2011

8th International Workshop

Strong Microwaves and Terahertz Waves: Sources and Applications

PROCEEDINGS



Nizhny Novgorod – St. Petersburg, Russia
July 9 – 16, 2011

Russian Academy of Sciences
Institute of Applied Physics

STRONG MICROWAVES AND TERAHERTZ WAVES: SOURCES AND APPLICATIONS

8th International Workshop

Nizhny Novgorod – St.-Petersburg, Russia
July 9 – 16, 2011

PROCEEDINGS

Nizhny Novgorod
2011

Workshop Chairman

Professor *A. G. Litvak*

Organized by

Institute of Applied Physics, Russian Academy of Sciences
GYCOM Ltd.
Novosibirsk State University

Sponsored by

Russian Academy of Sciences
Russian Foundation for Basic Research

All papers are printed as received

PLENARY

Microwave Plasma Assisted CVD Synthesis of Single Crystal Diamond at 180-300 Torr

Jes Asmussen[1,2], Y. Gu[1], and J. Lu[1]

[1]Michigan State University, East Lansing, MI 48824,USA, asmussen@egr.msu.edu
[2]Fraunhofer USA, Center for Coatings and Laser Applications, East Lansing, MI 48824, USA

Introduction

A new idea, first mentioned in [1], for a high efficient and potentially high power klystron is presented. It was triggered from the intention to use higher order modes and therefore larger cavities which would allow for either higher currents at equal current density or for higher frequencies with smaller beam port openings.

Instead of a round beam, like in standard klystrons, an annular cathode creates a hollow beam, which after compression and acceleration by the anode enters a bunching cavity, pill box type or coaxial. The cavity is driven by an azimuthally rotating higher order TM_{n10}-mode. Thus, the electrons are velocity modulated with a phase progressing in azimuthal direction. As a result, bunches placed along n interlaced corkscrew trajectories develop after the drift length. The output cavity is, as the input cavity, a round cavity operating in a circularly polarized TM_{n10}-mode.

A 30GHz tube, with two idler cavities, solenoid focusing and TM_{110}-mode multi-gap output cavity is simulated. With a beam voltage of 100 kV and a current of 1 A an output power of 36 kW could be reached. For higher modes and currents, electron efficiencies over 50% can be expected, keeping the same current density.

Input Cavity and Beam Formation

The input cavity is an annular ring cavity driven in an azimuthally rotating TM_{n10}-mode. Fig. 1 shows, for $n = 1$, the mode in the cavity and the development of a corkscrew modulated hollow beam in the drift space. Due to the annular arrangement and the higher order mode the beam area is larger then for a standard round beam. The radius of the hollow beam and the ratio of round to hollow beam area is given in the table for different mode numbers n at 30 GHz. Hereby the width of the annular ring was taken to be equal to the diameter of the round beam and an inner conductor with 2 mm diameter was assumed. The rapidly increasing area ratio allows for either higher currents at equal density or for smaller beam openings thus improving drastically the shunt impedance.

Idler cavities can be used, as in standard klystrons, to improve the bunching and increase gain and efficiency. The option to lower the current density at equal output power would also be advantageous since the plasma frequency becomes smaller and the drift space longer. Bunches stay together over a longer distance before they decohere. Extended output cavities are possible, which is essential to improve the efficiency at high frequencies.

TM_{n10} at 30 GHz	beam position radius in mm	area ratio A_0/A_n
0	0	1
1	3.5	46.7
2	5	66.7
3	6.8	90.7
4	8.6	114.7
5	10.4	138.7

Output Cavity

The output cavity is, as the input cavity, a round cavity with an annular beam port operating in a rotating TM_{n10}-mode excited by the corkscrew beam. It can be a single or multi gap cavity. For the latter a lower current density may be advantageous as mentioned above.

As an example, Fig. 2 shows the analytically calculated shunt impedance, i.e. the shunt impedance without beam port, of a coaxial 30GHz, TM_{n10}-mode, single gap cavity as a function of its inner conductor radius r_i. While for lower order modes, the impedance decreases strongly with increasing inner conductor r_i, this effect vanishes for higher order modes due to the small values of Bessel functions for small arguments and high orders. In view of the drop in shunt impedance, operating with higher order modes seems to be of no interest. On the other hand, a real cavity has a beam pipe and the impedance decays exponentially

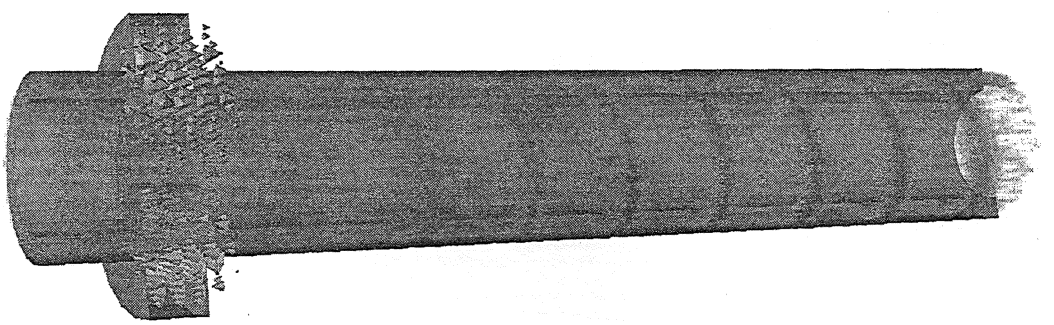

Fig. 1. Hollow beam modulated by a rotating TM_{110}-mode in a coaxial cavity

against the center of the opening. It is therefore important to keep the opening as small as possible in particular for high frequencies. This can be reached, at least partially, by decreasing the current density. In that way one may even overcompensate the loss in shunt impedance at higher modes. Alternatively, the beam current can be increased, resulting in an improved efficiency and higher output power as well.

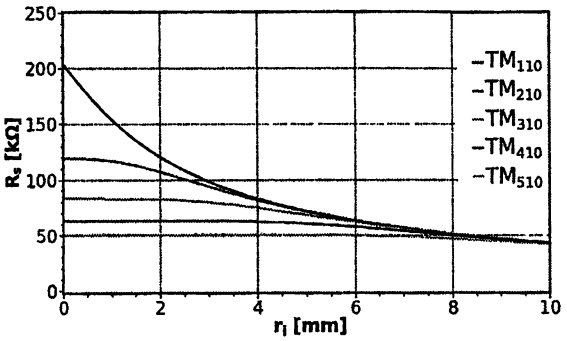

Fig. 2. Analytical shunt impedance over the inner conductor radius of a closed coaxial cavity for different mode numbers

For the special case of no inner conductor, the coaxial cavity becomes a pill box. Since an annular beam port is needed in order to achieve a decent shunt impedance, the central part of the cavity top and bottom cover has to be connected to the outer part by radial stems. This is important for the TM_{110} mode but not necessarily for higher modes because of the small dependence on the inner radius r_i for less than 2mm, s. Fig. 2. Nevertheless, this concept is also useful for higher modes. The stems can be extended through the whole beam tunnel, cutting it into sectors. Thus, the beam tunnel is kept under cut off, avoiding the TEM-mode and improving the mechanical stability. Then, however, the beam has to be generated by a sectional cathode in order to avoid electrons colliding with the stems. Corresponding simulation results can be found in [1].

Simulation Results

In order to evaluate the performance of the design, several simulations with the code GdfidL [2] have been performed. The beam voltage was assumed to be 100 kV and the current 1 A, 2 A and 3 A. Fig. 3 shows the simulation of a single gap 30 GHz coaxial output cavity, exited in the TM_{310} mode by 3 interlaced beams. The power extracted from the beam is 14,5 kW and remains the same for either a single or 3 interlaced beams with a total dc current of 1 A. Comparing this to 23.7 kW extracted by a single gap TM_{110} cavity, driven by a 1A beam, the result may be disappointing. However, since the current density in case of 3 beams in the TM_{310} cavity is 3.9 times less, it seems to be appropriate to decrease the beam port width or increase the beam current. Doing so and exiting the TM_{310} mode by 3 interlaced beams with a total dc current of 3 A yields a power of 100.35 kW in a single gap cavity. Fig. 4 shows the normalized velocity of the beam, as simulated by GdfidL. Ideal modulated beams have been used for a better comparison of different structures. This explains the tiny velocity spread of the spent beam. The results of simulations with 3 interlaced beams of 1 A and 3 A show an increase in efficiency from 14.5% to 30%.

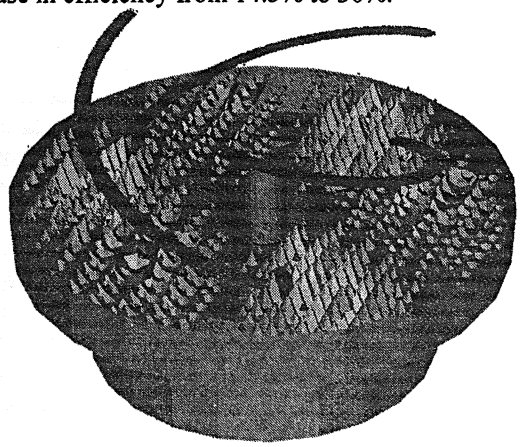

Fig. 3. Three interlaced beams entering a TM_{310}-mode output cavity

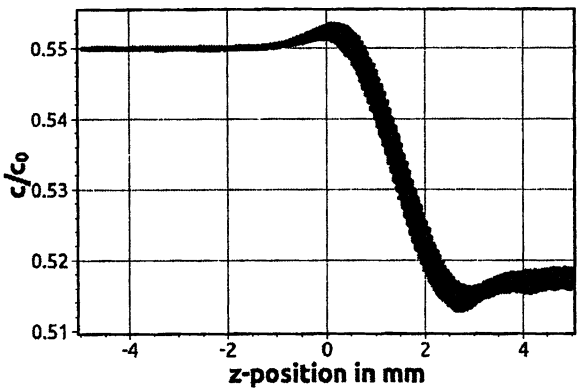

Fig. 4. Normalized velocity of 3 ideal modulated interlaced beams, decelerated by the TM_{310}-mode of a coaxial single gap cavity (0-2.8mm)

In earlier simulations 45 kW were extracted from a 100 kV, 1A beam by a 6-gap TM_{110} cavity. Using a coupling factor of 1:4 this resulted in 36 kW output power. Therefore, we are optimistic that an extended cavity driven in a TM_{310} or TM_{510} mode with a current of 3 A or 5 A, respectively, pushes the over all efficiency above 50%.

References

1. Grede, A., Henke, H. Concepts for circular defection modulated tubes and frequency multiplying millimeter wave sources //Proceedings of 2009 IEEE Int. Vac. Electr. Conf., Rome, 28-30 April 2009. P. 552-553.

2. *W. Bruns.* http://www.gdfidl.de

Hybrid Reactors – Prospects of Development and Application

E. A. Azizov

Institute of Tokamak Physics, NRC "Kurchatov Institute"

Practical application of the large-scale amount of knowledge accumulated over the past 60 years in the field of controlled fusion (CF) is now an urgent requirement of public in technologically advanced countries. Period of development of industrial fusion power, calculated up to 2050, seems too high, as take life by more than one generation. The fact that during this time scientists and engineers have to solve a huge number of scientific and technical problems the public is very weak informed. Among these problems, the achievement of steady-state controlled burning fusion plasma in a tokamak or stellarator, very high rates of energy gain in a laser or a pinch of CF in the modes with the required repetition rate of production of fission fuel and target technologies, materials with unique properties and so on.

At the same time much of the world and Russian fusion community believe that the accumulated scientific and technological capacity in CF is sufficient for the first fundamental step towards the practical use of the power of nuclear fusion reactions in the so-called hybrid (fusion-fission) reactors. Such reactors are needed to solve some fundamental problems of fission power, materials testing, parts and components of "pure" fusion reactors, as well as for fundamental research.

The basis of the hybrid reactor is a source of fusion neutrons (FNS) based on the tokamak, stellarator, a powerful multi-channel laser or multi-megawatt micropinches.

In the case of tokamak FNS is necessary to develop the installation, which would allow to generate flows of 14 MeV neutrons with an average power of 10-100 MW in steady-state mode or repetitive pulses. For the FNS based on lasers or heavy-duty micropinches necessary to ensure high reliability of periodic operation with high repetition rate and target systems with high efficiency.

Parameters of the demonstration and pilot FNS based on a steady-state tokamak with additional heating systems and control processes in a plasma with a high neutron yield (10-100 MW) were analyzed. The characteristics and scenarios of the physical prototype of tokamak based FNS were summarized.

Prospects for hybrid systems with a tokamak based FNS are compared with the prospects of effective hybrid systems use a multi-channel ultrapowerful lasers or micro-pinches with D-T targets, generating neutron flux due to fast compression by direct laser irradiation or pinch-effect, or due to homogeneous irradiation of soft X-rays, as the result of laser radiation and micro-pinch power convertion. For FNS tokamaks, also for laser or pinch FNS during their practical use for fusion power is estimated to be 10-15 years.

Megawatt Class Gyrotron Development at CPI

M. Blank, P. Borchard, P. Cahalan, S. Cauffman, K. Felch

CPI, Palo Alto, CA, USA, monica.blank@cpii.com

Several megawatt-class gyrotron oscillators in the 95 GHz – 170 GHz frequency range are currently under development at CPI.

A 95 GHz gyrotron capable of generating CW power levels in excess of 2 MW is currently being tested at CPI. [1] The gyrotron employs a single-anode electron gun that produces a 90-kV, 75-A electron beam for interaction with the $TE_{22,6,1}$ cavity mode. Output power from the cavity is transformed into a fundamental Gaussian beam using an internal converter that consists of a waveguide launcher and three focusing and phase-correcting mirrors. The Gaussian beam exits the tube through a chemical-vapor-deposition (CVD) diamond window. The spent electron beam is dissipated in a 40.6-cm diameter collector fabricated from a strengthened copper alloy. The collector nominally operates at a voltage of 61 kV relative to the cathode potential to minimize the amount of power absorbed in the collector and to improve efficiency.]

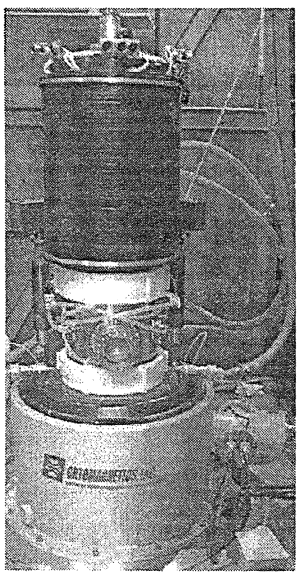

Fig. 1. Photograph of the 95 GHz oscillator installed in the test stand at CPI

A photograph of the 95 GHz gyrotron installed in the test stand is shown in Fig. 1. In recent tests on the gyrotron an output power of 1.92 MW was achieved with 40% efficiency at the nominal beam current of 75 A. Figure 2 shows the measured peak output power (circles) and efficiency (squares) as functions of cathode voltage for 75 A beam current and 27 kV body-to-ground voltage (or 27 kV collector depression). In Fig. 3, the peak output power (circles) and efficiency (squares) as functions of cathode voltage for 90 kV total accelerating voltage are plotted. As shown in Fig. 3, the peak output power remains nearly constant and efficiency, therefore, increases for cathode voltages as low at 61 kV, corresponding to 29 kV collector depression. Beyond 29 kV depression, output power and efficiency degrade.

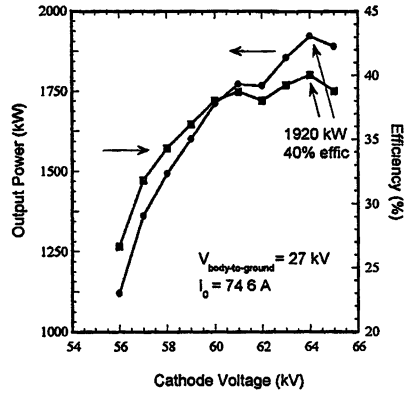

Fig. 2. Measured peak output power (circles) and efficiency (squares) as functions of cathode voltage for 75 A beam current and 27 kV body-to-ground voltage (or 27 kV collector depression)

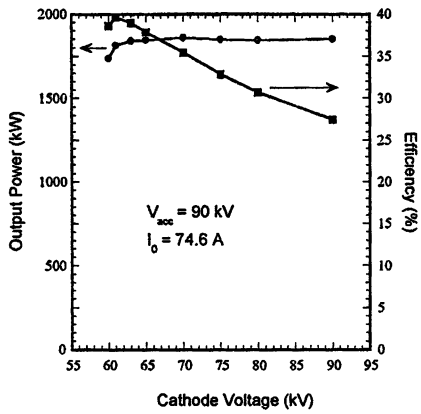

Fig. 3. Measured peak output power (circles) and efficiency (squares) as functions of cathode voltage for 90 kV total accelerating voltage

During the tests, a significant reduction in the amount of power absorbed in the beam tunnel compared with earlier versions of the tube was noted. The reduction in beam tunnel power is attributed to the use of a modified beam tunnel design to reduce the possibility of parasitic oscillations. [2]

Additional results of the recent tests and future plans will be presented.

In addition, the fabrication and test status for two other gyrotrons oscillators (1 MW at 170 GHz and 1.2 MW at 110 GHz) will be described.

References

1. Work supported by AFRL's Directed Energy Directorate contract number FA9451-04-C-0298.

2. *G. Gantenbein et al.* Experimental investigations and analysis of parasitic RF oscillations in high-power gyrotrons // IEEE Trans. Plasma Sci. 2010. V. 38, No. 6. P. 1168-1177.

Terahertz Electron Sources for EPR and DNP/NMR Spectroscopy

V.L. Bratman, A.E. Fedotov, and Yu.K. Kalynov

Institute of Applied Physics, Russian Academy of Sciences, Nizhny Novgorod, Russia
bratman@appl.sci-nnov.ru

Significant enhancement of magnetic fields has allowed in recent years transformation of magnetic resonance spectroscopy as an extremely informative tool for a study of the structure and dynamics of condensed media at the molecular level. Further progress in this direction is associated with increasing the sensitivity by orders of magnitude using sources of fairly powerful radiation with frequencies saturating the Electron Paramagnetic Resonance (EPR) transitions [1, 2]. In the case of Nuclear Magnetic Resonance (NMR) spectroscopy, such an increase in sensitivity is achieved due to the polarization transfer from the electronic subsystem to the nuclear subsystem (Dynamic Nuclear Polarization, DNP) which increases many times the response to resonant RF irradiation. Application of DNP allows one to distinguish very weak spectral lines, as well as to reduce dramatically (up to hundreds of times) the duration of experiments.

For modern NMR spectrometers with magnetic fields of 9.3-18.6 T, the irradiation frequencies and required powers in CW generation regime usually lie in the ranges 0.26-0.52 THz and 1-100 W, respectively. In fact, for the case where a small sample is placed in a special terahertz cavity combined with a spectrometer RF probe, CW power should not exceed a fraction of a watt. On the other hand, for some scenarios the required irradiation can also be provided by a sequence of very powerful and coherent short pulses.

In principle, stronger constant magnetic fields up to 35 T that are produced now in resistive and hybrid magnets could be also used for EPR and NMR spectroscopy, and correspondingly sources with frequencies of up to 1 THz may be needed for these applications in the nearest future.

At present, the terahertz radiation with required power is basically provided by conventional gyrotrons with poly-axial electron beams operated at the fundamental and second cyclotron harmonics. Several NMR spectrometers are already equipped with such gyrotrons having frequencies 0.26 - 0.46 THz. It should be noted that the conventional gyrotrons require quite a strong operating magnetic field approximately equal to the field in the spectrometer or half of this value for fundamental- or second-harmonic gyrotrons, respectively. Although the cost of such gyrotrons is many times lower than the cost of the spectrometers, and the effect achieved with their help greatly increases efficiency and simplifies measurements, this fact still markedly restricts the use of the DNP. Therefore, search for simpler sources or new methods for terahertz irradiation is a very important problem. Alternative sources of terahertz radiation with moderate continuous (average) power can be gyrotrons operated at higher cyclotron harmonics as well as several varieties of low-voltage generators with rectilinear electron beams, which will be discussed in this presentation.

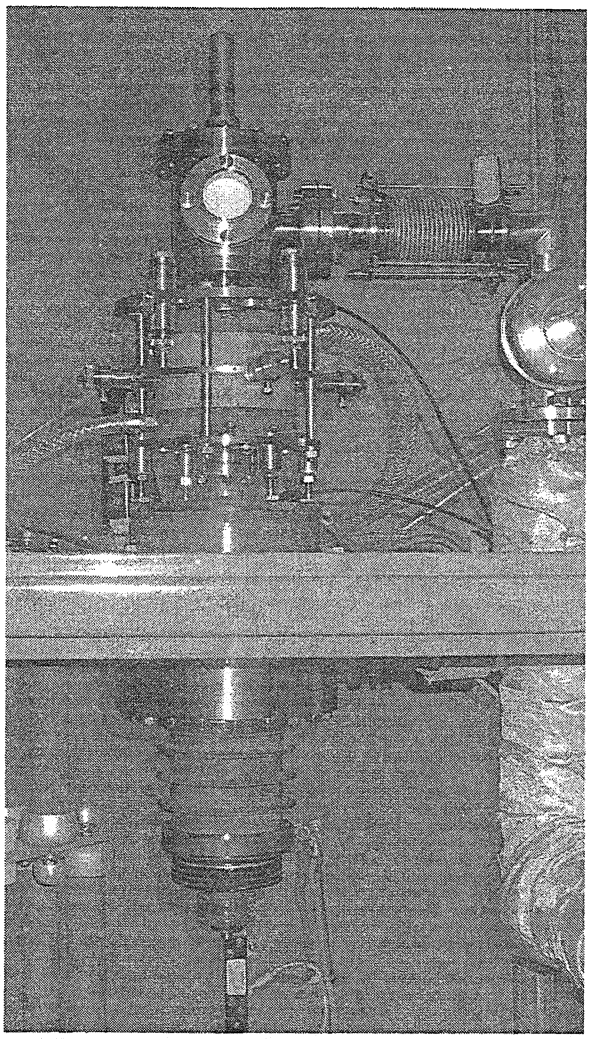

Fig. 1. Third-harmonic Large-Orbit Gyrotron with a radiation frequency of 1 THz and a power of 0.4 kW in 10-μs pulses [3].

The most difficult problem in the implementation of high-harmonic gyrotrons is discrimination of parasitic modes. It is well known that the solution of this problem is considerably simplified in the large-orbit gyrotrons (LOGs), where mono-axial electron beams are used instead of the poly-axial ones. Powerful pulsed generation at the third cyclotron harmonic with a frequency of up to 1 THz has already been successfully obtained in this way [3]. It is important to note that the electron-optical system developed in that LOG, namely a gun with a sharp reverse (cusp) of the magnetic field in the cathode-anode gap and the next region of gradual, thousands- of-times increase in the field along the axial coordinate, proved to be quite efficient and simple to operate in a wide range of

main parameters. Such a gun can presumably be employed in LOGs working in CW regime as well. In this case, a LOG has an important property that by using the same electron-optical system and slightly different resonator units, one can operate at different cyclotron harmonics and block the entire frequency range, which is interesting nowadays for EPR and DNP/NMR spectroscopy. According to calculations, the use of a nearly mono-axial electron beam with a voltage of 15 kV and a current of 0.3 A for a relatively low operating magnetic field of 3 to 6 T permits generation in the frequency range 0.26-0.52 THz with a sufficient output power of 10-50 W in CW regime in a LOG operated at the second and third cyclotron harmonics. Using a two times stronger magnetic field and a higher voltage, one can obtain in a similar oscillator at least 100 W in CW regime at frequencies of up to 1 THz. The experimental realization of similar CW terahertz LOGs will be started soon at the Institute of Applied Physics (see the presentation by Yu.K. Kalynov et al. in this book).

Along with the gyrotrons, several varieties of devices based on stimulated Cherenkov, transition, and Smith-Purcell radiation of electrons can be developed for the versions of DNP methods which require a relatively small continuous (average) power. In particular, modified versions of backward-wave oscillators (e.g., clinotrons) and Extended Interaction Klystrons, as well as orotrons (or Diffraction Radiation Generators) can claim this role. It is important that relatively weak magnetic fields generated by permanent magnets are required for the realization of all these terahertz devices.

Pulsed terahertz orotrons have been developed at the Institute of Applied Physics in collaboration with VNIIFTRI. The highest radiation frequencies of these oscillators already exceed 0.4 THz at an output power of the order of 100 mW and pulse durations from tens of nanoseconds to tens of milliseconds (see the Table and Fig. 2). Improving the technology for fabrication of orotron periodic systems should allow an at least twofold decrease in the operating periods and the achievement of frequencies up to 0.8-1.0 THz. Simultaneously, this will decrease the operating currents and will permit operation in long-pulse and CW regimes.

Table. Parameters of pulsed high-frequency orotrons

Structure period (μm)	140	100	82
Frequency (GHz)	100-300	260-370	170-410
Power (mW)	500-100	70-30	200-50

Powerful sources capable of generating coherent pulsed sequences in the pump-probe EPR methods and in DNP/NMR spectroscopy can be developed on the basis of gyro- and oro-multipliers driven by relatively low-frequency and low-power signals. The principle of operation of such devices is similar to that for the ordinary two-cavity klystrons. It is important that the drift section in gyro-multipliers with nearly mono-axial electron beams can be cutoff for the operating modes. This provides very strong separation of the cavities operated at different cyclotron harmonics and permits very effective particle bunching and obtaining a high output power. All the discussed sources look attractive alternatives to conventional gyrotrons in EPR and NMR studies.

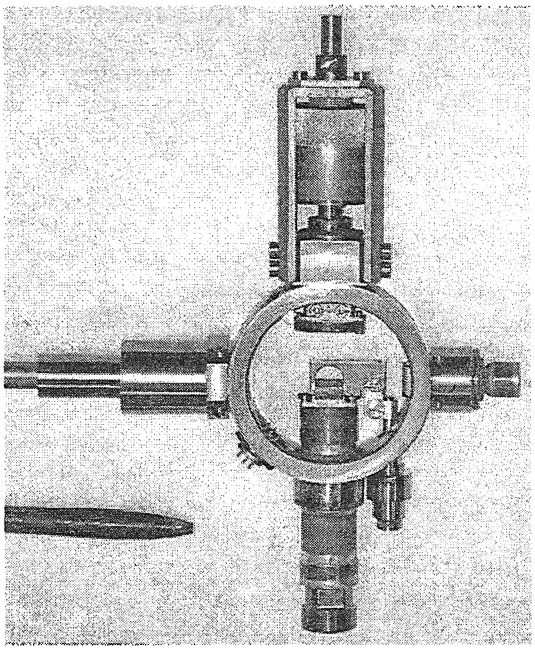

Fig. 2. Orotron with a frequency band of 0.14 - 0.41 THz (permanent magnet is not shown) [2].

This work was supported by the Russian Foundation for Basic Research (project Nos. 09-02-00637, 09-08-00457), and by the Presidium of the Russian Academy of Sciences (Program "Problems of physical electronics, charged particle beams and generation of electromagnetic radiation in high-power systems").

References

1. *Maly, T., Debelouchina, G.T., Bajaj, V.S., Hu K-N., Joo C.-G., Mak-Jurkauskas, M.L., Sirigiri J.R., van der Well P.C.A., Herzfeld, J., Temkin R.G., and Griffin, R.G.* Dynamic nuclear polarization at high magnetic fields // J. Chem. Phys. 2008. V. 128. P. 052211.

2. *Prisner, T.F., Griffin, R.G.* Perspectives of high-field dynamic nuclear polarization (DNP) // *NMR in Mechanistic Systems Biology, an output of EC-funded Coordination Action NMR-Life.* 2006-2009. P. 74-81.

3. *Bratman, V.L., Kalynov, Yu.K., and Manuilov, V.N.* Large-orbit gyrotron operation in the Terahertz frequency range // Phys. Rev. Lett. 2009. V. 102. P. 245101.

4. *Bratman, V.L, Dumesh, B.S., Fedotov, A.E., Makhalov, P.B., Movshevich, B.Z., Rusin, F.S.* Terahertz orotrons and oromultipliers // IEEE Trans. PS 2010, V. 39. P. 1466.

Interaction of THz Waves with Metals and Related Devices

J.-L. Coutaz[1], F. Garet[1], M. Nazarov[2], A. Shkurinov[2],
M. Sypek[3], E. Lheurette[4], and D. Lippens[4]

[1] IMEP-LAHC, UMR CNRS 5130, University of Savoie, 73376 Le Bourget du Lac Cedex, France, coutaz@univ-savoie.fr
[2] Department of Physics, M. V. Lomonosov Moscow State University, Russia
[3] Faculty of Physics, Warsaw University of Technology, and Orteh Sp. z o.o., Warsaw, Poland
[4] IEMN, UMR CNRS 8520, University of Lille 1, BP 60069, 59652 Villeneuve d'Ascq Cedex, France

The THz domain is usually described as the frequency range spreading approximately from 100 GHz up to 10 THz. But it may be also defined as the spectral region where the contributions of the conduction and displacement currents to the electromagnetic response of matter are in the same order of magnitude. This differs strongly from optics, for which only the displacement current and thus the related refractive index are important, and from microwaves, where most of the devices are based on or are included in electric/electronic circuits. It explains why devices and systems for manipulating THz beams could be made with dielectric materials, or with metals, or with both. As an example, we address in this paper some relevant topics concerning the interaction of THz waves with metals, and we describe some metallic devices allowing us to deviate or focus THz beams.

THz electromagnetic response of metals

Because the plasma frequency ω_p of pure metals is within the near UV range, and because intraband transitions involve slightly weaker energies, the electromagnetic response of metals in the THz domain is well described by the classical Drude model:

$$\varepsilon = \varepsilon_\infty - \frac{\omega_p^2}{\omega(\omega + j\Gamma)} \approx -\frac{\omega_p^2}{\omega(\omega + j\Gamma)}, \qquad (1)$$

where ω is the pulsation, Γ the damping pulsation, and ε_∞ the dielectric constant at higher frequencies. For example, $\omega_p = 2\pi \times 3570$ and $\Gamma = 2\pi \times 19.7$ THz for aluminum, leading to $\varepsilon \approx (-5+j40)\times 10^4$ at 1.5 THz [1]. It means that, for most of applications, metals in the THz domain may be considered as ideal conductors. Nevertheless, this is not the case when evanescent waves at the metal surface are involved in the studied phenomena. Indeed, such waves penetrate slightly in the metal, which is forbidden when the conductivity tends to infinity.

Determining ε in the far infrared, for example from reflectivity or ellipsometry measurements, is a difficult task due to the anticipated huge ε value. It is easier in transmission spectroscopy, but the response of the necessary very thin films differs from the bulk response [2]. It could indirectly be determined from surface plasmon (SP) experiment. However, the so-achieved values of ε show a large discrepancy with the Drude model. Typically, the losses (or resistivity) are two orders of magnitude larger than expected as reported by several groups [3]. This leads to a reduced SP propagation length over noble metals, and simultaneously to a smaller extension of the SP field in air. The possible explanations for such a discrepancy are linked to a larger density of defects in the skin depth region or to the presence of an oxidation layer at the metal surface [4]. We think [3] that the short SP propagation length results from the coupling between the SP and a quasi-plane wave propagating parallel to the metal surface. Indeed, in the THz range, the effective index of the SP wave is close to 1, and consequently the SP field map in air is very similar to a plane wave. Thus any perturbation, even at the microscopic scale, can lead to an exchange of energy between the 2 waves, and thus to the SP leaky behavior.

Towards negative-index metallic metamaterials

The high dielectric constant of metals may be decreased by designing sub-wavelength reliefs or details at the metal surface or in the metal film. As well, the SP velocity over such samples is strongly reduced. Such SPs are known as *spoof* SP. This could be also observed when SPs propagate over a periodically structured surface, like a diffraction grating, at the border of the Brillouin zones. Fig. 1 shows the SP effective index we determined from the SP reflection over an aluminum grating (period 0.3 mm) recorded in a Bragg geometry [3].

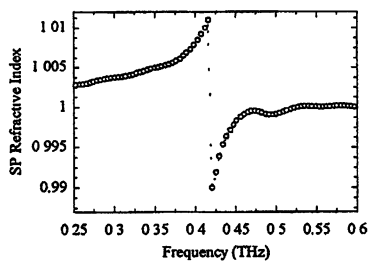

Fig. 1. Effective index of a THz SP propagating over a metallic grating in the vicinity of the border of the first Brillouin zone. The data are determined from the results of a Bragg reflection experiment.

Another way to reduce the dielectric constant of metallic samples is to design a metamaterial geometry with sub-wavelength cells. It is well known that such structures may even exhibit a negative refractive index (left-handed materials), provided the material shows simultaneously electric and magnetic resonances, which leads to negative permittivity and permeability. Usually, i.e. mostly in the microwaves domain, this is achieved by designing a device including both dipolar and loop structures. In the THz range, it is certainly easier to fabricate stacks of arrays of holes drilled in metal films, which exhibit a left-handed

character even if enlighten under normal incidence. The magnetic resonance arises from the inter-stack coupling of the currents flowing around each hole. We have manufactured and characterized such metamaterials, with elliptically-shaped holes to ensure a larger THz transmission [5]. Moreover, we have definitively demonstrated the left-handed property of the samples by performing a refractive experiment with a prism made with the metamaterials. For a given frequency band, the THz beam is deflected with a negative angle as regards to the right handed case [6].

2D-Optics with THz surface plasmons

Even if propagating over distances (tens of centimeters) shorter than expected, SP are still very interesting as a means to carry a THz signal or information over a metal surface, on which 2D quasi-optical elements may be designed to focus, split or reflect the SP THz beam. For example, we have designed diffraction gratings with elliptically shaped grooves, which couple an incident plane wave to a SP and focus the SP over the metal surface. More recently, we have observed efficient in-plane Bragg reflection and transmission of SP at a diffraction grating. Thanks to the potential of THz time-domain spectroscopy, we have analyzed in details the Bragg phenomenon, observing the THz signal reflection at each grating groove (Fig. 2 [7]).

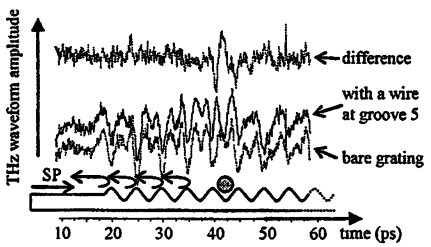

Fig. 2. SP temporal waveforms reflected by a diffraction grating. When a groove is filled with a wire, the THz signal reflected at this defect is seen in the difference signal.

3D-Optics with metallic diffractive components

As explained previously, metallic devices may constitute effective optical components to manipulate THz beams propagating in free space. It is known for years that sub-wavelength metal meshes are excellent polarizers for the far infrared. Binary-type (i.e. made of opaque and transparent zones) metal Fresnel lenses may also be substituted to refractive lenses with complementary or even better properties in some cases. Here we show that such metal diffractive lenses can be designed for focusing of axis a THz signal delivered by a scene in a passive imaging system, which is difficult to realize with refractive optics, because of the large and thick requested lens size, or with reflective optics, because of geometrical aberrations. The device is made of the composition of 2 Fresnel lenses (see pictures in Fig. 4) that ensure respectively the focusing and the deflection of the THz beam. Fig. 3 shows the recorded THz beam map near the focus (focal distance 70 mm, deviation angle 45° from the optical axis) [8].

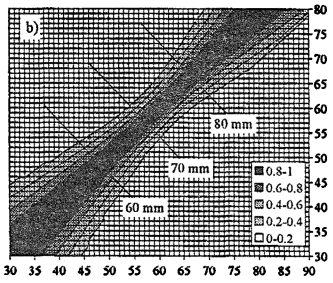

Fig. 3. Contour map of the THz beam amplitude at 0.5 THz extrapolated from the measurement of the beam parameters assuming the beam shape is Gaussian. The center of the device lies at $(x,z) = (0,0)$.

The focusing effect is a pure diffraction phenomenon that is observed in the over-wavelength regime. When the response of the same device is studied in the sub-wavelength regime, the directly transmitted beam is not diffracted (it corresponds to the zero order of diffraction), but it deflected as shown on Fig. 4 (full circles) [9]. We attribute this deflection to the slightly varying periodicity of the structure as seen in the photograph below. The effect is similar to the one of a gradient of the effective index of the structure. For a similar device with a constant periodicity, no deflection of the THz beam is observed (open triangles in Fig. 4).

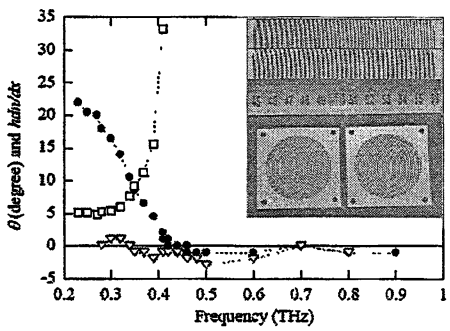

Fig. 4. Angle of deflection versus frequency of the THz beam directly transmitted by the diffractive lens. Full circles and open triangles are respectively for the structures with a varying periodicity (upper photograph) and a constant periodicity.

References

1. A. D. Rakic, Appl. Opt. **34**, 4755 (1995).

2. F. Garet, L. Duvillaret, and J.-L. Coutaz, *THz time-domain spectroscopy of nanometric-thick gold layers*, 29th IRMMW Conference, Karlsruhe, Germany (2004).

3. see references in M. Nazarov, and J.-L. Coutaz, *Terahertz surface waves propagating on metals with sub-wavelength structure and grating reliefs*, to appear in J. Infrared Milli. Terahz. Waves (2011).

4. N. Laman, and D. Grischkowsky, Appl. Phys. Lett. **90**, 122115 (2007); M. Gong, Tae-In Jeon and D. Grischkowsky, Opt. Express **17**, 17088 (2009).

5. S. Wang, *et al.*, Appl. Phys. Lett. **97**, 181902 (2010).

6. Ch. Croënne, *et al.*, Appl. Phys. Lett. **94**, 133112 (2009).

7. M. Nazarov, A. Shkurinov, and J.-L. Coutaz, *Bragg reflection of THz surface plasmon propagating over a diffraction grating*, submitted to IRMMW 2011.

8. A. Siemion *et al.*, Opt. Lett. 36, 1960 (2011).

9. E. Hérault *et al.*, J. Infrared Milli. Terahz. Waves **32**, 402 (2011).

Trends in High-Power Gyrotron Development

A.G. Litvak[1], G.G. Denisov[1], V.E. Zapevalov[1], V.E. Myasnikov[2], E.V. Sokolov[2], E.M. Tai[2], V.I. Ilin[3]

[1] Institute of Applied Physics Russian Academy of Sciences, 46 Ulyanov Street, Nizhny Novgorod, 603950, Russia
[2] GYCOM Ltd., 46 Ulyanov Street, Nizhny Novgorod, 603155, Russia,
[3] Kurchatov Institute, Kurchatov Square 1, Moscow, 123182, Russia

Introduction

Gyrotrons are the most powerful sources of millimetre wavelength radiation [1-5]. They are widely used in electro-cyclotron-wave systems of plasma fusion installations (e.g see [6, 7]). For the next generation of fusion installations gyrotrons with unit power at least 1 MW in CW regime are required. The present paper continues in the frames of SMP Conference proceedings [8] to monitor main achievements and general tendencies in MW-power gyrotron development. Additional emphasis is done to the gyrotron development in Russia.

First experiments with gyrotrons were done in 1964 [1-3]. In 70-s gyrotrons already were doing very well - we can mention here only two achievements: 28GHz/100kW/CW and 100GHz/1MW/100mks. The first application of gyrotrons for plasma fusion setups TM-3 and TUMAN-2 took place. In 80-s many scientific and industrial institutions worked on development of gyrotrons. Lots of scientific and technological tasks were solved at that time. Even nowadays young gyrotron researchers very often surprised that their "new" ideas were already published in 80-s. Real fruitful collaboration and simultaneously strong competition of the main gyrotron developers began in 90-s with start of ITER activity and wide use of gyrotrons at plasma installations. The requirement of 1MW/CW gyrotron operated at very high frequency (above 100GHz) was issued.

In the similar review papers of the previous conferences four first periods of "modern gyrotron history" in MW gyrotron development were discussed. In the period of 1995-1999 the following principal steps were made:

- efficient gyrotron operation was shown at very high-order modes. This solves the problem of cavity thermal loading.
- demonstration of a depressed collector in gyrotrons. This gave a great move in solving collector and power supply problems.
- gyrotron windows made of artificial diamond discs were developed. Such a window is still the only option for long-pulse megawatt tubes.

The achievements in the next period 1999-2002 were also very bright:

- demonstration of very long-pulse (hundreds seconds) operation of MW tubes equipped by diamond windows and depressed collectors.
- tests of short-pulse prototypes for multi-frequency and 1.5-2MW gyrotrons
- integration of MW gyrotron complexes at major fusion installations.

The period 2002-2005 showed:

- demonstration of CW operation of megawatt power gyrotrons,
- first tests of multi-frequency tubes,
- demonstration of very high gyrotron efficiency.

The important achievements of the period 2005-2008 are:

- Long pulse operation of 170 GHz gyrotrons for ITER at 1 MW power with efficiency exceeding 50%,
- First experiments on fast directional switching gyrotron wavebeams.

The present paper discusses the latest events between since last SPM Conferences – 2008-2011) in gyrotron development and progress trends of the development. The highlights of the period are:

- Demonstration of ITER required gyrotron parameters. Reliability tests of the gyrotrons;
- Experiments on fast modulation of megawatt power gyrotrons;
- Studies on multi-frequency and 1.5-2 MW gyrotron prototypes.

Demonstration of ITER required gyrotron parameters. Reliability tests of the gyrotrons

Requirements to ITER gyrotrons were formulated firstly in 2001. According to that requirements the 170 GHz gyrotrons are to provide at least 1 MW power in pulse of 400 seconds with efficiency exceeding 50%. In later years, the requirements to ITER gyrotrons were made more strict (pulse duration up to 3600 seconds) though the tokamak operation in the first 5 years probably will not require pulses longer than 400 s. Two teams developing gyrotron – Japanese and Russian ones – demonstrated gyrotron operation at 1 MW power in pulses exceeding 400 seconds with efficiency of 53-56%. It is important to note that two fabricated in 2009 and 2010 Russian gyrotrons showed very similar performance.

Reliability tests of the ITER gyrotron prototypes began. So in [7] it was demonstrated that using the ITER Japanese gyrotron prototype, repetitive operation with long pulse and high power was conducted. The operation with the set parameters as 800 kW/600 s with 20 min interval was performed at JAEA. Seventy two shorts of 88 ones were successfully continued to the end of the pulse. Detailed analysis of the

stop origins was done. The dominant interlocks are over current protection and arcing inside the gyrotron.

Similar reliability tests were done in Kurchatov institute with Russian gyrotron prototype. In series of 30 pulses with the same parameters only three pulses ended earlier than at the set time.

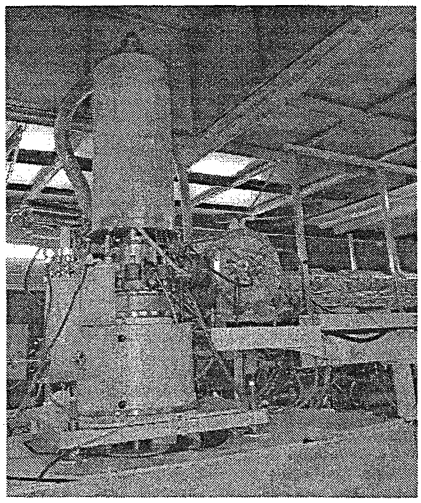

Fig. 1. Russian ITER gyrotron prototype in the test bench.

The results present usable reliability of gyrotrons for ITER. They also show there is a room for further development towards highly reliable gyrotron system.

Experiments of fast modulation of megawatt power gyrotrons

It was shown in modeling experiments that for ITER operation the gyrotrons can be effectively used to suppress NTM plasma instabilities. The suppression is more effective when the microwave radiation is modulated with a corresponding plasma island rotation time in the scale of milliseconds. Consequently ITER formulated a requirement to gyrotron output power modulation up to 1 kHz by a cathode voltage and up to 5 kHz by low current body or anode power supply. Such a modulation was successfully demonstrated with a 170 GHz gyrotron at megawatt power by Japanese team.

Studies on multi-frequency and 1.5-2 MW gyrotron prototypes

A gyrotron capable to operate at several frequencies is very attractive for plasma experiments. The use of step-tunable gyrotrons can greatly enhance flexibility and performance of ECRH/ECCD systems due to larger accessible radial range, possible replacement of steerable antennas, higher CD efficiency for NTM stabilization. Even two-frequency gyrotrons can bring real improvements of the system.

The main problems in development of multi-frequency gyrotrons are to provide: efficient gyrotron operation at different modes, efficient conversion of different modes into a Gaussian beam, reliable operation of broadband or tuneable window. Considering this three key problems one can say that first two of them are solved. Efficient gyrotron operation at several frequencies was demonstrated in many experiments. New synthesis methods allow design of efficient mode converters for multi-frequency gyrotrons. However realization of a CVD diamond window for a megawatt power level multi-frequency gyrotron met some real difficulties. Now several window concepts are under intensive study: Brewster-angle window, window with matched surfaces, double-disc resonant window, and travelling-wave tunable window. Hopefully the window problem will be solved soon.

There are two lines in development of gyrotrons with enhanced power: to advance conventional-type gyrotrons with cylindrical cavities and to develop more complicated gyrotrons with coaxial cavities. The main effort in the development of the coaxial tube is carried out by EU team. Many encouraging results (power about 2 MW in 1 ms pulses) have been obtained in short pulse experiments with a coaxial tube [7] though there are some open questions. IAP/GYCOM and JAEA/Toshiba study a possibility to use a higher order mode in a gyrotron conventional cavity. In particular in 2008/2010 two short-pulse (100 μs and 100 ms) gyrotron models operating with TE28.12 mode were tested at IAP/GYCOM. The models showed a very robust operation (microwave power up 2 MW with electronic efficiency of 34 %) at relatively high electron energies necessary to achieve the high goal power.

Conclusion

The achievements in gyrotron development are impressive and give hope of their successful use in future plasma fusion installations.

References

1. *A.V.Gaponov et al.* Induced synchrotron radiation of electrons in cavity resonators. Pis'ma ZhETF, 1965, 15, 430-435 (JETP Lett., 15, 2267-269).

2. *Gaponov A.V. et al.* Powerful millimeter-wave gyrotrons. // Int. J. of Electronics, 1981, v.51, No.4, pp. 277-302.

3. *G.Nusonovich.* Introduction to the Physics of Gyrotrons. The Johns Hopkins Univ. Press, 2004.

4. *K.L.Felch et al.* Characteristics and Applications of Fast-Wave Gyro-devices. Proceedings of IEEE, 1999, vol..87, No.5, pp.752-781.

5. *M.Thumm.* State-of-the-Art of High power Gyro-Devices and Free Electron Masers. Update 2010. Forschungcentrum Karlsruhe, Germany, 2011.

6. Special Issue; ECRH Physics and Technology for ITER. Nuclear Fusion, V.48, # 5, May 2008.

7. Special Issue: High-Power gyrotrons and their Applications. Journal of Infrared, Millimeter, and Terahertz Waves. V.32, Issue 3, March 2011.

8. *G.G.Denisov et al.* Megawatt gyrotrons for fusion research. State of the art and trends of development. Proc. of Int. Workshop "Strong Microwaves in Plasmas", Nizhny Novgorod. 2000, pp.967-986; 2003, pp. 29-45; 2006, pp. 62-75; 2009, pp. 15-26

ECRH with Advanced CW Systems

V. Erckmann[1], W. Kasparek[2], M.I. Petelin[3], A. Bruschi[4], W. Bin[4], H. Braune[1], R. van den Braber[5], N. Doelman[5], G. Gantenbein[6], H. P. Laqua[1], C. Lechte[2], L.Lubiako[3], N. B. Marushchenko[1], G. Michel[1], B. Plaum[2], M. Thumm[6], and the W7-X ECRH- teams at IPP Greifswald[1], IPF Stuttgart[2], and KIT[6]

[1]Max-Planck-Institut für Plasmaphysik (IPP), EURATOM-Association, D-17491 Greifswald, Germany
[2]Institut für Plasmaforschung, Universität Stuttgart, Pfaffenwaldring 31, D-70569 Stuttgart, Germany
[3]Institute of Applied Physics, RAS, 603950 Nizhny Novgorod, Russia
[4]Istituto di Fisica del Plasma, EURATOM-ENEA-CNR Association, I-20125 Milano, Italy
[5]Dept. of Mechatronic Equipment, TNO Science and Industry, NL-2600 Delft, The Netherlands
[6]Karlsruher Institut für Technologie, IHM, Association EURATOM-KIT, D-76021 Karlsruhe, Germany

Electron Cyclotron Resonance Heating (ECRH) and Current Drive (CD) play a key role in todays and future large-scale fusion devices [1]. Advanced ECRH systems must comply with various physics demands such as controlled plasma start-up from the neutral gas, steady state plasma stability control, impurity control, and performance optimization by plasma profile shaping. New fields of applications are still being discovered. The request for many different sophisticated applications, some of them are vital for steady state plasma control, and the increasing power demand results in a growing complexity of the systems. This is in conflict with the request for high Reliability, Availability, Maintainability, and Inspectability (RAMI), which arise from DEMO demands. 'Advanced' ECRH-components must therefore comply with both the complex physics demands and the requirement of operational robustness and reliability. The W7-X ECRH system is the first CW-facility of an ITER relevant size and is extensively used as a test bed for the investigation of innovative CW compatible components.

Gyrotrons operating in the 1 MW, CW range at relevant frequencies of 140 (W7-X) -170 (ITER) GHz have become state of the art [2, 3, 4]. They are, however, still in the prototype state and additional effort is required to arrive at a RAMI compliant design and robust series production. The transition from prototype achievements with the W7-X gyrotrons, where in general the performance was pushed to the very limits, to reproducible series production of units with high reliability and availability is a process with a comparable time scale as the prototype R&D itself [5]. The first series tube, which was delivered in 2005, met the specified parameters. The next series gyrotrons, which were based on the same design, failed to meet the full specifications and the phase from prototypes to industrial reproduction was characterized by an ongoing R&D since 2005 leading to significant improvements of several components: One critical component limiting the performance of the TED gyrotrons for W7-X is the collector. The strong power peaking at the turning points of the applied Vertical Field Sweeping (VFS) limits the total collector power to 1.3 MW, and consequently the rf-output power at a given efficiency. In recent experiments with a series gyrotron we have applied a combination of Transverse Field Sweeping (TFS) and VFS, which removes the power peaking and reduces the peak loading to about 62 % of the VFS-loading as seen from Fig 1.

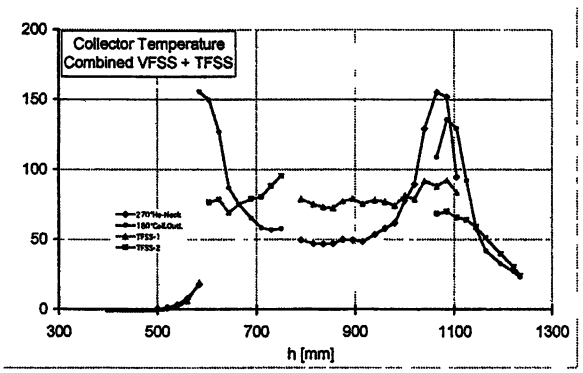

Fig. 1. Collector temperature distribution of the TED 1507-SN4R series gyrotron along the vertical distance h with Vertical Field Sweeping (dots) and combined Vertical- and Transverse Field Sweeping (squares).

The operation range could be extended beyond the previous limit with a related increase of the output power as seen from Fig. 2. Note, that there is still some power margin as the efficiency saturates and the power increases linearly with current. The result was obtained in long pulse operation (typ. 330 s) with a slow current ramp rate of typically 25 mA/s.

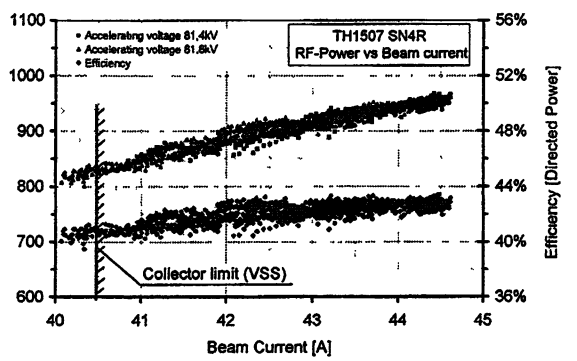

Fig. 2. Output Power (upper curve) and efficiency (lower curve) as a function of beam current. The collector limit for VSS is indicated.

Another important measure was the suppression of parasitic modes, which were limiting the performance, by an improved beam-tunnel design [5]. Tests with the SN 3R gyrotron showed, that without these

improvements reliable operation was achieved only at about 30 % reduced power.

For next-step reactor-type fusion devices RAMI aspects will become of crucial importance. A concentration of the R&D efforts towards a 'standard' type of gyrotron may help to improve the reliability. A 3-frequency (3-f) generic gyrotron is proposed, which is designed for 1.5 MW, but is operated at 1.0 – 1.2 MW. The chosen triplet of frequencies should be resonant with a simple single-disk window at multiples of $\lambda/2$. The W7-X (TED) [5] and ASDEX Upgrade (GYCOM) [3] gyrotrons have diamond windows with a resonant thickness of $4\lambda/2$ at 140 GHz. They are also transparent at 105 GHz corresponding to $3\lambda/2$ and 175 GHz at 5 $\lambda/2$. A possible set of modes, which are compatible with a 3-f design is $TE_{22,6}$ (104 GHz), $TE_{28,8}$ (140 GHz), and $TE_{34,10}$ (174 GHz) [6], or $TE_{17,6}$ (104.7 GHz) and $TE_{22,8}$ (140 GHz) as built by GYCOM. The extrapolation step from present-day achievements is moderate, as 2-f gyrotrons are already operating. The basic needs of many experiments may be satisfied choosing a frequency triplet of 174/140/104 GHz or, anchored at the ITER-frequency, at 170/137/102 GHz.

Transmission lines (TL) must have low losses and provide a reliable redistribution of the power to different launchers, which are selected according to the actual physics requirements. In the ITER baseline design, mechanical switches are foreseen in every TL to switch the power between the equatorial H&CD launcher and the upper launchers, which are dedicated for MHD-control. Replacing the mechanical switches by electronically controlled diplexers would allow to switch the power while keeping the gyrotrons running. Diplexers can operate as fast high power beam switches, power combiners, as well as power splitters. They are qualified to make more efficient use of the installed power while simplifying the ECRH-operation at the same time. The options to simplify power upgrades without the need for additional port space, to improve the efficiency for MHD-control techniques, and to share common antennas for ECRH and ECE-diagnostics are attractive. In recent high power experiments beam combination and arbitrary power distribution between two outputs was demonstrated using two gyrotrons at slightly different frequencies and tuning one of the diplexer mirrors [8].

Remote Steering Launchers (RSL) using simple corrugated square waveguides were proposed as a viable option for ITER and investigated with low and high power [9], but finally the Front Steering Launcher (FSL) was chosen for the baseline design. FSLs provide a wide angular steering range and a very narrow focusing of the individual RF beams. The choice was driven by physics arguments in both, the W7X and ITER devices. The challenging demands on MHD-stabilization (narrow beams must be steered to the resonant surfaces around q = 1, 1.5, and 2) for ITER, and the desirable (very) narrow power deposition (note the small minor radius of 0.5 m) for W7-X were the main drivers. For both FSLs, the W7-X equatorial launcher and the ITER Upper Launcher, a similar averaged power density (port through power/ port clearance) of 8-11 MWm^{-2} (baseline design) or twice this number assuming 2 MW/beam, is obtained.

Under RAMI aspects, however, FSLs with their delicate in-vessel steering mechanisms facing the burning plasma may not be acceptable. Improved concepts for remote steering are thus being investigated and will be used for the 1 MW, CW, high field side launch at W7-X. The average power density of such a simple structure would be about 100 MWm^{-2}, i.e. one (small) port would be sufficient to transmit the complete H&CD power for DEMO. Key points for the improvement of RSLs are the extension of the steering range and the development of optimized low-loss, high power CW structures (2 MW) [10, 11]. Furthermore, the development of mode conserving mitre bends with arbitrary angle, and the integration of vacuum valves and barrier windows in the waveguides are challenging tasks. For W7-X we have started conceptual design work on improved, CW-compatible, RSLs for the high field side launch. The conceptual design of the bend-area is sketched in Fig. 3 together with calculations on optimized wall shaping.

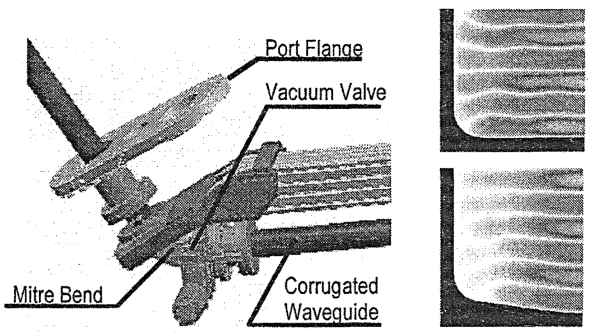

Fig 3. Left: Principal sketch of the W7-X N-port remote steering launcher assembly. Right: Field distribution in a standard square corrugated waveguide (top) and comparison with a shaped waveguide wall (bottom).

References

1. *V. Erckmann*, Fusion Eng. and Design, 84 (2009) 131-137.
2. *K. Sakamoto, et al.* Nature physics. 2007. V. 3.
3. *A.G. Litvak, G.G. Denisov, et al.*, J. Infrared Milli& TeraHz Waves (2011) 32: 337-342.
4. *K. Felch, M. Blank, et al.*, Journal of Physics: Conference Series 25 (2005), p. 13-23.
5. *M. Thumm* et al., this conference.
6. *S. Kern et al.*, IRMMW-THz 2008. 10.1109 /ICIMW.2008.4665582.
7. *W. Kasparek, et al.* Nucl. Fusion 48 (2008) 05401.
8. *W. Kasparek, et al.*, this conference.
9. *B. Plaum, et al.*, Fusion Science and Technology, Vol. 50 (2006), p. 1-14.
10. *G.G. Denisov, K.A. Fedorova, et al.*, Int. J. Infrared Milli Waves (2007) 28:923–935.
11. *B. Plaum, E. Holzhauer, and C. Lechte*, J. Infrared Milli Terahz Waves, to be published (2011).

Development of High Power mm-Wave and THz Sources at ENEA for Novel Biological Applications and Stand-off Detection

G.P. Gallerano[1], A. Doria[1], E. Giovenale[1], G. Messina[1] and I. Spassovsky[2]

ENEA, [1]Radiation Sources Laboratory, Via Enrico Fermi 45, 00044 Frascati (Rome) Italy, gianpiero.gallerano@enea.it
ENEA, [2]Mathematical Modelling Laboratory, 00044 Frascati

In this paper we present a brief report on the high power mm-wave and Terahertz sources available at ENEA-Frascati together with some design considerations for the development of new sources specifically devoted to novel biological applications and stand-off detection.

ENEA has a long term expertise on the construction of powerful short-pulse mm-wave and THz free electron sources [1]. A mm-wave Compact-FEL oscillator utilizing a microtron as electron beam source operates in the range 90–150 GHz providing an output power of 1.5 kW in 4 μs pulses.

A novel electron-wave interaction scheme has also been developed at ENEA-Frascati. This exploits the correlation between the energy and the phase of the electrons in a short bunch to maximize energy extraction from the electron beam and provide amplification in a single pass. Electrons are generated and accelerated by a S-band LINAC up to a energy of 2.3 MeV. Downstream the LINAC, a new radiofrequency device, called "Phase Matching Device" (PMD) acts on the electron beam to create the required correlation. The optimized electron beam passes through a 16 periods compact undulator to provide coherent radiation tunable from 400 to 800 mm (0.4–0.7 THz). Tunability can be exploited, beside varying the undulator gap, by making use of a new feature of this device: the possibility of changing the radiofrequency phase between the LINAC and the PMD.

Recently [2], a project entitled "Probing membrane dynamics with electromagnetic radiation and electric pulses" has been submitted to the Human Frontier Science Program (HFSP) to investigate a possible unified view of ultrafast electromagnetic interactions with cellular systems. One of the most important questions in bio-electromagnetics today is indeed whether cellular systems can rectify rapidly oscillating electric fields at frequencies which have pulse time durations ranging from pico- to microseconds. It has been demonstrated [3] that short duration electric pulses produce significant changes in cell membrane potential. The project hypothesizes that similar effects may occur also from millimeter and THz waves. The project will explore the interaction mechanisms using model membrane systems and electrically excitable cells (neurons) by applying electric pulses and RF carrier waves between 30 and 3000 GHz for possibly controlling cell function.

The source to be realized at ENEA within the HFSP project is a novel Electro-Magnetic pulser, capable of providing both nanosecond THz electromagnetic (EM) radiation pulses as well as electrostatic (ES) pulses in the same device, with identical time duration. The pulser will allow, for the first time, direct comparison of EM and ES pulses on biological systems, a major goal of the project. The pulser will provide a core measurement capability for the program as it will produce peak electric fields in the samples that are significantly higher than any reported to date, while keeping the average power low enough to avoid sample heating.

The pulser diagram is schematically reported in Fig. 1 [4]. The electron gun is composed by a 20 kV power supply charging a capacitor bank C0 that is the primary energy reservoir. A six-stage magnetic pulse compressor reduces the pulse from a discharge time of 1 μs down to about 30 ns and rises the voltage up to 350 kV. The final condenser of the compressor is connected to a transmission-line transformer made by three coaxial cables charged in parallel and discharged in series on a mismatched diode load raising the voltage up to 1.5 MV.

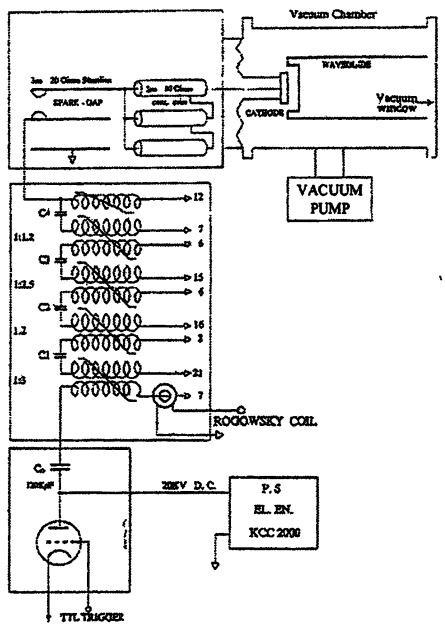

Fig. 1. Pulser schematic diagram

A peak current of about 5 kA allows the use of the pulser as a driver for an FEL that, with the reported electron beam parameters and the presence of a magnetic undulator (MU) of 8 periods of 2.5 cm of length and a parameter K = 0.8 at a gap of b = 8 mm, is capable to reach saturation at megawatt level at a central frequency of 200 GHz as reported in Fig. 2.

Another important field of application, in which high power THz sources could play a significant role is stand-off detection. The NATO Panel Group SET-124 has investigated the basic operation principles of stand-off detection of explosive using THz spectroscopy in the frequency range between 2 and 5 THz.

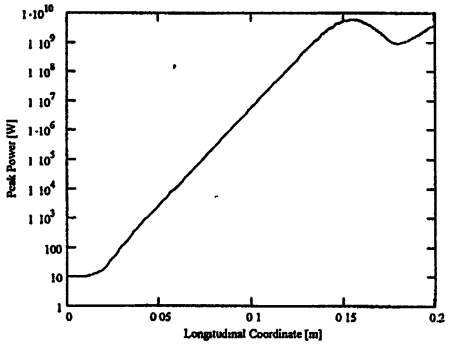

Fig. 2. FEL radiation power evolution along the MU

It has been shown that explosives can be detected under laboratory conditions both in transmission and reflection. However their presence in a real «scene» is much more difficult to detect, since the material obstructing the explosive (cloth, leather, luggage) is not always transparent in the above frequency range. MM-waves do show a better penetration to clothes and luggage, although they do not provide sufficiently selective fingerprints of explosive. However they can be used to detect metal objects or other materials that show a difference in index of refraction with respect to the human body. Moreover stand-off imaging of large areas, like e.g. airport halls, cannot rely on 'passive' techniques that detect tiny differences in the radiation thermally emitted by different objects, due to the high background noise and to the lack of sufficiently sensitive detectors.

Flashing the «scene» in a way similar to night photography would be needed to obtain a clear, phantom free, image of the area under surveillance, which could then allow to track suspect actions up to the security gate.

The ENEA mm-wave and THz sources satisfy the power requirements for illuminating a scene with a range of about 40 m. However, to be satisfactorily applied to stand-off detection, they need to operate at lower electron energy (to reduce shielding requirements) and with a pulse repetition rate suitable for acquiring real time images at typically 30 fps. When combined with an adequate collecting system, such a source can be specifically developed in the frame of a security program.

References

1. *Biedron S.G., Lewellen, J.W., Milton, S.V., Schneider, J.F., Gopalsami, N., Skubal, L., Li, Y., and Virgo, M., Gallerano, G P., Doria, A., Giovenale, E., Messina, G., Spassovsky, I.P.* Compact, High-Power Electron beam BasedTerahertz Sources" – Proceedings of the IEEE – 95, No. 8 (2007), 1666-1678.

2. *Gallerano, G.P, Ramundo Orlando, A , Siegel, P., Park, G.-S.,* Probing membrane dynamics with electromagnetic radiation and electric pulses" submitted to HFSP.

3. *Teissie, J.* Biophysical effects of electric fields on membrane water interfaces: a mini review, Eur. Biophys. J. 36 (2007) 967-972.

4. *Yovchev, I.G., Spassovsky, I.P., Nikolov, N.A., Dimotrov, D.P., Messina, G., Raimondi, P., Barroso, J.J. Correa, R.A.,* Numerical simulation of High Power Virtual Cathode reflex Triode Driven by Repetitive Short Pulse Electron Gun, IEEE Trans. On Plasma Science – 24, No. 3 (1996) 1015-1022.

Anomalous Phenomena at ECRH in Toroidal Devices and Low Threshold Parametric Decay Instabilities

E.Z. Gusakov, A.Yu. Popov

Ioffe Physical-Technical Institute of RAS, St. Petersburg, Russia, Evgeniy.Gusakov@mail.ioffe.ru

Electron cyclotron resonance heating (ECRH) at power level of up to 1 MW in a single microwave beam is often used in present day tokamak and stellarator experiments and planed for application in ITER for neoclassical tearing mode island control. Parametric decay instabilities (PDI) leading to anomalous reflection or absorption of microwave power are believed to be deeply suppressed in tokamak MW power level ECR O-mode and second harmonic X-mode heating experiments utilizing gyrotrons [1, 2]. According to theoretical analysis of PDI thresholds [1], the typical RF power at which these nonlinear effects can be excited at tokamak plasma parameters is around 1 GW. The physical reason for such a deep suppression is provided by strong convective losses of the daughter waves from the decay region either in the plasma inhomogeneity direction [3, 4] or along the magnetic field. Therefore it is taken for granted that wave propagation and absorption in these experiments is described by linear theory and predictable in detail.

However during the last decade a "critical mass" of observations has been obtained evidencing presence of anomalous phenomena in ECRH experiments at toroidal devices. First of all, non local electron transport was shown to accompany ECRH in some devices indicating that the RF power is not deposited in the regions predicted by standard theory, but is rather redistributed very quickly all over the plasma [5]. Secondly, fast ion generation and ion heating was observed during ECRH pulse under conditions when energy exchange between electrons and ions should be very low [6]. And finally, in 2009 the first observations of the backscattering signal in the 200 – 600 kW level second harmonic ECRH experiment at TEXTOR tokamak were reported [7]. This signal down shifted in frequency by approximately 1 GHz, which is close to the lower hybrid or ion Bernstein (IB) wave frequency under the TEXTOR conditions, was strongly modulated in amplitude at the m=2 magnetic island frequency. This observation performed at the modest RF power under conditions when no UHR, where the threshold can be lowered by the growth of the pump field or/and by decrease of the daughter wave group velocity [8], was possible for the pump wave provides an indication that probably a novel mechanism of the PDI excitation is associated with the presence of a magnetic island.

The novel low threshold mechanism of the PDI excitation was proposed in [9] based on analysis of the actual TEXTOR density profile. It was shown that the local maximum of the plasma density which is usually observed in the O-point of magnetic island at Textor [10] can lead to localization of the low frequency ion Bernstein (IB) decay wave and thus to suppression of IB wave convective losses in radial direction. A more complicated 2D analysis of the IB wave propagation accounting for the poloidal inhomogeneity of magnetic field in toroidal plasma have shown possibility of IB wave localization along the magnetic field direction as well [11]. The described possibility of IB wave 2D localization in a plasma waveguide provides an argument in favor of the PDI threshold lowering in the case of the waveguide eigen mode excitation. Assuming the IB wave damping, PDI pumping and convection in toroidal direction weak we account for them using the waveguide perturbation theory approach. It allows determination of the convective PDI gain in the third direction perpendicular to the radii and magnetic field. The power threshold for backscattering convective PDI was calculated in this case and shown to be

$$P_{th} \sim \frac{cH^2}{2\pi}\frac{\omega_i^2\omega_{ce}^2}{\omega_{pe}^4}\left(\frac{\rho^2}{\delta_y^2}\frac{1}{q_x^5\delta_x^3}\right)\Bigg|_0 \qquad (1)$$

where δ_x and δ_y stand for the width of the IB wave localization region in radial and poloidal direction accordingly, q_x is the IB wave number, ρ is the wave-beam radii and H is magnetic field. This threshold is more than four orders of magnitude lower than predictions of standard theory (in the range of 50 kW for the TEXTOR experiment parameters).

The drastic, compared to predictions of the standard theory [1, 2], decrease of the PDI threshold shown in this paper is explained by complete suppression of IB wave radial and poloidal convective losses and their substantial reduction in the third direction. This mechanism is based first of all on non-monotonous dependence of plasma density on radial coordinate. Such a dependence observed in tokamaks in the presence of magnetic islands [10] is associated with their magnetic confinement properties which, we believe, are not specific for the TEXTOR experimental conditions and may lead to easy PDI excitation in ECRH experiments in other toroidal devices where magnetic islands usually exist. In the absence of magnetic islands the hollow density profiles are also often observed at the discharge edge due to gas puffing and pellet injection or during ECRH experiments at low densities, where they are explained by a "density pump out effect" [12]. Moreover it should be mentioned that not only magnetic islands, but also blobs and drift wave density perturbations, which are as well elongated along magnetic field, in the case of intensive enough turbulence can result in IB wave trapping. Similar effect leading to reduction of PDI threshold can occur also on the plasma discharge axis.

It is important to stress that the backscattering convective PDI threshold can be overcome in the

presence of density bump at typical gyrotron power range not only in medium scale devices at modest parameters, but also in reactor scale machines at fusion plasma conditions. For example, Fig.1. shows the convective PDI gain dependence on the radial IB mode number calculated for big tokamak and fusion plasma parameters ($n=1.2\cdot10^{14}\text{cm}^{-3}$, $T_D=5$ keV; $H=27$ kGs; R = 2.96 m; a = 1.25 m; b = 2.10 m; $B_{pol}/B_{tor}\simeq0.1$) and extraordinary microwave beam (P = *1 MW*, $f_i=170$ GHz, $\rho=3$ cm) assuming for magnetic island density variation $\delta n/n=0.1$ and width $w=5$ cm. As it is seen, very high gain close to 10^5 is expected there which may lead to substantial anomalous reflection of heating power already at the convective instability stage.

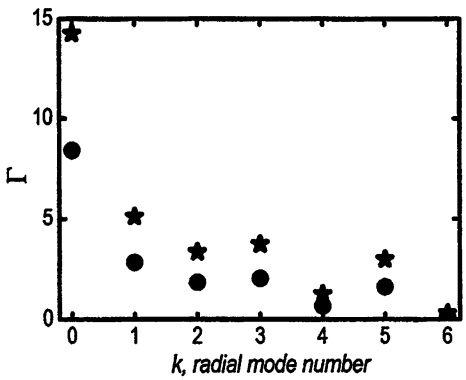

Fig. 1. Dependence of the IB wave gain on the radial mode number for fusion plasma parameters; Circles and stars correspond to poloidal mode numbers – $l=0$; – $l=2$.

It should be underlined, however, that at sufficiently high amplification value due to different feedback mechanisms the convective instability can lead to excitation of absolute PDI which grows slower, but saturates at much higher level due to nonlinear effects. The later instability can lead to strong anomalous reflection and, as a result, to fast variation of heating power deposition profile. In the present paper we consider excitation of the absolute instability on the base of the convective amplification introduced above for the hollow density profile in tokamak which exists due to gas puffing and due to magnetic island. It is shown that in both cases a 3D trapping of IBW leading to formation of the plasma cavity for this mode is possible. The threshold condition for the absolute PDI onset is obtained in the form similar to the expression of the homogeneous PDI theory

$$\gamma_0^2(P_{i0})=\nu_{IB}\nu_{EC}\frac{V_{damp}}{V_{\text{PDI}}} \qquad (2)$$

where the wave number decay condition mismatch is assumed vanishing; ν_{IB} and $\nu_{EC}^{-1}=\delta_x/c$ stand for damping of IB and convective loss rate of backscattered wave, whereas V_{PDI} and V_{damp} are volumes where decay and IBW damping take place accordingly. The growth rate of the instability in the case of the hollow density profile ($\delta n/n=0.1$, $w=5$ cm) calculated for ($n=1\times10^{14}\text{cm}^{-3}$, $T_D=T_e=3$ keV; $H=23$ kGs; R = 2.96 m; a = 1.25 m; b = 2.10 m; $B_{pol}/B_{tor}\simeq0.1$) and extraordinary microwave beam ($f_i=170$ GHz, $\rho=3$ cm) is shown in Fig.2.

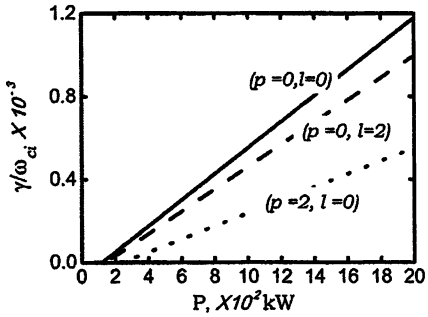

Fig. 2. Dependence of the absolute PDI growth rate on the pump power for different radial (p) and poloidal (l) modes.

As it is seen form Fig.2, the threshold value of less than 200 kW is predicted for the absolute PDI in this case. In the case of magnetic island in TEXTOR a much smaller threshold value of less than 1 kW is predicted due to much smaller V_{damp}.

The PDI saturation due to IBW stochastic damping, converting it into the ion plasma wave, is investigated and shown to limit the anomalous backscattering at the level of less than 1%. However it is shown that this saturation fails when the PDI pumping exceeds the ion plasma wave Landau damping.

A possible role of localized IBW in anomalous absorption of the gyrotron power due to low-threshold parametric excitation of electron Bernstein waves is also considered.

Financial support by RFBR grants 10-02-90003-Bel, 10-02-00887, NWO-RFBR grant 047.018.002; scientific school grant 6214.2010.2 is acknowledged.

References

1. *M. Porkolab et al.*, Nuclear Fusion 1988 V. 28, P. 239
2. *A.G.Litvak et al*, Phys. Fluids 1993 V. B 5. P. 4347
3. *A. D. Piliya* Proc. 10th Conf. Phenomena in Ionized Gases (Oxford). 1971 P. 320
4. *M.N. Rosenbluth* Phys. Rev. Lett. 1972 V. 29 P. 564.
5. *V.F. Andreev et al.* Plasma Phys. Control. Fusion 2004. V. 46. P. 319
6. *D. Rapisarda et al.* Plasma Phys. Control. Fusion 2007 V. 49. P. 309
7. *E. Westerhof et al.*, Phys. Rev. Let. 2009 V. 103. P. 125001
8. *E.Z. Gusakov et al.* Plasma Phys. Control. Fusion. 2007 V. 49. P. 631
9. *E.Z. Gusakov et al.* JETP Letters. 2010 V. 91. P. 655
10. *M. Kantor et al.* Plasma Phys. Control. Fusion 2009 V. 51. P. 055002
11. *E.Z. Gusakov et al.* Phys.Rev.Lett. 2010 V. 105 P. 115003
12. *H. Weisen et al.*, Nucl. Fusion 2001 V. 41, P. 1230.

Present Status of the 24 MW 170 GHz ITER EC H&CD System

M. Henderson[1], F. Albajar[2], S. Alberti[3], U. Baruah[4], T. Bigelow[5], B. Becket[1], R. Bertizzolo[3], T. Bonicelli[2], A. Bruschi[6], J. Caughman[5], R. Chavan[3], S. Cirant[6], C. Darbos[1], M. deBaar[7], G. Denisov[8], D. Farina[6], F. Gandini[1], T. Gassman[1], T.P. Goodman[3], R. Heidinger[2], J.P. Hogge[3], K. Kajiwara[9], W. Kasparek[10], A. Kasugai[9], S. Kern[12], N. Kobayashi[9], J.D. Landis[3], F. Li[3], A.Litvak[8], A. Moro[6], V.Myasnikov[8], C. Nazare[1], J. Oda[9], T. Omori[1], I. Paganakis[3], D. Parmar[4], B. Peters[5], P. Platania[6], B. Plaum[10], E. Poli[11], L. Porte[3], B. Piosczyk[12], D. Purohit[1], G. Ramponi[6], S.L. Rao[4], D. Rasmussen[5], D. Ronden[7], G. Saibene[2], K. Sakamoto[9], F. Sanchez[3], T. Scherer[12], S. Schreck[12], N.P. Singh[4], M. Shapiro[13], C. Sozzi[6], P. Spaeh[12], D. Straus[12], O. Sauter[3], E.Tai[8], K.Takahashi[9], R. Temkin[13], P. Thomas[1], M. Thumm[12], and H. Zohm[11].

[1] ITER Organization, St. Paul-lez-Durance, 13067 France;
[2] Fusion for Energy, C/ Josep Pla 2, Torres Diagonal Litoral-B3,E-08019 Barcelona – Spain
[3] CRPP, Association EURATOM-Confédération Suisse, EPFL Ecublens, CH-1015 Lausanne, Suisse
[4] Institute for Plasma Research, Near Indira Bridge, Bhat, Gandhinagar, 382428, India
[5] US ITER Project Office, ORNL, 055 Commerce Park, PO Box 2008, Oak Ridge, TN 37831, USA
[6] Istituto di Fisica del Plasma, Association EURATOM-ENEA-CNR, Milano, Italy
[7] Association EURATOM-FOM, 3430 BE Nieuwegein, The Netherlands
[8] Institute of Applied Physics Russian Academy of Sciences, 46 Ulyanov Street, Nizhny Novgorod, 603950 Russia
[9] Japan Atomic Energy Agency (JAEA) 801-1 Mukoyama, Naka-shi, Ibaraki 311-0193 Japan
[10] Institut fur Plasmaforschung, Universitat Stuttgart, Pfaffenwaldring 31, D-70569 Stuttgart, Germany
[11] IPP-Garching, Association EURATOM-IPP,D-85748 Garching, Germany.
[12] Karlsruhe Institute of Technology, Association EURATOM-KIT, Postfach 3640, D-76021 Karlsruhe, Germany
[13] MIT Plasma Science and Fusion Center, Cambridge, MA 02139, USA

A 24MW CW Electron Cyclotron Heating and Current Drive (EC H&CD) system operating at 170GHz is to be installed for the ITER tokamak. The EC system will represent a large step forward in the use of microwave systems for plasma heating for fusion applications. Present day systems are operating in relatively short pulses (≤10s) and installed power levels of ≤4.5MW, while the ITER EC system parameters are CW operation and 20MW injected power. The magnitude of the ITER system necessitates a worldwide collaboration. This is also reflected in the EC system that is comprised of the power supplies, sources, transmission line and launchers. A partnership between Europe, India, Japan, Russia, United States and the ITER organization is formed to collaborate on design and R&D activities leading to the procurement, installation, commissioning and operation of this system.

The ITER EC system (shown in figure 1) is comprised of four main sub-systems to be installed: 12 high voltage power supplies, 24 MW gyrotron power, the transmission lines and five launching antennas, and the additional ancillaries (control system, cooling, infrastructures, etc.). The functional requirements are to deliver ≥20MW at 170GHz for pulse lengths ≥3,600sec to the plasma for central heating, current drive and control some of the plasma instabilities.

The whole system is installed in three buildings. The power supplies (PS), gyrotrons and part of the transmission line (TL) are located in the RF building The TL pass through the Assembly hall building to the tokamak (bottom left), which houses the tokamak and the equatorial (EL) and upper (UL) launchers.

These subsystems are integrated together to provide a maximum operating flexibility and minimum downtime due to component failure by introducing a modular structure[1]. For example, a single power supply powers only two gyrotrons to allow control of the delivered power in increments of 2MW. In the event of failure a single PS, gyrotron, TL or launcher can be isolated to allow continued operation of the remaining EC plant.

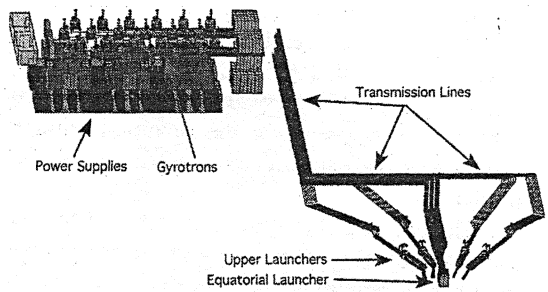

Fig. 1. The ITER EC system comprised of power supplies, gyrotrons, transmission lines and launchers

The power supplies consist of the main HVPS, body (BPS) and for some gyrotrons anode (APS) power supplies. The main HVPS provides the current (~90A) and roughly half the accelerating voltage (~55kV) of the electrons emitted from the gyrotron cathode. A pulse step modulated (PSM) concept is considered for the main HVPS, which provides high frequency modulation capabilities (≤5kHz) at competitive costs relative to thyristor systems[2]. The BPS provides the additional accelerating voltage (~45kV) in a depressed collector configuration to increase the electrical efficiency of the gyrotron to ≥50%.

The ITER in-kind procurement plans on the installation of three gyrotron types: a triode from Ja-

pan[3], a diode from Russia[4] and a 2MW co-axial from Europe[5]. India will also provide a single power supply and two gyrotrons (electing on one of the above types), which will be used as back-ups to the main 24MW system. All of the partners providing gyrotrons are performing prototype testing that aims at reliable demonstration of high power long pulse operation compatible with ITER specifications.

As mentioned above, the gyrotrons are to have an electrical efficiency of >50% (coupled power out the gyrotron window divided by the applied input power) and a pulse length of ≥3,600sec. The gyrotron output power is in a TEM_{00} mode that efficiently couples to the HE_{11} corrugated waveguide (63.5mm diameter), which forms the transmission line (TL). A matching optics unit (MOU) is inserted between the gyrotron and HE_{11} waveguide to reshape and orientate the beam for optimum coupling into the TL. An additional switch connected to a load is installed in the TL for gyrotron installation and conditioning.

The TL[6] guides the RF power from the gyrotron over a distance of ~160m to the launchers. In addition, the TL monitors the gyrotron output power, modifies the polarization for optimum plasma coupling and directs the power to either an equatorial or one of four upper launchers installed in the ITER ports via an in line switching system.. The routing of the TL through the three buildings was chosen to minimize the number of mitre bends (7 to 9 depending on the path to the EL or UL). The estimated transmission efficiency is ~90 to 92%, comparable to the ~95% transmission efficiency measured in the JAEA TL test stand[7].

Synthetic diamond windows[8] are placed at the entry of both the EL and UL, which create a vacuum and tritium barrier between the launchers and TL. The window prevents tritium from traveling from the launcher (at torus pressure) up the waveguide to the gyrotrons (note that the TL is also evacuated). All-metal valves are placed near the windows to provide a hard barrier in the event the diamond window fails and in-situ leak testing of the tritium confinement barrier.

The two launcher types (one EL and four UL) are used to inject the EC power into the plasma based on the physics requirements. The EL for central heating and current drive applications; the UL for control of magneto-hydrodynamic (MHD) instabilities.

The EL[9] has a total of 24 waveguide entries that are divided into sets of 8 beams on to three steering mirrors. The beams are steered in the toroidal (or horizontal) direction, which provides access from on axis to near mid radius and maximizes the driven current in side the plasma mid-radius

The four UL[10] ports each have 8 entries that are split in two sets of 4 beams. The UL has three fixed and one steering mirror for each beam set, these mirrors are used to focus and assemble the four beams such that the deposited power forms a peaked current density profile, optimum for the control of MHD instabilities[11-12], in particular the neoclassical tearing modes (NTMs) that can degrade the fusion performance by up to 50%. The NTMs are expected to occur on the q=3/2 and 2 flux surfaces for theplasma scenarios 2, 3a and 5 in the range of $\sim 0.55 \leq \rho_T \leq \sim 0.85$, where ρ_T is the square root of the normalized toroidal flux.

An optimized partitioning of the physics applications has been proposed[13-14] and integrated into the baseline design, which permits the application of EC power across nearly the entire plasma cross section. The EL covers a range of $\sim 0.0 \leq \rho_T \leq \sim 0.45$; and the UL a range of $\sim 0.3 \leq \rho_T \leq \sim 0.9$. Further optimization of this partitioning is under investigation including modification of the toroidal and poloidal steering angles to increase the access of each launcher as well as to improve the net driven current for steady state operation.

Previously, the EL and UL beams were to aim to provide co-current drive (current driven co-linear with the plasma current). The EL design has been modified to orientate one steering row to inject 8MW of power in the counter direction (driving current in the opposite direction of the plasma current). This would provide sufficient flexibility to either drive 20MW in the co-direction (by balancing 16MW in the EL and 8MW in the UL) or zero net current (8MW counter from the EL and 16MW in the UL). Note that the EL drives roughly twice the current as the UL.

This additional flexibility decouples the heating from the current drive functions. For example, pure on axis heating is useful for impurity control while avoids peaking of the central plasma current. The counter current drive can also be used to tailor the plasma current profile to either maintain a flat central shear for avoiding sawteeth or introducing a hollow profile for generating and sustaining an internal transport barrier.

The overall objective of these changes are to provide an EC system with the maximum flexibility to respond to the numerous needs for H&CD applications associated with the ELMy H-mode, hybrid and advanced scenarios envisioned for the ITER operation.

References

1. M. Henderson and G. Saibene, Nucl. Fusion **48** (2008) 054017.

2. D. Fasel *et al*, *Fusion Sci. Technol.* **53** (2008) 246.

3. K. Sakamoto *et al Nature* **3** (2007) 411–4.

4. G. Denisov *et al* Development in Russia of high power gyrotrons for fusion *Proc. 4th IAEA ECRH Technical Meeting (Vienna, Austria, May 2007).*

5. J.-P. Hogge *et al Fusion Sci. Technol.* **55** (2009) 204-212..

6. D. Rasmussen *et al* Design of the ITER electron heating *and current drive waveguide transmission line Proc. 4th* IAEA ECRH Technical Meeting (Vienna, Austria, May 2007).

7. Takahashi K. *et al,* to be published in Rev Sci Instrum.

8. R. Heidinger et al., Fusion Eng. Des. **82** (2007) 693.

9. Takahashi K. *et al* Nucl. Fusion **48** (2008) 054014.

10. M. Henderson et al Nucl. Fusion **48** (2008) 054013.

11. S. Gunter *et al Phys. Rev. Lett.* **87** (2001) 275001.

12. C. Angioni *et al Nucl. Fusion* **43** (2003) 455.

13. G. Ramponi et al, Nucl. Fusion **48** (2008) 054012.

14. M. Henderson et al, *et al* 2006 *Proc. 21st Int. Conf. on Fusion Energy 2006 (Chengdu, China, 2006)* IT/P2-15.

High-Gradient Collinear Two-Beam Electron Accelerator

Y. Jiang[1], S. V. Kuzikov[2], J. L. Hirshfield[1,3]

[1]Department of Physics, Yale University, New Haven, CT 06520, USA, jiang.yong@gmail.com
[2]Institute of Applied Physics, RAS, Nizhny Novgorod 603950 Russia, kuzikov@appl.sci.nnov.ru
[3]Omega-P, Inc., New Haven, CT 06510, USA, jay.hirshfield@yale.edu

Recently, we developed a self-consistent generic theory for a two-beam collinear accelerator based on use of a cascade of detuned multi-mode cavities [1, 2]. Two-beam accelerators transfer energy from a high-current drive beam to a low-current accelerated beam, with distinctive advantages as compared with the use of discrete RF sources to energize individual accelerator structures. The use of detuned cavities as elements in an accelerator structure has been shown to allow realization of moderate-to-high transformer ratios T for collinear acceleration, i.e. when the drive beam and accelerated beam move along a common axis. Furthermore, multi-mode excitation of the cavities can also be implemented. This latter approach, which can reduce the exposure time to high fields on cavity surfaces during each RF cycle, is expected to raise the RF breakdown threshold above what can be achieved for single-mode cavities. The accelerated beam in the detuned-cavity two-beam concept can be any species: electrons, positrons, muons, protons, or heavier ions; this paper focuses only on electrons (or positrons). The theory leads to interrelationships between the main parameters (acceleration gradient, transformer ratio, beam-to-beam power transfer efficiency) that permit systematic optimization to meet specific goals. The electron drive beam can evidently be generated with high efficiency; e.g., the 2.3-GeV, 100-A CLIC drive beam at CERN is expected to be formed with 95% RF-to-beam efficiency [3]. The principals enunciated here suggest that in future two-beam structures might operate with 150 MeV/m working acceleration gradients, as desired for a future multi-TeV collider. Proof-of-principle experiments will use the ~0.1-A, 6-MeV drive beam available from the Yale Beam Physics Lab S-band thermionic cathode RF gun, and a keV-range test beam. These experiments are aimed at confirming underlying principles of this novel acceleration concept. A cartoon illustrating the experiment is shown in Figure 1.

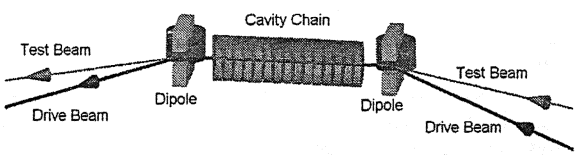

Fig. 1. Arrangement for planned 2-beam experiment

Our theory for a two-beam collinear accelerator using detuned cavities was, until recently, based on a simple circuit model [2]. This model does not easily allow calculation of transverse forces arising from loss of axisymmetry that can lead to beam breakup and/or beam deflection. Accordingly, a simulation approach is now being instituted, based on use of the SLAC T3P wake field code [4]. Preliminary use of this code has so far been limited to excitation of single-mode and bimodal cavities – either individually or in short structures – from wake fields arising from symmetrical bunched electron drive beams. Results from these studies are being compared to those from analytic theory to strengthen confidence in their utility, to predict what can be expected from experiments using the Yale drive beam, and to anticipate beam stability issues that may arise in a full-scale structure.

Due to space limitations, results discussed in this summary are limited to wake fields in structures composed of single-mode pillbox cavities. For a five-cavity structure, Fig 2 shows E-field maps at three instances during and following the passage of two final drive bunches. Each cavity is chosen to have a phase advance of $\pi/2$ near the drive frequency. Wake field simulations carried out demonstrated that the detuned beam-driven structure supports a travelling wave, since the field strength evolves sequentially in time with peak amplitudes in alternative cavities, and minimal values in adjacent cavities as these are 90° out of phase with one another.

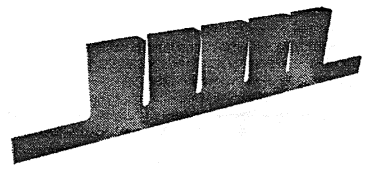

Fig. 2a. Wake fields in a 5-cavity pillbox structure as two bunches pass through the 1st and 5th cavities.

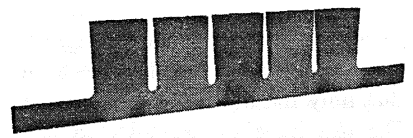

Fig. 2b. Same as Fig. 2a, 90° after exit of 2nd bunch

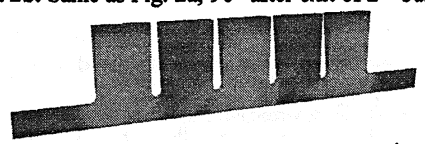

Fig. 2c. Same as Fig. 2a, 180° after exit of 2nd bunch

To simulate wake fields in an extended structure composed of either single- or multi-mode cavities, it was necessary to use two computational artifices to reduce the run times: first, is to artificially reduce the Ohmic Q's of the cavities as by increasing the resistivity of the wall material; and second, to introduce a "pre-bunch" sequence designed to cancel transient effects that arise during the cavity fill times [2]. As a result, simulations for structures with >30 cavities could be carried out in reasonable run times, using the T3P wake field code. Results are shown in Figs. 3 and 4 for a structure consisting of pillbox cavities with

TM_{010} mode frequencies slightly detuned from a drive bunch frequency of 2.856 GHz and with Q = 11,247 for nominal copper walls, but scaled down by a factor-of-100 for this simulation; and with no higher harmonic resonant modes.

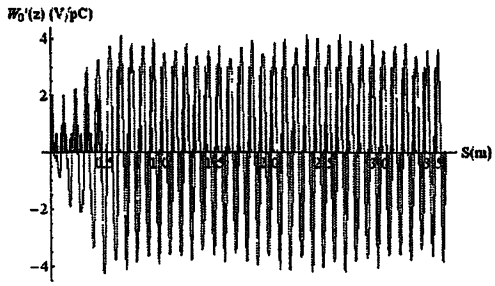

Fig. 3a. Simulated wake fields from drive and test bunch trains traversing an S-band detuned cavity structure

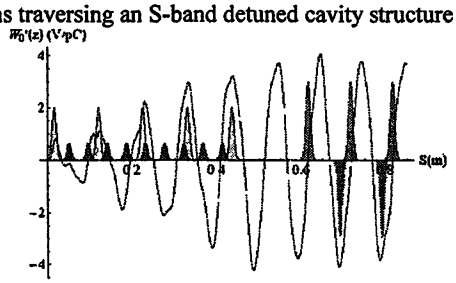

Fig. 3b. Same as Fig. 3a, zoomed at initial times, with the pre-bunch sequence in the interval $0 < S < 0.45$ m; the sequence of drive bunches are shown above the x-axis for $S > 0.6$ m; and the test bunches are shown below the x-axis

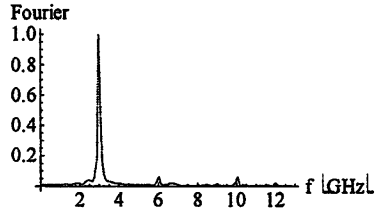

Fig. 3c. Fourier spectrum for wake field in Fig. 3a.

In Fig. 3, the drive bunch frequency is positively detuned from to the cavity frequency. The pre-bunch sequence suppresses the transient longitudinal higher-order modes. The clean Fourier spectrum in Fig. 3c shows that only the desired acceleration mode is excited. The test bunches are injected nearly 270° in phase behind the drive bunches. Similar results are found for negative detuning, but for the essential difference shown in Fig. 4 – as compared to Fig. 3b.

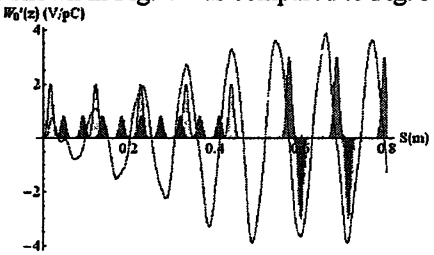

Fig. 4. Same as Fig. 3b, except for negative detuning

Here the test bunch is to be located 90° in phase behind the drive bunch. In this sequence – in contrast to that in Fig. 3—both drive and test bunches enjoy longitudinal stability. The head of the drive bunch experiences greater deceleration than does the tail, such that the beam breakup instability will be suppressed. Hence, negative detuning is preferable to positive.

For this S-band case, computations with a detuning of $Q\delta$ = -5.623 yield a transformer ratio of 13.6, an acceleration gradient per ampere drive current of 4.62 MV/A-m, based on taking a test-to-drive current ratio of 0.04. Here $\delta = \Delta f/f$, so $Q\delta$ = -5.623 corresponds to Δf = 1.43 MHz if one scales to nominal Ohmic Q for copper cavities. For the 30-bunch sequence used in this simulation, the computed power transfer efficiency is 27.8% including the energy deposited by the primary and secondary pre-bunches. For long pulse excitation, as in the planned experiments, the efficiency should grow to 54% after energy transfer between drive bunches and test bunches dominates.

For drive bunches that are sufficiently short, a detuned two-beam accelerator structure could be also be designed to run at, for example, 11.424 GHz (X-band). Here, for detuning $Q\delta$ = -5.623, the transformer ratio is 20.8 and the acceleration gradient per ampere drive current is 9.35 MV/A-m, taking a test to drive current ratio of 0.04. For a 30 bunch sequence, the power transfer efficiency is 41.8% including the energy deposited by the primary and secondary pre-bunches. In long pulse excitation, the efficiency should grow to a remarkable 83% after the energy transfer between the drive bunches and test bunches dominate.

Comparison of these results with those obtained from analytical theory [2] shows good agreement between the two when Ohmic losses in cavity walls are neglected. But with realistic losses in the copper walls, efficiency and acceleration gradient would be about a factor-of-2 smaller than the values cited here.

Conclusions: Preliminary simulations have been carried out using the SLAC T3P code to compute wake fields in a 2-beam collinear accelerator structure composed of a sequence of de-tuned pillbox cavities. Results are in agreement with analytic theory, and thus provide confidence for studies to assess beam stability issues for this new accelerator concept.

Acknowledgment: This work was sponsored by the US Department of Energy, Office of High Energy Physics. Discussions of great value were held with V.P. Yakovlev, S.Yu. Kazakov, Cho-Kuen Ng, and Kwok Ko.

References

1. *Kuzikov, S.V., Kazakov, S.Yu., Jiang, Y., Hirshfield, J.L.,* Asymmetric bimodal accelerator cavity for raising RF breakdown thresholds, Phys. Rev. Lett. 104, 214801 (2010).

2. *Kazakov, S.Yu., Kuzikov, S.V., Jiang, Y., Hirshfield, J.L.,* High-gradient two-beam accelerator structure, Phys. Rev. ST – Accel. & Beams, 13, 071303 (2010).

3. *Braun, H., Corsini, R., Delayahe, J. P., de Roeck, A., Dobert, S., Ferrari, A., Geschonke, G., Grudiev, A., Hauviller, C., Jeanneret, B.,* CLIC 2008 PARAMETERS, CERN-OPEN-2008-021, CLIC-Note-764 (2008).

4. *Candel, A., Kabel, A., Lee, L., Li, Z., Ng, C., Schussman, G., Ko, K.,* Wakefield Simulation of CLIC PETS Structure Using Parallel 3D Finite Element Time-Domain Solver T3P, Tech. Rep., SLAC-PUB-13670 (2009).

New Microwave Plasma Sources Based on the Latest Advances of Fundamental Gas-Discharge Physics

I.A. Kossyi

Prokhorov General Physics Institute of RAS, Moscow, Russia. kossyi@fpl.gpi.ru

Investigations of fundamental problems of microwave gas discharges, which carried out at the General Physics Institute of RAS (GPI) and at the Institute of Applied Physics of RAS (IAP) made it possible to create a new microwave plasma sources designed and suitable for physical laboratory research as well as for some applications.

The following physical phenomena, revealed and investigated at the GPI and IAP, provided the basis for these plasma sources (microwave plasmatrons):

-Low threshold microwave discharges (sparks) at a metal-dielectric interface [1-3];

- Thermal-ionization instability attaining strongly nonlinear phase [4, 5];

- "Plasma resonance" phenomenon consist in the totality of nonlinear processes, occurring where the plasma density of nonmagnetized plasma approaches the critical value $n_{ec} = \frac{m\left(\omega^2 + \nu_{eff}^2\right)}{4\pi e^2}$ on its essentially nonuniform profile (here, ν_{eff} is the effective frequency of electron-neutral collisions, ω is cyclic frequency of microwave radiation) [6].

Three type of microwave gas discharge plasma sources based on the listed phenomena have been elaborated, investigated and applied for some technologies in the GPI:

- Coaxial microwave plasmatron [7];
- "Microwave arc" [8] and
- "Biresonant" plasma source [9].

These microwave plasma sources schematically are shown on the Figs. 1-3.

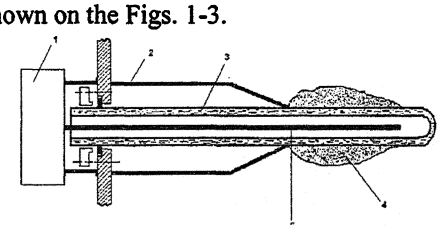

Fig. 1. Schematic of coaxial microwave plasmatron. 1 - magnetron; 2 - outer electrode; 3 - quartz tube; 4 - gas - discharge near - the - surface plasma layer; 5 - inner electrode – rod; 6 - wall of reactor chamber; 7 - plasma of "halo".

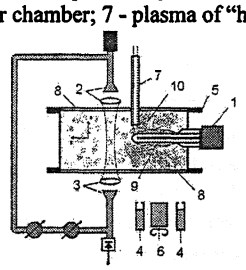

Fig. 2. Scheme of experiment. 1 - plasmatron; 2, 3 - hornlens antenna of microwave interferometer; 4 - optical spectrographs; 5 - vacuum chamber of reactor; 6 - photo - electron recorder FER-7; 7 - Langmuir probe; 8 - quartz windows; 9 - plasma layer created by surface e.m. wave; 10 - volume plasma generated by fast electrons and UV radiation.

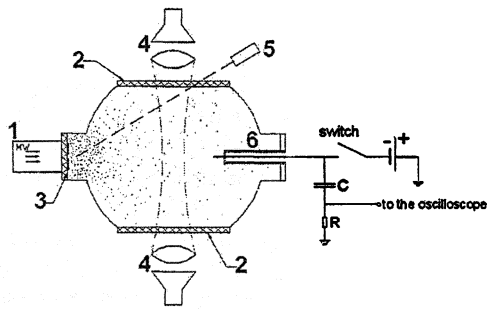

Fig. 3. Scheme of experiment with the "biresonant" plasmatron. 1 - cylindrical waveguide; 2 - diagnostic quartz window; 3 - plasma - forming window; 4 - horn-lens antennas of the microwave interferometer; 5 - optical spectrograph; 6 - Langmuir probe; 7 - metal chamber.

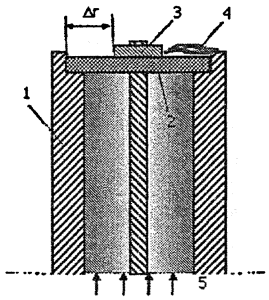

Fig. 4. Scheme of "Microwave Arc". 1 - outer electrode; 2 - quartz disk; 3 - inner electrode; 4 - discharge channels; 5 - microwave radiation

Results of experiments for studying the characteristics of plasma generated by the plasmatrons are described. Field of applications of a new microwave plasma sources are analyzed.

References

1. *Batanov, G.M., Bol'shakov, E.F., Dorofeyuk, A.A., Kossyi, I.A.* // J. Phys. D: Appl. Phys. 1996. V. 29. No. 6. P. 1641 - 1648.

2. *Batanov, G.M., Gritsinin, S.I. Kossyi, I.A.* et al. // J. Phys. D. Appl. Phys. 2002. V. 35. No. 20. P. 2687 - 2692.

3. *Batanov, G.M., Berezhetskaya N.K., Kossyi, I.A.* et al. // Eur. Phys. J., Appl. Phys. 2004. V. 26. No. 1. P. 11 - 16.

4. *Avetisov, V.G., Gritsinin, S.I., Kim, A.G., Kossyi, I.A.*, et al.// Pis'ma v Zhurnal Experim. I Teoretich. Fiziki. 1990. V. 51. iss. 6. P. 306 - 309. in Russian.

5. *Kim, A.G., Fraiman, G.M.* // Fizika Plasmy. 1983. V. 9. No. 3. P. 613 - 617. in Russian.

6. Generation of Nonlinear Waves and Quasi - Steady Currents in Plasma // Transact. GPI. 1988. V. 16. Moscow: Nauka. In Russian.

7. *Berezhetskaya, N.K., Kop'ev, V.A., Kossyi, I.A.*, et al. // Eur. Phys. J. Appl. Phys. 2008. V. 42, P. 327 - 337.

8. *Gritsinin, S.I., Davydov, A.M., Kossyi, I.A.* // XXXVII Intern (Zvenigorod) Conference on a Plasma Physics and Controlled Thermonuclear Synthesis. Abstracts. 2010. Zvenigorod. P. 364.

9. *Gritsinin, S.I., Davydov, A.M., Kossyi, I.A.* et al. // Plasma Physics Reports. 2011. V. 37. No. 3. P. 263 - 272.

High Power NovoFEL: Developments and New Results

G.N. Kulipanov and NovoFEL team

Budker Institute of Nuclear Physics, Novosibirsk, Russia, kulipanov@inp.nsk.su

In the Budker Institute of Nuclear Physics of the RAS Siberian Branch the creation of powerful FEL based on four-track energy recovery linac (ERL) with a maximum energy of 40 MeV is close to completion. The planned range of wavelength is between 240 and 5 μm, the expected radiation power varies from 1 kW in the long-wave range up to 10 kW in the short-wave range.

The first stage of Novosibirsk high power free electron laser (NovoFEL) had been commissioned in 2003. It is CW FEL based on non-superconducting low frequency (180 MHz) single-pass accelerator-recuperator with the following parameters. Electron energy – 12 MeV, charge per bunch – 1.5 nC, bunch repetition rate – 5.6 ÷ 22.5 MHz, maximum average current – 30 mA, bunch duration – 40 – 100 ps.

The radiation spectral range is 110 – 240 μm at the first harmonic, 60 – 117 μm and 40 – 80 μm at the second and third harmonics correspondingly. Maximum average power is up to 0.5 kW for the first harmonic. Maximum peak power is 1 MW, and repetition frequency 5.6 and 11.2 MHz. Relative spectral width is 0.25 – 1%. The radiation is completely spatial coherent, the degree of linear polarization is better than 99.6%.

To move to the region of higher frequencies of the terahertz range, the second stage of the free electron laser (FEL) is created.

Novosibirsk energy recovery linac has rather complicated magnetic system. One orbit for 12-MeV energy with terahertz FEL lies in vertical plane.

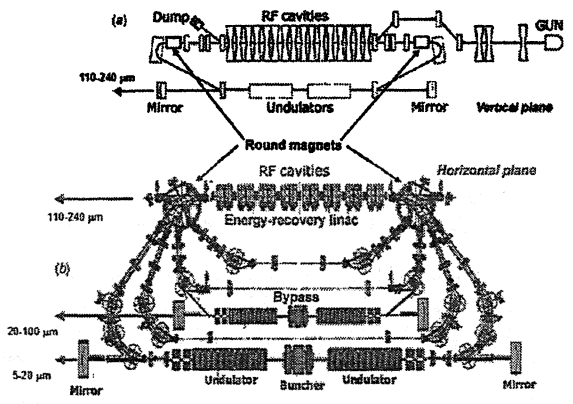

Fig. 1. The scheme of NovoFEL.

Other four orbits are in the horizontal plane. The beam is directed to these orbits by switching on of two round magnets. In this case electrons pass four times through acceleration RF cavities, obtaining 40-MeV energy. Than, (at the fourth orbit) the beam is used in FEL and decelerated four times.

At the second orbit (20 MeV) we have bypass with second FEL. When magnet of bypass are switched on, the beam passes through this FEL. The length of bypass is chosen to provide the delay, which necessary to have the deceleration instead acceleration at the third passage through acceleration cavities.

Now two of four horizontal orbits are assembled and commissioned. The electron beam was accelerated twice and then decelerated down to low injection energy. First multi-orbit ERL operation was demonstrated successfully.

The first lasing of the FEL at bypass was achieved in 2009. The radiation wavelength range now is 40-80 micron. The maximum gain was about 40%. The significant (percents) increase of beam losses took place during lasing. Therefore sextupole corrections were installed to some of quadrupoles to make the 180-degree bends second-order achromatic. It increased the energy acceptance for used electron beam.

Now the output power is about 0.5 kW at the 9 mA at the 9 mA ERL average current. Thus, the first in the world multiturn ERL operates for the far infrared FEL.

Laser radiation is transmitted from THz FEL and bypass FEL through nitrogen-filled optical beamlines to the experimental hall. To provide ultrahigh vacuum in the FEL and accelerator-recuperator, their vacuum volume is separated from the beamlines with the diamond window. Six user stations (metrology station, photochemistry station, biological station, introscopy and spectroscopy station, molecular spectroscopy station, gasdynamics station) are in use now for experiments.

Unique features of NovoFEL radiation, from one hand, require development of techniques for radiation imaging and characterization and, from other hand, enable the development of new metrological methods and techniques.

Our center has developed various experimental equipment for the THz range. First of all, there was developed a number of terahertz imaging techniques based on the relatively high power of radiation. We develop and apply 2D imaging systems of various types. There are commercially available thermal image plates of Macken Instruments Inc. and piroelectric cameras Pirocam III of Spiricon Inc. with 120x120 pixels and 12x12 mm in size.

The uncooled vanadium oxide 320x240 microbolometer focal plane array (MBFPA) was applied to direct recording "terahertz video" with frequency up to frames per second.

Spectral investigation can be made with three types of spectral devices: high resolution simple mesh Fabry-Perot interferometers; grating monochromators, which are especially useful for on-line spectral adjustment and harmonics measurement, and Bruker Fourier spectrometer for fine spectral measurements in a broad spectral range.

Keeping time-resolved experiments in mind, we have developed Schottky diode detector of two types: a fast detector with high sensitivity and ultra-fast detector. The latter device has now a rise time of about 20 ps and we plan to decrease the value in the near future. The detector allows us to observe and investigate a time structure of a single FEL pulse, which is very important for measurement of FEL parameters and their optimization.

In 2010, work on the FEL involved employees of Budker Institute of Nuclear Physics SB RAS, the Institute of Chemical Kinetics and Combustion SB RAS, the Institute of Cytology and Genetics SB RAS, the Institute of Inorganic Chemistry SB RAS, Rzhanov Institute of Semiconductor Physics. SB RAS, the Institute of Theoretical and Applied Mechanics SB RAS, the Technological Design Institute of Scientific Instrument, and the Scientific-Technological Center of Unique Instrumentation RAS (Moscow) as well as teachers, students and graduates of Novosibirsk State University and Novosibirsk State Technical University.

The themes of works using NovoFEL THz radiation in 2010-2011:

1. Study of the spectrum of electronic states in Si / CaF_2 BaF_2 / PbSnTe:In nanoheterostructures.

2. Investigation into the interaction of THz radiation with new functional resonant metamaterials for devices controlling the polarization, phase, intensity and direction of propagation of radiation.

3. Metamaterials based on precision micro- and nanoshells for terahertz and infrared ranges.

4. Investigation into the interaction of THz radiation with materials based on carbon nanotubes.

5. Production of carbon nanostructures with the help of NovoFEL radiation.

6. Determination of the fractional composition of nanoproducts of mechanical activation of double oxsides.

7. Exploration of composite silicon-polymer nanostructures.

8. Spectroscopy of attenuation total reflection (ATR).

9. Plasmon spectroscopy of surfaces and films.

10. Development of physical foundation of tomography, holography and metrology using a source of coherent monochromatic THz radiation.

11. Development of methods for flame diagnostics using the THz FEL.

12. Study of the impact of THz radiation on genetic material.

13. Exploration of the impact of THz radiation on stress-sensitive biological cell systems.

14. THz radiation influence of the katG and E.coli dps genes.

15. Study of the integrated proteomic response of E.coli to exposure by terahertz radiation.

Conclusions

At present, intense work on the creation of powerful FELs (> 1 kW of average power) is carried out worldwide. For the purposes of industrial applications, it is necessary to reach the average power level of about 10 kW.

In some cases, the problem is a rather wide radiation spectrum (usually, not less than 1-3%). For some industrial applications (for example, isotope separation) the required monochromaticity should be not worse than a few hundredths of percent.

The Novosibirsk terahertz free electron laser is becoming a user facility. We invite those researches who want to perform interesting experiments with a high power monochromatic coherent tunable THz radiation to carry out them in Novosibirsk.

References

1. *Antokhin E.A., Akberdin R.R. et al.* Commissioning of the accelerator-recuperator for the FEL at the Siberian Center for Photochemical Research // Journal of synchrotron radiation. – 2003. - Vol. 10, No 5. - P. 343-345.

2. *Antokhin E.A., Akberdin R.R. et al.* First lasing at the high-power free electron laser at Siberian center for photochemical research // Nucl. instrum. and meth. in phys. res. – 2004. – Vol. A528, No 1/2. - P. 15-18.

3. *Gavrilov N.G., Knyazev B.A., Kolobanov E.I., et al.* Status of the Novosibirsk high-power terahertz FEL // Nucl. instrum. and meth. in phys. res.. Sec. A. – 2007. – Vol. 575, No 1/2. - P. 54-57.

4. *Kulipanov G.N., Gavrilov N.G., Knyazev B.A. et al.* Research highlights from Novosibirsk 400 W average power THz FEL // Terahertz science and technology: The international electronic journal of THz. – 2008. – Vol. 1, No 2. - P. 107-125.

5. *Vinokurov N.A., Dementyev E.N., Dovzhenko B.A.et al.* Novosibirsk free electron laser: operation and second stage commissioning // Proc. of the Russian particle accelerator conf.: Ru-PAC 2008, 28 Sept. – 3 Oct. 2008, Zvenigorod, Russia. – Dubna, 2008. - P. 181-184.

6. *Vinokurov N.A., Dementyev E.N., Dovzhenko B.A. et al.* Novosibirsk free electron laser facility: two-orbit ERL with two FELs // Intern. particle accelerator conf., IPAC 2010, Kyoto, 23-28 May 2010: Proceedings. – S.l.: IPAC'10 OC/ACFA, 2010. - P. 2427-2429.

7. *Knyazev B.A., Kulipanov G.N. and Vinokurov N.A.* Novosibirsk terahertz free electron laser: instrumentation development and experimental achievements // Measurement science and technology. – 2010. – Vol. 21. - P. 054017 (13 p.)

8. *Knyazev B.A., Cherkassky V.S. et al.* High-power monochromatic terahertz radiation: metrological aspects // Proc. of the 20th IMEKO TC2 symposium on photonics in measurement. May 16-18, 2011, Linz, Austria. – Aachen: Shaker Verl., 2011. - P. 141-145.

Ultra-sensitive Cold-Electron Bolometers for High-Performance Cosmology Instruments

Leonid S. Kuzmin

Chalmers University, Gothenburg, Sweden, kuzmin@chalmers.se
LCN Alexeev NSTU, N. Novgorod, Russia,

Background

Science – achievements of the decade

Cosmic Microwave Background (CMB) measurements by the balloon telescope BOOMERanG (Balloon Observations of Millimetric Extragalactic Radiation and Geophysics) (Fig. 1) **are ranked by the journal Science in 10 Achievements of the Decade on the second place!** [1]

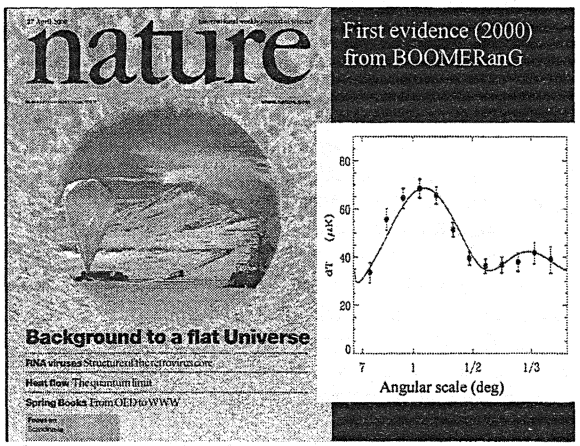

Fig. 1. In 2000, an experiment known as BOOMERanG measured the CMB in detail in patches of the sky. By measuring the distribution of the spots' sizes and fitting it with their theoretical model, scientists can probe the interplay and amounts of ordinary and dark matter in the early universe. They can also measure the geometry of space

These and following measurements have started transforming Cosmology from a largely qualitative endeavor to a precision science with a standard theory named the **Precision Cosmology** [1].

The **Chalmers Bolometer Group with collaborators** is the **only provider of the Cold-Electron Bolometers** for the **third flight of BOOMERanG** scheduled for 2013. We hope on successful participation in the BOOMERanG-3 project and possible progress in exploring the dark Universe.

Recent cosmology experiments have discovered that the Universe consists of 73 % Dark Energy, 23 % Dark Matter, and only 4 % ordinary matter. Indeed, in 2006, a Nobel Prize was awarded for the experimental observation of anisotropies in the Cosmic Microwave Background radiation, and the subsequent realization that the expansion of the Universe is controlled by unknown forces [1, 2]. Experiments to resolve the nature of these mysterious dark components will require **a new generation of ultra-sensitive detectors.** European balloon project BOOMERANG [2], Russian space observatory MILLIMETRON [3], and ESA space polarometer B-Pole relate to measuring the polarisation of the CMB in order to detect gravity waves in the early moments of the Big Bang.

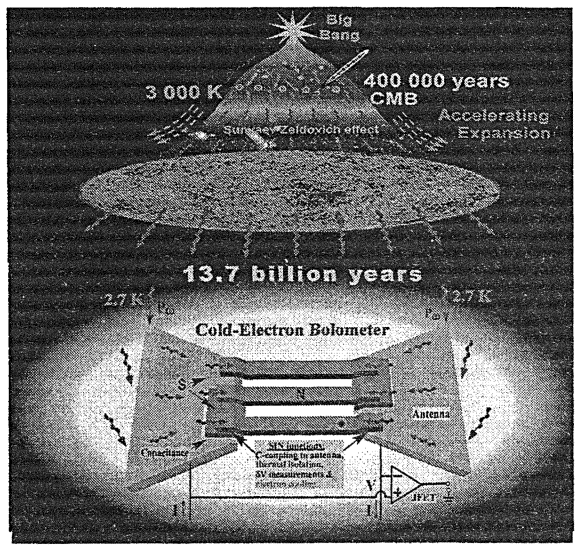

Fig. 2. Evolution of the Universe [1, 2] and a schematic view of the proposed CMB experiments with a Cold-Electron Bolometer (CEB). The novel concepts of 2D arrays of CEBs [4–6] are subject of development for BOOMERANG [2] and for MILLIMETRON [3] projects

2D Arrays of the Cold-Electron Bolometers

A novel concept of the ***Two-Dimensional array of Cold-Electron Bolometers (CEB) with dipole antennas*** is proposed for sensitive polarization measurements [4, 6] (Fig. 3). The main innovation is in combination of flexible parallel/series connections of CEB for DC with square distribution for RF signal. The parallel/series connection of CEBs in 2D array provides unlimited flexibility in matching to any readout from low-ohmic SQUID to high-ohmic JFET and CMOS readout. The CEB includes two Superconductor-Insulator-Normal (SIN) Tunnel Junctions with small nanoabsorber made of normal metal. Better noise performance are achieved by distribution of power between number of junctions increasing responsivity of each individual CEB. This mode of operation should lead to substantial improvements in sensitivity, dynamic range and reliability.

Fundamental sensitivity limits of the CEB arrays are below the photon noise $NEP = \sqrt{2}hfP_o$, which is referred to as the background-limited performance. This performance is better than any existing technology operating at the same optical power load. Estimations of the CEB noise with JFET readout show an opportunity to realize background-limited performance with NEP less than photon noise with NEP = $= 5 \cdot 10^{-17}$ W/Hz$^{1/2}$ at 350 GHz for an optical power load of 5 pW proposed for **BOOMERanG-3.**

Polarization resolution should be improved due to long arrays of dipole antennas with only narrow high ohmic orthogonal lines for dc connection at the ends

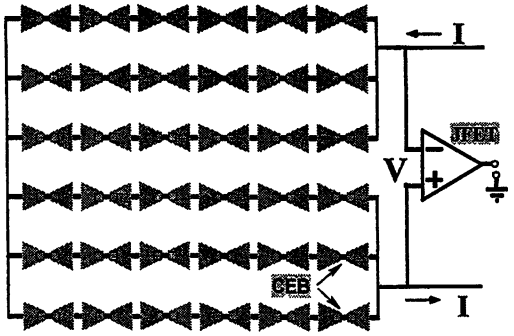

Fig 3. A 2D array of CEBs with single polarization dipole antennas and a JFET readout. This dipole antennas will be sensitive only to horizontal component of the RF signal. Reliability of 2D array is considerably increased due to parallel/series connections of CEBs

of arrays. Matching of Si substrate with vacuum could be done by Simulated Dielectric Antireflection Coating (SD-AR) or by classical AR coating or by using a Si phase Fresnel lens. However, the optimal option is visible as just a bare Si substrate of thickness $\lambda/4$ and a backshort behund the substrate.

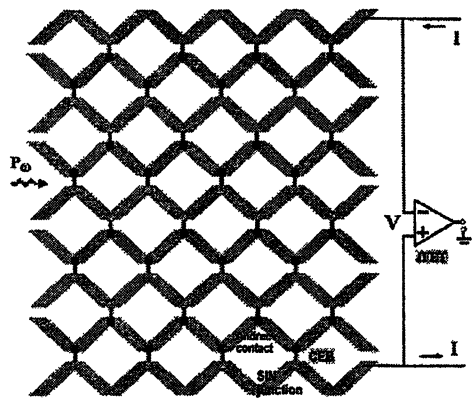

Fig. 4. A 2D array of CEBs with distributed cross-dipole antennas and a JFET readout. This multimode double polarization antennas are sensitive to both components of the RF signal. For analyzed array we use 4 CEBs in parallel and 8 rows of CEBs in series (N = 8)

A novel concept of the ***2D array of Cold-Electron Bolometers (CEB) with a Cross-Dipole Antennas*** is proposed for Ultra-Sensitive FTS (Fourier Transform Spectrometers) with measurements of both polarization components (Fig. 2). The optimal concept of the CEB including a Superconductor-Insulator-Normal (SIN) Tunnel Junction and an Andreev SN contact is proposed for better performance.

This concept provides better matching with JFET readout, suppresses charging noise related with Coulomb blockade due to small area of tunnel junctions, and decreases volume of a normal absorber for further improvement of noise performance. Reliability of 2D array is considerably increased due to parallel/series connections of several CEBs.

The 2D array of CEBs with distributed double polarization dipole antennas is sensitive to both components of an RF signal. Estimations of the CEB noise with JFET readout show an opportunity to realize NEP less than photon noise NEP = $4 \cdot 10^{-19}$ W/Hz$^{1/2}$ at 7 THz for an optical power load of 0.02 fW.

References

1. *Adrian Cho,* ***Insights of the Decade:*** **"Precision Cosmology"**. Science, **330,** p. 1615 (2010). http://www.sciencemag.org/site/special/insights2010/

2. **BOOMERANG** – balloon telescope: Measurements of CMB Polarization, Paolo de Bernardis, Rome University.
http://oberon.roma1.infn.it/boomerang/b2k/

3. **MILLIMETRON** – Russian Space Observatory led by Astro-Space Center; MSPU isresponsible for receiving system.
http://www.asc.rssi.ru/millimetron/eng/millim_eng.htm.

4. *Leonid Kuzmin,* "Two-Dimensional Array of Cold-Electron Bolometers for Ultrasensitive Polarization Measurements", to be published (2011).

5. *Peter K. Day, Henry G. LeDuc, Alexay Goldin, C Dowell, and Jonas Zmuidzinas.* Far-infrared/summillimeter imager-polarimeter using distributed antenna-coupled transition edge sensors. **5498,** p. 857-865, SPIE Proc. (2004).

6. *Leonid Kuzmin,* "Distributed Antenna-Coupled Cold-Electron Bolometers for Focal Plane Antenna", Proc of ISSTT conference, p. 154-158 (2008).

Ultrafast THz response of materials at extreme fields: Studies using laser-based and accelerator-based sources

D. Daranciang[1], J. Goodfellow[1], M. Fuchs[1], H. Wen[2], H. Loos[1], D. Reis[1], A. Fisher[1], A.M. Lindenberg[1]

[1]Stanford University/SLAC National Accelerator Laboratory, USA; aaronl@stanford.edu
[2]Advanced Photon Source, Argonne National Laboratory, USA

The generation of high intensity ultrafast terahertz (THz) single-cycle pulses provides new opportunities for all-optical application of biases to materials, and exploration of novel nonlinear responses at THz frequencies. Laboratory-based sources have reached pulse energies of 1-10 μJ and field strengths of order 1 MV/cm [1], and extending up to >10 MV/cm in the multi-cycle THz regime [2]. Complementary approaches using relativistic electron beams [3] to generate coherent transition radiation (CTR) at THz frequencies (in which each electron radiates in phase with it's neighbors) have reached similar maximum field strengths (of order 1 MV/cm) Here, we present recent experimental results obtained by extracting CTR radiation from relativistic electron beams generated at the Linac Coherent Light Source x-ray free electron laser, with electron bunch durations down to 50 fs and peak currents of 7 kA, generating THz pulse energies in excess of 100 μJ and fields that exceed 10 MV/cm, with bandwidth extending from 0.1 to 40 THz. These parameters represent a dramatic improvement over existing sources and open up novel opportunities in high field THz science. Extreme nonlinear responses are observed using silicon photodiodes as detector elements and we use this to carry out first THz nonlinear autocorrelation measurements of the pulse shape, with good agreement to models of the generated time-dependent electric field profile.

Figure 1 depicts an experimental schematic of terahertz extraction from the Linac Coherent Light Source. Highly compressed (τ = 50 to 200 fs FWHM), relativistic electron bunches with a charge q = 150 to 350 pC were generated by the SLAC National Accelerator Laboratory linear accelerator at a 10 Hz repetition rate and accelerated by 1 km of the accelerator to 14.5 GeV. A 2-μm-thick Be foil, tilted downward by 45°, was inserted into the electron beam, and the downward-emitted transition radiation was coupled out through a d = 1 in., 250-μm-thick diamond window, 5 in. away from the foil, into air. This light was reimaged onto a thermopile power meter for measurements of the pulse energy, reimaged onto a pyroelectric camera with 100 μm pixels for measurements of the spot size, or sent into a Michelson interferometer. As a check of the extracted energy, the electron beam energy loss was measured by the change in deflection of the electron bunch by a bending magnet located downstream of the foil, with the foil inserted and removed. For spectral characterization, the reflected beam from a Si beamsplitter was sent onto a pyroelectric detector for intensity normalization, the transmitted beam was sent into the interferometer, and a pyroelectric detector measured the linear autocorrelation at the output. A Si photodiode was the output detector for the nonlinear autocorrelations. In all cases, the radiation propagated approximately 2 m in air before being detected.

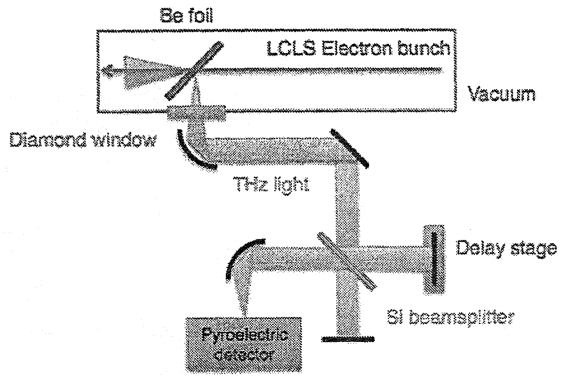

Fig. 1. Schematic of THz generation setup at the Linac Coherent Light Source (LCLS).

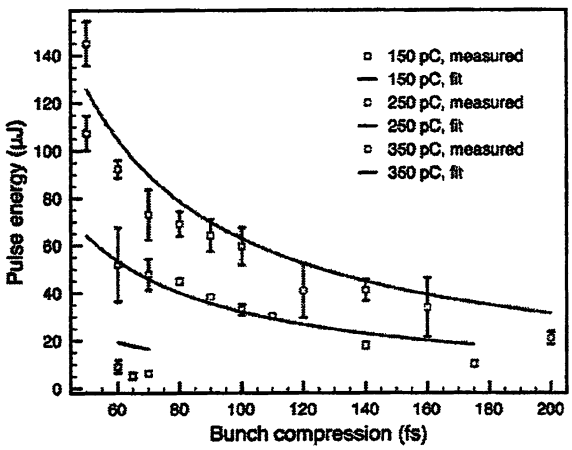

Fig. 2. Measurements of extracted THz energy as a function of pulse duration for different electron bunch currents. Observed scaling follows a Q^2/τ dependence as expected for CTR radiation (see text). Deviations at the shortest bunches reflect uncertainty in the actual bunch duration.

Results of measurements of the THz output energy on a thermopile power meter are shown in Figure 2. The most energetic pulses were obtained for q = 350 pC and τ = 50 fs, and under these conditions, the average pulse energy exceeded 140 μJ. We note that this measurement of τ likely represents an overestimate of the actual bunch duration, due to the abrupt cutoff of the spectrometer used to measure it, (Day-to-day variations in the photocathode injector and magnetic chicanes used to compress the bunch led to THz pulse energies of greater than 200 μJ for bunches

which also had a nominal length of $\tau = 50$ fs.) By plotting the pulse energy as a function of bunch charge and compression, we observe that the emitted energy follows a q^2/τ dependence. This can be explained by a simple model. The time-dependent electric field emitted by CTR depends upon the time-dependent bunch current, q/τ, so the emitted intensity is proportional to q^2/τ^2. Because we measure emitted energy, the time integral of this quantity is the observable, yielding a q^2/τ dependence.

By reimaging the extracted THz onto a pyroelectric camera a near-diffraction-limited spot size of 400 μm FWHM was measured, from which a peak electric field greater than 20 MV/cm is calculated, using the maximum pulse energy of 140 μJ for $\tau = 50$ fs. This calculation makes the simple approximation that the THz spatial profile near the focus is Gaussian, and assumes a Gaussian envelope for the time-dependent THz intensity. The far-field imaging used here prevents a diffraction-limited spot from being achieved, which would increase the peak field

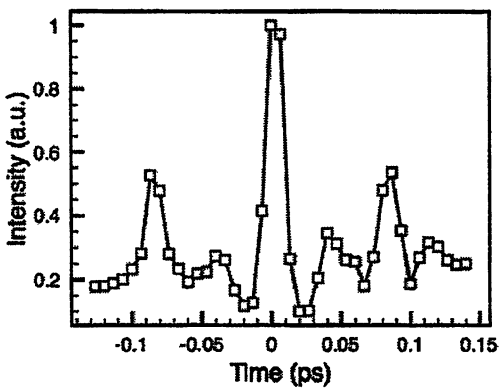

Fig. 3. Nonlinear THz autocorrelation of CTR THz puylses generated by 125 fs electron bunches.

In order to confirm the pulse energy measured by the thermopile, direct measurements of the electron beam energy loss were made. For $q = 350$ pC and $\tau = 50$ fs, the loss measured due to the foil is 2.9 mJ, which corroborates the pulse energy measurements shown in Figure 2 and is comparable to the energy loss due to the x-ray free electron laser process at LCLS. This measurement determines the upper limit for the energy that is extracted by the Be foil, and does not account for reflection losses on the diamond window, Coulomb scattering of the electron beam in the foil, the energy loss due to forward emitted THz from CTR, the small solid angle subtended by the 1" diameter diamond window, and losses due to reabsorption of the THz in air along the propagation length. These energy losses likely account for the disparity between the electron energy loss scans and the pulse energy measured at the thermopile.

The high intensities generated here enable us to observe a range of nonlinear THz responses in solids [4-6]. We observe in particular strong signals on silicon photodiodes (bandgap 1.1 eV ~ 270 THz, much higher than the cutoff frequency of the source). Insertion of a thin germanium crystal with bandgap 0.7 eV does not significantly change the signal level apart from reflection losses indicating that this is not a low-order multiphoton process driven by the high-energy tails of the THz spectrum. We made use of this nonlinear response to carry out the first ultrafast THz nonlinear autocorrelations, using the Michelson interferometer setup described above with a Si photodiode as detector. The measured nonlinear autocorrelation from a $q = 350$ pC, $\tau = 125$ fs electron bunch is shown in Figure 3. The shape of this spectrum is in good agreement with that expected from the double-horned uncompressed electron bunch temporal profile, thereby generating three peaks as observed. While direct knowledge of the nonlinear response is required to extract the most quantitative information (investigation currently in progress), these measurements indicate a relatively simple method for measuring THz pulse shapes at high-field THz sources.

References

1. *Hirori, H. et al.* Single-cycle terahertz pulses with amplitudes exceeding 1 MV/cm generated by optical rectification in $LiNbO_3$ // Appl. Phys. Lett. 2011. V. 98,. P. 519–522.

2. *Sell, A., Leitenstorfer A., Huber, R.* Phase-locked generation and field-resolved detection of widely tunable terahertz pulses with amplitudes exceeding 100 MV/cm. // Opt. Lett., 2008. V. 33, P. 2767-2769.

3. *Shen, Y. et al.* Nonlinear cross-phase modulation with intense single-cycle terahertz pulses // Phys. Rev. Lett. 2007. V. 99. P. 043901.

4. *Wen, H., Wiczer, M., Lindenberg, A.M.* Ultrafast electron cascades in semiconductors driven by intense femtosecond THz pulses // Phys. Rev. B 2008. V 78. P. 125203.

5. *Kuehn, W. et al.* THz-induced interband tunneling of electrons in GaAs // Phys. Rev. B 2010. V. 82. P. 075204.

6. *Hoffman, M.C. et al.* THz-pump--THz-probe spectroscopy of semiconductors at high field strengths // J. Opt. Soc. Am. B 2009. V 26. P. A29-A34.

Gyrotron Amplifiers and Gyro-BWOs with Helically Corrugated Waveguides

A. D. R. Phelps[1], V. L. Bratman[2], A. W. Cross[1], G. G. Denisov[2], C. R. Donaldson[1], W. He[1], C. W. Robertson[1], K. Ronald[1], S. V. Samsonov[2], C. G. Whyte[1], A. R. Young[1], L. Zhang[1]

[1]SUPA, Department of Physics, University of Strathclyde, Glasgow, G4 0NG, Scotland, UK, a.d.r.phelps@strath.ac.uk
[2]Institute of Applied Physics of the Russian Academy of Sciences, Nizhny Novgorod, 603950, Russia

This paper briefly reviews progress in gyro-devices with helically corrugated waveguides at frequencies from 10 to 100 GHz, pulse durations from tens of nanoseconds to CW and kWs to MWs power levels.

Gyro-traveling-wave tubes (gyro-TWTs) [1, 2] and gyro-backward-wave oscillators (gyro-BWOs) [1, 3] were considered early on in the development of microwave sources based on the electron cyclotron maser interaction. These fast-wave devices are linked via their names to the conventional slow-wave traveling-wave tubes and backward-wave oscillators based on Cherenkov interactions but they differ from them in that electrons move along helical trajectories and interact with fast waves. Because these fast wave interactions do not require wavelength-scale structures in the same way as conventional slow-wave TWTs and BWOs, they can provide much higher radiation powers at millimetre and sub-millimetre wavelengths. Until relatively recently gyro-TWTs and gyro-BWOs have not realised their full potential compared with the outstanding successes of some of the other members of the family of gyro-devices, namely gyrotrons and gyro-klystrons [4, 5]. The spread in electron beam velocities greatly reduces the performance of smooth waveguide gyro-TWTs and gyro-BWOs because the latter devices operate with significant values of the longitudinal wave number and hence the Doppler broadening of the cyclotron resonance results in poorer efficiency and reduced bandwidth. Gyrotrons and gyro-klystrons avoid this problem because they operate with longitudinal wave numbers very close to zero.

Many techniques have been applied to 'conventional' gyro-TWTs to improve their performance, including profiling the magnetic field and the waveguide cross-section [6–8] and applying distributed losses [9–11]. 'Conventional' gyro-BWOs [12,13] have received relatively less experimental attention. The authors of [14–17] proposed an alternative method allowing gyro-device operation with waves having simultaneously very high phase velocities and large group velocity, thus eliminating the high sensitivity to the particle-velocity spread. The idea of this method is a radical change in the dispersion of the operating wave, which is achieved by a transition from a waveguide with a smooth wall to a waveguide with a helical corrugation of the internal surface. For certain parameters, the helical corrugation efficiently couples the quasi-critical and traveling partial waves of the smooth oversized waveguide efficiently. A similar idea about coupling of the operating quasi-critical and auxiliary traveling waves on a helical corrugation was used, for a different purpose, earlier in gyrotrons [18]. As a result, in the region of small longitudinal wave numbers (high phase velocities), instead of the hyperbolic dispersion and a low group velocity typical of the smooth-waveguide modes, one of the eigenmodes can have a near linear dispersion with a sufficiently high group velocity. Such a wave can efficiently be used in gyro-TWTs and gyro-BWOs. In the case of a shallow corrugation, the dispersion of a helical waveguide can be found by the perturbation method [15, 16, 19], whereas for the deeper corrugation depths that are usually used in the present applications, one needs to use numerical calculation methods [20].

Unlike gyrotrons for which magnetron injection guns are usually used, the electron beams for helical gyro-devices have usually been produced either by (i) applying a "kicker" to impart rotational velocity to a thin rectilinear electron beam [17, 22-24] or (ii) using a cusp magnetic field configuration [21, 24-26].

Improving the efficiency of a helical gyro-BWO by energy recovery using a depressed collector has been demonstrated [27]. Impressive progress in gyro-devices with helical waveguides was reviewed in 2007 [28].

Helical waveguide gyro-devices have successfully operated in several frequency ranges including 8-10, 24, 33-35, 32-38 and 84-104 GHz.

Two examples of helical waveguides designed for a factor of 10 difference in frequency are shown in Fig. 1. A 84-104 GHz gyro-BWO, based on the helical waveguide shown in Fig. 1(b), is shown in Fig. 2. Although some of the early demonstrations of the benefits of applying the characteristics of helical waveguides to gyro-devices involved gyro-amplifiers [17, 23] there is also quite a lot of interest in gyro-BWOs [22, 26-30] based on helical waveguides.

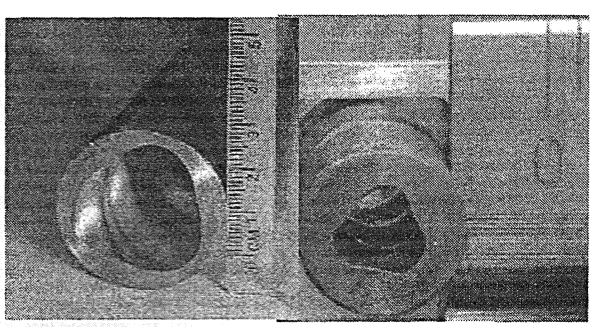

(a) (b)

Fig. 1. Helical waveguide (a) 8-10 GHz (b) 84-104 GHz

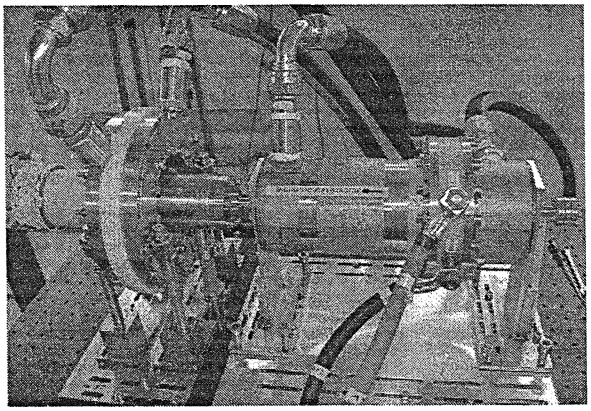

Fig. 2. 84-104 GHz gyro-BWO

Several of the early experiments both for gyro-amplifiers and gyro-BWOs were based on pulsed explosive-emission cathode guns and the trend has been for thermionic cathode electron guns to be introduced [24-28, 31] to provide the capability for longer pulses or CW operation. Cusp guns [24-26, 32, 33] for helical gyro-devices, while challenging to design have also received increasing attention. As the field of helical gyro-device research becomes more mature, the interest in increasing efficiency is motivating the development of depressed collector systems [27, 35-37].

References

1. *A. V. Gaponov*, Izv. Vyssh. Uchebn. Zaved., Radiofiz., **2**, No. 4, 443 (1959).

2. *V. V. Zheleznyakov*, Izv. Vyssh. Uchebn. Zaved., Radiofiz., **3**, No. 1, 57 (1960).

3. *R. H. Pantell*, Proc. IRE, **47**, 1146 (1959).

4. *A. V. Gaponov, M. I. Petelin, and V. K.Yulpatov*, Radiophys. Quantum Electron., **10**, Nos. 9–10, 794 (1967).

5. *J. L. Hirshfield and V. L. Granatstein*, IEEE Trans. Microwave Theory Tech., **MTT-25**, 522 (1977).

6. *P. E. Ferguson, G. Valier, and R. S. Symons*, IEEE Trans. Microwave Theory Tech., **MTT-29**,794 (1981).

7. *A. K. Ganguly and S.Ahn*, Int. J. Electron., **53**, 641 (1982).

8. *G. S. Park, J. J. Choi, S. Y. Park, et al.*, Phys. Rev. Lett., **74**, No. 12, 2399 (1995).

9. *K. R. Chu, H. Y. Chen, C. L. Hung, et al.*, Phys. Rev. Lett., **81**, 4760 (1998).

10. *M. Garven, J. P. Calame, B. G. Danly, et al.*, IEEE Trans. Plasma Sci., **30**, 885 (2002).

11. *D. E. Pershing, K. T. Nguyen, J. P. Calame, et al., IEEE* Trans. Plasma Sci., **32**, 947 (2004).

12. *S. Y. Park, R. H. Kyser, C. M. Armstrong, et al.*, IEEE Trans. Plasma Sci., **18**, 321 (1990).

13. *C. S. Kou, S. G. Chen, L. R. Barnett, et al.*, Phys. Rev. Lett., **70**, 924 (1993).

14. *G. G. Denisov, V. L.Bratman, A. D. R. Phelps, and S. V. Samsonov*, in: Digest 22nd Int. Conf. on Infrared and Millimeter Waves, Wintergreen, USA, 1997, p. 289.

15. *S. J. Cooke and G. G. Denisov*, Linear Theory of a Wide-Band Gyro-TWT Amplifier Using Spiral Waveguide, IEEE Trans. Plasma Sci., **26**, No. 3, 519-530 (1998).

16. *G. G. Denisov, V. L. Bratman, A. D. R. Phelps, and S. V. Samsonov*, IEEE Trans. Plasma Sci., **26**, No. 3, 508 (1998).

17. *G. G. Denisov, V. L. Bratman, A. W. Cross, et al.*, Phys. Rev. Lett., **81**, No. 25, 5680 (1998).

18. *A. L. Gol'denberg, G. S. Nusinovich, and A. B. Pavelyev*, in: Gyrotrons [in Russian], Inst. Appl. Phys., Gorky (1980), p. 91.

19. *N. F. Kovalev, I. M. Orlova, and M. I. Petelin*, Radiophys. Quantum Electron., **11**, No. 5, 449 (1968).

20. *G. Burt, S. V. Samsonov, K. Ronald, et al.*, Phys. Rev. E, **70**, No. 4, 046402 (2004).

21. *M. J. Rhee and W. W. Destler*, Phys. Fluids, **17**, 1574 (1974).

22. *S. V. Samsonov, V. L. Bratman, G. G. Denisov, et al.*, in: Proc. 12th Symp. on High Current Electronics, Tomsk, Russia, 2000, p. 403.

23. *V. L. Bratman, A. W. Cross, G. G. Denisov, et al.*, High-Gain Wide-Band Gyrotron Traveling Wave Amplifier with a Helically Corrugated Waveguide, Phys. Rev. Lett., **84**, No. 12, 2746-2749 (2000).

24. *V. L. Bratman, A. W.Cross, G. G. Denisov, et al.*, in: Proc. 5th Int. Workshop "Strong Microwaves in Plasmas", Nizhny Novgorod, Russia, 2002, p. 46.

25. *V. L. Bratman, G. G. Denisov, V. N. Manuilov, et al.*, in: Proc. 26th Int. Conf. on Infrared and Millimeter Waves, Toulouse, France, 2001, p. 5.

26. *V. L. Bratman, G. G. Denisov, S. V. Samsonov, et al.*, in: Abstr. of 3rd IEEE Int. Vacuum Electronics Conf., Monterey, USA, 2002, p. 359.

27. *S. V. Samsonov, G. G. Denisov, V. L. Bratman, et al.*, IEEE Trans. Plasma Sci., **32**, No. 3, 884 (2004).

28. *V. L. Bratman, G. G. Denisov, S. V. Samsonov, et al.* Radiophysics and Quantum Electronics, Vol. 50, No. 2, 96-107, 2007.

29. *W. He, K. Ronald, A. R. Young, et al*, Gyro-BWO experiments using a Helical Interaction Waveguide IEEE Trans. Electron Devices **52** (5), 839-844, (2005).

30. *W. He, A. W. Cross, A. D. R. Phelps, et al*, Theory and Simulations of a Gyrotron Backward Wave Oscillator Using a Helical Interaction Waveguide, Appl. Phys. Lett. **89** (9) 091504 (2006).

31. *A. W. Cross, W. He, A. D. R. Phelps, et al.*, Helically corrugated waveguide gyrotron traveling wave amplifier using a thermionic cathode electron gun, Appl. Phys. Lett. **90** (25) 253501 (2007).

32. *W. He, C. G. Whyte, E. G. Rafferty, et al.*, Appl. Phys. Lett. **93** (12) 121501 (2008).

33. *C. R. Donaldson, W. L. He, A. W. Cross, et al.*, IEEE Trans. Plasma Sci. **37** (11), 2153-2157 (2009).

34. *C. R. Donaldson, W. He, A. W. Cross, et al.*, A cusp electron gun for millimeter wave gyrodevices, Appl. Phys. Lett. **96** (14) 141501 (2010).

35. *L. Zhang, W. He, A. W. Cross, et al.*, Design of an energy recovery system for a gyrotron backward-wave oscillator, IEEE Trans. Plasma Sci. **37** (3), 390-394 (2009).

36. *L. Zhang, W. L. He, A. W. Cross et al.*, Numerical Optimization of a Multistage Depressed Collector With Secondary Electron Emission for an X-band Gyro-BWO, IEEE Trans. on Plasma Sci. **37** (12), 2328-2334 (2009).

37. *S. V. Samsonov, G. G. Denisov, I .G. Gachev, et al.* Development of helical-waveguide gyro-TWT and gyro-BWO, 34th Int. Conf. IRMMW-THz, Busan, South Korea 2009, pp. 448-449.

The Many Applications of ECH on the DIII-D Tokamak

R. Prater[1], J. Lohr[1], and the DIII-D Physics and Operations Teams

[1]General Atomics, P.O. Box. 85608, San Diego, California USA, prater@fusion.gat.com

Electron Cyclotron (EC) waves have been used in a very wide range of applications in discharges in DIII-D. Over the past decade, EC waves have become less an object of study and more a supplier of heat and current drive for other purposes in the experiments on DIII-D.

The characteristics [1] of EC wave heating (ECH) are quite different from those of neutral beam injection (NBI), the other main heating method for DIII-D. Unlike NBI, ECH power can be highly localized in space, giving a large power density. For most purposes, the heat conductivity along a flux surface is sufficiently large that the ECH and electron cyclotron current drive (ECCD) can be considered to be a function only of the normalized minor radius ρ. ECH power is deposited only in the electron fluid, unlike NBI which splits the power with most of the power going to ions, and also unlike NBI it does not provide either torque or a particle source. In these regards, ECH is an excellent proxy for plasma heating by fusion products. EC waves launched with a toroidal velocity component can provide a toroidal current [1], and for carefully chosen launch geometry the current density can be quite high since the radial extent of the current drive can be as small as $\Delta\rho = 0.02$. This narrow width can make the peak ECCD current density relatively large.

These unique chacteristics of ECH and ECCD support the application of EC power in a wide range of experiments on DIII-D. The ECH system on DIII-D has six gyrotrons operating at 110 GHz and producing power absorbed in the plasma up to 3.5 MW on a daily basis. The six launchers [2] can be independently aimed in the vertical and toroidal directions, and the incident polarization can be set to launch either the X-mode or O-mode for any launch angle. The frequency corresponds to the second harmonic of the electron cyclotron frequency at a magnetic field of 2.14 T, which is in the range of the normal operating space of DIII-D.

The ECH system is an important part of the DIII-D program. In the 2010 campaign, for example, there were 2524 discharges, for which substantial EC power was injected in 895, or 35 %. Applications of EC heating included torque-free electron heating for studies of intrinsic rotation and on the effect of core rotation on SOL flows; on the effect of pure electron heating on the H-mode threshold power; on T_e profile control for validation of the NBCD model; on RWM control in slowly rotating high beta plasmas; on suppression of some types of Alfven eigenmodes by ECH; on modeling ITER startup and rampdown; on 2nd harmonic preionization and heating; on modifying the temperature gradient for studying the transition to turbulence dominated by the trapped electron mode; and on QH-mode with co-injection of neutral beams. ECCD was applied to drive currents in the plasma in ITER demonstration steady-state discharges; for distributed current drive in support of fully noninductive operation at high beta; for control of neoclassical tearing modes for experiments on resistive wall modes in low rotation, high beta discharges; for neoclassical tearing mode control using oblique electron cyclotron emission as a diagnostic to determine robustly the optimum location of the ECCD; for studies of the validation of resistive MHD models; and for development of model-based current profile control. Some key results from recent applications of EC waves will be presented.

We are proposing to increase the ECH power to 15 MW (12 MW incident on the plasma). The primary objective is to have sufficient electron heating power that high performance discharges can be obtained with $T_e > T_i$ without introducing levels of torque that are unreasonable for fusion reactors. This is important because fusion reactors will have this condition due to the dominance of electron heating by fusion products, while gyrokinetic modeling indicates that the temperature ratio T_e/T_i has a strong influence on the types and amplitudes of turbulence that will dominate transport. Our studies have shown that gyrotrons operating at 117.5 GHz rather than 110 GHz will interface better with high performance configurations in DIII-D at the maximum toroidal field in DIII-D of 2.1 T. The power will be raised by developing new gyrotrons to operate at 1.5 MW of power, which raises the system power for six gyrotrons to 9 MW, and by adding three new gyrotron systems, for a total of 15 MW. In addition to supporting operation in the reactor regime of $T_e > T_i$, this system will contribute to overall program objectives by accessing the advanced steady-state conditions and suppressing multiple tearing modes that interfere with operation.

This work supported by the U.S. Department of Energy under DE-FC02-04ER54698.

References

1. *Prater, R.* Heating and current drive by electron cyclotron waves // Phys. Plasmas 2004. V. 11. P. 2349-2376.

2. *Ellis, R. A. Jr., Hosea, J., Wilson, J., Prater, R. and Callis, R.,* Design of a dual high-power, long pulse, steerable ECH launcher for DIII-D // 14th Topical Conf. Radio Frequency Power in Plasmas, AIP Conf. Proc. 2001. V. 595. P. 318-321.

Progress of Gyrotron Development in JAEA

Keishi Sakamoto, Ken Kajiwara, Yasuhisa Oda, Koji Takahashi, Kazuo Hayashi

Japan Atomic Energy Agency, 801-1, Mukoyama, Naka, Ibaraki 311-0193 Japan

Introduction

In Japan Atomic Energy Agency (JAEA), high power gyrotron developments are underway for a source of electron cyclotron heating and current drive (EC H&CD). For ITER application, where 20 MW EC H&CD system is planned[1,2], the development of 1MW 170GHz gyrotron has been carried out. In 2006, results of 1 MW / 800 s / 55%, 0.8 MW / 1 hr / 57% were obtained[3-5]. These satisfy the basic requirement of ITER for ITER Q=10 experiment. Followed this, a gyrotron reliability experiment, 5 kHz modulation, dual-frequency gyrotron development, have been carried out. The other activity in JAEA is a 110 GHz gyrtron development for JT-60SA, where 1.5 MW 4sec operation was demonstrated[6]. Here, the recent progress on the JAEA gyrotron development is reported, in particular, for 170 GHz gyrotron.

5 kHz full power modulation at CW

For the neo-classical-tearing (NTM) mode suppression for ITER, long pulse power modulation is required. The pulse duration in the modulation is limited by ~1 s at most in the present high frequency NTM suppression experiments, because of the overloads on the collector or a power supply system. When a finite beam current exists in the non-oscillation phase, large electron beam power hit the gyrotron collector. To avoid this, we performed a full beam current modulation at 5 kHz by the anode voltage switching of the triode electron gun. In Fig.1, the gyrotron and the power supply configuration of the JAEA test stand are shown. The body voltage V_{body}, which is equivalent to the depressed collector voltage is fed by the body power supply (BPS). The anode voltage V_{anode} is controlled to change a pitch factor of the electron beam keeping the beam acceleration voltage V_b constant. As the beam extraction voltage V_{ak} ($=V_{cathode}-V_{anode}$) decreases the beam current I_b does, and $I_b=0$ A at $V_{ak}=0$ kV. To realize the power modulation with the full beam current modulation, an anode switch composed of IGBT's (Insulated Gate Bipolar Transistor) is employed. If the anode switch is closed, the beam current is terminated. Fig.2 is an example of the 5 kHz full beam current and power modulation for 60 s at the output power of ~1.1 MW. Here, V_{dep}~24.3 kV, V_{catode}~-45.2 kV (main power supply voltage), I_{beam}~50A. As the beam current is zero at non-oscillation phase, the heat load on the collector is significantly decreased. It should be noted that the main power supply and the body power supply are CW operation. Consequently, the electron beam energy keeps a constant value, which is extremely important to obtain the stable RF oscillation for every pulse. It is concluded that the anode switching is simple and effective for CW power modulation. On ITER, long feeding cable run from the power supply (placed in the 1st floor of the RF building) to the anode terminal (2nd floor). The large capacity of the cable increases the rise time of the anode voltage, which causes the delay of the target mode excitation. To minimize the influence of the feed cable, we propose a double anode switch as shown in Fig. 3. In the modulation, flip-flop switching is done between SW1 and SW2, i.e., SW1 open and SW2 close (oscillation phase), and SW1 close and SW2 open (non-oscillation phase). The switch will be placed near the gyrotron in 2nd floor of ITER RF building.

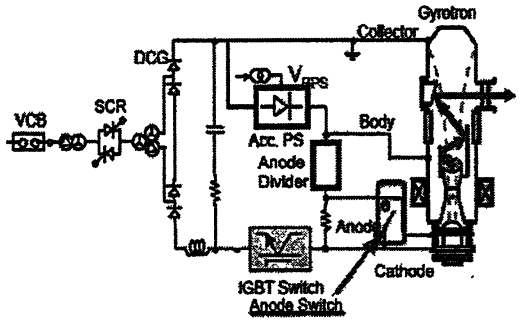

Fig. 1. Configuration of power supply of JAEA test stand and gyrotron with triode magnetron injection gun.

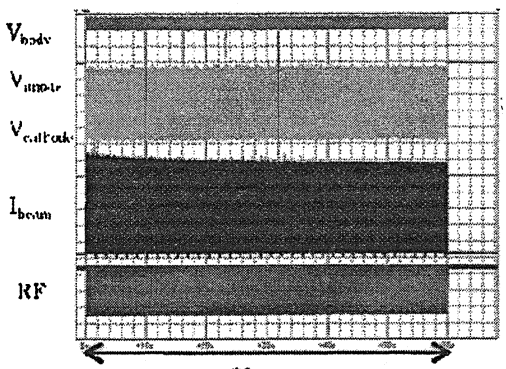

Fig. 2. Experimental result of full power modulation at 5 kHz with anode switching. Pulse duration is 60 s. RF power is ~1.1 MW.

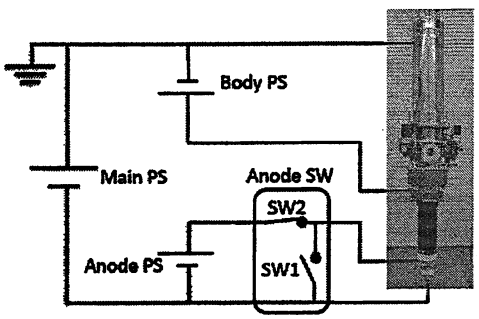

Fig. 3. Proposed power supply system for ITER to minimize the influence of the large capacitance of the long feed cable.

Reliability of the gyrotron

The reliability of the gyrotron is important for ITER operation. To demonstrate the reliability, repetitive power generation test was performed, which simulates the ITER operation[7]. The operation of 0.8 MW-600 s shots were repeated with an interval of 20~30 min. The total shots are more than 100 shots to obtain a statistical data. The electrical efficiency of each shot was in the 52 %-57 %. In Fig.4, the time history of the repetitive operation represented by the beam curent of the gyrotron is shown. After the morning conditioning shots, the repetitive operation was carried out in the afrernoon for 8-days. In the 88 trial shots, 72 shots was very stable 600 s operation, i.e., the success rate of 600 s shot was 82 %. Rest of the shots are terminated during the shot by the interlock. Reasons of the pulse termination are a photo-dignal increase measured by a photo-multiplier through the viewing port, sudden increase of the beam current, etc. One cause of the photo-signal increase is the mode transition resulting in the RF scattering in the tube. As a tentative conclusion, the gyrotron is reliable for ITER experiment. To increase the operational reliability further, the employment of the quick recovery system during the shot is effective in addition to the effort to suppress the interlock-event. For the fast recovery, the anode switch will be utilized to halt the beam current/power generation in a short time.

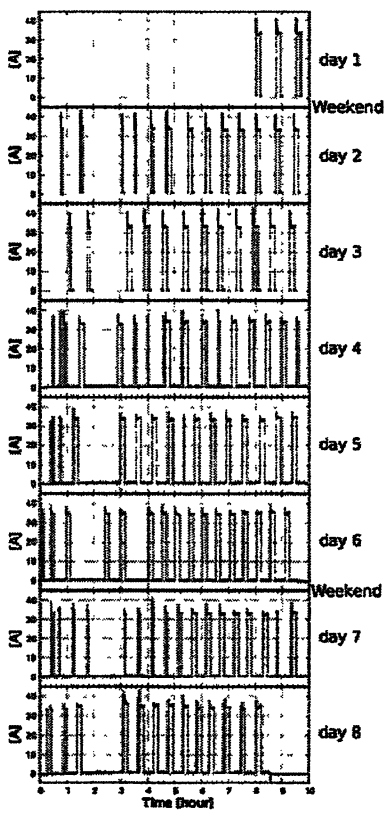

Fig. 4. Summary of pulse duration of repetitive operation of 10 min shots at 0.8 MW for 8 days. The interval of each shot is 20-30 min.

Dual frequency gyrotron

A development of a dual-frequency gyrotron is underway for a future advanced EC H&CD system. The design was made to satisfy the matching condition at the output window and to have a similar radiation angle from the window for both frequencies. As a result, modes of $TE_{31,11}$ and $TE_{25,9}$ are selected, which have frequencies of 170 GHz and 137 GHz, respectively. The oscillation is obtained by setting a proper magnetic field at the resonator (resonator filed). The optimum beam radius at the cavity is selected by setting a proper mirror ratio between the cavity field and MIG field. A pitch factor of the beam can be optimized by setting V_{ak} independently with the beam voltage. Up to now, the output power of 1.3 MW was obtained. And, 1 MW with efficiency of more than 30 % was also achieved for both frequencies. Further experiment will be continued aiming CW operation at both frequencies.

Conclusion

A progress of the ITER gyrotron development was described. The 5 kHz CW-relevant power modulation, which is inevitable for the NTM suppression of ITER plasma, was realized at 1.1 MW of each pulse. Here, the power was stable because the beam voltage is kept constant. In next, the double anode switching will be tried for ITER where the high capacitance long feeding cable is used.

For the ITER relevant operation, the 800kW/600s power generation was repeated for every ~30min. Temperature of all parts stabilized during the shot. High vacuum was kept during shot and returned to the original level by the next shot, and no influence is given to the following shots. The result indicates the gyrotron works in the ITER relevant operation. Finally, for the advanced EC H&CD system, the dual frequency gyrotron with the triode MIG is developed. By controlling the anode voltage, the optimum oscillation condition is obtained for both frequencies at the same beam voltage. This will make the EC H&CD system more attractive for fusion application.

References

1. *Henderson, M., et al,* An Overview of the ITER EC H&CD System // IRMMW-THz Conference, 21-25 Sept. 2009, Busan, Korea.

2. *Darbos, C., et al,* ECRH system for ITER // Proc. Of 18th Topical conf. on Radio Frequency Power in Plasmas, June 2009, Gent, Belgium, p.531 (2009).

3. *Sakamoto, K.*, et al, Nature Phys. 3 411 (2007).

4 *Kasugai, A.*,et al., Nuclear Fusion, 48, 5, 054009 (2009).

5. *Sakamoto, K.*, et al., Nuclear Fusion, 49, 9, 095019 (2009).

6. *Kobayashi, T.*, et al., Progress of high power and long pulse ECRF system development in JT-60// Proc of IAEA 23rd fusion energy conf., FTP/P6-13, Oct. (2010).

7. *Kajiwara, K.*, et al., J.Infrared, mm wave and terahertz waves, **32**, 3 329 (2010).

Status of Relativistic Electronics Research in Laboratories in the United States

E. Schamiloglu[1]

[1]Dept. of Electrical and Computer Engr., University of New Mexico, Albuquerque, NM 87131 USA, edl@ece.unm.edu

High power relativistic electronics basic research is ongoing in a handful of universities and government research laboratories in the U.S. This presentation provides a "snapshot" of some of these research activities. Five research topics emerge as dominating the research activities in recent years: novel cathode topologies for magnetrons, incorporating metamaterials in sources, novel source geometries, mode control (mode switching, phase locking, coherence), and continued developments in computational tools that have been responsible for all of the recent advances.

Novel Cathode Topologies for Magnetrons

Researchers at the University of New Mexico (UNM) and the U.S. Air Force Research Laboratory (AFRL) have been leading the effort on novel cathode topologies for magnetrons. The UNM group had developed the "transparent cathode" [1,2] for which two patents have been issued. The AFRL group has developed a "shaped cathode" [3]. Fig. 1 shows a schematic of a transparent cathode and a shaped cathode in a relativistic magnetron. Both of these cathodes have contributed to rapid start of oscillation, increased output power and efficiency, effective mode control, and operation over a much wider range of magnetic field in versions of the A6 magnetron.

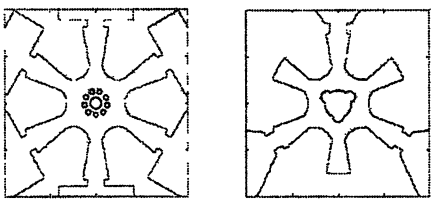

Fig. 1. Cross-sectional view of a relativistic magnetron with a transparent cathode (left) and a shaped cathode (right) [3].

Recently, researchers at AFRL reported simulations with improved magnetron performance using a metamaterial-inspired rodded cathode, shown in Fig. 2 [4]. Simulations of an L-band A6 magnetron demonstrate that the rodded quasi-metamaterial cathode allows the magnetron to automatically select one of the desired magnetron operating modes within a much broader range of the input operating parameters, as compared with the same magnetron working with a traditional smooth cylindrical cathode.

Incorporating Metamaterials in Sources

Researchers at MIT and AFRL have been leading the development of metamaterial structures for use in high power relativistic electronics. In 2005 MIT had demonstrated a 17 GHz high gradient accelerator using a photonic-band-gap structure [5]. Recently, in a collaboration with researchers at SLAC, the PBG structure was tested at an accelerating gradient of 65 MV/m yielding a breakdown rate of two breakdowns per hour at 60 Hz [6]. An accelerating gradient above 110 MV/m was demonstrated at a higher breakdown rate. Significant pulsed heating occurred on the surface of the inner rods of the PBG structure, with a temperature rise of 85 K estimated when operating in 100 ns pulses at a gradient of 100 MV/m and a surface magnetic field of 890 kA/m. Their hypothesis is that the moderate level electric field on the inner rods, about 14 MV/m, is enhanced at small tips and projections caused by pulsed heating, leading to breakdown.

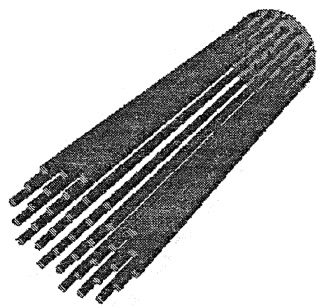

Fig. 2. Schematic of a quasi-metamaterial rodded cathode [4].

The Cerenkov maser consists of a hollow cylinder loaded with a dielectric material. Although the Cerenkov maser has been demonstrated, it suffers from the dielectric charging and eventually failing under high power conditions. Researchers at AFRL recently developed a dielectric Cerenkov maser formed using metallic microwave metamaterials in the form of concentric rings [7] (Fig. 3). Such an artificial dielectric does not suffer from charging. The researchers propose that metamaterials provide a practical new opportunity for vacuum electron devices, opening the means for new sources operating in the RF and microwave to THz regimes.

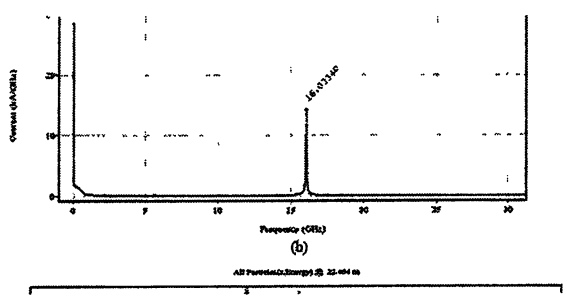

Fig. 3. Particle-in cell (PIC) simulation at 22.4 ns showing electron beam bunching in a Cerenkov maser using an artificial dielectric (rings shown in blue above the red electrons) [7].

Novel Source Geometries

Researchers the University of Michigan (UM) and UNM have been working on new source concepts. The UM group has developed using PIC simulations a recirculating planar magnetron in which the electron beam is negative mass unstable [8]. The negative mass instability in this case promotes rapid start-up of the magnetron. The experiment is presently under construction.

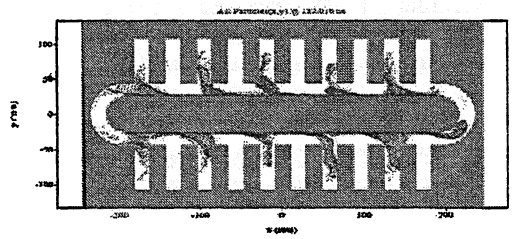

Fig. 4. Particle-in cell simulation at 132 ns with an axial magnetic field and radial electric field. The electrons (red) are negative mass unstable. (Figure courtesy of UM.)

The UNM group recently demonstrated a 70% efficient relativistic magnetron with diffraction output (MDO) [9]. This device was originally developed at the Institute of Applied Physics in Gorky in 1977. However, the efficiency of the device in experiment was poor and the device was no longer pursued. The UNM group revisited this device in PIC simulation following the publication from a group in Japan that noted that the original Russian design used an aperture that was cutoff for the radiation generated [10]. The Japanese group obtained 37% efficiency. The UNM group, through further refinements and the use of a transparent cathode instead of a solid cathode was able to demonstrate 70% efficiency.

Mode Control

Researchers at UNM have been studying RF mode switching in a relativistic MDO [11]. The idea is to use a weak input signal to rapidly switch the operating mode in the device when the applied magnetic field is close to the critical magnetic field that separates the operating point between two modes. This topic is discussed in an accompanying paper [12].

Development of Computational Tools

Researchers in relativistic electronics rely very heavily on the use of PIC codes. This was not always the case. Up until the mid-1990's or so the computational tools were useful qualitatively to yield additional insight into the physics of the operation of such sources. The fidelity of the simulations became so good that following the mid-1990's these computational tools are used to actually design relativistic electron sources. Today, in the U.S., no experiment with a source will be approved without a simulation yielding the necessary performance. This is why the use of these simulation tools is referred to as "virtual prototyping."

The University community in the U.S. uses the MAGIC PIC code [13] that runs on an ordinary PC. The state-of-the-art in PIC simulation tools is AFRL's ICEPIC [3], which runs on a massively parallel machine. These codes are continuously updated with additional physics (such as surface physics models, background plasmas, *etc.*) being incorporated. Algorithms are also evolving to take advantage of new types of hardware that are emerging.

Acknowledgments

The author wishes to thank the organizers for inviting him to present this overview. The content of this paper and presentation is the author's sole responsibility. The author is supported by grants from AFOSR and ONR.

References

1. *Fuks, M. I., Schamiloglu, E.* Rapid start of oscillations in a magnetron with a "transparent cathode" // Phys. Rev. Lett. 2005. V. 95, P. 205101-1-4.

2. *Bosman, H., Fuks, M., Prasad, S., Schamiloglu, E.* Improvement of the output characteristics of magnetrons using the transparent cathode // IEEE Trans. Plasma Sci. 2006. V. 34, P. 606-619.

3. *Fleming, T. P., Mardahl, P. J., Bowers, L., Cartwright, K. L., Bettencourt, M. T., Haworth, M. D.* Virtual prototyping of novel cathode designs for the relativistic magnetron // Comp. Sci. Engr. 2007. V. Nov/Dec, P. 18-28.

4. *Andreev, A. D., Hendricks, K. J.* Multi-cavity magnetron with the "rodded" quasi-metamaterial cathode // Phys. Plasmas 2011 (submitted).

5. *Smirnova, E. I., Kesar, A. S., Mastovsky, I., Shapiro, M. A., Temkin, R. J.* Demonstration of a 17-GHz, high-gradient accelerator with a photonic-band-gap structure // Phys. Rev. Lett. 2005. V. 95, P. 074801-1-4.

6. *Marsh, R. A., Shapiro, M. A., Temkin, R. J., Dolgashev, V. A., Laurent, L. L., Lewandowski, J. R., Yeremian, A. D., Tantawi, S. G.* X-band photonic band-gap accelerator structure breakdown experiment // Phys. Rev. S.T. Accel. Beams 2011. V. 14, P. 021301-1-11.

7. *Shiffler, D., Luginsland, J., French, D. M., Watrous, J.* A Cerenkov-like maser based on a metamaterial structure // IEEE Trans. Plasma Sci. 2010. V. 38, P. 1462-1465.

8. *French, D. M., Hoff, B. W., Lau, Y. Y., Gilgenbach, R. M.* Negative, positive, and infinite mass properties of a rotating electron beam // Appl. Phys. Lett. 2010. V. 97, P. 111501-1-3.

9. *Fuks, M. I., Schamiloglu, E.* 70% efficient relativistic magnetron with axial extraction of radiation through a horn antenna // IEEE Trans. Plasma Sci. 2010. V. 38, P. 1302-1312.

10. *Daimon, M., Jiang, W.* Modified configuration of relativistic magnetron with diffraction output for efficiency improvement // Appl. Phys. Lett. 2007. V. 91, P. 191503-1-3.

11. *Liu, M., Michel, C., Prasad, S., Fuks, M. I., Schamiloglu, E., Liu, C.-L.* RF mode switching in a relativistic magnetron with diffraction output // Appl. Phys. Lett. 2010. V. 97, No. 1, P. 251501-1-3.

12. *Fuks, M. I., Liu, M. Schamiloglu, E.* Mode switching and phase locking in a relativistic magnetron with diffraction output (this conference).

13. *Goplen, B., Ludeking, L., Smithe, D., Warren, G.* User-configurable MAGIC for electromagnetic PIC calculations // Comp. Phys. Commun. 1995. V. 87. P. 54-86.

The Basis of the Plasma Methods of Diagnostics and Detection of THz Radiation

A.B. Borodin[1], M.N. Esalkov[1], I.I. Kuritsin[1], A.A. Frolov[2], and A.P. Shkurinov[1]

[1] Department of Physics, M.V. Lomonosov Moscow State University, Moscow, Russia.
[2] Institute for High Energy Densities, RAS, Moscow, Russia

The paper studies both theoretically and experimentally simultaneous process of generation and detection of the THz pulsed radiation in the plasma optical breakdown. The algorithm of single-valued and correct reconstruction of the temporal profile of the initial THz pulse is suggested.

Simultaneous generation and THz pulse radiation detection in plasma breakdown named «ABCD technique» [1] allow us to create THz time-domain systems with an extraordinary spectral range. Self-descriptiveness and adequacy of the information obtained with the help of such systems is determined by mutual influence of generation and detection processes in plasma media. Each of them in itself is fairly hard to describe, but being combined together for proper interpretation of the received data they demand, first of all, the detection process simulation.

One of the methods of the THz pulsed radiation detection is connected with the detection of second harmonics (SH) $2\omega_0$ of laser radiation which appears as a result of nonlinear interaction of laser radiation at the carrier frequency ω_0 with THz wave in rarefied plasma, formed as a result of air photoionization [2].

We assume in our model that at some distance from the laser beam waist air ionization practically disappears due to the decrease of radiation intensity. Therefore, a sharp boundary appears which separates the area taken by the plasma from the area with non-ionized air. In connection with this we assume that THz radiation generation will take place owing to the propagation of laser pulse in this area of the sharp density gradient. This mechanism has been well known since 1962 and is called "transitional radiation" [3].

In this work to describe numerically the THz pulse and the detection SH generation process of laser radiation we used the Maxwell equations for electric field **E** and magnetic field **B** and also hydrodynamic equations for velocity **V** and **n** density of plasma electrons.

In the experiment and simulations we used Ti: Spp laser generating pulses at the wavelength $\lambda_0 = 0.8$ μm with duration $\tau_{FWHM} = 32$ fs and the power $W_1 = 1.2$ mJ. The dependence of the normalized spectral energy of THz radiation is shown in figure. The theoretical and experimental spectra have got two maxima, one of them is sharper and is around the frequency of 11 THz and corresponds to the radiation of at plasma frequency. The second peak – which is much more gentle and wide is in the low frequency area of the spectrum around 1.3 THz. We should note a good coincidence of the theoretical results here for the positions of the peaks in the theoretical and experimental radiation and detection spectrum.

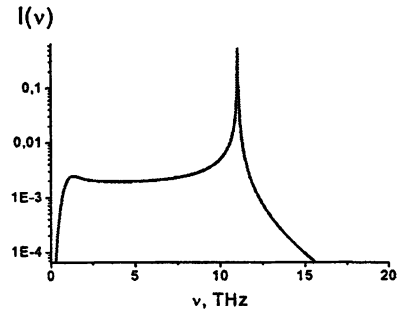

For the description of the THz detection in the plasma area we used the same model. Neglecting the difference of the group velocity of the laser and THz radiation from the speed of light, which is acceptable in rarefield plasma, we obtained the following expression for the radiation intensity at the doubled laser frequency

$$I_{2\omega} = -\frac{\omega_p^4 D^2 \tau^2}{16\pi c}\left(\left[e_L(e_L E_0) + \frac{1}{2}E_0\right]\times \right.$$
$$\left.\times\left[e_L(e_L e_T) + \frac{1}{2}e_T\right]\right)\frac{\partial}{\partial\xi}I_L^2\int_0^{\xi} d\zeta E_T(\zeta) \qquad (1)$$

where D – is the thickness of the effective plasma interaction area, τ – duration of the laser pulse, I_L – dimentionless intensity of the laser radiation at the fundamental frequency, e_L and e_T – polarization vectors of laser and terahertz radiations, $\xi = z - ct$ – is the longitudinal variable.

The expression obtained for the radiation intensity at the SH of the laser field (1) gives the opportunity to reconstruct the temporal profile of the THz pulse. Really, measuring the dependency $I_{2\omega}$ as the function of time, with the known plasma and laser parameters at the fundamental frequency, we can simulate the integral $\int_0^{\xi} d\zeta E_T(\zeta)$ which in its turn enables us to reconstract the temporal profile $E_T(\zeta)$ of the electric field of the true THz pulse.

References

1. *J. Dai, X. Xie, and X.-C. Zhang*, "Detection of broadband terahertz waves with a laser-induced plasma in gases," Phys. Rev. Lett. 97, 103903 (2006).

2. *I.A. Kotelnikov, A.V. Borodin, A.P. Shkurinov*, "Miltiphoton ionization of atom by dual color laser pulse" JETP, 139 (6) 1081 (2011).

3. *G.A. Askarian*, "Cherenkov and transition radiation from electromagnetic waves", JETP, 42 (5) 1360 (1962).

Impact of Low-Power Millimeter Waves on Cell Membrane Potential

P.H. Siegel[1] and V. Pikov[2]

[1]California Institute of Technology, Pasadena, CA, USA, 91125, phs@caltech.edu
[2]Huntington Medical Research Institutes, Pasadena, CA, USA 91105

Investigations on the biological impact of low levels of millimeter-wave energy date back to the first experiments on the generation and detection of these high frequency signals by Sir Jagadis Chunder Bose at the end of the 19th century. A bit more than a hundred years later, millimeter-wave transmission has become a ubiquitous commercial reality. Despite the widespread use of millimeter-wave transmitters for communications, radar and even non-lethal weapons systems, only a handful of researchers in the USA have funded programs focusing on millimeter-wave interactions with biological systems. As such, there is a growing need for a better understanding of the mechanisms of these interactions and their possible adverse and therapeutic implications. Independent of the health impact of long term exposure to high doses of millimeter-wave energy on whole organisms, there exists the potential for subtle effects on specific tissues or organs which can best be quantified in studies which examine real-time changes in cellular function as energy is applied. In this talk we present a series of experiments which show changes in neuron response with exposure to very low levels of millimeter wave power. The findings have implications for non-contact stimulation and control of neurologic function and might prove useful in a variety of health applications from suppression of peripheral neuropathic pain to the treatment of central neurological disorders.

1. Introduction

In 1901 Sir Jagadis Chunder Bose, often cited as the "father of millimeter-waves" is quoted as stating [1], "How lucky we are that the natural eye absorbs this radiation and protects us by veiling our sense against insufferable radiance in these days of space-signaling by Hertzian waves." 100 years later, we find ourselves in a world where we are continuously bathed in low power microwave and millimeter-wave radiation. The deployment of millimeter-wave, and soon THz, generators for wireless telecommunications [2], airport and checkpoint security screening [3], and even non-lethal crowd control weapons [4] has placed millimeter waves in the forefront of concerns over the unrestricted dose of RF energy in the public environment. This should have prompted renewed scientific interest in the effects of this wavelength range on biologic materials and organisms. However very few researchers and no US agencies are currently funding research in this field. Independent of the health impact of long term exposure to high doses of millimeter-wave energy on whole organisms, there exists the potential for subtle effects on specific tissues or organs which can best be quantified in studies which examine real-time changes in cellular function as energy is applied. In this talk we give results on some first experiments on cell membrane depolarization and neuronal stimulation as responses to levels of millimeter-wave power more than 1000 times below the MPE (maximum permissible exposure).

2. Results

Two independent types of measurements (optical and electrical) have been performed in vitro and in vivo to date, using both epithelial cells and neurons. One set of measurements involves fluorescent tagging of the fGFP plasmid to the inner lining of the lipid bilayer. On exposure to blue light, and when millimeter waves are present, a FRET process causes the fluorescent signature to shift from green to red if the membrane forms nanopores [Figs. 1-2]. This process has been recorded using 60 GHz exposures of 1 - 2 minutes at power levels below 1 mW/cm^2 [5]. A second series of measurements have been made on rat pup cortical slices using standard patch clamp techniques [Figs 3-6]. In these experiments membrane depolarization is observed through changes in action potential rise and fall times. In addition neural stimulation and suppression are observed at power levels below 1 microwatt/cm^2[6]. In a final set of measurements on leech neural ganglia [Figs. 7-8] using intracellular probes, similar suppression of AP firing rate and decrease in membrane resistance are observed with power levels of 10-100 microwatts/cm^2[7]. The data strongly suggests that stimulus-response pairing is present and that MMW interactions with tissue occur at much lower intensities than previously thought. The implications of the preliminary findings are widespread and impact the fields of environmental health and safety as well as providing the potential for positive therapeutic application.

References

1. *Peter H. Siegel*, "Sir Jagadis Chundra Bose: Traversing the interdisciplinary gap between physics and biology," IEEE Microwave Magazine, vol. 10, no. 2, pp. 119-121, 2009.

2. *G. Lawton*, "Wireless HD Video Heats Up," Computer, v. 41, pp.18-20, 2008.

3. *U.S. Transportation Security Adm.*, Imaging Technologies, Millimeter Wave Passenger Imaging Tech. Pilot, 2009.

http://www.tsa.gov/approach/tech/imaging_technology.shtm

4. *S. Levine* "The Active Denial System. A Revolutionary, Non-lethal Weapon for Today's Battlefield," ADA501865, 1-17, 2009.

5. *P.H. Siegel and V. Pikov*, "THz in Biology and Medicine: Towards Quantifying and Understanding the Interaction of Millimeter- and Submillimeter-Waves with Cells and Cell Processes," SPIE BiOS 7562: 75620H, 2010.

6. *V. Pikov, X. Arakaki, M. Harrington, S.E. Fraser and P.H. Siegel*, "Modulation of neuronal activity and plasma membrane properties with low-power millimeter waves in organotypic cortical slices," Journal of Neural Engineering, 7(4): 045003, 2010.

7. *V. Pikov and Peter H. Siegel*, "millimeter wave-induced changes in membrane properties of leech Retzius neurons," to appear in SPIE BiOS 2011.

Study of High T_e Plasma Characteristics of LHD Using High Power 77 GHz Gyrotrons

H. Takahashi[1], T. Shimozuma[1], S. Ito[1], S. Kubo[1], Y. Yoshimura[1], H. Igami[1], M. Nishiura[1], S. Kobayashi[1], Y. Mizuno[1], K. Okada[1], Y. Takita[1], I. Yamada[1], M. Yokoyama[1], T. Ido[1], A. Shimizu[1], K. Ida[1], S. Matsuoka[1], S. Satake[1], T. Mutoh[1] and the LHD experiment group[1]

[1]National Institute for Fusion Science, Toki 509-5292, Japan, takahashi.hiromi@LHD.nifs.ac.jp

Since 2006, the installation of 77 GHz gyrotrons with each output power of over 1 MW has progressed in the Large Helical Device (LHD) [1]. In the LHD, an ECRH system with seven gyrotrons, whose frequencies are 77, 82.7, 84 and 168 GHz, has been operated for plasma generation and heating. In the present state, three 77 GHz gyrotrons are operational for plasma experiments. The total injection power of ECRH to the plasma (P_{ECH}) significantly increased due to the installation of the 77 GHz tubes and reached a value of 4 MW. The actual value of the simultaneous injection power to LHD is slightly low (~3.7 MW) because the total input power for the gyrotrons is limited by the power capacity of the transformer.

The anode voltage (V_A) of the 77 GHz gyrotrons can be flexibly controlled using the preset waveform and the improvement of the electric efficiency was successfully achieved by applying stepwise V_A. Figure 1 shows the time evolution of (a) the applied voltage for collector V_C, for body V_B and for anode V_A, (b) the beam current I_C, the anode current I_A and the body current I_B and (c) the MOU output power for the latest-installed 77 GHz gyrotron. In this operation, enough low V_A not to start oscillation was applied for 100 ms. After that, V_A was increased to ~40 kV and the output power of 1.8 MW was stationary obtained for 1 s.

The charge neutralization of the gyrotron electron beam due to the ionization of the residual gas in the tube [2] is a key for the improvement of the electric efficiency by the stepwise V_A applying. Figure 2 shows the dependence of the MOU output power on (a) V_B, (b) T_1 and (c) I_C, where T_1 denotes the duration of the first step of the stepwise V_A. The electric efficiency η is also plotted in fig. 2 (c). The circles and triangles in fig. 2 (a) and (c) represent the results of the operations with the stepwise V_A and the regular V_A (rectangular waveform), respectively. T_1 was fixed at 100 ms for the case of the stepwise V_A in fig. 2 (a) and (c). In fig. 2 (b), the gyrotron operation parameters

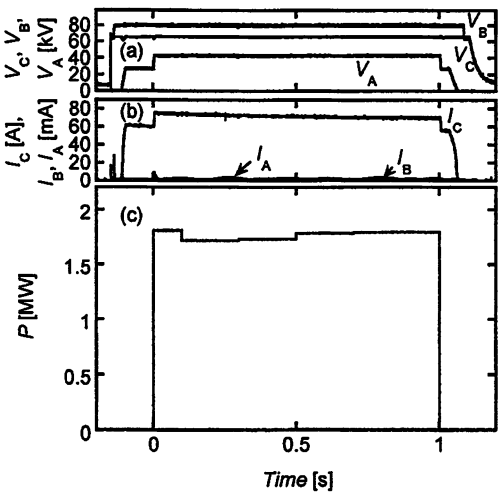

Fig. 1. The time evolution of (a) the applied voltage for collector V_C, for body V_B, for anode V_A, (b) the beam current I_C, the anode current I_A, the body current I_B and (c) the output power in the oscillation of 1.8 MW/ 1 s

were kept unchanged except for T_1. The oscillation duration T_p was set at 10 ms for all these operations in fig. 2 (a)–(c). As can be seen from fig. 2 (a), the operation with the regular V_A required 5~6 kV higher V_B to generate the similar output power with the stepwise V_A case. This means that the drop of the beam accelerating voltage occurred for the regular V_A case due to the space charge effect of the electron beam. Figure 2 (b) shows that the output power increased with the increase of the first step duration and was saturated for the longer duration than 50 ms. This indicates that the drop of the accelerating voltage recovered through the charge neutralization process in the T_1 phase and the space charge was fully neutralized for ~50 ms in the operation. These results suggest that the gyrotron operational parameters are able to be optimized for the fully accelerated electron beam by applying the stepwise V_A with the adequate T_1 duration, leading to the improvement of the output power and the electric efficiency as shown in fig. 2 (c).

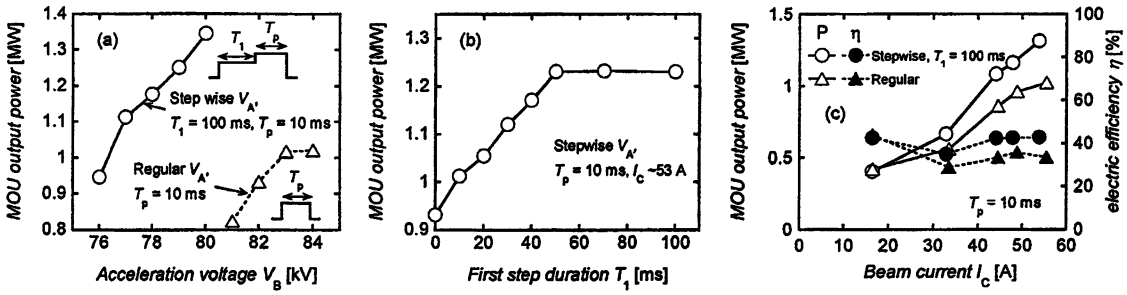

Fig. 2. The dependence of the MOU output power on (a) V_B, (b) T_1 and (c) I_C

These high power gyrotrons enabled us to achieve a higher electron temperature (T_e) than that previously obtained [3] and also to investigate characteristics of high T_e, low collisionality plasmas. In the 2010 experimental campaign, the central electron temperature T_{e0} of 20 keV at $n_e = 0.2 \cdot 10^{19}$ m^{-3} as a new record of LHD and $T_{e0} = 8.7$ keV at $n_e = 1.1 \cdot 10^{19}$ m^{-3} were successfully achieved with P_{ECH} ~3.7 MW.

HX-PHA, SXCCD and ECE measurement showed that there was a certain amount of superthermal electrons in the high T_e, low collisional plasmas. However, we have already confirmed that there was only small effect of the superthermal electrons for the bulk plasma temperature evaluation by the Thomson scattering measurement. An increase of superthermal electrons decreases the deposition power to bulk plasma because a part of the ECRH power is used for the production and/or the acceleration of the superthermal electrons [4].

These high T_e plasmas accompanied an electron internal transport barrier (e-ITB) [5]. The formation process of an e-ITB for high T_e plasmas was able to be observed due to the improvement of the accuracy of the Thomson scattering measurement [6]. Figure 3 shows the time evolution of (a)–(d) T_e and n_e profiles, (e) r_{in} and r_{out} and (f) T_e gradient at the effective minor radius of $r_{eff} = 0.078$ m, where r_{in} and r_{out} are the radial positions of the inner and the outer boundary of the local flattening in the T_e profiles, respectively. The rotational transform profile for a vacuum condition is attached in (a)–(d) and the rational surface of $\iota/2\pi =$ $= 0.5$ is located at r_{eff} ~0.25 m. ECRH was injected perpendicularly during $t = 0.21$–0.71 s with $P_{ECH} =$ $= 2.63$ MW. Highly accurate T_e profiles were successfully obtained by the accumulation of the intensity of Thomson scattered light through 20 discharges with the three YAG lasers all injected together.

At the beginning of the discharge, a flat T_e profile with a small bump was observed and a peaked T_e profile was formed at $t = 0.5$ s. After that r_{in}, which corresponds to the foot point of the e-ITB, moved outward. On the contrary, r_{out} shifted inward and the local flattening gradually shrunk. Fig. 3 (f) indicates that the T_e gradient increased during the discharge. Thus it is said that the increase of T_{e0} was due to r_{in} moving outward and the e-ITB growing. Recently, similar experiments were carried out with a longer pulse ECRH. In the experiments, it was found that r_{in} reached slightly inside position of the rational surface of $\iota/2\pi = 0.5$ and then the local flattening around the rational surface disappeared. After the healing of the local flattening, r_{in} stopped outward moving, namely the foot point of the e-ITB did not move across the rational surface.

The detailed verification of the role of the lower-order rational surface to determine the e-ITB structure and the study of the topology change in the magnetic surface during the e-ITB growing are the future works.

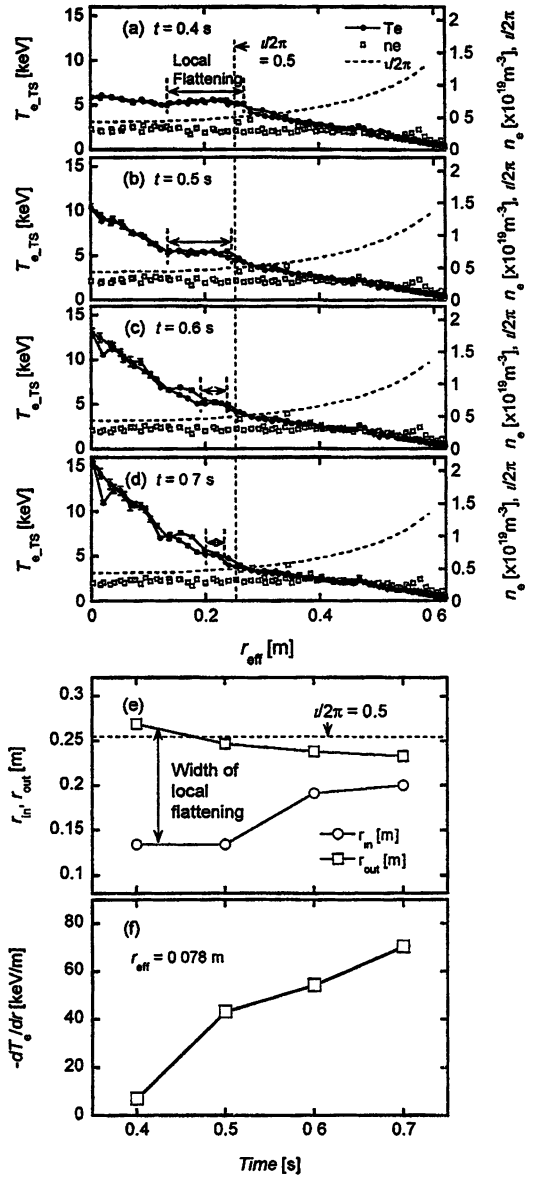

Fig. 3. The time evolution of (a)–(d) T_e and n_e profiles, (e) r_{in} and r_{out} and (f) T_e gradient at $r_{eff} = 0.078$ m

References

1. *Takahashi, H. et al.*, The Development of a 77-GHz, 1-MW ECRH System for the Large Helical Device, Fusion Sci. Technol. **57** (2010) 19.

2. *Nusinovich G. S. et al.*, Slow processes in startup scenarios of long-pulse gyrotrons // Phys. Plasmas **13** (2006) 083106.

3. *Takahashi, H. et al.*, High Te, low collisional plasma confinement characteristics in LHD // Proc. 23rd IAEA Fusion Energy Conference, Daejeon, Republic of Korea, October 2010, EXC/P8-15.

4. *Kubo, S. et al.*, ECRH and ECE in high T_e, low density plasmas of LHD // Proc. 16th Joint Workshop on ECE and ECRH, Sanya, China, April, 2010, I-5.

5. *Ida K. et al.*, Characteristics of Electron Heat Transport of Plasma with an Electron Internal-Transport Barrier in the Large Helical Device // Phys. Rev. Lett. **91** (2003) 085003.

6. *Yamada, I. et al.*, Improvements of data quality of the LHD Thomson scattering diagnostics in high-temperature plasma experiments // Rev. Sci. Instrum. **81** (2010) 10D522.

Pulsed Operation of ECR Ion Sources – Plasma Physics and Diagnostics

O. Tarvainen[1], T. Ropponen[1], V. Toivanen[1], T. Kalvas[1], J. Komppula[1], H. Koivisto[1], J. Ärje[1], P. Peura[1], J. Noland[2], I. Izotov[3], V. Skalyga[3], V. Zorin[3], T. Thuillier[4], T. Lamy[4], D. Küchler[5]

[1]University of Jyväskylä, Jyväskylä, Finland, olli.tarvainen@jyu.fi
[2]Lawrence Berkeley National Laboratory, Berkeley, CA, USA
[3]Institute of Applied Physics, RAS, Nizhny Novgorod, Russia
[4]LPSC, UJ F, CNRS/IN2P3, INPG, 53 rue des Martyrs, 38026 Grenoble Cedex, France
[5]CERN, Geneve, Switzerland

Electron Cyclotron Resonance Ion Sources (ECRIS) are magnetized plasma ion sources producing highly charged ions (HCI) from a variety of elements [1]. ECR ion sources providing DC beams are often operated as injectors for particle accelerators. Pulsed operation mode, used for specific applications and diagnostics, is typically realized by pulsing the microwave power supply. In this mode the temporal evolution of the plasma parameters and extracted ion beams can be divided in different regimes as follows: (A) plasma breakdown, preglow and the build-up of the charge state distribution (CSD), (B) steady-state and (C) afterglow plasma decay.

A. Plasma breakdown and preglow

The parameters affecting the plasma breakdown can be identified by considering the volumetric rate of ionizing collisions. For a given element (ionization cross section), the time to reach a critical electron density required to sustain the plasma, depends on neutral gas pressure and seed electron density. Both of these dependencies have been confirmed experimentally [2]. For the applications of pulsed operation it is often desirable to shorten the *e*-folding time of the electron density. The preferable choice is to supply seed electrons. Since the electron confinement time in a minimum-B ECRIS can extend up to seconds, it is obvious that the microwave pulse repetition rate and duty factor affect the seed electron density. The pulse pattern is often fixed by the application, leaving an independent supply of seed electrons the only viable choice to optimize the plasma breakdown characteristics. Experiments have demonstrated that a low power (~1 W) continuous microwave signal sustaining low density plasma and, therefore, acting as a source of seed electrons, significantly reduces the delay between the leading edge of the primary microwave pulse and the plasma breakdown making the breakdown time independent of the neutral gas pressure [2].

The initial low density plasma stage can be described by the theory of microwave induced plasma breakdown in simple magnetic traps under cyclotron resonance conditions [3]. Each time an electron traverses the ECR zone it either gains or loses transverse velocity depending on the phase difference of its cyclotron motion and the microwave electric field. At low energies the bounce period, τ_b, of the electron in the trap is much longer than its cyclotron period, τ_c. Thus, the phase difference in consecutive resonance crossings can be considered as random resulting to a net energy gain averaged over the electron population (stochastic heating). When τ_b approaches τ_c, i.e. $\tau_b \sim$ 20-100 times τ_c, the electron energy is limited due to the loss of the phase randomization disturbing the process. At low plasma density this limit can be reached by a significant fraction of the electrons, forming a so-called superadiabatic electron energy distribution function (EEDF), characterized by high average electron energy. Increasing electron density eventually causes the loaded Q-value of the plasma chamber to drop due to enhanced cyclotron damping and the microwave power becomes insufficient to maintain the superadiabatic EEDF. The abrupt shift of the EEDF towards the steady-state double-Maxwellian [1] causes the average electron energy to collapse. At the same time the loss rate of electrons is increased dramatically as their collision rate is multiplied. This in turn leads to a transient peak of the plasma potential and a burst of ions from the plasma.

The transient peak of extracted ion currents of low and medium charge states, representing the prevailing CSD, is called *preglow*. The preglow transient, exceeding the steady-state beam currents by a factor up to 7, has been studied in experiments and simulations [4] since it could be utilized for applications requiring fast and efficient ionization of radioactive elements. The duration (FWHM) of the observed preglow is typically 1-5 ms depending on the charge state. In conventional ECR ion sources the preglow caused by the shift of the EEDF is often overlapping with gradual build-up of the CSD determined by ionization and charge exchange rates. Saturation of the EEDF and particle densities, i.e. electrons and all ion charge states, is reached in ~ 10^1 - 10^2 ms (order of magnitude) depending on the microwave frequency.

Plasma breakdown and ignition transient can be studied with e.g. bremsstrahlung, plasma diamagnetism and plasma potential diagnostics, characterization of the plasma-microwave coupling and measurement of the extracted ion beam currents. The described sequence of plasma processes explaining the preglow and associated time scales is strongly supported by the data obtained through these diagnostic methods (see e.g. [5] and references therein).

B. Diagnostics of steady-state plasma through pulsed operation

Long pulse operation of ECRIS is valuable for diagnostics purposes of the steady-state plasma as the

progress towards saturation of various plasma parameters can be monitored. For example, plasma diamagnetism and bremsstrahlung emission can provide information on the electron heating time scale and the plasma energy content (density and temperature). Such experiments reveal information on different electron loss channels, i.e. collisional scattering and rf-induced pitch-angle scattering, and cavity properties of the plasma chamber [6]. Furthermore, the measurement of the temporal evolution of the plasma potential and energy spread of the extracted ion beams has provided insight to beam transport issues related to pulsed and continuous operation of the ion source.

C. Plasma decay and afterglow

Two decay "modes" of ECRIS plasma have been classified [1]: (a) turbulent, hot-electron plasmas exhibit decay dictated by diffusive processes (Bohm diffusion) and (b) non-linear afterglow, characterized by instabilities, expelling charged particles in bursts. The observed plasma decay is often a combination of the two. Theory and experiments suggest that in the case of diffusive decay the decay time of each charge state Z is proportional to Z^{-2} [7]. The decay time of highly charged ions (HCI) is a few milliseconds while low charge states (LCI) take up to hundreds of milliseconds to disappear. The model for the "quiescent" plasma decay does not explain the observed burst of highly charged ions occurring immediately after the microwave turn-off nor the instabilities often experienced during the afterglow. Both of these observations have been associated with non-linear effects, for which the dynamics of the plasma potential and EEDF play an important role.

It is believed that HCI are trapped in a potential dip, generated by well-confined hot electrons in the plasma core, while LCI occupy the peripheral region of the plasma [1]. Turning off the microwave power causes a bunch of cold electrons to enter the loss cone of the magnetic bottle as the energy transfer from the microwaves to the perpendicular component of electron velocity is interrupted. The sudden escape of electrons and loss of ion confinement is further observed as a burst of extracted ion beam currents of HCI exceeding their steady-state currents by a factor up to 5. This transient, whose duration is on the order of a millisecond, is referred to as *afterglow*. At least two factors are believed to contribute to the fact that HCI exhibit a more pronounced afterglow than LCI: (1) the effect of the potential dip on the electrostatic confinement gets stronger with increasing charge state and, (2) the potential dip is presumably located inside the (closed) resonance zone where the spatial distribution of ions is dominated by HCI. The afterglow transient has been applied for the production of heavy ion beams (Pb^{29+}) for the LHC accelerator at CERN [8].

Observed afterglow instabilities are most likely driven by the electron losses. Weakly confined cold electrons with high collision rate are the first ones to leak from the plasma. The process distorts the electron velocity distribution function, $f_e(v)$, as the hot well-confined electrons remain trapped. Thus, the situation is prone to Whistler instabilities stemming from the anisotropy of the afterglow electron energy distribution, i.e. the positive slope of the electron velocity distribution function; $\partial f_e/\partial v > 0$. The instability has been observed to repeat periodically as the hot electron density slowly falls off with time exciting waves that can restore a stable distribution as they abruptly expel hot electrons into the loss cone. Plasma diagnostics [6,7] have shown that the observed instability is indeed associated with enhanced loss rate of hot electrons. Furthermore, the results imply that the loss mechanism is concentrated to radial direction.

Figure 1 shows an example of the temporal evolution of oxygen beam currents extracted from the JYFL 14 GHz ECRIS (500 W pulsed at 10 Hz / 50 % duty factor i.e. 50 ms pulses). The currents have been normalized to their steady-state values. LCI exhibit preglow and afterglow peak is observed only for HCI.

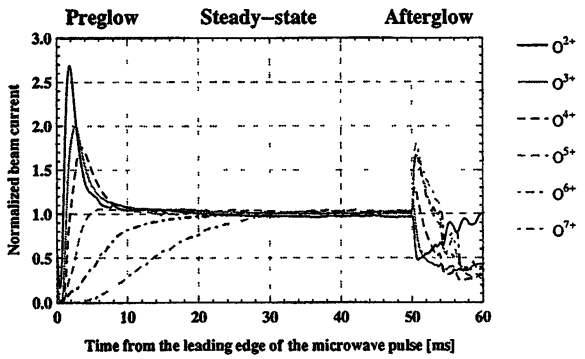

Fig. 1. Pulsed oxygen beam currents of a 14 GHz ECRIS.

References

1. *Geller, R.* Electron Cyclotron Resonance Ion Sources and ECR Plasmas // Bristol: Institute of Physics Publishing, 1996.

2. *Tarvainen, O., Ropponen, T., Toivanen, V., Ärje, J., Koivisto, H.* Plasma breakdown diagnostics with the biased disc of electron cyclotron resonance ion source // *Plasma Sources Sci. Technol.* 18 (2009) 035018.

3. *Suvorov, E.V., Tokman, M.D.* Theory of microwave breakdown of low-density gas at electron cyclotron resonance in magnetic mirror systems // *Sov. J. Plasma Phys.* 15, 540, (1989).

4. *Izotov, I.V., Sidorov, A.V., Skalyga, V.A., Zorin, V.G., Lamy, T., Latrasse, L., Thuillier, T.* Experimental and theoretical investigation of the preglow in ECRIS // *IEEE Trans. Plasma Sci.*, 36, 4, Part 2, (2008), p. 1494.

5. *Ropponen, T. et al.* Studies of plasma breakdown and electron heating on a 14 GHz ECR ion source through measurement of plasma bremsstrahlung // submitted to *Plasma Sources Sci. Technol.*(2011).

6. *Noland, J., Tarvainen, O., Benitez, J., Leitner, D., Lyneis, C., Verboncoeur, J.* Studies of electron heating on a 6.4 GHz ECR ion source through measurement of diamagnetic current and plasma bremsstrahlung // Plasma Sources Sci. Technol. 20 (2011) 035022.

7. *Tarvainen, O., Ropponen, T., Toivanen, V., Kalvas, T., Ärje, J., Koivisto H.* Diagnostics of plasma decay and afterglow transient of electron cyclotron resonance ion source // *Plasma Sources Sci. Technol.* 19 04502, (2010).

8. *Küchler, D., O'Neil, M., Scrivens, R.* First experience with the operation of the GTS-LHC ion source at 18GHz // *Proc. of ECRIS08*, Chicago, IL USA, JaCoW.org.

Recent Progress on the 1 MW, 140 GHz, CW Series Gyrotrons for W7-X

M. Thumm[a,1,2], H. Braune[b], G. Dammertz[a,1], G. Gantenbein[a,1], V. Erckmann[b], S. Illy[a,1], S. Kern[a,1], W. Kasparek[c], C. Lechte[c], W. Leonhardt[a,1], C. Liévin[d], G. Michel[b], F. Noke[b], F. Purps[b], A. Samartsev[a,1], A. Schlaich[a,2], M. Schmid[a,1], T. Schulz[b]

[a]Karlsruhe Institute of Technology (KIT), Association EURATOM-KIT, Kaiserstr. 12, D-76131 Karlsruhe, Germany
[1] Institute for Pulsed Power and Microwave Technology (IHM)
[2] Institute of High Frequency Techniques and Electronics (IHE)
[b]Max-Planck-Institut fuer Plasmaphysik, Teilinstitut Greifswald, Association EURATOM-IPP, Wendelsteinstr. 1, D-17491 Greifswald, Germany
[c]Universitaet Stuttgart, Institut fuer Plasmaforschung (IPF), Pfaffenwaldring 31, D-70569 Stuttgart, Germany
[d]Thales Electron Devices, 2 Rue Marcel Dassault, F-78141 Vélizy-Villacoublay, France

A 10 MW, 140 GHz ECRH system with a pulse duration of 30 minutes is currently under construction for the stellarator W7-X at Greifswald. The RF power will be provided by 10 gyrotrons. A European collaboration has been established to develop and build 9 (out of 10) tubes each with an output power of 1 MW for continuous wave (CW) operation. This contribution reports on recent results with the series gyrotrons.

Introduction

The stellarator W7-X at IPP Greifswald will use ECRH as the basic heating and current drive system. In the first stage W7-X will be equipped with a 10 MW ECRH system operating at 140 GHz in continuous wave (CW) [1]. The complete system will be provided by KIT in collaboration with IPF and IPP, including the design, development, construction, installation and integrated tests of all components required for stationary plasma heating on site at IPP Greifswald. At Thales Electron Devices (TED) seven series gyrotrons have been ordered. First operation and long pulse conditioning and the factory acceptance test (FAT) of these gyrotrons is taking place at the test facility at KIT where pulses up to 180 s at full power are possible, 30 minutes shots at full power can be done only at IPP where the site acceptance test (SAT) is being performed. Including the pre-prototype tube, the prototype tube and a 140 GHz CPI-tube, ten gyrotrons will be available for W7-X. The first TED series tube SN1 delivered 0.92 MW output power at an efficiency of almost 45 % with a fundamental Gaussian output mode purity of 97.5 % [2,3].

The following series gyrotrons starting from SN2 up to SN5 suffered from parasitic oscillations in the beam tunnel due to different dielectric properties of the BeO/SiC attenuation ceramics [4]. A modification of the beam tunnel structure was proposed and tested successfully by KIT using two modular short pulse megawatt-class gyrotrons [4]. The present contribution reports on FAT and SAT acceptance tests of series gyrotron SN3a, still equipped with the old beam tunnel, and SN4R employing the improved beam tunnel.

Experimental results

Up to March 2010 the series gyrotron SN3a was operated and tested at KIT at short (few ms) and long pulses. The operation and the dependence of the output power and stable oscillation region of the cavity mode ($TE_{28,8}$) on different parameters was investigated. In particular, scans of the output power versus the cathode voltage have been performed for different magnetic field values in the cavity and the cathode region. Since this gyrotron is still equipped with the original beam tunnel which tends to support parasitic oscillations the maximum achievable output power is limited. The operation of the gyrotron beyond this limit is usually associated with a strong reduction of output power, enhanced stray radiation level and an increased amount of absorbed RF power in the beam tunnel region which may result in a thermal overload. It has been found that around 0.7 MW output power can be generated at a beam current of approximately 40 A very reliably, avoiding any evidence of spurious beam tunnel oscillations.

Thermographic IR camera measurements and analyses of the output beam pattern at different distances from the window gave a TEM_{00} mode content of 97%, which verifies the high quality of the internal mode converter and mirror system.

Long pulses up to 3 minutes were performed with a CW load at full power (0.7 MW) at an efficiency of 37 % in single- stage depressed collector (SDC) mode for energy recovery. The increasing temperature of the cavity is associated with an expansion of the cavity diameter and results therefore in a small reduction of the oscillation frequency. The typical drop of the frequency during the first second of the pulse is about 260 MHz (to be compared with 140.33 GHz at the start).

As a standard procedure the W7-X gyrotrons have to pass a reliability test during the acceptance tests in order to show a reproducible and stable operation within a pulse sequence.

Figure 1 shows the temperature increase in the calorimetric load during this reliability study. The gyrotron has been operated in 3 min pulses at 0.69 – 0.72 MW output power and a duty cycle of 10 % (13 pulses). All parameters were kept constant, except the beam current: it was increased slightly from 38.7A in the morning to 40.2A in the evening. All pulses were successful, one pulse (no. 6) was pre-terminated due to an arc in the pre-load.

At KIT a pulse length of up to 30 min (and even longer) is only possible at a beam current of less than

30 A due to the limitation of the HV power supply. Tests at full power were performed at IPP Greifswald. Figure 2 shows a very stable behavior of the total RF power during a 28 min pulse. The increase of the output power between 16 min and 23 min is caused by adjusting the body voltage and optimizing the boosting procedure to stabilize the electron beam current.

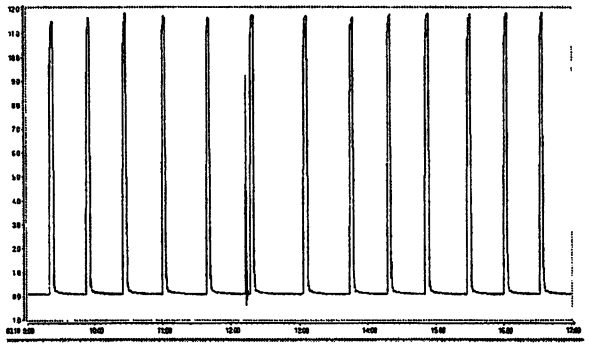

Fig. 1. Temperature increase (11.3 – 11.8 °C) in the calorimetric load for 13 successive pulses with 3 min length each (duty cycle 10%) of SN3a.

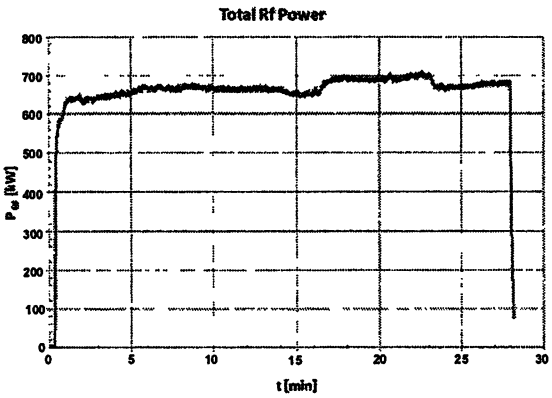

Fig. 2. Output power for a 28 min pulse of SN3a. Variation of the power after 16 min is due to adjustment of body voltage and beam current.

As already mentioned before, experimental studies on beam tunnel oscillations have been performed at KIT with a modular step-frequency-tunable gyrotron and a coaxial-cavity gyrotron [3,5]. It has been shown that parasitic oscillations in the original beam tunnel of the W7-X gyrotron are the reason for the limitation of the output power. The corresponding frequencies could be measured with a new precise frequency measurement system. It has been found that several frequencies in the range of 119-132 GHz have been excited simultaneously with the 140 GHz cavity mode. Then an improved beam tunnel with irregularly longitudinally slotted copper rings was experimentally employed resulting in a parasitic-free operation of the gyrotron.

Series gyrotron SN4R was mounted with such an improved beam tunnel and has been tested at KIT and IPP. The FAT at KIT resulted in reliable 0.86 MW operation in 3 min pulses at 10% duty cycle with an efficiency of approximately 36 % (with SDC). No parasitic beam tunnel oscillations have been observed and a TEM_{00} mode purity of 97 % has been measured. An output power saturation at electron beam currents higher than 40 A resulted in the low overall efficiency. After transfer to IPP Greifswald the tube delivered during the SAT 1.02 MW output power as derived from the calorimetrically measured power in the load plus transmission and load reflection losses. The efficiency is 41% at a pulse duration of nearly 6 minutes (Fig. 3). The pulse length was limited by arcing in the stainless steel GYCOM load at a power level of 0.95 MW behind an optical transmission line of 8 mirrors. Operation with longer pulse duration was possible at the reduced power level of 0.85 MW in the load. Measurements on the symmetry of the magnetic field in the KIT gyrotron magnet revealed that the reduced power at KIT might be due to a slight field misalignment which is currently under further investigation.

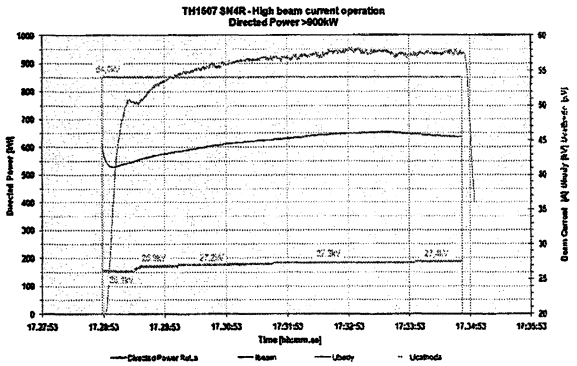

Fig. 3. Output power (left ordinate), beam current, body voltage and cathode voltage (right ordinate) for a 350 s pulse of SN4R.

Conclusions

Experiments with the TED series gyrotron SN3a for the ECRH system of the stellarator W7-X show a very reliable and stable operation at a reduced output power of 0.7 MW. Series gyrotron SN4R with a new improved beam tunnel achieved 1 MW output power in long pulse operation without any parasitic oscillations in the beam tunnel.

Acknowledgement

This work, supported by the European Communities under the contract of Association between EURATOM and Karlsruhe Institute of Technology (KIT), was carried out within the framework of the European Fusion Development Agreement (EFDA). The views and opinions expressed herein do not necessarily reflect those of the European Commission.

References

1. V. Erckmann, et al., Fusion Sci. & Techn., **52**, 291, 2007.
2. G. Dammertz, et al., IEEE TPS, **34**, 173, 2006.
3. M. Thumm, et al., IEEE TPS, **35**, 143, 2007.
4. G. Gantenbein et al., IEEE TPS, **38**, 1168, 2010.
5. S. Kern, et al., 34th IRMMW-THz, Busan, Korea, September 21-25, 2009, T4C01.

CVD Diamond Films Grown in Millimeter-Wave Plasma-Assisted Reactor

A.L. Vikharev, A.M. Gorbachev, V.V. Chernov, A.V. Kozlov, D.B. Radishev

Institute of Applied Physics RAS, Nizhny Novgorod, Russia, val@appl.sci-nnov.ru

Diamond films grown using microwave plasma assisted CVD technology possess a number of unique properties [1, 2]. For scientific and industrial application it is important to produce high quality films with rapid growth rates and good uniformity over large area substrates. Deposition of such diamond films can be performed in a novel millimeter-wave plasma-assisted reactor [3, 4]. This system has many advantages over the microwave reactors operating at frequency 2.45 GHz which are widely used nowadays [1].

The millimeter-wave plasma-assisted CVD reactor is based on 15 kW gyrotron operating at frequency 28 GHz, Fig.1. The gas discharge in the reactor is localized and maintained by using crossing beams of electromagnetic waves. This allows to produce a uniform gas discharge over a substrate having a diameter of up to 100 mm.

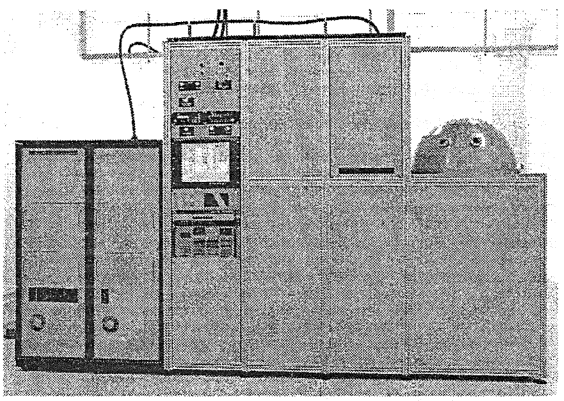

a

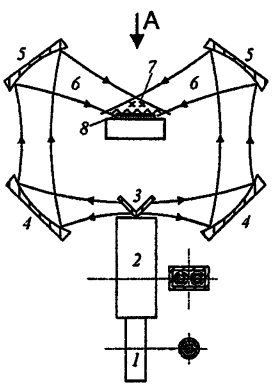

b

Fig. 1. Photograth of the gyrotron-based system (a) and the schematic diagram of plasma reactor (b): 1 — circular waveguide, 2 — wave beam spliter, 3—plane mirrors, 4—bottom focusing mirrors, 5—top focusing mirrors, 6 — wave beams, 7 — discharge plasma, 8 — substrate holder.

The diamond film deposition was carried out at wide variation of process parameters. Two gas mixtures Ar–H_2–CH_4 and Ar–H_2–CH_4–N_2 were used. The substrate temperature at the deposition was from 500 to 900 C and the gas pressure was 150-300 Torr.

For understanding the growth conditions of diamond films the investigations of the plasma parameters (electron density and gas temperature) in CVD reactor were made. Gas kinetic temperature and electrons concentration and their dependence on external parameters – incident microwave power, operating pressure and gas mixture composition were studied by method of optical emission spectroscopy.

The series of experiments on deposition of nanocrystalline diamond (NCD) films on the surface of silicon substrates was performed. The substrates were seeded by two methods: spin coating and bias. In the spin coating processes the diamond nuclei were particles (the average sizes were equal to 4 nm and 40 nm) of detonation nanodiamond dissolved in suspension. NCD films were deposited on the substrates having a diameter of up to 75 mm. Thickness of each film was equal to a few hundred nanometers. Seeding type influence on uniformity and surface roughness of diamond films was researched. Dependence of NCD film properties on gas mixture content in growth process was investigated also. For illustration Fig. 2 shows an optical photo and SEM image of NCD film, correspondingly, grown at the following parameters: gas mixture $Ar/H_2/CH_4$ - 97/2/1, pressure p=300 Torr, microwave power P= 7 kW, substrate temperature T_s=700°C.

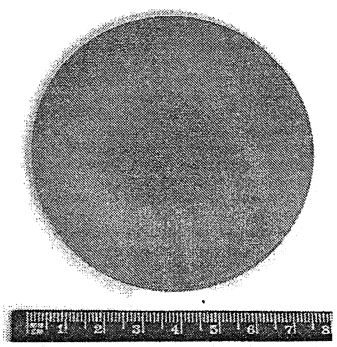

a

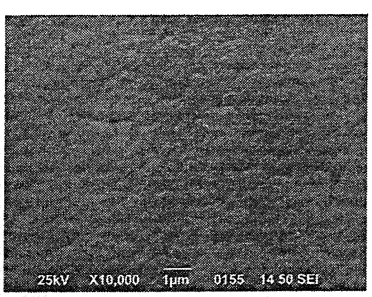

b

Fig. 2. Photograth (a) and SEM image (b) of the substrate after deposition, thickness of NCD film is 350 nm.

The general view of the thin diamond film without the silicon substrate is shown in Fig. 3.

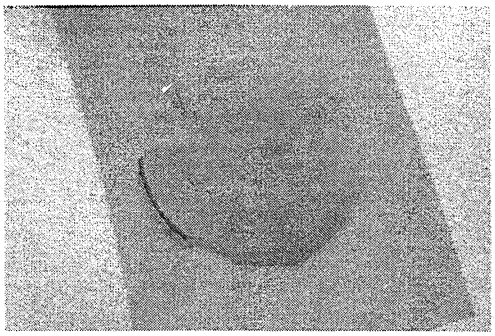

Fig. 3. Photograph of free standing diamond film, thickness is 1 micron.

The series of experiment was performed on deposition of thin diamond films on the surface of molybdenum cathodes. The main tasks were to design and test new types of cold cathodes employing diamond for using them in high-power RF devices. The diamond films with different morphology, composition, size of the crystals were deposited and the emission properties of the cathodes that utilize such films were studied.

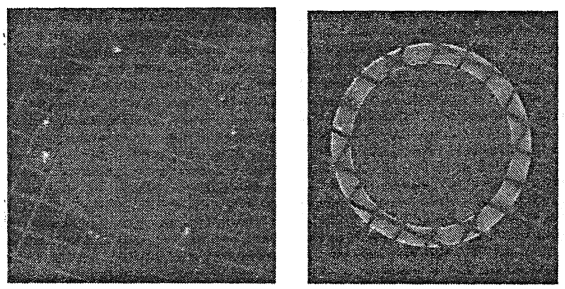

(a) (b)

Fig. 4. Photos of the emitting surfaces when high-voltage pulse is applied (peak voltage ~100 kV, pulse duration ~100 ns). (a) - uncoated cathode, (b) - cathode coated with a diamond film.

The diamond films were deposited on molybdenum cathodes of cylindrical shape of 20 mm in diameter with wide edge (molybdenum cup 4 mm tall with 2 mm thick walls). The films with thickness of 8-10 μm and high content of the diamond phase sp^3 were grown. The deposition was done under the pressure 200 Torr in gas mixture Ar/H2/CH_4=210/100/2. Figures 4 and 5 present photos of the cathodes when a high-voltage pulse (100 kV) is applied, the Raman spectrum of the grown film, and oscillograms of the emission currents for the both cathodes.

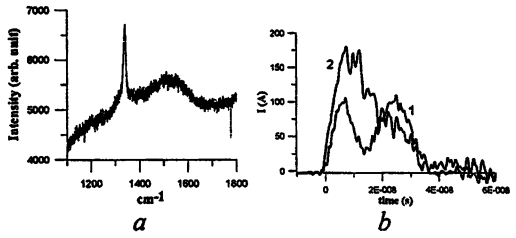

a *b*

Fig. 5. Raman spectrum of diamond film (a) and emission currents (b) created by cathodes: 1 - uncoated molebdenum cathode, 2 - cathode with a diamond film. The distance between cathode and slit anode is 3.5 mm.

The deposition of the diamond film results in more uniform emission from the cathode surface and is accompanied with an increase in the emission current. Thus, the diamond film improves the emission properties of the cathode.

Also the two-dimensional self-consistent numerical model describing the behavior of microwave discharge in crossing beams of electromagnetic waves was developed and numerical modeling of discharge in such CVD reactor was made. Calculations showed that in two crossing wave beams over substrate it is possible to obtain plasma that covers large area substrates. In spite of the fact that the electron concentration has maximums in antinodes of standing wave, the density distribution of atomic hydrogen has high uniformity. This is explained by fast diffusion of hydrogen atoms in heavily heated gas.

This work was partially supported by the Russian Foundation for Basic Research (project No. 11–08–01092).

References

1. *Diamond Films Handbook*, ed. by J. Asmussen and D. K. Reinhard, New York, Marcel Dekker, 2001.

2. *O.A. Williams, M. Nesladek, M. Daenen, S. Michaelson, A. Hoffman, E. Osawa, K. Haenen, R.B. Jackman* // Diam. Relat. Mater., 2008, V.17, P.1080

3. *A.L. Vikharev, A.M. Gorbachev, A.V. Kozlov, V.A. Koldanov, A.G. Litvak, N.M. Ovechkin, D.B. Radishev, Yu.V. Bykov, M. Caplan* // Diam. Relat. Mater., 2006, V.15, P.502

4. *A.L. Vikharev, A.M. Gorbachev, A.V. Kozlov, D.B. Radishev, A.B. Muchnikov* // Diam. Relat. Mater., 2008, V.17, P.1055

Advanced Plasma Heating and Control Schemes using ECRH at ASDEX Upgrade

D. Wagner[1], J. Stober[1], H. Höhnle[2], W. Kasparek[2], G. Grünwald[1], F. Leuterer[1], F. Monaco[1], S. Müller[1], M. Münich[1], M. Schubert[1], H. Schütz[1], H. Zohm[1] and ASDEX Upgrade Team

[1]Max Planck Institut für Plasmaphysik, Association EURATOM-IPP, D-85748 Garching, Germany
[2]Institut für Plasmaforschung, Universität Stuttgart, D-70569 Stuttgart, Germany

Introduction

Seven gyrotrons are currently in operation in the Electron Cyclotron Resonance Heating (ECRH) system at the ASDEX Upgrade tokamak. An older system in operation since 1996 is equipped with four gyrotrons, operating at 140 GHz with 500 kW output power and 2 s pulse length. In the "old" ECRH system, the launching angle and the polarization can only be changed in-between ASDEX Upgrade discharges. Recently the ECRH system was extended with three step-tunable gyrotrons with an output power close to 1 MW at 140 GHz and around 800 kW at 105 GHz. The pulse length of the new gyrotrons is 10 s corresponding to the maximum flat top time of ASDEX Upgrade discharges. The new gyrotrons are equipped with a single stage depressed collector and a single disc CVD diamond window. In its final stage the system will employ four step-tunable gyrotrons. Depending on an ongoing vacuum output window development, the fourth gyrotron will eventually become a four-frequency gyrotron with two additional intermediate operating frequencies between 105 and 140 GHz [1].

In the new ECRH system, one quasi-optical Matching Optics Unit (MOU) is connected to each gyrotron. The MOU is connected to a non-evacuated HE_{11} corrugated waveguide transmission line (I.D. = 87 mm), including up to 6 miter bends. In the MOU, an individual pair of phase correcting mirrors is required for each frequency. The two mirrors also provide the alignment of the gyrotron output beams at different frequencies with respect to the optical beam axis of the MOU mirrors and the waveguide transmission line. Each MOU contains a spherical load, capable of 1 s, 1 MW. Additionally, each gyrotron can be connected to a common all-stainless-steel long-pulse load, capable of 10 s, 1 MW. The output beam of the transmission line can be connected to the launcher or to a short-pulse calorimetric load via a switching mirror. The calorimetric load at the torus can be used to measure the efficiency of the transmission line and to test the transmission line prior to plasma experiments. The launcher has a fast steering capability that allows for poloidal steering with velocities up to 10°/100 ms. Directional couplers built into the second phase correcting mirror in the MOU as well as in the last miter bend mirror of the transmission line are used for power monitoring and polarization measurements. Other capabilities of the new system include fast power modulation up to 25 kHz and control of the launching angle during a plasma discharge by the ASDEX Upgrade control system.

Extension of the ECRH operation space

In the past the main mode of operation for the ECRH on ASDEX Upgrade was the second harmonic extraordinary mode (X2). This heating scenario is limited by the cutoff electron density ($1.22 \cdot 10^{20}/m^3$ for $B_t = 2.5$ T, f = 140 GHz, $T_e = 2$ keV). Since 2007 ASDEX Upgrade operates with fully tungsten covered plasma facing components. Central heating with ECRH plays a key role in suppressing tungsten accumulation in the plasma center. The requirement of central heating for impurity control further limits the operational space using X2-mode heating.

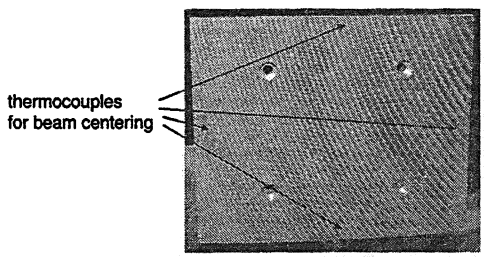

Fig. 1. ASDEX Upgrade inner wall tile with holographic reflector grating and indicated positions of the thermocouples.

The frequency step-tunability (105, 140 GHz) of the new ASDEX Upgrade ECRH system allows for four different heating scenarios (X2, O2, X3, O1) [2, 3]. Additionally, both launcher and polarizer angle can be changed remotely during the discharge. Access to plasmas with higher densities is possible by using the O2-mode. Unlike the X2-mode which is fully absorbed at the resonant surface in the plasma, heating in the O2-mode exhibits only partial absorption of approximately 70 % of the injected power. For this reason two tiles of the inner wall have been replaced with holographic reflectors that reflect the non-absorbed part of the beam again with O2-mode polarization allowing for a second pass through the resonant layer (Fig.1, 2). That way the absorption can be increased up to 90 %. The holographic reflector is equipped with thermocouples underneath its surface, close to the edges. First successful measurements of the beam position using feed forward controlled launcher movements were performed. In future these thermocouples will give a feedback signal to the fast steerable launcher in order to make sure that the beam stays in the center of the reflector, even when the plasma density changes. In a proof of principle experiment, X2-heating was used to pre-heat the plasma at densities below the X2-cutoff. When the density increased, the polarization was changed for O2-mode

heating during the discharge and the pulse continued (Fig. 3). To monitor ECRH stray radiation in cases with non-perfect absorption, three sniffer probes have been installed around the ASDEX Upgrade torus. The signals from the sniffer probes are also used for an interlock in case of excessive stray radiation.

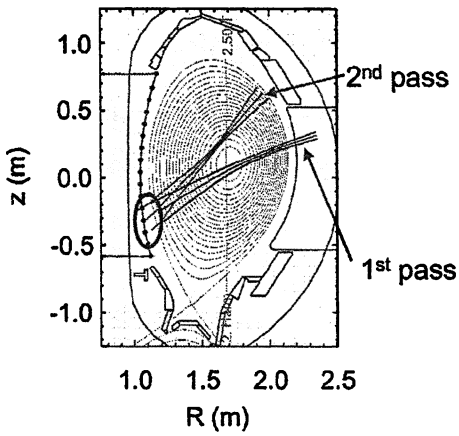

Fig. 2. Poloidal cross section of ASDEX Upgrade with injected and reflected beam path for the O2 heating scenario.

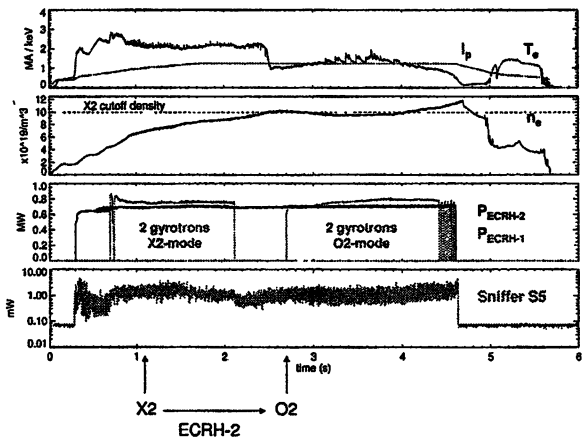

Fig. 3. Shot parameters of discharge #24107. Plasma current I_p, electron temperature T_e, central electron density ne, injected ECRH power of the old (PECRH-1) and the new ECRH system (PECRH-2) and signal from the sniffer probe in Sector 5). The frequency of both ECRH systems was 140 GHz. The old system (ECRH-1) was polarized for X-mode, whereas the polarization of system 2 was changed from X to O between $t = 1.1$ s and $t = 2.7$ s.

One possibility to achieve an ITER-like safety factor of $q_{95} = 3$ is a reduction of the magnetic field by ~30 %. Central heating with the third harmonic X3-mode is possible by tuning the new gyrotrons to the lower frequency (105 GHz). Central absorption is only 70–90 % in this case. A heating scenario was found with a toroidal magnetic field of 1.8 T where the X2 resonant layer is located at the pedestal top on the high field side and acts as a beam dump for the X3 shine through (Fig. 4).

Heating at a higher toroidal magnetic field above the range for X2 heating could be achieved by applying the ITER-like O1 scheme. This was successfully demonstrated with a toroidal field of 3.2 T and 105 GHz gyrotron output frequency. In this heating scenario the O1-mode resonance is located at the high field side whereas the X1-mode exhibits a cutoff at the low field side close to the launching antenna (Fig. 5). This results in a high sensitivity in the measurement of the cross-polarization of the ECRH beam, since one of the three sniffer probes installed at ASDEX Upgrade is located next to the launching antenna [4].

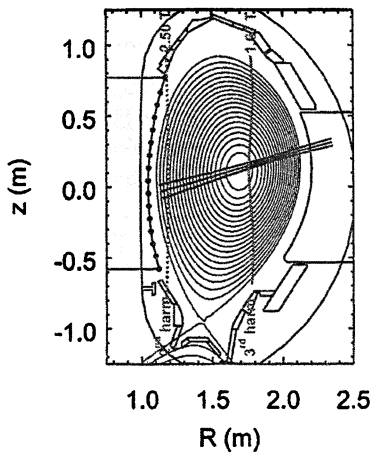

Fig. 4. Poloidal cross section of ASDEX Upgrade resonant layers and beam path for the X3 heating scenario at 1.8 T.

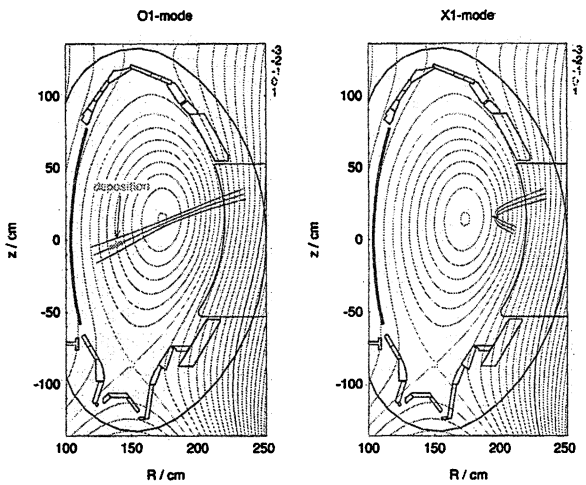

Fig. 5. Poloidal cross section of ASDEX Upgrade with beam paths for the O1- and X1-modes .

References

1. *Wagner, D. et al.,* Recent Upgrades and Extensions of the ASDEX Upgrade ECRH System // J. Infrared, Millimeter and Terahertz Waves. 2010. № 6. P. 519–522.

2. *Höhnle, H. et al.,* Extension of the ECRH operational space with O2 and X3 heating schemes to control tungsten accumulation in ASDEX Upgrade // submitted to Nuclear Fusion.

3. *Höhnle, H. et al.,* O2- and X3-Heating Experiments on ASDEX Upgrade // Proc. 16th Joint Workshop on ECE and ECRH (EC-16), edited by R. Prater, 2010. P. 124–130.

4. *Wagner, D. et al.,* Feed Forward Polarization Control during ECRH discharges at ASDEX Upgrade // Fusion Science and Technology. 2010. V. 58, № 2. P. 658–665.

Recent Progress in R&D of Synthesis of Large Single-Crystal Diamond Wafers by Using MWPCVD

H. Yamada, A. Chayahara, Y. Mokuno, N. Tsunouchi, H. Umezawa, S. Shikata

Diamond Research Lab., AIST, Osaka, Japan, yamada-diamond@aist.go.jp

Diamond is one of the wide band gap materials, which has several characteristics superior to those of others; wider band gap, higher thermal conductivity, and so on [1]. Therefore, this material has been considered to be a promising material to realize future high performance electronic devices. One of the problems for the realization is difficulty to make its large wafer. For example, in case of silicon, its standard size is 300 mm (12 inches) in diameter. Wafer size of silicon-carbide, which is other hopeful wide band gap material, has been enlarged continuously. Recently a wafer with 150 mm (6 inches) in diameter was reported [2]. On the other hand, normally available size of the commercialized single-crystal diamond (SCD) is usually less than 10 mm of its edge length [3], while wafers with several inches in diameter is considered to be required for the use of semiconductor industries.

Artificial SCD can be made in several ways. For example, one may use high-pressure-high-temperature method (HPHT), which uses more than 1 GPa of pressure and 1000 deg. C of temperature in a press apparatus, and carbon sources are transferred onto a seed crystal to be grown as diamond crystal. This method may be the most standard way to produce diamond for mechanical use, e.g. cutting and polishing. However, because size of such press apparatus becomes huge to make inch size diamond, this method is considered to be practically not suitable for large size wafer. Plasma chemical vapor deposition (CVD) is another way to make diamond. Among several ways of plasma CVD, microwave plasma CVD (MWPCVD) is widely used to make plate shape diamond because this method can make diamond in relatively stable manner with relatively high growth rate.

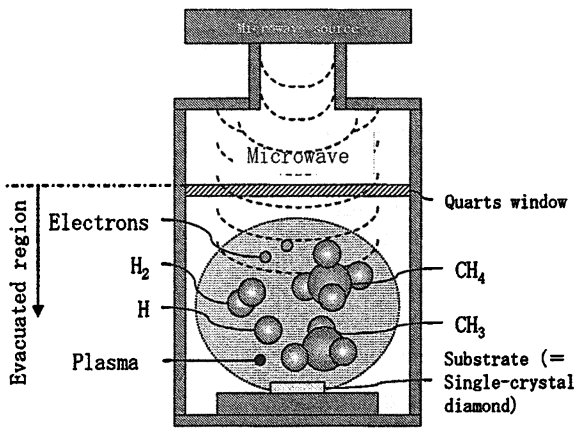

Fig. 1. Schematic of MWPCVD

Figure 1 shows principle of this method. Microwave which is generated by, for example, magnetron, is introduced into an evacuated region where the pressure there is typically less than ≈10kPa. Electrons in that region absorb the power of MW, and collide with source gases. This collision ignites and maintains plasma. We usually use plenty amount of hydrogen and small amount of methane. Depending on purposes, in addition, we introduce small amount of impurities, such as nitrogen, oxygen, and boron. These molecules are dissociated into radicals in the plasma and diffuse onto the top surface of the SCD substrate.

If one adopts 915 MHz of MW frequency, for example, growth over 4-6 inches area is possible [4]. Practical point which makes difficult to obtain inch size wafer of single crystal diamond is that (1) such size seed crystal is not available and (2) technique to process such size freestanding wafer is not well developed.

In case of silicon and silicon carbide, growth surface of the seed crystal can be enlarged during the growth [5]. In other words, the crystal enlarges horizontally as well as vertically as shown in Fig.2 (a). However, in case of SCD, usually the growth area *shrinks* during the growth as shown in Fig. 2 (b). This difference in the growth modes makes difficult to obtain large size seed crystal.

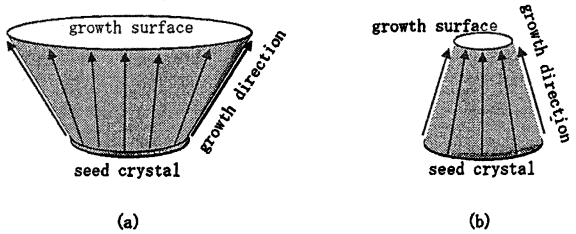

Fig. 2. Growth modes (a) crystal enlarges horizontally as well as vertically, and (b) crystal enlarges vertically but shrinks horizontally.

Therefore, Mokuno, et al. conducted three-dimensional growth as shown in Fig. 3. After growth of a (100) direction, side surface is cut and polished to bear (010) surface. Then, another diamond layer is grown on this (010) surface. These processes are repeated several times in several {100} surface, then enlarged area is available as shown in the 3rd figure in Fig. 3 from left [6].

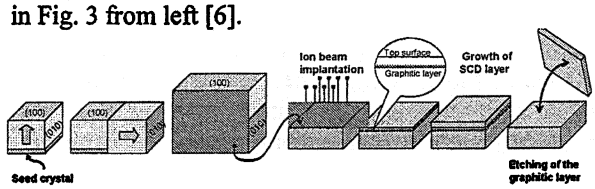

Fig. 3. Processes to make free standing wafers with large area.

They have also succeeded in fabrication free-standing wafers from this enlarged seed crystal by

using ion implantation technique. High energy ion beam is irradiated onto the top surface of the seed crystal, and then graphitic layer is created beneath the top surface. After that, SCD layer is deposited onto this surface followed by selective etching of this graphitic layer [6]. Above techniques make us possible to produce freestanding SCD plates with over 10×10 mm^2 in area, while is much larger than common size. One of the important characteristics of the technique to make freestanding wafers by using ion implantation is that the crystallographic characteristics of the seed crystal are mirrored to the synthesized freestanding wafer. This means that one may be able to obtain freestanding wafers with the same characteristics with each other if one applies this technique on an identical seed crystal.

By the way, the growth rate of the SCD is typically less than or around 1μm / hr. With the use of concentrated plasma and introduction of supplemental impurities, growth rate can be enhanced up to ≈100 μm / hr. However, this is still not sufficient; to enlarge 10 mm size seed crystal up to 25mm size one, for time period of 150×3=750 Hr, growth is required to be maintained stably. Therefore, we have decided to develop another method to obtain large wafer more efficiently. That is so-called "mosaic wafer" [7], where relatively small pieces of SCD plates are jointed into one larger size wafer. We found that the key of this method is to match the crystallographic characteristics of plate to be jointed with each other, and that the use of "clone" plates, which is made from one identical seed crystal, is efficient to obtain improved junction of the plates. We succeeded in fabricating wafers with are over 20×20 mm^2, as shown in Figure 4, which consists of four 10×10 mm^2 size SCD plates. If device size is smaller than these jointed plates, this type of wafer is considered to be practically not so different from monolithic wafer.

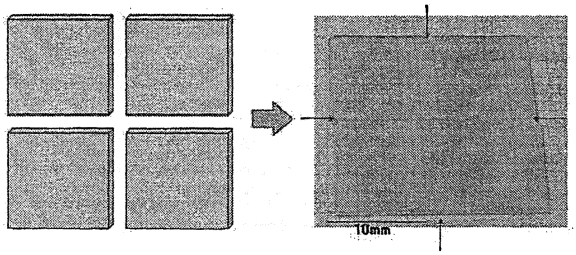

Fig. 4. Inch size mosaic wafer; 4 plates (left) are jointed (right) where arrows indicates their junctions.

To achieve stable and rapid growth of such SCD wafers, optimization of the discharge condition is important. However, it is sometimes not easy to guess plasma distribution experimentally. For example, ignition of plasma is not obtained when the substrate holder thickness is changed only 1 mm. Experimental and economical point of views, numerical simulation to study distributions of plasma parameters and predict optimization condition is considered to be useful [9]. We have developed original model of MWP and conducted numerical simulation for actual configuration which is used in experiments as shown in Figs. 5 (a) and (b). Distributions of electric field strength and electrons from the downstream of the waveguide to the inside of the chamber are calculated as shown in Figs. 5 (c) and (d), respectively. In addition, distributions of gas-temperature, velocity, and source gas species are also calculated as shown in Fig. 5 (e). These numerical results help us to consider mechanism of the growth and improved condition/configurations.

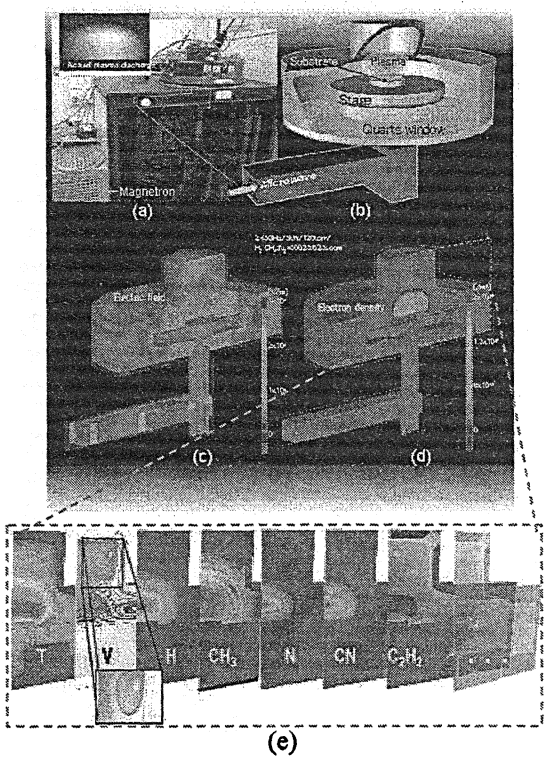

Fig. 5. Sample results of numerical simulation

Further developments of all of above subjects are ongoing. We are now going to establish technique to fabricate freestanding wafer with 2 inches in diameter.

References

1. S. Koizumi, C. Nebel, and M. Nesladek: Physics and Applications of CVD Diamond (Wiley-VCH, Weinheim, 2008).

2. W. Palmour, et al., The 8th ECSCRM, Oslo, Norway, Aug. 29 - Sep. 2, 2010.

3. For example, EDP Co., http://www.d-edp.jp/index.html; Element six., http://www.193.120.252.126/cvd/page.jsp?211 pageid=100&lang=en.

4. E. Sevillano and B. Williams, Diamond Films and Technol. 8 (1998) 73.

5. W. C. Dash, J. Appl. Phys. 30, 459 (1959).

6. Y. Mokuno, et al., Diamond Relat. Mater. 18 (2009) 1258.

7. M. W. Geis, et al., Appl. Phys. Lett. **58** (1991), 2485.

8. H. Yamada, et al., Appl. Phys. Express 3 (2010), 051301.

9. H. Yamada, et al., J. Appl. Phys. 101 (2007), 063302; Jpn. J. Appl. Phys. 50 (2011), 01AB0201.

Detection of Intense THz Wave with Air-Plasma Photonics

Xiaofei Lu[2] and X.-C. Zhang[1,2]

[1]Wuhan National Laboratory for Optoelectronics, Huazhong University of Science and Technology, Wuhan 430074, China
[2]Center for Terahertz Research, Rensselaer Polytechnic Institute, Troy, NY 12180 USA

With the successful developments in THz wave emitters in past 20 years, ultra-broadband, sensitive, and time-resolved THz wave detectors remain challenging. This paper presents recent development of THz wave detectors with air-plasma photonics. This presentation reports (a) balanced THz wave air-biased-coherent-detection, [1] and (b) generation of elliptical polarized THz wave using double helix electrodes.

1. Balanced THz wave air-biased-coherent-detection (ABCD)

Conventional THz-ABCD [2] uses a concept of heterodyne detection: introducing a modulated bias field-induced second harmonic (SH) as a local oscillator, mixing THz field-induced SH with the local oscillator through interference, and finally isolating the cross term at modulation frequency through a lock-in amplifier (LIA). Although the DC offset terms will be ignored automatically by LIA, the noises from these terms still limit the SNR and even saturated the LIA. In early works with electro-optic sampling techniques or optical heterodyne detection, a balanced detection is utilized based on a polarization geometry, which cancels out laser fluctuation down to the laser or photodiode shot noise limit.

In this paper, we introduce a balance detection scheme based on conventional THz-ABCD. Utilizing the tensor property of third order nonlinear susceptibility, SH pulses with two orthogonal polarizations are detected by two separated photomultiplier tubes (PMTs) simultaneously. The differential photocurrent from the two PMTs with a balanced detection circuit cancels the offsets and therefore reduces the common noise resulting from laser fluctuation. A factor of two improvement of SNR is achieved.

The prerequisite in this balanced detection scheme is the isotropic tensor property of $\chi^{(3)}$ in gases. In an isotropic media, the third-order susceptibility tensors have three independent non-zero components: $\chi^{(3)}_{yyxx}, \chi^{(3)}_{xyxy}, \chi^{(3)}_{xyyx}$ and $\chi^{(3)}_{xxxx} = \chi^{(3)}_{yyxx} + \chi^{(3)}_{xyxy} + \chi^{(3)}_{xyyx}$ with the four subscripts corresponding to polarizations of 2ω, THz (or bias field), ω, and ω beams, respectively. To produce a differential signal, we select two $\chi^{(3)}$ elements: $\chi^{(3)}_{xxxx}$ and $\chi^{(3)}_{yyxx}$. $\chi^{(3)}_{xxxx}$ represents that all four waves are in x polarization, and $\chi^{(3)}_{yyxx}$ represents that 2ω, THz field (or bias field) in y polarization, while fundamental beam ω is x polarization. Thus, if the polarization of THz field is oriented at certain angle with respect to the polarization of ω beam, the produced 2ω beam will have two orthogonal components. Fig. 1 shows a schematic of balanced ABCD for broadband THz waves. The detection scheme is similar to conventional THz ABCD. However, the polarization of each beam is controlled separately and rotated to certain angle with respect to each other, which is shown in the grey circle of Fig. 1.

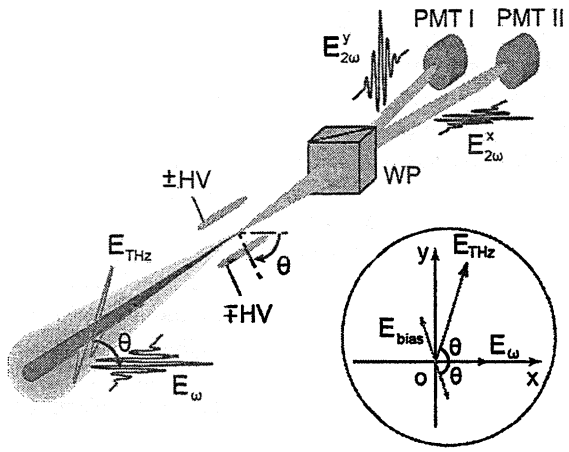

Fig. 1. Schematic of balanced ABCD for THz waves. WP: Wollaston prism. PMT: photomultiplier tube. The polarization of each beam and the experimental coordinate are shown inside the grey circle.

Fig. 2 shows detected THz waveforms with individual $I^x_{2\omega}$ and $I^y_{2\omega}$ component of second harmonic. The balanced signal ($I^x_{2\omega} - I^y_{2\omega}$) is obtained by using a current subtraction circuit. Fig. 2 demonstrates the concept of balanced ABCD. By introducing a polarization dependent geometry, two out of phase signals are detected separately by two detectors. In this case, a subtraction will help to reduce the noise fluctuation since the background noise are correlated while maintaining the signal. A factor of two improvement of SNR is achieved.

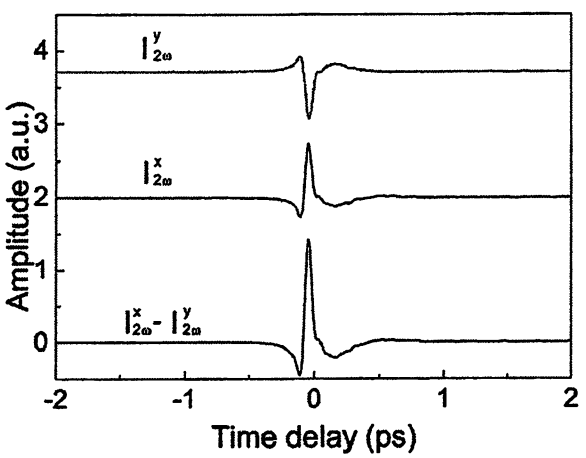

Fig. 2. Each component measured in balanced ABCD. Waveforms are offset vertically for clarity.

2. Generation of elliptical polarized THz wave using double helix electrodes

In this part, we present a experimental study of elliptical polarization properties of generated THz waves from a laser-induced plasma with a pair of double helix electrodes. We demonstrate that temporal propagation effects are indispensable for understanding the THz wave generation process and influence the THz polarization substantially. We observe a remarkable properties change of the elliptical THz polarization state with various electrodes design. Such ellipticity is a result of a sensitive dependence of the velocity mismatch between propagation of the optical pulses and generated THz pulses. Extensive numerical simulations were performed combining transient current model with pulse velocity retardation, which includes the longitudinal propagation effects responsible for polarization control of THz waves.

In the laser-induced ionization process, electrons released from molecules or atoms exhibit a net drifting current after passage of the laser pulses when they experience an asymmetric electrical field. This drifting current, which contributes to the far-field THz radiation, is aligned with the direction of an external DC field [3] or asymmetric optical field [4-5]. In our experiment with a pair of double helix electrodes, during the travel of the ionization front, which associates with the propagation of intense laser pulses, the induced net electron current is revolving along the filament due to the longitudinal variation of applied DC electrical field. Furthermore, due to the velocity mismatch between THz wave and optical beam, we find that the produced THz wave will travel ahead of optical excitation, which will eventually lead to a phase difference between the produced s and p components of THz pulse in the far field due to the retarded radiation.

An elliptically polarized wave can be resolved into an arbitrary set of mutually orthogonal component waves with their polarization perpendicular to each other and with a fixed phase change. By recomposing the THz electric fields obtained at two orthogonal directions, it is feasible to derive the elliptical trajectories if the THz pulse is elliptically polarized. In our experiment, the polarization of THz waves was obtained by composing the THz electric fields in two orthogonal directions measured by EO sampling technique, which is shown in Fig. 3. An elliptical THz polarization trajectory with an ellipticity $e = 0.5$ was observed on X-Y plane in Fig. 3(a) and (b). In the presence of the external helical electrical field, the handedness of elliptically polarized THz waves can be manipulated by the longitudinally revolving the direction of DC field.

In conclusion, we have demonstrated a balanced heterodyne air-biased-coherent-detection scheme for broadband terahertz waves by utilizing the tensor nature of third order nonlinear susceptibility. Moreover, we demonstrate that the polarization of far-field THz radiation can be significantly modified through manipulation of revolving electron transient current in laser filament with a pair of double helix electrodes.

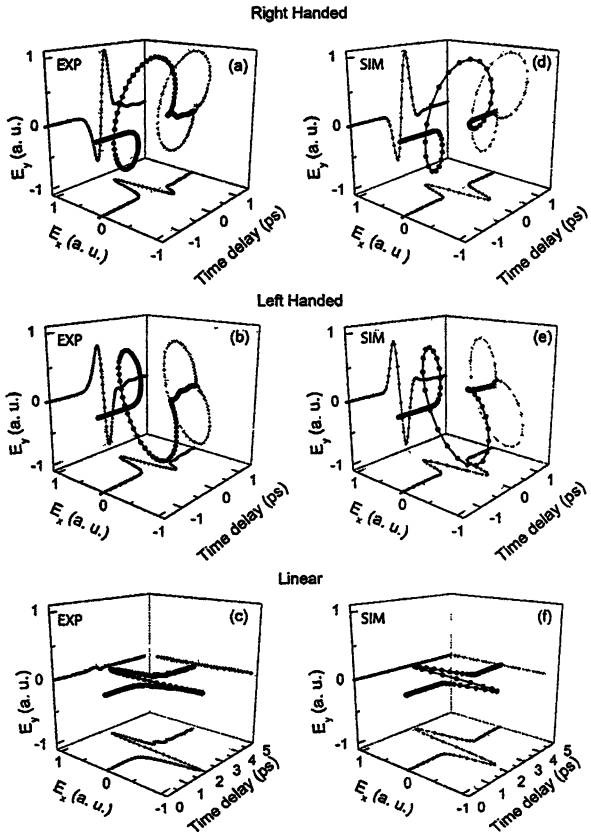

Fig. 3. Temporal evolution of electrical field vector of (a) right-handed and (b) left-handed elliptically polarized and (c) linear polarized THz pulses. Simulated temporal evolution of electrical field vector of (d) right-handed and (e) left-handed elliptically polarized and (f) linear polarized THz pulses. EXP: experimental results. SIM: simulation results.

References

1. *Lu, X. F., and Zhang, X.-C.* Balanced terahertz wave air-biased-coherent-detection // Appl. Phys. Lett. 2011. V. 98. P.151111.

2. *Karpowicz, N., Dai, J. M., Lu, X. F., Chen, Y. Q., Yamaguchi, M., Zhao, H. W., Zhang, X.-C., Zhang, L. L., Zhang, C. L., Price-Gallagher, M., Fletcher, C., Mamer, O., Lesimple, A., Johnson, K.* Coherent heterodyne time-domain spectrometry covering the entire "terahertz gap" // Appl. Phys. Lett. 2008. V. 92. P. 011131.

3. Houard, A., Liu, Y., Prade, B., Tikhonchuk, V. T., Mysyrowicz, A. Strong enhancement of terahertz radiation from laser filaments in air by a static electric field // Phys. Rev. Lett. 2008. V. 100. P. 255006.

4. *Dai, J. M., Karpowicz, N., Zhang, X.-C.* Coherent polarization control of terahertz waves generated from two-color laser-induced gas plasma // Phys. Rev. Lett. 2009. V. 103. P. 023001.

5. *Wen, H. D., Lindenberg, A. M.* Coherent terahertz polarization control through manipulation of electron trajectories // Phys. Rev. Lett. 2009. V. 103. P. 023902.

Symposium S

HIGH POWER MICROWAVE SOURCES

Powerful Masers and Lasers with Two-Dimensional Distributed Feedback

N. S. Ginzburg[1], N. Yu. Peskov[1], A. S. Sergeev[1], A. V. Arzhannikov[2], P. V. Kalinin[2], S. L. Sinitsky[2] and M. Thumm[3]

[1]Institute of Applied Physics, Nizhny Novgorod, Russia, ginzburg@appl.sci-nnov.ru
[2]Novosibirsk State University, Novosibirsk, Russia
[3]Karlsruhe Institute of Technology, Karlsruhe, Germany

Introduction

Two-dimensional (2D) distributed feedback is an effective method of production of high-power spatially-coherent radiation from an active media that is spatially extended along two coordinates, including relativistic electron beams of sheet and annular geometry. For FEMs an effective transverse (azimuthal) mode selection has been demonstrated experimentally under the transverse size of about 20 - 25 wavelengths and narrow-frequency microwave pulses of multi-MW power have been generated in the Ka- and W-bands using planar and coaxial geometry [1, 2].

At present, theoretical and experimental studies of generators of coherent radiation based on 2D feedback are continued in several directions including

- synchronization of radiation of two parallel sheet electron beams,
- experiments and modeling of coaxial Cherenkov BWO with external synchronizer based on 2D Bragg structure,
- advance of long-pulse FEL with 2D distributed feedback into THz waveband,
- development of quantum wall lasers with 2D distributed feedback.

Planar FEM driven by two parallel sheet e-beams

Current experiments at high-current accelerator "ELMI" (BINP, Novosibirsk) are aimed to development of two-stage sub-mm FEM exploiting an inter-cavity scattering [3]. For these experiments simultaneous generation and transport of two parallel intense sheet electron beams have been realized.

At the first stage of present experiments these beams were used to drive two parallel FEM channels, which were synchronized via transverse wave fluxes arise in the region of upstream 2D Bragg reflectors. State of art of these experiments is discussed in [4].

Powerful THz FEL with hybrid Bragg resonator

Advanced Bragg structures based on coupling between propagating and cutoff modes have been proposed for powerful long (microsecond) pulse THz-band FELs [5]. Advantage of Bragg structures of this type is the ability to provide mode selection in oversized system over y-coordinate directed between plates (fig. 1). It is attractive to compose a resonator with advanced Bragg structure as an up-stream reflector and to use a 2D Bragg structure as down-stream reflector (fig. 1), which allows to increase the system size over x-coordinate [6].

Results of simulation of FEL with such hybrid resonator operating at the frequency of 1 THz are presented in fig. 2. We suppose this FEM to be driven by 5.5 MeV electron beam with current density of 130 A/cm and pumped in the wiggler of 4 cm period and ~ 2 kOe transverse field amplitude (the gain parameter is $C \approx 1.4 \cdot 10^{-4}$). Lengths of the sections were taken to be $l_1 = 35$ cm (corrugation depth 1.2 μm), $l_2 = 28$ cm (corrugation depth 2 μm) and $l_0 = 195$ cm. The gap between plates was 3 mm (10 wavelengths) the width of the resonator and the sheet electron beam was 35 cm (about 10^3 wavelengths).

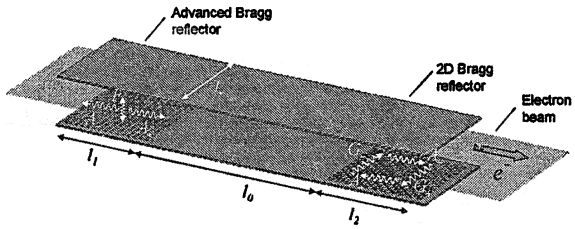

Fig. 1. Scheme of planar FEL with hybrid resonator composed from advanced up-stream and two-dimensional down-stream Bragg reflectors. Arrows mark the directions of partial waves propagation.

Simulations demonstrates establishment of the steady-state oscillations regime (fig. 2, *a*) and spatial synchronization of radiation (fig. 2, *b*). The main amplification takes place in the regular section. Output 2D Bragg mirror provides a relatively small reflection into the backward wave and the scattering into the transversely-propagating "synchronization" waves. As a result, 60% of the radiated power is extracted with the forward propagating wave. At the efficiency ~ 2% the output power reaches 350 MW.

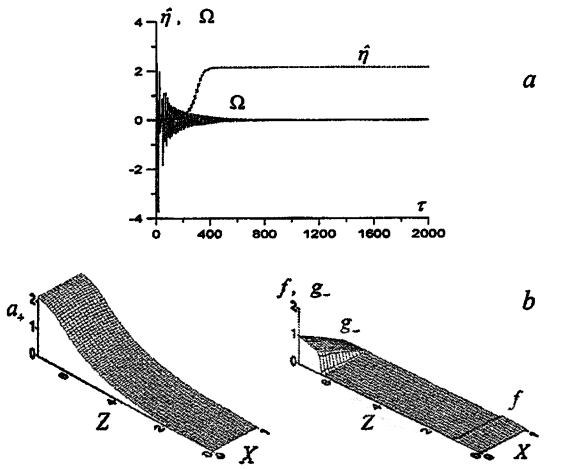

Fig. 2. **(a)** Time dependence of normalized efficiency and frequency shift from the Bragg frequency under the optimal parameters. **(b)** Spatial distributions of partial wave-beams in the steady-state regime.

Cherenkov BWO with 2D Bragg synchronizer

The use of 2D feedback mechanism is attractive also for Cherenkov devices [7]. Cherenkov masers are based on rectilinear electron beams, which simplify electron-optical system of the oscillator and make it possible to exploit more intensive electron beams in comparison with FEMs.

Experimental study of Ka-band coaxial BWO was started based on microsecond accelerator "Saturn" 200 keV / 150 A. (IAP RAS). Tubular electron beam was formed from a thermionic cathode with a mean diameter of 5 cm. The slow wave structure provide interaction of the beam with $TM_{0,1}$ wave of the coaxial waveguide. This wave was reflected from the cathode side by the cutoff narrowing. The 2D Bragg structure positioned at the collector side of the interaction space, provides the feedback loop for two counter propagating waves of $TM_{0,1}$ type and two azimuthally propagating waves of $TE_{16,0}$ type having opposite rotation. According to the 3D simulation this structure possess reflection zone for operating wave in the vicinity of 30 GHz with the power reflection coefficient of about 60%.

Simulations of coaxial BWO demonstrated that in the regime of "free oscillations" (without the 2D Bragg structure) multifrequency generation of different azimuthal harmonics n occurs. Installation of external 2D Bragg synchronizer results in establishment of a single frequency oscillation at the azimuthally symmetrical mode (fig. 3).

Results of the first experiments are presented in fig. 4. In configuration with external synchronizer stable narrow band generation has been observed. Calorimetric measurement indicates the power level of 1 – 1.5 MW in up to 500 ns pulses, that corresponds to electron efficiency of 5 – 10%.

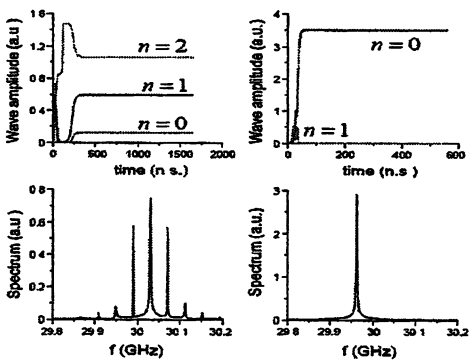

Fig. 3. Results of simulations of Ka-band coaxial BWO with (right column) and without (left column) 2D Bragg synchronizer: Time dependence of amplitudes of different azimuthal harmonics (top) and radiation spectrum (bottom).

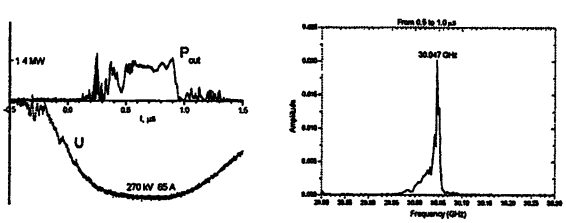

Fig. 4. Typical oscilloscope traces of the diode voltage and RF-pulse (left) and corresponding frequency spectrum (right) in Ka-band coaxial BWO with 2D Bragg synchronizer driven by the "Saturn" accelerator.

Lasers with 2D distributed feedback

In optics, 2D distributed feedback can be realized based on a dielectric structures (films) with double-periodic modulation (fig. 5) [8]. Laser active medium provides an isotropic amplification of all the partial waves independently of direction of their propagation. Within semi-classical approach nonlinear dynamics of 2D DFL is studied and spatial synchronization of radiation from extended active medium is demonstrated. In steady-state single-frequency regime the partial waves amplitudes distribution is similar to those of the fundamental mode of the 2D Bragg resonator. We should also mention the scalability feature of the system. If we increase the dimensions $l_{x,z}$ and proportionally scale down population inversion ρ_e (i.e. decrease pump intensity per square unit) and coupling coefficient α keeping $l_{x,z}\rho_e = const$ and $l_{x,z}\alpha = const$, then the distributions of partial waves in steady-state regime will not change and the total power output of the laser will proportionally scale up: $P / l_{x,z} = const$. Presently quantum wall hetero lasers with 2D distributed feedback is developed in collaboration between IAP RAS and IPM RAS (N.Novgorod).

This work was partially supported by the Russian Federal Program "Scientific and Pedagogical Staff for Innovative Russia" for 2009-2013.

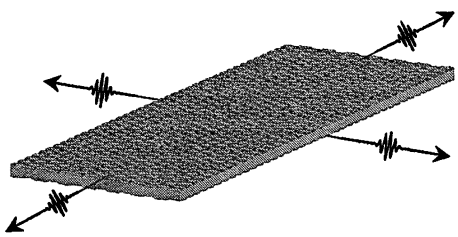

Fig. 5. Scheme of 2D distributed feedback laser (DFL). Arrows mark the directions of the output radiation.

References

1. *Arzhannikov A.V., e.a.* Generation of spatially-coherent radiation in planar free-electron maser with two-dimensional distributed feedback. // JETP Lett. 2008. V.87, No.11. P.618-622.

2. *Konoplev I.V., e.a.* Co-axial Free-Electron Maser based on two-dimensional distributed feedback // Phys. Rev. E. 2007. V.76. P.056406.

3. *Arzhannikov A.V., e.a.* Intercavity scattering scheme for two-stage generation of sub-mm radiation based on planar 2D Bragg FEM // Proc. of 6 Int. Workshop "Strong microwaves in plasma", N.Novgorod, Russia, 2005. P.228.

4. *Arzhannikov A.V., e.a.* Planar FEM driven by two microsecond sheet e-beams // presented at this conference.

5. *Ginzburg N.S., e.a.* Teraherz band free electron lasers based on coupling propagating and cut-ff modes // JETP Lett. 2010. V.91. P.286-289.

6. *Ginzburg N.S., e.a.* Powerful terahertz Free electron lasers with hybrid Bragg reflectors // Phys. Rev. ST-AB. 2011. V.14. P.042001.

7. *Ginzburg N.S., e.a.* Cherenkov masers with 2D distributed feedback // Tech. Phys. Lett. 2010. V.36, No.2. P.77-86.

8. *Baryshev V.R., e.a.* Dynamics of lasers with two-dimensional distributed feedback // Opt. Comm. 2008. V.281. P.4879.

High Power Pulsed Terahertz Gyrotrons

M.Yu. Glyavin, A.G. Luchinin

Institute of Applied Physics, Nizhny Novgorod, Russia, glyavin@appl.sci-nnov.ru

The important and promising direction of gyrotron development is investigations in the sub-terahertz (sub-THz) and terahertz (THz) frequency bands. Development of compact, simple and reliable sources of coherent sub-THz and THz radiation is important for numerous applications, which include plasma physics, spectroscopy, detection and imaging of explosives and weapons, new medical technology, etc. Gyrotrons are much more compact than powerful free electron lasers because they do not require large accelerators or high-voltage modulators. From the other hand the gyrotrons can produce essentially higher output power comparing with solid state devices.

However, to provide cyclotron resonance between gyrating electrons and fast waves excited in smooth waveguides at THz frequencies near cutoff, high magnetic fields are necessary: in the range of 40 T for the fundamental harmonic interaction at the radiation frequency of 1 THz; at higher harmonics magnetic field decreases inversely proportional to the cyclotron harmonic number. It should be emphasized that at the sub-THz and THz frequencies ohmic losses in gyrotron cavities become drastically important for the operation and the efficiency of the device. There is a known way to diminish the role of this factor, namely, enlargement of the transverse cavity size and a corresponding increase in the radial index of the operating mode. So, the frequency enhancement needs operating at high order modes to store the reasonable scale of interaction region. The progress in frequency increasing was delayed by problem of mode competition at high order harmonic modes operation and impossibility realized non-volatile pulsed coils with strong enough magnetic fields and effective cooling for fundamental harmonic operation. It should be taken into account that typically magnetic field, which can be produced in cryomagnets with a large enough inner bore, do not exceed 20 T. Higher magnetic fields can be realized only with the use of pulsed or hybrid solenoids.

In the design of gyrotrons operating with pulsed magnetic fields a number of specific requirements were taken into account. First, to provide cyclotron resonance condition accurately enough, magnetic field should be reproducible from pulse to pulse and its value during the microwave radiation pulse should vary by less than 0.1%. Second, conductivity of a resonator wall should meet contradicting requirements: on the one hand, this conductivity should be rather poor to allow varying magnetic field to penetrate into the resonator; on the other hand its inner surface should have conductivity high enough to provide reasonably low level of ohmic losses. Finally, the tube and the solenoid should be strong enough to withstand mechanical stresses caused by high pulsed magnetic fields.

In the beginning of 1980s at the IAP RAS the fundamental-harmonic gyrotron with a strong pulsed magnetic field was realized [1]. In these experiments, a frequency up to 0.65 THz with a power of 40 kW was obtained for pulse duration of 50 μs and step frequency tuning from pulse to pulse. A high output power of 375 kW at the frequency of 0.33 THz has been obtained in 3 μs pulses in the Massachusetts Institute of Technology (MIT) [2].

In the recent years terahertz gyrotrons got remarkable achievements in experimental research. Gyrotrons with a pulsed solenoid developed at the FIR FU (Fukui, Japan) demonstrated the excitation of 1 THz frequency with a several tens Watt power level at the second cyclotron harmonic [3]. The solenoid based on an original ice-protected technology and maximum field intensity was up to 20.5 T. The pulse magnet was powered by a capacitor bank with a stored energy up to 300 kJ. The operation modes seem to be $TE_{1,12}$ and $TE_{4,12}$ with frequencies 0.9 THz and 1.01 THz and pulse durations up to 1 ms and 0.5 ms, respectively [4].

The most powerful pulsed THz tubes have been developed at IAP RAS. A 50 T solenoid was made of a composite cable consisting of a 40%Nb-60%Ti alloy mechanically reinforced in an outer copper shell for a compact (overall size about 400 mm) demountable THz gyrotron tube. For reducing ohmic heating and stabilizing the operation, the solenoid was cooled by liquid nitrogen, which reduces the resistance by a factor of 7 in comparison with the room temperature resistance. The cable was wired directly on a thin stainless steel gyrotron body. This allowed the significant reduction of the solenoid inner bore diameter (up to 6 mm) and the energy required for obtaining the necessary magnetic field. Magnetic field was produced in the course of discharge of a bank of capacitors. The voltage and the coil current in 1.5 ms pulses did not exceed 2.5 kV and 6 kA, respectively (total storage energy was about 5.6 kJ). The pulse-to-pulse reproducibility of the magnetic field was within 0.05%. Due to limitations caused by cooling the pulsed solenoid, the repetition rate was limited by one shot in a minute.

When the magnetic field is varied, a number of modes with frequencies close to 1 THz are excited. Detection of microwave power was made by a silicon point contact diode and by the dummy load, which has the sensitivity allowing for detecting the microwave energy in single shots at a 10 mJ level. To measure the THz frequency the method based on mixing the gyrotron signal with the signal from a millimeter-wave frequency synthesizer was used.

For a magnetic field of 38.5 T and an electron beam having parameters 24 kV and 3 A, the $TE_{17,4}$ mode was excited at a frequency of 1.02 THz with pulse duration of 40 μs and the power averaged over the pulse being up to 5 kW. The highest frequency of 1.3 THz with pulse duration of 30 μs and the power

averaged over the pulse about 0.5 kW has been observed with the field close to 48 T [5, 6]. After more than 3500 pulses with magnetic field intensity higher than 35 T no any changes at the coil operation observed.

There are some plans to developed internal mode converter and improved solenoid cooling allowing the operation with higher repetition rate (up to 2 Hz) and high average power [7] but up to present the tube operation limited by coil mechanical strength and cooling facilities and have no success.

For high density plasma diagnostic the sub-THz radiation at significantly higher than present power level is needed [8]. To increase output power to sub-MW level, fundamental harmonic gyrotron with operating frequency 0.33 THz was developed at the IAP RAS based on the coil with field intensity up to 15 T. The solenoid consists of 10 sections with water cooling and the pulse duration about 2.5 ms with the repetition rate about 1 Hz was obtained. The calculated gyrotron efficiency at fundamental harmonic for helical electron beam with voltage 70 kV, current 60 A is closed to 0.3. During preliminary single shorts tests with 1.2 MW beam power, 0.4 MW/30 μs microwave radiation was measured by dummy load.

One of the interesting applications of THz radiation is the detection of concealed sources of ionizing radiation [9]. The idea is to focus powerful THz wave beam in a small spot for getting the RF electric field strong enough to break down the air if the background ionization level is sufficiently elevated. The peculiar feature of this method is the fact that the radiation can be focused in a small volume in which in the absence of additional sources of ionizing radiation can be no free electrons to initiate the breakdown. Correspondingly, it should take some time for a free electron to reach the region where strong THz field is focused and initiate there a breakdown. So there should be a certain statistical lag time for initiating the breakdown after the gyrotron is turned on, while at longer wavelengths there are always some free electrons in the focal spot and, hence, such delay is absent.

For this goal in a joint project with the Center on Applied Electromagnetics University of Maryland the 0.67 THz gyrotron which will deliver the power in the range of 0.1-0.2 MW in single-shot pulses is under development [10]. The microwave pulse duration will be several tens of microseconds. The operating frequency was dictated by an atmospheric window where the transmission losses are at the 50 dB/km level and in the case of wave beam propagation over the distance of about 20 m the wave power will be attenuated by about 1 dB. The coil with liquid nitrogen cooling was successfully tested and preliminary tube test has been started.

As already mentioned, the high harmonic operation needs an improved mode selection. The problem of high harmonic operation can be mitigated by employing a so-called large-orbit electron beam, where all the electrons encircle the axis of the cavity. Based on this advantage, Bratman et al (IAP RAS, Russia) developed a large-orbit gyrotron operated at 1 THz in the third harmonic of $TE_{3,7}$ mode. The output power of 0.4 kW was successfully realized and the operating magnetic field was greatly decreased to 13.6 T [11]. The main advantages of this tube are internal mode converter to Gaussian beam and microwave pulses repetition frequency up to 0.1 Hz. Some other promising approaches for selective high harmonic excitation such as step-cavity with mode conversions [12] and two mirrors cavity [13] are discussed as well. For example, calculations predict the possibility $TE_{32,5}/TE_{32,6}$ modes excitation with a frequency close to 2 THz in a step (diameter difference about 0.1 mm) cavity which can be installed in a tube described in Ref. [5].

Despite the problems of high ohmic losses, parasitic modes discrimination, small scale, and requirement of strong operating magnetic fields the THz frequency has been achieved by the pulse gyrotrons. Today it is clear that relatively small-size tubes with a kilowatts level of output power at the frequencies of 0.3-1.5 THz will be available soon for many applications.

References

1. *Flyagin, V. A., Luchinin, A.G, Nusinovich, G. S.* Submillimeter-wave gyrotrons: Theory and experiments // Int. J. IRMM Waves, 1983, V. 4, P. 629-637.

2. *Kreischer, K., Grimm, T., Guss, W., Temkin, R.* The operation of a megawatt gyrotron in the submillimeter waveregion // Technical Digest of the International Electron Devices Meeting, 1989, P. 751-754

3. *Idehara, T., Tsuchiya, H., Watanabe, O. et al.* The first experiment of a THz gyrotron with a pulse magnet // Int. J. IRMM Waves, 2006, V. 27, P. 319-331.

4. *Idehara, T., Saito, T., Mori, H., et al.* Long Pulse Operation of the THz Gyrotron with a Pulse Magnet // Int. J. IRMM Waves, 2008, V. 29, No. 2, P. 131-141.

5. *Glyavin, M. Yu., Luchinin, A. G., Golubiatnikov, G. Yu.* Generation of 1.5-kW, 1-THz Coherent Radiation from a Gyrotron with a Pulsed Magnetic Field // Phys. Rev. Lett., 2008, V. 100, P. 015101.

6. *Glyavin, M. Yu., Luchinin, A. G.* Powerful terahertz gyrotrons based on pulsed magnets // Int. J. of Terahertz Science and Technology, 2009, V. 2, No. 4, P. 150-155.

7. *Read, M., Ives, L., Neilson, J., Nusinovich, G.* Development of a High Power Pulse THz Gyrotron, IEEE Int. Vacuum Electronics Conf., 2007, P. 347-348.

8. *Skvortsova, N. N., Batanov, G. M., Sarksyan, K. A. et al.* Opportunities for plasma diagnostics in fusion devices // *Strong Microwaves in Plasmas: sources and applications. Ed. A G. Litvak*, 2009, Nizhny Novgorod, V. 2. P. 384-391.

9. *Granatstein, V. L., Nusinovich, G. S.* Remote sensing of an elevated level of background ionization with a 1 THz, 1 kW Gyro-BWO // 51 Annual Meeting of the APS-DPP, 2009, paper BO6-2, P. 29.

10. *Nusinovich, G.S., Pu, R., Antonsen, Jr., T.M., et al.* Development of THz-range gyrotrons for detection of concealed radioactive materials // Int. J. IRMM&THz Waves, 2011, V. 32, P. 380-402.

11. *Bratman, V. L., Kalynov, Yu. K., Manuilov, V. N.* Large-Orbit Gyrotron Operation in the Terahertz Frequency Range // Phys. Rev. Lett., 2009, V. 102, P. 245101.

12. *Bratman, V., Idehara, T., Kalynov, Yu., et al.* Design of powerful and compact THz oscillator // Int. J. IRMM Waves, 2006, V. 27, P. 1063-1071.

13. *Ginzburg, N., Zotova, I., Zaslavskii, V., et al.* Submillimeter planar gyrotrons with transverse diffraction output of radiation // Technical Phys. Lett., 2011, V. 37, P. 79-82.

High Power THz Technologies Opened by High Power Radiation Sources – Gyrotron FU CW Series

T. Idehara, F. Horii, Y. Fujii, I. Ogawa, T. Saito, T. Fujiwara[1], T. Suehara[2] and R. Dupree[3]

Research Center for Development of Far-Infrared Region, University of Fukui (FIR FU), Fukui 910-8507, Japan
[1]Institute of Protein Research, Osaka University, Suita, Osaka 565-0871, Japan
[2]International Center for Elementary Particle Physics, University of Tokyo, Tokyo 113-0033, Japan
[3]Center for NMR, The University of Warwick, Coventry CV4 7AL UK

Gyrotrons are extremely high power radiation sources even in THz frequency region comparing with conventional radiation sources. We have developed gyrotron FU CW series for application to many high power THz technologies. Up to the present, nine CW gyrotrons were developed. Each gyrotron has its own objective and was optimized for respective application subject. Now, the applications are extended to wide fields including DNP-NMR measurement, ESR echo experiment, direct and precise measurement on hyperfine structure of positronium, experiment on effective operation of Bloch oscillator using semiconductor super lattice, etc. In this paper, we will introduce such high power THz technologies opened by high power THz radiation sources.

1. Introduction

At the present, a high power THz radiation source such as a high frequency gyrotron is a key technology in order to extend the application to high power THz technologies. High power THz spectroscopy open new areas of material research such as DNP enhanced NMR spectroscopy for analysis of protein structure and polymer surface, the first experiment of direct measurement on hyperfine structure of positronium, high frequency ESR echo measurement in THz region for study on quick relaxation phenomena concerning electron behavior and X-ray detected magnetic resonance (XDMR) experiment to probe the resonant precession of the magnetization caused by a THz-wave pump field. For such applications, we are developing in our research center FIR FU high power CW terahertz radiation sources – Gyrotron FU CW Series which consists of nine CW gyrotrons.[1)] In this paper, two examples of the applications are introduced.

2. 600 MHz, 300 MHz and 200 MHz DNP-NMR Spectroscopy

We have already applied our Gyrotrons FU CW II and VI for 600 MHz DNP-NMR, Gyrotron FU CW VII for 300 MHz DNP-NMR and Gyrotron FU CW IV for 200 MHz DNP-NMR. Table 1 summarizes the parameters of each DNP-NMR spectroscopy.

Table 1

Summary of DNP-NMR spectroscopy using Gyrotron FU CW Series as high power sub-THz radiation sources

	600MHz-DNP	300MHz-DNP	200MHz-DNP
Used gyrotron	FU CW II and VI	FU CW VII	FU CW IV
Freq. of gyrotron f	394.3 GHz frequency tubable	187 GHz	131.3 GHz
Freq. of NMR F	600 MHz	285MHz	200 MHz
Enhancement E	22	70	40
Institutions	Osaka Univ.	Warwick Univ.	Univ. Fukui

Fig. 1 shows the enhancement of 600 MHz NMR absorption signal with the irradiation of gyrotron output.[2)] Comparing with NMR signal without the irradiation (lower trace), the enhancement factor is 10.4. The maximum factor achieved up to the present is around 20 which enables us to shorten the measurement time for protein study drastically.

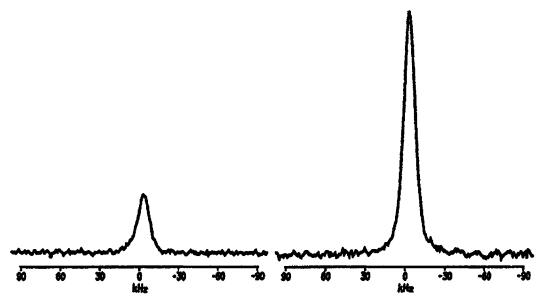

Fig. 1. 600 MHz DNP measurement result. ^{13}C-NMR absorption signal for u-glucose is enhanced by irradiation of gyrotron output. Enhamcement factor $E = 4.4$ at 14.1 T.

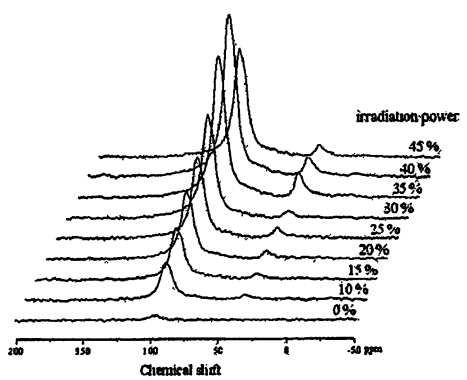

Fig. 2. 200 MHz DNP/CP/MAS ^{13}C NMR spectra with the duty ratio as a parameter. The enhancement factor E reaches around 32 at the duty ratio of 40%. After that, E decreases because of the heating effect of the irradiation.

Fig. 2 shows 200 MHz-NMR spectra at -175°C for Cl ^{13}C-enriched glucose dissolved in DMSO-d_6/D_2O/H_2O containing 4-amino-TEMPO. Gyrotron FU CW IV operates in the pulse mode. The repetition rate is 5 Hz and the output power typically 30 W. The

avraged irradiation power is changed by changing the duty ratio up to 45 percent, so that the averaged output power is changed up to 13.5 W. As seen in the figure, the enhancement factor is increased with the averaged irradiation power increased. The highest enhancement factor observed up to the present is around 40. We are intending to use TOTAPOL as a radical to achieve a drastic increase of the enhancement factor. Hopefully, the factor will reach around 100 or higher.

3. Direct measurement of hyperfine structure of positronium

A positronium which consists of an electron and a positron has two states, ortho- and para- states. The ortho-state is triplet and the para-state singlet. The life times of both states are 142 ns and 125 ps, respectively. Therefore, almost all cases, positroniums exist in ortho-state. The energy level of ortho-state is higher than that of para-state by around 203.4 GHz. The energy difference has not been measured directly, because we had no high power radiation source with such a high frequency. Now, we are trying it by using Gyrotron FU CW V as a radiation source.[3] In Fig. 3, is illustrated the experimental setup.

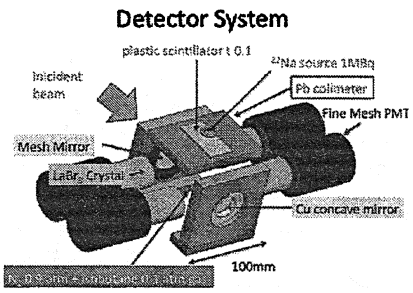

Fig. 3. The experimental setup for direct measurement of hyperfine structure of positronium.

The output power of TE_{03} mode from Gyrotron FU CW V is converted to a Gaussian mode and injected into Fabry-Perot resonator. The output power at the vacuum window is 0.5 to 0.6 kW. Inside the Fabry-Perot resonator, the equivalent power irradiated on the positroniums is estimated to be around 10 kW.

When positroniums are irradiated by such a high power sub-THz radiation with the frequency closed to 203.4 GHz, ortho-states transit to para states. Then, para states decay immediately with 2γ ray emission. If we can sweep the frequency of the radiation and observe the γ ray emission simultaneously, the energy difference can be decided directly.

Fig. 4 shows the preliminary result using Gyrotron FU CW V with output frequency of 203.03 GHz and the equivalent irradiation power inside the resonator is around 10 kW. The vertical axis is the difference between γ ray counts per second with and without irradiation of gyrotron output. This means the signal rate of the level transition from ortho- to para-state. It is estimated as 3.88±0.84 mHz. The statistical error σ=0.84 mHz. The transition signal rate was confirmed with 4.6σ. This is the first experiment on the direct measurement of the level transition from ortho- to para-state using high power sub-THz radiation with the power of around 0.5 kW.

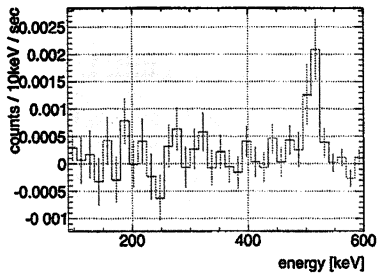

Fig. 4. The preliminary result of transition of states from ortho- to para-state. The signal rate is estimated as 3.88±0.84 mHz. The transition was confirmed with 4.6σ.

This is a preliminary experiment using a frequency fixed radiation source – Gyrotron FU CW V. In order to determine the energy difference between both states, the frequency of the radiation source should be varried. Now, the development of a frequency-tunable gyro-BWO is proceeding for application to the final analysis on the hyperfine structure of positronium. The designed output power and the tunable range are higher than 1 kW and ±1.6 GHz near the center frequency of 203.4 GHz.

4. Summary

In FIR FU, we are developing high power sub-THz radiation sources – Gyrotron FU CW Series, for application to many high power THz technologies. Among these technologies, DNP-NMR spectroscopy for analyses of complicated protein molecules and polymer surface and the first direct measurement on hyperfine structure of positronium are being advanced as follows,

1) A 600 MHz DNP-NMR spectroscopy was developed at Osaka University by using Gyrotron FU CW II as a radiation source. The maximum enhancement factor is around 22. This is the DNP enhancement result at the highest magnetic field of around 14.1 T. In addition, 300 MHz and 200 MHz DNP-NMR measurements are succeeded at Warwick University and University of Fukui, respectively. At the present, the enhancement factors for both cases are 70 and 40.

2) The direct measurement on level transition from ortho- to para- of positronium has been carried out successfully by use of Gyrotron FU CW V as a radiation source. A Fabry-Perot resonator was used to store the radiation energy. The equivalent irradiation power in the resonator is around 5. The signal rate of the level transition is estimated as 3.88±0.84 mHz.

The development of a frequency tunable gyro-BWO for direct measurement on the hyperfine structure is under way.

References

1. *T. Idehara et al.*, Thin Solid Films 519 (2008) 1503-1506.

2. *Yoh Matsuki et al.*, Physical Chemistry Chemical Physics 12, (2010) 5799-5803.

3. *Akira Miyazaki et al.*, Materials Science Forum Vol. 666 (2011) pp 133-137.

High Power Nanosecond Microwave Oscillators with Phase Synchronization

V.V. Rostov[1], A.A. Elchaninov[1], A.I. Klimov[1], V.Yu. Konev[1], I.V. Romanchenko[1], G.A. Mesyats[2], M.I. Yalandin[3]

[1]Institute of High Current Electronics SB RAS, Tomsk, Russia, rostov@lfe.hcei.tsc.ru
[2]Lebedev Physical Institute RAS, Moscow
[3]Institute of Electrophysics UrB RAS, Ekaterinburg, Russia

Recently the development of high-power microwaves (HPM's) has become more and more intensive. On this pathway, nonconventional circuit designs, new active media and generation modes can provide possibilities to master record-breaking parameters and new applications of HPM's. In this context, of interest are multi-channel oscillators with high coherence due to shock excitation by supply voltage of short rise time. The paper briefly reviews our experimental research in phase synchronization on two types of two-channel nanosecond X-band HPM sources of Cherenkov superradiance (SR) pulses, of which one ensures a peak power of 300 MW in each channel and the other, being based on Gunn diodes, ensures a peak power of 20 W in each channel at a pulse duration of 11 ns.

Synchronization of two SR channels

The background for research in the possibility to synchronize electrodynamically independent SR channels was the data of our previous S-band [1] and X-band [2] experiments that demonstrate high stability of the pulse-to-pulse phase distribution. The rms phase deviation on the time scale was found to approximate the rise time dispersion of supply voltage. A fundamentally important problem in understanding the experimental results is the conditions of picosecond stabilization of the explosive electron emission (EEE) delay, which is generally variable in a wide range in response to slightly varying field strength at the edge of a cylindrical cathode. For the EEE delay not to destabilize the microwave pulse phase pattern, its dispersion may not go beyond the range from several to tens of picoseconds. The field emission current density (up to 10^{10}–10^{11} A/cm^2 [3]) required for the so short EEE delay apparently approximates its limiting level due to weakening of the local field of strength $E_{loc} \sim (3–6) \cdot 10^8$ V/cm by the field of the electron space charge near the emitters. As disclosed in the experiments reported in [4–6], the cathode that are best suited in this case are dense graphite cathodes with an extremely thin edge of about 0.1–0.3 mm and metal dielectric film (MD) cathodes. In particular, an increase in root-mean-square EEE delay from 2–3 to 8 ps in 10^4 pulses was observed in experiments with two-channel injection of two parallel beams from identical graphite cathodes [4]. The lifetime of MD cathodes (50-μm copper on a glass fiber plastic substrate) was found to increase in [6]: the EEE delay increased slowly in about 10^6 pulses.

For experiments, a laboratory mockup (Fig. 1) based on a SINUS-200 high-voltage accelerator with a forming line of impedance 30 Ohm and electrical length 9 ns was designed and manufactured [6]. The accelerator allowed repetitive pulsed operation with a pulse repetition frequency up to 100 Hz. In the self-breakdown mode, the main gas gap switch ensured TEM pulses of amplitude up to 300 kV in a coaxial transmission line.

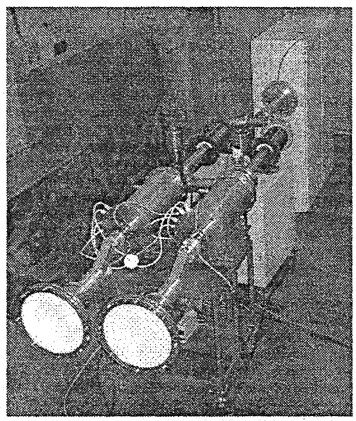

Fig. 1. Two-channel system for the generation of SR pulses of duration 1 ns and peak power up to 0.3 GW in a channel.

The electrical length of the transmission lines downstream of a coaxial T-branch was more than half of the pulse duration. This ensured reliable decoupling between the channels. The vacuum diodes and the slow-wave structures of the generators were identical in geometry and were placed in solenoids with series dc supply. The magnetic field was 0.5 T. At the first stage of experiments, a peaking spark gap switch (peaker) based on a nonlinear line with an unsaturated ferrite section was located in each channel upstream of the T-branch [6]. At the next stage, the peakers were removed and the voltage pulse transmission channels were each incorporated with an identical NiZn ferrite nonlinear line (30 cm) whose saturated state was specified by an external solenoid with a constant axial magnetic field (H_0 up to 50 kA/m). With no and with a low magnetic field, the transmitted voltage pulse was sharpened to about the same degree (from 3 ns at the input to ≈ 1 ns downstream of the peakers). As H_0 was increased, the differential detector signal, which is proportional to the voltage derivative, increased 2–2.5 times to a certain maximum level in the range $H_0 \approx$ 15–25 kA/m. Thus, the maximum rate of rise of the voltage is estimated to be

430 kV/ns. The shift of the pulse rise time (by about 100 ps per 3 kA/m) allowed control of the relative phase within more than the full oscillation period. As a result, the characteristic dispersion of the phase difference at fixed H_0 in each channel was kept at a level of several picoseconds as before [1], but independent control was made possible.

"Double-barreled" Gunn oscillators

Phase synchronization on a steep portion of the rate of rise of the modulator voltage was studied in [7] as applied to electrodynamically decoupled X-band Gunn oscillators [8] producing microwave pulses with a peak power of 20 W and pulse duration of 11 ns. This method was proposed earlier [9] and assumes that phase synchronization is due to shock excitation of a waveguide resonator by the Gunn diode current pulse just before microwave oscillation arises. In this case, the formation of a domain is strictly timed with a current jump of about the oscillation period.

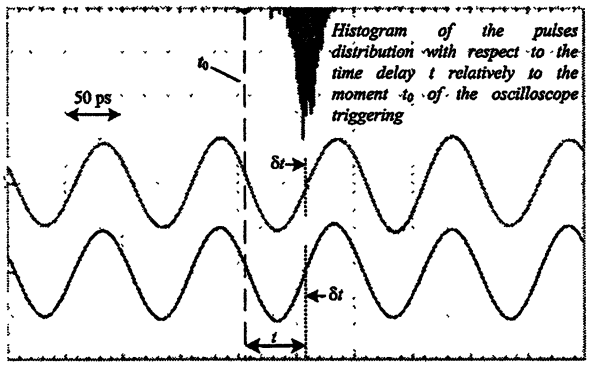

Fig. 2. Histogram of the pulses distribution with respect to the time delay t relatively to the oscilloscope triggering.

In this paper, the phase synchronization of microwave oscillation was realized by applying a modulator voltage pulse with clearly defined sharpening of the rise time to a Gunn diode. Methods of measurements were similar to those used in [6]. A TDS6254C Tektronix digital oscilloscope was triggered on a steep of the modulator voltage rise time. The dependence of the phase difference instability of the oscillators was investigated at a rate of rise of the voltage dU/dt corresponding to the steep of the pulse rise time just before microwave oscillation arises. It is found that the rms deviation σ of the time delay δt corresponding to a fixed phase of two oscillators (Fig. 2) is less than the rms deviation of the time delay t of this phase with respect to the modulator pulse rise time: $\sigma_{\delta t} = 1.8$ ps and $\sigma_t = 8.6$ ps, respectively. The deviation $\sigma_{\delta t}$ decreases from 0.18 to 0.1 rad with increasing dU/dt from 6.6 to 14.2 ps. According to estimations, the operating mode of the Gunn oscillators is likely to be associated with a strong effect of the microwave electric field on the domain behavior.

Conclusion

The research results give confidence that the development of multi-channel nanosecond HPM sources is quite promising. This field offers a wide range of activity in theoretical development and selection of optimum types of generators to increase the duration of coherent signals. In particular, coherence of several electron generators with limited pulse duration can be ensured in a mode similar to the operating mode of Gunn diodes with a dominating, in our viewpoint, transit-time mechanism. Limitation of the pulse duration in each particular case can be specific and, according to a specified degree of coherence, can impose more or less rigid requirements on the stability of the voltage pulse shape with a certain optimum steep of the rate of rise and division accuracy for the channels. In engineering terms, there are no obstacles to design in the near future 4-channel and then 8-channel superradiance systems with a common high-voltage modulator.

This work was supported in part by RFBR, Grants: 10-08-00420a, 10-08-00277a, and 11-02-00097.

References

1. *Afanasev, K.V., Bykov, N.M., Gubanov, V.P., Elchaninov, A.A., Klimov, A.I., Korovin, S.D., Rostov, V.V., Stepchenko, A.S.* A High-Power Periodic Nanosecond Pulse Source of Coherent 8-cm Electromagnetic Radiation // Tech. Phys. Lett. 2006. V. 32, No. 11, pp. 925–927.

2. *Grishin, D.M., Lyubutin, S.K., Mesyats, G.A., Rostov, V.V., Rukin, S.N., Slovikovsky, B.G., Timoshenkov, S.P., Ulmaskulov, M.R., Sharypov, K.A., Shpak, V.G., Shunailov, S.A., and Yalandin, M.I.* Generation of Gigawatt 10-GHz Pulses with Stable Phase // Tech. Phys. Lett. 2008. V. 34, N. 10, pp. 822–824.

3. *Mesyats, G.A. Explosive Electron Emission.* Ekaterinburg, Russia: URO-Press. 1998. P. 248.

4. *Yalandin, M.I., Reutova, A.G., Ulmasculov, M.R., Sharypov, K.A., Shpak, V.G., Shunailov, S.A., Klimov, A.I., Rostov, V.V., Mesyats, G.A.* Picosecond Stability of Injection of Parallel High-Current Pulsed Electron Beams // *Tech. Phys. Lett.* 2009. V. 35, N. 9, pp. 804–807.

5. *Yalandin, M.I., Reutova, A.G., Sharypov, K.A., Shpak, V.G., Shunailov, S.A., Ulmasculov, M.R., Rostov, V.V., Mesyats, G.A.* Stability of Injection of a Subnanosecond High-Current Electron Beam and Dynamic Effects Within Its Risetime // *IEEE Trans. on Plasma Sci.* 2010. V.38, N. 10, pp. 2559–2564.

6. *Elchaninov, A.A., Klimov, A.I., Kovalchuk, O.B., Mesyats, G.A., Pegel, I.V., Romanchenko, I.V., Rostov, V.V., Sharypov, K.A., Yalandin, M.I.* Coherent Summation of Power of Nanosecond Relativistic Microwave Generators // *Tech. Phys.* 2011. V. 56, N.1, pp. 121–126.

7. *Konev, V. Yu., Gubanov, V. P., Klimov, A. I., Kovalchuk, O. B., Rostov, V. V., Sharypov, K. A., Yalandin, M. I.* Phase stabilization of nanosecond Gunn oscillators // Instrum. and Exp. Techniques. 2011 (to be published).

8. *Gubanov, V. P., Klimov, A. I., Kovalchuk, O. B., Konev, V. Yu., Rostov, V. V.* An X-band nanosecond Gunn-effect generator // Instrum. and Exp. Techniques. 2010. V. 53, No. 5. P. 710–713.

9. *Vvedensky V. Yu., Andriyanov A. V., Ermilov E. A.* An Oscillator of coherent nanosecond microwave pulses // Instrum. and Exp. Techniques. Rus. 1975. No. 1. P. 114–115.

Development of High Power Gyrotrons in the Sub Terahertz Region for Application to CTS Measurement

T. Saito[1], Y. Tatematsu[1], N. Yamada[1], S. Ogasawara[1], R. Ikeda[1], I. Ogawa[1], T. Idehara[1], V. N. Manuilov[2]

[1] Research Center for Development of Far-Infrared Region, University of Fukui, Fukui 910-8507, Japan
[2] Nizhny Novgorod State University, Radiophysical Faculty, Nizhny Novgorod 603600, Russia

High power sub terahertz pulse gyrotrons are under development in FIR FU for application to CTS measurement on a fusion plasma device. Up to now, pulse sub terahertz radiation exceeding 60 kW at about 390 GHz has been obtained from a gyrotron with second harmonic oscillation. This paper reports detailed study of oscillation characteristics of the gyrotron. Try for still higher power is also described.

Introduction

Recently high frequency gyrotrons have been applied to various fields. Among those, use of a sub terahertz high power gyrotron for collective Thomson scattering (CTS) diagnostics in a fusion plasma device is a very challenging task. For a power source of CTS, gyrotrons for electron heating with frequencies from tens of GHz to 140 GHz are now used and physics data have been recently obtained from several devices [1, 2]. However, electromagnetic waves with these frequencies suffer from strong plasma dispersion effects. Moreover, background electron cyclotron emission becomes a large noise source. Then, the parameter range (CTS range) in which CTS measurement is effective is limited. Use of a higher frequency gyrotron in the sub-terahertz range will resolve these problems [3, 4]. In fact, as plotted in Fig. 1, the CTS range is extended to a much higher density region by using a 400 GHz gyrotron. This is of particular significance in the Large Helical Device in NIFS, in which the high density regime is considered to be an alternative path to a fusion reactor [5].

We have started development of a high-power, sub terahertz pulse gyrotron with a frequency around 400 GH and have demonstrated more than 50 kW at 350 GHz and about 40 kW at 390 GHz in the first stage [6]. Succeeding to this result, a sealed-off gyrotron tube has been fabricated to realize assemble of the gyrotron parts with high accuracy and operation at a good vacuum condition [7].

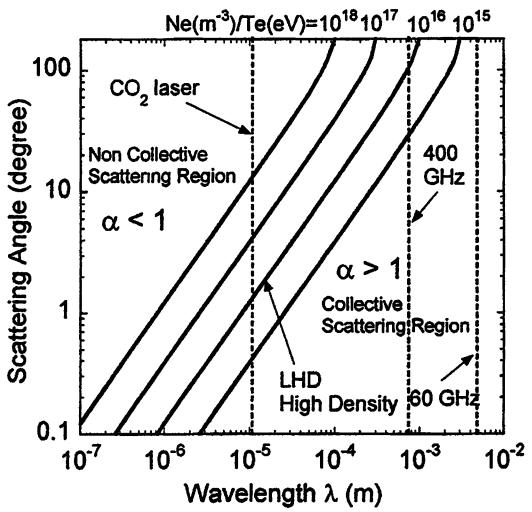

Fig. 1. Collective scattering region is shown for the wavelength of the power source. Parameter is the ratio of the electron density in m^{-3} to the electron temperature in eV. The symbol α represents the Salpeter parameter

Experimental Results and Discussion

The electro dynamic design of the sealed-off gyrotron is the same as that of the former gyrotron tube of demountable type. The dimensions of the cavity resonator are 2.99 mm in diameter and 12 mm in length. The electron gun is designed to inject an electron beam with a diameter around 1.9 mm with a good quality [8]. This gyrotron has no internal mode convertor. The oscillation power is radiated vertically upward through a vacuum window made of c-axis cut sapphire crystal. Operation of the gyrotron is in pulse mode. The pulse length is several microsecond and the repetition rate is less than 10 Hz.

A group of second harmonic oscillation modes such as the $TE_{3,7}$, $TE_{1,8}$ and $TE_{17,2}$ modes has been adopted rather than the $TE_{8,5}$ mode in the new gyrotron because the $TE_{8,5}$ mode suffered from mode competition with the fundamental $TE_{4,3}$ mode. The $TE_{3,7}$, $TE_{1,8}$ and $TE_{17,2}$ modes are further isolated from the competing $TE_{4,3}$ mode. The electron beam can be coupled to each of the $TE_{3,7}$, $TE_{1,8}$ and $TE_{17,2}$ modes.

Figure 2 shows the oscillation intensity measured with a pyroelectric detector as a function of the magnetic field strength B_c at the cavity for the case of the beam voltage $V_k = 50$ kV and the beam current $I_b = 4$ A. The oscillation mode turns successively from the $TE_{3,7}$ mode to the $TE_{8,5}$ mode with increasing B_c. Each

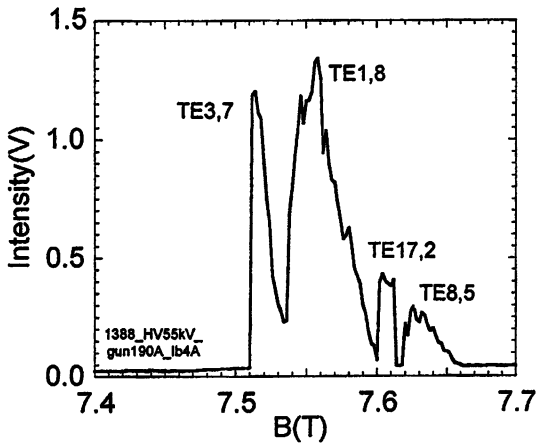

Fig. 2. Oscillation intensity is plotted as a function of the magnetic field strength at the cavity. Labels near each peak indicate the oscillation mode

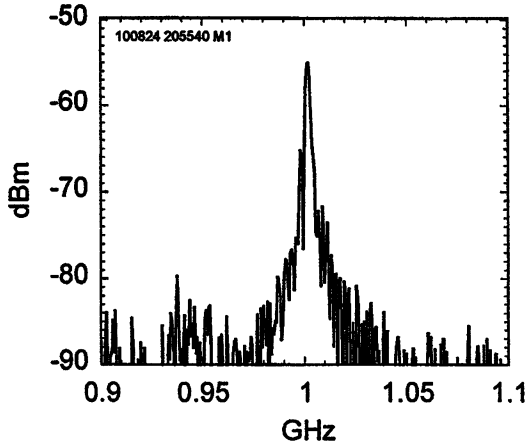

Fig. 3. Frequency spectrum of the $TE_{1,8}$ mode measured with a heterodyne receiver system

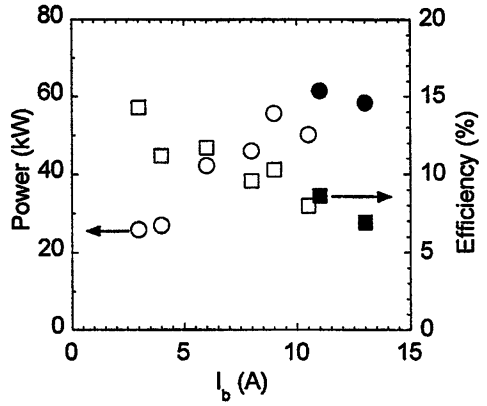

Fig. 4. Output power and oscillation efficiency are plotted as functions of the beam current with circles and squares, respectively. The open symbols correspond to V_k = 60 kV and closed symbols correspond to V_k = 65 kV

mode has been identified from frequency measurement with a Fabry-Perot interferometer and a heterodyne receiver system. The $TE_{3,7}$, $TE_{1,8}$ and $TE_{17,2}$ modes are free from mode competition with the $TE_{4,3}$ mode. However, the $TE_{8,5}$ mode often oscillates simultaneously with the $TE_{4,3}$ mode for large V_k and I_b. Mode transition becomes continuous for higher V_k and I_b. Among these modes, the $TE_{1,8}$ mode is strongest in a wide range of V_k and I_b.

The frequency width is one of the important factors for a gyrotron to be applied to the CTS measurement. Figure 3 depicts a typical frequency spectrum of the $TE_{1,8}$ mode measured with the heterodyne receiver with a harmonic mixer. The 3 dB frequency width is about 3 MHz, which is almost determined by the pulse width. This width is narrow enough for CTS measurement.

The output power P was measured with a water load installed just outside of the vacuum window. Figure 4 plots P of the $TE_{1,8}$ mode as a function of I_b. The open circle represents P for V_k = 60 kV and the closed circles stand for P for V_k = 65 kV. Each data point was obtained with careful adjustment of the operation conditions such the electron beam radius R_b by changing the current of the auxiliary coils installed at the cathode region. The output power increases with I_b and attains at 57 kW for V_k = 60 kV but a slightly decreases at I_b larger than 9 A. This was likely due to deterioration of the beam quality at large I_b. The design of the electron gun was optimized for V_k = 65 kV. Then, operation voltage was increased to 65 kV after suppression of surface discharge on the atmosphere side of the insulator ceramic of the electron gun. Then, further increase in P was obtained. It has reached 62 kW at I_b = 11 A. However, decrease in P at larger I_b still remains.

Figure 4 also shows the window power efficiency. It is as high as about 15 % for low I_b. However, it decreases with I_b down to about 7 % at I_b = 13 A. This is likely due to due to deterioration of the beam quality. Increase in V_k resulted in only a slight recovery of the efficiency. Moreover, theoretical calculation of the oscillation power of the $TE_{1,8}$ mode has shown difficulty to obtain power more than 100 kW with this mode. This is due to coupling between the electron beam and the oscillating electric field at a low peak at an outer radius.

The $TE_{17,2}$ mode has a coupling peak at R_b slightly larger than the present value. Then, we have replaced the electron gun with a new one that emits an electron beam more suitable for oscillation of the $TE_{17,2}$ mode. Experiments with the new electron gun are now ongoing for higher power.

Conclusions

We have demonstrated more than 60 kW radiation at a sub terahertz frequency with second harmonic operation of a gyrotron. This oscillation was free from mode competition with a fundamental mode.

References

1. *Nielsen S.K. et al.*,Temporal evolution of confined fast-ion velocity distributions measured by collective Thomson scattering in TEXTOR // Phys. Rev. 2008. V. E77, 016407.

2. *Kubo S. et al.*, Collective Thomson scattering of high power ECRH beam in LHD // Rev. Sci. Instrum. 2010. V. 81, 10D535.

3. *Notake T. et al.*, Subterahertz gyrotron development for collective Thomson scattering in LHD // Rev. Sci. Instrum. 2008. V. 79, 10E732.

4. *Saito T. et al.*, Development of terahertz gyrotrons and their application to LHD CTS // Journal of Physics: Conference Series 2010. V. 227, 012013.

5. *Ohyabu, N. et al.*, Phys. Rev. Lett. 2006. V. 97, 055002.

6. *Notake T. et al.*, Development of a Novel High Power Sub-THz Second Harmonic Gyrotron // Phys. Rev. Lett. 2009. V. 103, 225002.

7. *Saito T. et al.*, Development of high power sub terahertz gyrotrons for application to CTS measurement // IRMMW and THz 2010, Th-E1.5.

8. *Manuilov V. N. et al.*, Electron gun for powerful short pulse gyrotron with operating magnetic field 8 T // Int. J. Infrared and Milli. Waves 2008. V. 27, P.1103-1112.

Recent Progress on Plasma Relativistic Microwave Electronics at General Physics Institute

P.S. Strelkov

A.M. Prokhorov General Physics Institute RAS, Moscow, Russia

The review gives a brief description of the fundamentals of plasma relativistic microwave electronics, which have been being developed since 1972 by A.A. Rukhadze [1]. Fig. 1 presents a scheme of the experimental device – plasma microwave oscillator that was constructed in 1982 at the our Institute [2].

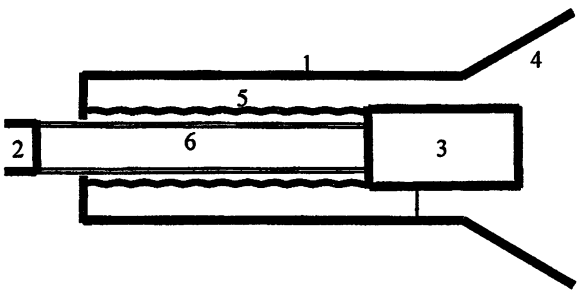

Fig. 1. Schematic of the plasma relativistic microwave oscillator. 1 – metal waveguide, 2 – cathode, 3 – collector, 4 – horn, 5 – plasma, 6 – relativistic electron beam.

The main elements of the oscillator are an annular thin-walled plasma inside a circular-cross-section metal waveguide and an annular relativistic electron beam the radius of which is less than the plasma radius. The beam and plasma propagate along the lines of the longitudinal magnetic field. This scheme is still in use. The review continues with presenting some analytic results that were obtained by A.A. Rukhadze and M.V. Kuzelev for this scheme [3].

The review also outlines the progress that has been made in our experiments up to 2007. A 50-MW plasma microwave oscillator has been constructed that is tunable from 4 to 28 GHz. The Cherenkov excitation of a slow plasma wave with the E01 mode has been demonstrated [4]. It has been revealed that an electromagnetic plasma wave reflected from the end of the plasma waveguide is suppressed due to its interaction with the fast cyclotron wave of the electron beam (the normal Doppler effect) [5]. This result made it possible to lower the parasitic feedback and to create a plasma microwave amplifier with a power of 60—90 MW, operating at frequencies of 9 and 13 GHz, the amplification coefficient being up to 30 dB [6].

The report focuses on the experimental studies and numerical simulations of relativistic microwave devices that were carried out after 2007. Numerical simulations were done in collaboration with V.P. Tarakanov, the author of the KARAT code [7], which was used in the simulations

Earlier experiments were carried out with single shot regime. In 2007, a relativistic plasma microwave oscillator capable of operating in a periodic pulsed regime was constructed [8]. But the traditional scheme of the collector did not allow this regime to be implemented in practice because of the strong gas emission from the collector and the production of a high-density collector plasma. A fundamentally new design of the collector unit made it possible to perform experiments with periodic pulses. At present, microwave generation at a level of 50 MW is achieved in the frequency range of 6 to 20 GHz in 50 pulses in one second [9]. The duration of a microwave pulse is approximately equal to the duration of the current pulse of an electron beam (70 ns). By varying the plasma density, it is possible to vary the emission spectrum of 50 pulses (Fig. 2).

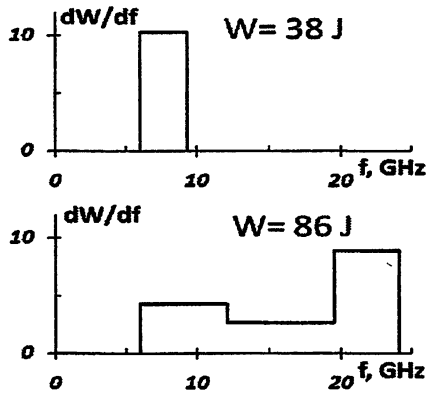

Fig. 2. Spectra of 50 microwave pulses generated at a low and a high plasma density.

We have created a system that ensures injection of each pulse of an electron beam into a plasma of given density according to a computer program that has been chosen beforehand. The objective of the relevant experiments is to generate a sequence of microwave pulses at a frequency assigned by this program. The frequency of each microwave pulse is to be recorded by an oscilloscope with a frequency band of up to 20 GHz, but we do not have such an oscilloscope. Our experience in putting a high-frequency microwave oscillator into operation in a rep-rated regime has enabled us to create a low-frequency microwave oscillator in which the frequency of each microwave pulse was recorded by the available oscilloscope with a frequency band of up to 4 GHz.

In our project on plasma microwave amplifiers, we switched from a high-frequency (9—13 GHz) to a low-frequency (2—3 GHz) microwave amplifier in 2007. The reason was the same: the possibility of recording the emission spectrum in each microwave pulse by the available oscilloscope. According to the experience in working with a high-frequency microwave amplifier, the magnetic field was chosen so that

the backward plasma wave cannot propagate under conditions of the normal Doppler effect. It was demonstrated that the amplifier operated at two frequencies, 2 and 3.2 GHz, and emitted an H_{11} mode with a power of 30 and 70 MW, respectively, the amplification coefficient being about 30 dB. The duration of a microwave pulse was less than 100 ns, which is shorter than the duration of the current pulse of an electron beam [9]. A detailed analysis of the amplifier operation at the frequency 3.2 GHz revealed that the noises in the emitted microwaves were suppressed at a sufficiently high input signal power [10]. This effect was also captured by numerical simulations. The electromagnetic field of the input signal modulates the electron beam in velocity in the entrance part of the plasma waveguide. When this modulation is deeper than the stochastic modulation in the absence of input signals, the noises are efficiently suppressed [11]. We thus achieved a low noise level in a longer plasma waveguide, with the result that the microwave pulse duration became equal to the duration of an electron current pulse (450 ns). Finally, we investigated the problem of whether the frequency can be continuously tuned in a certain band. This problem can be solved directly by continuously varying the frequency of the input signal with a power of 50—100 kW and measuring the emitted microwave power. Since we do not have the required microwave source, we measured the amplification coefficient at four fixed frequencies, 2.4, 2.7, 2.8, and 3.1 GHz, and also recorded the emitted microwave power while continuously varying the length of the plasma waveguide. The experimental data so obtained allow us to state that the emitted maximum microwave power was 90+/-20 MW at any frequency in the band from 2.4 to 3.1 GHz, the amplification coefficient was 30 dB, and the signal-to-noise ratio was also 30 dB.

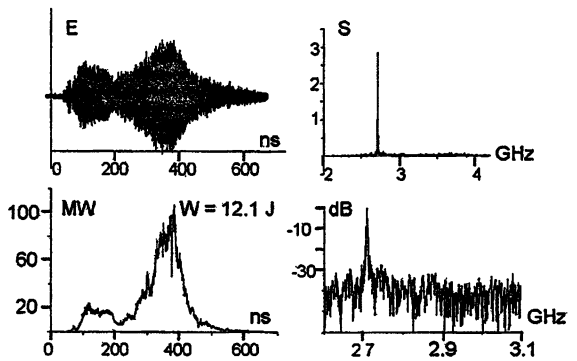

Fig. 3. Parameters of the microwave pulse for a 2.73-GHz input signal: (a) time evolution of electric field strength, (b) spectrum of signal (a), (c) time evolution of the microwave power, and (d) spectrum of the microwave power.

In order to achieve an optimum emission power, it is sufficient to vary only one parameter — the plasma density. The plasma density can be specified by an arbitrary computer program and can be varied electronically from pulse to pulse. The pulse repetition rate in this case should not exceed one kilohertz.

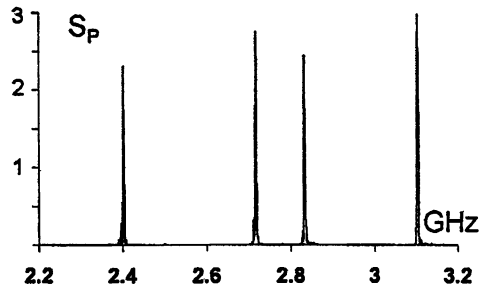

Fig. 4. Output power microwave spectra for different frequencies of the input signal.

References

1. *L.S.Bogdankevich, A.A.Rukhadze.* Excitation on Longitudinal Electromagnetic Waves in a Restricted Plasma by Injection of Relativistic Electron Beams // JETP, 1972. V. 62, No.1, P. 233-246. (in Russian).

2. *M. V. Kuzelev, F.Kh.Mukhametzyanov, M.S. Rabinovich, A.A. Rukhadze, A.G. Shkvarunets, P.S. Strelkov.* Relativistic plasma UHF generator // Sov. Phys. JETP, 1982. V. 54, P. 780 - 785.

3. *M. V. Kuzelev, A.A.Rukhadze, P.S Strelkov.* Plasma. Relativistic Microwave Electronics //Mosk. Gos. Tekch. Univer. im. Baumana, Moscow, 2002 [in Russian].

4. *P. S. Strelkov and D. K.* Ul'yanov Emission Spectra of a Cherenkov Plasma Relativistic Maser // Plasma Physics Reports, 2000. V. 26, No. 4, P. 303–307.

5. *P.S.Strelkov, A.V.Ponomarev, and I.L. Bogdankevich.* Normal Doppler Effect in Experiments on the interaction of Relativistic Electron Beams with Plasma // Plasma Physics Reports, 2007. V. 32, No. 4. P. 329 -337.

6. *A. V. Ponomarev and P. S. Strelkov* 50-MW Broadband Plasma Microwave Amplifier // Plasma Physics Reports, 2004. V. 30, No. 1, P. 62–68.

7. *V.P.Tarakanov.* User's Manual for Code "Karat"//Berkley Research Associates, Springfield, VA., 1992.

8. *I. L. Bogdankevich, D. M. Grishin, A. V. Gunin, I. E. Ivanov, S. D. Korovin, O. T. Loza, G. A. Mesyats, D. A. Pavlov, V. V. Rostov, P. S. Strelkov, and D. K. Ul'yanov.* Repetitively Rated Plasma Relativistic Microwave Oscillator with a Controllable Frequency in Every Pulse // Plasma Physics Reports, 2008. V. 34, No. 10, P. 855-859.

9. *O. T. Loza, D. K. Ul'yanov, P. S. Strelkov, I. E. Ivanov, and R. V. Baranov.* Increase in the Average Radiation Power of a Plasma Relativistic Microwave Generator // Bulletin of the Lebedev Physics Institute, 2011. V. 38, No. 4, P. 120-122.

10. *Bogdankevich I.L., Ivanov I.E., Loza O.T., Strelkov P.S., Ul'yanov D.K., Garate E.* Relativistic Plasma Microwave Amplifier Tunable within 2–3 GHz Frequency Band // Technical Physics Letters, 2007. V. 33, No. 6, P. 480–482.

11. *I.E.Ivanov, P.S.Strelkov, and D.V.Shumeiko.* Radiation Spectrum of a Relativistic Plasma Microwave Amplifier // Journ.of Communic. Tecnol. and Electronics, 2009. V. 54, No. 9, P. 1035-1041.

12. *I.L.Bogdankevich, I.E.Ivanov, and P.S.Strelkov.* Experimental Study and Numerical Simulation of a Relativistic Plasma Microwave Amplifier// Plasma Physics Reports, 2010. V. 36, No. 9, P. 762-771.

Amplification, Self-Transparency and Compression of Ultrashort Electromagnetic Pulses Propagating along Quasi-Stationary Electron Beam

I.V. Zotova[1], N.S. Ginzburg[1], A.S. Sergeev[1], M.I. Yalandin[2], M.R. Ulmaskulov[2], K.A. Sharypov[2]

[1]Institute of Applied Physics RAS, N. Novgorod, Russia, zotova@appl.sci-nnov.ru
[2]Institute of Electrophysics RAS, Ekaterinburg, Russia

Development of powerful electromagnetic pulse generator [1] based on superradiance stimulates studies for further transformation of such pulses.

The first part of this paper is devoted to amplification of SR pulse by quasi-stationary electron beams based on Cherenkov mechanism of interaction. This process is significantly different from the well-known mechanism for amplification of monochromatic signals in CW regime. Due to the slippage of input SR pulse over electrons input pulse accumulates energy of various fractions of electron beam and effectively amplified. This process is accompanied by SR pulse shortening. The first experiments on observation of SR pulse amplification propagating along quasi-stationary electron beam in the dielectric loaded waveguide were performed in [2]. As a result Ka-band ~200 MW pulses with unique short duration less than 100 ps were obtained.

The second part is devoted to effects appearing under cyclotron resonance interaction of ultrashort microwave pulse with rectilinear electron beam [3]. These effects can be considered as a classical analogy of well-known effects of optical pulse propagation through passive (without inversion) two-level media/ Similar to optics these effects include self-induced transparency and self compression of incident e.m. pulse [4]. Furthermore the motion of electrons introduces some additional opportunities. In particular for backward propagation of e.m. pulse through electron beam the stopping of pulse occurs with formation of standing solitons having zero group velocity.

Cherenkov Amplification of SR Pulses by Quasi-Stationary Electron Beams

The process of amplification of short e.m. pulse by quasi-continues electron beam under Cherenkov synchronism condition $\omega \approx h(\omega)V_0$ in the dielectric loaded waveguide can be described by equations [2]:

$$\frac{\partial a}{\partial Z}+\frac{\partial a}{\partial \tau}=\frac{1}{\pi}\int_0^{2\pi} e^{-i\theta}d\theta_0, \quad \frac{\partial^2\theta}{\partial Z^2}=\mathrm{Re}\left(a e^{i\theta}\right) \qquad (1)$$

Here $Z=Cz\omega/V_0$, $\tau=C\omega\left(t-z/V_0\right)\left(\beta_{gr}^{-1}-\beta_0^{-1}\right)^{-1}$, $\theta=\omega t-hz$ is electron phase, a is normalized pulse amplitude, C is the gain parameter proportional to beam current and coupling impedance with operating mode.

Simulations of Eqs.(1) were performed for experimental parameters. The interaction space represented the cylindrical waveguide (radius R=0.45 cm, length 24 cm) with hollow quartz insert. Transverse structure of radiation corresponds to TM_{01} mode. For particles energy 300 keV, beam current 1 kA and injection radius R_0=0.2 cm gain parameter is $C\sim 0.1$ and normalized interaction length is ~ 25. Evolution of input pulse with amplitude $a_0=2$ and duration $T=10$ (that corresponds to 300 ps incident signal with peak power ~50 MW) is presented in Fig. 1.

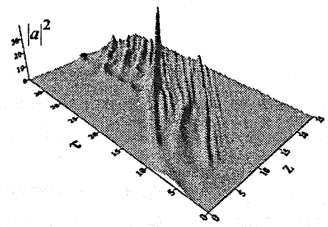

Fig. 1. Amplification of input SR pulse by electron beam.

The level of noise modulation of electron density corresponds to power ~30 MW. It is seen from Fig.1 that the back front of input pulse constantly fed by electrons without initial modulation and effectively amplified. For simulation parameters power amplification gain is ~7. This process is accompanied by significant shortening of input pulse duration in 4-5 times.

For observation of SR pulses amplification the experimental set-up (Fig. 2) based on two accelerator RADAN, synchronized with accuracy ~300 ps was build up. The first accelerator was used to drive the 37 GHz generator of SR pulses based on relativistic BWO. Typical SR pulse with power 50 MW and duration ~300 ps is shown in Fig. 3a. This pulse through the diagnostic waveguide was transmitted to amplification section formed by dielectric loaded waveguide. In this section after reflection from cut-off neck SR pulse was amplified by electron beam with current 1.2 kA and duration up to 2.5 ns from second accelerator RADAN.

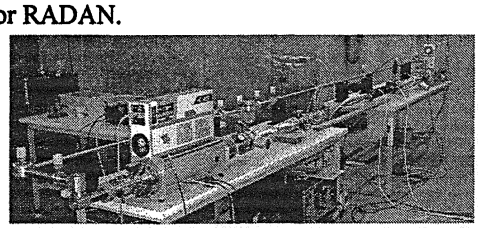

Fig. 2. Experimental set-up for observation of Cherenkov amplification of Ka-band SR pulse.

Results of experiments are presented in Fig.3. In absence of input signal regime of self-amplification of spontaneous emission (SASE) was realized with duration ~2.5 ns and power level ~30 MW (Fig.3b). When amplification section was driven by input SR pulse the short single amplified output pulse is observed (Fig. 3c). Peak power of output pulse was ~200 MW

(power amplification gain ~4). Amplification was accompanied by shortening of e.m. pulse duration up to 100 ps. It should be noted that the duration of the observed subgigawatt pulses is the record for the Ka-band and corresponds to 5-6 periods of RF oscillations.

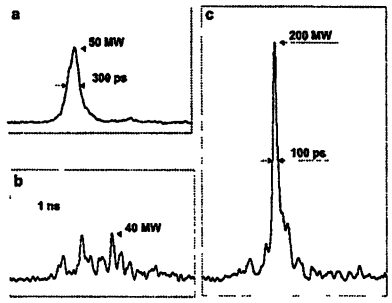

Fig. 3. Experimental results on observation of Cherenkov amplification of SR pulse in Ka band: (a) - typical input pulse from generator of SR pulses, (b) – multispike regime in absence of input pulse, (c) – amplified output pulse.

Electromagnetic Pulse Self-Compression and Stopping under Cyclotron Resonance Interaction with Rectilinear Electron Beam

Let's consider the interaction of initially rectilinear electron beam guided by magnetic field $\vec{H} = \vec{z}_0 H_0$ with backward propagating electromagnetic pulse in waveguide under cyclotron-resonance condition $\omega + hV_{\|} \approx \omega_H$, $\omega_H = eH_0/mc\gamma$ is the gyrofrequency. Evolution of incident e.m. pulse can be described by equations [3]:

$$\frac{\partial a}{\partial Z} - \frac{\partial a}{\partial \tau} = p, \quad \frac{\partial p}{\partial Z} + ip\left(\delta + |p|^2\right) = a. \qquad (2)$$

Here $\tau = \sqrt{G}\omega\left(t - z/V_{\|0}\right)\left(\beta_{gr}^{-1} + \beta_{\|0}^{-1}\right)^{-1}$, $Z = \sqrt{G}\,\omega z/c$, a and p are normalized pulse amplitude and electrons transverse momentum, δ is the initial cyclotron resonance mismatch, G is the parameter proportional to electron current. We assume that an incident pulse enters the output cross-section. In the input cross section all electrons have zero transverse momentum.

Simulations of Eqs. (2) show that for rather small energy of incident e.m pulse the cyclotron absorption is observed. However similar to optics with increasing of initial pulse energy the self-transparency effect occurs when the e.m. pulse propagates practically without damping. In this case the initial pulse transforms to one or several solitons which amplitudes and duration obey the relation

$$|a(Z,\tau)| = \frac{2}{(1+U)^{3/4}}\left[\operatorname{sech}\frac{2}{\sqrt{1+U}}(Z - U\tau)\right]^{1/2}, \qquad (3)$$

where U is soliton velocity. Moreover under certain conditions forming of solitary wave accompanied by self-compression of initial e.m. pulse. The peak power of output pulse in this case in ~3.5 time exceeds the input pulse power while effective pulse duration decreases in more than 4 times. According to estimations for compression of Ka band SR pulse with peak power 1.2 GW and duration of 350 ps in waveguide with radius 0.45 cm the current of electron beam should achieve ~ 450 A for energy 300 keV. Thus the peak power of output pulse achieves ~3.5 GW for duration ~80 ps (Fig. 4). The compression length is about 10-15 cm.

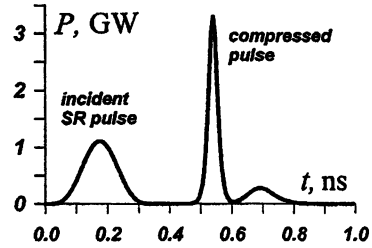

Fig. 4. SR pulse self-compression.

It is easy to see from Eqs. (3) that soliton with zero group velocity $U = 0$ can exist. Formation of standing soliton is shown in Fig. 5. For full stopping of 1.2 GW, 300 ps SR pulse the current of electron beam should increase up to ~1 kA.

It is important to note that the effect of light stopping attracts the considerable attention in optics [5]. In the process of photo-induced transparency formation of a transparency window within the zone of resonance absorption under action of strong pump wave is accompanied by extremely slow group velocity of the reference light wave. In the considered case due to nonlinear resonance medium motion the stopping occurs in the frame of more simple single photon process in the absence of pump wave

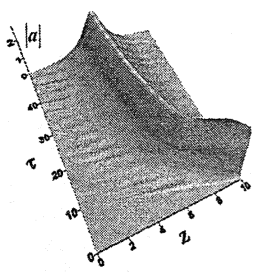

Fig. 5. SR pulse stopping under cyclotron resonance interaction with backward rectilinear electron beam

References

1. *Korovin S.D., Eltchaninov A.A., Rostov V.V., et al* Generation of Cherenkov superradiance pulses with a peak power exceeding the power of driving short electron beam // Phys. Rev. E 2006. V. 74, P. 016501-016509.

2. *Yalandin M.I., Reutova A.G., Ulmaskulov M.R., et al* Nonlinear compression of ultrashort SR pulse in the process of amplification by quasi-stationary electron beams // JETP Lett. 2010. V. 91, No. 11. P. 620-625.

3. *Ginzburg N.S., Sergeev A.S., Zotova I.V* Self-Induced Transparency and Electromagnetic Pulse Compression in a Plasma or an Electron Beam under Cyclotron Resonance Conditions // Phys.Rev.Lett. 2010. V. 105, P. 265001-265005.

4. *Allen L., Eberly J.,* Optical Resonance and Two-Level Atoms, Wiley, N. Y., 1975.

5. *Phillips D.F., Fleischhauer A., Mair A., et al* Storage of Light in Atomic Vapor // Phys. Rev. Lett. 2001, V.86, 783-787.

Beam-spreading Surfaces for Millimeter-wave Matched Loads

A. Bruschi[1], W. Bin[1], S. Cirant[1], F. Dell'Era[1], F. Gandini[2], V. Muzzini[1]

[1] Istituto di Fisica del Plasma, Consiglio Nazionale delle Ricerche, Milano, Italy, bruschi@ifp.cnr.it
[2] ITER Organization., Saint Paul Lez Durance, France

Introduction

A number of calorimetric matched loads designed for absorption of high power (up to 2 MW, CW) millimeter-wave beams (from 105 to 170 GHz) have been built at IFP for testing gyrotrons and high-power components in different ECRH systems [1]. Loads are based on hollow copper spheres coated with a layer of ceramic absorber. A shaped mirror in front of the entrance distributes the power on the inner wall. The loads have different cooling layouts depending on pulse duration, consisting of spiral channels (from 1 to 20 in parallel) electroformed on the outer shell. A back-reflecting preload prevents the escape of radiation out of the load, reducing the overall reflectivity down to around 2%.

The coating selected for the inner surface is a critical item in the loads based on the internal deposition of absorbing ceramics. The one presently in use, Cr_2O_3, was demonstrated to withstand a power density of a few MW/m^2, that can be easily exceeded locally due to accumulation of radiation and interference phenomena after multiple reflections in the load [2]. In order not to exceed the coating capability during long pulses and to guarantee the durability in repetitive operations, the final power density incident onto the inner surface, sum of the first and the successive reflections, must be as uniform as possible.

Spreading mirror design

The spreading mirror shape can be calculated on the basis of the desired first-pass deposition and the power distribution of the incoming beam. It is an axisymmetric surface with a precisely determined shape, solution of a differential equation for the mirror quote as a function of radius, such that it gives a primary power distribution on the internal load surface. The design of the mirror surface for a narrow Gaussian beam and a constant power distribution onto the absorbing surface is described below.

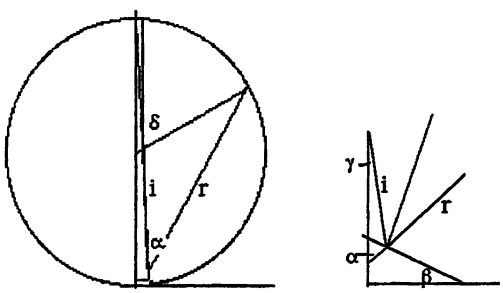

Fig. 1. Geometrical model showing the spherical load, incident (i) and reflected (r) beam axes (left); close-up of the spreading mirror surface (right). The mirror surface is hit by each ray describing the beam in a point with local inclination angle β with respect to the horizontal plane.

Fig.1 shows the geometry of the load: a narrow beam (i) enters from the top in a large vessel (in this case a sphere), slowly expands due to diffraction, then impinges on a small mirror of suited shape. The radiation is then reflected (r) and spreads on the internal surface where it can be absorbed, diffused or reflected again, depending on the local properties of the coating. Considered the cylindrical symmetry of the problem (r=radial coordinate), the shape of the mirror that performs the desired spreading (i.e. a given power distribution on the vessel) is given by the function y(r) describing the mirror surface. First, we assign a power distribution function on the mirror surface (P(r)) and on the vessel surface (f(d));

$$\int_{\Sigma}\frac{dP}{dr}dr = Pm_{tot} = \int_{S}\frac{dP}{dS}dS = 2\pi R^2\int_0^{\pi} f(\delta)\sin\delta d\delta \quad (1)$$

where Σ and S are the mirror and load inner surfaces respectively, Pm_{tot} the power reflected by the mirror and δ the angle at the center corresponding to the reflection point on the mirror. A simplified differential equation giving the function y(r) can be obtained expliciting (1) as a function of r: for this purpose we pass switch to the variable α (angle at the mirror), approximating it with the angle at the surface, i.e. α~δ/2

$$f(\alpha)=\frac{dP}{d\alpha}\frac{d\alpha}{d\delta}\frac{1}{2\pi R^2\sin\delta}=\frac{dP}{d\alpha}\frac{1}{4\pi R^2\sin(2\alpha)} \quad (2)$$

and then to the variable r:

$$f(r)=\frac{dP}{dr}\frac{1}{\frac{d\alpha(r)}{dr}}\frac{1}{4\pi R^2\sin(2\alpha(r))} \qquad \alpha=\gamma+2\beta \quad (3)$$

with γ and β both depending on r, and:

$$\beta=-\arctan\left(\frac{dy(r)}{dr}\right) \qquad \frac{d\alpha(r)}{dr}=\gamma'(r)-2\frac{y''(r)}{1+(y'(r))^2} \quad (4)$$

For a Gaussian beam whose divergence is negligible and completely contained in the mirror surface, which power spreads uniformly on the sphere, the following relations can be written:

$$\frac{dP}{dS}=\frac{2P_{tot}}{\pi w^2}e^{-2\frac{r^2}{w^2}} \qquad \frac{dP}{dr}=\int\frac{dP}{dS}2\pi r d\theta = 4r\frac{P_{tot}}{w^2}e^{-2\frac{r^2}{w^2}} \quad (5)$$

and

$$\gamma(r)=0 \quad \gamma'(r)=0 \quad f(\delta)=\frac{Pm_{tot}}{4\pi R^2} \quad Pm_{tot}=P_{tot} \quad (6)$$

from which the simplified differential equation:

$$y''(r)\sin(-4\arctan(y'(r))) = \frac{2r}{w^2} e^{-\frac{2r^2}{w^2}} (1+(y'(r))^2) \quad (7)$$

can be numerically solved for y(x) with the appropriate boundary conditions.

In real applications, it is better to avoid backward reflection where the beam enters the vessel, on one side, while the beam divergence and the finite mirror size are not negligible, in general, on the other. This leads to the following constraints (small angles approximation):

a) $f(\delta)=0$ for $\delta<\delta 0=a/R$ where a is the radius of the shaded spot.

b) $\gamma(x)=x/r$ where r is the curvature radius of the phase-front of the beam on the mirror.

Equation (7) should therefore be generalized considering that a uniform spreading does not prevent always from local accumulations. For the present design of the loads a proper function of δ is chosen, avoiding the equatorial region overloading, since that region would reflect the unabsorbed power towards the load entrance [2]. The solution for the surface depends on the beam shape but not much on the beam frequency; the geometrical optics approximation after the beam reflection is found adequate. It is worth saying that the same concept has been applied to find analogous solutions in the case of cylindrical (conical) loads, as the one used in the FTU transmission line [3]. In Fig. 2 the profiles obtained with this method for two loads are shown on the left. On the right, instead, the absorbed power densities expected along a meridian for different input polarizations and a given primary illumination are shown, where entrance and mirror are respectively at angles 0 and π.

Phase-scrambling surface design

In case of input beams that are not well qualified or exceed the mirror dimension, a scrambling surface can be inserted around the spreading mirror, up to the radius where the side-lobes hit the coated surface with a power density exceeding the 1-2 MW/m^2 range. The phase-scrambling surface is designed to diffuse uniformly the power in all directions, no matter of the beam shape in input. It is made by machining a flat surface with a coarse-grained texture of holes drilled with a nearly random depth from zero to the radiation half wavelength.

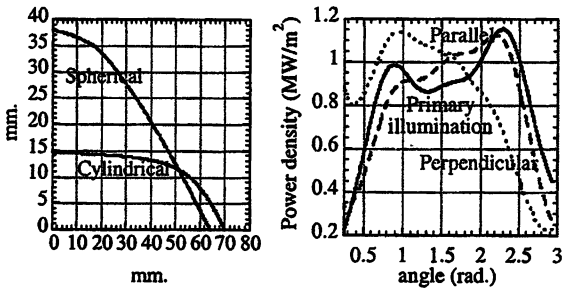

Fig. 2. Left: Mirror profiles obtained with the differential equation method for a spherical and a cylindrical load. **Right:** Deposition profiles at different polarizations obtained with a primary illumination for uniform distribution.

A correction to a pure random distribution have to be applied, due to the construction technique used for machining the surface. In fact, part of the surface of the holes drilled at lower depth is removed by the drilling of deeper holes, as shown in Fig. 3. If ε is the average fraction of surface that is removed, and $\{x_i\}$ a set of random numbers chosen in the interval (0,1), the balance of the remaining surfaces at different depth is obtained by imposing a depth:

$$<\eta_i>=\frac{\lambda}{2}\left((1+\varepsilon)-\sqrt{(1+\varepsilon)^2-4\varepsilon<x_i>}\right)/(2\varepsilon) \quad (8)$$

The distribution of depths computed for a mirror for 170 GHz, with 40000 holes on the surface and ε=0.2 is shown in Fig. 3. The balance of surfaces at different depth makes the reflected power to combine with random phases in the axial direction. The scrambling mirror has been tested at low power showing direct reflection of ~3%, while the remaining power is diffused at wide angles [4]. The scrambling surface is not to be inserted in correspondence of the axis of a MW-power beam, during operations in air, being its machining not enough smooth in order to prevent arcs at high power densities.

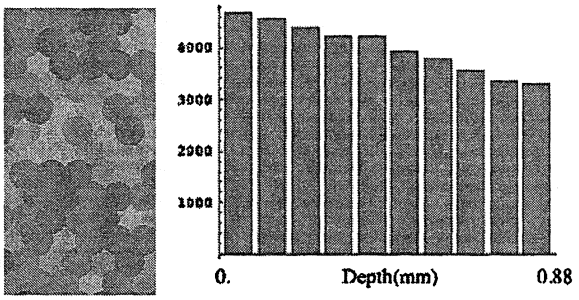

Fig. 3. Left: Pattern of holes drilled at random depth: deeper holes (dark gray) remove part of the surface of the shallower holes (in light gray). **Right:** Distribution of holes with respect to depth, to balance surfaces at different depth.

Conclusions

The design concepts for both diffusing and scrambling mirrors are presented in this paper. They have been validated with calculations and measurements in the past years. The loads for which these mirrors are designed, which have the advantage to be static and easily cooled, have been already tested, showing a low overall reflectivity.

References

1. *Cirant, S., et al.* A Family of Calorimetric Loads for High Power Millimetric Wavelength Beams // *Strong Microwaves in Plasmas*, edited by Institute of Applied Physics. Russian Academy of Sciences 2006. V.2. P. 586.

2. *Bruschi, A., Cirant, S., Gandini, F., et al.* Design of a high-power load for millimetre-wave Gaussian beams // Nucl. Fusion 2003. V. 43, No. 11. P. 1513–1519.

3. *Bruschi, A., Gandini, F., Muzzini, V. et al.* Calorimetric loads for high power transmission lines at millimeter wavelengths // Fus. Eng. Des. 2001. V. 56-7, P. 649–54.

4. *Bruschi, A., Bin, W., Cirant, S. et al.* High-power millimeter-wave calorimetric beam absorbers // Fusion Sci. Technology 2008. V. 53, No. 1. P. 62–68.

High-Power, Terahertz Gyrotron with Frequency Tunability

T.H. Chang[1], N.C. Chen[1], C.P. Yuan[1], Y.S. Yeh[2], and C.L. Hung[3]

[1]Department of Physics, National Tsing Hua University, Hsinchu, 300, Taiwan
[2]Department of Electro-Optical Engineering, Southern Taiwan University, Tainan
[3]National Penghu University of Science and Technology, Taiwan

The gyrotron backward-wave oscillator (gyro-BWO) uses a frequency tunable scheme at terahertz regime. Unlike step-tunable type where oscillation frequencies change discretely, this scheme continuously adjusts the oscillation frequency smoothly. The continuous frequency tuning can be achieved by varying either the magnetic field or the beam voltage in a non-resonant structure. The talk reports our recent findings in the underlying physics as well as the experimental devices developed.

Introduction

The gyrotron backward-wave oscillator (gyro-BWO) is a frequency-tunable source, which can be operated at high frequency and high power. The oscillation of gyro-BWO is formed by internal feedback consisting of a forwardly moving electron beam and a backwardly propagating wave. Gyro-BWO has been demonstrated to be highly efficient and broadband. The next goal is to increase the operating frequency into the low terahertz range, which is associated with a highly over-moded condition. Severe mode competition is expected.

The operating mode is the TE_{01} waveguide mode with fundamental cyclotron harmonic (s=1). The circular TE_{01} mode has the lowest propagating loss of all cylindrical waveguide modes, but it was chosen mainly because the mode converter has been successfully developed and the mode-selective circuit is relatively easy to construct. Major competing modes, for example, TE_{21}, TE_{31}, TE_{02}, TE_{61}, and TE_{32}, are shown in Table I.

TABLE I. Operating parameters

Operating mode	$TE_{01}^{(1)}$ ℓ=1
Competing transverse modes	$TE_{21}^{(1)}$, $TE_{31}^{(1)}$, $TE_{02}^{(2)}$, $TE_{61}^{(2)}$, $TE_{32}^{(2)}$
Competing axial modes	$TE_{01}^{(1)}$ ℓ=2,3,...
Tapered section length (L_1)	0.7-2.7 cm
Lossy section length (L_2)	0.2-0.6 cm
Waveguide radius (r_w)	0.189-0.193 cm
Beam current (I_b)	0-5 A
Beam voltage (V_b)	40-120 kV
Magnetic field (B_0)	38-44 kG
Guiding center position (r_c)	0.466-0.476 r_w
Velocity ratio ($\alpha = v_\perp/v_z$)	1
Velocity spread ($\Delta v_z/v_z$)	0%

The frequency can be tuned by changing either the magnetic field B_0 or the beam voltage V_b. In addition to transverse mode competition, however, axial mode competition occurs. The operating mode $TE_{01}^{(1)}$ can be further classified into different axial modes (ℓ = 1, 2, 3...) A mode with a favorable field profile, normally the fundamental axial mode, tends to be the dominant axial mode, which determines the axial mode competition. Recently, the distributed loss was founded to be effective in selectively suppressing the competing axial modes. The distributed loss scheme was adopted to achieve a smooth and stable tuning and the effect of this approach on the suppression of the competing modes was discussed.

This study reports the development of $TE_{01}^{(1)}$ gyro-BWO at W-band. All the operating parameters are shown in Table I.

Simulation Results

Figure 1 shows the geometry and the linear field profiles of the gyro-BWO under study. It depicts the interaction structure and the loss profile. The radius of the waveguide is slightly down tapered from 0.193 cm to 0.189 cm (taper angle 0.11°). In addition to the uniform section at both ends, it consists of two sections, a taper section (L_1, copper) and a lossy section (L_2, loss).

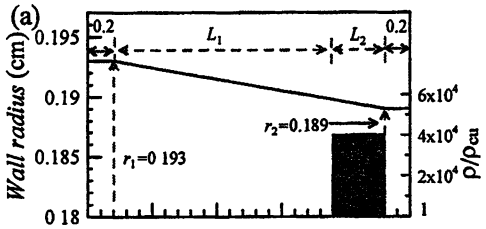

Fig. 1. Interacting structure and profile of distributed loss.

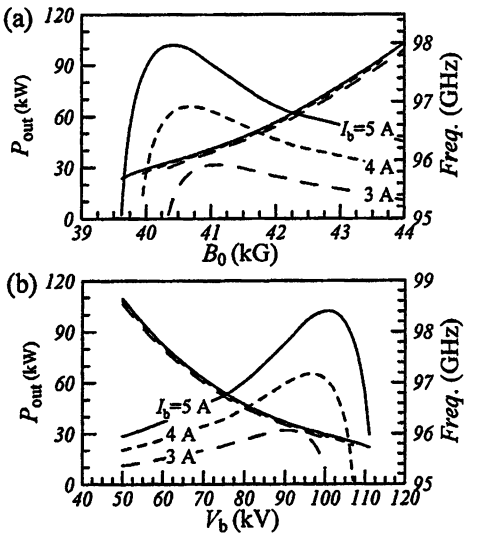

Fig. 2. Calculated output power P_{out} and oscillation frequency f vs. tuning parameters: (a) the magnetic field B_0 and (b) the beam voltage V_b. The interaction structure is shown in Fig. 3 and other parameters are listed in Table I.

Figure 2 plots output power and oscillation frequency as functions of (a) magnetic field B_0 and (b)

beam voltage V_b. The calculated results [1] show that the peak output power of the stable $TE_{01}^{(1)}$ gyro-BWO is 102 kW when using 5 A and 100 kV electron beam, corresponding to an efficiency of 20 %. The oscillation frequency can be smoothly tuned. The 3-dB tuning range by the magnetic field is about 1.8 GHz. Figure 2(b) presents the voltage tunings for 3 A, 4 A, and 5 A at B_0 =40.4 kG.

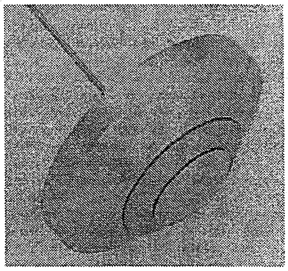

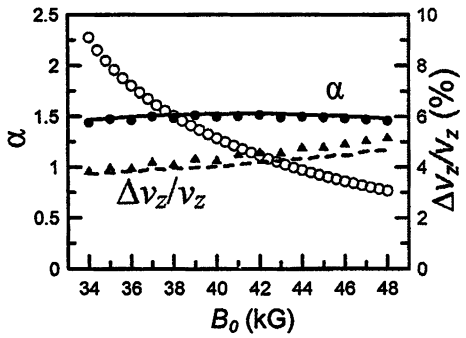

Fig. 3. (a) Photo of the cathode. (b) Velocity ratio α and velocity spread ($\Delta v_z / v_z$) versus the magnetic field B_0 with a variable trim coil current. Both EGUN (solid and dashed lines) and CST (solid dots and triangles) are presented. The open circles depict α without the correction of the variable trim field.

Figure 3 shows the velocity ratio α and axial velocity spread ($\Delta v_z / v_z$) versus the magnetic field B_0. The solid and dashed lines represent the velocity ratio and spread from EGUN simulations [2], respectively. The open circles show the velocity ratio when the trim field is not applied. The results of CST are also plotted. The solid dots and triangles show velocity ratio and spread, respectively. With the help of the variable trim field, the value of α is almost constant from 3.4 to 4.8 Tesla. The velocity spread is slightly changed, but still within the acceptable region. Basically, the results of EGUN and CST agree well.

Figure 4 is the photo of our new 5 Tesla superconducting magnet just delivered. The room temperature bore is 15 cm in diameter and the uniform region is 30 cm.

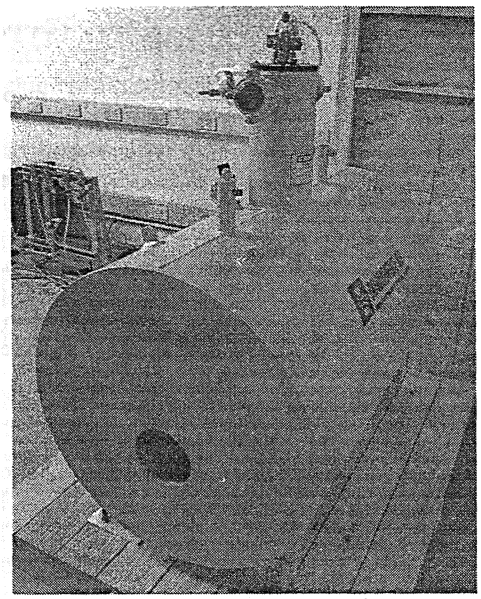

Fig. 4. Photo of our new 5-T superconducting magnet

Conclusions

The high-performance TE_{01} mode converter is ready [3]. The new magnetron injection gun (MIG) and the new superconducting magnet are both under test. Two gyro-BWO experiments at W-band will be conducted readily. One is the normal gyro-BWO [1] and the other is reflective gyro-BWO [4, 5].

Acknowledgement. The authors would like to thank the National Science Council of the Republic of China, Taiwan, for financially supporting this research under Contract Nos. NSC 98-2112-M-007-003-MY3 and NSC 99-2923-M-007-005-MY3.

References

1. *T. H. Chang, C. F. Yu, C. L. Hung, Y. S. Yeh, M. C. Msiao, and Y. Y. Shin*, W-band TE01 gyrotron backward-wave oscillator with distributed loss, Phys. Plasmas **15**, 073105 (2008).

2. *C. P. Yuan, T. H. Chang, N. C. Chen, and Y. S. Yeh*, Magnetron injection gun for a broadband gyrotron backward-wave oscillator, Phys. Plasmas, **16**, 073109 (2009).

3. *T. H. Chang, C. S. Lee, C. N. Wu, and C. F. Yu*, Exciting circular TEmn modes at low terahertz region, Appl. Phys. Lett. **93**, 111503 (2008).

4. *T. H. Chang, T. Idehara, I. Ogawa, L. Agusu, C. C. Chiu, and S. Kobayashi*, Frequency tunable gyrotron using backward-wave components, J. Appl. Phys. 105, 063304 (2009).

5. *N. C. Chen, T. H. Chang, C. P. Yuan, T. Idehara and I. Ogawa*, Theoretical investigation of a high efficiency and broadband sub-terahertz gyrotron, Appl. Phys. Lett. **96**, 161501 (2010).

Compact Sources of Medium-Power Millimeter-Wave Radiation

V.L. Bratman, A.E. Fedotov, and P.B. Makhalov

Institute of Applied Physics, Nizhny Novgorod, Russia, fedotov@appl.sci-nnov.ru

The medium-power millimeter-wave generators and amplifiers are widely used in radars and space telecommunications, in nuclear magnetic resonance (NMR) spectroscopy for dynamic nuclear polarization methods, and as input sources for powerful amplifiers. For generation of the millimeter waves with CW or an average power level from tens of watts to several kilowatts, slow-wave devices such as traveling-wave tubes (TWTs), backward-wave oscillators (BWOs), and extended-interaction klystrons – oscillators and amplifiers (EIOs and EIAs, respectively) are widely used. Traditionally, these radiation sources are based on utilizing thin rectilinear electron beams. Such pencil-like beams are guided through thin cylindrical channel cuts in slow-wave structures of helix, folded-waveguide, or coupled-cavity type, so that the electrons interact with slow spatial harmonics of microwave field. The amplitude of a slow harmonic decreases drastically towards the center of the channel on the scale

$$\Lambda = \frac{\beta\gamma\lambda}{2\pi}, \qquad (1)$$

where β, γ, and, λ are the normalized electron velocity, the electron Lorentz factor, and the operating wavelength, respectively. At the millimeter waves, this scale is fairly small; for example, $\Lambda = 0.17$ mm for W-band device with a moderate operating voltage of $U = 30$ kV. Hence, for such a device, a very thin electron beam with very high energy density is needed, which hinders the guiding of the beam in proximity of the slow-wave structure wall, especially in CW regime. Correspondingly, slow-wave devices are not capable of radiation of a kilowatt or higher level of average power, and gyro-devices with a fairly strong magnetic field should be employed.

In order to mitigate the described difficulty, a new concept of medium-power slow-wave devices of the millimeter-wavelength range is proposed in this paper. Like in relativistic Cherenkov devices [1], the proposed scheme of a slow-wave radiation source is based on using a hollow thin-wall electron beam moving in a corrugated waveguide (Fig. 1). The use of a hollow cylindrical beam allows increasing significantly the diameter of a transient channel as well as decreasing the required current density and heat load at the interaction structure wall. In contrast to the high-current relativistic devices where shallow corrugation of the waveguide wall is used, a relatively deep corrugation is needed in non-relativistic generators to provide electron-wave coupling.

The discussed scheme can be applied for the realization of various types of radiation sources, such as TWT-amplifiers, frequency-tunable BWO-oscillators, two- and multi-sectioned extended-interaction klystrons (including frequency multipliers), and so on. To demonstrate the feasibility of the scheme, consider one of the simplest variants, namely, an orotron. The starting current of the orotron with a hollow electron beam is

$$I_{st} \approx I_A \frac{\beta^3\gamma^3 N}{2\pi Q L^2 K^2}, \qquad (2)$$

where $I_A \approx 17$ kA, N and Q are the wave norm and quality factor, respectively, L is the cavity length, and K is the electron-wave coupling coefficient. Estimations on the basis of Eq. (2) allow one to expect the realization of orotrons operated in CW regime with fairly high operating voltages, at least up to 60 and 20 kV at long and short millimeter waves, respectively.

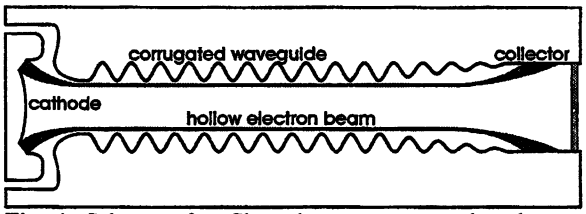

Fig. 1. Scheme of a Cherenkov-type source based on a hollow electron beam

Ka-band orotron design

As an example of the concept, a Ka-band orotron with an operating voltage of 31 kV has been designed. The TM_{010} mode of a 50-mm wavelength waveguide with an azimuthally symmetrical sinusoidal corrugation of the wall can be excited by an electron beam with an outer diameter of 4 mm and a thickness of 0.2 mm. The choice of the lowest operating transverse-magnetic mode TM_{01} allows avoiding the problem of transverse mode competition. The large corrugation depth of 1.7 mm ensures strong coupling between the electrons and the operating mode. Since for a deep corrugation, the minimum structure diameter is less than the cutoff diameter for the TM_{01} mode, the slow-wave structure operates as a coupled-cavity structure at the 2π-mode rather than the orotron structure. This feature takes place for the operating mode with the lowest radial index and an azimuthally symmetrical corrugation.

According to numerical simulations, an utput power of 1.5 kW can be obtained for the electron current 1 A. The moderate ohmic losses (less than 0.8 kW) permit the CW oscillation regime. A single-stage depressed collector with a potential of 25 kV will provide rather high overall electron efficiency up to 25 %.

The designed interaction structure seems to be quite simple and robust for manufacturing, in comparison with traditional coupled-cavity structures of medium-power Ka-band devices. The required

hollow electron beam with thin walls and small parasitic transverse pulsations of electrons can be formed in a traditional two-electrode Pierce-type electron gun with a moderate emission density and following beam compression in an increasing magnetic field. Another very attractive possibility is a very compact electron gun based on using a cathode with high current density of 40 A/cm^2 immersed in a uniform magnetic field.

It is important that the output parameters close to parameters of technological gyrotrons can be obtained in a device with fairly low guiding magnetic field of 0.3 T accessible with permanent magnets. The experimental realization of Ka-band orotron is being prepared.

Prospects at short-millimeter waves

The preliminary simulations performed for a W-band device show the possibility of realizing the similar source with TM_{010} operating mode. The corrugated waveguide with minimal radius of 0.9 mm, period of 1 mm and corrugation depth of 0.6 mm can provide effective generation for operation voltage of 30 kV. According to calculations of slow-wave structure properties, the diffraction and ohmic Q-factors are approximately equal to each other, therefore for this device the power absorbed by the structure walls amounts to approximately a half of the power extracted from electron beam. The density of heat load on a corrugated waveguide wall can be as high as 0.5 kW/cm^2, hence the ohmic losses limit the possible average power on a level of 0.5-1 kW, which, however, is higher than the experimentally demonstrated average power level for devices with rectilinear electron beams [2]. Simulations show that and a magnetic field of 0.6 T is sufficient for the beam guiding.

The further increase in the orotron frequency is hampered by a dramatic decrease in the beam radius. This difficulty can be avoided by using higher operating modes, for example, TM_{12} or TM_{13}. For an effective mode selection, the two longitudinal slots in the waveguide walls can be used, as in a relativistic orotron [3]. Such an orotron with a frequency of 260 GHz and an output power of 10-50 W would be employed, in particular, for the dynamic nuclear polarization in NMR spectroscopy.

Another possibility of increasing the beam radius at short waves is use of travelling waves in TWTs or BWOs instead of the cutoff waves in orotrons. In particular, a 220 GHz BWO with TM_{01} operation mode in a waveguide with rectangular corrugation can be based on the electron beam with an outer diameter of 1.3 mm. An output power of 100 W can be obtained in such an oscillator with possibility of smooth frequency tuning.

One should note that in the proposed devices the medium level of output power is achievable for fairly low guiding magnetic fields of 0.3 and 1.2 T at long and short millimeter waves, respectively, in contrast to the high magnetic field needed for gyro-devices. The possibility of beam focusing using a periodic permanent-magnet (PPM) system will be the subject of the further research.

References

1. *Levush, B., Antonsen, T., Bromborsky, A., Low W.R., Carmel, Y.* Relativistic backward-wave oscillators: Theory and experiment // Phys. Fluids B. 1992. V. 4, No.7. P. 2293-2299.

2. *Thesis A.J., Meadows C.J., Freeman R., True R.B., Martin J.M., Montgomery K.L.* High-average-power W-band TWT development // IEEE Trans. Plasma Sci. 2010. V. 38, No. 6. P. 1239-1243.

3. *Bratman, V.L., Gubanov, V.P., Denisov, G.G., Korovin, S.D., Polevin, S.D., Rostov, V.V., Smorgonskii, A.V.* The relativistic orotron - A high-power source of coherent millimeter microwaves // Soviet Technical Physics Letters. 1984. V. 10, No.7. P. 339-340.

Mode Switching and Phase Locking in a Relativistic Magnetron with Diffraction Output

M.I. Fuks, M. Liu, E. Schamiloglu

Dept. of Electrical and Computer Engr., University of New Mexico, Albuquerque, NM 87131 USA, fuks@ece.unm.edu

Using computer simulations we demonstrate a possibility to switch neighboring modes using a short (~10 ns), weak (~10^5 W), single frequency RF signal in the 6-cavity highly efficient gigawatt magnetron [1] (Fig. 1) with diffraction output (MDO), in which any eigenmode can be used as the operating one owing to symmetrical nature of such magnetrons. This investigation is primarily focused on application in radars in which operation with variable frequency from pulse to pulse is necessary in order to render its location difficult to find. Above all, we study the possibility to realize phase control in such magnetrons using an input RF signal for coherent summation of power.

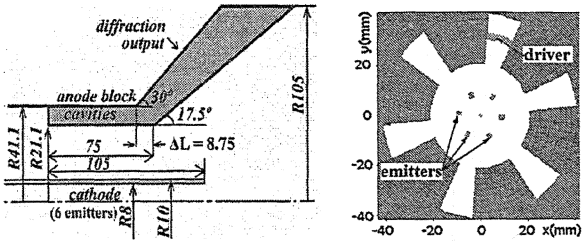

Fig. 1. Design of the high efficient MDO [1]. Right: cross section of the anode block. The position of a driver inserting an input signal and optimal positions of emitters relatively cavities for electron hub that drifts counter-clockwise around the cathode are shown.

We consider all scenarios of mode switching on the basis of common properties of dynamical systems with two stable states separated by an unstable saddle point [2]. In particular, we show [3] that the switched mode persists in spite of the elimination of the short input RF signal that caused the switching. The closer the value of the applied axial magnetic field H is to the critical value H_{00} that corresponds to the unstable state that bounds regions of synchronous interaction of electrons with neighbor modes where bifurcation of their frequencies occurs (Fig. 2), the weaker is the input signal that is required for mode switching. In principle, a very small signal is necessary for mode switching as the field H approaches the value H_{00}. For example, using the particle-in-cell (PIC) code MAGIC [4] for the different approaches we found that only $P_{in} \approx 10$ kW is sufficient for mode switching when $\Delta H / H_{00}$ is about 0.5% and computer noise is suppressed; however, increasing noise level leads to the erosion of the boundary that results in an uncertainty where it is impossible to predict for each magnetron start-up what mode will be generated when the difference $\Delta H / H_{00}$ is so small. Since it is impossible to account for the real noise level in simulations, we give more realistic results for $\Delta H / H_{00} \geq 2\%$ that will be refined in forthcoming experiments.

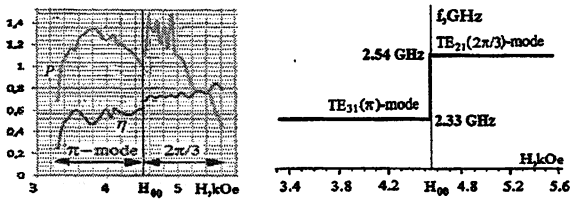

Fig. 2. Regions of synchronous interaction of electrons with the fundamental harmonic of the $\pi-$mode and the first negative harmonic of the $2\pi/3-$mode for applied voltage $U = 400$ kV with rise time $\tau_U = 4$ ns (P, GW is power of radiation, η is electron efficiency).

This raises the question of whether the switched mode "remembers" the initial phase φ of the weak, short input signal (in simulations we use a 15 ns pulse duration input RF pulse that starts simultaneously with the applied voltage). We insert the input signal using a "driver" with azimuthal current density $j_\theta = j_0 \sin(\omega t + \varphi)$ that is placed in one of magnetron cavities (Fig. 1 right) and whose power is measured as $P_{in} = \int_V j_\theta E_\theta dV$, where E_θ is the field excited by this driver in volume V and ω is the cyclic frequency. In experiments with an MDO we plan to inject the input signal through a coaxial line whose inner conductor connects with one of vanes that separates cavities of an anode block. The idea of such a device is similar to coaxial extraction of radiation [5]. The compromise between P_{in} and the portion of generated power that will flow out through such a coupler will be achieved through proper choice of its position.

We found that mode switching depends not only on the amplitude and frequency of the input signal, but also on its initial phase φ (Fig. 3).

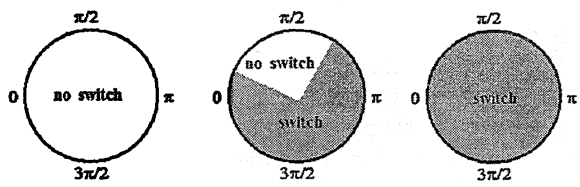

Fig. 3. Dependences of mode switching (from the $TE_{21}-$mode to the $TE_{31}-$mode) on the initial phase φ of the input signal with frequency $f = 2.33$ GHz for $P_{in} < 10$ kW (left); $P_{in} \approx 60$ kW (middle) and $P_{in} \geq 200$ kW (right) when $H = 4.6$ kOe, $U = 400$ kV and $\tau_U = 0.2$ ns.

Such a regular dependence as in Fig. 3 (middle) can occur when each time a magnetron starts identically (noise is absence). In this case the phases of the generating wave are locked to the rise τ_U of the applied voltage. For some initial phases φ interference

of the input RF signal with the corresponding spectral component of the Fourier integral over τ_U can lead to a suppression of the initial amplitude of the switching mode that mode switching will be not achieved.

The fact that reproducible behavior of the magnetron is determined by the voltage rise time when the noise level is very small is supported by demonstration [6] of coherent summation of radiation from two backward wave oscillators with common applied voltage and sub-nanosecond rise time.

Change of voltage rise time leads not only to change in phase of the generating wave (Fig. 4, left), but also can lead to the generation another wave (Fig. 4 right). Instability in the applied voltage leads to a change in the frequency of radiation, and, as a consequence, to a decrease in the interval of correlation that limits the pulse duration for coherent summation of power for magnetrons. If the available difference in phases, for example, is $\Delta\varphi = \pi/4$, then the correlation interval is $\tau_\varphi \approx 40$ ns for $\Delta U/U = 5\%$ and $\tau_\varphi > 100$ ns for $\Delta U/U < 1\%$. Thus, random phasing can be caused not only by a high level of electron noise, but also from the jitter of the voltage rise time τ_U and instability of the voltage pulse.

Phase control occurs for both the unswitched mode (when frequency locking is absence) and the switched mode. For example, for the case shown in Fig. 3 (middle) the difference of phases of the radiated field when $\Delta\varphi_{in} = \pi/2$ is $\Delta\varphi_{out} \approx 0.7\pi$ for the switched $\pi-$mode and $\Delta\varphi_{out} \approx 0.9\pi$ for the $2\pi/3-$ mode.

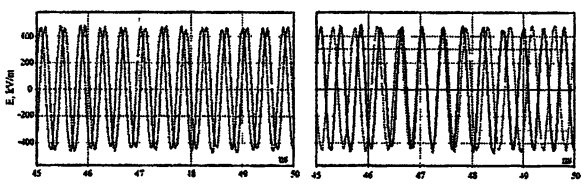

Fig. 4. Close-up view of radiated fields of the TE_{21}-mode with $\tau_U = 1$ ns and $\tau_U = 4$ ns (left) and that of the same MDO generating the TE_{31}-mode with frequency f = 2.33 GHz when $\tau_U = 0.2$ ns and the TE_{21}-mode with f = 2.54 GHz when $\tau_U = 2$ ns (right).

The dependence of *f(H)* in Fig. 2 raises the question, why apply an input RF signal for mode switching if there is a simpler way - by changing the field H near its critical value H_{00}? Rapid variations in H is difficult to implement; however, it is not pertinent to variations in the applied voltage U, which like H affects the azimuthal drift velocity v_e of electrons and, as a consequence, the regions of synchronous interaction of electrons with considered modes. In Fig. 5 these regions are shown as the dependence *f(U)* for a magnetic field H = 4.52 kOe that corresponds to the value H_{00} in Fig. 2. Then the regions in Fig. 5 are separated by the critical value of applied voltage U_{00} = 400 kV. However, rapid mode switching by voltage variation offers a problem: the dependence of the boundary for the applied voltage and magnetic field separating synchronous regions of neighboring modes on the time variant voltage presents a hysteresis-like dependence: when the voltage increases, the boundary that corresponds to the bifurcation of the modes shifts to larger voltages; when the voltage decreases, the boundary shifts to lower voltages. In doing so, the hysteresis loop enlarges with increasing rate of voltage variation overlapping both neighboring synchronous regions for pulse durations of several 10's ns that are typical for relativistic microwave oscillators (Fig. 5). This occurs not only owing to the high stability of generating modes as was demonstrated in [3] for the π–mode and the 2π–mode in the well-known A6 magnetron, but also because of different contributions to synchronism of rotating magnetic fields induced by change of the applied voltage $\pm dU/dt \rightarrow \pm rot_r \vec{H}$. The magnetron begins to generate the mode corresponding to the synchronous voltage U, which occurs with a short rise time τ_U that is less than the characteristic fill time Q/ω of magnetron cavities by EM energy (here Q is the loaded quality factor).

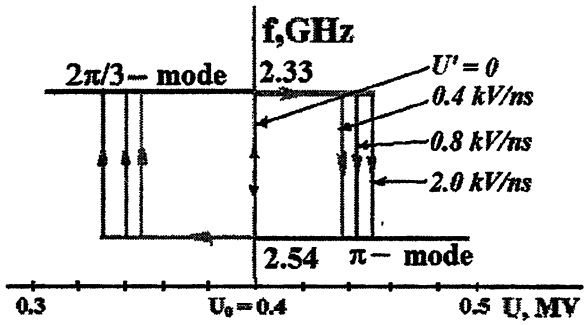

Fig. 5. Dependences of radiation frequency on voltage for different $U' = dU/dt$.

In conclusion, the authors wish to thank M. Petelin for useful discussions on phase control.

References

1. *Fuks and E. Schamiloglu,* 70% efficient relativistic magnetron with axial extraction of radiation through a horn antenna // IEEE Trans. Plasma Sci. 2010. V. 38. No. 6. P. 1302-1312.

2. *A.A. Andronov, A.A. Vitt, and S.E. Khaikin,* Theory of Oscillations (Pergamon Press Ltd., Oxford, UK, 1966).

3. *M. Liu, C. Michel, S. Prasad, M. Fuks, E. Schamiloglu and C.-L.Liu,* RF mode switching in a relativistic magnetron with diffraction output // Appl. Phys. Lett. 2010. V. 97, No. 1, P. 251501-3.

4. *B. Goplen, L. Ludeking, D. Smithe, and G. Warren,* User-configurable MAGIC for electromagnetic PIC calculations, Comp. Phys. Commun. 1995. V. 87. P. 54-86.

5 H.A.H. Boot, Magnetron with long anode//Crossed-Field Microwave Devices, edited by E. Okress. New York, Academic Press, 1961. V. 2. P. 218-223.

6. *A.A. Elchaninov, K.V. Afanas'ev, A.I. Klimov, O.B. Kovalchuk, G.A. Mesyats, V.V. Rostov, K.A. Sharypov, M.I.Yalandin,* Experimental demonstration of coherent power summation for relativistic X-band HPM oscillators, Proc.XVI Int Symp. on High Current Electronics, Tomsk, Russia. 2010. P. 404-407.

Limiting Currents of Strongly-Magnetized Electron Beam in Uniform Transport Channel

M.B. Goykhman, A.V. Gromov, N.F. Kovalev, A.V. Palitsin

IAP RAS, Nizhny Novgorod, Russia

High-current relativistic electron beams, emitted from cold emission cathodes, are successfully used for generation of microwave pulses with gigawatt-level power and duration of several tens nanosecond. In order to develop oscillators with higher power levels we need more detailed information about electron beam's properties, especially thin walled strongly magnetized ones, those are employed in such oscillators.

Thin-walled electron beams usually are formed in two-electron coaxial guns with edged graphite cathodes in strong longitudinal magnetic field that also provide a transportation of the beams through the interaction space of oscillator. A thickness of cathode's edge ordinarily doesn't exceed 1 mm. A formed electron beam has the same thickness. We consider basic properties of tubular beams with off-center axes, as it is shown in Fig. 1. Such situation often appears in experiments with oscillators.

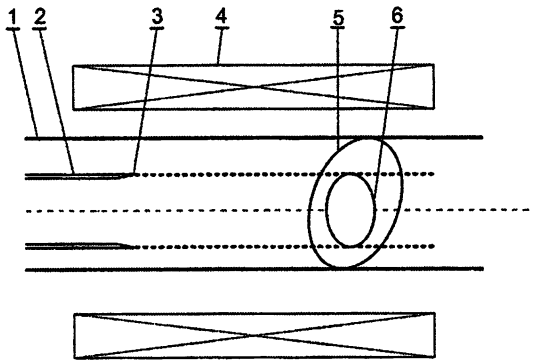

Fig. 1. Two-electrode electron gun with magnetized edge cathode. 1 – anode tube, 2 – cathode, 3 – emitting edge, 4 – solenoid, 5 – cross section of anode tube, 6 – cross section of electron beam.

The fist part of the report presents the analytical demonstration that limiting current of electron beam with given arbitrary cross section in the tube with arbitrary cross section is reached if the beam is equipotential and electron's relativistic factor

$$\gamma = \gamma_0^{1/3}, \qquad (1)$$

where $\gamma_0 = 1 + \frac{eU_0}{mc^2}$ and U_0 - accelerating voltage. The Fedosov's problem [1] is solved for non co-axial electron beam and regular channel. It is demonstrated, that formed electron beam is equipotential and electron's relativistic factor is defined by expression

$$\gamma = \sqrt{2\gamma_0 + 0.25} - 0.5. \qquad (2)$$

Both this assertions are illustrated by solutions of approximate nonlinear partial defferential equation

$$\frac{\partial^2 \gamma}{\partial z^2} + \frac{\partial^2 \gamma}{\partial y^2} + \frac{2}{a^2}(\gamma_0 - \gamma) - \frac{\chi}{a}\frac{\gamma}{\sqrt{\gamma^2 - 1}} = 0, \qquad (3)$$

where $\chi = 4\pi \frac{eJ}{mc^3}$, J - linear current density and $a = a(y,z)$ - function that is proportional to distance between the beam and the wall of channel.

Equation (3) was applied to investigation of steady states of thin-walled electron beams in out-off-alignment channel, in particular, "virtual cathode curve" is obtained and that allows defining the cross-section of the beam after virtual cathode.

References

1. *A.I. Fedosov, E.A. Litvinov, S.Ya. Belomytsev and S.P. Bugaev.* On account of characteristics of an electron beam forming in diodes with magnetic insulation // Izv. VUZov, Fizika (in Russian), No. 10, P. 134-135, 1977.

Corkscrew Modulated Hollow-Beam Klystron

A. Grede, H. Henke

Technische Universitaet, Berlin, Germany, henke@tu-berlin.de

Introduction

A new idea, first mentioned in [1], for a high efficient and potentially high power klystron is presented. It was triggered from the intention to use higher order modes and therefore larger cavities which would allow for either higher currents at equal current density or for higher frequencies with smaller beam port openings.

Instead of a round beam, like in standard klystrons, an annular cathode creates a hollow beam, which after compression and acceleration by the anode enters a bunching cavity, pill box type or coaxial. The cavity is driven by an azimuthally rotating higher order TM_{n10}-mode. Thus, the electrons are velocity modulated with a phase progressing in azimuthal direction. As a result, bunches placed along n interlaced corkscrew trajectories develop after the drift length. The output cavity is, as the input cavity, a round cavity operating in a circularly polarized TM_{n10}-mode.

A 30GHz tube, with two idler cavities, solenoid focusing and TM_{110}-mode multi-gap output cavity is simulated. With a beam voltage of 100kV and a current of 1A an output power of 36kW could be reached. For higher modes and currents, electron efficiencies over 50% can be expected, keeping the same current density.

Input Cavity and Beam Formation

The input cavity is an annular ring cavity driven in an azimuthally rotating TM_{n10}-mode. Fig. 1 shows, for n=1, the mode in the cavity and the development of a corkscrew modulated hollow beam in the drift space. Due to the annular arrangement and the higher order mode the beam area is larger then for a standard round beam. The radius of the hollow beam and the ratio of round to hollow beam area is given in the table for different mode numbers n at 30GHz. Hereby the width of the annular ring was taken to be equal to the diameter of the round beam and an inner conductor with 2mm diameter was assumed. The rapidly increasing area ratio allows for either higher currents at equal density or for smaller beam openings thus improving drastically the shunt impedance.

Idler cavities can be used, as in standard klystrons, to improve the bunching and increase gain and efficiency. The option to lower the current density at equal output power would also be advantageous since the plasma frequency becomes smaller and the drift space longer. Bunches stay together over a longer distance before they decohere. Extended output cavities are possible, which is essential to improve the efficiency at high frequencies.

TM_{n10} @ 30 GHz	beam position radius in mm	area ratio A_0/A_n
0	0	1
1	3.5	46.7
2	5	66.7
3	6.8	90.7
4	8.6	114.7
5	10.4	138.7

Output Cavity

The output cavity is, as the input cavity, a round cavity with an annular beam port operating in a rotating TM_{n10}-mode excited by the corkscrew beam. It can be a single or multi gap cavity. For the latter a lower current density may be advantageous as mentioned above.

As an example, Fig. 2 shows the analytically calculated shunt impedance, i.e. the shunt impedance without beam port, of a coaxial 30GHz, TM_{n10}-mode, single gap cavity as a function of its inner conductor radius r_i. While for lower order modes, the impedance decreases strongly with increasing inner conductor r_i, this effect vanishes for higher order modes due to the small values of Bessel functions for small arguments and high orders. In view of the drop in shunt impedance, operating with higher order modes seems to be of no interest. On the other hand, a real cavity has a beam pipe and the impedance decays exponentially against the center of the opening. It is therefore important to keep the opening as small as possible in particular for high frequencies. This can be reached, at least partially, by decreasing the current density. In that way one may even overcompensate the loss in shunt impedance at higher modes. Alternatively, the

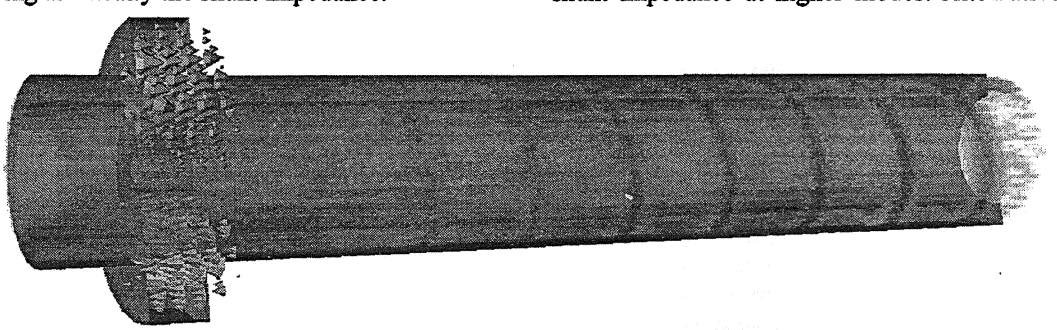

Fig. 1. Hollow beam modulated by a rotating TM_{110}-mode in a coaxial cavity

beam current can be increased, resulting in an improved efficiency and higher output power as well.

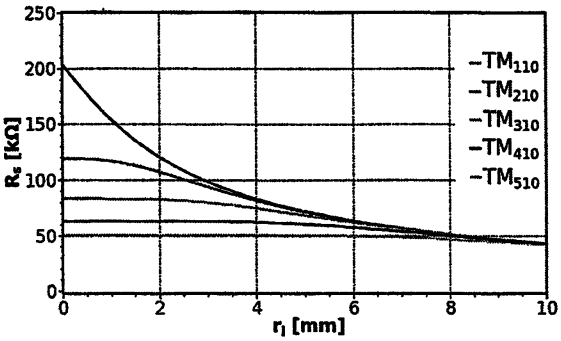

Fig. 2. Analytical shunt impedance over the inner conductor radius of a closed coaxial cavity for different mode numbers

For the special case of no inner conductor, the coaxial cavity becomes a pill box. Since an annular beam port is needed in order to achieve a decent shunt impedance, the central part of the cavity top and bottom cover has to be connected to the outer part by radial stems. This is important for the TM_{110} mode but not necessarily for higher modes because of the small dependence on the inner radius r_i for less than 2mm, s. Fig. 2. Nevertheless, this concept is also useful for higher modes. The stems can be extended through the whole beam tunnel, cutting it into sectors. Thus, the beam tunnel is kept under cut off, avoiding the TEM-mode and improving the mechanical stability. Then, however, the beam has to be generated by a sectional cathode in order to avoid electrons colliding with the stems. Corresponding simulation results can be found in [1].

Simulation Results

In order to evaluate the performance of the design, several simulations with the code GdfidL [2] have been performed. The beam voltage was assumed to be 100 kV and the current 1A , 2A and 3A. Fig. 3 shows the simulation of a single gap 30GHz coaxial output cavity, exited in the TM_{310} mode by 3 interlaced beams. The power extracted from the beam is 14,5 kW and remains the same for either a single or 3 interlaced beams with a total dc current of 1A. Comparing this to 23.7kW extracted by a single gap TM_{110} cavity, driven by a 1A beam, the result may be disappointing. However, since the current density in case of 3 beams in the TM_{310} cavity is 3.9 times less, it seems to be appropriate to decrease the beam port width or increase the beam current. Doing so and exiting the TM_{310} mode by 3 interlaced beams with a total dc current of 3A yields a power of 100.35kW in a single gap cavity. Fig. 4 shows the normalized velocity of the beam, as simulated by GdfidL. Ideal modulated beams have been used for a better comparison of different structures. This explains the tiny velocity spread of the spent beam. The results of simulations with 3 interlaced beams of 1A and 3A show an increase in efficiency from 14.5% to 30%.

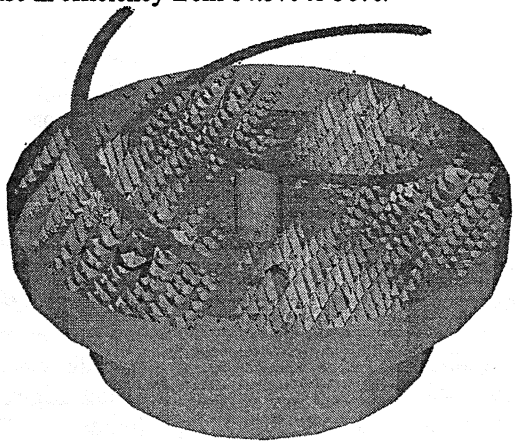

Fig. 3. Three interlaced beams entering a TM_{310}-mode output cavity

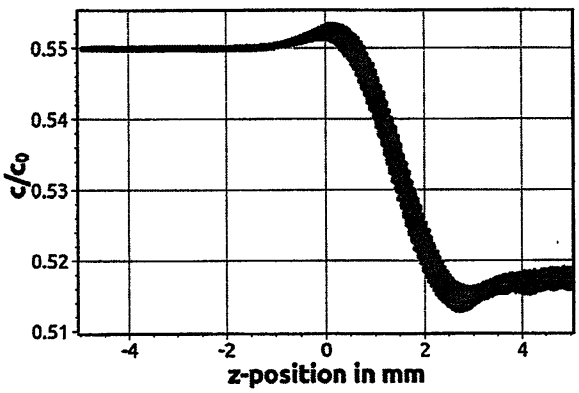

Fig. 4. Normalized velocity of 3 ideal modulated interlaced beams, decelerated by the TM_{310}-mode of a coaxial single gap cavity (0-2.8mm)

In earlier simulations 45kW were extracted from a 100 kV, 1A beam by a 6-gap TM_{110} cavity. Using a coupling factor of 1:4 this resulted in 36kW output power. Therefore, we are optimistic that an extended cavity driven in a TM_{310} or TM_{510} mode with a current of 3A or 5A, respectively, pushes the over all efficiency above 50%.

References

1. *Grede, A., Henke, H.* Concepts for circular defection modulated tubes and frequency multiplying millimeter wave sources //Proceedings of 2009 IEEE Int. Vac. Electr. Conf., Rome, 28-30 April 2009. P. 552-553.

2. *W. Bruns.* http://www.gdfidl.de

Desktop MW Superradiant Free-electron Laser at THz Frequencies

Yen-Chieh Huang, Chia-Hsian Chen, Kuan-Yan Huang

Department of Electrical Engineering, National Tsinghua University, Hsinchu 30013, Taiwan, ychuang@ee.nthu.edu.tw

A free-electron laser (FEL) is often criticized for its bulky size, high cost, and complex setup. We present in this paper a MW-peak-power, single-pass THz FEL with a greatly reduced size, cost, and complexity.

Electron bunching is the key mechanism for generating high-brightness radiation. When an electron bunch length is shorter than the radiation wavelength, the small radiation phase allows the radiation fields from all electrons to coherently add up to a large field. This process is termed as electron superradiance [1]. A long train of periodic electron bunches can further enhance the radiation brightness at harmonics of the bunching frequency. This radiation process is dubbed as comb-pulse superradiance in this paper. The focus of this paper is to study THz comb-pulse superradiance from an electron pulse train with a length much longer than the individual pulse length. Without external seeding, it is difficult for a single-pass THz FEL operating in the self-amplified-spontaneous-emission mode to reach saturation due to the space-charge debunching force associated with a low energy electron beam. As will be shown below, using a pre-formed electron pulse train at THz frequencies to drive the FEL can effectively solve this problem. Our scheme neither increases the length of a beam line nor introduces energy spread to an electron beam, permitting the design of an ultra-compact electron radiation source at THz frequencies.

Figure 1 shows the configuration of the proposed superradiant FEL, wherein a short undulator is installed immediately after the emittance-compensating solenoid of a THz pulse train photoinjector. The fast electron pulse train is produced by illuminating the photocathode of the injector with a THz laser pulse train. The pre-bunched electron pulses generate comb-pulse superradiance in the undulator. The solenoid magnet is the only focusing element of the FEL.

In practice, the radiation field generated from the trailing electrons of an electron pulse could be amplified when slipping toward the leading electrons. The amplification process is stopped when the electrons lose a significant amount of their kinetic energy to the radiation wave and fall off synchronization with the radiation field. The acceleration process in a photoinjector could also degrade the electron bunching. Therefore, we used the space-charge tracking code ASTRA [2] to simulate the acceleration of a pulse-train beam at 2 THz propagating from the photocathode of a S-band 1.6-cell photoinjector to the FEL entrance at z = 50 cm. The peak acceleration field was set at 120 MV/m and the peak solenoid field was set at 3.15 kG to focus the beam at z = 50 cm. Since generating a transversely flattop, circular laser beam for a photoinjector is within reach of today's laser technology, we adopted a radial distribution of electrons at the cathode. Table 1 summarizes the input and output beam parameters for the photoinjector simulated by ASTRA. The fundamental bunching frequency is blue shifted to 2.4 THz due to the velocity bunching in a RF accelerator. The peak bunching factor is reduced from 0.85 at the cathode to 0.21 at the undulator entrance.

If the radiation frequency is chosen to be the fundamental bunching frequency at 2.4 THz according to Table 1, it can be calculated from the FEL synchronism condition that the corresponding undulator period, peak undulator field, and undulator parameters are 18 mm, 8.3 kG, and, 0.98, respectively. By using the beam parameters in Table 1 and a helical undulator, we continue to study the superradiant FEL by using the simulation code GENESIS [3]. Both ASTRA and GENESIS take into account the longitudinal space charge field, which is responsible for the dominant longitudinal plasma oscillation in the beam. Owing to the fast energy extraction from the electrons in a superradiant FEL, it is advantageous to adopt a tapered undulator to maintain the FEL synchronism condition over a longer distance.

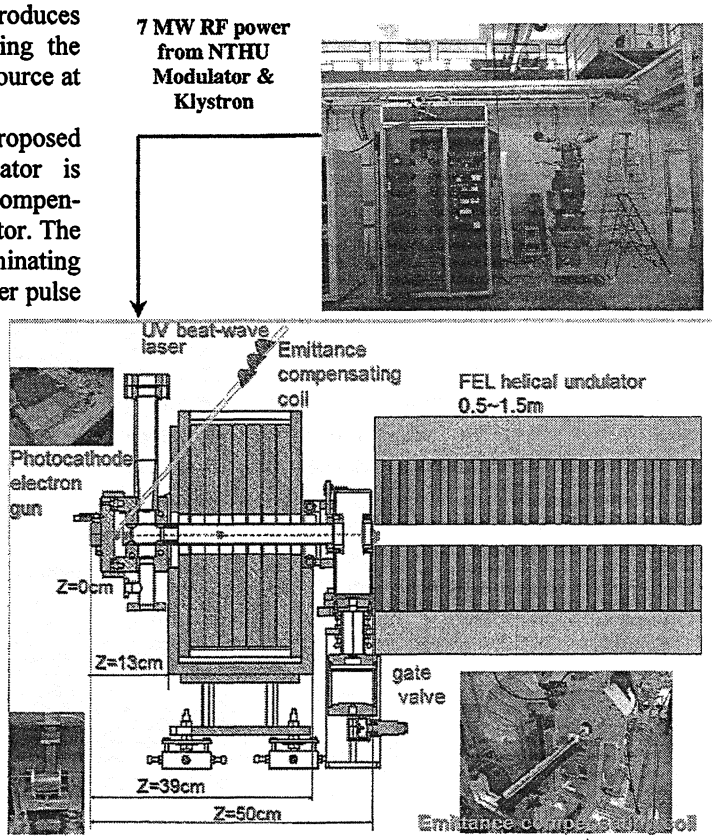

Fig. 1. Schematic of the proposed ultra-compact superradiant FEL driven by a THz-pulse-train photoinjector. The pre-bunched electron pulses are injected into an undulator to generate electron superradiance.

Table 1. Summary of the input and output beam parameters at z = 0 and 50 cm with a 120-MV/m peak acceleration gradient in the photoinjector.

Input Beam Parametes at $z = 0$						
peak gradient	Charges	rms beam radius (mm)	σ_M	σ_μ	micro-pulse rate	Bunching factor @ 2 THz
120 MV/m	1 nC	0.6	4.25 ps	50 fs	2 THz	0.85

Output Beam Parameters at z = 50 cm				
rms beam energy (γ)	rms energy spread $\Delta\gamma$	rms beam radius (mm)	rms emittance (10^{-6} π-m)	bunching factor (@ 2.4 THz)
11.9	7.4×10^{-2}	6.3×10^{-2}	6.88	0.21

Figure 2(a) shows the FEL radiation power at 2.2 THz versus undulator length with 20% linear taper (blue curve) and without taper (green curve) in the undulator parameter between z = 60 and 150 cm. Without the taper, the FEL radiation power saturates at about 0.8 m in the undulator, reaching a power level of 10.7 MW; whereas with the taper, the power increases another 4 MW in the tapered section. Figure 2(b) shows the corresponding bunching factors versus distance in the two undulators. It is seen that the bunching factor first decreases due to the space charge force and then increases due to the fast build-up of the FEL power. If the driving beam was not initially bunched to radiate strongly enough to re-grab the electron bunches, this THz superradiant FEL would be otherwise impossible. With a tapered undulator, the bunching factor retains a nontrivial value between 60 and 150 cm in the undulator, facilitating the growth of the FEL power in that undulator section.

To show the dependence of the radiation power on the initial bunching factor, Fig. 3 plots the FEL power versus distance in the 20% tapered undulator for bunching factors of 0.01, 0.1, and 0.2. Apparently, a larger initial bunching factor helps build up the FEL power. Even with 1% bunching at the undulator entrance, the proposed superradiant FEL can produce MW-level radiation power.

We present in this paper a superradiant FEL at THz frequencies and found a new regime of FEL operation, where space charge debunching is overcome by radiation re-bunching when a low-energy electron pulse train is just injected into an undulator. By using nominal beam parameters from a S-band THz-pulse-train photoinjector [4], we show in simulation that MW-level radiation power at THz frequencies is achievable from a meter long, sinlge-pass undulator. The proposed THz superradiant FEL employs a short undulator directly attached to an emittance compensating coil of the electron gun without using any additional beam-focusing elements. This compact design allows the construction of a MW FEL at THz frequencies on an ordinary desk. We also show that, with 20% linear taper in the final 90-cm section of a 1.5-m undulator, the FEL radiation power can be increased by more than 35%. The spectral property of this FEL with and without external seeding is our next subject of study.

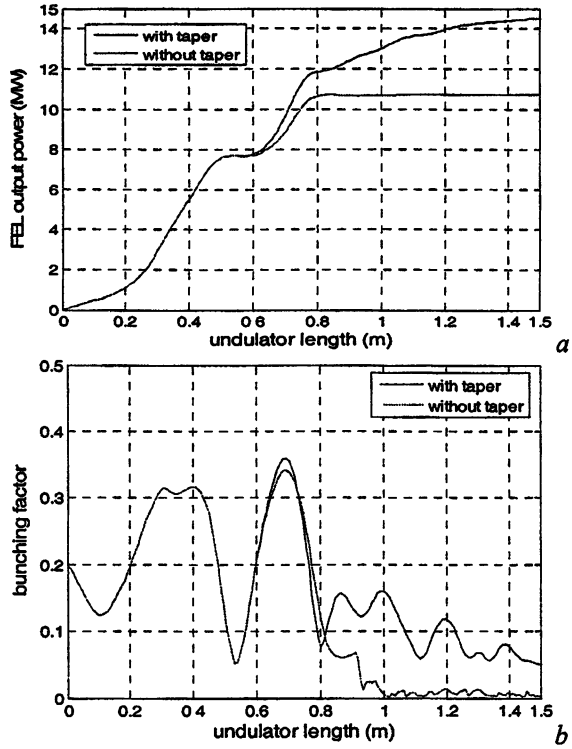

Fig. 2. (a) The FEL radiation power at 2.2 THz with (blue curve) and without (green curve) tapering the undulator parameter. With 20% linear taper between 60 and 150 cm, the FEL radiation power increases by another 4 MW. (b) The corresponding bunching factors versus distance for the two undulators. The bunching factor first decreases due to the space-charge debunching, but quickly shoots up to a higher value due to the fast buildup of the FEL power.

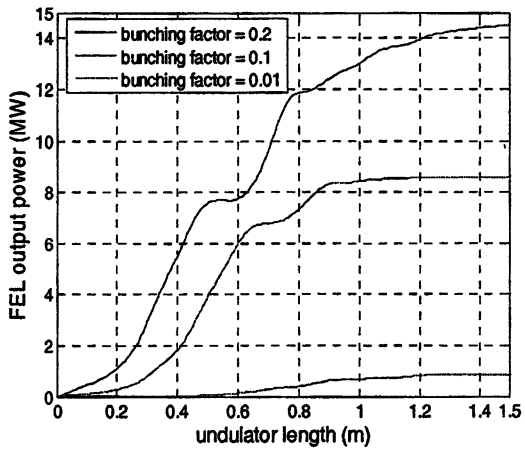

Fig. 3. The effect of initial bunching factor on the FEL radiation power from the 20% tapered undulator. To obtain MW-level radiation power, the bunching factor should be higher than 1%.

This work is supported by National Science Council under Contract NSC 99-2112-M-007 -013 -MY3.

References

1. Avi Gover, "Superradiance and stimulated-superradiant emission in pre-bunched electron-beam radiators. I. Formulation", Phys. Rev. ST AB, 8, 030701 (2005).
2. K. Floettmann, ASTRA User Manual, available at: http://www.desy.de/mpyflo/Astra_dokumentation.
3. Sven Reiche, GENESIS User Manual, available at: http://corona.physics.ucla.edu/~reiche/
4. Yen-Chieh Huang, Chia-Hsian Chen, An-Ping Lee, Wai-Keung Lau, Sheng-Guang Liu., "Laser-beat-wave photoinjector," Nucl. Instr. and Meth. A (2010), doi:10.1016/j.nima.2010.02.009.

A Coaxial-Waveguide Gyrotron Backward-Wave Oscillator with Tapered Waveguide Cross Section

C.L. Hung[1], Y.S. Yeh[2], T.H. Chang[3]

[1]National Penghu University of Science and Technology, Penghu, Taiwan, hung8282@npu.edu.tw
[2]Southern Taiwan University, Tainan, Taiwan
[3]National Tsing Hua University, Hsinchu, Taiwan

The gyrotron backward-wave oscillator (gyro-BWO) is a frequency-tunable source of high-power millimeter-wave radiation. Recently, mode competition problems in high-power gyrotron oscillators have been reduced using coaxial structures. A coaxial structure may be suitable for a gyro-BWO with good mode selectivity. This study analyzes the characteristics of a tapered coaxial-waveguide gyro-BWO using a single-mode, self-consistent nonlinear code. The longitudinal geometry of the interaction structure is tapered to investigate the effects of tapering on the start-oscillation currents of the coaxial gyro-BWO. Additionally, the tapered waveguide method is applied to increase the efficiency of the coaxial gyro-BWO.

Introduction

The gyrotron backward-wave oscillator (gyro–BWO) is a high-power, coherent millimeter-wave source that is based on the electron cyclotron maser interaction. When a nonresonant structure is used, the oscillation frequency of the gyro-BWO can be continuously tuned over a wide range by adjusting either the applied magnetic field or the beam voltage.

The efficiency of the gyro-BWO with a uniform interaction structure is lower than that of other gyrotron devices. Uptapering the magnetic field and/or downtapering the cross-section of the waveguide significantly enhances the efficiency of the gyro-BWO [1-2]. Nonlinear analysis has revealed that properly tapering the magnetic field can enhance the efficiency of the gyro-BWO from 10-15% to 30% [1]. A gyro-BWO with a downtapered interaction structure produced a peak power of a factor of two–higher than that of a uniform tube [2].

Although the efficiency of a gyro-BWO can be enhanced by a down-tapered interaction structure, a gyro-BWO with a down-tapered interaction structure is more susceptible to axial mode competition. The field of the higher-order axial modes can penetrate more deeply into the downstream circuit than can that of the fundamental axial mode, so the start oscillation current of the higher-order axial modes are lowered by a larger effective interaction length [3]. The distributed losses at the down-stream end of the interaction structure can be used to suppress the higher-order axial modes [4].

Not only does axial mode competition occur, but also the electron beam can interact with any transverse waveguide mode at any cyclotron harmonic when the beam-wave resonance condition is satisfied. Most gyro-BWOs use either cylindrical or rectangular waveguides as their interaction structures. Various transverse modes may oscillate and compete with the operating mode. Coaxial cavities have been proposed to reduce problems of transverse mode competition in a high-power gyrotron [5]. The competing transverse modes are suppressed using a coaxial cavity with a tapered and/or corrugated center conductor to decrease selectively the diffractive quality factor. Therefore, a gyro-BWO with a tapered coaxial structure may be able to exhibit mode selectivity. Moreover, the efficiency of a gyro-BWO can be greatly enhanced by tapering cross-section of the waveguide. Therefore, this study analyzes the linear and nonlinear characteristics of a coaxial gyro-BWO with a tapered waveguide cross section.

Numerical Method and Results

The beam-wave interaction in a coaxial waveguide is analyzed using a single-mode, self-consistent nonlinear code [6]. This code is based on the particle-tracing technique and a slow-time scale formulation. The guiding centers of all electrons are assumed to be uniformly distributed on a circle of radius r_c. The transverse field is approximated by that of a uniform waveguide, while the axial field profile is self-consistently evaluated using the field equation and the electron dynamical equations. After an iterative procedure, the oscillation frequency and the field amplitude at the beam entrance are determined under the outgoing (above the cutoff frequency) or evanescent (below the cutoff frequency) wave boundary conditions.

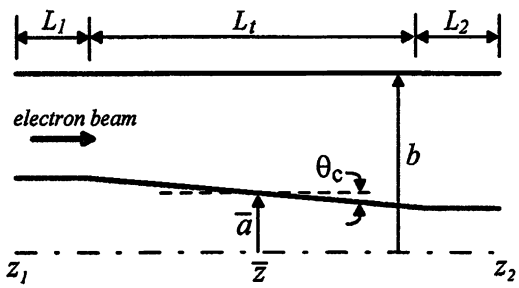

Fig. 1. Schematic drawings of the coaxial gyro-BWO with tapered inner wall radius.

This study considers coaxial waveguides with a slightly tapered inner radius $a(z) = \bar{a} + \Delta a(z)$ and a uniform outer radius b, where $\bar{a}$ is the average value of $a(z)$ (Fig. 1). If $|\Delta a| << \bar{a}$, k_{mn}^2 can be expanded in terms of $\bar{C}(= b/\bar{a})$ and Δa, then k_z becomes [5]

$$k_z^2 = \frac{\omega^2}{c^2} - \bar{k}_{mn}^2 \cdot (1 - 2\frac{\Delta b_{eq}}{b}) \qquad (1)$$

where

$$\Delta b_{eq} = \left(\frac{\overline{C}^2}{\overline{\chi}_{mn}} \frac{d\chi_{mn}}{dC}\bigg|_{\overline{C}}\right) \cdot \Delta a \qquad (2)$$

and $\Delta a(z) = (z - \overline{z}) \cdot \tan\theta_c$.

According to Eq. (2), if the change of the inner wall is small ($|\Delta a| << \overline{a}$), then the change of the equivalent waveguide radius is proportional to $(d\chi_{mn}/dC) \cdot \Delta a$. For TE_{52} mode, Fig. 2 indicates that the coaxial waveguide with a down-tapered inner wall ($\theta_c < 0$) is equivalent to a hollow waveguide with a down-tapered outer wall when $C > 2.0$, but to a hollow waveguide with an up-tapered outer wall when $C < 2.0$.

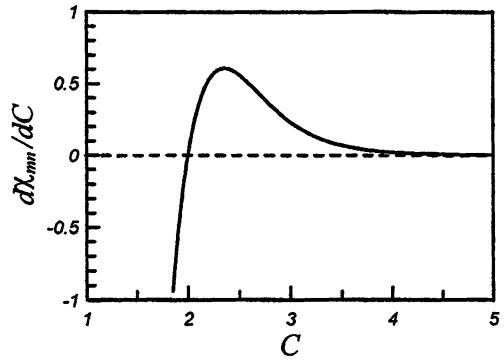

Fig. 2. Dependence of the derivative $d\chi_{mn}/dC$ on the parameter C (=b/a) for TE_{52} mode.

Figure 3 plots the start-oscillation currents and the start-oscillation frequencies of TE_{-52} (s=1) mode as functions of the taper angle θ_c. At $\overline{C}$ =2.0 the start-oscillation currents is almost independent of the taper angle θ_c because the derivative $d\chi_{mn}/dC$ is zero. However, the start-oscillation currents is highly affected by the taper angle θ_c at $\overline{C}$ =2.5. As the taper angle θ_c increases above a certain value θ_{cut} ($\theta_{cut} > 0$) or decreases under $-\theta_{cut}$ (θ_{cut} = 0.18° for B_o=13.0 kG), the oscillation frequency below cutoff in parts of the tapered interaction structure become cutoff for. Then, the effective interaction length is shortened by either down-tapering or up-tapering the inner wall, so the start-oscillation current increases rapidly with the absolute value of the taper angle $|\theta_c|$.

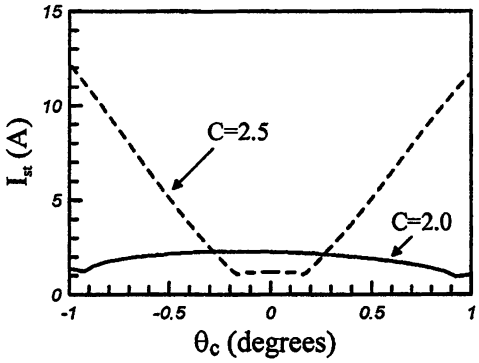

Fig. 3. Start-oscillation current vs the taper angle θ_c for $\overline{C}$ =2.0 and $\overline{C}$ =2.5.

Figure 4 plots the efficiency of TE_{-52} (s=1) mode as a function of the taper angles θ_c at B_0=12.6 kG and a beam current of 10 A. The efficiency increases to a maximum value as the taper angle θ_c decreases from zero to a negative value. The efficiency decreases as the taper angle θ_c increases from zero to a positive value. This characteristic is consistent with a gyro-BWO with a hollow interaction structure [2].

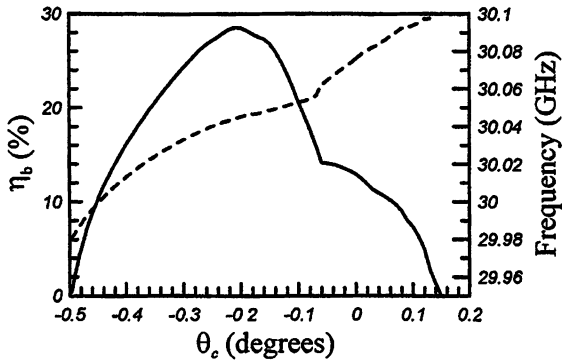

Fig. 4. Calculated efficiency (solid line) and frequency (dashed line) vs the taper angle.

Conclusions

This study investigated the effects of a tapering waveguide cross-section on the characteristics of a coaxial gyro-BWO. The effects of tapering on the start-oscillation currents depend on the derivative $d\chi_{mn}/dC$ at $\overline{C}$. Therefore, a gyro-BWO with a tapered coaxial structure can exhibit mode selectivity. Moreover, the efficiency of a coaxial gyro-BWO can be greatly increased from 12.9% to 28.5% at a beam current of 10 A by tapering of the inner wall.

Acknowledgement

The authors would like to thank the National Science Council of the Republic of China, Taiwan, for financially supporting this research under Contract Nos. NSC 99-2923-M-007-005-MY3 and NSC 99-2221-E-346-003.

References

1. *A. K. Ganguly, and S. Ahn.* Nonlinear analysis of the gyro-BWO in three dimensions // Int. J. Electron. 1989. V. 67, No. 2. P. 261-276.

2. *M. T. Walter, R M. Gilgenbach, P. R. Menge, and T. A. Spencer.* Effects of tapered tubes on long-pulse microwave emission from intense e-beam gyrotron-backward-wave-ocillators // IEEE Trans. Plasma Sci. 1994. V. 22, No. 5. P. 578-584.

3. *K. F. Pao, T. H. Chang, C. T. Fang, S. H. Chen, C. F. Yu, and K. R. Chu.* Dynamics of mode competition in the gyrotron backward-wave oscillator // Phys. Rev. Lett. 2005 V. 95, 185101.

4. *K. F. Pao, C. T. Fang, T. H. Chang, C. C. Chiu, and K. R. Chu.* Selective suppression of high order axial modes of the gyrotron backward-wave oscillator // Phys. Plasmas. 2007. V. 14, 093301.

5. *O. Dumbrajs, and G. S. Nusinovich.* Coaxial gyrotrons: past, present, and future // IEEE Trans. Plasmas Sci. 2004. V. 32. No. 3. P. 934-946.

6. *C. L. Hung and Y. S. Yeh.* Stability analysis of a coaxial-waveguide gyrotron traveling-wave amplifier // Phys. Plasmas. 2005., V. 12, 103102.

Short-wavelength Tunable Bragg Reflectors based on Coupling of Propagating and Cutoff Waves: Modeling and "Cold" Tests

P.V. Kalinin[1], A.V. Arzhannikov[1,2], S.A. Kuznetsov[2], S.L. Sinitsky[1], N.S. Ginzburg[3], A.M. Malkin[3], N.Yu. Peskov[3], A.S. Sergeev[3] and V.Yu. Zaslavsky[3]

[1]Budker Institute of Nuclear Physics SB RAS, Novosibirsk, Russia, pkalinin@inp.nsk.su
[2]Novosibirsk State University, Novosibirsk, Russia
[3]Institute of Applied Physics, RAS, N. Novgorod, Russia

Operation principles of advanced Bragg structures

Advanced Bragg structures based on coupling of propagating and cutoff modes have been proposed [1] to advance FELs into THz-bands. Increase of the oversize factor that is necessary for operation in this band leads to (1) dramatic reduction of selectivity of traditional Bragg structures (which are based on coupling of two counter-propagating waves having high group velocities) [2] due to overlapping of the Bragg reflection zones for different waveguide modes and (2) significant drop of absolute values of the reflection coefficient. Similar to gyrotrons the implication of the cutoff wave into the feedback loop results in mode spectrum purification because the distance between the cut-off waveguide modes is much higher than between the paraxial waves.

Advanced Bragg reflector (ABR) of the planar geometry (fig. 1) is formed from two metal plates having distance a_0 between them and corrugated as

$$a = a_0 + (a_1/2)\cos(\bar{h}z), \qquad (1)$$

where $\bar{h} = 2\pi/d$, d is the period and a_1 is the depth of corrugation. This structure provides the feedback loop including two counter-propagating TEM waves

$$\mathbf{E} = \mathbf{y}_0 \,\mathrm{Re}\left[A_+ e^{i\omega t - ihz} + A_- e^{i\omega t + ihz}\right] \qquad (2)$$

and a cutoff TM_n wave

$$\mathbf{E} = \mathbf{z}_0 \,\mathrm{Re}\left[B \sin\left(\frac{\pi n y}{a_0}\right) e^{i\omega t}\right] \qquad (3)$$

under the Bragg resonance condition

$$h \approx \bar{h}. \qquad (4)$$

Thus, the period of the advanced Bragg structure is about twice higher than the period of traditional one that is also beneficial at short-wavelength bands.

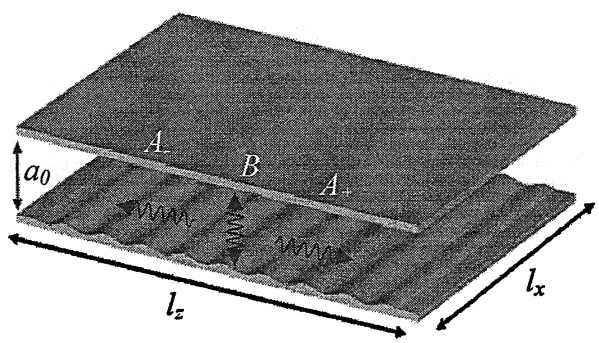

Fig. 1. Scheme of the planar Bragg structure based on coupling of propagating ($A_\pm$) and cutoff (B) waves.

Advanced Bragg structure provides narrow-band reflection near the cutoff frequency $\omega_c = \pi nc/a_0$ of the wave B. Thus, geometrical parameters of the system satisfy the relation

$$a_0 \approx nd/2. \qquad (5)$$

One more advantage of the advanced Bragg structure is tunability of the reflection by varying the distance between the plates a_0 According to the simulations (see fig. 2a) the reflection zone is shifted together with the cutoff frequency ω_c.

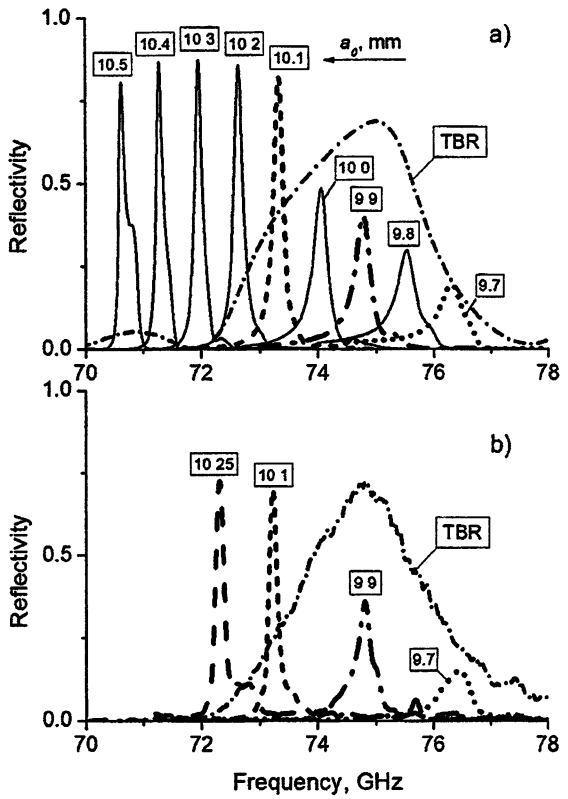

Fig. 2. Results of **(a)** simulations and **(b)** measurements of advanced Bragg reflector at various values of the gap a_0 (l_x = 100 mm, l_z = 60 mm, d = 4 mm, a_1 = 0.1 mm) in comparison with the traditional Bragg reflector (TBR, l_x = 100 mm, l_z = 60 mm, d = 2 mm, a_1 = 0.15 mm).

Results and discussions

The first "cold" tests of the advanced Bragg structures were carried out in the millimeter band near 75 GHz using the BWO scalar network analyzer (SNA). The advanced Bragg reflector for these tests was composed of two parallel copper plates with the rectangular 1D corrugation. The structure parameters

were as following: $l_x = 100$ mm, $l_z = 60$ mm, $d = 4$ mm, $a_1 = 0.1$ mm. According to (2)-(4) such structure should provide resonance coupling of the propagating TEM waves and the quasi-cutoff wave of TM_5-type at the gap $a_0 \approx 10$ mm. During the tests the gap was slightly varied near this value. The accuracy of the a_0 adjustment was ±0.05 mm. To excite the structure an adiabatic horn with the extension from the waveguide transverse section of 3.6 mm × 1.8 mm (SNA output size) to 100 mm × 10.1 mm was used. This horn forms the quasi-TEM wave from the $TE_{1,0}$ wave of standard rectangular waveguide with the power efficiency of 90%.

For comparison the properties of traditional Bragg reflector (TBR) of the same size ($l_x = 100$ mm, $l_z = 60$ mm) and the corrugation depth $a_1 = 0.15$ mm were studied. Period of the traditional reflector corrugation was 2 mm to provide coupling of forward and backward TEM waves at 75 GHz.

Simulations of the advanced Bragg reflector (fig. 2a) were carried out using 3D code HFSS and compared with the results of "cold" tests for different values of a_0 (fig. 2b). One can see the results of measurements coincide well with numerical simulations. The reflection band of the advanced Bragg structure is much sharper than of the traditional one. Absolute value of the reflection provided by advanced Bragg structure is also higher.

As discussed above, the resonance frequency strongly depends on the gap between plates. The shift of the reflection zone with variation of a_0 is shown in fig. 2a. Small differences between "cold" tests and simulations can be explained by the uncertainty of the measurements (~ 10 - 15%) conditioned by precision of positions of the plates forming the structure as well as by admixture of high-order modes in the forward and backward fluxes.

Advanced Bragg reflector of sub-mm wavelengths

To estimate possibility of the advanced Bragg reflectors to operate in the sub-millimeter and terahertz band FELs it is important to investigate the selective properties of such structures at higher oversize parameter $a_0/\lambda \sim 10 - 20$. In fig. 3 result of simulation is presented for the structure with the following parameters: $l_z = 47$ mm, $d = 0.47$ mm, $a_0 = 5$ mm, $a_1 = 0.08$ mm. As one can see the advanced Bragg structure with the oversize parameter $a_0/\lambda \approx 10$ remains narrow-band reflectivity ($\Delta\lambda/\lambda \approx 0.5\%$) at the frequency band of 600 GHz.

Reflector with such corrugation is manufactured currently and "cold" tests of this structure at 600 GHz are in progress using the wideband BWO spectrometer in Novosibirsk State University.

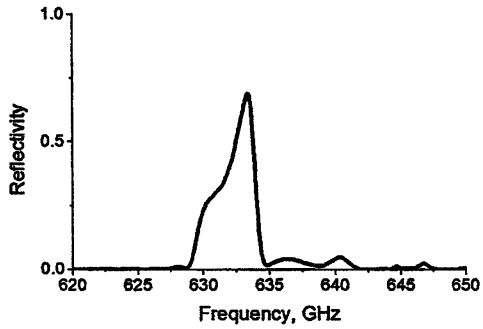

Fig. 3. Results of simulations of advanced Bragg structure ($l_z = 47$ mm, $d = 0.47$ mm, $a_0 = 5$ mm, $a_1 = 0.08$ mm) in sub-mm wavelength band.

Conclusion

Advanced Bragg reflectors were simulated and designed for FELs operating in the frequency bands of 75 GHz and 600 GHz. Results of "cold" tests at 75 GHz demonstrated good agreement with the simulations. Narrow-band reflection in the vicinity of the cutoff frequency of the trapped wave was measured and high selective properties of the Bragg structures of such type were proved. Tunability of the reflector was achieved in the frequency band of about 4% when varying distance between plates.

Coupled-wave analysis together with 3D simulations demonstrates that advanced Bragg structures are able to provide selectivity up to transverse size ~10 - 20 wavelengths [3]. Compatibility with transportation of an intense electron beam encourages the use of novel Bragg reflectors in powerful long-pulse FELs up to THz frequencies [4].

This work was partially supported by the Russian Federal Program "Scientific and Pedagogical Staff for Innovative Russia" for 2009-2013, Grants of the Government of Russian Federation (# 11.G34.31.0033), The Russian President Grant for young Ph.D. scientists (# MK-5530.2011.2) and the Russian Foundation for Basic Research

References

1. *Ginzburg N.S., e.a.* Improving selectivity of free electron maser with 1D Bragg resonator using coupling of propagating and trapped waves // Phys. Rev. ST-AB. 2005. V. 8. P. 040705.

2. *Bratman V.L., e.a.* FEL's with Bragg reflection resonators: CARMs versus ubitrons // IEEE J. Quant. Electr. 1983. V.19, No.3. P. 282-293.

3. *Ginzburg N.S., e.a.* Tunable terahertz band planar Bragg reflectors // Appl. Phys. Lett. 2009. V. 95. P. 043504.

4. *Ginzburg N.S., e.a.* THz FEL with Bragg resonator based on coupling of propagating and trapped waves // JEPT Lett. 2010. V.91. P. 286-289.

Design of a Powerful CW Terahertz Large-Orbit Gyrotron

Yu.K. Kalynov, V.L. Bratman, V.N. Manuilov, and A.Sh. Fix

Institute of Applied Physics, Nizhny Novgorod, Russia, kalynov@appl.sci-nnov.ru

The project is aimed at creating a powerful continuous-wave oscillator with radiation frequencies in a range of 0.26 to 0.52 THz using a fairly low supply voltage of 30 kV. For this purpose, a Large-Orbit Gyrotron (LOG) operated at the second, third, and fourth cyclotron harmonics has been chosen.

Unlike the conventional gyrotrons, an electron beam describing a helical trajectory around the cavity axis (a nearly monoaxial beam) is used in the LOG. This configuration provides the maximum coupling of the electron beam with operating cavity modes whose azimuthal indices are equal to the resonant harmonic number, and the spectrum of potentially dangerous parasitic modes is simultaneously essentially rarefied when operated at high cyclotron harmonics. LOGs give a possibility to excite several cyclotron harmonics using the same electron gun, magnetic system, and collector for generation in a specified range of frequencies by changing only the cavity unit and rearranging an output window.

The formation of an electron beam with shape close to the monoaxial one is impossible in a classical magnetron-injection gun. After experiments with various types of guns, a system with a magnetic-field cusp in the anode-cathode gap was successfully employed in a THz LOG [1]. The same type of a gun will be used in this project (Fig. 1). The gun is calculated for much lower electron energy of 30 keV, an electron beam current of 1A, and a pitch-factor of 1.5. This gun should operate in the regime of thermal limitation of emission. Calculated magnetic field at the cathode is 1.7 mT. The magnetic field passes through zero at a distance of 0.6 mm from the emitter centre, and after the field reversal reaches a value of about 30 mT at the input of the transportation tunnel. Then the imparted transverse electron velocity increases many times in a smoothly increasing magnetic field. A trajectory analysis has confirmed the possibility of the formation of an electron beam with parameters necessary for effective gyrotron operation. Specifically, the transverse velocity spread is 0.25–0.14, the corresponding pitch-factors are 1.5–2.0, and a deflection of the leading particle centers from the device axis is much less than the operating wavelength and does not exceed 0.09 mm.

A fairly strong magnetic field should be provided in the cathode part of the beam formation system where a special coil that compensates the rather large component of the main solenoid magnetic field creates a necessary oppositely directed field at the cathode. The main solenoid and the cathode coil are combined in the same cryostat to simplify the power supply of the magnetic system. The cryomagnet is calculated for the creation of a magnetic field with an induction of up to 5 T inside the gyrotron cavity. Parameters of the cathode coil are chosen such that the currents in the windings of the coil and the main solenoid are close to each other.

Since the electron beam in the LOG is strongly concentrated near the device axis, conventional methods of the beam utilization at a collector are ineffective. One of the possible techniques is that the beam as a whole is turned in a transverse magnetic field to the collector surface and is spread over this surface by rotation of the transverse magnetic field component around the collector axis (Fig. 2). For this, a system of three pairs of rectangular coils located one opposite to another around the external surface of a cylindrical

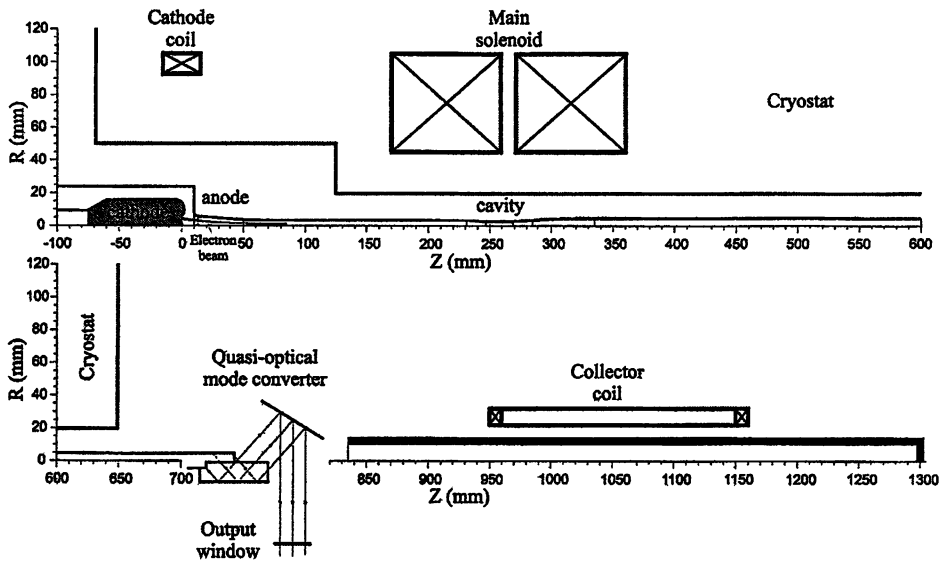

Fig. 1. General scheme of a CW Terahertz Large-Orbit Gyrotron

collector will be used (Fig. 3). The coils are connected to a three-phase power supply, and due to this a rotating magnetic field of constant amplitude is created near the collector axis and a circular trace with a uniform azimuthal distribution of electrons at the collector surface is provided. A cylinder with an internal diameter of 20 mm and a length of 450 mm is used as the collector. Its external surface is cooled by water. Calculated value of the average thermal power at the internal surface does not exceed 0.5 kW/cm^2.

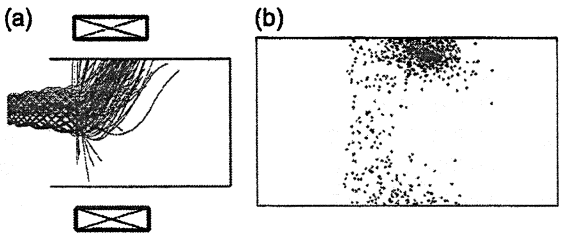

Fig. 2. Trajectories of particles (a) and a circular trace of the electron settling area (b) at a fixed instant of time

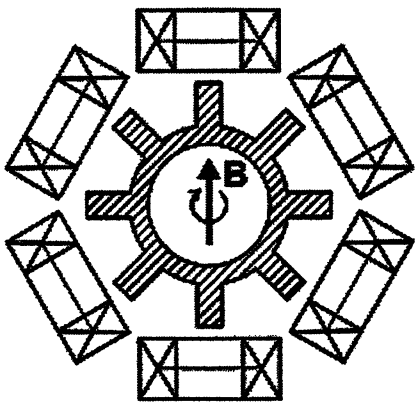

Fig. 3. Scheme of the collector with a system of coils

Like in the previous experiments, a conventional gyrotron cavity in the form of a section of a weakly irregular circular waveguide will be used in the CW LOG. In the case of operation at the third cyclotron harmonic, the cavity is calculated for a frequency of 0.394 THz and a corresponding magnetic field of 4.9 T. The $TE_{3,7}$ mode, which is used in a pulsed terahertz LOG [1], is chosen as the operating one. The corresponding cavity diameter is 5.85 mm. The chosen cavity length of 19 mm ensures a threefold excess of the operating beam current over the minimum starting current. Calculated ohmic losses in the cavity walls are close to 70 % of the power generated, and an average calculated thermal loading of 0.5 kW/cm^2 is admissible for the CW generation regime. The calculated output power is 1.2 kW. If the magnetic field is increased up to 5 T, then selective generation of the $TE_{2,5}$ mode in the same cavity at the second cyclotron harmonic with a radiation frequency of 0.267 THz and a power of up to 3.5 kW becomes possible.

Use of the cavity with a diameter of 6 mm and a length 15.5 mm will provide generation of the $TE_{2,5}$ mode with a frequency of 0.26 THz and a power of up to 5 kW at the second cyclotron harmonic in a field of 4.9 T.

Although the supply voltage of 30 kV is fairly low, calculations show that the developed gun and magnetic system can also be used to excite the fourth cyclotron harmonic and reach an operating frequency of 0.52 THz. For this purpose, a more complex and selective electrodynamics system in the form of Coupled Resonators with Mode Conversion (CRMC) is needed. Due to such a configuration, the interaction length can be increased almost two times, which markedly reduces the starting current of the LOG. Calculations of the fourth-harmonic LOG with coupled $TE_{4,7}$ and $TE_{4,8}$ modes in cavities (with diameters 4.699 and 5.283 mm, respectively) show that the power generated at a frequency of 0.52 THz is 160 W. In this case, ohmic losses in the output cavity are very large and require special techniques to reduce them.

An output quasi-optical converter will be mounted inside the LOG for transformation of the operating mode into a Gaussian wave beam. This is convenient both for transport and use of the radiation. The converted radiation will be extracted from the gyrotron through an output BN window with a diameter of 66 mm. The resonant thickness of the disk at a radiation frequency of 0.394 THz is 2.1 mm. Simultaneously, this thickness is resonant for frequencies 0.263 and 0.525 THz. Estimates show that the window losses are high enough and the window should be water-cooled.

The project implementation can, in particular, satisfy a considerable part of the requirements for coherent radiation sources in high-field DNP-NMR spectroscopy and a study of the gas-discharge phenomenon [2], as well as opens up new opportunities for diagnostics of various media and examination of the surface of rigid bodies, in technology, medicine, and a number of other areas.

The authors are grateful to I.V. Bandurkin and N.A. Zavolsky for assistance in the calculations.

This work was supported by the Russian Foundation for Basic Research (project No. 09-08-00457) and the Presidium of the Russian Academy of Sciences (Program "Problems of physical electronics, charged particle beams and generation of electromagnetic radiation in high-power systems").

References

1. *Bratman, V.L., Kalynov, Yu.K., and Manuilov, V.N.* Large-Orbit Gyrotron Operation in the Terahertz Frequency Range // Phys. Rev. Lett. 2009. V. 102, No. 24. 245101.

2. *Koldanov, V.A., Bratman, V.L., Golubev, S.V., et al.* Plasma Terahertz Discharge in Argon at High and Medium Pressures // Proc. of 8th Int. Workshop "Strong Microwaves and Terahertz Waves: Sources and Applications," Nizhny Novgorod. 2011. edited by A.G. Litvak.

Gyrotron Affected by Modulated Reflection: New Experiments

N.K. Kharchev[1], G.M. Batanov[1], Yu.V. Bondar[1], L.V. Kolik[1], D.V. Malakhov[1], A.E. Petrov[1], K.A. Sarsyan[1], N.N. Skvortsova[1], M.I. Petelin[2], Yu.V. Novozhilova[2], A. Cappa[3], J. Martinez[3], A. Tolkachev[3]

[1]Prokhorov General Physics Institute RAS, Moscow, Russia, khar@fpl.gpi.ru
[2]Applied Physics Institute RAS, Nizhniy Novgorod, Russia
[3] EUROATOM-CIEMAT, Madrid, Spain

1. In the previous experiments [1, 2] the modulation of gyrotron reflected power at relatively low frequencies (200-400 Gz) was used. It was shown, that the value of gyrotron power is modulated on the same frequencies for the optimal ratio between phases of direct and reflected signals. The explanation of these results was presented in [3].

2. In presented experiments the new mechanical method of reflected power modulation with rotating disk was used. This method permits to increase the modulation frequency up to 1-5 kHz. At first step the modulation frequency was 1-2 kHz. Figure 1 presents a disc with a groove. This is a basic element of a mechanical modulator. The depth of the groove is equal to a quarter wavelength gyrotron. Maximum rotation speed is 70000 rpm. According to the theory discussed in [3], such a groove depth should give the maximum amplitude modulation of the gyrotron radiation under the influence on gyrotron weak reflection from a rotating surface.

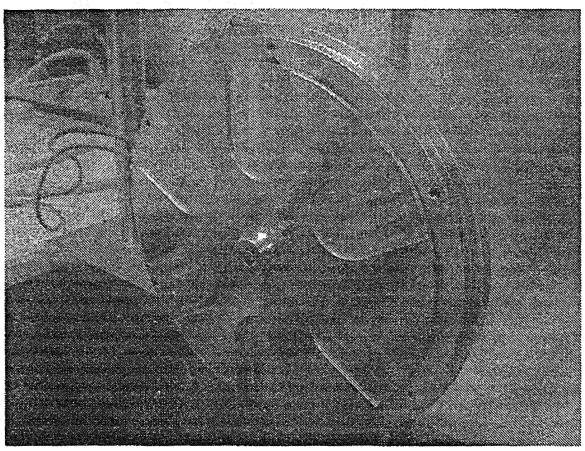

Fig. 1. Mechanical modulator. Maximum disk rotation speed 70000 rpm. The depth of the grooves is equal to a quarter wavelength of gyrotron.

3. The special receiver signal arrangement, consisting of four detectors, was used for simultaneous measurements of space distribution of gyrotron Gaussian beam power. The value of signals was measured near of beam edge in perpendicular to the beam axis plane. It was shown that for every pair of detectors (with opposite location to every one) the phases of power level periodical changes were opposite. These results can be explained with some weak transformation of gyrotron modes during stationary generation regime. Specifically established a quasi-optical coupler allowed to receive the signal from the center of the radiation beam of a gyrotron. Figure 2 shows the signal obtained with this quasi-optical coupler. Signal proportional to the level of reflected radiation from the mechanical modulator. Modulator was rotated at 1100 rpm. Modulation frequency is about 1 kHz.

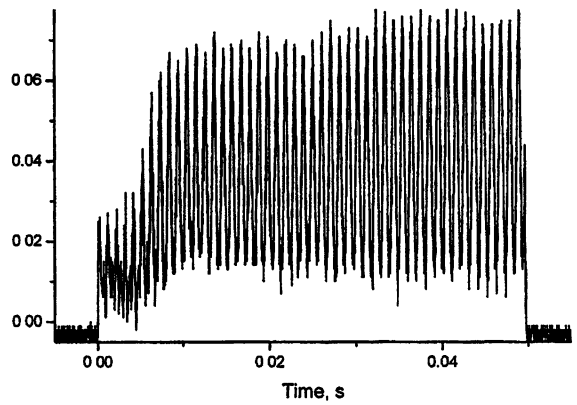

Fig. 2. Signal received by the detector from the center of the beam reflected from a mechanical modulator. Rotational speed of the modulator is 10 000 rpm.

4. Special units were used for simultaneous measurements of two perpendicular linear polarization of gyrotron radiation electric field. It was shown that the main change of gyrotron radiation polarization up to 7-10 degree takes place in the edge part of Gaussian beam power level periodical changes were opposite. These results can be explained with some weak transformation of gyrotron modes during stationary generation regime.

The work is supported by RPPI project 11-08-01129-a (Russia project).

References

1. *Fernandez A.,Kharchev N. et al.* Int. J. of Infrared and Millimeter Waves,2007,V.28,№ 9. P. 705-711.

2. *Kharchev N. et al.* Zh. Prikladnaya Fizika (Rus) (6) p. 158-165(2009)

3. *Novozhilova Yu. et al.* Conf. digest of the 29 Int.Conf.on Infrared and Millimeter Waves. 2004, Karlsruhe (Germany), p. 229-230.

Nanosecond Optically Controlled Switches for Sub-Terahertz Radiation

M.L. Kulygin, G.G. Denisov, V.I. Belousov, Yu.V. Rodin and A.A. Vikharev

Institute of Applied Physics RAS, Nizhny Novgorod, Russia, kmaxim@appl.sci-nnov.ru

Recent progress in optically controlled microwave switches opens the way to efficiently commutate powerful radiation up to terahertz frequencies. The switches are based on an induced photoconductivity effect in semiconductor elements changing properties of resonant systems they are built in [1, 2]. The prospective applications – plasma heating, radars, particle accelerators, and spectroscopy – often require switching rapidness up to nanoseconds and coherence of output pulse packets between each other. The switches studied in this work could be one of the most promising to satisfy these requirements.

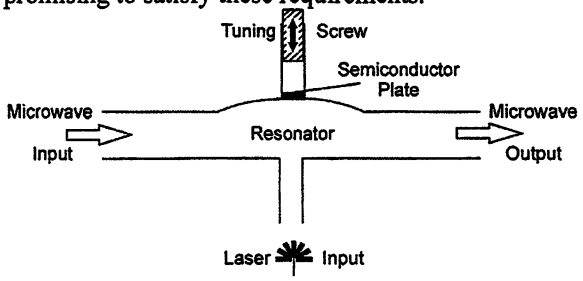

Fig. 1. Layout of the semiconductor switch for microwave radiation

Fig. 1 represents a layout of the semiconductor switch with one-side copper waveguide widening resonator. It is surrounded with two symmetrical pieces of standard single TE_{10} eigenmode rectangular waveguide for the input and the output of the commutated microwave radiation. The resonator also has two attached pieces of subcritical waveguide for eigenmode coupling. The lower waveguide is also used as the input for laser emission.

The semiconductor plate is located at the junction of the resonator and the upper waveguide. The working principle of the resonator is similar to a notch filter [3] which suppresses the passing microwave with a selected frequency to the level of about -40 dB. The screw located above the plate is used for mechanical tuning of the frequency. Illuminating the plate by an appropriate laser emission significantly changes the resonator frequency and its quality factor so the previously reflected signal can pass through it unchanged. This is the switching.

In this study all calculations are based on the simplified theory of switches [4]. We have a set of Maxwell's equations for the fields E and H in vacuum and semiconductor media:

$$rot\vec{E} = -\frac{1}{c}\frac{\partial \vec{H}}{\partial t}, \qquad (1)$$

$$rot\vec{H} = \frac{1}{c}\left(\varepsilon\frac{\partial \vec{E}}{\partial t} + 4\pi e N(\vec{r},t)\mu\vec{E}\right). \qquad (2)$$

Here c is a light velocity, ε is a permittivity, e is an electron charge, and μ is total charge carrier mobility for the semiconductor. N is total charge carrier density (electrons and holes) in the semiconductor, also time dependent:

$$\frac{\partial N}{\partial t} = D\Delta N + g(\vec{r},t) - G_1(N - N_e). \qquad (3)$$

Here D is an ambipolar diffusion coefficient, $g(r, t)$ is a source of photoconductivity [4], G_1 is a charge carrier recombination constant obtained from auxiliary measurements of the semiconductor sample, and N_e is a typical equilibrium density for room temperature. All typical semiconductor constants can be found in [5].

For numerical simulations of the system (1)-(3) we use an own software based on a modification [6] of the well-known Finite Difference Time Domain (FDTD) method [7]. This also includes Unsplit Perfectly Matched Layer (UPML) absorbing boundary conditions [8] at all the ends of waveguides, Ohmic loss boundary conditions at the positions of copper walls, and a transparent unidirectional TE_{10} wave source near the input.

We supposed our numerical model to make adequate calculations at the microwave frequency band between 50 and 100 GHz. So the spatial grid step is 25 μm, and 0.1 μm in the photoconductivity layer due to big difference of charge carrier density. The basic time step is 117 fs; it corresponds to a Courant number [7] value of 0.99. The time step is automatically adjusted by the software to keep the equation (3) stable all over the time of simulation:

$$dN(\vec{r},t) << N(\vec{r},t), \qquad (4)$$

where dN means an increment to the density at each time step.

The simulation software consumes about 10 Mbytes of memory. On a modern personal computer the calculation performs at about 0.5 ns per a processor core per a minute of real time. The total times of simulation did not exceed 100 ns.

A working sample of the switch for 70 GHz is displayed at Fig. 2.

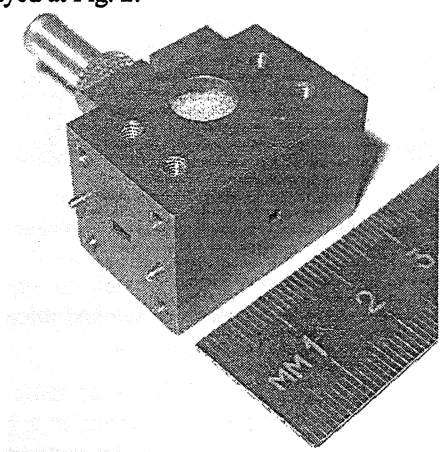

Fig. 2. Photo of the nanosecond switch for 70 GHz

The longest dimension does not exceed 3 cm. The microwave input 3.6 × 1.8 mm standard waveguide with connection pins and screw holes can be seen at the left side; it is symmetrical to the output. The lower side has the input for laser emission. The semiconductor plate is installed through the hole at the center. The frequency tuning screw with its flange is located on the higher side.

We have performed several experiments with the switch. The TE_{10} microwave from a frequency tunable source with power less than 1W is fed to the input of the switch through a directional coupler to suppress the reflected signal. The pulse laser emission beam is focused at the semiconductor plate. The output is connected to a detector that transforms microwave energy to an electric voltage. The output of the detector is loaded with a 50 Ohm resistor to achieve a nanosecond level of performance. Then the detected output signal is directed to an oscilloscope. The digital oscilloscope has a frequency bandwidth of 500 MHz and a sampling rate of $5 \cdot 10^6$ samples per second.

For this study we use a femtosecond titan-sapphire (Ti:Sa) laser complex consisting of a main Ti:Sa optical laser with diode pumping, a Ti:Sa optical regenerative amplifier and a parametric infrared amplifier. The main laser has pulse duration of 50-100 fs, wavelength of 750-830 nm, pulse repetition rate of 75.4 MHz, and average power of 500 mW (the pulse energy is about 10 nJ). The regenerative amplifier decreases the repetition rate to 1 kHz but increases the average power to 2.5 W (the pulse energy to 2.5 mJ). The parametric amplifier increases laser emission wavelength up to 2 μm providing an ability to observe a red boundary of photo effect and its influence on switching. The laser emission is guided to the switch through its 2mm input.

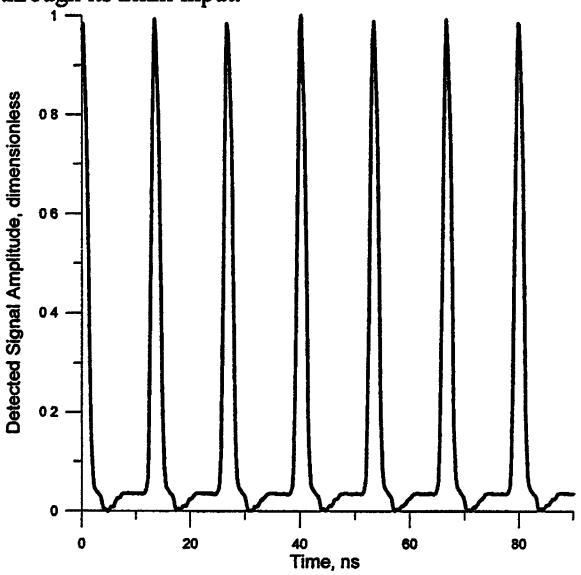

Fig. 3. Output signal as a response to series of laser pulses

A typical response of the switch to repetitive main laser pulses is series of the switched microwave pulse packets. Fig. 3 displays it as an oscillogram curve of the detected signal amplitude. We can see the same repetition rate to the laser of 13.6 ns. The rise time of the microwave pulses is about 1 ns, the fall time is about 2 ns.

The switch demonstrates nanosecond level of performance. It provides a broad frequency tuning range of about 10% so it has low requirements for fabrication precision. It remains operational in wide range of driving laser parameters so there is a possibility of using inexpensive modern 1.06 μm infrared lasers instead of bulky optical multi-cascade sets. The switch seems to be especially useful for molecular coherent spectroscopy. Attached to a source of coherent microwaves it can modulate the monochromatic source to series of packets with nanosecond duration. And all the packets at the output of the switch have phases linked to each other. So there is a possibility to expand the spectrum of molecular analysis and improve its resolution.

Although we tested the switch at commutated microwave power less than 1W we expect the switch to withstand much higher power.

Today the authors also have drafts for 260 GHz IEA WR3 standard waveguide-based switch.

The authors thank B. V. Shishkin and I. E. Ilyakov for their assistance in experiments, V. V. Korchagin and E. A. Novikov for the switch fabrication, and V. Ya. Aleshkin for useful discussions.

References

1. *Vikharev, A. A., Denisov, G. G., Kocharovsky Vl. V., et al.* A high-speed quasi-optical wave phase switch based on the induced photoconductivity effect in silicon // Tech. Phys. Lett. 2007. V. 33, No. 9. P. 735-737.

2. *Kulygin, M. L., Denisov, G. G., Rodin, Yu. V.* Optically controlled semiconductor microwave modulator with nanosecond response // Tech. Phys. Lett. 2011. V. 37, No. 4. P. 368-370.

3. *G. G. Denisov, S. V. Kuzikov and D. A. Lukovnikov.* Simple millimeter wave notch filters based on rectangular waveguide extensions // Int. J. of IRMM Waves 1995, V. 16, No. 7, P. 1231.

4. *M. L. Kulygin, G. G. Denisov, Vl. V. Kocharovsky.* Modeling of dynamic effects in a laser-driven semiconductor switch of high-power microwaves // Int. J. of IRMM and THz waves (IJIM), Springer 2010, V. 31, Issue 1, P. 31-40.

5. *O. Madelung.* Semiconductors, Data Handbook. Springer, 2003.

6. *M. L. Kulygin* (2006 Jun 19). Numerical investigation of three-dimensional multi-mode electrodynamic systems of electronic microwave devices, Ph.D. report monograph. IAP RAS, Nizhny Novgorod, Russia, P. 12-47.

7. *A. Taflove.* Computational electrodynamics: the finite-difference time-domain method, Boston, MA: Artech House, 1995.

8. *S. D. Gedney.* An anisotropic perfectly matched layer – absorbing medium for the truncation of FDTD lattices // IEEE Trans. Antennas and Propagation 1996, V. 44, No. 12, P. 1630.

A Short-Period RF Undulator

J.L. Hirshfield[2,3], S.V. Kuzikov[1], Th.C. Marshall[2,4], G.V. Sotnikov[2,5], A.A. Vikharev[1]

[1]Institute of Applied Physics, Nizhny Novgorod, Russia, kuzikov@appl.sci-nnov.ru
[2]Omega-P, Inc., Yale University, New Haven, CT
[3]Yale University, New Haven, CT
[4]Columbia University, New York, NY
[5]NSC/KIPT, Kharkov, Ukraine

Introduction

An undulator made of static magnets typically has a period of a few centimeters. In order to produce synchrotron radiation of short wavelengths (~ 1 nm) in such undulator a 1.5 GeV electron beam is necessary. Instead of expensive high energetic electron beam a beam of a moderate energy (≤ 300 MeV) in RF undulator with period ranging from several millimeters to sub-millimeters is appealing. Additionally the RF undulator can provide fast dynamic control of polarization, wavelength, undulator K parameter, can have wide aperture (~ 1 cm), and to bring other attractive features [1, 2].

In order to become a competitive alternative to the traditional undulator, the RF undulator must, of course, have as high strength of wiggling fields as magnetic fields in existing permanent magnets (B ~ 1 T). In particular, the K parameter should be about unity in RF undulator of the 10 mm period. Because powers of modern millimeter and sub-millimeter RF sources like a magnicon or a relativistic gyroklystron are limited by several tens of megawatts, necessary undulator fields can be obtained in so-called storage cavities only. Design of such cavities should take into account many constraints like: emittance growth in presence of powerful RF fields, Ohmic wall losses, breakdown, and surface pulse heating.

Travelling wave RF undulators

A travelling wave undulator can be made of low-loss resonant ring where an operating wave moves toward the beam which traverses one of arms. Among low-loss waves there are TE_{01} mode in smooth circular cross-section waveguide and HE_{11} in corrugated waveguide of the impedance type. Both modes have low surface fields in an oversized waveguide. Because the first mode requires bigger diameter to turn [3] and consequently requires higher RF power and energy, the HE_{11} mode is preferable.

The 34 GHz room-temperature RF undulator which exploits superposition of the HE_{11} and HE_{12} modes to minimize diffraction losses in mitre bends is shown in Fig. 1. Calculations show, in order to obtain parameter K = 0.4 in the waveguide of L = 250 mm length, about 120 MW input power, 470 ns filling time (loaded Q-factor is $5.1 \cdot 10^4$ at waveguide radius 26.5 mm) are necessary. Surface electric field is ~ 20 MV/m. Ohmic quality ($Q_{ohm} = 31 \cdot 10^4$) here is twice more than diffraction quality ($Q_{diff} = 15.2 \cdot 10^4$) caused by scattering in mitre bends. The mentioned high input power level is explained by big total volume which cannot be reduced because waveguide radius reduction causes more diffraction losses.

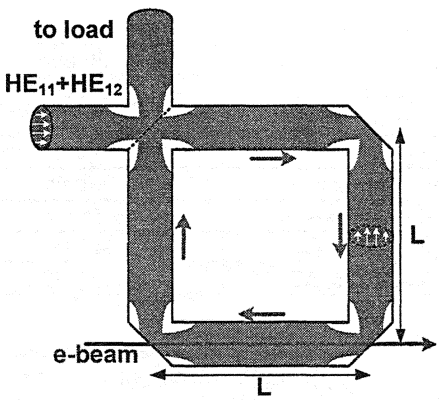

Fig. 1. HE_{11} resonant ring

Beam dynamics in a standing wave RF undulator

In the standing wave RF undulator an operating mode consists of a co-propagating wave and a counter propagating wave (Fig. 2). The counter propagating wave causes the desired FEL quiver electron motion with relativistic Doppler up-shift of Compton photons. The forward wave also interacts with the electrons and generates low frequency microwave radiation. Unfortunately, this wave produces spatially-growing beam oscillations which have an amplitude of the mm-scale. This is a kind of the undesirable beam instability. The view along the beam axis in Fig. 2 shows such beam motion. The reason of this instability is that co-propagating wave in oversized waveguide moves synchronously with moving electrons far enough so that some electrons acquire the positioning shift in one direction, other electrons do the shift in the opposite direction.

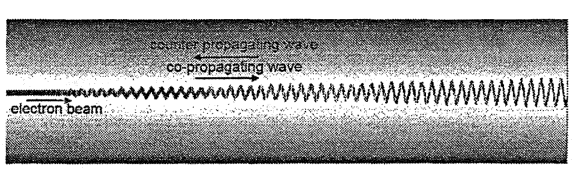

Fig. 2. Electron beam motion in standing wave undulator with identical co-propagating and counter propagating waves (f = 34 GHz, K = 0.1, R = 14 mm)

A cavity with different co- and counter propagating modes

In order to avoid the mentioned undesirable instability a co-propagating mode should have a transverse structure which excludes an interaction with the

beam. In Fig. 3 the counter propagating mode is the TE_{01} wave which has almost maximum fields at beam location, the co-propagation mode TE_{02} has zero fields at this place (Fig. 4). Both modes do not have normal to wall fields. The TE_{01} and TE_{02} modes are converted each to other by ladder-like converters in both ends of the undulator. Calculations show that very high conversion efficiency (diffraction losses at level – 50 dB) is achievable. Input coupler in a form of the perforated section couples selectively the TE_{02} mode in undulator with the TE_{01} coaxial mode. Parameters of the 34 GHz undulator with K = 0.4 are summarized in the Table:

waveguide radius, R	12 mm
main section length, L	250 mm
Ohmic quality, Q_{ohm}	67800
loaded quality, Q_L	33900
coupling, χ	0.8%
RF pulse duration, τ	320 ns
beam shift off axis, r_b	6.55 mm
RF input power, P_{in}	34 MW
temperature rise, ΔT	133 °C

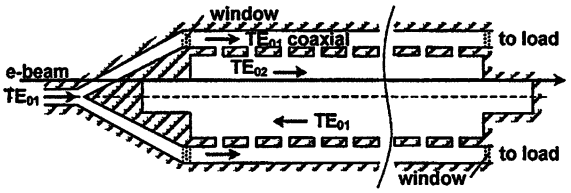

Fig. 3. Conceptual sketch of the two-mode undulator

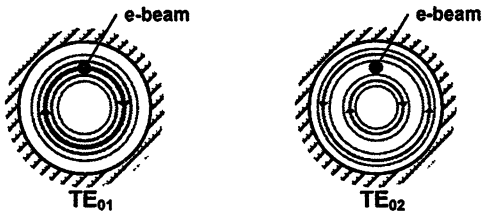

Fig. 4. Cross-section of the resonator showing azimuthal transverse electric fields of co- and counter propagating modes and a location of electron beam

Another possible version is TE_{01}–TM_{11} undulator which has on-axis beam, but surface electric field is not zero. The closer TM_{11} mode to cut off the less the surface field. That is why, an undulator with near to cut off TM_{11} wave seems promising.

A cavity with a TM mode near cut off

In this undulator the operating TM_{11} mode is excited in barrel-like cavity (Fig. 5). Near cut off frequency both co- and counter propagating modes have high phase velocities and can not be in synchronism with electron beam long time. Beam dynamics simulations show that mentioned beam instability is avoided in this case. In cavity, those length equals tens of wavelengths, an electric field consists mainly of E_z component, so the surface field is not high. A corrugation is necessary, in order to provide coupling of the TM_{11} mode with TE_{11} waves of two powering phase-locked RF sources. Polarization of the operating mode can be easily controlled by polarizations of the input TE_{11} waves. The cavity has the smallest volume in comparison with TM_{11} undulator where the operating mode is far from cut off. This factor leads to relatively small input power and input pulse duration. For example, 34 GHz undulator with K = 0.4 and effective length 250 mm (cavity radius R = 5.33 mm) requires P_{in} = 20 MW and τ = 70 ns. These parameters provide low surface electric field (~ 1 MV/m) and comfortable temperature rise (16°C). A disadvantage of this scheme is that frequency of output photons is proportional to $2\gamma^2$ (γ – is a Lorentz factor) like in a DC undulator instead of $4\gamma^2$ like in RF undulators with far from cut off waves.

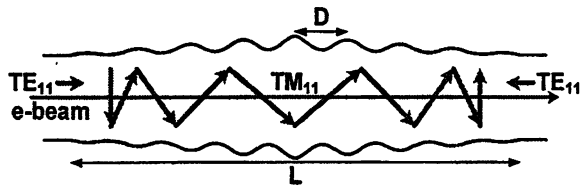

Fig. 5. Conceptual design of the cavity with near to cut off TM_{11} mode

"Cold" RF undulator

In order to reduce input power, it is natural to reduce Ohmic losses by using cryogenically cooled systems. Because a superconducting RF undulator is rather expensive and is able at relatively low RF frequencies ≤ 1 GHz, it is attractive to use at Ka-band a copper undulator to be cooled by liquid nitrogen (T≈80° C). In particular, the copper cooling down to liquid nitrogen temperatures promises about 3 times loss reduction with anomalous skin effect taken into account.

Conclusion

Among the considered schemes the HE_{11} resonant ring is distinguished by simplest design, low surface fields, but the feeding requires huge RF power. The TE_{01}/TE_{02} resonator (off-axis beam) with short efficient mode converters and coaxial coupler requires a moderate power, has low surface fields, but pulse heating temperature is rather high. The undulator with near to cut off TM_{11} mode is very attractive due to many reasons (low input power, low surface fields, simple design), but frequency up-shift is two times less in comparison with other considered versions.

References

1. *T. Shintake, K. Huke, J. Tanaka, I. Sato and I. Kumabe,* Development of microwave undulator // Japanese J. of Appl. Phys., 1983, 22, p. 844–851.

2. *S. Tantawi et al,* Phys. Rev. ST Accel. Beams, 8, 2005, 042002.

3. *A. Bogdashov, G. Denisov, D. Lukovnikov, Y. Rodin, J. Hirshfield,* Ka-band resonant ring for testing components for a high-gradient linear accelerator // IEEE Trans. on Microwave Theory and Techniques, 2005, vol. 53 Issue 10, p. 3152–3155.

High Power Test of Active Microwave Pulse Compressor with Switch Employing Electron Beam Triggering

O.A. Ivanov[1], A.L. Vikharev[1], M.A. Lobaev[1], A.M. Gorbachev[1], V.A. Isaev[1], J.L. Hirshfield[2,3], S.H. Gold[4], and A.K. Kinkead[5]

[1]Institute of Applied Physics RAS, Nizhny Novgorod, 603600 Russia, lobaev@appl.sci-nnov.ru
[2]Omega-P, Inc., New Haven, Connecticut 06510, USA
[3]Department of Physics, Yale University, New Haven, Connecticut 06511, USA
[4]Plasma Physics Division, Naval Research Laboratory, Washington DC, USA
[5]LET Corporation, Washington DC, USA

Time compression of RF pulses [1, 2] is a promising direction for development of a source of high-power nanosecond microwaves. Microwave compressors can be used in linear particle accelerators and in radars. The method of active compression is based on energy storage in a high Q-factor cavity over a time exceeding its settling time, with consequent rapid release of the energy into a load (Q-switching). The main element of an active compressor, which determines the level of power in the output pulse, is a switch for extracting energy from the storage cavity. The switch should have short activation time (~10 ns) and high electric breakdown threshold. Up to now, the best results have been obtained for active compressors with plasma switches [2-4], although the achieved results are still far from those required for accelerators. Restrictions to the achievable peak power of the compressed pulses are associated with the appearance of multipactor discharges on the surface of gas-discharge tubes in the switch and an uncontrollable electric breakdown of the gas in the tubes [2].

The power of compressed pulses in active microwave pulse compressors may be increased by using a new type of the switch employing electron beam triggering [5]. The results of high power tests of the active microwave pulse compressor with such switch are presented in this work. The use of an electron beam allows one to position the active element outside of the high-field region within the compressor, and hence to increase the magnitude of switched power significantly.

The operation of the compressor is based on a sharp increase in the $TE_{02} \rightarrow TE_{01}$ mode conversion coefficient during electron beam injection in the switch Fig. 1. In a compressor with a new switch, the energy is accumulated on TE_{02} mode and extracted on TE_{01} mode. The switch consists of the taper (4) in which modes are converted ($TE_{02} \rightarrow TE_{01}$ and $TE_{01} \rightarrow TE_{02}$), and section (5) of the circular waveguide with its length chosen in such a way as to ensure that the TE_{01} modes reflected from cone (4) and cavity (7) sum up in phase opposition. As a result, the total coefficient of the $TE_{02} \rightarrow TE_{01}$ mode conversion in the switch amounts to 2–3%. Switch cavity (7) is formed by diaphragm (6), a section of the cylindrical waveguide and output diaphragm (9), which acts as the anode. Sharp-edge explosive emission cathode (8) is located behind the diaphragm. Note that the phase of the signal reflected from the switch cavity is significantly dependent on whether the cavity is in or out of resonance. For example, if one brings resonator (7), which was initially tuned to resonance, out of it, the phase of the signal reflected from the cavity changes by ~180°, and the TE_{01} modes reflected from conical taper (4) and resonator (7) start summing up in phase. In this case, the $TE_{02} \rightarrow TE_{01}$ conversion coefficient increases up to ~40–90% (depending on incline of taper 4). As a result, the microwave energy stored in the compressor at the TE_{02} mode is emitted from it into the TE_{01} mode.

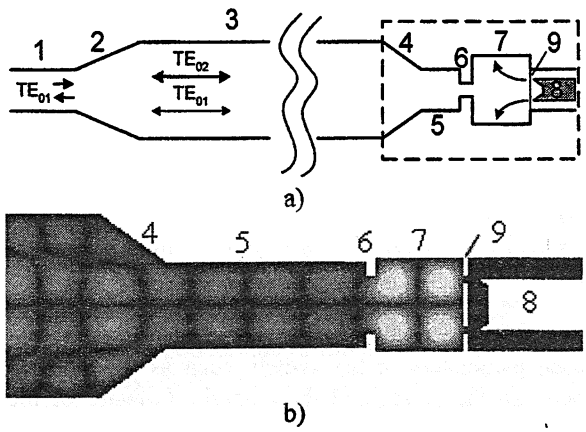

Fig. 1. Schematic diagram of the single-channel compressor with new switch: 1 – input TE_{01} mode waveguide, 2 – taper, 3 – cylindrical waveguide cavity, 4 – conical taper, 5 – waveguide section, 6 – diaphragm, 7 – switch resonator, 8 – cathode, 9 – anode (special diaphragm); (b) Instantaneous distribution of the amplitude of the electric field in the storage resonator and the switch

The schematic diagram of a microwave compressor with new switch at a frequency of 11.424 GHz is illustrated in Fig. 2. The compressor was excited by using a magnicon [6] at the (0.5-8)-megawatt level of power. Each of the compressor channels was a single-channel compressor with the switch employing electron beam triggering, Fig.1. The storing resonator was formed by conical taper, a cylindrical waveguide 130 cm long and 80 mm in diameter, and the switch that has been described above. In order to decouple the magnicon (2) from the reflected signal, the single-mode 3-dB directional coupler (5) was used. The microwave power fed into branch I was divided in two in branches III and IV. In the energy storage regime the power reflected from the resonators into branches III and IV was added in the output branch, II. In this case no microwave power entered branch I (the electromagnetic waves reflected from each compressor channel were added with opposite phases in this

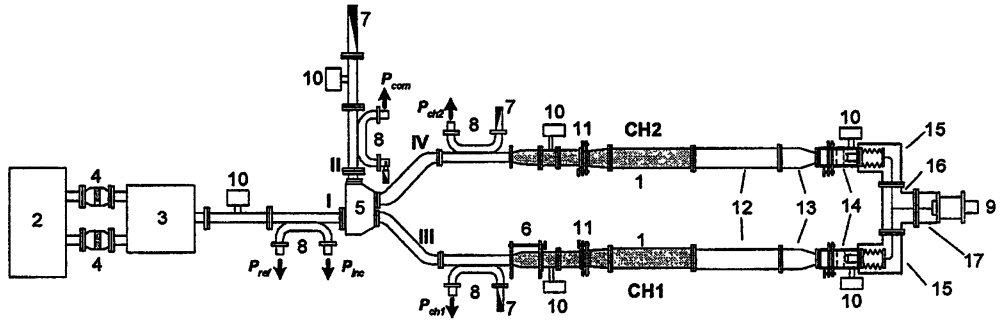

Fig. 2. Schematic diagram of the experimental set-up for tests of two-channel microwave compressor with switches employing electron beam triggering: (1) single-channel of the compressor; (2) magnicon; (3) combiner; (4) output window; (5) single-mode 3-dB hybrid coupler; (6) phase shifter; (7) matched load; (8) 55.5-dB directional coupler; (9) high-voltage pulser; (10) ion pump; (12) section of cylindrical waveguide, (13) cone taper, (14) switch, (15), (16), (17) screen.

branch). The phase difference $\Delta\varphi = 0$ required for division of the input power of the magnicon in two between branches III and IV of the single-mode 3-dB directional coupler was set by using the phase shifter (6).

The compressor was pumped out by ion pumps (10) down to the pressure of $(3\text{-}5)\cdot10^{-7}$ Torr. The compressor was switched from the regime of microwave energy storage into the regime of its output by means of electrically controlled switches employing electron beam triggering. The electron beam was produced simultaneously in the switches of the both channels by one and the same high-voltage pulse generator (4). A high-voltage pulse with amplitude of 100 kV and FWHM of 100 ns was fed simultaneously to the both cathodes of compressor.

The experiments showed that the parameters of the compressed pulse depended significantly on the used parameters of the switch, such as the distance between the anode and the cathode, Q-factor of the switch cavity, and the inclination angle of the switch horn, at which the $TE_{01} \rightarrow TE_{02}$ mode conversion occurs. Therefore, these parameters were varied during the experiments in order to optimize the operation of the compressor.

The experiments demonstrated that as one passes over from the horn with a transformation ratio of 40% to the horn with a transformation ratio of 90%, the power gain increased by more than two times. As the distance between the anode and the cathode decreased from 3.8 mm to 1.3 mm, the stability of operation of the both channels increased and a higher power gain was achieved. However, the further decrease in the size of this gap to 0.9–1 mm started to shortening of the compressed pulse by 4–5 ns due to faster bridging of the gap by the cathode plasma. Moreover, when the both channels of the compressor operated simultaneously, the decrease in the beam current occurred in each switch, which led to incomplete removal of the energy from the compressor.

The oscillogram of the pulse with the best parameters is shown on Fig. 3.

The two-channel compressor with new switches was tested at a high power level and a frequency of 11.424 GHz. The compressed pulses obtained for the incident power in the range 1.5–7 MW had the power of 25–90 MW, duration of 25–35 ns, and the power gain of 12.5–16.

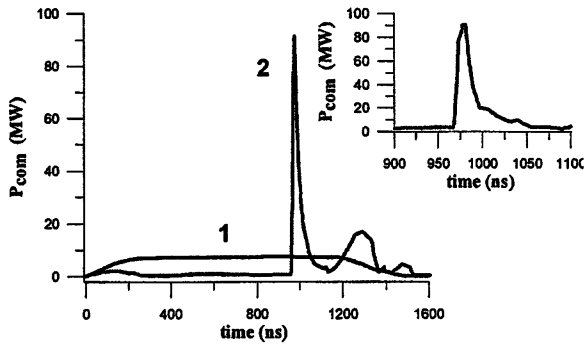

Fig. 3. Oscillogram traces of the incident (1) and the compressed pulse (2). Power of the compressed pulse – 90 MW, compression ratio – 12.5, power of the incident pulse – 7.4 MW

References

1. *Vikharev A.L., Gorbachev A.M., Ivanov O.A., Isaev V.A., Kuzikov S.V., Lobaev M.A., Hirshfield J.L., Gold S.H., Kinkead A.K.* High power active pulse compressor using plasma switches // Phys. Rev. ST AB 2009. V. 12, 062003

2. *Tantawi S.G., Nantista C.D., et. al.* High-power multimode X-band rf pulse compression system for future linear colliders // Phys. Rev. ST AB 2005, V. 8, 042002

3. *Ivanov O.A., Vikharev A.A., Gorbachev A.M., Isaev V.A., Lobaev M.A., Vikharev A.L., et. al.* Active quasioptical Ka-band RF pulse compressor switched by diffraction grating // Phys. Rev. ST AB 2009. V. 12, 093501

4. *R.A. Alvarez, D. P. Byrne, R. M. Johnson* Some properties of microwave resonant cavities relevant to pulse-compression power amplification // Rev. Sci. Instrum. 1986. V. 57, P. 2475.

5. *Ivanov O.A., Isaev V.A., Lobaev M.A., Vikharev A.L., Hirshfield J.L.* A resonance switch employing an explosive-emission cathode for high-power RF pulse compressors // Applied Physics Letters. 2010. V. 97, 031501

6. *Gold S.H., Nezhevenko O.A., Yakovlev V.P., et. al.* Status report on the 11.424 GHz magnicon amplifier // *High Energy Density Microwaves*, edited by R. M. Phillips. AIP Conference Proceedings 474, New York: American Institute of Physics, 1999. P. 179.

Generation of Multi-megawatt Terahertz Pulses Based on Superradiance of Picosecond Electron Bunches

N. S. Ginzburg[1], I. V. Zotova[1], A. M. Malkin[1], A. S. Sergeev[1]

[1]Institute of Applied Physics RAS, Nizhny Novgorod, Russia, ginzburg@appl.sci-nnov.ru

Recently significant progress has been achieved in generation of ultrashort electromagnetic pulses in centimeter and millimeter waveband based on superradiance (SR) of high-current electron bunches [1]. Generated pulses are characterized by record (gigawatt) peak power. As it was shown theoretically and experimentally at particle energies ~ 300 keV, current ~ 1 kA and the bunch durations ~ 1 ns the most effective mechanism of SR pulses generation is the Cherenkov one, realized in a periodic slow-wave structure.

The advancement of SR sources further into short wave ranges can be obtained by using the emission of electron bunches moving in the undulator field. In this case the particles energy should be increased up to 4-5 MeV and the bunch duration should be about several picoseconds. The bunches formed by photo-injection guns possess the necessary characteristics [2]. In this paper under assumption that the electron bunch propagates in a planar waveguide a theoretical analysis and KARAT PIC code simulations of above process were performed. In both approaches we analysis SR effects in the co-moving with electrons reference frame K'. In particular this, allows to simplify the numerical simulation procedure significantly, because at relativistic factor values $\gamma \sim 10$ the length of undulator of about several meters according to Lorentz transformations turns into several tens of centimeters, whereas the length of picosecond electron bunch in the rest reference frame stretches up to several centimeters. Besides the radiated wavelength transforms from the submillimeter to millimeter range. Proportionality of all scales, including the transverse size of the bunch, allows us to simulate the processes without using significant computational resources, finding then the parameters of radiated pulses in the lab frame using again the relativistic transformations.

We consider here a two-dimensional model assuming that an electron bunch with a length of l moves in a planar waveguide with the gap between plates b_0. Electrons oscillate in a planar undulator field with vector potential:

$$\vec{A}(z,t) = \mathrm{Re}\left(\vec{x}_0 A_u \exp[ih_u z]\right), \qquad (1)$$

where $d = 2\pi/h_u$ is the undulator period, A_u is an amplitude. Further analysis will be conducted in the co-moving reference frame where the undulator field transforms into propagating pump wave

$$\vec{A}'(z',t') = \mathrm{Re}\left(\vec{x}_0 A'_u \exp[i\omega' t + ih' z]\right), \qquad (2)$$

where $\omega' = \gamma V_{\|} h_u$, $h' = \gamma h_u$. In K' the electron bunch (layer) of finite length l' can be divided into a set of macroparticles differing by initial location z'_0. The particles interacting via ponderomotive force that can be presented in the form [3]:

$$F'_{pond}(z') = \frac{2\pi e^2 \rho' c \alpha_i^2 \varepsilon}{\omega' b_0} f_{pond}\left(k(z' - z'(z'_0))\right)$$
$$f_{pond}(X) = \mu_+ \cos(\mu_+ X), \; X > 0 \qquad , \qquad (3)$$
$$f_{pond}(X) = \mu_- \cos(\mu_- X), \; X < 0$$

where $\mu_{\pm} = (h' \pm k)/k$, $k = \omega'/c$ This force is sign-variable and attracting near the particle. Thus the dynamics of particles can be described by the following equations:

$$\frac{dZ}{d\tau} = \bar{p}, \; \frac{d\bar{p}}{d\tau} = \frac{\omega_p^2 \alpha_i^2 \varepsilon}{2\omega^2 b_0} \int_0^L f_{pond}\left(Z(Z_0) - Z(\bar{Z}_0)\right) d\bar{Z}_0, \qquad (4)$$

where $Z = \omega' z'/c$, $L = \omega' l'/c$, $\bar{p} = p'/mc$, $\tau = \omega' t'$, $\omega_p = \sqrt{4\pi e^2 \rho'/m}$, $\alpha_i = eA'_u/mc^2$. At initial moment all of the electrons are uniformly distributed over the longitudinal coordinate in the interval $[0, B]$. Normalized amplitudes of the component of scattered field which is radiated in the direction which is opposite to direction of pump wave are given by

$$\left|\alpha_s^+\right| = \frac{i\omega_p^2 \alpha_i}{2\omega^2} \left| \int_0^B \exp\left(2iZ(\bar{Z}_0)\right) d\bar{Z}_0 \right|. \qquad (5)$$

Simulations of Eqs.(4) shows that due to attracting feature of pondermotive force (3) the bunching of particles developed (Fig.1a). Correspondingly in some instant of time (Fig.1b) a coherent summation of fields radiated by most of particles takes place and the generated field constitutes a short SR pulse. Initial level of signals corresponds to the level of radiation of the bunch without modulation and in fact is determined by the front edges of electron pulse. This radiation in the case under consideration is a seed initiating the further development of SR process.

We simulated the radiation of the electron bunch with particles energy of 5 MeV, with duration in the lab frame ~10 ps, charge of 50 nC/cm and the transverse size ε~2 mm oscillating in the field of undulator with period of 4 cm and field amplitude of 1 kOe. The radiation was assumed to take place in a planar waveguide with the gap between plates of 3 mm. In the rest frame K' the length of the bunch was 4 cm. The undulator field transforms into a wave with a wavelength of 4 mm and the power density of 4 GW/cm.

As follows from Fig.1b the normalized radiation power is 150 and the pulse duration is ~2, which corresponds to the power density of 9.5 MW/cm and duration of 100 ps. By means of Lorentz transformations we obtain the power density of the radiation of the forward propagating wave in the lab frame of 3.8 GW/cm. Radiation frequency is 1.5 THz and the pulse duration decreases down to 10 ps. Note that in the rest

frame the pump pulse was about 25 wavelength. In the lab frame it corresponds to 25 period undulator with a total length of about 1 m.

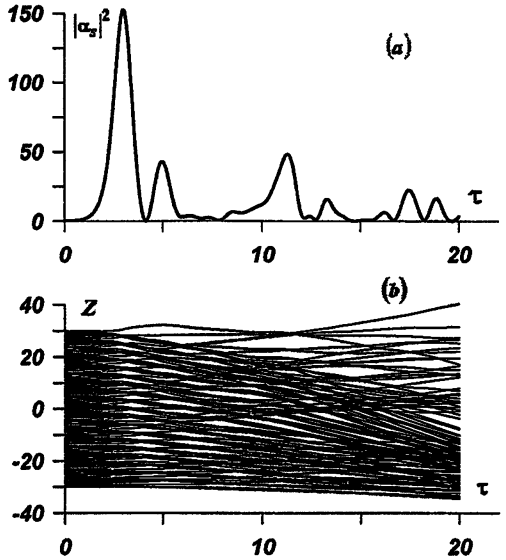

Fig. 1. Formation of SR pulse (a) and electrons bunching (b) (average model). $L = 60$.

The analysis of SR process within the model that employed the averaged ponderomotive force approach does not account for a number of important factors, including Coulomb interaction of the particles. This consideration we supplemented by a direct PIC simulation in the rest frame. Initial geometry of a bunch in the planar waveguide is presented in Fig. 2a This figure also shows the eqiupotential lines of the electrostatic field of the bunch. Under conditions when in the rest frame the length of the bunch is sufficiently larger than its width and the distance between waveguide plates, the intrinsic field of the bunch has mainly transverse E_x component. Longitudinal E_z component is significant only near the bunch edges. Thus the presence of metallic plates leads to strong reduction of the space charge forces which encumbers the bunching and besides leads to entirely expansion of the bunch. Note that for focusing of particles in the transverse direction a small longitudinal magnetic field H=10 kOe was used. Neglecting the transverse inhomogeneity of the undulator field this field was approximated by a TEM wave. Fig. 3 shows the SR pulse having in the rest frame power density 2MW/cm and duration of 100 ps. After transformation to the lab frame the power of the forward wave increases in $2\gamma^2$=400 times reaching 800 MW/cm and the pulse duration decreases γ=10 times down to 10 ps. Longitudinal bunching in the SR process with a period of 2 mm is illustrated by Fig. 2b. It is interesting to note that the time of development of the process in the rest frame is about 200-300, still the bunch moving with a velocity close to the speed of light passes the distance of about 1 m. Thus the simulation conducted is an example of unconventional use of relativity theory in applied problems.

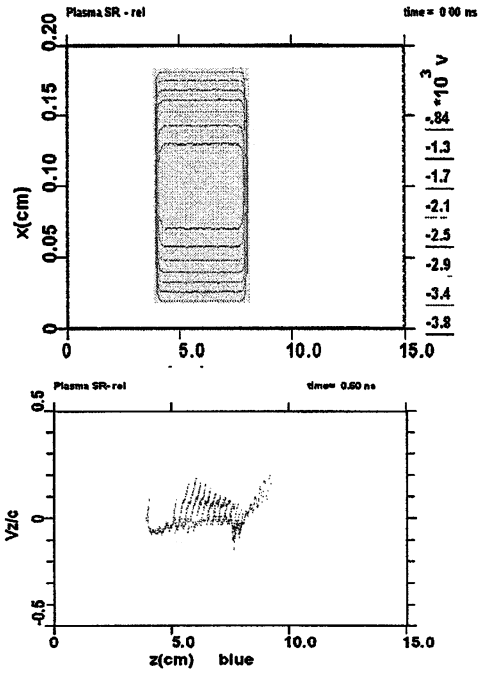

Fig. 2. Initial position of electron bunch and equipotential lines (a). Phase plane demonstrated electron bunching at the moment 0.6 ns (b).

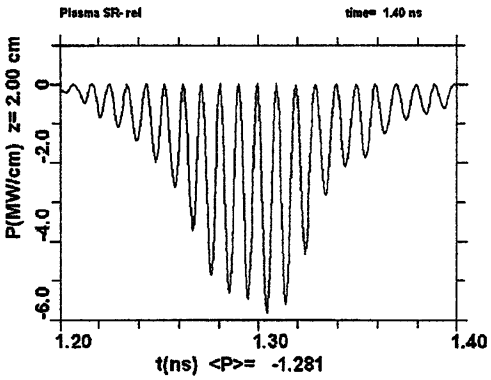

Fig. 3. SR pulse in PIC simulations

References

1. *Korovin S.D., Eltchaninov A.A., Rostov V.V., et al* Generation of Cherenkov superradiance pulses with a peak power exceeding the power of driving short electron beam // Phys. Rev. E 2006. V. 74, P. 016501-016509.

2. *Kurennoy S.S., Schrage D.L., Wood R.L., Young L.M., Schultheiss T., Christina V., Rathke J.* Development of photoinjector RF cavity for high-power CW FEL // Nucl. Instr. & Meth. in Phys. Res. A 2004. V.528, Iss 1-2, P. 392-396.

3. *Ginzburg N.S., Sergeev A.S.* Superradiance of electron bunch moving in the periodic magnetic field // Sov. JETP Lett. 1991. V.54, P.445-448.

Three-Dimensional Numerical Studies of Non-Uniform Emission in Magnetron Injection Guns

A.V. Malygin[1], I.Gr. Pagonakis[1], S. Illy[1], K.A. Avramides[3], B. Piosczyk[1], S. Kern[1], M. Thumm[1,2]

Karlsruhe Institute of Technology, Association EURATOM-KIT
[1]Institut für Hochleistungsimpuls- und Mikrowellentechnik (IHM)
[2]Institut für Hochfrequenztechnik und Elektronik (IHE) D-76131 Karlsruhe, Germany
[3]SECE, National Technical University of Athens, Zographou GR-15773, Greece

In gyrotron devices, a magnetron injection gun is used for the generation of the helical electron beam. Ideally, the gun emits a hollow electron beam with azimuthally uniform distribution. In a real gun, this is not always the case, as is seen in experimental results [1]. In normal situations, the primary reasons for the inhomogeneous emission of the electron beam are the azimuthal temperature variation and the non-uniform emissive surface around the emitter. The question is how the azimuthally non-uniform emission from the cathode affects the beam quality. To study this problem two gyrotron guns have been simulated with the use of the three-dimensional, electrostatic and parallel code *Ariadne* [2]. In order to study how the degraded beam affects the mode coupling and the stability of the wave-particle interaction in the cavity we initiated numerical studies using the non-stationary, self-consistent multi-mode cavity code *Euridice* [3].

Gun Simulation

The non-uniform emission effects on the beam properties of a low-power 15 kW, 28 GHz experimental gyrotron gun, designed at KIT, and the refurbished first prototype EU 2 MW, 170 GHz ITER coaxial gyrotron gun [4] have been studied. The non-uniform emission was analytically defined by the current density equation $j(r, \varphi)=j_0 (1 + \varepsilon \cos(n\varphi))$, where $j_0=I_b/A_e$ is the nominal current density, I_b is the total beam current, A_e is the emitter ring surface area, while ε and n, are the amplitude and the harmonic number of the non-uniformity, respectively.

Non-uniform emission leads to the degradation of the beam quality which could affect the gyrotron operation. Firstly, as is shown in Fig. 1, for the low-power gyrotron, and in Fig. 2 for the high-power gyrotron, a deformation of the electron beam takes place. The mechanism of that deformation is based on the radial drift of the electrons due the azimuthal component of the electric field which comes by the non-azimuthal space charge density [5].

This deformation could increase the competition between modes which are in close vicinity to the main mode in the given frequency range. In addition, as is shown in Fig. 3 and Fig. 4, the pitch angle distribution becomes wider under the influence of the non-azimuthal space charge density. Therefore, a significant number of electrons have a high alpha value (up to 2 in the low power gyrotron and up to 1.8 in the high power gyrotron). This could lead to an increase of the trapped charge in the area between the cathode and the resonator which could initiate instabilities in the electron beam [6].

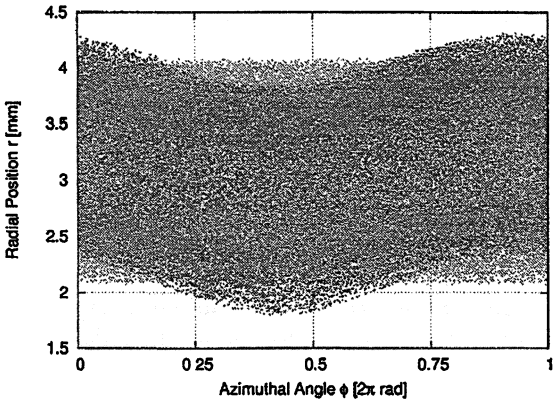

Fig. 1. Radial electron position versus azimuthal position at the cavity for uniform (green) and non-uniform (red) emission with ε=0.5 and n=1 for a low-power 28 GHz gyrotron.

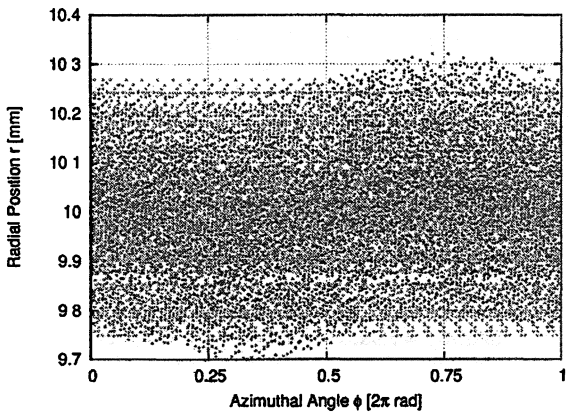

Fig. 2. Radial electron position versus azimuthal position at the cavity for uniform (green) and non-uniform (red) emission with ε=0.5 and n=1 for the high-power 170 GHz coaxial gyrotron.

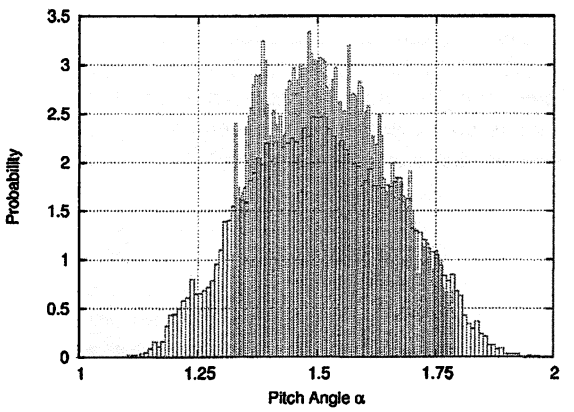

Fig. 3. Pitch-angle distribution of the electron beam at the cavity for uniform (green) and non-uniform (red) emission with ε=0.5 and n=1 for the low-power gyrotron.

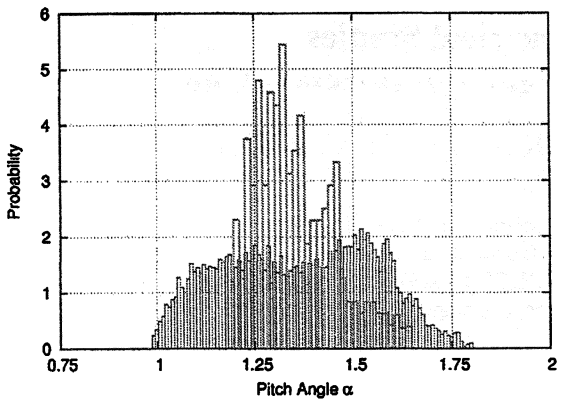

Fig. 4. Pitch-angle distribution of the electron beam at the cavity for uniform (green) and non-uniform (red) emission with ε=0.5 and n=1 for the high-power gyrotron.

Cavity Simulation

In order to check possible effects on the cavity operation, we initiated numerical studies using the non-stationary, self-consistent multi-mode cavity code *Euridice*. The initial electron beam properties at the entrance of the cavity are specified by the results of the gun simulation using the *Ariadne* code.

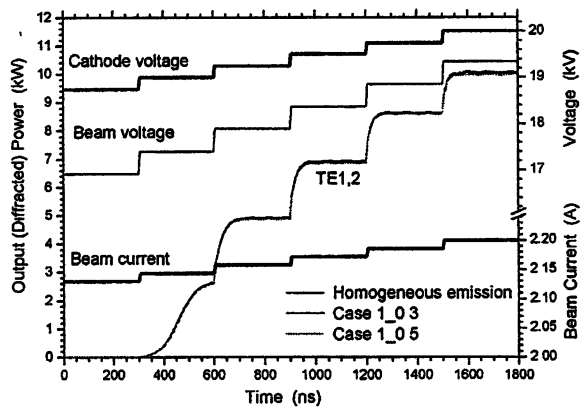

Fig. 5. Start-up scenario for the low power gyrotron for the uniform (black) and two non-uniform cases, with ε=0.3 and n=1 (red) and ε=0.5 and n=1 (green)

Fig. 5 presents a start-up scenario obtained from *Euridice* simulations for the low-power 28 GHz gyrotron. As one can see from this figure there is no significant difference between the uniform and the non-uniform case. Possible reason for the small influence of the non-uniform emission could be that all neighboring modes have a much lower coupling coefficient compare to the operating mode and due to that there is no excitation of the neighboring modes. In spite of the fact that the distribution functions for pitch-angle and for the guiding centers spread becomes wider, the average parameters are still almost the same and this keeps the efficiency almost the same for the uniform and non-uniform case. The investigation of the effect of the non-uniform emission on the cavity of the high-power gyrotron is in progress.

Conclusions

Non-uniform electron emission leads to similar effects in both gyrotrons. The beam width is slightly increased, which could lead to the excitation of one or more spurious modes. Additionally, the existence of an electron population with high alpha could contribute to the generation of a beam halo by magnetically trapped electrons. This could lead to enhanced beam instabilities and may limit the maximum allowed pitch-angle of the electron beam.

Acknowledgments

This work was partly supported by Fusion for Energy under the grant contract No. F4E-2009-GRT-49-01 and within the European Gyrotron Consortium (EGYC). The views and opinions expressed herein reflect only the author's views. Fusion for Energy is not liable for any use that may be made of the information contained therein. EGYC is a collaboration among CRPP, Switzerland; KIT, Germany; HELLAS, Greece; CNR, Italy

References

1. *C.D. Marchewka et al.*, Non-uniform cathode emission studies of a MIG Gun, Joint 30th Int. Conf. Infrared Millimeter Waves and 13th Int. Conf. THz Electronics, Conference Digest, Sept. 19-23 2005, Williamsburg, USA.

2. *I. Gr. Pagonakis and J.L Vomvoridis*, The self-consistent 3D trajectory electrostatic code Ariadne for gyrotron beam tunne simulation, Joint 29th Int. Conf. Infrared Millimeter Waves and 12th Int. Conf. THz Electronics, Conference Digest, 27 Sept.- 1 Oct. 2004, Karlsrihe, Germany.

3. *K.A. Avramides, et al.*, EURIDICE, National Technical University of Athens, unpublished, 2008.

4. *J.-P. Hogge et al.*, "First experimental results from the European Union 2-MW coaxial cavity ITER gyrotron prototype", *Fusion Science and Technology*, 55, Feb. 2009, pp. 204-212.

5. *I. Gr. Pagonakis, J.L. Vomvoridis*, Evolution of nonuniform electron beam in a cylindrical beam tunnel, IEEE Transaction on Plasma Science, vol. 32, pp 890-898, 2004.

6. *V.N. Manuilov, S.A. Polushkina*, Behavior of helical electron beams in gyrotrons with high pitch factors, Radiophysics and Quantum Electronics, vol. 52, pp. 714-721, 2009.

Dynamic Processes in the Helical Electron Beams with High Pitch-Factor

V.N. Manuilov

Nizhny Novgorod State University, N.Novgorod, Russia, manuilov@rf.unn.ru

The data of numerical simulation of gyrotron magnetron-injection guns (MIGs) forming Helical Electron Beams (HEBs) with high pitch-factor are presented. Different beam topology as well as gyrotron MIGs of different wavelengths (λ=12 mm and 3.5 mm) are considered. The HEBs parameters for the regimes with various coefficients of reflection from the magnetic mirror are found.

Introduction

HEBs are used in gyrotrons as the energy source of radiation. The efficiency of gyrotrons strongly depends on the achievable level of the pitch-factor $g=v_{\perp 0}/v_{\parallel 0}$. Here $v_{\perp 0}$, $v_{\parallel 0}$ are the mean electron velocities of rotational and longitudinal motion in the working space. HEBs are formed by magnetron-injection guns (MIGs) [1], which are characterized by the sufficient oscillatory velocity spread $\delta v_{\perp}$ (about 20-30%, [1]) of electrons and trapped configuration of the magnetic field distribution (Fig. 1, 2). It makes the essential part of particles reflect from the magnetic mirror even for moderate values of the pitch-factor, $g \approx 1.3 - 1.5$ [1] and causes in the beam such dynamic processes as accumulation of the space charge in the trap, additional depression of the emitter electric field, development of the beam instabilities including space charge and potential oscillations and so on. So, studying the mentioned above processes allows to make it possible to predict beam parameters with more accuracy and might specify the ways to improve the beam quality and finally the gyrotron efficiency.

Below the process of establishing of HEBs parameters (oscillatory velocity distributions, time dependencies of locked charge, passing to the cavity current and some others) are investigated numerically. MIGs with different beam topology (regular intersecting, boundary and laminar beams) are studied. Corresponding angles φ between the emitter and the magnetic field line are φ=12°, 18° and 26°. Comparison of the dynamic processes in the formation systems of the centimeter and millimeter wavelengths gyrotrons is performed. The regimes with high "cold" (calculated without taking into account the space charge forces) pitch-factor $g_0 \geq 2$ are investigated.

The numerical dynamic model based on the PIC-method takes into account two-dimensional magnetic- and electric field distributions including the own beam space charge fields and the action of the secondary emission from cathode caused by the reflected from the magnetic mirror electrons bombarding cathode surface [1, 2]. The combined action of such factors as thermal velocities and emitter roughness is also included into the numerical model.

Results of Simulation

Two typical MIGs of centimeter (Fig.1) and millimeter (Fig.2) wavelengths gyrotrons are investigated numerically. The first one operates in the regime close to the critical one, while the second uses strongly overcritical regime. The value of the beam current I was assigned such as to ensure that $t_f=I/I_L \approx 0.1$ (I_L is the Langmuir current of the gun).

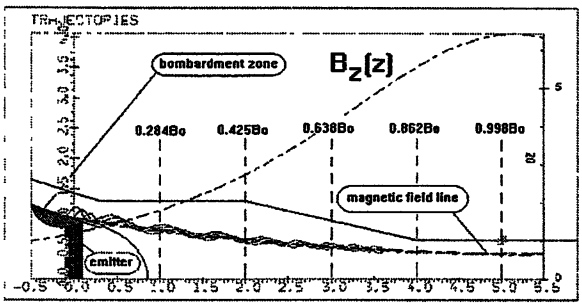

Fig. 1. MIG of the centimeter wavelength gyrotron. The ratio of the current magnetic field intensity to the operating magnetic field B_0 in different planes is specified.

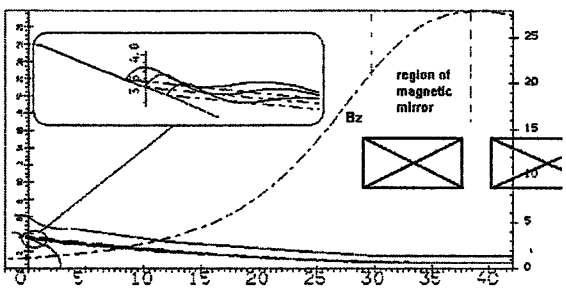

Fig. 2. MIG of the millimeter wavelength gyrotron. The axial magnetic field distribution Bz and the electron trajectories near the emitter are shown.

The accumulation of locked space charge Q_r leads to significant depression of the pitch-factor calculated from dynamic model in comparison with the data of static one, which neglects the reflected electrons. Moreover, dynamic model shows that if g_0 is high enough, the further increasing of pitch-factor is not possible (Fig.3). In such regimes the accumulation of the space charge in the trap is so strong that caused by this factor additional depression of the emitter electric field totally compensates the attempts to increase pitch-factor by increasing the anode potential or magnetic compression ratio. Big deviation between results of static and dynamic codes occurs when the reflection coefficient exceeds some critical value $KR>KRmax\approx 0.05$. In such regimes the strong oscillations of the locked charge as well as potential inside the beam are developed , and not only g value, but also velocity spread becomes close to constant and does not depend on the cold pitch-factor because the magnetic mirror does not let pass the "bad" electrons to the cavity.

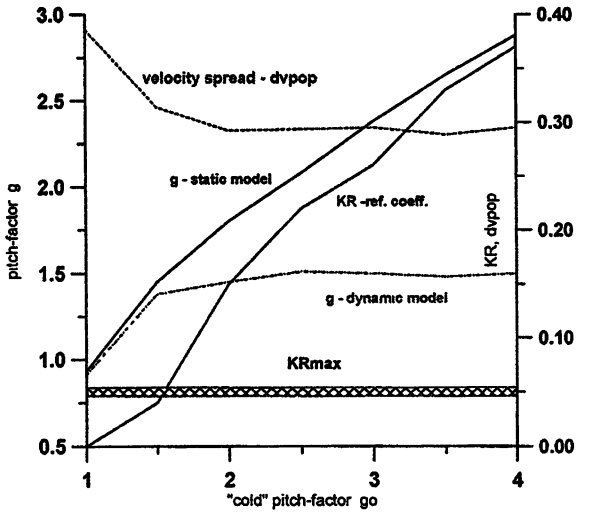

Fig. 3. Dependencies of the pitch-factor, velocity spread and reflection coefficient form the magnetic mirror for MIG of the centimeter wavelength gyrotron with regular intersecting HEB as functions of cold pitch-factor.

The quality of HEB can be improved by turning to the boundary or laminar beam. In such case the bombardment area of the cathode and locked into the trap space charge are decreased essentially (see tab. 1).

Table1. Value of the normalized locked charge Q_r/Q_0 in HEBs with different topology. MIGs of centimeter wave length gyrotrons. Q_0 is the charge of the primary (coming to the cavity) beam.

g_0	Regular intersecting beam	Boundary beam	Laminar beam
2.0	1.2	1.0	0.7
4.0	2.8	2.3	2.4

Increasing of the angle φ eliminates the oscillations of space charge and potential at least till the values $g_0 \leq 3.0$ and grows up the maximum achievable value of the operating pitch-factor g_{max} from 1.48 (φ=12°) to 1.65 (φ=26°).

In millimeter wave region gyrotrons the qualitative picture of the HEBs behavior for high pitch-factors is close to the features observed in centimeter wavelengths gyrotrons. At the same time some parameters differs essentially. In particular the starting value of the ratio Q_r/Q_0 when the intense space charge oscillations are developed, as well as the value of the corresponding operating pitch-factor g becomes essentially lower. Ratio Q_r/Q_0 decreases from 0.8-1.0 in MIG Fig.1 to 0.4-0.5 for the system Fig. 2 (see Fig. 4 and tab. 2). Corresponding value of g reduces from 1.5-1.6 to 1.3 approximately even for gyrotrons with the wavelength $\lambda \approx 3$ mm. The value of g_{max} also drops down to 1.3-1.35 even for laminar beam. The region of intense potential oscillations becomes essentially shorter and located mainly near the area of the magnetic mirror. Possible reason for the mentioned differences is essentially longer distance L between the emitter and the cavity and higher magnetic compression ratio α. In centimeter wavelength gyrotrons L corresponds to 20-25 periods of the cyclotron frequency approximately ($\alpha \approx 5$), while in millimeter wave region it grows up to some hundreds ($\alpha \approx 25$-30 or even more) . Such big distance (and passing time) is enough for essential part of electrons to get additional energy during the longitudinal oscillations even when the operating pitch-factor g is rather moderate. Then such particles can bombard the cathode and initiate the intense secondary emission, which is the main factor in the development of the beam instability.

Table 2. Value of the normalized locked charge Q_r/Q_0 in MIGs Fig. 2. Figures in brackets present g values in the operating regime calculated from the static model [1].

g_0	Regular intersecting beam	Boundary beam	Boundary beam with shaped cathode
1.75 (1.32)	0.42	0.15	0.05
2.15 (1.52)	0.60	0.35	0.14
3.22 (1.84)	0.85	0.65	0.35

The space charge oscillations can be suppressed also in MIGs with the special shape of the cathode behind the emitter. Here the angle of inclination to the axis is higher then on the emitter. It increases the retarding component E_z of the electric field and makes it more difficult for reflected electrons to bombard the zone of the cathode located in smaller magnetic field. As a result, the locked charge becomes essentially smaller, especially for moderate values of the operating pitch factor (see tab. 2 and Fig. 4).

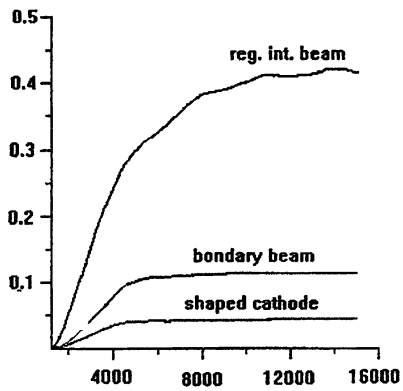

Fig. 4. Time dependence of the normalized locked charge Q_r/Q_0 for MIG Fig.2, g=1.32.

References

1. *P.V. Krivosheev, V.K. Lygin, V.N. Manuilov, Sh.E. Tsimring.* Numerical Simulation Models of Focussing Systems of Intense Gyrotron Helical electron Beams, *Int. J. of Infrared and MM waves*, 2001. V. 22, no. 8, P. 1119-1146.

2. *V.N. Manuilov.* Space Charge Oscillations in Gyrotron Magnetron-Injection Guns with High Pitch-Factor. Book of Abstract of the 10-th International Vacuum Electronic conference (IVEC2009), Rome, Italy, 28-30 April 2009, pp. 90-91.

Low Voltage Non-Adiabatic Electron Gun for Technological Gyrotron

A.L. Goldenberg[1], M.Yu. Glyavin[1], V.N. Manuilov[2], M.V. Morozkin[1]

[1]Institute of Applied Physics, N. Novgorod, Russia, glyavin@appl.sci-nnov.ru
[2]Nizhny Novgorod State University, N. Novgorod, Russia, manuilov@rf.unn.ru

Technological gyrotrons with moderate level of output power (about 10 kW) and operating frequency 24-30 GHz are used in many applications such as ceramic sintering, growing of diamond discs, sources of multi-charge ions, and so on. Gyrotron based technological complexes have been developed at IAP RAS/GYCOM [1]. Typical value of accelerating voltage U_0 in these devises is about 15-30 kV. But for several kW output power level, essentially lower, "quasi-kitchen" value of U_0 close to 3-5 kV is preferable. It simplifies the scheme of the system and makes it smaller and less heavy, significantly reduces the x-ray radiation from the collector and, after all, makes it much cheaper. Simple estimations show that $U_0 = 5$ kV and beam current $I_0 = 3$ A is enough to get the output power level of 3-5 kW.

In technological gyrotrons, as well as in the other devices of this type, the magnetron-injection guns (MIGs) are usually used to form the helical electrons beams (HEBs) with suitable beam quality. But simple adiabatic estimations show that low accelerating potential ($U_0 = 5$ kV) together with rather low value of operating magnetic field $B_0 \approx 0.5$T, typical for the second harmonic operation (needed to reduce the energy consumption at the solenoid), leads to large sizes of anode and cathode and, more important, to the non-adiabatic behavior of the beam near emitter. It is close to the case of injection of the electron beam with big angle $\varphi \approx 70$-$80°$ with respect to the magnetic field line. Besides, well known disadvantages of MIGs are strong influence of the emitter roughness on the velocity spread and uncontrolled increase of the emitter current caused by the electrons reflected from the magnetic mirror. These factors limit the maximum achievable value of pitch-factor considerably. The last two features can be eliminated if we switch from the typical for MIGs temperature limited regime to the space charge limited regime. So, for low-voltage technological gyrotrons non-adiabatic formation systems (NAFS) operated in the space charge limited regime are preferable.

Below the results of numerical optimization and experimental tests of the low-voltage NAFS are presented. The schematic view of the MIG is shown in Fig. 1 and photo of the MIG is presented in Fig. 2. The injector of the electron gun consists of a concave annular cathode, part of which is covered with the emitting layer, and two anodes – internal and external. The magnetic field in the gun region is the scattering field of the main solenoid, which forms the magnetic field in the cavity region. For correction the magnetic field in the gun region a relatively low-power additional solenoid is used. In the considered gun, the influence of nonuniformities of the emitter electric field and the spatial charge field is excluded or considerably decreased. Firstly, the gun operates in the mode of total spatial charge, and, therefore, the electric field on the surface of a virtual cathode in such a gun is zero, and so small-scale inhomogeneities of the surface and the emissive properties of the cathode are not important for the beam formation. Secondly, the anodes of the injector gun are located both outside and inside the electron-motion area, which makes it possible to exclude or drastically decrease the difference of the electric field on the inner and outer boundaries of the electron beam. All this factors reduces the velocity spread in comparison with traditional magnetron-injection gun and give a chance increase transverse energy of an electron beam.

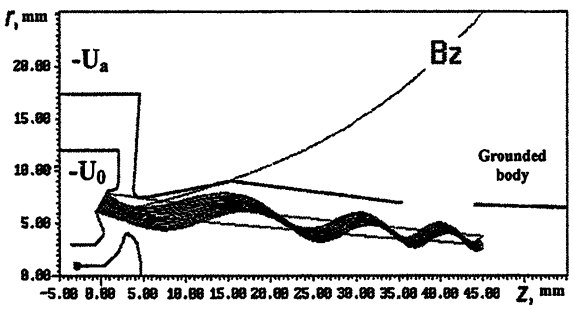

Fig. 1. MIG geometry, electron beam trajectory and axial magnetic field distribution *Bz*.

The gun is aimed to be used in the 28GHz CW gyrotron with the output power of 3-5 kW ($U_0 = 5$ kV, $I_0 = 3$ A, calculated efficiency without CPD about 20%). It is necessary to note, that the specific feature of the gun is very high value of the perveance 10^{-5}A/V$^{3/2}$ that is at least in order of magnitude higher that in traditional MIGs.

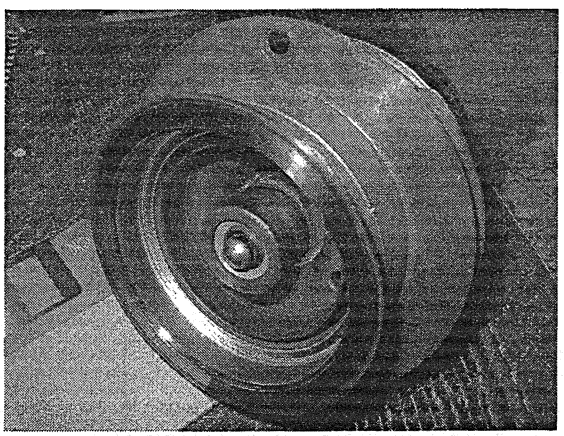

Fig. 2. General view of the developed non-adiabatic MIG

Numerical simulation of the gun was performed within two-dimensional static model using the code EPOS [2]. The value of cathode current was found directly from the condition $E_c = 0$. Here E_c is the value of the electric field on the emitter surface.

The optimized form of the electrodes (Fig.1) allows intersect the reflected electrons by the inner and outer anodes. According to calculations [2] the gun provides moderate value of the oscillatory velocity spread $\delta v_\perp$=14% for high HEB pitch factor g = 1.8 [3].

The numerical analysis has shown the possibility to use the NAFS also for high power nuclear fusion gyrotrons. The obtained velocity spread $\delta v_\perp \leq 14\%$ while the pitch factor g = 1.8 for the gyrotron with a beam voltage 80 kV, beam current 35 A and operating frequency 170 GHz [4]. At the same time, for traditional MIGs of this frequency range gyrotrons, typical values are $g \approx 1.3$ and $\delta v_\perp \approx 30\%$.

The measurements of the beam parameters were carried out by the well known retarding potential method [5]. The modified version of an analyzer has been used. To protect overheating of the analyzer grid and target the measurements have been carried out in the scaling regime. In this regime accelerating voltage, beam current, and magnetic field were reduced according to similarity scaling relations: $U = U_0 / k$, $I = I_0 / k^{3/2}$, $B = B_0 / k^{1/2}$. The NAFS tests was made with the scaling coefficient k = 10.

Preliminary experimental investigation of the beam properties was carried out with the diode configuration of the gun. It was found that in the initial gun design the essential part of the current is intersected by the upper anode. According to experimental data and the numerical simulation, one of the possible reasons is the parasitic emission from the cathode region near the emitter. To verify it the calculation of the heat transfer inside the gun body by the QuickField™ simulation software was carried out. The calculated temperature distribution on the cathode is shown in Fig. 3. Using this data the thermal isolation of the cathode parts was upgraded and additional anti-emission coating was evaporated near the emitter.

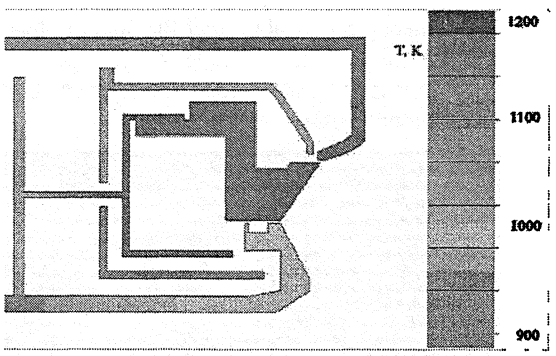

Fig. 3. Temperature distribution on the cathode

Unfortunately, these steps have not solved the problem of the high beam current intersection. The next assumption was inaccurate alignment of the electron gun. Calculations had shown the high sensitivity of the developed MIG to the positional shift of electron gun the elements (Table 1).

The gun is also sensitive to positioning in the magnetic field and, so, the required installation accuracy (including possible temperature drift) looks close to 0.1 mm. To reduce the intersection of the electron beam, the outer anode shape was slightly altered and the outer anode diameter near the end of the first trajectory step was increased. Along with that, to minimize the effects of misalignment and increase the control over the electron beam, the configuration of the electron gun was changed to the triode one. It allows decreasing of the emitter bombardment by the reflected electrons and caused by this factor secondary emission.

Table 1. Dependence of the beam parameters on the emitter shift relative to other gun elements.

Δz, mm	$\delta v_\perp$	g
0	0.22	1.8
+0.2	0.80	2.8
-0.1	0.16	1.6

After modification of the gun geometry and manufacturing technology it was possible to form the HEB with pitch-factor $g > 2$, velocity spread less than 15% and suitable (70% or more) ratio of the passing to the cavity current to the cathode one – $K = I_{cavity} / I_{cathode}$ (Fig. 4).

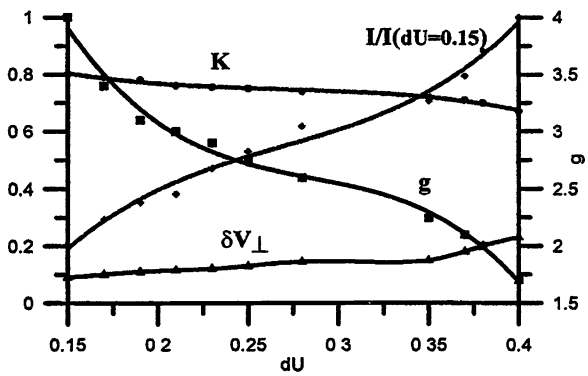

Fig. 4. Measured dependencies of the K value, pitch-factor g, velocity spread and total beam current vs. relative anode-cathode voltage $dU = (U_0 - U_a) / U_0$ in the scaling regime.

The NAFS looks suitable for both medium power gyrotrons for technological applications and high power gyrotrons for nuclear fusion. Despite the high sensitivity to the positioning accuracy, such systems may provide significantly better beam quality than traditional adiabatic MIGs.

References

1. *Bykov Yu., Eremeev, A., Glyavin, M., et al.* 24-84 GHz Gyrotron Systems for Technological Microwave Applications // IEEE Trans. on Plasma Science, 2004, V. 32, P. 67-72

2. *Krivosheev, P. V., Lygin, V. K., Manuilov, V. N., Tsimring, Sh. E.* Numerical Simulation Models of Focusing Systems of Intense Gyrotron Helical electron Beams // Int. J. of Infrared and MM waves, 2001, V. 22, P. 1119-1146.

3. *Goldenberg, A.L., Glyavin, M. Yu., .Zavolsky, N. A., Manuilov,* V. N. Technological gyrotron with low accelerating voltage // Radiophysics and Quantum Electronics, 2005, V. 48, P. 741-747

4. *Goldenberg, A. L., Manuilov, V. N., Glyavin, M. Yu.* Electron-Optical System of a High-Power Gyrotron with Nonadiabatic Electron Gun // Radiophysics and Quantum Electronics, 2005, V. 48, P. 461-465

5. *Avdoshin, E. G., Goldenberg, A. L.* Experimental investigation of the adiabatic guns of gyrotrons // Radiophysics and Quantum Electronics, 1973, V. 16, P. 1241–1246.

Conceptual Design of a High Voltage Electron Gun as a Driver of High Power Millimetre Wave Oscillators

F. Mirizzi[1], E. Di Palma[2], I. Spassovsky[2], V. Surrenti[2], G. Dattoli[2]

[1]Associazione EURATOM-ENEA sulla Fusione, C.R. Frascati, Frascati (Rome), Italy, francesco.mirizzi@enea.it
[2]ENEA C.R. Frascati, Dept. UTAPRAD-MAT, via E. Fermi 45, 00044 Frascati, Italy

The design of a high-voltage thermionic electron gun is a very challenging task, mainly because the maximum electric field at the cathode surface has to be maintained below a safety value of 10 kV/mm. In addition the gun must generate a high quality electron beam with reference to velocity and pitch ratio spreads.
With the aim of allowing the design and realization of high power millimetre wave oscillators, mainly for the needs of future experimental machines and reactors for Nuclear Fusion, the preliminary analysis and numerical study of a non-adiabatic, electrostatically pumped beam in the diode part of the gun, followed by an adiabatic compression in the drift section, has been carried out.
The results of the analysis indicate the concrete possibility of realizing an electron gun with optimum beam energy higher than 700 keV, a beam current in the 10-50 A range and a velocity spread lower than 1%. The paper reports the available encouraging results in this direction.

Introduction

Recently there were a considerable research efforts to develop high power, high frequency (millimeter and submillimiter wave) sources based on high voltage electron beams. These devices, the best known of which are the Free Electron Laser (FEL) and the Cyclotron Autoresonance Masers (CARM) are inherently high power and produce high frequencies by a Doppler-shift effect which scales differently proportional of the relativistic mass ratio γ. However the Gyrotrons for now are unbeaten leaders dominating the millimeter wave region with their simplicity, high efficiency and moderate beam energy (about 100 keV). In submmilimiter range gyrotrons suffer from need to work at the harmonic of the cyclotron frequency because of the limitations of superconducting solenoids. For being good competitors with the gyrotrons, both FEL and CARM require high quality electron beam. There is a substantial difference between FEL and CARM regarding the beam energy. The FELs, due to their nature, uses an electron beam with energy above one MeV. In contrast the CARM could operate easily with beam energy below 1 MeV. The new high voltage power supply available today make the CARM source much more competitive than FEL. The second crucial problem is the design of the high-voltage and high-current electron beam operating at long pulse duration and voltage above 500 kV.

Electron Gun Design

In the design of any power microwave device there are several issues to be considered. Starting from the available literature [1, 2, 3] the design criteria have been set up with respect to different parameter related to the diode configuration and electron beam parameters.

The desired operating frequency ($f \sim 350$ *GHz* in our case), and the beam energy of 700 keV determine the magnetic field (B_0) at the interaction region and the cathode potential.

Defined the cathode potential φ around 600 – 700 kV, we can calculate the relativistic factor:

$$\gamma_0 = 1 + \varphi / \varphi_0 \approx 1 + 2\,\varphi_{(MV)}$$

where φ_0 is the reduced electron rest energy. Accordingly to $B_0 = f(\mathrm{GHz})\gamma_0/28s$, where s is the harmonic number [3], finally with the normal Doppler shift we can adjust the desired operating frequency.

Table 1 reports the fixed values of the gun parameters. All those parameters are in agreement with the literature and set the electric field over the cathode surface less than 10 kV/mm in order to avoid the breakdown.

Table 1. The design project parameters

Anode-cathode distance$(D_a\text{-}D_g)/2$	200 mm
Magnetic field along the cavity	7 T
Pitch ratio $\alpha = v_\perp/v_{||}$	<0.5
Axial and transverse velocity spread	<1%
Electric field at the cathode surface (E_c)	<10 kV/mm

Using the commercially available code CST [4], with particle tracking package, we performed a numerical simulation of the gun configuration reported in fig. 1. The magnetic field guiding the beam was generated by an analytical axial profile computed considering two coils. The first one, the gun coil, is located at the gun part. It produces a low magnetic field of about Bc ≈ 0.2 T. The second one is positioned along the cavity and produces a magnetic field B_0 up to 7 T.

The primary goal of this design is to generate a high quality electron beam which is necessary for an efficient interaction with the cavity mode.

In order to increase the operating frequency with a moderately low magnetic field the electron beam has to interact with a significant Doppler shift. That means an high quality and very laminar electron beam has to be created with a transverse velocity spread smaller than 1% and pitch ratio $\alpha = v_\perp/v_{||} \approx 0.5$.

As a first step to reduce the velocity spread produced by the thermoionic emission, in our design we propose an emitter ring as a circular crown with a width of 3 mm, located at the cathode front face (Fig. 1).

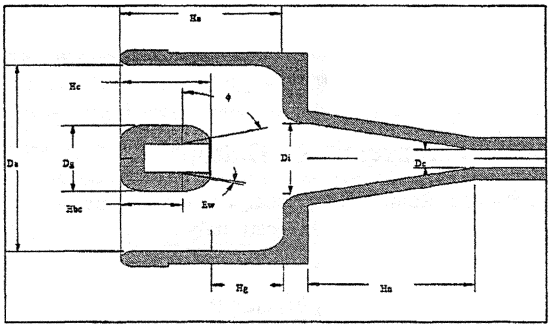

Fig. 1. The two-dimensional gun geometry used for electron beam analysis

In table 2 we report the variable parameters used in the simulation in order to optimize the velocity spread and the pitch ratio.

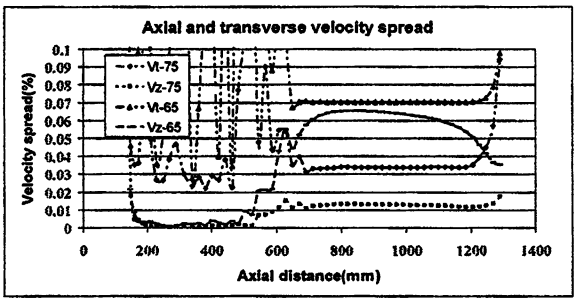

Fig. 2. Optimized velocity spread by varying the ϕ parameter (ϕ =65°,75°)

The ϕ parameter is very important to control the transverse velocity spread. It depends on the position of the emitter ring on the cathode surface.

In figure 2 we report the spread velocity calculated by varying the ϕ angle from 65° to 75° with a fixed magnetic compression ratio *fm*. The spread was calculated with the following statistic:

$$\delta v = \langle \Delta v \rangle / \langle v \rangle \text{ with } \Delta v = |v - \langle v \rangle|$$

Starting from this configuration we have optimized the initial pitch ratio α. It depends on the diode configuration. It is also proportional to the electric field E_c and inversely proportional to B_c.

Table 2. Limits of variate parameters

Cathode potential	650÷750 kV
Beam current	10÷40 A
Ring emitter width(E_w)	> 3 mm
Cathode-Diaphragm distance(H_g)	120÷160 mm
Aperture diaphragm(D_i)	220÷260 mm
Magnetic field at the cathode(B_c)	<0.2 T
Emitter ring angle(ϕ)	65°÷75°
Magnetic field compression ratio(f_m)	20÷50
Neck parameter(H_n)	300÷500 mm

By varying those parameters around the value reported in Table 2 we have got considerably good results (Figure 4) showing that the beam characteristic can be constrained within the value of Table 1. Furthermore by using an adiabatic tapering of the axial magnetic field the pitch ratio α has been increased to desirable value of 0.5÷0.6.

Figure 3 shows the pitch ratio vs beamlet direction at different magnetic field over the emitter ring; as we can see α decreases with the increase of the magnetic field (B_c).

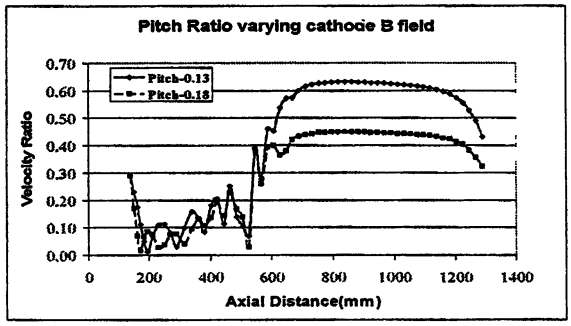

Fig. 3. Effect of the cathode magnetic field variation on the pitch ratio α(B_c=0.13T,0.18 T)

When varying B_c it is important to vary the neck parameter (H_n) in order to maintain the adiabaticity and to obtain the right value of α.

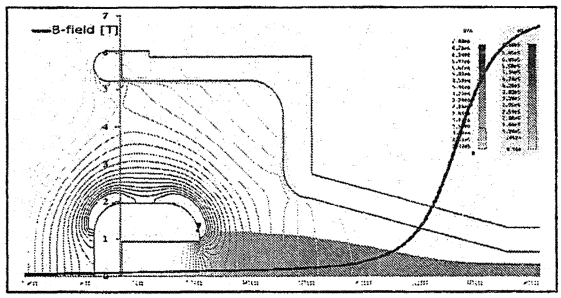

Fig. 4. 2D map of absolute value of electrostatic field, the axial magnetic field profile and electron beam trajectory obtained with optimized parameters.

Conclusion

The first attempt to design a high voltage electron gun shows optimistic results. However the velocity spread and especially the transverse one and the cathode surface field are still above the values required by the project. In a forth incoming investigation we will improve the performances of this parameters by design the cathode geometry and reshaping directly the electric field.

References

1. *Nusinovich, G. S., Latham,* P. *E., and Dumbrajs,* O. Theory of relativistic cyclotron masers // Phys. Rev. E July 1995. V. 52, No. 1. P. 998–1012.

2. *McCowan, R. B., Pendleton, R.A., Fliflet, A. W.* Design of an Electron Gun for a 280 GHz // Naval Research Laboratory Washington DC, Report. n° 6785, 1991 P. 1–17.

3. *Tsimring, S. E.* Electron Beams and Microwave Vacuum Electronics// edited by Wiley-Interscienze 2007

4. *CST Microwave Studio,* CST GMbH, Buedinger Str. 2a, D-64289, Darmstadt, Germany.

Technological Gyrotron with the Wide-Band Fast Frequency Sweeping

M.Yu. Glyavin, A.G. Luchinin, M.V. Morozkin

Institute of Applied Physics, N. Novgorod, Russia, glyavin@appl.sci-nnov.ru

The CW gyrotron-based systems [1] developed by IAP RAS jointly with GYCOM Ltd. (N. Novgorod, Russia) are successfully used for fabrication of nanostructured ceramics and composites, sintering of fine metal powder compacts and ceramic-metal composites, annealing of semiconductors and dielectrics, microwave plasma assisted CVD diamond growth. These systems operating in the range of 24-30 GHz differ advantageously in their functional capabilities and microwave source efficiency [2]. Technological systems composed of gyrotrons, the set of power supplies, transmission lines, microwave ovens and computer controls are used in laboratories and industrial centers of Russia, USA, Germany, Japan and China for microwave material processing. Some data on these systems are summarized below.

CW gyrotrons for technological applications
(PM – permanent magnet, OC – oil-cooled,
WC – water cooled, CM – cryomagnet)

Frequency, GHz	24	24	24	28	82.6	300
Output power, kW	5	7	30	15	35	2.5
Efficiency, %	30	45	50	35	50	15
Voltage, kV	15	20	33	25	25+15 CPD	15
Magnetic system	PM	OC	WC	OC	CM	CM

The 24 - 28 GHz systems with 10 - 15 kW output power are used as microwave sources for powering the electron cyclotron resonance ion sources capable of producing a high total ion current and high average ion charge [3, 4].

Further enhancement of both the ion current and ion charge can be achieved by an increase in the effective volume of ECR plasma in weakly inhomogeneous magnetic field using the multi-frequency microwave radiation [5]. Alternatively, radiation with wide frequency spectrum or fast frequency sweeping can be used. In the latter case the frequency band should be at least 2% and the sweeping time rate is defined by plasma diffusion time. Theoretical estimation gives the required sweeping frequency close to 1 kHz.

Such wide-band gyrotron frequency tuning is impossible in resonance zone of a single mode due to the high cavity Q-factor (about 1000) but can be implemented by a mode switching induced by the magnetic field variation. For this goal the two points are important: a coil inductance L must be small enough for the attainment of the necessary characteristic time $t = L / R$ and the skin effect in the gyrotron body must be minimized. A modified version of the second harmonic technological gyrotron was developed to satisfy these requirements.

The TE_{23} and TE_{03} modes were selected as operating ones. The frequency difference for these modes is close to 2%. The design parameters of operating regime are: the 23-24 kV voltage, 2-3 A beam current, 23% in efficiency. To minimize the skin effect, the tube body and cavity were made from stainless steel with the thickness of about 1 mm. The thin copper layer was deposited on the cavity inner surface by the electroforming method to reduce the ohmic losses. In contrast with previous technological gyrotrons, the cavity radius R_0 was significantly increased as well as the optimal electron beam radius. The new version of the triode electron gun was developed for this gyrotron. The cathode radius is equal to 30 mm, the electron beam radius in the cavity R_b is close to $R_0 / 3$. The calculated value of the pitch-factor is $g = 1.2$ and the velosity spread is $\delta v_\perp = 0.11$ for the beam current $I = 2$A. The anode voltage is formed by the pass of the anode current produced by the reflected electrons through the anode resistor.

General view of the tube is shown in Fig. 1. An additional low inductance coil is wired directly on the tube body in the cavity region. The current through the coil, required for 2% magnetic field variation in presence of the main field ($B_0 \approx 0.5$ T) corresponding to the 28 GHz second harmonic operation, is close to 10 A. The standard oil cooled main solenoid is used for this gyrotron. The power consumption of the solenoid is about 12 kW. The tube has a direct microwave output through the circular 40 mm waveguide with a brazed-in BN window. The thickness of BN disk was optimized to obtain the minimum reflected power in the both modes. Calculated value of the reflected power is about 0.5%.

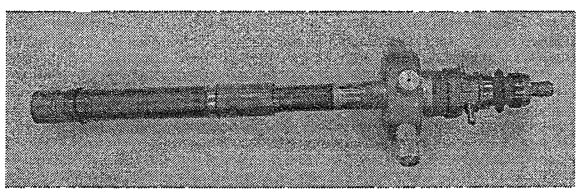

Fig. 1. General view of the gyrotron.

Some data of the gyrotron operation in the regime without frequency sweeping are presented in Fig. 2. The horizontal axis is the time in seconds, the left axis – output power in kW, the right one – the efficiency in percents. The output power of about 10 kW (upper plot) and 20% efficiency were obtained in experiments for both modes what are close to the design values. On the left side of the plot the magnetic field corresponds to the TE_{03} mode. After the change in the main coil current (time ~ 500 s from the beginning) the other mode, TH_{23}, was excited. The beam current was limited to a 2.5 A by the high voltage power supply. We hope to increase efficiency up to 30% operating with a 3 A beam current.

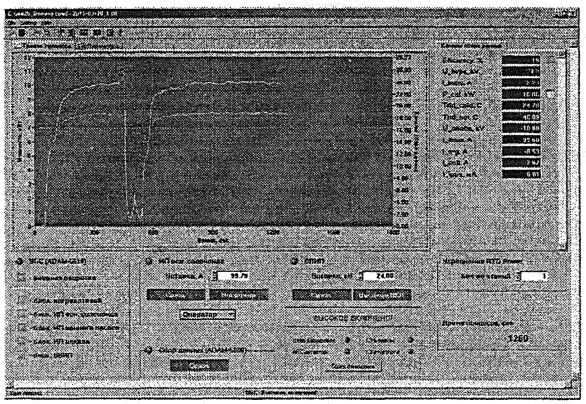

Fig. 2. Experimental curves of the output power and efficiency

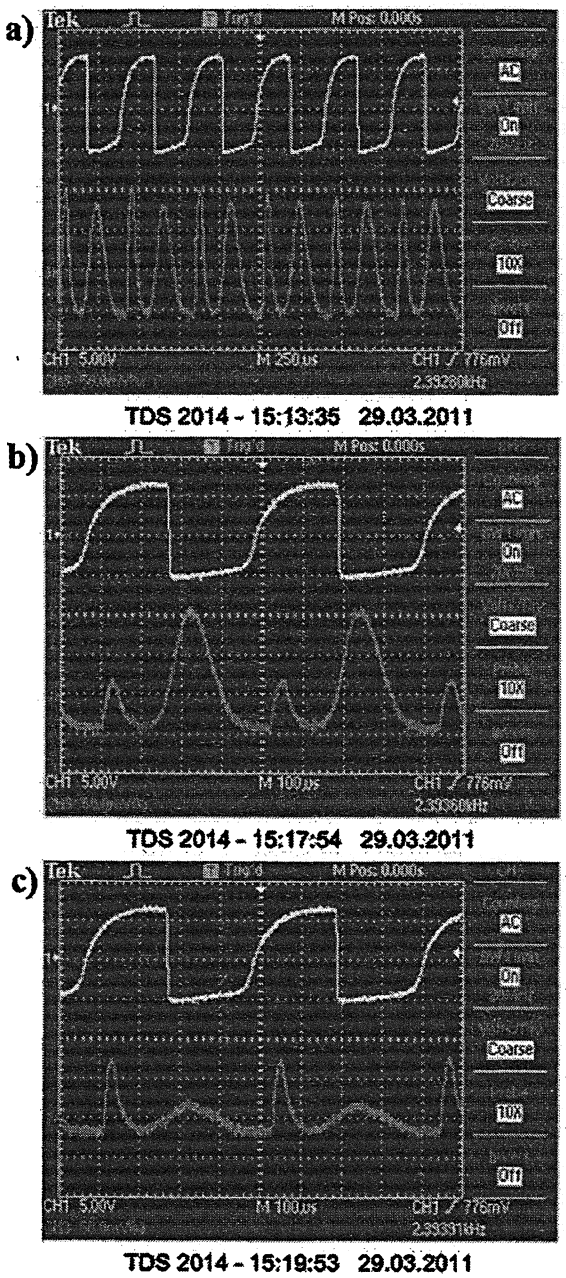

Fig. 3. Oscillograms of the additional coil current and microwave power from the RF detector. The plots (b) and (c) correspond to the resonance absorption of different modes by frequency meter

The results of frequency sweeping are shown in Fig. 3.

The sweeping frequency up to 2 kHz was realized. The frequencies of two operating modes were measured by a resonance frequency meter and were equal to 28.1 GHz (TH_{23} mode) and 28.7 GHz (TE_{03} mode). Preliminary calculation has shown that both modes can be converted with high efficiency to the Gaussian beam by a united mode converter.

The capacity for fast power modulation makes this type of gyrotron as a promising instrument for many microwave processing applications. The example of power modulation by the additional coil current variation is shown in Fig. 4.

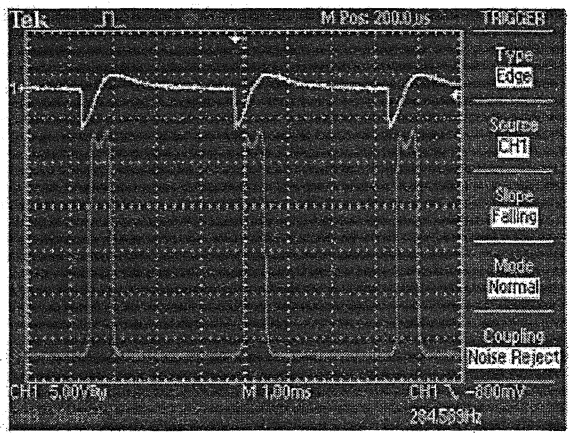

Fig. 4. Power modulation by the additional coil current

Thus, the technological gyrotron with the wide-band fast frequency sweeping has been developed, manufactured and tested. This gyrotron can be used to increase the multicharged ion current in ECR-ion sources or to improve the homogeneity of microwave field distribution the applicator of the gyrotron based sintering systems. In contrast to a wide band gyro-BWO or gyro-TWT the developed gyrotron is less sensitive to a load.

References

1. *Bykov, Yu., et al.* 24-84 GHz Gyrotron Systems for Technological Microwave Applications // *IEEE Trans. on Plasma Science*, 2004, 32, 1, 67-72

2. *Morozkin, M. V., Glyavin, M. Yu., Denisov, G. G., Luchinin, A. G.,* A high-efficiency second harmonic gyrotron with a depressed collector // Int. J. IRMM Waves, 2008, V. 29, P. 1004-1010

3. *Bykov, Yu., et al.,* 28 GHz 10 kW gyrotron system for electron cyclotron resonance ion source // Rev. Sci. Instrum. 2004, V. 75, P. 1437-1439

4. *Leitner, D., et al.*, Status report of the 28 GHz superconducting electron cyclotron ion source VENUS // *Rev. Sci. Instruments*, 2006, V. 77, 03A302

5. *Vondrasek, R. C.; Scott, R.; Pardo, R. C.*, ECRIS Operation with Multiple Frequencies // Review of Scientific Instruments, 2006, V. 77, 03A337

Numerical Simulation of Non-stationary Operation of Oscillator with Reflection from Output Remote Load

Yu.V. Novozhilova[1], N.M. Ryskin[2], S.A. Usacheva[2]

[1]Institute of Applied Physics RAS, Nizhniy Novgorod, Russia, river@appl.sci-nnov.ru
[2]Saratov State University, Saratov, Russia, usasva@mail.ru

It is well known that even small time-delayed reflection from the output load considerably influences the spectrum of gyrotron output radiation (see e.g. [1, 2]). Taking into account this influence is important for plasma diagnostics, controlled fusion and other applications where narrow or continuously tunable spectrum should be provided. Dynamics of various oscillators driven by the signal reflected from remote load was considered earlier in many papers. However, the main attention has been paid to such non-stationary phenomena as self-modulation and transition to chaos [3]. In this paper, we focus our interest to such problems as stability of eigenmodes, transient processes, and possibility of switching between various modes by external driving. We consider the case of large delay time which is typical for millimeter and submillimeter (terahertz) devices. Large delay usually leads to multistability, i.e. coexistence of many stable steady states. Thus, mode competition phenomena are significant.

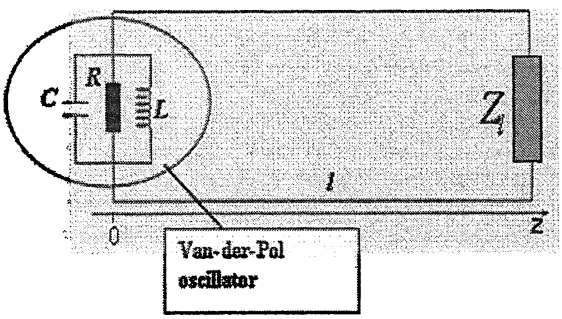

Fig. 1. A Van der Pol oscillator connected with a remote load

We consider a simple model of a Van der Pole oscillator with reflection from the remote load (Fig.1), which is a universal model for description of any oscillator with fixed field structure. Such a system is described by the following equation for slowly varying complex amplitude

$$\dot{A}-\left(\lambda-A^2\right)A=\rho e^{i\psi}A\left(t-\Delta t\right), \qquad (1)$$

where λ is the parameter of excitation. The $A(t-\Delta t)$ term in the right-hand side of (1) corresponds to the reflected signal, Δt is the delay time and $\rho\exp(i\psi)$ is the complex reflection factor; ρ is the product of reflection coefficient and the number of half-wavelength at feedback loop divided by Q-factor of the circuit. Further we assume $\Delta t=1$ which is always possible to obtain by normalization of the variables.

The number of admitted single-frequency solutions (longitudinal modes) $A=A_0\exp(i\omega t)$ with real frequency in such a system is finite and is determined by ρ. The amplitudes and frequencies of modes are described by formulas

$$A_0^2=\lambda+\rho\cos\theta, \qquad (2)$$

$$\omega=-\rho\sin\theta \qquad (3)$$

Here $\theta=\omega-\psi$ is the signal phase shift at the time of feedback loop passing. If

$$\rho<1 \qquad (4)$$

there is only one single-frequency mode exists. At $\rho>1$ excitation of several one-frequency modes is possible. With the increase of ρ, a new mode appears at $\rho\cos\theta=-1$, which corresponds to the touch of the straight line and the sinusoid in Fig. 2. The new mode at the touching condition is degenerated and at the further increase of ρ splits into two ones (e.g. modes 5, 6 in Fig. 2).

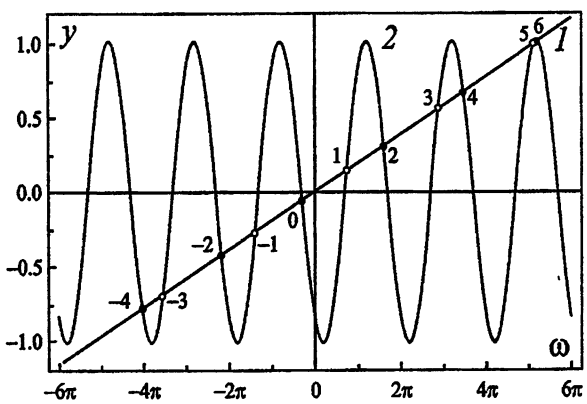

Fig. 2. The graphic solution of (3) at $\rho=16.335$, $\psi=-0.309\pi$. *1* — straight line $y_1=\omega/\rho$, *2* — sine curve $y_2=-\sin\theta$. Self-stable modes are marked by black circles, self-unstable — by light circles

The longitudinal mode uniqueness condition (4) can be interpreted in terms of the well-known theory of self-oscillator locking by external harmonic force [4]. The reflected wave acts as an external force, which locks the frequency of the oscillator, if the reflected wave frequency is situated near the auto-oscillator free frequency within locking-band wide of ρ. When there is only one longitudinal mode of delay line in the locking-band (at $\rho<1$), there is the single one-frequency mode in the system. On the contrary, when there are more than one longitudinal modes of delay line within the locking band, there are more than one (but finite number) one-frequency modes in the system (fig. 2).

We studied stability of the single-mode solutions with respect to two kinds of perturbations: 1) slow

evolution of amplitude and frequency of the mode ("self-perturbations") 2) perturbations which frequencies relatively far from that of the mode [5]. In the latter case perturbations are composed of two satellites with frequencies, symmetrically spaced from the fundamental frequency. Correspondingly the evolution of satellites can be treated as a parametric process when the satellites are pumped by the fundamental mode [6].

At $\rho<1$, the corresponding single mode is stable relatively to both types of perturbations. At $\rho\cos\theta=-1$ the degenerate mode (Fig. 2, modes 5 and 6) has zero increment relatively to "self-perturbations" and can be stable, unstable or neutral relatively to satellite instability.

At $\rho>1$, when the number of modes is large, self-stable and self-unstable states are alternating (Fig. 2). Modes, which amplitudes increase due to the load reflection are self-stable (modes with even numbers in Fig. 2), and modes which amplitudes decrease due to the reflection (modes with odd numbers in Fig. 2), are self-unstable: this effect again can be explained in terms of locking of a self-oscillator by weak external force [4].

On the other hand, at $\rho>1$ modes with frequencies located near edges of the set of the frequency band can decay into pair of satellites with frequencies symmetrically spaced from the eigenfrequency. The fundamental mode with frequency nearest to the free running oscillator frequency is always stable.

Numerical modeling shows that transition from an unstable mode occurs to a stable mode with nearest frequency. For the case of decay of a self-unstable mode, the beginning of the transient process has an exponential character (Fig. 3a). For the case of satellite instability, the transient looks like growing modulation of the amplitude caused by beating of two modes terminating by rapid switch to the stable mode (Fig. 3b).

The possibility of switching between stationary modes is investigated at short-time influence by an external driving. The similar way of gyrotron frequency control was considered earlier in [7].

This work is supported by the RFBR grants No. 09-02-00707 and 11-02-01411.

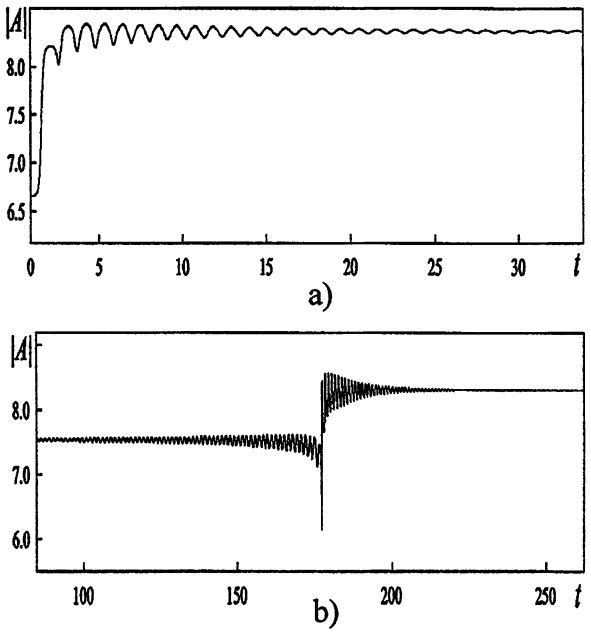

Fig. 3. Examples of transient processes for the case of self-instability (a) and satellite instability (b)

References

1. *Batanov, G. M., Kolik, L. V., Novozhilova, Yu. V. et al.* Response of a gyrotron to small-amplitude low-frequency-modulated microwaves reflected from a plasma // Tech. Phys. 2001. V. 46. P. 595-600.

2. *Dumbrajs, O., Glyavin, M. Y., Zapevalov, V .E., Zavolsky, N.A.* Influence of reflections on mode competition in gyrotrons // IEEE Trans. Plasma Sci. V. 28. 2000. P. 588-596.

3. *Lang, R., Kobayashi, K.* External optical feedback effects on semiconductor injection laser properties // IEEE J. Quantum Electron. 1980. V. 16. P. 347-355.

4. *Rabinivich, M.I., Trubetskov, D.I.* Oscillations and Waves in Linear and Nonlinear Systems. Kluwer Academic, Dordrecht. 1989, 577 p.

5. *Novozhilova, Yu. V.* Parametric instability in an oscillator with delayed reflection from the load // Appl. Nonlin. Dynamics. 2011. V. 19. No. 2 (in Russian).

6. *Bloembergen, N.* Nonlinear Optics, Ed. Benjamin, New York, 1965.

7. *Nusinovich, G. S., Sinitsyn , O. V., Antonsen, T M.* Mode switching in a gyrotron with azimuthally corrugated resonator // Phys. Rev. Lett. 2007. V. 98. 205101.

The Method for Measuring the Spectra of Nanosecond High-Power Microwave (HPM) Sources

S.E. Fil'chenkov, N.G. Kolganov, S.P. Mar'ev, A.V. Palitsin, Yu.V. Rodin

IAP RAS, Nizhny Novgorod, Russia

We present a new method, schematically given in Fig. 1, for measuring spectra of nanosecond high-power microwave sources. This method is based on iterative processing of detected signals after passing them through band-pass filters. Our iteration procedure to reconstruct the high-frequency filling in measured time envelopes is similar to the procedure used in Refs. [1, 2].

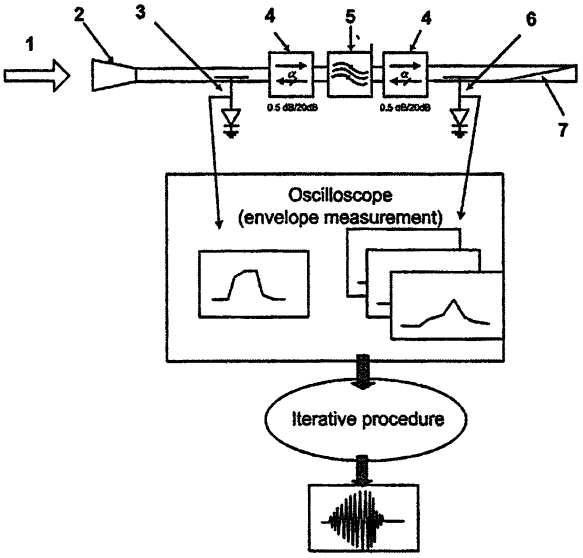

Fig. 1. Spectrum measurement scheme. 1 – microwave radiation; 2 – receiving antenna; 3 – microwave sensor for pulse measurement prior the filter; 4 – ferrite isolator; 5 – band–pass tunable filter; 6 – microwave sensor for pulse measurement after filter; 7 – matched load.

Measurement consists of three stages. The first stage measures the signal envelope, $A(t)$. The second stage registers the envelopes of the signals passed through the filters with different central frequencies, $A_k(t)$. The final stage involves an iterative procedure that numerically reconstructs the initial microwave signal and its spectrum.

Our numerical procedure requires to know the transmission function of the filters, $L_k(\omega)$, before hand. These functions were measured with network analyzer Agilent E5071C and one of them for a particular frequency out of tuning range from 8 to 12 GHz is shown in Fig. 2. Having these functions we numerically "propagate" a candidate signal through these filters. The envelopes of obtained signals are replaced with the detected envelopes. Thus the procedure automatically changes phases of the signals:

$$\alpha^{(i)}(t) = \arg\left(F^{-1}\left[\sum_k F\left\{ A_k(t) e^{i\alpha_k^{(i)}(t)} \right\} \frac{1}{L_k(\omega)} \right] \right), \quad (1)$$

$$\alpha_k^{(i+1)}(t) = \arg\left(F^{-1}\left[F\left\{ A(t) e^{i\alpha^{(i)}(t)} \right\} L_k(\omega) \right] \right),$$

where $\alpha^{(i)}(t)$ - signal's phase on i^{th} iteration prior the filters; $\alpha_k^{(i)}(t)$ - signal's phase on i^{th} iteration after k^{th} filter; F and F^{-1} - direct and inverse Fourier transformation. A resulting signal is used as candidate for the next iteration.

The procedure outputs a full microwave signal $A(t)\cdot\alpha(t)$ and its spectrum $F\{A(t)\cdot\alpha(t)\}$. Presented iterative procedure (1) is similar to the one described in Ref. [2], where single reflectionless dispersive medium was considered instead of a set of filters.

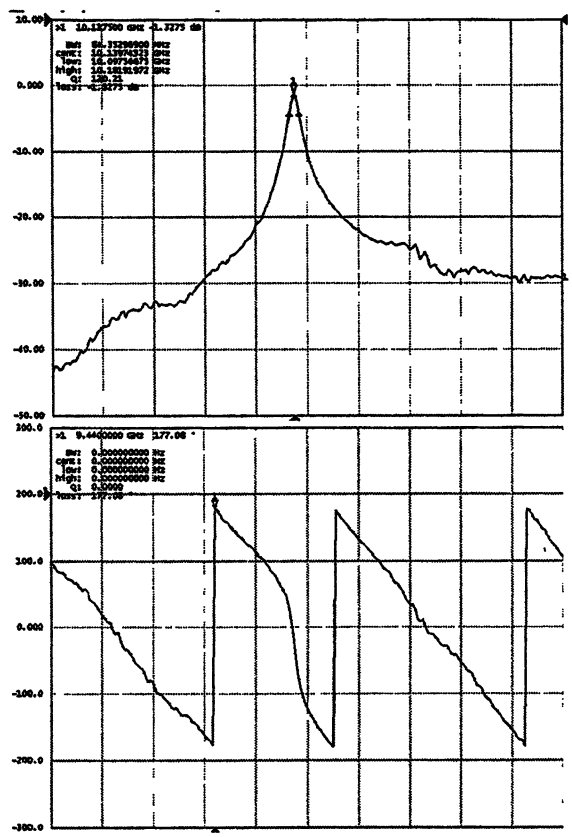

Fig. 2. Amplitude and phase characteristics of the tunable filter used in experiments.

We have confirmed the convergence of our method by applying the iterative procedure to a representative set of test signals and one of them is shown in Fig. 3. Overall error of spectrum reconstruction usually was less than 1%. Such a good accuracy of the iterative procedure requires two conditions to be met. The fist condition is that the combined frequency span of all filters to be broader than the frequency span of the signal $\Delta\omega$. The second condition is that each filter has the bandwidth comparable or less than $\Delta\omega$. Moreover, method has a low sensitivity to central frequency offset of the filters (Fig. 4).

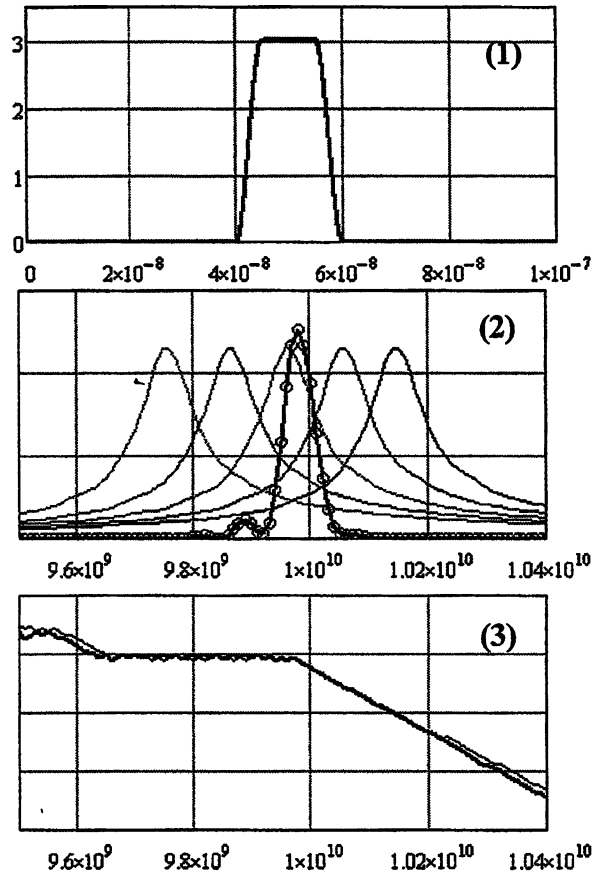

Fig. 3. Reconstruction of test signal's spectrum using five filters. (1) – envelope of a test signal; (2) – initial and reconstructed amplitude spectra that coincide and characteristics of five filters, used for reconstruction; (3) – initial and reconstructed phase spectra.

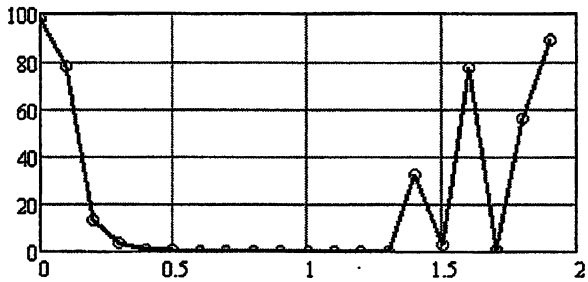

Fig. 4. The error of spectrum reconstruction as a function of the central frequency offset of filters expressed in fractions of a bandwidth.

We have experimentally tested our method by measuring output radiation of a Gigawatt-level X-band relativistic backward wave oscillator (BWO). In this experiment a single tunable band-pass filter was used instead of a set of filters. The central frequency of the filter was adjusted from one pulse to another, so required envelopes of signals were acquired in consecutive pulses with an assumption that the frequency, power and other characteristics of pulses were invariable. The output spectrum of iterative procedure is shown in Fig. 5(a). For comparison the spectrum, independently measured by heterodyne method, is shown in Fig. 5(b). Central frequencies and shapes of amplitude spectra coincide with good accuracy. The time, required for calculation of this spectrum, was about 30 sec on PC with Pentium 4, 2.8 GHz processor and 1.5 GB memory).

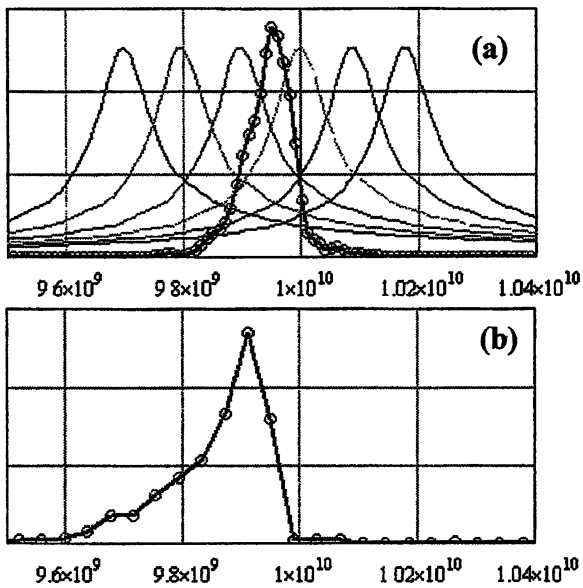

Fig. 5. Experimentally measured spectrum of HPM nanosecond pulses (a) – by the presented method, based on iterative procedure; (b) – by heterodyne method.

In conclusion, a hardware realization of our method doesn't require broadband equipment since only envelopes of microwave pulses are to be measured. It demonstrates good accuracy and can be implemented in a device with small dimensions and weight. This was confirmed numerically on a representative set of test signals as well as experimentally on output radiation of a Gigawatt-level X-band relativistic BWO. An extension of this method towards higher frequency bands (such as Ka-band) is straightforward subject to availability of filters.

References

1. *Katsenelenbaum B.Z., Semenov V.V.* // Radiotekhnika I Electronika, No. 12, 1967, P. 244-251.
2. *Kuzikov S.V.* Optimization and synthesis of passive pulse compressors based on reflectionless cavities // Int. J. IRMMW, Vol. 19, No. 5, 1998, P.771-784.

Short Wavelength FEM based on Bragg Coupling of Propagating and Cutoff Waves: Recent Results and Prospects

N.Yu. Peskov[1], N.S. Ginzburg[1], A.K. Kaminsky[2], A.M. Malkin[1], E.A. Perelstein[2], S.N. Sedykh[2], A.S. Sergeev[1], V.Yu. Zaslavsky[1] and I.V. Zotova[1]

[1]Institute of Applied Physics, Nizhny Novgorod, Russia, peskov@appl.sci-nnov.ru
[2]Joint Institute for Nuclear Research, Dubna, Russia

Improving Selectivity of Bragg FEM

The use of Bragg resonators in the form of shallow-corrugated waveguides was proposed [1] to provide narrow-frequency operation of free-electron masers (FEM) at Ka-band. During the last years in collaboration between JINR and IAP RAS such Bragg FEM has been realized at the linac LIU-3000 (JINR) and applied to study pulse heating effect in high-gradient accelerating structures [2].

Many possible applications of the FEM require shortening radiation wavelength. However traditional Bragg resonators with the feedback loop, which is based on coupling of two counter-propagating waves having high group velocities, lose their selectivity with increase of the oversize factor that is necessary for the short wavelengths FEM operation. This problem can be solved using a new type of Bragg structures based on coupling of propagating and quasi-cutoff waves [3]. In this scheme a beam of wiggling electrons interacts with a propagating wave, which is coupled at the Bragg corrugation with a quasi cut-off mode. The main advantage of novel FEM scheme is provision of higher selectivity over transverse mode index than traditional schemes of Bragg FEM. Similar to gyrotrons implication of the cutoff wave into feedback loop results in mode spectrum purification because distance between cut-off waveguide modes is much higher than between paraxial waves. To decrease Ohmic losses associated with excitation of cut-off mode it is attractive to section the interaction space and to use two-mirror scheme of the resonator (Fig. 1) with the up-stream Bragg reflector based on quasi-cutoff feedback mode and conventional Bragg reflector with rather small reflectivity as a down-stream reflector [4]. Under the optimal parameters oscillation frequency in such scheme is close to the frequency of the cutoff wave excited in the up-stream mirror. The 3D simulations demonstrate that advanced Bragg structures are able to provide selectivity up to transverse size ~ 10 - 20 wavelengths [4]. Based on such resonators MW-level long-pulse FEMs can effectively operate at THz frequency band [5].

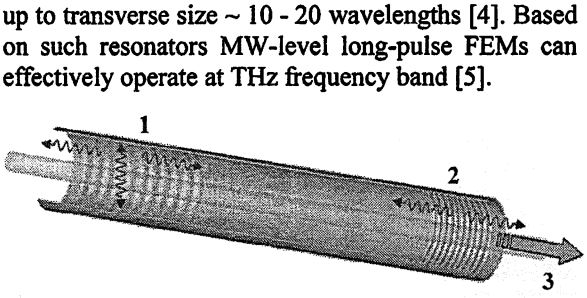

Fig. 1 Scheme of FEM with hybrid two-mirror resonator formed from advanced up-stream (1) and traditional down-stream (2) Bragg reflectors. Propagation of electron beam (3) and e.m. fluxes in each mirror are shown.

Basic model of advanced Bragg FEM

Advanced Bragg structure (Fig. 1) represents a section of a cylindrical waveguide having shallow axially symmetric corrugation $r = r_0 + r_1 \cos(h_1 z)$ ($h_1 = 2\pi/d_1$, d_1 is the period and r_1 is the amplitude of corrugation, r_0 is the mean waveguide radius) and provides coupling of quasi-cutoff wave

$$\vec{E} = \mathrm{Re}\left(B(z,t)\vec{E}_B(r_\perp)e^{i\omega_c t}\right) \quad (1)$$

and two counter propagating waves

$$\vec{E} = \mathrm{Re}\left(\left[A_+(z,t)e^{-ih_1 z} + A_-(z,t)e^{ih_1 z}\right]\vec{E}_A(r_\perp)e^{i\omega_c t}\right) \quad (2)$$

under the Bragg resonance condition

$$k \approx h_1. \quad (3)$$

Here ω_c is the cutoff frequency and functions $E_{A,B}(r_\perp)$ specify transverse structure of the waves corresponding to the modes of a regular waveguide. Electron beam is synchronous to the propagating wave A_+. Mutual scattering of the partial wave beams and excitation of the synchronous wave can be described in quasi-optical approximation by the following system of equations:

$$\frac{\partial A_+}{\partial Z} + \frac{\partial A_+}{\partial \tau} + i\alpha_1 B = J, \quad -\frac{\partial A_-}{\partial Z} + \frac{\partial A_-}{\partial \tau} + i\alpha_1 B = 0,$$
$$\frac{iC}{2}\frac{\partial^2 B}{\partial Z^2} + \frac{\partial B}{\partial \tau} + \sigma B + i\alpha_1 (A_+ + A_-) = 0, \quad (4)$$

with the electron excitation factor J, which can be found from the electron motion equations

$$\left(\frac{\partial}{\partial Z} + \beta_\parallel^{-1}\frac{\partial}{\partial \tau}\right)^2 \theta = \mathrm{Re}\left(A_+ e^{i\theta}\right). \quad (5)$$

Output traditional Bragg reflector possesses corrugation $r = r_0 + r_2 \cos(h_2 z)$ and provides mutual scattering of two counter propagating waves (2) under the resonance condition $2k \approx h_2$, which can be described by the equations

$$\frac{\partial A_+}{\partial Z} + \frac{\partial A_+}{\partial \tau} + i\alpha_2 A_- = J, \quad -\frac{\partial A_-}{\partial Z} + \frac{\partial A_-}{\partial \tau} + i\alpha_2 A_+ = 0. \quad (6)$$

Amplification of the synchronous wave A_+ in the regular section of the resonator is described by the equations (5), (6) where one should put $\alpha_2 = 0$. In simulation we assumed that external energy fluxes are absent so the amplitudes of partial waves $A_\pm$ on the corresponding boundaries vanish and all the partial waves free escape from the cavity. In (3)-(6) the following normalized variables and parameters are used [4, 6]: $Z = zkC$, $\tau = \omega_c t C$, $A_\pm$ and B are the normalized wave amplitudes, C is the gain parameter, θ is electron phase in respect to the synchronous wave, Δ is detuning from the undulator synchronism, σ is the Ohmic losses parameter, $\alpha_{1,2}$ are the coupling coefficients of the partial waves in the advanced and traditional Bragg structures correspondingly.

Prove-of-principle experiment at Ka-band

Experimental study of novel FEM scheme was performed at LIU-3000 (0.8 MeV / 150 A / 200 ns). The operating transverse velocity was pumped in 6-cm period wiggler with transverse field of 0.12 T and reversed guide field of 0.15 T. Two-mirror resonator of total length of about 60 cm was constructed with (1) advanced Bragg reflector of the period of 10.6 mm, which operates via coupling of two counter-propagating $TE_{1,1}$ waves with quasi-cutoff $TE_{1,2}$ wave and provides rather narrow reflection zone near the designed frequency, and (2) traditional Bragg structure with the period of 5.3 mm, which provides reflection of the $TE_{1,1}$-wave into the backward wave of the same type (Fig. 2).

Simulations of the FEM in the frame of the approach described above demonstrated establishment of a single-mode single-frequency oscillation regime for experimental conditions. In accordance with the simulations stable single-mode operation at the frequency of 30.2 GHz was observed under designed parameters (Fig. 3). The output power was measured at the level of 15 MW.

The main advantage of the considered FEM scheme is stabilization of the oscillation frequency for the beam having jitter of parameters during the RF-pulse or from pulse to pulse. This was corroborated by results of the experiment, where oscillation at the fundamental mode of the resonator at the frequency close to the cutoff frequency of the wave *B* (with accuracy of electron frequency shift) was obtained at any wiggler fields from the zone of self-excitation.

Project of sub-mm Bragg FEM

Simulations were carried out to advance JINR-IAP FEM into sub-mm wavelengths. To generate 2-mm radiation we consider shortening the wiggler period up to 3 cm and increasing the beam energy up to 1.5 MeV, which can be done at LIU-3000 when using additional accelerating sections. Two-mirror

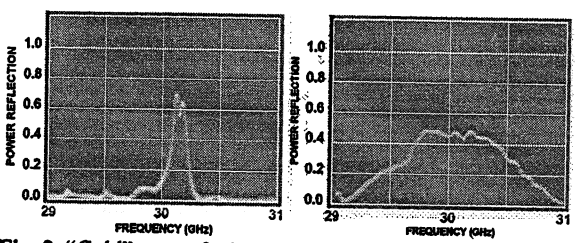

Fig. 2. "Cold" tests of advanced (left) and traditional (right) Bragg reflectors.

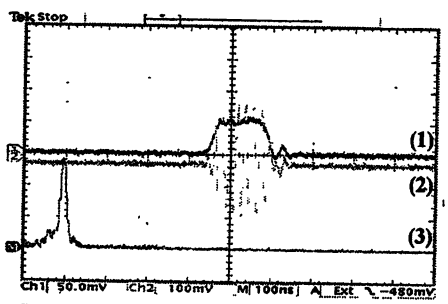

Fig. 3. Typical oscilloscope traces of (1) RF-pulse (100 ns / div.), (2) heterodyne beating signal and (3) frequency spectrum (50 MHz / div.).

Bragg resonator of the novel type is responsible for selection over the radial mode index. Advanced up-stream Bragg structure with radius of 0.52 cm and period of ~ 0.2 cm would provide the feedback loop for the operation wave $TE_{1,1}$ via excitation of quisi-cutoff wave of $TM_{1,5}$ type. Down-stream Bragg reflector of traditional type would have period of ~ 0.1 cm and operate via two counter-propagating $TE_{1,1}$ waves. For the corrugation amplitude of ~ 0.01 cm the wave coupling coefficients are $\alpha_1 = 1.4$, $\alpha_2 = 1$. The reflectors would be $l_1 = 6$ cm and $l_2 = 2$ cm with the regular section of 34 cm long.

Simulations of the FEM demonstrated establishment of a single-mode single-frequency oscillation regime for given parameters. The main amplification of the synchronous wave takes place after input mirror, thus, amplitude of the cutoff mode *B* in advanced Bragg structure is relatively small and Ohmic losses in the resonator made from copper ($\sigma \approx 5 \cdot 10^{-3}$) does not exceed 5%. At the same time, small power reflection from the output mirror (about 20%) provides favorable for interaction with e-beam structure of the synchronous wave, thus, rather high electron efficiency of ~ 10% and output power ~ 10 MW. Simulations show that over full zone of the oscillator self-excitation radiation frequency is close to the frequency of the cutoff wave when beam energy variation $\Delta\gamma/\gamma \approx 15\%$ (Fig. 4). This proves stability of novel FEM scheme to the change in beam parameters.

This work was partially supported by the Russian Foundation for Basic Research (#10-02-01395 and #10-08-01269) and the Russian Federal Program "Scientific and Pedagogical Staff for Innovative Russia" for 2009-2013.

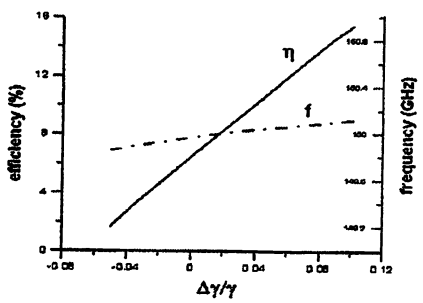

Fig. 4. Simulation of 150 GHz FEM with advanced Bragg reflector based on LIU-3000. Electron efficiency and oscillation frequency for the beam having jitter of energy.

References

1. *Bratman V.L., e.a.* FEL's with Bragg reflection resonators: CARMs versus ubitrons // IEEE J. Quant. Electr. 1983. V.19, No.3. P.282-293.

2. *Kaminsky A.K., e.a.* Demonstration of powerful 30-GHz FEM operation with resonant load // Tech. Phys. Lett. 2010. V.36, No.5. P.37-42.

3. *Ginzburg N.S., e.a.* Improving selectivity of free electron maser with 1D Bragg resonator using coupling of propagating and trapped waves // Phys. Rev. ST-AB. 2005. V.8. P.040705.

4. *Ginzburg N.S., e.a.* Tunable terahertz band planar Bragg reflectors // Appl. Phys. Lett. 2009. V.95. P.043504.

5. *Ginzburg N.S., e.a.* THz FEL with Bragg resonator based on coupling of propagating and trapped waves // JEPT Lett. 2010. V.91. P.286-289.

Numerical Simulations of a Co-Harmonic Gyrotron

D.A. Constable[1], I.V. Bandurkin[2], A.V. Savilov[2], W. He[1], C.G. Whyte[1], C.W. Robertson[1], A.D.R. Phelps[1], A.W. Cross[1], V.L. Bratman[2] and K. Ronald[1]

[1]SUPA, Department of Physics, University of Strathclyde, Glasgow, G4 0NG, Scotland,
[2]Institute of Applied Physics, Russian Academy of Science, Nizhny Novgorod, Russia.
K.Ronald@strath.ac.uk

Results from numerical simulations have demonstrated the principle of a co-harmonic gyrotron, operating with a novel cavity. Such a cavity is capable of generating coherent radiation at both the 2nd and 4th harmonics of the electron cyclotron frequency simultaneously, at frequencies of 37.5 GHz and 75 GHz. Further results are presented here, including refinements to the output section of the cavity, as well as on the on-going testing of the cavity and its associated components, which are required to generate the operating modes of interest.

Introduction

Gyrotrons [1-3] have long been considered as one of the most effective devices for generating and amplifying [4] coherent, high-power radiation within the mm-band. This is achieved through the use of the cyclotron resonance maser (CRM) instability [5], whereby a beam of electrons undergo bunching within an applied magnetic field, and emit radiation as a result. However, with increasing pressures for ever higher frequencies, scaling gyrotrons for operation within the sub mm-band has been problematic.

These problems are associated with the inherent ancillary difficulties associated with operation at high frequencies. The frequency of operation, ω, is constrained by the beam dispersion shown below where s is the harmonic of operation, ω_c is the cyclotron frequency and k_z and v_z are the axial wave-number and velocity of the wave and electrons, respectively. Most gyrotrons are operated close to cut-off, and so the $k_z v_z$ term is small. ω_c is defined in terms of e and m_0, the electronic charge and rest mass, respectively, B_z the applied magnetic flux density and γ the relativistic correction factor.

$$\omega = s\omega_c + k_z v_z$$

$$\omega_c = \frac{eB_z}{\gamma m_0}$$

Therefore, it can be seen that if operating at a low harmonic, a large magnetic field will be required for high frequency radiation. Conversely, if operating at a high harmonic, the current required to start a given high frequency, close to cut-off mode, will often be enough to also generate a lower frequency, undesired mode, which would then dominate the output radiation.

Previously, work has been presented on a novel interaction region [6,7], for use as a gyrotron cavity. Such a cavity features an azimuthal corrugation, as shown in Fig. 1, in order to achieve co-harmonic generation of $TE_{2,2}$ and $TE_{4,3}$ signals, occurring at the 2nd and 4th harmonics, with the frequencies of the two being in an exact integer ratio. In order to facilitate pure output of the 4th harmonic, a specially designed output aperture was also designed, in order to trap the 2nd harmonic within the cavity.

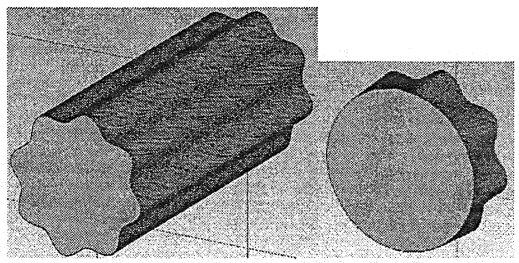

Fig. 1. Representation of a) the corrugated interaction region, and b) the output taper

Magic 3-D Results

Investigations using the PIC code Magic 3-D have focused on an electron beam of 60 kV, 5-10 A, with a pitch factor of 1. The magnetic field used to confine the electron beam is 0.7 T. While the simulations display the intended co-harmonic behaviour occurring at the 2nd and 4th harmonics (as shown in Fig. 2), the output signal is dominated by the 2nd harmonic.

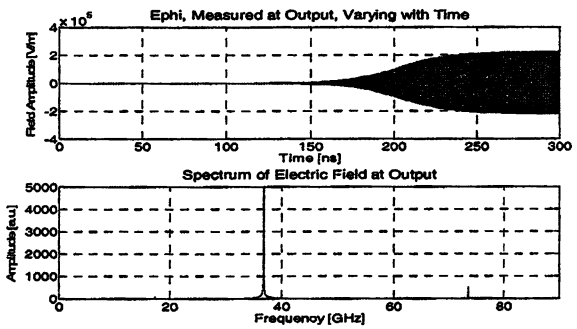

Fig. 2 Azimuthal electric field, and its FFT, of the co-harmonic gyrotron

Analysis of the modal content of the detected signal indicates the presence of mode converted $TE_{2,1}$ and $TM_{2,1}$ signals. Such mode conversion has also been confirmed through a subsequent analysis of the structure in CST Microwave Studio. Through a lengthening of the output taper, the degree of mode conversion can be reduced.

$TE_{2,1}$ Mode Launcher

More recent endeavours have focused on measuring the mode conversion experimentally and testing the improvements predicted by the lengthening the output taper. To that end, the cavity and output section have been constructed, and are currently awaiting cold-testing. In order to achieve this, input

couplers to produce $TE_{2,1}$ [8] and $TE_{4,1}$ signals, with a large degree of mode purity, have been designed, constructed and tested. Additionally, ripple wall mode converters [9] have been designed and are presently undergoing construction and testing, to allow the production of the two operating modes of the cavity.

In order to accurately cold-test the co-harmonic interaction cavity, it is necessary to generate both the $TE_{2,2}$ and $TE_{4,3}$ modes. As a result, this has necessitated the development of a method for first launching the $TE_{2,1}$ and $TE_{4,1}$ modes. This is accomplished through the introduction of a number of longitudinal slots in the outer wall of a cylindrical waveguide, in order to preferentially favour a specific $TE_{m,1}$ mode. An input $TE_{1,0}$ signal is provided by a rectangular feed section, which is then side-wall coupled into the main section of the device, as shown in Fig. 3, below.

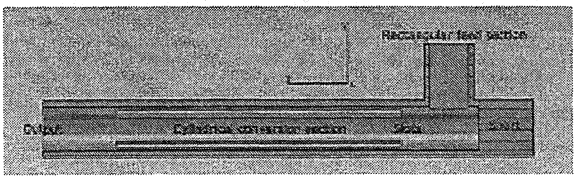

Fig. 3 Cross-sectional view of the $TE_{2,1}$ launcher

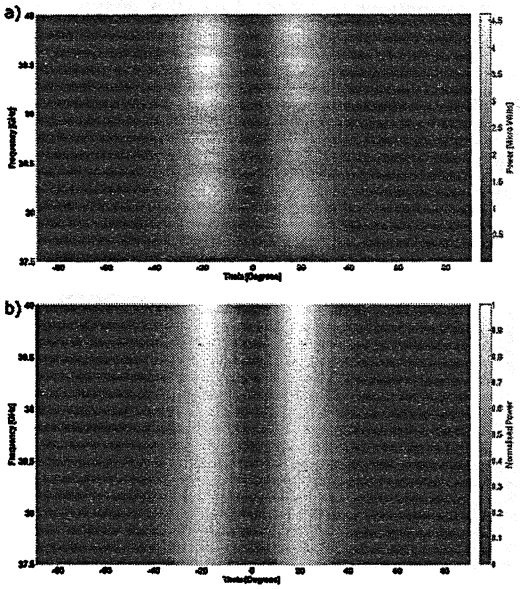

Fig. 4 Power of the E_φ component, for a) a constructed launcher, and b) an analytically predicted $TE_{2,1}$ mode

Two such devices have been constructed, demonstrating good experimental agreement when compared with the performance predicted by CST Microwave Studio. The launchers display transmission parameters of better than -5 dB, across a range of ~ 10% within the Ka-band. Most importantly, the launchers demonstrate a high degree of mode purity, as shown in Fig. 4. In addition, the launchers have been shown to be scalable, with similar devices constructed for operation within the W-band, demonstrating output of the $TE_{4,1}$ mode. Recently conversion of the $TE_{2,1}$ mode generated in such a launcher to the $TE_{2,2}$ mode required to cold test the cavity components has been demonstrated.

Sectioned Cavity Multipliers

Recently, it has been proposed that sectioned gyro-multipliers may offer advantages for operation in the sub-mm wave part of the spectrum by mitigating surface smoothness and manufacturing problems to the benefit of wall losses [10]. This concept is currently being numerically investigated at Strathclyde and progress to date will be reported on a 4th harmonic device operating at ~1.4 THz.

Acknowledgments

This work was supported by the UK Engineering and Physical Sciences Research Council, the UK Royal Society and the Russian Foundation for Basic Research. Thanks are also extended to Mr. Davy Barclay for his invaluable assistance with the construction of several aspects of the experimental apparatus.

References

1. *Flyagin, V.A., et al.*, The gyrotron // *IEEE* Transactions on Microwave Theory and Techniques, 1977, V.MTT-**25**, P. 514-521.

2. *Flyagin, V.A. and G.S. Nusinovich,* Gyrotron oscillators // Proceedings of the IEEE, 1988, V. **76**, P. 644-656.

3. *Ronald K. et al.,* Observations of dynamic behaviour in an electron cyclotron maser oscillator // J. Phys. D: Appl. Phys., 2001, V .34, P. L17-L22

4. *He W., et al.,* Axis-encircling electron beam generation using a smooth magnetic cusp for gyrodevices // Appl. Phys. Lett., 2008, V. 93, A. 121501

5. *Sprangle, P. and A.T. Drobot,* Linear and self-consistent nonlinear theory of the electron cyclotron maser instability // IEEE Transactions on Microwave Theory and Techniques, 1977, V. MTT-**25**, P. 528-544.

6. *Constable, D.A., et al.,* A co-harmonic gyro-oscillator with a novel interaction cavity // Proc. 2009 IEEE International Vacuum Electronics Conference, 2009, Rome, Italy.

7. *Bandurkin I.V. et al.,* Experimental study of a fourth-harmonic gyromultiplier // Phys. Plasmas, 2009, V. 16, A. 07070

8. *Constable, D.A., et al.,* A novel cylindrical $TE_{2,1}$ mode converter // Review of Scientific Instruments, 2010, V. **81**, A. 094702.

9. *Levine, J.S.,* Rippled wall mode converters for circular waveguide // International Journal of Infrared and Millimeter Waves, 1984, V. **5**, pp.937-952

10. *Bandurkin, I.V., et al.,* High-harmonic gyrotron with sectioned cavity // Phys. Plasma, 2010, V.17, A. 073101.

Forced Synchronization of a Two-Mode Electronic Maser

E.N. Peregorodova, S.A. Usacheva, N.M. Ryskin

Saratov State University, Saratov, Russia, usasva@mail.ru

Development of compact high power millimeter and submillimeter (terahertz) sources is of great importance for broad application in spectroscopy, space research, military and many other perspective fields [1]. Such devices naturally utilize essentially multimode "oversized" electrodynamic structures. Mode competition phenomena strongly affect dynamics of gyrotrons, free-electron lasers and many other devices [2]. Therefore the problem of control of radiation spectrum is of primary importance. One of possible solutions is driving by an external synchronizing signal. For example, in [3] using short-pulse driving signal for switching of radiation frequency of a high-power gyrotron used for plasma heating was studied.

In this work we investigate analytically and numerically the problem of synchronization of a two-mode electronic maser in case of non-synchronous interaction (cross-saturation). The system is described by the following equations for complex slowly varying amplitudes of the modes $A_{1,2}$:

$$\begin{aligned} \dot{A}_1 &= \lambda_1\left[1-|A_1|^2-\beta_1|A_2|^2\right]A_1 + fe^{i\omega t}, \\ \dot{A}_2 &= \lambda_2\left[1-|A_2|^2-\beta_2|A_1|^2\right]A_2, \end{aligned} \qquad (1)$$

where f and ω are amplitude and frequency of external driving, $\lambda_{1,2}$ are excitation parameters, and $\beta_{1,2}$ are coefficients of nonlinear coupling, which characterize cross-saturation of the modes. In the case of free-running oscillator ($f=0$) (1) become the well-known equations describing competition of two modes [4].

Note that this problem previously has been addressed in several works [5,6] mostly by using analytic methods of oscillation theory. However, the picture of synchronization cannot be completely understood without extensive numerical simulation.

Recall that the free-running system can exhibit the regimes of single-mode generation of either first ($\beta_1<1$, $\beta_2>1$) or second ($\beta_1>1$, $\beta_2<1$) mode, two-mode generation ($\beta_{1,2}<1$) and bistability regime ($\beta_{1,2}>1$) [4]. We perform analytical study of stability conditions for single-mode and two-mode oscillation regimes of the driven system and plot the resonant curves and synchronization tongues (i.e. areas stability of the single-frequency oscillation on the frequency of external driving). Also we present the results of detailed numerical simulation revealing the mechanisms of transition to the synchronous regime. As a result, we plot the phase diagrams on the driving amplitude-frequency parameter plane. Note that the numerical results are in excellent agreement with analytic ones (see [7] for details).

Consider the case when $\beta_1<1$, $\beta_2>1$, i.e. when the free-running system exhibits the regime of first mode generation. In Fig. 1 the example of phase diagram on the ω, f plane is presented. At small values of f two-frequency regime is observed when the frequency of external driving and the first mode natural frequency present in the spectrum. We name this regime as type I two-frequency regime. If ω is small, the classical mechanism of phase-locking which is widely described in literature [4] is observed.

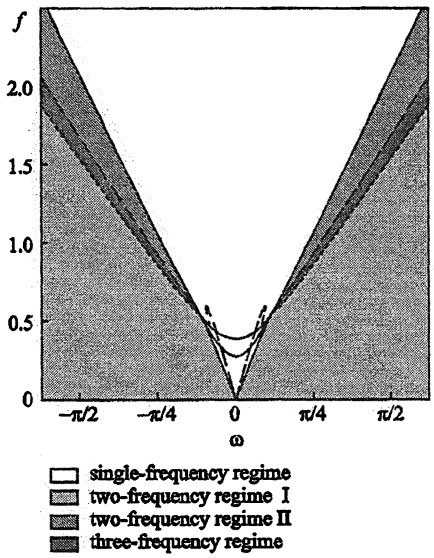

Fig. 1. Phase diagram on the plane of parameters f, ω for $\lambda_{1,2}=1$, $\beta_1=0.5$, $\beta_2=1.5$.

However, with the increase of ω excitation of the second mode becomes possible with the increase of the external driving amplitude. Since the excitation of the second mode is induced by driving with frequency close to that of the first mode, we call this effect asynchronous excitation. As a result, three-frequency oscillation appears. Further increase of f leads to complete suppression of the first mode natural frequency, and the regime of oscillations becomes two-frequency again. Now in the spectrum there are frequencies of external driving and of the second mode. We name this regime as a type II two-frequency regime. The next increase of f leads to suppression of the second mode and transition to the single-frequency synchronous regime.

Now consider the case when $\beta_{1,2}<1$, i.e. the free-running system exhibits two-mode oscillation. Note that this situation was considered in [3] in connection with the problem of frequency switching of the gyrotron.

We choose the following values of parameters: $\beta_1=0.5$, $\beta_2=0.5$, $\lambda_{1,2}=1$. The corresponding phase diagram is presented in Fig. 2. So far as we are driv-

ing the system generating two-frequency oscillation, at small amplitude of external driving the oscillation becomes three-frequency. With the increase of f the transition to the synchronous regime occurs. First, depending on ω, either locking or suppression of the first mode natural frequency takes place. The II-type two-frequency regime appears. Further increase of f leads to asynchronous suppression of the second mode.

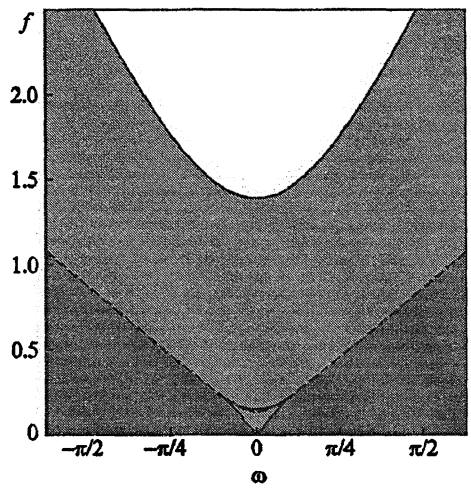

Fig. 2. Phase diagram on the plane of parameters f, ω for $\lambda_{1,2}=1$, $\beta_1=0.5$, $\beta_2=0.5$.

As one can see from the phase diagram presented on Fig. 2, the domain of synchronization breaks away from the horizontal axes i.e. the threshold of synchronization appears.

We considered the case of driving the oscillator in the bistability regime ($\beta_{1,2}>1$) as well. In that case, the synchronization tongue also has a bistable nature, i.e. the form of synchronization domain depends on the initial conditions. The details of numerical results are presented in [7].

The results presented in the paper might be helpful for solution of the problem of frequency control of multimode electronic masers.

This work is supported by Russian Foundation for Basic Research grant No. 11-02-01411.

References

1. *Booske, J.H.* Plasma physics and related challenges of millimeter-wave-to-terahertz and high power microwave generation // Phys. Plasmas. 2008. V. 15. 055502.

2. *Nusinovich, G.S.* Review of the theory of mode interaction in gyrodevices // IEEE Trans. Plasma Sci. 1999. V. 27. P. 313.

3. *Nusinovich, G.S., Sinitsyn, O.V., Antonsen T.M.* Mode switching in a gyrotron with azimuthally corrugated resonator // Phys. Rev. Lett. 2007. V. 98. 205101.

4. *Rabinovich, M.I. Trubetskov, D.I.* Oscillations and Waves in Linear and Nonlinear Systems. Dordrecht: Kluver, 1989.

5. *Nusinovich, G.S.* Theory of synchronization of multimode electron microwave oscillators.// Radiophys. Quant. Electron.1975. V.18. P.1689.

6. *Melnikova V.A., Tarantovich T.M.* Mode competition and locking states of a self-exited oscillator // Radiophys. Quant. Electron. 1975. Vol. 19. P. 817.

7. *Peregorodova, E.N., Usacheva, S.A., Ryskin N.M.,* Synchronization of the system of two competing modes by external harmonic signal // Izv. VUZ. Applied Nonlinear Dynamics. 2011. V. 19, No. 3 (to be published).

Nonstationary Simulation of a Second-Harmonic Sub-Terahertz Frequency-Tunable Gyrotron

S.T. Han[1], A.G. Rozhnev[2], N.M. Ryskin[2]

[1]Korean Electrotechnology Research Institute, Ansan, R. of Korea,
[2]Saratov State University, Saratov, Russia, RyskinNM@info.sgu.ru

Powerful frequency-tunable continuous-wave (CW) gyrotrons are of great importance for dynamic nuclear polarization (DNP) spectroscopy and some other applications. In [1] principles of design and results of experimental investigation of a CW second-harmonic 460-GHz gyrotron were reported. Smooth frequency tuning within 1 GHz by variation of the guiding magnetic field was measured. Since frequency tunability is achieved owing to successive excitation of high-order axial modes [2], one can expect strong mode-competition non-stationary effects.

In this paper, we perform numerical investigation of non-stationary processes in a second-harmonic gyrotron with parameters nearly the same as reported in [1]. The system is described by the following dimensionless equations:

$$i\frac{\partial F}{\partial t}-\frac{\partial^2 F}{\partial x^2}=-\frac{I_0}{2\pi}\int_0^{2\pi}p(\varphi_0)\,d\varphi_0\,, \qquad (1)$$

$$\frac{dp}{dx}+ip\left(|p|^2-1+\Delta\right)=iF\,, \qquad (2)$$

where F is normalized RF field amplitude, p is normalized electron transversal momentum, I_0 is normalized beam current and Δ is frequency mismatch parameter. Eqs. (1), (2) are supplemented with the boundary conditions for electrons

$$p(x=0)=\exp(i\varphi_0)\,,\ \varphi_0\in[0;2\pi]$$

and the nonlocal boundary condition for the field describing a transition of a uniform waveguide into an output horn [3,4]

$$F(L,t)=-i\kappa_L\int_0^t G\left[\kappa_L^2(t-t')\right]\frac{\partial F(L,t')}{\partial x}dt'\,, \qquad (3)$$

where G is the Green function, and κ_L is a parameter determined by angle of the output horn ψ [3, 4] (Fig. 1). Similar boundary condition is applied for field at the left boundary, $x=0$.

In contrast with the perfectly-matching boundary conditions [5], (3) allows correct account of singularity of the reflection factor near cut-off frequency. This method was successfully applied for simulation of various non-stationary phenomena in a gyrotron with non-fixed longitudinal RF field structure including self-modulation and transition to multi-mode "high-dimensional" chaotic operation [6, 7].

Linearization of the equations (1), (2) leads to the following equations:

$$\frac{d^2F}{dx^2}+i\Omega F=iI_0J,$$
$$\frac{d^2J}{dx^2}+i\Delta\frac{dJ}{dx}-\Delta^2J=\left(i(n\Delta-1)F+n\frac{dF}{dx}\right), \qquad (4)$$

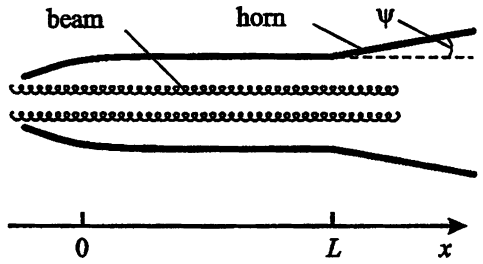

Fig. 1. Schematic of a gyrotron cavity

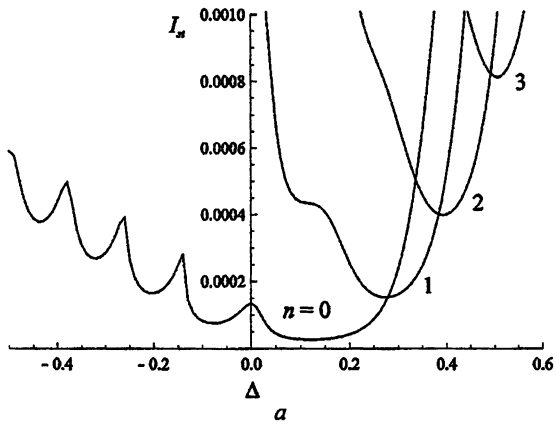

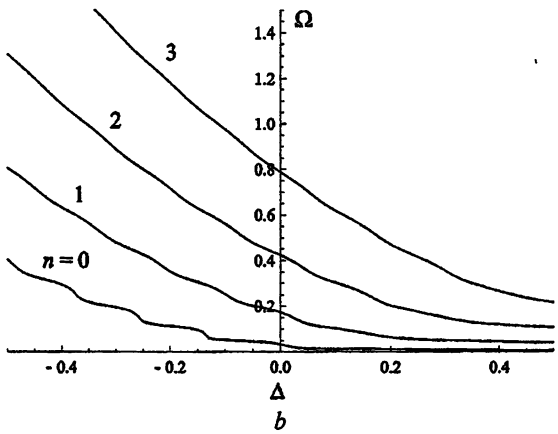

Fig. 2. Start-oscillation current (a) and frequency (b)

with boundary conditions

$$J(0)=\frac{dJ(0)}{dx}=0 \qquad (5)$$

for the RF current and the boundary conditions (3) for the field which can be rewritten as follows:

$$\frac{dF}{dx}+i\chi_{0,L}(\Omega)F=0\,,$$
$$x=0,L\,, \qquad (6)$$

where $\chi_{0,L}(\Omega)$ are given in [3, 4].

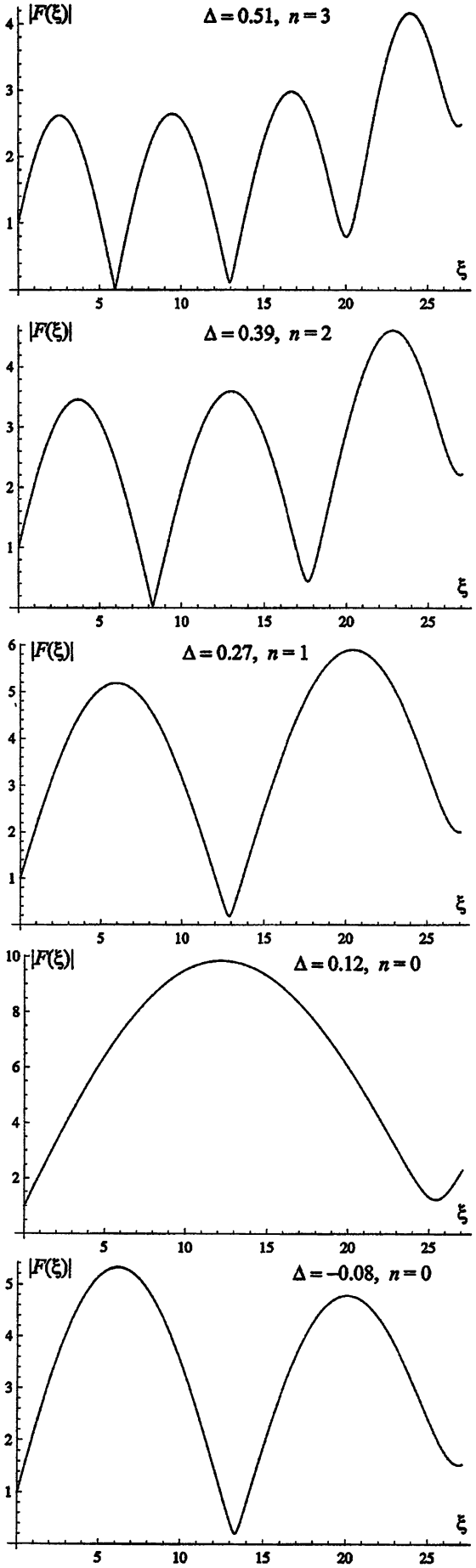

Fig. 3. Field vs. normalized coordinate profiles for various eigenmodes

Solving Eqs. (4)-(6) we calculate start-oscillation current and frequency tuning using the linear theory and compare the results with the experimental ones presented in [1]. In Fig. 2 example of I_{st} and Ω versus the mismatch parameter Δ is shown for fundamental ($n=0$) and higher-order ($n=1,2,3$) axial modes. These curves have the form typical for beam-wave interaction near cut-off frequency (see e.g. [4]). For negative mismatch $\Delta<0$ the beam interacts mainly with backward RF wave and the system operates as a gyro-backward-wave oscillator. In this domain frequency tuning by variation of the magnetic field is possible (cf. [2]).

In Fig. 3 examples of the field profiles $F(x)$ are presented. One can see that with the increase of frequency mismatch the $F(x)$ profile becomes more complicated and the number of maxima increases.

We also adopt the non-linear code developed in [6, 7] for the case of second-harmonic gyrotron and observe non-stationary transient phenomena caused by competition of the fundamental and higher-order axial modes.

This work is supported by Russian Foundation for Basic Research grant No. 11-02-01411.

References

1. *Torrezan, A.C., Han, S.-T., Mastovsky, I., Shapiro, M.A., Sirigiri, J.R., Temkin, R.J., Barnes, A.B., Griffin, R.G.* Continuous-wave operation of a frequency-tunable 460-GHz second-harmonic gyrotron for enhanced nuclear magnetic resonance // IEEE Trans. Plasma Sci. 2010. V. 38. P. 1150.

2. *Chang, T.H., Idehara, T., Ogawa, I., Agusu, L., Kobayashi, S.* Frequency tunable gyrotron using backward-wave components // J. Appl. Phys. 2009. V. 105, 063304.

3. *Rozhnev, A.G.* // J. Commun. Technol. Electron. 2000. V. 45. Suppl. 1. P. 95.

4. *Kuznetsov A.P., Kuznetsov, S.P., Rozhnev, A.G., Blokhina, E.V., Bulgakova, L.V.* Wave theory of a traveling-wave tube operated near the cutoff // Radiophys. Quantum Electron. 2004. V. 47. P. 356.

5. *Ginzburg, N.S., Zavol'skii, N.A., Nusinovich, G.S., Sergeev, A.S.* // Radiophys. Quantum Electron. 1986. V. 29. P. 89.

6. *Blokhina, E.V., Rozhnev, A.G.* Chaos and hyperchaos in a gyrotron // Radiophys. Quantum Electron. 2006. V. 49. P. 799.

7. *Blokhina, E.V., Kuznetsov, S.P., Rozhnev, A.G.* High-dimensional chaos in a gyrotron // IEEE Trans. Electron Devices, 2007, V. 54. P. 188.

2 MW, 170 GHz Coaxial-Cavity Gyrotron for ITER: Results Obtained with a Short Pulse Pre-Prototype at KIT

T. Rzesnicki[1], B. Piosczyk[1], S. Illy[1], J. Jin[1], S. Kern[1], I. Gr. Pagonakis[1], A. Samartsev[1], A. Schlaich[1] and M. Thumm[1,2]

Karlsruhe Institute of Technology (KIT), Association EURATOM-KIT,
[1]IHM, [2]IHE, 76131 Karlsruhe, Germany

Introduction

In difference to conventional hollow waveguide cavity gyrotrons which are under development for ITER in Japan and Russia, the EU is investigating a coaxial-cavity gyrotron with the potential to generate an RF output power of 2 MW in continuous wave (CW) operation [1]. The coaxial arrangement reduces mode competition and decreases voltage depression due to the electron beam space charge, thus resulting in an increase of the limiting current. Therefore stable single-mode operation can be obtained even with volume modes of very high order enabling a reduction of the Ohmic cavity wall loading and thus an increase of the generated mm-power of a gyrotron up to the multi-megawatt range. One consequence of the use of very high-order volume modes is the significant increase of the complexity of the quasi-optical (q.o.) RF output system needed for conversion of the cavity mode into the fundamental free space Gaussian mode. The main design specifications for the coaxial-cavity gyroton which is under development are given in *Table 1*.

Table 1. Design parameters for the coaxial-cavity gyrotron

Operating cavity mode	$TE_{34,19}$
Frequency, f	170 GHz
RF output power, P_{out}	2 MW
Beam current, I_b	75 A
Accelerating voltage, U_C	90 kV
Velocity ratio, α	~ 1.3
Cavity magnetic field, B_{cav}	6.87 T
Efficiency with SDC	> 50 %

For verification of the design of critical components of the industrial 170 GHz, 2 MW, CW prototype [2] a short-pulse pre-prototype tube is used at KIT. The main components of this tube are as far as possible the same as in the industrial design. The experimental condition at KIT has been improved by installation of a normal conducting (nc) coil which allows it to increase the cavity magnetic field to the nominal value of 6.87 T. In addition, the previously used beam tunnel has been replaced by a modified version with longitudinal slots in the cooper rings, which destroy the azimuthal symmetry. Further on, a new q.o. RF output system with a launcher designed with a novel optimization method [3] has been installed. With those modifications an RF output power of 2.2 MW has been obtained with an output efficiency of ~30 % in non-depressed collector operation (pulse length ~1 ms). As shown in Fig. 1, the experimental results are in good agreement with the theoretical predications. With the modified beam tunnel stable single-mode gyrotron operation has been obtained without parasitic RF oscillations. The quality of the RF output beam with a fundamental Gaussian mode content of 96 % was in agreement with the design simulations of the new launcher. In comparison with the previous RF system, the amount of the internal stray losses was reduced to about 7 % of the output power. However, this value is for unknown reasons still larger then the estimated value of 3 to 4 % based on numerical analysis of the q.o. system.

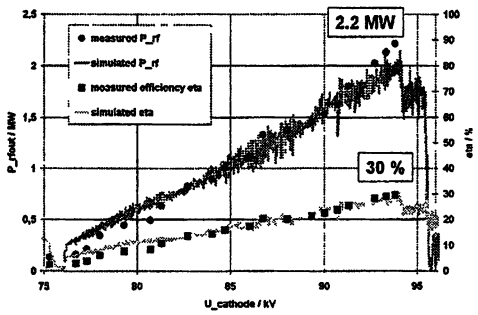

Fig. 1. RF output power and gyrotron efficiency vs. cathode voltage measured and calculated at nominal magnetic field.

Experimental Results

Due to problems with the electron gun (leakage of the ceramic insulators) the experiments had to be interrupted in 2010. To be able to continue the studies on the performance (internal stray losses, conversion efficiency) of the q.o. output coupler an old electron gun, previously used in the 165 GHz coaxial gyrotron, has been adapted for operation at 170 GHz at reduced magnetic field of ~6.67 T (without the nc-coil). After a long lasting conditioning stable single mode operation has been obtained with RF output power up to 1 MW as shown in Fig. 2.

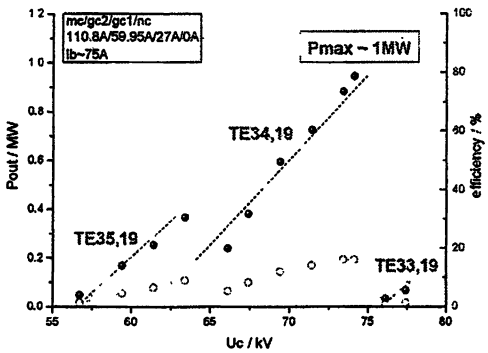

Fig. 2. RF output power and gyrotron efficiency vs. cathode voltage measured at reduced magnetic field in operation with the reactivated 165 GHz electron gun.

These conditions are very well suited for testing of an alternative launcher antenna designed [4] and

manufactured at IAP, Nizhny Novgorod. In difference to the KIT launcher the corrugations of the inner wall of the IAP launcher have a smoother structure. Before installing the launcher in the gyrotron, its performance has been measured at low power. For these tests, the converter has been installed in the KIT toroidal mirror system and the output field profile has been measured at several positions in- and outside the q.o. coupler. From the measured data (amplitude and phase) the mode conversion efficiency to the fundamental free space Gaussian mode has been calculated. Fig. 3 shows both the measured field pattern and the phase distribution of the IAP launcher in comparison to the previously studied KIT launcher. A detailed analysis has shown that both launchers have a conversion efficiency of around 96 %.

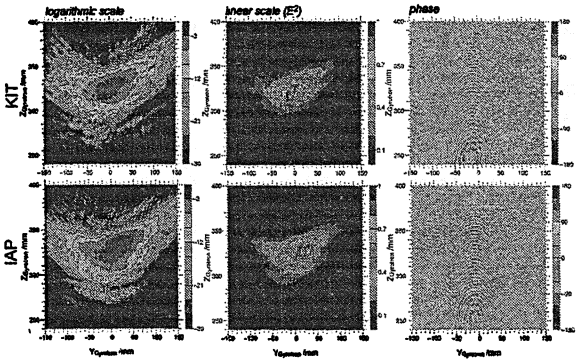

Fig. 3. Low power measurement results of the radiated field (amplitude and phase) from the KIT- (top) and IAP-launcher (bottom) antenna.

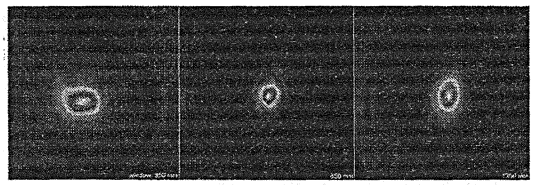

Fig. 4. RF beam profile as obtained with the IR-camera for the q.o. system with the IAP-launcher: at window position (left), at a distance of 500 mm (middle) and 1000 mm (right) outside the gyrotron output window.

An important parameter for characterization of the quality of a q.o. output coupler is the information about the internal RF-stray radiation losses. The amount of the internal stray radiation caused by the non ideal conversion can only be measured correctly if there are no additional losses due to an incorrect position of the microwave beam at the gyrotron window. Therefore, at first the position of the RF output beam at the window plane has been verified by measuring the RF-beam profile. In Fig. 4 the measured pattern is shown as well at the window plane and outside the gyrotron. The results show that the RF beam has the right width and is well centred within the output window. In order to estimate the amount of the RF stray radiation inside the tube, three independent measurements have been used: (1) calorimetric measurement of the dissipated power in an internal absorber, (2) calorimetric measurement of the stray RF power through a relief window and (3) relative measurement of the RF power through the relief window by using a sensitive bolometer. The measured values have been compared with the results obtained by using the KIT-launcher in the gyrotron under very similar conditions. In Table 2 the results are summarized. The values of the calorimetric measurements (two upper lines) are normalized to the RF output power. Previously a calibration of the stray RF-losses radiated through the relief window relative to the total internal stray radiation has been performed. With this calibration, the amount of the total internal RF stray losses is estimated to be ~5.5% for the IAP-launcher in comparison to ~7 % for the KIT design.

Table 2. Comparison of the stray radiation measurements results performed with the IAP- and KIT-launcher.

Launcher:	*IAP*	*KIT*	*ratio IAP/KIT*
Internal load*	0 0162	0 020	**0.81**
calorimeter on the relief window*	0 0036	0 0045	**0.80**
bolometer on the relief window	0 032	0 042	**0.78**

*measured power related to Pout

Summary and Outlook

Recent experiments with the short-pulse coaxial-cavity prototype gyrotron at KIT have been mainly dedicated to the verification of the performance of an IAP-launcher. Obtained results (both at low and high power) have confirmed the high conversion efficiency of the antenna. The measured amount of the stray losses was about 20 % lower compared with the KIT-launcher. The aim of the ongoing activities is concentrated on an improvement of the properties (conversion efficiency, stray radiation losses) of the q.o. output system. For that a set of mirrors with non-quadratic phase-correcting surface contour has been optimized and will be tested. In addition, a smoothened version of the KIT launcher has been designed.

Acknowledgment. This work was supported by Fusion for Energy (F4E) under grant contract No. F4E-2008-GRT-049(PMS-H.CD)-01 and within the European Gyrotron Consortium (EGYC). EGYC is a collaboration among CRPP, Switzerland; KIT, Germany; HELLAS, Greece; CNR, Italy; ENEA, Italy. The views and opinions expressed herein only reflect the authors' view. Fusion for Energy is not liable for any use that may be made of the information contained therein.

References

1. *T. Rzesnicki, et al.*, 2.2-MW Record Power of the 170-GHz European Pre-Prototype Coaxial-Cavity Gyrotron for ITER, *IEEE Transactions on Plasma Science*, Vol. 38, No. 6, pp. 1141-1149, 2010

2. *J.-P. Hogge et al.*, First experimental results from the European Union 2-MW coaxial cavity ITER gyrotron prototype, *Fusion Science and Technology*, 55, Feb. 2009, pp. 204-212.

3. *J. Jin, et al.*, Novel Numerical Method for the Analysis and Synthesis of the Fields in Highly Oversized Waveguide Mode Converters, *IEEE Transactions on Microwave Theory and Techniques*, Vol. 57, No. 7, pp. 1661-1668, 2009.

4. *A. V. Chirkov, et al.*, Use of Huygens's principle for analysis and synthesis of the fields in oversized waveguides, *Radiophys. Quantum Electron.*, vol. 49, no. 5, pp. 344-353, 2006.

Development of Helical-Waveguide Gyro-TWT at IAP

S.V. Samsonov, A.A. Bogdashov, G.G. Denisov, A.G. Eremeev, I.G. Gachev, V.V. Holoptsev, V.Yu. Ivanov, G.I. Kalynova, S.Yu. Kornishin, V.S. Kurkin, V.N. Manuilov, V.V. Maslov, S.V. Mishakin, I.V. Plotnikov, T.M. Smirnova

Institute of Applied Physics, Russian Academy of Sciences, Nizhny Novgorod, Russia, samsonov@appl.sci-nnov.ru

The gyrotron traveling wave tube (gyro-TWT) is known as a broad-frequency-band variety of gyrotron-type amplifiers having potentialities for production of the highest averaged or CW power in millimeter wavelength range [1-3].

In this paper we present recent experimental results and currently developing projects on gyro-TWTs which are based on a concept of using a helically corrugated waveguide radically changing dispersion of the operating eigenwave [4]. The gyro-TWTs under discussion are driven by nearly axis-encircling electron beams interacting at the second cyclotron harmonic with the $TE_{2,1}$ mode, which is scattered on the 3-fold helical corrugation into counter-rotating forward propagating $TE_{1,1}$ mode [5, 6].

Recent result on this activity at the Institute of Applied Physics (Nizhny Novgorod, Russia) includes realization of a CW Ka-band gyro-TWT. This amplifier was designed and made in the frame of a contract with the Southwest University of Science and Technology (China). According to the contract the amplifier should provide CW output power higher than 1 kW for frequency band 30-31 GHz and is supposed to be used for technological applications.

The gyro-TWT was designed to operate with 30 kV / 0.7 A electron beam produced by an MIG-like electron gun. According to the design and simulations the gyro-TWT was predicted to have a maximum output power of 3.5-4 kW and gain of 26-29 dB with instantaneous -3 dB bandwidth of about 5% at the center frequency of 30.5 GHz for electron beam having a pitch factor of 1.2 and perpendicular velocity spread of 15-20%.

The amplifier uses a DC oil-cooled main solenoid with magnetic field of about 0.57 T and a conventional TWT with power of 10-20 W as an RF driving source (Fig.1). The mid-power TWT (preamplifier) can be driven by a master oscillator with a power of few milliwatts. The gyro-TWT interaction region is about 50 cm long and includes two sections of the helical waveguide separated by a -3dB 3-cm long sever to prevent the reflection oscillations (Fig.2). The measured with a Vector Network Analyzer dispersion of the operating wave of the helical waveguide is in agreement with 3D simulations with accuracy of higher than 0.3%. According to a cold test, an input coupler provides transformation of more than 80% of input power in the form of a fundamental mode of a standard WR-28 waveguide into circularly polarized $TE_{1,1}$ mode at the entrance of the helical gyro-TWT structure for frequencies between 29.5 GHz and 31.5 GHz.

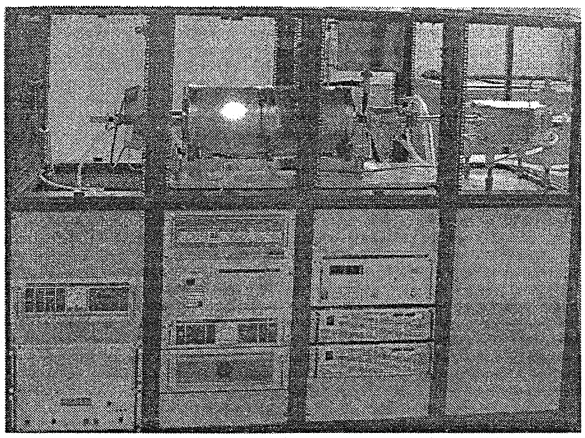

Fig. 1. A photograph of the gyro-TWT setup: the upper section includes the gyro-TWT tube with a collector coil immersed in a DC solenoid followed by a mode converter, 4-mirror box and a calorimetric load; the lower sections include the power supplies, a preamplifier, control, interlock, interface units, an oil pump, a heat exchanger etc.

"Hot" tests of the gyro-TWT were started in 2009. Several tubes were made each of those was carefully tested in the experiments using all available adjustable parameters including beam voltage, current, main and cathode magnetic field, axial and perpendicular position of a tube in the coils, drive RF power and frequency. As a result one tube was selected with parameters marginally satisfying the contract requirements. The results on this tube are presented below.

In available accelerating voltage range produced by an HV power supply (15-30 kV with power of up to 20 kW) the best operation of the gyro-TWT was found to take place at the value of 21 kV. Any 1 kV shift from the optimum (with the corresponding optimization of the magnetic fields) resulted in about 10% drop in the maximum power and bandwidth (at higher voltages limited by the self oscillations at frequencies within the operating band).

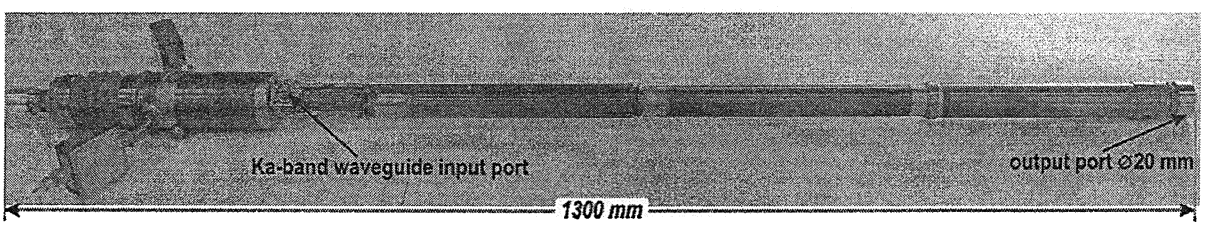

Fig. 2. A photograph of the gyro-TWT tube

At the zero-drive-stable operation the measurements showed that a regime with maximum output power (which amounted to 4 kW) and regimes with maximum instantaneous bandwidth (all parameters fixed except the drive frequency) had been realized at different values of magnetic field (Fig. 3).

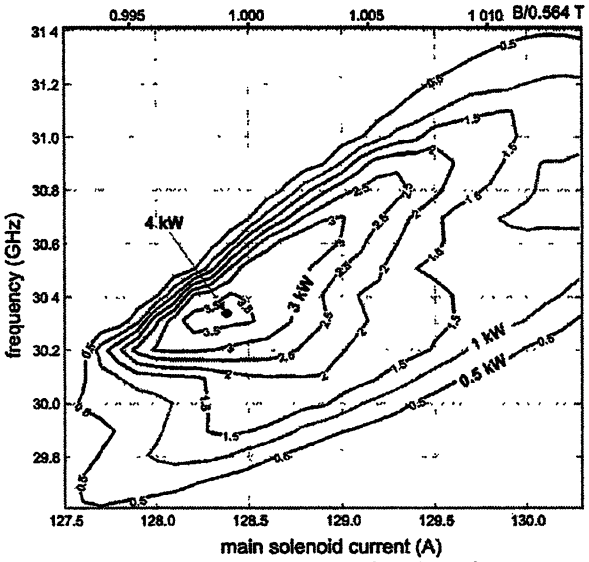

Fig. 3. Measured output power as a function of main solenoid current (magnetic field in the interaction volume) and frequency at constant RF drive power of about 8 W and beam of 21 kV / 0.87 A.

In the regime with a relatively high output power and simultaneously wide instantaneous bandwidth the power exceeded 1 kW in the frequency interval of nearly 30-31 GHz with the maximum of 2.8 kW at 30.7 GHz (Fig. 4). Frequency tuning accompanying by the corresponding adjustment of the magnetic field enabled the output power higher than 1 kW for the range 29.8-31.2 GHz with the maximum of 4 kW.

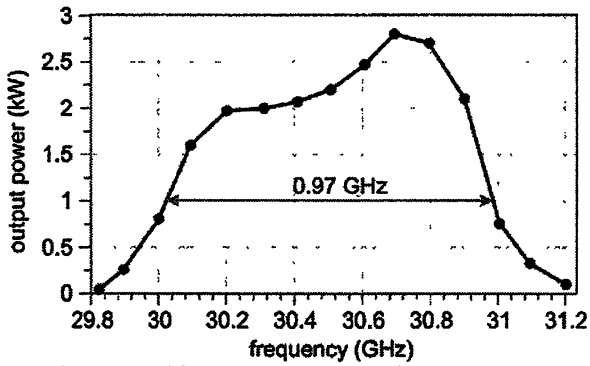

Fig. 4. Measured instantaneous band at beam parameters of 21 kV / 0.87 A, RF drive power of about 8 W and main solenoid current of 129.2 A

A possible reason of the fact that the measured instantaneous bandwidth (about 3%) was almost 1.5 times less that the designed value could be a significantly lower beam quality than it was predicted by the gun simulations. The beam-wave interaction simulations based on a 1D simplified model and on a 3D PIC code showed a very good agreement with the measurements for an electron beam having pitch-factor of 1.05 and velocity spread of about 40%. According to the same simulations reduction of the velocity spread to a reasonable value of 20% should result in 40-50% broadening of the bandwidth. Therefore special attention to the careful gun design and manufacturing with possible minimization of impact of spurious factors were undertaken for further projects of the gyro-TWTs.

Two other gyro-TWTs are currently under technical design and manufacturing. The common features of these two projects are the operation with CW or average output power of about 10 kW, the use of "warm" DC magnets, the use of single-stage depressed collectors, absence of any absorbers inside the operation volume and operation with a relatively low gain of about 20 dB with a consequent use of a relatively high-power (but commercially available) preamplifiers. It is interesting to note that for the higher power gyro-TWT (compared to the tube described above) the design is even simpler and main parameters such as efficiency and frequency band are higher.

The first gyro-TWT is designed to operate in a pulse (100 us duration) regime with a pulsed power of up to 150 kW, duty factor of 10% and instantaneous bandwidth of about 10% at Ka-band. It will be driven by an electron beam with energy of 70 keV and current of 7-10 A with the collector voltage depression by at least 20 kV.

Another gyro-TWT is designed for CW operation with output power of 8-12 kW and instantaneous bandwidth of 8.5-7% at Q-band. It is supposed to use an electron beam with current of 1.5 A and particles' energy of 40 keV half of which will be recovered to the power supply due to deceleration of the beam at the collector.

References

1. *K.R. Chu, H.Y. Chen, C.L. Hung, et al.* Theory and experiment of ultrahigh gain gyrotron traveling wave amplifier // IEEE Trans. Plasma Sci. 1999. V. 27. P. 391.

2. *M. Garven, J.P. Calame, B.G. Danly, et al.* A gyrotron-travelling-wave tube amplifier experiment with a ceramic loaded interaction region // IEEE Trans. Plasma Sci. 2002. V. 30. P. 886.

3. *M. Blank, P. Borchard, S. Cauffman, F. Felch* W-band gyro-amplifiers at Haystack Ultra-Wide Satellite Imaging Radar // in Digest of Joint 32nd Int. Conf. on IR and MM Waves and 15th Int. Conf. on THz Electronics, Cardiff, UK, 2007. P. 364-366.

4. *G.G. Denisov and S.J. Cooke* New microwave system for a gyro-TWT // in Digest 21st Int. Conf. IR&MM Waves, Berlin, Germany, 1996, P.AT2.

5. *G.G. Denisov, V.L. Bratman, A.D.R. Phelps, S.V. Samsonov* Gyro-TWT with a Helical Operating Waveguide: New Possibilities to Enhance Efficiency and Frequency Bandwidth // IEEE Trans. on Plasma Science. 1998. V.26. P.508.

6. *S.V. Samsonov, V.L. Bratman, G.G. Denisov, et al.* Broadband Gyro-TWTs and Gyro-BWOs with Helically Rippled Waveguides // in Proc. of 5th Int. Workshop "Strong Microwaves in Plasmas", Nizhny Novgorod, Russia, 2002. P. 46-61.

Compression of FM Pulses from an X-Band Relativistic BWO up to Power of 3 GW

S.V. Samsonov, V.L. Bratman, G.G. Denisov, N.G. Kolganov, S.V. Mishakin

Institute of Applied Physics, Russian Academy of Sciences, Nizhny Novgorod, Russia, samsonov@appl.sci-nnov.ru

In a series of publications, the well-known phenomenon of passive pulse compression (reduction in duration accompanied with an increase in amplitude), widely used in optics, has been proposed and investigated both theoretically and in low-power proof-of-principle experiments [1, 2] as a method of achieving microwave radiation with multigigawatt peak powers. The method is based on generation of a frequency modulated (FM) pulse by a relativistic backward-wave oscillator (RBWO) following its compression due to propagation through a dispersive medium (DM) in the form of a hollow metallic waveguide with helical corrugation of the inner surface. In this paper we present the pulse compression experiment in which multigigawatt peak power of X-band radiation has been achieved.

The experimental setup comprises two key elements (Fig.1): the source of FM radiation - an RBWO and the DM - a helical-waveguide (HW) compressor.

A helical-waveguide of the compressor due to a relatively shallow helical corrugation of the inner wall resonantly couples a pair of circularly polarized partial modes of the unperturbed waveguide, having significantly different group velocities where one mode is far from the cutoff and the other mode is close to cutoff [1]. As a result, in the frequency region of their resonant coupling, an eigenmode appears having a strong frequency dependent group velocity, which is favorable for the pulse compression. In contrast to a smooth or axially symmetric corrugated waveguide, the helical corrugation allows the frequency regions with zero or negative group velocity of the eigenwave, to be avoided. This ensures good RF matching of the compressor to the input source over a suitably wide frequency band.

In the experiment under discussion, a five-fold sinusoidal corrugation was used which coupled a circularly polarized $TE_{3,1}$ mode having large group velocity with a near-cutoff counter-rotating $TE_{2,2}$ mode. The use of these relatively high-order modes ensured sufficient RF breakdown strength at gigawatt power level [2]. The HW consisted of 4 aluminum sections and had a total length of the regular corrugation of 972 mm, bounded from each side by three-period sections with linearly increasing/decreasing amplitude of corrugation for adiabatic conversion of the radiation from the incident $TE_{3,1}$ mode into the operating eigenwave of the HW, at the input, and back to the $TE_{3,1}$ mode, at the output (Fig.1). The most favorable frequency region for the pulse compression is a part of the dispersion characteristic where the operating wave group velocity has a large negative gradient as a function of frequency, which, for the HW under consideration, is the region from 9.5 to 10 GHz (Fig. 2). Therefore, in order to be effectively compressed, an input pulse should have a negative frequency sweep within the mentioned frequency interval.

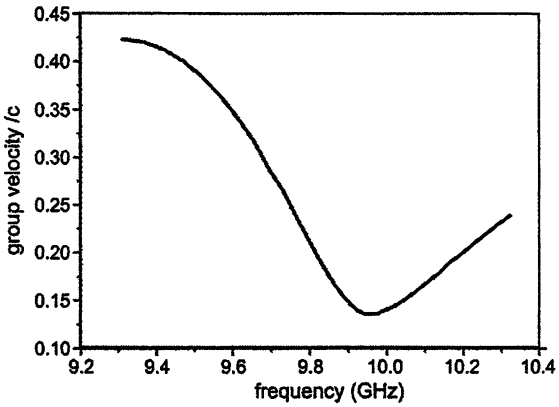

Fig. 2. Group velocity (normalized to the speed of light) of the HW operating wave as a function of frequency

Relativistic backward-wave oscillator. According to the design and simulations, the RBWO oscillation frequency should smoothly sweep from 10 to 9.5 GHz when the accelerating voltage gradually changes in time from 600 to 300 kV while its peak output power should amount to 0.4-0.9 GW for beam current of 5-9 kA.

The experiments were performed using a SINUS-6 accelerator where an accelerating voltage pulse was formed by a combination of a Tesla transformer and a coaxial transmission line. Usually the accelerator produces pulses of voltage up to 600 kV and current of 6-7 kA with about 15-ns long flat top and 5 to 10-ns long rising/falling edges. Because of the principle of operation of the SINUS-6 accelerator it is very problematic to realize the necessary voltage sweep for the RBWO pulse by modifying the external circuit.

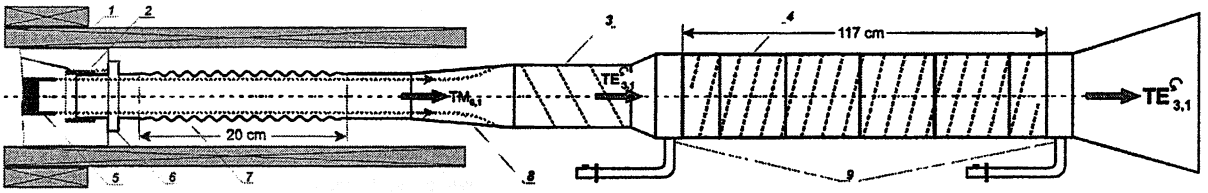

Fig. 1. Scheme of the experimental setup: 1 – solenoid with additional coil; 2 – moveable dielectric cylinder; 3 – mode converter; 4 – HW compressor; 5 – cathode; 6 – resonant reflector; 7 – BWO slow-wave structure; 8 – electron beam; 9 – ~50-dB couplers.

Nevertheless, it was experimentally found how to realize an appropriate voltage drop "internally" [3]. To achieve this change in voltage a dielectric cylinder was introduced into the region of the magnetically insulated coaxial diode where the electron beam was formed. Presumably due to some plasma effects, this dielectric insert led to a significant decrease (with characteristic time of 10-20 ns) of the diode impedance during the process of explosive-emission beam generation, resulting in a decrease in the accelerating voltage and an increase in the beam current at the top of the pulse (Fig. 3a). Moreover, varying the axial distance between edges of the cathode and dielectric insert, $L_{C\text{-}D}$, within several millimeters we could control the magnitude of the voltage drop and hence control the frequency sweep interval, which was used in the final experimental optimization of the combination of the RBWO with the compressor.

At optimum configuration, when the top-pulse voltage decreased from 550 to 350 kV and beam current increased from 8 to 9.5 kA the RBWO generated radiation with power of 0.6-0.8 GW when frequency sweeping from 10 to 9.6 GHz during about 15 ns (Fig. 3b). The frequency sweep was measured by means of a heterodyne technique, when a small fraction of output radiation from the RBWO was nonlinearly mixed with radiation of a pulsed magnetron at a fixed frequency, resulting in a waveform at the intermediate frequency. The power of the output radiation was obtained by processing of RF detector signal, detector voltage-power calibration and data from a calorimeter measuring the total RF energy in the pulse.

Combination of the RBWO and the HW compressor. The RBWO was combined with the HW compressor in a common vacuum system via a mode converter which transformed the power from the RBWO in the form of the $TE_{0,1}$ mode into the incident operating mode of the compressor, namely, the circularly polarized $TE_{3,1}$ mode (Fig. 1). The output power was radiated through a horn terminated with a 300mm-diameter 0.3mm-thick lavsan window and then absorbed in a calorimeter with an aperture of 600 mm in diameter. Two identical couplers with RF detectors situated up- and down-stream the compressor (Fig. 1) enabled monitoring both corresponding waveforms in one shot.

As a result of experimental optimization a 4.5-fold power amplification due to the compression was achieved. The maximum peak power of the compressed pulse was measured to be as high as 3.2 GW while its halfwidth amounted to 2.2 ns with a total pulse energy of 9.7±0.2 J (Fig. 3b). Another important for some applications result from this configuration is a demonstration of ability to change significantly the RF pulse duration (in a range of about 2-10 ns) from shot to shot by small variation in the geometry of the system (changing $L_{C\text{-}D}$ distance) which can be performed by a distant control without breaking the vacuum. At such a large variation in the pulse width (by almost 5 times) the output pulse energy can be kept almost constant (with variation of less than 20-30%).

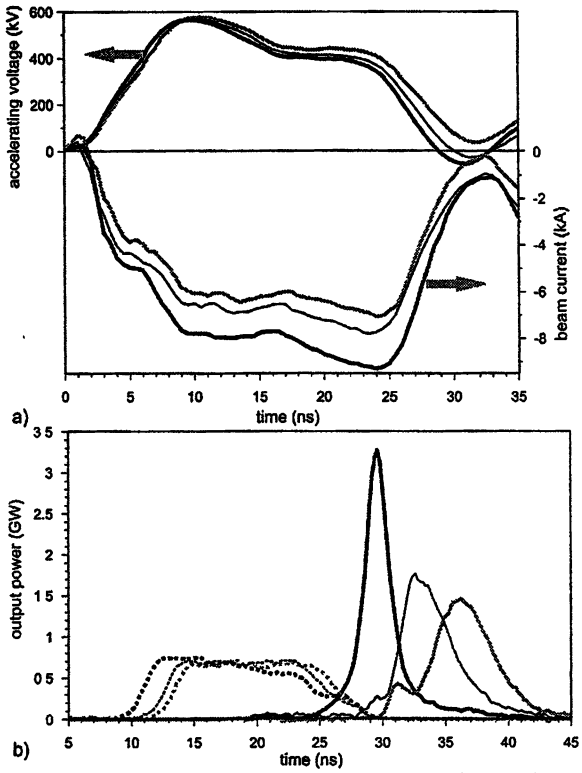

Fig. 3. Measured pulses for a combination of RBWO and compressor: a) accelerating voltage and beam current of the RBWO; b) detector signals (after processing and normalization to the power) from couplers up-stream (dashed lines) and down-stream (solid lines) the compressor at different distances $L_{C\text{-}D}$, (11 mm – grey thick lines, 9 mm – black thin lines, 8 mm – black thick lines).

Let us also note that the achievable power compression ratio by the method discussed is approximately proportional to the input FM pulse width. Therefore if the duration of the RBWO accelerating voltage pulse (which should have a negative slope) is increased from 15 ns, as used in the experiment presented, to 40-50 ns and the HW compressor is proportionally elongated a further 3-fold power increase of the compressed pulse is achievable.

This work was supported by the Russian Foundation for Basic Research (Grant 10-02-00975) and by the Presidium RAS (Program "Problems of physical electronics, charged particle beams and generation of electromagnetic radiation in high-power systems").

References

1. *Samsonov, S.V., Phelps, A.D.R., Bratman, V.L., Burt, G., Denisov, G.G. et al.* Compression of Frequency-Modulated Pulses using Helically Corrugated Waveguides and Its Potential for Generating Multigigawatt rf Radiation // Phys. Rev. Lett. 2004. V. 92, 118301.

2. *Bratman, V.L., Denisov, G.G., Samsonov, S.V., Cross, A.W., Ronald, K., Phelps, A.D.R.* Method for achievement of a multigigawatt peak power by compressing microwave pulses of a relativistic backward-wave oscillator in a helical waveguide // Radiophys. Quantum Electron. 2007. V. 50, No. 1. P. 36-48.

3. *Bechasnov, A.M., Bratman, V.L., Kolganov, N.G., Mishakin, S.V., Samsonov, S.V.* Voltage-tuned relativistic backward wave oscillator // Tech. Phys. Lett. 2010. V. 36, No. 2. P. 140–143.

Periodic Giant RF Pulse Formation in Electron Masers

I. V. Bandurkin, G. G. Denisov, S. V. Kuzikov, A. V. Savilov, A. A. Vikharev

Institute of Applied Physics, N.Novgorod, Russia, savilov@appl.sci-nnov.ru

In the physics of the quantum generators of coherent electromagnetic radiation (quantum lasers and masers), there exist well-known principles for production of extremely high-power optical pulses, which are successfully generated in a system with modulation of its quality factor Q (Q-switching or giant pulse formation) [1]. Naturally, it could be interesting to use a similar approach in classical electron masers (Fig. 1 a), and develop periodical-pulse generators of intensive rf radiation. This could be interesting for some applications associated with using coherent nanosecond rf radiation such as a spectroscopy, broadband radars, and high-gradient particle accelerators.

As electron masers are based on the use of a moving active media, a principal point is the relation between the group velocity of the interacting rf wave, V_{gr}, and the electron velocity, V_e. The period of rf pulse circle inside the cavity, $T = 2L/V_{gr}$, corresponds to the length of the electron beam moving through the cavity $L_T = L_f + L_b$, where $L_f = L(V_e - V_{gr})/V_{gr}$ and $L_b = L(V_e + V_{gr})/V_{gr}$ correspond to the forward and backward motion of the rf pulse, respectively. As $L_b / L_f > 1$, the most natural solution is a Q-switched backward-wave oscillator (BWO), where the counter-propagating rf pulse extracts the energy of a great number of electrons.

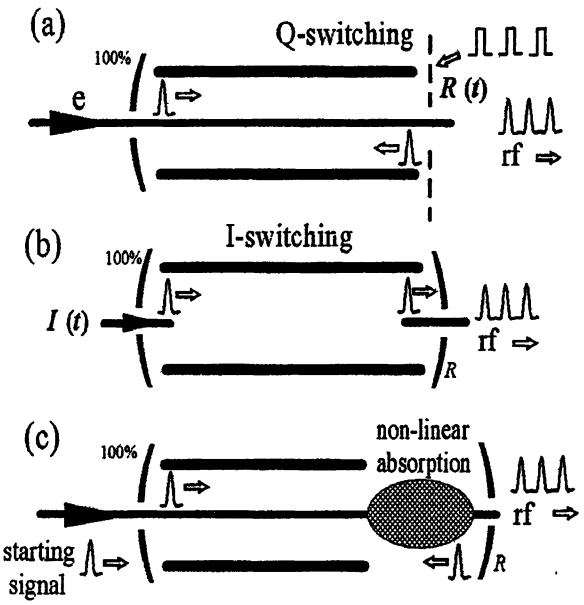

Fig. 1. Schematics of pulses-periodic electron based on the active Q-switching (a), the electron-current switching (b), and the passive Q-switching (c).

The Q-switch is assumed to be a fast, electrically-controlled element. Presently, the fastest switches are semiconductors excited by laser pulses [2], thereby promoting photoconductivity (Fig. 2). GaAs has the property of being converted from a nearly-ideal dielectric into a good conductor, on a femtosecond time scale. GaAs can have an extremely fast relaxation time in the range of 0.1 - 0.6 ns.

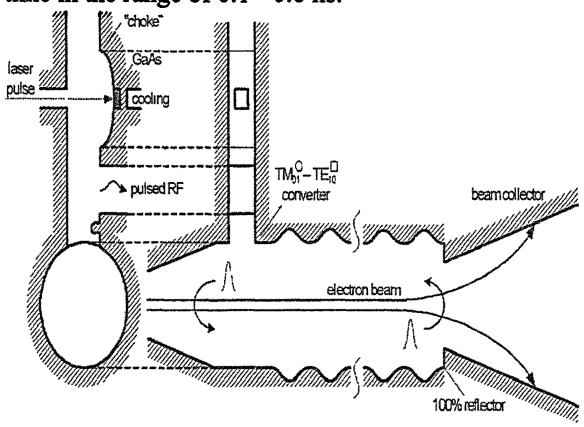

Fig. 2. Schematic of pulse-periodic BWO with resonant choke-type GaAs Q-switch. Resonant Q-switch is controlled by laser: $\lambda = 870$ nm, $W = 10$–100 nJ, rpt = 70 MHz.

According to simulation, the use of the Q-switching in a BWO can ensure realization of stable periodic generation of short powerful rf pulses. As compared to the conventional regime of the stable generation of a BWO with no feedback, in the Q-switched BWO the averaged electronic efficiency can be increased by an order of magnitude, whereas the peak power of output rf pulses is 40-50 times higher (Fig. 3).

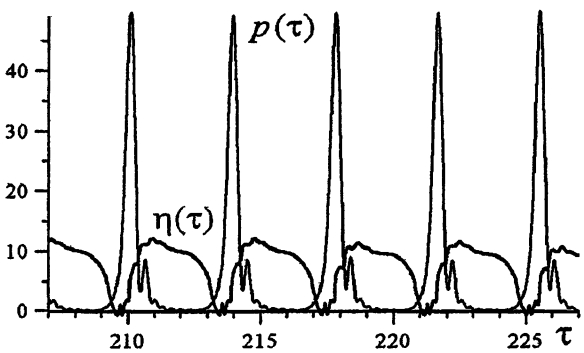

Fig. 3. Simulations of the Q-switched BWO, the stage of stationary pulse-periodic generation. Normalized output rf power, p, and normalized electron efficiency, η, versus the normalized time, τ. For the comparison, in the case of the stationary BWO with no feedback, $p = \eta \approx 1$.

The optimal regime of the Q-switched BWO is realized in the situation, when $V_e \approx V_{gr}$ and, therefore, $L_b / L_f >> 1$. In this situation, the averaged electron efficiency is high, as almost all electron beam interacts with the operating backward rf pulse. In addition, the self-generation from "idle" fraction of the e-beam (entering to the cavity during the non-

operating forward motion of the rf pulse) does not spoils the pulse-periodic generation imposed by the Q-switching.

The length of the output rf pulse is practically independent of the duration of the "feedback pulse", $R(t)$. This length just corresponds to the frequency band of the effective (resonant) electron-wave interaction. The Q-switching cannot impose a shorter length of the rf pulse by means of shortening the "feedback pulse"; in this case the rf-pulse spectrum includes components, which cannot effectively extract the electron energy and, therefore, which are not amplified by the electron beam.

As an example, a low-efficiency weakly-relativistic (20 keV) Cherenkov BWO with the length $L=5\lambda$ operates in the conventional regime of the stable generation with efficiency of 4%; correspondingly, the output rf power P_{rf}/P_e (normalized to the e-beam power) is also 4%. According to simulations, the use of the Q-switching in this BWO provides the pulse-periodic generations with the averaged efficiency of 40% and P_{rf}/P_e=170%. In the case of a relativistic (400 keV) BWO, the efficiency in the conventional regime is higher (15-20% in the case of $L\sim10\lambda$). For this BWO, simulations predict Q-switched operation with the efficiency of 70% and $P_{rf}/P_e = 320\%$.

A disadvantage of the BWO is that the length of the operating cavity is limited by the danger of the instability of the periodic pulse generation imposed by the Q-switching. The operating cavity can be significantly longer in the case of the resonant TWT, as it cannot be excited without the feedback (mirrors). Simulations predict that in the case of the resonant Q-switched TWT the peak power of the output rf pulses is at least 2-3 time higher as compared to the BWO. However, a disadvantage of the TWT if that the operating fraction of the e-beam (which interacts with the forward propagating rf pulse) is significantly shorter than the "idle" fraction (which passes through the cavity during the "idle" backward motion of the rf pulse) (Fig. 4). Therefore, the averaged efficiency of the pulse-periodic generation is low, as the "idle" e-beam fraction does not radiate.

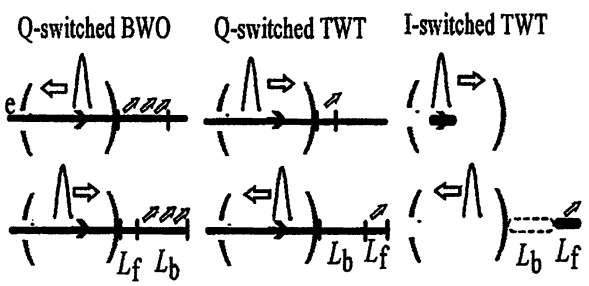

Fig. 4. Operating and "idle" fractions of the electron beam in the cases of Q-switched BWO, Q-switched TWT, and I-switched TWT.

A very prospective solution of this problem is just to cut off the "idle" fraction and, therefore, to use a periodic switching of the electron beam (Fig. 4). In this case, the whole modulated e-beam takes part in the electron-wave interaction. It is important that in the case the Q-switching is not needed. Actually, the rf pulse is formed by several axial modes of the long operating cavity. In order to provide the short rf-pulse, proper phases should be imposed upon these modes. In the case of the Q-switching, the modes form the rf pulse close to the output reflector only when it provides the feedback ($R\neq0$). In the case of the I-switching, the modes form the rf pulse inside the electron-wave interaction region only when the e-bunch presents there ($I\neq0$). Thus, numerical simulations of the I-switched resonant TWT (Fig. 5) demonstrate results, which are very similar to the Q-switched resonant TWT. A similar regime of I-switching can be organized also in the resonant BWO.

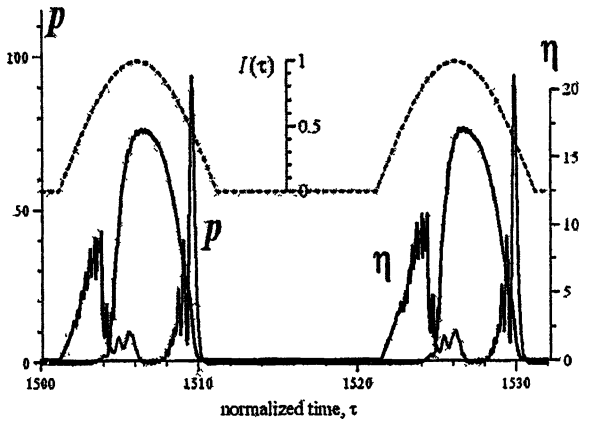

Fig. 5. I-switched resonant TWT, the stage of stationary pulse-periodic generation. Normalized output rf power, p, normalized electron efficiency, η, and the normalized e-beam current, I, versus the normalized time, τ.

Similar to the quantum lasers, it is attractive to organize a passive Q-switching in electron masers. In such a regime, electrons should amplify the operating powerful rf pulse, but do not amplify all small-signal spurious noises. Naturally, a single high-power input rf pulse is needed to start such oscillator (Fig. 1). It is important that the electron beam is a nonlinear media itself. The character (resonant or non-resonant) of the electron-wave interaction is determined by the amplitude of the operating wave. If the frequency of the input rf signal is relatively far from the frequency corresponding to the exact resonance, then this pulse is amplified only if its amplitude is high enough. Having based on this approach, it is possible to organize in a resonant BWO (with no active Q-switching and I-switching) quasi-stable pulse-periodic regimes of operation, when a single high-power input rf pulse induces generation of a series consisting of 20-30 output rf pulses.

References

1. *R. Paschotta.* Field Guide to Laser Pulse Generation. SPIE Press, Bellingham, WA (2007).

2. *A. A. Vikharev, G. G. Denisov, Vl. V. Kocharovski, S. V. Kuzikov et al.* Tech. Phys. Lett. 33, 735 (2007).

Quasi-Optical Theory of Submillimeter Relativistic Surface-Wave Oscillators

N.S. Ginzburg, A.M. Malkin, A.S. Sergeev, V.Yu. Zaslavsky

Insitute of Applied Physics RAS, Nizhny Novgorod, Russia, ginzburg@appl.sci-nnov.ru

At present, surface wave oscillators attract considerable attention as a source of millimeter and submillimeter radiation. In these oscillators rectilinear electron beam excites an evanescent slow wave of a periodic structure. The large number of successful experimental testing of such oscillators was carried out both with subrelativistic and relativistic electron beams [1-5]. For analysis of nonlinear dynamics of surface wave oscillators typically a 2D PIC code simulations are being carried out. In the case of relativistic electron beam for arrangement of synchronous Cherenkov type interaction it is sufficient to use a periodic structure with a shallow corrugation. Due to small corrugation depth it is possible to apply a quasi-optical approach for description of formation of surface wave and its excitation by a sheet electron beam.

We consider a 2D model of surface wave oscillator (Fig. 1) with microwave system formed by planar waveguide with the gap between plates b_0. We assume that one of the plates at the finite length l has a shallow sinusoidal corrugation $b(z)=b_1\cos(\bar{h}z)$, where $\bar{h}=2\pi/d$, d is the corrugation period, $b_1 << d$ is the corrugation amplitude.

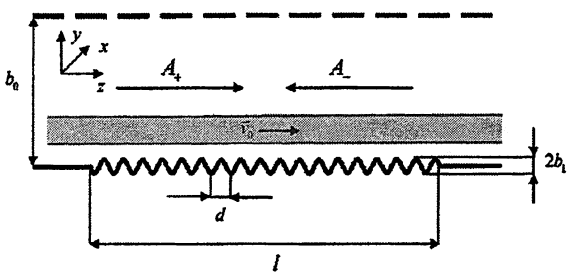

Fig. 1. A schematic diagram of planar surface-wave generator.

Radiation near a corrugated surface can be presented as a sum of two counter-propagating wave-beams with the following component of magnetic field

$$H_x=\mathrm{Re}\left[A_+(z,y,t)e^{i(\omega t-kz)}+A_-(z,y,t)e^{i(\omega t+kz)}\right] \quad (1)$$

$k=\omega/c$. Correspondingly the longitudinal component of electric field given by realations

$$E_z=-\mathrm{Re}\frac{i}{k}\left[\frac{\partial A_+}{\partial y}e^{i(\omega t-kz)}+\frac{\partial A_-}{\partial y}e^{i(\omega t+kz)}\right] \quad (2)$$

In the frame of quasi-optical approach the free diffraction of wave-beams at $y>0$ is described by parabolic equations. Due to corrugation under Bragg resonance condition $\bar{h}\approx 2k$ the coupling of wave-beams (1) occurs that can be described by the surface magnetic currents induced at the plane y=0:

$$\begin{aligned}&\frac{\partial A_+}{\partial z}+\frac{\partial A_+}{c\partial t}+i\frac{\partial^2 A_+}{\bar{h}\partial y^2}=i\alpha A_-\delta(y),\\&-\frac{\partial A_-}{\partial z}+\frac{\partial A_-}{c\partial t}+i\frac{\partial^2 A_-}{\bar{h}\partial y^2}=i\alpha A_+\delta(y),\end{aligned} \quad (3)$$

where $\delta(y)$ is the delta function, $\alpha=\bar{h}b_1/4$ is the coupling parameter.

Based on Eqs (3) let us find dispersion relation. Under assumption $b_0\to\infty$ one can present solution in the region $y>0$ as $A_\pm\sim e^{i(\Omega\mp\Gamma z+g_\pm y)}$, where $g_\pm=i\sqrt{-\bar{h}(\Omega/c\mp\Gamma)}$ are the transverse wave numbers and get a dispersion equation for the normal eigenwaves propagating over infinite corrugated

$$g_+g_-=-\bar{h}^2\alpha^2 \text{ or } \frac{\Omega^2}{c^2}-\Gamma^2=\frac{\bar{h}^2\alpha^4}{4} \quad (4)$$

As seen from Fig. 2 a dispersion curve of the normal wave is located below the light cone that corresponds to evanescent slow wave with exponential amplitude decay. For $\Gamma=0$ (so-called π-mode) a transverse decrement is given by: $|g_\pm|=\bar{h}^2b_1/4$.

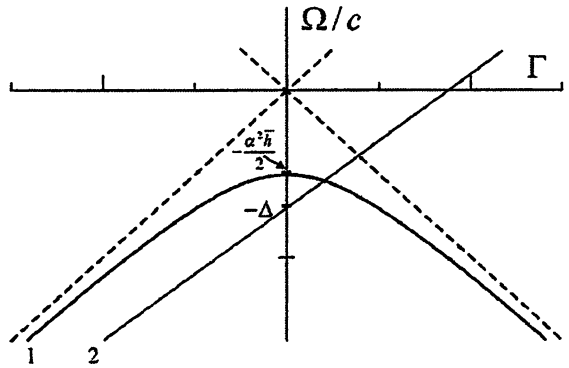

Fig. 2. (1) Normal surface-wave dispersion diagram. (2) Beam line $\Omega/c=-\Delta+\beta_\parallel\Gamma$.

We assume now that rectilinear electron beam moves along the corrugated surface. In the process of Cherenkov-type interaction the electron bunching is caused by the longitudinal component of electric field E_z which is given by (2). Correspondingly, taking into account the excitation of the forward wave A_+ by electron RF current the equations describing nonlinear dynamics of surface-wave oscillators can be presented in the form

$$\begin{aligned}&\frac{\partial\hat{A}_+}{\partial Z}+\frac{\partial\hat{A}_+}{\partial\tau}+i\frac{\partial^2\hat{A}_+}{\partial Y^2}+\sigma\hat{A}_+\delta(Y)=\\&\quad=i\hat{\alpha}\hat{A}_-\delta(Y)-\frac{1}{B_e}\frac{\partial}{\partial Y}(JF(Y)),\\&-\frac{\partial\hat{A}_-}{\partial Z}+\frac{\partial\hat{A}_-}{\partial\tau}+i\frac{\partial^2\hat{A}_-}{\partial Y^2}+\sigma\hat{A}_-\delta(Y)=i\hat{\alpha}\hat{A}_+\delta(Y).\end{aligned} \quad (5)$$

Here $F(Y)$ is the function describing the unperturbed the electron current density. Amplitude of RF current: $J = 1/\pi \int_0^{2\pi} e^{-i\theta} d\theta_0$ can be found from electron motion equations

$$\left(\frac{\partial}{\partial Z} + \beta_0^{-1}\frac{\partial}{\partial \tau}\right)^2 \theta = \mathrm{Re}\left[\frac{\partial \hat{A}_+}{\partial Y} e^{i\theta}\right], \qquad (6)$$

$$\theta|_{z=0} = \theta_0 \in [0, 2\pi), \quad \left(\frac{\partial}{\partial Z} + \beta_0^{-1}\frac{\partial}{\partial \tau}\right)\theta\Big|_{z=0} = \hat{\Delta}.$$

Here $\theta = \omega_0 t - k(\omega_0) z$ is the electron phase with respect of the forward wave, $\hat{\Delta} = (1-\beta_0)/\beta_0 G$ is the synchronism detuning. It should be noted that this detuning has obligatory positive value, $\Delta > 0$. Thus the synchronous interaction occurs only due to coupling between forward and backward waves and formation of evanescent slow-wave described by Eq. (5). In the equations (5), (6) we used following normalization:

$$Z = Gkz, \quad Y = \sqrt{2G}ky, \quad \tau = G\omega t, \quad \hat{A}_\pm = \frac{eA_\pm \mu}{mc\omega\gamma_0 G^{3/2}},$$

$\hat{\alpha} = \alpha/\sqrt{2G}$, $G = (2\sqrt{2}\frac{eI_0}{mc^3}\frac{\mu}{\gamma}\lambda)^{2/3}$ is the gain parameter, I_0 is the electron current, $\mu \approx \gamma_0^{-2}\beta_0^{-3}$ is the bunching parameter, $\sigma = k\varepsilon / G$ is Ohmic losses parameter, ε is the skin depth.

Boundary conditions for the wave-beams (1) at the edges of corrugated region correspond to the absence of external energy fluxes: $\hat{A}_+|_{Z=0} = 0$, $\hat{A}_-|_{Z=L} = 0$, where $L = Gkl$ is normalized system length.

In practice the sheet electron beam should be transported in the vacuum channel formed by the planar waveguide. If this gap is sufficiently large $\sqrt{2G}kb_0 >> 1$ the position of the second plate does not affect the characteristics of electron-wave interaction due to exponential decay of surface wave in y direction. Nevertheless it allows in numerical simulation to present the solution of Eqs (5) as sum of the modes of regular planar waveguide.

On the basis of Eqs (5), (6) we simulate the powerful relativistic submillimeter surface wave oscillator at wavelength of 0.6 mm. We take the electron energy 1 MeV, the current density 0.2 kA/cm, the corrugation period 0.236 mm, depth $2l_0 \approx 0.08$ mm. Corresponding normalized parameters $G = 1.9\times10^{-3}$, $\hat{\Delta} \approx 30$, $\hat{\alpha} \approx 8.7$, $\sigma \approx 6\times10^{-2}$, $L \approx 0.3$. In Fig. 3 the process of establishment of steady-state oscillations is shown. Profile of partial wave-beams in this regime is plotted in Fig. 4 that is closed to evanescent wave. The negative oscillations frequency shift also indicate on formation of slow wave. For practical application it is important to note that normalized efficiency corresponds to rather high electron efficiency about 25 %. The total radiation power of about 200 MW/cm with rather limited Ohmic losses at the level of 10 % from radiation power. Thus for the relativistic electron beam which excites slow-wave over smooth corrugation surface we have rather effective radiation outcoupling.

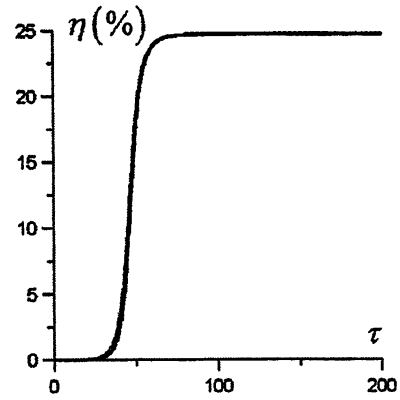

Fig. 3. Establishment stationary regime of oscillation in planar surface-wave generator.

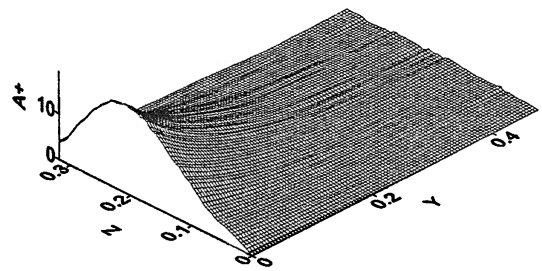

Fig. 4. Spatial profile of partial wave amplitude $A_+(Z,Y)$ in the stationary regime of oscillations.

Note in conclusion that based on a quasi-optical approach for further increasing radiation power it is possible to suggest two dimensional surface-wave oscillator with double periodic corrugation:

$$b(z,x) = b_1/2\left[\cos\left(\bar{h}_x x + \bar{h}_z z\right) + \cos\left(\bar{h}_x x - \bar{h}_z z\right)\right].$$

Similar to FEM with 2D distributed feedback coupling of four partial wave-beams will occur. Two of them will propagate in transverse X direction and synchronize radiation of large size sheet electron beam.

This work is supported by the Russian President grant for young Ph.D. scientists (Grant No. MK-5530.2011.2)

References

1. *A.N Vlasov., A.G Shkvarunets., J.S Rodgers, et al.* // IEEE Trans. Plasma Sci. 2000,V.28, P. 235

2. *S. P Bugaev., V. A , Cherepenin, V. I Kanavets., et al.* // IEEE Trans. Plasma Sci. 1990.V.18. P. 525

3. *Bratman V. L., Denisov G. G., Ofitserov M. M., et al.* // *IEEE Trans. Plasma Sci.*, 1987.V. 15. P. 2

4. *V. L. Bratman, A.E. Fedotov, P.B Makhalov.* // Appl. Phys. Lett. 2011.V.98. 061503.

5. V.L. Bratman, A.E. Fedotov, P.B. Makhalov, et al. // Appl. Phys. Lett. 2009. 94, 061501.

Planar FEM Driven by Two Microsecond Sheet E-beams

S.L. Sinitsky[1,2], A.V. Arzhannikov[1,2], V.T. Astrelin[1,2], N.S. Ginzburg[3], P.V. Kalinin[1,2], S.A. Kuznetsov[1,2], N.Yu. Peskov[3], A.S. Sergeev[3], V.D. Stepanov[1,2], M. Thumm[4], V.Yu. Zaslavsky[3]

[1]Budker Institute of Nuclear Physics SB RAS, Novosibirsk, Russia, sinitsky@inp.nsk.su
[2]Novosibirsk State University, Novosibirsk, Russia
[3]Institute of Applied Physics RAS, Nizhny Novgorod, Russia
[4]Karlsruhe Institute of Technology, Karlsruhe, Germany

Introduction

In previous stage of the experiments on the ELMI-device (BINP, Novosibirsk) the operation of 4-mm single channel free electron maser (FEM) with planar geometry and two-dimensional (2D) distributed feedback was studied [1]. In this scheme the spectrum measurements using heterodyne diagnostics demonstrated single-mode oscillation regime in the vicinity of 75 GHz with pulse duration of about 300 ns at tens megawatt power level. These results provided a background for development of two-stage generator of sub-mm radiation exploiting an intercavity scattering in two-channel FEM driven by two parallel sheet beams [2]. At the first step of experimental realization of this idea we studied simultaneous generation and transport of two sheet electron beams 0.8 MeV / 1–2 kA / 3 μs having the cross-section of 0.4 cm × 7 cm in the slit channels [3], which are similar to the electrodynamic system of two-channel FEM. Electron-optical experiments demonstrated that these beams can be transported in vacuum channels with the cross section of 0.95 cm × 9 cm at the length of 1.5 m in the guide magnetic field of 1÷1.7 T. The paper presents results of experiments on generation of mm radiation in two parallel FEM with 2D distributed feedback driven by these two beams.

Experimental setup

Scheme of the present experimental set-up for generation of mm radiation in two-channel FEM is shown in Fig. 1. Microwave system of each channel is a planar hybrid Bragg resonator [4] formed by upstream 2D and the down-stream 1D Bragg reflectors of the length of 20 cm each and regular waveguide section of 32 cm long. To eliminate influence of parasitic modes due to reflection by side walls of the 2D reflector we used the wave dispersers with comb surface [4] which consists of conducting segments inclined at a random angle with period of 2 cm.

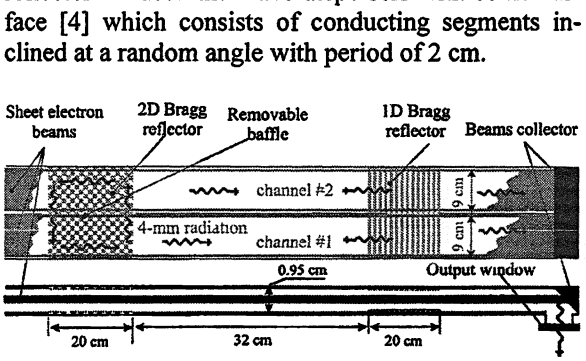

Fig. 1. Scheme of the experiment (side and top views)

In the first series of experiments the two channels of FEM were separated by a baffle in the region of 2D Bragg reflectors. Nevertheless some interchannel diffraction coupling can take place in the output section. After passing the resonators the electron beams are transported to the collectors. Here after the beam cross-sections expansion using diverging magnetic field the beams are dumped in the graphite which surface is inclined at 45° to the beam direction. The mm-waves outgoing from the resonators also pass these channels to the beam collectors where these waves are reflected to the output windows (see Fig. 1). From these windows the radiation by means of circular waveguides is transported to a special shielded measuring room.

The RF-pulse is measured by detectors on "hot carriers" in Ka- and W-bands. The spectral measurements of the radiation in W-band at this stage of the experiments were carried out by means of 4-channel spectral diagnostics including the set of waveguide couplers, band-pass filters and Shottky diodes. The pass-bands of each channel are shown in Fig. 2. The energy of the radiation pulse is measured by TK Absolute Power/Energy Meter.

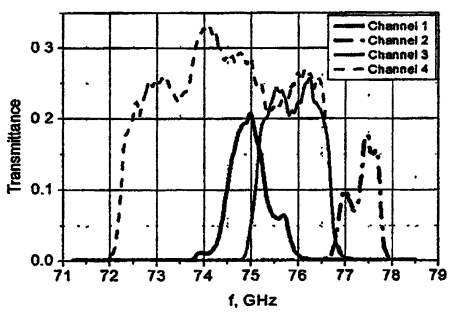

Fig. 2. Sensitivities of the spectral channels

Experimental results

Results of the first experiments on generation of mm radiation in two-channel FEM are shown in Fig. 3 and presents oscilloscope traces of the diode voltage, beam current and RF-pulse in typical shot. Analyzing the data obtained from the 4-channel spectral diagnostics (see Fig. 4) we find that in the shots with a high radiation power the main spectral fraction (about 70 % power) is contained in the 1st band (74.5–75.5 GHz), about 30 % in the 2nd (77–77.8 GHz) and the 3rd channel detects some part of the radiation from 1st band due to the band overlapping. If one subtracts the contribution of the 1st and

3rd channels from the signal of 4th channel taking into account the integrals of sensitivity for each channel the result should be close to zero (see Fig. 4). It means that the radiation power in the range of 72.3–74.5 GHz is rather small in comparison with 1st and 2nd bands.

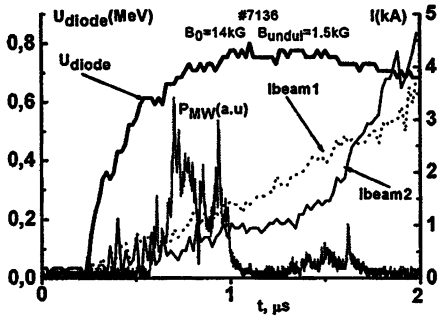

Fig. 3. Typical traces of the diode voltage U_{diode}, beam currents in two FEM channels I_{beam1}, I_{beam2} and radiation power in the 1st band of spectral diagnostic P_{MW}

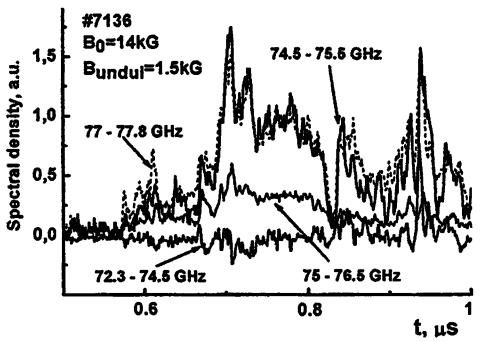

Fig. 4. Power signals divided by integrals of sensitivity in W-band

As a result, the experiments demonstrate that the main part of the generated radiation detected in 1st frequency band, which corresponds to the designed frequencies and belongs to excitation of the operating modes of hybrid Bragg resonators [4]. Admixture of the radiation in the 2nd band is related to parasitic coupling of TEM and TE_2 waves on the down-stream 1D reflector and the plasma coming from the diode.

The next series of measurements were aimed to study the radiation power in these two bands as a function of the undulator field amplitude at various values of the guide magnetic field. This dependence for the 1st band is presented in Fig. 5. Increase of the

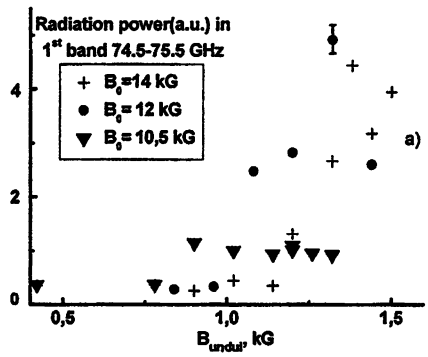

Fig. 5. Radiation power averaged during RF-pulse vs the undulator field at various guide magnetic fields. Measurement errors of data do not exceed 7 %

undulator field above some threshold provides rapid growth of the radiation power from noise-level to the maximal value, which depends on the guide magnetic field. This behavior agrees well with the simulation [5], however the maximums measured in the experiments are slightly shifted to higher undulator fields. Direct comparison of theoretical and experimental results is difficult in our case because the beginning of mm-wave generation occurs at different energies of the electrons which is also dependent on the undulator field. Similar behavior of the radiation power is observed in the 2nd frequency band but at few times lower power level.

The measurement of the energy of the radiation pulse for the frequencies higher 70 GHz by means of TK Absolute Power/Energy Meter gave the value of about 2-4 J and the average power 10-20 MW from each channel of the FEM.

Conclusion

Present experiments at "ELMI" accelerator is aimed to development multichannel sub-mm generator. At this preliminary stage we demonstrated possibility of formation of two parallel sheet beams with acceptable parameters for generation of mm radiation when driven two-channel FEM.

We should note that in all series of the experiments the signals from the "hot carrier" detectors, which measured the radiation power from two channels of the FEM, had practically the same shapes and time behavior. At the next stage we plan to improve selectivity of the resonator to suppress parasitic generation. Also, heterodyne measurements of the radiation spectrum will be performed. Demonstration of synchronization of radiation in two FEM channels will be done when the baffle between channels in the up-stream 2D Bragg structure will be removed.

This work is supported by grant 11.G34.31.0033 of the Government of Russian Federation.

References

1. *A.V. Arzhannikov, N.S. Ginzburg et al.* Investigation of Mode Structure for MM-Wave Radiation Pulses Generated by Planar FEM at 2-D Distributed Feedback // Proc. of 16th Int. Conf. on High-Power Particle Beams, Oxford, UK, 2006. P. 19.

2. *A.V. Arzhannikov, N.S. Ginzburg et al.* Intercavity Scattering Scheme for Two-stage Generation of submillimeter Radiation on the Base of Planar 2D Bragg FEM // Proc. of Int. Workshop "Strong microwaves in plasmas", Nizhny Novgorod, Russia, 2006. V. 1. P. 228-232.

3. *S.L. Sinitsky, A.V. Arzhannikov et al.* Simultaneous Generation and Transport of Two Microsecond Sheet REBs in Application to Multichannel FEM // IEEE Trans. on Plasma Sci. 2009. No. 10. P. 1885-1889.

4. *A.V. Arzhannikov, N.S. Ginzburg et al.* Generation of Spatially Coherent Radiation in Free Electron Masers with Two Dimensional Distributed Feedback // JETP Lett. 2008. V. 87, N. 11. P. 618-622.

5. *A.V. Arzhannikov, N.V. Agarin et al.* Operation of High-power Planar FEM with Two-dimensional Bragg Reflectors // Proc. of 13th Int. Conf. on High-Power Particle Beams, Nagaoka, Japan, 2001. V. 1. P. 244-247.

Gyrotron Complexes for Technological Applications

E.A. Soluyanova[1], Yu.V. Bykov[2], A.V. Chirkov[2], G.G. Denisov[2], E.A. Kopelovich[2], V.B. Orlov[1], A.B. Pavelyev[2], E.V. Sokolov[1], E.M. Tai[1]

Gycom Ltd, Nizhny Novgorod, Russia, solu@mail.internet2.ru
*Institute of Applied Physics, Nizhny Novgorod, Russia

Experience of Russian CW gyrotrons for technological applications started in the 1970s. On the whole, more than 30 CW gyrotron systems were manufactured and delivered to customers. "Classic" CW gyrotrons operate in oil magnets at the second magnetic field harmonic and have the longitudinal operating waveguide mode output. The typical operating frequencies are from 24 to 30 GHz, the voltage does not exceed 25 kV, the output power is up to 25 kW, and the efficiency, up to 40 %. However, the total efficiency of the gyrotron complex does not exceed 20 % due to high power consumption in oil magnets.

The progress in frequency, output power and efficiency enhancement was achieved due to operation at the first cyclotron harmonic in superconducting magnets. Development of such systems was due to applications in ceramic sintering and sources of multicharged ions. The series of CW gyrotrons manufactured in the 1990s had frequencies of 40–85 GHz, output power of up to 40 kW, operating voltage of up to 50 kV, and overall efficiency of more than 30 %. Design features included quasi-optical built-in converters of operating waveguide mode to the Gaussian wave beam, lateral direction of wave beam output, and the triode-type electron gun. The gyrotrons were installed in the cryomagnet warm bore on the cathode side, with the setting bore diameters ranging from 110 to 140 mm. The disadvantages of those systems were low efficiency of the quasi-optical mode converter and, consequently, a high level of the stray radiation lost in the vacuum volume. The stray radiation heats the gyrotron body and the cathode, and the time of full thermo-stabilization reaches 40–50 minutes. That limits the maximum HF energy during a single switching-on and, correspondingly, does not allow operating in the real CW regime with an output power of more than 25 kW.

In the last decade, design of technological CW gyrotrons has been optimized. The tubes are equipped with the CPD collector and a high-efficiency built-in converter. Main design features include the diode-type electron gun with a high-temperature LaB_6 cathode, minimized geometrical dimensions, and a stainless-steel water-cooled body. Actually, the body is used as an absorber of stray radiation. The design principles are similar to those for high-power CW gyrotrons used in plasma heating applications. The maximum output power is limited by the possibility of the boron nitride output windows. The final output parameter of gyrotron systems are as follows: output power up to 50 kW, operating frequency 40 ÷ 85 GHz, beam voltage < 30 kV, beam current < 4 A, anode voltage < 20 kV, anode current < 0.1 A, filament power < 500 W, efficiency 45 ÷ 50%, cooling water flow ~4 l/s, input cooling water pressure ~3 bar.

Whenever necessary, CW gyrotrons can be provided with all accessories of a gyrotron complex, namely, a matching optic unit, a cryomagnet, a waveguide line, a calorimetric load, a test bench, two highvoltage power supplies, power supply units for the cryomagnet, gyrotron filament and ion pump, a water cooling system, high voltage, arc and water flow rate protection, and an automated control unit. A typical scheme of the gyrotron system without power supplies and a control rack is shown in Fig. 1. During operation, the systems showed good controllability and high reliability. Further progress is associated with the use of liquid-free magnets.

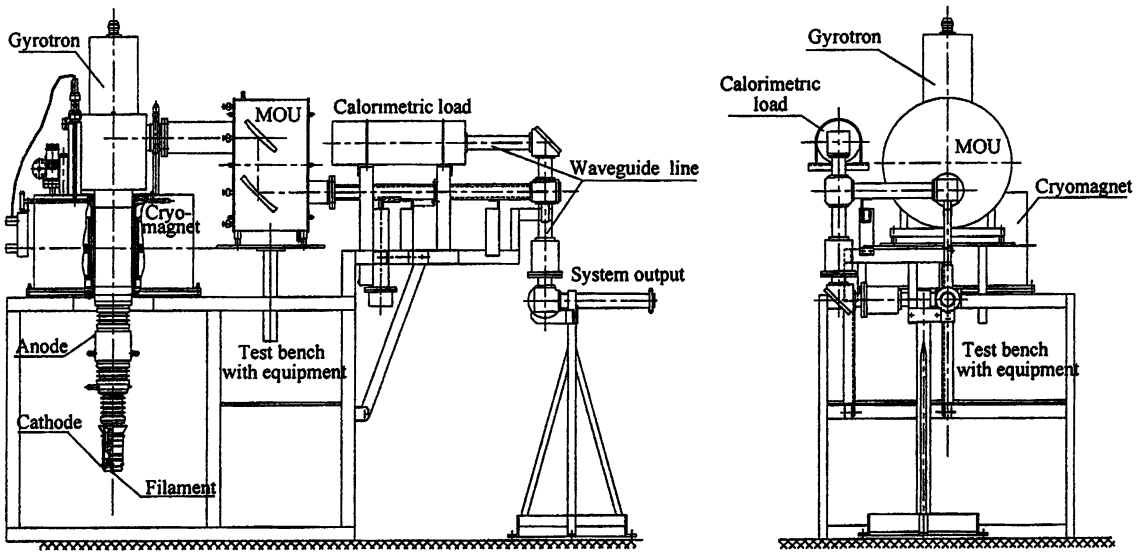

Fig. 1. Typical scheme of the gyrotron system

Experimental Investigation of the S-band Relativistic Cherenkov Microwave Oscillator without a Guiding Magnetic Field at the Repetitively Pulsed Modes

E. M. Totmeninov, S. A. Kitsanov, P.V. Vykhodtsev

Institute of High Current Electronics, Tomsk, Russia, e-mail: totm@lfe.hcei.tsc.ru

I. Introduction

An attempt to realize a repetitively pulsed operation mode of a Cherenkov microwave oscillator without an external magnetic field was made in this research. The generator belongs to the class of the devices such as MILO [1] and vircator [2] in which an external magnetic field is not required to generate high-power microwave radiation (pasotron [3] is a nonrelativistic analogue of this device). In the previous experiments, single modes of oscillator operation were realized for the electron energies of 0.5 MeV [4] and 1.2 MeV [5]. In the process of experimental investigation of the oscillator for the electron energy of 0.5 MeV it was found out that replacement of a velvet-covered cathode for a metal-dielectric blade one results in essential decrease of the oscillator efficiency and increase of generation instability up to its complete absence. Thus, basing on the results of the work [4], it appears to be reasonable to check the operation of the given oscillator using a velvet-covered cathode for the electron energy of 1.2 MeV both in a single and in a repetitively pulsed mode. The latter is particularly actually since from the point of view of practical application, microwave oscillators operating in a repetitively pulsed mode are of the most interest. Information concerning the lifetime of the velvet-covered cathode and anode grid of the oscillator seems to be interesting as well. It is expedient as well to carry out analogous investigations for the oscillator developed for the electron energy of 0.5 MeV since increased lifetime of the velvet-covered cathode and anode grid is to be expected owing to the less values of the electron current density and beam energy.

II.Experimental setups

The experiments were performed on the SINUS-7 nanosecond repetitively pulsed electron accelerator [6] with voltage pulse duration was ≈ 50 ns and the pulse repetition frequency was up to 50 Hz. Electrons were emitted from a ~70-mm-diameter velvet-covered cathode placed inside a focusing stainless steel electrode [4]. The anode grid of the generator was a 0.2-mm-diameter stainless steel wire with a square mesh. The electrodynamic system of the oscillator consists of an anode grid (G) and a corrugated slow-wave structure (SWS) of the mean diameter which is ~1.3 times greater than the wavelength (Fig. 1.). The electrochemical treatment of the storage electrode surface was used to increase its electric strength. The microwave power was measured using a calibrated waveguide-to-stripline coupler and integration of the power flux density over radiation pattern measured with a short dipole antenna. The oscillation frequency was measured by a TDS 7404 oscilloscope with a built-in fast-Fourier-transform converter.

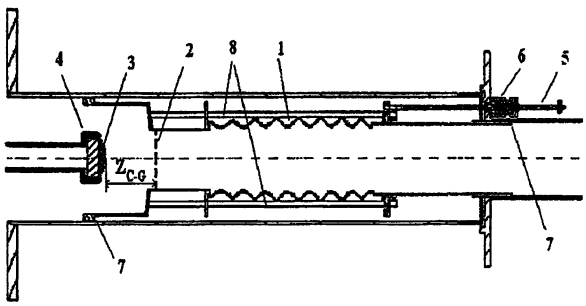

Fig. 1. Schematic design of the oscillator: *1* – SWS, *2* – anode grid, *3* – velvet-covered cathode on a metal base plate, *4* – storage electrode, *5* – rod for changing the anode-cathode gap $Z_{C\text{-}G}$ without vacuum breakdown of system, *6* – vacuum seal, *7* – plungers, *8* – studs.

III. Oscillator for 1.2 MeV electron energy

The electrodynamic system of the oscillator previously designed for 1.2 MeV electron energy [5] and 12-mm anode grid mesh side was used in this experiment. The butch mode of 20 pulses with a 10-Hz repetition frequency was chosen for testing the anode grid and velvet-covered cathode lifetimes. Increasing the number of pulses in a butch over 30 results in the anode grid destroy. At the repetition frequency exceeding 10 Hz, the electron accelerator operation becomes more unstable. Successive batches were alternated with a ~5 min rest and every 500 accelerator pulses were alternated with a ~30 min rest, respectively. Electron beam parameters were stabilized after the first 1-2 pulses of a batch. The diode voltage and the diode current averaged amplitudes were ≈1.1 MV and ≈12 kA, respectively (Fig. 2*a*). The microwave peak power values were, respectively, 2.1 ± 0.4 GW using the waveguide-to-stripline coupler and 1.8 ± 0.3 GW using the antenna. Thus, the average microwave peak power was about 2.0 ± 0.4 GW. The oscillator efficiency calculated using the total diode current value was 15 ± 3%. The average microwave pulse width was about 17 ns at the oscillator frequency 4.04 GHz (Fig. 2 *b*). The standard deviation of microwave signal amplitudes was not greater than 10%. It was shown earlier [4,5] that only about 60-70% of the total diode current passes into the drift tube region. The oscillator efficiency can be estimated as ≈ 23% taking into account the current passed through the anode grid rather than the total diode cur-

rent. The anode grid was destroyed after ≈3000 accelerator pulses.

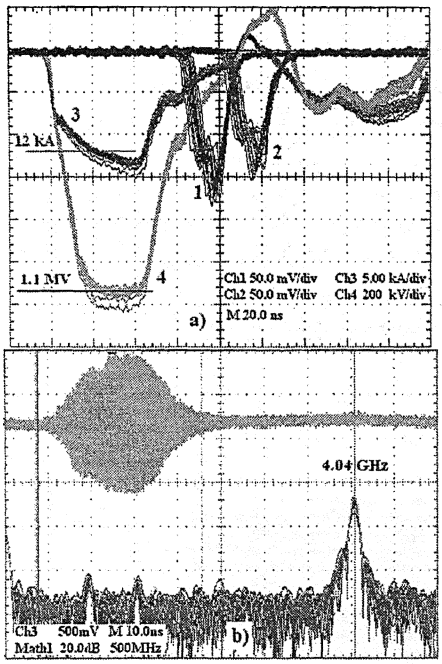

Fig. 2. Waveforms of detected signals from the coupler (1) and antenna (2), diode current (3), diode voltage (4): *a*) – 20-pulses batch mode with a 10-Hz repetition frequency, *b*) – RF signals from a waveguide-stripline coupler and its spectrum.

IV.Oscillator for 0.5 MeV electron energy

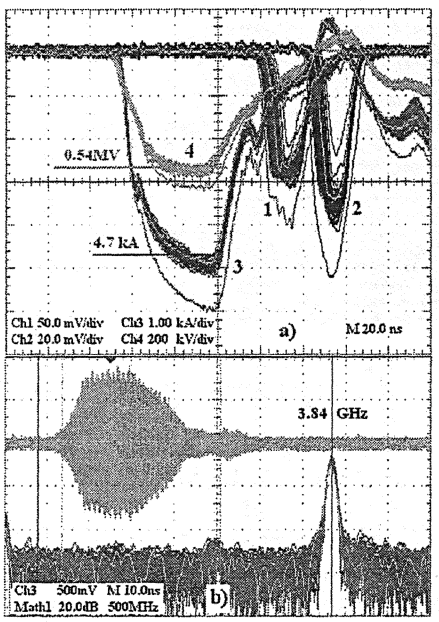

Fig. 3. The waveforms at a 60-pulses batch mode with a 30-Hz repetition frequency.

The electrodynamic system of the oscillator previously designed for 0.5-MeV electron energy [4] and 4-mm anode grid mesh side was used in this experiment. The butch mode of 60 pulses with a 30-Hz repetition frequency was chosen for testing the anode grid and velvet-covered cathode lifetimes. The diode voltage and the diode current averaged amplitudes were ≈0.54 MV and ≈4.7 kA, respectively (Fig. 3*a*). The microwave peak power values were, respectively, 0.2 ± 0.04 GW using the waveguide-to-stripline coupler and 0.21 ± 0.04 GW using the antenna. Thus, the average microwave peak power was about 0.21 ± 0.04 GW. The oscillator efficiency calculated using the total diode current value was 8 ± 2%. The average microwave pulse width was about 15 ns at the oscillator frequency 3.84 GHz (Fig. 3*b*). The standard deviation of the microwave signal amplitudes was not greater than 10%. Microwave radiation parameters remained stable up to the moment of vacuum breakdown of the system. This can testify to the absence of essential degradation of the velvet-covered cathode emissive ability. The oscillator efficiency can be estimated as ≈ 12% taking into account the current passed through the anode grid rather than the total diode current. External visual examination of the anode grid (after 11000 accelerator pulses) showed that it was undamaged.

V. Conclusion

Thus, in the experiment, the repetitively pulsed Cherenkov oscillators without a guiding magnetic field were realized. In the batch modes with the pulse rate of 10 Hz and electron energy of 1.2 MeV the oscillator efficiency was 15% at 2.0 GW output power and carrier frequency 4.04 GHz. The lifetime of the anode grid was about 3000 pulses. For the electron energy of 0.5 MeV and pulse rate of 30 Hz the oscillator efficiency was 8% at 0.21 GW output power and carrier frequency 3.84 GHz. The lifetime of the anode grid and velvet-covered cathode exceeded 11000 pulses. The standard deviation of the microwave signal amplitudes was not greater than 10% that is optimistic for oscillator without a guiding magnetic field.

References

1. *M.D. Haworth, G. Baca, James N. Benford, et al.*, "Significant pulse-lengthening in a multigigawatt magnetically insulated transmission line oscillator", *IEEE Trans. Plasma. Sci.* Jun. 1998. V. 26, No. 3. P. 312–319.

2. *S.A. Kitsanov, A.I. Klimov, S.D. Korovin, et al.*, "A vircator with electron beam premodulation based on high-current repetitively pulsed accelerator", *IEEE Trans. Plasma. Sci.* Feb. 2002. V. 30. P. 274–285.

3. *G.S. Nusinovich, Yuval Carmel, A. G. Shkvarunets et al.*, "The Pasotron: Progress in the Theory and Experiments", *IEEE Trans. Electron Devices.* May 2005. V. 52, No. 5. P. 845–857.

4. *E.M. Totmeninov, A.I. Klimov, V.V. Rostov* "Relativistic Cherenkov Microwave Oscillator without a Guiding Magnetic Field for the Electron-Beam Energy of 0.5 MeV", *IEEE Trans. Plasma. Sci.* 2010. V. 38, Issue 10. Part 2. P. 2944–2947.

5. *E.M. Totmeninov, A.I. Klimov, V.V. Rostov* "Relativistic Cherenkov Microwave Oscillator without a Guiding Magnetic Field", *IEEE Trans. Plasma. Sci.* July 2009. V. 37, No. 7. P. 1242–1245.

6. *S.D. Korovin, V.V. Rostov*, "Repetitively pulsed high current electron accelerators on basis of the TESLA transformer", *Rus. Phys. J.* Dec. 1996. V. 39, No. 12. P. 21–30.

Last Test Results of 170 GHz / 1 MW / 50% / CW Gyrotron for ITER

S.V. Usachev[b], L.G. Popov[b], V.I. Ilin[c], M.V. Agapova[b], G.G. Denisov[a], A.Ph. Gnedenkov[b], V.N. Ilin[b], A.P. Khvostenko[c], A.N. Kostyna[b], A.N. Kuftin[a], A.G. Litvak[a], V.I. Malygin[a], V.E. Myasnikov[b], V.O. Nichiporenko[b], V.N. Novikov[c], V.G. Rukavishnikova[b], E.V. Sokolov[b], E.A. Soluyanova[b], E.M. Tai[b], V.G. Usov[a], Yu.M. Yashnon[b], V.E. Zapevalov[a]

[a] Institute of Applied Physics, 46 Ulyanov Street, Nizhny Novgorod, 603950, Russia
[b] GYCOM Ltd., 46 Ulyanov Street, Nizhny Novgorod, 603155, Russia
[c] Tokamak Physics Institute, RRC "Kurchatov Institute", 1 Kurchatov Sq., Moscow, 123182, Russia

Test results of ITER gyrotrons V-10 and V-11 obtained in the Kurchatov Institute facility are presented. Output power of 1MW with total efficiency of 53-55% was attained. Pulses were extended up to 1000 sec at 800-kW power for V-10 and at 850-kW power for V-11. For the gyrotron V-10 reliability of 90% was demonstrated by the train of ten 800 kW / 600 sec pulses.
At 1 MW regime maximal pulse duration of 578 sec was reached for the V-10 gyrotron. The gyrotron V-11 is conditioning now to provide high reliability of 1 MW / 400 sec pulses according to ITER requirements.

Intoduction

The long term development of Russian 170 GHz / 1 MW / 50% / CW gyrotron for ITER is coming to the final stage. The gyrotron design was elaborated by GYCOM/IAP and a lot of experimental prototypes of ITER gyrotron were manufactured and tested [1, 2]. Furthermore the special gyrotron test facility in Kurchatov Institute was constructed. It has evacuated transmission line with 1-MW terminal load, all necessary auxiliary equipment and CW power supplies.

The last gyrotrons V-10 and V-11 were produced following conventional GYCOM/IAP design of 170 GHz / 1 MW / CW gyrotron and equipped with especial liquid cooling system of DC break ceramic insulator. Perfluormetildecalin which is used as a coolant is one of fluorocarbon liquids and has enough electrical strength to prevent arcing. These two gyrotrons differ in launcher manufacture technology and anti-dynatron coating type of cathode parts.

Fig.1 shows the gyrotron V-10 installed into LHe-free cryomagnet ("Cryomagnetics", USA) and connected through the matching optics unit (MOU) to evacuated transmission line.

Test Results of ITER Gyrotrons V-10 and V-11

V-10

At first at 100-ms pulse duration operational regime was optimized. At operational beam voltage of 71-72 kV and beam current of 44-45 A output power of 1MW was attained. Total efficiency of 53-55% was reached at retarding voltage of ~30 kV.

It was found that output power 50% modulation is provided when retarding voltage is modulated by ~7 kV.

After gyrotron conditioning and operating regimes optimizing the pulse duration of 1000sec at 800kW power was attained. Fig. 2 demonstrates calorimetry traces recorded in the terminal load in this regime. Operation reliability was examined by 600sec pulse train (10 pulses) with duty factor 1:6. Only 1 pulse was stopped by cut-off protection system at 510 sec. Test was carried out under ITER representatives' supervision.

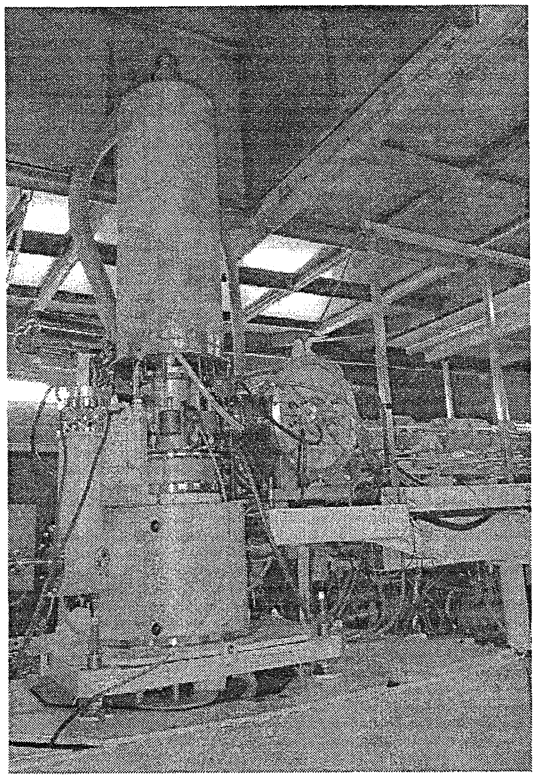

Fig. 1. ITER gyrotron in the test facility in Kurchatov Institute

At 1 MW regime maximal pulse duration of 580sec was reached. During test there were also measured fractions of stray radiation absorbed in MOU (~3%) and emanating through relief window (~4%). Diamond window losses were determined as ~0.1%. Due to very high total efficiency collector dissipation power did not exceeded 800 kW.

Unfortunately in 1-MW power regime current instabilities appeared at beam current of 45A. During first 350-450 sec all the signals were rather stable. Beam current stability was supported by automatic control system through a feedback embedded into heater circuit. At some critical point both body current and beam current started to rise. Control system which follows up both beam current value and its derivative reduced heater power up to zero but neverthe-

less in a few seconds beam current rose from 45 A to ~53 A when HV was tripped by current interlock.

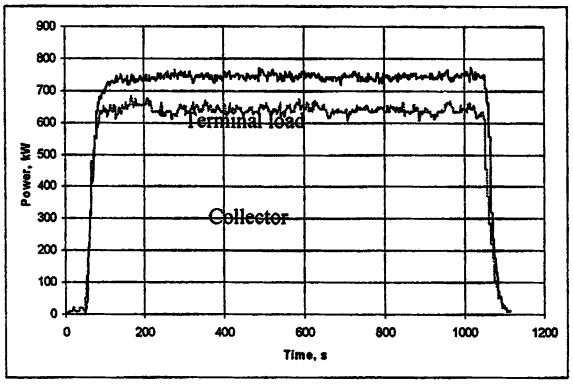

Fig. 2. Power calorimetry traces in the collector and in the terminal load of the gyrotron V-10

Long pulse operation at 1MW power was renewed by modification of gun magnetic field. To check a reliability of this regime a series of 1MW/400s pulses was made. Seven of them were successful. One pulse was terminated by gyrotron arcing and one pulse by cut-off protection. In neither of pulses spontaneous beam current rise was watched. So the main ITER originaly specified parameters (1MW/50%/400s) were attained.

V-11

Behavior and characteristics of the gyrotrons V-10 and V-11 are very similar. At operational beam voltage of about 70 kV and beam current of 45A output power of 1MW with efficiency of 55% was attained. Due to better anti-dynatron cathode coating in V-11 body current dropped to 3-5mA being compared with 40-50mA value for V-10. New technology of dimple-wall launcher manufacture didn't result in essential reduction of stray radiation level.

For this gyrotron current instability in 1-MW regime was also watched at the same beam voltage of 70kV and beam current of 45A in original gun magnetic field configuration. But due to better anti-dynatron cathode coating and thus lower body current it was possible to provide its stable operation at current of 39A corresponding to 900kW output power. After gun magnetic field was modified similarly to V-10 case pulse length of 400s at 1MW output power was attained. Test is continuing now.

In the table 1 the results of the last gyrotron tests are summarized.

Table 1. Summary of test results

N	Power at MOU outlet kW	Efficiency %	Pulse duration sec
V-10	~750	~54	1000
			600 (90% good pulses)
	~960	~53	578
		~55	400 (7 good pulses)
V-11	~850	~53	1000
	~960	~55	400
			(test is continuing)

To date the main original ITER requirements have been attained. There are some optional specifications under ITER discussion to provide now:

- Gyrotron reliable operation in 1-MW regime at pulse elongation to 1000 s
- Ensuring of a gyrotron service time up to 5 years
- Development and manufacture of ITER gyrotron on-site infrastructure components.

Conclusions

The prototype V-10 of ITER gyrotron with upgraded body insulation and liquid cooling of DC-break ceramic has been manufactured and tested. Max pulse duration of 1000s was reached at 0.8 MW power and 34-A beam current. 800kW/600sec regime reliability of 90% was demonstrated.

After modification of gun magnetic field 1-MW 400 sec pulse regime at 45-A beam current was attained.

Gyrotron V-11 with improved processing of dimple-wall mode converter has been manufactured. It has also upgraded anti-dynatron coating of non-emitting cathode parts. During short period of test pulse duration of 1000s was attained at 900-kW output power and 39-A beam current. Pulse duration of 400s was attained at 1MW output power and 45-A beam current. Test is continuing.

Both gyrotrons meet the ITER original specification (1MW/50%/400s).

References

1. *M.V.Agapova et al.*, Proc. 6th Inf. Workshop "Strong Microwaves in Plasmas". Ed. A.G. Livak. Nizhny Novgorod, 2006, v.1. pp. 107-112.

2. *L.G.Popov et al.*, Proc. 7th Inf. Workshop "Strong Microwaves in Plasmas". Ed. A.G. Livak. Nizhny Novgorod, 2009, v.1. pp. 95-99.

A Study of Harmonic Multiplying Gyrotron Traveling-wave Amplifiers with Distributed Wall Losses and Attenuating Severs

Y.S. Yeh[1], C.L. Hung[2], T.H. Chang[3], Y.C. Lo[1], C.W. Hung[1]

[1]Department of Electro-Optical Engineering, Southern Taiwan University, Tainan 710, Taiwan, yihsen@mail.stut.edu.tw
[2]Department of Communication Engineering, National Penghu University of Science and Technology, Penghu 880, Taiwan
[3]Department of Physics, National Tsing Hua University, Hsinchu 300, Taiwan

The high power and broad bandwidth capabilities of gyrotron traveling-wave amplifiers (gyro-TWTs) make them attractive sources in the millimeter wave range. Unlike conventional linear beam devices, the electron beam used in a gyrotron exhibits transverse motion at the electron cyclotron frequency. The electron cyclotron harmonic operation by the proper choice of a transverse electric (TE)-mode and a harmonic number has been an attractive solution to meet the demand for high-frequency amplifiers alleviating the drive frequency and magnetic field requirement [1, 2]. However, the additional degree of freedom provided by the multitude of cyclotron harmonics in a gyro-TWT also generates several spurious oscillations.

Distributed-loss gyrotron traveling-wave amplifiers with high-gain, broadband, and millimeter-wave capabilities have been demonstrated. Most structures with distributed wall losses are stabilized in gyro-TWTs that operate at low beam currents. Attenuating severs are added to the interaction circuit of a distributed-loss gyro-TWT to prevent high beam currents that result in mode competition [3].

This study proposes Ka-band and W-band harmonic multiplying gyro-TWTs, using distributed wall losses and attenuating severs, to improve the stability of the amplification and the performance of the amplifiers. By amplifying a TE_{11} (s=1) drive wave, the second harmonic component (s=2) of the beam current initiates a TE_{21} wave to be amplified. A nonlinear self-consistent code, based on a slow time scale formulation, is developed to evaluate the performance of stable gyro-TWT amplifiers. The electron beam interacting with multiple waveguide modes (TE_{mn}) is presumed. Thus the structural nonuniformity must be sufficiently weak to prevent mode conversion.

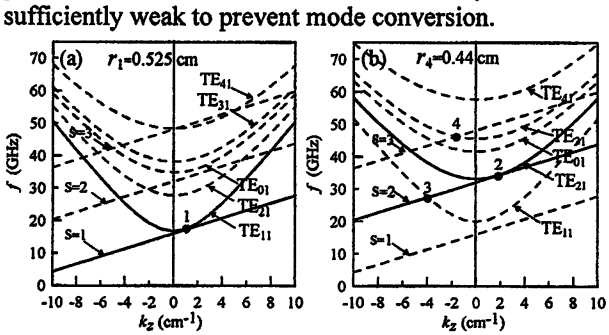

Fig. 1. $\omega - k_z$ diagram of the transverse electric waveguide modes and the cyclotron harmonic beam-wave resonance lines in the Ka-band harmonic multiplying gyro-TWT.

Figure 1 (a) and (b) plot the $\omega - k_z$ diagram of the transverse electric waveguide modes as well as the cyclotron harmonic beam-wave resonance lines at the wall radii r_1=0.525 cm and r_5=0.44 cm, respectively. The interactions in the forward wave region (points 1 and 2) are sources of absolute instabilities where as those in the backward wave region (points 3 and 4). The gyro-TWT has five sections, which are a lossy section, a taper section, a severed and two copper sections, as depicted in Fig. 2(a). The parameters of the gyro-TWT are beam voltage V_b =60 kV, magnetic field B_0 =6.272 kG, guiding center radius r_c =0.25 cm, and perpendicular-to-parallel velocity ratio α =1.5. In Fig. 2(b), the loss values of the lossy and severed sections are assumed to be $\rho_1 / \rho_{cu} = 1.41 \times 10^5$ and $\rho_4 / \rho_{cu} = 1.5 \times 10^6$, respectively.

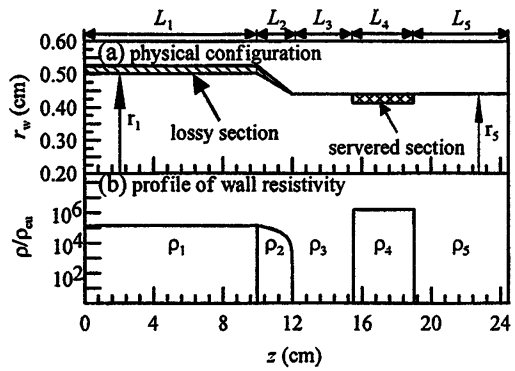

Fig. 2. The proposed structure shown in (a) $r_W(z)$ and (b) $\rho / \rho_{cu}(z)$ in the Ka-band harmonic multiplying gyro-TWT.

For absolute instabilities, the gyro-TWT is susceptible to the $TE_{21}^{(2)}$ (positive-k_z mode), $TE_{11}^{(2)}$ (negative-k_z mode), and $TE_{31}^{(3)}$ (negative-k_z mode) [points 2, 3 and 4 in Fig. 1(b)]. The minimum start-oscillation current at which the three modes begin is 14.5 A (when the absolute instability $TE_{31}^{(3)}$ mode occurs) where L_5=5 cm and $\rho_4 / \rho_{cu} = 1.5 \times 10^6$.

Figure 3 plots the saturated output power as functions of frequency at different axial velocity spreads of the electron beam. The output power of the gyro-TWT amplifier is sensitive to the quality of the electron beam. For an axial velocity spread of 5%, the peak power of 240 kW corresponds to a saturated gain of 54 dB at interaction efficiency of 31 %. The full width at half maximum bandwidth is 1.3 GHz, approximately 3.8% of the center frequency.

The structure is also employer for a W-band harmonic multiplying gyro-TWT. The $\omega - k_z$ diagram of the W-band harmonic multiplying gyro-TWT at the

wall radii r_1=0.1795 cm and r_5=0.1492 cm are shown in Fig. 4. The gyro-TWT has a lossy section, a severed section and copper sections, as depicted in Fig. 5. The parameters of the gyro-TWT are beam voltage V_b =60 kV, magnetic field B_0 =18.81 kG, guiding center radius r_c =0.09 cm, and perpendicular-to-parallel velocity ratio α =1.5. For absolute instabilities, the minimum start-oscillation current at which the $TE_{21}^{(2)}$ mode begins is above 10.0 A (point 2 in Fig. 4) where L_5=4 cm and $\rho_4 / \rho_{cu} = 1.0 \times 10^5$.

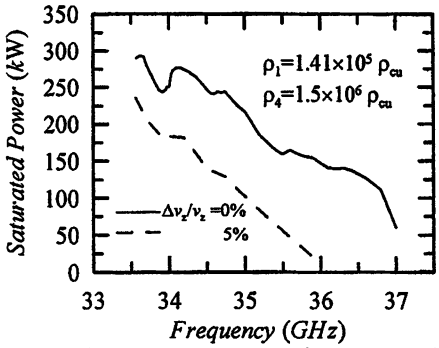

Fig. 3. Saturated output power versus frequency at different axial velocity spreads of the electron beam in the Ka-band harmonic multiplying gyro-TWT.

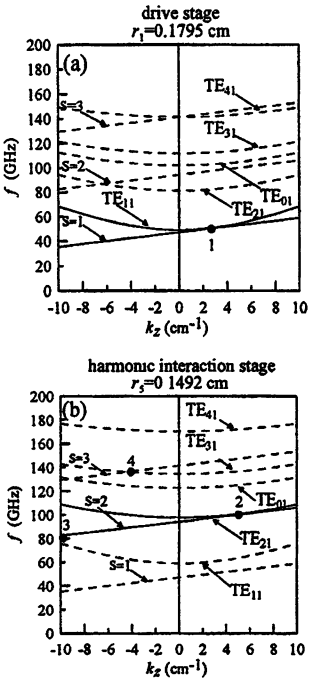

Fig. 4. $\omega - k_z$ diagram of the transverse electric waveguide modes and the cyclotron harmonic beam-wave resonance lines in the W-band harmonic multiplying gyro-TWT.

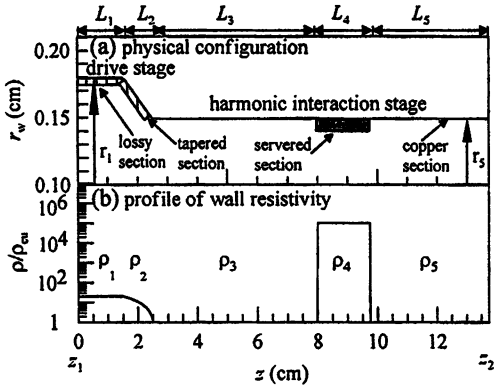

Fig. 5. The proposed structure shown in (a) $r_W(z)$ and (b) $\rho / \rho_{cu}(z)$ in the W-band harmonic multiplying gyro-TWT.

The W-band harmonic multiplying gyro-TWT is predicted to yield a peak output power of 122.4 kW at 97.9 GHz with an efficiency of 27.5 %, a saturated gain of 22 dB and a 3 dB bandwidth of 1.14 GHz for a 60kV, 7.42 A electron beam with an axial velocity spread of $\Delta v_z / v_z$=8% in Fig. 6.

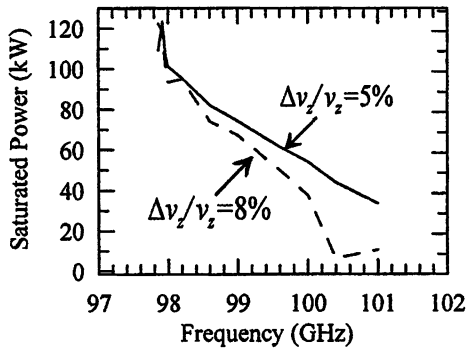

Fig. 6. Saturated output power versus frequency at different axial velocity spreads of the electron beam in the W-band harmonic multiplying gyro-TWT.

References

1. *Chu, K. R., Guo, H. and Granatstein, V. L.* Theory of the harmonic multiplying gyrotron traveling wave amplifier, Phys. Rev. Lett., 1997. V. 78, No. 24, P. 4661-4664.

2. *Guo, H. Chen, S. H. Granatstein, V. L. Rodgers, J. Nusinovich,G. Walter, M. Levush, B. and Chen, W. J.* Operation of a highly overmoded, harmonic-multiplying, wide-band gyrotron amplifier, Phys. Rev. Lett., 1997. V. 79, No. 3, P. 515-518.

3. *Y. S. Yeh, J. H. Cheng, L. K. Chen, C. W. Hung, C. Y. Lo, and C. W. Liao,* Stable harmonic multiplying gyrotron traveling-wave amplifier with distributed wall losses and attenuating severs, Phys. Plasmas, 2008. V. 15, P. 023109.

A Pulsed Multimegawatt Gyroklystron

N.I. Zaitsev, Yu.Yu. Danilov, A.K. Gvozdev, S.V. Kuzikov, M.A. Moiseev, M.I. Petelin, M.E. Plotkin and S.A. Zapevalov

Institute of Applied Physics of the Russian Academy of Sciences,
46 Ulyanov Street, Nizhny Novgorod, Russia.

For any kind of coherent radiation sources, one of methods for power enhancement is expanding the RF interaction space. For instance, high-order mode gyrotrons have reached ~1 MW powers at frequencies up to 170 GHz [1-3]. By adding upstream cavities, such a gyrotron might be converted to a klystron-type amplifier. Experimentally studied since 1967 [4], gyroklystrons presently deliver pulse powers of tens megawatts at the centimeter wave band [5] and hundreds kilowatts at the millimeter wave band [6, 7]. Our paper describes an internationally funded experiment [8] aimed to develop a pulsed gyrolkystron at 30 GHz: one of frequencies for using in future electron-positron colliders.

Our experimental set-up is based on a ~400 kV/ ~250 A/ ~1mcs pulser and up to 2.4 T cryomagnet. A tubular beam of helical-trajectory electrons was formed with a triode magnetron injection gun with a 90 mm diameter cathode. The electron pitch factor measured by means of an analyzer [9] with an adjustable magnetic mirror reflector proved to be 1.3. To check the good electron beam quality, the beam was used to excite the TE5.3.1 mode in an optimized barrel-like cavity. This free running gyrotron delivered 20 MW pulsed power with 50% efficiency.

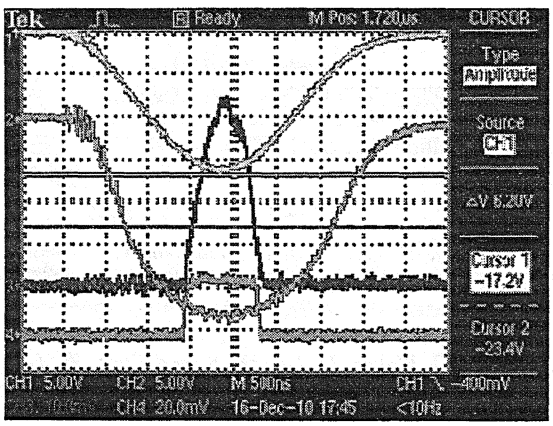

Fig. 1. Traces: 1) – cathode voltage (20 kV/V), 2) – beam current (4 A/V), 3) – output RF power, 4) – input RF power

The same electron beam was used to drive a gyroklystron operating at the TE5.2.1 mode in the input cavity and the TE5.3.1 in the output cavity. The 30 dB amplifier delivered 15 MW at 40 % efficiency, the bandwidth being 50 MHz. Typical plots of the beam voltage and current as well as of the input and output RF powers are shown in Fig. 1. The measured phase instability was within 10 degrees.

In the 3-cavity configuration, the gyroklystron operated at TE5.2.1, TE5.2.1 and TE5.3.1 modes with 36 dB gain, other characteristics being the same as in the 2-cavity configuration.

Now we are planning a research on gyroklystrons that would operate at still higher order modes; new electrodynamic components [12] will be used.

References

1. *A. Kasugai, R. Minami, K. Takahashi et al.*, "Development of a 170 GHz High-Power and CW Gyrotron for Fusion Application", 30 Intl. Conf. on IR and MM Waves, USA, 2005, pp. 17-18.

2. *A. Litvak, G. Denisov, M. Agapova et al.*, "Recent Results of Development in Russia of 170 GHz Gyrotron for ITER". The 35-th Int. Conference on Infrared, Millimeter and Terahertz Waves, 2010, Conference Digest, p.Tu.-E1.1.

3. *T. Rzesnicki, B. Piosczyk, S.Kern et al.*, "2.2 MW Record Power of the 170 – GHz European Preprototype Coaxial – Cavity Gyrotron for ITER", IEEE Trans. Plasma Science, 2010, vol. 38, № 6, pp. 1141-1149.

4. *A. Andronov, V. Flyagin, A. Gaponov et al.*, "The gyrotron: high-power source of millimetre and submillimetre waves", Infrared Physics. 1978, V. 18, No.5-6, pp. 385-393.

5. *Lawson W., Gouveia S., Hogan B, Granatstein V.*, "Experimental results of four cavity 17 GHz gyroklystron", Proc. IVEC 2003, Seoul, pp. 344-345.

6. *E. Zasypkin, I. Gachev, I. Antakov, E. Sokolov*, "W-band pulsed 300 kW gyroklystron amplifier", Proc. IR&MMMW Conf., 2001, Toulouse, pp. 586-588.

7. *Blank M., Borhard P., Cauffman S., Felch K.*, "Broadband W-band gyrotron amplifier development,"Proc. IR & MMW Conf., Shanghai, 2006, p.198.

8. *Zaitsev N.I., Ilyakov E.V., Kuzikov S.V. et al.*" Pulsed high-order volume mode gyroklystron", Radiophysics and Quantum Electronics, 2005, Vol. 48, No. 10–11, pp. 737-740.

9. *A.K. Gvozdev, N.I. Zaitsev, S.A. Zapevalov et al.*, "A Magnetic Analyzer of a Helical Electron Beam Based on a Controlled Magnetic Mirror", Instruments and Experimental Techniques, 2011, vol. 54, № 2, pp. 230 – 233.

10. *M. Petelin, V. Erckmann, J. Hirshfield et al.*,"New concepts for quasi-optical structures for use with gyrotron systems", *IEEE Trans-ED*, 2009, No.5, pp. 561-565.

Preliminary Design of 300GHz/200kW/CW Gyrotrons for Fusion Research

V.E. Zapevalov, A.V. Chirkov, G.G. Denisov, A.N. Kuftin, A.G. Litvak, M.A. Moiseev, N.A. Zavolsky

Institute of Applied Physics, Russian Academy of Sciences, Nizhny Novgorod, Russia, zapev@appl.sci-nnov.ru,

Some advanced fusion experiments and promising technological applications require RF sources with CW powers of about 200 kW and frequencies of at least 300 GHz [1]. In the framework of this project, the program aimed at the design of a 300 GHz gyrotron producing an output power of 200 kW in the continuous-wave regime was implemented at IAP RAS in cooperation with the industrial company GYCOM Ltd. Gyrotron specifications are shown in Table 1.

Table 1

Frequency, GHz	300 ± 2
Maximal CW output power, kW	at least 200
Range of CW output power, kW	0.5 – 200
Maximal beam voltage, kV	60
Maximal beam current, A	20
Output window diameter, mm	88
Output mode	wave beam
Overall dimensions (approx.), m	0.4(W)×0.4(D)×2.7(H)

The gyrotron tube should be used together with the 12T liquid-Helium-free cryomagnet of JASTEC Co. (Japan) [2] or its analogue with the diameter of the "warm" bore equal to 100 mm.

Based on the analysis of the scientific and technical data, the general design concept of the gyrotron has been developed and possible operating modes and the value of the accelerating voltage have been chosen.

Several possible operating modes like the $TE_{22,8}$, $TE_{25,10}$, $TE_{31,12}$ were considered. Their main parameters are summarized in Table 2, where ν denotes the Bessel functions derivation roots corresponding to each mode, R_{cav} is the cavity radius, p_{ohm} is the specific ohmic load of the cavity, R_0 is the average radius of the electron beam in the cavity, R_{cath} is the average radius of the cathode emitter, and Q_{ohm} is the ohmical Q-factor.

Table 2

mode	$TE_{22,8}$	$TE_{25,10}$	$TE_{31,12}$
ν	52.7	63.3	77.76
R_{cav}, mm	8.39	10.07	12.37
p_{ohm}, kW/cm^2	2.5	2.1	1.7
R_0, mm	3.7	3.7	3.7
R_{cath}, mm	21.5	24.3	30.0
Q_{ohm}	30000	36000	44300

Finally, based on the analysis of technical limitations, the $TE_{22,8}$ mode was chosen as the operating on for this gyrotron tube, which allowed us to check different scientific and technical solution. The results of this activity are summarized in this report.

Gyrotron Design

The gyrotron has the same basic design concept as the earlier developed 110-170 GHz gyrotrons [1] and, partly, the 300 GHz/4kW/CW gyrotron [2]. Specifically, this includes the use of a quasi-diode gun with a LaB_6 cathode, a built-in mode converter to transform the cavity mode to a wave beam with the radial directed output, and an electron beam collector, all components rated for the CW operation. The magnetic system of the tube includes a 12 T cryomagnet and, optionally, a cathode coil for fine adjustment of the electron beam parameters.

Cavity

Stable single-mode CW oscillation in an oversized cavity with high efficiency η, becomes a rather complicated problem at the 300 GHz [3]. The results of detailed numerical simulation of the gyrotron prototype demonstrate that its efficiency is limited by the limitation imposed on the density of the ohmic loss in the cavity walls, voltage depression, and mode competition as well. The dependences of the output power and specific ohmic loss at the cavity wall on the beam current in different cavities are shown in Figure 1. The dependences of the efficiency on the beam current are shown in Figure 2. The possibilities to improve the gyrotron efficiency have been theoretically identified.

The use of a potential depressed collector (CPD) gives us the possibility to improve the gyrotron efficiency remarkably. Figure 3 presents the energy distribution function of the worked-out electron beam. Efficiency without CPD reaches 23.05 % without after-cavity interaction (ACI), and 22.12 % with ACI. Efficiency with CPD and 0% electron reflection is 39.6%, (U_0–Urec =34 kV, and the power of the main high-voltage source P_e=680 kW), and efficiency with CPD and 1% reflections is 42.8 %, (U_0–Urec=31 kV, P_e =620 kW).

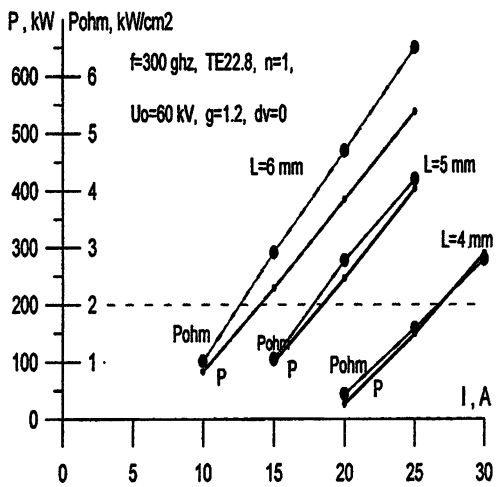

Fig. 1. Output power and specific ohmic loss vs. beam current at different cavities.

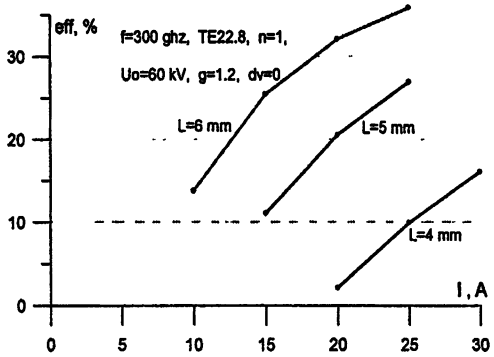

Fig. 2. Output power and specific ohmic loss vs. beam current at different cavities.

To achieve the highest efficiency, it is very important to provide minimal misalignment of the tube subsystems and the magnetic field axis [3] with a typical limiting value of 0.15–0.2mm.

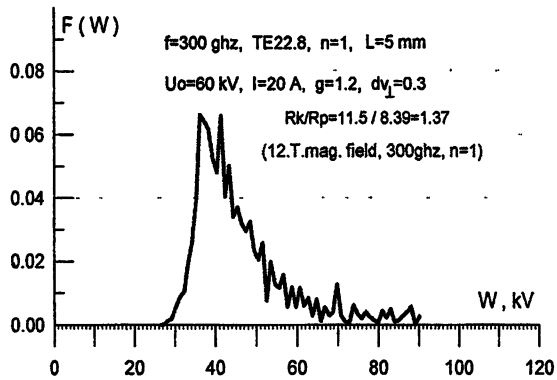

Fig. 3. Energy distribution in the worked-out electron beam.

Electron gun and collector

Formation of a high-quality helical electron beam (HEB) with the required parameters is one of the main problems in creation of high-efficiency gyrotrons.

The gyrotron has a triode-type electron gun, thus the anode voltage and the accelerating (beam) voltages can be controlled separately. Figure 4 shows a photo of the gun prototype without an emitter ring and an anode.

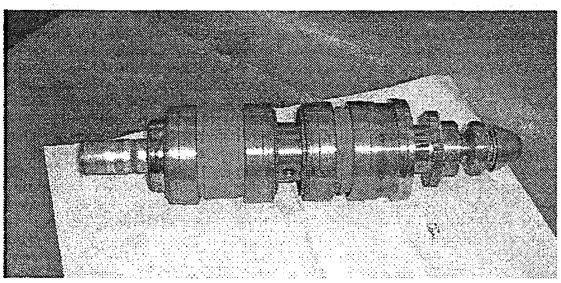

Fig. 4. Photo of the gyrotron gun prototype.

Configuration of the electrodes in the designed gun is optimized using electron trajectory analysis codes in order to obtain the electron beam with specified parameters. Simulations were performed allowing for initial velocities [4]. The calculated parameters of the electron gun are as follows: the cathode emitter radius is 21.5 mm, the electron beam voltage U_o = 60 kV, the beam current is up to 20 A, and the pitch factor is 1.2. The cathode emitter of the gyrotron tube is a high temperature LaB6 cathode.

As a result of the numerical simulation, the shapes of the gun electrodes were optimized and the dependence of the HEB velocity spread and ratio of oscillatory energy to the total energy in the beam current was obtained. The tube collector was designed to withstand up to 900 kW electron beam power for the CW regime of operation.

Mode converter and output window

The mode converter separates RF radiation from the worked-out electron beam, transforms a complicated cavity mode to a paraxial wave beam with an optimized structure and allows one to minimize the harmful effect of possible reflections of the RF power back to the gyrotron. The converter includes a specially shaped waveguide end and three profiled mirrors, to provide low diffraction losses inside the tube, the optimal RF power distribution over the output window, and the matching of the output wave beam with the transmission line. The amplitude and phase distributions at the converter output are presented in Fig. 5. The TEM_{00} mode content is 99.54 %.

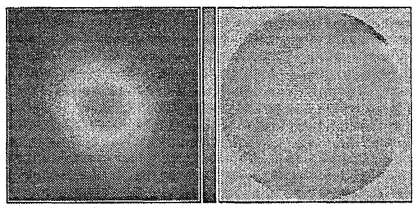

Fig. 5. Amplitude and phase distributions

In the output window of the 300GHz/200 kW CW gyrotron, a CVD-diamond disk nearly 80 mm in diameter will be used, which have a low RF loss level.

Conclusion

Design versions of the 300 GHz/ CW, gyrotron with output power 200 kW, including its specific property details are presented. The main and specific technical problems of the 300 GHz gyrotron and its entire facility are outlined and discussed. The experimental-industrial 300 GHz CW gyrotron prototype will be designed and made to order.

References

1. *A.G.Litvak, G.G.Denisov, M.V.Agapova, et al.* Recent Results of Development in Russia of 170 GHz Gyrotron for ITER // *The 35-th Int. Conference on Infrared, Millimeter and Terahertz Waves*, 2010, Sept.5- Sept.10 Roma, Italy, *Conference Digest*, p.Tu.-E1.1

2. *V.Bratman, M.Glyavin, T. Idehara, et al* Review of Sub-Terahertz and Terahertz Gyrodevices at IAP RAS and FIR FU // *IEEE Transactions on Plasma Science*, 37, 1, P. 36-43, (2009)

3. *V.E.Zapevalov.* Increasing Power and Efficiency of gyrotrons Fusion Science and Technology, August 2007 –Vol.52, No2, P. 340-344

4. *A.N.Kuftin, V. K. Lygin, V.E Zapevalov et al.* Int. J. of Infrared and Millimeter waves, 20 (1999), no.3, P.361-382

Development of 395 GHz Gyrotrons for DNP Spectroscopy on the Basis of Experience of Elaboration of a 260 GHz Gyrotron

V.E. Zapevalov, A.N. Kuftin, V.N. Manuilov, M.A. Moiseev, A.B. Pavelyev, A.S. Sedov, N.A. Zavolsky

[1]Institute of Applied Physics, Nizhny Novgorod, Russsia, zapev@appl.sci-nnov.ru

Dynamic nuclear polarization (DNP) is an important technique to enhance nuclear magnetic resonance (NMR) signals in spectroscopy [1]. It requires high power microwave sources with continuous output power about several tens of watts and operating frequencies 250 GHz and above. Currently among all the relatively compact sources of electromagnetic radiation only gyrotrons fully satisfy these requirements [2]. In this paper we present the results of theoretical and experimental investigation of this area carried out at the IAP RAS.

One of these devices – a 260 (258.9) GHz gyrotron was developed, manufactured and tested at IAP RAS in cooperation with the industrial company GYCOM. This gyrotron setup is a part of a complex experimental system for DNP spectroscopy at the Institute of biophysical chemistry of Frankfurt-am-Maine University (Germany).

The gyrotron tube has a conventional design with axial output at the operating mode. The gyrotron has triode-type electron gun and so the anode and accelerating (beam) voltages could be controlled separately. The configuration of electrodes of the designed gun is optimized using electron trajectory analysis codes in order to get the electron beam with given parameters. The calculated parameters of the electron gun are the following: electron beam voltage U_0=15 kV, anode voltage U_a=12 kV, beam current – up to 0.5 A. The cathode emitter of the gyrotron tube is of high temperature type made of LaB_6.

The gyrotron parameters are optimized to achieve the highest stability of output power and operating frequency at the calculated electron beam parameters. The radius of the cavity is chosen R_c=1.84 *mm* in order to have the given operating frequency 260 GHz at the operating mode $TE_{2,3}$. The length of the cavity allows us to have the diffraction quality Q_{dif}=6000 in order to provide effective excitation of the operating mode. Due to considerable ohmic losses in the cavity, output waveguide and window, the efficiency of the gyrotron is about 1 %. Requirements for stability of magnetic field value in the cavity, cooling of the cavity, voltage and current of power supplies are defined to provide the stability of frequency not worse than $3*10^{-5}$.

The main part of the magnetic system for the gyrotron is a superconducting cryomagnet. The longitudinal distribution has a homogeneous part of maximal magnetic field whose length is 36 mm with accuracy 0.2 %. For fine adjustment of the magnetic field in the electron gun an additional normally conducting coil is used.

The gyrotron output window is made of a selected boron nitride (BN) single disk with a diameter 20 mm. Its thickness is chosen according to the non-reflection passing conditions of the output RF signal.

To provide proper vacuum condition the gyrotron tube includes a built-in vacuum pump. The cathode filament power supply is designed to feed the gyrotron cathode filament with direct current and to sustain the preset value of the gyrotron electron beam current automatically.

A photo of the gyrotron tube is shown in Fig. 1. A maximum CW power of 200 W for accelerating voltage 16 kV and current 0.3 A was obtained in the course of the experimental tests. Fig. 2 presents the experimental dependence of the output power on the accelerating voltage for constant beam current. During more than 8 hours of CW operation the frequency stability of $5*10^{-6}$ was demonstrated and it increased the sensitivity of the spectrometer in this system. A comparison of experimental and theoretical data has made it possible to estimate the properties of the electron beam and cavity ohmic losses for submillimeter wave operation.

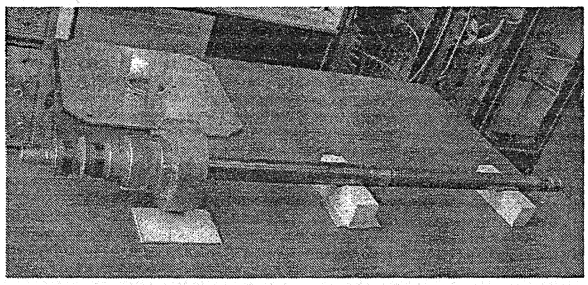

Fig. 1. The general view of gyrotron tube

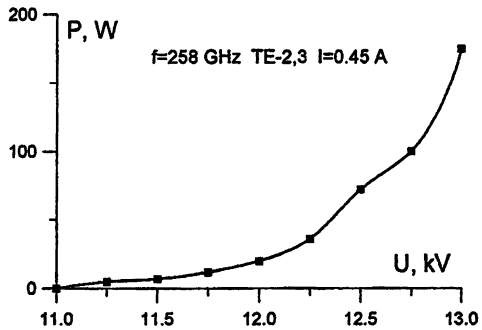

Fig. 2. 260 GHz gyrotron output power vs. accelerating voltage

Fig. 3 presents general view of gyrotron set-up at the Institute of biophysical chemistry. Application of the 260 GHz gyrotron to the developed DNP spectrometers in Frankfurt has opened the following opportunities: to improve NMR sensitivity of solid state NMR experiments at low temperatures, to reach unexpected high DNP enhancements on in-situ DNP experiments at 9.2 T on aqueous solutions at room temperature [3].

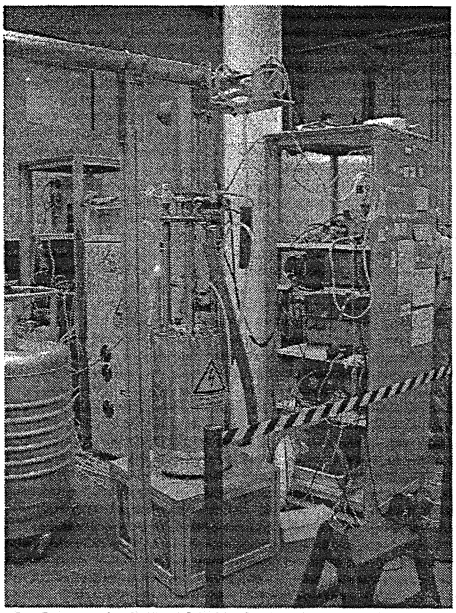

Fig. 3. General view of 260 GHz gyrotron set-up.

Traditional gyrotron oscillators provide RF radiation at the fixed frequencies. Some frequency tuning is possible while using operating modes TE_{mpq} with different axial variations q, but achievable tuning curve is very non-homogeneous. Next investigation shows the possibility to create a device like gyro-BWO as an improvement of existing 260 GHz gyrotron oscillator. For such tube some frequency tuning may be realized. In this tube version cavity output has to be directed to the side of electron gun. Numerical calculations show the increase of the bandwidth of frequency tuning half times compared to «ordinary» cavity of the same length. Problems of an output system, wideband converter and window for this system are under consideration now.

Summarizing experience of previous developments nowadays the 395 GHz/100W/CW gyrotron at the second harmonic of gyro-frequency is under development in the IAP RAS. The gyrotron has in general the same principal design concept as the earlier developed 300 GHz/4kW/CW gyrotron [2]. This includes the use of a quasi-diode gun with a LaB_6 cathode, a build-in mode quasi-optical converter (QOC) to transform cavity mode to wave beam with radial directed output, and an electron beam collector, all designed for CW operation. Magnetic system of the tube includes a 8 T cryomagnet of GYCOM or 8 T cryomagnet of JASTEC (Japan) and optionally a cathode coil for fine adjustment of electron beam parameters. The output power of this device is expected to achieve the level of 100 W. Efficiency and output power of 395 GHz gyrotron on length of cylindrical part of the cavity are shown in Fig. 4. For QOC the conventional style was chosen due to small scale corrugation necessary for improved version. Structure of output radiation at the window of 395 GHz gyrotron are shown in Fig. 5.

With the view of using complex signal for advanced DNP NMR spectroscopy it's very attractive to use the amplifier. One of the variants under the consideration for this DNP setup is gyroklystron. It allows for example to generate pulse periodic signals which can significantly improve the DNP efficiency. Numerical simulations show that it is necessary for the external solid-state source to have power level of 0.1 W to achieve the output power of gyroklystron of about 100 W. In this case the gain is about 1000. However the given system requires a substantially greater length of homogeneous magnetic field section.

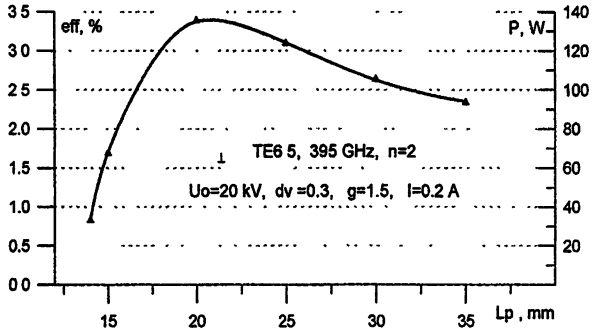

Fig. 4. Efficiency and output power of 395 GHz gyrotron vs. length of cavity.

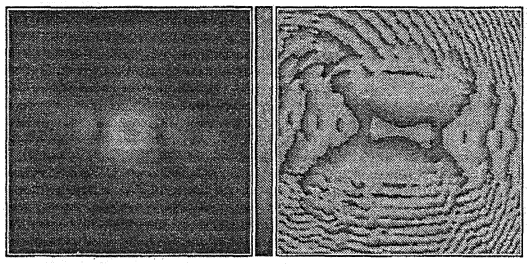

Fig. 5. Structure (amplitude and phase) of output radiation in 395 GHz/100W/CW gyrotron.

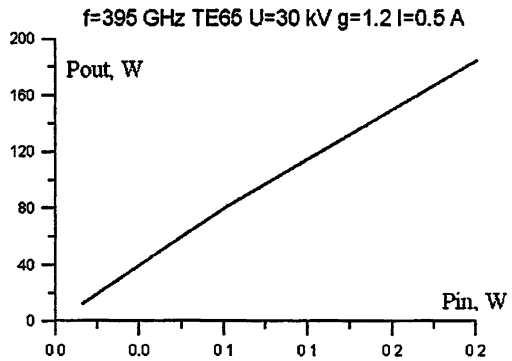

Fig 6. Output power of 395 GHz gyroklystron vs. input power

References

1. *J. Ardenkjaer-Larsen, B. Fridlund, A. Gram, G. Hansson, L. Hansson, M. Lerche, R. Servin, M. Thaning and K. Golman* Increase in signal-to-noise ratio of > 10, 000 times in liquid-state NMR // *Proc. Natl. Acad. Sci. U. S. A.*, 2003, 100, 10158–10163

2. *V.Bratman, M.Glyavin, T.Idehara, Yu.Kalynov, A.Luchinin, V.Manuilov, S.Mitsudo, I.Ogawa, T. Saito, Y.Tatematsu, V.Zapevalov* Review of Sub-Terahertz and Terahertz Gyrodevices at IAP RAS and FIR FU // *IEEE Transactions on Plasma Science*, 37, 1, 36-43, (2009)*Vasyl Denysenkov , Mark J. Prandolini , Marat Gafurov , Deniz Sezer , Burkhard Endeward and Thomas F. Prisner* Liquid state DNP using a 260 GHz high power gyrotron// *Phys. Chem. Chem. Phys.*, 2010 12, 5786-5790

Symposium H

CURRENT DRIVE AND PLASMA HEATING BY MICROWAVES IN NUCLEAR FUSION DEVICES

Control Oriented Application of High Power EC Waves

M.R. de Baar[1,2], J. Citrin[1], S. Djordjevic[2], G.M.D. Hogeweij[1], G. Witvoet[1,2], M. Steinbuch[2]

[1] Association EURATOM-FOM, POBox 1207, 3430 BE Nieuwegein, The Netherlands
[2] Eindhoven Technical University, Mechanical Engineering, POBox 513, 5600 MB Eindhoven, The Netherlands

The ITER ECRH system is conceived to provide maximum flexibility to respond to the numerous needs for H&CD applications associated with the ELMy H-mode, hybrid and advanced scenarios envisioned for the ITER operation [1]. This implies that a number of control of scenarios will be developed to allow high efficiency operation close to, but within, the operational boundaries. Particular emphasis has to be given to turbulence suppression for optimal performance and the amelioration or control of Magneto-hydrodynamic modes. The actuation strategies and distributed control designs for these applications need to be considered in detail. In this paper we discuss (i) the control oriented modelling for the controllability analysis of the magnetic flux distribution in ITER Hybrid modes using high power distributed Electron Cyclotron waves and (ii)the systematic design of a sawtooth controller actuated with high power EC-waves.

In ITER Hybrid modes, the ion temperature profile is assumed to stays close to the critical gradient for the onset of ion temperature gradient (ITG) driven transport. In such conditions, the inverse gradient length of the ion temperature profile scales with 1+s/q, in which q is the safety factor and s is the magnetic shear. Both q and s are functions of the poloidal magnetic flux $\Psi(t, x)$ in the radial co-ordinate x. Work by Citrin et al. [2] suggests that control of Ψ could be applied for the optimisation of the ion temperature profile in ITER hybrid modes.

A model-based control strategy for the analysis of the control of closed loop control of Ψ actuated with EC-waves only is set-up, following [3]. The Ψ (t, x) profile evolution is modelled as a partial differential equation (PDE). This model allows for investigating the effect of the input (*viz.* the position of the EC-driven contribution of the current j_{ec}), on the output (viz. the desired target Ψ profiles). The model will be used to identify the reachable $\Psi(t, x)$ profiles. The parameters used in this work are identical to those in simulations [2] done with the CRONOS [4, 5] suite of codes.

The model presented in [3] can be re-formulated in a spatially discretized form

$$\partial\Psi(t, x_i)/\partial t = (\eta(x_i)/\mu_0 a^2)(c_1(x_i)\Psi_{i+1} - c_2\Psi_I + c_3(x_i)\Psi_{i-1}) + \\ + \eta(x_i)R_0 (j_{bc}(x_i) + j_{nbi}(x_i) + j_{ec}(t, x_i),$$

where $\eta(x)$, $j_{bc}(x)$, and $j_{nbi}(x)$ are considered to be space-dependent parameters. j_{ec} (t,x_i) is considered as a spatially distributed input. This can be rewritten in a state-space

$$d\Psi_i(t)/dt = \mathbf{A}\Psi_i(t) + \mathbf{Bu}, \text{ and } y_i = \mathbf{C}\Psi_i(t)$$

where u and y are inputs and output respectively [6]. The formalism is widely used in control engineering, for the analysis and design of controllers. Here we assume that the system is fully observable, which means that the minimal input/output realization is determined by the $j_{ec}(x_i)$ deposition. The exact influence of the $j_{ec}(x_i)$ deposition, i.e. the input **u**, on the system dynamics **A** can be quantified using the controllability matrix. In general, the system is fully controllable if the controllability matrix has full rank, which according to the Cayley-Hamilton theorem is determined by the first N x N columns of the controllability matrix. The key element in determining the controllability of the $\Psi(t)$ profile is to use the Hankel singular value decomposition (SVD) of the controllability and observability Gramians. If the SVD decrease rapidly, this means that the Hankel singular value $\sigma_i \sim 0$ corresponds to the unreachable sets. Then, the system behavior is almost fully determined by the first few balanced states with $\sigma_i > 0$. The minimal input/output realization is determined by the highest σ_i.

The Hankel singular value σ_i can be interpreted as the energy contribution of the ith component of the balanced state to the input/output behavior of the system.

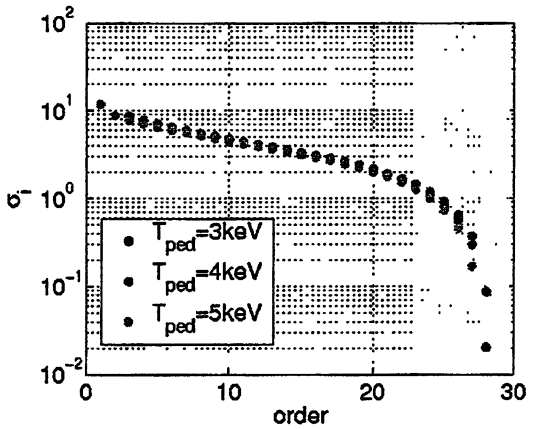

Fig. 1. Hankel Singular Values. Only 27 SVs of a total of 101 SV are shown to be relevant for the system dynamics. This implies that a number of Ψ-profiles, but not all can be «reached» by ECCD

Figure 1 illustrates the first 27 largest singular values σ_i with i = 1, 2, ... 27 for an ITER Hybrid scenario with a plasma current Ip of 12 MA. The pedestal temperature has been varied: T_{ped} = 3 keV, 4 keV and 5 keV. The Hankel singular values σ_i for i > 27 decrease rapidly. The low numerical rank of the Gramian results in the rapid decay of the eigenvalues. This implies that not all Ψ profiles are reachable from the chosen actuation strategy. The subspace of magnetic fluxes corresponding to the eigenvalues σ_i with i > 27 can be considered as unreachable.

Hence the j_{ec} deposition at a specific location affects the input energy required to shape the $\Psi(t, x)$ profile. The controllability analysis shows that the system behaves as a model of much lower order. This has to be considered for designing a real-time controller.

Now we turn to the second subject of this presentation, the design of a sawtooth controller. A low complexity sawtooth model, based on the Kadomtsev reconnection with a Porcelli critical shear condition has been implemented in the real-time simulation environment of Matlab Simulink [7]. This model successfully mimics the basic and well-known effect of EC co-current deposition on the sawtooth period: shortening the period for depositions inside $q = 1$ and lengthening it otherwise. This implemented model was then used as a case study for systematic analysis and structured controller design for the sawtooth instability. Identification simulations were performed to gain insight in the dynamics around various operating points.

This analysis revealed that the sawtooth model acts as a low-pass filter, although its behaviour for on-axis deposition locations is quite different from more outward depositions. The transition seemed to correspond with the transition from single $q = 1$ situations to the case with multiple $q = 1$ surfaces. Based on the identiffed frequency response functions both an integral (I) and a proportional-integral-integral (PII)-controller were designed, maximizing the closed-loop performance while satisfying stability and robustness specifications. Time simulations showed its success for both slow and fast changing set points; as expected convergence is much faster for small period set points than for large ones.

Next, the influence of slow actuation and detection was investigated. The launcher installations on current day tokamaks are relatively slow, making their dynamics dominant over the sawtooth dynamics themselves. On the one hand, this can simplify analysis, as only the sawtooth DC-gain and the closed-loop launcher dynamics are relevant for controller design. On the other hand, it calls for a redesign of the launcher mechanics, as it restricts the achievable closed-loop performance to a large extent.

The usefulness of model-based control approach to fusion power is evident from the obtained results, but a rigorous mathematical proof of its validity is an important topic of future research. Furthermore, the work presented here focuses on the $\Psi(t,x)$ profiles and ST periods. The current work only considers the nominal case where various plasma parameters remain constant and disturbances are hardly present. Future work will involve an investigation of changing plasma conditions on the identified plants, an identification of plasma disturbance dynamics, and the influence of these on the controller design and closed-loop performance. In future research the focus should be broadened in order to derive a controller for the whole operating range of the ECCD mirror. Possible research directions include injection locking [8] or hybrid controller switching techniques or extremum seeking algorithms [9].

References

1. *M. Henderson and G. Saibene*, Nucl. Fusion 48 (2008) 054017.

2. *J. Citrin et al.*, Nucl. Fusion 50 115007 (2010)

3. *E. Witrant et al.*, Plasma Phys. Contr. Fusion 49 1075 (2007).

4. *V. Basiuk et al.*, Nuc. Fusion 43 (2003) 822

5 *J.F. Artaud et al.*, Nuc. Fus 50 043001 (2010)

6 *S. Djordjevic et al.*, Proc. 38tth EPS conference on plasma physics (Strasbourg, France, 2011) and the references therein.

7. *G. Witvoet et al.* accepted for publication in Nuc. Fusion (2011).

8. *G. Witvoet et al.*, submitted to Nuc. Fus.

9. *J. Bolder et al.*, to be submitted to Nuc. Fus.

Status Update on the DIII-D ECH System

Y.A. Gorelov[1], J. Lohr[1], M. Cengher[1], D. Ponce[1], M. Shapiro[2] and R.A. Ellis[3]

[1]General Atomics, P.O. Box 85608, San Diego, CA 92186-5608 USA, gorelov@fusion.gat.com
[2]Massachusetts Institute of Technology, Plasma Science and Fusion Center, 167 Albany St, Cambridge, MA 02139, USA
[3]Plasma Physics Laboratory, Princeton University, Princeton, NJ 08543, USA

The gyrotron system on the DIII-D Tokamak is comprised of six Communications and Power Industries (CPI) diode tubes operating at 110 GHz. Five of the six gyrotrons have been tested at 1 MW, 5 s pulses and 500–600 kW 10 s pulses and one has generated about 80 % of these powers. The maximum rf power injected into DIII-D at the second harmonic of the electron cyclotron (EC) resonance has been 3.5 MW during simultaneous 5 s pulses of all six gyrotrons. The gyrotron thermal design is adequate for 10 s pulses at 1 MW, but the pulse length is presently limited to 5 s to prolong the collector fatigue lifetime.

Significant upgrades to the rf transmission system were made in 2010. In order to increase the total efficiency of the rf transmission, all six waveguides have been rerouted to decrease the total number of miter bends by fifteen, increasing the transmitted power by 200 kW for the entire system. The angular alignment of rf beams after the matching optics unit (MOU) focusing mirrors at the waveguide input has been improved. The launcher mirrors have all been redesigned for improved heat transfer and fatigue lifetimes. Both poloidal and toroidal steering mirror motion now uses electric motors in place of air turbines, yielding higher speed poloidal scans and greater positioning accuracy.

Preparation for installation of a 7th gyrotron has been in progress since August 2010. The frequency of this depressed collector diode gyrotron will be 110 GHz, with output rf power expected to be 1.2–1.3 MW. The 8th gyrotron for the DIII-D system is in the design stage. Also a depressed collector diode tube, this gyrotron is being designed for 117.5 GHz, 1.8 MW output in short pulses with operational parameters of 10 s pulses at 1.5 MW generated.

1. Gyrotrons

Six CPI gyrotrons with chemical-vapor-deposition (CVD) diamond windows have been in routine operation on DIII-D since 2008 [1]. Despite the increasing number of gyrotrons, the overall gyrotron reliability for plasma experiments remained stable at more than 82%. After repairing the collector failures of the first three gyrotrons and improving the collector sweep method at both CPI and DIII-D [2], no additional collector problems were encountered on this type of gyrotron. Calorimetric monitoring of the gyrotron internal losses has been providing additional information for optimal operation and for the output rf power estimation. Direct rf power measurements were completed with a high power, long pulse dummy load from Calabazas Creek Research [3] installed near the tokamak launchers. This information has been used, and continues to be, for the correction of the internal gyrotron ohmic losses in full power operation and for an estimation of a total injected rf power inside the DIII-D vessel.

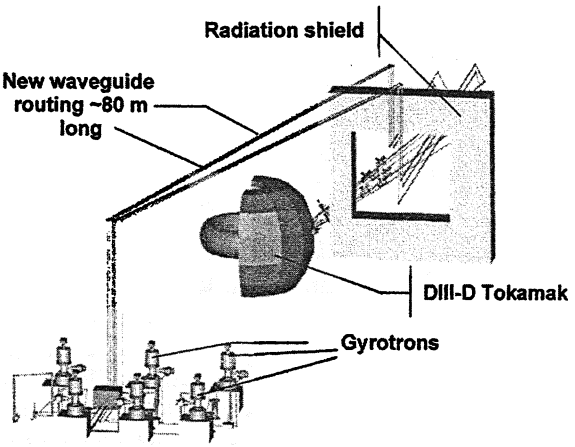

Fig. 1. DIII-D ECH system layout

Although all six CPI gyrotrons of the VGT-8110 series have CVD diamond windows, the parameters of these windows are different. The first three tubes have a diamond disk diameters of 57 mm and disk thickness of 1.14 mm with $\tan^{TM}=1.4\cdot10^{-4}$. The others have a disk diameter of 73.5 mm and thickness of 1.71 mm and $\tan^{TM}=1.0\cdot10^{-4}$. The apertures of all the windows are the same: 50.8 mm. The last three tubes of this gyrotron production series have polished diamond disks that allow us to monitor the light output from the gyrotrons.

2. Waveguide transmission lines

The DIII-D ECH transmission line system is comprised of six evacuated windowless transmission lines up to 80 meters in length with transmission efficiency from 72.4 % to 80.9 %. Each waveguide line includes an MOU with focusing mirror, waveguide dummy load switch, waveguide isolation valve, two polarizers and up to ten miter bends. The corrugated waveguides are circular with a diameter of 31.75 mm. The waveguides are pumped to an internal pressure of $1.33\cdot10^{-4}$ Pa.

In addition to rerouting the wavguides, the alignments of the rf beams to the first waveguide were improved. At the waveguide input the Gaussian rf beam excites the HE_{11} waveguide mode with a maximum efficiency of 98 %. At small tilt angles, $\cup$ (less than 2 deg), and small offsets, $\otimes$ (less than 3 mm), the purity fractional decrease for the HE_{11} mode scales as $\cup^2$ and $\otimes^2$, respectively.

The overall performance of the transmission lines is dependent on the input alignment. To estimate the quality of the rf beam after the reflection from the MOU mirror, the gyrotron beam was measured by an infrared camera at varying distances from the mirror

after passage through ~40 cm of waveguide. Based on these data, the mode content for every rf line was calculated and the alignment was adjusted. The purity of HE_{11} mode in the rf beam for the best line is 94.4 % (see Table 1).

Table 1. Alignment results of rf beams into the waveguide transmission lines and final mode content of HE_{11}

	Tilt Angle (deg)		Offset (mm)		HE_{11}(%)
	Before	After	Before	After	
Lion	1.00	0.10	0.84	0.40	92
Scarecrow	1.58	0.14	3.20	0.16	88.3
Tin Man	2.44	0.10	2.00	0.20	91.4
Leia	0.50	0.10	1.50	0.50	94.4
Luke	1.87	0.40	2.00	0.40	84.6
Han	0.06	0.06	0.25	0.25	90.9

3. Launchers

Three fully articulating dual launchers [4], which can steer the rf beams poloidally and toroidally through ±20° in each direction are installed on DIII-D. All are designed and built by Princeton Plasma Physics laboratory. Each launcher has a fixed focusing mirror followed by a flat steering mirror. Two of the six focusing mirrors were damaged during the past two experimental campaigns on DIII-D. The focusing mirrors were made from stainless steel with a thin layer of copper on the surface. A finite element thermal calculation predicts that these mirrors should withstand a front surface temperature of 880 °C for pulse lengths up to 10 s with incident rf power of 850 kW from the existing gyrotrons, Fig. 2.

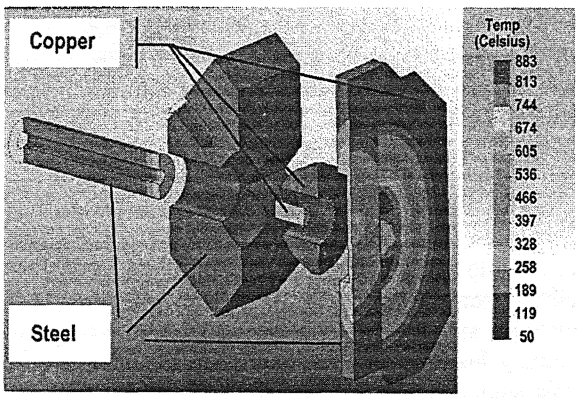

Fig. 2. Old design of a fixed focusing launcher's mirror after 5 s rf pulse with incident rf power of 850 kW

However, in 2008 local stress cracking of the copper surface was found on some focusing mirrors. In some cases, the copper was melted exposing the stainless steel to the rf beam. Rapid thermal runaway and extensive melting resulted.

An upgrade of the launcher mirrors was completed in 2011. All focusing mirrors were replaced by new ones from solid Al-15 Glidcop construction. A finite element electromagnetic analysis, made by Princeton Plasma Physics Laboratory (PPPL), indicates that a solid Glidcop mirror will withstand electromagnetic forces during disruptive tokamak shots. The design goal for these mirrors is to allow the operation of gyrotrons with 1.5 MW output rf power (1.2 MW at the launcher) for 10 s pulses every 15 minutes. The solid Glidcop mirror has superior thermal and stress performance over the stainless mirror with the plated copper design. Stresses in the critical reflecting surface region are in the range that should provide a fatigue life of nearly 4000 tokamak shots with rf pulses of 10 s. It is expected that these mirrors will be replaced periodically.

The existing steerable mirrors of the launchers are made from stainless steel, copper plated on the front surfaces, with inlaid copper bars. The design allows for heat diffusion while minimizing eddy current forces. The steerable mirrors were also beginning to develop slight dimpling on surfaces near the center and which was evidence of thermal fatigue. The new design, also installed on all launchers, has steerable mirrors made from a more substantial copper block with inlaid stainless steel bars brazed in place.

4. Summary

Six gyrotrons at 110GHz have been in routine operation on plasma experiments on DIII-D since 2002. New rf beam alignment and the rerouting of all six waveguides have increased the total efficiency of the transmission lines. Upgraded versions of the PPPL launchers, particularly the new design of the focusing and steerable mirrors, open up possibilities for the operation of new gyrotrons with output power of 1.5 MW and with pulse length up to 5 s.

This work supported in part by the U.S. Department of Energy under DE-FC02-04ER54698, DE-FC02-93ER54186 and DE-AC02-09CH11466.

References

1. *Lohr, J., Cengher, M., Doane, J. L., Gorelov, Y. A., Moeller, C. P., Ponce, D. and Prater, R.,* The multiple gyrotron system on the DIII-D tokamak // J. Infrared Millimeter and Terahertz Waves 2010. V. 32. P. 253.

2. *Felch, K., Blank, M., Borchard, P., Cahalan, P., Cauffman, S., Chu, T. S. and Jory, H.,* Improved collector analyses and measurements on high-power gyrotrons // Proc. 14th Joint Workshop on Electron Cyclotron Emission and Electron Cyclotron Resonance Heating, edited by A. Lazaros, 543 (2006); http://www.hellasfusion.gr/images/stories/ec14/papers/87.pdf.

3. *Ives, L., Mizuhara, M., Neilson, J. and Marsden, D.* CW waterload for gaussian mode gyrotrons // IEEE Trans. Plasma Sci. 1999. V. 237. P. 531.

4. *Ellis, R. et al.,* Design of the dual high power, long pulse steerable ECH launcher for DIII-D // Proc. 14th Topical Conf. of Radio Frequency Power in Plasma, AIP Conf. Proc. 2011. V. 595. P. 318-321.

Electron Cyclotron / Bernstein Wave Heating and Current Drive Experiments using Phased-array Antenna System in the QUEST

H. Idei[1], H. Zushi[1], K. Hanada[1], K. Nakamura[1], A. Fujisawa[1], M. Hasegawa[1], N. Yoshida[1], M. Sakamoto[2], H. Watanebe[1], K. Tokunaga[1], Y. Nagashima[1], A. Ejiri[3], M. Sakaguchi[4], E. Kalinnikova[4], M. Ishiguro[4], S. Tashima[4], A. Fukuyama[5] H. Igami[6], S. Kubo[6], S.K. Sharma[4], T. Ryokai[4], H.Q. Liu[4], M. Isobe[6], K. Nagaoka[6], H. Nakanishi[6], N. Nishino[7], S. Kawasaki[1], H. Nakashima[1] A. Higashijima[1], Y. Takase[3], T. Maekawa[8], O. Mitarai[9], M. Kikuchi[10] and K. Toi[6]

[1] Research Institute for Fusion Science, Kasuga, Japan, idei@triam.kyushu-u.c.jp
[2] Plasma Research Center, Tsukuba Univ., Tsukuba, Japan
[3] Department of Complexity Sci. and Eng., Univ. of Tokyo, Kashiwa, Japan
[4] Interdisciplinary Grad. School of Eng. Sci., Kyushu Univ., Kasuga, Japan
[5] Department of Nuclear Engineering, Kyoto Univ., Kyoto, Japan
[6] National Institute for Fusion Science, Toki, Japan
[7] Mechanical System Engineering, Hiroshima Univ., Hiroshima, Japan
[8] Graduate School of Energy Science, Kyoto Univ., Kyoto, Japan
[9] Inst. of Ind. Sci. and Tech. Research, Tokai Univ., Kumamoto, Japan
[10] Japan Atomic Energy Agency, Naka, Japan

1. Introduction

The spherical tokamak (ST) has a capability to attain higher b than conventional tokamaks. The Q-shu university experiment with steady state spherical tokamak (QUEST) was proposed at Kyushu University, and the QUEST device has been constructed [1]. A final target of the project is the steady state operation with relatively high beta (<10 %) in the ST configuration under controlled plasma wall interactions (PWI). For the steady state tokamak operation, the plasma current drive method should be established. Electron Bernstein wave heating and current dive (EBWH/CD) is one of attractive candidates to sustain the steady-state ST plasma. In the ST experiments, the plasma frequency may become larger than the electron cyclotron frequency in the operating density range due to the rather low magnetic field, and electron cyclotron waves cannot propagate into the plasma beyond the cutoff layer. In the EBWH/CD experiments, some mode conversions from the electron cyclotron (electromagnetic) wave to the electron Bernstein[B]- (electrostatic) wave are required. In the O-X-B mode conversion experiments, the launching angle and elliptical polarization state should be controlled to attain the high mode conversion efficiency from the O/X-mode wave to the B-mode wave. A phased-array antenna (PAA) system, which enabled us to control the launching angle (with parallel refractive index $N_{//}$) and elliptical polarization state, was proposed and has been developed for the EBWH/CD experiments in the QUEST. The experimental scenarios have been considered by a multiple-ray tracing analysis, including non-optimum mode conversion cases. The antenna was set up below the mid-plane in the QUEST along the multiple ray analysis to conduct the current drive experiments. The heating and current drive experiments have been begun using a CW PAA in the QUEST.

2. Development of Phased-array Antenna

The 8.2 GHz LHCD system in the previous TRIAM-1M tokamak has been planed to be used for the EBWH/CD experiments in the QUEST. In the system, a maximum power of 200 kW generated by 8 klystrons was transmitted using 16 rectangular fundamental waveguide (WR-137) lines in the CW operation. An orthomode transducer (OMT) was developed to control launching polarization state in the antenna system. The two orthogonal electric field components were mixed to excite arbitrary elliptical polarization states with the intensity and phase control at the OMT. The 8 OMT square waveguide outputs were led into the PAA to control the launching angle. The elliptically polarized O-mode wave was obliquely injected in the O-X-B mode conversion experiments. The PAA output aperture was composed of the 8 [4×2] squared waveguide phased-array ports here. Recently, 16 [4×4] element PAA has been developed to excite 2-dimensional symmetric narrow-field distributions. Figure 1 (a) and (b) show the intensity contour plots of the E_x fields radiated from the 8 [4×2] and 16 [4×4] PAAs at the propagating position z = 0.2 m, respectively. The phase array was adjusted at x = 0.082 m and y = 0.012 m in Fig. 1 (a), while it was

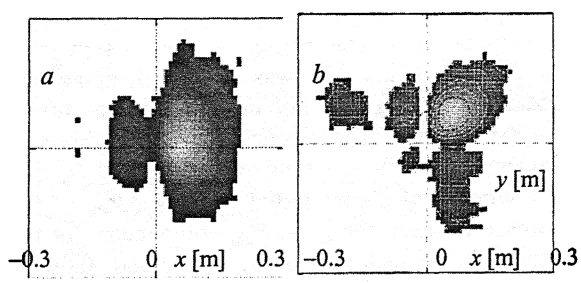

Fig. 1. Intensity contour plots of the E_x fields radiated from the 8 [4×2] and 16 [4×4] PAAs at the propagating position z = 0.2 m

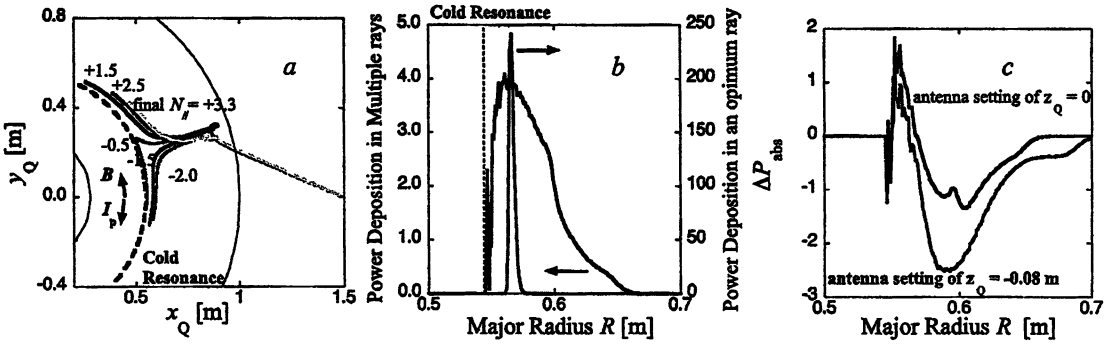

Fig. 2. (*a*) Ray trajectories with $N_{//}$ varying along propagations, (*b*) Power deposition profiles, P_{abs}, in the multiple ray analysis and in an optimum case with the [4×2] antenna, and (*c*) Radial profiles ΔP_{abs} of differences between [+/–] P_{abs} components for the antenna vertical positions of z_Q = 0 m and –0.08 m

done at 0.082 m in both of the x and y directions in Fig.1 (b). The radiation fields evaluated from Kirchhoff integrals could explain the measured fields even at the side-lobe parts. The heat load and thermal stress in the CW 200 kW operation were analyzed with finite element codes. The 8 [4×2] and 16 [4×4] antennae were made from Oxygen-Free Copper and Aluminum, respectively. The thermal stresses due to the heat load in the CW operation were analyzed to be moderate in both of the antennae.

3. Multiple Ray Analysis

In the non-optimum ray tracing in the O-X-B mode conversion, the tunneling effect through the evanescent layer should be properly treated. The ray position after the tunneling was searched in the high-density side beyond the cutoff [2]. This approach was implemented into the TASK/WR code [3] for the multiple-ray tracing.

Figure 2 (a) shows calculated ray trajectories in the O-X-B mode conversion at a toroidal tokamak cross-section until the B-wave was fully absorbed due to Doppler-shifted resonances with $N_{//}$ varying along the propagations. Here, a coordinate (x_Q, y_Q, z_Q) system with an origin at the QUEST device was taken in the multiple ray analysis. The initial poloidal refractive indexes were scanned with a fixed initial toroidal index, respectively. Figure 2 (b) shows a broad power deposition profile in the multiple ray analysis with the various $N_{//}$ evolutions, as well as a peaked profile in an optimum case. The refractive index spectra excited at the [4×2] PAA were taken into consideration. The change of the $N_{//}$ sign from plus [+] to minus [–] was observed along the propagation, which was not desired for the current drive experiments. The antenna setting position was considered to excite the field with the fixed $N_{//}$ sign [4]. Figure 2 (c) shows radial profiles ΔP_{abs} of the difference between the [+/–] P_{abs} components for the antenna vertical positions of z_Q = 0 m and -0.08 m. Here, [–] P_{abs} component had a contribution to increase the plasma current. The [–] P_{abs} component was significantly large at the antenna setting of z_Q = = –0.08 m. The experiments have been conducted with the [4×2] PAA set up at z_Q = –0.08 m.

4. Experimental Results

The non-inductive RF plasma current drive experiments have been begun using the developed [4×2] PAA. The plasma current (< ~15 kA) was started up with an aspect ratio of 1.5 and sustained by only RF injection. In the RF startup experiments, the vertical magnetic field B_z with two pairs of the poloidal magnetic coils (PFC1-7/2-6) was ramped up to about 3 mT. The toroidal magnetic field was 0.133 T. Figure 3 (a) shows reconstructed magnetic flux surfaces of the 12 kA discharge. The hard X-ray intensity from current-carrying forward electrons accelerated by the RF injection was increased in the energy range of 10~30 keV, following the I_p evolution. The long pulse discharge of 10 kA was attained for 40 s. Recently, the single-null divertor configuration with the high plasma current (< ~ 25 kA) was attained in the 17 s plasma sustainment. The new density window to sustain the plasma current was also observed in the hjgher density (over-densed) range.

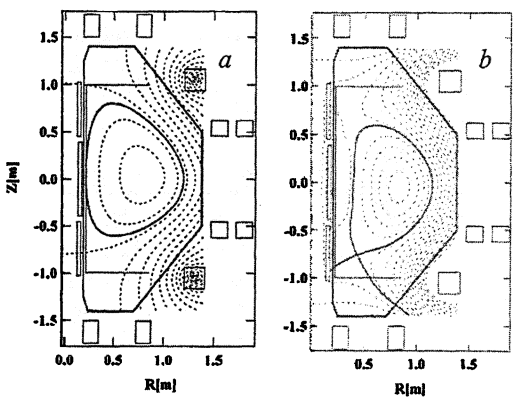

Fig. 3. (*a*) Reconstructed flux surfaces in the 12 kA limiter discharge, (*b*) Reconstructed flux surfaces in the divertor discharge with the plasma current (< ~ 25 kA)

References

1. *Hanada, K. et al.*, Proc. of the 22nd IAEA Fusion Energy Conference (2008), FT/P3-25.

2. *Igami, H. et al.*, Plasma Phys. Control. Fusion **48** (2006) 573.

3. *Fukuyama, A.*, Fusion Engineering and Design, **53** (2001) 71.

4. *Forest, C.B. et al.*, Phys. Plasmas, **7** (2000) 1352.

Controlled High-Power Microwave Diplexers

W. Kasparek[1], R. van den Braber[2], N. Doelman[2], E. Fritz[2], V. Erckmann[3], F. Hollmann[3], G. Michel[3], F. Noke[3], F. Purps[3], W. Bongers[4], B. Krijger[4], E. Eminoglou[4], M. Petelin[5], L. Lubyako[5], A. Bruschi[6], J. Stober[3], D. Wagner[3], B. Plaum[1], E. Filipovic[1], M. Saliba[1], and teams at the contributing institutes[1-6]

[1] Institut für Plasmaforschung, Universität Stuttgart, D-70569 Stuttgart, Germany
[2] Dept. of Mechatronic Equipment, TNO Science and Industry, NL-2600 Delft, The Netherlands
[3] Max-Planck-Institut für Plasmaphysik, EURATOM Association, D-17491 Greifswald, and D-85748 Garching, Germany
[4] FOM Institute for Plasma Physics "Rijnhuizen", NL-3439 Nieuwegein, The Netherlands
[5] Inst. of Applied Physics, Russian Academy of Science, 603950 Nizhny Novgorod, Russia
[6] Istituto di Fisica del Plasma, EURATOM-ENEA-CNR Ass., I-20125 Milano, Italy

Introduction

In Electron Cyclotron Resonance Heating (ECRH) systems, high-power diplexers can serve as power combiners, slow and FAst DIrectional Switches (FADIS) to toggle the power from continuously operating gyrotrons between two launchers, and as discriminators of low-power Electron Cyclotron Emission (ECE) signals from high-power ECRH using a common transmission line and antenna [1]. In the frame of a development activity for advanced ECRH, a resonant diplexer was developed for application at ASDEX Upgrade for MHD-stabilization experiments and in-line ECE. In the following, we describe the compact, waveguide-compatible design with a feedback-controlled mirror drive for tracking of the resonator to the gyrotron frequency and results from high-power, long-pulse tests with the 140-GHz ECRH system for the stellarator W7-X. Plans for application on ASDEX Upgrade and options for ITER are discussed.

Diplexer design and experimental test set up

The potential of diplexers for ECRH has triggered the development of several prototypes [1] satisfying different physics needs with different technical approaches. Driven by the physics demands for advanced NTM-control experiments at ASDEX Upgrade, we have, among many other design options, chosen a resonant diplexer [2], as shown in Fig. 1, top. Special features of this device are the narrow resonances in the output 2 ("resonant channel"), being periodic with the free spectral range of $\Delta f_F = c/L$ (c is the speed of light, L is the round-trip length of the resonator), and broad transmission bands with periodic notches in output 1 ("non-resonant channel"), depicted in Fig. 1, bottom. These design features are particularly well suited for FADIS, because of the steep resonant slope, and for power combination, as two gyrotrons operating at slightly different frequencies of the order of $0.5 \cdot \Delta f_F$ (or odd-numbered multiples thereof) can be combined to one output channel. Last but not least, in-line ECE experiments are feasible due to the good isolation from the power channel.

The diplexer is based on a 4-mirror ring resonator with gratings as beam splitters, which can be used in quasi-optical as well as in corrugated waveguide systems. Due to integrated HE_{11}-TEM_{00}-mode converters, it readily fits into a straight corrugated waveguide section of the transmission system at ASDEX Upgrade [3].

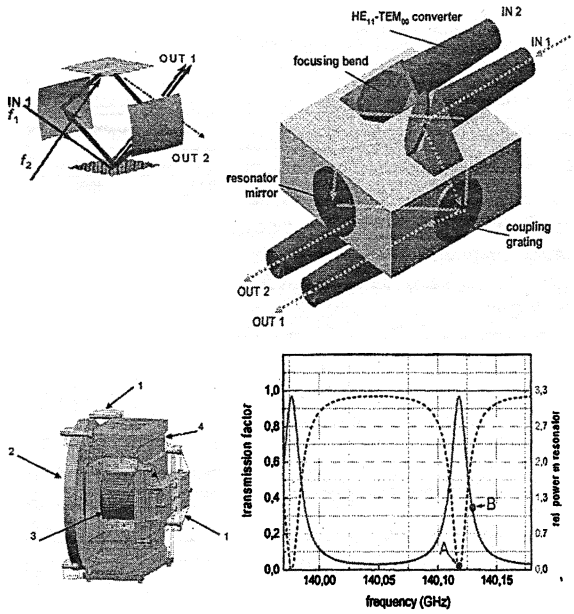

Fig. 1. Compact resonant diplexer. Top: principle (left), mechanical design (right). Bottom: resonator mirror with drive (left), transmission function with operation points A and B (right; dashed line: non-resonant channel 1-1; solid line: resonant channel 1-2)

To cope with frequency variations of free-running gyrotrons (frequency chirp at the beginning of the pulse, erratic frequency jumps during the pulse, frequency dependence on the output power, etc.), a fast drive for the resonator mirror was developed. It is controlled by the output power signals of the diplexer and an optional real-time frequency measurement; this allowed tracking of the slope (operation point B in Fig. 1) or the peak (point A) of the diplexer resonance to the gyrotron frequency on a 20-ms timescale.

The diplexer had been investigated by extensive low-power measurements [1]. Afterwards it was installed in the beam duct of the ECRH system on W7-X [4] for high-power tests. Here, the beams from one or two gyrotrons could be coupled to the input(s), where the TEM_{00}-HE_{11} interfaces had been removed. The transmitted power at the two outputs was measured by directional couplers, and finally was dumped into two cw calorimetric loads.

High-power tests

Several diplexer applications were investigated during the tests. "Slow" switching of the continuous power from one tube between two output channels by controlled mirror movement is shown in Fig. 2. Fast switching by frequency-shift keying of the gyrotron (using few kV modulation of the body voltage) with optimum contrast was demonstrated, and tracking the notch of the diplexer to the gyrotron as is needed for in-line ECE experiments was possible.

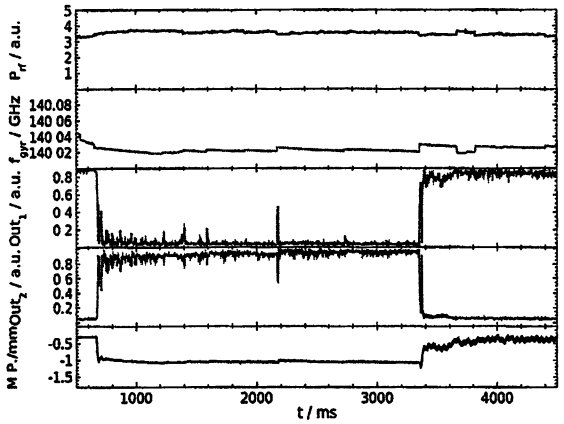

Fig. 2. Switching of the input power at IN1 between both output channels by diplexer mirror control only. The RF signal P_{rf} (top) and the gyrotron frequency f_{gyr} (2nd from top) are displayed together with the normalized output power in the non-resonant (OUT_1, 3rd from top) and resonant output channel OUT_2 (4th from top) and the mirror position M.P. (bottom) as a function of time. The feedback control of the mirror is activated in the time 680 ms < t < 3350 ms

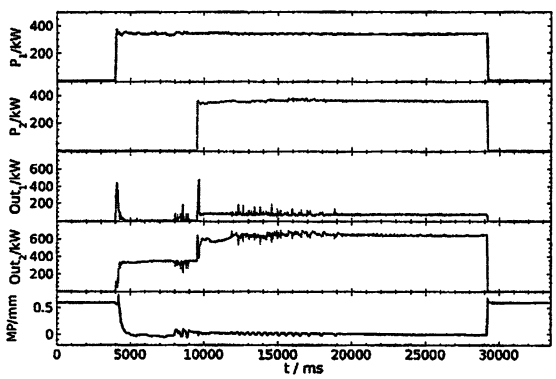

Fig. 3. Beam combination of two gyrotrons operating at slightly different frequencies with diplexer frequency tracking to dip. The RF power of gyrotron 1 (P_1, top) at IN1 and gyrotron 2 (P_2, 2nd from top) at IN2, respectively, are displayed together with the output power in channel OUT1 (3rd from top) and OUT2 (4th from top) as a function of time. The controlled mirror position MP is shown at the bottom

When feeding two gyrotrons to the diplexer, stable power combination with an output contrast of 90 % could be reached, as shown in Fig. 3.

Application on ASDEX Upgrade

At present, a proof-of principle experiment on synchronous NTM stabilization on ASDEX Upgrade is in preparation. Furthermore, the diplexer will be used for in-line ECE at ASDEX Upgrade to demonstrate the applicability of this technique in CW systems [5]. For further optimization, compact diplexers, which use an eigenmode in the resonator corresponding to the HE_{11} mode in waveguide, are being developed; they allow direct connection of corrugated waveguide without the use of HE_{11}-to-TEM_{00} converters, and are very efficient mode filters in the resonant output. The design is very compact without enhancing the power load on the mirrors, and thus ideally suited for integration into large ECRH systems [1].

Options for ITER, Conclusions

In the 170-GHz ECRH system of ITER [6], 24 gyrotrons are connected via corrugated HE_{11} waveguide to three upper launchers (UL, mainly for NTM stabilization) and one equatorial launcher (EL, mainly for central heating and current drive). The replacement of the mechanical waveguide switches between the launchers by diplexers and the integration of the diplexer control into the control system of the experiment would strongly increase the system performance: Any desired distribution of the power between the ULs and the EL according to the needs of the experiment – while running the gyrotrons continuously-becomes possible. For efficient NTM-mode stabilization, the switching of the gyrotrons from the EL to the UL in phase with the island rotation frequency can be instantaneously started by a voltage modulation of only a few kV. Then in a few milliseconds the diplexers are tracked towards point B (Fig. 1), to achieve the maximum power modulation for the ULs, while the remaining asynchronous power is still available at the EL. For any power upgrade at a late stage, additional gyrotrons could be fed into the second inputs of the diplexers to provide power combination.

In conclusion, diplexers will improve the flexibility and efficiency, especially for large ECRH systems employing many transmission lines and launchers, while simultaneously reducing the complexity.

Acknowledgments

This work was carried out in the frame of the virtual institute "Advanced ECRH for ITER" (collaboration between IPP Garching and Greifswald, KIT Karlsruhe, IPF Stuttgart, IAP Nizhny Novgorod, and IFP Milano), supported by the Helmholtz-Gemeinschaft deutscher Forschungszentren.

The work by TNO and FOM has been carried out in the frame of the ITER-NL project, supported by the Dutch Ministry of Economic Affairs, in the "Fonds Economische Structuurversterking" program.

References

1. *A. Bruschi et al.*, IEEE Trans. Plasma Sci. PS-38, art. no. 5460918, 1427-1438 (2010).

2. *M.I. Petelin*, 6th Workshop on High Energy Density and High Power RF, AIP Conf. Proc. 691, 251-262 (2003).

3. *D. Wagner et al.*, Fusion Sci. Technol. 52, 313-320 (2007).

4. *V. Erckmann et al.*, Fusion Sci. Technol. 52, 291 (2007).

5. *W.A. Bongers et al.*, Progress of CW compatible implementations of line-of-sight ECE..., this conference.

6. *M.A. Henderson et al.*, Nucl. Fusion 48, 054013 (2008).

RF-Experiments at the WEGA-Stellarator

H.P. Laqua[1], A. Ben Rhouma[2], E. Chlechowitz[4], B. Chouli[5], H. Laqua[1], S. Marsen[1], T. Stange, M. Otte[1], J. Preinhaelter[3], J. Urban[3]

[1] Max-Planck-Institut für Plasmaphysik, EURATOM Ass., D-17491 Greifswald, Germany
[2] University of Rostock, Faculty of Electrical Engineering, D-18059 Rostock, Germany
[3] Institute of Plasma Physics, EURATOM/IPP.CR Ass., 182 00 Prague, Czech Republic
[4] HSX Plasma Laboratory, University of Wisconsin, Madison, USA
[5] Université Pierre et Marie Curie, Ecole Polytechnique, Université Paris XI, INSTN

Introduction

WEGA is a classical $l = 2$ stellarator with five field periods ($m = 5$), a major radius of $R = 72$ cm and a maximum effective plasma radius of a=11 cm, respectively. The toroidal magnetic field coils can be operated at 0.5 T for about 20 s. With additional vertical field coils for varying the radial plasma position, the machine has a very flexible magnetic configuration. For plasma generation, two microwave heating systems operating at a frequency of 2.45 GHz (altogether 26 kW, cw) and 28 GHz (10 kW, cw), respectively, and a transformer with a capacity of 440 mVs for Ohmic heating are available. The 28 GHz microwaves are launched quasi-optically by a movable mirror system, which is installed inside the vacuum vessel. Thus the toroidal launch angle and the launch position can be varied. Additionally, both polarisation parameters (orientation and ellipticity) can be arbitrarily chosen. A specially designed waveguide converts the TE02 gyrotron mode into the HE11 mode for the quasi-optical transmission. The 2.45 GHz System consists of two TE11 transition lines for 20kW and 6 kW, respectively, with different circular antennas in front of the plasma. Both lines are equipped with directional couplers and stub tuners for matching. Both heating system can be modulated with up to 12 kHz at variable modulation amplitudes. Helium was the operating gas in most experiments. In some special cases hydrogen and argon were used. WEGA is also used as a test-bed for the Wendelstein7-X machine control and data acquisition system.

Over-dense plasma heating

The WEGA stellarator is used for fundamental research on plasma-wave interaction under steady-state conditions. The combination of different rf frequencies generates beneficial synergy effects, which makes it possible to reach otherwise inaccessible plasma conditions. The 2.45 GHz resistive R-wave heating enables the density threshold of $1 \cdot 10^{19}$ m^{-3} to be overcome for 28 GHz (OXB) **O**rdinary-e**X**traordinary-**B**ernstein-mode conversion heating and current drive with electron Bernstein waves (EBW) in over-dense plasmas, where the EBWs generate a hot (>10 keV) electron population and suprathermal electron Bernstein wave emission (EBE). The transition into the OXB-heated plasma is accompanied by a fast increase of the central density and a sharp decrease of the microwave stray-radiation level due to the high absorption of the Bernstein waves even at low electron temperatures as shown in Fig. 1. The logical interconnection of both signals is routinely used by the W7-X prototype control system to detect the transition automatically and to switch-off the auxiliary 2.45 GHz heating. The plasma is then exclusively OXB-heated. This heating scenario is also foreseen for W7-X at ultra-high densities above $2.5 \cdot 10^{20}$ m^{-3}. The long discharge time and the flexible control system enables the variation of magnetic field, plasma position and gas flux during the discharge in order to optimize the parameter in the OXB-phase. The EBE makes use of the inverse (BXO)-mode conversion process; thus the precise measurement of the k-spectrum of the emitted wave makes it possible to investigate the details of the conversion process. Both the OXB-heating, OXB-current drive and the suprathermal EBE are modeled with ray-tracing calculations that take into account a non-thermal electron distribution function. This is absolutely necessary because the Bernstein wave heated plasma expresses a strong non-thermal electron component. The spatial localization and the energy distribution of the suprathermal electrons is measured with a soft-X pulse height analyzer with pinhole imaging, making use of the long stationary discharge time. The long discharge time also enables sensitive measurements with power modulation.

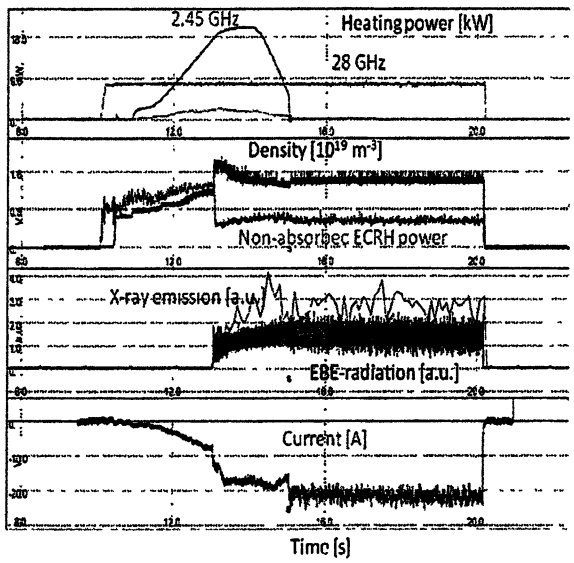

Fig. 1. Overdense plasma heating by OXB-mode conversion. Signals from the top: heating power, density and 28 GHz stray radiation, X-ray emission and EBE-radiation, plasma current

Rf-current drive

Below the 28 GHz cut-off density and well above the 2.45 GHz cut-off density at typically $2 \cdot 10^{18}$ m^{-3}, the 28 GHz ECRH enables the 2.45 GHz waves to couple to very high-energetic electrons (> 0.3 MeV) and to drive currents >100 A/kW with lower hybrid waves in steady state. It is a Landau-damping type interaction that mainly increases the parallel electron momentum. A synchrotron like broad ECE radiation spectrum measured by ECE-radiometer is generated by the high energy electron component. Its energy distribution is measured by γ-ray detectors using Geiger-Mueller type gas counters with different thicknesses of lead screening. Even with a lead screening of 28 mm, which correspond to γ-energies of more than 1 MeV, a significant count rate well above the background rate could be detected.

At energies above 200 keV, the electron confinement in WEGA becomes highly asymmetric for co- and counter propagating electrons. Thus the rf-driven current no longer depends on the $N_{//}$ spectrum of the emitting antenna, but can only be driven with electrons that are propagating in the direction with stable trajectories. A current reversal is only possible with a reversal of the magnetic field direction. This current drive mechanism is different from the well known Fish-Boozer- and Ohkawa-type schemes [1, 2] and could also be meaningful for high energy ions in fusion devices.

MeV electrons

The generation of MeV electrons at WEGA opens the possibility to investigate the predicted stagnation orbits [3], which also occur for runaway electrons in tokamaks experiments and for energetic α-particles in fusion reactors. These orbits are located at the equatorial plane at the plasma edge and do not encircle the magnetic axes. In WEGA, the fast electrons are located at a 30 mm thick layer at the low-field side of the plasma and could be completely collected by a probe moving through that region. Their average energy was estimated to be 1.7 MeV. The main γ-radiation orginates from the toroidal position, where in-vessel components approach the plasma at the low field side; this indicates that the MeV electrons are finally colliding with components. The particle trajectories in the poloidal projection are shown in Fig. 2 for different energies.

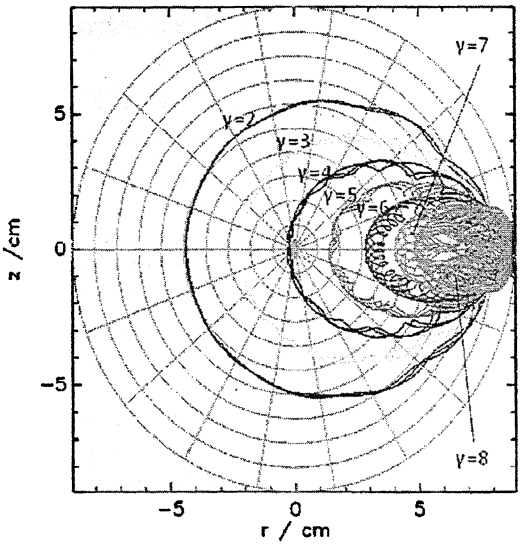

Fig. 2. Poloidal projection of the electron trajectories with initial zero pitch angle for different relativistic γ–values

Antenna development

The coupling of the 2.45 GHz rf-waves was investigated with different antenna types. The best coupling was found with an open double cut circular antenna with a symmetric *k*-spectrum. In order to test the current drive mechanism, a front bended tube was used which emits circular polarized waves only in one direction. An antenna rotation of 180° did not change the current direction as it was expected due to the high energy particle orbit. Recently, a new LH-type grill antenna of circular cross-section with variable $N_{//}$ values between 2 and 4 was designed and built. Additionally, the flexible antenna allows a coupling optimization by varying the antenna-plasma distance during the plasma operation. Unfortunately this antenna could not yet reach the performance of the open mono-waveguide antennas, since a proper matching has not yet been achieved.

References

1. *Fisch, Nathaniel J.* Theory of current drive in plasmas.: Rev. Mod. Phys. 59 (1987), Jan, Nr. 1, S. 175–234. http://dx.doi.org/10.1103/RevModPhys.59.175. – DOI 10.1103/RevModPhys.59.175.

2. *Ohkawa T.*, General Atomic Report No. 4356.007. 001 (1976).

3. *Zehrfeld H.P.D., Fussmann D., Green B.J.*: Plasma Physics. V. 23, № 5, p. 473-489, 1981 General Atomic Report No. 4356.007.001 (1976).

Sawtooth Control in the Presence of Fast Ions

M. Lennholm[1,2,3], T. Blackman[4], F. Bouquey[2], I. T. Chapman[4], C. Darbos[2,5], L-G. Eriksson[1], G. Giruzzi[2], J.P. Graves[6], D.F. Howell[4], E. Corbel[2], F. Turco[2,7] and JET EFDA Contributors

[1]European Commission, B-1049 Brussels, Belgium, morten.lennholm@jet.efda.org
[2]CEA, IRFM, F-13108 Saint-Paul-lez-Durance, France.
[3]EFDA Close Support Unit, Culham Science Centre, Abingdon OX14 3DB, UK
[4]EURATOM/CCFE Fusion Association, Culham Science Centre, Abingdon OX14 3DB, UK
[5]ITER Organization, Route de Vinon sur Verdon - 13115 St Paul Lez Durance - France
[6]Association EURATOM-Confédération Suisse, EPFL, CRPP, CH-1015 Lausanne, Switzerland
[7]Oak Ridge Associated Universities, Oak Ridge, Tennessee

Sawteeth relaxations, caused by an m = 1 Magneto Hydrodynamic (MHD) instability, periodically flatten the plasma temperature profile. At the time of such a relaxation, a sawtooth crash, the temperature inside a certain minor radius, the sawtooth inversion radius, drops abruptly, while the temperature outside this radius increases. The sawtooth inversion radius lies close to the poloidal flux surface at which the safety factor q is equal to unity. Following a sawtooth crash the temperature profile peaks up slowly until the next sawtooth crash occurs. Sawtooth crashes often trigger Neoclassical Tearing Modes (NTMs) and experimental evidence shows that this becomes more likely when the time between consecutive sawtooth crashes, the sawtooth period, increases. As NTMs degrade the plasma confinement and may lead to plasma disruptions, it is important either to avoid triggering them or to stabilise them. In a burning plasma sawteeth will assist in removing helium ash from the plasma centre but they will also reduce the central alpha particle heating. Thus it is desirable to control the sawtooth period, in order to strike an optimal balance between allowing maximum central alpha heating, facilitating helium ash removal and avoiding NTM triggering.

In the part of parameter space considered here, the Porcelli model [1] commonly used to determine when a sawtooth crash will occur, can be reduced to:

$$s_1 > s_{crit} \quad \text{and} \quad s_1 > (c/\hat{\rho})\delta W \qquad (1)$$

where both inequalities have to be fulfilled for a sawtooth crash to occur. Here s_1 is the shear $s = (r/q)(dq/dr)$ at the q = 1 surface, $\hat{\rho}$ is the normalised, thermal, ion Larmor radius and δW is the potential energy functional associated with the relevant m = 1 mode. s_{crit} and c are essentially determined by layer physics near the q = 1 surface. At a sawtooth crash the q = 1 surface becomes small or disappears and hence s_1 and $(c/\hat{\rho})\delta W$ are abruptly reduced before increasing on a diffusive timescale until (1) is fulfilled again and the next crash occurs.

The value of δW and hence the sawtooth period is strongly affected by fast ions. While central fast ions are stabilising, trapped fast ions with turning points near q = 1 can be both stabilising and destabilising depending on details of their orbits [2]. Without significant fast ion pressure, $(c/\hat{\rho})\delta W$ does not reach s_{crit} and the sawtooth crash occurs when $s_1 = s_{crit}$. With higher central fast ion pressures, $(c/\hat{\rho})\delta W$ grows rapidly following a sawtooth crash and, unless the sawtooth crash has occurred prior to $(c/\hat{\rho})\delta W$ reaching s_{crit}, the crash will be delayed until $s_1 > (c/\hat{\rho})\delta W$. The stabilising effect of fast ions, in particular fusion produced alpha particles, is likely to result in very long sawteeth in ITER, while the stabilising effect of Neutral beam (NBI) ions with energies in the 100keV range and of Ion Cyclotron Resonance Frequency (ICRF) accelerated ions in the MeV range have been documented on several tokamaks [3, 4].

The sawtooth period can be controlled by modifying δW and/or s_1. In JET Deuterium plasmas, H and He3 minority ICRF near the q = 1 surface has been seen to significantly increase or decrease the sawtooth period in plasmas with strongly stabilising central fast ion populations. As the ICRF driven current is very small in the He3 case, these experiments suggests that δW rather than s_1 is modified supporting the fast ion orbit explanation of [2]. Increasing the fast ion energy by decreasing the He3 concentration was seen to lead to an increased influence on the sawteeth in agreement with this theory as describe in [4].

Sawtooth control through the modification of s_1 using localised Electron Cyclotron Current Drive (ECCD) has been demonstrated both under conditions without fast ions (TCV [5]) and in plasmas where a central fast ion pressure was generated either by NBI (ASDEX Upgrade – 60–100 keV fast ions [3]) or by ICRF (Tore Supra – MeV fast ions [6]).

In the Tore Supra experiments [6], 2–4 MW central ICRF was used to increase the central fast ion pressure, increasing the sawtooth period from the ohmic value (25 ms) to 70–100 ms. By adding 300 kW co- current or counter-current ECCD and varying the ECCD location from mid-radius to the plasma centre, scanning the poloidal ECCD injection angle, the sawtooth period was reliably reduced to ~30 ms when the ECCD was absorbed in a fairly narrow region near the q = 1 surface. When ECCD was absorbed outside this destabilisation region, the sawtooth period remained largely unaffected. The switch between long and short sawteeth was very abrupt and it proved impossible to find ECCD locations which resulted in intermediate sawtooth periods. The destabilisation region was just inside q = 1 in the case of co-current drive while it was slightly further out, overlapping q = 1, in the case of counter current drive in good

agreement with the locations at which the ECCD driven current is expected to achieve the largest increase in s_1. When these experiments were repeated with pulsed, rather than continuous ECCD, injecting a series of 50 ms pulses at 950 ms intervals, the ECCD pulses with absorption in the destabilisation region, resulted in short sawteeth and, more interestingly, these short sawteeth persisted for 200–300 ms after the end of the ECCD pulse. In discharges with varying ICRF power and plasma density, the sawtooth period was seen to increase with density and ICRF power in the absence of ECCD destabilisation, while the period of the destabilised sawteeth remained close to the ohmic value, independently of density and ICRF power. It should, however, be noted that above a certain density ECCD was no longer able to affect the sawtooth period, probably due to the reduced ECCD current drive efficiency at high density. When these discharges were repeated without central ICRF, only a very small sawtooth period variation was observed. This is not very surprising, as the experiments were carried out at large (30°) toroidal ECCD injection angles, resulting in broad driven current profiles and modest modifications in s_1. It is, however, remarkable that an ECCD power which hardly affect the sawtooth period in plasmas without ICRF has such a strong effect in ICRF heated plasmas, possibly explaining the JET observations as well.

Though the bi-stable nature of the sawtooth period is puzzling, very abrupt changes in sawtooth period are also characteristic of JET experiments with significant fast ion populations. An explanation could be that the simultaneous temporal evolution of s_1 and δW means that, while $s_1 > (c/\hat{\rho})\delta W$ determines the time of the sawtooth crash in the absence of ECCD destabilisation, a small increase in s_1 caused by ECCD may result in s_1 reaching s_{crit}, triggering the sawtooth, before $(c/\hat{\rho})\delta W$ exceeds s_{crit} thereby eliminating the fast ion stabilising effect. A small reduction of δW induced by phased ICRF absorbed near $q = 1$ could have the same effect.

The narrow radial ECCD/ICRF deposition range required to destabilise sawteeth makes real time control of the absorption location a necessity for reliable NTM avoidance and helium ash removal. Real time sawtooth period control using steerable ECCD beams has been demonstrated on Tore Supra, with central ICRF generated fast ions [6, 7] and in ECCD only plasmas on TCV [5], while experiments on JET have demonstrated real time sawtooth period control using variable frequency ICRF [8].

In the Tore Supra experiments, when using a simple PID sawtooth period controller, the bi-stable nature of the sawtooth period led to oscillatory control loop behaviour when the requested sawtooth period was in the unachievable range [7]. To remedy this, a 'search and maintain' control scheme was developed. This controller initially moves the poloidal injection angle until sufficiently short sawteeth are achieved, at which time the injection angle and measured sawtooth inversion radius are memorised. In the remainder of the control phase the injection angle required to maintain the difference between the ECCD absorption radius and the sawtooth inversion radius is found from a real time sawtooth inversion radius measurement, using look-up tables to translate ECCD injection angles into absorption radii. As the 'search' part of the algorithm finds the ECCD location, initially required for destabilisation, the look up tables only needs to indicate the change in ECCD radius associated with modest poloidal injection angle variations. Using the 'search and maintain' controller, short sawteeth have successfully been achieved and maintained for > 4 s during an ICRF heated Tore Supra discharge [6].

In the JET experiments, the operating frequency of the ICRF generators was changed in real time within a 1MHz interval surrounding the nominal operation frequency allowing the resonance location to be varied within a range of ~6 cm (~20 % of the minor radius of the $q = 1$ surface). This modest range is (just) sufficient to achieve a significant sawtooth period variation. The rate of change of this frequency is limited to 75 kHz/s due to the need to move mechanical matching elements in order to keep acceptable matching throughout. In closed loop experiments it was demonstrated that the sawtooth period could be controlled in the range from 30 ms to 60 ms [8].

Though promising results have been achieved demonstrating the ability of both ECCD and ICRF in controlling the sawtooth period of fast ion stabilised sawteeth, further development is required before these methods can be reliably extrapolated to future machines in which sawtooth control may well be essential.

Acknowledgments: This work supported by EURATOM was carried out in the framework of the European Fusion Development Agreement. The views and opinions expressed do not necessarily reflect those of the European Commission.

References

1. *Porcell F., Boucher, D., Rosenbluth, M.N.* Model for the sawtooth period and amplitude // Plasma Phys. Control. Fusion 1996. V. 38. 2163.

2. *Graves, J. et al.* Sawtooth-Control Mechanism using Toroidally Propagating Ion-Cyclotron-ResonanceWaves in Tokamaks // Phys. Rev. Lett. 2009. V. 102. 065005.

3. *Mueck, A. et al.* Sawtooth control experiments on ASDEX Upgrade // Plasma Phys. Cont. Fusion 2005. V. 47. 1633.

4. *Graves, J. et al.* Experimental verification of sawtooth control by energetic particles in ion cyclotron resonance heated JET tokamak plasmas // Nucl. Fusion 2010. V. 50. 052002.

5. *Paley, J. I. et al.* Real time control of the sawtooth period using EC launchers // Plasma Phys. Control. Fusion 2009. V. 51. 124041.

6. *Lennholm, M. et al.* Demonstration of Effective Control of Fast-Ion-Stabilized Sawteeth by Electron-Cyclotron Current Drive // Phys. Rev. Lett. 2009. V. 102. 115004.

7. *Lennholm, M. et al.,* Closed Loop Sawtooth Period Control Using Variable Eccd Injection Angles On Tore Supra // Fusion Sci. and Tech. 2009. V. 55. P. 45.

8. *Lennholm, M. et al.* Feedback Control of the Sawtooth Period through Real Time Control of the Ion Cyclotron Resonance Frequency // submitted for publication in Nucl. Fusion 2011.

Physics Study of ECCD in Heliotron J

K. Nagasaki[1], N.B. Marushchenko[2], S. Yamamoto[1], K. Sakamoto[1], Y. Turkin[2], T. Mizuuchi[1], H. Okada[1], K. Hanatani[1], T. Minami[1], K. Masuda[1], S. Kobayashi[1], S. Konoshima[1], M. Takeuchi[1], Y. Nakamura[2], S. Ohshima[4], K. Mukai[2], H.Y. Lee[2], K. Mizuno[2], S. Murakami[6], Y. Moriya[6], Y. Yoshimura[5], G. Motojima[5], Á. Cappa[7], F. Sano[1]

[1]Institute of Advanced Energy, Gokasho, Uji, Kyoto University, Japan, nagasaki@iae.kyoto-u.ac.jp
[2]Max-Planck-Institut für Plasmaphysik, Greifswald, Germany
[3]Graduate School of Energy Science, Gokasho, Uji, Kyoto Univ., Japan
[4]Kyoto Univ. Pioneering Research Unit for Next Generation, Gokasho, Uji, Japan
[5]National Institute for Fusion Science, Toki, Japan
[6]Department of Nuclear Engineering, Kyoto University, Kyoto, Japan
[7]Laboratorio Nacional de Fusión, EURATOM-CIEMAT, Spain

Noninductive current plays an important role in the realization of high-performance plasmas and the sustainment of steady-state plasmas in toroidal fusion devices. Although no Ohmic current is required for equilibrium in stellarator/heliotron (S/H) systems due to generation of the confinement magnetic field by external coils, noninductive currents such as bootstrap current and NB current (Ohkawa current) flows as well as in tokamaks. These currents give rise to modification of the rotational transform profile, thereby affecting the equilibrium and stability. We have observed in the S/H device, Heliotron J, that MHD activity of the m/n = 2/1 mode is excited when the rotational transform increases from 0.48 to 0.50 by bootstrap current and NB driven current [1]. Furthermore, a transition onset to an improved confinement mode in NBI plasmas has been observed in relation to the noninductive current [2].

Electron cyclotron current drive (ECCD) is recognized as being a useful scheme for stabilizing MHD instabilities in tokamaks. In S/H systems, ECCD is expected to be an effective current drive scheme to suppress the non-inductive current and to tailor the rotational transform profile, particularly in low-shear devices. In Heliotron J, we have conducted ECCD experiment [3, 4], and successfully demonstrated that net zero current state was maintained by cancelling the bootstrap current with ECCD. From the viewpoint of diagnostics, S/H systems have the advantage of achieving an accuracy of 0.1 kA using conventional Rogowski coils due to no Ohmic current.

The coil system of Heliotron J is composed of an L=1/M=4 helical coil, two types of toroidal coils A and B, and three pairs of vertical coils. The configuration is scanned by varying the current ratios in each coil, making it possible to investigate the properties of noninductive current over a wide range of magnetic configurations. We have recently installed an upgraded EC launching system in the Heliotron J in order to extend the controllability of EC driven current [5]. The upgraded 70-GHz launching system consists of an ellipsoidal mirror and a steerable flat mirror. The steerable mirror enables us to change the beam angle flexibly in the toroidal and poloidal directions.

Second harmonic X-mode ECCD experiments have been conducted using the upgraded launching system [6]. A localized ECH power of 400 kW is possible to inject up to 200 ms. Figure 1 shows the $N_{\parallel}$ dependence of the measured toroidal current. We define the current flowing in the Fisch-Boozer direction as positive. In ECH plasmas, the toroidal current is composed of the bootstrap current and the EC current. These currents can be separated by comparing the experimental results obtained for clockwise and counter-clockwise magnetic fields, since the flow direction of the bootstrap current is reversed by reversing the magnetic field, while that of the EC current associated with the B strength is not. For near-ripple-top heating case (Fig. 1(a)), the EC driven current increases with $N_{\parallel}$ in the Fisch-Boozer direction. For near-ripple-

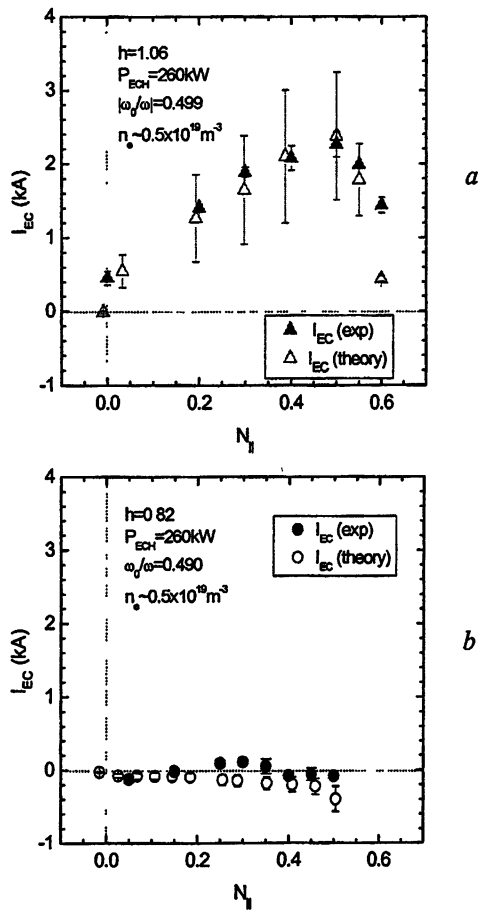

Fig. 1. $N_{\parallel}$ dependence of EC driven current, (a) near-ripple-top-heating and (b) near-ripple-bottom heating

bottom heating (Fig. 1(*b*)), on the other hand, the EC driven current is almost zero regardless of $N_{\parallel}$.

A numerical simulation using TRAVIS code [7, 8] is performed for the Heliotron J configuration to calculate the ECCD. The absorption is decomposed into the contributions from trapped and passing electrons by analyzing during integration along the resonance line. The CD efficiency is calculated by applying the adjoint approach with parallel momentum conservation taken into account. As shown in Fig. 1, the TRAVIS calculation quantitatively agrees well with the experimental results for the magnetic configurations conducted in the experiments. The collisional limit model overestimates the EC driven current by a factor of 4–5, indicating that the trapped particle effect is required to explain the experimental results.

The EC current is also calculated by GNET code using a Monte Carlo technique in 5-D phase space [9]. The GNET code solves a linearized drift kinetic equation as a time-dependent initial value problem. A technique similar to the adjoint equation for dynamic linearized problems is used, and the linearized drift kinetic equation for the deviation from the Maxwellian background is solved. The radial diffusion of trapped particles is taken into account. The calculation results show that the dependence of EC driven current on the magnetic configuration including reversal of the flow direction at a ripple bottom heating is reproduced by GNET.

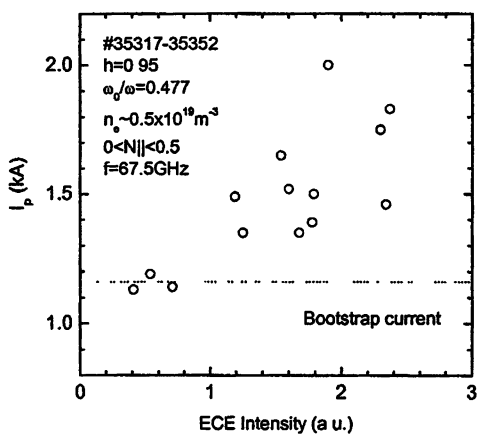

Fig. 2. Relation between EC driven current and ECE intensity. $N_{\parallel}$ is scanned from $N_{\parallel} = 0.0$ to $N_{\parallel} = 0.5$

We have observed enhancement of ECE signals by one order of magnitude and high correlation with the toroidal current as shown in Fig. 2. Since the optical thickness at this low density is gray, $\tau \sim 1$, and the stored energy is weakly changed during the $N_{\parallel}$ scan, the ECE signal reflects not only the bulk T_e but also the high-energy tail. The oblique launch shifts the EC absorption in higher energy range, increasing the population of high-energy electrons.

The EC driven current in S/H systems is not so high as that in tokamaks due to high magnetic ripple. However, it is comparable to bootstrap current, and it can modify the rotational transform profile. A one-dimensional current diffusion equation is solved to calculate the time evolution of rotational transform profile. Figure 3 shows a calculation result on the rotational transform profile. An inductive current is driven at the initial phase, and the rotational transform profile goes to the final state after the *L/R* current diffusion time. The rotational transform has a local maximum or minimum, depending on the flow direction of EC driven current. This suggests that ECCD has a potential to control interchange instability and/or Alfven eigenmodes. MHD control experiment using ECCD will be conducted in the forthcoming experimental campaign.

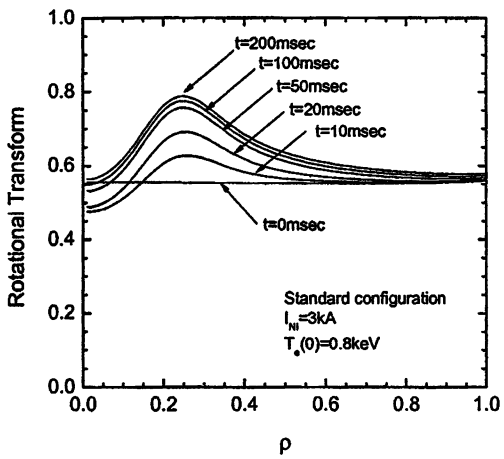

Fig. 3. Time evolution of rotational transform profile. The noninductive current of $I_{NI} = 3$ kA is assumed to initially flow at $\rho = 0.2$ with the width of $\Delta\rho = 0.1$

The authors are grateful to the Heliotron J staff for conducting the experiments. This work was performed with the support and under the auspices of the Collaboration Program of the Laboratory for Complex Energy Processes, IAE, Kyoto University, and the NIFS Collaborative Research Program (NIFS08KOAR010, NIFS10KUHL030), the NIFS/NINS project of Formation of International Network for Scientific Collaborations, and a Grant-in-Aid for Scientific Research, MEXT.

References

1. *G. Motojima, et al.*, Plasma and Fusion Res. **3** (2008) S1067.
2. *S. Kobayashi, et al.*, 11th IAEA TM on H-mode Phys. Trans. Barriers (Tsukuba, 2007) (http://www-jt60.naka.jaea.go.jp/h-mode-tm-11/index.html).
3. *G. Motojima, et al.*, Nucl. Fusion **47** (2007) 1045.
4. *K. Nagasaki, et al.*, Nucl. Fusion **50** (2010) 025003.
5. *K. Nagasaki, et al.*, Contrib. Plasma Phys. **50** (2010) 656.
6. *K. Nagasaki, et al.*, submitted to Nucl. Fusion.
7. *N.B. Marushchenko, et al.*, Fusion Sci. Technol. **55** (2009) 180.
8. *N.B. Marushchenko, et al.*, Phys. Plasmas **18** (2011) 032501.
9. *Y. Moriya, et al.*, submitted to Plasma Fusion Res.

LH Current Drive in Spherical Tokamak. Theory and Experiment

O.N. Shcherbinin, E.Z. Gusakov, V.V. Dyachenko, M.A. Irzak, S.A. Khitrov, A.N. Saveliev

A.F. Ioffe Physico-Technical Institute, RAS, St. Petersburg, Russia, o.shcherbinin@mail.ioffe.ru

At present, the method of Lower Hybrid Current Drive (LHCD) is not used in Spherical Tokamaks (ST) because of the accessibility problem, since STs operate usually with high enough densities at comparatively low magnetic field, so that $\omega_{pe} \gg \omega_{Be}$. For instance, in Globus-M condition [1] initial $N_{||}$ necessary for wave penetration into the central region should be greater than 7–10 ($N_{||}$ – component of refractive index parallel to magnetic field). Effective excitation of these waves is a complicated technical problem, however been launched such waves would be absorbed at the plasma periphery due to the Landau damping. Luckily, the strong poloidal inhomogeneity of the magnetic field in spherical tokamaks (due to low aspect ratio and high elongation) provides the possibility of using an alternative approach. It was proposed in [2] that the waves with comparatively low slowing factors (≈3–5) excited by the "grill" antenna in the equatorial plane should be slowed down in poloidal rather than toroidal direction. For this account the waveguides should be stacked vertically, one atop the other, with the broad side parallel to toroidal direction. The waves propagate at first at the plasma periphery, their $N_{||}$ is increased due to the poloidal inhomogeneity, and finally they penetrate into the dense plasma and are absorbed by the Landau mechanism in the vicinity of the "poloidal" resonance.

The described approach has been used in preparation of the LHCD experiments on the low aspect ratio tokamak Globus-M. The obtained results are refered here as examples of general approach. Standard regime taken for simulation: R = 0.36 m, a_0 = 0.24 m, B_0 = 0.4 T, I_p = 0.25 MA, vertical elongation – 1.6, triangularity– 4 cm, $n_0 = 4 \cdot 10^{19}$ m^{-3}, $n_b = 1 \cdot 10^{17}$ m^{-3}, T_{e0} = 400eV. The operating frequency was 2.45 GHz.

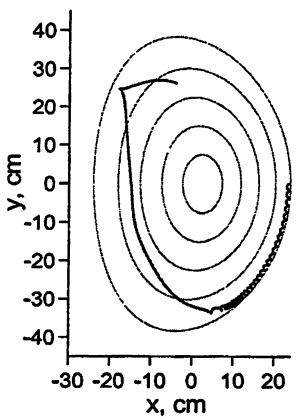

Fig. 1. The wave ray projection on the poloidal cross-section calculated by ray tracing technique at $Npol = -2.9$

Self-consistent modeling of the grill operation was carried out with GRILL3D code [3] using plane, 1D inhomogeneous plasma model. The problem of wave propagation was solved in a plasma slab with parameters imitating the Globus-M equatorial region. As a result, the surface impedance matrix was calculated. Then this matrix was used as a boundary condition for 3D simulation of antenna operation. The basic grill configuration consisted of 10 waveguides with adjoining broad sides, stacked vertically ("poloidal" grill), so that the waveguide electric field (of fundamental TE_{10} mode) was aligned with poloidal direction. Waveguide openings width was equal to 10 mm, the septum width was 4 mm; phase shift between adjacent waveguides could be varied.

It was found out that, in spite of severe complications caused by low value of magnetic field in spherical tokamaks, there is a fairly wide range of experimental conditions when multi-waveguide antenna (grill) aligned poloidally and placed in the equatorial plane excites LH waves which propagate in peripheral plasma layer in a sort of plasma waveguide. Due to the strong plasma poloidal inhomogeneity those waves experience slowing down and finally reach the warm core of the discharge, where they are absorbed by electrons via the Landau mechanism (Fig. 1). The antenna characteristics influence the spectrum of waves excited in plasma only partly. It was found out that from various field patterns "imposed" by the antenna the plasma "accepts" only those permitted to propagate inside the plasma waveguide. Also a very strong poloidal asymmetry in the plasma transparency was found. The allowed direction of poloidal propagation is determined by the direction of toroidal magnetic field. At most experimenal conditions the overall reflection coefficient in grill operation is estimated as 20–30 %, which is still very high. However varying the phasing of grill waveguides one can find some favorable conditions when the antenna coupling with plasma waveguide gets rather high and the reflection reduces down to several percents.

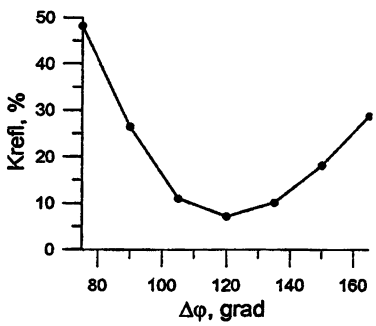

Fig. 2. The total reflection coefficient in dependance on the phase shift between waveguides for density profile $\sim(1-r^4)^2$

LH waves propagation and absorption in the 2D inhomogeneous ST plasma was modelled independently by the ray tracing code (using a Hamiltonian with gradient terms corrections [4]) and by the full-

wave 2D code [5]. It was shown that the LH waves excited poloidally turn gradually in toroidal direction (against plasma current, that is favorable for current drive perspective), increase $N_{||}$ and finally enter the bulk plasma where the RF energy is absorbed. The parallel refractive index growth is shown to be enhanced by the poloidal resonance, which is specific for 2D inhomogeneous plasmas at frequencies equal to several times the LH resonance frequency. The location of poloidal resonances in a cold Globus-like plasma is determined by two conjoint conditions [5]:

$$\varepsilon + \eta \frac{B_\theta^2}{B^2} = 0, \qquad (1)$$

and

$$\frac{\partial}{\partial r}\left(\varepsilon + \eta \frac{B_\theta^2}{B^2} \right) = 0. \qquad (2)$$

At simultaneous fulfillment of both conditions, N_θ (and therefore $N_{||}$) tends to infinity. That is why it is called the "poloidal" resonance. In practice the exact fulfillment of this condition in a warm plasma is not necessary, $N_{||} \approx 10$ will be quite sufficient for effective Landau damping [6], (compare Fig. 1 and Fig. 3).

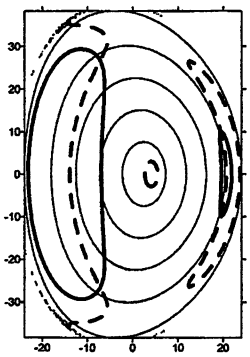

Fig. 3. The location of the poloidal resonance at Ip=180 kA. Condition (1) – solid line, condition (2) – broken line

Finally, the LHCD was modeled for plasma parameters close to those of the tokamak Globus-M using the modified version of the Fast Ray Tracing Code (FRTC) [7]. This version takes into account the additional terms in the LH dispersion relations described in [4]. FRTC solves the LH wave equation in the cold plasma ray approximation, well justified for frequencies above the LH resonance frequency, and calculates iteratively the LH power deposition into the plasma electrons together with electron quasilinear diffusion coefficient. The latter is used in calculations of the electron distribution function in a simple 1D Fokker-Planck equation with a correction to the collision operator to account for important 2D effects due to pitch angle scattering. The spectrum computed for "poloidal" grill was used for modeling being imitated by 25 groups of 100 rays started from different spatial positions evenly distributed along the poloidal position of the LH antenna. The LHCD of up to 100kA have been demonstrated.

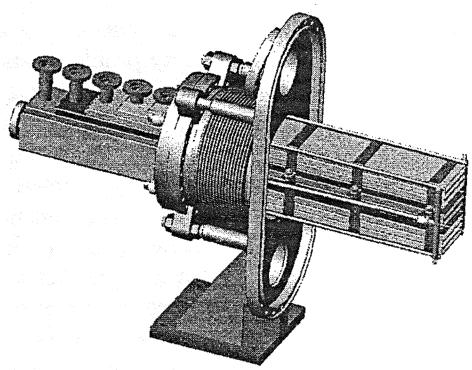

Fig. 4. The design of the 10-waveguide poloidal grill

The construction of the poloidal grill was developed by use of standard waveguides with inner cross-section 90×10 mm and wall width of 2 mm. The antenna can be moved along its axis and be turned around it. No multi-junction scheme is used, since a maximum flexibility in varying waveguide phasing is needed in experiments. So phase shifters will be installed in each wave channel.

This work has been supported by the Russian Foundation for Basic Research grant 09-02-01336a.

References

1. *Gusev, V.K. et al.* Spherical tokamak Globus-M // Technical physics 1999. V. 44, № 9. P. 1054.

2. *Esterkin, A.R. et al.* RF heating in Globus-M tokamak at lower hybrid frequencies // Spherical Torus'97. Proc. Int. Workshop, St. Petersburg, Russia, 1997. V. 1. P. 265.

3. *Irzak, M.A., Shcherbinin, O.N.* Theory of waveguide antennae for plasma heating and current drive // Nuclear Fusion. 1995. V. 35, № 11. P. 1341.

4. *Gusakov, E.Z., et al.,* New regions of transparency for intermediate-frequency waves in an inhomogeneous magnetoactive plasma // Pis'ma v ZhETF. 1997. V. 65, № 1. P. 26, (JETP Lett. 1997. V. 65. P. 25).

5. *Irzak, M.A.* Full-wave 2D modeling of LH heating in Globus-M tokamak // Proc.of the 30th EPS Conf. on CFPP, St. Petersburg, (2003), ECA. V. 27A, P-2.175.

6. *Gusakov, E.Z. et al.* Lower hybrid wave excitation and propagation in the spherical tokamak Globus-M // Plasma Phys. Control. Fusion. 2010. V. 52. P. 075018.

7. *Esterkin, A.R.* and *Piliya, A.D.* Fast ray tracing code for LHCD simulation // Nucl. Fusion. 1996. V. 38, № 11. P. 1501.

Conceptual Design of an ECRH System for JET

C. Sozzi[1], G. Giruzzi[2], M. Lennholm[3,4], A. Parkin[5], G. Aiello[6], M. Bellinger[5], J. Bird[5], F. Bouquey[2], H. Braune[7], A. Bruschi[1], P. Butcher[5], R. Clay[5], E. de la Luna[3,9], G. Denisov[10], T. Edlington[5], J. Fanthome[5], D. Farina[1], J. Farthing[5], L. Figini[1], S. Garavaglia[1], J. Garcia[2], M. Gardener[5],T. Gerbaud[11], G. Granucci[1], J. Hay[5], M. Henderson[12], S. Hotchin[5], V.N. Ilyin[13], M. Jennison[5], W. Kasparek[14], P. Khilar[5], N. Kirneva[13], D. Kislov[13], S. Knipe[5], A. Kuyanov[13], X. Litaudon[2], A.G. Litvak[10], A. Moro[1], S. Nowak[1], V. Parail[5], B. Plaum[14], G. Saibene[15], P. Späh[6], D. Strauss[6], E. Trukhina[13], A. Vaccaro[6], A. Vagdama[5], V. Vdovin[13], and JET EFDA Contributors

JET-EFDA, Culham Science Centre, Abingdon OX14 3DB, UK;
[1]Istituto di Fisica del Plasma CNR, Euratom Association, 20125 Milano, Italy; sozzi@ifp.cnr.it
[2] CEA, IRFM, 13108 Saint-Paul-lez-Durance, France; [3] EFDA Close Support Unit, Culham Science Centre, Abingdon OX143DB, UK; [4] European Commission, B-1049 Brussels, Belgium; [5] CCFE, Culham Science Centre, Abingdon OX14 3DB, UK; [6] Karlsruhe Institute of Technology, D-76021 Karlsruhe, Germany; [7] Max-Planck-IPP, Euratom Association, D-17491 Greifswald, Germany; [9] Laboratorio Nacional de Fusion, Asoc. EURATOM-CIEMAT, 28040, Madrid, Spain; [10] Institute of Applied Physics, Nizhny Novgorod 603155, Russia; [11]LPTP, Ecole Polytechnique, 91128 Palaiseau, France; [12]ITER Organization, 13108 Saint-Paul-lez-Durance, France; [13]RRC 'Kurchatov Institute', Moscow, Russia; [14]Institut für Plasmaforschung der Universität Stuttgart, D-70569 Stuttgart, Germany; [15]Fusion for Energy, 08019 Barcelona, Spain

ECRH will be one of the essential tools in ITER for scenario formation (ELMy H-mode, advanced steady state, hybrid) and plasma control (NTMs and current profile). In the perspective of ITER construction and operation the availability of a full performance ECRH system in JET would be desirable for a number of reasons. To evaluate the feasibility of installing such a multi-MW ECRH system on JET a preliminary conceptual system design has recently been developed by an EU-Russia team.

At first the main physics objectives of an ECRH system on JET have been considered: a) control of the ratio between electron and ion temperature (T_e/T_i) and of the impurities; b) control of the current profile in hybrid and advanced scenarios; c) control of the period of sawteeth; d) neoclassical tearing modes avoidance and suppression [1].

In order to fulfil all the objectives, the system should be able to deposit the ECRH power over almost the full range of plasma minor radii. The possible technical solutions have been evaluated starting from the options for the gyrotron sources available in a reasonable time: double frequency gyrotrons at 113–150 GHz (modification of AUG's sources) and 170 GHz (in development for ITER). The physics study has also been constrained by the limited room for the antenna: one single equatorial port, hosting two multi-beam steering systems. Extensive beam-tracing calculations [2] have shown that the 170 GHz option offer better performances in the toroidal field interval 2.7–3.1 T, with off axis current drive available in a significantly wider range. As an additional consideration, selection of 170 GHz also offer the opportunity of an effective technological synergy with the development of the ECRH system for ITER. The physics study also established that a minimum of 10 MW absorbed in the plasma is adequate for some of the tasks (a, c, d) and marginally adequate for others (b) [2, 3]. The width of the deposition profile is also a critical parameter for MHD control.

Following the assessment of the physics requirements the main design choices of the system were fixed; 12 MW of installed power, an extended range launcher (≈30° poloidally, ±30° toroidally also allowing counter current drive) located in a single equatorial port and 12 evacuated transmission lines fed by 12 depressed collector 170 GHz gyrotrons with at least 20 s pulse duration, with kHz power modulation and real time control capability at least for beam steering in poloidal direction. A further requirement was the use of the steering unit developed for the ITER Upper Launcher.

Such full scale performance specifications are, in most cases, achieved by using multiple launcher systems and these specifications therefore translate into rather demanding requirements on the JET antenna. Its present design uses two nearly identical modules, situated one above the other, each occupying half of the available volume in the port. Each module includes 6 tapered waveguide terminations; 6 focusing mirrors with ellipsoidal surface redirecting the 6 beams towards the poloidal steering mirror; one ITER steering mechanism providing the poloidal steering of a flat mirror, which redirects 6 beams towards the toroidal steering mirror; one toroidal steering mechanism moving a flat mirror, which redirects 6 beams towards the plasma or towards a side mirror, depending on the required toroidal injection angle. One fixed side mirror, shared by the upper and lower modules, redirects (for certain toroidal injection angles) 6 or 12 beams towards the plasma. Two types of beam trajectories are possible in the launcher: single bounce, for which the beams are deflected by the toroidal mirror directly towards the plasma; double bounce, for which the beams deflected by the toroidal mirror hit the fixed side mirror before reaching the plasma. Toroidally perpendicular injection is possible in both the cases, while co-current and counter-current injection are obtained with 1 and 2 bounces respectively.

* See the Appendix of F. Romanelli et al., paper OV/1-3, 23rd IAEA Fusion Energy Conference (2010).

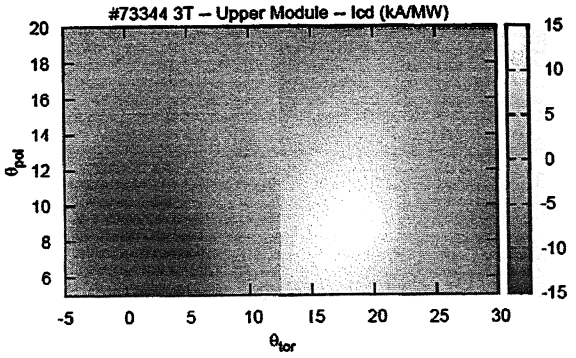

Fig. 1. Total current drive efficiency (in kA/MW) along the steering range for advanced scenario reference shot 73344. scaled to 3T magnetic field. θ_{tor} and θ_{pol} coordinates refer to the rotation of the toroidal and poloidal steering mechanisms respectively. Transition from two to one bounce is at 12.5°

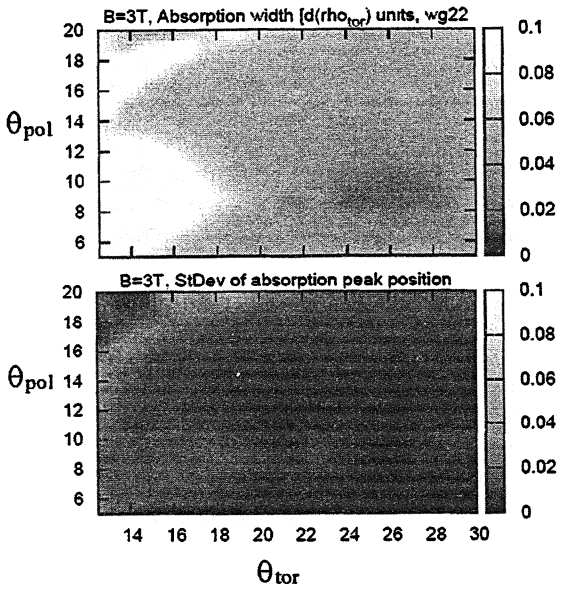

Fig. 2. Top color map shows the width of the power absorption (or driven current) layer in normalized radius ρ_{tor} for one waveguide (WG22), co-current launching range. The same color code is used in the bottom plot, representing the standard deviation around the average position of the peak of the driven current. The comparison between the two plots shows that everywhere in the steering range the width of the driven current channel is dominated by the single beam absorption layer and not by the spread of their relative positions

The RF power input to the launcher is provided by 2×6 corrugated waveguides of 63.5 mm inner diameter arranged as a centred pentagon, each terminated with a taper 911 mm long and 120 mm in aperture diameter. The taper aperture is directly connected with the main flange of the port. The taper has a double function: improve the waveguide HE-Gaussian beam coupling and moving the effective beam waist back into the waveguide, allowing better focusing of the beam in the plasma. Each beamline is equipped with its own focusing mirror positioned in front of the waveguide. The precise pointing of each focusing mirror can be used as a further parameter to ensure optimal beam overlapping for applications which are critically dependent on the maximum power/driven current density attainable. In this launcher design the ITER steering mechanism can be implemented without any modification, since the two steering movements are mechanically decoupled. Moreover this layout provides a nearly continuous range of toroidal injection angles.

This conceptual design has been implemented in the GRASP Physics Optics tool and the propagation of the beams in the optics system has been studied. Such calculations supplied a detailed input for both the evaluation of the thermal load on the launcher components and for an accurate tuning of the size and position of the mirrors in order to avoid diffractive losses and edge effects. Finally, the resulting optical model has been linked with the GRAY code[2] to perform the beam tracing (see Fig. 1 and 2).

A preliminary port integration study considering all the main aspects of the mechanical design including the port-plug structure, the mirrors support, the toroidal steering mechanism, the closure flange and feedthroughs has been conducted. A finite elements model of the full structure has been implemented and the structural analysis under very conservative assumptions concerning disruption forces has been performed. Also a preliminary thermal expansion analysis has been executed [4].

The plant design performed [5] has assumed the use of a version of the GYCOM/IAP diode-type depressed collector gyrotron sources being developed for ITER, fed with –65 kV, 50 A (main) and 30 kV, 50 mA (body). The possible options for the needed power supplies, including partial re-use of refurbished existing units have been considered.

Other topics analysed in this conceptual design have been port allocation, transmission line routing and technology, tritium segregation, auxiliary systems including cooling and cryosystems, and buildings. Reasons for the choice of the system specifications will be detailed as well as the evaluation of the required resources, of the time planning and of the risk analysis.

This work was supported by EURATOM and carried out within the framework of the European Fusion Development Agreement. The views and opinions expressed herein do not necessarily reflect those of the European Commission.

References

1. *Giruzzi, G.*, Objectives, physics requirements and conceptual design of an ECRH system fo JET // Nucl. Fusion 51 (2011) 063033.

2. *Farina, D., Figini, L.* Investigation of electron cyclotron wave absorption and current drive in JET // Nucl. Fusion 50 (2010) 095007.

3. *Nowak, S.*, Feasibility of an ECRH system for JET: Neoclassical Tearing Modes stabilization // Proceed. of the 16th Joint Works hop on ECE and ECRH (World Scientific, Singapore, 2011).

4. *Spaeh, P.*, Structural design and analysis of an ECRH Launcher for JET.// ICOPS-SOFE conference Chicago, Illinois June 26-30, 2011 paper #11465.

5. *Lennholm, M.* ECRH for JET: A feasibility study // in Fusion Eng. and Design,. Article in press: doi:10.1016/ j.fusengdes.2011.01.136.

Initiation of Closed Flux Surfaces and Subsequent Current Ramp-up by ECH/ECCD in the LATE Device

H. Tanaka, T. Maekawa, M. Uchida, F. Watanabe, Y. Noguchi

Graduate School of Energy Science, Kyoto University, Kyoto, Japan, h-tanaka@energy.kyoto-u.ac.jp

Initiation of toroidal current in tokamaks usually done by induction from primary current in central solenoid coils because this method is very simple and easy. However, for the high performance and low cost fusion reactor, the volume of central space should be reduced and therefore sufficient volt-seconds for inductive start-up will not be provided [1]. Experimental studies on non-inductive start-up and formation of tokamak configuration have been carried out in many devices so far. Among them, utilization of microwaves in the electron cyclotron (EC) range of frequency has a remarkable advantage for the reactor design because it needs only small launchers remote from the plasma and can avoid the plasma-facing problem and severe neutron irradiation.

In the LATE (Low Aspect Ratio Torus Experiment) device, we investigate the physical bases on initiation of toroidal current and ramp-up by electron cyclotron heating and current drive (ECH/ECCD). The vacuum chamber is a stainless steel cylinder with an inner diameter of 100 cm and a height of 100 cm. The center post is also a stainless steel cylinder with an outside diameter of 11.4 cm, enclosing 60 turns of toroidal field coil. We have a 5 GHz klystron ($P_{inj} \leq \leq 200$ kW, pulse width ≤ 70 ms), and four 2.45 GHz magnetrons (one of them $P_{inj} \leq 5$ kW, CW, and others $P_{inj} \leq 20$ kW, pulse width ≤ 2 sec). Those microwaves are launched from low field side on the midplane obliquely to the toroidal field direction. The angle between the axis of launchers and the toroidal field is ~80 degree at each injection point. The polarization of electric field is usually linearly polarized one, where the electric field lies on the midplane and mainly in O-mode.

When a weak vertical field Bv is superposed to the toroidal field Bt and a microwave pulse is injected, breakdown occurs at the electron cyclotron resonance (ECR) layer and a toroidal ECR plasma is produced. The equilibrium current flows and compensates the charge separation due to the opposite directions of the field gradient and curvature drifts of electrons and ions, resulting in generation of toroidal current, so called pressure driven current in the open field configuration [2]. When the injected microwave power is sufficient, the toroidal current Ip increases enough to form closed flux surfaces (CFSs) [3]. Figure 1(a) shows waveforms of Ip for various Bv which is kept constant during a discharge. Figure 1(b) replots the Ip time evolution as a function of product of major radius of the current center and Bv, showing the trajectory of toroidal force balance condition. The open circles show the points on formation of CFSs found by reconstruction of poloidal flux distribution from magnetic measurement. Trajectories show that an efficient mechanism of current generation should work when the CSFs are formed. Considering the single particle orbit of electrons in the open field configuration, some electrons whose vertical drift is canceled out by inclination of field lines can make a circular orbit around the torus and carry the plasma current in the same direction of existing one. Such electrons may be supplied by ECH and Coulomb scattering from low temperature bulk electrons efficiently and drive the current till CFSs are formed.

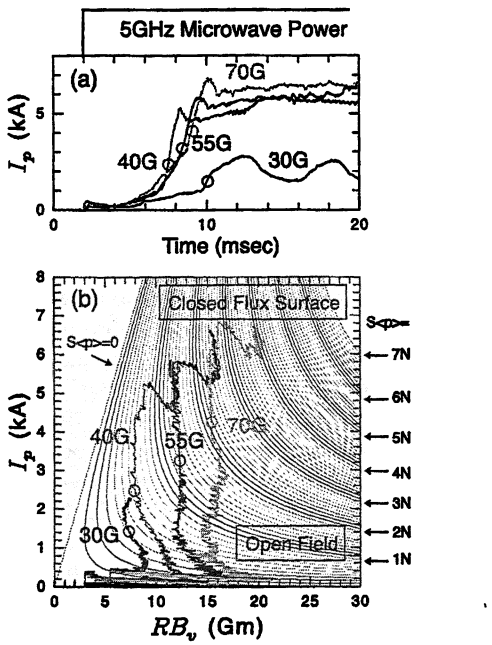

Fig. 1. (*a*) Waveforms of Ip when Bv is kept constant. (*b*) Replot of Ip as a function of product of major radious of the current center and Bv

After the formation of CFSs, ECCD mechanism becomes functioned and Ip ramps up by increasing Bv and decreasing the decay index. When a 5 GHz microwave pulse of P_{inj} = 190 kW and width = 70 ms is injected, Ip ramps up at the rate of ~260 kA/s and reaches 20 kA [4]. Magnetic measurement shows that the negative electric field about ~0.05 V/m is induced by the self-inductance. The line-averaged electron density is $n_e \sim 4 \cdot 10^{11}$ cm^{-3} and exceeds the plasma cut-off density for the 5 GHz microwave, suggesting EC heating by electron Bernstein (EB) waves. The bulk electron temperature is estimated to be $T_e \leq$ ~100 eV from the impurity line radiations of OV, OIII, CV and CIII. The bulk electron contribution to poloidal beta βp^{bulk} is estimated to be ~0.05, while βp obtained from magnetic measurement is ~1.5, indicating the presence of high energy electrons. Hard X-ray energy spectra are obtained by pulse height analysis (PHA) system with CdTe detectors. The energy range of photons expands to higher energy as Ip increases and exceeds 200 keV. These data show that several percent

of electrons in population are heated and get relativistic energy of ~100 keV, have the main part of plasma pressure and carry the plasma current.

From the view point of MHD force balance, the isotropic pressure does not support pressure gradients along magnetic field. The plasma pressures parallel to and perpendicular to the magnetic field ($p_{//}$ and $p_{\perp}$, respectively) are obtained by magnetic measurement and equilibrium analysis. It is shown that the $p_{//}$ is much smaller than $p_{\perp}$ outside the last closed flux surface (LCFS) but becomes comparable at the inside. This result suggests that the inside current is carried mainly by passing electrons, while some portion of the outside current may be generated as a result of the toroidal precession of trapped electrons.

Because the density in the plasma core is more than the plasma cutoff density, the electrons should be accelerated by EB wave. In these experiments, microwave power is injected obliquely to the toroidal field mostly in O-mode. The O-mode wave meets the plasma cutoff layer and excites the slow X-mode wave, which is converted to EB wave at the upper-hybrid resonance (UHR) layer [5]. In principle, waves with high parallel refractive index $N_{//}$ are effective for accelerating electrons along the magnetic field because resonant electrons gain the parallel momentum and the energy from the waves at the ratio of $\delta p_{//} / \delta \varepsilon = N_{//} / c$. In the low aspect ratio torus plasma, the $N_{//}$ spectrum upshifts largely as the wave propagates toward inside as R^{-1}, and further up-shift is expected due to the poloidal magnetic field. Then, the injected microwave may be mode-converted to the high $N_{//}$ EB wave and supports the high energy electron tail against the reverse electric field effectively.

In order to study the heating characteristics in EC-sustained spherical tokamak, we changed the toroidal magnetic field strength, i.e., the position of the fundamental ECR layer R_{ECR} shot by shot. When we inject 2.45 GHz microwaves with $P_{inj} = 60$ kW in total and set Bt = 720 G and $R_{ECR} = 20.6$ cm, the plasma current is ramped up to 10 kA with ~10 times the plasma cutoff density (Fig. 2). From multi-channel microwave interferometer data, the position of UHR layer is estimated to be located between the fundamental ECR layer and the second harmonic one. The current profile does not expand beyond the second harmonic ECR layer. Signals of 20 ch extreme ultraviolet (XUV) detector array show that the XUV emissions near the fundamental ECR layer increase significantly. The impurity line radiation of OV increases much compared with those of lower excitation level such as OIII and CIII, showing that the bulk electron temperature is increased. Even CV line (excitation energy = 304 eV) can be observed. On the other hand, when we set Bt = 672 G and $R_{ECR} = 19.2$ cm and injected the same 60 kW power, the plasma current is ramped up to the same value (10 kA) but the density is low and only ~3 times the plasma cutoff density. In this case, the current profile expand beyond the second harmonic ECR layer to low field side. The plasma pressure becomes slightly larger and portion of $p_{\perp}$ increases, especially outside of the LCFS, suggesting the increase of trapped electrons. These experimental results denote that, in the former case, EB wave heat both high energy electrons to drive the plasma current and bulk electrons effectively, while in the latter case, EB wave does not heat the bulk electron effectively, but produce high energy trapped electrons.

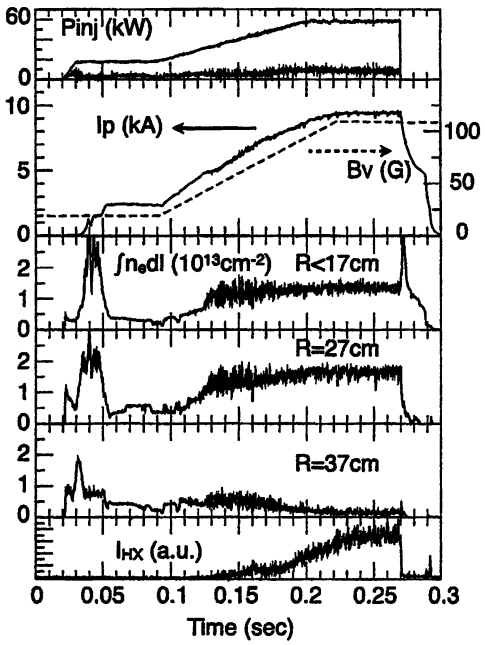

Fig. 2. Typical waveforms with 2.45 GHz microwave at Bt = 720 G and $R_{ECR} = 20.6$ cm

We also investigate the effects of externally applied magnetic perturbations (MPs) on the transport of both bulk and high energy electrons in EC-sustained spherical tokamak. Four coils for MPs are wound around radial ports on midplane outside the vacuum chamber. When MPs with $\sim 10^{-4}$ times the toroidal field strength is applied to the plasma with Ip = 7 kA produced by injecting 2.45 GHz, 30 kW microwave, the plasma current increases to 8 kA and the density in the plasma center becomes twice. The slope of X-ray energy spectrum becomes steep, indicating that the high energy electron energy decreases. This preliminary result supports the possibility of controlling the high energy tail distribution by MPs.

References

1. *Tobita, K., Nishio, S., Enoeda, M., et al.*, Compact DEMO, SlimCS: design progress and issues // Nucl. Fusion 2009. V. 49. P. 075029.

2. *Nishi, S., Sakabe, T., et al.*, Current Circulation and Equilibrium in Toroidal Electron Cyclotron Resonance (ECR) Plasmas in the LATE Device // Plasma Phys. Control. Fusion V. 52. P. 125004.

3. *Yoshinaga, T., Uchida, M., et al.*, Spontaneous Formation of Closed-Field Torus Equilibrium via Current Jump Observed in an Electron-Cyclotron-Heated Plasma // Phys. Rev. Lett. 2006. V. 96. P. 125005.

4. *Uchida, M., Yoshinaga, Y., et al.*, Rapid Current Ramp-Up by Cyclotron-Driving Electrons beyond Runaway Velocity // Phys. Rev. Lett. 2010. V. 104. P. 065001.

5. *Maekawa, T., Tanaka, S., et al.*, Wave Trajectory and Electron-Cyclotron Heating in Toroidal Plasmas // Phys. Rev. Lett. 1978. V. 40. P. 1379.

Progress of CW Compatible Implementations of Line-of-Sight ECE Measurements Within Waveguide Based ECRH Transmission Systems

W.A. Bongers[1], W. Kasparek[2], M. Petelin[3], L. Lubyako[3], E. Eminoglu[1,2], M.R. de Baar[1,4], V. van Beveren[1], R. van den Braber[5], N. Doelman[5], A.J.H. Donné[1,4], V. Erckmann[6a], A.P.H. Goede[1], B. Krijger[1], P.W.J.M. Nuij[4], B. Plaum[2], J. Stober[6b] and D. Wagner[6b]

[1]FOM-Institute for Plasma Physics Rijnhuizen, Association EURATOM-FOM, Trilateral Euregio Cluster, PO Box 1207, 3430 BE Nieuwegein, The Netherlands, www.rijnhuizen.nl, W.A.Bongers@rijnhuizen.nl
[2]Institut für Plasmaforschung Universität Stuttgart, 70569 Stuttgart, Germany
[3]Institute for Applied Physics, RAS, 603950, Nizhny Novgorod
[4]Eindhoven University of Technology, NL-5600 MB Eindhoven, The Netherlands
[5]TNO department of Opto-Mechatronics, 2628 CK Delft, The Netherlands
[6]Max Planck Institut für Plasmaphysik, Association EURATOM-IPP,[a]D-17491 Greifswald, [b]D-85748 Garching, Germany

It is known that effective control of plasma instabilities, like neoclassical tearing modes or sawteeth, can be obtained by locally applied Electron Cyclotron Heating and Current Drive (ECRH/CD). Central island deposition of ECCD leads to suppression, where the efficiency can be enhanced by synchronizing the phase of the mm-wave power modulation with the poloidal rotation of the island. To provide the feedback signal, required to control and to direct the ECCD power, real time detection and precise localization of the islands is necessary. To guarantee high positional accuracy and timeliness a solution with Electron Cyclotron Emission (ECE) measurements along the same line of sight of the incident mm-wave beam was demonstrated on TEXTOR [1] in a quasi-optical set-up [2].

Further development, implementation and tests of in-line CW ECE separation systems for feedback control for ASDEX and ITER featuring oversized corrugated waveguides are presented:

1) Combination of non-resonant Mach Zehnder diplexer with dielectric plate beam splitters [3, 4] and a resonant Fast Directional Switch, FADIS [5, 6].

2) Pure grating based diplexers [7] as alternative for 1 but without dielectric plates.

Advantage of line-of-sight ECE

It has been demonstrated at TEXTOR that a line-of-sight ECE/ECRH system has the advantage that the sensed data can be readily interpreted without any assumptions on the plasma equilibrium [1]. Moreover, drifts in the system calibration and alignment are self-compensating. The ECE signal was used to actively feedback on the injection angle and on the power modulation of the ECRH.

Implementation Progress

The challenge of such a collinear system is that the typical signal level seen by the detector is on the nano-watt level, whereas the ECRH systems work at the mega-watt level and strong filtering is needed to separate the gyrotron frequency from the ECE radiation in neighboring frequency channels. A line-of-sight system is in preparation for ASDEX-Upgrade, (87 mm waveguides) equipped with a combination of tunable FADIS, as ECE separator, and fixed tuned dielectric plate Mach-Zehnder Filter (MZF).

The requirements, layout and design of MZF are given in [3, 4], see Fig. 1 for the design and filter curves. Important is that the ECE separation system has to accommodate possible (startup) frequency changes of the gyrotron (~0.3 GHz), whilst providing sufficient attenuation (~50 dB) in the oversized parts to prevent breakdown of the standard waveguide notch filter protecting the ECE detection system. Since the FADIS notch width is only a few MHz wide for at least 20 dB suppression, FADIS must be synchronously tuned. If in this case FADIS is combined with the MZF at least 50 dB total suppression on 140 GHz is obtained. In the worst case with no or wrong FADIS tuning, the combination gives only 36 dB isolation for single-mode HE_{11} reflection from arc (multi-mode (plasma) reflection is no problem (76 dB) [6].

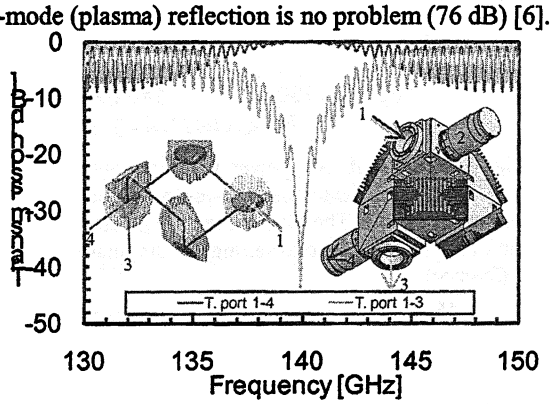

Fig. 1. The transmission curve of the polarization independent Mach-Zehnder-type two-beam interferometer build from a 87 mm corrugated oversized waveguide (left) is shown. The input flange (1), the terminators (2, 3) and the cooled mitre bends are visible. Route 1–3 (yellow curve) is used as filter, which offers a minimum of 30-dB suppression of the gyrotron stray radiation over a 0.3 GHz band during start-up frequency droop of the gyrotron (< 1 s time)

Preliminary high power tuning tests of FADIS, using the gyrotrons of the W7-X ECRH system (in Greifswald) [5], have shown the results of two operation control ways: both output channel power feedback and measured frequency feed forward. As result FADIS could be synchronized, by changing its cavity path length, in a few tenths of a second after the start of the gyrotron pulse. Further optimization is needed. By also sensing the phase information [4] at the FADIS output ports the control performance may be further improved. This phase information should provide

a monotonically increasing or decaying function around the optimum of the cavity length. At first the idea was to mix part of the input signal of FADIS (from gyrotron) with a part of the resonant output. This concept worked but needs a complicated setup with extensive calibration, not very practical for high power setup. Then the signal was obtained by simply mixing both the outputs of FADIS at two different phase shifter settings, see Fig 2 and Fig. 3 for setup and results.

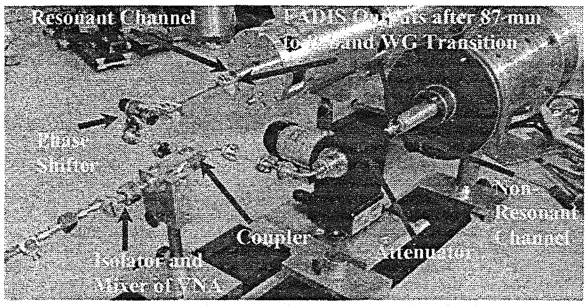

Fig. 2. Low power setup at IPF: both the outputs of FADIS are mixed to form the signal, compensated by additional attenuator and phase shifter for amplitude and path differences

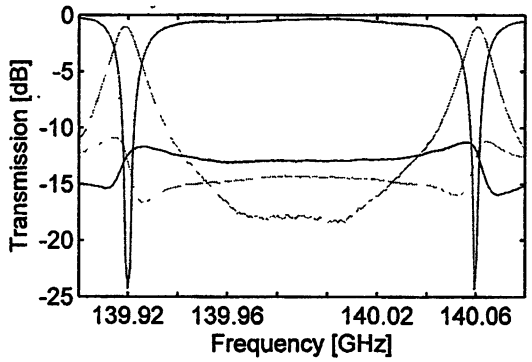

Fig. 3. Results of low power measurements: the red and green curves indicate the non-resonant and the resonant output of FADIS. The blue curves are measured at the output of the coupler for two settings of the phase shifter (180° difference)

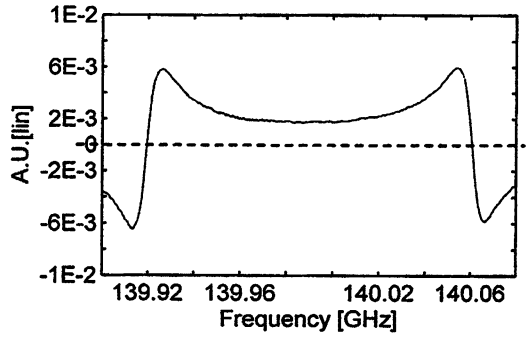

Fig. 4. Sensor-curve obtained by subtracting signals from the mixers after the magic tee. The control objective for FADIS should be to drive this signal to zero. The desired monotonic behavior is shown for a limited stroke of the mirror (note, although the graph is plotted against frequency, a similar behavior is obtained for the cavity length of the active mirror

To make both mixing signals, with 180° phase difference, simultaneous available, a magic tee (4-port 180° hybrid splitter) was used instead of the 3-port coupler. This resulted in two blue curves as shown in Fig. 3. These new curves have an extended dynamic range from 5 to 15 dB, well suited as FADIS control signals. Subtracting these signals gives the control-sensor curve, see Fig. 4. At high power the system in Fig. 2 extended with a magic tee could then be connected to the output mitre-bend couplers of FADIS.

A possible upgrade

The above ECE/ECRH configuration including the quasi-optical resonant FADIS may be supplemented with a broad-band non-resonant diplexer in combination with an universal mechanically tunable polarizer shown in Fig. 5, both based on gratings [7]. The ECE measurement would be performed within a ~20 % frequency band.

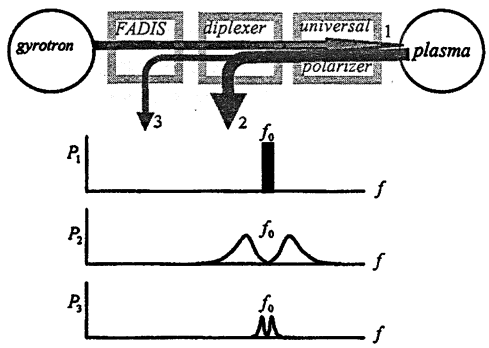

Fig. 5. Upgrade for line-of-sight system by pure grating based diplexer in combination with universal polarizer

Conclusion

Successful tearing mode control has been demonstrated at TEXTOR using the line-of-sight ECE/ECRH concept. As a next step an inline separation system scheme is proposed which combines a polarization independent MZF in tandem with FADIS. Attainability of the line-of-sight is supported by experiments, innovations of control signals sensing and alternative approach of diplexers. Next development steps include demonstration on AUG and a possible implementation for ITER.

Acknowledgements

This work is supported by Centre of Excellence grant 047.018.002

References

1. *Hennen, B.A. et al.*, PPCF., 52 (2010) 104006.
2. *Oosterbeek, J. W.* et al., RSI, 79 (2008), , 093503.
3. *Bongers, W. A. et al.*, FS&T. 55 (2009) P. 188-203.
4. *Bongers, W. A. et al.*," Utilization of collinear ECE detection/ECRH heating for active stabilization of plasma instabil.", Proc. and Pres. IRMMW 2010, sept. 5–10, Rome.
5. *Kasparek, W. et al.*, FS&T., "High-Power Performance of a Res. Diplexer for adv. ECRH", to be publ. May 2011.
6. *Kasparek, W. et al.*, "Development of compact resonant diplexers for ECRH: Design, recent results, and plans". Proc. and Pres. EC16 2010, Sanya, China, 12–15 April.
7. *Petelin, M.I., Caryotakis, G., Tolkachev, A.A. et al.*, High Energy Density Microwaves, AIP Conference Proc. and Pres. 474, California, Oct. 1998. P. 304-315.

ECCD Calculations in ITER by Means of the Quasi-Optical Code

A.A. Balakin[1], N. Bertelli[2,3], M.N. Buyanova[1], E. Westerhof[2]

[1]Institute of Applied Physics, Nizhny Novgorod, Russia
[2]FOM-Institute for Plasma Physics Rijnuizen, Association EURATOM-FOM, Nieuwegein, The Netherlands
[3]Princeton Plasma Physics Laboratory, Princeton, NJ 08540, USA

One of the main aims of the ITER electron cyclotron resonance heating (ECRH) system, in particular of the ITER ECRH Upper Port Launcher, is the control of MHD instabilities such as neoclassical tearing modes (NTMs). NTMs can be stabilized by application of a local current driven within the magnetic island to replace the 'missing' bootstrap current. This has resulted in the introduction of a figure of merit for NTM stabilization η_{NTM} of a driven current density j_{CD} as the ratio of j_{CD} to j_{bs}, i.e. $\eta_{NTM} \equiv j_{CD}/j_{bs}$ [1, 2]. The requirement, for full suppression an NTM can then written in the form $\eta_{NTM} > C_{supp}$ where C_{supp} is a constant of order unity. The actual value of C_{supp} is a topic of active debate [3, 4]. Theoretical considerations [5, 6], show that it depends amongst others on the marginal island size and the dominant physical effect limiting the neoclassical growth of the tearing mode for island sizes below this marginal size (finite parallel transport or ion polarization current) as well as on the EC driven current density profile width. A minimum value of C_{supp} appears to be obtained for the width of ECCD profile w_{CD} between one and two times the marginal island size. For smaller deposition widths, C_{supp} increases as $\sim 1/w_{CD}$. Considering that for a given ECCD power the value of $\eta_{NTM}\, w_{CD}$ is fixed by the physical parameters of both the plasma and ECCD system, the minimum required ECCD power for full suppression is realized for driven current density profile widths smaller than one to two times the marginal island width. In case of ITER this results in the criterion that w_{CD} should be smaller than about 5 cm. An accurate prediction of the EC driven current density profile is thus required in order to optimize the design of the beam launcher in experiments. A systematic study with a QO code including an ECCD calculation has been performed in order to quantify the consequences of the quasi-optical effects for the EC driven current density for the case of the ITER ECRH Upper Port Launcher.

The routine performing the adjoint calculation of the ECCD efficiency as given in the work of Lin-Liu *et al.* [7] has been implemented in the QO code taking into account the effect of the wave polarization. ECCD calculations are shown for ITER reference scenarios 2, 3a and 5 for beams launched from the Upper Port Launcher lower and upper steering mirrors directed at the m/n = 3/2 and m/n = 2/1 rational surfaces (Fig. 1). For all these cases, a comparison with the beam-tracing code TORBEAM [8] is done. In particular, the same ECCD routine mentioned above has been implemented in TORBEAM. For the case of ITER reference scenario 2, a comparison of the EC power deposition profile as obtained by the QO code and TORBEAM is also presented, correcting the results presented in Ref. [9] in which the broadening predicted by the QO code was overestimated due to small differences in the equilibria. The present calculations show that quasi-optical effects give a significant broadening in comparison with beam tracing calculations in the range of 15–30 % (Table 1). A similar broadening is obtained for the EC driven current density profile. In addition we find a significant reduction of the peak of the EC driven current density. This corresponds to a reduction of the achievable NTM figure of merit as typically $\eta_{NTM,QO} \rightarrow 0.85\, \eta_{NTM,TB}$ (Table 2). The main reason for the broadening of the power deposition and driven current density profiles in the QO calculations is the finite wave vector spectral width of the beam as determined by the size of the beam waist [10]. In addition, an estimate of the effect of the radial diffusion of the current carrying superthermal electrons on the EC driven current density is obtained by using the formula presented in Ref. [11] which combines the width of the EC power deposition profile with the effect of the radial diffusion. By this formula, with an effective radial diffusion at the rate of 0.1 or 0.3 m^2s^{-1}, already a strong decrease in the peak of the EC driven current density profile occurs.

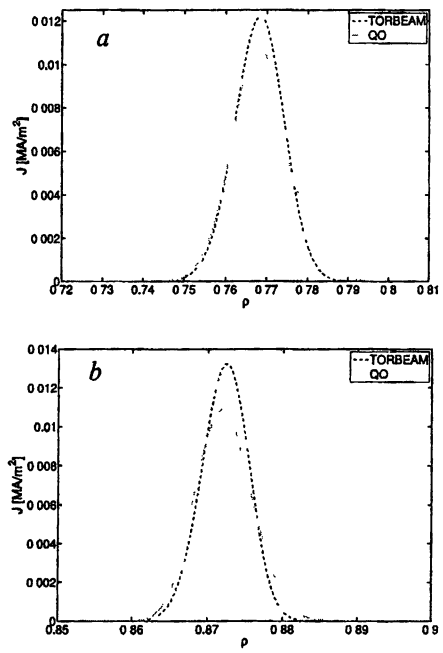

Fig. 1. Example of ECCD profiles as a function of the normalized poloidal flux for beams launched from the Upper Port Launcher LSM directed at the m/n=3/2 (figure (*a*)) and the m/n = 2/1 (figure (*b*)) rational surface in ITER reference scenario 2. The solid curves show the result of the quasi-optical code (QO) whereas the dashed curves show the results from TORBEAM

Table 1. Width of the ECCD profiles for both the QO calculations, $w_{CD,QO}$, and TORBEAM $w_{CD,TB}$. The last column provides the ratio $w_{CD,TB}/w_{CD,QO}$.

scenario	mirror	*m/n*	$w_{CD,QO}$	$w_{CD,TB}$	ratio
2	LSM	3/2	0.0071	0.0060	0.85
		2/1	0.0037	0.0031	0.84
	USM	3/2	0.0105	0.0088	0.84
		2/1	0.0065	0.0052	0.80
3a	LSM	3/2	0.0081	0.0080	0.99
		2/1	0.0047	0.0039	0.83
	USM	3/2	0.0115	0.0098	0.85
		2/1	0.0067	0.0067	0.88
5	LSM	3/2	0.0043	0.0043	0.77
		2/1	0.0023	0.0023	0.70
	USM	3/2	0.0072	0.0072	0.86
		2/1	0.0048	0.0048	0.83

Table 2. The maximum value of the EC driven current density (in MA/m^2) for both the QO calculations, $J_{CD,QO}$, and TORBEAM, $J_{CD,TB}$ and their ratio.

scenario	mirror	*m/n*	$J_{CD,QO}$	$J_{CD,TB}$	ratio
2	LSM	3/2	0.0108	0.0122	0.88
		2/1	0.0110	0.0132	0.83
	USM	3/2	0.0095	0.0107	0.89
		2/1	0.0078	0.0096	0.81
3a	LSM	3/2	0.0147	0.0146	1.01
		2/1	0.0159	0.0176	0.90
	USM	3/2	0.0130	0.0147	0.88
		2/1	0.0116	0.0123	0.94
5	LSM	3/2	0.0092	0.0113	0.81
		2/1	0.0098	0.0129	0.76
	USM	3/2	0.0080	0.0086	0.93
		2/1	0.0066	0.0074	0.89

It should be noted that in addition to the quasi-optical effects and the effect of radial diffusion leading to a broadening of the driven current density profile and a concomitant reduction of the maximum driven current density there are various other effects that can give rise to additional profile broadening. These include, in particular, relative misalignment of the multiple beams in case of the ITER ECRH system [12] and effective beam broadening due to scattering off density fluctuations [13, 14]. On the other hand, higher driven current densities might be obtained including a more complete momentum conserving electron-electron collision operator in the current drive efficiency calculations [15], or coming from quasi-linear effects that may occur when the higher power density that is achieved inside a magnetic island are properly accounted for [16]. Also the requirement on the EC driven current density profile might be relaxed when the additional stabilizing effect of the EC heating is accounted for [17].

The work in this paper has been performed in the framework of the NWO-RFBR Centre of Excellence on Fusion Physics and Technology (grant 047.018.002). This work, supported by the European Communities under the contract of Association between EURATOM/FOM, was carried out within the framework of the European Fusion Program. The views and opinions expressed herein do not necessarily reflect those of the European Commission. The work of AAB and MNB has also been supported by RFBR grant No. 09-02-00972.

References

1. *Perkins F.W., Harvey R.W.*, Criteria for Suppression of Neoclassical Tearing Modes // Bull. Am. Phys. Soc. 2000. V. 45. P. 278.

2. *Zohm H., Heidinger R., Henderson M., et.al.*, Comparison of the performance of different options for the ITER ECRH Upper Launcher // JPCS. 2005. V. 25. P. 234

3. *Isayama A., et al*, Neoclassical tearing mode control using electron cyclotron current drive and magnetic island evolution in JT-60U // Nucl. Fusion. 2009. V. 49. P. 055006.

4. *Petty C.C., La Haye R.J. et.al*, Complete suppression of the $m = 2/n = 1$ neoclassical tearing mode using electron cyclotron current drive in DIII-D // Nucl. Fusion2004. V. 44. P. 243.

5. *Sauter O., Henderson M.A. et.al*, On the requirements to control neoclassical tearing modes in burning plasmas // PPCF. 2010. V. 5. P. 025002.

6. *Bertelli N., De Lazzari D., and Westerhof E.*, Requirements on localized current drive for the suppression of neoclassical tearing modes // 2011 subm. to Nucl. Fusion.

7. *Lin-Liu Y.R., Chan V.S., Prater R.*, Electron cyclotron current drive efficiency in general tokamak geometry // Plas. Physics. 2003. V. 10. P. 4064.

8. *Pereverzev G.V.*, Beam tracing in inhomogeneous anisotropic plasmas // Phys. Plasmas. 1998. V. 5. P. 3529.

9. *Balakin A.A., Balakina M.A., Westerhof E.*, ECRH power deposition from a quasi-optical point of view // Nucl. Fusion. 2008. V. 48. P. 065003.

10. *Bertelli N., Balakin A.A., Westerhof E., Buyanova M.N.*. ECCD calculations in ITER by means of the quasi-optical code // Nucl. Fusion. 2010. V. 50. P. 115008.

11. *Bertelli N., Westerhof E.*, Consequences of finite transport on the effectiveness of ECCD for neoclassical tearing mode stabilization in ITER // Nucl. Fusion. 2009. V. 49. P. 095018.

12. *Henderson M.A. et al*, Overview of the ITER EC upper launcher // Nucl. Fusion. 2008. V. 48. P. 054013.

13. *Tsironis C., Peeters A.G., et al.*, Electron-cyclotron wave scattering by edge density fluctuations in ITER // Plas. Physics. 2009. V. 16. P. 112510.

14. *Bertelli N., Balakin A.A., Westerhof E., et.al*, The influence of the edge density fluctuations on electron cyclotron wave beam propagation in tokamaks // Journal of Phys. Conf. Ser. 2010. V. 260. P. 012002.

15. *Marushchenko N.B., Maassberg H., Turkin Yu.*, Electron cyclotron current drive calculated for ITER conditions using different models // Nucl. Fusion. 2008. V. 48. P. 054002.

16. *Rosa P.R. da S., Ziebell L. F.*, Current drive by EC waves in the presence of magnetic islands and transport // PPCF. 2008. V. 50. P. 095002.

17. *De Lazzari D., Westerhof E.*, On the merits of heating and current drive for tearing mode stabilization // Nucl. Fusion. 2009. V. 49. P. 075002. Erratum: Nucl. Fusion. 2010. V. 50. P. 079801.

A Low-Dimensional Model System for Quasi-Periodic Plasma Perturbations

D. Constantinescu[1], O. Dumbrajs[2], V. Igochine[3], K. Lackner[3], R. Meyer-Spasche[3], H. Zohm[3] and ASDEX Upgrade team[3]

[1]Department of Applied Mathematics, University of Craiova, Association Euratom-MECI, Romania
[2]Institute of Solid State Physics, University of Latvia, Association Euratom-UL, Latvia, olgerts.dumbrajs@lu.lv
[3]Max-Planck Institut für Plasmaphysik, Association Euratom-IPP, Germany

Larger scale plasma instabilities not leading to an immediate termination of a discharge frequently result in periodic nonlinear perturbations of the plasma (sawteeth, ELMs, FIR-NTMs, etc.) [1–3]. A low-dimensional description of their dynamics appears useful to understand qualitatively their reaction to changes in the driving parameters (e.g. heating power), or to illustrate the possible action of control techniques (e.g. pellet injection for ELM mitigation). Several authors have introduced model nonlinear dynamic systems with a small number of degrees of freedom which can illustrate the generic characteristics of such oscillations. In these models, one focuses on physically "relevant" degrees of freedom, without attempting to simulate all the details of the fundamentally nonlinear tokamak phenomena. Such degrees of freedom often involve the plasma macroscopic quantities such as pressure or density.

A number of zero-dimensional models for the L–H bifurcation involving nonambipolar losses, radial electric field shear reduction of anomalous transport and ion poloidal viscous damping have been proposed. By introducing spatio-temporal variation into these models it is possible to obtain limit-cycle behavior resembling ELMs (see review [4] and references therein). In Ref. 5 the dynamical consequences of a pressure-driven "coherent" mode, which interacts with the turbulence in a specific manner, are investigated. Varying only the two parameters related to the coherent mode, the bifurcation properties of the system have been studied. These were found to be remarkably rich: sawteeth, "compound sawteeth" with partial crashes, "monster" sawteeth, metastability, intermittency, chaos, periodic and "grassy" ELMs in appropriate regions of parameter space. A minimal (low-dimensional) dynamical model of the sawtooth oscillations is presented in Ref. 6. Here it is assumed that the sawtooth is triggered by a thermal instability which causes the plasma temperature in the central part of the plasma to drop suddenly, leading to the sawtooth crash. It is shown that this model possesses an isolated limit cycle which exhibits relaxation oscillation, in the appropriate parameter regime, which is the typical characteristics of sawtooth oscillations. A single parameter hysteresis model is used in Ref. 7 to describe experimental data on sawtooth crash in the ASDEX Upgrade tokamak. The model is based on hysteresis which arises due to the fact that the value of the current density gradient (approximated for the H-mode discharges studied there, by the temperature gradient) at the $q = 1$ surface required to turn on the instability is greater than the gradient required to maintain the instability, once it is turned on. The value of the hysteresis parameter can be chosen such that the model reproduces correctly the two time scales of the sawtooth crash in the ASDEX Upgrade tokamak: the slow rise time (~7 ms) and the rapid crash time (~50 μs).

In this paper we formulate a minimal possible model for interaction of driver part of the system (typical changes in profiles or profile gradients) with relaxation of instabilities which depend on global quantities. Such a situation is encountered frequently in different processes in the plasma. Here we confine ourselves to the most simple and general assumptions taking into account the two different time scales of underlying dynamics. We wish to describe a complex process by means of the model whose characteristics can be easily explained in terms of relaxation and drive. To be minimalist in the approach we consider only two equations: the first being responsible for the instability dynamics (MHD force balance) and the second for the energy conservation. The model can be generalized to include external perturbations, for example, the pellet injection to influence ELMs, or the electron cyclotron current drive to influence sawteeth.

Equations

Our low-dimensional model is given by the system of two equations

$$\begin{cases} \dfrac{d^2}{dt_n^2}\xi_n = \left(p_n' - 1\right)\cdot\xi_n - \delta\cdot\dfrac{d}{dt_n}\xi_n \\ \dfrac{d}{dt_n}p_n' = \eta\cdot\left(h - p_n' - \alpha\cdot\xi_n^2\cdot p_n'\right) \end{cases} \tag{1}$$

Here ξ is the displacement of the magnetic field, p' is the pressure gradient, δ is dissipation, η is the ratio between the normal heat diffusion and heat diffusion due to perturbations, h is the power input into the system, α is the ratio between the anomalous heat diffusion and the normal heat diffusion, and the index n means that quantities are normalized. Introducing the variables $y = \sqrt{\alpha}\cdot\xi_n$ and $z = p_n'$, we can rewrite the system (1) in the form of a system of three parameter-dependent first order ordinary differential equations

$$\begin{cases} \dfrac{dx}{dt} = (z-1)y - \delta\cdot x \\ \dfrac{dy}{dz} = x \\ \dfrac{dz}{dt} = \eta\cdot\left(h - z - y^2 z\right) \end{cases} \tag{2}$$

which reminds the celebrated Lorenz system in the chaos theory. The most important feature of our system is the fact that the instability can develop only above the critical input power $(h>1)$ which is a typical behavior of the plasma in such regimes. In what follows we consider δ and η as independent parameters for a fixed heating $(h=1.5)$ and calculate numerically dynamical zones for various types of oscillations. The results are presented in Fig. 1.

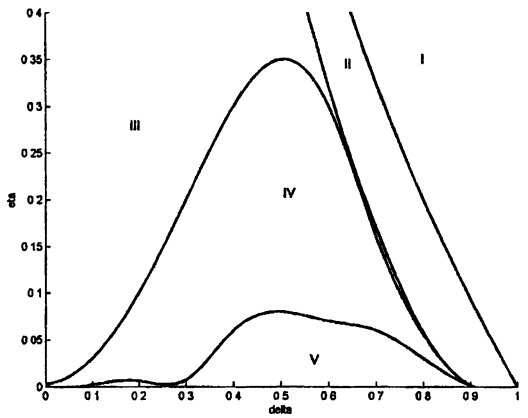

Fig. 1. Dynamical zones of oscillations in the (δ,η) plane. In zone I there are damped oscillations, in zone II simple periodic oscillations, in zone III double periodic oscillations, in zone IV chaotic oscillations, and in zone V ELM/sawtooth type oscillations

Pellet injection

It is well known that by injecting pellets into the plasma it is possible to mitigate ELMs. It is remarkable that our model can describe this phenomenon. Let us perturb the first equation of the system (2):

$$\begin{cases} \dfrac{dx}{dt} = -\left\{1-\left[z+P(t)\right]\right\} y - \delta x \\ \dfrac{dy}{dt} = x \\ \dfrac{dz}{dt} = \eta\left[h - z - y^2 z\right] \end{cases} \quad (3)$$

To simulatethe pellet injection, the perturbation $P(t)$ can be chosen in the following form:

$$P(t) = a \cdot \exp\left\{-\left[t - t_{period}\,\mathrm{int}\left(t/t_{period}\right) - \delta_P\right]^2 / b\right\}. \quad (4)$$

Here a is the perturbation amplitude, t_{period} is the perturbation period, δ_P is the perturbation shift, and b is the perturbation width. This perturbation changes the plasma stability, but does not affect the power balance equation which is the case of a real pellet. To illustrate how this model works, we choose the following values of the system parameters: $\eta = 0.009$, $\delta = 0.2$, $h = 1.5$ which leads us into the space where ELMs exist (zone V, in Fig. 1). Perturbation parameters are: $a = 5$, $t_{period} = 50$, $\delta_P = 2$, and $b = 1$. The resulting temporal dependence of the pressure gradient is shown in Fig. 2.

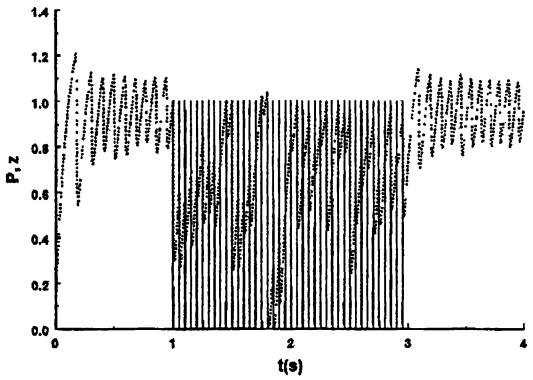

Fig. 2. ELMs (dashed) with pellet injection. Pellet injection was switched on at t = 1s and switched off at t = 3s. Perturbations are shown by black vertical lines. Their amplitude is normalized to unity

It can be seen that the pellet injection increases the ELM frequency almost by a factor two. After pellet injection stops, the number of ELMs is almost the same as before of injection. It is interesting to note that not all pellets trigger an ELM. For example, the pellets at t = 1.4 s, 1.7 s, 1.95 s, 2.35s, and 2.8 s do not trigger an additional ELM (z continues to rise in spite of pellet injection). This prediction coincides with experimental observations that not all pellets induce new ELMs. Thus, our model can be used for analysis of the plasma behavior also under influence of external factors.

References

1. *Zohm, H.* Plasma Phys. Control. Fusion. 1996. V. 38. P. 105.
2. *Hastie, J.* Astrophysics and Space Science 1998. V. 256. P. 177.
3. *Günter, S. et al.* Nucl. Fusion 2004. V. 44. P. 524.
4. *Connor, J.W.* Plasma Phys. Control. Fusion. 1998. V. 40. P. 191.
5. *Thyagaraja, A., Haas, F.A., Harvey, D.J.* Phys. Plasmas. 1999. V. 6. P. 2380.
6. *Bora, M.P. and Sarmah, D.* Comm. Nonlinear Sci. and Numerical Simulation 2008. V. 13. P. 296.
7. *Dumbrajs, O., Igochine, V., and Zohm, H.* The Open Plasma Physics Journal. 2008. V. 1. P. 9.

Plasma Start-up and Current Generation by RF Waves in Spherical Tokamak Globus-M

V.V. Dyachenko[1], F.V. Chernyshev[1], V.K. Gusev[1], S.A. Khitrov[1], N.A. Khromov[1], M.M. Larionov[1], A.D. Melnik[1], A.N. Novokhatsky[1], Yu.V. Petrov[1], N.V. Sakharov[1], O.N. Shcherbinin[1], A.E. Shevelev[1], A.Yu. Stepanov[1], S.E. Bender[2], A.A. Kavin[2], S.E. Lobanov[2]

[1] A.F. Ioffe Physico-Technical Institute, St.Petersburg, Russia, v.dyachenko@mail.ioffe.ru
[2] D.V. Efremov Research Institute, St.Petersburg, Russia

Non-solenoidal plasma start-up and current ramp-up is an important problem on the way to compact fusion reactors. A number of experiments have demonstrated such possibility due to absorption of electromagnetic waves in vicinity of the electron cyclotron resonance for plasma formation and then current start-up [1, 2, 3, 4]. In our case the non-resonant scenario of plasma and current generation by RF power of LH frequency range was used. Plasma current up to 17 kA was achieved with average density $(1–3)\cdot10^{18}$ m^{-3} and 10–20 eV electron temperature. Experimental data indicate that the plasma current could be determined by high energy "tail" in electron energy distribution function.

An experiment on RF plasma start-up and current rump-up was carried out on the spherical tokamak Globus-M (R = 36 cm, a = 24 cm, A = 1.5) [5]. The RF generator with 920 MHz frequency and 100 kW power was used in the experiment. The pulse duration was up to 100 ms. The wave excitation was performed by comb-like antennae: one of them excited mostly poloidally slowed waves (PSA) with Ntor ≈ ≈ (1–15) и Npol = 7 [6] and the other – toroidally slowed waves (TSA) with Ntor ≈ (7–8) и Npol ≈ 1. (Fig. 1). The RF power was fed through the one end of the antenna, whereas the other end was loaded by matching resistance. The excited spectrum is expected to be symmetrical in both directions from the antenna.

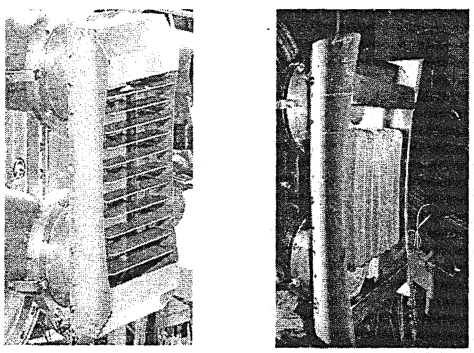

Fig. 1. Photo of PS (*left*) and TS (*right*) antennae

The gas puffing was programmed and optimized. Inductive toroidal electric field was not excited. Quasi-stationary toroidal magnetic field (B_{t0} = 0.4T) and weak vertical magnetic field (B_V ≈ 2–2.5 mT) were applied before the RF pulse. The value of B_V at the breakdown stage was chosen to obtain maximal rate of the current increase at the discharge start. The evolution of the plasma parameters during the discharge is shown in Fig. 2. One can distinguish three stages of the discharge formation. At the RF start (3–4 ms) the ionization takes place (see the initial peak in D_α radiation), and the plasma fills all the volume of the torus. Both antennae are equally effective on the plasma formation stage. Then after 3–5 ms time, the toroidal current arises up to the value of 4–5 kA. The current direction was dependent on the direction of B_V. At the next stage of the discharge, the vertical magnetic field was enhanced fluently to increase the plasma current. In this phase the induced current is approximately proportional to B_V . At achieving some optimal level the current ceased to increase and passed into saturation phase. The achieved maximum of the current was (15–17) kA at plasma density $(1–3)\cdot10^{18}$ m^{-3} and electron temperature (15–20) eV. An attempt to increase the plasma density by intense gas puffing led to decrease of the current. Contamination of the plasma by impurities influenced negatively the current ramp-up phenomenon. RF current drive began from minimal RF power of 20 kW, but when the power exceeded the 40–50 kW value the RF current terminated probably due to impurity accumulation. The current ramp-up phenomenon exists at decreasing of B_{t0} down to 0.2 T. The TS antenna shows smaller efficiency in electron beam and current generation.

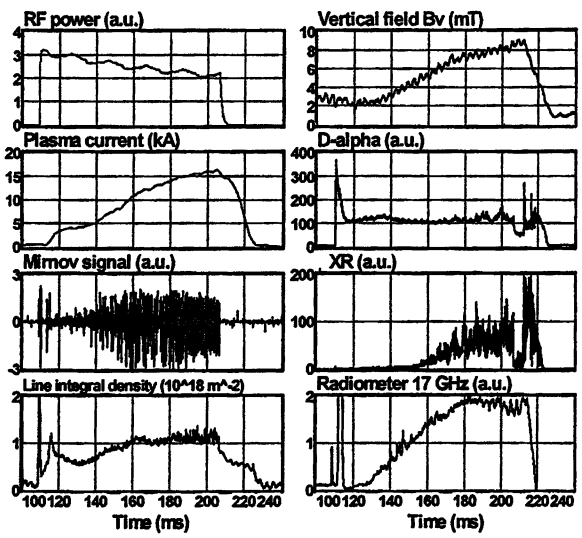

Fig. 2. Waveforms of plasma parameters (sht#26715)

The current ramp-up was accompanied by increase of synchrotron and HXR radiation, which evidenced the generation of high energy electrons. The synchrotron radiation was observed in a broad fre-

quency range 12–36 GHz with small delay after the current start. The radiation temperature can be evaluated as several keV. The HXR radiation was analyzed by a spectrometer in perpendicular direction to the current in the energy range (0.2–0.9) MeV. The last value can be taken as the upper limit of electron energy. Interesting is the fact that CX diagnostic observes the fluxes of high energy neutral particles in these discharges. Their "tails" outspread up to 1.5 keV, and "effective" temperature amounts (200–300) eV . The frequency analysis of plasma RF radiation was provided in frequency range (400–1000) MHz. It reveals the appearance of some satellites of pumping frequency at the level – (30–40) dB which are shifted in low frequency side on ion cyclotron value for plasma outer edge. Essential increase of radiation was observed also in 400–500 MHz frequency range. RF radiation takes place in current ramp-up stage only and vanishes in the stationary current phase. Reconstruction of last closed magnetic surface by Variable Current Loop method [7] shows that LCFS appears beginning from (3–4) kA current and then moves inward during the discharge.

Discussion. As to plasma formation similar experiments at different frequency range were carried out on a lot of tokamaks (for example [8, 9]). The estimation shows that in our case the primary electrons can easily gain the oscillation energy up to (20–50) eV at input power of 20–30 kW, which is greater than ionization potential of hydrogen and is sufficient for plasma creation.

The initial current arose at stationary phase of the vertical field, when the toroidal inductive electric field is absent entirely. One can suggest two mechanisms for explaining the observed phenomena. The first of them can have RF wave nature. The modeling shows that the waves with N_{tor}> 3–5 can easily enter the primary plasma. The most slowed components can be absorbed by Landau mechanism. The 2D simulation predicts the existence of RF fields up to several tens of V/cm at 40 kW of input power [10], which is much greater than Dreiser field ($E_{cr} \cong$ (5–7) 10^{-2} V/cm) and makes it possible to produce run-away electrons. In addition, the observation of low frequency satellites and ion "tails" could evidence the developments of parametric decay processes. The "cold" lower hybrid resonance arises in the plasma at (150–200) MHz frequencies and resonant acceleration of electrons and ions could take place if suitable waves appear in the plasma. The increase of vertical B_V helps to confine the fast electrons and sustain the current.

The second possible mechanism is the direct electron acceleration in the fields on antenna elements (like described in [11]). But in our case the oscillation energy of electrons can not be greater than 500–1000 eV. The most probable is a hybrid scenario: RF fields on the antenna surface produce two groups of fast electrons running along and against the toroidal field. The vertical field B_v saves only one of them, shifting it inside the chamber. Then they interact with less slowed waves and gain higher energy, sustaining plasma current.

Conclusion. The work presents the first use of "lower hybrid" waves for the double purpose – creating a target plasma and ramp-up and driving the plasma current in a spherical tokamak. The comb-like antennae with a broad wave spectrum produced the plasma current up to 17 kA. The further progress depends on understanding of electron acceleration mechanism.

This work was supported by the RFBR grant 09-02-01336a.

References

1. *Shevchenko V.F., O'Brien M R., Taylor D. et al.* Electron Bernstein wave assisted plasma current start-up in MAST // Nucl. Fusion. 2010. V. 50. P. 1-5.

2. *Fjiri A , Takase Y., Sugiyama J. et al.* Non-inductive Plasma Current Start-up by EC and RF Power in the TST-2 Spherical Tokamak // Proc. of the 22 IAEA Conference, (2008), EX/P6-6.

3. *Tanaka H., Maekama T., Uchida M. et al.* Non-Solenoidal Formation of Spherical Torus by ECH/ECCD in LATE // Proc. of the 22 IAEA Conference, 2008, EX/P6-8.

4. *F. Jobes, J. Stevens, R. Bell et al.* Formation of a 100-kA Tokamak Discharge in the Prinston Large Torus by Lower Hybril Waves // Phys. Rev. Let. 1984. V. 52, № 12. P. 1005-1007.

5. *Gusev V.K. et al* Spherical tokamak Globus-M // ZhTF. 1999. V. 69. P. 58-62. or Tech. Phys. 1999. V. 44. P. 1054.

6. *Dyachenko V.V, Chernyshov F.V., Chugunov I.N. et al.* Non-inductive Plasma Current Start-up and Drive by RF Powerin the Globus-M Spherical Tokamak // Proc. of the 37 EPS Conf. on Plasma Physics, Dublin. 2010. P.5.151.

7. *Amoskov V. Bender S. et al.*"Plasma boundary reconstruction from external magnetic measurements in the Globus-M tokamak using the variable current loop method" // Plasma Devices and Operations. 2001. V. 9. P. 159-172.

8. *Budnikov V.N, Dyachenko V.V. et al.* // Proc. of the 19-th Conf. on CFPP, Insbruck, 1992. P. 997-1000.

9. *Gryaznevich M., Shevchenko V., Sykes A,* Plasma Formation in START and MAST Spherical Tokamaks // Nucl. Fusion, 46 (2006) S573-S583.

10. *Irzak, M. A.*, Full-wave 2D modeling of LH heating in Globus-M tokamak // Proc.of the 30th EPS Conf. on CFPP, St. Petersburg, (2003), ECA V. 27A. P-2.175.

11. *Fuchs V., Demers Y., Jacquet P. et al* Interaction of tokamak edge electrons with lower hybrid antenna electric field spectra // Plasma Phys. Control. Fusion, (1999), A495-A505.

Design of Auxiliary ECR Heating System for the Gas Dynamic Trap

E.D. Gospodchikov[1], A.G. Shalashov[1], O.B. Smolyakova[1], P.A. Bagryansky[2], V.I. Malygin[1], V.N. Gorbatushkov[1], V.Kh. Amirov[2], M. Thumm[2,3]

[1]Institute of Applied Physics, RAS, Nizhny Novgorod, Russia, ags@appl.sci-nnov.ru
[2]Novosibirsk State University, Novosibirsk, Russia, [3]Karlsruhe Institute of Technology, Karlsruhe, Germany

The large mirror device Gas Dynamic Trap (GDT) in Budker Institute of Nuclear Physics, Novosibirsk is proposed as a fusion neutron source to test and validate inner wall components of ITER and future thermonuclear fusion reactors [1]. Relative to previous magnetic mirror neutron sources, the GDT facility uses simpler axisymmetric magnets and consumes less tritium providing about 2 MW/m^2 neutron flux. Recent results with high $\beta = 0.6$ provide a firm basis for extrapolating to a fusion relevant high-flux neutron source [2]. Another important application of the GDT neutron source is nuclear waste processing based on fusion driven burning of minor actinides [3]. In this paper we discuss physics and design of a new system for electron cyclotron resonance heating (ECRH) presently under construction for the GDT device which is aimed at increasing the bulk electron temperature in the trap volume and in the long run the efficiency of the neutron source.

The main part of the GDT setup is an axially symmetric magnetic mirror with high mirror ratio. Confined plasma consists of two ion components: the background ions with a temperature of about 200 eV and density $2\cdot10^{19}$ m^{-3} confined in a gas-dynamic regime, and the hot ions, which are produced as a result of oblique injection of high-power (up to 5 MW) hydrogen or deuterium beams into plasma. The distribution function of the hot component is essentially anisotropic in the velocity space; therefore the density and pressure of hot ions are peaked in the mirror points providing conditions for the fusion reactions. Presently the mean energy of the hot ions is about 9 keV, and their density near the mirror points reaches $5\cdot10^{19}$ m^{-3}. Energy confinement times of hot ions as well as their velocity spread are determined basically by the collisional slowing-down on the bulk electrons. Since $\tau_{el} \propto T_e^{3/2}$ the electron drag force is rapidly decreasing with the electron temperature increase. This makes the electron temperature to be the most important parameter which determines the efficiency of the neutron source.

One of the possibilities to increase the electron temperature in the GDT is provided by the auxiliary ECRH system discussed in the present paper. This system based on two 450 kW / 54.5 GHz gyrotrons has a pulse duration longer than the typical NBI-driven discharge (about 5 ms). Evident and attractive feature of ECRH is direct power transfer into the electron component which may be comparable to the power transmitted to electrons due to the ion slowing-down (1.5 MW). Power balance analysis shows that the auxiliary ECRH can provide essential enhancement of electron temperature: up to 350 eV (in case of full absorption) instead of 200 eV achieved in present-day experiments with 5 MW NBI heating. This corresponds to enhancement of the hot-ion confinement time from 2.3 ms to 5 ms what drastically increases the efficiency of neutron-flux production.

The key physical issue of the GDT conditions is that all conventional and widely used ECRH geometries are not accessible. The so-called transverse launch of the gyrotron radiation with respect to the ambient magnetic field shows low efficiency for GDT plasmas even at the fundamental harmonic due to relatively low electron temperature and small scales of the device. Indeed, the total optical depth for the ordinary (O) mode may be estimated as

$$\tau^{\text{O-mode}} = \int 2\,\mathrm{Im}\,\mathbf{k}\cdot d\mathbf{l} \approx \pi \beta_e^2\, qkL_B \ll 1,$$

where $\beta_e = (T_e/m_ec^2)^{1/2} \sim 0.02$, $q = \omega_{pe}^2/\omega_{ce}^2 \sim 1$ is the ratio between the electron plasma and cyclotron frequencies, $k = \omega_{ce}/c$ is the vacuum wavenumber corresponding to 54.5 GHz, and $L_B \sim 10$ cm is the magnetic field inhomogeneity scale. Quasi-transverse launch of the extraordinary (X) mode is impossible at the fundamental harmonics due to plasma refraction and posses the same low efficiency at the second harmonic as the fundamental O-mode. Fortunately, the fundamental X-mode may be effectively absorbed while propagating quasi-longitudinally along the magnetic field at large enough longitudinal refractive index $N_\parallel \sim \beta_e^{-1/3}$, the total optical depth is then [4]

$$\tau^{\text{X-mode}} \approx \tfrac{8}{\sqrt{\pi}} \beta_e^{1/3} q^{2/3} (1-q)^{3/2} kL_B \sim 10.$$

However, the qausi-longitudinal launch of waves with high-enough $N_\parallel$ is physically impossible at the GDT conditions. The solution proposed is based on a peculiar effect of radiation trapping in an inhomogeneous magnetized plasma column. Under specific conditions *oblique* launch of gyrotron radiation results in X-mode propagating longitudinally in the vicinity of the cyclotron resonance, what provides effective single-path absorption of the injected RF power. The physics of the radiation trapping may be understood as following. A wave beam injected obliquely from a vacuum posses $N_\parallel < 1$ which is nearly constant of the plasma-vacuum boundary. During propagation in plasma the longitudinal refractive index increases as

$$\Delta N_\parallel^2 \approx \Delta\varepsilon_- (\cos^2\theta + \varepsilon_\parallel)/(\varepsilon_- + \varepsilon_\parallel)_{\text{at injection point}},$$

where $\varepsilon_- = 1 - \omega_{pe}^2/(\omega - \omega_{ce})$, $\varepsilon_\parallel = 1 - \omega_{pe}^2/\omega^2$, and $\Delta\varepsilon_-$ is variation of ε_- along the radiation path, θ is the wave propagation angle. Evidently, if $|N_\parallel| > 1$ at a plasma border, then radiation cannot escape the

plasma volume at least as a geometro-optical ray. A ray is reflected back to the plasma core, and propagates towards the electron cyclotron resonance (ECR) where both ε_- and $N_\parallel$ are increasing. Finally the ray reaches the vicinity of the ECR with $N_\parallel \sim \beta_e^{-1/3}$ sufficient for a single-pass absorption. Note that due to increasing ε_- the trapping does not occurs if the injection port is close enough to the ECR surface.

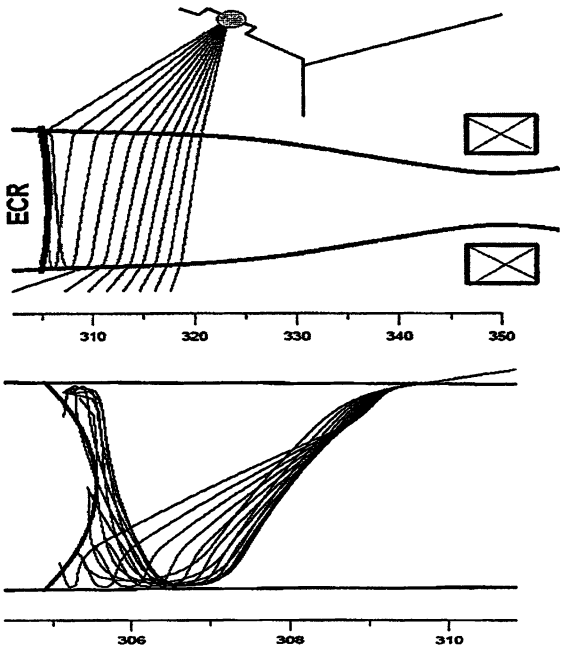

Fig. 1. Top – geometric-optical rays for a set of launching angles 15° – 70°. Bulk plasma density is $1.5 \cdot 10^{19} m^{-3}$. Bottom – rays launched with the same angle 55° for a set of plasma densities $0.5–2.5 \cdot 10^{19} m^{-3}$

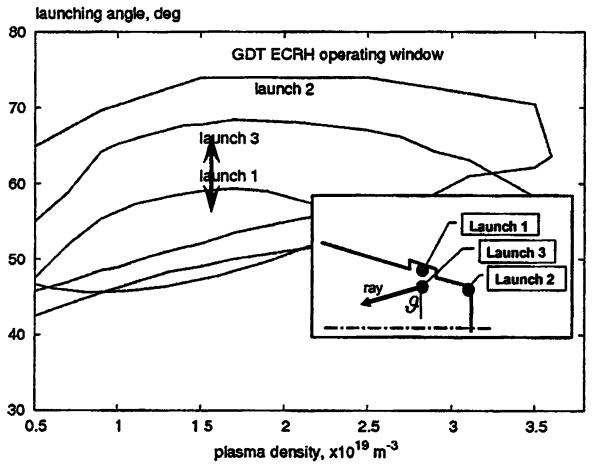

Fig. 2. Operating windows in angle–density plot for tree positions for the ECRH launcher. Launch 1 has been selected for manufacturing

In the present communication we investigate numerically a number of optimized ECRH scenarios based on the proposed mechanism. In the example shown in Fig. 1 we demonstrate how a set of rays may be splitted into trapped and untrapped fractions depending on the initial launching angle. All trapped rays are 100 % absorbed. Also we show that trapping is still possible for various plasma densities. Calculations are summarized in Fig. 2 where the trapping regions are mapped in the plasma density – launching angle diagram. Here we consider three possible positions for the last mirror shown in the inset. After some discussion the "launch 1" point was chosen for the reference design presented below. Correspondingly, this geometry allows operating in the density range $0.5–2.5 \cdot 10^{19} m^{-3}$ using a 50°–55° angular window.

The auxiliary 450/900 kW 54.5 GHz ECRH system is now under construction at the GDT. Design of the proposed fundamental harmonic X mode ECRH launch system is shown in Fig. 3. The start-up of the first gyrotron line is expected in Spring 2012. This system can provide essential enhancement of the electron temperature application up to 300–400 eV. According to computer simulations, in this temperature range the GDT neutron source is quite attractive in comparison with the accelerator based systems [1].

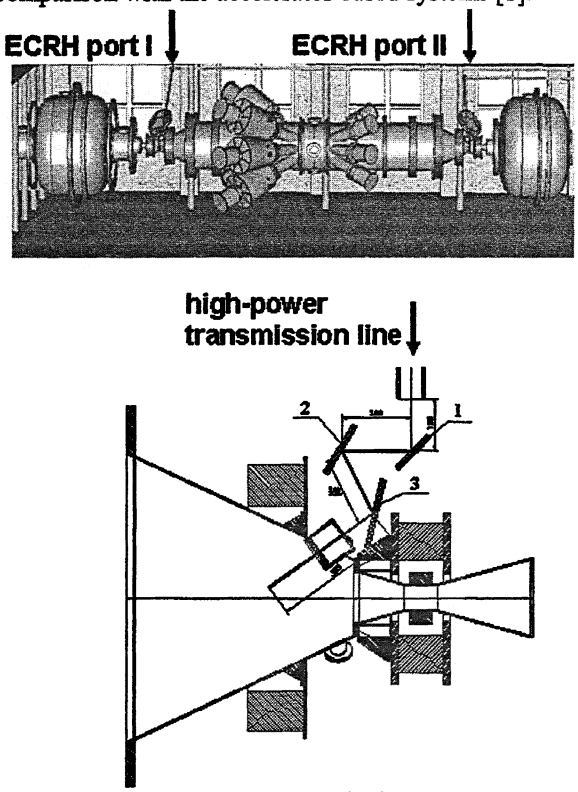

Fig. 3. Top – overview of the GDT facility and positions of the ECRH ports. Bottom – schematic of one of the ECRH launchers (currently under construction in Novosibirsk)

In conclusion we would mention another promising application of ECRH for creating a hot electron population for improved confinement, which is a matter of our future research. The work is supported by Russian Ministry for Education and Science (grant No. 11.G34.31.0033) and RFBR (grants No. 10-02-00441, 11-02-00403).

References

1. *Bagryansky, P.A., Ivanov, A.A., Kruglyakov, E.P., et al.* // Fusion Eng. Des. 2004. V. 70. P. 13–33.

2. *Ivanov, A.A. et al.* // Fus. Sci. Tech. 2010. V. 57. P. 320.

3. *Noack K., Rogov A., Anikeev A.V., et al.* // Annals of Nuclear Energy. 2008. V. 35. P. 1216–1222.

4. *Gospodchikov E.D. Suvorov E.V.* // Radiophys. and Quantum Electronics. 2005. V. 48 (8). P. 641–647.

Novel Quasi-Optical Approach to Studying the Linear Mode-Conversion in Magnetic Fusion Devices

A.A. Balakin, M.N. Buyanova, E.D. Gospodchikov, A.G. Shalashov

Institute of Applied Physics of Russian Academy of Sciences, Nizhny Novgorod, Russia, balakin@appl.sci-nnov.ru

The problem of linear coupling (also known as linear interaction or mode conversion) between high-frequency normal waves propagating in smoothly inhomogeneous magnetized plasmas has a long history. The studies were initiated by Ginzburg in his works on the "tripling" of radio signals in the ionosphere [1]. Under astrophysical conditions, the linear interaction between waves is of considerable importance in description of the mechanism of radiation escape from dense plasmas, for example, from the solar corona [2]. In recent years, interest in the linear mode conversion in electron cyclotron resonance frequency range has increased appreciably in connection with the problems of high-frequency plasma heating and diagnostics in toroidal magnetic traps used in studies of controlled thermonuclear fusion. This is related to achievement of improved plasma confinement in modern tokamaks and to the development of alternative systems like spherical tokamaks and optimized stellarators, which are characterized by comparatively low magnetic fields and high plasma densities [3]. The confinement regimes in which the density in the central regions of a plasma column exceeds its critical value for the propagation of electromagnetic waves used in conventional electron cyclotron (EC) plasma heating and diagnostic schemes, such as the ordinary (O) wave at the fundamental EC harmonic or the extraordinary (X) wave at the second harmonic, are realized increasingly often. The resonance absorption of the electromagnetic waves in spherical tokamaks is also proven to be inefficient, since the EC absorption can be realized only at fairly high harmonics of the electron gyrofrequency due to a weak magnetic field. One of the most promising ways to overcome these difficulties is based on conversion of the electromagnetic waves into the short wavelength electrostatic waves, the so-called electron Bernstein (B) waves, which have no density cutoffs and may be effectively absorbed at high cyclotron harmonics. In large-scale magnetic fusion devices, electron Bernstein waves may be effectively excited via two-step mode conversion process (O–X–B conversion) in which an ordinary wave launched from the low field side is converted in the vicinity the cutoff surface to a slow extraordinary wave, which, in turn, is converted near the upper hybrid resonance to an electron Bernstein wave. The efficiency of the entire process is determined mainly by the O to X mode (O–X) conversion which is sensitive to the value of the parallel refractive index of the incident O wave with respect to an external magnetic field in the coupling region.

In the present communication we present a new computational tool for studying the mode conversion problems in toroidal fusion devices, in particular, the O-X-B heating of over-dense plasmas. It is based on the unique quasi-optical (QO) beam tracing code developed at IAP RAS [4, 5], which is amended by analytical procedure for linking the solutions in front of and behind the mode-coupling region where the quasi-optical approximation does not work. Analytical procedure is based on a solution of a full-wave problem in a simplified (but three-dimensional) geometry adequately described the wave physics inside the mode-coupling region [6]. First applications of this code are discussed. In particular, for the first time the role of diffraction and aberration effects is identified for mode-coupling problems in this frequency range.

Recently it has been understood that the one-dimensional approximation may be insufficient to describe the O–X conversion in toroidal magnetic configurations, in which density and magnetic field vary along different directions resulting in *intersection* of the cut-off surfaces. In some sense, this may be attributed to variation of a magnetic field on flux surfaces. A non-one-dimensional extension of the theory of the O–X coupling has been developed by Gospodchickov *et al.* [6–9] and, independently, by Popov *et al.* [10–12]. The theory is based on a new reference problem in which the linear interaction region is formed by intersection of two flat cut-off surfaces and the system is homogeneous along the intersection line. Thus, a tokamak-like geometry has been reduced to the two-dimensionally inhomogeneous problem shown in Fig. 1.

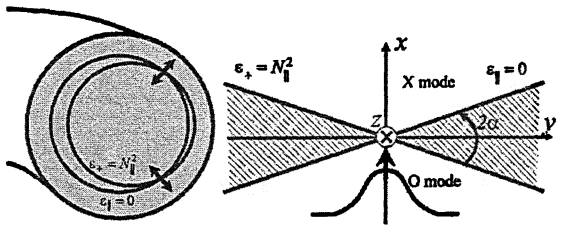

Fig. 1. *Left*: the cut-off surfaces in a poloidal cross-section of a tokamak. *Right*: the O–X transformation region in 2D geometry, where the plasma density and the magnetic field intensity vary in the *xy* plane; the evanescent region for left-hand polarized waves is dashed

The main two-dimensional effect found in analytical theory is that the coupling region acts as a filter selecting the optimal beam structure. Indeed, when a plane wave falls on the interaction region, behind this region a structure is formed that follows the optimal beam profile. Gaussian incident beam remains Gaussian after passing the transformation region, although the beam parameters change. The incident beam is widened if its width is less than the optimal beam width and narrowed otherwise. Thus, the spatial filter

formed in the coupling region imposes a certain spatial scale that weakly depends on the initial width of the incident beam.

Unfortunately, above mentioned exact analytical approach is applicable only in local vicinity of the transformation point. On the other hand, a quasi-optical beam tracing code [4, 5] can accurately describe wave beam propagation far from this point. In this code the propagation and absorption are treated self-consistently using the weakly relativistic, warm dispersion relation. Opposite to other known codes, this quasi-optical code is capable of treating correctly wave beams of arbitrary shape in the presence of strongly inhomogeneous media and absorption as well as in media with strong spatial dispersion. Such conditions are found, for example, in the region around the EC resonance where the warm plasma dispersion is strongly varying. Recently, a verification of the quasi-optical method has been performed in the case of a simplified plasma model in which an analytical, exact solution of the full wave equation exists: good agreement between the quasi-optical calculations and the analytical solution has been found [13].

Recently the quasi-optical code has been upgraded for treatment of mode-coupling problems with the help of the analytical procedure for linking the solutions in front of and behind the mode-coupling region where the quasi-optical approximation is not applicable. As an example of first use of this code, dependences of the O-X transformation coefficient on the flux-surface label ρ is presented in Fig. 2 for different wave beams propagated in TCV-like tokamak plasmas [14]. As one expects the dependence of the transformation coefficient over the flux-surface have a plateau at some middle region where both approximations (the quasi-optical and the analytical solution) are valid. Differences at the edge of the plasma ($\rho = 1$) and near the refraction point take place due to errors in analytical and quasi-optical solutions correspondingly.

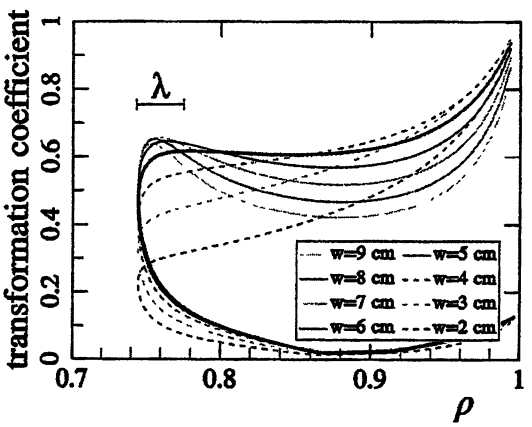

Fig. 2. Transformation coefficient for different widths of wave beams. One can see an optimal beam width (black thick curve) which have highest transformation efficiency. Here ρ is the flux surface label, for example the square root of the normalized poloidal or toroidal flux. Generally $\rho = 1$ on the boundary of the plasma and $\rho = 0$ in the centre

Another feature shown in Fig. 2 is the presence of optimal beam width which has the maximal value of the transformation coefficient. Exactly such value of 5 cm for beam width is predicted by analytical formulas for selected magnetized plasma configuration. The developed tool demonstrates a next step in evolution of beam-tracing techniques and can be a good alternative to complicated full-wave numerical codes.

The work in this paper has been performed in the framework of the NWO-RFBR Centre of Excellence on Fusion Physics and Technology (grant 047.018.002) and has also been supported by RFBR (grants Nos. 09-02-00972, 11-02-00403) and Russian Ministry for Education and Science (state contract No. 14.740.11.0607).

References

1. *Ginzburg, V.L.* The Propagation of Electromagnetic Waves in Plasmas, 2nd ed. (Nauka, Moscow, 1967; Pergamon, Oxford, 1970).

2. *Zheleznyakov, V.V.* Radiation in Astrophysical Plasmas (Kluwer, 1996).

3. *Laqua, H.P.* Electron Bernstein wave heating and diagnostic // Plasma Phys. Control. Fusion. 2007. V. 49. P. R1–R42.

4. *Balakin, A.A., Balakina, M.A., Smirnov, A.I., Permitin, G.V.* Scalar equation for wave beams in a magnetized plasma // Plas. Phys. Rep. 2007. V. 33. P. 302.

5. *Balakin, A.A., Balakina, M.A., Westerhof, E.* ECRH power deposition from a quasi-optical point of view // Nucl. Fusion. 2008. V. 48. P. 065003.

6. *Shalashov, A.G., Gospodchikov, E.D.* On the O-X mode coupling in 3D sheared magnetic field // Plasma Phys. Control. Fusion. 2010. V. 52. P. 115001.

7. *Gospodchikov, E.D., Shalashov, A.G., Suvorov, E.V.* On influence of 2D inhomogeneity on electromagnetic mode conversion near the cut-off surfaces in magnetized plasmas // Plasma. Phys. Contr. Fusion. 2006. V. 48. P. 869.

8. *Shalashov, A.G., Gospodchikov, E.D., Suvorov, E.V.* On the structure wave fields in the region of linear interaction between ordinary and extraordinary waves in two-dimensionally inhomogeneous magnetoactive plasmas // JETP. 2006. V. 103. P. 480.

9. *Husainov, T.A., Gospodchikov, E.D., Shalashov, A.G.* Curvature effects on linear mode-conversion of electron cyclotron waves in tokamak plasmas / Proc. of 8th International Workshop "Strong Microwaves and Terahertz Waves: Sources and Applications". 2011.

10. *Popov, A. Yu., Piliya, A. D.* Conversion of normal waves in the electron-cyclotron frequency range at the critical surface in a cold anisotropic plasma inhomogeneous in two dimensions // Plasma Phys. Rep. 2007. V. 33. P. 109.

11. *Popov, A. Yu.* On O–X mode conversion in spherical tokamaks // Plasma Phys. Control. Fusion. 2007. V. 49. P. 1599.

12. *Popov, A. Yu.* On O–X mode conversion in 2D inhomogeneous plasma with a sheared magnetic field // Plasma Phys. Control. Fusion. 2010. V. 52. P. 035008.

13. *Maj, O., Balakin, A.A., Poli, E.* Effects of aberration on paraxial wave beams: beam tracing versus quasi-optical solutions // Plasma Phys. Control. Fusion. 2010. V. 52. P. 085006.

14. *Pochelon, A. et al.*, Electron Bernstein wave heating of over-dense H-mode plasmas in the TCV tokamak via O-X-B double mode conversion // Nucl. Fusion. 2007. V. 47. P. 1552.

Curvature Effects on Linear Mode-Conversion of Electron Cyclotron Waves in Tokamak Plasmas

T.A. Husainov, E.D. Gospodchikov, AG. Shalashov

Institute of Applied Physics of Russian Academy of Sciences, Nizhny Novgorod, Russia, eggos@mail.ru

This paper continues the series of studies of linear mode coupling in non-one-dimensionally inhomogeneous magnetized plasmas, see [1] and references therein. More precisely, we study the conversion of ordinary (O) waves to extraordinary (X) waves near the plasma cut-offs in the electron cyclotron resonance frequency range in toroidal plasmas. This process plays an important role in excitation of the electron Bernstein waves, which in turn provide an effective way for high-frequency heating and diagnostics of overdense plasma in spherical tokamaks and optimized stellarators.

Recently it has been understood that conventional one-dimensional approach [2] may be insufficient to describe the O–X conversion in toroidal magnetic configurations, in which plasma density and ambient magnetic field vary along different directions resulting in *intersection* of the cut-off surfaces. This case is shown schematically in fig. 1 (right). Propagation regions for the O and X waves are separated by the evanescent region defined by condition $\varepsilon_{\parallel}(\varepsilon_{+}-N_{\parallel}^2)<0$ where $N_{\parallel}=ck_{\parallel}/\omega$ is the wave refractive index parallel to the magnetic field

$$\varepsilon_{\parallel}=1-\omega_{pe}^2/\omega^2,\quad \varepsilon_{\pm}=1-\omega_{pe}^2/[\omega\,(\omega\pm\omega_{ce})],$$

ω, ω_{ce} and ω_{pe} is, correspondingly, the wave, electron cyclotron and plasma frequencies, and. Here the cut-off surface $\varepsilon_{\parallel}=0$ is a part of a flux surface with the critical plasma density ($\omega_{pe}=\omega$); however due to variation of the magnetic field, the cut-off surface $\varepsilon_{+}-N_{\parallel}^2=0$ does not correspond to a flux surface. Tokamak symmetry implies that the system is homogeneous in the toroidal direction represented by the z-axis in fig. 1. After toroidal curvature is neglected, propagation of the O and X waves may be treated as a two-dimensionally inhomogeneous problem. Indeed, the mode conversion actually occurs as a tunnelling of the electromagnetic radiation throughout the non-slab two-dimensional evanescent region shown in fig. 1. The earlier studies of this process were performed under assumption that the cut-off surfaces are flat since the entire O-X coupling region is small. In the present paper we study the effects of the flux-surface curvature but taking into account only a toroidal magnetic field. Effects of a poloidal magnetic field have been studied separately in [1].

Following [2] we will use Stix representation for the field components in the Cartesian coordinate system with the z-axis directed along the external magnetic field:

$$\sqrt{2}E_{\pm}=E_x\pm iE_y=(F_x\pm iF_y)\exp(ik_0N_{\parallel}z-i\omega t),$$

$$E_z=F_z\exp(ik_0N_{\parallel}z-i\omega t),$$

here $k_0=\omega/c$. In the vicinity of the O-X coupling region one obtains the following wave equations for the slow wave amplitudes:

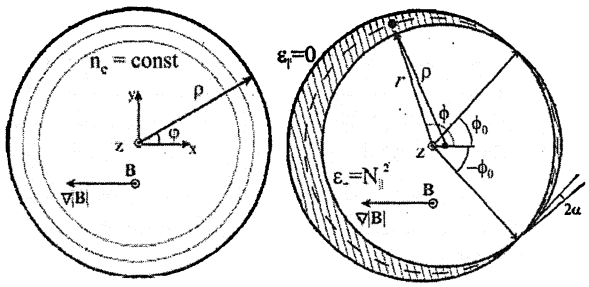

Fig. 1. Original cylindrical coordinates ρ,φ centered around the magnetic axis (left) and new cylindrical coordinates r,ϕ with the origin shifted over $\Delta\rho$ from the magnetic axis. The evanescent region for the right-polarized waves formed by two cut-off surfaces is shown in dashing

$$\begin{cases} N_{\parallel}(i\partial/\partial x-\partial/\partial y)F_{\parallel}=\sqrt{2}k_0\left(\varepsilon_{+}-N_{\parallel}^2\right)F_{+} \\ N_{\parallel}(i\partial/\partial x+\partial/\partial y)F_{+}=\sqrt{2}k_0\,\varepsilon_{\parallel}F_{\parallel} \end{cases} \quad (1)$$

which are valid in a weakly inhomogeneous medium with a scale $k_0L\gg1$. The only difference of the subsequent analysis from those published in [2] is more complicated dependence of ε_{+} and $\varepsilon_{\parallel}$ on spatial coordinates.

Let us assume the simplest toroidal magnetic field model – surfaces of constant pressure are formed by concentric circular tori; thus the plasma density $n_e(\rho)$ depends on a minor radius ρ only. With a same accuracy the magnetic field strength is inversely proportional to the distance to the axis of symmetry, $B=B_0L_B/R$ where $R=L_B+\rho\cos\varphi$, φ is an angle the from equatorial plane, see fig. 1 (left). In a local vicinity on the cut-off region all spatial dependences may be approximated by linear functions, under these assumptions

$\varepsilon_{\parallel}\approx g_{\parallel}(\rho-\rho_0)$, $\varepsilon_{+}\approx g_{+}(\rho-\rho_0-\Delta\rho\cos\varphi+\rho_1)+N_{\parallel}^2$, where ρ_0 is the "radius" of the cut-off region, $g_{\parallel}=|n_e'/n_e|=1/L_n$ is the inverse density variation scale, $g_{+}=g_{\parallel}Y/(1+Y)$, $\Delta\rho=\rho_0(L_n/2L_B)/(1+Y)$, $\rho_1=[1/(1+Y)-N_{\parallel}^2]/g_{+}$, $Y=\omega_{ce}/\omega$ at $\rho=0$. Up to the small terms $O(\rho_1/\rho_0)$ and $O(\Delta\rho/\rho_0)$ both cut-off surfaces are formed by two circles with centers shifted by $\Delta\rho$ in horizontal direction and radii differed by ρ_1. To describe this geometry it is more convenient to introduce a new polar coordinates (r,ϕ) with the origin exactly between the centers of two cut-off surfaces, see fig. 1. Also it is convenient to shift the r-coordinate $\tilde{r}=r-\rho_0+\rho_1/2$ such that $\tilde{r}$ is small inside the O-X coupling region. Finally one obtains $\varepsilon_{\parallel}\approx g_{\parallel}[\tilde{r}+(\Delta\rho\cos\phi-\rho_1)/2]$ and

$\varepsilon_+ - N_\parallel^2 \approx g_+ [\tilde{r} - (\Delta\rho\cos\phi - \rho_1)/2]$. Substituting these expressions into (1), the one obtains the reference wave equations in the new coordinates:

$$\begin{cases} \dfrac{N_\parallel e^{+i\phi}}{\sqrt{2}k_0 g_+}\left(i\dfrac{\partial}{\partial\tilde{r}} - \dfrac{1}{\rho_0}\dfrac{\partial}{\partial\phi}\right)F_\parallel = \left(\tilde{r} - \dfrac{\Delta\rho}{2}\cos\phi + \dfrac{\rho_1}{2}\right)F_+ \\ \dfrac{N_\parallel e^{-i\phi}}{\sqrt{2}k_0 g_\parallel}\left(i\dfrac{\partial}{\partial\tilde{r}} + \dfrac{1}{\rho_0}\dfrac{\partial}{\partial\phi}\right)F_+ = \left(\tilde{r} + \dfrac{\Delta\rho}{2}\cos\phi - \dfrac{\rho_1}{2}\right)F_\parallel \end{cases}$$

The most effective coupling is expected when the wave field is localized close to the intersections of the cut-off surfaces, which have the following coordinates in the poloidal plane: $\tilde{r} = 0$, $\phi = \pm\phi_0$ with $\phi_0 = \arccos(\rho_1/\Delta\rho)$. Thus, $\Delta\rho$ and ϕ_0 fully characterize the geometry of the cut-off region. Indeed, with new dimensionless variables

$$A_\parallel = \frac{F_\parallel}{\sqrt{g_\parallel}}\exp\left(\frac{\tilde{r}}{2\rho_0} + \frac{i\phi}{2}\right),\ A_+ = \frac{F_+}{\sqrt{g_+}}\exp\left(\frac{\tilde{r}}{2\rho_0} - \frac{i\phi}{2}\right) \quad (2)$$

$$\xi = \frac{-\tilde{r}}{L_\nabla},\ \Delta\xi = \frac{\Delta\rho}{2L_\nabla},\ \kappa = \frac{L_\nabla}{\rho_0},\ L_\nabla^2 = \frac{N_\parallel}{k_0\sqrt{2g_+ g_\parallel}},$$

the reference wave equations may be rewritten as

$$\begin{cases} (i\partial/\partial\xi + \kappa\partial/\partial\phi)A_\parallel = (\xi + \Delta\xi(\cos\phi - \cos\phi_0))A_+ \\ (i\partial/\partial\xi - \kappa\partial/\partial\phi)A_+ = (\xi - \Delta\xi(\cos\phi - \cos\phi_0))A_\parallel \end{cases} \quad (3)$$

These are generalization of Eqs. (11) obtained in [2] over the cylindrical geometry; here ξ is equivalent to the coordinate x', and ϕ is equivalent to the poloidal coordinate y'. Note that some cylindrical effects are introduced by the field renormalization (2) – these are the additional phase shift over the poloidal coordinate accounting for variation of wave polarization due to rotation of the normal to a flux surface, and the additional cylindrical focusing.

As in our previous papers [1, 2], an arbitrary wave field can be represented as,

$$A_+ = A^+ + A^-, \qquad A_\parallel = A^+ - A^-,$$

where the components A^+ and A^- correspond to the waves that propagate, respectively, in the positive and negative directions along the radial coordinate in the region of geometrical optics (or WKB limit). In new field variables Eqs. (3) takes the following form:

$$\begin{cases} (i\partial/\partial\xi + \xi)A^- = (\kappa\partial/\partial\phi - \Delta\xi(\cos\phi - \cos\phi_0))A^+ \\ (i\partial/\partial\xi - \xi)A^+ = (\kappa\partial/\partial\phi + \Delta\xi(\cos\phi - \cos\phi_0))A^- \end{cases}.$$

Introducing $A^- = A_\xi^-(\rho)\cdot A_\phi^-(\phi)$, $A^+ = A_\xi^+(\rho)\cdot A_\phi^+(\phi)$ one obtains

$$\left(d^2/d\xi^2 + \xi^2 + i\right)A_\rho^+ = \lambda\kappa^2 A_\rho^+, \quad (4)$$

$$\left(-d^2/d\phi^2 + \delta^2(\cos\phi - \cos\phi_0)^2 - \delta\sin\phi\right)A_\phi^+ = \lambda A_\phi^+, \quad (5)$$

with $\delta = \Delta\xi/\kappa = \rho_0\Delta\rho/2L_\nabla^2$. Equation (4) is fully equivalent to the same equation obtained for the flat cut-off surfaces; it solution corresponded to the propagating in the positive direction wave may be expressed in terms of the parabolic cylinder functions:

$$A_\rho^+ \propto D_{i\nu}\left(\sqrt{2}e^{i\pi/4}\xi\right),\ \nu = \lambda\kappa^2/2.$$

Equation (5), that defines the poloidal structure of the wave field, obviously differs from its analogue obtained for the flat cut-off surfaces. While the latter may be solved in terms of Hermite polynomials, equation for poloidal modes for the cylindrical cut-off surfaces have no explicit analytical solutions, however it may be easily solved numerically. Equation (5) should be considered as a Sturm-Liouville problem with boundary condition $A_\phi^+(\phi) = -A_\phi^+(\phi + 2\pi)$. Solutions of this problem form a complete set of orthogonal modes $\Phi_n(\phi)$ corresponded to a real valued and discrete spectrum of eigenvalues λ_n.

The general solution for the forward (incident or transmitted) wave takes the following form:

$$A^+(\xi,\phi) = \sum_{n=0}^{\infty} A_n\Phi_n(\phi)D_{i\nu_n}\left(\sqrt{2}e^{i\pi/4}\xi\right),\ \nu_n = \lambda_n\kappa^2/2,$$

where A_n are the constant coefficients that can be identified as projections of the wave field over the poloidal modes $\Phi_n(\phi)$ at some point ξ before the coupling region where the incident field is known. Corresponding reflected wave ($A^- \to 0$ at $\xi \to +\infty$) is

$$A^-(\xi,\phi) = \sum_{n=0}^{\infty}(-1)^{n+1}\sqrt{i\nu_n}\,A_n\Phi_n(-\phi)D_{i\nu_n - 1}\left(\sqrt{2}e^{i\pi/4}\xi\right).$$

The above two expressions give full solution of the problem, i.e. allow reconstructing wave fields that are transmitted through and reflected from the coupling region for any given structure of the incident beam.

An example of application of the developed theory to a realistic tokamak configuration (FTU) is presented in fig. 2. One can see oscillations formed by interference of the incident and reflected beams close to the cut-off surface, and the incident and transmitted beams formed far from the interaction region

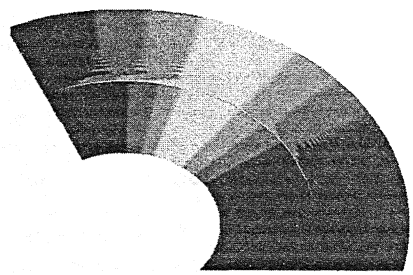

Fig. 2. Field distribution $|A^+|$ in the poloidal cross-section for Gaussian incident beam $\propto \exp[-(\phi - \pi/3)^2/\delta\phi^2]$ with $\delta\varphi = \pi/6$. Tokamak parameters correspond to $\delta = 60$, $\kappa = 0.022$, and $\varphi_0 = \pi/3$

The work has been supported by RFBR (grants No. 09-02-00972, 11-02-00403) and Russian Ministry for Education and Science (state contract No. 14.740.11.0607).

References

1. *Shalashov, A.G., Gospodchikov. E.D.* On the O-X mode coupling in 3D sheared magnetic field // Plasma Phys. Control. Fusion. 2010. V. 52. P. 115001.

2. *Gospodchikov, E.D., Shalashov, A.G., Suvorov, E.V.* On influence of 2D inhomogeneity on electromagnetic mode conversion near the cut-off surfaces in magnetized plasmas // Plasma Phys. Contr. Fusion. 2006. V. 48. P. 869.

Analysis of LHCD Efficiency on FT-2 Tokamak

S.I. Lashkul, A.B. Altukhov, A.D. Gurchenko, V.V. Dyachenko, L.A. Esipov, M.Yu. Kantor, D.V. Kouprienko, M.A. Irzak, A.N. Saveliev, V.V. Rozhdestvensky, S.V. Krikunov, S.V. Shatalin*, A.Yu. Stepanov

A.F. Ioffe Physico-Technical Institute Politekhnicheskaya 26, 194021, St. Petersburg
*St. Petersburg State Polytechnical University, 195251, Russia

The experiments with LHCD generation has been carried out on the FT-2 tokamak (R = 0.55 m, a_L = 0.08 m). The experiments were performed at plasma currents of I_{pl} = 19–40 kA and a toroidal magnetic field of B_T = 2.2 T. In the steady state phase of the discharge, the RF power at the frequency f = 920 MHz P_{RF} = 50÷200 kW was input from the low field side by using a two waveguide grill. The discharge duration was Δt_{pl} = 50 ms, and the RF pulse duration Δt_{RF} was varied from 5 to 14 ms.

The dependence of the LHCD efficiency $\eta_{exp} = \Delta U I_{pl} \langle n_e \rangle R / U_{OH} P_{LHW}$ on the grill phasing $\Delta\varphi$ and RF oscillator power has been determined experimentally in a wide range of plasma densities [1]. The highest LHCD efficiency was observed at $\Delta\varphi = \pi/2$, Fig. 1. It is shown that, for higher plasma currents (i.e., at higher electron temperatures), LHCD is suppressed when the plasma density reaches its LH resonance value $n_{LH} \sim 3\ 10^{19}$ m^{-3}, rather than when parametric decay comes into play, as was observed in regimes with lower currents and accordingly, lower electron temperatures T_e. It is found that the additional impurity influx caused by the bombardment of the diaphragm by high energy electron beams substantially reduces the LHCD efficiency. The recalculated for Z_{eff} = 1 experimental quantity η_{CD} well correlates with line dependence on $\langle T_e \rangle$ obtained for larger tokamaks [2].

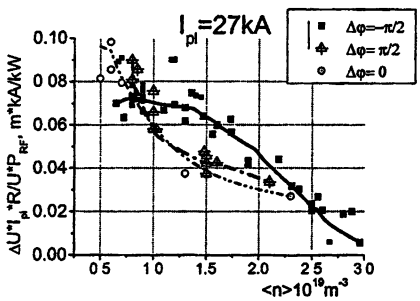

Fig. 1. Normalized LH driven current $I^N_{RF} = (-\Delta U/U_{OH})I_{PI}$ versus density at different $\Delta\varphi$. The injected LHW power is 100 kW

In order to analyze the experimentally observed LHCD effect and its dependence on the value and sign of the antenna phasing, the spectra of the excited LH waves have been calculated using the GRILL3D code for three values of the phase shift, $\Delta\varphi = \pm\pi/2$ and 0. It is shown that the spectra of slowed down RF waves are bidirectional (with respect to the plasma current) and that the RF power spectrum $P(N_z)$ has several maxima. For $\Delta\varphi = \pi/2$, the maxima correspond to the parallel refractive indices $N_{||}$ = –9, –1.7, 3, and 20. Using the Fast Ray Tracing Code (FRTC) [3] with allowance for the calculated spectrum $P(N_z)$ of the excited LH waves and the measured plasma parameters, we found the value and direction of LHCD. The magnetic equilibrium of the plasma column was calculated using the ASTRA code for the radial plasma profiles and parameters of the FT-2 tokamak. The FRTC solves the wave equation for LH waves in the ray approximation in the cold plasma model, which is well applicable for frequencies exceeding the LH resonance frequency. The quasi-steady electric field and the action of LHCD on the equilibrium plasma parameters were not taken into account in these calculations.

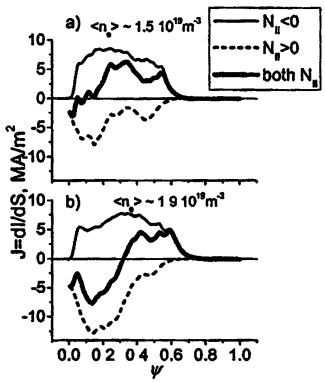

Fig. 2. Modeling by FRTC code the current density profile components for two different $\langle n \rangle$. I_{PL} = 27 kA, P_{RF} = 100 kW, $\psi = \rho/a_L$

The calculated LHCD radial profiles $J=dI/dS$, MA/m2, where ψ is the relative radial coordinate of the magnetic surface is shown in Fig. 2. In the case of asymmetric excitation $\Delta\varphi = \pi/2$ for the initial plasma current I_{pl} = 27 kA, central electron temperature $T_e(r = 0\ \text{cm})$ = 450 eV, and RF power P_{RF} = 100 kW, the inductive plasma current at $\langle n_e \rangle = 0.9 \cdot 10^{19}$ m^{-3} can be completely replaced with the total LH-driven current, which is the sum of two oppositely directed currents. For higher plasma densities, $1.5 \cdot 10^{19}$ m^{-3} $n_e(0) = 2.6 \cdot 10^{19}$ m^{-3}, the inductive current is replaced only partially, I_{RF} = 14.6 kA.

The simulations revealed the important role of the synergetic effect caused by the interaction of different spectral components of the excited RF waves. An LH wave with the slowing down factor $N_{||} = -1.8$ efficiently drives the current only in the presence of even slower waves with $N_{||} = -9$. Waves with $N_{||} = -9$ alone are insufficient to drive the current; however, interacting with thermal electrons, they are capable of accelerating these electrons to velocities at which electrons efficiently interact with the main spectral component with $N_{||} = -1.8$.

Main experiments are carried out at relatively large for installation plasma currents $I_{pl} \sim 36$ kA ($q \sim 4$) and $P_{RF} = 100$kW. LHCD is accompanied by an increase in the plasma density and the intensity of the spectral line of the CIII impurity. Moreover, the intensity of 2- to 10-MeV bremsstrahlung hard X-ray (HXR) emission caused by the escape of runaway electrons onto the diaphragm and the chamber wall also undergoes typical variations. Additional impurity influx from the wall obviously resulted from the fan or Parail-Pogutse instability (PPI) which produces the runaway electron flux at the limiter and the wall of the chamber [4]. Experimental confirmations of the conclusion about reconstruction of the plasma current profile could be SXR, TS data and observed effect of abrupt suppression of MHD oscillations taking place during LHCD [1].

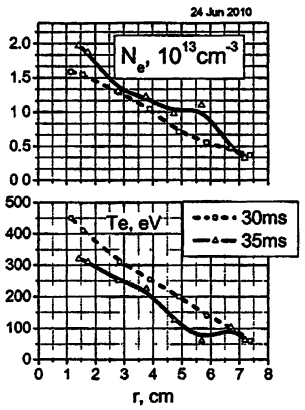

Fig. 3. $T_e(r)$ and $n_e(r)$ measured by TS diagnostic in LHCD experiment

Fig. 3 illustrates changes in $T_e(r)$ and $n_e(r)$ measured by TS diagnostics in LHCD experiment. RF pulse duration $\Delta t_{RF} = 5$ms (from 30 to 35ms). The data is indicative of noticeable cooling of the plasma column at LHCD because some part of the plasma current (~25 %) is carried by super thermal and runaway electrons generated by LHW. At the same time the plasma density rise is observed. It seems to be associated with the rise of particle confinement time at ITB formation. Density profile steeping at the middle radii, as one can see in figure 3 at r = 5.5÷7cm, is also confirmed by spectral observations.

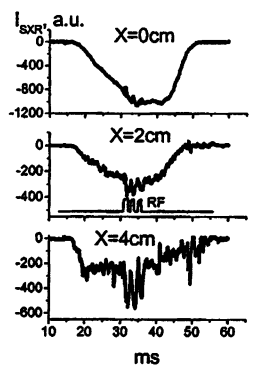

Fig. 4. Chord SXR signals modulated by RF meander

Space distribution of the above-thermal electrons generated by LHW, when the RF input is modulated by three consecutive pulses of 1.2 ms duration, is analyzed with 14-channel SXR diagnostics. Additionally modulated SXR signals are observed mainly at chords $X = 2$ cm and X = 4 cm, Fig. 4. So, according to the experimental data, generation of above-thermal electrons occurs basically at middle radii that correspond to data modeling (see heavy curve in Fig. 2).

The essential rise of HXR emission observed experimentally during LHCD is determined by above-thermal electrons generated by LHW and then accelerated in residual vortex toroidal electrical field and thus contributing to runaway beams. On the other hand, if the loop voltage at LHCD is small, HXR can be lower than the OH level. Fig. 5 demonstrates such a case when during meander RF pulses U_{pl} signal falls down to the level at which HXR signal remains at OH level or decreases below it. During interval between pulses, when U_{pl} rises, HXR signal increases dramatically because the comparatively long-living above-thermal electrons generated by LHW are accelerated by higher U_{pl}.

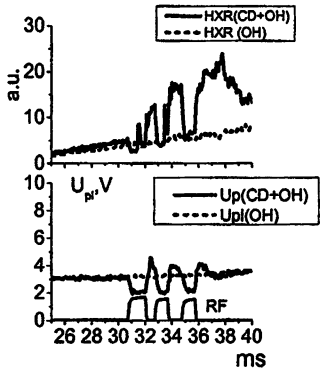

Fig. 5. Comparison of HXR levels and loop voltage signals for OH (dotted lines) and OH+LHCD in the experiment with modulation by meander of the launched LHW

Recently LHCD experiment at $\langle n_e \rangle = 0.9\ 10^{19}$ m^{-3} with longer LHW pulse duration $\Delta t_{RF} = 14$ ms ($P_{RF} = 100$ kW and the inductive plasma current $I_{pl} = 35$ kA) reveals rise of $T_e(y = 0$ cm) from 400 eV to 600 eV before end of RF pulse. During LHCD the abrupt powerful (ΔP_{RF} ~20÷30 kW) radiation increase had been registered by collimated bolometer, which can be associated with synchrotron emission generated by runaway beam (not impurity radiation). The paper presents and analyses the data of the microwave synchrotron emission (SE).

References

1. *S.I. Lashkul, A.B. Altukhov et al.* Analysis of the Efficiency of Lower Hybrid Current Drivein the FT-2 Tokamak // Plasma Physics Reports. 2010. V. 36, № 9. P. 751–761.

2. *V. Pericoli-Ridolfini, 1.E. Barbato et al.* High Plasma Density Lower-Hybrid Current Drive in the FTU Tokamak // Physical Review Letters. V. 82, № 1. 93.

3. *A.D. Piliya and A.N. Saveliev,* Preprint No. JET_R(98)01 (JET Joint Undertaking, Abingdon, 1998).

4. *V.V. Parail and O.P. Pogutse,* in Reviews of Plasma Physics, Ed. by M.A. Leontovich and B.B. Kadomtsev (Atomizdat, Moscow, 1982; Consultants Bureau, New-York, 1986). V. 11.

Nonlinear Evolution of Fast Ion Driven Modes at Mariginal Stability in Tokamak Plasmas

M. Lisak[1], J. Zalesny[2], G. Galant[1,2] and V.E. Semonov[3]

[1]Department of Earth and Space Sciences, Chalmers University of Technology, Göteborg, Sweden, email: mietek.lisak@chalmers.se
[2]West Pomeranian University of Technology, Szczecin, Poland
[3]Institute of Applied Physics, Nizhny Novgorod, Russia

Energetic particle driven Alfvénic instabilities are often observed in present-day fusion experiments and they are of major importance for the next step burning plasmas. These instabilities are excited in a broad range of frequencies and exhibit a variety of nonlinear scenarios for the mode amplitude and frequency evolution, from a steady-state saturated amplitude, to a bursting one. The nonlinear evolution, together with the linear stability criteria and the characteristic values of the amplitudes of the Alfvénic modes, are essential for understanding the global transport of the energetic particles and hence particle re-distribution and losses.

In MAST, as with other machines with neutral beam injection (NBI), a «hard» non-linear regime is observed, especially at low frequencies (e.g. Fig. 1), resulting in bursting amplitude evolution and in rapid frequency sweeping.

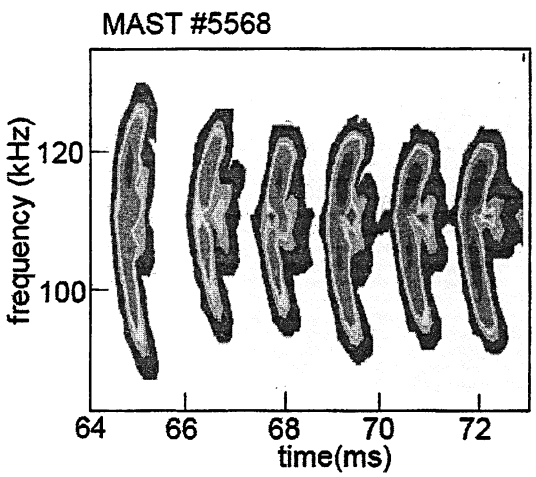

Fig. 1. Magnetic spectrogram of a MAST experiment with constant NBI power, showing rapid frequency sweeping

In contrast, Alfvèn eigenmodes (AEs) excited by ICRH-produced ions at JET show usually the «soft» excitation regimes (e.g. Fig. 2). In these nonlinear scenarios, the mode frequency remains close to the linear AE eigenfrequency and the structure of the mode remains similar to the linear one.

The current nonlinear research is focused around the idea that, in spite of the significant differences in the nature of the modes (e.g. shear Alfvén or CAE), and in the corresponding excitation mechanisms, the nonlinear evolution of these modes, when driven just above their excitation threshold, is determined by competition between the electromagnetic field of the modes and the relaxation processes of the fast particles driving these modes. This leads to a 1-D bump-on-tail

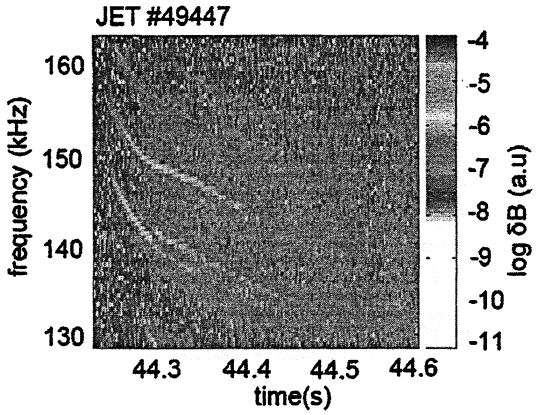

Fig. 2. Magnetic spectrogram of a JET experiment with slowly increasing ICRH power, showing a variety of soft non-linear regimes

model for the mode evolution. In particular, we present an extension of the existing single–mode theory [1, 2], to the case of two weakly linearly unstable modes driven resonantly by fast ions near the instability thresholds. We treat the problem as one-dimensional and assume that the two plasma eigenmodes with wave numbers k_i and frequencies ω_i, $i = 1; 2$, have phase velocities ω_i/k_i being close to each other and lying on the positive slope of the fast ion velocity distribution function. The discussion is restricted to the isolated, but close, resonances, for which the frequency separation is much less than the corresponding bounce frequencies. We apply a perturbative analysis which is based on the assumption of small deviations of the particles from their unperturbed orbits. The basic assumption of this model is that linear dissipation from background plasma γ_d and the energetic particle drive for instability γ_L give a net growth rate $\gamma = \gamma_L - \gamma_d > 0$ that satisfies the condition $\gamma_L - \gamma_d << \gamma_L$, i.e. it is assumed that mode excitation takes place just above instability threshold. By applying the perturbative procedure to solve the Boltzman equation for fast particles together with the Amper law, we obtain the equation time evolution of the slowly varying wave amplitude A_1 (see below).

The equation for the second wave amplitude A_2 is obtained by exchanging indices 1 and 2. Note that $\Delta k = k_1 - k_2 << k_1$ and $\Delta\omega = \omega_1 - \omega_2 << \omega_1$, and that the collisional processes are modeled via «annihilation» (Krook), dynamical friction and diffusion operators characterized by the parameters ν, α and β, respectively. The nonlinear equation system for the mode amplitudes was examined numerically and the

$$\frac{dA_2}{dt} = \gamma A_2 - 2\gamma_2 \int_0^{t/2} d\eta \{\eta^2[(ek_1/m)^2 A_2(t-\eta)A_1(t-\eta-\chi)A_1^*(t-2\eta-\chi)\, e^{i\eta(\eta+\chi)\alpha^2}$$

$$+ (ek_2/m)^2 A_1(t-\eta)A_2(t-\eta-\chi)A_2^*(t-2\eta-\chi)\, e^{i\eta(\eta+\chi)\alpha^2} + (ek_2/m)^2 A_2(t-\eta)$$

$$A_1(t-\eta-\chi)A_2^*(t-2\eta-\chi)e^{i\eta(\eta+\chi)\alpha^2} e^{-i\left(\frac{\omega_1}{k_1}-\frac{\omega_2}{k_2}\right)k_1\eta}\, \eta(\eta+\frac{\Delta k}{k_2}(\eta+\chi))\}e^{-\nu(2\eta+\chi)-\beta^2\eta^2(2/3\eta+\chi)}$$

results show that depending on the type of relaxation process different nonlinar regimes take place. It was found that in the case, when the dominant relaxation processes are modeled via the Krook or diffusion collisional, the non-linear evolution of the wave amplitude may exhibit four main regimes: a steady-state, periodic amplitude modulation, chaotic and explosive regimes, see Figs. 3–5 and 8. This is in contrast to the case when dynamical friction is the dominant collision process, where the explosive evolution of the wave amplitude was found to be the only possible behavior, i.e., within the context of the perturbation theory the mode reaches arbitrarily large amplitude in a finite time, see Figs. 6 and 7.

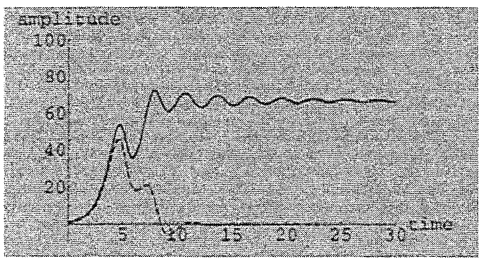

Fig. 3. $\nu = 5$, $\alpha = 0$, $\beta = 0$

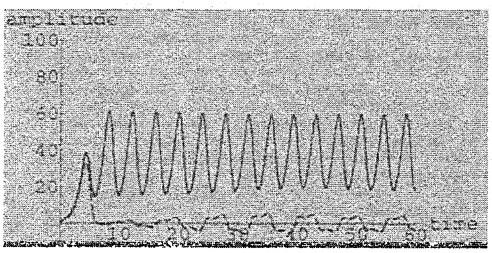

Fig. 4. $\nu = 4$, $\alpha = 0$, $\beta = 0$

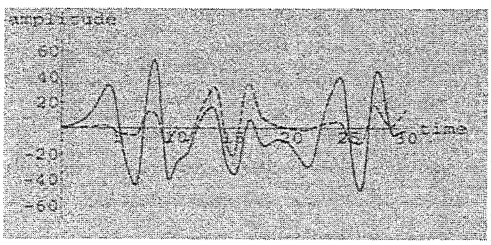

Fig. 5. $\nu = 2.5$, $\alpha = 0$, $\beta = 0$

In addition, it was found that the finite separation in the phase velocities of the two modes weakens the interaction strength between the modes.

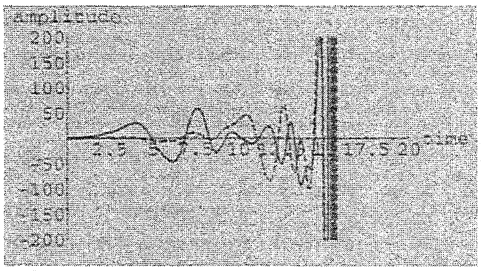

Fig. 6. $\nu = 2.3$, $\alpha = 0$, $\beta = 0$

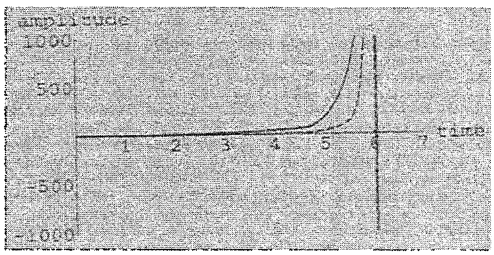

Fig. 7. $\nu = 0$, $\alpha = 10$, $\beta = 0$

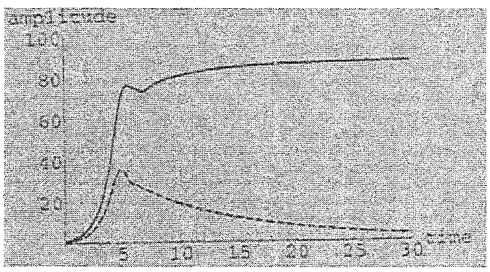

Fig. 8. $\nu = 5$, $\alpha = 2.5$, $\beta = 0$

References

1. *Berk, H.L., Breizman, B.N., Pekker, M.S.* Nonlinear Dynamics of a Driven Mode near Marginal Stability // Phys. Rev. Lett. 1996. V. 76. P. 1256.

2. *Lilley, M., Breizman, B.N., Sharapov, S.E.* The destabilizing effect of dynamical friction on fast particle-wave-driven waves in a near-threshold non-linear regime // PRL. 2009. V. 102. P. 195003.

Transmission Line for Megawatt Power Gyrotron Test Stand

V.I. Malygin[1], G.G. Denisov[1], A.V. Chirkov[1], V.N. Gorbatushkov[1]
E.M. Tai[2], E.A. Solujanova[2], V.I. Ilin[3]

[1]Institute of Applied Physics Russian Academy of Sciences, Nizhny Novgorod, Russia, malyg@appl.sci-nnov.ru
[2]GYCOM Ltd., Nizhny Novgorod, Russia
[3]Institute of Tokomak Physics National Research Centre "Kurchatov Institute", Moscow, Russia

Introduction

The development of 170 GHz continuous wave (CW) gyrotrons megawatt level of the microwave power for ITER ECW system at IAP/GYCOM is successful. A set-up for testing 1MW / 170 GHz / CW gyrotrons and measuring their wave beams parameters has been constructed at ITP NRC "Kurchatov Institute". This test stand includes the microwave beam measuring set-up and the transmission line for testing of CW gyrotrons megawatt level of the output power.

Measurement of wave beam parameters

Test of the gyrotron begins with the measurement of wave beam parameters (amplitude and phase distributions), using the thermo-vision method of measurement of power distributions [1] and 3D wave beam field reconstruction from power measurements in a few cross sections [2, 3]. The gyrotron microwave beam measuring set-up at ITP NRC "Kurchatov Institute" is shown on Fig. 1.

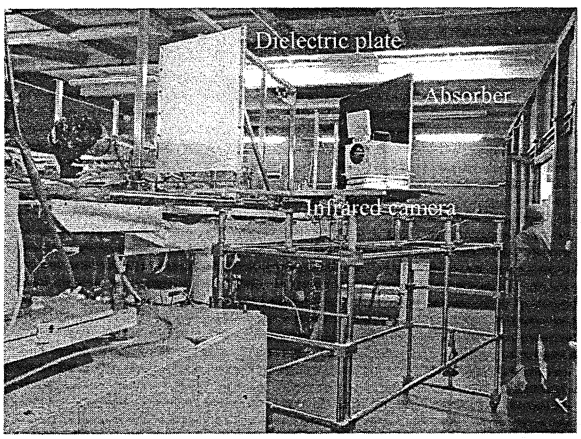

Fig. 1. Gyrotron microwave beam measuring set-up at ITP NRC "Kurchatov Institute"

As a result of the thermo-vision measurements and phase reconstruction procedure the amplitude and phase distributions of a wave beam at the output of a gyrotron flange are found (Fig. 2). In particularly the parameters of the field distribution of a wave beam at the output flange of a gyrotron "Vesuvius 10" are following:

- Radii of a wave beam at e^{-1} level of intensity: $r_x = 15.8$ mm, $r_y = 16.5$ mm;
- Radii of a wave beam phase front curvature: $R_x = -3749$ mm, $R_y = 4179$ mm;
- Gaussian contents: $\eta_{a,ph}$ (η_a) = 95.4 % (98.7 %).

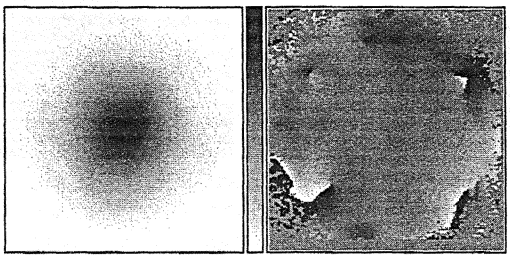

Fig. 2. Amplitude and phase distributions of a wave beam at the output flange of the gyrotron "Vesuvius 10"

Transmission line on the test stand

The evacuated transmission line for testing of 1 MW / 170 GHz / CW gyrotrons consists of two mirror matching optics unit (MOU), aluminum corrugated circular waveguides Ø88.9 mm, a miter bend, a miter bend with bi-directional coupler, a quasi-optical switch, 1MW / CW load and a small calorimetric load (Fig. 3).

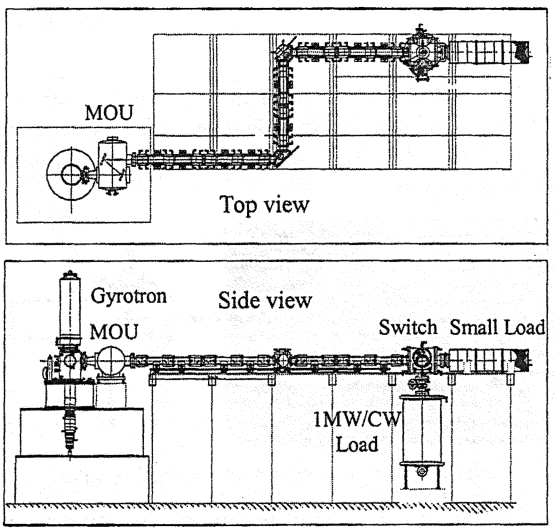

Fig. 3. Evacuated transmission line for testing of 1 MW / 170 GHz / CW gyrotrons at ITP NRC "Kurchatov Institute"

The bellows are installed in each straight part of corrugated waveguides for compensating of thermo expansions of the transmission line. MOU filters and absorbs parasitic radiation from gyrotron and converts with help of two shaped mirrors (Fig. 4) the gyrotron wave beam into HE_{11} mode at the entrance of the corrugated waveguide. Two shaped mirrors of MOU are calculated and fabricated using measurements of gyrotron wave beam parameters [3]. The efficiency of conversion of the gyrotron wave beam to HE_{11} mode is $\eta_{a,ph} = 0.98$. HE_{11} mode propagates in a corrugated waveguide practically without losses (0.0006% / m) to the quasi-optical switch (Fig. 5), which turns a wave beam to the 1MW / CW load or to a small load.

When the quasi-optical switch turns a wave beam to a small calorimetric load, it is possible to measure power in short pulses (less 150 ms) and if the quasi-optical switch turns a wave beam to the 1 MW / CW load, then a small calorimetric load absorbs reflecting and dissipating power in the transmission line.

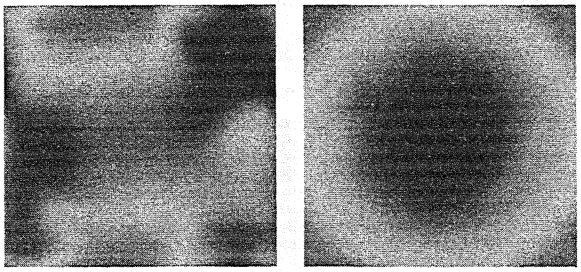

Fig. 4. Surfaces of two shaped MOU mirrors

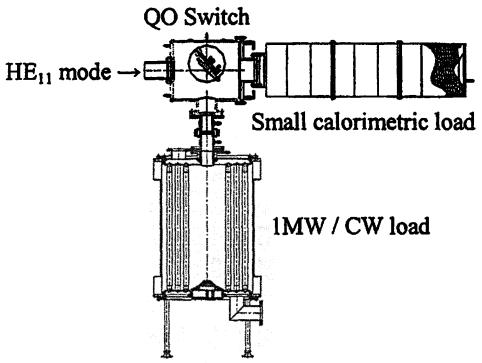

Fig. 5. Quasi-optical switch to 1 MW / CW load or to a small calorimetric load

It is possible to monitor the behavior of transmitted power of the gyrotron and reflected power from the load by means of bi-directional coupler in the miter bend (Fig. 6).

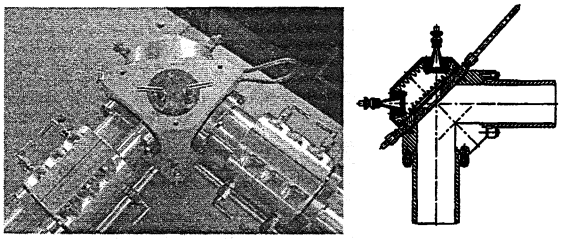

Fig. 6. Miter bend with bi-directional coupler

Time traces (Fig. 7) of the main gyrotron parameters show real CW behavior of the gyrotron.

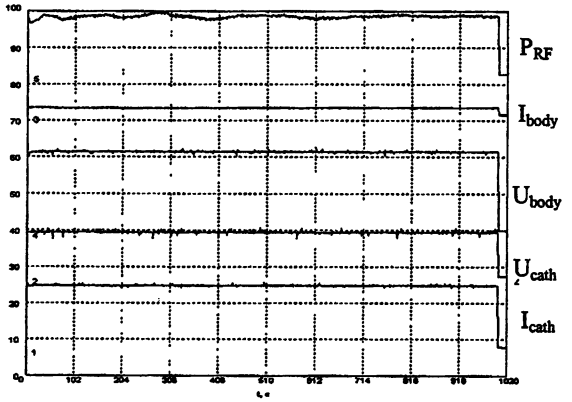

Fig. 7. Time traces (from top to bottom) for RF power, body current and voltage, cathode voltage and current

The balance of powers in the evacuated transmission line is following:

Power at the output of a gyrotron flange	1 MW	100 %
Power absorbed in MOU	30 kW	3 %
Power absorbed in 1 MW / CW load	920 kW	92 %
Power absorbed in a small calorimetric load	20 kW	2 %
Power absorbed in a quasi-optical Switch	30 kW	3 %

The industrial production prototype of the ITER gyrotron "Vesuvius 10" (Fig. 8) was successfully tested at this test stand with power 1 MW in 570 seconds pulses and 0.8 MW in 1000 second pulses.

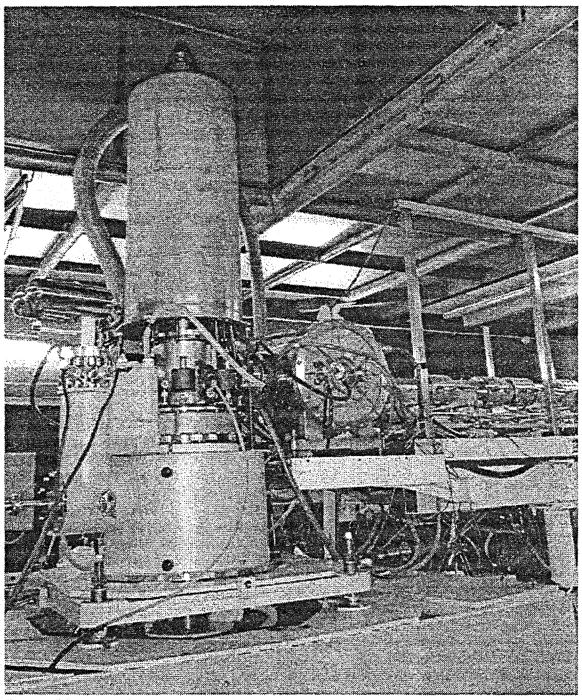

Fig. 8. Industrial prototype ITER gyrotron "Vesuvius 10" in the test stand at ITP NRC "Kurchatov Institute"

Conclusion

The evacuated transmission line for testing of 1 MW / 170 GHz / CW gyrotrons in the test stand at ITP NRC "Kurchatov institute" is very reliable and convenient in an operation. This test stand makes possibility also to measure wave beam parameters, using moveable measuring set-up.

References

1. *Kuznetsov S.O. and Malygin V.I.* Determination of gyrotron wave beam parameters // International Journal of Infrared and Millimeter Waves. 1991. V. 12, № 11. P. 1241-1252.

2. *Chirkov A.V., Denisov G.G., Aleksandrov N.L.* 3D wave beam field reconstruction from intensity measurements in a few cross sections // Optics Communications. 1995. V. 115. P. 449-452.

3. *Chirkov A. V.* Analysis and synthesis of the spatial structure of the field in high-power microwave beams // Radiophysics and Quantum Electronics. 2007. V. 50, № 3. P. 209-215.

Analysis of the Main Transmission Line for the Conceptual Design of an ITER-like LHCD System

F. Mirizzi[1], S. Ceccuzzi[1]

[1]Associazione EURATOM-ENEA sulla Fusione, C.R. Frascati, Frascati (Rome), Italy, francesco.mirizzi@enea.it

Introduction

The preliminary design of the LHCD system for ITER, lately carried out in the frame of the EFDA task WP08-HCD-03-01 "LH4IT" (EU contribution to the ITER LHCD development plan), has been mainly focused on the launcher and its main microwave components. The system, made by 48 independent modules, each one generating 500 kW, has been designed in order to couple a maximum RF power of 20 MW CW at 5 GHz to the ITER plasma.

Toshiba is presently developing a 5 GHz, 500 kW prototype klystron for the LHCD system of the South Korean KSTAR tokamak. The latest obtained results show a promising output power of 300 kW for 800 s and 450 kW for 20 s [1].

The successful tests of Passive Active Multijunction (PAM) launchers on FTU [2, 3] and on Tore Supra [4] allow considering this launcher a highly realistic (convincing) candidate for the LHCD system for ITER. This launcher presents its better performances at plasma density very close to cut-off. It can be then allocated flush to the vacuum vessel wall or in the port shadow, which is in a very safe position, sufficiently far from the harsh burning plasma environment.

The Main Transmission Line

In the frame of the above mentioned EFDA task the design of the Main Transmission Line (MTL) has been only outlined because, at the time, the real path of the MTL was not yet established and its length was not known. These elements, following the recently defined almost definitive positioning of the LHCD sources with reference to the ITER load assembly and the definition of the ITER port allotted for the launcher, can be now better evaluated.

Each independent MTL, with an estimated average length of 70 m, transports the nominal 500 kW generated by a single klystron. To limit the transmission losses below an acceptable threshold of 5 %, moderately oversized circular waveguides excited in the very effective TE°_{01} mode must be used. At 5 GHz, mode TE°_{01}, the optimum performances are assured by the standard circular C 16 waveguide (R = = 67.05 mm) that can transmit up to 7.6 MW with an inner maximum electric field lower than 6kV/cm and transmission losses less than 5 % up to length of about 100 m.

The $TE^{\square}_{10}$ to TE°_{01} mode converter

The klystron's output rectangular waveguide (the WR 187 standard) must be coupled to the MTL circular waveguide (the C 16 standard) and, at the same time, the $TE^{\square}_{10}$ mode in the rectangular waveguide must be converted into the TE°_{01} mode in the circular waveguide. At the end of the MTL, the inverse mode conversion (TE°_{01} to $TE^{\square}_{10}$) is necessary to conveniently feed the launcher's input rectangular waveguide.

Several converter concepts have been examined, including the very complex, from the practical realisation point of view, Marié converter [5] and the classical $TE^{\square}_{10}$ to TE°_{11} followed by the TE°_{11} to TE°_{01}, snake-like, mode conversion scheme [6]. The numeric simulations have demonstrated that this second conversion scheme, due to its inner smooth geometry, is the most suitable taking into account the nominal 500 kW transported by each independent MTL. The assembly of the two involved mode converters results however in a very long component, so that alternative shorter solutions have been also examined.

The chosen $TE^{\square}_{10}$ to TE°_{01} mode converter is given in figure xx. It is a variant of the so-called "wrap-around" mode converter. It results in a very short component but it is a little bit complicate to realize. The simulation results are very convincing.

Bends

Two different ITER ports (no. 11 and no. 9) are presently allotted for the LHCD launcher. Independently from the final choice, the MTLs include four 45 deg bends and one 100 deg (port 9) or 60 deg (port 11) bend.

The ITER layout imposes to split the 48 MTLs of the LHCD system in two rows of 24 lines each. Taking into account the flanges' diameter, the average width of a row can be then evaluated in about 4320 mm.

The narrower bending radius is about 350 mm on the axis of the waveguide, thus the larger bending radius is about 4500 mm.

Bends made with smooth oversized waveguides generates spurious modes that must be neutralized by an appropriate design of the bends. Several alternatives have been proposed to circular bends [7] in order to limit number and amplitudes of spurious modes, but most of them have been demonstrated not suitable for the narrower radius bends. Sine and cosine shaped bends as well as parabolic and hyperbolic bends have been also studied, but the results have been not satisfactory from the scattering matrix point of view. The best results have been obtained with classical corrugated wall waveguides. The 350 mm and the 530 mm radius bends have been optimized with the help of a commercial FEM code (the ANSYS electromagnetic HFSS code). The remaining bends with larger bending radius are to be optimized in the next future. The experience shows that the mode conversion attitude of bends decreases as the bending radius increase, thus bends with larger bends could be easier to optimize.

Mode Filters

The C 16 waveguide (R = 67.05 mm) is above cut-off at 5 GHz for all the modes given in the following table.

Modes above cut off at 5GHz in the C 16	
TE modes	TE_{01} TE_{02} TE_{11} TE_{12} TE_{21} TE_{22} TE_{31} TE_{41} TE_{51}
TM Modes	TM_{01} TM_{02} TM_{11} TM_{12} TM_{21} TM_{31}

All of them can be potentially generated by accidental and/or deliberate discontinuities or bends in the MTL. Trapped modes can produce likely destructive effects in the MTL, so that they must be effectively filtered. Mode filters must not reject unwanted spurious modes, but must absorb them to avoid their trapping in some region of the MTL. Also in this case several mode filter typologies have been analyzed, the most effective being the corrugated wall mode filter with absorbing inserts. In this initial phase, a mode filter with ten corrugations has been studied and optimized with HFSS. The obtained results, in terms of mode attenuations (S_{12} for all the modes above cut-off), are very encouraging. It must be pointed out that the study has been limited to ten corrugations because of limitations on the available computing resources. By doubling the number of corrugations, the attenuation for each mode is increased by 3dB, thus increasing the mode filter effectiveness.

Conclusions

The preliminary design of the MTL for an ITER-like LHCD system has been further developed by studying microwave components, like $TE^{\square}_{10}$ to TE°_{01} mode converters, bends with low mode conversion efficiency and effective mode filters in order to avoid likely destructive effects on the waveguides due to extremely high electric fields determined by trapped resonant modes in some section of the MTL.

The results are not considered conclusive, but further studies must be carried out to obtain more efficient results.

In addition thermal analysis must be started to verify possible cooling needs for the MTL.

References

1. *Do H. et al.*: Test results of the 5GHz, 500kW CW prototype klystron for the KSTAR LHCD system // Paper presented to the 26th SOFT, 27 September – 1 October 2010, Porto, Portugal (to be published in Fusion Engineering and Design).

2. *Mirizzi F. et al.* The test of a PAM launcher on FTU: the first step toward the LHCD launcher for ITER // Fusion Eng. Des. V. 74, 1- 4, 237-242 (2005).

3. *Pericoli Ridolfini V. et al.*: LHCD and coupling experiments with an ITER-like PAM launcher on the FTU tokamak // Nucl. Fusion. V. 45 (2005) 1085-1093.

4. *Ekedahl A. et al.*, Validation of the ITER-relevant PAM LHCD launcher on long pulses in Tore Supra // Nuc. Fusion, V. 50, No. 11, 112002 (2010).

5. *G.R.P. Marié*: British Patent 805510, 1958.

6. *Thumm M.*: High-power millimeter-wave mode converters in overmoded circular waveguides using periodic wall perturbations // Int. J. of Electronics, V. 57, No. 6, (1984), 1225-1246.

7. *Plaum B.:* Optimization of oversized waveguide components using a genetic algorithm. Fusion Eng. Des. V. 53 (2001), 499-503.

The Effect of the ITER Stray Magnetic Field on the Operation of the EU 2 MW Coaxial-Cavity Gyrotron

I.Gr. Pagonakis[1], F. Li[2], S. Alberti[2], S. Illy[1], B. Piosczyk[1], J.-P. Hogge[2], S. Kern[1], A. Ferran[3], M. Henderson[4], C. Darbos[4]

[1] Karlsruhe Institute of Technology (KIT), Association Euratom-KIT, IHM, 76131 Karlsruhe, Germany, ioannis.pagonakis@kit.edu
[2] Centre de Recherche en Physique des Plasmas, Association Euratom - Confédération Suisse, EPFL Ecublens, Station 13, CH-1015 Lausanne, Switzerland
[3] Fusion for Energy, C/ Josep Pla2, Torres Diagonal Litoral-B3, E-08019 Barcelona-Spain
[4] ITER Organization, St. Paul-lez-Durance, 13067 France

Introduction

The gyrotron performance is intrinsically associated to the electron beam trajectories and properties, which are related to the gyrotron magnetic field structure. In an application where these gyrotrons are used in an EC-system, such as the one foreseen for ITER, different gyrotrons are placed in close vicinity of other ones and also in vicinity of the tokamak. In this situation the stray magnetic field (SMF) of the neighboring gyrotrons and/or the tokamak might affect the electron beam properties trajectories and consequently the gyrotron operation. Since these fields in general break the cylindrical symmetry commonly assumed in electron beam propagation codes, for taking into account the effect of stray fields one needs to use a three-dimensional code.

In this work, the degradation of the electron beam properties at the cavity and the collector of the refurbished 1st prototype 170 GHz, 2 MW EU gyrotron for ITER has been numerically studied for the stray magnetic field at the ITER-ECRH building. The three-dimensional, self-consistent, electrostatic and parallel code *Ariadne* [1] has been used.

Stray Magnetic Field Sources

The tokamak SMF comes by the tokamak coils and the toroidal plasma current. Since the distance between the center of the tokamak and the position of the gyrotron is more than 100 m, the tokamak coil SMF could be considered negligible. However, the SMF generated by the toroidal tokamak plasma current should be taken into account. In such distances, the toroidal plasma SMF could be analytically approximated by the magnetic dipole equation. Figure 1 shows the magnetic field of the dipole with magnetic moment $6.56 \cdot 10^9 \, Am^2$, which corresponds to the highest magnetic field operation scenario. The gyrotron hall is located, as it is show in Fig. 1, in horizontal distance between 100 m and 130 m from the tokamak while the gyrotron cavities are located 11.65 m above the tokamak center.

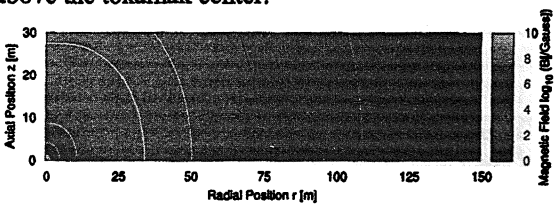

Fig. 1. The tokamak stray magnetic field

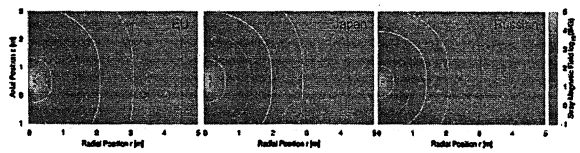

Fig. 2. The stray magnetic field of the European, Japanese and Russian gyrotron

The SMF of the European, Japanese and Russian gyrotrons could be also calculated analytically by the integration of Biot-Savart's law. A comparison of the stray magnetic field of the three magnets is presented in Fig. 2. The highest SMF is generated by the European gyrotron, while the lowest one is generated by the Russian gyrotron. It should be noted that the closest distance between two gyrotrons in the ECRH building has been determined as 5 m.

Finally, an additional stray magnetic field could be caused by the ferromagnetic materials which are used for the EC-building construction. In particular S355J0 steel I-Beams are located in close vicinity to the gyrotrons. In order to estimate the effect of these materials to the magnetic field of the gyrotron, the magneto-static problem has been numerically solved using the commercial code COMSOL Multi-Physics. The main conclusion of this work is that the effect of I-Beams in the ECRH-building is not significant for the gyrotron operation. In particular, the change of the main magnetic field taking into account the effect of the I-beam is estimated less than the Earth magnetic field (~0.5 G).

Simulation Results

The SMF effect of the tokamak and one neighboring gyrotron on the operation of the refurbished 1st prototype European gyrotron has been studied separately. In particular, the electron beam has been simulated for several distances between the EU gyrotron and the tokamak and between two EU gyrotrons. The SMF causes a deformation of the electron beam, as is shown in Fig. 3. In addition, a long tail in the high values is also observed in the pitch angle distribution, as is shown in Fig. 4, which could limit the collector depression voltage and could contribute to the generation of the harmful electron beam halo. The main beam parameters versus the distance from the center of the tokamak and the neighboring gyrotron are presented in Fig. 5 and Fig. 6, respectively. The beam radius and the transverse velocity spread are not affected by the SMF, in contrast to the thickness of the beam and the pitch angle. In particular, the width of

the beam increases significantly for distances less than 80 m from the tokamak and less than 3.5 m from the neighboring gyrotron, while the pitch angle remains slightly higher than the nominal value even for the nominal distances.

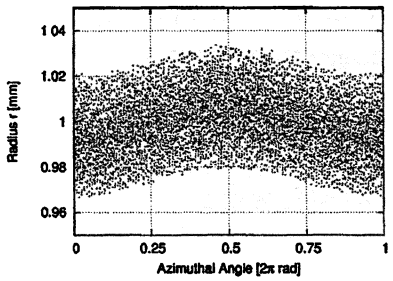

Fig. 3. The deformation of the electron beam at the cavity due to the tokamak SMF at 80 m

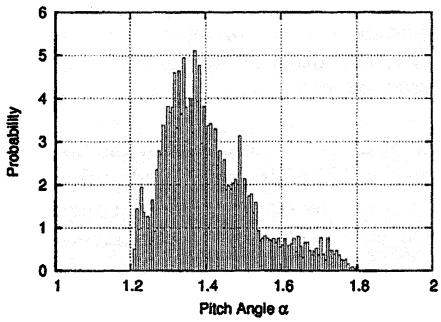

Fig. 4. The pitch angle electron distribution at the cavity under the influence of the tokamak SMF at 80 m

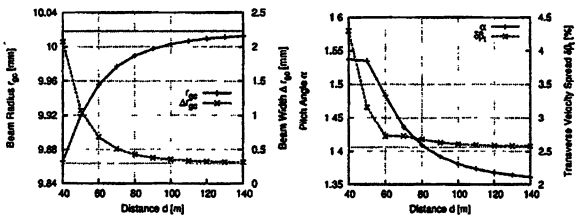

Fig. 5. The beam parameters at the cavity versus the horizontal distance between tokamak and gyrotron

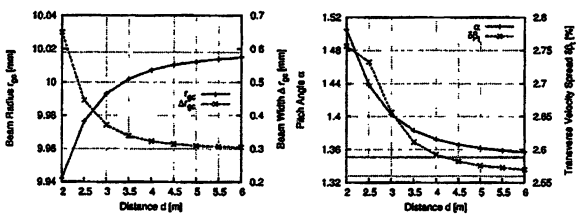

Fig. 6. The beam parameters at the cavity versus the distance between two gyrotrons

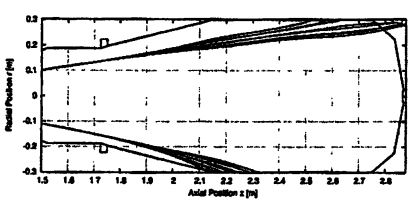

Fig. 7. The electron beam trajectories in the collector region under the influence of the tokamak SMF at 80 m

On the other hand, the collector operation seems to be affected more by the SMF of the tokamak and the neighboring gyrotron. The SMF affects the electron beam trajectories as it is shown in Fig. 7. The magnetic field lines are plotted for several phases of the axial sweeping of the collector for the closest and the opposite side of the collector to the tokamak. Due to the radial component of the SMF, the electron beam is significantly tilted. As a results, some beam electrons are guided by the magnetic field line on some parts of the collector surface which are not appropriately cooled (right part in Fig. 7). In addition, the area where the beam energy is distributed could be decreased significantly for some azimuthal angle of the collector (bottom part in Fig. 7). The tilt of the beam and the width of the beam collection area are presented in Fig. 8 and Fig. 9 for the tokamak SMF and the gyrotron SMF, separately. It is shown that even for the nominal distances, the tilt and the width are significantly deviated by the SMF of the tokamak and the neighboring gyrotron.

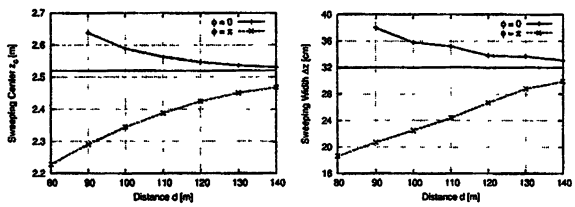

Fig. 8. The center and the width of the sweeping on the collector wall under the influence of the tokamak SMF

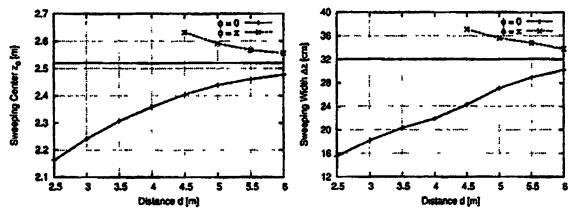

Fig. 9. The center and the width of the sweeping on the collector wall under the influence of a neighboring gyrotron SMF

Conclusions

The main conclusions of this work are the following: (i) concerning the wave-particle interaction in the gyrotron cavity, the stray magnetic field effects are negligible, (ii) in the collector region, however, stray magnetic field effects are significant and implement mitigating actions are required such as adding compensating coils in the collector region.

Acknowledgments

This work was supported by Fusion for Energy under the grant contract No. F4E-2009-GRT-34-01 and within the European Gyrotron Consortium (EGYC). The views and opinions expressed herein reflect only the author's views. Fusion for Energy is not liable for any use that may be made of the information contained therein. EGYC is a collabo-ration among CRPP, Switzerland; KIT, Germany; HELLAS, Greece; CNR, Italy; ENEA, Italy.

References

I. Gr. Pagonakis and J.L Vomvoridis, The self-consistent 3D trajectory electrostatic code Ariadne for gyrotron beam tunne simulation // Joint 29th Int. Conf. Infrared Millimeter Waves and 12th Int. Conf. THz Electronics, Conference Digest, 27 Sept. – 1 Oct., Karlsruhe, Germany.

Laboratory Reproduction of Auroral Cyclotron Emission Processes

D.C. Speirs[1], S.L. McConville[1], K.M. Gillespie[1], A.D.R. Phelps[1], R. Bingham[1,3], A.W. Cross[1], C.W. Robertson[1], C.G. Whyte[1], W. He[1], M. King[1], I. Vorgul[2], R.A. Cairns[2], B.J. Kellett[3] and K. Ronald[1]

[1]SUPA Department of Physics, University of Strathclyde, Glasgow, G4 0NG, Scotland
[2]School of Mathematics and Statistics, University of St. Andrews, St. Andrews, KY16 9SS, Scotland
[3]Space Physics Division, STFC, Rutherford Appleton Laboratory Didcot, OX11 0QX, England
K.Ronald@strath.ac.uk

A scaled laboratory experiment has been constructed at the University of Strathclyde to replicate major features of the auroral kilometric radiation phenomenon [1, 2] in a controlled environment at microwave frequencies [3–5]. 2D and 3D simulations are also being conducted to predict the experimental radiation power, spectrum, wave polarisation and propagation as well as analysing the evolution of cyclotron electron beams in the absence of transverse radio boundaries [6–10]. Theoretical studies are being undertaken at the University of St Andrews to analyse the evolution of the instability using plasma kinetic theory [11–14]. The results of these studies confirm the proposition that sufficient free energy in the magnetically compressed descending electron current exists to explain satellite observations of the magnetospheric wave generation.

Geophysical and Astrophysical Background

Auroral Kilometric Radiation (AKR) emissions [15, 16] occur at frequencies of ~300 kHz polarised in the plasma X-mode [17] with efficiencies of ~1–2 % [1, 2] in the polar regions of the Earth's magnetosphere. Here, in a region of low density plasma ($\omega_{ce}>10\omega_{pe}$) ~3200 km above the Earth's surface electrons are accelerated down towards the Earth whilst undergoing magnetic compression hence acquiring a horseshoe distribution function in velocity space. Theory has suggested that this distribution is unstable to cyclotron emission [11–14, 18–20]. Over a range of frequencies from the low RF bands to the microwave bands, many magnetised astrophysical bodies exhibit such polar emissions, including planets with a dipole-like magnetic field and certain stars, e.g. UV-Ceti and CU-Virginis.

Experimental Reproduction

The experiment injects an initially mainly rectilinear electron beam from an explosive emission cathode through a sparse anode mesh into a system of solenoids presenting a progressively increasing magnetic field. This adiabatically compresses the electron beam in a manner similar to the polar magnetosphere. The centre of the cathode was domed to vary the vector of the electric field across the ring of the velvet emitter. This induced an initial velocity spread on the electron beam. Given sufficient magnetic compression (a factor of ~30 was possible) the spread on the electron beam becomes exaggerated leading to the formation of a horseshoe velocity distribution. At the maximum plateau field of the solenoid system the electrons were held at a fixed cyclotron frequency over a length of 20 cm, where they were brought into resonance with electromagnetic modes of a cylindrical waveguide.

Experimental measurements demonstrated the formation of a horseshoe distribution function in velocity space at B-fields of ~0.18 T and 0.47 T which in turn excited the near cut-off TE_{01} and TE_{03} waveguide modes at frequencies of 4.42 GHz and 11.7 GHz respectively [3, 4]. The polarisation and propagation properties of these modes are comparable to the X-mode observed in the magnetosphere. The frequencies were determined by Fourier transform of the AC waveform captured with a real time oscilloscope. Peak microwave output power was calculated by integrating over the antenna patterns measured by rectifying detectors in stub waveguide receiving apertures. Typically ~19–35 kW was measured corresponding to a peak rf conversion efficiency of ~1–2 % depending on the degree of magnetic compression. This is comparable with the magnetospheric estimates [3, 5].

In the polar magnetosphere there exists a background plasma which may in principle be capable of absorbing the cyclotron emissions from the electron beam. Indeed, wave generation is observed only in those regions where the background plasma frequency is depressed below the cyclotron frequency, although it has been proposed that this absorption may be mitigated with a slight Doppler tuning associated with excitation of a slightly backwards propagating wave [21]. To reproduce the inhibiting effect of a background thermal plasma a quasi-Penning trap was constructed and inserted into the interaction waveguide. This trap enabled generation of a background plasma consistent with the magnetospheric ratios of plasma to cyclotron frequency. Recent results have shown the impact the background plasma has on inhibiting the growth of the cyclotron instability.

Numerical Simulations of the Experiment

2D and 3D simulations of the experiment have been carried out using the PiC code KARAT. The 2D simulations have predicted the horseshoe velocity distribution formed by magnetic compression of the electron beam as it transits from the gun region into the interaction space. Given the correct form for the electron velocity distribution the code has also been able to accurately predict the wave generation modes, efficiency and spectra [6]. 3D PiC simulations [7]

have enhanced this predictive capability by allowing all possible mode couplings to be simulated. Work is currently in progress comparing the predictions of these simulations with the growth of the electromagnetic wave as the cyclotron frequency is increased above transverse resonance, hence measuring the sensitivity of the instability to the Doppler shift. Results to date appear to indicate that the emission favours backward wave coupling which shows stronger tolerance to the high levels of velocity spread.

Numerical Simulations of Unbound Emissions

Given that the 2D PiC code KARAT has been suitably benchmarked against the behaviour of the experiment, it becomes interesting to consider its predictions for the magnetospheric case where the electron beam radiates into a region which lacks well defined wave boundaries. In this condition the code, tested against the experimental data is being used to bridge the gap between the experiments with well defined metallic radiation boundaries to the more tenuous boundaries which are believed to exist in the Polar magnetosphere. A region of uniform magnetic field was defined and an electron current allowed to stream through this region. A radially gradiated lossy dielectric was defined surrounding the electron trajectories to attenuate the wave signals before they reached the edges of the simulation. The wave production was estimated by a measure of the electromagnetic energy at the cyclotron frequency flowing through a cylindrical boundary just inside the dielectric region. These simulations indicated that in the absence of the external wave boundaries the instability grows more slowly over the spatial scale requiring a plateau field ~metres in extent for frequencies in the gigahertz range. The radiation spectrum was dominated by the cyclotron frequency whilst the wave polarisation and propagation have near X-mode properties, although the observed wavefronts appear to indicate a slight preference for backward wave excitation. The estimated conversion efficiencies (~1 %) are again comparable with the experimental peak efficiencies and the magnetospheric observations [9].

Conclusions and Future Work

The results presented in this paper support the premise that the descending electron flux in the auroral magnetosphere offers sufficient free energy given sufficient magnetic compression to explain the satellite observations of the AKR emissions. The wave spectrum, generation efficiency, polarization and propagation properties observed in the experiment and predicted by the numerical simulations agree well with the satellite observations and correlate well with the predictions of the theoretical analysis undertaken at St Andrews. Further work is ongoing to remove the transverse radiation boundaries from the experiment to study direct X-mode emissions from the apparatus.

Acknowledgements

This work was supported by the EPSRC and the STFC Centre for Fundamental Physics. The authors would like to thank Prof. A. Savilov and Prof. V.L. Tarakanov for helpful discussions and Mr. I.S. Dinwoodie and Mr. D. Barclay for their skills in building the apparatus.

References

1. *D.A. Gurnett* // Journal of Geophysical Research. 1974. V. 79. P. 4227-4238.
2. *P.L. Pritchett & R.J. Strangeway* // Journal of Geophysical Research. 1985. V. 90. P. 9650-9662.
3. *S.L. McConville et al.* // Plasma Physics & Controlled Fusion. V. 50, A. 074010 (2008).
4. *K. Ronald et al.* // Plasma Sources Science & Technology 2008. V. 17, A.035011.
5. *K. Ronald et al.* // Physics of Plasmas. 2008. V. 15, A.056503.
6. *D.C. Speirs et al.* // Plasma Physics & Controlled Fusion. 2008. V. 50, A.074011.
7. *K.M. Gillespie et al.* // Plasma Physics & Controlled Fusion. 2008. V. 50, A.124038.
8. *D.C. Speirs et al.* // Journal of Plasma Physicsıo 2005. V. 71. P. 665-674.
9. *D.C. Speirs et al.* // Physics of Plasmas. 2010. V. 17, A. 056501.
10. *K. Ronald et al.* // Plasma Physics & Controlled Fusion. 2011. V. 53, A.074015.
11. *R.A. Cairns et al.* // Physica Scripta. 2005. V. T116. P. 23- *I. Vorgul et al.* // Physics of Plasmas. 2005. V. 12. P. 1-8.
12. *I. Vorgul. et al.* // Physics of Plasmas. V. 18, A. 056501.
13. *R.A. Cairns et al.* // Physics of Plasmas. 2011. V. 18, A. 022902.
14. *G.T. Delory et a.,* // Geophysical Research Letters. 1998. V. 25. P. 2069-2072.
15. *R.E. Ergun et al.* // The Astrophysical Journal. 2000. V. 538. P. 456-466.
16. *J.E. Allen & A.D.R. Phelps* // Rep. Prog. Phys. 1977. V. 40. P. 1305-1368.
17. *R. Bingham & R.A. Cairns* // Physics of Plasmas, 2000. V. 7. A. 3089-3092.
18. *R. Bingham & R.A. Cairns,* // Physica Scripta, 2002,V.T98, P.160-162
19. *R. Bingham et al.* // Contributions to Plasma Physics. 2004. V. 44. P. 382-387.
20. *A.V. Savilov et al.* // Physics of Plasmas. 2007. V. 14, A. 113104.

EBW Current Drive and Plasma Heating in MAST-Upgrade

A.N. Saveliev[1], V.F. Shevchenko[2]

[1]Ioffe Physical Technical Institute, St Petersburg, Russia, alexander.n.saveliev@mail.ioffe.ru
[2]EURATOM/CCFE Fusion Association, Culham Centre for Fusion Energy, Abingdon, Oxon, UK

Electron Bernstein waves (EBWs) have a potential to provide highly localized heating and current drive (CD). EBWs are predominantly electrostatic and they damp on electrons near electron cyclotron harmonics without momentum injection into the plasma. These features represent a powerful tool for understanding transport and stability phenomena by locally perturbing the plasma and providing a complementary CD method in addition to neutral beams. The Mega-Ampere Spherical Tokamak (MAST) [1] has a large cylindrical vacuum vessel and the recently proposed upgrade to MAST would enable a number of launcher positions for RF power injection.

In the present work we explore the potential of EBW heating and CD on MAST over a range of parameters. A new centre column together with additional poloidal field coils and new power supplies for toroidal and poloidal fields are planned for MAST [2]. They will provide a longer pulse capability at higher toroidal magnetic field. At a later stage it is planned to add at least 1MW of EBW heating. Together with the increased NBI power these upgrades move MAST toward fully non-inductive operation at high beta. EBW may provide highly localised near-axis and off-axis heating and CD without any momentum transfer to the plasma. EBW heating and CD are based on resonant absorption near EC harmonics. Hence they must be optimized for every particular application in a given magnetic configuration. EBW can be an efficient tool providing local profile control capability. Also highly localised controllable electron temperature perturbations can be beneficial in plasma transport studies.

The present work explores the feasibility of EBW in the MAST-U parametric space. Analysis is focused on 3 main tasks: optimisation of launch parameters and launch frequency to achieve maximum efficiency for off-axis EBW CD; achievement of efficient near central counter-CD and finally achievement of efficient near central EBW heating with close to zero EBW CD effects. Modelling has been conducted with the EBW&BANDIT code package [3] using a "steady state" reference scenario with near zero loop voltage. The package unites self-consistently a code solving the electromagnetic wave (EMW) to EBW coupling problem with the use of the 1D approach [4], the EBW ray-tracing code and a Fokker-Planck code BANDIT-3D [5] which calculates EBW power deposition and driven plasma current. Typical simulation run-time of this program package takes a few minutes on a moderate workstation with a single processor. Clear heating and CD effects have been identified for different launch configurations and frequencies.

It has been found in this study that for the specified magnetic equilibrium and plasma parameters of the MAST-U tokamak the optimum frequency for near axis counter-CD is approximately 19.4 GHz. It can provide up to 0.1 A/W CD efficiency with localisation $\delta r/a < 0.1$. Near central heating (with almost zero CD effect) can be achieved at the same frequency of 19.4 GHz with $Z = -12.5$ cm off-midplane launch. Efficient off-axis EBW CD can be achieved at a higher frequency of 25 GHz at the $2\omega_{ce}$ harmonic or with 19.4 GHz at reduced toroidal field. CD efficiency up to 0.075 A/W is achievable near $r/a \approx 0.5$ and $r/a \approx 0.7$.

Finally the sensitivity of the EMW-EBW mode conversion (MC) process has been modeled for various launch positions against pitch angle variations in the MC layer. A gradual shift of the MC maxima and decrease of the MC window width with pitch angle increase are demonstrated in the paper. It is found that the EMW-EBW mode conversion is less sensitive to pitch angle variations for far off-midplane launch in comparison with near off-midplane launch.

Acknowledgements

This work was funded partly by the RCUK Energy Programme under grant EP/I501045 and the European Communities under the contract of Association between EURATOM and CCFE. The views and opinions expressed herein do not necessarily reflect those of the European Commission. The work was also supported by the RFBR grant 10-02-00887-a.

References

1. *Cox M. et al.*, The Mega Amp Spherical Tokamak // Fus. Eng & Des. 1999. V. 46. P. 397.

2. *Lloyd B.* Recent Advances in ST Research and Prospects for New ST Capabilities // Proc. 36th ICOPS-SOFE 2009 Conference, San Diego, USA, 31 May-5 June 2009.

3. *Saveliev A. N.* Electron Bernstein waves in spherical torus plasmas // Proc. Varenna-Lausanne Int. Workshop on Theory of Fusion Plasma, Varenna 2006, CP871, 215.

4. *Pilya A.D. and Tregubova E.N.*, Linear conversion of electromagnetic waves into electron Bernstein waves in an arbitrary inhomogeneous plasma slab // PPCF. 2005. V. 47. P. 143–154.

5. *O'Brien M.R. et al.* // Proc. IAEA Technical Committee Meeting on Advances in Simulation and Modelling of Thermonuclear Plasmas, Montreal, 1992. P. 527.

Low-Pressure Off-resonant Discharge for the Extreme-Ultraviolet Source

A.G. Shalashov, S.V. Golubev, E.D. Gospodchikov, A.V. Vodopyanov

Institute of Applied Physics of Russian Academy of Sciences, Nizhny Novgorod, Russia, ags@appl.sci-nnov.ru

Intense investigations aimed at creating a radiation source for high-resolution projection lithography with a wavelength of 13.5 nm ±1 % are now being performed worldwide. The line radiation of multiple-charged tin ions (more than 100 tin ion radiation lines with charges from +6 to +11 fit in the above interval) is used in the most efficient radiation sources. Installations with high-power lasers or various types of pinches are mostly used to obtain such plasma, see e.g. [1] and references therein. In addition to the substantial progress in this field, the systems being developed have a series of disadvantages. In particular, there are problems caused by the short lifetime of the source, the contamination of optical elements by evaporated substances and high-speed ions. Thus, the search for new extreme-ultraviolet (EUV) sources remains a problem of great interest.

EUV source based on a low-pressure discharge in tin vapors sustained within a magnetic trap by high-power millimeter-wave electromagnetic radiation under conditions of electron cyclotron resonance (ECR) was proposed demonstrated experimentally in [2]. In this source, shown schematically in fig. 1, tin vapor plasma is injected into a straight axisymmetric magnetic trap using a vacuum arc source. Electrons heated by microwave radiation perform additional ionization during their flight through the magnetic trap, and multiply charged tin ions with radiation lines fitting the EUV range are formed. The use of millimeter range radiation and miniature vacuum arc plasma generators make it possible to create sources of relatively small size (with a transverse size of the radiating area of $a \sim 1$ mm) with quite high plasma density (up to 10^{14} cm^{-3}), making the described method quite attractive for creating an almost point EUV source.

Gyrotron radiation with frequency of 75 GHz, a power of up to 50 kW, and an pulse length of 150 μs was used for additional plasma heating. The magnetic field strength of the trap mirrors was 4 T so that ECR conditions at the fundamental harmonic ware met inside the trap volume. The detected EUV intensity in the range of 13.5 nm ±1 % was about 25 W per spatial angle of 2π sr, what corresponded the specific luminescence power 100 W cm^{-3} and the efficiency of about 1 % for the conversion of the micro-wave radiation absorbed in the plasma to the EUV radiation in the desired wavelength range.

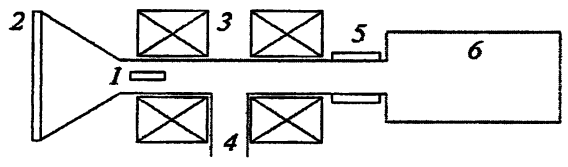

Fig. 1. Scheme of the installation: (1) plasma generator, (2) microwave window, (3) magnetic coils, (4) pump-out channel, (5) magnetic cloak, (6) EUV detector or ion extractor and time-of-flight analyzer of ion spectrum [1]

A key problem discussed in the present paper concerns the physics of high-frequency heating in this system. Tin ions injected into the trap from a vacuum-arc discharge form a narrow plasma column streamlined along the confining magnetic field with the transverse dimension comparable with or even less than the wavelength of the rf radiation. Conventional mechanism based on the electron cyclotron resonance (ECR) wave absorption in warm plasmas seems to be not effective due to small radial dimensions. However, under these conditions the role of plasma cut-offs significantly reduces due to possibility of direct wave tunneling through the evanescent regions. Consequently the rf radiation may absorbed with high efficiency in a vicinity of the upper hybrid resonance (UHR). This idea is supported by the previous experiment in which EUV radiation with a power of about 2 W per spatial angle of 2π sr was detected in the desired range for strongly off-resonant conditions (magnetic field strength of 1 T in the trap mirrors).

To model qualitatively this situation we study rf absorption in a plasma cylinder with non-uniform density $n_e(r)$ placed in an uniform external magnetic field directed along the cylinder axis z. Axially symmetric modes with $E, B \propto \exp(i\omega t - i n_\parallel k_0 z)$ are described by the Maxwell equations in cylindrical coordinates with the cold plasma dielectric response as

$$\partial E_\varphi / \partial r = -E_\varphi / r - i k_0 B_z, \; \partial B_\varphi / \partial r = -B_\varphi / r + i k_0 \varepsilon_\parallel E_z,$$

$$\partial E_z / \partial r = -n_\parallel k_0 g E_\varphi / \varepsilon_\perp + i k_0 (1 - n_\parallel^2 / \varepsilon_\perp) B_\varphi,$$

$$\partial B_z / \partial r = i k_0 (n_\parallel^2 - \varepsilon_\perp + g^2 / \varepsilon_\perp) E_\varphi - n_\parallel k_0 g B_\varphi / \varepsilon_\perp.$$

Here $k_0 = c/\omega$, $\varepsilon_\parallel(r) = 1 - \omega_p^2 / \omega(\omega + i\nu)$,

$$\varepsilon_\perp(r) = 1 - \frac{\omega_p^2 (1 + i\nu/\omega)}{(\omega + i\nu)^2 - \omega_c^2}, \; g(r) = \frac{\omega_p^2 \omega_c}{\omega[(\omega + i\nu)^2 - \omega_c^2]},$$

and ω, ω_c and ω_p are, correspondingly, the wave, electron cyclotron and plasma frequencies, ν is an effective frequency that define damping rate at the UHR (collisional or due to the spatial dispersion). The above equations are solved numerically using the novel impedance technique [3] generalized over the cylindrical geometry. As a result one can calculate the excitation of the ordinary (O) and extraordinary (X) electromagnetic modes of a plasma column, including distribution of all field components, related refection and absorption with all mode conversion effects typical of non-uniform plasma being taken into account.

Some examples of calculated RF power absorption efficiency are shown in fig. 2. Absorption of the X mode is maximal at small $n_\parallel$, while absorption of the O mode is maximal at large $n_\parallel$, which is very close to the optimal value for the O-X mode coupling in a plane stratified plasma, $n_\parallel^{opt} = 1/\sqrt{1 + \omega/\omega_c}$ [3]. One can see that direct absorption of the X mode is more

efficient than the absorption through the O-X mode conversion. This is a natural consequence of a small plasma size that enables traveling of the X mode through the evanescent region before the UHR. The damping is most efficient when the plasma density is close to the critical one defined by condition $\omega_p = \omega$, however it is still quite effective (e.g. for multi-pass absorption) for the much higher densities.

Wave absorption occurs near the UHR defined by

$$\omega = \omega_{UH}(r) \approx \sqrt{\omega_p^2(r) + \omega_c^2}\,. \qquad (1)$$

Due to low collisionality, $\nu/\omega \sim 10^{-4}$, studied damping mechanism is characterized by extremely narrow power deposition (width $\sim a\nu/\omega$), and high field intensity inside the absorption zone. However power deposition may be essentially broadened due to longitudinal inhomogeneity or non-linear effects, or combination of both. For the first effect, let us assume that the magnetic field strength $B(z)$ varies along the plasma axis slowly as compared to the wavelength. Then at each cross-section z wave absorption is roughly described by above model, but it occurs at different radial positions corresponded to varying ω_c in Eq. (1). Due to fast electron motion along the magnetic field the absorbed power is spread over the z-axis. Therefore, scan over B, e.g. shown in fig. 2, may be mapped to dependence over the radius. Example of such mapping is shown in Fig. 3. Note that the power is deposited to outer parts of a plasma column, and the absorption zone becomes narrower while plasma density deviates from the critical one.

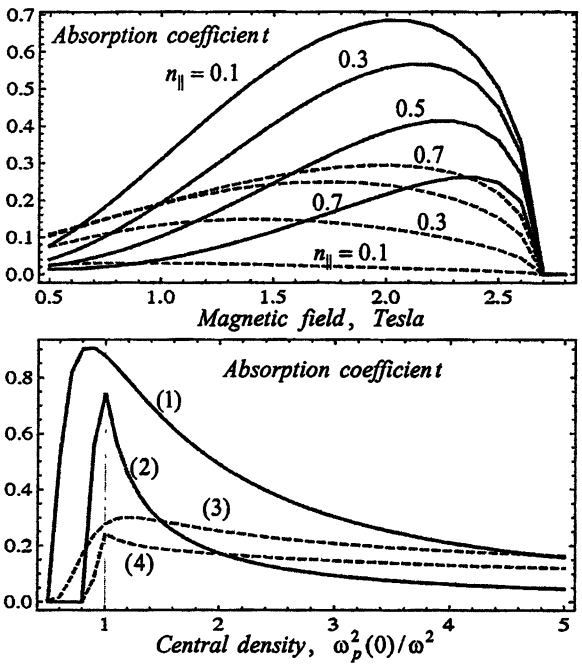

Fig. 2. RF power absorption efficiency at 75 GHz vs. magnetic field strength for different $n_\parallel$ (top) and vs. plasma density at $r = 0$ measured in critical densities (bottom). Solid lines—X mode, dashed lines—O mode. Labels in the bottom plot are (1) X mode, $n_\parallel = 0.1$ and $B = 2$ T, (2) X mode, $n_\parallel = 0.1$ and $B = 1$ T, (3) O mode, $n_\parallel = 0.65$ (optimal) and $B = 2$ T, (4) O mode, $n_\parallel = 0.52$ (optimal) and $B = 1$ T. Electron density profile is $n_e = n_0\,[1-(r/a)^8]^2$ with $n_0 = 10^{14}$ cm^{-3} and $a = 1.5$ mm. Electron temperature is $T_e = 50$ eV

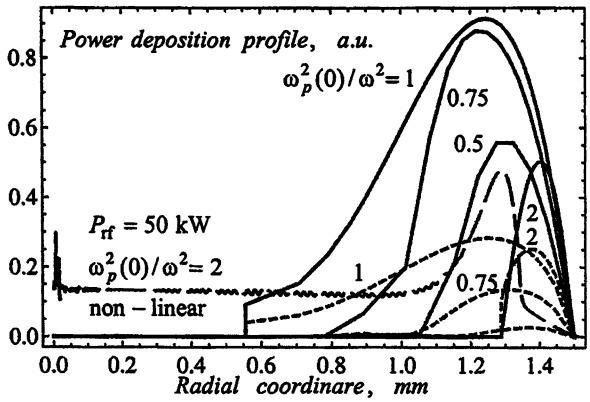

Fig. 3. RF power deposition profile at 75 GHz for different densities. Solid lines—X mode, $n_\parallel = 0.1$, dashed lines—O mode, $n_\parallel = 0.65$ (optimal), long dashed lines—X mode, $n_\parallel = 0.1$, non-linear regime. Other parameters are as in fig. 2

For high enough power flux the rf pondermotive force acting on plasma electrons results in spatial broadening of the UHR zone providing flat power deposition profile as shown in fig. 3. This may be described as follows. Plasma redistribution along the magnetic field is governed by the Boltzmann law:

$$n_e(r,z) = n_e^{lin}(r)\exp(-|E_r^2|_{UHR}/4\pi n_e T_e), \quad (2)$$

where n_e^{lin} is the non-perturbed density profile. Resonant field intensity inside the absorption zone may be estimated from approximate conservation of the tangential (non-resonant) field $E_\varphi \cong \text{const}$ and the normal electric displacement $D_r = \varepsilon_\perp E_r - igE_\varphi \cong 0$ as

$$|E_r^2|_{UHR} \approx |g/\varepsilon_\perp|^2\, 4\pi S_{rf}/c\,,$$

$S_{rf} = P_{rf}/2\pi a l$ is the density of an injected rf power, l is a focusing length, and $g/\varepsilon_\perp$ is a function of plasma density n_e. Thus, algebraic equation (2) may be solved for unknown n_e, which then is used for calculation of the power deposition profile by means of the linear model described above. Theoretical estimate for the total power absorption coefficient is

$$\eta^{non\text{-}lin} \sim (\nu/\omega)(P_0/P_{rf})\eta^{lin},\ P_0 = 2\pi a l c n_e T_e,$$

where $P_0 \approx 150$ MW for the discussed experiment. One see that non-linearity increases the heating efficiency when $\nu/\omega > P_{rf}/P_0 \sim 3\times10^{-4}$, and the total absorbed power can not exceed $(\nu/\omega)P_0 \sim 10$ kW. Proposed plasma discharge of a novel type allows to optimize the efficiency and cost of EUV source, in particular by increasing the plasma density above the "critical" value for the ECR discharge, increasing the rf frequency and reducing the confining magnetic field below the gyro-resonance.

The work is performed in frame of federal targeted program "Scientific and pedagogical labor force for an innovative Russia" for 2009 – 2013, and supported by RFBR (gr. No. 10-02-00441, 11-02-00403).

References

1. *Vodopyanov, A.V., Golubev, S.V., et al.* // Bulletin of Rus. Acad. of Sci.: Physics. 2011. V. 75, No. 1. P. 64.

2. *Vodopyanov, A.V., Golubev, S.V., Mansfeld, D.A. et al.* // JETP Letters. 2008. V. 88. P. 95–98.

3. *Shalashov, A.G., Gospodchikov, E.D.* // Physics–Uspekhi. 2011. V. 54, No 2. P. 145–165.

On Interpretation of Multi-Scale Pulsed Regimes of Electron Cyclotron Instabilities in a Mirror Confined Plasma Produced by ECR Discharge

A.G. Shalashov, S.V. Golubev, E.D. Gospodchikov, D.A. Mansfeld, M.E. Viktorov

Institute of Applied Physics of Russian Academy of Sciences, Nizhny Novgorod, Russia, ags@appl.sci-nnov.ru

In the present communication we discuss a possible mechanism responsible for the complex temporal patterns of quasi-periodic pulses of electromagnetic radiation and related precipitation of energetic electrons detected at a laboratory setup based on a magnetic mirror trap with plasma sustained by a gyrotron radiation (SMIS37, IAP RAS, Nizhny Novgorod). These experiments were aimed to simulate nonlinear wave-particle interactions in space plasmas and in particular to demonstrate the role of background plasma as a possible trigger of maser instability. A new regime of instability has been revealed during the plasma decay after the ECR power switch-off [1]. The instability develops when the plasma density becomes low enough, so that the electron plasma frequency is much less than the electron gyrofrequency. It was interpreted as a special regime of relaxation oscillations in the decaying plasma, in which a decrease in the wave energy losses provides repeated recovery of the instability conditions and thus serves as an effective source of free energy. At this stage, we observe the periodic excitation of electromagnetic waves which propagate nearly perpendicular to the magnetic field and cause precipitation of energetic electrons to the trap ends, what can be explained by similar mechanisms as the quasi-periodic regimes of instabilities under natural conditions, e.g., in pulsating auroral plasma cavities and similar systems.

The main features of the instability were reproduced by the simplest model of two-level maser proposed in [2]. The electron distribution function formed by ECR discharge in the mirror trap comprises two fractions, one of them being a small energetic addition to the other component which is much cooler and denser. The quasilinear interaction of hot resonant electrons with the electromagnetic wave exponentially increasing at the linear stage of instability reduces its transverse energy; as a result, some hot electrons fall within the loss cone and leave the trap. These losses reduce the instability growth rate and, finally, restrict the increase in the electromagnetic energy density in the system. The joint evolution of the hot-electron density N and the density of the electromagnetic energy E can be qualitatively described by the following balance equations [1, 2]:

$$\begin{cases} \dot{N} = -\kappa E N, & \kappa \approx h/T_h \\ \dot{E} = (\gamma - \nu) E, & \gamma \approx hN \end{cases} \qquad (1)$$

The first equation describes the rf-field-induced losses of hot electrons with effective temperature T_h, while the second equation describes the change of the wave energy in terms of the relation between the linear instability growth-rate γ and dissipation ν. Here the dissipation is governed by electron collisions with the background plasma thus $\nu(t)$ is assumed to be known function monotonically decreasing during the plasma decay after the ECR power switch-off. This particular feature is responsible for the operation of the cyclotron maser in absence of a direct pump.

The above model describes relatively well some essential features of the measured data such as time of beginning of the burst activity, pulse duration and typical interval between pulses. However, it does not reproduce complex temporal patterns regularly observed in the experiment, in which the interval between spikes may become irregular, single spikes join in bursts, and a kind of stochastic generation regime is sometimes detected. Typical examples of such activity are shown in Fig. 1 (top). The important feature of these data is that different patterns were observed quite randomly for the same experimental conditions.

This random switching between different nonlinear regimes of electron cyclotron instability may be explained as a result of self-modulation of a plasma cyclotron maser due to coherent interference of two (or more) unstable waves resulting in spatial modulation of amplification. Let us consider a simplest case of two counter-propagating modes with complex amplitudes $a_+(t)$ and $a_-(t)$ such as the wave field is

$$\propto a_+ \exp(ik\xi - i\omega t) + a_- \exp(-ik\xi - i\omega t).$$

Although direction of the spatial coordinate is not important for further analysis, note however that in an axisymmetric trap it is most likely the azimuthal direction. A standing wave formed by the coherent counter-propagating modes result in modulation of the hot electron density at the second harmonic,

$$N = [n(t) + \mathrm{Re}\, n_\sim(t) \exp(2ik\xi)] N_0.$$

This results in the same modulation of the growth-rate (amplification gain) and in Bragg scattering that couples the counter-propagating modes. Taking all these effects into account, one obtains the following modification of the basic maser equations (1):

$$\begin{cases} \dot{n} = -(|a_+^2| + |a_-^2|) n - a_+ a_-^* n_\sim^* - a_+^* a_- n_\sim \\ \dot{n}_\sim = -(|a_+^2| + |a_-^2|) n_\sim - a_+ a_-^* n \\ \dot{a}_+ = \tfrac{1}{2}(n - \nu) a_+ + \tfrac{1}{2} a_- n_\sim \\ \dot{a}_- = \tfrac{1}{2}(n - \nu) a_- + \tfrac{1}{2} a_+ n_\sim^* \end{cases} \qquad (2)$$

Here all densities are normalized over the initial density N_0 of hot electrons, all times and frequencies are normalized over the initial growth rate $\gamma_0 = hN_0$, the wave amplitudes are chosen such that the wave energy is scaled in terms of initial hot-electron energy,

$$E/N_0 T_h = |a_+^2| + |a_-^2|,$$

and superscript star denotes a complex conjugate. Note that Eqs. (2) have much in common to equations

of multimode fiber lasers with frequency-degenerate modes, especially ring lasers [3], although solutions studied below are quite different because of very different parameters typical for a plasma maser. Another important distinction from optical systems is an indirect pumping mechanism due to decreasing losses instead of direct pump of inversion in lasers (we assume that $\nu = \nu_0 \exp(-\nu_1 t)$).

Peculiar feature of the proposed model is its sensitivity to small variations of initial conditions in the parameter range typical of described experiments. In particular, different temporal patterns may be obtained for the same parameters except dispersion of initial amplitudes of the counter-propagating waves as shown in Fig. 1 (bottom). Note that some spread in initial amplitudes is very natural due to its thermal origin. Once excited, both modes compete for the same resources, namely a free energy stored in hot electrons, so one mode typically dominates over another. The resulted maser dynamics show rather complex behavior similar to what was observed in the experiment. Further details may be found in the figure caption.

Thus, the self-modulation of the cyclotron maser may explain qualitatively the variety and randomness of the observed data. The proposed model is very simple so it does not require knowledge of the details such as particular type and characteristics of the unstable modes. However, quantitative modeling requires more elaborated model which accounts wave traveling outside the generation region as well as plasma inhomogeneity in radial direction. These researches will be published elsewhere.

The work has been supported by RFBR (grants No. 09-02-00822, 10-02-00441) and Russian Ministry for Education and Science (state contract No. 14.740.11.0607).

References

1. *Vodopyanov, A.V., Golubev, S.V., Demekhov, A.G., Zorin, V.G., Mansfeld, D.A., Razin, S.V., Shalashov, A.G.* Observation of pulsed precipitations of fast electrons and cyclotron origin of the burst activity in a decaying plasma of ECR discharge // JETP. 2007. V. 104, No. 2. P. 330–342.

2. *Shalashov, A.G., Vodopyanov, A.V., Golubev, S.V., Demekhov, A.G., Zorin, V.G., Mansfeld, D.A., Razin, S.V.* Maser based on cyclotron resonance in a decaying plasma // JETP Letters. 2006. V. 84, No. 6. P. 314–319.

3. *Khanin, Ya.I.* Fundamentals of laser dynamics. Cambridge: International Science Publ. Ltd. 2006. P. 182.

4. *Golubev, S.V., Shalashov, A.G.* Cyclotron-resonance maser driven by magnetic compression of rarefied plasma // Phys. Rev. Lett. 2007. V. 99. P. 205002.

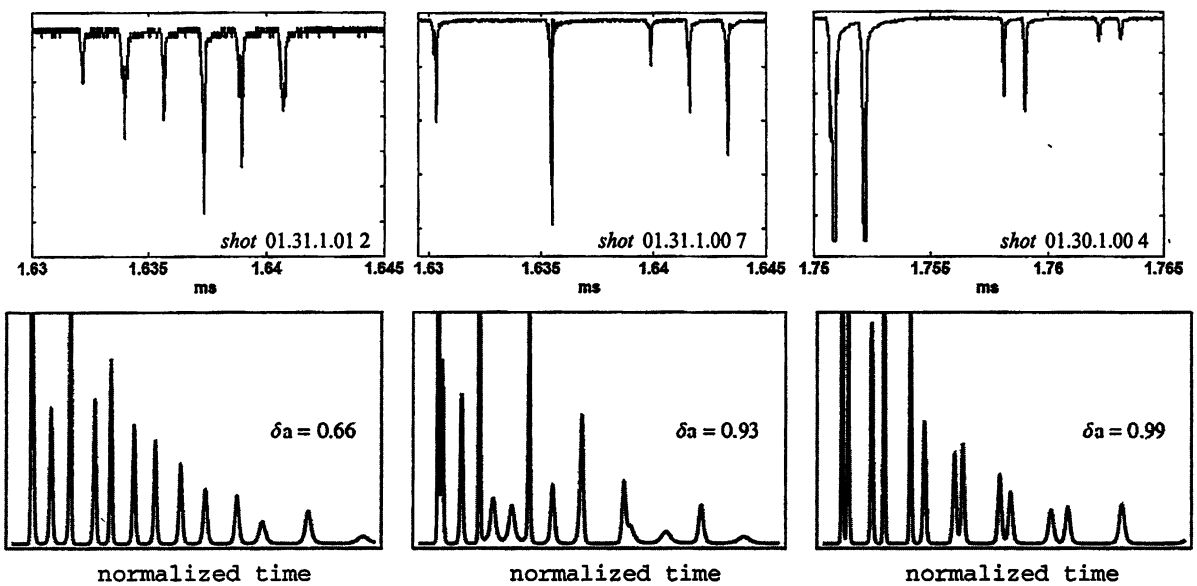

Fig. 1. On top – oscillograms of the signals from the pin diode measured precipitations of hot (10–500 keV) electrons from a trap after the ECR power is switched-off. In this experiment, nitrogen plasmas are formed with an initial density of 10^{13} cm^{-3}, an electron temperature of about 300 eV, a hot-electron density of 10^{10}–10^{11} cm^{-3}, and an effective hot-electron temperature of 10 keV. On bottom – precipitations of hot electrons dn/dt calculated basing on Eqs. (2) for different ratios δa between the initial amplitudes of two competing modes. One can see quasi-periodic (left), chaotic (center) and double-burst (right) regimes similar to those observed experimentally. Time is normalized over initial groth-rate γ_0; in order to match the experimental date one should assume $\gamma_0 \sim 10^7$ s^{-1} what corresponds well to the cyclotron instability of the extraordinary mode at the fundamental harmonic [1, 4]. Plasma decay is modeled by $\nu(t) = \nu_0 \exp(-\nu_1 t)$ with $\nu_0/\gamma_0 = 1.05$, $\nu_1/\gamma_0 = 0.0003$. Initial conditions are $a_+ = 10^{-2}$, $a_- = 10^{-2}\,\delta a$, $n = 1$, $n_- = 0$ at $t = 0$. Note that relative phase between initial a_+ and a_- is not important for these regimes, so we consider here the real valued solutions of Eqs. (2)

Suppression of Anomalous Power Reflection from Plasma by the Resonant Microwave Frequency Broadening

V.I. Arkhipenko[1], E.Z. Gusakov[2], L.V. Simonchik[1], M.S. Usachonak[1]

[1]Institute of Physics NAS of Belarus, Minsk, Belarus, simon@imaph.bas-net.by
[2]Ioffe Physical-Technical Institute of RAS, St-Petersburg, Russia, evgeniy.gusakov@mail.ioffe.ru

The parametric decay instability (PDI) excitation is a reason for anomalous reflection of electromagnetic waves in laser fusion experiments. The anomalous backscattering is also accompanying RF heating experiments in magnetic confinement devices as in the case of electron Bernstein wave heating where the PDI excited in the UHR due to relatively low power thresholds [1] is often observed [2]. Moreover, as it was shown recently [3], due to non monotonous density profile and magnetic field inhomogeneity, the backscattering PDI can be easily excited at second harmonic ECR heating in tokamaks and stellarators, as well, leading to anomalous backscattering [4], ion acceleration [5] and presumably to redistribution of the heating power. Therefore the development of the PDI control methods is essential and actual.

In the present report we demonstrate the way how the pump wave frequency broadening can be used as an effective tool for suppression of inhomogeneous magnetized plasma backscattering PDI. The experiment is performed at linear plasma device "Granit" [6] in magnetized inhomogeneous argon plasma at pressure ~2 Pa, maximal plasma density ~$5\cdot10^{12}$ cm^{-3} and electron temperature T_e ~1 – 2 eV. Using microwave at frequency $f_0 = \omega_0/(2\pi) = 2.4$ GHz the electron plasma wave (EPW) pump was excited in plasma by a waveguide. The dispersion relation for this mode is $k_\perp^2 = \left(\omega_{pe}^2(r,z) / \omega_0^2 - 1 \right) k_\parallel^2$, where $k_\parallel$ and $k_\perp$ are the parallel and perpendicular (relative to the magnetic field) wave vector components. Propagating toward decreasing electron density to the point of plasma resonance, where $\omega_0 \sim \omega_{pe}(0, z)$ the wave slows down and its electric field increases drastically (more than 10^3 times). After that the collisional absorption of wave as well as its interaction with electrons via Landau mechanism should take place in the vicinity of the resonance leading to the wave absorption. Measurements of fast component of electron distribution function have verified the slowing down of EPW in this area. The observations of the of stimulated backscattering instability $l_0 \rightarrow l_0' + s$ excited in the vicinity of the resonance at pump power $P_0 > 20$ mW have confirmed an electric field increase there. It was shown that above a certain threshold ($P_0 \cong 30$ mW) the absolute decay instability is excited which manifests itself as a coherent process with the limited number of oscillatory modes excited leading close to the threshold to BS spectrum possessing narrow lines (Fig. 2, *a*).

The non-monochromatic pump is produced in two ways, namely, by using the harmonic frequency modulation of pump or two frequency pump. The enhanced scattering [6] technique is applied to study the decay ion acoustic wave. For this purpose the probing EPW at frequency $f_p = 2.35$ GHz $< f_0$ and small power ($P_p < 5$ mW) is launched into plasma by the same waveguide system. In the vicinity of its own resonance point the probing wave is effectively back scattered off the parametrically driven small scale IA wave. The scattered wave amplitude is proportional to the IA one, unless the later is too high.

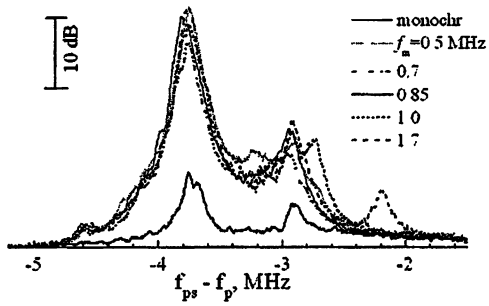

Fig. 1. BS signal spectra at harmonic frequency modulation (deviation is 5 MHz)

The harmonic frequency modulation of pump. The strong resonant suppression of the most dangerous absolute inhomogeneous plasma PDI is observed at a minimal frequency deviation (less than 1 %) when the modulation frequency is equal to frequency separation of the stable lines observed in the backscattering spectrum which correspond to ion acoustic wave eigen modes excited in the plasma by the absolute PDI (Fig. 1, f_m = 0.85 MHz). It is important to note that frequency modulation leads not only to resonant suppression of the IA wave generation, the

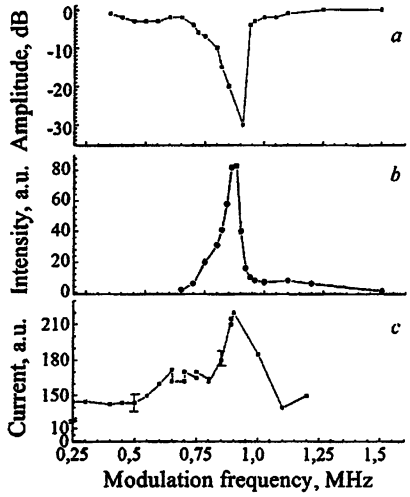

Fig. 2. Dependences of the BS signal (*a*), plasma luminosity growth (*b*) and the super thermal (>20 eV) electron current (*c*) on the modulation frequency (δf = 7.5–12 MHz)

probing wave BS, and accordingly anomalous reflection, but also to the enhancement of the pump wave absorption in the vicinity of the resonance point. The last statement is confirmed by observations of resonant growth of the plasma luminosity (Fig. 2, *b*) and super thermal electron production at energy higher than 20 eV (Fig. 2, *c*) in the decay region initiated by the pump frequency modulation switching on. We used the retarding potential about 20 V on the analyzer in order to exclude the contribution of thermal electrons with average energy of about 2 eV.

Two frequency pump. Taking into account that fast harmonic pump frequency modulation could be technically difficult we have investigated also influence of the pump amplitude modulation and complimentary pump on the absolute instability. It was shown, in particular, that weak pump amplitude modulation is not able to suppress the BS instability. On contrary, a possibility of deep resonant instability suppression by launching of an additional (small power) pump wave possessing a frequency shifted by the value equal to the frequency separation of ion acoustic eigen modes was demonstrated. The parametric decay instability $l \rightarrow l' + s$ was excited by the EPW pump at frequency $f_0 = 2335$ MHz and power of about 40 mW resulting in red-shifted satellite observed in BS spectrum (Fig. 3, *a*). When additional EPW at frequency $f_p = f_0 + 5$ MHz and small power ($P_p \sim 15$ mW) was launched into plasma by the same waveguide system a complicated BS spectrum consisting of two pump lines and two down shifted satellites was observed (Fig. 3, *b*). At high enough pump frequency difference $|f_p - f_0| \geq 2$ MHz (Fig. 3, *b* and *f*) the complementary pump do not influence the primary pump BS spectrum. However, as it is seen in Fig. 3, *c* and *e*, at frequency difference $|f_p - f_0| \approx$ ≈ 1 MHz the main pump BS decreases by several orders of magnitude, thus indicating the next to total absolute PDI suppression. At $|f_p - f_0| < 1$ MHz the BS signal recovers, however possessing different spectrum shown in Fig. 3, *d*. A more detailed analysis of suppression efficiency shows that the pump frequency difference corresponding to easier and deeper suppression of the absolute instability is equal to the frequency difference of ion acoustic eigen modes

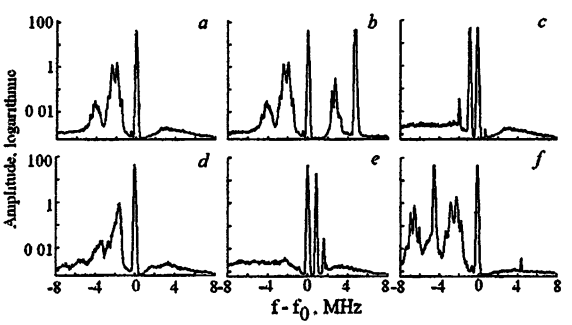

Fig. 3. Scattered signal spectra at different frequencies of additional pump wave. (A) – monochromatic pump $f_0 =$ $= 2335$ MHz, (B–F) – frequency differences are +5 MHz, +1, 0, –1 and –5 MHz correspondingly

excited by the instability and observable as separate lines in BS spectrum in Fig. 3, *a*.

As in the case of harmonic modulation, the parametric decay instability suppression is accompanied by the recovery of microwave power absorption as demonstrated using measurements of the plasma luminosity (Fig. 4, *a*) and fluxes of accelerated electrons (Fig. 4, *b*).

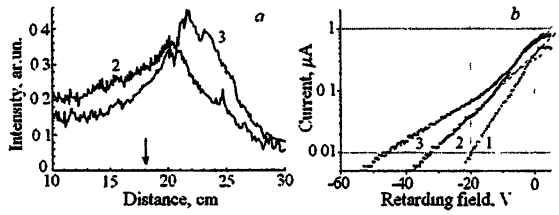

Fig. 4. Axial plasma luminosity distribution (*a*) and analyzer voltage current characteristics (*b*) registered at pump frequency difference of 5 MHz (2) and 1 MHz (3), 1 – background plasma. Arrow corresponds to the resonance position.

The observed PDI resonant suppression effect is interpreted in terms of the three-wave dynamic system nonlinearity leading in the presence of pump frequency modulation or secondary pump to coupling of the PDI eigen modes and, as a result, to energy losses for the fastest growing mode, backscattering decrease and recovery of microwave power absorption. Keeping in mind that excitation of discrete frequency spectrum due to creation of feedback loop, when the part of energy carried out convectively by a daughter wave from the decay region is retuned back is the common feature of absolute PDIs, the proposed experimental arrangement for the PDI control, in our opinion, is not specific for our experiment and can be utilized in a high power microwave plasma heating experiments.

Financial support of BRFBR-RFBR grants (F10R-010, 10-02-90003) is acknowledged.

References

1. *Gusakov, E.Z., Surkov, A.V.* Induced backscattering in an inhomogeneous plasma at the upper hybrid resonance // Plasma Phys. Control. Fusion 2007. V. 49. P. 631–640.

2. *Laqua, H.P.* Electron Bernstein wave heating and diagnostic // Plasma Phys. Control. Fusion 2007. V. 49. R1–R10.

3. *Gusakov, E.Z., Popov, A.Yu.* Low Threshold Parametric Decay Backscattering Instability in Tokamak Electron Cyclotron Resonance Heating Experiments // Phys. Rev. Lett. 2010. V. 105. 115003.

4. *Westerhof, E., Nielsen, S. K. et al* Strong Scattering of High Power Millimeter Waves in Tokamak Plasmas with Tearing Modes // Phys. Rev. Lett. 2009. V. 103. 125001.

5. *Rapisarda, D. et al.* The role of a fast ion component on the heating of the plasma bulk // Plasma Phys. Control. Fusion 2007. V. 49. P. 309–324.

6. *Arkhipenko, V.I., Budnikov, V.N. et al.* Parametric Decay Instability of an Inhomogeneous Plasma in a Frequency-Modulated Pump Wave // Plasma Phys. Reports. 2000. V. 26. P. 314–319.

«Micropulses» Generation in ECR Breakdown Stimulated by Gyrotron Radiation @ 37,5 GHz

V. Skalyga, I. Izotov, S. Razin, A. Sidorov, V. Zorin

Institute of Applied Physics RAS, Nizhny Novgorod, Russia, sval@appl.sci-nnov.ru

Realization of the European programme for neutrino oscillations research, "Beta Beam" project [1], requires that high-power short-pulse (tens of microseconds) beams of multicharged ions of radioactive gases (e.g. ^{6}He or ^{18}Ne) be created. Present work is devoted to experimental investigation of possibility of such short pulsed (< 100 μs) ion beams creation.

The quasi-stationary generation of short pulsed beams under conditions of quasi-gasdynamic plasma confinement was shown in recent experiments [2]. Another way of such beams creation based on preglow effect was proposed [3, 4]. In present work it was demonstrated that in the case when duration of microwave (MW) pulse is less than formation time of preglow peak, realization of a regime when ion current is equal to zero during MW pulse and intense multicharged ions flux appears only when MW ends is possible. Such pulses after the end of MW were called "micropulses". In present work generation of micropulses was observed in experiments with ECR discharge stimulated by gyrotron radiation @ 37,5 GHz, 100 kW. In this case pulses with duration less than 30 μs were observed. Probably the same effect was observed in GANIL where 14 GHz radiation was used and pulses with duration about 2 ms were registered [5].

Experimental Setup

The experimental research presented in this work was carried out on the SMIS 37 [6, 7] shown schematically in fig. 1.

A gyrotron generating linearly polarized radiation at the frequency of 37.5 GHz, with the power up to 100 kW, and pulse duration up to 1.5 ms was used as a source of pulsed microwave radiation. In the greatest majority of the experiments the field in the magnetic plugs of the system was 2 Tesla. The operating gas was injected into the trap along the axis of the magnetic system through a 20-cm long quartz tube with internal diameter of 5 mm; the tube was soldered at the center of the input quartz window.

Ion extraction and ion beam formation were achieved by means of a traditional two-electrode extracting system. A plasma electrode was placed at an arbitrary distance from the trap plug. Maximum 55 kV voltage was supplied to the extractor. Total ion current was measured by a Faraday cup mounted on the magnetic trap axis. The cup had an input window 35 mm in diameter and intercepted the entire ion beam passed through the extractor puller.

Spectral analysis of the extracted beam of positive ions was performed by means of a magnetostatic analyzer.

Experimental Results

In experiments on SMIS 37 the preglow effect was successfully observed [7]. The preglow peak duration in this case was about 20 μs, and that is much shorter than in traditional ECRIS [3, 4]. An example of the ion current oscillogram is presented in fig. 2.

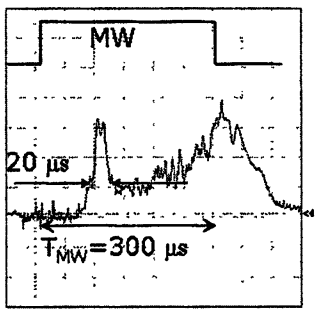

Fig. 2. Oscillogram of total ion current. The shape of MW pulse is schematically shown above the oscillogram

The next obvious step is reduction of MW duration till the ion current pulse would not satisfy certain requirements. In fig. 3 the evolution of Ar^{4+} current shape with MW pulse duration reduction is shown.

Such short pulse after the end of microwaves was called "micropulse". Temporal evolution of ion beam

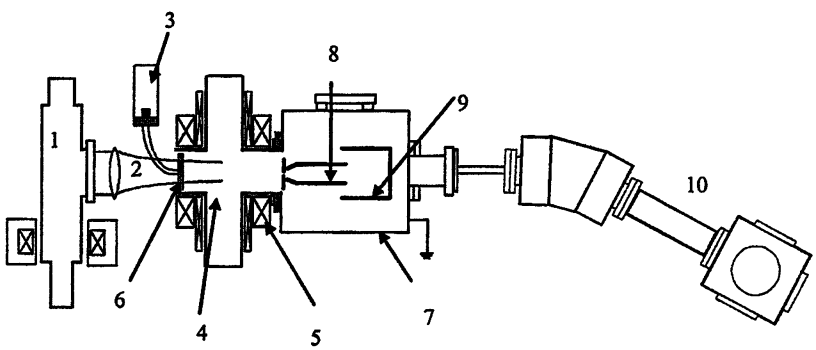

Fig. 1. SMIS 37 experimental stand. 1 – gyrotron, 2 – MW beam, 3 – pulsed vacuum valve, 4 – discharge chamber, 5 – magnetic trap coils, 6 – quartz window, 7 – diagnostic chamber, 8 – extractor, 9 – Faraday cup, 10 – ion analyzer

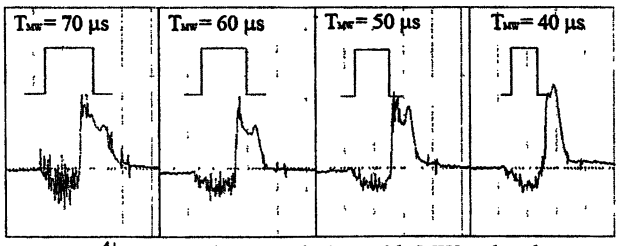

Fig. 3. Ar^{4+} current shape evolution with MW pulse duration reduction

current may be described in frame of the model developed in [8]. In the beginning of the breakdown while plasma density is low electrons could accumulate a lot of energy which could course an efficient ionization after the end of MW pulse. Fast density growth and average electron energy decrease after MW pulse leads to intense peak of ion current. So nature of micropulses looks very close to afterglow, but with starting of afterglow peak not from steady state regime of discharge but from breakdown stage.

In such conditions the average ion charge in this peak could be high enough. Corresponding ion spectrums in nitrogen and argon are presented in fig. 4 and fig. 5.

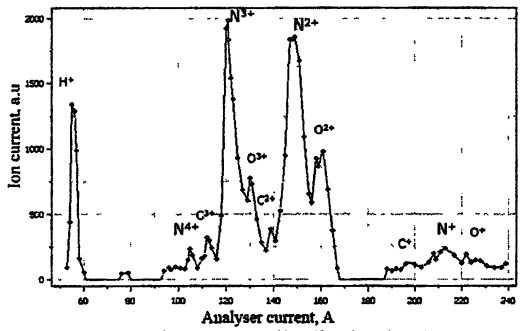

Fig. 4. Ion charge state distribution in nitrogen

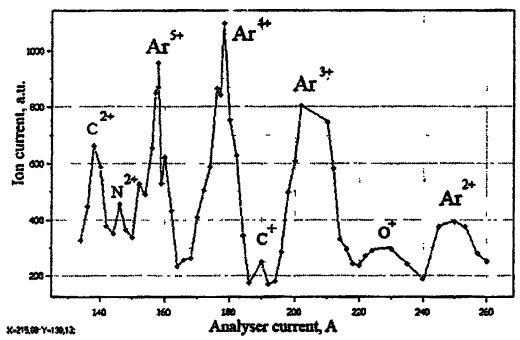

Fig. 5. Ion charge state distribution in argon

Conclusion

In present work it was shown that intensity of such micropulse could be slightly higher than intensity of preglow peak at the same conditions but with longer MW pulse. The generation of micropulses of nitrogen and argon multicharged ions with current of a few mA and length about 30 μs after MW pulse with duration of 30–100 μs was demonstrated. The low level of impurities, high current density and rather high average charge make possible to consider such micropulse regime as promising way for creation of a short pulsed ion source.

Acknowledgements

Work was performed in frame of realization of federal targeted program "Scientific and pedagogical labor force for an innovative Russia" for 2009–2013 yy.

We acknowledge the financial support of the European Community under the European Commission Framework Programme 7 Design Study: EUROnu, Project Number 212372. The EC is not liable for any use that may be made of the information contained herein.

Work was partly performed with support of RFBR grant #11-02-97056-p_povolj'e_a.

References

1. http://beta-beam.web.cern.ch/beta-beam/.

2. *Skalyga V.A., Zorin V.G., Izotov I.V., Vodopyanov A.V. and Golubev S.V., et al.* Short-pulse ECR: A source of multiply charged ions // Technical Physics. 2010. N. 55. V. 12. P. 1797-1801.

3. *Thuillier T., Lamy T., Latrasse L., Geller R., Izotov I., Sidorov A., Skalyga V., Zorin V., Marie-Jeanne M.* Study of pulsed electron cyclotron resonance ion source plasma near breakdown: The Preglow // Review of Scientific Instruments, 79, 02A314 (2008).

4. *Izotov I., Sidorov A., Skalyga V., Zorin V., Lamy T., Latrasse L., Thuillier T.,* Experimental and Theoretical Investigation of the Preglow in ECRIS // IEEE Transactions on Plasma Science. 2008. V. 36, No. 4. P. 1494-1501.

5. *Maunoury L. et al.* // Review of Scientific Instruments. 79, 02A313 (2008).

6. *Golubev S.V., Razin S.V., Vodopyanov A.V., Zorin V.G.* // Transactions of Fusion Technology. 35, 288 (1999).

7. *Zorin V.G. et al.*, ECR breakdown of heavy gases in open mirror traps // proceedings of the 8th International Conference on Open Magnetic Systems for Plasma Confinement, July 5-9, 2010, Novosibirsk, Russia, Fusion Science and Technology. V. 59, Nb. P 140-143.

8. *Skalyga V., Zorin V., Izotov V., Sidorov A., Lamy T., Sortais P., Thuillier T.* Gas Breakdown in ECR ion Source // Review of Scientific Instruments. V.77, № 3. P. 03A325-1 – 03A325-3, (2006).

Present Status of ITER Equatorial EC Launcher Design and R&D

K. Takahashi[1], K. Kajiwara[1], Y. Oda[1], N. Kobayashi[1], K. Sakamoto[1], T. Omori[2] and M. Henderson[2]

[1] Japan Atomic Energy Agency, 801-1, Mukoyama, Naka, Ibaraki 311-0193 Japan
[2] ITER Organnization, St. Paul-lez-Durance, 13067 France

Introduction

An electron cyclotron heating and current drive (EC H&CD) system is an indispensable tool to improve fusion plasma performance. The system is prepared in ITER as well. The ITER EC H&CD system (Fig. 1) consists of twenty-four 170 GHz, 1 MW gyrotrons, a transmission line composed of twenty-four waveguide lines and five antennas launching millimeter (mm) wave beam power into plasma. The gyrotrons are placed in the RF building and the launchers are installed in both equatorial (one) and upper port (four) of the vacuum vessel in the tokamak building. The one side of the transmission line is connected to the gyrotrons and the other side is to the launchers. The equatorial launcher (EL) had the torus diamond windows at the interface between the launcher and the transmission line. Although it was changed that windows were installed in the port cell area, far back from the end of the launcher, the window development was included as one of the design and R&D items of the launcher.

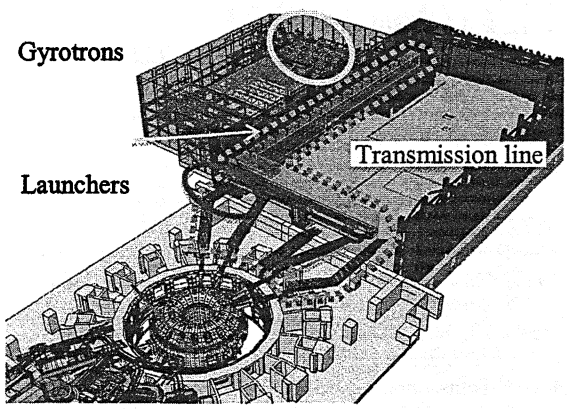

Fig. 1. ITER EC H&CD system : Gyrotrons and transimission line and launchers

Equatorial Launcher

The schematic picture of the ITER equatorial EC launcher (EL) is shown in fig. 2. It shall be capable of injecting a 170 GHz, 20 MW millimeter (mm) wave beam into plasma. A toloidal steering of the beams ($20° \leq \Theta_T \leq 40°$) is also required. The launcher design has been modified to a partial quasi-optical (QO) layout consisting of the movable mirrors, the focusing mirrors and the dog-legged waveguide lines without changing the opening size of the blanket shield modules (BSMs) located in front, resulting some advantages such as a simpler configuration and a possible reduction of fabrication cost. The transmission efficiency of the mm wave beam on the QO layout is kept to be 99.5 % [1]. This modification also derives the reduction of heat load on the steering mirror to be one-third of the reference design, which relaxes the thermal design of the mirrors [1–2].

The IO physics team proposed that the EL should have the capability of the counter injection of some beam power and the titling of the beams toward the plasma center so that the pure heating and more power deposition in the central region of plasma could be performed. The EL has three bundles of the injection beam and each has eight beam lines. Therefore the middle one has been flipped off and the top and the bottom are poloidally tilted toward the plasma center by 5°. In order to perform this modification without degrading the propagation capability of the beams and increasing the peak heat load on the mirrors' surface, some parts of the BSMs have been cut and the shape of both mirrors has been modified. The position of both the steering and the fixed mirrors has also been shifted back to increase the space for the cooling pipes of the BSMs. The reasonable assembly and refurbishment of the BSMs' can be done with this modification. It is obtained that the degradation of the transmission efficiency of the beam is only 0.3 % and the peak heat load on the mirror is equivalent to the reference design.

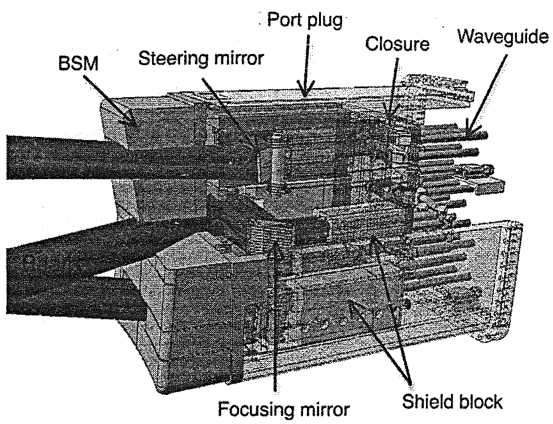

Fig. 2. Present design of ITER equatorial EC launcher : The 20 MW power is provided by three beam bundles and one of them is injected for the evolution of counter current drive

Based on this QO design, the full scale EL mock-up was fabricated. The mirrors are located in front of the waveguide structure composed by the waveguide lines. One of the line is authentic and mm wave can propagate in the line. Figure 3 shows the results of the low power experiment; the field pattern of the beam at the mirrors and the target that is 2 meters away from the outlet of the BSM opening and the comparison between the experiment and the calcula-

tion [3]. It was confirmed that the experimental results were agreed with the calculation. This indicates that the QO arrangement with a pair of optical mirrors is applicable to the optimum mm-wave design of the launcher. The high power experiment was preliminary carried out. The mock-up was connected to the end of the ITER relevant transmission line via the torus diamond window that are described in the next section. Transmission of 0.5 MW – 0.4 s and 0.16 MW – 10 s was successfully demonstrated. The field patterns in the beam duct qualitatively measured by an infrared camera indicate that some power deposition of stray RF are concerned.

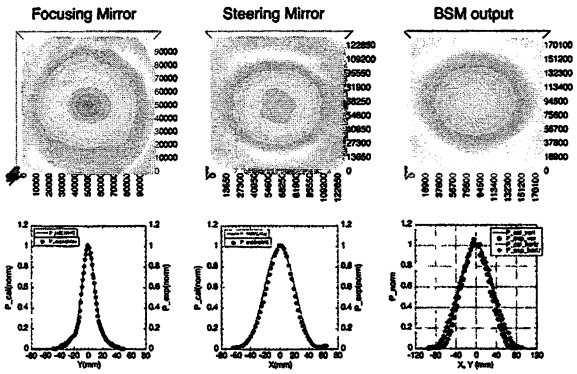

Fig. 3. The results of the field pattern measurement at low power: Power profile at the focusing mirror (*left*), the steering mirror (*middle*) and 2m away from the BSM opening (*right*)

Window development

Figure 4 shows the digital photograph of the torus window prototype fabricated on the current design basis. A pair of copper cylinder is brazed to both sides of the disk edge and they are welded to a stainless steel window housing that has a cooling water channel. A pair of stainless steel corrugated waveguide is inserted to both side of the window disk and welded to the window housing. The inner diameter of the waveguide is 63.5 mm that is the same size of the ITER transmission line. The gap between the waveguide and the disk is 0.5 mm. A thin copper layer ($\leq$ 5 μm) is coated onto the inner surface of the corrugation to minimize ohmic wall loss due to the high order modes propagation in the waveguides.

Transmission of both 430 kW and 740 kW was demonstrated and the successful pulse length was 100 s on both cases. Temperature increase of cooling water was saturated to be 0.18 °C in 25 s at the transmitted power of 430 kW. The vacuum pressure in the waveguide is increased at the beginning of the pulse and saturated when the RF power become stable. When the transmission power/pulse length of the propagated wave is 430 kW / 30 s, the deposited power into the window cooling water was measured to be 30 W. Then, the loss tangent of the diamond disk was estimated to be $5.54 \cdot 10^{-6}$, which was the lowest value that had ever obtained. It should be noted that the deposited power includes the power (or heat) penetrated into the copper cylinder that are brazed to the window disk and the window housing. Therefore, it is expected that the loss tangent of the diamond disk itself is lower than the above.

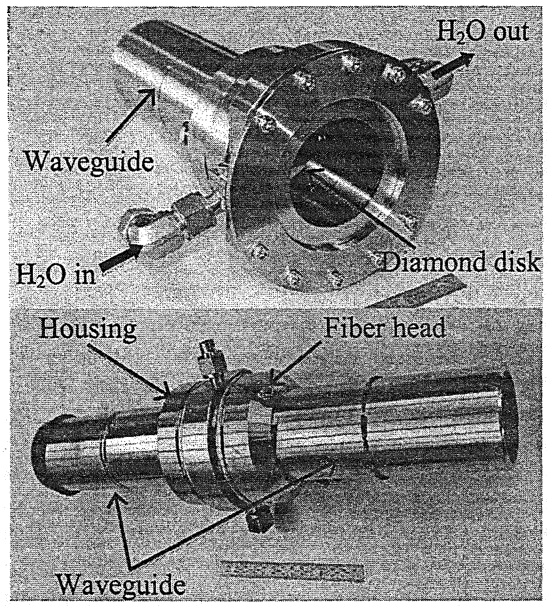

Fig. 4. Photograph of a torus diamond window prototype for ITER EC H&CD system

Conclusion

The EL design to perform the high efficient transmission of mm waves power and to reduce the heat load on the mirrors is obtained assuming the HE11 mode propagation in the transmission line. The efficiency is 99.5 %. The EL mock-up was fabricated based on the design and the RF transmission experiments were carried out. Some stray RF radiation in the beam duct was qualitatively obtained. The torus window mock-up was fabricated based on the current design and the high power RF transmission experiment was carried out. The loss tangent of the diamond disk was evaluated to be $5.54 \cdot 10^{-6}$, which was the lowest value that had ever obtained.

References

1. *Takahashi, K. et al.* Improved design of an ITER equatorial EC launcher // Nucl. Fusion. 2008. V. 48, № 5. P. 054014.

2. *Kajiwara, K. et al.* Design of a high power millimeter wave launcher for EC H&CD system on ITER // Fusion Eng. Design 2009. V. 84. P. 72.

3. *Takahashi, K. et al.* Progress of ITER Equatorial Electron Cyclotron Launcher Design for Physics Optimization and toward Final Design // Fusion Eng. Design to be published.

Generation of Wideband Electromagnetic Radiation Under Magnetic Compression of a Mirror-Confined Plasma Produced by ECR Discharge

M.E. Viktorov, S.V. Golubev, E.D. Gospodchikov, I.V. Izotov, D.A. Mansfeld, A.G. Shalashov, A.V. Vodopyanov

Institute of Applied Physics of Russian Academy of Sciences, Nizhny Novgorod, Russia, mikhail.viktorov@appl.sci-nnov.ru

In the present paper we demonstrate the use of a laboratory setup (SMIS37, IAP RAS, Nizhny Novgorod, [1]) based on magnetic mirror trap with plasma sustained by powerful millimeter-wave gyrotron radiation under the electron cyclotron resonance (ECR) conditions aimed at identifying the role of the adiabatic magnetic compression as a possible driver of electron cyclotron instability. The generation of bursts of electromagnetic radiation associated with the explosive development of the cyclotron instability of a magnetized plasma, and accompanied by precipitations of energetic particles from a trap, has been observed in a wide range of plasma parameters in various conditions: in the magnetospheres of the Earth and other planets, in the Solar coronal loops, as well as in laboratory magnetic traps. In such systems variations of temporal and spatial structure of magnetic field may be of importance. In the context of a laboratory setup, the use of adiabatic increase of the magnetic field provides the effective energy pump in a hot anisotropic electron component.

Heating under the ECR conditions allows to create a two-component plasma containing cold dense component with an isotropic velocity distribution, and less dense component of hot electrons with anisotropic distribution function (with a predominance of the transversal to the magnetic field momentum as compared to the longitudinal one). Parameters of the initial plasma were $N_e \sim 10^{13}\,\mathrm{cm}^{-3}$, $N_h \sim 5\cdot10^{10}\,\mathrm{cm}^{-3}$, $T_e \sim 300$ eV, $T_h \geq 10$ keV. The new regime of cyclotron instability has been revealed during the plasma decay after ECR heating switch-off when the plasma density becomes low enough, so that the electron plasma frequency is much less than the electron gyrofrequency [2]. In such plasma, instability development is determined by the substantial difference in the lifetimes of the trapped hot and cold plasma components. Density of the cold plasma component decreases rapidly after the ECR heating switch-off, thus creating conditions for the excitation of waves propagating across the magnetic field. The experiment described in [2] showed the existence of quasi-periodic bursts of energetic electron flux precipitating from the trap ends and synchronous pulses of microwave radiation of plasma in a direction nearly perpendicular to the ambient magnetic field.

Present research is aimed at direct observation of microwave radiation which causes precipitation of energetic electrons from the trap. A set of microwave receivers with different transmission bands was used for spectrum measurements. Every receiving channel includes two filters: band-pass filter and low-pass filter that provides good suppression of high frequencies. Filters were designed to exclude the light-striking of stray radiation of a gyrotron in the detection bandwidth. All receivers were calibrated such that allowed to measure an absolute value of a microwave intensity escaping from the plasma volume.

According to the theory of cyclotron instabilities [3] it is usually assumed that the resonant interaction of electromagnetic waves with anisotropic hot electrons occurs at the center of the magnetic trap where the magnetic field strength, and hence the electron gyrofrequency, are minimal. But the present experiment shows that the electromagnetic radiation is generated at frequencies significantly higher than the value of the electron gyrofrequency at the trap center. However the frequency of the detected electromagnetic radiation has increased following the confining magnetic field strength what proves the cyclotron mechanism of the instability development.

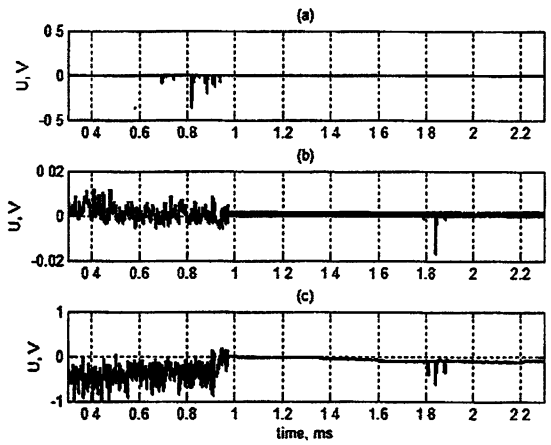

Fig. 1. Typical signals from receivers: (a) microwave radiation in direction longitudinal to the ambient magnetic field at 6–18 GHz frequency range (the whistler mode), (b) microwave radiation in direction perpendicular to the ambient magnetic field at 18–26 GHz frequency range (the fast extraordinary mode), (c) signal of hot electrons precipitated from the trap. The gyrotron was switched-off at 1 ms

In experiments the electron gyrofrequency at the trap center was in frequency range of 10–15 GHz. At the same time the instability was detected as series of quasi-periodic broadband pulses of electromagnetic radiation in 25–27 GHz frequency range with typical pulse duration of 1–10 microseconds. Synchronously a precipitation of energetic (≥10 keV) electrons was observed. Typical signals are shown in Fig. 1 and Fig. 2. The maximum amplitude of the signal on microwave detectors has reached a value of 300 mV which corresponds to the radiation power of 5 mW. Taking into account the value of solid angle which is covered by the receiver and the distance to the trap

center one can derive the total emitted power of 3 W. For this kind of signals it is a significant quantity to prove the stimulated nature of radiation.

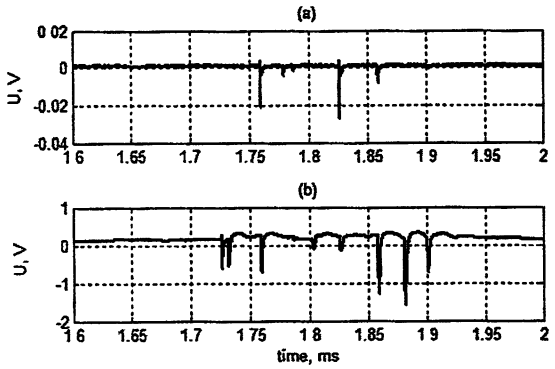

Fig. 2. Bursts of microwave radiation of the plasma have a rich temporal structure with strictly defined typical periods: (*a*) microwave radiation in direction perpendicular to the ambient magnetic field at 18–26 GHz frequency range, (*b*) signal of hot electrons precipitated from the trap

In all experiments bursts of microwave radiation and precipitations of hot electrons under cyclotron instability were observed approximately after 1 ms next to gyrotron switch-off. It was suggested to use this time to pump additional energy into plasma using adiabatic compression of the magnetic field [4]. New power supply system allowed to increase magnetic field strength twice during the experimental shot and achieve 3.15 T maximum magnetic field in the plug. During the magnetic field ramp-up, the ECR pump was launched at the moment when the magnetic field is resonant to the gyrotron radiation, what resulted in the ECR breakdown and initiation of the non-equilibrium plasma discharge. After the end of the ECR pump, magnetic field continued to grow up about 30% before the first burst instability develops. During this time interval, the energy of hot electrons was adiabatically increased (mainly for transverse motion), resulting in more favorable conditions for the development of the electron cyclotron instabilities. The schemes of the experiments with the magnetic field rump-up and without it are shown in Fig. 3.

In these experiments, the sequences of pulses which were generated in conditions of constant confining magnetic field were compared with the sequences of pulses detected in a time-varying (adiabatically increasing) magnetic field both at the stage of ECR heating and the plasma decay. It was demonstrated that the magnetic compression leads to a sufficient increase of burst intensity and their number in accordance with the theoretical predictions based on the model of a cyclotron maser.

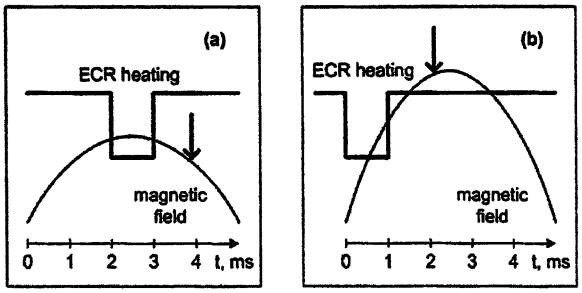

Fig. 3. The scheme of the experiment: (*a*) ECR heating in a constant magnetic field, (*b*) ECR heating during adiabatic increase of the magnetic field. The upper trace stands for the gyrotron microwave pulse and the lower trace for the magnetic field strength. The vertical arrow schematically shows the moment of cyclotron instability development in rarefied plasma

In addition to the diagnostics described above, a diamagnetic probe was used for measurement of the plasma pressure variation during the burst activity. Data from the diamagnetic probe allowed estimations of the total energy losses accompanying the instability development. Such analysis shows that about 2/3 of the initial energy stored in the hot plasma component is taken away by hot precipitating electrons. Thus, the cyclotron instability plays a major role in energy balance of the decaying plasma providing much faster losses of the hot component as compared to those due to the Coulomb collisions.

The present paper shows that the magnetic compression can provide an effective mechanism to enhance burst activity of the plasma. The setup has been upgraded and the system for spectrum analysis has been developed. In this sense our laboratory setup can be used for modeling much wider range of fundamental processes in the plasma.

The work has been supported by RFBR (grants No. 09-02-00822, 10-02-00441) and Grant of President of RF #MK-7563.2010.2.

References

1. *Vodopyanov, A.V., Golubev, S.V., Demekhov, A.G., Zorin, V.G., Mansfeld, D.A., Razin, S.V., Trakhtengerts, V.Yu.* Laboratory modeling of nonstationary processes in space cyclotron masers: first results and prospects // Plasma Physics Reports. V. 31, № 11. 2005. P. 927–937.

2. *Vodopyanov, A.V., Golubev, S.V., Demekhov, A.G., Zorin, V.G., Mansfeld, D.A., Razin, S.V., Shalashov, A.G.* Observation of pulsed precipitations of fast electrons and cyclotron origin of the burst activity in a decaying plasma of ECR discharge // JETP. 2007. V. 104, No. 2. P. 330–342.

3. *Gaponov-Grekhov, A.V., Glagolev, V.M., Trakhtengerts V.Yu.* Cyclotron resonance maser with background plasma // Sov. Phys. JETP 53, 1146 (1981).

4. *Golubev, S.V., Shalashov, A.G.* Cyclotron-resonance maser driven by magnetic compression of rarefied plasma // Phys. Rev. Lett. 2007. V. 99. P. 205002.

Symposium T

TERAHERTZ SOURCES, DIAGNOSTICS AND NONLINEAR INTERACTIONS

Subterahertz Generation by Magnetized Plasma at Two-Stream Instability of High Current 1-MeV REB

A.V. Arzhannikov[1,2], A.V. Burdakov[1-3], P.V. Kalinin[1,2], S.A. Kuznetsov[1,2], M.A. Makarov[1], K.I. Mekler[1], S.V. Polosatkin[1,2], V.V. Postupaev[1,2], A.F. Rovenskikh[1], S.L. Sinitsky[1,2], V.F. Sklyarov[1,3], V.D. Stepanov[1,2], Yu.S. Sulyaev[1], M.K.A. Thumm[2,4], L.N. Vyacheslavov[1,2]

[1]Budker Institute of Nuclear Physics SB RAS, Novosibirsk, RF, arzhannikov@inp.nsk.su
[2] Novosibirsk State University, Novosibirsk, Russia
[3] Novosibirsk State Technical University, Novosibirsk, Russia
[4]Karlsruhe Institute of Technology, Karlsruhe, Germany

Introduction and background

One of possible ways to generate submillimeter and THz radiation is to use a process of transformation of plasma waves into electromagnetic radiation at strong Langmuir turbulence [1]. We had already described some implementation of such method at the GOL-3 experiments [2, 3], wherein the mechanism of plasma heating was recognized as the excitation of strong Langmuir turbulence (LT) via a two-stream instability induced by the propagating high current beam. The detailed theoretical consideration of LT-induced electromagnetic emission from turbulent plasmas distinguishes two main processes responsible for the electromagnetic radiation emission during the beam-plasma interaction at GOL-3. First, plasmon scattering on plasma density fluctuations yields electromagnetic emission at the plasma frequency ω_p ("ω_p-process"). Second, plasmon-plasmon merging results in production of photons in the vicinity of the double plasma frequency $2\omega_p$ ("$2\omega_p$-process"). For plasma densities 10^{14}–10^{15} cm^{-3}, corresponding output radiation frequencies are located in the range from mm to sub-mm waves, $\omega_p/2\pi \cong 90-283$ GHz, $2\omega_p/2\pi \cong 180-566$ GHz.

In this paper, we present studies of LT-induced submm-wave emission from GOL-3 plasmas during injection of the 10-μs-REB. We intentionally focused on investigating the $2\omega_p$-emission from the plasma at plasma density $n \approx 10^{14}$–10^{15} cm^{-3}, and magnetic field strength of 4 T.

Experimental setup

Experimental studies are carried out at the multiple-mirror magnetic trap GOL-3 ($B_{max}/B_{min} \cong 4.8/3.2$). An electron beam with the current up to 10 kA/cm^2 and the particle energy up to 0.5 MeV is injected during 10 μs through one end of a plasma column and propagated through the plasma on the distance of 12 m. Registration of the electromagnetic emission was performed at two distances: about of 80 and 180 cm from the beam injection plane wherein the magnetic field strength is B ≅ 4 T (See Fig. 1). Diamagnetic signals demonstrate the maximum efficiency for the beam-plasma interaction in this area of the plasma column. Information about the intensity of the beam-plasma interaction was obtained by comparison of measurements of electron beam parameters before its injection into the plasma and the energy distribution function of the beam electrons after passing through the plasma column.

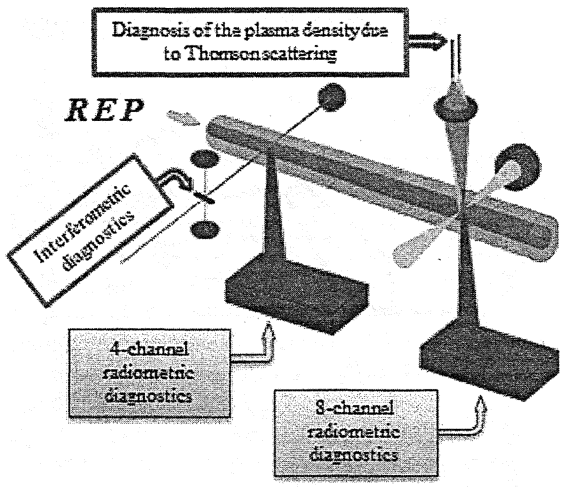

Fig. 1. Schematic of the radiometric experiment at the GOL-3 facility

As soon as frequency spectrum of sub-THz radiation and its dynamics during the beam injection are essentially depend on plasma parameters we apply a Thomson scattering diagnostic system based on Nd-glass laser (1.054 μm). The laser generates two independently triggered pulses with 10–20 J energy and 20–30 ns duration each. This system allows us to measure the plasma density in six points over plasma column diameter for the distance 140 cm from the beam injection point. In some experiments the Thomson scattering system was also used to measure the velocity distribution function of heated plasma electrons. Time dynamics of the plasma density is registered in the cross-section at the distance 80 cm by Michelson interferometer based on a CO_2-laser.

We developed two radiometric systems capable of measuring power of sub-mm emission. One of them has four parallel frequency-shifted spectral bands in the interval from 210 up to 430 GHz. The other radiometric system covers 8 channels in the interval from 100 up to 650 GHz. We use filters with a relative transition bandwidth of ~15 % and 50 dB out-of-band attenuation at 20–60 GHz frequency shift of adjacent transmission bands.

After passing through the filters, radiation beams are focused by aspheric teflon lenses ($f = 40$ mm, CA Ø70 mm) into the receiving horn antennas of the Shottky-detector units. Each detector, initially developed for operation at frequencies 210–450 GHz, is equipped with a built-in 900 MHz-band operational preamplifier and has the response time better than 2 ns. At 50 Ω loading resistance, the detector Volt-Watt sensitivities and dynamic ranges precisely measured with calibrated 280 GHz-solid-state radiation-source are within 1000–4000 V/W and 50 dB, respectively. The broadband calibration of the detectors with a tunable backward-wave oscillator has shown an acceptable level of their sensitivity up to ~530 GHz.

Results of experiments

In our previous experiments we established that spectrum of the emitted radiation essentially depends on the plasma density in the investigated area of the plasma column. For example, in the case of constant plasma density of $n_0 \approx 3 \cdot 10^{14}$ cm^{-3} during 6 μs of the electron beam injection we measured approximately constant ratio between the signals for three frequency bands [3]: 275 GHz, 312 GHz, and 350 GHz with the maximal radiation power at the frequency 312 GHz.

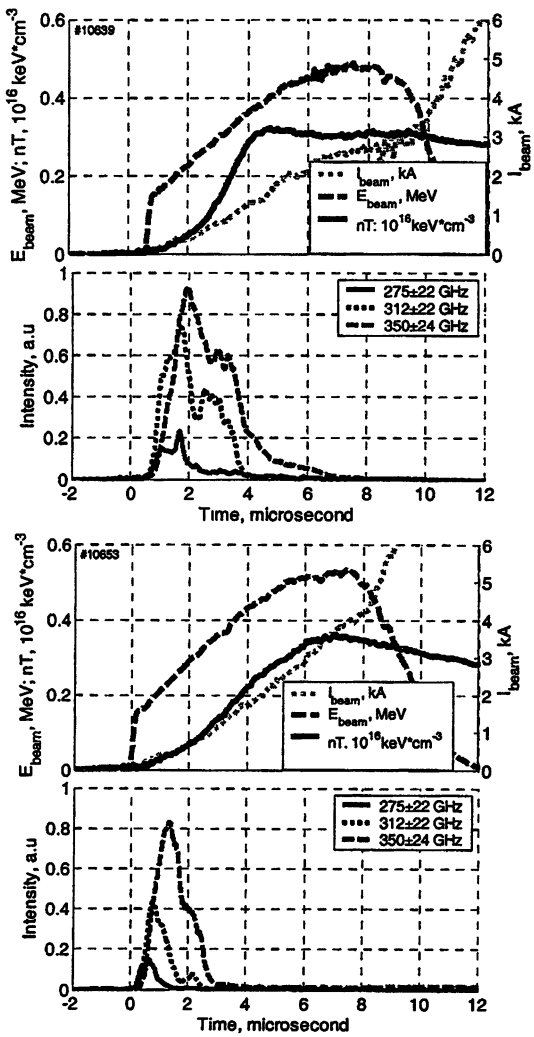

Fig. 2. Two shots at different plasma densities reached during the beam injection: PL10639 – $n_e \approx 5 \cdot 10^{14}$ cm^{-3}, PL10653 – $n_e \approx 7 \cdot 10^{14}$ cm^{-3}. Beam current in tens of kA

The opposite case is when the plasma density increases during the beam injection time. This occurs when the ionization degree of hydrogen at the beam injection start is about 50 % and then it increases up to 100 % with the increase of the plasma electron temperature up to 2–3 keV. For the final value of the plasma density $n_e \approx 5 \cdot 10^{14}$ cm^{-3} the dynamics of the emitted radiation in selected frequency bands is demonstrated by results of the measurements in the shot PL10639 and for $n_e \approx 7 \cdot 10^{14}$ cm^{-3} in the shot PL10653. One can see that increase in the plasma density during the injection time produces some shifting of the position of the maximum of the spectral power density. We also demonstrate in the experiments that increase of the frequency for the maximal power is not the only effect but also the spectral interval of the generated radiation is narrowed during the increase of the plasma density.

Such behavior of the distribution of EM-radiation power over frequency channels can be explained by the frequency spectrum of generated EM-radiation dependences on the ratio of electron gyrofrequency to the Langmuir frequency. When the ratio decreases the EM-radiation spectrum has to be more narrow [4]. On the base of this dependence we are waiting to achieve a small width of the generated spectrum by the increase in the plasma density value and by usage more lower strength of the magnetic field. Future experiments will be devoted to the e-beam injection into more dense plasma at magnetic field with essentially lower strength.

Acknowledgements

Support of this research by Russian Federation Government Grant N 11.G34.31.0033, by Contract #16.740.11.03.77 of Ministry Education and Science of the Russian Federation.

References

1. *Kruchina, E.N. et al.* Strong Langmuir turbulence as a source of radio emission// JETP Lett. 1980. V. 32, № 6. P. 419-423.

2. *Kuznetsov, S.A. et al.* Quasi-Optical Spectral System for Submm-Wave Radiometry of Turbulent Plasma // Proc. of the 39th European Microwave Conference, 2009, Rome, Italy. P. 173-176.

3. *Arzhannikov, A.V. et al* Subterahertz Generation by Strong Langmuir Turbulence at Two-Stream Instability of High-Current 1-MeV REBs // NSU Bulletin, Series: Physics. 2010. V. 5, №. 4. P. 44-49.

4. *Tirsky, V.V. et al.* Concerning the Elecromagnetic Radiation Spectrum of a Hot Plasma with Langmuir Turbulence in a Magnetic Field // Physica Scripta. 2001. V. 64. P. 353-359.

Superconducting Hot Electron Bolometer as THz Mixer, Direct Detector and Single-Photon Counter

G.N. Goltsman

Moscow State Pedagogical University, Moscow, Russia, goltsman@mspu-phys.ru

We present hot-electron superconducting sensors: terahertz mixers, direct detectors and single-photon counters. These sensors have already demonstrated a performance that makes them devices-of-choice for many terahertz and optical applications.

The superconducting hot electron bolometer (HEB) mixers (Fig. 1) based on ultrathin films of NbN combine the best sensitivity at the frequencies well above 1 THz and a gain bandwidth of about 6–7 GHz [1, 2] which make them suitable for most sensitive instruments being developed in the far IR region for astronomical and atmospheric studies.

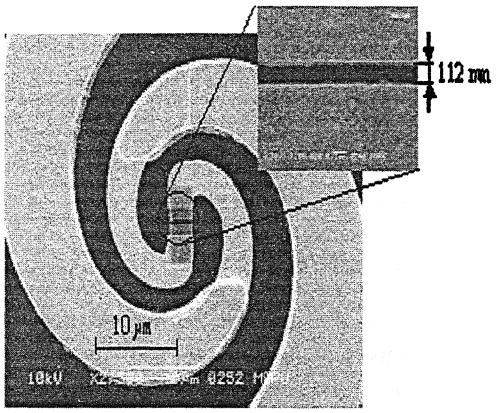

Fig. 1. A SEM image of a part of an HEB chip including the logarithmicspiral antenna and the mixing element at its apex. The inset is a close-up of the central part of the chip; the length of the mixer is 112 nm

Figure 2 shows the results of the gain bandwidth measurements for two devices 0.12 and 0.35 μm long. The data can be approximated using $P(f) \sim [1+(f/BG)^2]^{-1}$, with $B_G = 6.5$ GHz and $B_G = 3.5$ GHz for 0.12 and 0.35 μm, respectively.

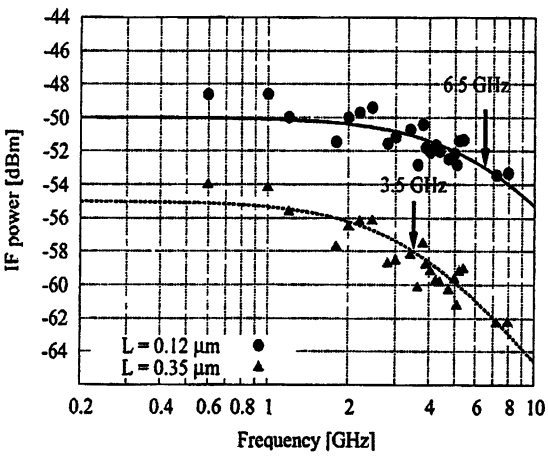

Fig. 2. The gain bandwidth measurement data for two HEB mixers with different lengths of the mixing element: 0.12 μm (circles) and 0.35 μm (squares). The solid lines are the fits $P(f) \sim [1+(f/B_G)^2]^{-1}$, with $B_G = 6.5$ and 3.5 GHz

Direct detectors made from NbN and MoRe films are operated in 0.3–3 THz range exhibit response time as low as 50 ps and 1 ns respectively with noise equivalent power (NEP) of $3 \cdot 10^{-13}$ W $Hz^{-1/2}$ (NbN) and $5 \cdot 10^{-14}$ W $Hz^{-1/2}$ (MoRe). Another versions of these detectors have a broadband sensitivity in 0.1–30 THz range with the same response time and exhibit higher NEP but much higher dynamic range.

A promising type of the photon counting detector is superconducting single-photon detector (SSPD). The SSPD is patterned from 4-nm-thick NbN film as 120-nm-wide and meander-shaped strip that covers a square area of 10×10 μm. At wavelength $\lambda \leq 1.3$ μm quantum efficiency (QE) of our best devices approaches 30 % at 2 K with 35 ps timing jitter. The single-photon counting was observed at wavelength up to 5.6 μm with QE of ~ 1 %. Simultaneously, at 2 K the SSPD has negligibly low dark counts of $2 \cdot 10^{-4}$ s^{-1}. It provides NEP value of 10^{-20} $W/Hz^{1/2}$ at $\lambda \leq 1.3$ μm and 10^{-18} $W/Hz^{1/2}$ at 5 μm. Our recent investigations allowed us to develop an SSPD with photon-number resolving capability. Single-, two-, three- and four-photon absorptions were clearly observed [3].

Further development of SSPD was to form it as parallel-connected strips. Such SSPD has a new quality: the ability to resolve the number of simultaneously absorbed photons, because the amplitude of the detector response is proportional to the number of incident photons. Simultaneously duration of the photoresponse decreased to 200 ps, enabling up to 1 GHz counting rate.

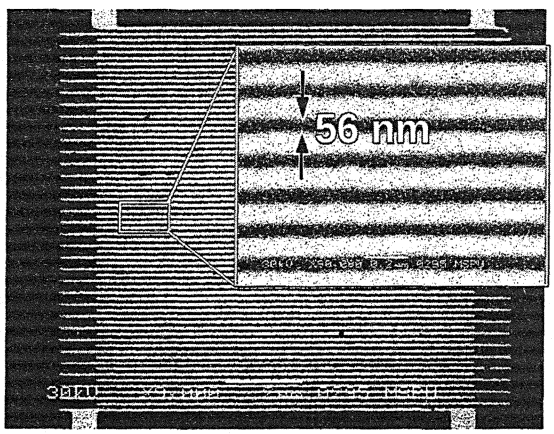

Fig. 3. SEM image of parallel-wire SSPD. Black is NbN film, white is the etched areas. We manage to produce 56-nm-wide strip retaining high superconducting properties

In an effort to move into the middle IR we managed to develop a SSPD with a strip width of 54 nm while preserving the superconducting properties. Fig. 3 presents a SEM image of the parallel-wire SSPD with 10×10 μm area and consisting of 46 strips

each 56-nm-wide. These detectors show more than an order of magnitude higher sensitivity at a wavelength of 5 μm. These results open the way to the development of the practical mid-infrared single photon detector.

SSPD can be efficiently coupled with a single mode optical fiber and thus can be easily integrated into a practical commercial dual-channel receiving system. The system has already found a number of practical applications in experiments on optical coherence tomography, detection of radiation from the quantum dots with high temporal resolution, as well as in quantum cryptography.

THz direct detectors and HEB mixers are used in a wide range of applications ranging from THz imaging for security (observation of hidden drugs, explosives and weapon) and medicine (THz probing of human tissues) to radioastronomy observation of stellar formation (space observatories Herschel and Millimetron). SSPD due to their high quantum efficiency and picosecond timing resolution has already been successfully applied for non-destructive testing of CMOS integrated circuits, study of single-photon sources and quantum dot luminescence, and for quantum cryptography enabling quantum key distribution over 250 km distance.

References

1. *I. Tretyakov, S. Ryabchun, M. Finkel, A. Maslennikova, N. Kaurova, A. Lobastova, B. Voronov, G. Gol'tsman* Low noise and wide bandwidth of NbN hot-electron bolometer mixers // Applied Physics Letters 98, 033507, 2011.

2. *S.A. Ryabchun, I.V. Tretyakov, M.I. Finkel, S.N. Maslennikov, N.S. Kaurova, V.A. Seleznev, B.M. Voronov, and G.N. Goltsman.* NbN Phonon-Cooled Hot-Electron Bolometer Mixer with Additional Diffusion Cooling // 20th International Symposium on Space Terahertz Technology, Charlottesville, 20-22 April 2009. P. 151-154.

3. *A.V. Divochiy, F. Marsili, D. Bitauld, A. Gaggero, R. Leoni, F. Mattioli, A. Korneev, V. Seleznev, N. Kaurova, O. Minaeva, G. Goltsman, K.G. Lagoudakis, M. Benkhaoul, F. Levy, A. Fiore.* Superconducting nanowire photon number resolving detector at telecom wavelength // Nature Photonics. 2008. V. 2. P. 302-306.

Performance of Sensitive Terahertz Photodetectors Based on $Pb_{1-x}Sn_xTe(In)$

D.E. Dolzhenko[1], V.I. Chernichkin[1], L.I. Ryabova[1], A.V. Nicorici[2], D.R. Khokhlov[1]

[1]M.V. Lomonosov Moscow State University, Moscow, Russia, khokhlov@mig.phys.msu.ru
[2]Institute of Applied Physics, Kishinev, Moldova

Recently, terahertz technologies have received a lot of attention due to attractive possibilities for numerous applications in medicine, ecological monitoring, security systems, high-resolution spectroscopy, and many other fields. One of the most challenging tasks in this area deals with applications in the space astronomy. For instance, the direct detector sensitivity goal for the BLISS instrument $3 \cdot 10^{-20}$ W/Hz$^{1/2}$ [1] requires improvement of the state-of-the-art by 2–3 orders of magnitude.

Several technologies are now considered as a base for reaching this goal. These technologies include quantum dot detectors, kinetic inductance detectors, superconducting transition edge sensors, hot electron bolometers (HEB). At this time, the lowest optical NEP of $3 \cdot 10^{-19}$ W/Hz$^{1/2}$ is reported for a Ti-based nanoHEB [2]. One of the major drawbacks of these technologies is extremely low operating temperature – not higher than 100 mK in most of the cases.

In this paper, we report on an alternative possibility based on unique features of a narrow-gap semiconductor – $Pb_{1-x}Sn_xTe(In)$ (for a review, see [3]). Making use of these features allows construction of an extremely sensitive direct detector of terahertz radiation demonstrating NEP as low as $6 \cdot 10^{-20}$ W/Hz$^{1/2}$ at the wavelength of 350 μm and much higher operating temperature of 1.5 K.

Doping of the lead telluride with indium in an amount exceeding concentration of other impurities and defects results in the Fermi level pinning effect. A consequence of this effect is homogenization of electrical properties of the semiconductor. High sample homogeneity gives rise to enhanced carrier mobility reaching 10^5–10^6 cm^2/V·s at low temperatures. Position of the pinned Fermi level E_0 may be tuned by alloying. It crosses the gap in the tin content range ($0.22 < x < 0.28$) providing appearance of the semiinsulating state for this range of alloy compositions. Conductivity of the material in the semiinsulating state ($0.22 < x < 0.28$) is defined by activation from the impurity local level E_0, and therefore the free carrier concentration is very low n, $p < 10^8$ cm^{-3} at temperatures $T < 10$ K. This makes very attractive the idea to use this material as a photodetector.

External infrared illumination leads indeed to the substantial increment of the material conductivity at the temperatures $T < 25$ K. High amplitude of photoresponse at the low temperatures is a consequence of the persistent photoconductivity effect: the photoresponse increases linearly in time providing a kind of «internal integration» of the incident radiation flux. When the radiation is switched off, the conductivity relaxes very slowly. The characteristic relaxation time $\tau > 10^4$ s at $4.2 \text{ K} < T < 10$ K, then it sharply decreases with the temperature rising, and $\tau \sim 10^{-2}$ s at $T \approx 20$ K. The effect is defined by the specifics of impurity states that form DX-like centers.

Two approaches have been used to explore spectral characteristics of the photoconductivity. In the first approach which may be called "low-background", a sample is completely screened from the background radiation, therefore the measurements can start from the "dark" conductivity state. The illumination source may be a cryogenic blackbody located in the same measurement cell [4], or an external blackbody being at the room or somewhat lower temperature [5, 6]. In the latter case, the sample field of view is restricted to the blackbody opening by a stop aperture cooled to the liquid helium temperature. A series of cold filters is used to "cut" a certain spectral line from the blackbody spectrum.

This experimental approach was used in [5, 6] for $Pb_{0.75}Sn_{0.25}Te(In)$. A series of cold filters were used to extract a certain spectral line in the terahertz range. It has been demonstrated that the persistent photoconductivity is observed in $Pb_{0.75}Sn_{0.25}Te(In)$ for the wavelengths of the incident terahertz radiation of 90, 116 μm [5], 176, 241 μm [6]. It is very important to note that the respective quanta energies are considerably lower than the ground impurity state thermal activation energy. It means that the local states which are responsible for this photoresponse at terahertz frequencies are not the ground impurity states that pin the Fermi level at ~20 meV below the conduction band bottom, but some other metastable local states lying close to the conduction band edge.

The question remains how far in wavelength does the photoconductivity spectrum expand. Another experimental approach has been used to clarify this question. In this approach which may be called "high-background", only standard cryogenic equipment is used, and the background illumination is not screened off. Therefore the concentration of non-equilibrium long-lived free electrons is very high at low temperatures. At the same time, photoexcitation is provided by strong pulses of terahertz laser radiation, and the photoresponse due to laser pulses may be observed even on top of the high concentration of free background electrons [7, 8].

In the experiments described in [7, 8], photoconductivity has been excited by ~100 ns long pulses of a terahertz gas laser with optical pumping. The laser wavelength was 90, 148, 280 or 496 μm with the power in a pulse up to 30 kW. The laser power could be varied by introduction of attenuators in the laser beam. The sample temperature varied from 4.2 to 30 K.

A considerable photoconductivity signal was observed at all laser wavelengths used up to 496 μm. The photoconductivity kinetics and its sign depended on the sample temperature. At T = 4.2 K, the positive photoconductivity with the characteristic time considerably exceeding the laser pulse length has been observed. As the temperature rose to T = 25 K, the photoconductivity sign has changed to the negative one, and the time profile of the signal reproduced the laser pulse time profile [7]. It has been shown that the positive persistent photoconductivity observed at T < 10 K is due to photoionization of metastable impurity states, whereas the negative photoconductivity with short relaxation time that prevails at higher temperatures T ~ 25 K corresponds to heating of free electrons with a laser pulse.

The data of [8] demonstrate that the red cut-off wavelength corresponding to the ionization energy of metastable impurity states which are responsible for the positive persistent photoconductivity in $Pb_{1-x}Sn_xTe(In)$ in the terahertz spectral range is at least higher than 496 μm.

One of the ways to increase the signal-to-noise ratio of photodetectors is integration of the incident signal. In terms of this, the persistent photoconductivity effect observed in $Pb_{1-x}Sn_xTe(In)$ gives a significant advantage for terahertz photodetecting systems based on these materials compared to the case of ordinary single photodetectors since it provides "internal" integration of the incident radiation flux. On the other hand, this advantage is valuable only if there exist a way to quench quickly the persistent photoconductivity. The most efficient way of such a quenching in $Pb_{1-x}Sn_xTe(In)$ samples is application of strong radiofrequency pulses to sample contacts. Using this technique, the long-living photoexcited free electrons may be localized for less than 10 μs. Therefore it became possible to operate in the regime of periodical accumulation and successive fast quenching of the photoresponse. Moreover, application of radiofrequency pulses in some special regime results in giant increment of the quantum efficiency up to ~ 100 (see [3]).

In this paper, we report on the performance of a laboratory model of the terahertz radiometer based on $Pb_{1-x}Sn_xTe(In)$ operating in the regime of periodical accumulation and successive fast quenching of the persistent photoconductivity, at the terahertz frequency of 350 μm. The $Pb_{0.75}Sn_{0.25}Te(In)$ sample was mounted in a closed metallic vacuum cell which was immersed in the liquid helium. The cryogenic blackbody was located in the same cell, but it was separated from the sample compartment by a stop aperture of 1.1 mm in diameter. The stop aperture had a direct thermal contact with the helium bath. A combination of two terahertz filters pressed to the stop aperture was used to select the spectral transmission line. The first filter was a band-pass filter with the center at 350 μm and the Q-factor 4. The filter transmission coefficient was 0.7 in the band, being less than 0.001 outside the band, except for a small spectral region at the double frequency, at which the transmission was several percent. To exclude the influence of this second transmission line, a low-pass filter was used in combination with the first one. Its transmission edge corresponds to about 200 μm with the transmission coefficient 0.9 at low frequencies. The filters were produced by the QMC Instruments. The helium vapor pressure in the cell was kept at 10^{-1} mbar to allow effective sample and blackbody cooling. The blackbody was heated from 0.5 K to 10 K above the cell temperature. The blackbody temperature T_b was controlled by a low-temperature Cu-Cu(Fe) thermocouple. The sample area was 0.3×0.2 mm. The sample temperature was varied from 4.2 K to 1.5 K by pumping off the helium vapor.

Even in the absence of the blackbody radiation, a sawtooth-like conductivity signal has been detected. The source of the terahertz radiation were the walls of the cell. As the cell temperature T_c decreased from 4.2 to 1.5 K, the amplitude of the signal decreased accordingly. The signal amplitude was considerable even at the quenching frequency of 100 Hz.

In order to provide chopping of the incident radiation flux, the blackbody heater was loaded by AC voltage from the internal source of a SR830 (Stanford Research Instruments) lock-in amplifier. A diode was connected in series with the heater to provide modulation of the blackbody temperature at the not doubled local source frequency. The amplitude and the shape of the blackbody temperature modulation was controlled by the thermocouple. It turned out that it was possible to modulate effectively the blackbody temperature at the frequency of 0.3 Hz. The saw-tooth like signal from the sample was loaded to the lock-in input. The signal-to-noise ratio appeared to be 1 already at $T_b = 4.7$ K for $T_c = 4.2$ K and $T_b = 2.7$ K for $T_c = 1.5$ K. These values correspond to NEP = $3 \cdot 10^{-17}$ W/Hz$^{1/2}$ at $T_c = 4.2$ K and NEP = $6 \cdot 10^{-20}$ W/Hz$^{1/2}$ at Tc = 1.5 K. The latter value nearly hits the requirements for the future space instruments. These data look very promising especially taking into account that the operating temperature is much higher than that for the analogs.

References

1. *C.M. Bradford, M. Kenyon, W. Holmes, J. Bock, T. Koch,* Proc. SPIE 7020, 70201O (2008).

2. *B.S. Karasik, R. Cantor,* arXiv:1009.4676v1 [astro-ph.IM] (2010).

3. *B.A. Volkov, L.I. Ryabova, D.R. Khokhlov,* Phys. Uspekhi 45, 819 (2002).

4. *B.A. Akimov, N.B. Brandt, L.I. Ryabova, D.R. Khokhlov,* Sov. Tech. Phys. Lett. 6, 544 (1980).

5. *D.R. Khokhlov, I.I. Ivanchik, S.N. Raines, D.M. Watson, J.L. Pipher,* Appl. Phys. Lett. 76, 2835 (2000).

6. *K.G. Kristovskiy, A.E. Kozhanov, D.E. Dolzhenko, I.I. Ivanchik, D. Watson, D.R. Khokhlov,* Phys. Solid State 46, 122 (2004).

7. *D. Khokhlov, L. Ryabova, A. Nicorici, V. Shklover, S. Ganichev, S. Danilov, V. Bel'kov,* Appl. Phys. Lett. 93, 264103 (2008).

8. *A.V. Galeeva, L.I. Ryabova, A.V. Nikorich, S.D. Ganichev, S.N. Danilov, V.V. Bel'kov, D.R. Khokhlov,* JETP Lett. 91, 35 (2010).

The Use of Quantum and Thermal Fluctuations for Calibration of the Terahertz Wave Spectral Brightness

G.Kh. Kitaeva

Faculty of Physics, M.V. Lomonosov Moscow State University, Moscow, Russia, kit@qopt.phys.msu.ru

Among different approaches for compact table-top terahertz wave (THz) sources, optical methods were in the forefront for the past few decades. They are advantageous not only due to possibility of effective THz generation by means of conversion of the optical laser energy into the THz gap, but also due to opportunity of room-temperature detection using the same laser source in the inverse process of the THz-to-optical conversion. Nevertheless, the problem of measurement of absolute radiometric quantities still remains as not properly solved for the THz radiation. Developing of radiometric standards for such parameters as THz radiation intensity, energy flux, spectral power density, and others, seems to become an actual task in the nearest future.

Recently we studied the schemes for detection of continuous-wave and nanosecond-pulsed THz radiation, based on parametric frequency conversion of the terahertz radiation into the optical range [1, 2]. These schemes enable to calibrate the most universal and informative parameter of the THz radiation, the spectral brightness (radiance) [2, 3]. Under nonlinear-optical detection, the THz radiation is involved as an idler radiation into the parametric processes of sum-frequency and difference-frequency generation, so that the output optical signals at the shifted frequencies are proportional to the input THz spectral brightness. Being expressed in terms of the mean numbers of photons per optical output mode, $N_{1'}^{sum,dif}$, and per terahertz input mode, N_2^{THz}, this linear relation takes the form

$$N_{1'}^{sum,dif} = \left|U_{1'2}^{sum,dif}\right|^2 N_2^{THz}. \qquad (1)$$

The mean number of photons per mode $N_2^{THz} \equiv \left\langle a_2^+ a_2 \right\rangle$ represents a spectral brightness of the THz source in quantum units, since it is directly proportional to the radiometric spectral brightness B_ω [4]:

$$B_\omega = \frac{\hbar \omega_{THz}^3}{8\pi^3 c^2} N_2^{THz}. \qquad (2)$$

The optical-to-terahertz conversion coefficients $\left|U_{1'2}^{sum,dif}\right|^2$ can be calibrated using the signals of spontaneous parametric down- and up-conversion of the pump radiation, which necessarily accompany the induced generation processes. This idea comes from the first work [5] of D.N. Klyshko, who proposed the use of zero-vacuum electromagnetic field fluctuations for the absolute calibration of the spectral radiance in the optical range via the process of spontaneous parametric down-conversion (SPDC). The specificity of the terahertz range requires significant developing of theoretical foundations of this method. The Stokes SPDC signals, corresponding to the THz idler frequencies, are proportional not only to effective brightness of quantum fluctuations (that is equal to N_{vac}=1 photon/mode), but also to brightness of the thermal field fluctuations N_T:

$$N_{1'}^{SPDC} = \left(\left|U_{1'1}^{dif}\right|^2 - 1\right)(1 + N_T). \qquad (3)$$

SPDC signals appear at the difference frequencies $\omega_{1,s} = \omega_0 - \omega_{THz}$ (ω_0 is the optical pump frequency). Under the equilibrium conditions, effective brightness of the thermal fluctuations is determined by the crystal temperature T and depends strongly on the THz frequency:

$$N_T = \left[\exp(\hbar\omega_{THz} / k_B T) - 1\right]^{-1}. \qquad (4)$$

Since N_T is not small in the THz range, additional spontaneous anti-Stokes signals are generated at the sum frequencies $\omega_{1,as} = \omega_0 + \omega_{THz}$ (as for example, see Fig. 1). Intensities of these so called "spontaneous parametric up-conversion" (SPUC) signals are determined by the thermal fluctuations only:

$$N_{1'}^{SPUC} = \left(\left|U_{1'1}^{sum}\right|^2 - 1\right) N_T. \qquad (5)$$

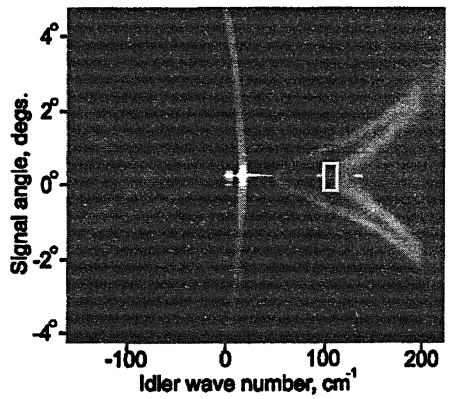

Fig. 1. Frequency-angular spectra of SPDC (positive idler wave numbers) and SPUC (negative idler wave numbers), recorded in the *eee*-geometry in a periodically poled lithium niobate crystal. The pump wavelength is 514.5 nm. The white rectangle denotes area where the THz-induced difference-frequency signal appears under detection of the forward-propagating THz wave

If the nonlinear crystal is transparent at optical and THz frequencies, conversion and amplification coefficients are connected by the relations $\left|U_{1'2}^{sum,dif}\right|^2 = \left|U_{1'1}^{sum,dif}\right|^2 - 1$. This makes a base for absolute calibration of the thermal fluctuations brightness, of the local crystal temperature inside the

laser beam, and of the input THz radiation spectral brightness. For these purposes, the signals at Stokes and anti-Stokes optical frequencies have to be measured at the output of the crystal when the THz radiation is switched off (P_{SPDC}, P_{SPUC}) and on ($P_{SPDC+DFG}$, $P_{SPUC+SFG}$). Then the THz spectral brightness and the local crystal temperature are determined as

$$N_2^{THz} = \frac{1}{(\Delta p_s)^{-1} - (\Delta p_{as})^{-1}}, \qquad (6)$$

and

$$T = \frac{\hbar\omega_{THz}}{k_B \ln(\Delta p_{as} / \Delta p_s)}, \qquad (7)$$

taking the relative DFG- and SFG-caused increments, $\Delta p_s \equiv (P_{SPDC+DFG} - P_{SPDC})/P_{SPDC}$ and $\Delta p_{as} \equiv (P_{SPUC+SFG} - P_{SPUC})/P_{SPUC}$. By this way, both the thermal fluctuations and the input THz radiation are calibrated simultaneously, using the quantum fluctuations as an internal reference.

Nevertheless, effects of absorption of the terahertz radiation in the nonlinear crystal usually cannot be neglected. Idler-radiation losses in the crystal were considered specially in the low-gain and constant pump approximations. It was found, that the conversion coefficients are directly determined by the crystal nonlinear transfer function, $T(\Delta k) \equiv \equiv \frac{1}{L}\int_{-L/2}^{L/2} \chi(x) e^{i\Delta kx} dx$, and absorption $y_2 \equiv \alpha_{THz} L_{THz}/2$ of the THz waves along their path $L_{THz} = L/\cos\vartheta_2$ inside a crystal (L is the crystal length, ϑ_2 is the angle of propagation),

$$U_{1'2}^{dif,sum} = -i\rho e^{-y_2/2} T(\Delta k) . \qquad (8)$$

For the case of collinear propagation of optical and THz waves, $\rho = 2\pi E_0 \sqrt{\omega_1 \omega_{THz} / n_1 n_{THz}}\, L/c$. At the same time, the amplification coefficients have another dependence on the absorption coefficient α_{THz} and the complex phase mismatch Δk :

$$U_{1'1}^{dif,sum} = 1 + \rho^2 D(\Delta k),$$
$$D(\Delta k) = \sum_m \chi^*_m \frac{e^{i(\Delta kL + 2\pi m)/2} T(\Delta k) - \chi_m}{i(\Delta kL + 2\pi m)}, \qquad (9)$$

Here, χ_m are Fourier harmonics of the spatial distribution of the second-order crystal susceptibility $\chi(x)$,

$$\chi_m = \frac{1}{L}\int_{-L/2}^{L/2} \chi^{(2)}(x) e^{-i2\pi mx/L} dx . \qquad (10)$$

Thus, the pre-calculated THz loss coefficient $\kappa(\omega_{THz})$ should be taken into account in the measuring procedure in the case if absorption and reflection losses of the incident THz radiation in the crystal are essential:

$$N_{THz} = \frac{\kappa(\omega_{THz})}{(\Delta p_s)^{-1} - (\Delta p_{as})^{-1}} . \qquad (11)$$

$\kappa(\omega_{THz})$ is dependent on the crystal THz absorption (y_2) and reflection (R_{THz}) coefficients as

$$\kappa(\omega_{THz}) = \frac{2}{1 - R_{THz}} \cdot \frac{e^{-y_2} - 1 + y_2}{\left(1 - e^{-y_2}\right)^2} . \qquad (12)$$

Fig. 2 shows the results of calculations of $\kappa(\omega_{THz})$, made for the case of pure and 5% Mg-doped congruent lithium niobate crystals of a 1 mm length, for collinear DFG and SFG processes with forward-propagating THz waves [2]. As it is seen, κ is far from 1 even at low THz frequencies and has to be taken into account under the THz calibration with such type of crystals.

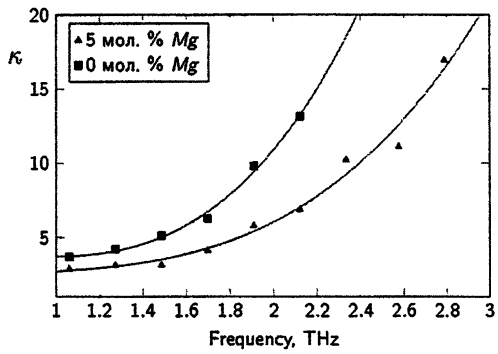

Fig. 2. Estimated spectral dependences of the loss coefficient $\kappa(\omega_{THz})$ for 1-mm long pure (upper squares) and 5% Mg-doped (lower triangles) congruent lithium niobate crystals [2]

This work was supported by the Federal Agency of Science and Innovations of the Russian Federation (state contract No.02.740.11.0223) and by the Russian Foundation for Basic Research, project Nos.10-02-00427 and 09-02-92003.

References

1. *Kitaeva, G. Kh., Penin, A. N., Tuchak, A. N.* Generation and detection of terahertz radiation by means of periodically and aperiodically poled crystals // Opt. Spectrosc. 2009. V. 107, No. 4. P. 521-528.

2. *Kitaeva, G.Kh., Kovalev, S.P., Penin, A.N., Tuchak, A.N., Yakunin, P.V.* A method of calibration of terahertz wave brightness under nonlinear-optical detection // J. Infrared Milli. Terahz. Waves. 2011. V. 32 (online first).

3. *Kitaeva, G.Kh., Penin, A.N., Tuchak, A.N., Shepelev, A.V., Yakunin, P.V.* Measurement of the spectral brightness of terahertz radiation in the process of nonlinear optical detection // JETP Lett. 2010. V. 92, No. 5. P. 291-294.

4. *Klyshko, D.N.* Photons and Nonlinear Optics. New York: Gordon and Breach. 1988. P. 9-12.

5. *Klyshko, D.N.* Utilization of vacuum fluctuations as an optical brightness standard // Sov. J. Quantum Electron. 1977. V. 7, No. 5. P. 591-594.

Field Effect Transistors for Terahertz Detection and Emission

Wojciech Knap, Nina Dyakonova, Dominique Coquillat, Frederic Teppe

TERALAB &L2C Universite Montpellier 2 and CNRS, Montpellier, 34095 France
E-mail: knap @univ-montp2.fr

We review a few recent results concerning the physics and applications of Field Effect Transistors (FETs) as Terahertz detectors and emitters. Particulary we stress results concerning dependance of THz detection and emission on high/quantizing magnetic fields and the geometry of the transistor channel.

1. Introduction

THE channel of a field effect transistors (FETs) can act as a resonator for plasma waves. The frequency of plasma waves propagating this resonator depends on its dimensions, and for gate lengths of a micron and sub-micron (nanometer) size can reach the sub-Terahertz or Terahertz (THz) range. The interest in the applications of FETs for THz spectroscopy started at early 90's with a pioneering theoretical work of Dyakonov and Shur [1] who predicted that a steady current flow in a FET channel can become unstable against generation of plasma waves. These waves can, in turn, lead to the emission of electromagnetic radiation at the plasma wave frequency. This work was followed by another one where the same authors have shown that nonlinear properties of the 2D plasma in the transistor channel can be used for detection of THz radiation [2]. THz emission in nW power range from submicron InGaAs and GaN FETs has been observed both at cryogenic and room temperatures [3–5]. THz detection by FETs is due to nonlinear properties of the transistor, which lead to the rectification of the ac current induced by the incoming radiation. The photoresponse appears in the form of a dc voltage between source and drain. This voltage is proportional to the radiation intensity (photovoltaic effect). The more information on the state of the art of the FETs as the emitters and detectors can be found in review papers [6–7].

In the present paper, we present an overview of most recent results concerning THz detection and emission by FETs. The dependance of THz detection and emission on high/quantizing magnetic fields and the geometry of the transistor channel are discussed.

2. Detection in quantizing magnetic fields

Very interesting physical effects were recently observed while studying THz detection in quantizing magnetic fields. The photovoltaic detection signal was investigated as a function of the gate voltage and magnetic field using InGaAs/InAlAs FETs and GaAs/AlGaAs FETs. Oscillations analogous to the Shubnikov-de Haas oscillations as well as their strong modification at the cyclotron resonance condition were observed [8, 9].

The measured photoresponse dependences as functions of magnetic field, B, revealed a pronounced oscillating behavior periodic with 1/B. The amplitude of the photoresponse signal but also its polarity oscillated with the magnetic field. The measured magnetoresistance also revealed oscillations periodic in 1/B, correlated with those of the photoresponse. The period of both types of oscillations was the same and changed with the gate voltage in the same manner. The most remarkable effect is a $\pi/2$ phase shift between the photoresponse and magnetoresistance oscillations. Both effects (the periodicity and the phase shift) are explained by Lifshits-Dyakonov theory [10].

3. Emission from GaN/AlGaN transistors

As already mentioned in the introduction, the interest in the applications of FETs for THz spectroscopy started at early 90's with a pioneering theoretical work of Dyakonov and Shur [1] who predicted that a steady current flow in a FET channel can become unstable against generation of plasma waves. These waves can, in turn, lead to the emission of electromagnetic radiation at the plasma wave frequency. THz emission in nW power range from submicron InGaAs and GaN FETs has been observed both at cryogenic as well as at room temperatures [3–5]. However, in most experiments, the emission did not depend on the gate voltage as predicted in [1].

Only recently a tunable THz emission has been observed at room temperature from AlGaN/GaN-based high electron mobility transistors [15]. The emission appeared in a threshold-like manner, and was accompanied by a drop in the drain current. For a spectral analysis of the radiation a Fourier transform spectrometer under vacuum has been used.

As mentioned above, in earlier experiments [3–5] mainly a broadband, gate independent emission was observed. A possible explanation was given only recently by M. Dyakonov [16]. The main reason is that the transistor geometry is very different from the one-dimensional model adopted in [1]. In a standard experimental situation, the width W of the gate is much larger than the gate length L. Under such conditions the oblique plasma waves also can propagate. In such geometry, the gated region is not a resonator, but rather a waveguide with a continuous spectrum of plasma waves. In Ref. 16, an analysis of the instability was extended to a more realistic case when W>>L, and it was shown that in such a geometry an additional new mode of instability dominates, which is localized near the gate boundaries and results in a broad spectrum of the plasma oscillations.

In conclusion, we have presented an overview of experimental results on plasma excitation in field ef-

fect transistors with nanometric gates. We observed also nonresonant overdamped plasma modes in room temperture detection experiments. Recent results on voltage-tunable THz emission from GaN based FETs were discussed as well. Results on THz detection and emission allow one to propose them as new valuable elements for THz imaging and spectroscopy. Their real importance comes from the fact that using modern microelectronic technology many of these elements can be easily integrated into arrays to make focal plane arrays (detectors) or high power emitters (sources).

References

1. *M.I. Dyakonov, M.S. Shur*, "Shallow water analogy for a ballistic field effect transistor: New mechanism of plasma wave generation by dc current", Phys. Rev. Lett., vol. 71, p. 2465-2468, 1993.

2. *M.I. Dyakonov, M.S. Shur*, "Plasma wave electronics: novel terahertz devices using two dimensional electron fluid," IEEE Trans. Electron Devices, v. 43, p. 380-387, 1996.

3. *W. Knap, J. Łusakowski, T. Parenty, S. Bollaert, A. Cappy, V.V. Popov, M. S. Shur*, "Terahertz emission by plasma waves in 60 nm gate high electron mobility transistors", Appl. Phys. Lett., v. 84, p. 3523-3525, 2004.

4. *N. Dyakonova, F. Teppe, J. Łusakowski, W. Knap, M. Levinshtein, A. P. Dmitriev, M. S. Shur, S. Bollaert, A. Cappy*, "Magnetic field effect on the terahertz emission from nanometer InGaAs/AlInAs high electron mobility transistors", J. Appl. Phys., v. 97, p. 4313-4317, 2005.

5. *N. Dyakonova, A. El Fatimy, J. Łusakowski, W. Knap, M. I. Dyakonov , M. A. Poisson, E. Morvan, S. Bollaert, A. Shchepetov,Y. Roelens, Ch. Gaquiere, D. Theron, and A. Cappy*, "Room temperature terahertz emission from nanometer field-effect transistors", Appl. Phys. Lett., v. 88, p. 141906-141908, 2006.

6. *W. Knap, F. Teppe, N. Dyakonova, D. Coquillat, J Łusakowski*, "Plasma wave oscillations in nanometer field effect transistors for terahertz detection and emission", J. Phys.: Condens. Matter, v. 20, 384205, 2008.

7. *W. Knap, M. Dyakonov, D. Coquillat, F. Teppe, N. Dyakonova, J. Łusakowski, K. Karpierz, G. Valusis, D. Seliuta, I. Kasalynas, A. El Fatimy, T. Otsuji*, "Field Effect Transistors for Terahertz Detection: Physics and First Imaging Applications", J. Infrared Milli Terahz Waves, v. 30, 1319, 2009.

8. *S. Boubanga-Tombet, M. Sakowicz, D. Coquillat, F. Teppe, N. Dyakonova, W. Knap, K. Karpierz, J. Łusakowski*, Terahertz Detection by Field Effect Transistor in High Magnetic Fields: Influence of Shubnikov – de Haas and Cyclotron Resonance Effects, Appl. Phys. Lett., v. 95, p. 072106- 072108, 2009.

9. *O.A. Klimenko, Yu.A. Mityagin, H. Videlier, F. Teppe, N.V. Dyakonova, C. Consejo, S. Bollaert, V.N. Murzin, and W. Knap*, Terahertz Response of InGaAs Field Effect Transistors in Quantizing Magnetic Fields, Submitted to Appl. Phys. Lett, May 2010.

10. *M. Lifshits, M. Dyakonov*, Photovoltaic effect in a gated two-dimensional electron gas in magnetic field, Phys. Rev. B, v. 80, 121304, 2009.

11. *W. Knap, F. Teppe, Y. Meziani, N. Dyakonova, and J. Lusakowski, F. Boeuf and T. Skotnicki, D. Maude, S. Rumyantsev and M. S. Shur*, App. Phys. Lett., v. 85, p. 675-677, 2004.

12. *R. Tauk, F. Teppe, S. Boubanga, D. Coquillat, W. Knap, Y.M. Meziani, C. Gallon, F. Boeuf, T. Skotnicki, C. Fenouillet-Beranger, D.K. Maude, S. Rumyantsev, M.S. Shur*, Appl. Phys. Lett., v. 89, p. 253511-253513, 2006.

13. *A. Lisauskas, U. Pfeiffer, E. Öjefors, P.H. Bolìvar, D. Glaab, and H.G. Roskos*, "Rational design of high-responsivity detectors of terahertz radiation based on distributed self-mixing in silicon field-effect transistors" J. Appl. Phys., v. 105, 114511, 2009.

14. *F. Schuster, H. Videlier, D. Coquillat, M. Sakowicz, F. Teppe, B. Dupont, B. Giffard, W. Knap*, "Imaging above 1 THz limit with Si-MOSFET detectors", accepted IRMWW Conference Rome 2010.

15. *A. El Fatimy, N. Dyakonova, Y. Meziani, T. Otsuji, W. Knap, S. Vandenbrouk, K. Madjour, D. Théron, C. Gaquiere, M.A. Poisson, S. Delage, P. Pristawko, C. Skierbiszewski*, AlGaN/GaN high electron mobility transistors as a voltage-tunable room temperature terahertz sources J. of Appl. Phys., v. 107, p. 024504-024507, 2010.

16. *M.I. Dyakonov*, Boundary Instability of a Two-dimensional Electron Fluid, Semiconductors, v. 42, p. 984-988, 2008.

Imaging with a High-Power Monochromatic Terahertz Source: Techniques and Applications

B.A. Knyazev[1,2]

[1] Budker Institute of Nuclear Physics, Novosibirsk, 630090, Russia
[2] Novosibirsk State University, Novosibirsk, 630090, Russia

Introduction

Gradually appearing high-power terahertz sources necessitates the development of adequate imaging techniques. The Novosibirsk free electron laser (NovoFEL) is nowadays the most intense source of terahertz radiation [1]. It generates a monochromatic coherent radiation as a continuous stream of 100-ps pulses with a repetition rate of 5.6 MHz. Now the radiation wavelength of the laser can be precisely tuned within spectral ranges of 120–240 μm and 40–80 μm. The average power of radiation at the user stations, depending on the wavelength, can vary from ten's to several hundred Watts.

The unique features of the NovoFEL radiation, on the one hand, necessitate elaborating techniques for radiation imaging and characterization and, on the other hand, enable the development of new methods and techniques for many applications. In this paper our attention will be focused on a comparative description of four real-time imaging techniques [2] and the results achieved with their help in a number of applications. All experiments described in this paper have been carried out at a wavelength of about 130 μm.

Imaging devices

We used both indirect and direct terahertz imaging. In the first case "secondary" recorders (Princeton Instruments PI Max2 intensified CCD camera or nitrogen-cooled AsIn-matrix thermal recorder), sensitive to visible or near-infrared radiation, were used for registration of thermal fingerprints of the terahertz beam. Many screens non-transparent to both terahertz and NIR radiation were employed for terahertz radiation sensing in the combination with the thermal recorder (TR). Because of a low matrix size (128×128) and geometrical restrictions in optical systems, the TR-based device possessed a low spatial resolution (see the Table) and was mostly used for THz beam tracing.

A set of Macken Instruments temperature-sensitive phosphor plates (TSPP) enabled sensing terahertz radiation via thermal quenching of visible-light luminescence induced by mercury lamp [3], which was recorded with PI Max2. This device has a large plate size, 75×75 mm, but a low sensitivity, and was used in the applications when wide field was critically important, e. g. for recording of holograms in the THz range.

A thermal-sensitive Fizeau interferometer (TSFI) operated as an absolute meter of THz power density distribution [4]. It consists of a BK7 glass plate illuminated with a plane wave from a semiconductor laser (λ = 656 nm). Interference pattern is produced by the beams reflected from front and rear glass surfaces. After opening the shutter, PI Max2 camera records the change of the interference pattern (Fig. 1) that enables the reconstruction of THz power density distribution (5.1 J/cm^2 per fringe). Obviously, this device operates only in a transient mode, but has a good time and space resolution (see the Table).

Table

	TR	TSFI	MBFPA	TSPP	
				Pl. #7	Pl. #8
Δx (mm)	2	0.3	0.3	1	2
Δt (s)	DS*	0.02	0.02	0.4	1.3
Sensitivity	High	Medium	Very high	Very low	Low
f (fps)	25	10–50	10–50	4–25	4–25

* depends on screen thermal characteristics

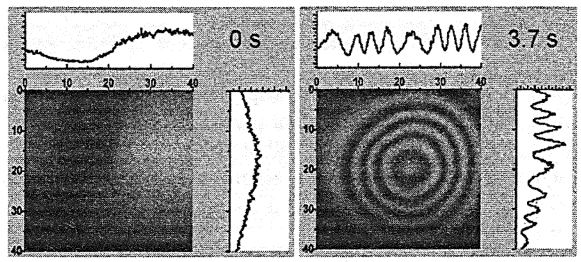

Fig. 1. FEL beam image: Interferograms recorded with TSFI before exposition and at 3.7 s after opening the shutter (frames selected from a video recorded with a repetition rate of 17 frames per second)

An uncooled microbolometer focal plane array (MBFPA) [4] is directly sensitive to terahertz radiation. High sensitivity, as well as good space and time resolutions (see the Table) of the device, enables obtaining high quality images in real time. Figure 2 demonstrates the images registered with three devices using the same optical system. It is worthy to mention that the mechanism of sensitivity of the vanadium oxide microbolometers appears to be mostly the "parasitic" antenna effect on electric contacts, but not heating of sensitive elements directly by terahertz radiation [2].

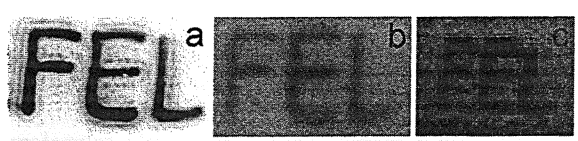

Fig. 2. Images of the "FEL" mask recorded by (*a*) the microbolometer focal plane array; (*b*) with the temperature sensitive phosphor plate and (*c*) with the thermal recorder

New applications of terahertz imaging

Talbot effect. The Talbot effect (TE), the self-imaging of periodical structures illuminated by monochromatic coherent radiation, has been first observed in the terahertz spectral range and applied to measurements of distances, FEL wavelength and distortion of wavefront passing through gas or condense matter. Some images of a 2D grid of openings with a period of 2 mm obtained with the MBFPA in the Talbot main and fractional planes are shown in Fig. 3. It is clearly seen the applicability of the effect to many metrological goals. A unique opportunity for one-shot recording of phase-shifting holograms gives the Talbot "quarter-plane" (Fig. 3, *c*), because, according to the theory, each of the double-frequency circles has $\pi/2$ phase shift.

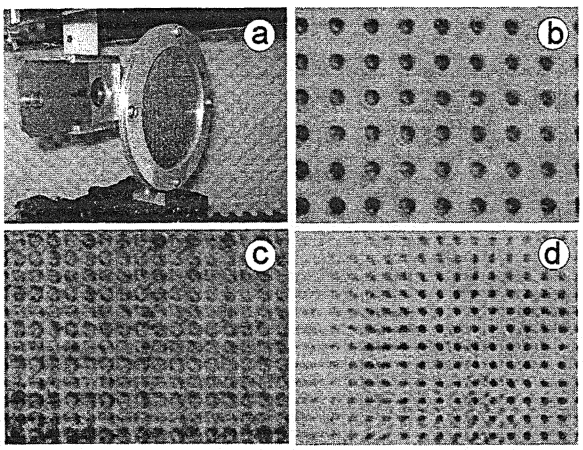

Fig. 3. Talbot effect: (*a*) the experimental setup, (*b*) an image recorded in a main Talbot plane ($Z_T = 2Np^2/\lambda$, where p is a grid period and N is a Talbot plane number), (*c*) an image in a ($N + \frac{1}{4}$) fractional Talbot plane, and (*d*) the distortion of FEL wavefront by a $f = 50$ mm TPX lens; $\lambda = 126$ μm

Terahertz speckles. The imaging devices were applied to real-time detection and imaging of different objects illuminated with directional or scattered coherent terahertz radiation. The images of rough objects were observed to have a speckled structure, which was used for the implementation of speckle photography, the detection of concealed objects, including automatic movement sensing, and detection of interior structure of bulk objects.

Surface plasmons. An optical system consisting of the MBFPA and a Fresnel polyethylene lens was used for the imaging of the 2D distribution of intensity of the terahertz wave transmitted along gold-air interface in the experiments with surface plasmons. The measurements using a Goley cell are presented in [6].

Holography. Experiments on the "classic" in-line holography enable reaching a spatial resolution in the retrieved images of 0.4 mm that is about three radiation wavelengths [7]. Reference-beam holograms were recorded using a modified Mach-Zehnder interferometer.

Tomography. A "classic" tomography system was developed for the terahertz region and applied for recording tomographic projections using TSPP. Because of strong diffraction in the terahertz range, tomography in this region is a "diffraction tomography," and the development of new methods for object reconstruction is very important.

Optical coherent tomography. Feasibility of the examination of inner structure of thick layered objects using 100-ps FEL pulses by optical coherent tomography technique has been demonstrated. The setup consisted of a Michelson interferometer with a thin polypropylene beamsplitter, computer-controlled moving mirror and MBFPA.

References

1. B.A. Knyazev, G.N. Kulipanov, N.A. Vinokurov. Novosibirsk terahertz free electron laser: Instrumentation development and experimental achievements // Meas. Sci. Technol. V. 21, 054017, 13 p. 2010.

2. B.A. Knyazev, V.S. Cherkassky, Y.Y. Choporova et al. Real-time imaging using a high-power monochromatic terahertz source: comparative description of imaging techniques with examples of application // Journal of Infrared, Millimeter, and Terahertz Waves, 2011, DOI: 10.1007/s10762-011-9773-x.

3. B.A. Knyazev, V.V. Kubarev. Real-time wide-field imaging using a tunable terahertz free electron laser and a thermal image plate. Infrared Physics and Technology, V. 52, 14, 2009.

4. N.A. Vinokurov, B. A. Knyazev, G. N. Kulipanovet et al. Visualization of radiation from a high-power terahertz free electron laser with a thermosensitive interferometer. Technical physics, V. 52, p. 911-919, 2007.

5. M.A. Dem'yanenko, D.G. Esaev, B.A. Knyazev et al. Imaging with a 90 frames/s microbolometer focal plane array and high-power terahertz free electron laser. Appl. Phys. Lett. V. 92, 131116, 2008.

6. V.V. Gerasimov, B.A. Knyazev, A.K. Nikitin, G.N. Zhizhin. Experiments on generation of surface plasmons using terahertz radiation of a free-electron laser. These Proceedings.

7. Yu.Yu. Choporova, V.S. Cherkassky, B.A. Knyazev. In-line and reference-beam holography experiments at Novosibirsk free electron laser. These Proceedings.

The Control of THz Generation in a Dual-Color Pulse by Molecular Alignment

Wenxue Li, Min Li, Haifeng Pan, Jian Wu, Heping Zeng

State Key Laboratory of Precision Spectroscopy, East China Normal University, Shanghai 200062, People's Republic of China
hpzeng@phy.ecnu.edu.cn

Strong THz radiation is of significant importance for many applications such as nonlinear THz spectroscopy and THz biology. With the promise to acquire strong THz radiation at remote targets without detrimental absorption attenuation by water vapor in air, THz generation by optical filament in gases [1, 2] is especially catching our eyes, and its dynamic control could be attained by tuning the pump pulse chirp and pump beam profile [3, 4]. Enhanced THz generation has been demonstrated in static electric field biased intense filament, two partially overlapped parallel filaments, or dual-color filaments in air, which could be well explained by the so-called plasma current model [5]. For the THz enhancement driven by dual-color filaments in air, the intensity and polarization of the generated THz radiation could be controlled by adjusting the relative phase. On the other hand, impulsive molecular alignment could induce ultrafast birefringence in air, and molecular alignment induced cross-phase modulation was demonstrated efficiently for remote control of intense femtosecond filaments. Furthermore, some unique effects have been revealed in molecular alignment mediated THz generation driven by dual-color filaments in air [6].

We demonstrated an all-optical way to control the THz generation and to implement the ultrafast THz polarization switching driven by dual-color fs laser pulses [7], where the impulsive field-free molecular alignment functioned as a transient dynamic wave-plate to modulate the relative phase of the dual-color components with its fundamental wave (FW) and second harmonic (SH) wave orthogonally polarized. An evident polarization switching of THz radiation was observed. The intensity of the THz generation could also be promoted or decreased by the focusing or defocusing effects induced by the molecular alignment in air.

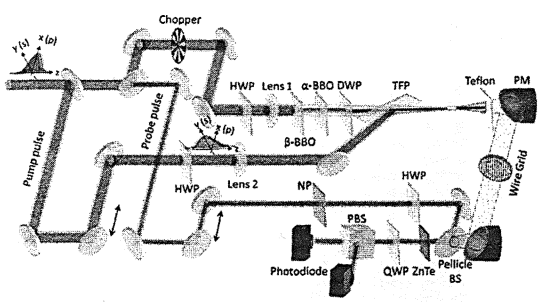

Fig. 1. Experimental set up

The orthogonally polarized dual-color pulse was generated by focusing the pulse through β-BBO crystal, and the parallel components were obtained via a dual-color wave plate (DWP). The air molecules were aligned by pump pulse through collinear combination with dual-color pulse by a thin film polarizer. The THz radiation was detected by EO sampling. The result indicated the measured THz intensity as a function of the M-pulse time delay, which periodically followed molecular alignment signals. As the refractive index change of pre-aligned molecules could be expressed as

$$\delta n(r, t) = 2\pi\rho_0\Delta\alpha/n_0(<<\cos^2\theta_\perp(r, t)>>-1/3) \quad (1)$$

where $\Delta\alpha$, ρ_0 and n_0 denote the molecular polarizability difference, initial molecular density, and linear refractive index, respectively, the cross-(de)focusing effect caused in parallel (perpendicular) aligned molecules induced a positive (negative) refractive index change of medium, which increased (decreased) the field intensity and plasma photon-current and in the end led to the increase (decrease) of the THz generation. For the parallel polarized components of the dual-color pulse, around zero time delay, the dual-color pulse intensity increased due to the increase of refractive index caused by spatial cross-phase modulation (XPM) between dual-color pulse and M-pulse, which induced the enhancement of THz generation. After the zero time, the baseline of THz radiation decreased because of the decrease of dual-color pulse intensity caused by the plasma defocusing effect. The polarization of generated THz always kept the same for parallel polarized FW and SH components, although the THz intensity changed.

For FW⊥SH, which was perpendicular and parallel to the M-pulse polarization. The change of THz intensity had the similar periodic modulation with the change of FW pulse caused by alignment-induced (de)focusing effect, whose intensity was more than the SH one. The cooperation or competition between the molecular alignment, plasma, and Kerr effects on the THz generation also occurs for orthogonally polarized FW and SH components of the dual-color pulse. The great interesting for the orthogonally polarized dual-color pulse was that the molecular alignment-induced cross-phase modulation could rotate the polarization of THz radiation at different time revivals. For the orthogonally polarized FW and SH components, the experienced molecular alignment revivals was opposite and so the refractive index change was also opposite. For example, for the perpendicular molecular alignment revivals whose molecular axis perpendicular to the FW polarization, the refractive index was decreased. Oppositely, the molecular axis

was parallel to the SH, which increased the SH component. The change of refractive index increased and decreased the propagation velocities of the FW and SH components, respectively.

In summary, we demonstrated that molecular alignment could be used as an ultrafast way to control the intensity and polarization of THz radiation. For the orthogonally polarized components of dual-color pulse, the molecular alignment could be used as a transient wave plate, which rotated the polarization of THz radiation through changing the phase delay between FW and SH wave. The use of molecular alignment makes the control of THz radiation in femtosecond scale.

References

1. *W. Hoyer, A. Knorr, J. V. Moloney, E. M. Wright, M. Kira, and S. W. Koch*, Photoluminescence and Terahertz Emission from Femtosecond Laser-Induced Plasma Channels // Phys. Rev. Lett. 2005. V. 94, 115002.

2. *C.C. Cheng, E.M. Wright, and J.V. Moloney*, Generation of Electromagnetic Pulses from Plasma Channels Induced by Femtosecond Light Strings // Phys. Rev. Lett. 2001. V. 87, 213001.

3. *J. Dai, X. Xie, and X.-C. Zhang*, Terahertz wave amplification in gases with the excitation of femtosecond laser pulses // Appl. Phys. Lett. 2007. V. 91, 211102.

4. *X.-Y. Peng, C. Li, M. Chen, T. Toncian, R. Jung, O. Willi, Y.-T. Li, W.-M. Wang, S.-J. Wang, F. Liu, A. Pukhov, Z.-M. Sheng, and J. Zhang*, Strong terahertz radiation from air plasmas generated by an aperture-limited Gaussian pump laser beam // Appl. Phys. Lett. 2009. V. 94, 101502.

5. *K.Y. Kim, A.J. Taylor, J.H. Glownia, and G. Rodriguez*, Coherent control of terahertz supercontinuum generation in ultrafast laser-gas interactions // Nature Photonics 2008. V. 2, 605.

6. *J. Wu, Y. Tong, M. Li, H. Pan and H. Zeng*, THz generation by a two-color pulse in prealigned moleculse // Phys. Rev. A 2010. V. 82, 053416.

7. *M. Li, H. Pan, Y. Tong, C. Chen, Y. Shi, J. Wu, and H. Zeng*, All-optical Ultrafast polarization switching of terahertz radiation by impulsive molecular alignment // Submitted to Opt. Lett.

High Power THz Activities at SNU

G.S. Park[1], S.H. Min[1], M.A. Sattorov[1], O.J. Kwon[1], R.K. Barik[2], A. Bera[2]

[1] Center for THz-Bio Application Systems, Department of Physics and Astronomy, Seoul National University Seoul, Korea
gunsik@snu.ac.kr

[2] School of Electrical Engineering and Computer Sciences, Seoul National University, Seoul, Korea

A overview of high power terahertz activities of Seoul National University is presented. Microfabrication issue for high power devices is also described.

In 2009, a Center for THz-Bio Application Systems (CTBAS) was established. This center comprises more than 20 institutions over the Korea. The goal of this center is to develop THz sources, detectors, antennas, waveguides and other passive devices using MEMs and nano technologies; novel systems for each THz-Bio applications; investigate the THz spectroscopy and its interaction with bio-molecules such as DNA, RNA glucan, protein, etc.; clinical T-ray imaging.

Aiming to develop THz-Bio research, a high power femtosecond beam-line was developed at Pohang accelerator laboratory (PAL), Pohang [1]. Have developed an inexpensive and compact THz free electron laser (FEL) at Korea Atomic Energy Research Institute (KAERI) [2]. The wavelength range of the FEL is 100–1200 μm. The peak power of the FEL beam is more than 100 W. The size of the FEL system is much smaller than that of usual FELs operating in the world. The main idea to decrease its size is to use a compact microtron accelerator.

The micro-fabricated THz devices based on cavity [3] open grating structures [4] and metamaterials [5–10] were designed and successfully tested at Seoul National University. In addition to that, recently an upgrade of already developed and tested x-band high-power high-current relativistic devices is carried out to increase its operating frequency from 10 GHz to 0.1–0.2 THz [11–12].

A miniaturized continuous-wave (CW) vacuum electronic devices (VEDs) utilizing micro-fabrication technique are developed (Fig. 1). This device operated at 0.1 THz and expected output power is 15 W.

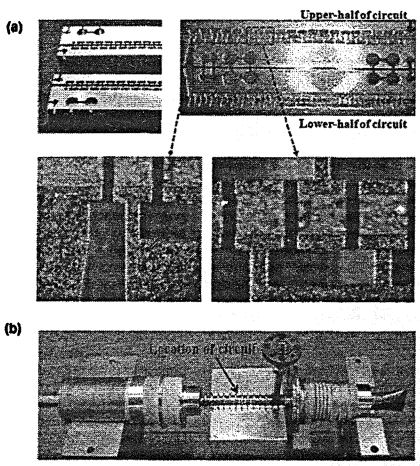

Fig. 1. LIGA-fabricated circuit (*a*) and W-band device assembly (*b*)

Nowadays, a study on open structure based THz devices is carried out. In this study, the interaction of inclined electron beam with the high frequency (HF) field close to the surface of the slow-wave structure with the real HF field distribution is considered. It is demonstrated that the electron interaction with the transversal electrical field induces the selective settling of the electrons on the comb lamellas, and the power is then taken away from the modulated electron flow in the grating slot resonators.

Low transition threshold and increased radiation intensity from counter-streaming electron beams was achieved for 0.5 THz two-step LIGA fabricated device (Figs. 2–3).

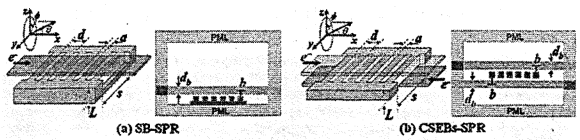

Fig. 2. Conceptual SPR illustrations (left) and schematic simulation models (right) of (*a*) a single beam Smith-Purcell radiation (SBSPR) on the metal grating and (*b*) counter-streaming electron beam SPR (CSEB-SPR) on the metal slab perforated by hole arrays.

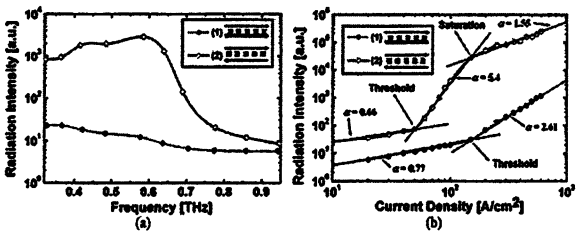

Fig. 3. Numerical FDTD-PIC simulation, MAGIC results with the condition of Fig. 2

The various types of metamaterials were investigated theoretically and experimentally [9–10]. The electromagnetic response of a metallic metamaterial to fast-moving electrons is studied by numerical simulations. The considered metamaterial is a one-dimensional array of slits perforated on a metallic film and is found to generate Cerenkov wakes when the electron beam travels near its surface. There is no energy threshold (Fig. 4) for the generation of such wakes, which would be promising to lower the operation energy of the electron beam in compact Cerenkov free-electron-lasers. Moreover, by analyzing the spectral dependence of the Cerenkov light, it is possible to map the dispersion relation of the guided modes supported by the metamaterial.

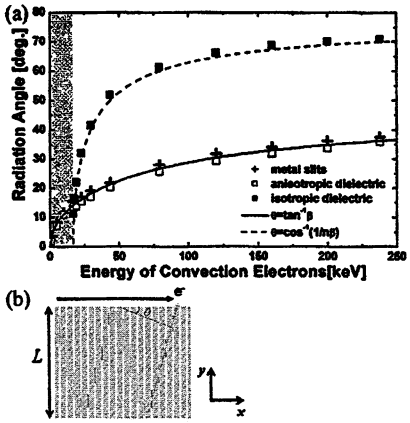

Fig. 4. Simulated radiation angles for metal slits structure and its effective dielectric media are compared at various beam energies. (*b*) Contour plot of the *Hz* field distribution for the metamaterial at 20 keV

The superradiant SPR phenomenon occurring from CSEBs has fascinating aspects in that it opens up opportunities to investigate a powerful THz wave generation from micro- and nano-devices in practice as well as an enhanced transmission of electronically excited surface plasmon polariton (SPP) modes.

The gigawatt level THz relativistic high-power machines was designed and studied during last 2 years, aiming to obtain more than 100 MW (Fig. 5).

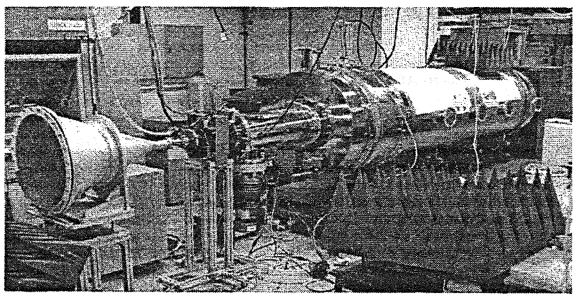

Fig. 5. HPM device

References

1. *Y.U. Jeong, B.C. Lee, S.K. Kim, S.O. Cho, B.H. Cha, J. Lee, G.M. Kazakevitch, P.D. Vobly, N.G. Gavrilov, V.V. Kubarev and G.N. Kulipanov*, Nucl. Instr. Meth. A 475, 47 (2001).

2. *Kwon, et al.*, Micro-fabricated Millimeter Wave Vacuum Electronic Devices. IRMMW-THz-2010, Rome, Italy (2010).

3. *M.A. Sattorov, et al.*, Beam-wave interaction in THz Clinotron. IRMMW-THz-2011, Texas USA, accepted for oral presentation.

4. *Y.M. Shin, et al.*, Microfabrication of millimeter wave vacuum electron devices by two-step deep etch X-ray lithography. Appl. Phys. Lett. **88**, 091916 (2006).

5. *S.T. Han, et al.*, Investigation on a microfabricated folded waveguide traveling-wave tube oscillator. IEEE T-ED **52** (5), 702-708 (2005); *S.T. Han, et al.*, Design of Folded Waveguide Traveling-Wave Tube. Microwave and Opt. Technol. Lett. **30**, 161 (2003).

6. *J.H. Won, M.A. Sattorov, J.K. So, K.H. Jang and G.S. Park*, Phase shifted EIO. Application number: 10-2008-0133580, 2008.

7. *Y.M. Shin, et al.*, Superradiant terahertz Smith-Purcell radiation from surface plasmon excited by counter-streaming electron beams. Appl. Phys. Lett. **90**, 031502 (2007).

8. *Y.M. Shin et al.*, Frequency-dependent refractive index of one-dimensionally structured thick metal film. Appl. Phys. Lett. **91**, 031102 (2007).

9. *J.K. So, et al.*, Cerenkov radiation in metallic metamaterials. Appl. Phys. Lett. **97**, 151107 (2010).

10. *J.K. So and G.S. Park*, THz Surface Plasmons on 1D Plasmonic Metamaterials with Disorder. IVEC 2011, Bangalore, India.

11. *H.C. Jung, et al.* Transmission of gigawatt-level microwave using a beam-rotating mode converter in a relativeistic backward-wave oscillator. Appl. Phys. Lett. 96, 131502 (2010).

12. *S.H. Min, et al.*, Mode conversion of high-power electromagnetic microwave using coaxial-beam rotating antenna in relativistic backward-wave oscillator. IEEE Trans on Plasma Science **38** (6), 1391-1397 (2010).

Direct Terahertz Detection by On-chip InGaAs/GaAs Field-Effect-Transistor Array

V.V. Popov[1], D.M. Ermolaev[2], K.V. Maremyanin[3], N.A. Maleev[4], V.E. Zemlyakov[2], V.I. Gavrilenko[3], S.Yu. Shapoval[2]

[1]Kotelnikov Institute of Radio Engineering and Electronics (Saratov Branch), Russian Academy of Sciences, Saratov, Russia, popov@soire.renet.ru

[2]Institute of Microelectronic Technology and High-Purity Materials, Russian Academy of Sciences, Chernogolovka, Moscow region, Russia

[3]Institute for Physics of Microstructures, Russian Academy of Sciences, Nizhny Novgorod, Russia

[4]Ioffe Physical Technical Institute, Russian Academy of Sciences, St. Petersburg, Russia

Recent years have witnessed further progress in terahertz (THz) detection based on plasmonic nonlinearities in a field-effect transistor (FET) with two-dimensional (2D) electron channel, which was originally proposed in [1]. Both the resonant and non-resonant THz detection by resonant and forced plasma oscillations, respectively, have been demonstrated [2]. For symmetry reasons, the detection response is zero in 2D electron channel with identical boundary conditions at its opposite ends if there is no DC bias current flowing in the transistor channel. Therefore, in order to obtain a photovoltaic THz plasmonic photoresponse (with no DC bias current in the channel), one has to ensure some asymmetry in the transistor channel.

An antenna element effectively coupling THz radiation to FET device is needed to obtain good detector responsivity suitable for practical applications. In a grating-gate FET plasmonic detector [3], the grating gate of large area (comparable with typical cross-section area of a focused THz beam) acts as an effective aerial matched antenna. Required asymmetry in the grating-gate FET structure is commonly created by applying DC drain current in the FET channel. However, strong drain current causes large voltage drop across a long channel of the grating-gate FET structure and, hence, different unit cells of a large-area grating-gate FET structure turn out to be under different effective gate voltages. As a result, the net responsivity of the grating-gate FET detector decreases for strong drain currents.

In this work, we investigate non-resonant THz photovoltaic detection by a one-dimensional (1D) array of individual identical FETs fabricated on a single chip [4]. Although such detector array has no supplementary antenna elements, it demonstrates much greater responsivity than reported previously for any plasmonic THz detector based on an antenna-coupled isolated FET.

Each FET in the array is based on GaAs/InGaAs/AlGaAs heterostructure. The 2D electron channel is formed in a 12-nm-thick undoped InGaAs layer with 40-nm-thick δ-doped AlGaAs carrier-supplying layer, and 400-nm-thick undoped GaAs buffer layer formed on the (100) surface of 450-μm-thick semi-insulating (SI) GaAs substrate (Fig. 1). 50-nm-thick cap GaAs layer is n-doped with Si up to $6\cdot10^{18}$ cm^{-3}. The top surface of the mesa is passivated by deposition of thin silicon nitride layer. The electron density in the channel is $3\cdot10^{12}$ cm^{-2} with the electron effective mass $0.061m_0$, where m_0 is the free-electron mass, and room temperature mobility is 5900 cm^2/V·s. The top metallization of the transistor array is formed with 65-nm-thick Ti/Au/Ti by a standard lift-off process.

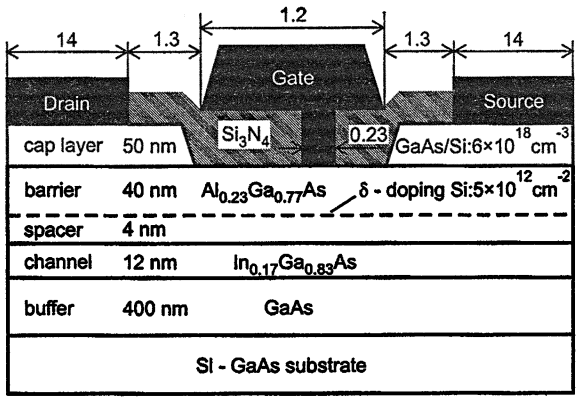

Fig. 1. Schematic of an individual FET in the array. All lateral dimensions are given in microns

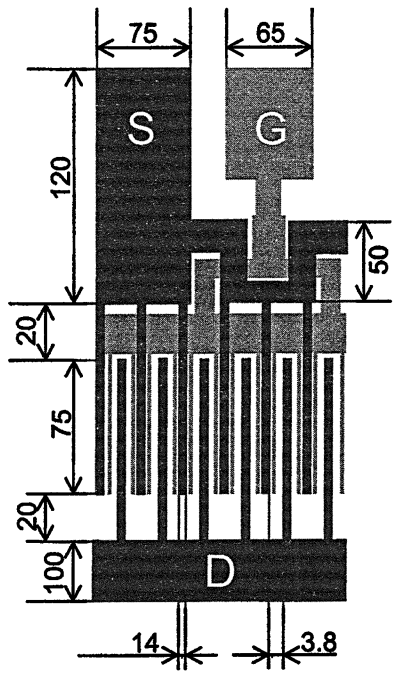

Fig. 2. Top view of the unit cell of FET array (each unit cell contains 12 similar FETs). The entire array is formed by repetition of 16 unit cells from right to left. All dimensions are given in microns

Top view of the unit cell of the FET array is shown in Fig. 2. Each FET in the array is biased by

the same gate voltage applied to a common gate lead. All individual FETs in the array are electrically connected in parallel and, hence, have common source and drain leads. Individual FETs are densely arranged in the 1D array in such a way that they can interact electromagnetically. The entire array of 192 similar FETs has the length of 3.6 mm. Terahertz radiation is incident normally upon the plane of the array from the top with the polarization of THz electric field across the FET contact fingers. Therefore, the entire grid of all FET metal fingers forms a specific type of antenna that couples the FETs to incident THz radiation. The short-period metal grid (with the period much shorter that THz radiation wavelength) is a broadband antenna because the amplitude of the near-field of such an antenna coupled to the FET channels is essentially independent of the incident THz wave frequency [5]. The gate finger in each FET of the array is placed in a position shifted to the source contact which yields necessary asymmetry enabling the photovoltaic response in each FET.

The DC photocurrent/photovoltage was measured between the source and drain leads of the array at liquid nitrogen temperature and at room temperature for zero DC drain bias current. Backward wave oscillator (BWO) was used as a monochromatic source of sub-THz radiation with the output power of about 1 mW in frequency range 0.415–0.72 THz. Terahertz radiation from the BWO was mechanically chopped at frequency 350 Hz and taken to the sample through an oversized circular metal waveguide with a tapered end which allowed focusing THz radiation onto the spot area of 6 mm in diameter covering the entire FET array.

Measured photocurrent is shown in Fig. 3 as a function of the gate voltage, U_g, at frequency 0.587 THz for T = 77 K and T = 300 K. Source-to-drain conductance of the entire FET array as a function of the gate voltage (depletion curve) measured at room temperature is also shown in Fig. 3. It is seen from Fig. 3 that the photoresponse greatly increases when FETs are driven to the channel cut-off at $U_g \approx -1$ V, which is characteristic of the non-resonant detection regime.

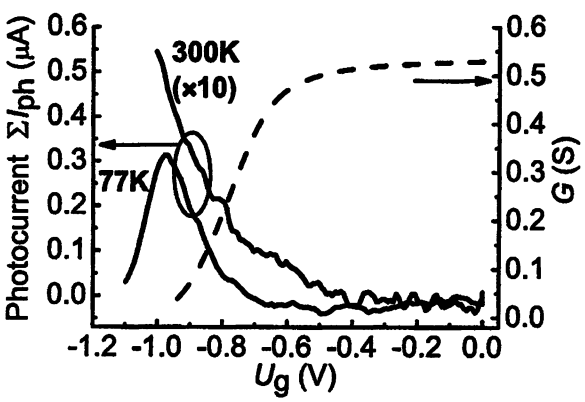

Fig. 3. Measured photocurrent at different temperatures (solid curves) and the source-to-drain conductance (dashed curve) of the FET array as functions of the gate voltage

Because the position of the gate finger is shifted to the source contact in each FET (see Fig. 1), the THz voltage, U_a, induced by the FET-array antenna is applied mainly between the gate and source contacts in every FET. Although different FETs in the array are coupled electromagnetically, they are uncoupled electronically since the electron channels of different FETs are isolated of each other. Therefore, the photocurrent I_{ph} is generated in each FET independently of the other FETs in the array. Since all FETs in the array are connected in parallel, the measured photocurrent ΣI_{ph} is the sum of photocurrents generated by every FET. Relating the measured photocurrent to the THz power incident upon the entire FET array area 3.6×0.075 mm, we estimate the FET array photocurrent responsivity as 0.05 A/W at T = 300 K for $U_g = -1$ V, which yields the photovoltage responsivity of 960 V/W per a transistor. This is the greatest responsivity ever reported for uncooled THz plasmonic detectors. Neither a supplementary antenna coupler nor a dc bias current is needed to be applied for achieving the strong THz photovoltaic response.

This work was supported by the Russian Foundation for Basic Research (Grant Nos. 11-02-92101, 10-02-93120, 08-02-00962, and 08-02-97034), the Russian Government Program "Scientific and Educational Brainpower for Innovation in Russia" (project. No. P1211), and by the Russian Academy of Sciences Program "Fundamentals of Nanotechno-logies and Nanomaterials." The work was performed under umbrella of the GDR-I project "Semiconductor Sources and Detectors for Terahertz Frequencies".

References

1. *Dyakonov, M., Shur, M.* Detection, mixing, and frequency multiplication of terahertz radiation by two-dimensional electronic fluid // IEEE Trans. Electron Devices. 1996. V. 43, No. 3. P. 380-387.

2. *Knap, W., Dyakonov, M., Coquillat, D., Teppe, F., Dyakonova, N., Łusakowski, J., Karpierz, K., Sakowicz, M., Valusis, G., Seliuta, D., Kasalynas, I., El Fatimy, A., Meziani, Y. M., Otsuji, T.* Field effect transistors for terahertz detection: Physics and first imaging applications // J. Infrared Millim. Terahertz Waves 2009. V. 30, No. 12. P. 1319-1337.

3. *Marem'yanin, K.M, Ermolaev, D.M., Fateev, D.V., Morozov, S.V., Maleev, N.A., Zemlyakov, V.E., Gavrilenko, V.I., Popov, V.V., Shapoval, S.Yu.* Wide-aperture detector of terahertz radiation based on GaAs/InGaAs transistor structure with large-area slit grating gate // Tech. Phys. Lett. 2010. V. 36, No. 4. P. 365-368 [Pis'ma v Zh. Tekh. Fiz. 2010. V. 36, No. 8. P. 39-47].

4. *Popov, V.V., Ermolaev, D.M., Maremyanin, K.V., Maleev, N.A., Zemlyakov, V.E., Gavrilenko, V.I., Shapoval, S.Yu.* High-responsivity terahertz detection by on-chip InGaAs/GaAs field-effect-transistor array // Appl. Phys. Lett. 2011. V. 98, No. 15. P. 153504 (3 p.).

5. *Muravjov, A.V., Veksler, D.B., Popov, V.V., Polischuk, O.V., Pala, N., Hu, X., Gaska, R., Saxena, H., Peale, R.E., Shur, M.S.* Temperature dependence of plasmonic terahertz absorption in grating-gate gallium-nitride transistor structures // Appl. Phys. Lett. 2010. V. 96, No. 4. P. 042105 (3p.).

THz/sub-THz Radiation Detectors. Requirements and Restrictions

F. Sizov

Institute of Semiconductor Physics, Nauki Av., 41, Kiev 03028, Ukraine, sizov@isp.kiev.ua

THz technologies now are important trends in different areas of human activity. Yet some aspects of this multidisciplinary subject remain relatively unexplored. To be widely used, one of the important components of these technologies, are detectors. There are a lot of achievements in low-temperature detector parameters for space THz technology applications (see, e.g., [1]) but there are many challenges for detectors and arrays which require further improvements in their sensitivity at elevated compared to sub-K operation temperatures. That will make the systems much less complicated and bulky.

The current status of THz/sub-THz detectors is considered taking into account the operation temperature, spectral band, sensitivity and bandwidth. To choose one or another sensing system and detector type one should follow the application purposes. Of the many promising THz detectors, particularly if the application is broadband, only a few may currently be suitable to be assembled into arrays (especially at elevated temperatures) which require background limited sensitivity, high degree of integration and processing in real time imaging.

Requirements and restrictions of direct detection and heterodyne type detectors to be used in application in active or passive imaging systems are briefly discussed. Advantage of the heterodyne imaging systems (and, e.g. in high resolution spectroscopy) over those with direct detection detectors become apparent (at least in the range of $\nu \leq 1$ THz where the sensitivity of fast non-linear detectors are high and the intermediate frequency bandwidth $\Delta\nu_{IF}$ is several GHz), and when imaging is performed with narrow band sources (e.g., interstellar molecular line emission). Also it takes place when for active systems coherent scene illuminators are used. Thus in the case of narrow band signals and if the local oscillator (LO) frequency is narrow (e.g., high resolution spectroscopy $\nu/\Delta\nu \sim 10^6$), because of suppressing of thermal noise of unwanted signals, the high S/N ratio is possible that makes them preferable over the direct detection ones.

Because of suffering the complication to diplex of two signals (the signal itself and from the LO one) and as a rule the absence of relatively powerful LOs, for heterodyne imaging arrays inherent are small number or single detectors.

Direct detection imaging systems are generally more sensitive in broad spectral region because of, e.g for important figure of merit the noise equivalent difference temperature (NEDT) the relationship $NEDT_{Dir}/NEDT_{Het} \sim \Delta\nu_{IF}/\Delta\nu$ is applicable. Here $\Delta\nu$ is the direct detection system spectral region width, and this is the case, e.g., of thermal sources, and thus $\Delta\nu_{IF}/\Delta\nu \ll 1$. Thus for broader bandwidth spectroscopy or imaging the direct detection systems are preferred and detectors easier can be assembled into arrays. But in mm and sub-mm regions to reach the sensitivity of heterodyne systems the direct detection ones, as a rule, to reduce inherent thermal noise, require higher level of cooling and they lack the phase information processing advantages present in heterodyne systems.

The detection sensitivity is particularly important at ambient temperature applications, since in THz/sub-THz region the spectral radiant exitance is small and the current available THz sources produce low power outputs. Moreover THz/sub-THz radiation suffers from the large attenuation in the air. These problems drive the demand for high sensitivity of uncooled or slightly cooled (≥77 K) detectors.

The number of detectors in the array is a key parameter that determines the information capabilities, and the response speed of the system. The accumulation time τ_{acc} at each sensitive element is proportional to the number M_e of sensitive elements in array, and inversely proportional to the frame rate f_r, and the number of picture dots M: $\tau_{acc} \approx 1/f_r \cdot (M_e/M)$. In imaging applications, the most important are multi-element arrays and they are available and used, e.g., in astronomy. These arrays are deeply cooled to $T \leq 1$ K (e.g., TES (transition edge sensors) detectors with SQUID (superconducting quantum interference device) readouts, semiconductor and hot-electron superconductor bolometers) with noise equivalent power (NEP) $\sim 10^{-18}$–10^{-15} W/Hz$^{1/2}$ depending on the wavelength bands under consideration, as photon noise limitations depend on the spectral band and resolution. Also extrinsic detectors in arrays (e.g., doped Ge and Si) operating at low temperature conditions are used above 1 THz but as a rule current arrays require an amplifier per each pixel.

For a lot of ambient temperature imaging applications at thermal background limit the broad spectral band arrays with detector NEP ~ 10^{-13} W/Hz$^{1/2}$ would be sufficient for short range (several meters) passive imaging, though it is still well below the thermal background limit at room temperature conditions with spatial resolution limited only by beam diffraction (NEP ~ 10^{-14}–10^{-16} W/Hz$^{1/2}$ in dependence of radiation frequency and spectral bandwidth). Also for real-time uncooled imaging systems appropriate readout electronics for detector arrays is required. At the moment most of the uncooled detectors are limited to NEP ~ 10^{-12}–10^{-10} W/Hz$^{1/2}$ and most of them hardly can be assembled into arrays.

Quantum detectors can't operate at $\lambda > 400$ μm at any reasonable temperatures (higher compared to sub-K operation) because of high thermal generation rate of carriers. In this spectral range thermal (e.g. different kind of bolometers – heat sensitivity detectors) or pare breaking detectors are the choice.

Ultimate performance characteristics of THz/sub-THz detectors taking into account only the fluctuations in the number of photons from the background determine the possible limiting detector performance characteristics but only the detector technology can determine what characteristics are achievable in sub-THz and THz frequency regions.

Background limited detectors and focal-plane arrays (FPAs) on platforms above the atmosphere (background temperature from T~3 K to T~30 K) using cold optics (T < 5 K) enable the capability to study the cosmic microwave background (CMB), the galaxies formation and evolution, etc. These detectors are based on heating of the sensitive element electron subsystem.

Intrinsic temperature fluctuation noise of thermal detector defines its upper NEP limit NEP = $= (4k_BT^2G)^{1/2}$, where G is the effective thermal conductance. In conventional uncooled microbolometers for IR wavelength region (λ ~10–50 μm) at T ~300 K, the heat capacity C ~$2\cdot10^{-9}$ J/K (for bolometer sensitive element volume ~50×50×0.5 μm) and G ~10^{-7} W/K (α-SiH or VO_x bolometers), which define time constant τ =C/G ~20 ms. Approaching background and quantum limits performance the only way to detect fainter signals is to accumulate for long times or low C and G values. At 65 mK the thermal conductance can be G ~$3\cdot10^{-14}$ W/K [2] that together with low C values due to small detector volume (~10^{-2} μm^3) and low temperature operation leads to reasonable time constants of ms range.

Qualitative leap in both bolometer and high sensitivity and quick response can be obtained by radiation warming its subsystem with low heat capacity, which is weakly interacting with hit sink (e.g. low background). Such subsystem can be electrons in semiconductor or superconductor weakly interacting with the lattice (via phonons). Electron heat capacity is many orders lower compared to the lattice one in conventional thermal IR detectors. The optical NEP achieved now in such kind of low temperature bolometers is $NEP_{opt} = 3\ 10^{-19}$ W/Hz$^{1/2}$, ($\lambda \approx 460$ μm, detector temperature $T_d = 50$ mK) [2].

Use of background limited FPAs at environmental conditions (with high absorptive atmosphere) give the opportunity, e.g. to provide the passive vision on human bodies and identifications the drugs and explosives, etc.

Some existing uncooled detector and arrays characteristics also based on new materials are compared and discussed in application to THz/sub-THz technologies together with their compatibility with readout electronics. The requirements to uncooled or slightly cooled detectors and arrays sensitivity operating under BLIP (background limited performance) conditions naturally are much less compared to deeply cooled ones and because of it THz technologies require relatively powerful broadband emitters or sophisticated technologies and new materials to realize BLIP (NEP ~10^{-14} W/Hz$^{1/2}$) for implementation, e.g., in the long range (≥30 m) real time passive imaging.

Really, now almost no uncooled detectors and arrays can satisfy these requirements of operation in the passive regime for real-time broadband imaging in the THz frequency range $\nu \sim$ (0.2–3) THz. Because of it THz imaging applications are still away in comparison with IR system feasibilities (frequently operating at BLIP conditions) and their consumer applications are stymed by the cost, size and weight.

Some uncooled Schottky Barrier Diodes (SBDs) used as direct detectors reaching NEP ~10^{-12} W/Hz$^{1/2}$ at ν~0.1 THz can be used for short range (~5 m) passive imaging. But these detectors have some kind of limitations to be used in large arrays both as the direct detection detectors and the heterodyne ones. Recently NEP =$4\cdot10^{-12}$ W/Hz$^{1/2}$ was achieved for these direct detection detectors (TIFT ErAs-InGaAs SBDs) at 0.639 THz what is about two orders of magnitude better that for typical GaAs Schottky diodes [3]. For uncooled SBD mixers ($\Delta\nu/\nu \sim 0.008$) NEP ≈ $4\cdot10^{-15}$ W/Hz$^{1/2}$ at $\nu = 0.5$ THz [4].

Some near video frame rate (f_r ~10 Hz) passive THz/sub-THz imagery systems are operating with uncooled small number of detectors in linear arrays but most of them are utilizing low temperature superconducting microbolometer linear arrays (f_r ~10 Hz) [5] or superconducting TES bolometer matrix arrays (f_r ~20 Hz) [6].

To achieve diffraction limited performance in THz/sub-THz region the detector area is necessary to become large which in many cases is impossible. Because of it between the small detector sensitive element (≤2–10 μm) microantennas are imposed. The effectiveness of introducing the radiation power from the antenna to the sensitive element depends much on radiation frequency, detector impedance, substrate thickness and its dielectric properties, etc. A lot of antenna types were shown to efficiently couple THz radiation. Their modeling still is important in designing the front ends of THz detectors because of relative lack of experimental data especially for uncooled or cooled to 77 K detectors on the base of semiconductors.

References

1. 22nd Int. Symp. Space THz Technol. 2011. April 26-28, Tucson, USA.

2. *Karasik B.S., Cantor R.* Optical NEP in hot electron nanobolometers // 21st Int. Symp. Space THz Technology 2010. Oxford, 23-25 March, P. 291-297.

3. http://www.darpa.mil/mto/programs/tift/pdf/MTT_ THz_ Workshop.pdf.

4. *Siegel P.H., Dengler R.J.* THz heterodyne imaging part // J. IR MM waves. 2006. V. 27, P. 465-480.

5. *Luukanen A.R., Aikio M., Grönholm M., et. al.* Design and performance of a passive video-rate THz system demonstrator // Proc. SPIE 2011. P. 8022-6.

6. *Becker D.T., Beall J.A., Cho H.-M., et. al.* High-resolution passive video-rate imaging at 350 GHz // Proc. SPIE 2011. P. 8022-5.

Nonlinear Terahertz Wave Photonics

A.P. Sukhorukov, D.O. Saparina, A.N. Kalish

Lomonosov Moscow State University, Moscow, Russia, apsmsu@gmail.com

In this report the recent results in nonlinear THz photonics which developed rapidly over the past decade are discussed [1, 2]. We present exploring methods for generating coherent radiation with nonlinear frequency conversion; consider dynamics of THz beams and pulses propagation in nonlinear media; show all-optical switching of THz radiation; and exhibit management of THz media properties.

In the terahertz region is easy to generate extremely short pulses of a small number of field oscillations. The equations for these envelopes are

$$\frac{\partial E_1}{\partial z} = \Gamma_2 \frac{\partial^3 E_1}{\partial \tau^3}, \quad \frac{\partial E_2}{\partial z} = \nu \frac{\partial E_2}{\partial \tau} \beta \frac{\partial E_1^2}{\partial \tau} + \Gamma_1 \frac{\partial^3 E_2}{\partial \tau^3}. \quad (1)$$

The wideband signals are expanding rapidly due to the group velocity mismatch ν and group velocity dispersion Γ, which greatly reduces the efficiency of nonlinear interaction of pulses (Fig. 1, 1 layer).

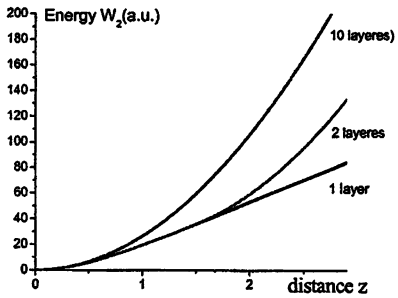

Fig. 1. SH energy via the distance in layered medium with alternating signs of dispersion

For their localization is proposed to create a layered medium with varying signs of group velocity mismatch ν and group velocity dispersion Γ. On the example of SHG the fruitfulness of photonic crystals with controlled dispersion is shown in Fig. 1. Such photonic crystals are indispensable for THz pulses.

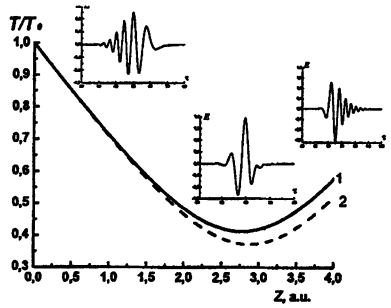

Fig. 2. Dynamics of pulse compression with a quadratic phase modulation. In the inset shows the profiles of the field at the entrance, at the point of compression, and beyond

We are also exploring the possibility of compression of long pulses to single-cycle pulses in a nonlinear medium with the electron and ion dispersion

$$\frac{\partial E}{\partial z} - a\frac{\partial^3 E}{\partial \tau^3} + b\int_{-\infty}^{\tau} E d\tau' - gE^2\frac{\partial E}{\partial \tau} = 0. \quad (2)$$

Another advanced metamaterials can have negative electric and magnetic susceptibilities. In such double-negative media, phase and group velocities are oppositely directed, and a negative refraction at the boundary occurs. This unusual property makes focusing properties of the meta-plate. As a result, the waveguide propagation in plane-layered metamaterials (analog lens line) can be observed, and localized modes can be excited in an open flat meta-cavity (Fig. 3).

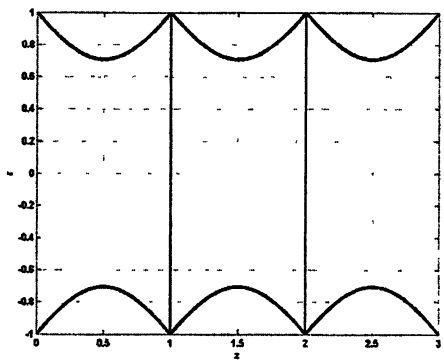

Fig. 3. Basic mode of three-layered meta-cavity with $L = 3$ (l_1=l_2=l_3=1), $R_1 = R_2 = 1$, $n_1 = 1$, $n_2 = -1$, $n_3 = 1$; $L_{eff} = 1$

In the metamaterial layer a negative phase shift occurs, so that the optical length of meta-cavity is

$$L_{opt} = \sum n_i l_i. \quad (3)$$

In the case of the flat mirrors $R_1 = R_2 = \infty$ a resonance condition $\varphi_c = \pi q$ is satisfied if

$$f_q L_{opt} = cq/2; \quad q = 0, \pm 1, \pm 2... \quad (4)$$

As $L < Lopt$ then the length of the meta-cavity can be smaller than the wavelength of terahertz radiation.

Waveguide mode limited in cross-section exists due to periodic focusing on the interface between metamaterial and dielectric layers. Beam diffraction in a stratified medium is convenient to characterize the effective length

$$L_{opt} = \sum l_i / n_i. \quad (5)$$

The eigen frequencies of meta-cavity, taking into account the phase incursion between the mirrors and diffraction shift are expressed by the following formula:

$$2L_{opt} f_{nmq} / c = \\ = q + (n+m+1)\pi^{-1} \arccos\sqrt{\left(1-\frac{L_{eff}}{R_1}\right)\left(1-\frac{L_{eff}}{R_2}\right)}. \quad (6)$$

If $L_{dif} = 0$ diffraction phase shift is equal to zero and, all transverse modes have the same frequency

$$f_{nmq} = \frac{cq}{2L_{opt}}. \quad (7)$$

Eigen frequencies of Hermit-Gaussian modes are shown in Fig. 4.

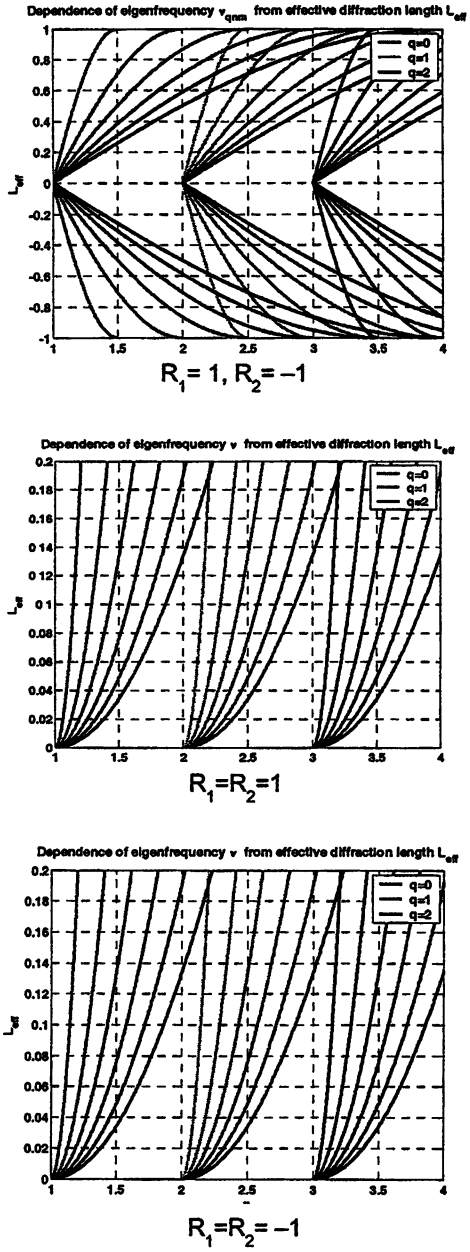

Fig. 4. Dependence of the eigen frequencies on the effective length for cavities (down) with convex-concave, convex-convex and concave-concave mirrors

In the case of zero effective length mirror curvatures should satisfy the condition:

$$n_1 / R_1 = n_N / R_2 \quad (8)$$

The stable modes are formed provided

$$0 \le \hat{g}_1 \hat{g}_2 \le 1 \quad (9)$$

where $\hat{g}_1 = 1 - L_{eff} / R_1$.

In the negative metamaterials the dynamics of nonlinear interactions dramatically is modified, as the ray vectors may be oppositely directed. It changes the nature of the energy exchange between the waves. We discuss some typical cases.

In the defocusing media with negative nonlinearity beams repel each other, and there is an effect of total internal reflection. We developed the theory of the total internal reflection in time domain on the base of two equations for the slowly varying amplitude of optical pulse and the slowly varying profile of terahertz pulse:

$$i\left(\frac{\partial A}{\partial z} + \frac{1}{u}\frac{\partial A}{\partial t}\right) + \frac{k_2}{2}\frac{\partial^2 A}{\partial t^2} - a\omega E_\Omega A + k_2 g |A|^2 A = 0 \quad (10)$$

$$\frac{\partial E_\Omega}{\partial z} + \frac{n_\Omega}{c}\frac{\partial E_\Omega}{\partial t} - \sigma\frac{\partial^3 E_\Omega}{\partial t^3} + \frac{\partial}{\partial t}(\eta E_\Omega^2 + b|A|^2) = 0$$

where σ is the dispersion coefficient in the terahertz frequency range, and u is the group velocity and $k_2 = \partial^2 k / \partial \omega^2$ is the GVD coefficient.

We consider the effect of the interaction of a weak probe optical pulse with a strong inhomogeneity created by extremely short pulses. The trajectory of the pulse in the limit in case of transmission becomes

$$\frac{d\tau}{dz} = \pm\sqrt{\delta^2 - k_2^2 (U(\tau) - U(\theta))} \quad (11)$$

with $U(\tau) = 2k_2^{-1} a\omega E_\Omega(\tau)$. If GVM is not greater than the critical value, we obtain the trajectory of the reflection (Fig. 5).

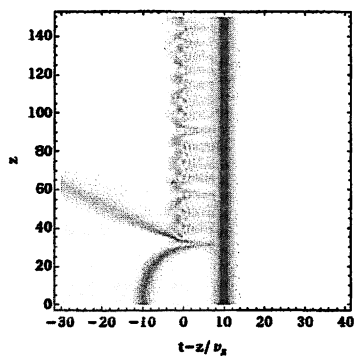

Fig. 5. Trapping a weak optical pulse by low frequency THz pulse when light pulse does not penetrate through the inhomogeneity.

We also study the properties of terahertz beams and pulses on a metal or a metamaterial surface taking into account diffraction and dispersion phenomena. Spatio-temporal phase dislocation formation and trapping dark and bright solitons is analyzed in detail.

This work was supported by grants RFBR № 09-02-01028, № 10-02-90010, № 11-02-00681.

References

1. *X. -C. Zhang and J. Xu.* Introduction to THz wave photonics, Springer, 2010.

2. *A.P. Sukhorukov, D.O. Saparina, A.N. Kalish.* THz and infrared surface wave beams and pulses on gyrotropic, nonlinear and metamaterial interfaces // Journal of Infrared, Millimeter, and Terahertz Waves. 2011 (to be published).

Plasma Mechanisms of THz Radiation Generation

E.V. Suvorov, R.A. Akhmedzhanov, D.A. Fadeev, I.E. Ilyakov, V.A. Mironov, and B.V. Shishkin

Institute of Applied Physics, Russian Academy of Sciences, Nizhny Novgorod, Russia, suvo@appl.sci-nnov.ru

The review of experimental and theoretical activity in the Institute of Applied Physics RAS on the generation of terahertz (THz) radiation in the plasma of optical discharge produced due to the focusing of femtosecond optical radiation in the open air is presented below. This way of THz radiation generation possesses a number of advantages such as the absence of destruction threshold which allows the use of arbitrary high laser pulse intensity, the absence of sharp resonances and "forbidden" frequency gaps typical of solids, rather high generation efficiency in some generation schemes. Besides, this is a very interesting process from the point of view of fundamental physics.

The main part of IAP facility designed for investigations on optoelectronics is SPITFIRE laser system which provides 50 fs pulses at 780 nm wavelength with the averaged power 3–5 W with the repetition rate 1 kHz (pulse energy about 3 mJ). Discharge in the ambient air is initiated by focusing of fs laser pulses either by axicon lens or by traditional spherical lenses with different focal distances. There is also the possibility to apply a dc electric field (up to 15 kV/cm) to the discharge region transverse to the propagation direction of optical pulses, and to add the admixture of the optical radiation at the second harmonics using conventional way of generating the second harmonics by nonlinear BBO crystal. A specially designed detection system is used for measuring the radiation pattern and polarization distribution of generated THz pulses; it includes InSb bolometer at cryogenic temperature, greed polarizer and opaque screen with small hole in it, movable in the plane orthogonal to the beam axis (for more details see [1, 2]).

In experiments on THz radiation emitted from the plasma of axicon discharge, (scheme proposed in [3]), the axisymmetric radiation pattern of Cherenkov type (with the maximum of radiated THz power, corresponding to the angle of axicon lens) was obtained (see Fig. 1, *a*).

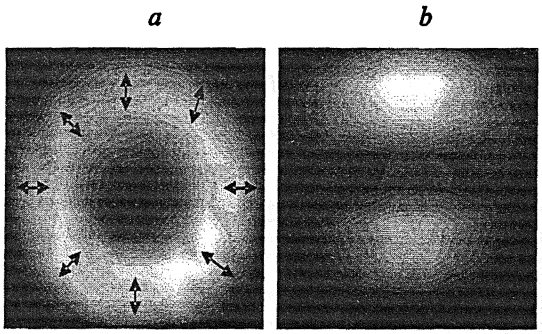

Fig. 1. Radiation pattern and polarization distribution of THz radiation from axicon discharge a) and from the discharge produced by focusing fs radiation with spherical lens

Polarization of THz radiation is radial and also possesses axial symmetry which assumes that low-frequency currents responsible for THz radiation either are of radial direction or are longitudinal with respect to the discharge axis. What was more unexpected, there was practically no reaction of THz radiation characteristics to the applying to the discharge region of a dc electric field up to maximum values (above 10 kV/cm). This means that low-frequency intrinsic electric field generated in a plasma in the process of optical break-down and plasma filament formation are of essentially higher value [4] (see also [5]).

More rich variety of experimental results was obtained for the optical discharges produced due to the focusing of fs optical radiation with conventional spherical lenses. First of all, the radiation pattern of THz radiation is of quadrupole type (Fig. 1, *b*) in a wade range of focusing distances (from 5 to 80 cm), integral polarization and the direction of linear quadrupole being transverse to the polarization of optical pulse (horizontal in Fig. 1, *b*). Second, unlike to the case of axicon discharge applying of large enough external dc electric field results in essential increase of THz radiation generation efficiency (more than 200 times with maximum dc electric field of order of 10 kV/cm); radiation pattern of THz radiation becomes bell-shaped with the maximum at the discharge axis and its polarization is linear and parallel to the external dc electric field.

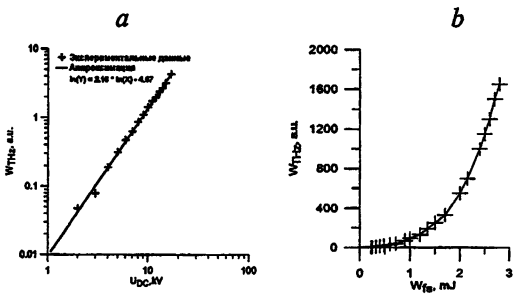

Fig. 2. Dependence of the energy of generated THz pulses on the applied dc field with maximum energy of optical radiation – a), and on the energy of optical pulses with maximum applied dc field

Quadratic scaling in Fig. 2, *a* demonstrates that generated THz field is proportional to the applied dc field. It should be stressed that dependence of THz energy pulses of the energy of optical pulses in Fig. 2, *b* demonstrates no signs of saturation.

And finally, there is a rather specific modification of radiation pattern with the variation of applied electric field intensity (see Fig. 3).

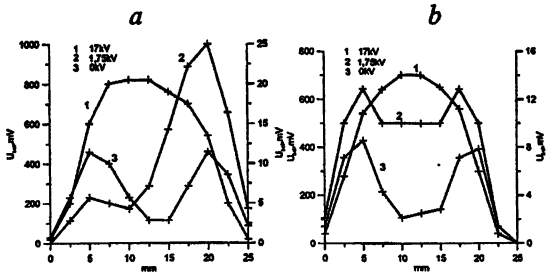

Fig. 3. Modification of THz radiation intensity along the vertical direction in Fig. 1, *b* with the dc electric field variation: *a*) vertical dc field, *b*) horizontal dc field

In the case a) increase of dc field results in suppression of one maximum with simultaneous increase of another one, with the further increase of dc field this maximum is shifted to the axis of a discharge, while in the case b) two maxima are increasing together and the well between them becomes less and less pronounced and disappears after all. simultaneously, resulting after all in a single hump structure with the maximum at the discharge axis. It should be noted also that that the change of the direction of a dc field to the opposite leads to the change in positions of suppressed and increased maxima.

The laser spark produced by bi-chromatic optical radiation was also investigated as a source of THz radiation, using nonlinear BBO crystal for generation the second harmonics of optical radiation. Known results concerning strong dependence of generation efficiency on the phasing between optical fields at the fundamental and at the second harmonics as well as a tremendous increase of THz radiation generation efficiency - addition of about 10 % in intensity of optical radiation at the second harmonics with optimal phasing results in about 5 orders of magnitude increase in generation efficiency. Dependence of THz pulse energy on the energy of optical pulses at the fundamental corresponds to power dependence with the index four which is in a good agreement with generally adopted model of four wave mixing, but also corresponds to the alternative model, proposed by IAP group [1] (see also below). For BBO crystal cut at type I synchronism the optimal angle of its orientation has been found corresponding to maximum THz radiation generation efficiency; the possibility of polarization control for THz radiation has been demonstrated as well.

For comparison of THz radiation generation efficiency in various schemes an absolute calibration of InSb bolometer was performed. The energy of THz pulses was estimated as $W_{THz} \approx \frac{c}{4\pi} S \int_{-\infty}^{\infty} E^2(t)dt$, where aperture S of THz radiation was taken from "knife-edge" measurements, and the waveform $E(t)$ of THz pulses was obtained from elipsometry measurements using ZnTe EO crystal. Calibration has been performed for few values of THz pulse energy (difference in value up to 50 times); all of them give the similar sensitivities different from each other by the factor less than 1.5 and well in accordance of independent measurements based on the reaction of the bolometer to the well calibrated signal at 140 GHz [6]. Basing on the absolute calibration the efficiency of conversion the optical radiation into THz one is estimated as 10^{-8} for the discharge produced by focusing with axicon or spherical lenses, $2 \cdot 10^{-6}$ with applying a dc electric field about 10 kV/cm to the region of discharge, produced by focusing with spherical lenses and up to $3 \cdot 10^{-4}$ for the discharge in bi-chromatic fs laser field with about 10 % admixture of the second harmonics and optimal phasing.

For qualitative understanding of obtained experimental results we develop some alternative theoretical approaches with taking into account specific features of tunnel ionization of neutral atoms in the electric field of optical pulses. The probability of tunnel ionization is defined by well known Keldysh formula:

$$\frac{\partial n}{\partial t} = 8\omega_H n_0 \exp\left(-\frac{2E_H}{3|\vec{E}|}\right),$$

where besides various constants the most important is the dependence on the instant value of optical field modulus. For optical fields essentially lower than the characteristic atomic field E_H ionization process has a form of short spikes, corresponding to maximum values of optical field. It may be shown that the low-frequency current in 0D approximation is governed by the equation:

$$\frac{\partial \vec{j}}{\partial t} = \frac{e^2}{m}\langle n\vec{E}\rangle,$$

where the averaging is performed over all high frequencies. For monochromatic optical field this averaged value is zero, while for bi-chromatic field non-zero contribution follows from mixing of first $\left(\overline{n_\omega \vec{E}_\omega}\right)$ and second $\left(\overline{n_{2\omega}\vec{E}_{2\omega}}\right)$ harmonics of electron density and optical field. Such simple model provides good qualitative explanation of main experimental results such as dependences of generation efficiency on mutual phasing and polarizations of optical fields at the first and at the second harmonics, dependences on the intensities of optical radiation at both harmonics, polarization of generated THz radiation and others [1].

A sophisticated model has been proposed for explanation of observed non-symmetric (quadrupole) radiation pattern, which is based on the hydro-dynamical model for electron fluid with anisotropic pressure, formed in the process of tunnel ionization (for more details see [7]).

References

1. *R.A. Akhmedzhanov et al.* // JETP. 2009. V. 109, № 3. P. 370.

2. *R.A. Akhmedzhanov et al.*, Radiophysics and Quantum Electronics. 2009. V. 52, № 7. P. 482–493.

3. *S.V. Golubev et al.* // JETP Letters. 2004. V. 79. P. 361.

4. *R.A. Akhmedzhanov et al.* // JETP Letters. 2008. V. 88. P. 569.

5. *V.A. Kostin et al.* // Opt. Lett. 2010. V. 35. P. 247.

6. *S.B. Bodrov et al.* // Opt. Expr. 2009. V. 17. P. 1871.

7. *N.A. Zharova et al.* // Phys.Rev. E. 2010. V. 82. P. 056409.

Methods of Microwave Spectrometry in the Development of the THz Frequency Range

V.L. Vaks

Institute for Physics of Microstructures RAS, Nizhny Novgorod, Russia, vax@ipm.sci-nnov.ru

Introduction

Over the last twenty years the terahertz (THz) frequency range has gained popularity all around the world. Many groups in different countries have focused their efforts on development and elaboration of THz technique and its applications to various problems. The most promising and vast fields of applications include security systems, medicine and biology. Many papers have successfully reported detection of characteristic absorption bands of some explosives [see, for example, 1] in the THz frequency range. Studying of biomolecules spectra in THz frequency range are also widely performed [see, for example, 2]. All above and other results are obtained with using of THz spectrometers based on quasioptics technique: photoconductive switches [3] illuminated by ultrashort laser pulses, and optical rectification [4] using ultrashort laser pulses in nonlinear crystals. To date, the quasioptics technique permitted spectral resolution only of about 0.1 cm^{-1} (3 GHz) with the additional complication of frequency instability. Fourier Transform IR spectroscopy, FTIR, is also widely applied for studying of various substances in THz frequency range [see for example, 5]. The typical spectral resolution of the FTIR analysis is about 0.5–4 cm^{-1}.

In fact, for some applications, where one expects wide absorption bands, the spectral resolution, provided by quasioptics technique and FTIR, is enough. However, many problems, like, for example, molecules identification, require analysis with high spectral resolution. The spectral analysis with resolution of about kHz is also essential when providing detection, quantification, and monitoring of certain gases in multi-component mixtures that can be marker gases in exhaled breath for noninvasive diagnostics; toxic gases or explosives vapors in ambient air; reagents or intermediate products in chemical reactions for *hi-tech*. In this case high resolution enables one to obtain high level of discrimination between chemical species, i.e. reliability of analysis.

To provide a required resolution, spectroscopic characteristics of a radiation sources are to meet requirements for measurements at Doppler line resolution ($\sim 10^{-6}$) and frequency measurements with accuracy $10^{-8} \div 10^{-10}$.

Today there exist several sources of coherent radiation of the THz frequency range, including back wave oscillators (BWO), free electron lasers, molecular lasers and quantum-cascade lasers.

The BWOs sources operate mostly in the subterahertz (subTHz) frequency range. The maximal generation frequency is about 1.5 THz.

Free electron lasers are known as tunable sources of high power THz radiation but they are large scale, high cost and do not have the necessary frequency stability for laboratory or field applications.

Optically pumped molecular lasers can operate at the THz frequencies but are bulky, power consumable, and can be tuned only within narrow emission lines, which do not always coincide with strong absorption lines of substances under investigation.

Quantum cascade lasers (QCL) are shown to be promising for many applications, because of output power (tens of mW) and possibility of frequency tuning. Although for high precise spectroscopy the QCL frequency still has to be stabilized and frequency controlled.

In the present paper we report an application of microwave approach to development of high precise technique of the THz frequency range. A special paragraph is focused on employment of a spectrometer for medical problems and security systems.

Microwave approach in development of high-precise THz technique

The traditional approach to obtain high-stable generators has involved frequency multiplication of high-stable reference synthesizers. Over the last few years, the development of new device technologies and application of advanced techniques to frequency multiplier design have resulted in a very good level of performance throughout mm frequency band. These multipliers are based mainly on Schottky diodes. However, for a successful operation in the THz range, it is necessary to increase cut off frequency of Schottky diodes (SD) that has proven quite difficult due to fundamental restrictions. Furthermore, use of superlattice structures (SL) are expected to be more effective for frequency transformation and detection, since the lower values of inertness and parasitic capacitances and presence of negative differential conductivity (up to 1 THz) on the volt-ampere characteristic.

In the present paper output radiation in the THz and subTHz frequency ranges is generated with using frequency multiplier and harmonic mixer, based on SL device [6].

A. THz Frequency Synthesizer

The application of harmonic mixers based on SL allows essentially simplifying a THz synthesizer's scheme and improving reliability and stability of the BWO operation in synchronization mode for all generation range (up to 1.25 THz). We have elaborated synthesizers operating in the frequency ranges 667÷857 GHz, 789÷968 GHz, 882÷1100 GHz. Cornerstone of the synthesizers design is a PPL system by 37th÷55th harmonics of reference synthesizer (with upper frequency up to 20 GHz). In fact this means

that a prefabricated synthesizer (for example Agilent) can be used as a reference. For synthesizer 882÷1100 GHz, a 3-mm wavelength synthesizer is employed as a reference.

B. THz Solid-state spectrometer

Application of the SL multipliers and mixers has also advanced a method of nonstationary microwave spectroscopy to the THz frequency range. The advantages of a nonstationary method include high sensitivity, real-time measurements and opportunity of *in situ* studies. The operation of nonstationary spectrometers can be realized in a phase switching [7] or fast passage regime [8]. In the presented paper we report a nonstationary spectrometer with phase switching. The spectrometer is based on a solid-state radiation source (Gunn generator) and operates in the range 0.5–2.5 THz (Fig. 1).

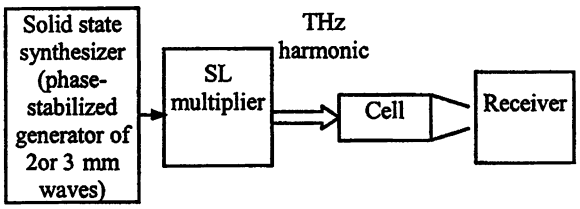

Fig. 1. General block-schema of solid state nonstationary spectrometer

In the proposed scheme a signal of reference generator is multiplied by means of a solid state device. Gas molecules interact with the resonance THz harmonic. A high quality resonator cell can be used to increase power intensity of a resonance mode and to reduce the others.

Application of high-precise THz spectroscopy

A. Noninvasive medical diagnostics: exhaled breath analysis

Together with department of Radiation therapy of Nizhny Novgorod Oncology Hospital, we have carried out experimental studies of NO concentration dynamics in the exhaled breath of oncological patients before/after radiation therapy. The studies have demonstrated an increase of NO concentration (in 2–3 times) in exhaled breath of lung cancer patients after a session of radiation therapy (see table 1).

Table 1. Concentration of NO in exhaled breath of oncopatients before/after radiation therapy (RT)

	NO Concentration (before RT), %vol.	NO concentration (after RT), %vol.
Patient N 1	0.018	0.075
Patient N 2	0.015	0.034
Patient N 3	0.012	0.022

B. Remote detection of explosives substances

The THz nonstationary spectrometer has been also employed for studying of explosives vapours compositions. Registration of vapours, evaporated from surface during natural decomposition is a promising way for remote detection of explosives. The results of analysis of explosives vapour composition are given in table 2.

Table 2. Explosives vapour composition

	Gases, found in explosives vapors
TNT	NO, N_2O, NO_3, NH_3, acetone, CO, CH, CH_2
RDX	NO, N_2O, CH, CH_2, acetone
NG	NO, NH_3, CH, CH_2

C. Heavy water spectra

We have analyzed several water samples: ^1H_2O – normal distilled water; heavy water/normal water - HDO (~51%) and ^1H_2O (49%); heavy water/superheavy water – D_2O (~ 99%) and T_2O (~1%); normal water/heavy water/superheavy water – ^1H_2O (~ 56%) D_2O (~ 43%) and T_2O (≤ 1%). The results have shown that in both subTHz and THz spectra, there are lines which, as judged by their frequency positions and intensities, cannot be assigned to $HD^{16}O$ and $HD^{18}O$ transitions. We assume that these "extra" lines may belong to HTO transitions.

Acknowledgment

This work is financially supported by Teradec 5281, RFBR 10-08-01124-a, Program of the Physical Sciences Department RAS «The modern problems of radiophysics» Program of the Presidium RAS "The problems of physical electronics, beams of charged particles and generation of E-field radiation in the systems of high power".

References

1. *William R. Tribe, et al.* Hidden object detection: security applications of terahertz technology // Terahertz and Gigahertz Electronics and Photonics III, edited by R. Jennifer Hwu, Proc. of SPIE Vol. 5354 (SPIE, Bellingham, WA, 2004).

2. *Anis Rahman, et al.* Ultrasensitive label-free detection and quantitation of DNA hybridization via terahertz spectrometry // Proc. SPIE 7568, 756810 (2010).

3. *G. Matthäus, et al.* Microlens coupled interdigital photoconductive switch // Appl. Phys. Lett. 93, 091110, 2008.

4. *D. Talbayev, et al.* Terahertz wave generation via optical rectification from multiferroic BiFeO3 // Appl. Phys. Lett. 93, 212906, 2008.

5. *T. Globus, et al.* Low THz Spectroscopy of Some Widely Used Explosives // Terahertz Physics, Devices, and Systems IV: Advanced Applications in Industry and Defense, edited by Mehdi Anwar, Nibir K. Dhar, Thomas W. Crowe, Proc. of SPIE Vol. 7671, 76710C, (2010).

6. *K.F. Renk, et al.* Semiconductor superlattice frequency multiplier for generation of submillimeter waves Joint 29th International Conference on Infrared and Millimeter Waves and 12th International Conference on Terahertz Electronics, September, 2004, Karlsruhe, Germany, M5.5, 125-126.

7. *V.L. Vaks, A.B. Brailovsky, V.V. Khodos.* Millimeter Range Spectrometer with Phase Switching – Novel Method for Reaching of the Top Sensitivity // Infrared & Millimeter Waves. 1999. V. 20, № 5. P. 883-896.

8. *V.V. Khodos, D.A. Ryndyk, V.L. Vaks.* Fast passage microwave molecular spectroscopy with frequency sweeping // Eur. Phys. J. Appl. Phys. 2004. V. 25. P. 203-208.

Reflected Signal Analysis in Standoff TDS Terahertz Probing

A.A. Angeluts[1], M.M. Nazarov, A.P. Shkurinov, P.M. Solyankin

[1]International Laser Center of Moscow State University, Leninskie Gory, GSP-1, 119991, Moscow, Russia, andrew_aa@inbox.ru

Terahertz time-domain spectroscopy (THz-TDS) provides non-destructive capabilities to investigate substances. This region is very promising for various organic molecules having absorption lines due to rotation, phonon and collective vibrational modes. Sometimes the reflection mode of THz spectroscopy is the only method for quantity characterization of media. This method is very demanded for distant measurements, for instance for industry control and security. Other virtue of reflection THz-TDS is the ability to get spectral information about shielded object.

To investigate spectral property of substance we used a model of linear Lorentz oscillators [1] for real and imaginary parts of permittivity $\varepsilon = \varepsilon' + i\,\varepsilon''$:

$$\varepsilon'(f) = \varepsilon_0 + \sum_j \frac{S_j f_j^2 (f_j^2 - f^2)}{(f_j^2 - f^2)^2 + \Gamma_j^2 f^2} \quad (1)$$

$$\varepsilon''(f) = \sum_j \frac{S_j f_j^2 f \Gamma_j}{(f_j^2 - f^2)^2 + \Gamma_j^2 f^2} \quad (2)$$

where f is frequency, f_i are resonant frequencies, S_i are oscillator strengths, Γ_i are relaxation coefficients.

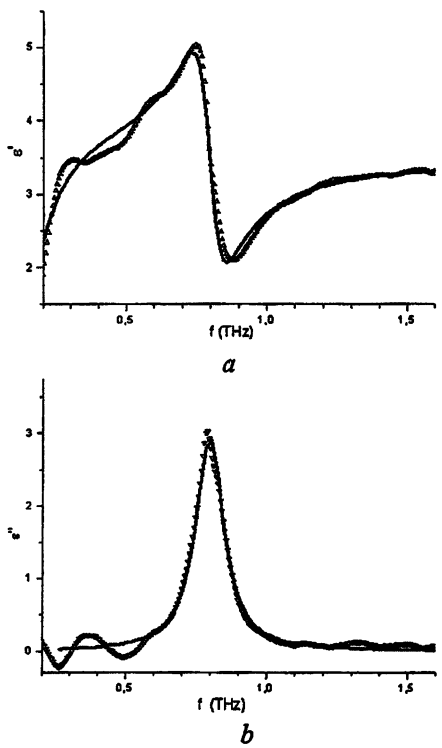

Fig. 1. Permittivity spectra of carbamide peroxide: *a* – real and *b* – imaginary parts. Continuous lines are calculated with equations (1) and (2). Dotted curves are experiment results in [2]

To obtain values of ε_0, ω_i, S_i, and Γ_i we should apply the iterative fit algorithm to experimental data. Fig. 1 shows results of fitting of experimental curves from [2] by model (1) and (2). The fitting parameters are: $\varepsilon_0 = 3.44$, $\omega_1 = 0.8$ THz, $S_1 = 0.4$, $\Gamma_1 = 0.12$. The data are in good agreement with a fit based on the Lorentz model for the dielectric function

In real experiment we can get dependence of reflection coefficient for *p*- or *s*-polarization (R_p or R_s) on THz frequency f (detailed descriptions see in [3]). To obtain the substance parameters we should transform experimental complex reflection coefficient $R_p(f)$ or $R_s(f)$ to absorption and refraction index spectra.

Sometimes we need to perform substance recognition. Often it is needed in industry control and security. To simplify spectral recognition we propose to calculate complex reflection spectra and to compare it with experimental spectra.

To transform permittivity spectra to reflection spectra we used simple Fresnel equations for *s*- and *p*-polarization.

$$R_p = \frac{n^2(f)\cos(\theta_0) - \sqrt{n^2(f) - \sin^2(\theta_0)}}{n^2(f)\cos(\theta_0) + \sqrt{n^2(f) - \sin^2(\theta_0)}} \quad (3)$$

$$R_s = \frac{\cos(\theta_0) - \sqrt{n^2(f) - \sin^2(\theta_0)}}{\cos(\theta_0) + \sqrt{n^2(f) - \sin^2(\theta_0)}} \quad (4)$$

Here complex refraction index $n^2 = \varepsilon$, θ_0 – incident angle.

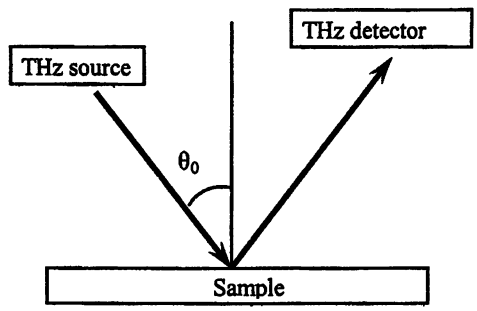

Fig. 2. Scheme of experiment

Fig. 2 shows the scheme of reflection spectra measurements. Before measurements we need to register reference spectra S_{ref} from mirror placed instead of sample. Then we register emission spectra S_{sample} reflected from sample surface. Reflection spectra R of the sample is: $R = S_{sample}/S_{ref}$.

Fig. 3 shows the reflection spectra of carbamide peroxide for various incident angles. One can see the different behavior of amplitude and phase of reflection spectra. From comparison of Fig. 3, *a* and Fig. 3, *b* we can conclude that s-polarization is more preferable for sharp angles, which more corresponds to real standoff device.

Our results demonstrate possibility of resonant substances detection and recognition even in ambient conditions and hidden under dielectric shield. This simple technique enables distant characterization or recognition in the THz range.

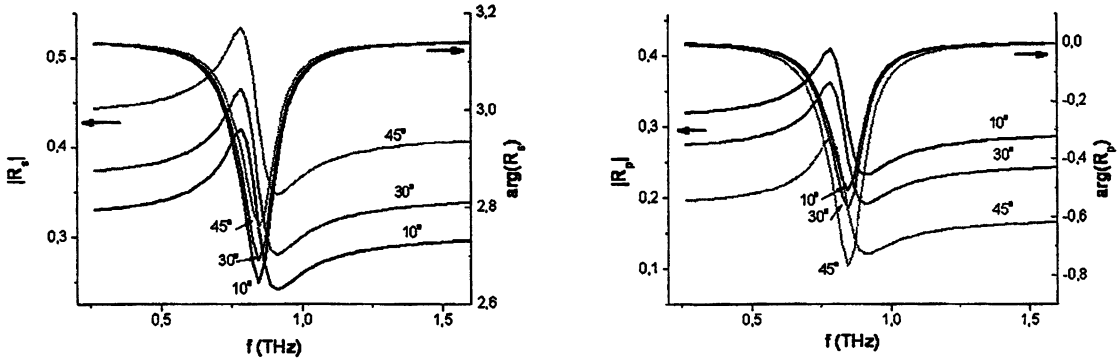

Fig. 3. Amplitude and phase of reflection spectra of carbamide peroxide: *a* – for s-polarization, *b* – for p-polariza-tion. Incident angle values are given near corresponded curves

References

1. *K. Yamamota, Md.H. Kabir, K. Tominaga.* Terahertz time-domain spectroscopy of sulfur-containing biomolecules // J. Opt. Soc. Am. B. 2005. V. 22. P. 2417.

2. *A.A. Angeluts, A.A. Golubkov, V.A. Makarov, A.P. Shkurinov.* Permittivity spectra reconstruction of parallel-sided plate by angular dependence of transmission spectra // JETP Letters. 2011, V. 93. P. 209-212.

3. *M.M. Nazarov, A.P. Shkurinov, E.A. Kuleshov, V.V. Tuchin.* Terahertz time-domain spectroscopy of biological tissues // Quantum Electronics. 2008. V. 38. P. 647-654.

Ultra-Thin Submillimeter Wave Absorbers for Bolometric Applications

S.A. Kuznetsov[1,2], A.V. Arzhannikov[1,2], A.G. Paulish[1,3], A.V. Gelfand[1,3], P.A. Lazorskiy[1,3]

[1]THz Research Laboratory, Novosibirsk State University, Novosibirsk, Russia
[2]Budker Institute of Nuclear Physics SB RAS, Novosibirsk, Russia
[3]Institute of Semiconductor Physics SB RAS, Novosibirsk Branch "TDIAM", Novosibirsk, Russia

Introduction

The rapid development of research in the range of submillimeter or terahertz waves of the electromagnetic spectrum demands adequate 2D matrix receivers for radiation detection, which are desired to be inexpensive, uncooled, easy-to-use, fast-response, sensitive, high-resolved, large-formatted, and capable of operating in real time. By now, implementation of THz matrix receivers maximally satisfied the aforementioned conditions faces serious instrumental restrictions arisen from specificity of the conventional solutions [1, 2]. The key drawback of commonly used THz sensors based on semiconductor and superconductor structures is connected with high complexity of their on-chip micro/nano-element integration & micro/nano-machining fabrication, unsuitable for large-format array mass production, or with the necessity of cryogenic environment. Similarly, the attempts for direct adaptation of modern room-temperature IR bolometric and pyroelectric array cameras, as well as fluorescence-quenching-based thermal image plates to THz imaging typically reveal either the problems of faint susceptibility or dimension restrictions for the radiation sensitive area, poorly applicable for handling radiation beams with diameters above 20 mm. Due to the aforementioned limitations, the high-quality THz imaging is typically realized via a time-consuming procedure of 2D raster scanning in a scheme with single detector measurements.

One of the prospective approaches to the real-time THz imaging is the uncooled bolometric detector based on a 2D array of micro-Golay cells (MGC) and optical readout system, which was recently proposed by our group and realized for the far infrared region [3, 4]. The alternative scheme for bolometric detection of THz radiation can be built using the principle of terahertz-to-IR conversion [5]. Both the MGC array detector and the THz-to-IR converter are estimated to be flexible to the choice of the operating wavelength and have no principle constraint on the array's overall dimensions. It is essential that adaptation of these detectors to the submm-wave band became feasible due to elaboration of the concept of electrically thin electromagnetic absorbers with a close to unity absorptivity within a desired frequency range [6-8]. Such absorbers are considered as a kind of metamaterial structures and are typically implemented in a configuration of a high-impedance or artificial impedance surface (HIS/AIS), which is represented by a subwavelength frequency-selective surface (FSS) of a capacitive type placed over a thin metal-backed dielectric substrate [6, 9]. Unlike the classical Salisbury, Jaumann, or Dallenbach electromagnetic absorbers based on unfavorably thick quarter-wave absorbing layers [10], the AIS-absorbers are capable of attaining the excess of at least several tens for the free-space wavelength λ ratio to the absorber thickness d. The condition $\lambda/d >> 1$ is essential for decreasing the absorber's heat capacity that allows achieving high sensitivity and low response time of the bolometric detector. It is noteworthy that the increase of the λ/d ratio inevitably leads to decreasing the absorption bandwidth, making AIS-absorbers ideally suitable for bolometric detectors with a high spectral resolution.

In this communication we present the results of experimental development of spectrally selective high-performance AIS-based absorbers with wavelength-to-thickness ratios $\lambda/d \cong 40$-180 designed for bolometric applications at frequencies 0.1–0.4 THz. To maximize the absorption resonance Q-factor, as well as the λ/d ratio, the absorbers are implemented on basis of low-loss bulk materials, such as polypropylene dielectric films and high-conductivity aluminum metallization, that distinguishes them from any types of absorbers realized before. The concepts of MGC imaging array and THz-to-IR converter with integrated AIS-absorbers are considered, and efficiency of the proposed approach is demonstrated in "THz-to-IR conversion" experiments on imaging submm-wave beams from a backward wave oscillator of the milliwatt output radiation power level.

Selected results

Figs. 1, 2 illustrate implementation results for the ultra-thin polarization-selective AIS-absorbers designed for the frequency range 0.3–0.36 THz. The photolithographically-patterned split-ring resonator arrays (SRR), optimized in Ansoft HFSS™ software, were utilized as vias-free FSSs to realize the AISs of the "FSS + grounded dielectric slab" configuration. Polypropylene (PP) with thickness d = 20 μm was used as the AIS dielectric substrate, further metallized from both sides via thermal vacuum deposition of aluminum (Al) 0.4 μm thick to form the high-conductivity metallization of the "grounded" and FSS layers.

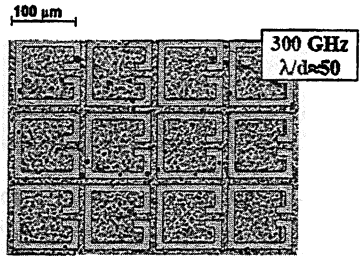

Fig. 1. Micrograph of the topological pattern for SRR FSS fabricated on PP surface: example of the 300GHz-absorber with $\lambda/d = 50$

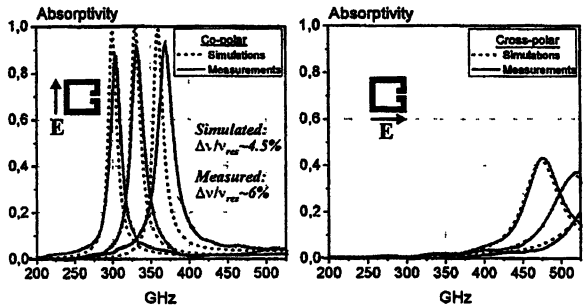

Fig. 2. Spectral response of three different 20μm-PP-based absorbers optimized for near-unity co-polar absorbance at 300, 330 and 360 GHz (λ / d ratios are 50, 45 and 41 respectively)

The developed AIS-absorbers were used to design a simple and flexible bolometric system for active THz imaging employing the scheme of terahertz-to-IR conversion [5]. In this scheme a THz beam is visualized via detecting THz-induced thermal heating of the absorber by a conventional infrared camera (Fig. 3, 4). It is noteworthy that the proposed imaging system operates in real time and suits well for imaging THz beams of a milliwatt CW power level or higher, though the negative effects of the "comet tail" and blooming can be identified on the registered images (Fig. 4). These effects can be reduced via

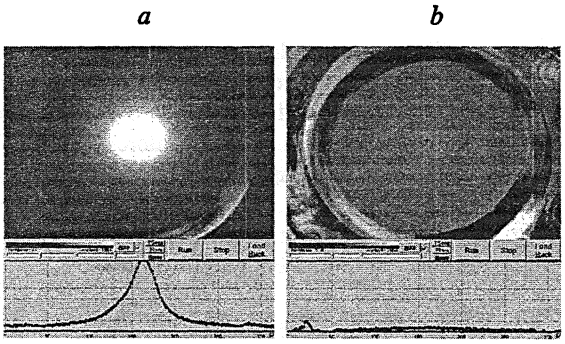

Fig. 3. IR images of the BWO beam focused upon "0.3 THz absorber" with clear aperture diameter 32 mm: a) co-polar excitation (E ⊥ SRR gaps, 0.3 THz); b) cross-polar excitation (E ∥ SRR gaps, 0.3 THz). BWO radiation power is 3 mW. The bottom graphs indicate intensity distribution along the horizontal line traced through the red crosshair

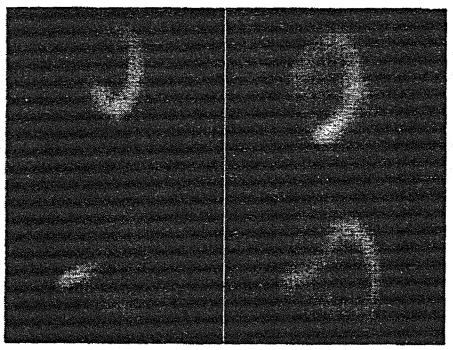

Fig. 4. Screen shots from the recorded movie at real-time THz imaging: motions of the focused submm-wave beam along the converter surface

employing the AIS-absorbers with a thinner dielectric substrate and an appropriately redesigned FSS pattern (see e.g. Fig. 5).

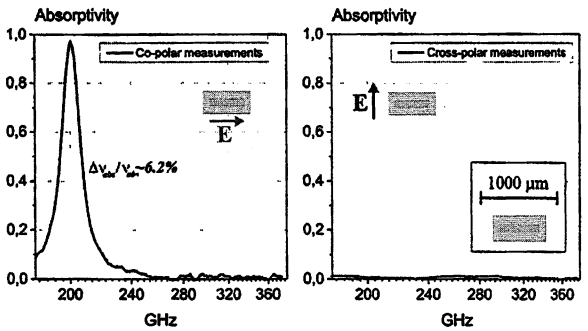

Fig. 5. Measured spectral absorptivity for the ultra-thin AIS-absorber with wavelength-to-thickness ratio $\lambda / d = 100$ optimized for near-unity co-polar absorption at 200 GHz. The AIS is realized on basis of 15 μm PP film and FSS of the "gangbuster" type (FSS unit cell is shown in the inset)

Acknowledgments

This work is supported by the grant 11.G34.31.0033 of the Russian Federation Government and the contract 16.740.11.0377 via the Federal Target Program. We also acknowledge Dr. D. G. Esaev for granting the high-sensitive IR bolometric camera and Dr. M. A. Dem'yanenko for the assistance with IR measurements.

References

1. *Yun-Shik L.* Principles of Terahertz Science and Technology // Springer. 2009.

2. *Sizov F.* THz radiation sensors // Opto-Electron. Rev., 2010. V. 18, No. 1. P. 10–36.

3. *Gelfand A. V. et al.* Uncooled matrix IR detector based on optoacoustic cells and optoelectronic reading system // Opt. Memory & Neural Networks. 2009. V. 18, No. 1. P. 25–28.

4. *Kuznetsov S. A. et al.* Implementation of Novel Type of IR-THz Receivers Based on Matrix Structures of Optoacoustic Cells // Proc. of the 40th European Microw. Conf. (EuMC-2010). 2010. P. 61–64.

5. *Kuznetsov S. A. et al.* Bolometric THz-to-IR converter for terahertz imaging // Appl. Phys. Lett. 2011. In press.

6. *Luukkonen O. et al.* A thin electromagnetic absorber for wide incidence angles and both polarizations // IEEE Trans. on Antennas and Propagation. 2009. V. 57, No. 10. P. 3119–3125.

7. *Tao H. et al.* Highly flexible wide angle of incidence terahertz metamaterial absorber: Design, fabrication, and characterization // Phys. Rev. B. 2008, V. 78, Iss. 24. P. 241103-1-4.

8. *Liu X. et al.* Infrared Spatial and Frequency Selective Metamaterial with Near-Unity Absorbance // Phys. Rev. Lett. 2010. V. 104. P. 207403-1–4.

9. *Balanis C. A.* Modern Antenna Handbook // Wiley-Interscience. 2008.

10. *Vinoy K. J., Jha R. M.* Radar absorbing materials: from theory to design and characterization // Kluwer Academic Publishers. 1996.

Low-Frequency Transition Radiation from a Femtosecond Laser-Induced Air-Breakdown Plasma with Sharp Boundaries

A.V. Borodin[1], M.N. Esaulkov[1], A.A. Frolov[2], I-Chen Ho[3], A.P. Shkurinov[1]

[1] Physics Department of M.V. Lomonosov Moscow State University , Moscow, Russia, borodin_msu@mail.ru
[2] IHED RAS, Moscow, Russia,
[3]Center for Terahertz Research, Rensselaer polytechnic Institute, Troy, USA

Femtosecond optical breakdown plasma is one of the most promising sources of strong Terahertz radiation. It provides both high field amplitude and the most broadband spectrum. Several physical mechanisms contribute to the generation process simultaneously, depending on the experimental conditions.One can distinguish Four-Wave Rectification (FWR) mechanism due to nonlinearity of neutrals, photocurrent mechanism and emission due to the ponderomotie force.

FWR is the dominating mechanism if the two-color laser excitation is used. Nevertheless, one can also observe the transition radiation with maximum spectral intensity in the far-infrared frequencies for both single-color and two-color excitation. This radiation origins from the spatial inhomogenity of the plasma and the optical pulse.

Under specific conditions, the transition radiation can be of the same order with the emission caused by FWR and photocurrent mechanisms. This effect was first observed by Hamster et al. [1]: at variable pressures, the THz emission strongly increased when $\omega_{plasma}\tau_{pulse} \approx 1$. Changing the plasma frequency via varying pressure or optical pulse intensity, we can obtain a strong resonant contribution of transition radiation, which can overcome the emission caused by ponderomotive forces and be comparable with the FWR radiation, as we show in our work.

Two important conditions for observing this transition radiation are sufficiently short laser pulse and a possibility of a broadband Terahertz detection. For this purpose, we use a spectrometer with an ABCD detection [2] system which allows for the most broadband coherent detection in Terahertz domain. We also compare experimental results and theoretical modeling.

We investigated detection process in plasma under different conditions(pulse duration, probe power and orientation of polarization) theoretically and experimentaly.

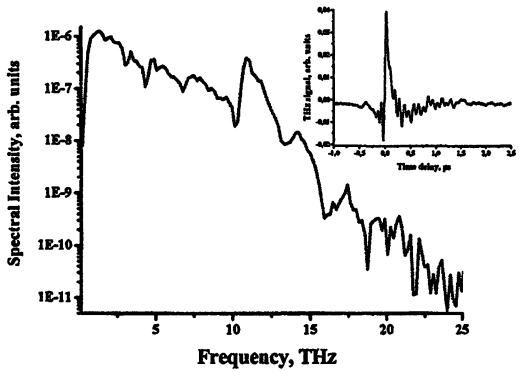

Fig. 1. A measured time-domain waveform(inset) and it's Fourier transform spectrum

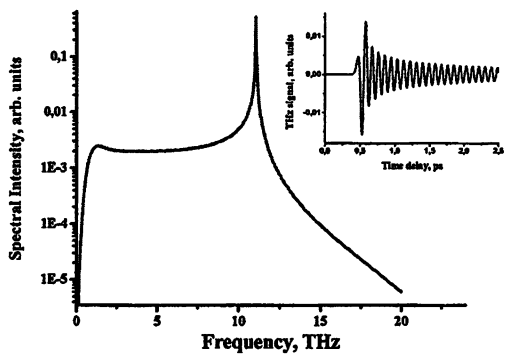

Fig. 2. Theoretical THz waveform(inset) and it's Fourier transform spectrum

References

1. *Hamster, H., Sullivan, A., Gordon, S., White, W., abd Falcone, R.W.,* Subpicosecond, electromagnetic pulses from intense laser-plasma interactionrs // Phys. Rev. Lett. 1993. V. 71, No. 17. P. 2725–2728.

2. *I-Chen Ho, Xiaoyu, X.-C. Zhang.* Design and perfomance of reflective terhertz air-biased-coherent-detection for time-domainous media // Optic Express. 2010 . V. 18, No 3. P. 2872–2883.

In-line and Reference-Beam Holography Experiments at Novosibirsk Free Electron Laser

Yu.Yu. Choporova[1,2], V.S. Cherkassky[2], B.A. Knyazev[1,2]

[1]Budker Institute of Nuclear Physics, Novosibirsk, Russia, choporenok@ya.ru
[2]Novosibirsk State University, Novosibirsk, Russia

Introduction

Many experiments in the terahertz region have been performed using low-power short-pulse wide-band sources. Methods for pulsed terahertz holography with a time domain spectroscopy technique are very different from the methods of classical optics commonly used in visible spectral range. Appearance of intense monochromatic terahertz sources (quantum cascade lasers, free electron lasers) enables the implementation of classical variants of optical methods in the terahertz range. This paper is devoted to the implementation of classic holographic techniques in the terahertz spectral range using a terahertz free electron laser as a source of radiation.

Experimental setup

The experiments were performed at the "Spectroscopy and radioscopy" (SpIn) user station. Radiation of the Novosibirsk free electron laser (FEL) [1], following as a continuous stream of 100-ps pulses with a frequency of 5.6 MHz, entered at the user station through a thin polypropylene film after passing a 16-m long beamline filled with dry nitrogen. Average power of the radiation in these experiments was about 50 W. The radiation was plain polarized that allowed attenuating of the beam power with a photolithographic polarizer. The laser beam at the station had the Gaussian shape $I = I_0 \exp(-2r^2 / w^2)$ with a waist $w = 9$ mm. The beam divergence was about 0.004 rad. The radiation was completely spatially coherent. All experiments were performed at the radiation wavelength 130 μm.

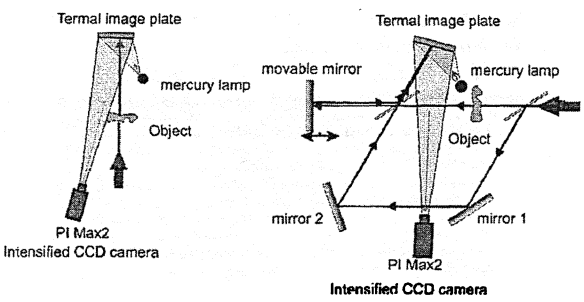

Fig. 1. Experimental schematics for (*a*) in-line and (*b*) reference-beam holography systems

Experimental schematics for two holographic techniques, which were used in the experiments, are presented in Fig. 1. The objects under study were directly illuminated by the laser beam. Masks, made of 100 μm-thick metal foil, were used as amplitude objects (see, e. g. the inset in Fig. 2). Phase objects were made from teflon plates, plastic films and other semi-transparent materials.

Availability of imaging devices with acceptable time and space resolution and high dynamic range is critically important for implementation of classic holography schemes in the terahertz range. The absence of commercially available devices designed for imaging of high-power terahertz radiation requires the development of novel imaging methods and techniques or adapting the existing ones. Three devices were used for the imaging. There characteristics are described in detail in [2]. The microbolometer focal plane array is a rather sensitive device, but the small physical size of the array, 16.36×12.24 mm, imposes restrictions in its applications, when a large field of view is required.

A temperature sensitive phosphor image plate (TSPP), developed by Macken Instruments Inc. [3] for imaging near- and mid-infrared radiation, was applied to THz-imaging. The plate has size of the sensitive area equal to 75×75 mm, which enables recording directly large images. Luminescence of the TSPP (in visible spectral range) was excited by UV radiation of a mercury lamp. A fingerprint of THz beam was detected via thermal quenching of the luminescence that was recorded with a PI Max2, 1024×1024 pixel, Princeton Instruments intensified CCD camera. To convert the recorded pattern into standard digital hologram (THz power density distribution), a simple processing described in [4] is to be performed.

In-line holography

In-line, or Gabor, holography (Fig. 1, *a*) setup does not require any optical elements, which is an additional advantage in the terahertz region.

Reconstruction process was performed using the procedure described in [5]. The diffraction of a plane reference wave by the recorded hologram is described by the Fresnel-Kirchhoff integral

$$\Gamma(\xi,\eta) = \frac{i}{\lambda}\int_{-\infty}^{\infty}\int_{-\infty}^{\infty} h(x,y)E_R(x,y)\frac{\exp\left(-i\frac{\pi}{\lambda}\rho\right)}{\rho}, \quad (1)$$

where $h(x, y)$ is the hologram function and ρ is the distance between a point in the hologram plane and a point in the reconstruction plane. Because the wave field $\Gamma(\xi, \eta)$ is a complex function, both the intensity and the phase can be calculated. Reconstructed object is formed at the position of the original object, but in the opposite direction from the CCD. Calculation of expression (1) was performed using the discrete fast Fourier transform. Sampling increment of the hologram determines experimentally the distance on the

hologram (mm), which corresponds the distance between two adjacent pixels. This value determines the Nyquist's frequency of the transformation.

An example of in-line digital hologram (obtained after primary data processing), which was recorded at a distance d = 237 mm, and reconstructed real image of an amplitude object is shown in Fig. 1, *a*, *b* respectively. The mask size was 10x10 mm, but though the Gabor conditions were not completely satisfied, quality of the image may be considered as very good. An example of reconstructed image of a phase object – "FEL"-shaped foam polyethylene is shown in Fig. 2, *d*.

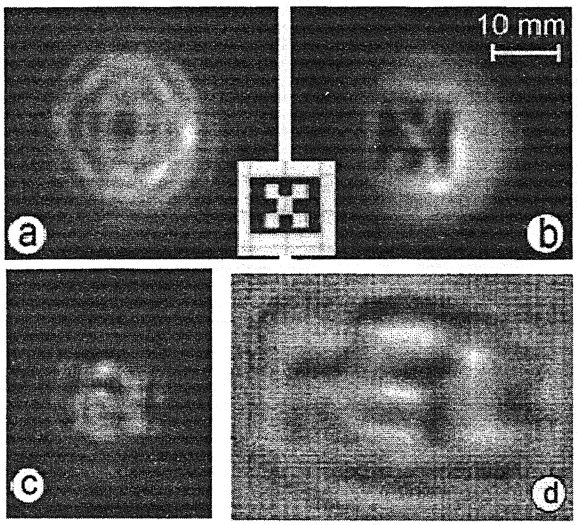

Fig. 2. (*a*) A hologram and (*b*) reconstructed image of an amplitude object; (*c*) a hologram and (*d*) reconstructed image of a phase object

Spatial resolution of the reconstructed real images was determined for an amplitude mask. A spatial resolution of 0.4 mm at a wavelength of 0.13 mm for the amplitude objects (see plot in Fig. 3) was achieved for the Gabor scheme.

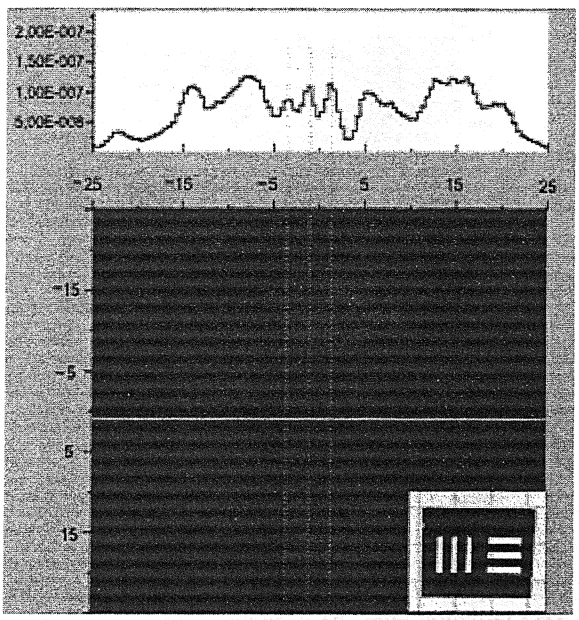

Fig. 3. A cross-section of intensity distribution across the reconstructed images of amplitude object shown in the inset

Reference-beam holography

A modified Mach-Zehnder interferometer [6] was employed for recording reference-beam holograms. Thin plastic films were used as beam splitters. A short pulse length of the FEL limits the coherence length and consequently imposes a restriction on the geometry of this device. A movable mirror enabled a varying optical path length in one of the interferometer arm and matching the arms length when an object was placed in the lower one. In such scheme both off-axis and in-axis holograms can be recorded. The experiments on the in-axis holography, where object and reference waves were coaxial, have been carried out. Phase objects were reconstructed in this scheme better then the amplitude ones (Fig. 3).

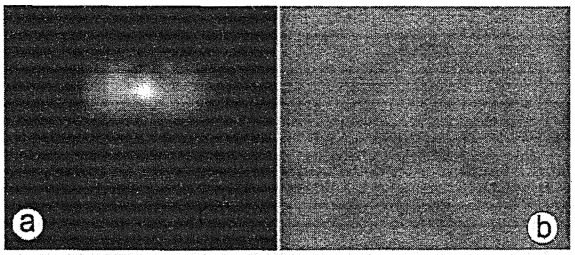

Fig. 3. Reconstructed real (*a*) and imaging (*b*) parts of a phase object

Summary

Two classic holographic techniques in the terahertz spectral range have been implemented using radiation of the Novosibirsk free electron laser. The temperature sensitive phosphor image plate was first applied as an imaging device for THz holography. Reasonable quality of the digitally reconstructed objects has been achieved in the terahertz range.

References

1. *B.A. Knyazev, G.N. Kulipanov, N.A. Vinokurov.* Novosibirsk terahertz free electron laser: Instrumentation development and experimental achievements // Meas. Sci. Technol. V. 21, 054017, 13 p. 2010.

2. *B.A. Knyazev, V.S. Cherkassky, Y.Y. Choporova, V.V. Gerasimov, M.G. Vlasenko, M.A. Dem'yanenko, D.G. Esaev.* Real-time imaging using a high-power monochromatic terahertz source: comparative description of imaging techniques with examples of application. Journal of Infrared, Millimeter, and Terahertz Waves, 2011.

3. http://www.macken.com/thermal.shtml

4. *Knyazev B.A., Kubarev V.V.* Real-time wide-field imaging using a tunable terahertz free electron laser and a thermal image plate // Infrared Physics and Technology, V. 52, 14, 2009.

5. *Schnars, U., Jüptner, W.* 1994 Digital reconstruction of holograms in hologram interferometry and shearography // Appl. Opt. 1994. V. 33. P. 4373–4377 (Reprinted in, Hinsch K and Sirohi R (ed.) 1997, Holographic Interferometry–Principles and Techniques (SPIE, Milestone Series, v. 144) p. 656–60).

6. *P.K. Shukla, K.K. Sarangpani, S. Talwar, G.S. Purbia, S.V. Nakhe, H.S. Vora.* A modified Mach Zender interferometer for the study of coherence of laser // Proc. The Education and Training in Optics and Photonics Conference (ETOP), Marseille, France, Oct. 23th–27th, 2005.

Role of the Multiphoton Ionization in Generation of Broadband Terahertz Radiation from Optical Breakdown Plasma

M.N. Esaulkov[1], A.V. Borodin[1], I.I. Kuricyn[1], I.A. Kotelnikov[2], A.P. Shkurinov[1]

[1]Moscow State University, Moscow, Russia, esaulkov_mich@mail.ru
[2]Budker Institute of Nuclear Physics, Novosibirsk, Russia

Generation of Terahertz pulses in laser-induced plasma still raises theoretical and practical interest since it offers the most broadband spectrum and high peak electric field (up to hundreds kV/cm). The most efficient THz generation occurs under two-color plasma excitation using both first and second harmonics of optical pulse.

Since the bandwidth of the emitted THz spectrum is proved to be limited by the laser pulse duration, we conclude that it is caused by an instantaneous process occurring in plasma. The instantaneous nonlinearity of neutral atoms and molecules contributes to the total emission, but strong radiation is achieved only when the plasma is formed. We conclude thus that the photoionization process itself makes the largest contribution to the total emission. The coherent motion of photoelectrons is equivalent to a surge of photocurrent which can emit dipole-like radiation with a broadband spectrum in Terahertz frequency domain. The role of photocurrent in the process of generation was first proposed in 2007 by Kim et al [1].

In this work, we focus our attention on the process of multiphoton ionization in case of two-color excitation beam. Since the photoionization is a strongly nonlinear process, the influence of second harmonics field is not additive and needs to be carefully investigated using a quantum mechanical approach. To avoid complicated calculations, we apply a semi-classical Imaginary Time Method (ITM) approach to calculate the ionization probability and the electron momentum acquired in a two-color ionization process. We investigate the ω to 2ω phase ψ and polarization dependences for the multiphoton ionization (MPI) regime.

It is found that the second harmonics field plays two different roles in formation of photocurrent. First, it modulates the probability of photionization according to the cosine law:

$$P_{mpi} \sim \exp[I/4\ \varepsilon^2\gamma^2(\cos(2\psi))]. \qquad (1)$$

Second, it results in formation of a nonzero average momentum acquired by the electron during the optical pulse, including the initial momentum it receives while leaving the parent atom or molecule. The momentum also has the dependence on ω to 2ω phase ψ and angle between polarizations θ:

$$\alpha_x \sim \varepsilon\gamma^2\sin(\psi)\cos(\theta)/2\ln(2\gamma). \qquad (2)$$

This approach introduces the ability of accurate control of initial electron momentum and for modulation of ionization probability (thus the plasma density), through variation of ω to 2ω phase.

We observe the change in the probability of photoionization experimentally by recording the fluorescence intensity at 391.4 nm vs the phase ψ between ω and 2ω (see fig. 1).

The modulation of the initial electron momentum manifests in rotation of the emitted THz wave polarization if the ω beam is slightly elliptic. Observation of this fact is visible on fig. 2.

The low-frequency radiation emission of the photoelectrons has a dipole-like character and thus most of energy is emitted in forward direction. The direction diagram is formed by interference pattern of the array of point dipole sources distributed along the plasma region.

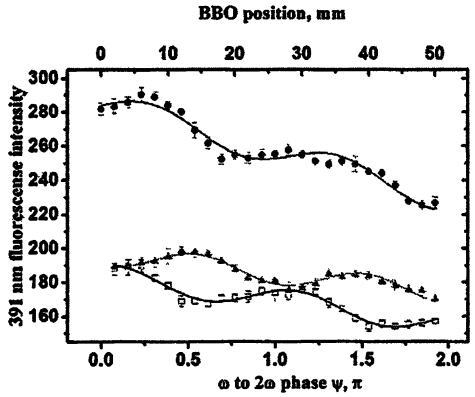

Fig. 1. Fluorescence intensity of the first negative band of N_2^+ (proportional to plasma density) at different points of plasma column vs phase shift between ω and 2ω

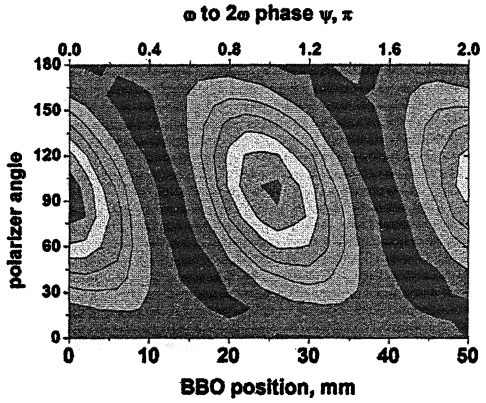

Fig. 2. Measured THz radiation intensity as a function of polarizer angle and ω to 2ω phase

However, the experimental investigation shows somewhat different direction pattern. A 320×240 microbolometer detector array [2] is used to obtain the spatial profile of terahertz radiation intensity. The THz radiation after the generator was collimated and then focused with two off-axis parabolas on the detector array.

The radiation formed a ring structure when the detector plane was moved behind the focal plane of the parabolic mirror (see fig. 3). This equals the fact that Terahertz radiation is directed into a cone.

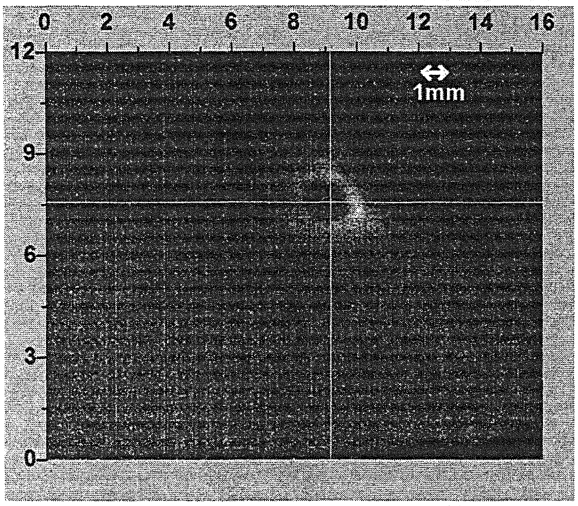

Fig. 3. Ring-shaped spatial profile of THz radiation observed with a microbolometer array

To confirm this conclusion, we investigate the spatial profile of the Terahertz radiation using an iris diaphragm placed behind the plasma filament and a time-domain technique. We use an ABCD detecting system to obtain the maximal bandwidth of 7 THz.

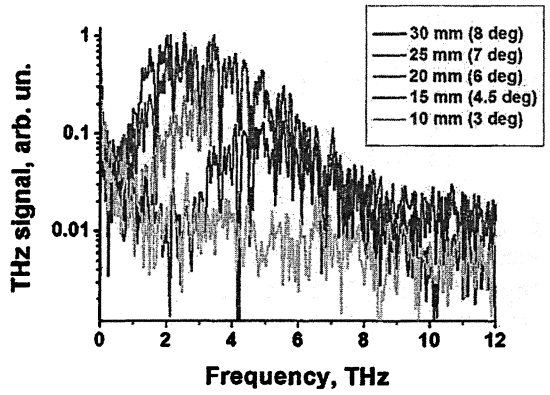

Fig. 4. Dependence of the THz spectrum detected with ABCD system on the clear iris aperture diameter. Iris is located at 95 mm from plasma

We find that the emitted Terahertz spectrum has a strong angular dependence. At small angles, below 4 degrees from the laser beam direction, only highest components of spectrum (above 3 THz) are observed. At wider angles, the contribution of low frequency part of spectrum becomes significant, so that most of the energy below 3 THz propagates between 4 and 8 degrees from the optical beam axis (see fig. 4). We thus confirm a cone-shaped Terahertz emission pattern for lowest part of the spectrum.

Conical spatial profile was predicted for the Terahertz emission from laser filaments by several groups [3], [4]. However, we should understand the difference between this conical profile and our observed signal. In [3] and [4], slow ponderomotive forces caused longitudinal oscillation of electrons and thus the emission profile was expected to be conical and radially polarized. The maximum spectral intensity was achieved at plasma frequency ω_p.

In our case, the polarization of the emitted signal shows strong correlation with the direction of the initial momentum of electrons released by the field ionization process. We thus conclude that we observe a dipole-like radiation pattern disturbed by the absorption of terahertz radiation in the plasma string. If no plasma absorption existed, we would observe the $\cos^2\theta$ pattern of emission. In reality, at small angles the lowest frequency components of Terahertz radiation is absorbed and cannot reach the detector.

In conclusion, properties of the emitted Terahertz radiation are mostly defined by the photoionization process and subsequent coherent motion of electrons and, in other hand, by the absorption in the plasma region.

References

1. *Kim, K.Y., et al.* Terahertz emission from ultrafast ionizing air in symmetry-broken laser fields // Opt. Express. 2007. V. 15, No. 8. P. 4577–4584.

2. *Demyanenko, M.A., et al.* Microbolometer detector arrays for the infrared and terahertz ranges // J. Opt. Technol. 2009. V. 76, No. 12. P. 739–743.

3. *D'Amico C, et al.* Forward THz radiation emission by femtosecond filamentation in gases: theory and experiment // New Journal of Physics. 2008. No. 10. P. 1–18.

4. *Balakin, A.V., et al.* Terahertz emission from femtosecond laser focus in a two-color scheme // J. Opt. Soc. Am. B. 2009. V. 27, No. 1. P. 16–26.

The Diffraction of One Period Terahertz Electromagnetic Waves

A.A. Ezerskaya, D.V. Ivanov, S.A. Kozlov

Saint-Petersburg State University of Information Technologies, Mechanics and Optics, Saint-Petersburg, Russia.
a.a.ezerskaya@gmail.com

The techniques for generating THz radiation as well the physics behind the propagation of short pulses have a long history [1], however recent advances in novel, highly efficient generation techniques created an additional interest to the physics of few-cycle pulses and opened a door for a variety of new applications [3] including medicine, security control, and material characterization.

We obtain analytical expressions for the general spatial distribution of the time spectra of one-period in the plane wave sources with broad temporal, and narrow spatial in the areas of Fresnel and Fraunhofer diffraction and spatial-temporal field pattern in the Fraunhofer diffraction.

Consideration of the features of the diffraction field dynamics and spectra of the paraxial wave by a few oscillations in dielectric media was carried out for the Gaussian boundary spatial distribution of field.

For the radiation is linearly polarized along x and its spectrum at $z = 0$

$$C_x(k_x,k_y,\omega) = \pi\rho^2 \exp\left(-\frac{\rho^2(k_x^2+k_y^2)}{4}\right) G_0(\omega), \quad (1)$$

where ρ is the spatial size of pulse, k_x and k_y are frequencies of temporal and spatial spectrum respectively, $G_0(\omega)$ is the initial temporal spectrum of the pulse near the axis, the spatial spectrum of a wave at an arbitrary distance z can be described by the following relation

$$G(x,y,\omega,z) = \frac{1+i\frac{2cz}{\rho^2 n(\omega)\omega}}{1+\left(\frac{2cz}{\rho^2 n(\omega)\omega}\right)^2} \exp\left(\frac{x^2+y^2}{\rho^2}\frac{1+i\frac{2cz}{\rho^2 n(\omega)\omega}}{1+\left(\frac{2cz}{\rho^2 n(\omega)\omega}\right)^2}\right) \times$$

$$\times \exp\left(-i\frac{n(\omega)\omega z}{c}\right) G_0(\omega), \quad (2)$$

In a transparent dielectric medium for one-period waves at the boundary of the form

$$E(t) = E_0 \frac{t}{\tau} \exp\left(-\frac{t^2}{\tau^2}\right), \quad (3)$$

the temporal evolution of wavepacket in the far field region takes the form:

$$E(x,y,t',z) = E_0 \cdot A^3(x,y,z) \cdot \frac{T(z)}{\tau} \times$$

$$\times \left[1-2\left(A(x,y,z)\frac{t'}{\tau}\right)^2\right] \exp\left(-\left(A(x,y,z)\frac{t'}{\tau}\right)^2\right), \quad (4)$$

где $A(x,y,z) = \frac{1}{\sqrt{1+\left(\frac{2T(z)}{\tau}\right)^2 \cdot \frac{x^2+y^2}{\rho^2}}}$,

$$T(z) = \frac{n_0\rho^2}{2cz},$$

and "delay time",

$$t' = t - \frac{n_0}{c}\left(z - \frac{x^2+y^2}{2z}\right).$$

Near the axis of the pulse the expression for the field (4) becomes simpler, and it can be written in the form

$$E(0,0,t',z) = T(z)\frac{\partial E_0(t')}{\partial t'}. \quad (5)$$

In the region of the Fraunhofer diffraction on axis of beam the temporal spectrum of the radiation field is shifted towards higher frequencies in comparison with the spectrum at the input; however at the periphery of beam – to the low frequencies.

We estimate the typical diffraction distances for one period on the emitter THz waves with the Gaussian traversal profile, assuming that the pulses of τ=0,2 ps with the transverse spatial spreading of ρ=3 мм. As follows from this figure, the main part of the radiation energy is in the frequency interval from ν_{min} = 0.25 THz up to ν_{max} = 2.25 THz (e^{-1} level).

At the distances much smaller than $z_1 = 25\,mm$, for the wavepacket under consideration the condition is satisfied, so that the wave structure does not change substantially yet. However, for the distance much larger than z_2 = 22,5 cm, the regime of Fraunhofer diffraction is realized and THz radiation transforms into a spherical wave. The traverse size of the light spot in this diffraction regime grows, for example, on a distance of 1 m it becomes 10 cm. In far field region the one-period wave become 1,5 period, and its spectrum is shifted towards higher frequencies.

Was shown that the diffraction of Gauss(25) the one-period wave become 1,5 period, and near the optical axis the maximum of frequency is shifted to high frequencies, whereas the frequency is shifted downwards far from the optical axis.

References

1. *Volkov A.A., Gorshunov B.P., Kozlov G.V.* Dynamical properties of superconducting materials. Works GPIAS, v. 25, p.112-161, Moscow, Science, 1990 (In Russian).

2. *Zhang X.-C., Xu.* Introduction to THz wave photonics. N. Y.: Springer Science+Business Media, 2009. 249 p.

Emission of Terahertz Waves in the Interaction of a Short Laser Pulse with an Underdense Plasma Slab

A.A. Frolov

Joint Institute for High Temperatures RAS, Moscow, Russia, frolov@ihed.ras.ru

The generation of the terahertz electromagnetic radiation is investigated when a short laser pulse with the carrier frequency ω_0, duration τ, the radius of the pulse focal spot R_L and energy W_L is incident from vacuum on an underdense plasma slab with the thickness $2d$. A new mechanism for generating terahertz radiation is considered that is associated with the growth of an antisymmetric leaking mode of the slab under the action of the ponderomotive forces of the pulse. The spatiotemporal distribution of terahertz waves is investigated and it is shown that they propagate into vacuum in the form of electromagnetic field pulses with a frequency close to the plasma frequency ω_p and a duration equal to the reciprocal of the damping rate of the anti-symmetric leaking mode of the plasma slab. The angular, spectral, and energy parameters of the terahertz radiation are investigated. It is shown that the radiation energy is emitted predominantly along the normal to the slab boundary into a cone the angle of which decreases as the size of the focal spot of the laser pulse R_L increases (fig. 1). For a thin plasma slab ($k_p d \le 1$), the analytical expression for angular dependence of the terahertz radiation energy is obtained

$$\frac{dW_{THz}}{d\Omega} = \frac{\omega_p^2}{\omega_0^2}\frac{k_p^2 R_L^2 \omega_p \tau}{16\sqrt{\pi}}\frac{V_E^2}{4c^2} W_L \cos\theta \times$$

$$\times \frac{\sin^2 k_p d}{k_p d} \exp\left\{-\frac{1}{2}k_p^2 (L^2 + R_L^2 \sin^2\theta)\right\} \quad (1)$$

here $k_p = \omega_p / c$, c is the speed of light, V_E is the electron oscillatory velocity in the laser field, $d\Omega = 2\pi \sin\theta d\theta$ is a solid angle θ element. Fig. 1 indicates agreement the analytical formula (1) and the result of numerical calculations. The spectral parameters of the terahertz radiation are examined. It is demonstrated that, for a short laser pulse, the terahertz radiation spectrum has a sharp peak at the plasma show frequency and that this peak narrows substantially with increasing the pulse spot size. As the laser pulse duration τ increases, the spectral line at the plasma frequency disappears and a broad peak arises at a frequency comparable to the reciprocal of the pulse duration (fig. 2). The total energy of the terahertz radiation is calculated and its dependence on the size of the focal spot of the laser pulse is examined (fig. 3). A comparison with earlier results (see [1]) shows that, for a laser pulse with large transverse sizes, the radiation

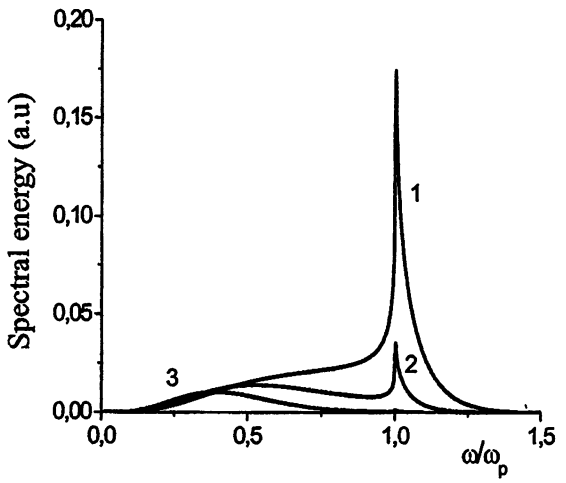

Fig. 2. Spectrum of the terahertz radiation for the parameters $(k_p R_L)^2 = 2$ and $k_p d = 1$. Curves *1–3* are for the laser pulse durations $(\omega_p \tau)^2 = 8, 12, 20$, respectively

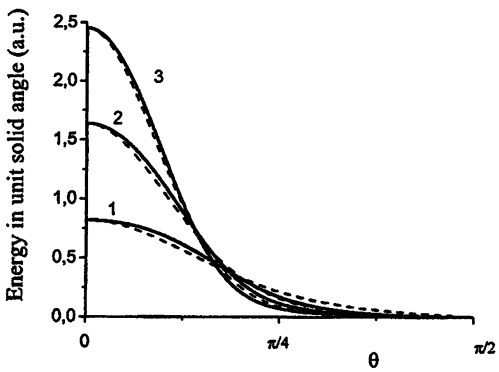

Fig. 1. Angular dependence of the terahertz radiation energy for a laser pulse with the duration $\omega_p \tau = \sqrt{2}$ and a plasma slab with the thickness $k_p d = 1$. Curves *1–3* are for the focal spot radii $(k_p R_L)^2 = 4, 8, 12$, respectively. The solid curves the results of numerical calculations, and the dashed curves are plotted from analytic formula (1)

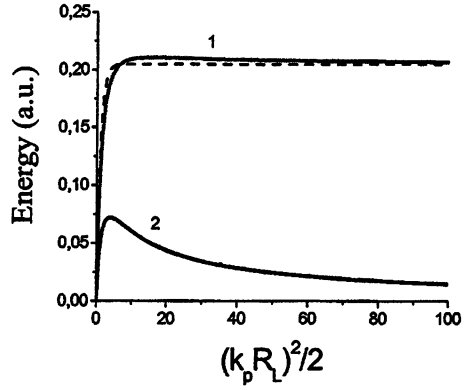

Fig. 3. Dependence of the total energy of the terahertz radiation on the focal spot radius R_L for $k_p d$=1. Solid curve *1* is obtained from the results of numerical calculations, dashed curve shows analytic dependence (2). Solid curve *2* corresponds to the energy of the transition radiation from a laser pulse at the boundary of a plasma half-space ($k_p d \to \infty$)

energy from the slab is much higher than the energy emitted by a plasma half-space (fig. 3). The analytical dependence the total energy of the terahertz radiation W_{THz} from parameters of a laser pulse and plasma slab is obtained

$$W_{THz} = \frac{\omega_p^2}{\omega_0^2}\frac{\sqrt{\pi}\omega_p\tau}{8}\frac{v_E^2}{4c^2}W_L\frac{\sin^2 k_p d}{k_p d}\times$$

$$\times \exp\left(-\frac{1}{2}\omega_p^2\tau^2\right)\left\{1-\exp\left(-\frac{1}{2}k_p^2 R_L^2\right)\right\}. \quad (2)$$

Fig. 3 demonstrates correspondence the result of numerical calculations and the analytical formula (2). The dependence of the total energy of the terahertz radiation from the thickness of the plasma slab is examined (fig. 4). It is shown that terahertz waves are excited most efficiently when the pulse length is comparable to the slab thickness (fig. 4). According to the presented estimates, the interaction of a femtosecond laser pulse with gas jets can generate megawatt-level terahertz radiation power.

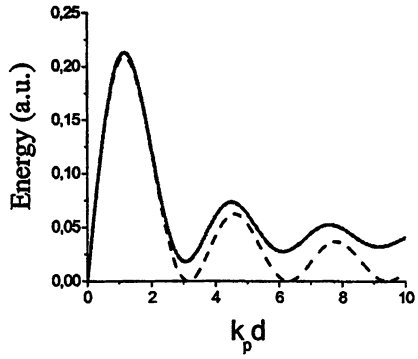

Fig. 4. Dependence of the total energy of the terahertz radiation on the plasma slab thickness *d*. The solid curve is constructed from the results of numerical calculations, and the dashed curve is plotted from analytic dependence (2)

Reference

1. *Gorbunov L.M., Frolov A.A.* Transition radiation generated by a short laser pulse at a plasma-vacuum interface // Plas. Phys. Rep. 2006. V. 32, № 10. P. 850-865.

Experiments on Generation of Surface Plasmons using Terahertz Radiation of a Free-Electron Laser

V.V. Gerasimov[1,2], B.A. Knyazev[1,2], A.K. Nikitin[2,3], G.N. Zhizhin[3]

[1]Budker Institute of Nuclear Physics SB RAS, Novosibirsk, Russia, einy@ngs.ru
[2]Novosibirsk State University, Novosibirsk, Russia
[3]Scientific and Technological Center for Unique Instrumentation RAS, Moscow, Russia

Introduction

Surface plasmons (SPs) of the visible and middle IR ranges have been studied well and are widely used in surface science, spectroscopy, and sensing. In the terahertz (THz) range, however, the understanding of the SP phenomenon, let alone its use, is far from being complete. The cause is not only the recent lack of well-developed sources and detectors of THz radiation but the specific properties of THz SPs. These peculiarities are as follows: 1) SP refractive index exceeds that of light in the surrounding medium only by hundredths or even thousandths of a percent; 2) SP field extends into air (if it is the medium adjacent to the metal) over 100λ (here λ is the radiation wavelength in free space); 3) as small as hundredths to thousandths of the total SP field energy is transported in the metal, which results in small absorption of SPs and large propagation length, reaching tens of centimeters or even meters.

A comprehensive review of our experiments on the generation of terahertz surface plasmons (THz SPs) performed at Novosibirsk free-electron laser (FEL) lately will be presented in the talk.

Experimental setup

The experiments were performed at the Novosibirsk the free-electron laser (FEL) (Siberian Center for Photochemistry Research) generating within spectral ranges 120–240 μm and 40–70 μm a continuous stream of 100-ps pulses with a repetition rate of 5.6 MHz, the average power of the radiation at the user stations being around hundred watts [1].

Fig. 1 sketches the device we used in the experiments. The collimated monochromatic THz radiation produced by FEL passes trough rotatable wire polarizer P_1 using for the intensity control and lithographic polarizer P_2 for the polarization rotation. After reflection from the plane and cylindrical mirrors the beam is focused at the entry mouth of the element transforming bulk radiation into SPs. The element was elaborated by Prof. D. Grischkowsky and coworkers and is characterized by high transformation efficiency [2]. It is a bar (prism) with two axial cuts of the lower facet. Both the cuts and the facet are covered with a nontransparent gold film. Brought close to the sample (a shaded box) the metallized base of the prism and the sample surface form a waveguide able to lead modes of the TM type. These modes (the single-mode regime – preferable) diffract at the exit mouth of the element and are partially converted into SPs. The diffracted bulk waves are blocked by absorber A, while the SPs slip under it. Detector D, fixed at the edge of the sample and provided with an aperture, indicates the arrival of the SPs. To change the distance run by the SPs the sample is installed on a computer-controlled, horizontally moving platform. Detector D is able to move in the plane of incidence in order to measure the SP field distribution in air.

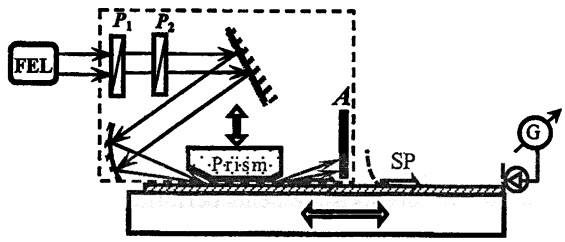

Fig. 1. Scheme of the attachment for measuring the THz SP propagation length L and the field decay δ in air

Much effort was made to get rid of the parasitic bulk waves (BWs) produced by the incident FEL radiation due to its diffraction on the input element. We have developed a simple method for the detection of such BWs propagating in air at grazing angles to the sample surface, which guides THz SPs [3]. The method is based on the rough permanence of the detector signal as a standard paper strip put on the surface and crossing the SP track at a right angle is moved along the track.

To separate the BWs and SPs with overlapping fields we suggested to use a right cone geodesic prism [4] formed on the guiding surface and having its axis normal to the SPs track. While detecting the SPs to the angle $\gamma = \arcsin[\tan(\alpha)\cdot(\pi-2)\cdot\kappa']$, here α is the angle between the cone's axis and the generating line, κ' is the real part of the SPs, the prism lets the BWs proceed with going in the plane of incidence.

To screen the detector from the parasitic BWs we advanced the decision put forward first by E. S. Koteles and coworkers [5] to place the input element and the detector on adjacent sample facets joint by a rounded edge. We suggested putting the detector below the specimen and lead the SPs to it by a glass hemi cylinder with its surface cowered with a gold film joining the specimen surface and the detector (Fig. 2).

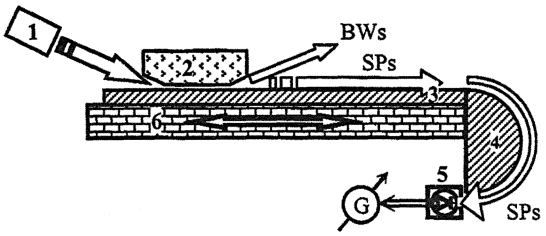

Fig. 2. Scheme of the attachment for measuring the THz SP propagation length with the detector being completely screened from the parasitic bulk waves (BWs). Here: 1 – FEL; 2 – Grischkowsky element; 3 – specimen; 4 – glass hemi cylinder; 5 – detector; 6 – horizontally moveable platform

Results

We have found that: 1) using the aperture method one can convert a monochromatic radiation into THz SPs on a clean metal surface with very low efficiency, which necessitates using very sensitive detectors for examination of the SP characteristics; 2) the efficiency increases up to the value of several percent with the waveguide method [2]. In this case the incident radiation is first converted into a TM waveguide mode, which is partially transformed into SPs after diffraction at the waveguide outlet. The plasmons excited in this way by FEL can be detected and probed with an uncooled pyroelectric or Golay detector; 3) intensity measurements performed for THz SPs generated on evaporated gold along the track and the normal to the surface indicated that the real SP propagation length L and depth of penetration into air δ are much smaller than those calculated by the Drude model for metal permittivity.

We interpreted the above mentioned facts in the following way. Low SP excitation efficiency with the aperture method at THz frequencies can be explained by the local character of the FEL-SPs interaction and small value of their fields overlap integral due to large SPs penetration depth δ into air. The waveguide method enables the observer to fit phase velocities of the TM-mode and the SPs by varying the gap between the Grischkowsky prism base and the specimen surface. While the discrepancy between the experimental and calculated values for L and δ can originate from a great natural difference between crystalline and evaporated gold, let alone the unrecorded SP radiation losses on the surface inhomogeneities.

A method for determining the optical constants of real metal surfaces at THz frequencies from measured L and δ has been elaborated and tested on gold, copper and aluminum [6]. No other optical method enables researchers to do this due to the high reflectivity of metals. The method implies excitation of SPs on the sample surface by the probing radiation and measurements of the SPs propagation length and penetration depth in air. It is well known that solving the dispersion equation for SPs in a given guiding structure, one can determine two its parameters provided the complex refractive index $\kappa = \kappa' + j\cdot\kappa''$ (here j is the imaginary unit) of the surface wave is measured. Specifically, in case of a two-layer structure composed of a plane metal surface and adjacent air, the equation having the following form:

$$\kappa = \sqrt{\frac{\varepsilon_1 \cdot \varepsilon_2}{\varepsilon_1 + \varepsilon_2}} \qquad (1)$$

(where $\varepsilon_1 = \varepsilon_1' + j\cdot\varepsilon_1''$ and $\varepsilon_2 = \varepsilon_2' + j\cdot\varepsilon_2''$ are the dielectric functions of the metal and that of air, accordingly) may be resolved relative to ε_1' and ε_1''.

So, the only problem in the THz SP refractometry of real conducting surfaces is the determination of κ, which consists of κ' and κ''.

To determine κ'' we measured the value of L related to κ'' by $L = (2k_0\cdot\kappa'')^{-1}$, where $k_0 = 2\pi/\lambda$, using the acknowledged "two-prism method", implying measurements of the SP intensity at two points or more along the track.

To determine κ' we realized the noninterferometric technique based on two facts: 1) at THz frequencies, the magnitude of SP decay length δ can be measured with a photo detector array or a single moveable detector; 2) the value of δ depends on κ as

$$\delta = \left[k_o \cdot \mathrm{Re}\left(\sqrt{\kappa^2 - \varepsilon_2}\right)\right]^{-1}. \qquad (2)$$

With regard to the relation between L and κ'', one can solve eq. (2) relative to κ' and obtain the following formula [6]:

$$\kappa' = \frac{k_o^2\delta^2\kappa''\varepsilon_2''}{2\cdot\left[1+k_o^2\delta^2\cdot(\kappa'')^2\right]} + \sqrt{\frac{1}{1+k_o^2\delta^2\cdot(\kappa'')^2}} \times$$
$$\times\left[\frac{1}{k_o^2\delta^2} + (\kappa'')^2 + \varepsilon_2' - \frac{k_o^2\delta^2\cdot(\varepsilon_2'')^2}{4\cdot\left[1+k_o^2\delta^2\cdot(\kappa'')^2\right]}\right]. \qquad (3)$$

The permittivity of gold estimated by the method at $\lambda = 130$ μm equals $\varepsilon_1 = -877 + j\cdot 610$, while its value calculated by the Drude model is $\varepsilon_1 = -101641 + j\cdot 284090$. Such a great difference can be explained, in our opinion, by the difference in the physical properties of real metal surfaces and bulk metals. The method is of great practical importance as there is no other way to attain the purpose because of the high reflectivity of metals at THz frequencies.

References

1. *B.A. Knyazev, G.N. Kulipanov, N.A. Vinokurov.* Novosibirsk terahertz free electron laser: instrumentation development and experimental achievements // Measurement Science and Technology. 2010. V. 21. P. 054017.

2. *M. Gong, T.-I. Jeon and D. Grischkowsky.* THz surface wave collapse on coated metal surfaces // Optics Exp. 2009. V. 17. P. 17088.

3. *V.V. Gerasimov, B.A. Knyazev, A.K. Nikitin, V.V. Nikitin.* Method for identifying diffraction satellites of THz surface plasmons // Techn. Phys. Lett. 2010. V. 36. P. 1016.

4. *G.D. Bogomolov, G.N. Zhizhin, A.K. Nikitin, B.A. Knyazev.* Geodesic elements to control terahertz surface plasmons // Nuclear Instrum. & Methods in Physics Research (A). 2009. V. 603 (1/2). P. 52.

5. *Koteles E.S. and McNeill W.H.* Far infrared surface plasmon propagation // Int. J. Infr. & Millim. Waves. 1981. V. 2 (2). P. 361.

6. *V.V. Gerasimov, B.A. Knyazev, A.K. Nikitin and G.N. Zhizhin.* A way to determine the permittivity of metalized surfaces at terahertz frequencies // Appl. Phys. Lett. 2011. V. 98. P. 1.

Terahertz Pulse Reflective Tomography System

V.G. Bespalov, A.A. Gorodetsky, Y.V. Grachev, E.V. Novoselov,
O.A. Smolyanskaya, S.A. Kozlov

Saint-Petersburg State University of Information Technologies, Mechanics and Optics, Saint-Petersburg, Russia,
grachev_y@mail.ru

The original scheme of broadband terahertz reflective tomography presented in the report. It is possible to obtain internal structure of layered object in normal direction to surface. We got tomograms of multilayer glue compositions, floppy disk, CD, human tooth in THz rays.

We use semiconductor crystal InAs placed in strong magnet field and irradiated by femtosecond pulses as a source of broadband THz radiation [1]. The laser beam from a femtosecond laser FL-1 splits by semitransparent mirror 1 at the probe beam and pump beam. Probe beam aligned by system of mirrors M to the electro-optical detection path, which consists of electro-optical crystal CdTe 9, phase-shifting plates $\lambda/4$ 10, the Wollaston prism 11 and the balanced detector 12. The signal from the balanced detector is sampled on the frequency of the chopper 5 by lock-in amplifier, further digitized and recorded on a computer. Pump beam is passed through a controlled delay line 2, incident on the generator 3, which consists of a crystal InAs, placed in a magnetic field, and the teflon filter. THz radiation was collimated by a first parabolic mirror 4, pass through beamsplitter from HRFZ-Si 7, focused by second parabolic mirror 4 on the object 6. THz radiation reflected from the object, going backward to the second off-axis parabolic mirror 4 and beamsplitter 7. Reflected THz radiation is focused by TPX lens 8 with a focus of 5 cm on electro-optical detector – cadmium tellurite crystal, cut along the [110]. Setup scheme presented on fig. 1. In our experiments, the diameter of the THz beam on the object was 1–2 mm. It was associated with a diameter of femtosecond radiation spot lighting crystal semiconductor InAs, since the optical system carries the image of the illuminated part of the crystal to the object.

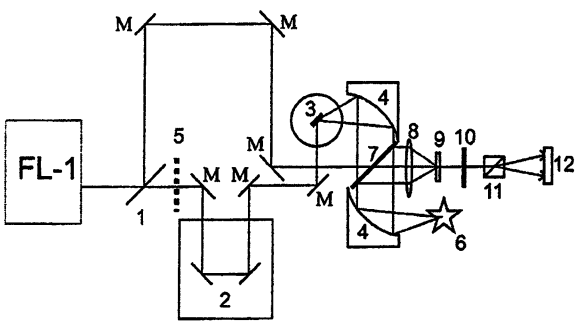

Fig. 1. THz reflective tomography setup

First object we study is metal mirror, because it's high reflectivity. Normalized reflection signal from metal mirror shown on fig. 2. Analysis of temporal form of THz pulse shown that generated pulse has one-cycle oscillation. Width of positive part of pulse on half-height is 1 ps. Smaller oscillation follow after main oscillation. It correspond to dispersive properties of environment, mainly caused by water vapor.

One-period pulse same as first but in opposite phase observed in time area 24–28 ps. It's amplitude is 0,65 a.u. This delayed pulse correspond to pulse mirroring from silicon-air surface of 1-mm beamsplitter.

Next pulse at 39–42 ps phased with main pulse correspond two passes of THz pulse in 3-mm crystal CdTe with parallel planes.

Last showed pulse with opposite phase correspond second pass of THz pulse in beamsplitter.

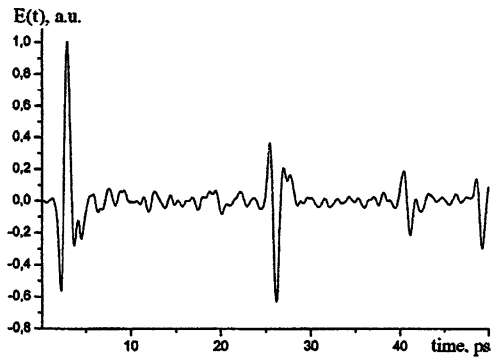

Fig. 2. Waveform of THz pulse reflected from metal mirror

In second part reflection from layered structures was studied. CD in a plastic envelope and floppy disk has been selected as simple structures.

We measured the reflected THz pulse from a plastic envelope (fig. 3, *a*), from the CD (fig. 3, *b*) and from the whole object (fig. 3, *c*).

Upon reflection from the plastic envelope, clearly visible peaks of reflection from the first and second layer of the envelope, and the second peak in opposite phase with the first. Upon reflection from the CD, recorded almost identical primary structure. It is expected, since that part of CD metalized.

More complex structure reflecting the THz pulse was observed in the case of a floppy disk because it was a series of dielectric surfaces. Since the thickness of a magnet disk is only 50 microns, the reflections of the THz pulse with a duration of about 1 ps (corresponding to the length of the path of light in a vacuum of 300 microns) from the front and rear surfaces overlaped and formed the structure of the two peaks (fig. 4, *a*).

The pattern of the reflection from whole floppy disk, allows to reveal the internal structure – reflection from the blind disk from the front surface of protective layer and the proper floppy disk are clearly visible (fig. 4, *b*). Magnet disk have a maximum coefficient of reflection among other parts.

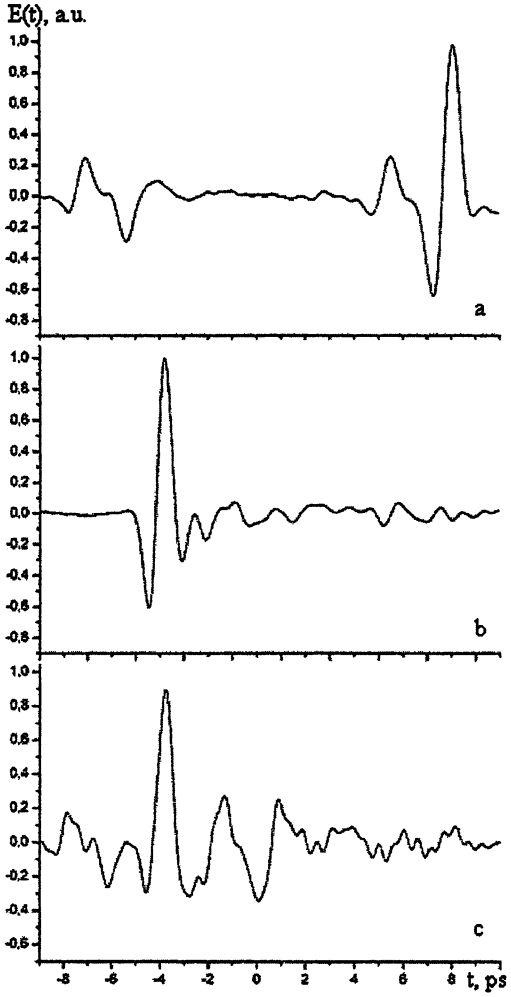

Fig. 3. Waveform of THz pulse reflected from plastic envelope, CD and CD in envelope

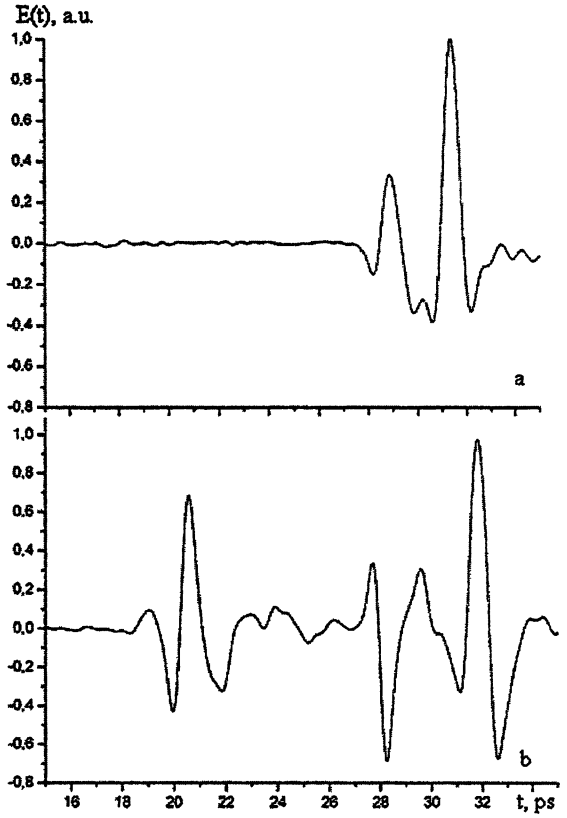

Fig. 4. Waveform of THz pulse reflected from magnet disk whole floppy disk

References

1. *V.G. Bespalov, V.N. Krylov, S.E. Putilin and D.I. Stasel'ko* Lasing in the far IR spectral range under femtosecond optical excitation of the InAs semiconductor in a magnetic field // Optics and Spectroscopy. 2002. V. 93, № 1. P. 148-152.

THz Radiation Causes Abnormal Mitoses in A_L Cells

Henning Hintzsche[1], Christian Jastrow[2], Thomas Kleine-Ostmann[2], Thorsten Schrader[2], Ernst Schmid[3] and Helga Stopper[1]

[1] Institut für Pharmakologie und Toxikologie, Universitaet Würzburg, Germany
[2] Physikalisch-Technische Bundesanstalt (PTB), Braunschweig, Germany
[3] Institut für Zellbiologie, Center For Integrated Protein Science, Universitaet München, Germany

Terahertz radiation is electromagnetic radiation in the frequency range from 0.1 to 10 THz [1]. Effects of this kind of radiation have not been investigated thoroughly in the past [2]. In the present study [3], the effect of 0.106 THz radiation on mitotic human-hamster hybrid cells was investigated. Cells were exposed for 30 minutes with different power densities from 0.043 to 4.3 mW/cm². Figure 1 shows the irradiation setup consisting of a regular cell culture incubator modified for irradiation experiment.

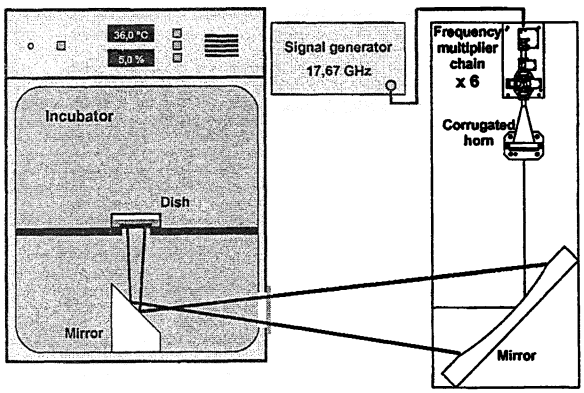

Fig. 1. Setup for field exposure experiments at 0.106 THz. A signal from a generator is sextupled and directed from below onto the µ-dishes containing the cells. The frequency multiplier chain is shown from above (tilted by 90°) for clarity

As a positive control, cells were treated with the insecticide Trichlorfon. All in all, more than 6,000 mitotic cells were analyzed. All of the mitotic phases were looked at, but it turned out that ana- and telophases were affected primarily (Fig. 2).

The frequency of mitotic disturbances was increased after irradiation with 0.043 and 0.43 mW/cm². After irradiation with 4.3 mW/cm², no further elevation could be observed (Fig. 3).

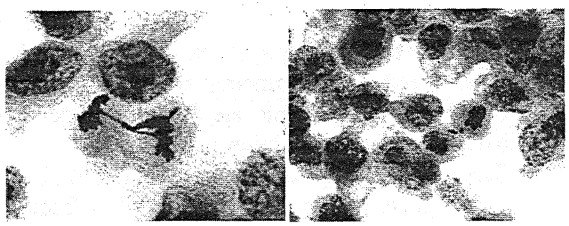

Fig. 2. AL cells with spindle disturbances in the ana- (*left*) and telophase (*right*) of the cell cycle

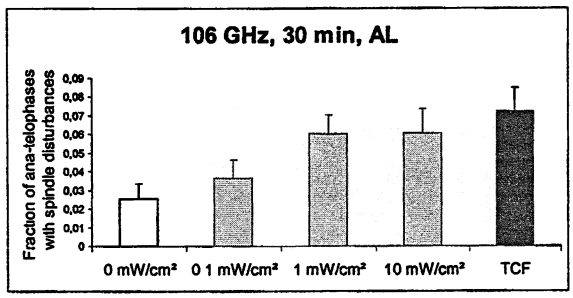

Fig. 3. Ana-telophases with spindle disturbances after exposure to 0.106 THz radiation at different power densities or incubation with trichlorfon (TCF) determined in two replicate experiments. Data are shown as mean ± standard error

References

1. *P.H. Siegel*, Terahertz technology in biology and medicine //.IEEE Transactions on Microwave Theory and Techniques. 2004. V. 52. P. 2438-2447.

2. *A. Korenstein-Ilan, A. Barbul, P. Hasin, A. Eliran, A. Gover and R. Korenstein*, Terahertz radiation increases genomic instability in human lymphocytes. Radiat Res. 170, 224-234 (2008).

3. *H. Hintzsche, C. Jastrow, T. Kleine-Ostmann, H. Stopper, E. Schmid, and T. Schrader*, Terahertz radiation induces spindle disturbances in human-hamster hybrid cells, Radiat Res, 175(5), 569-74. (2011).

Terahertz Discharge in Argon at High and Medium Pressures

V.A. Koldanov, V.L. Bratman, S.V. Golubev, Yu.K. Kalynov, A.G. Litvak, S.V. Razin, A.V. Sidorov, V.A. Skalyga, V.G. Zorin

Institute of Applied Physics RAS, Nizhny Novgorod, Russia, vkold@appl.sci-nnov.ru

This paper presents the results of experimental investigations of the discharge in argon in a focused beam of terahertz wave under near-atmospheric and medium (few tens Torr) pressures. These studies have been motivated by fundamental research reasons on the one hand and possible applications of terahertz discharge plasmas on the other hand.

The compact large-orbit gyrotron (LOG) [1] with maximum pulse power of about 600 W at frequency 0.55 THz and pulse duration 8 μs has been used as a radiation source. Terahertz beam with linear polarization has been focused into the focal spot $2*3.5*\lambda^2$ by two-mirror quasi-optical system near the center of discharge chamber (fig. 1). The additional short-focus mirror placed in the focal zone of the beam has been used for terahertz intensity increase by the 10–15 times (according to our numerical simulations).

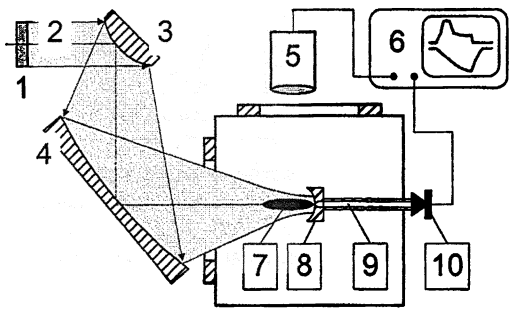

Fig. 1. Schema of the experimental setup. 1 – gyrotron output window; 2 – terahertz beam; 3, 4 – defocusing and focusing mirrors; 5 – photomultiplier or streak-camera; 6 – oscilloscope; 7 – discharge; 8 – short-focus mirror; 9 – waveguide (metal tube); 10 – detector

The discharge chamber was first evacuated to a pressure of 10^{-2} Torr, and then filled with argon to the required pressure. Photomultiplier, streak-camera, camera, and terahertz detectors of transition wave (installed on a movable metal tube) have been used for the discharge diagnostic. To produce seed electrons required for breakdown stabilizations, we use an additional continuous glow discharge at the edge of the additional mirror.

At high pressure range (0.2–2 atm.) a terahertz discharge is formed near the focus of the additional focusing mirror (fig. 2). The spatial structure of the discharge appears significantly non-uniform and has typical transverse scales that are shorter than the wavelength. In this case, the overall dimensions of the discharge region are many times larger than the dimensions of the focal spot of the additional focusing mirror. Moreover, the dimensions of the discharge area are much larger than the focal spot formed by the focusing system. Thus, it can be expected that the discharge, which is formed in the area of the maximum electric field, propagates into the region with the fields that are significantly below the breakdown threshold.

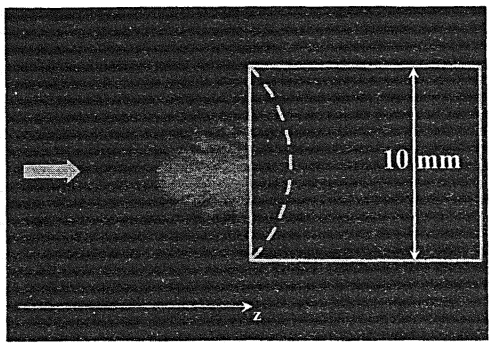

Fig. 2. Photo of the terahertz discharge in argon under a pressure 0.3 atm. Terahertz radiation falls from the left, and the additional focusing mirror is situated on the right (shown schematically)

This assumption has been confirmed by studying the spatial-temporal dynamic of the optical radiation of the discharge by means of a streak-camera FER-27. As seen at figure 3 the ionization front of the discharge moves toward the terahertz radiation with velocity of about 10^5 cm/s. Note that the glow is observed only in a relatively narrow region of the discharge front, which can be associated with strong attenuation of the terahertz radiation by the plasma.

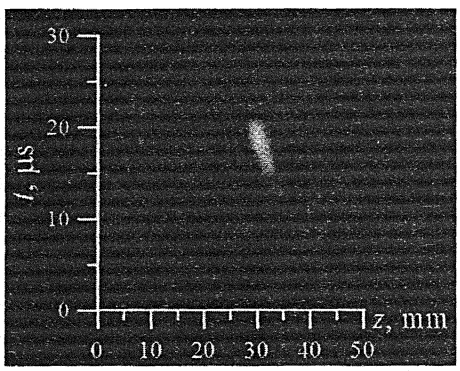

Fig. 3. Streak-camera image of the discharge in argon at pressure 0.5 atm

At high pressures the intensity of total optical emission of the discharge (the signal from the photomultiplier) increases during the entire terahertz pulse and decreases sharply after the end of the pulse (fig. 4). At the same time plasma of terahertz discharge leads to significant (up to 10 times) attenuation of transmitted terahertz. The density of the formed plasma can be estimated on the basis of these results. Our calculations show that the plasma density of the terahertz discharge is about $(5–8)\cdot10^{14}$ cm^{-3}, which is somewhat lower than the critical density for the used frequency.

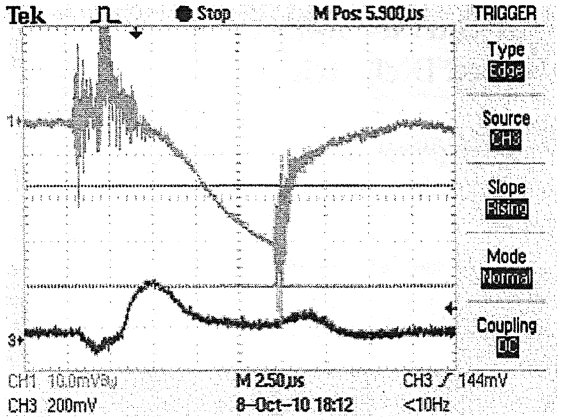

Fig. 4. Traces of optical emission of the discharge (ch. 1) and transmitted from the discharge terahertz power (ch. 3) in argon at pressure 500 Torr

At medium pressure (5–100 Torr) discharge looks like quasi-uniform plasma jet (fig. 5) with typical length 1–2 cm and diameter 2–3 mm.

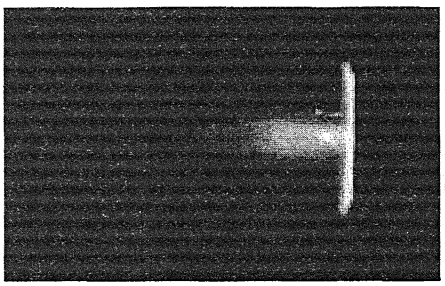

Fig. 5. Photo of the terahertz discharge in argon at pressure 10 Torr. Terahertz radiation falls from the left, and the additional focusing mirror is situated in the right (not shown)

According to streak-camera images of the plasma optical emission the discharge is formed in the focal area of the short-focus mirror and moves toward the terahertz radiation with velocity of about 10^5 cm/s at medium pressure as well as at high pressure. In contrast to high pressure, optical emission of medium-pressure plasma is observed not only in a relatively narrow region of the discharge front, but at all its length (fig. 6).

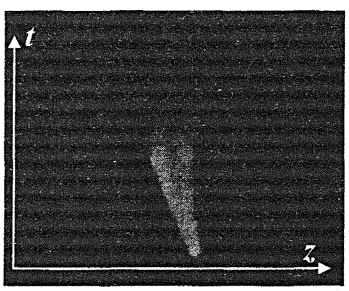

Fig. 6. Streak-camera image of the discharge in argon at pressure 58 Torr

Another feature of medium-pressure discharge is an after-glow effect – optical emission of the plasma continues a long time after the end of terahertz pulse. This effect is especially noticeable at relatively low discharge pressures. Moreover, at pressures lower than 50 Torr the maximum of total discharge emission occurs after the end of terahertz pulse with typical decay of about a few microseconds (see fig. 7).

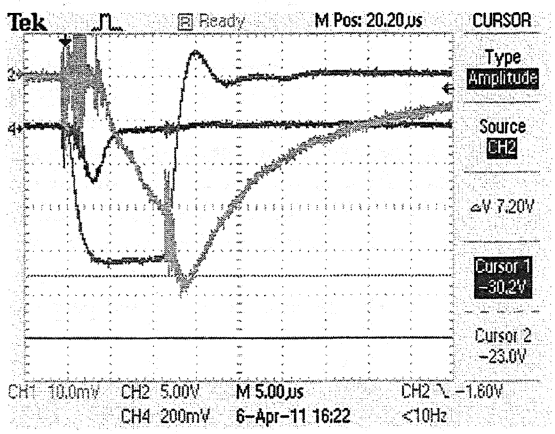

Fig. 7. Traces of optical emission of the discharge (ch. 1), high-voltage LOG pulse (ch. 2) and transmitted from the discharge terahertz power (ch. 4) in argon at pressure 12,5 Torr

One of possible explanations of this effect is probably connected with significant increase of role of electron-ion recombination in total plasma emission. The electron gas cooling after the end of terahertz pulse can lead to increase of recombination rate and correspondingly to recombination emission growth.

In presented study the terahertz discharge was regular and stable at argon pressures higher than 7 Torr. At lower pressures the breakdown threshold exceeds the maximum field of terahertz beam because of high rate of electron diffusion losses on the one hand and low rate of electron energy increases on the other hand [2]. Further investigations are to aim at significant increase of terahertz field magnitude for dense multi-charged ions plasma production.

This work has been supported by the Russian Foundation for Basic Research (projects 09-02-12154-ofi_m, 09-02-97084-r_povolzhye_a and 11-02-97072-r_povolzhye_a).

References

1. *V.L. Bratman, Yu.K. Kalynov, and V.N. Manuilov.* Large-Orbit Gyrotron Operation in the Terahertz Frequency Range // Phys. Rev. Lett. 2009. V. 102. P. 245101.

2. *A.D. McDonald.* Microwave breakdown in gases // New York: Wiley, 1966.

THz Emission from the Near-Surface Ionization of Large-Area DC-Biased Dielectric

V.A. Kostin, N.V. Vvedenskii

Institute of Applied Physics, Nizhny Novgorod, Russian Federation, vkl@appl.sci-nnov.ru

In this report we present the results of studying the generation of electromagnetic waves in the scheme which employs femtosecond laser pulse falling angularly on the boundary of the dielectric (photoconductive) medium. This laser pulse ionizes the near-surface layer of the dielectric medium so that an ionization front is formed as it is shown on the figure 1. The velocity of the ionization front V_{if} is determined by the velocity of the laser pulse V_L and the angle of incidence θ: $V_{if} = V_L/\cos\theta$. The dielectric is biased with DC electric field directed perpendicularly to its boundary.

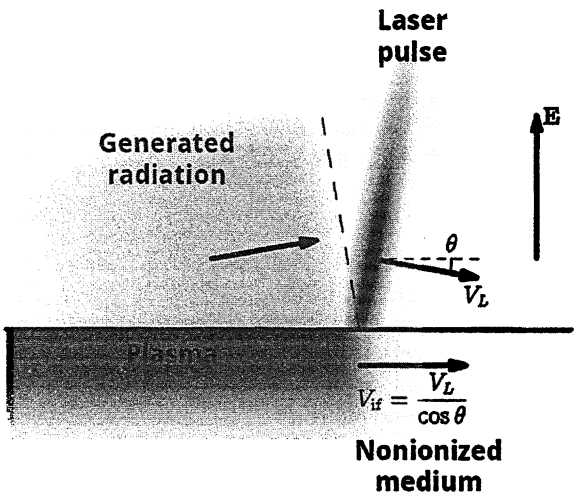

Fig. 1. Schematic of the conversion of static electric field to electromagnetic radiation

We find the generated emission by the solution of the Maxwell equations for the electric **E** and magnetic **B** fields,

$$\nabla \times \mathbf{B} = (4\pi/c)\,\mathbf{j} + (\varepsilon_0/c)\,\partial\mathbf{E}/\partial t, \qquad (1)$$

$$\nabla \times \mathbf{E} = -(1/c)\,\partial\mathbf{B}/\partial t, \qquad (2)$$

and the semiclassical equation for the current density of free carriers **j**,

$$\partial\mathbf{j}/\partial t + \nu\mathbf{j} = (Ne^2/m_{eff})\,\mathbf{E}. \qquad (3)$$

Here, c is the velocity of light in vacuum, ε_0 is the dielectric permittivity of non-ionized medium, N is the free carrier density, $e = |e|$ is the elementary charge, m_{eff} is the effective reduced mass of free carriers, ν is the collision frequency. To simplify the problem we assume that the dielectric and the born plasma layer have sharp boundaries: $N = N_0$ at $|x| < a$ and $N = 0$ otherwise, $\varepsilon_0 = \varepsilon_*$ at $x < a$ and $\varepsilon_0 = 1$ otherwise, a is the half-width of the plasma layer, x, y, z are the Cartesian coordiantes, N_0 is the maximum carrier density, ε_* is the permittivity of the dielectric medium. We assume the velocity V_{if} to exceed the velocity of light in the dielectric and in the surrounding space. In this case the fields before the ionization front are unchanged. Therefore, we can set up the initial conditions on the ionization front,

$$\mathbf{E}(\xi = 0) = D_e/\varepsilon_0(x)\,\mathbf{x}_0, \qquad (4)$$

$$\mathbf{B}(\xi = 0) = 0,\ \mathbf{j}(\xi = 0) = 0, \qquad (5)$$

and seek the solution in the terms of steady-state wave, when all the fields depend only on the variables x and $\xi = t - z/V_{if}$. In (5), D_e is the electric displacement of the external DC bias. The conditions of continuity of tangential fields at $|x| = a$ and the radiation conditions at $|x| \to \infty$ complete the setup of the problem.

We apply the Laplace transform to the equations (1)–(3) and solve the equation set obtained taking into account the boundary conditions. When the collisions are absent, $\nu = 0$, the found Laplace images are the meromorphic functions of the Laplace variable. Due to this fact the solution for the fields and the current density in time domain inside the plasma can be decomposed into a sum over the poles of the Laplace images,

$$\{\mathbf{E}, \mathbf{B}, \mathbf{j}\} = \sum\{\mathbf{E}_j, \mathbf{B}_j, \mathbf{j}_j\}\exp(-i\omega_j\xi). \qquad (6)$$

The individual terms in this sum correspond to leaky even transverse magnetic eigenwaves, which can travel along the plasma slab with the phase velocity equal to V_{if}. The frequencies ω_j of these waves have complex dependencies on the parameters a, V_{if}, and ε_*, so that the spectra of generated radiation can vary significantly with the change of any of these parameters.

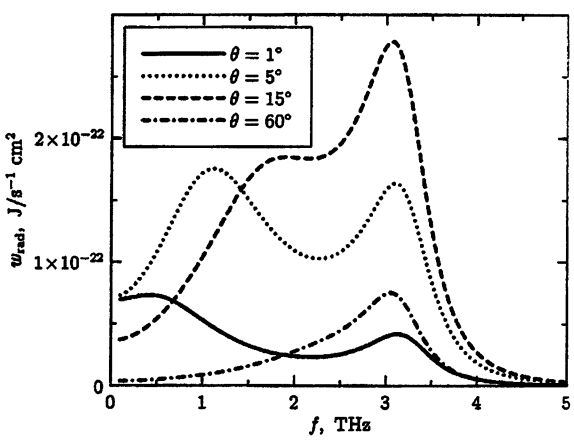

Fig. 2. The spectral density of generated radiation w_{rad} for various values of the angle of incidence θ

As an example, the spectral density of radiated energy for different values of the angle θ, i.e. for various values of V_{if}, is plotted on the figure 2. Here the GaAs is taken as the ionizable medium, $\varepsilon_* = 12.9$, the plasma frequency $\omega_p = (4\pi N_0 e^2/\varepsilon_* m_{eff})^{1/2} = 2\cdot 10^{13}$ s^{-1},

$\nu = 5 \cdot 10^{12}\ s^{-1}$, $D_e = 200$ kV/cm, $a = 3$ μm. In this case the position of the maximum in the radiation spectrum lies inside the THz frequency range near the plasma frequency or below it depending on θ, and the spectrum can be easily tuned by simple changing of angle of incidence. The radiated energy per unit area of the ionized surface can be evaluated as 7 nJ/cm^2 for $\theta = 15°$.

To conclude, the conversion of static homogeneous electric field into the electromagnetic radiation by the ionization front travelling inside the dielectric medium is investigated. The electromagnetic fields are calculated with the use of the exact Maxwell equations and semiclassical equation for the current of freed carriers. We find the dependencies of the spectrum, the polarization, the radiation pattern of the generated radiation, and the conversion efficiency on the incidence angle of the laser radiation and the spatial distribution of the free-carrier concentration which can be controlled reasonably easily by tuning laser pulse parameters. We determine the optimal conditions for the effective electromagnetic waves generation and designate the new ways to control the spectrum, the polarization, and the radiation pattern of the generated electromagnetic pulses for creation of the compact, effective, and tunable terahertz sources with the use of the dielectric media.

This work was supported by RFBR (Grant Nos. 11-02-01416, 09-02-01490, and 10-02-01250).

Broadband THz Emission from a Plasma Formed by the Ionizing Bessel Beam

V.A. Kostin, N.V. Vvedenskii

Institute of Applied Physics, Nizhny Novgorod, Russian Federation, vkl@appl.sci-nnov.ru

In this report, we present the results of studying THz emission from a superluminous ionization front produced by a femtosecond Bessel beam propagating in a gas medium. The emission is caused by excitation of the current pulse behind the ionization front due to the action of the field of ionizing laser pulse or of the external static electric field.

To describe the emission processes, explain the given experimental results and find out new possibilities to control parameters of THz radiation (e.g., the spectrum, the efficiency, and the radiation pattern), we develop a new approach based on the solution of a system of equations including exact Maxwell's equations for self-consistent electric **E** and magnetic **B** fields, the equation for the electron current density **j** in cold plasma

$$\partial \mathbf{j}/\partial t + \nu \mathbf{j} = (Ne^2/m)\,\mathbf{E} + \mathbf{S}, \qquad (1)$$

and the ionization equations for the time-dependent plasma density N

$$N = \sum N_\alpha,\ \partial N/\partial t = (N_{\alpha 0} - N_\alpha)\, w_\alpha. \qquad (2)$$

Here, e and m are the electron charge and mass, respectively; N_α, $N_{\alpha 0}$, and w_α are the density of ions, the initial density of neutrals, and the average probability of ionization per time unit, which are related to the particles of the α sort (for example, oxygen and nitrogen in the case of air ionization), respectively; ν is the effective collision frequency of electrons with heavy particles, which is determined by the gas pressure and electron temperature, **S** is the nonlinear driving term connected with the action of exciting fields (the laser field or the external electrostatic field) on free electrons. This driving term can independently include the contribution from the ponderomotive force of the laser pulse, its own electric field or also the second harmonic of the laser pulse.

The above equations are solved both analytically and numerically in cylindrical coordinates (r, φ, z), under the assumption that all fields and currents depend only on the variables $\xi = t - z/V_{if}$, r and φ; here $V_{if} > c$ is the velocity of the ionization front. The initial conditions are zero values of **B**, **j**, and N_α for $\xi \to -\infty$ and $\mathbf{E} = \mathbf{E}_0$, where $\mathbf{E}_0$ is the value of the external electrostatic field. The boundary conditions for the fields are the radiation conditions for $r \to \infty$.

To find the analytical solution, we assume that the laser field is non-zero for $\xi < 0$ within a small interval $\Delta\xi$ of order of the laser pulse duration. During this interval $\Delta\xi$, the laser pulse produces distributions of plasma density $N(r)$ and current density $\mathbf{j}_0(r, \varphi)$. Then, we solve the Maxwell equation and Eq. (1) with $\mathbf{S} = 0$ in the domain $\xi > 0$ with the initial conditions at $\xi = 0$. These conditions are $\mathbf{E} = \mathbf{E}_0$, $\mathbf{B} = 0$, and $\mathbf{j} = \mathbf{j}_0$. By setting such initial conditions for the fields, we assume that the period of the THz field generated by the plasma is much longer than the duration of the ionizing laser pulse and, hence, we can neglect the polarization response of the plasma at the THz frequency, which emerges during the time of the laser pulse action. For the sake of simplicity, we also assume that $N(r) = N_0$ for $r < a$ and $N(r) = 0$ for $r > a$ and use the conditions of continuity of the tangential electric and magnetic fields at $r = a$. We find solutions by applying the Laplace transform with respect to ξ.

Such analytical treatment shows that the main properties of the generated radiation such as spectrum and polarization depend strongly on the initial current distribution $\mathbf{j}_0(r, \varphi)$ on the ionization front and the value and the direction of the external electric field $\mathbf{E}_0$. The axisymmetric ponderomotive force creates axisymmetric initial current $\mathbf{j}_0$ having longitudinal and radial components. In opposite, the own electric field of the laser pulse or its second harmonic produce the initial current with azimuthal variation.

The symmetric part of the initial current and the longitudinal component of the external electric field result in the symmetric conical emission with radial polarization. The unanticipated fact is that the frequency corresponding to the maximum of the THz spectrum and the spectrum width are determined by the electron collision frequency and are almost independent of the maximum plasma frequency which is much greater than the collision frequency for plasma channels created by axicon-focused laser pulses [1]. For example, when the external longitudinal electric field is absent and the plasma cylinder is thin enough, $a \ll c/\omega_p$, and the condition $(a\omega_p \sin\theta/c)^2 \times \ln[c/a\nu \sin\theta] \ll 1$ is fulfilled, $\omega_p = (4\pi N_0 e^2/m)^{1/2}$ is the plasma frequency, the spectrum of the generated radiation at relatively low frequencies $|\omega| \ll \omega_p/\sin\theta$ can be described through the simple formula

$$|B_{\varphi\omega}|^2 = (2\pi I_0^2 \sin\theta/c^3 r)\, |\omega|/(\omega^2 + \nu^2). \qquad (3)$$

Here, I_0 is the total initial longitudinal current created by the ponderomotive force and $\theta = \arccos c/V_{if}$. The THz spectrum determined by the collision frequency agrees well with the spectrum obtained in experiments and is confirmed also by the results simulating numerically the dynamics of the field and plasma during ionization of the ambient air by axicon-focused laser pulses [1]. The characteristic radius of the plasma channel and the value of maximum plasma density are strongly dependent on the values of the laser pulse duration, the energy of the laser pulse, and the focusing angle. However, the spectrum of the THz radiation, which was found numerically, depends weakly on these parameters and its shape is close to that yielded by equation (3).

On the contrary, the non-symmetric part of the initial current and the transverse component of the external electric field result in the non-symmetric solution. The position and the width of the peaks in the spectrum are determined by the real and imaginary parts of the complex frequencies of the natural leaky hybrid waves propagating along the plasma cylinder with the phase velocity equal to the velocity of the ionization front V_{if}. The values of the complex frequencies of the leaky natural waves and their amplitudes depend strongly on the plasma density, the velocity and transverse size of the ionization front, and on the value of internal losses associated with the spatial inhomogeneity of the plasma density and with the collisions of electrons with heavy particles; and the amplitudes depend also on the spatial distribution of the initial current density on the ionization front. In the most cases only one natural wave is excited effectively. When the plasma cylinder is thin, $a << c/\omega_p$, and intrinsic losses in plasma are minor, the complex frequency of this wave is close to $\omega_p/2^{1/2}$ [2, 3, 4]

The ratio between energies of symmetric emission excited by the ponderomotive force and non-symmetric emission excited by the laser electric field itself is determined by the laser pulse duration. When few-cycle ionizing laser pulses (with the pulse duration not much longer than the optical field period) are used, the energy of the non-symmetric part grows dramatically [4, 5]. The non-symmetric initial current density depends strongly on the carrier-envelope phase (CEP) of the laser pulse, hence the conversion efficiency depend strongly on CEP too. Our simulations reveal the value of CEP which corresponds to the most efficient THz waves generation. We show that for the single-cycle laser pulse of millijoule energy it is possible to obtain very high conversion efficiency and the corresponding THz radiation of a gigawatt power level.

For Bessel beams generated by axicons with focusing angles of 3°–15° and air of atmospheric pressure, the *forced* THz emission based on the use of the static external electric field is much weaker than the *self-induced* emission unlike the case of the conventional filamentation of the laser pulse [6, 7].

This work was supported by RFBR (Grant Nos. 11-02-01416, 09-02-01490, and 10-02-01250) and the Ministry of Education and Science of the Russian Federation.

References

1. *Kostin, V.A., Vvedenskii, N.V.* Ionization-induced conversion of ultrashort Bessel beam to terahertz pulse // Opt. Lett. 2010. V. 35. P. 247.

2. *Golubev, S.V., Suvorov, E.V., Shalashov, A.G.* On the possibility of terahertz wave generation upon dense gas optical breakdown // JETP Lett. 2004. V. 79. P. 361.

3. *Bystrov, A.M., Vvedenskii, N.V., Gildenburg, V.B.* Generation of terahertz radiation upon the optical breakdown of a gas // JETP Lett. 2005. V. 82. P. 753.

4. *Gildenburg, V.B., Vvedenskii, N.V.* Optical-to-THz wave conversion via excitation of plasma oscillations in the tunneling-ionization process // Phys. Rev. Lett. 2007. V. 98. P. 245002.

5. *Silaev, A.A., Vvedenskii, N.V.* Residual-current excitation in plasmas produced by few-cycle laser pulses // Phys. Rev. Lett. 2009. V. 102. P. 115005.

6. *Houard, A., Liu, Y., Prade, B., Tikhonchuk, V.T., Mysyrowicz, A.* Strong enhancement of terahertz radiation from laser filaments in air by a static electric field // Phys. Rev. Lett. 2008. V. 100. P. 255006.

7. *Löffler, T., Jacob, F., Roskos, H.G.* Generation of terahertz pulses by photoionization of electrically biased air // Appl. Phys. Lett. 2000. V. 77. P. 453.

Ultra-Fast Phenomena on Powerful Terahertz NovoFEL

V.V. Kubarev[1], G.N. Kulipanov[1], E.N. Chesnokov[2], O.A. Shevchenko[1]

[1]Budker Institute of Nuclear Physics, Novosibirsk, Russia, V.V.Kubarev@inp.nsk.su
[2]Institute of Chemical Kinetics and Combustion, Novosibirsk, Russia

Light pulse structure of THz NovoFEL

Novosibirsk terahertz free electron laser (THz NovoFEL) generates continuous train of sufficiently long (100–150 ps) pulses [1]. The peculiarity allows us to have narrow laser line. But later is possible only when modulation instability is suppressed [2]. Period of the instability $T = L_s/c = 74\ \lambda/c = 30$–$60$ ps, where L_s is slippage length and λ is wavelength. Negative detuning between electron and light repetition frequencies is effective method of suppression of the instability (Figs. 1, 2). Eearly we observed the modulation instability and its suppression in frequency domain by Fourier spectrometer which showed spectra and coherency. But the instability was practically not observed in time domain because it was impossible to measure one by our sampling oscilloscope due to a jitter of perturbations from pulse to pulse [2]. Now we use our ultra-fast Schottky diode detector [3] with the direct 30 GHz LeCroy oscilloscope and have full clear picture of the phenomenon in time domain (Fig. 2). One can see that the full coherent stabilized regime #1 transforms in the multimode regime with correlated sub-pulses #2 when the sub-pulses with slippage period appear as a result of decreasing of the stabilization factor. Then the sup-pulses stay practically uncorrelated in the resonance point #3 [2]. For a positive detuning we observe decreasing of number of generated independent sub-pulses with practically constant maximal pulse power due to saturation effect (#4–#5). Last regime can be used for some user applications when shot pulse radiation is need.

The measuring of light pulse structure is necessary not only for study of the instabilities but has a routine application in determination of real laser pulse power.

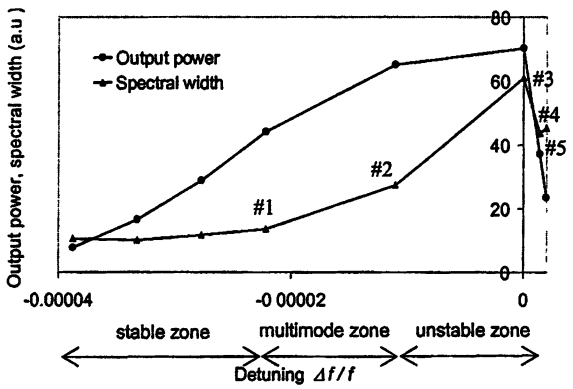

Fig. 1. Output NovoFEL cw power and its spectral width versus detuning between electron and light repetition frequencies. Numbers #1–#5 near spectral width curve mark light pulse pictures in Fig. 2

Thus maximal pulse power of NovoFEL was about of 400 kW in regime with repetition frequency of 11.2 MHz and cw power of 400 W, and about 250 kW in regime at repetition frequency of 22.4 MHz and cw power of 500 W.

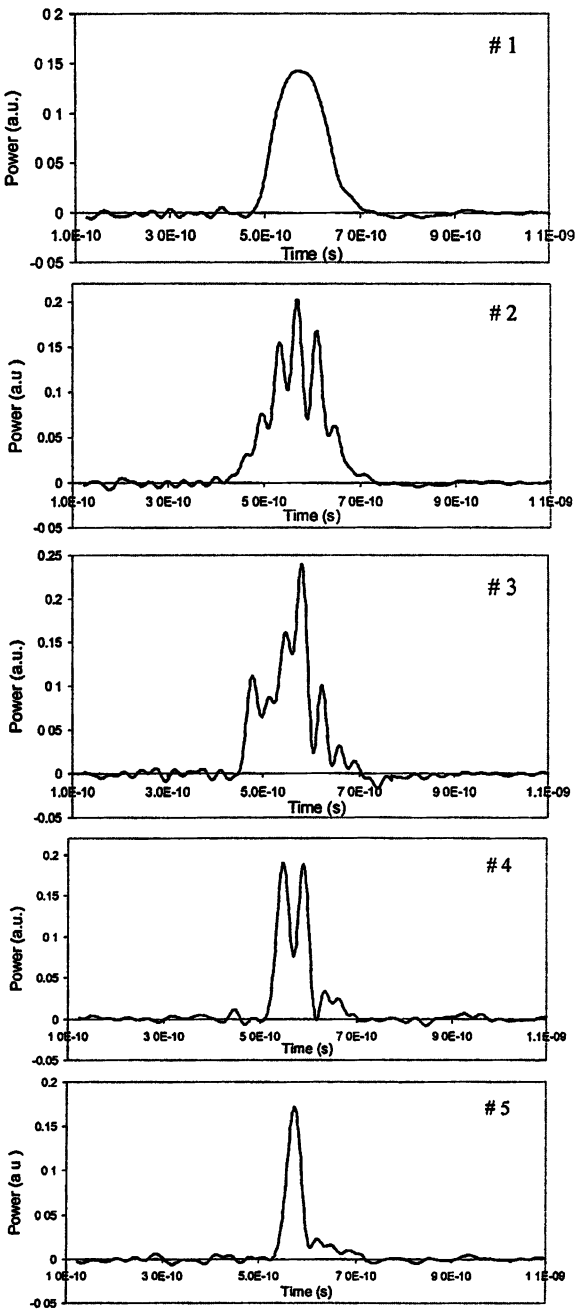

Fig. 2. Terahertz NovoFEL light pulses for different detuning marked in Fig. 1. Laser wavelength is 130 μm

Free induction decay of molecular transitions

Phenomenon of THz free induction decay in gases is coherent radiation of molecules excited by coherent laser pulse in result its transitions in ground state. We first observed the process directly in picoseconds time range using our ultra-fast Schottky diode detector. Some illustrations of such experiments are shown in Figs. 3–4.

First experiment (Fig. 3) was made with gas cell filled D_2O vapor. Center of laser line was tuned in the rotational transition of D_2O molecule with wavenumber of 70.3 cm^{-1}. Initially molecules absorb laser radiation and when radiate part of the power as free induction decay signal.

More strong effect one can see for HBr vapor (Fig. 4) due to more radiation efficiency of the molecules.

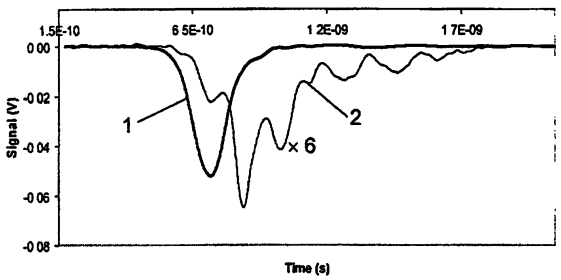

Fig. 3. Free induction decay in D_2O vapor: laser pulse after cell without (1) and with (2) the vapor. Wavenumber of D_2O rotational transition is 70.3 cm^{-1}

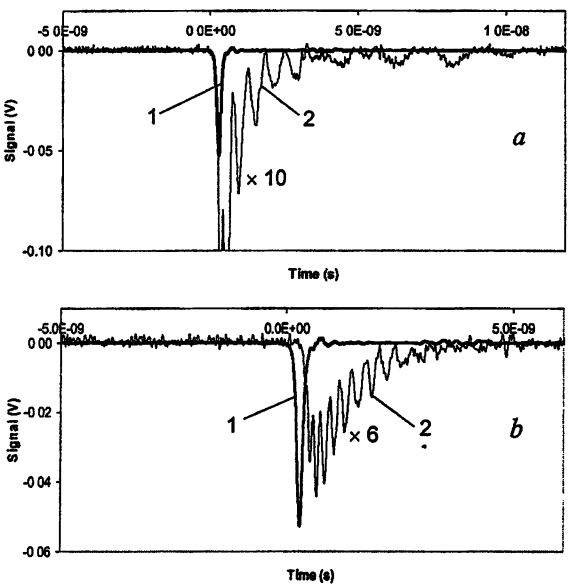

Fig. 4. Free induction decay in HBr vapor: laser pulse after cell without (1) and with (2) the vapor in the case of low (*a*) and middle (*b*) vapor density. Wavenumber of HBr doublet rotational line is $\nu = 66.71$ cm^{-1} and $\Delta\nu = 0.02$ cm^{-1}

The experiments coincide very well with simulations based on linear Lorentz dispersion theory of gases. Free induction signal contains full spectral information about gas medium in the excited spectral range. Therefore we plan to use this phenomenon for ultra-fast high-resolution spectroscopy. In addition to widely used in present time slow femtosecond scanning time-domain spectroscopy, such technique allows us to investigate ultra-fast unrepeated phenomena because measuring time of a spectrum can be only some nanoseconds. For example last four oscillations of signal in Fig. 4a) are coursed by doublet structure of the absorption line unresolved in our spectral devices.

Dynamic of THz optical discharge

Continuous THz optical discharge was one of the demonstrations of high pulse power of NovoFEL [4]. According a classical model, dynamic of the discharge presents a fast appearing and heating of free electrons during of the light pulse. Then slow decay takes place between FEL pulses with character diffusion time ~ 100 ns [5]. Measuring of real parameters of the dynamic is need for future user application of the phenomenon. It can be made in some pump-probe experiment. Such experiment is one of our activities in the present time.

References

1. *Gavrilov N.G., Knyazev B.A., Kolobanov E.I., Kotenkov V.V., Kubarev V.V., Kulipanov G.N., Matveenko A.N., Medvedev L.E., Miginsky S.V., Mironenko L.A., Oreshkov A.D., Ovchar V.K., Popik V.M., Salikova T.V., Scheglov M.A., Serednyakov S.S., Shevchenko O.A., Skrinsky A.N., Tcheskidov V.G., Vinokurov N.A.* Status of the Novosibirsk high-power terahertz // Nucl. Instr.&Meth. 2007. A575. P. 54-57.

2. *Kubarev V.V., Kulipanov G.N., Kolobanov E.I., Matveenko A.N., Medvedev L.E., Ovchar V.K., Salikova T.V., Scheglov M.A., Serednyakov S.S., Vinokurov N.A.* Modulation instability, three mode regimes and harmonic generation at the Novosibirsk terahertz free electron laser // Nucl. Instr.&Meth. 2009. A 603. P. 25-27.

3. *Kubarev V.V., Ovchar V.K. and Palagin K.S.* Ultra-fast Terahertz Schottky Diode Detector // Conference digest of the 34th international conference on infrared, millimeter and terahertz wave. Busan. Korea. 21–25 Sept. 2009. report 09030439.

4. *Bolotin V.P., Kayran D.A., Knyazev B.A., Kolobanov E.I., Kotenkov V.V., Kubarev V.V., Kulipanov G.N., Matveenko A.N., Medvedev L.E., Miginsky S.V., Mironenko L.A., Oreshkov A.D., Ovchar V.K., Popik V.M., Salikova T.V., Serednyakov S.S., Skrinsky A.N., Shevchenko O.A., Scheglov M.A., Vinokurov N.A., Zaigraeva N.S.* Status of the Novosibirsk high power free electron laser // Conference digest of the 2004 Joint 29-th international conference on infrared and millimeter waves and 12-th international conference on terahertz electronics. Sept. 27–Oct. 1. 2004. Karlsruhe. Germany. P. 55-56.

5. *Bolotin V.P., Knyazev B.A., Kolobanov E.I., Kotenkov V.V., Kubarev V.V., Kulipanov G.N., Matveenko A.N., Medvedev L.E., Oreshkov A.D., Persov B.Z., Popik V.M., Salikova T.V., Serednyakov S.S., Shevchenko O.A., Scheglov M.A., Vinokurov N.A.* Quasi-continuous submillimeter optical discharge on Novosibirsk free electron laser: experiments and elementary theory // Proc. Joint 30th International Conference on Infrared and Millimeter Waves & 13th International Conference on Terahertz Electronics. 19–23 September 2005. Williamsburg. USA. P. 126-127.

Terahertz Generation in Laser Cluster Interaction

Manoj Kumar[1], V.K. Tripathi

[1]Indian Institute of Technology Delhi, New Delhi, India, manojailum@gmail.com

A scheme of terahertz (THz) generation [1, 2] by two collinear laser pulses of finite spot size in a clustered gas is investigated theoretically [3]. The lasers quickly ionize the atoms of the clusters, converting them into plasma balls and exert a ponderomotive force on the cluster electrons, producing a beat frequency longitudinal current of limited transverse extent. The current acts as an antenna to produce beat frequency terahertz radiation. As the cluster expands under the hydrodynamic pressure, plasma frequency of cluster electrons ω_{pe} decreases and approaches $\sqrt{3}$ times the frequency of laser, resonant heating and expansion of clusters occurs. On further expansion of clusters as ω_{pe} approaches $\sqrt{3}$ times the terahertz frequency, resonant enhancement in THz radiated power occurs.

Theoretical model

Consider a gas jet target embedded with atomic clusters of radius r_{c0} and density n_c. Two collinear laser beams propagate through it with electric fields $\mathbf{E}_j = \hat{x}A_j e^{-i(\omega_j t - \mathbf{k}_j z)}$, where, $A_j^2 = A_{j0}^2 e^{-(t-z/v_g)^2/\tau_L^2} \times$ $\times e^{-r^2/r_0^2}$, where $j = 1, 2$, v_g is the group velocity of lasers and τ_L is the pulse duration of laser and $\omega = (\omega_1 - \omega_2)$ is in the terahertz range $(\omega << \omega_1, \omega_2)$. The lasers quickly ionize the atoms of clusters, converting them into plasma balls. After solving the equation of motion for cluster electrons under the electric fields of lasers, and it gives the electron excursions and quiver velocities,

$$\Delta_j = \frac{e\mathbf{E}_j}{m(\omega_j^2 - \omega_{pe}^2/3 + i\nu\omega_j)}, \qquad \mathbf{v}_j = \frac{e\omega_j\mathbf{E}_j}{mi(\omega_j^2 - \omega_{pe}^2/3 + i\nu\omega_j)}, \tag{1}$$

where m is the mass of electron and ν is the electron-ion collision frequency and $\omega_{pe} = (4\pi n_e e^2/m)^{1/2}$ is cluster electron plasma frequency. The lasers heat the cluster electrons at a time average rate (averaged over the laser periods) as

$$\frac{d}{dt}\left[\frac{3}{2}T_e\right] = -\frac{e}{2}\mathrm{Re}\left[\mathbf{E}_1^*.\mathbf{v}_1 + \mathbf{E}_2^*.\mathbf{v}_2 + \mathbf{E}_1.\mathbf{v}_2^* + \mathbf{E}_2^*.\mathbf{v}_1\right]. \tag{2}$$

The clusters undergo expansion, due to the pressure associated with heated electrons [4, 5]. For electron excursion less than a Debye length and cluster radius $\Delta_j << (v_{th}/\omega_{pe})$, r_c, one may take the expansion to be hydrodynamic and expansion velocity equal to the sound velocity $c_s = (T_e/m_i)^{1/2}$, as the cluster expands its radius increases and the plasma frequency decreases, $\omega_{pe}^2 = \omega_{pe0}^2 (r_c/r_{c0})^{-3}$. From the Fig. 1, we may note that cluster heating rises sharply when the electron density in the cluster approaches three times of the critical density, i.e. $\omega_{pe} = \sqrt{3}\,\omega_1$. As further expansion of the cluster detunes this resonance, the temperature decreases slowly with time due to adiabatic cooling.

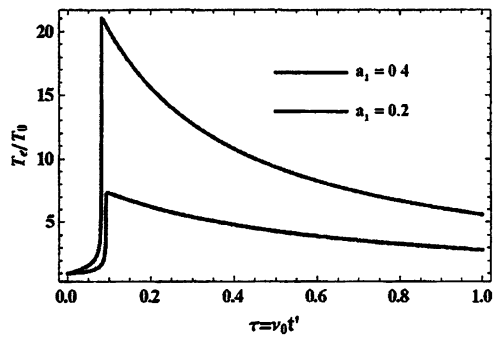

Fig. 1. Normalized cluster electrons temperature (T_e/T_0) as a function of normalized time $(\tau = \nu_0 t')$ for normalized amplitudes $a_1 \approx a_2 = 0.2, 0.4$

The lasers exert a ponderomotive force on the cluster electrons at the beat frequency $\omega = \omega_1 - \omega_2$, $\mathbf{k} = \mathbf{k}_1 - \mathbf{k}_2$,

$$\mathbf{F}_p^c \equiv e\nabla\phi_p^c = -\frac{e}{2c}(\mathbf{v}_1 \times \mathbf{B}_2^* + \mathbf{v}_2^* \times \mathbf{B}_1). \tag{3}$$

The velocity of cluster electrons under the ponderomotive force is

$$\mathbf{v}' = \frac{i\omega\,\mathbf{F}_p^c}{m(\omega^2 - \omega_{pe}^2/3 + i\nu\omega)}. \tag{4}$$

The nonlinear current density at ω, $\mathbf{k}$ is,

$$\mathbf{J}_{\omega,k}^{NL} = -n_a e\mathbf{v}' = \hat{z}\frac{n_c r_{c0}^3 e A_1 A_2^* e^{-i(\omega t - kz)}}{6mc}\frac{\omega_{pe}^2/\omega_1^2}{(\omega^2 - \omega_{pe}^2/3 + i\nu\omega)}. \tag{5}$$

If the plasma cylinder were of large (infinite) radius, the axial current density would cause only the electrostatic fields. However, when the plasma cylinder radius is finite there is discontinuity in the dielectric constant that produces the magnetic field. For cylinder radius less than the THz wavelength, ponderomotive force driven current can be taken to be unmodified by the self-field and the nonlinear current source can be treated like a wire antenna as far as the radiation field is concerned. The vector potential at a far

point $\mathbf{r}(r,\theta,\phi)$ due to all the clusters in cylinder of length L and radius r_0, where r_0 is the spot size of laser,

$$\mathbf{A}(\mathbf{r},t)=\hat{z}\frac{\pi n_c r_{c0}^3 eA_1A_2^* e^{-i(\omega(t-r/c)}}{3mrc^2}\frac{(e^{i\omega(1-\cos\theta)L/c}-1)}{i\omega(1-\cos\theta)/c}\times$$
$$\times\int_0^{r_0}\frac{\omega_{pe}^2/\omega_1^2}{(\omega^2-\omega_{pe}^2/3+iv\omega)}J_0\left(\frac{\omega\rho_i}{c}\sin\theta\right)\rho_i d\rho_i. \quad (6)$$

For far field, the electric field and magnetic field of the THz is

$$\mathbf{E}_r(\mathbf{r},t)=\hat{z}\frac{\pi n_c r_{c0}^3 eA_1A_2^* e^{-i(\omega(t-r/c)}}{3mrc^2}\frac{(e^{i\omega(1-\cos\theta)L/c}-1)}{(1-\cos\theta)}I,$$

$$\mathbf{B}_r(\mathbf{r},t)=(\hat{r}\times\hat{z})\frac{\pi n_c r_{c0}^3 eA_1A_2^* e^{-i(\omega(t-r/c)}}{3mrc^2}\frac{(e^{i\omega(1-\cos\theta)L/c}-1)}{(1-\cos\theta)}I,$$

where,

$$I=\int_0^{r_0}\frac{\omega_{pe}^2/\omega_1^2}{(\omega^2-\omega_{pe}^2/3+iv\omega)}J_0\left(\frac{\omega\rho_i}{c}\sin\theta\right)\rho_i d\rho_i.$$

The normalized radiated terahertz power is

$$\frac{\mathbf{S}_{av}r^2}{P_0}=\hat{r}\frac{\pi(n_c r_{c0}^3)^2}{9}\frac{v_{th}^2}{c^2}\frac{r_0^2\omega_2^2}{c^2}\frac{\omega_{pe0}^4}{\omega_1^4}\left|\frac{eA_{20}}{m\omega_2 v_{th}}\right|^2\times$$
$$\times\frac{e^{-2\tau^2/v_0^2\tau_{L1}^2}\sin^2[\sin^2[\theta/2]\omega L/c]\cos^2[\theta/2]}{\sin^2[\theta/2]}I_1^2, \quad (7)$$

where,

$$I_1=\int_0^1\frac{\rho_i' e^{-2\rho_i'^2}(1-\omega_{pe0}^2/3\omega^2(r_c/r_{c0})^{-3})(r_c/r_{c0})^{-3}}{(1-\omega_{pe0}^2/3\omega^2(r_c/r_{c0})^{-3})^2+v_0^2/\omega^2(T_e/T_{e0})^{-3}}\times$$
$$\times J_0\left(\frac{\omega r_0}{c}\rho_i'\sin\theta\right)d\rho_i',$$

where, $\rho_i'=\rho_i/r_0$. The normalized radiated total terahertz power is,

$$\frac{P_{THz}}{P_0}=\int_0^{2\pi}\int_0^{\pi}(\bar{S}_{av}r^2/P_0)\sin\theta d\theta d\Phi$$

$$\frac{P_{THz}}{P_0}=\frac{2\pi^2(n_c r_{c0}^3)^2 e^{-2\tau^2/v_0^2\tau_{L1}^2}}{9}\frac{v_{th}^2}{c^2}\frac{r_0^2\omega_2^2}{c^2}\frac{\omega_{pe0}^4}{\omega_1^4}\left|\frac{eA_{20}}{m\omega_2 v_{th}}\right|^2$$
$$\int_0^{\pi}\frac{\sin^2[\sin^2[\theta/2]\omega L/c]\cos^3[\theta/2]}{\sin[\theta/2]}I_1^2 d\theta. \quad (8)$$

From the Fig. 2, the angular distribution of the emitted radiation depends upon the length of the cluster plasma. For the larger L, peak is located at an angle 20°, if we decrease the length of plasma the peak is shifted from 20° to 30°. From the Fig. 3, the THz power rises slowly with time, acquire a maximum at the resonance condition, where $\omega_{pe}=\omega\sqrt{3}$. This resonance enhancement in the THz radiation occurs for a limited duration then falls off with time. The laser excitation of terahertz radiation requires laser intensity $\geq 10^{15}$ w/cm^2 and the pulse duration should be larger than the 100 fs. The THz power goes as square of laser spot size (as long as the THz wavelength is bigger than the spot size of laser). It scales linearly with square of $(n_c r_c^3)$, square of laser amplitude, fourth power of cluster electron plasma frequency and the inverse square of laser frequency. The plasma region on the scale of Rayleigh length produced by the lasers work as a dipole antennae of THz radiation. The energy conversion efficiency for our parameters is $\sim 10^{-4}$.

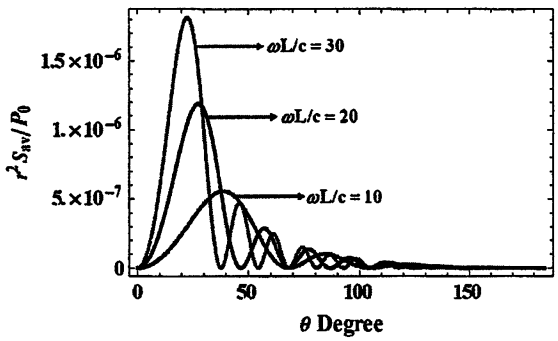

Fig. 2. Normalized THz power ($\mathbf{S}_{av}r^2/P_0$) as a function of θ for the different values of $\omega L/c = 10, 20, 30$ with normalized amplitude $a_2 = 0.2$

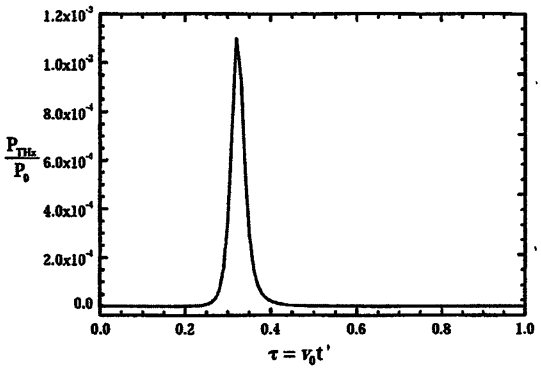

Fig. 3. Normalized total THz power (P_{THz}/P_0) as a function of normalized time ($\tau = v_0 t'$) with normalized amplitude $a_2 = 0.2$

References

1. *Nagashima, T., Hirayama, H., Shibuya, K., Hangyo M., Hashida, M., Tokita, S., Sakabe, S.,* Terahertz Radiation from Argon Clusters Irradiated by Intense Femtosecond Laser Pulses // Opt. Express. 2009. V. 17, No. 12. P. 8807-8812.

2. *Gildenburg, V.B., Vvedenskii, V.V.,* Optical-to-THz Wave Conversion via Excitation of Plasma Oscillations in the Tunneling-Ionization Process, 2007 // Phys. Rev. Lett. V. 98, No. 24. P. 245002-245006.

3. *Kumar, M., Tripathi, V.K.,* Terahertz generation by nonlinear mixing of laser pulses in a clustered gas // Plasma. 2011. V. 18, No. 5, P. 053105-05.

4. *Ditmire, T., Donnelly, T., Rubenchik, A., Falcone, R., Perry, M.,* Interaction of intense laser pulses with atomic clusters // Phys. Rev. A. 1996. V. 53, No. 5. P. 3379-3402.

5. *Kumar, M., Tripathi, V.K.,* Rayleigh scattering of a Gaussian laser beam from expanding clusters // Phys. Plasma. 2009. V. 16, No. 12. P. 123111-05.

THz Absorption in the Nanodispersed Oxide Materials

V.I. Mukhin[1], A.N. Khodan[2], M.M. Nazarov[1]

[1] Lomonosov Moscow State University, Moscow, Russia, ppvadim@rambler.ru
[2] Frumkin Institute of Physical Chemistry and Electrochemistry, Russian Academy of Sciences, Moscow, Russia

Physical and functional properties of nanodispersed materials remain studied insufficiently. Nanomaterials and its physical and chemical modifications can be applied for creation of new devices and functional mediums using the effects of selective absorption, internal or external photoelectric effect, variable refractive index and others.

This paper presents THz spectroscopy study of refraction and absorption in nanostructured aluminum oxyhydroxides (NOA) and its modification by surface silica (NOAM). NOA materials possess very high porosity ~ 99 % and specific surface up to 320 m^2/g [1]. Chemical composition of NOA can be described as $Al_2O_3 \cdot nH_2O$ with n ranging from 1 to 3.7 and dependent on the synthesis temperature. Initial structure of NOA can be described as 3D network consisting of supramolecular nanofibrils with diameter about 5–7 nm and average length 100–150 nm. XRD show diffused halo from the amorphous phase.

High temperature annealing change the phase state of NOA and influence the chemical composition: n becomes ~ 0.1 for γ- and θ-Al_2O_3 phase and is approaching to 0 for α-Al_2O_3. Using 4 hours isochronous annealing the following phase transitions were observed: supramolecular system transforms to amorphous oxide at 100°C, which in turn transforms to γ-Al_2O_3 at 650–900 °C, and α-Al_2O_3 is formed at ≥ 1100 °C.

Chemical composition of NOAM can be presented as $Al_2O_3 \cdot nH_2O \cdot kSiO_2$ where k ranging from 0.06 to 0.25. The temperatures of isochronous phase transition in NOAM is shifted about 100–200 °C for supramolecular to amorphous transformation, and crystallization of γ-Al_2O_3 starts at 1000–1200 °C.

Using TGA measurements the values of n were estimated at different annealing temperatures:

T, °C	20	100	200	380	520	650	900	1000	1200
NOA	3.72	1.45	1.06	0.88	0.58	0.27	–	–	–
NOAM	3.70	2.86	1.94	1.57	1.45	1.33	0.95	0.88	0.46

Pulse THz spectroscopy was used to obtain absorption and refraction spectra of NOA and NOAM specimens [2], and specific values of absorption and refraction of the main structural component – fibrils – were calculated using Bruggeman effective medium model [3], Fig. 1.

Estimation of refraction index of the fibrils in NOA and NOAM was about 3±0.25, it is similar to that in sapphire [4].

THz absorption decreases with the higher temperature of annealing, what can be simply explained by the dehydration of NOA and NOAM materials. Hydrophobization of NOAM surface leads to the smaller absorption in relation to the equally processed NOA samples.

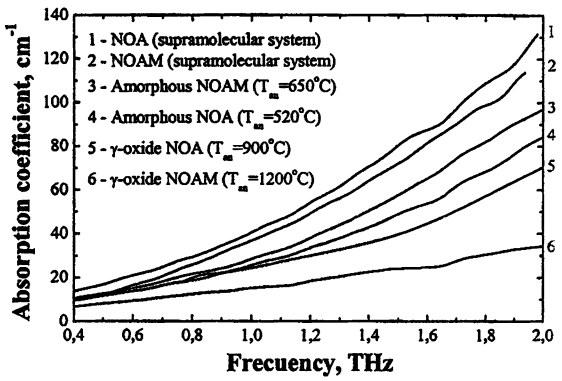

Fig. 1. Absorption spectra of NOA and NOAM for supramolecular phase, amorphous oxide and γ-oxide

We sort out several states of water in NOA and NOAM materials: molecular water with hydrogen bonding in the fibrils in supramolecular state and/or physically adsorbed water at the surface of other alumina phases, hydroxyls inside of the NOA structure and chemically adsorbed water at the surface. It was proved that the pulse THz spectroscopy is sensitive to one or several monoatomic layers of water at the surface of alumina.

Results of this study could be used for calculation of absorption and refraction spectra of any dispersed media consisting of alumina nanoparticles.

NOA and NOAM materials not have resonances in THz range that makes them applicable for elaboration of composite functional matrixes and porous substrates with chemically modified surface. This allows studying spectra of small quantities of molecules deposited at the surface of NOA or NOAM.

References

1. *J.-L. Vignes, C. Frappart, T. di Costanzo, J.-C. Rouchaud, L. Mazerolles, D. Michel* Ultraporous monoliths of alumina prepared at room temperature by aluminium oxidation // Journal of Materials Science, Feb. 2008, v. 43, 4, p. 1234-1240.

2. *M.M. Nazarov, A.P. Shkurinov, E.A. Kuleshov* Terahertz time-domain spectroscopy of biological tissues // Quantum Electronics, 2008, 38, № 7, p. 647-654.

3. *L.A. Golovan, V.Yu. Timoshenko, P.K. Kashkarov* Optical properties of porous-system-based nanocomposites // Physics-Uspekhi, 2007, 50, p. 595-612.

4. *H. Walther, N. Koroteev, M.O. Scully* Frontiers in nonlinear optics. – Bristol and Philadelphia: Institute of Physics Publishing, 1993, p. 221.

Subwavelength Structures in Metal Film for THz Surface Plasmon Control

M.M. Nazarov[1], A.Y. Ryabov[1], I.Yu. Denisyuk[2]

[1]Department of Physics of M.V. Lomonosov Moscow State University, Russia; maxim@lasmed.phys.msu.ru
[2] ITMO, Saint-Petersburg, Russia

Surface plasmons (SP) are collective excitations of free electron gas at the surface of a conductor [1]. They are interesting due to their field localization at the surface, but in THz frequency SP field confinement is problematic because metals are almost ideal conductors here [2]. THz SP waves propagate over tens of cm, sensing devices or more complex 2D systems are foreseen, in which information is carried or enhanced by THz SP's. But the fact that the SP waves are loosely bound creates difficulties in realizing useful devices because of the lack of field confinement. Slowing down the THz SP velocity without introducing a considerable dispersion is necessary for keeping SP strongly localized on a non ideal surface and thus to reduce its expansion in the surrounding dielectric medium over the metal.

Substance properties may be engineered by subwavelength structuring (SWS). In visible range it can be nanoparticles or diffraction gratings, more sophisticated devices are difficult to produce in nanometer scale. For terahertz frequency range ($\lambda = 0.3$ mm) wavelengths and sizes of plasmon devices became thousand times larger, and complex structures for plasmons studies are produced with grate accuracy.

We study the interaction of propagating and localized SP on sub-wavelength corrugated or drilled surfaces, formation of standing surface waves for a the local field enhancement [3, 4]. We use the time-domain THz transmission and reflection techniques to perform the experiments [2, 4] and modeling to explain them.

We start with an extraordinary transmission (EOT) through an array of the subwavelength holes with sizes smaller than the wavelengths. We analyze the effect of the shape and the size of the hole, thickness of the metal film and of the substrate on a transmittance spectrum of a free space and of surface waves. We have investigated four samples, each being different by a particular size of the structure, relative to the base structure, depicted of fig. 1 (a).

For describing EOT in the THz range the authors [5] applied the Fano model (considering the resonance, which has an asymmetrical profile, resulting from the interference of two processes (non-resonant and resonant)), to describe the EOT of SWS. The first process (localized SP) is governed by the size of the holes, the second process – by the period structure (diffraction to the propagating SP). Our expression for effective dielectric function, similar to [1] of SWS is:

$$\varepsilon_{eff}(\omega) = \varepsilon_\infty \left(1 - \frac{{\omega_p}^2}{\omega^2 + i\gamma_p \omega}\right) +$$

$$+ \sum_j \varepsilon_{d,j} \frac{({\omega_{pl,j}}^2 + {\omega_p}^2) - \omega^2 - i\gamma_j \omega}{{\omega_{pl,j}}^2 - \omega^2 - i\gamma_j \omega},$$

where the first term is a "plasma" contribution (Drude model with effective parameters $\varepsilon_\infty = \frac{\pi^2 d^2 \varepsilon_h}{8a^2}$, ${\omega_p}^2 = \frac{\pi^2 c^2}{a^2 \varepsilon_h}$, γ_p). In second term $\omega_{pl,j} = 2\pi c \sqrt{\left(\frac{m}{d_x}\right)^2 + \left(\frac{n}{d_y}\right)^2}$ describe SP excitation by diffraction orders m and n. The expression $\varepsilon_{eff}(\omega)$ contains 4 unknown parameters (ε_∞, γ_p, $\varepsilon_{d,j}$, γ_j) which we will vary to describe the transmission (see fig. 1 (b)) and reflection spectra of a slab with such a dielectric function. Note that all resonance frequencies are fixed by the structure sizes. Reflection experiments helped us to study film substrate role for the EOT.

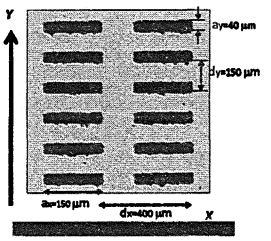

a

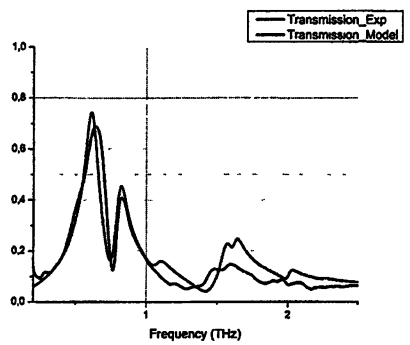

b

Fig. 1. (*a*) sample photograph and sizes, (*b*) transmission spectra, experiment and model

A good agreement with experiment allows us to assign all spectral features of EOT to particular modes of SP excitation. Angular dependencies allows to separate resonances related to the diffraction (structure period) form resonances related to a single hole. Interaction of propagating and localized SP leads to narrowband features in transmission spectrum. For the broadband THz pulse high frequency region corresponds not to SWS but to wavelength-size surface corrugation for SP manipulating. The spectrum of the broadband SP transmitted through the such grating exhibits band gaps originating in a Bragg effect.

Finally we utilize SWS for transmission of surface (unlike free space wave in previous case) waves – SP. Reduced effective dielectric function $\varepsilon_{eff}(\omega)$ predicted SP slowing down on such SWS, that we observe in preliminary experiment. For that purpose we launched a broadband SP along the metal bar

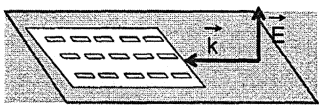

a

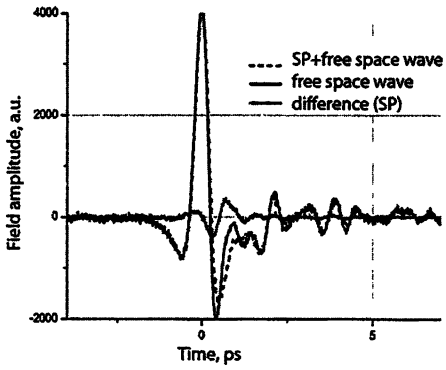

b

Fig. 2. (*a*) experiment configuration (*b*) temporal forms of the pulses transmitted through the surface with and without SWS

(fig. 2). For the next measurement we placed a piece of SWS on SP way. The difference between two signals (fig. 2 b) provides the form of delayed SP.

In conclusion: we describe transmission of a subwavelength perforated metal film by effective dialectic function, assign spectral features to different modes of plasmon excitation, demonstrate possibility of THz SP slowing down (localization enhancement) on such a structure.

Acknowledgements

The work is partly supported by RFBR grant: 11-02-01470-a.

References

1. *H. Raether*, Surface Plasmons on Smooth and Rough Surfaces and on Gratings. Springer Tracts in Modern Physics 111. New York: Springer-Verlag. (1988)

2. *M. Nazarov, F. Garet, D. Armand, A. Shkurinov, J.-L. Coutaz*, Comptes-Rendus Physique 9, 232-247 (2008).

3. *A.V. Andreev, M.M. Nazarov, I.R. Prudnikov, A.P. Shkurinov*, JETP Letters 90, 177-180, (2009).

4. *M. Nazarov, A.A. Angeluts, A.P. Shkurinov, J.L. Coutaz*, IRMMW-THz2010 technical digest on CD, We-P.46, (2010).

5. *A. Agrawal, Z. Valy Vardeny, A. Nahata*, Engineering the dielectric function of plasmonic lattices // Opt. Express. V. 16, No. 13, 9601. (2008).

Optical Susceptibilities of Carriers in the Terahertz-Frequency Range and Generation in Semiconductors with Controlled Nanostructures

Yu.V. Malevich[1], E.V. Moisseenko[2], M. M. Nazarov[1],
A.V. Shepelev[3], A.P. Shkurinov[1], V.A. Skuratov[4]

[1] M.V. Lomonosov Moscow State University, Moscow, Russia
[2] Nuclear Safety Institute of Russian Academy of Sciences, Moscow, Russia
[3] Gubkin Russian State University, Moscow, Russia, shepelev@rambler.ru
[4] Joint Institute for Nuclear Research, Dubna, Russia

I. Both generation and application of THz-frequency signals cause the necessity of dynamic control over the parameters of the THz radiation that can be done by means of the electric field. For controlling the optical properties of semiconductors one can take into account the interaction of THz-radiation with free carriers. A strong influence of the external field on parameters of semiconductor plasma opens possibilities for controlling parameters of THz radiation and nonlinear effects. The characteristic modulation time is defined by the carriers relaxation time (about 10^{-12} s), i.e. has the same order of magnitude as a THz wave period. Besides, the THz radiation field can act as this external field.

For the calculation of an influence of an external quasi-static electric field on the optical susceptibilities of the semiconductor plasma all main mechanisms of carrier scattering and relaxation were accounted. For AIIIBV semiconductors the calculations of the response of the complex dielectric constant of carrier plasma on the external field were done numerically. This allowed computing the dependencies of the real and imaginary parts of the dielectric constant on the temperature, external field, carrier concentration and THz radiation frequency. An analysis based on generalized Fresnel equations showed a significant variation of the reflection and absorption index of the semiconductor under the influence of the electric field.

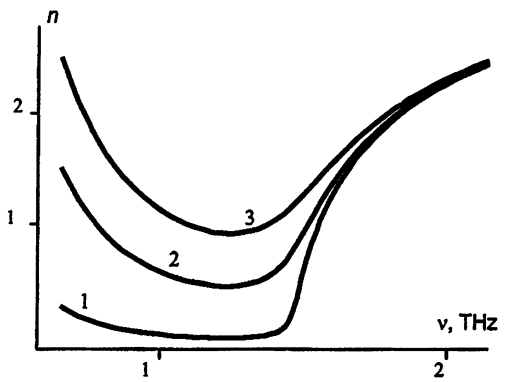

Fig. 1. Refractive index real part vs frequency. $T = 40$ K, carriers concentration $1.5\,10^{16}$ cm^{-3}. 1 – $E = 5\cdot10^4$ V/cm, 2 – $E = 2\,10^4$ V/cm, 3 – $E = 0$

In case when an external field is a THz radiation field itself, the dependence of the dielectric constant on the field results in nonlinear susceptibility appearance and harmonics generation.

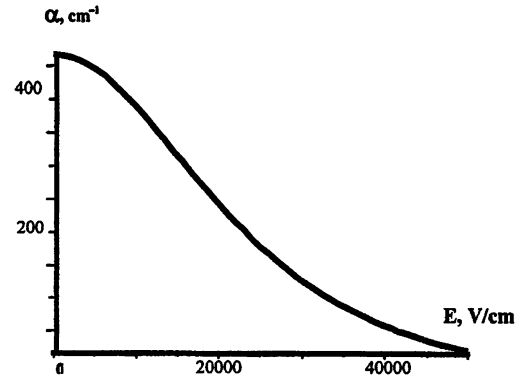

Fig. 2. Absorption coefficient vs electric field. $T = 40$ K, frequency 1.5 THz, carriers concentration $1.5\cdot10^{16}$ cm^{-3}

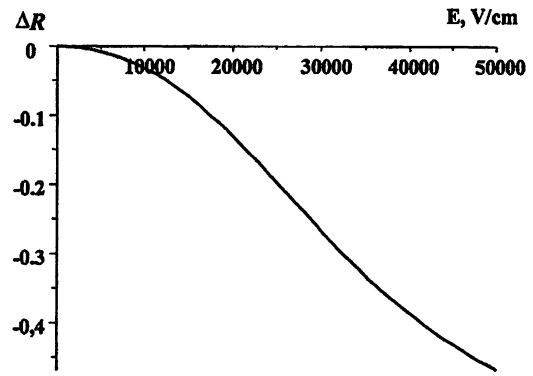

Fig. 3. Reflectivity change ΔR vs external field. T = 40 K, frequency 1THz, carriers concentration 10^{16} cm^{-3}

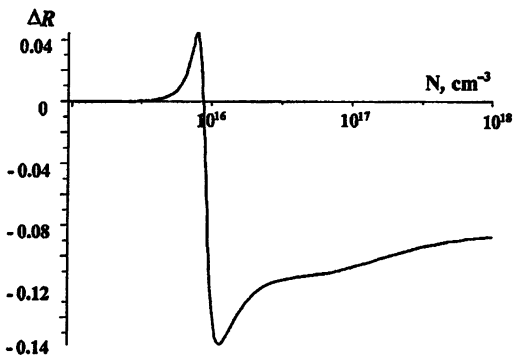

Fig. 4. Reflectivity change ΔR vs carriers concentration. T = 40 K, frequency 1 Hz, $E = 2\cdot10^4$ V/cm

II. Local internal semiconductor fields play an important role in the process of non-coherent conversion of the femtosecond-pulsed laser radiation into THz-range. Efficiency of this method increases in semiconductor materials with irregularities or defects that can be explained by appearance of intracrystalline fields and by decreasing of the carrier relaxation time. For formation of such fields, we have used the high-energy ion-beam technique which provides a unique possibility for fabrication of controlled low-dimension structures near the surface of a semiconductor crystal. As a result, the local electric fields appear in the bulk of a semiconductor. By this way we have achieved a 10-times increase of the THz wave generation efficiency in GaAs.

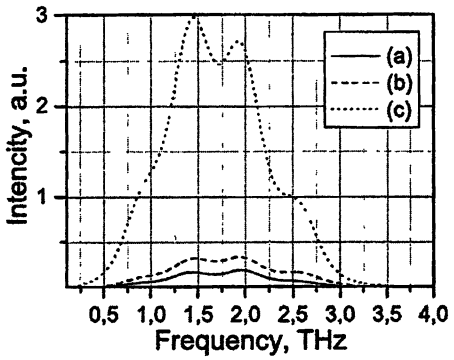

Fig. 5. Spectral dependencies of the intensity of THz radiation for nonirradiated GaAs samples (*a*) and for the GaAs samples of various heavy-ions fluence: 10^{13}cm^{-2} (*b*), $2\cdot10^{11}$cm^{-2} (*c*). The measurements were carried out under the room temperature

It is characteristic that samples with the fluence of 10^{13} cm^{-1} the efficiency of this conversion decreases. It is explains by the fact that with such high fluence disordered regions around ion trajectories cover each other and the contact areas and thus areas with the high value of the field disappear.

On the other hand, the control of experimental conditions provided the possibility to estimate the relation between the properties of defects and parameters of the THz wave radiation. For this purpose, a detailed study was made for dependence of THz generation on the heavy-ions fluence, temperature and intensity of optical radiation.

The crutial fact for the interpretation of temperature dependences is that with the considerable change with temperature of the relaxation time of photoexited carriers (more than for an order in the temperature range from 30 K to 350 K) the THz emission spectrum changes negligibly. Besides we should take into account that in our experiments, the energy of the laser pulse was 2 nJ, the diameter of the irradiated area of the order of 0.6 mm, dissipation index 10^4 cm^{-1}. Consequently, the concentration of the photoexcited carriers was of the order of 10^{16} cm^{-3}, i.e. less or the same then that the concentration of equilibrium carriers. The concentration of the photoexcited carriers remains practically unchanged if the temperature changes while the concentration of equilibrium carriers grows considerably with the temperature grows.

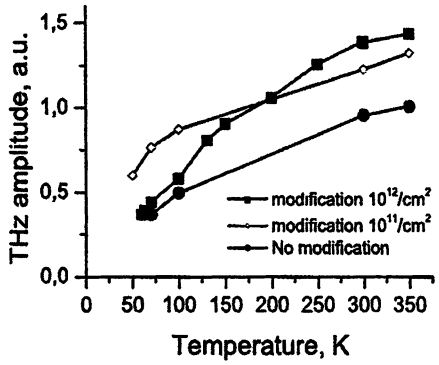

Fig. 6. Efficiency of the THz conversion vs the temperature for the samples of different heavy-ions fluence

This fairly convincingly justifies that the main reason for the appearance of the THz are the currents appearing as a result of the oscillations of the electron-hole plasma of both photoexcited and equilibrium carriers, excited as a result of the diffusion of the photoexcited carriers. The grows of the efficiency of generation with temperature finds the natural explanation to the grows of the concentration of the equilibrium carriers and the appropriate current grows. A faster efficiency grows in irradiated samples with temperature grows is explained by two reasons. One of them is the defect levels depletion appearing in the forbidden zone when irradiated by heavy ions, because the concentration of the defect levels grows with the fluence grows. The other reason is the presence in the irradiated samples of areas with lower effective width of the forbidden zone.

Acknowledgements. This work has been partially supported by Federal Agency of Science and Innovations of the Russian Federation (state contract No.02.740.11.0223) and by the RFBR, grants 10-02-90032-Бел_а and 10-10-02-00427.

References

1. *Moisseenko, E.V., Shepelev, A.V.* Control over the parameters of THz waves interacting with semiconductor free carriers // SPIE Proc. V. 7993, p. 24 (2011).

2. *Nazarov, M.M., Shepelev, A.V., Shkurinov, A.P., Skuratov, V.A., Zagorski, D.L.* Heavy ions irradiated crystal GaAs as an active non-linear matrix for the generation of THz radiation // Radiation Measurements, v. 43, p. 5591-5593, 2008.

Low-Frequency Molecular Motions: Gaseous and Solid State Approaches

I.N. Smirnova[1,2], A. Cuisset[2], A.V. Kargovsky[1], M.M. Nazarov[1], D.A. Sapozhnikov[1], O.P. Cherkassova[3], R. Bocquet[2] and A.P. Shkurinov[1]

[1]Departament of Physics and International Laser Center of M. V. Lomonosov Moscow State University, Moscow, Russia, irina.smirnova.ru@gmail.com

[2]Laboratoire de Physico-Chimie de l'Atmosphère, l'Université Littoral Côte d'Opale, Dunkirk, France

[3]Institute of Laser Physics SB RAS, Novosibirsk, Russia

THz frequency domain (0.1–10 THz or 3.33–333 cm^{-1}), corresponding to energies of a few meV, presents a challenging range for vibrational spectroscopy. For gas phase, even obtaining spectra is still a difficult task, because of the low sensitivity of the THz time-domain spectroscopy (THz-TDS) method in short-path realization. Despite the fact, that THz-TDS is nowadays widely used and the measurement of absorption spectra of substances, above all in solid state phase, is not a problem, the interpretation of observed spectra remains a highly nontrivial task. The aim of this work is to demonstrate the successful registration and assignment of observed bands in THz range in case of both solids and gases and to reveal the peculiarity of the spectra analysis and assignment in this range.

In case of gaseous samples THz frequency range corresponds to rotations and vibrations. For small molecules like H_2O or HCl the rotational bands in the THz range are narrow and thus the spectra are easily detected by the standard technique and the attribution of observed bands is not complicated. In case of big molecules, the measurements and the assignment are much more complex. In this section we will discuss the acquisition and evaluation of spectra of organophosphorous compounds, like TMP (trimethyl phosphate), TEP (triethyl phosphate) and DEMaP (diethyl (2-methylallyl) phosphonate)[1]. The pressure of saturated vapors of these gases is extremely low (100 Pa) and it was necessary to use a very sensitive spectrometer to measure the spectra. In our case we used the FTIR spectrometer based on AILES beamline of synchrotron SOLEIL, Paris, France, opened for external users in 2008. The AILES beamline was focused onto the entrance iris of a high resolution Bruker IFS 125 Fourier transform interferometer containing interferometer containing a composite Mylar beamsplitter suitable for the THz spectral range. The detector was a helium-cooled silicon bolometer equipped with an optical frequency filter with a bandpass of 33–330 cm^{-1}. A vacuum pump was used to cool the bolometer allowing the detection of frequencies as low as 20 cm^{-1}. All the studied compounds were purchased from Aldrich Chemical Co with a stated purity higher than 97 % and were used, without purification, by direct injection of the saturated vapor pressures at room temperature in the cell. To increase the sensitivity, the spectrometer was connected to a multipass cell adjusted to reach a 150 m optical path length. The exceptional properties of the AILES beamline, the combination of a high brilliance source with a long interaction length, gave spectra with a good S/N ratio. Typically, S/N > 100 was achieved with recording times from few minutes at low and high? resolution.

In Fig. 1 (center) the measured spectra of TEP and DEMaP and their chemical structures are presented for demonstration of the sensitivity of the THz domain to molecular structure.

For assignment of measured bands the calculations of gas spectra were performed using Gaussian 03. For TEP and DEMaP, semi-empirical density functional theory using the Becke three parameter hybrid exchange functional and the correlation functional B3LYP has been used for the determination of the conformational landscape and for the calculations of the harmonic frequencies of each of the stable conformers. Nine torsional axes including CH_2-CH_2 and CH_2-CH_3 axes provide the conformational flexibility of TEP. In the case of DEMaP, the influence of the [CH_2(C=CH_2)CH_3] group on the conformational flexibility was not taken into provide account in the

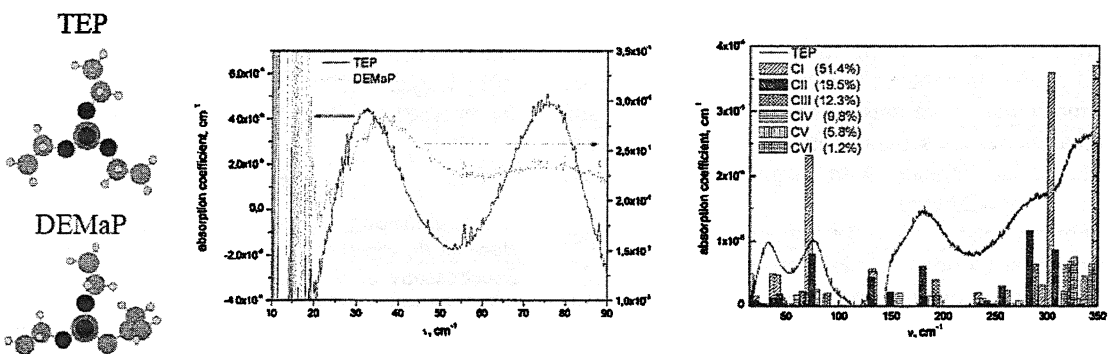

Fig. 1. (left) Structures of studied molecules. (center) Absorption spectra in THz domain of TEP and DEMaP measured by FTIR (AILES beamline of synchrotron SOLEIL, France). (right) Assignment of TEP absorption spectrum by consideration of 6 conformers

conformational account in the conformational analysis and only the four torsional axes belonging to the methoxy groups were considered. In order to locate the minima, relaxed potential energy surfaces (PES) scans have been performed at the Hartree-Fock/6-31+G(d,p) level of theory using the dihedral angles O=P-O-C and P-O-C-C as internal coordinates. Each minimum observed on the PES scans has been used as initial trial geometries for a geometry optimization at the B3LYP/6-311G++(3df,2p) level of theory. All the optimizations were done using the TIGHT and GDIIS convergence criteria, ensuring adequate convergence and the reliability of the computed frequencies, especially for the low frequency modes. The same method and basis set were used for the geometry optimizations and the harmonic frequency calculations. After identification of the most stable conformer, the relative energies of the other different conformers including the zero point vibrational contribution were determined. Only the stable conformations with a significant population will be taken into account in the discussion. For DEMaP molecule the structure optimizations and the harmonic frequency calculations were performed at ab initio second-order perturbed Møller-Plesset (MP2) level of theory limited to the 6-311G+(d,p) basis set taking into account the full electronic core correlation. Compared to the DFT semi-empirical method, the MP2 calculations for DEMaP yielded, in this specific case, a better prediction of the frequencies and the intensities of the largest amplitude modes. For the other molecules studied, the B3LYP/6-311G++(3df,2p) level of theory was sufficient to obtain a rather good agreement between predictions and observations.

Due to the consideration of full conformer landscape the performed assignment of spectra was very successful. For example, in the Fig. 1 (right) the TEP spectrum with 6 conformers is presented. As we can see, the spectral features in the range 200–300 cm^{-1} could be explained only by the impact of non-principal conformers. Also in THz absorption spectrum of TMP, that has two main conformers at room temperature, we have picked out the impact of separate conformers.

In case of molecular crystals the situation becomes more complicated, because the absorption properties are influenced by intermolecular and intramolecular structure of the substance. The vibrations represent small translational and rotational motions about their equilibrium positions; they are called external modes, in contrast to internal modes, which are intramolecular vibrations. Usually the internal and external modes are separated in frequency. But in case of molecular crystals with large molecules these ranges are overlapping.

For demonstration of the impact of different types of molecular motions on THz absorption spectra a set of corticosteroids (progesterone, 17α-hydroxyprogesterone (17-OP) and cortisone) was examined. The THz absorption spectra were measured by a THz-TDS spectrometer with cryostat for reducing the temperature (at room temperature the bands of solids are broad) in the range 17.8–300 K.

For successful spectra assignment in case of solids it's important to take into account the unit cell of the molecular crystal. Solid-state DFT calculations were performed in DMol3 (version 4.4) with "fine" grid sizes. Molecules within the unit cell were optimized within the cell parameters specified by the room-temperature X-ray diffraction study as reported in the Cambridge Structural Database. All normal-mode analyses were performed in the harmonic limit since the consideration of vibrational anharmonicity is beyond the capabilities of any atom-centered solid-state DFT code currently available. The performed calculations allow us to assign the observed bands in all three hormone crystals.

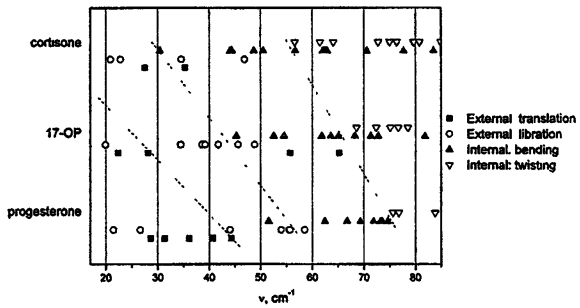

Fig. 2. Ranges of different type vibrations in case of corticosteroid hormones based on calculations

The ranges of external (subdivided into translation and libration) and internal (bending, twisting) vibrational modes for progesterone, 17-OP and cortisone crystal that has $P2_12_12_1$ space symmetry are presented in Fig 2. Notice, that progesterone crystal has no hydrogen bond, 17-OP has 1 intermolecular hydrogen bond and cortisone has 2 intermolecular hydrogen bonds. The appearance of hydrogen bonds reveals in red- shift of ranges of different vibrations. Also we can see that the frequency ranges of different type vibrations are limited in frequency.

In summary, in present work the successful assignment of absorption spectra in THz frequency domain in case of gases on the example of organophosphorous compounds and solids on the example of hormones has been presented. The contribution of conformers in gas phase and the importance of the lattice consideration have been shown. The dependence of hydrogen bond quantity on frequency ranges of different types of vibrations has been demonstrated.

References

1. *Smirnova, I.N., Cuisset, A., Hindle F., Mouret G., Bocquet R., Pirali O., Roy P.* Gas-Phase Synchrotron FTIR Spectroscopy of Weakly Volatile Alkyl Phosphonate and Alkyl Phosphate Compounds: Vibrational and Conformational Analysis in the Terahertz/Far-IR Spectral Domain // J. Phys. Chem. B. 2010. V. 114, No. 50. P. 16936–16947.

Analysis of Spectral Features of Cyclopentaphenanthrene Derivatives in THz Frequency Range

O.P. Cherkasova[1], A.V. Kargovsky[2], M.M. Nazarov[2], D.A. Sapozhnikov[2], I.N. Smirnova[2], A.P. Shkurinov[2], E.V. Fedulova[2]

[1]Institute of Laser Physics SB RAS, Novosibirsk, Russia, chrom@laser.nsc.ru
[2]Departament of Physics and International Laser Center, M.V. Lomonosov Moscow State University, Moscow, Russia

Terahertz time-domain spectroscopy (THz-TDS) is a powerful tool to probe low-energy vibrational modes of organic molecules. The bands observed in vibrational spectra of molecular crystals in THz range correspond both to external and to internal vibrational modes and the vibrational bands are determined both by structure of molecule itself and by the structure of crystal. The estimation of roles of external and internal impacts in observed vibrational bands and their assignment are among the main topics of low-frequency spectroscopy. The cyclopentaphenanthrene derivatives are aggregated into the molecular crystals of two space groups P_{212121} and P_{21}, in general. These molecules have similar general structure and differ only by the position of side groups. The variety of these compounds allows the formulation of different ranges, in which all molecules belong to the same space group and have the same number of molecules in the cell. The molecules could be bound by van der Waals and/or stronger hydrogen forces in molecular crystals. The influence of a crystal lattice motions on the THz spectra can also be analyzed and the spectral features associated molecular motions can be highlighted. Thus, the cyclopentaphenanthrene derivatives are convenient object for study of a nature of low-frequency vibrations. Simultaneous assays of THz-TDS and Raman spectra as well as the use of quantum chemical calculations allow performing a complete analysis of vibrational spectra of molecular crystals in THz range. The aim of this work is study THz and Raman spectra of progesterone, 17α-hydroxyprogesterone and cortisone in the frequency range 3–110 cm^{-1} in the temperature range from 18 K to 300 K. These substances exist in form of molecular crystals of the same orthorhombic space group P_{212121} with 4 molecules per unit cell. The density functional theory (DFT) calculations are used for the qualitative interpretation of the experimental data. All observed bands were assigned using DMol[3] simulations.

We used the substances in the form of polycrystalline powders without further purification purchased from Koch-Light Laboratories Ltd, UK. The description of the THz-TDS apparatus was given in [1]. The Raman spectra were recorded as in [2]. THz and Raman spectra were fitting by Lorenz dipole oscillator model and experimental frequencies were obtained.

Substances under study (fig. 1) have intensive features in the THz frequency region. The room temperature spectra of P are very similar. The only difference between THz and Raman spectra was observed near 70 cm^{-1} where the spectral maximum in the THz absorption is shown in Raman spectra by just a shoulder.

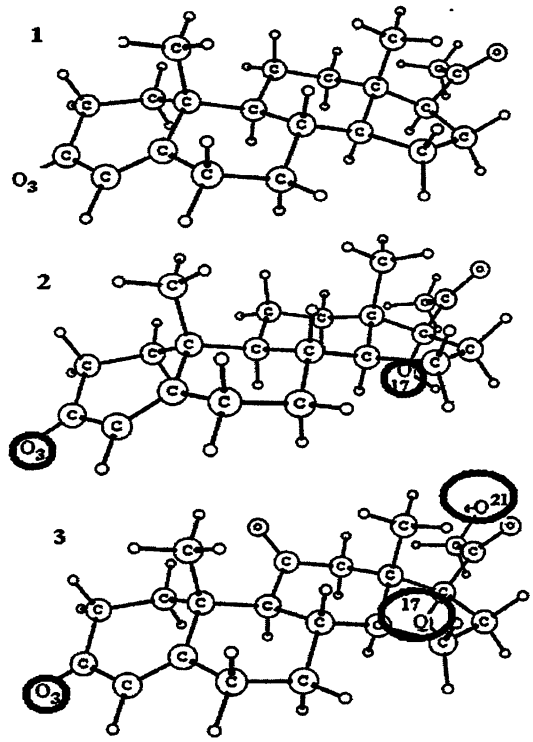

Fig. 1. Conformation of the progesterone (1), 17α-hydroxyprogesterone (2) and cortisone (3) molecules. C – carbon atom, O – oxygen atom, small circle – hydrogen atom

The progesterone room temperature Raman spectrum has several basic bands at 30 (ν_1), 37 (ν_2), 53 (ν_3) and 99 cm^{-1} (ν_4), which are assigned to external modes (sliding, ν_1 and ν_2) and internal modes (ν_3, bending and ν_4, twisting). The THz absorption spectra have several narrow absorption bands at 41 (ν_1), 55 (ν_2), 70 (ν_3) and 98 cm^{-1} (ν_4), which correspond to internal modes (ν_1-ν_3, bending, and ν_4, twisting). The decrease of the temperature only makes the Raman and THz lines sharper and their shift to the higher wavenumbers takes place. The temperature shift is the maximum for internal modes, namely twisting (ν_4) (fig. 2). The different temperature dynamics of the band positions and intensities of the motions of the similar type may be concerned with the change of the planarity of the molecular arrangement with the temperature decrease. Such temperature behavior is typical for the hydrogen bond free molecular arrangements of the ultimate density.

The 17α-hydroxyprogesterone is differ from progesterone by only a presence of the OH-group in the C^{17} position of the steroid nucleus that is resulted in the formation of a hydrogen bond between the O^3 and O^{17} atoms from two neighboring molecules ("head to tail") (fig. 1), which stabilizes the molecules within the

layer and does not allow itself to deform the molecule at lower temperatures. A comparison of the spectra of progesterone and 17α-hydroxyprogesterone shows that for the last substance bands are shifted toward lower frequencies, illustrating the effect of hydrogen bonds [3]. The THz absorption and Raman spectra of 17α-hydroxyprogesterone are different. THz absorption spectrum of 17α-hydroxyprogesterone has only two well defined absorption maxima at 53 (ν_2) and 66 cm^{-1} (ν_3). These bands correspond to the bending of molecules. Raman spectrum has several basic bands at 25 (ν_1), 36 (ν_2), 51 (ν_3) and 66 cm^{-1} (ν_4), which are assigned to external modes (ν_1, sliding, and ν_2, libration) and internal modes (bending, ν_3 and ν_4). Upon cooling the changes of relative intensities of the bands and their sharpening up are observed, thus some broad at room temperature bands split into several narrower bands, but the positions of bands is almost not shifted (fig. 2).

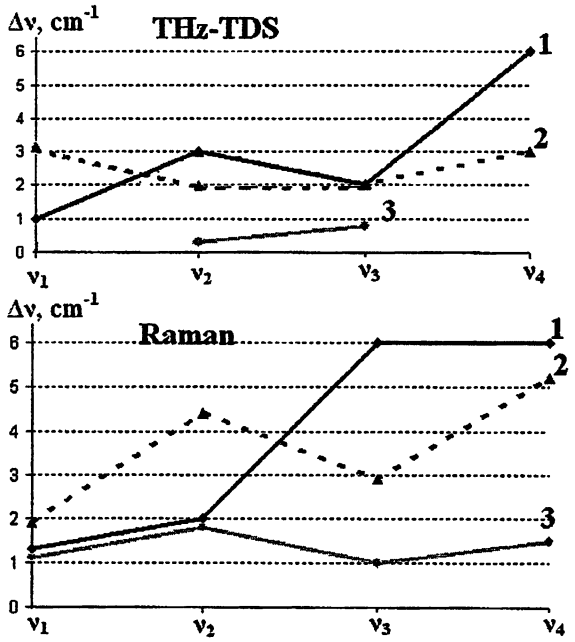

Fig. 2. The temperature shifts (Δν, cm^{-1}) for basic bands in THz and Raman spectra. 1 – progesterone, 2 – 17a-hydroxyprogesterone, 3 – cortisone

Hydroxylation of 17α-hydroxyprogesterone at the C^{11} and C^{21} positions of the steroid nucleus provides the cortisone (fig. 1). In the crystal packing of cortisone two types of helical coils are formed by hydrogen bonding. Head to tail (O^{21}-O^3) bonding occurs in coil 1 generated by the screw axis in the *b*-direction of unit cell, and head to head (O^{17}-O^{21}) bonding occurs in coil 2 generated by the screw axis in the *c* direction. The molecules in the type 1 coil are oriented with the thickness of the steroid nearly parallel to the *b* axis. The *b* axis almost passes through the C^{11}-O^{11} double bond so that the carbonyls are stacked over each other and the self association in this coil is much stronger than in the type 2 coils [4]. The cortisone molecules cannot move one against another in the plane (translation modes), and even in the low frequency region all molecules are bound together so hard, that any libration movement leads to twisting. The bands observed in vibrational spectra of cortisone crystals in THz range correspond to internal modes. Raman spectrum has four broad bands, at 35 (ν_1, bending), 40 (ν_2, bending of end group), 62 (ν_3, twisting) and 75 cm^{-1} (ν_4, twisting), which at 83 K shift to the higher frequencies and their bandwidths reduce. The temperature shift is the maximum for ν_4, twisting (fig. 2). THz absorption spectrum of cortisone has two intensive absorption maxima at 64.5 (ν_4, twisting) and 78.5 cm^{-1}. The bands get narrow upon cooling that allows resolving more peaks. We analyzed the temperature dynamics of the bands at 44.6 (ν_1, twisting), 52 (ν_2, bending), 57.5 (ν_3, bending) and at 64.5 cm^{-1}. As there is in Raman spectra, the maximal temperature shift is observed for twisting motions (ν_1 and ν_4) (fig. 2).

Thus, the cyclopentaphenanthrene derivatives progesterone, 17α-hydroxyprogesterone and cortisone were studied in THz frequency range. Substances under study have several intense features, which were assigned using $DMol^3$ simulations and the estimation of external and internal impacts in observed vibrational bands was made. It was obtained, that external modes in progesterone are observed in the range up to 45 cm^{-1}, in 17α-hydroxyprogesterone – up to 30 cm^{-1} and in the cortisone there is no sliding. We observe the different temperature dynamics of the THz and Raman band positions if the temperature goes down. The maximal temperature shift is observed for twisting motions. Such temperature behavior depends on ability of a molecule to form hydrogen bonds. So, the absence of hydrogen bonds can explain high mobility of the molecules in the crystal of progesterone and maximum band shifts. In the crystal 17α-hydroxyprogesterone there is one hydrogen bond that is resulted to rigid position of molecules within the layer and the absence of band shifts. Cortisone has two different types of hydrogen bonds which lead to a weakening of tight coupling in the layer and the appearance of coupling between the layers.

References

1. *N.N. Brandt, A.Yu. Chikishev, A.V. Kargovsky, M.M. Nazarov, O.D. Parashchuk, D.A. Sapozhnikov, I.N. Smirnova, A.P. Shkurinov and N.V. Sumbatyan,* Terahertz Time-Domain and Raman spectroscopy of the sulfur-containing peptide dimers: low-frequency markers of disulfide bridges // Vibrational Spectroscopy. 2008. V. 47. P. 53-58.

2. *O.P. Cherkasova, V.A. Volodin, V.A. Minaeva, B.F. Minaev, G.V. Baryshnikov.* Temperature dynamics for low-frequency Raman spectra of progesterone, 17α-hydroxyprogesterone and cortisone // Vestnik Novosibirsk State University. Series: Physics. 2010. V. 5, issue 4. P. 176-180.

3. *A. Szyczewski, K. Hołderna-Natkaniec, I. Natkaniec* Progesterone and testosterone studies by neutron scattering and nuclear magnetic resonance methods and quantum chemistry calculations // Journal of Molecular Structure. 2004. V. 693. P. 49-71.

4. *W.L. Duax, D.A. Norton* Atlas of steroid structure // New York: Plenum press, 1975.

Terahertz Scanning Near-Field Microscopy for Diagnostics of Semiconductor Microstructures

V.N. Trukhin[1,3], A.O. Golubok[2,3], A.V. Lyuteckii[1], B.A. Matveev[1], N.A. Pihtin[1], L.L. Samoilov[1,3], I.D. Sapozhnikov[2], I.S. Tarasov[1], M.L. Felshtyn[2], D.P. Hor'kov[1]

[1]Ioffe Physical Technical Institute RAS, Saint-Petersburg, Russia, valera.truchin@mail.ioffe.ru
[2]Institute for Analytical Instrumentation RAS, Saint-Petersburg, Russia
[3]National Research University of Information Technologies, Mechanics and Optics, Saint-Petersburg, Russia

Terahertz scanning near-field microscope is a new powerful diagnostic instrumentation to the analytical arsenal of nanotechnology. It makes it possible to image nanoobjects with characteristic dimensions of tens nanometers and simultaneously determine the optical properties in terahertz wave region [1].

We report on experimental research results of the near-field interaction occuring between a metallic probe and an object surface via the evanescent field. The amplitude and phase spectrum of the scattered THz radiation which contains information about the properties of the complex "probe-nanoobject" system were investigated by means of the THz scanning near-field microscope. It is a combination of a THz time-domain spectrometer with a scanning probe microscope (SPM) operating in tapping mode. The coherent THz radiation was generated by LT-GaAs antenna excited by 90 femtosecond optical pulses from a modelocked Ti-sapphire laser, generating at 800 nm central wavelength and the 80 MHz pulse repetition rate with an average power of 0.9 W. Tentatively the laser output beam was divided into two – a pump and a probe. The THz radiation generated by the pump beam was collimated and then focused onto the tungsten tip, and the reflected THz pulses were detected by a receiver. A 1-mm-thick (110) ZnTe crystal was used in electro-optical sampling arrangement to detect the THz radiation. The temporal profile of THz electric field was mapped out by varying the delay between the pump pulse and the probe pulse. The THz system was in open laboratory air. The THz waveform signal to noise ratio with no probe near Au sample was normally around $2 \cdot 10^4$ for our THz-TDS setup.

Terahertz scanning near-field microscope operates in forward scattering geometry and employs harmonic signal demodulation to extract the signal of near-field scattering. The signal of near-field scattering is separated from full scattering signal by means of double lock-in technique.

InAs and GaAs semiconductor samples with different concentration of free carriers were investigated. It was shown that spectral and lateral distribution of THz near-field components depends on concentration of the free carriers. Surface distribution of free carriers' concentration was determined by the use of these properties in various semiconductor structures, such as AlGaAs-GaAs-AlGaAs laser and heterojunctions based on silicon and indium arsenide.

The semiconductor structures based on GaAs and InAs were grown on a semiconductor substrate by chemical vapor deposition from organometallic and hybrid sources (MOCVD). Figure 1 shows the topography (dashed line) of the cleavage of the p-InAsSbP(Zn)/n-InAs/n^+-InAs sample and the simultaneously recorded dependence of the differential THz signal (solid line). On the topography obtained by AFM the transition between the doped and undoped regions of InAs is not observed. Nevertheless this transition is clearly visible in the differential THz signal and has dimensions that far exceed the spatial resolution.

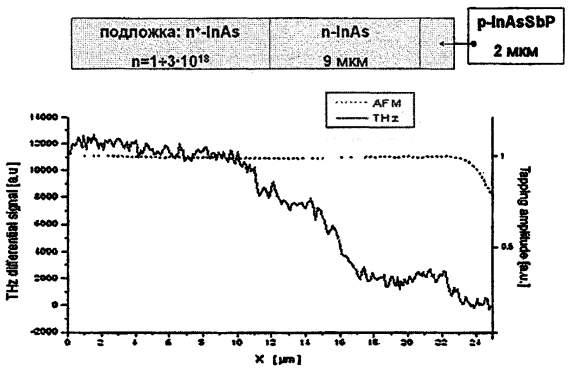

Fig. 1. The topography (dashed curve) and the dependence of the THz differential signal (solid line) recorded synchronously. Sample – p-InAsSbP(Zn)/n-InAs/n^+-InAs

Waveforms and the corresponding spectral distribution of the scattered THz radiation registered for different points of scanning the sample had a different character. Using the Drude model and the corresponding analytical expressions for the amplitude of the THz field scattered from a "probe-object" system near the probe, carrier concentration in the structure in the undoped region was evaluated as $3 \cdot 10^{15}$.

In this study, we investigate the effect of the interaction of THz near-field components of electromagnetic field with semiconductor nano-objects close to the AFM probe. These results indicate that using THz near-field microscope one can determine the distribution of carrier concentration in semiconductor microstructures. The transition regions between the layers with different concentration of electron-hole plasma were determined with lateral resolution ~100 nm. The characterization of the near-field spectrum in a fixed point of the sample allowed to estimate the concentration of the free carriers.

References

1. *Zhang X.-C., Jingzhou Xu.* Introduction to THz Wave Photonics // Springer. 2009. 246 p.

A Thermoacoustic Sensor for Detecting High-Power Microwave and THz Pulses

V.A. Vdovin

V.A. Kotelnikov Institute of Radioengineering and Electronics of RAS, Moscow, Russia, vdv@cplire.ru

Hot-carrier semiconductor detectors that are cooled with liquid nitrogen or uncooled are currently widely used to detect the shape of the envelope of high-power nanosecond microwave pulses in the centimeter- and millimeter-wave ranges [1].

In this paper, the new microwave sensor based on the use of the thermoacoustic effect is presented [2]. The operation principle and the design of this sensor were described in [3]. The sensor is located in free space and is designed to record microwave pulses having durations from 1 to 500 ns in the frequency range 3–3000 GHz with a pulse repetition rate of up to 5 kHz.

The operation principle of this device is based on the fact that when electromagnetic radiation is absorbed in a medium, a mechanical stress arises, which leads to an excitation of the acoustic pulse whose shape is determined by both the properties of the absorber and the temporal profile of the electromagnetic signal. A distinctive feature of the proposed design is the use of a layered structure comprising a radiotransparent window, an absorbing medium in the form of a nanometer-thick metal film, and a liquid. The choice of metal films with thicknesses about several nanometers is due to their ability to absorb efficiently incident electromagnetic waves. In particular, for an aluminum film deposited on a quartz substrate, the maximum absorption coefficient amounts to 60 % and is observed for the film thickness ranging from 2 to 3 nm [4]. Theoretical analysis of the excitation of an acoustic pulse in the quartz–aluminum film–liquid layered structure showed that signal generation takes place in two stages [5]. At the first stage, the microwave energy is absorbed in the film and heat is released. Next, the heat diffuses almost instantaneously into the liquid. Its thermal expansion forms the acoustic signal.

To ensure that the acoustic signal repeats the shape of the microwave pulse, the following condition should hold:

$$l_{abs}/c \ll \tau, \qquad (1)$$

where τ is microwave pulse duration, c is the sound speed, and l_{abs} is the size of the heat-release area. Physically, this means that the size of the heat-release area should be sufficiently small to ensure the release of the heating-produced mechanical stress during times which are much shorter than the pulse duration.

The calculated working range 3–3000 GHz of the tested thermoacoustic sensor is determined by the design of the input layered structure and specified by the properties of the absorbing material, i.e., an aluminum film in our case. The lower boundary 3 GHz is rather conventional and depends on the transverse size of the input window of the sensor and the density of microwave energy on the surface of the absorbing film. The upper boundary 3000 GHz is determined by the condition $\delta \gg l_0$, where δ is the skin depth of the absorber material and l_0 is the mean free path of conduction electrons in a metal at room temperature. Using films of other metals, e.g., chromium, one can significantly raise the upper boundary of the working band.

The tests were performed as follows. An sensor detector was placed in the wave field of the transmitting antenna of a microwave oscillator. Structurally, the sensor is manufactured as a cylinder of 60 mm in diameter and 100 mm in height. The diameter of the input radiotransparent window is 20 mm (Fig. 1). A microwave pulse was sent to the input window of the detector, passed through quartz glass *1*, and reached aluminum film *2* deposited on the internal surface of the quartz glass. A three-layer structure with the aluminum film having a thickness of 3.5 nm was used in the experiments.

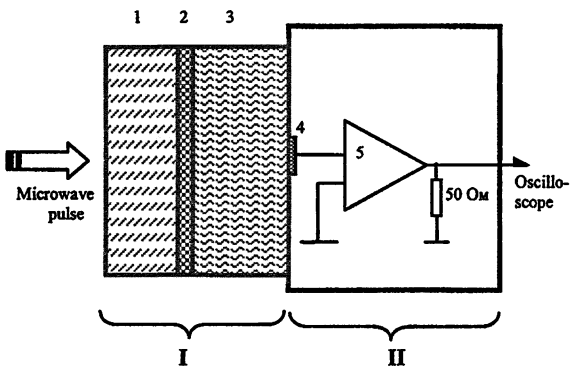

Fig. 1. Scheme of the detector sensor the shape of a microwave pulse: system converting a microwave signal into an acoustic pulse (I), system receiving and recording an acoustic signal (II), quartz substrate (*1*), aluminum film (*2*), liquid layer (*3*), acoustic receiver (*4*), and wideband preamplifier (*5*)

The aluminum film made contact with liquid layer *3*. In the film and the adjacent liquid, the microwave radiation was converted to an acoustic pulse which was recorded by wideband acoustic receiver *4*. The thickness of the distilled-water layer amounted to 4 mm. This water layer ensured a 2.67- μs time delay of the acoustic pulse, which allowed one to avoid the influence of strong electromagnetic pickup at the moment of microwave pulse generation. On the other hand, such a thickness of the water layer had almost no influence on the time profile of the acoustic pulse, which passed through it, due to a small value of the ultrasound attenuation coefficient at the frequencies corresponding to the spectral composition of the recorded pulse. A polyvinylidene fluoride (PVDF) film with a thickness of 28 μm was used as an acoustic

receiver. It was glued on the surface of the material having an acoustic impedance almost equal to the impedance of PVDF. The receiver used in the experiment allowed one to detect acoustic signals in a band of about 20 MHz with a sensitivity of 5 μV/Pa, which was determined by the resonance in the bulk of the PVDF film and its piezoelectric moduli. The receiver signal was recorded by digital oscilloscopes.

The circuit for recording nanosecond microwave pulses was experimentally checked by a relativistic generator of millimetric-range surface wave available in V.A. Kotelnikov Institute of Radioengineering and Electronics of RAS. This device produced radiation pulses with a power of up to 3 MW and a wavelength of about 8 mm. The energy of a pulse did not exceed 1 mJ. The microwave-pulse envelope, which was recorded by the hot-carrier germanium detector cooled with liquid nitrogen, is shown by a solid line in Fig. 2 (curve *1*).

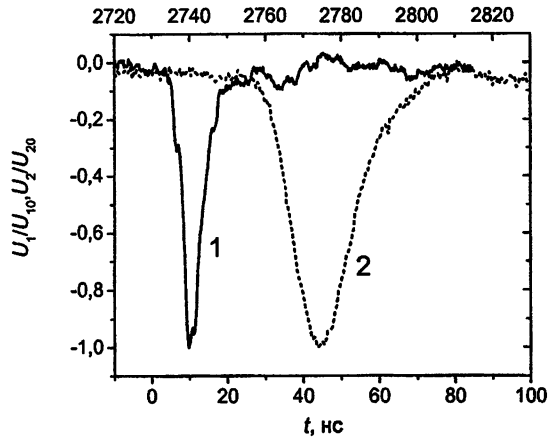

Fig. 2. Microwave pulse signals produced by a surface-wave oscillator and recorded by the hotcarrier detector ($U1$; curve *1*) and the thermoacoustic detector ($U2$; curve *2*). The signals are normalized to their maximum values. The lower time axis refers to curve *1*, and the upper one, to curve *2*. The horizontal scale is the same for both curves, but is shifted by the time $t \sim 2.7$ μs due to the delay in the arrival of the acoustic pulse

The duration of the microwave-pulse envelope, measured at half-maximum of the peak power, amounted to 5.2±0.4 ns, which was determined by the duration of a current pulse. The acoustic sensor was placed at a distance of 10 cm from the cone-shaped horn antenna of 40 mm in diameter. The profile of the detected acoustic signal is shown by the dashed line in Fig. 2 (curve *2*). The acoustic signal had the shape of a single-polarity pulse with a duration of 18±2 ns at half-maximum of the peak-power. The limited bandwidth of the acoustic receiver does not allow one to reproduce the shape of the microwave-pulse envelope, which is shown by a solid line in Fig. 2. The acoustic pulse had a delay time of about 2.7 μs with respect to the pulse recorded by the hot-carrier detector, which was stipulated by the propagation of the acoustic pulse through a 4-mm-thick water layer. The duration of the acoustic-pulse edge was equal to about 20 ns and corresponded to the receiver passband equal to 20 MHz.

The sensitivity of the thermoacoustic detector is determined by the acoustic sensor, its noises, and the characteristics of layer structure I. The sensitivity of the sensor with a 28-μm-thick PVDF film and water used as a liquid in contact with the Al film was 0.5 V/mJ. A 10-ns pulse duration was used in calculations. The sensitivity of a sensor with ethyl alcohol is an order of magnitude higher. The minimum detectable microwave signal is determined from the condition that the amplitude of the acoustic pulse is equal to the rms value of the noise pressure produced on the piezoelectric transducer either by thermal noise or action of the external electromagnetic disturbance. From estimates, the action of the disturbances was two orders of magnitude higher than the thermal noise level and created an rms pressure of ~40 kPa or an electric voltage of 20 mV at the acoustic sensor. In this case, the minimal energy of the 10-ns microwave pulse, recorded by the thermoacoustic sensor, was 0.04 mJ.

Thus, the thermoacoustic sensor demonstrated a sufficient level of noise immunity of the output signal, as well as the possibility of precise detection of microwave pulse with time resolution no worse than 20 ns. To detect microwave pulses with durations 1 ns and longer, we produce acoustic receivers based on plates of lithium niobate piezocrystals with a thickness of 20 μm.

The duration of the detected pulses can be decreased further by using optical interference methods for detecting mechanical displacements of the surface of the metal film which absorbs microwaves. However, this method can be used only to detect pulses with sufficiently high pulse repetition rates.

References

1. *Dagys, M., Kancleris, Z., Simniskis, R., et al.* The Resistive Sensor: A Device for High-Power Microwave Pulsed Measurements // IEEE Antennas Propagat. Mag. 2001. V. 43, No. 5. P. 64-78.

2. *Andreev, V.G., Vdovin V.A. and Karabutov A.A.* Thermoacoustic method for detection of powerful microwave pulses // Radiophys. Quantum Electron. 2003. V. 46, No. 8/9. P. 787-793.

3. *Andreev, V.G., Vdovin V.A.* A Thermoacoustic Sensor for Recording High-Power Nanosecond Microwave Pulses // Instrum. Exp. Tech. 2009. V. 52, No. 2. P. 226-229.

4. *Andreev, V.G., Vdovin V.A. and Voronov P.S.* An Experimental Study of Millimeter Wave Absorption in Thin Metal Films // Tech. Phys. Lett. 2003. V. 29, No. 11. P. 953-958.

5. *Andreev, V.G., Vdovin V.A.* Generation of acoustic waves by powerful microwaves pulses by using thin metallic films // Quantum Electron. 2005. V. 48, No. 10/11. P. 896-900.

Symposium A

HIGH POWER MICROWAVE APPLICATIONS (INCLUDING ACCELERATORS, RADARS, GAS DISCHARGES, MATERIALS PROCESSING, BIOMEDICAL APPLICATIONS etc.)

Quasi-Optimal Filtering of a Non-Coherent Sequence of Echo Signals in a Nanosecond Radar

A.B. Blyakhman, I.N. Zamyatina, V.I. Irkhin

Federal Research and Production Center
"Nizhny Novgorod Research Institute of Radiotechnics",
N. Novgorod, Russia

In the high-power nanosecond radar [1], the jitter in the transmitter causes pulse-to-pulse transmitted signal amplitude and shape variations. This instability results in the dynamic range reduction and migration of the echo signal over range cells within the azimuth burst, degrading the quality of optimum filtration and affecting azimuth and range cells.

This talk describes a theoretical model with a Gaussian enveloped transmitted signal with distortions simulating the signal jitter. The phase jitter of a signal spectrum can be simply described as a set of slowly varying sine functions, which simulate parasitic modulation of a powerful electron beam in the power stage resonator of the transmitter.

The model demonstrated that variation of signal phase spectrum caused by only two sine distortions leads to variation of the signal's shape and duration as well as its displacement along the time axis. Thus, besides the primary displacement along the time axis due to object motion, the echo signal will undergo a secondary displacement due to distortion of the transmitted signal phase spectrum.

The use of "intra-cycle" correlation processing reduces distortion of the shape of the transmitted signal (approximating it to the Gaussian shape) and precludes the effect of secondary displacement of the echo signal due to distortion of the phase spectrum of the transmitted signal. The supporting function in this method is a replica of the transmitted signal formed by means of a directional coupler introduced between the transmitter output and the radiating element of the antenna system.

The use of "inter-cycle" correlation processing, wherein the echo signal from the previous clock cycle is adopted as the supporting function, makes it possible to compensate for linear variations of the signal spectrum from cycle to cycle and prevents displacement of the cross-correlation function (CCF) along the time axis due to object motion (both linear motion and uniformly accelerated motion in increments of t^2). This method allows for CCF to be accumulated within, for instance, the beam of the antenna system, and thereby provides an improved range cell and an optimum integration of returned signal energy within an azimuth burst.

To verify the findings, experimental results were analyzed for: 1) a return signal from helicopter propeller blades, 2) a return signal from a hang-glider. The return signal from the real object in adjacent cycles differs from the Gaussian function (while the transmitted signal is a signal having a Gaussian envelope): its shape and amplitude vary and it is displaced along the time axis (fig. 1). The variation of the shape and amplitude of the return signal is due, on the one hand, to distortion of the transmitted signal phase spectrum and, on the other hand, to object motion peculiarities. The primary displacement of the signal along the time axis is determined by the motion of the object, and the secondary displacement – by distortion of the phase spectrum of the transmitted signal. Inter-cycle cross-correlation processing helped to reduce distortions of the shape of return signals and to preclude migration of the return signal within the range cell in an azimuth burst (fig. 2), also permitting of optimum filtering in azimuth to be employed. Efficiency of accumulation in azimuth is determined by the size of step (spatial period of sampling) along the object's flight track, which is given by $d = V / F_{rep}$ (where V is velocity of the object and F_{rep} is the repetition frequency of transmitted signals. Therefore, to increase the information content of the radar data, it is necessary to maximize transmitted signal repetition frequency. The information content of a radar image is also determined by the azimuth cell.

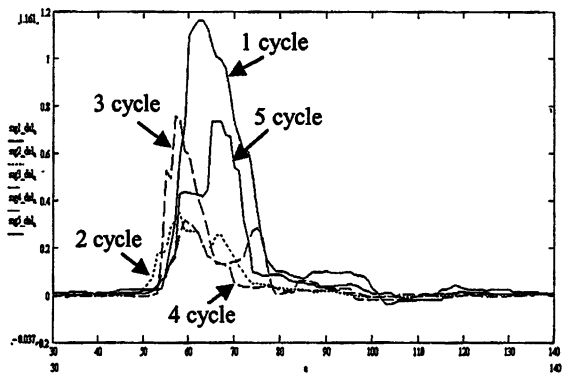

Fig. 1. Returned signal from a hang-glider in 5 adjacent clock cycles

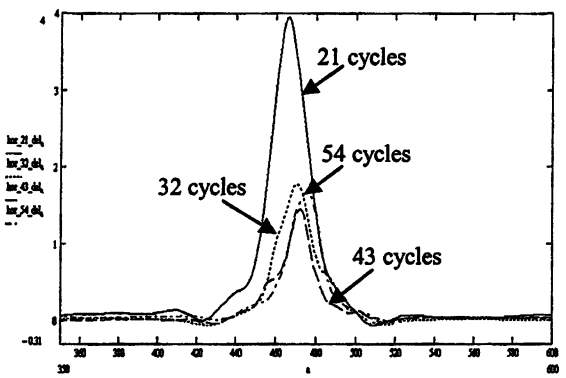

Fig. 2. CCF between returned signals of adjacent clock cycles for moving hang-glider

A multifold improvement of the azimuth cell for an antenna system that performs scanning within a designated angular sector can be achieved by using monopulse methods for measuring angular directions along with algorithms equivalent in their efficiency to synthetic aperture techniques. The signal processing algorithms include the measurement of angular (azimuth) directions to the target $\hat{\alpha}(t)$ within an azimuth burst by a monopulse method and subsequent synthesis of spatial frequencies in accordance with the measurements. In this case, the synthetic spatial frequencies will correspond to equivalent rectilinear motion of the carrier within the width of a real beam, where each angular direction has a respective Doppler frequency:

$$\hat{F}_d = \frac{2 \cdot R_0 \cdot \hat{\alpha} \cdot \Omega}{\lambda}$$

(Ω is the angular scanning rate of the antenna beam at range R_0 within the designated sector, λ is the wavelength of the radar). As a result, a synthetic signal is obtained whose phase varies quadratically just as in the case of rectilinear motion of the antenna system. Processing of such a signal is based on the use of a dechirping filter, which yields a resolution cell along the synthetic aperture of

$$\delta L_{rot} = \frac{\lambda}{2 \cdot \Theta_b}$$

(where Θ_b is the beamwidth of the antenna system). Thus, the entire aperture of a real antenna is used in the course of scanning to synthesize the beam, and the resolution cell in an angular direction is potentially equal to a half of the real aperture d in the respective angular plane: $\delta L_{rot} = d / 2$.

References

1. *Blyakhman, A., Clunie D., Mesyats, G., Harris, R., Petelin, M., Postoenko, G., Wardrop, B.* Nanosecond Gigawatt Radar: Indication of Small Targets Moving Among Heavy Clutter // Proc. of IEEE 2007 RADAR Conference, Boston, USA. 2007. P. 61-64.

Progress on Euclid & ANL/AWA Collaboration on Dielectric Wakefield Accelerator Development

A.D. Kanareykin[1,2]

[1]Euclid Techlabs LLC, Gaithersburg, MD USA alexkan@euclidtechlabs.com
[2]St. Petersburg Electrotechnical University "LETI", St. Petersburg, Russia

We present here our recent results of the Euclid Techlabs LLC/AWA of Argonne National Laboratory collaboration on wakefield high energy acceleration of electron bunches in dielectric based accelerating structures. This program concentrates primarily on Cherenkov radiation studies providing efficient high energy generation aimed at a future 1 TeV linear collider and a X-ray FEL light source. We report here on recent experiments in high power Cherenkov radiation and corresponding dielectric material developments and characterizations. Progress in diamond, quartz and microwave lowloss ceramic structure development in GHz and THz frequency ranges is presented. Beam breakup (BBU) effects and transverse bunch stability has been discussed as well. We have reported on recent progress on tunable dielectric based structure development. A Ka-band double layer structure with a tunable ferroelectric layer to permit frequency adjustment has been successfully beam tested at AWA recently. A special subject of our report is transformer ratio enhancement scheme providing energy transfer efficiency for the dielectric based wakefield acceleration.

Dielectric loaded accelerator (DLA) structures using low-loss microwave ceramics or quartz and excited by a high current electron beam or an external high frequency high power RF source have been under extensive study recently [1–3]. The basic wakefield RF structure is very simple – a cylindrical, dielectric loaded waveguide with an axial vacuum channel is inserted into a conductive sleeve. A high charge, (typically 20–40 nC), short, (1–4 mm) electron drive beam generates TM01 mode electromagnetic Cherenkov radiation (wakefields) while propagating down the vacuum channel [1, 2]. Following at a delay adjusted to catch the accelerating phase of the wakefield is a second electron (witness) beam. The witness beam is accelerated to high energy by the wakefield produced by the drive beam. A series of proof of principle experiments have been successfully performed in microwave frequency range at Argonne's Wakefield Accelerator AWA [1, 2, 6–10]. THz wakefields have been successfully generated by the UCLA/SLAC collaboration too [3].

A linear collider concept based on drive beam generation from an RF photoinjector and employing dielectric structures [1] for power extraction and acceleration has been proposed [4]. The collider is based on a modular design with each module providing 100 GeV net acceleration. High frequency (20 GHz) RF power extracted from the drive beam using a low impedance dielectric structure is used to power the main linacs, which are based on high impedance high gradient dielectric loaded accelerating structures [2, 4, 10]. Dielectric structures have been shown to sustain high fields for short RF pulse lengths and can be used as RF power generation devices [2, 6, 10].

X-ray free-electron lasers (FELs) are expensive instruments and a large part of the cost of the entire facility is driven by the accelerator. Using a high-gradient dielectric wake-field accelerator (DWA) instead of a conventional accelerator may provide a significant cost saving and reduction of the facility size [5]. Currently, AWA and Euclid collaboration investigates using a collinear DWA to provide the electron beam to drive a CW x-ray FEL light source [5]. As an initial case study, a straw-man facility using a 100 MV/m loaded gradient, 850 GHz quartz DWA to generate the beam for the FEL has been considered. This configuration provides for 10 parallel beams operating at 10 kHz all driven by a single 100 kHz beam. A collinear DWA accelerator generates a beam of 8 GeV, 50 pC/bunch, ~1.2 kA of peak current, in less than 100 meters [5].

The advantages and potential problems of using dielectric for loading an accelerating structure are discussed in references [2, 6, 10] and are only summarized here. The advantages are: 1) simplicity of fabrication: the device is simply a tube of dielectric surrounded by a conducting cylinder – this is a great advantage for high frequency (> 20 GHz) structures compared to conventional structures where extremely tight fabrication tolerances are required, and the relatively small diameter of these devices also facilitates placement of quadrupole lenses around the structures; 2) dielectrics potentially exhibit high breakdown thresholds relative to copper at high GHz and THz frequencies; 3) reduced sensitivity to the single bunch beam break-up (BBU) instability: note that the frequency of the lowest lying HEM11 deflecting mode is lower than that of the TM01 accelerating mode; 4) easy parasitic mode damping [2, 6, 10].

Potential challenges of using dielectric materials in a high power RF environment are breakdown and thermal heating, same as for all-metal conventional accelerating structures. Formula presenting longitudinal wake function [2, 6, 10] clearly shows that the high gradient can be reached by using the small aperture structure ($\sim a^{-2}$) that, in turn, requires low emittance ε_N, high charge Q drive beam (or bunch train) to be generated and transferred through the DLA structure [2, 6, 10]. The power extraction has to be provided for the two-beam accelerator design [4]. 26 GHz wakefield power extractor has been successfully demonstrated in 2009, and 30 MW power level has been reached for the ~10 ns pulse [2]. Beam handling is always a special issue for the decelerating section of a high charge wakefield accelerator [2, 6].

It should be also noted that expected problems with dielectric charging are easily mitigated by using a dielectric with low dc conductivity.

Microwave and THz DLA required high brightness high charge drive beam providing >200 MV/m accelerating gradient that has to be sustained by the dielectric material of the structure loading [2, 6, 10]. Low loss microwave ceramics, fused silica, and CVD polycrystalline and single crystal diamonds have been considered as materials for dielectric based accelerating structures to study of the physical limitations encountered driving > 100 MV/m at microwave [2] and > GV/m at THz [3, 6] frequencies in a dielectric based wakefield accelerator [10]. A 100 MV/m gradient has been demonstrated with an X-band standing wave resonator [2]. THz radiation has been generated recently by a short ~10 GV/m pulse within a 100 μm diameter dielectric fiber [3].

The electrical and mechanical properties of diamond make it an ideal candidate material for use in dielectric RF structures: high breakdown voltage, extremely low dielectric losses and the highest thermoconductive coefficient available for removing waste heat from the device [6, 10]. Currently we consider fused silica and CVD diamond as our primarily candidates for the high gradient DLA structure loadings [10]. The cylindrical diamond dielectric tubes that are manufactured via a relatively simple and inexpensive chemical vapor deposition (CVD) process, plasma assisted CVD have been considered in [6, 10]. Our initial work was based on 100 μm and 5 mm scale tubes with fundamental frequencies in the 0.1–1.0 THz range; promising results were obtained using the plasma assisted and hot-filament CVD process. Recently the 5 mm inner diameter, 2.5 cm long and 500 μm thick high electronic quality "white" diamond tube has been fabricated for 35 GHz structure and characterized with SEM, micro-Raman and microphotoluminescence spectrum analysis [6, 10].

The frequency of a metallic accelerating structure is defined by its geometry. DLA structures, on the other hand, have another important parameter that determines the frequency spectrum – the dielectric constant of the loading material [6, 7]. We have proposed a new technique that allows control of the dielectric constant (and consequently the frequency spectrum) for dielectric waveguides by incorporating ferroelectric layers [6, 7]. The most noteworthy feature of the tunable DLA is the replacement of a single ceramic by a composite of two layers. The inner layer is ceramic, with permittivity typically in the range of 4–36. The outer layer is made of BST ferroelectric, placed between the ceramic layer and the copper sleeve. The DLA structure tuning is achieved by varying the permittivity of the ferroelectric layer by temperature changes or by applying an external DC electric field across the ferroelectric [6]. Recently, a novel low loss BSTM ferroelectric material has been developed and used in dielectric based accelerators as a method of frequency tuning [7]. Measurements showed an excellent tuning capability through control of either temperature or DC bias voltage. A wakefield experiment using an accelerated witness beam successfully demonstrated this technique using the first tunable DLA structure. During the experiment, the energy of a witness bunch at a fixed delay with respect to the drive beam was measured while the temperature of the structure was scanned over a 50 °C range. The energy change corresponded to a change of more than half of the nominal structure wavelength [7].

The transformer ratio is defined as the ratio of the maximum energy gain of the witness bunch to the maximum energy loss experienced by the drive bunch (or a bunch within a multidrive bunch train) [2, 6]. This plays an important role in the collinear wakefield acceleration scheme. A high transformer ratio is desirable since it leads to a higher overall efficiency under similar conditions (e.g. the same beam loading, the same structure, etc.) [2, 4–6]. One technique to enhance the transformer ratio beyond the ordinary limit of 2 is to use a ramped bunch train [2, 6, 8]. The first experimental demonstration observed a transformer ratio only marginally above 2 due to the mismatch between the drive microbunch length and the frequency of the accelerating structure [8]. Recently, we revisited this experiment with an optimized microbunch length using a UV laser stacking technique at the ANL/AWA facility and measured a transformer ratio of 3.4. Measurements and data analysis from these experiments are presented in detail in [9].

This work is supported by the US Department of Energy, Russian Foundation of Basic Research (RFBR), and the program "Scientific and Pedagogical Staff of Innovative Russia" of the Ministry of Education and Science of Russian Federation.

References

1. *W. Gai, P. Schoessow, B. Cole, R. Konecny et al.* Phys. Rev. Lett. 1988. V. 61. P. 2756.

2. *W. Gai,* AIP Conf. Proc. 2009. V. 1086, Melville, New York. P. 3.

3. *M.C. Thompson, H. Badakov, A.M. Cook, J.B. Rosenzweig et al.* Phys. Rev. Lett. 2008. V. 100. P. 214801.

4. *W. Gai, M. Conde, J.G.Power and C.Jing.* 2010, Proc. Int. Part. Accel. Conf. IPAC'10, Kyoto, Japan. P. 3428.

5. *C. Jing, J. Power, and A. Zholents.* ANL/APS LS-326, http://www.aps.anl.gov/Science/Publications/lsnotes/

6. *A. Kanareykin.* Journal of Physics. 2010. Conf. Ser. V. 236. P. 012032.

7. *C. Jing, A. Kanareykin, J.G. Power, M. Conde et al.* Phys. Rev. Lett. 2011. V. 106. P. 164802.

8. *C. Jing, A. Kanareykin, J.G. Power, M. Conde et al.* Phys. Rev. Lett. 2007. V. 98. P. 144801.

9. *C. Jing, J.G. Power, M. Conde, W. Liu et al.* Phys. Rev. ST-Accelerator Beams. 2011. V. 14. P. 021302.

10. *A. Kanareykin.* AIP Conference Proceedings. 2010. NY. V. 1299. P. 286.

An ECR Ion Source with a High Power – High Frequency Gyrotron, the 60 GHz «SEISM» Project

T. Lamy[1], F. Debray[3], I.V. Izotov[2], M. Marie-Jeanne[1], A.V. Sidorov[2], V.A. Skalyga[2], P. Sortais[1], T. Thuillier[1], C. Trophime[3], E. Verney[3], N. Vidal[3], V.G. Zorin[2]

[1] LPSC, Université Joseph Fourier Grenoble 1, CNRS/IN2P3, Institut Polytechnique de Grenoble 53, rue des Martyrs, 38026 Grenoble Cedex, France, lamy@lpsc.in2p3.fr
[2] Institute of Applied Physics of Russian Academy of Sciences, 46 Ulyanov Street, 603950, Nizhny Novgorod, Russia
[3] LNCMI CNRS UJF INSA UPS, 25 rue des Martyrs, B.P. 166 38042 Grenoble cedex 9, France

Electron Cyclotron Resonance Ion Sources (ECRIS) are able to deliver higher and higher charge states and ionic current intensities, thanks to the increase of microwaves (MW) frequencies and magnetic field induction like predicted by Geller [1]. Nowadays, additional characteristics are expected from ECRIS for specific applications. For example, high ionization efficiency in one charge state is required for the production of radioactive ion beams, this characteristics is particularly important for an accelerator project: the Beta Beam project.

A neutrino facility: the Beta Beam project

The study of neutrinos properties is of great interest for fundamental physics, especially with the goal to develop theories beyond the standard model and to get better knowledge of the universe birth. The availability of intense neutrinos beams would ease neutrinos studies. EUROnu [2] is a European design study entitled "A High Intensity Neutrino Oscillation Facility", aiming to study three different concepts of neutrino facilities. One of these concepts called "Beta Beams" consists in the production, the ionization, the acceleration and then the storage of high energy radioactive ions undergoing beta decay in long straight sections of a storage ring, leading to high energy neutrinos beams. For the radioactive ions, several schemes have been developed (production and acceleration of ^{6}He, ^{18}Ne, ^{8}B or ^{8}Li); let's focus on the gaseous ones like ^{6}He. Radioactive atoms are produced continuously ($5\cdot10^{13}$ pps) by the impact of a high energy proton beam on a target. Then they have to be extracted from the target, transported toward an ion source where they are ionized and then injected into a Rapid Cycling Synchrotron (10 Hz repetition rate – 50 μs bunches) for initial acceleration. The use of a high efficiency ECRIS with bunching capabilities [3], would allow to directly adapt the production to the RCS injection. This paper describes the concept of such an ECRIS.

Parameters for an ECRIS for Beta Beams

The plasma density of "Minimum-B" ECRIS varies as the square of the ECR frequency, presently the highest MW frequency used is 28 GHz in large devices using sophisticated magnetic structures (superconductors) allowing to satisfy magnetic field scaling laws [4]. These devices can deliver either cw beams, either pulsed ones (by pulsating the MW power) using the afterglow and preglow effects [5, 6]. For Beta Beams, the "ideal" ECRIS has to deliver $5\cdot10^{12}$ ions in 50 μs pulses, 10 times per second, corresponding to $^{6}He^{+}$ beam current peaks of 16 emA. Our ECRIS prototype will have a low volume (0.25 l) and will be based on a cusp magnetic configuration [7]. The generation of short pulses require a high ionization rate (so a high initial gas density), this one associated with a high ionization degree leads to a high plasma density that can be obtained with high ECR frequency [8]. The source (which will be fed by $5\cdot10^{13}$ ^{6}He per second), will be fully emptied after each MW pulse, the helium flux between each pulse will give a plasma density of $2\cdot10^{10}$ ions/cm^3 which is equivalent to an ECR cutoff frequency of less than 1.5 GHz. In order to allow high frequency operation, a high flux of additional gas and a high MW power will be necessary in order to maintain the plasma density. The ideal device delivering high power and high frequency MW are the gyrotrons developed by GYCOM, so the ECRIS prototype will be operated with a 60 GHz (50μs – 10 Hz) gyrotron allowing a $4.46\cdot10^{13}$ cm^{-3} plasma density. The magnetic field will present a closed ECR zone at 2.14 T in the plasma chamber, magnetic inductions of 6T at the injection, 3T at the extraction, about 100 mm between the two maxima, and a 4T radial magnetic field at the ring cusp in the center plane. Moreover the magnetic field lines crossing the ECR zone will not intercept the walls before passing through the high field values.

Magnetic field of the 60 GHz SEISM prototype

Preliminary 2D simulations of the magnetic field of the SEISM (Sixty GHz ECR Ion Source using Megawatt Magnets) prototype have shown that the radially cooled polyhelix technology developed at LNCMI was suitable to generate the expected magnetic field. The 3D simulations allowed to make the final magnetic design. The helices are copper tubes with a helical slit performed by a wire electrical discharge machining. The thickness of this slit is fixed by glued insulators like shown on Fig. 1.

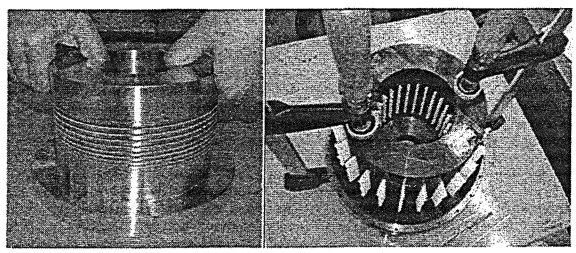

Fig. 1. An helix with its slit maintained by glued insulators

The helices are cooled down by high pressure (~28 bars) demineralized water flowing from the center to the outside through the slits. 4 helices are assembled around a plasma chamber like seen on Fig. 2.

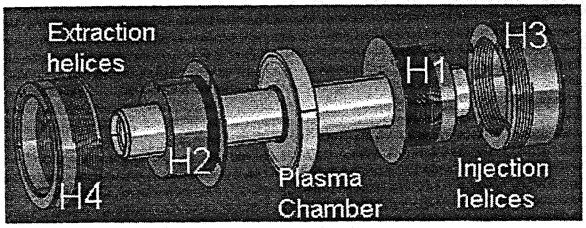

Fig. 2. Helices assembly around the plasma chamber

Fig. 1 shows the result of the simulation performed with 4 helices with a current intensity of 30000 A.

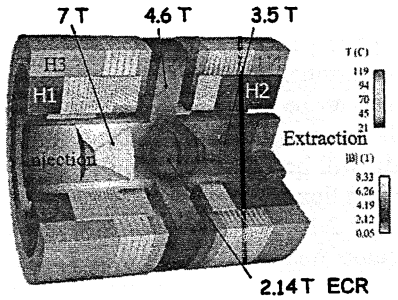

Fig. 3. 3D magnetic field simulation of the SEISM prototype

The results of the simulations show that the magnetic field induction expected could be achieved and even exceeded.

After the mechanical design and the prototype building, the structure was installed at the LNCMI high field facility in order to measure the magnetic field induction. The setup is shown Fig. 4 with the electrical cables and the water pipes for cooling.

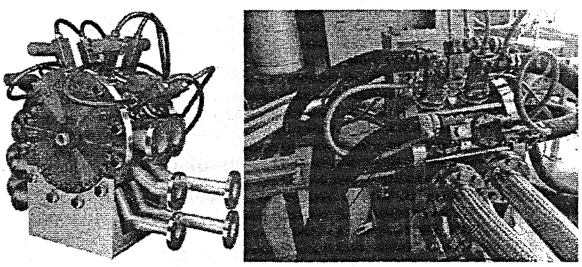

Fig. 4. SEISM prototype (left) and setup for magnetic field measurements (right).

Radial and axial magnetic field inductions have been measured on 4 axis of the prototype from 1500 up to 15000 A. Fig. 5 shows the norm of the magnetic induction at 15000 A (1.5 MW) on the revolution axis of the prototype and the iso-B surfaces around the zero field which is close to the center (~ –10 mm). These measurements show that the magnetic field obtained is very close to the simulated one, so the magnetic field at 30000 A should be very close to the expected one. The 1T iso-B surface gets closed without touching the plasma walls for a current intensity in the helices of about 12000 A. In order to characterize the performances of the prototype, first plasma and beam experiments will be performed in the next months at 28 GHz with the GYCOM gyrotron available at LPSC, then the magnetic field will be measured up to 30000 A, before the 60 GHz gyrotron delivery to Grenoble by the Institute of Applied Physics (Nyzhni Novgorod-Russia) fall 2012.

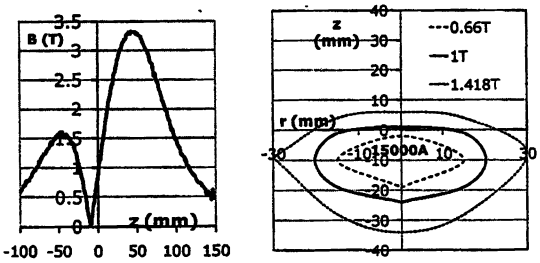

Fig. 5. Norm of the magnetic field induction at 15000 A: on axis (left), closed iso-B lines around the zero field

Perspectives of ECRIS developments

The improvement of ECRIS characteristics is usually obtained by increasing the ECR frequency and the magnetic field induction. The development of our ECRIS prototype with the polyhelix technology has been successful for a low cost and limited development time. This success allows to develop a unique programme in the world: the study of magnetic field influence on the efficiency of high frequency-high power MW ECRIS. These studies are not possible with present superconducting technologies. After Beta Beam dedicated studies, we will develop minimum-B magnetic structures allowing the highest ECR frequency ever used in such devices.

We acknowledge the financial support of the European Community under the European Commission Framework Programme 7 Design Study: EUROnu, Project Number 212372. The EC is not liable for any use that may be made of the information contained herein.

References

1. *R. Geller,* Electron cyclotron resonance multiply charged ion sources // IEEE Trans. Nucl. Sc. 1976. V. NS-23, No. 2. P. 904-912.

2. http://www.euronu.org/

3. *P. Sortais,* ECR technique for RIB production // Radioactive beams for nuclear physics and neutrino physics, Rencontres de Moriond, Les Arcs, France (March 17–22, 2003) http://moriond.in2p3.fr/mor_fr.html.

4. *S. Gammino, G. Ciavola,* ECR ion sources and scaling laws // Proc. of 14th Int. Conf. On cycl., capetown (1995) 377.

5. *O. Tarvainen et al.*, Pulsed Operation of ECR Ion Sources – Plasma Physics and Diagnostics // in these proceedings.

6. *Izotov I.V. et al.,* Experimental and Theoretical Investigation of the Preglow in ECRIS // IEEE Transactions on Plasma Science. 2008. V. 36, No. 4. P. 1494-1501.

7. *Rashid M.H. et al.*, New spindle cusp zero-B field for ECR ion and plasma sources // Proceedings of ECRIS 2008, Chicago, IL USA (15–18 sept. 2008). http://accelconf.web.cern.ch/accelconf/ecris08/papers/mopo-23.pdf

8. *Zorin V.G. et al.*, ECR breakdown of heavy gases in open mirror traps // Fusion Sci. Technol. 2011. V. 59, No 1T. P. 140-143.

Homoepitaxial Single Crystal Diamond Growth at Different Synthesis Parameters

A.B. Muchnikov, A.L. Vikharev, A.M. Gorbachev, D.B. Radishev

Institute of Applied Physics RAS, Nizhny Novgorod, Russia, mab1@appl.sci-nnov.ru

The interest in single crystal diamond (SCD) is caused by its unique properties and the prospects of its application in many fields of science and technology [1]. Homoepitaxial SCD growth by microwave plasma chemical vapor deposition (MPACVD) is studied currently by many research teams using continuous (CW) and pulsed (PW) wave regimes of reactor operation. To achieve the high rates, one should choose the synthesis conditions in 2.45 GHz MPACVD reactor with a high microwave power density (MWPD) in plasma [2–4]. In a real CVD reactor there always exist limitations for the maximum MWPD. They may be connected, among other things, with the design of the reactor, the maximum power of the microwave source, and the method of substrate cooling. Therefore, it is of interest to find whether the SCD growth rate can be increased (while retaining the quality) at fixed microwave power and power density.

This paper presents a comparative study of the homoepitaxial SCD growth for the CW and PW operation regime of the MPACVD reactor at high MWPD 200 W/cm^3. Different methods were used to reach high microwave power density: 1) CW regime at relatively high gas pressure without local increase of electric field, 2) CW regime using local increase of electric field by changing the reactor geometry (substrate holder configuration) at moderate gas pressure and 3) PW regime at high gas pressure.

The growth was performed in a 2.45 GHz MPACVD reactor described in [4]. SCDs were grown on single crystalline type Ib (100) HPHT diamond substrates, size 2.5×2.5×0.3 mm, thickness 300 microns. The growth temperature was 900 °C during all experiments. The nitrogen content in all grown SCD samples did not exceed 1 ppm.

Figure 1 shows the dependences of the MWPD in the plasma on the gas pressure for CW regime (solid lines) and for PW regime (dash lines). MWPD (in Fig. 1) was calculated as the ratio of the accepted mean microwave power and the discharge volume measured by plasma radiation.

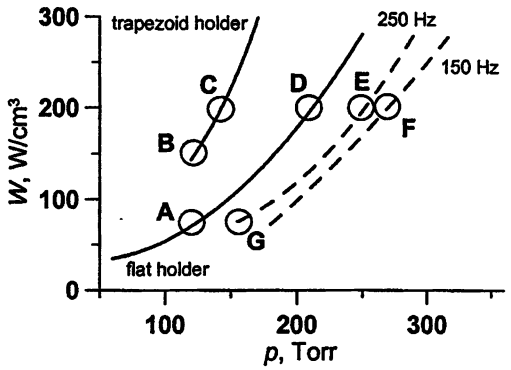

Fig. 1. Dependence of the MWPD on the gas pressure for an incident mean microwave power of 2.7 kW: solid lines – CW regime (for two different substrate holder configurations, flat and trapezoid) and dash lines – PW regime (for pulse repetition rates 150 and 250 Hz). Letters A, B, C, D, E, F, G (circles) mark the parameters, for which the comparison of the SCD growth was made

The circles and letters A, B, C, D, E, F and G in Fig. 1 show the parameters, at which the SCD growth was carried out. In CW regime the growth at points B and C was performed at the substrate holder in the shape of truncated cone (trapezoid holder) and at points A and D at the flat substrate holder. In PW regime the SCD growth was carried out at the flat substrate holder (points E, G and F in Fig. 1). It is seen from Fig. 1, that the same values of the MWPD are achieved at higher gas pressure when one passes from CW to the PW regime. In PW regime the plasma dimensions depend on peak microwave power. Therefore the same MWPD 200 W/cm^3 at pulse repetition rate 250 Hz and 150 Hz can be achieved for pressure 250 Torr and 260 Torr (points E and F in Fig. 1, respectively).

SCD sample	Pressure p, Torr	MWPD, W/cm^3	Growth rate G, μm/h	CH_4, %	Raman FWHM, cm^{-1}	Growth parameters in Fig. 1
Sample 1	120	80	5	4	2.0	CW (A)
Sample 3	120	150	1.5	4	2.0	CW (B)
Sample 4	120	150	5	8	2.2	CW (B)
Sample 8	120	150	20	12	1.7	CW (B)
Sample 5	145	200	3.5	4	1.8	CW (C)
Sample 7	145	200	8	8	1.8	CW (C)
Sample 2	210	200	5	4	1.7	CW (D)
Sample 6	210	200	11	8	1.9	CW (D)
Sample 3p	250	200	9	4	1.9	Pulsed, 250 Hz (E)
Sample 6p	260	200	12	4	1.8	Pulsed, 150 Hz (F)
Sample 7p	260	200	22	8	2.3	Pulsed, 150 Hz (F)
Sample 8p	155	80	5.7	4	2.2	Pulsed, 250 Hz (G)
Sample 9p	155	80	5.9	4	2.1	Pulsed, 250 Hz (G)

For illustration Fig. 2 and Fig. 3 show an optical photo and SEM image of two samples (Sample 6p and 7p, correspondingly. Surface morphology of all samples is quite smooth without microscopic defects such as cracks and unepitaxial crystallites. Note that the surface of Sample 6p has the growth hillocks in some places. Probably, the growth hillocks originated from defects at the substrate surface.

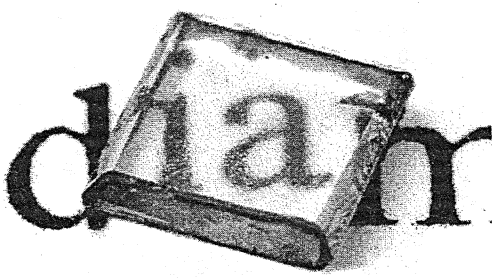

Fig. 2. Optical photo of Sample 6p after growth, thickness of CVD layer 130 microns

Comparison of the SCD growth at points C, D, E and F, Fig. 1, shows that for an equal MWPD of 200 W/cm^3, the growth rate was higher at a higher gas pressure, see Table. The experiments were performed at different methane content (4 % and 8 %) and the different conditions: flat and trapezoid configurations of the substrate holder at CW regime and flat substrate holder at PW regime (pulse repetition rate 150 and 250 Hz).

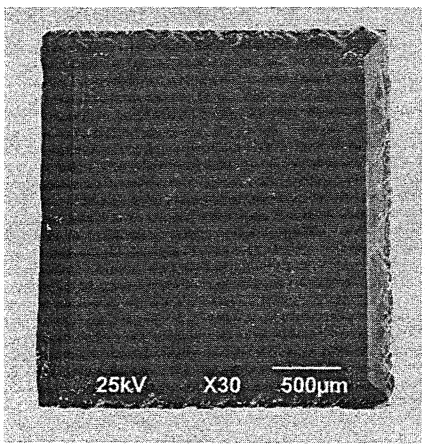

Fig. 3. SEM image of Sample 7p after growth, thickness of CVD layer 185 microns

For a methane content of 4 % and 8 %, the growth rate at 210 Torr (flat holder, point D, Fig. 1) is about 1.4 times higher than at 145 Torr (trapezoid holder, point C, Fig. 1). Note that the gas pressure, at which these experiments were performed differed by 1.45 times. Thus, the difference in SCD growth rates can be explained in the same way as in [5], namely, by the fact that the density of [CH_3] and [H] near the surface of the diamond substrate is proportionally higher in the case of a high gas pressure, than when the pressure is lower. But the result of comparing the SCD growth at points D and F in Fig. 1 shows the following.

For experiments with 4 % methane content the growth rate in PW regime, (point F) was 12 µm/h, but in CW regime (point D) the growth rate was 5 µm/h. In PW regime the gas pressure was about 1.24 times higher than in CW regime, but the growth rate differs by 2.4 times. For experiments with 8% methane content the growth rate in PW regime (point F, Fig. 1) was 22 µm/h, but in CW regime (point D, Fig. 1) the growth rate was 11 µm/h. In this case the growth rate differs by 2 times. Thus in PW regime the growth rate is higher than in CW regime not only due to the increase of gas pressure and consequently due to the proportional growth of [CH_3] and [H] near the diamond surface.

The maximum growth rate 22 µm/h in PW regime was obtained at 150 Hz and 260 Torr (point F in Fig. 1) for Sample 7p. The growth of Sample 3p and Sample 6p (points E and F in Fig. 1) showed that the decrease of pulse repetition rate from 250 Hz to 150 Hz caused the 30 % increase of SCD growth rate at practically the same gas pressure (250 and 260 Torr) and the same Raman FWHM (quality). One can only hypothesize about the reasons of the dependence of the growth rate on the pulse repetition rate. The hydrocarbon conversion reactions proceed by the well-known scheme [6] with different characteristic times. In the PW regime, the formed gas flows contribute to stirring of the gas mixture and change the transport of chemically active particles to the substrate surface. Thus, the growth species flow o the substrate surface, growth species density and dynamics near surface can depend on the parameters of microwave pulses and their repetition rate. These hypotheses require further development, both theoretical and experimental.

This work was partially supported by the Russian Foundation for Basic Research (project No. 09–08–00019.

References

1. *Koizumi S., Nebel C. and Nesladek M.* // Physics and Applications of CVD Diamond, WILEY-VCH Verleg Gmbh &Co. KGaA, Weinheim, 2008.

2. *Achard J. Tallaire A., Sussmann R., et al.* // J. Crystal Growth, 2005. V. 284 P. 396.

3. *Yamada H. Chayahara A., Mokuno Y., Shikata S.* // Diam. Relat. Mater. 2008. V. 17 P. 1062.

4. *Muchnikov A.B., Vikharev A.L., Gorbachev A.M. et al.* // Diam. Relat. Mater. 2010. V. 19. P. 432.

5. *Achard J., Silva F., Tallaire et al.* // J. Phys. D: Appl. Phys. 2007. V. 40. P. 6175.

6. *Goodwin D.G., Butler J.E.* / Handbook of Industrial Diamonds and Diamond Films, edited. by M.A. Prelas, G. Popovici, L.K. Bigelow. Marcel Dekker Inc. 1998. P. 527.

Some Problems in the Theory of High-Gradient Accelerating Structures

G.S. Nusinovich[1], T.M. Antonsen[1], Jr., O.V. Sinitsyn[1] and K.L. Jensen [2]

[1]Institute for Research in Electronics and Applied Physics, University of Maryland, College Park, MD 20742-3511, USA
gregoryn@glue.umd.edu

[2] Vacuum Electronics Branch, Naval Research Laboratory, Washington D.C., 20375-5320, USA

In this talk, results of theoretical studies of factors limiting high-gradient operation of room-temperature accelerating structures will be presented. These studies were done by our group which includes G. S. Nusinovich, T. M. Antonsen, Jr., O. V. Sinitsyn, students W. Zhu, D. G. Kashyn and A. Keser and affiliated members K. Jensen and I. Haber.

It is known that the initial conditioning of accelerating structures allows for a significant increase in the accelerating gradient while simultaneously keeping the breakdown rate reasonably low. Then, after a certain period of high-gradient operation at the achieved gradient the breakdown rate starts to grow and results in unreliable operation of such structures. Post mortem inspection of such structures shows that initially carefully fabricated and well polished surfaces are greatly deteriorated in that numerous craters, cracks and micro-protrusions are evident.

There are known many theories aimed at explaining these observations. However, so far the reasons for this phenomenon are not well understood, so the further studies are warranted. Our group is trying to contribute to this important area of research. Our initial steps were overviewed in Ref. 1. This paper will describe the present status of our research.

The main areas of our studies are:

A) Heating of microcracks by the RF magnetic field and corresponding stresses [2]. It was shown that the presence of cracks can significantly increase the heating of surfaces of metallic accelerating structures. It was found that the maximum stress occurs at the bottom of a crack and this is quite insensitive to the orientation of the magnetic field relative to the crack, whereas the rate of temperature rise at the edge of a crack depends on the orientation of the magnetic field relative to the crack.

B) Heating and melting of small metallic particles of the size of the skin depth (metallic dust) by the RF magnetic field in single shots [3] and in rep-rate [4] regimes. First, following Ref. 5, in these studies the ratio of a typical particle size to the skin depth was determined for particles shaped as cylinders of a different orientation and spheres. Then, the temperature dependence of the skin depth was taken into account and the amplitude of the RF magnetic field and the corresponding pulse duration were determined which result in the heating and melting of such a particle in a single pulse [3]. Later, a similar study [4] was carried out for devices (accelerating structures as well as high-power microwave sources) operating in rep-rate regimes. There, effect of the duty cycle was analyzed as well as the difference between the thermal radiation of a heated particle from the blackbody radiation.

C) Heating of small micro-protrusions on the surface of accelerating structures. First, we analyzed penetration of the RF electric field into an axially symmetric protrusion on the surface of a metallic structure with finite conductivity. In this study [6], the field outside the protrusion was determined using the point-charge model proposed in Ref. 7. This model allows one to analytically describe the potential and RF electric field amplification in the vicinity of the conductor by assembling a number of point charges on top of each other. The most realistic surfaces can be obtained by using a dipole point-charge model. Then, the electric potential and the field inside a small protrusion can be found by using the Laplace's equation and this solution is matched with the potential outside by using proper boundary conditions. After the field and the current density $j = \sigma E$ inside the protrusion are determined (the current density corresponds to the Fowler-Nordheim field emitted current from the protrusion apex), the heat equation can be solved to determine the temperature rise inside the protrusion. This approach allows us to determine conditions (accelerating gradient, field amplification factor, protrusion height-to-base ratio, pulse duration) resulting in the protrusion melting. At present, we are adding to our treatment the Nottingham and Thomson effects.

D) Regarding the same problem of microprotrusion heating we performed also another study [8] in which we compared the role of two effects: a) the microwave heating caused by penetration of the RF magnetic field into microprotrusion of a radius on the order of the skin depth and b) the Joule heating caused by the field emitted current, i.e. the effect of the RF electric field magnified by a sharp protrusion. Corresponding expressions for the power densities of both effects were derived and the criterion for evaluating the dominance of one of these two is formulated. This criterion is illustrated by the discussion of an example with parameters typical for recent experiments at the Stanford Linear Accelerator Center (SLAC) National Accelerator Laboratory.

E) Ion bombardment of micro-protrusions. Some researchers believe that ion bombardment can be the most important reason for heating and melting micro-protrusions on structure surfaces. At the same time, however, it is known [9] that field emitted cathodes operated in microwave fields have emission stability substantially higher than

that in static fields. This fact can be explained [9] by weakening of the ion bombardment in microwave fields in comparison with the ion bombardment in DC fields. Following Ref. 9, we started our study [10] from analyzing this effect by using Kapitsa's method based on introducing the ponderomotive force describing the field outside sharp micro-protrusion. Then, we used more direct analytical calculations in the framework of a simple model and concluded with simulations based on the used of the PIC code WARP. First resukts of our studies were described in Ref. 10. Recently, in addition to results described in Ref. 10, we also studied the effect of the electron dark field emitted from the protrusion apex on the ion motion.

F) Besides the studies of metallic accelerating structures listed above, also some work on the non-stationary, self-consistent theory of multipactor (MP) phenomena in dielectric-loaded accelerating structures was carried out. The work started with the development of a non-stationary self-consistent two-dimensional (2D) model of MP in such structures [11]. Results obtained with this model were later compared [12] with some experimental data. Good agreement between the theory and experiments was observed for tubes with relatively large (with respect to wavelength) inner diameter (ID). Tubes with smaller ID resulted in a discrepancy between the two. Such disagreement could be caused by 1) neglecting the axial motion of electrons in our 2D model and 2) insufficiently accurate modeling of the space charge fields [13]. Our group is currently working on the development of a three-dimensional model of MP that would allow us to address those problems.

This work is supported by the Office of High Energy Physics of the U.S. Department of Energy. The authors are indebted to S. Tantawi and V. Dolgashev for insightful discussions.

References

1. *G.S. Nusinovich,* Structures and Breakdown (plenary presentation) // 13th AAC Workshop, AIP Conf. Proc., 1086, Melville, New York, p. 38-46 (2009).

2. *W. Zhu, J. Mizrahi, T. M. Antonsen, Jr., and G.S. Nusinovich,* Temperature rise and stress induced by microcracks in accelerating structures // Phys. Rev. Special Topics – Accelerators and Beams, 13, 121003 (2010).

3. *G.S. Nusinovich, D. Kashyn, and T.M. Antonsen, Jr.,* Possible role of rf melted microparticles on the operation of high-gradient accelerating structures // Phys. Rev. Special Topics – Accelerators and Beams, 12, 101001 (2009).

4. *G.S. Nusinovich, D.G. Kashyn, and T.M. Antonsen, Jr.,* Effect of Metallic Dust on Operation of Rep-Rate, High-Power Microwave Devices // IEEE Trans. Plasma Sci. (to be published).

5. *L.D. Landau and E.M. Lifshitz,* Electrodynamics of Continuous Media, (Pergamon Press, Oxford, 1960).

6. *D.G. Kashyn, G.S. Nusinovich, T.M. Antonsen, Jr., and K.L. Jensen,* 14th Advanced Accelerator Concepts Workshop (AAC-2010), Annapolis, MD, 13–19 June 2010, Eds. S. Gold and G. S. Nusinovich, AIP Conf. Proc., 1299, p. 387-392; also, "Heating of microprotrusions in high-gradient accelerating structures"// Submitted to Phys. Rev. Special Topics – Accelerators and Beams.

7. *K.L. Jensen, Y.Y. Lau, D.W. Feldman, and P.G. O'Shea,* Phys. Rev. ST Accel.& Beams, 11, 081001 (2009); also *K.L. Jensen,* J. Vac. Sci. Technol. B 29, 02B101 (2011).

8. *G.S. Nusinovich and T. M. Antonsen, Jr.,* Role of rf electric and magnetic fields in heating of micro-protrusions in accelerating structures // Paper 1105/5097 in arXiv.org> physics, submitted on 25 May 2011.

9. *G. Fursey,* Field Emission in Vacuum Microelectronics // Kluwer Academic/Plenum Publishers, New York, 2005, p. 63.

10. *G.S. Nusinovich, D. Kashyn, T. Antonsen, Jr., and I. Haber,* Ion Bombardment of Microprotrusions in High-Gradient Accelerating Structures // 14th Advanced Accelerator Concepts Workshop (AAC-2010), Annapolis, MD, 13–19 June 2010, Eds. S. Gold and G.S. Nusinovich, AIP Conf. Proc., 1299, Melville, New York, p. 382-386 (2010).

11. *O.V. Sinitsyn, G.S. Nusinovich, and T.M. Antonsen, Jr.,* Self-consistent nonstationary two-dimensional model of multipactor in dielectric-loaded accelerator structures // Physics of Plasmas, 16, 073102 (2009).

12. *O.V. Sinitsyn, G.S. Nusinovich, and T.M. Antonsen, Jr.,* Studies of Multipactor in Dielectric-Loaded Accelerator Structures: Comparison of Simulation Results with Experimental Data // AIP Conference Proceedings, vol. 1299, p. 302-306, 2010.

13. *O.V. Sinitsyn, G.S. Nusinovich, and T.M. Antonsen, Jr.,* Multipactor dynamics in dielectric-loaded accelerator structures // Proceedings of the 2011 Particle Accelerator Conference, March 28 – April 1, 2011, New York, NY, paper TUP011.

Growth of Isotope ^{12}C-enriched Polycrystalline and Single Crystal Diamond Films by Microwave Plasma Assisted CVD

V.G. Ralchenko[1], A.P. Bolshakov[1], A.V. Inyushkin[2], A.N. Taldenkov[2], E.E. Askinazi[1], I.I. Vlasov[1], A.V. Polsky[1], A.F. Popovich[1], A.V. Khomich[3], V.I. Konov[1], V.A. Panchenko[2]

[1]A.M. Prokhorov General Physics Institute RAS, Moscow, Russia, ralchenko@nsc.gpi.ru
[2]National Research Center "Kurchatov Institute", Moscow, Russia
[3]Institute of Radio Engineering and Electronics RAS, Fryazino, Russia

Diamond has the highest thermal conductivity (TC) at room temperature (RT = 298 K) among all known materials, with TC value up to 2000–2400 W/mK for most perfect and pure type IIa single crystal natural stones. The best synthetic chemical vapor deposition (CVD) polycrystalline diamond wafers and single crystals grown from microwave plasma also fall in this top TC range [1]. The record high TC of CVD diamond is one of the benefits for its application in high power microwave electronics and high power multispectral optics (from UV to Terahertz range, and, to longer, millimeter waves).

The ultimate opportunity to achieve even higher TC values relays on purification of isotopic composition of diamond. The natural isotope content in diamond is 98.93% ^{12}C and 1.07% ^{13}C, the isotope ^{13}C being "an impurity" for propagating phonons, resulting in a finite thermal resistance even in absence of point and extended defects.

Synthetic single crystal (SC) diamonds grown by a high pressure-high temperature (HPHT) technique with ^{12}C-enriched precursor (^{12}C 99.93%) showed the 50 % increase in TC, up to 3320 W/mK @ RT [2]. Here we report on growth of isotopically "purified" polycrystalline (PC) and SC CVD diamond films in a microwave plasma and evaluation of their TC.

Transparent PC and SC films were produced in a microwave plasma CVD system ARDIS-100 (2.45 GHz) from H_2-CH_4 mixtures using either isotopically enriched methane (99.96%^{12}C) or "normal" methane. The PC sample was a kind of sandwich prepared by deposition of the first 170 μm thick layer of normal diamond on 57 mm diameter Si substrate at 1.2%CH_4, substrate temperature 820 °C, and growth rate of 1.5 μm/h. Then it was overgrown by 290 μm thick ^{12}C diamond layer at the same conditions.

The 210 μm thick epitaxial SC diamond film was grown on (100) oriented type Ib HPHT diamond substrate (4×4×0.5 mm) at 4%CH_4 in H_2, pressure 120 Torr, substrate temperature 950–1130 °C, and growth rate of 7.4 μm/h. Then the SC layer was separated from the substrate by laser cutting, and polished.

In-plane TC ($k_{\|}$) was determined in the temperature range of 80 K to 420 K by classical method of stationary thermal gradient measured with a resistor thermometer for PC, or with the chromel-constantan thermocouple of 25 μm diameter for SC. For the bi-layered PC film the TC for ^{12}C layer was found from the difference in TC between the sandwiched sample and the substrate. The systematic error was less than 3 % for PC and less than 15 % for SC. The perpendicular TC ($k_{\perp}$) was determined by a laser flash technique.

We found $k_{\|}$ = 2510 W/mK at RT for ^{12}C polycrystalline film that is 32 % higher than the value of 1900 W/mK measured for 0.5 mm thick PC with natural isotope abundance (Fig. 1), both samples being produced at identical growth parameters except the methane gas source. Even higher TC $k_{\perp}$ = 2600 W/mK was measured for this ^{12}C PC film perpendicularly to the film plane [3]. The isotopic effect increases with temperature decrease, the maximum TC of 4700 W/mK is reached at T = 160 K.

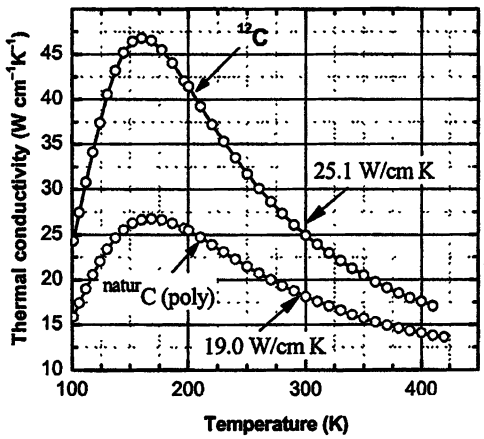

Fig. 1. Temperature dependence of thermal conductivity $k_{\|}$ of polycrystalline diamond films with natural abundance ^{nat}C (bottom) and isotopically enriched layer ^{12}C (top). The sample size 12×2×0.46 mm

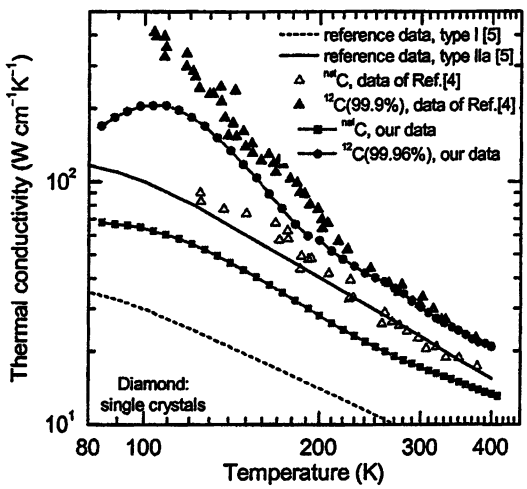

Fig. 2. The measured temperature dependence of TC for SC diamonds: epitaxial ^{12}C layer, sample size 3.4×1.5×0.36 mm (circles), and type Ib HPHT diamond substrate (squares). The literature data [4] are shown for HPHT ^{12}C (99.9 %) sample (full triangles) and type IIa natural diamond (open triangles). Also given are reference data for type Ia and type IIa diamonds (dashed and solid lines) [5]

In case of ^{12}C SC sample the measured thermal conductivity approaches 3100 W/mK at RT (Fig. 2), that is still 7 % lower compared to the TC of 3320 W/mK for HPHT ^{12}C (99.9 %) SC produced by General Electric Co [4]. The maximum TC k_{max}= 20500 W/mK is reached at T = 104 K. This improvement in k_{max} by the factor of four compared to ^{12}C PC sample is due to the absence of grain boundaries and a reduction in structural defects and impurities in the SC.

The photoluminescence (PL) spectrum (Fig. 3) of the PC sample taken at 488 nm excitation wavelength revealed the presence of nitrogen and Si impurities in the material, identified as N-vacancy and Si-vacancy color centers. The width of 1st order Raman peak is 2.2–3.5 cm^{-1}, reflecting variation of defect abundance and stress over the sample. Nevertheless, the presence of 2nd order Raman peak confirms rather good crystallinity of the PC diamond.

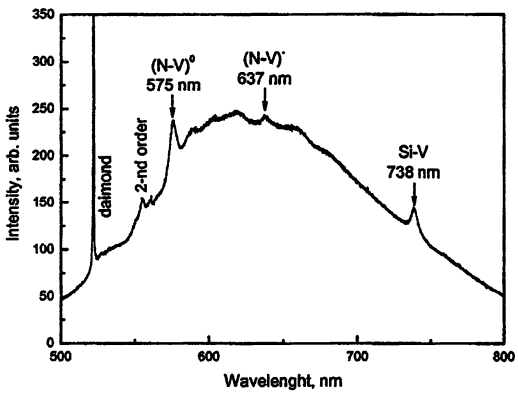

Fig. 3. PL spectrum, vertically extended to show nitrogen and Si related defects, in polycrystalline ^{12}C film

In contrast, the SC sample showed better quality: very narrow ($\Delta\nu$ = 1.7 cm^{-1}) Raman peak at 1332 cm^{-1}, and no significant features related to N and Si defects in PL spectrum (Fig. 4).

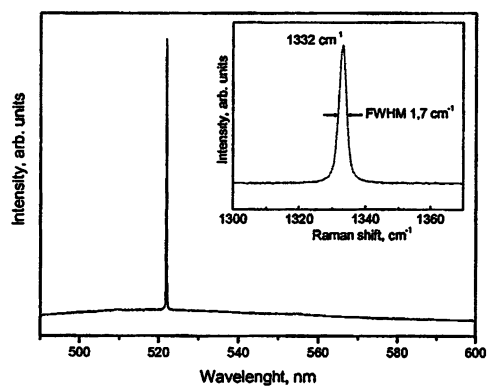

Fig. 4. PL spectrum of SC ^{12}C sample. Insert: Raman spectrum

To our knowledge this is first TC measurement of ^{12}C SC diamonds at temperatures around and lower of that (T_{max}) for maximum TC.

Our value of k_{max} is still a factor of two lower than k_{max}= 41000 W/mK (Fig. 2) measured by Wei et al. [4] using optical "mirage effect" method, their result being the highest TC for any dielectric material measured so far.

In view of extraordinary TC the isotopically enriched CVD diamond can be used as ultimate material for passive and active electronic devices, optical and microwave components when the thermal management problem is critical.

Table. Prices for isotopically enriched CH_4 and CO gases

Gas	$^{nat}CH_4$	$^{12}CH_4$ (99.95%)	^{12}CO (99.95%)
Price, $/liter	0.1	145*	7.7*

*Cambridge Isotope Labs, Feb 2011

Due to low consumption of CH_4 for growth process the normal methane cost contributes less than 1 % to the total production cost of optical quality PC diamond wafers. As the price for commercial isotopically enriched (99.95 %) $^{12}CH_4$ increases by three orders of magnitude (Table), the direct use of ^{12}C methane results in very high total cost of PC diamond (the rise by 3–4 times). A solution could be a conversion of cheaper ^{12}CO to $^{12}CH_4$ with diamond production cost rise of about 40 % only. Thus the growth of ^{12}C diamond with extreme thermal conductivity looks economically viable even at unoptimized (laboratory) process parameters.

This work was supported in a part by Physical Sciences Chapter of RAS (Program "Physics of new materials and structures, project A70); Ministry of Education and Science, State Contract No.16.513.11.3081; and Russian Fund for Basic Research: grants No. 09-02-00759 and No.10-02-90038-Bel.

References

1. *A.V. Sukhadolau, E.V. Ivakin, V.G. Ralchenko, A.V. Khomich, A.V. Vlasov, A.F. Popovich.* Thermal conductivity of CVD diamond at elevated temperatures // Diamond Relat. Mater. 2005. V. 14. P. 589-593.

2. *T.R. Anthony, W.F. Banholzer, J.F. Fleischer, L. WEi, P.K. Kuo, R.L. Thomas, R.W. Pryor.* Thermal diffusivity of isotopically enriched ^{12}C diamond // Phys. Rev. B. 1990. V. 42. P. 1104-1111.

3. *A.V. Inyushkin, V.G. Ralchenko, A.N. Taldenkov et al.* Singificant increase in thermal conductivity of polycrystalline CVD diamond upon isotopic enrichment // Bull. Lebedev Phys. Inst. 34 (2007) 329-333.

4. *L. Wei, P.K. Kuo, R.L. Thomas, T.R. Anthony, W.F. Banholzer.* Thermal diffusivity of isotopically modified single crystal diamond // Phys. Rev. Lett. 1993. V. 70, No. 2. P. 3764-3767.

5. *C.Y. Ho, R.W. Powell, P.E. Liley.* Thermal conductivity of the elements // J. Phys. Chem. Ref. Data. 1972. V. 1, No. 2. P. 279-425.

Plasma Enhanced Chemical Vapor Deposition of High-Enriched Silicon and Germanium Isotopes

P.G. Sennikov[1], N.V. Abrosimov[4], S.V. Golubev[2], A.V. Vodopyanov[2], D.A. Mansfeld[2], O.N. Godisov[3], D.A. Pryakhin[6], V.I. Shashkin[6], M.N. Drozdov[6], H.-J. Pohl[5]

[1] G.G. Devyatykh Institute of Chemistry of High-Purity Substances RAS, Nizhny Novgorod, Russia, pgsen@rambler.ru
[2] Institute of Applied Physics RAS, Nizhny Novgorod, Russia
[3] Centrotech Spb LLC, Sankt-Petersburg, Russia
[4] Leibniz-Institut for Crystal Growth, Berlin, Germany
[5] VITCON Projektconsult GmbH, Jena, Germany
[6] Institute for Physics of Microstructures RAS, Nizhny Novgorod, Russia

Isotopes of silicon and germanium, both in the form of thin films and of bulk crystals, find their increasing application in fundamental and applied investigations. High-purity crystals of some of isotopic species of germanium have been produced for the first time in the early 90s by the team of Russian and American researchers from RRC "Kurchatov Institute" and Lawrence Laboratory in Berkley [1]. The isotopically enriched tetrafluoride was used as the initial substance which was transformed into polycrystalline powder by chemical methods via the stage of oxide formation with subsequent formation of compacts sample, its purification by zone melting and growth of monocrystals. At present time due to realization of a number of international projects on registration of rare nuclear physics transformations, a great interest is being shown in large amounts of highly enriched and high-purity monocrystalline germanium-76 isotope. The same technological scheme is used for its production.

In case of silicon isotopes this sequence of operations does not lead to the required result both in isotopic and chemical purity of the target product. That is why at the end of the 90s the Russian ("Centrotech" Spb LLC, IChHPS RAS) and German ("Vitron" Company, Leibnitz Institute of Crystal Growth, Physical and Technical Federal Center) have developed a method for production of silicon isotopes comprising chemical transformation of fluoride into hydride, its thermal decomposition with subsequent growth of a single crystal from polycrystal by crucibleless zone melting [2]. High-purity and highly enriched silicon (with the content of ^{28}Si 99.994 %), produced in amount of several kilograms, is used in the experiments on fabrication and diagnostics of a physically substantiated reference mass ("Avogadro" program) as well as in different fundamental investtigations in the field of solids and information science [3].

Development of the direct method for production of silicon and germanium from the plasma mixture of their tetrafluorides and hydrogen is of interest due to simplification of technology and associated decrease in isotopic dilution (actual, first of all, for silicon). However, high bonding energy in fluoride molecules as well as the necessity to attain high degree of isotopic purity set rigid requirements to discharge type and reactor design.

In present report the main results are discussed on development of scientific fundamentals for plasma chemical method for production of silicon and germanium in elementary form; at the same time this approach can be expanded on isotopes of other elements having volatile chlorides.

Experiments were conducted in specialized laboratory set-ups with generation of plasma by HF (13.56 MHz) and ECR (24 GHz) discharge.

To develop the technology for production of layers and of bulk silicon crystal in the set-up with HF discharge and quartz reactor, its tetrafluoride with natural isotopic composition was used. For production of germanium isotopes in the same set-up, $^{74}GeF_4$ fluoride was used with enrichment of 83 % with respect to germanium. With selected conditions the deposition rate of silicon polycrystalline powder was 0.2 g/hour at conversion degree of about 60 %. Corresponding parameters for germanium deposition were 0,8 g/hour and more than 80 %, respectively. Pilot silicon polycrystals were grown by Czochralski method with natural isotopic composition of p-type with specific resistance of ρ = 0.3 Ohm·cm, carrier concentration $p = 6 \cdot 10^{16}$ cm^{-3} and oxygen concentration $1 \cdot 10^{18}$ cm^{-3}.

^{74}Ge (85 %) single crystal, produced by single growth with Czochralski method, was characterized by ρ = 2 Ohm·cm, $n = 1 \cdot 10^{15}$ cm^{-3} and oxygen concentration $1 \cdot 10^{16}$ cm^{-3}.

Thus, to our opinion, the plasma chemical method after its small debugging can provide the production of high-purity single crystals of germanium with any degree of enrichment at powder deposition rate of several grams per hour and conversion degree up to 90%. In case of silicon isotopes it is quite realistic to increase the deposition rate by two times and to increase the conversion degree up to 70 %. The degree of isotopic dilution will be determined by reactor material and by the level of preparation of the set-up in whole. It is necessary to pay special attention to development of the efficient system for collection of non-reacted products of plasma chemical transformation.

$^{28}SiF_4$, containing more than 99.999 % of this isotope, was used to produce ^{28}Si isotope with ultimately high enrichment. Experiments were carried out in set-up with ECR discharge maintained by gyrotron of continuous operation at 24 GHz with high deposition rate. Structural elements, previously being in contact with natural silicon, were completely replaced.

As a result, the silicon layers were produced with thickness of 2 mkm and enrichment of 99.9986± ±0.0003 % upon substrates from molybdenum and silicon, previously enriched up to 99.9959±0.0003 % within the framework of Avogadro project (measurements were conducted by SIMS method). The obtained isotopic enrichment of silicon is a record-breaking value for the present time.

Acknowledgements

The authors would like to acknowledge A.Ju. Safronov and A.I. Glasunov for isotopic enrichment of SiF_4, Ju.N. Drozdov for X-ray and B.A. Andreev for IR and Raman study of samples, H. Riemann and P. Becker for very useful discussions.

The work was financially supported by ISTC Project 3736, RFBR projects 08-08-12076-ofi and 10-08-01323-a.

References

1. *Itoh K., Hansen W.L., Haller E.E. et al.* High purity isotopically enriched ^{70}Ge and ^{74}Ge single crystals: Isotope separation, growth and properties // J. Mater. Res. 1993. V. 8, No. 6. P. 1341-1347.

2. *Becker P., Schiel D., Pohl H.-J. et al.* Large scale Production of highly enriched ^{28}Si for the precise determination of the Avogadro constant // Meas. Sci. Technol. 2006. V. 17. P. 1854-1860.

3. *Becker P., Pohl H.-J., Riemann H., Abrosimov N.* Enrichment of silicon for better kilogram // Phys. Status Solidi A. 2010. V. 207, No.1. P. 49-66.

Dielectric Structures for Two-Beam Accelerators, with Parameters Ranging from GHz to THz

S.V. Shchelkunov[1], J.L. Hirshfield[1,2], M.A. LaPointe[1], T.C. Marshall[2], G. Sotnikov[3], Wei Gai[4], M. Conde[4], J. Power[4], D. Mihalcea[4]

[1]Yale University, New Haven, CT 06511, USA, sergey.shchelkunov@gmail.com
[2]Omega-P, Inc, New Haven, CT 06510, USA
[3]NSC Kharkov Institute of Physics and Technology, 61108 Kharkov, Ukraine;
[4]Argonne National Laboratory, Argonne, IL, 60439,USA

Dielectric-lined structures are appealing candidates for a future collider or other accelerators because they offer simplicity and cost-effectiveness, withstand high fields, and can be configured to provide direct energy transfer from the drive bunch train to accelerated bunches without intermediate coupling elements (waveguides, input/output couplers, etc). Promising versions are those that have two distinct adjacent channels – one for the drive bunch train and the other for the accelerated bunches – because these versions can exhibit both high transformer ratio and appreciable gradients, while not requiring sophisticated means to profile the drive bunches or the drive bunch trains to obtain desired performance [1, 2, 3].

An overview of recent work (at Yale University and Argonne National Lab., USA) on two-channel rectangular and coaxial dielectric lined structures (Fig. 1) is presented covering numerous topics such as a recently conducted proof-of-principle experiment. We shall also describe theoretical investigations of cm-scale (GHz) and mm-scale (THz) structures that are excited by a ramped bunch train, together with an extensive study of bunch stability issues. The described work is supported by US Department of Energy, Office of High Energy Physics.

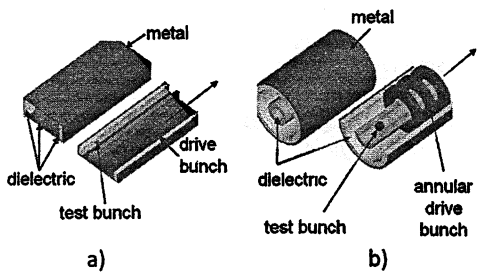

Fig. 1. Examples of two-channel rectangular (a), and coaxial (b) dielectric-lined structures. Note that the number of drive bunches may be greater than one

A recently conducted proof-of-principle experiment with a rectangular 10-cm long two-channel module is the first experiment to test the 2-channel DWA concept. The experimental objective was to design, build, and test a 2-channel dielectric wakefield structure and compare results with theory model predictions via observations of the test bunch energy acceleration and transverse kick. The experiment was carried out at the AWA beam-line (Argonne National Lab). The structure is designed to have a maximum transformer ratio (TR) of ~12.5:1. It is excited by a single drive bunch, and operates mainly in the LSM_{31} mode (~ 30 GHz). The time-delayed test bunch is produced off-axis on the same photocathode where the drive bunch is produced. The dielectric liner is cordierite (dielectric constant ~ 4.76). Details of the experimental setup are described in [4]. One notes that the 10–15 nC drive bunch was typically off the channel center by 2–3 mm [Fig. 2]. However, this did not prevent obtaining data to confirm the theory.

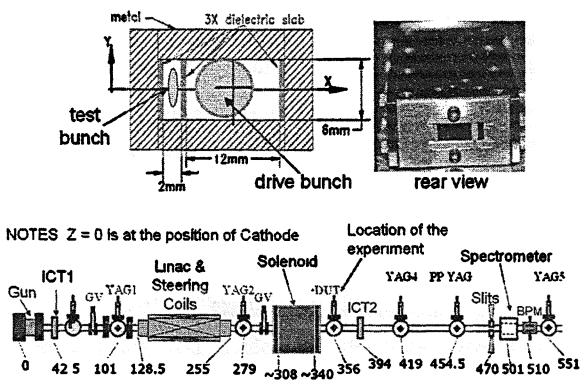

Fig. 2. (Top, left) Cross-section of the apparatus (dielectric slab thicknesses, from left to right, are 1.26, 2.03 and 1.06 mm); and (bottom) its position in the AWA beam line

Data were collected for different delays between the drive bunch and the test bunch, including measurements of the energy gain or loss received by test electrons, and the horizontal kick they received. The latter is processed to obtain the value of the horizontal deflecting force responsible for bunch deflection [5]. Space limitations prevent us from presenting here the results for more than one value of test bunch delay.

With a delay of ~11 mm or ~37 ps [Fig. 3], a jitter of 50–60 keV, and an energy slit error of 77 keV required recalibration of the data. The resulting inferred energy loss was up to 65 keV, while the energy gain was in the range 65–150 keV; the average energy change was ~50 keV. The horizontal kick that led to the typical shifts presented in Fig.3 ranged from –2.45 to –5.2 mrad, averaging –3.9 mrad. When the aforementioned values are scaled to a 50 nC drive bunch charge, excellent agreement is found between theory and the measurements [Fig. 4]. To have loss, the accelerating force F_z (re-computed for a 50 nC drive bunch) must be up to –2.85 MeV/m; to have the observed gains, F_z must be between 2.85 and 6.7 MeV/m; to have the obseved x-kicks, the horizontal deflecting force F_x (re-computed for a 50 nC drive bunch) must range between –1.72 and –3.6 MeV/m, and be on average –2.8 MeV/m. All these values (pointed at by the arrows) can be found on the $F_z(z)$ and $F_x(z)$ theoretical curves just where the test bunch was located.

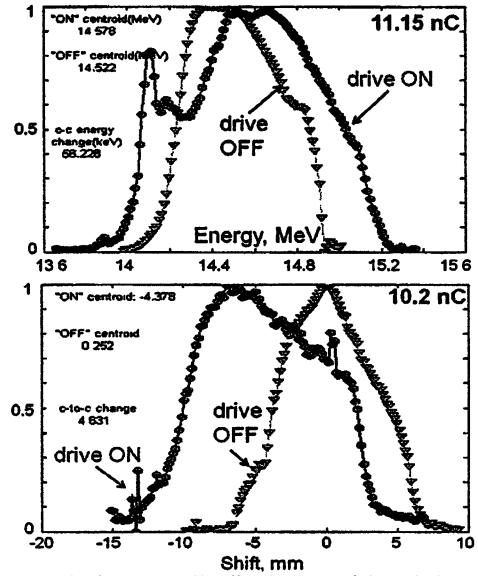

Fig. 3. Typical energy distributions, and bunch horizontal distributions (observed in 80–85 % of shots) when the delay was ~11mm; distributions are normalized to unity

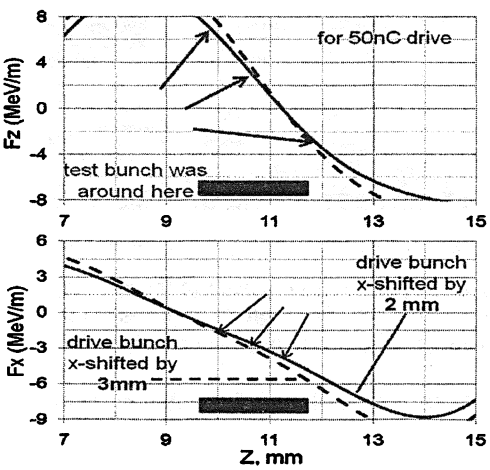

Fig. 4. Theoretical simulations of F_z and F_x as obtained by use of CST Microwave Studio for the test channel

In summary, the theory model predictions are well confirmed by the experimental data. Considering Fig. 4, one may note that moving a narrower bunch to a delay of 9 mm would allow both high acceleration and low deflection. However in general, deflection in a rectangular configuration is an intrinsic feature. An exceedingly far better choice for accelerator applications is a coaxial geometry, where inherent symmetry implies no undesirable deflection [3].

The planned near-term proof-of-principle experiment with a coaxial structure will be installed and operated at AWA-Argonne in 2011–2012. The structure uses two alumina (dielectric constant ~9.8) 100 mm long pipes. The outer pipe has OD 30.16 mm, and ID 27 mm; the inner pipe has OD 8 mm, and ID 4.8 mm. The structure is to be driven by a single 14 MeV annular bunch having charge up to 50 nC. The structure is to be mainly excited in the TM_{02}-mode. This module is predicted to exhibit TR 6.2:1, and acceleration gradient 18 MV/m. The experimental objectives are the same as they were for the rectangular module.

Another experiment that may be conducted in collaboration with AWA-Argonne after the planned upgrades [6] is to test the so-called ramped bunch train (RBT) concept [7]. In [8], a cm-scale example of this was described for coaxial geometry, and a recipe was obtained to enhance TR up to ~17:1 following only four drive bunches. Most importantly, the proposed scheme ensures that all the drive bunches undergo the same deceleration.

Coaxial mm-scale structures are promising candidates as acceleration modules for a future multi-TeV collider because they should provide high transformer ratio and large accelerating gradient, should have transverse forces acting on the accelerated bunch that are focusing, and can be designed to have weak drive bunch instabilities that permit utilizing the drive trains over long distances [3, 9]. In [10], an example is given for a mm-scale coaxial module that would operate in the TM_{02}-mode at ~912 GHz, and when driven by one 6 nC bunch would exhibit ~520 MV/m accelerating gradient in a ~100 micron-diameter inner channel. [The outer channel has OD ~1 mm]. The RBT concept is under further study, and drive and test bunch stability issues are being investigated as well [9, 10].

References

1. *Changbiao Wang, et al.,* Rectangular Dielectric-loaded Structures for Achieving High Acceleration Gradients // AIP Conf. Proc. 877, p. 910-917 (2006).

2. *Wanming Liu and Wei Gai,* Wakefield generation by a relativistic ring beam in a coaxial two-channel dielectric loaded structure // Phys. Rev. ST-AB, V. 12, 051301 (2009) and references therein.

3. *G.V. Sotnikov, T.C. Marshall, and J.L. Hirshfield,* Coaxial two-channel high-gradient dielectric wakefield accelerator // Phys. Rev. ST-AB, V. 12, 061302 (2009) and references therein.

4. *S.V. Shchelkunov, et al.,* Status of Dielectric-Lined Two-Channel Rectangular High Transformer Ratio Accelerator Structure Experiment // Procs of 2011 Particle Accelerator Conf., MOP107, link: http://www.c-ad.bnl.gov/pac2011/proceedings/papers/mop107.pdf and refs. therein.

5. *J.L. Hirshfield, et al.,* A Fast Kicker Using a Rectangular Dielectric Wakefield Accelerator Structure // Particle Accelerator Conference 2009 Procs, paper FR2RAC03, link: http://trshare.triumf.ca/~pac09proc/Proceedings_091005 papers/fr2rac03.pdf and references therein.

6. *M.E. Conde, et al.,* Upgrade of the Argonne Wakefield Accelerator Facility (AWA) and Commissioning of a new RF Gun for Drive Beam Generation // Procs of 2011 Particle Accelerator Conf., MOP008, link: http://www.c-ad.bnl.gov/pac2011/proceedings/papers/ mop008.pdf.

7. *C. Jing, et al.,* Increasing the transformer ratio at the Argonne wakefield accelerator // Phys. Rev. ST-AB, V. 14, 021302 (2011) and references therein.

8. *G.V. Sotnikov and T.C. Marshall,* Improved ramped bunch train to increase the transformer ratio of a two-channel multimode dielectric wakefield accelerator // Phys. Rev. ST Accel. Beams, V. 14, 031302 (2011).

9. *G.V. Sotnikov, et al.,* Accelerated Bunch Stability in a Coaxial Dielectric Structure When its Symmetry is Broken // AIP Conf. Proc. 1299, p. 342-347 (2010).

10. *T.C. Marshall, G.V. Sotnikov, and J.L. Hirshfield,* A THz Two-Channel Dielectric Wakefield Structure for High Gradient Acceleration // AIP Conf. Proc. 1299, p. 336-341 (2010).

High Gradient Accelerator Structures R&D at SLAC*

J.W. Wang for the SLAC Team and Collaborators

SLAC National Accelerator Laboratory, Menlo Park, U.S.A. jywap@slac.stanford.edu

It has always been our goal to design ultra high-gradient room-temperature RF linear accelerators. We have to pay special attention on the physics of several important phenomena which limit their performance: electron field emission, dark current, pulse heating, RF breakdown and cavity damage.

High Gradient Performance for Room Temperature Linear Collider NLC/GLC

One of the important requirements for the future e^+e^- linear collider is to demonstrate stable, long-term operation at the high gradient in order to optimize the machine cost [1]. The tests of various prototype structures as shown in Fig. 1 have been done predominantly at 11.424 MHz. Figure 2 shows that our X-band test structures reached the maximum practical gradients in the range of 60–80 MV/m after considerable RF processing.

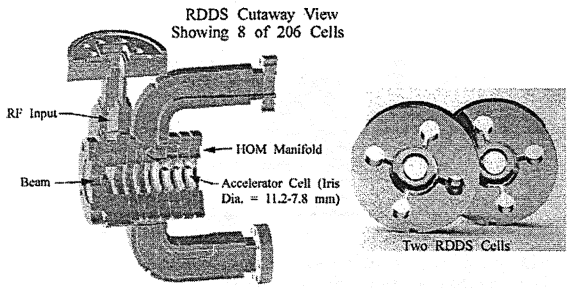

Fig. 1. Prototype accelerator structures for the NLC/GLC main linac. RDDS stands for Rounded Damped Detuned Structure. HOM stands for Higher Order Mode

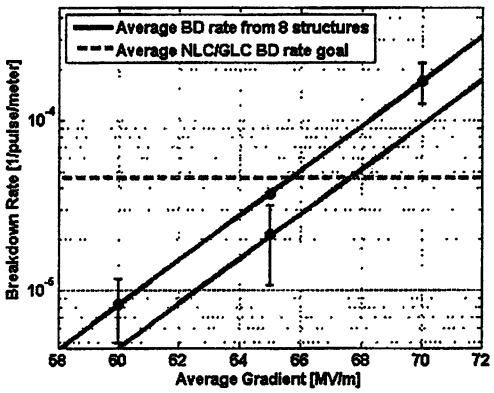

Fig. 2. Average breakdown rates for a series of NLC test structures as a function of accelerating gradient after 500 hours (upper line) and 1500 hours (lower line) of RF processing

US High Gradient Collaboration

Figure 3 shows the US High Gradient Collaboration is part international collaboration in high gradient research [2]. The main challenge is to know what the reliably achievable accelerating gradient is and to understand the mechanism behind it.

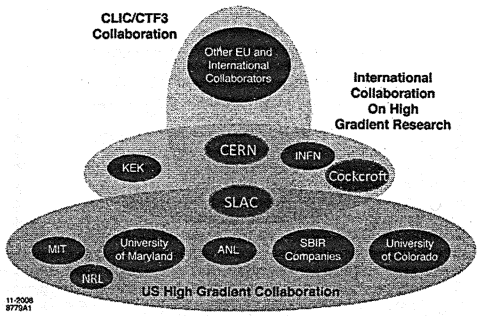

Fig. 3. Collaboration on High Gradient Accelerator Structures at SLAC, US and worldwide

For years, this collaboration has made some very encouraging progress in basic RF breakdown physics, frequency scaling, geometry dependence, material choices and surface processing techniques.

Basic Physics Research on Short/Compact Accelerator Structures

It was believed in the past that Field Emission is the initial cause of RF breakdown. At a microscopic field of several GV/m, field emitted current can approach $10^{11}A/m^2$ and above, the Joule losses in an emitter can heat it in a few or tens of nanoseconds to the point of vaporizing some of its contents to form a sheath or plasma spot over the emitter, eventual explosion or meltdown, metal droplets, and expanding damage in the form of craters. Recently a systematic study [3] with some structures showed in Fig. 4 casted some doubt on this belief, that pulse heating, somewhere in the cavity where the magnetic field is high, to induce thermal fatigue and thermal stresses beyond the elastic limit of the cavity metal may be the original cause.

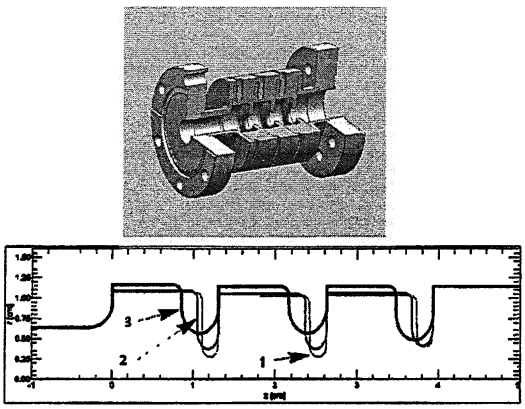

Fig. 4. Three short disk-loaded standing-wave structures shown in top picture with respective ratio of aperture radius over wavelength of (1) 0.105, (2) 0.143 and (3) 0.215

* Work supported by U.S. Department of Energy, contract DE-AC03-76F00515

As shown in Fig. 5, the RF breakdown data do not correlate well with the gradient or peak surface fields, however, correlate very well to the peak surface heating caused by the surface magnetic field.

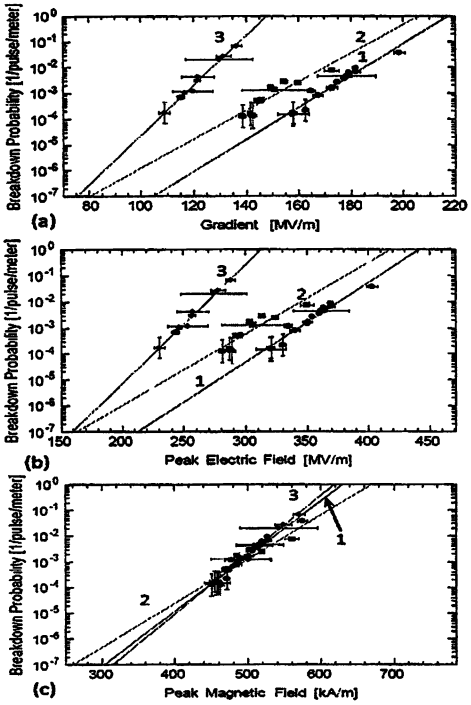

Fig. 5. Comparison of breakdown probabilities for three different structures. Their respective ratios of aperture to RF wavelength are given in Fig. 4

Basic Physics Research on Full Size Accelerator Structures

In recent years, a CERN-SLAC-KEK collaboration on high gradient X-band structure research has been established in order to demonstrate the feasibility of the CLIC baseline design for the main linac stably operating at more than 100 MV/m loaded accelerating gradient [4]. Several prototype CLIC structures were successfully fabricated and high power tested. They operated at above 100 MV/m with a breakdown rate that meets the CLIC linear collider specifications of $<5\cdot10^{-7}$/pulse/m. Figure 6 shows a prototype X-Band accelerator. Figure 7 shows satisfactory operation results with lower than required RF breakdown rate at the average gradient of more than 110 MV/m.

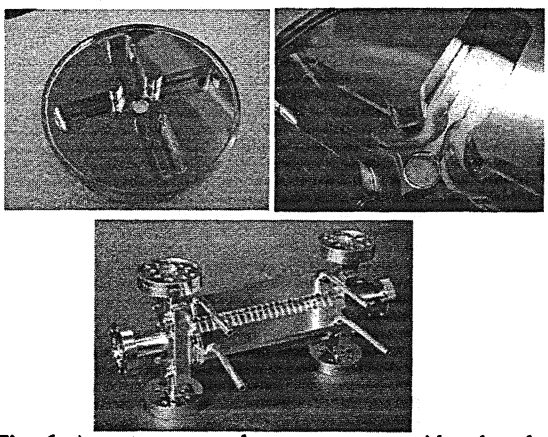

Fig. 6. A prototype accelerator structure with a length of 24 cm (bottom) and its typical accelerator cups with the features for high-order mode damping (top)

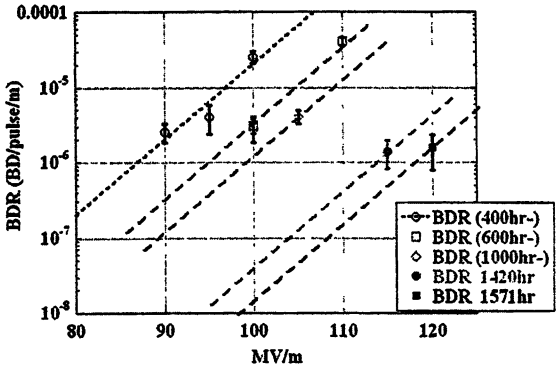

Fig. 7. Average breakdown rates for a CLIC main linac prototype structure called T24 as a function of accelerating gradient after certain hours of RF processing

Material Studies Using Pulsed Heating Experiments

In order to better understand the RF breakdown mechanism due to pulse heating, the material studies with various tolerances to surface fatigue were carried [5]. Figure 8 shows the test set-up, where the 3 in" diameter samples are mounted onto the cavity end cap. Figure 9 shows the pulse heating damages.

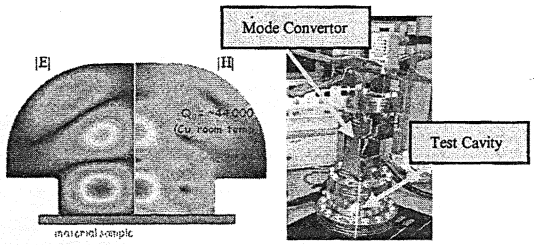

Fig. 8. TE_{013} cavity (left) and its connection to a circular to WR90 waveguide mode convertor (right)

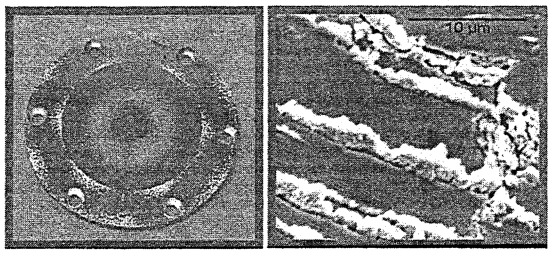

Fig. 9. Copper pulsed heating sample tested to 110 °C showing (a) pulsed heating ring and (b) SEM image showing a typical surface area within the pulsed heating ring

Each sample was tested to a peak pulsed heating temperature of approximately 110 °C and remained at this temperature for approximately $10\cdot10^6$ RF pulses. In general, the results showed the possibility of pushing the gradient limits due to pulsed heating fatigue by the use of copper zirconium and copper chromium.

References

1. *J. Wang and T. Higo, Beam* Dynamics Newsletter, No. 32, SLAC-PUB-10370 (2004).
2. *S. Tantawi,* Talk in 5th Collaboration Meeting on X-Band Accelerator Structures, SLAC, U.S. (2011).
3. *V. Dolgashev, et al.* Applied Physics Letters, V. 97, No. 17 (2010).
4. *J. P. Delahaye, IPAC10,* THPEA012, Kyoto, Japan.
5. *L. Laurent, et al.* Phys. Rev. Spec. Topics, 14 (2011).

Microwave Sintering of Functional Layers in Design of Planar Solid Oxide Fuel Cells

V.A. Sadykov[1,2], V.V. Usoltsev[1,2], N.F. Eremeev[1,2], A.N. Salanov[1], N.V. Mezentseva[1], T.S. Kharlamova[1], S.N. Pavlova[1]; O.F. Bobrenok[3], A.S. Ulihin, N.F. Uvarov[4], O.L. Smorygo[5], A.V. Arzhannikov[1], P.V. Kalinin[1,6], M.K.A. Thumm[7]

[1]Boreskov Institute of Catalysis, Novosibirsk, Russia, sadykov@catalysis.ru
[2]Novosibirsk State University, Novosibirsk, Russia
[3]Kutateladze Institute of Thermal Physics, Novosibirsk, Russia
[4].Institute of Solid State Chemistry and Mechanochemistry, Novosibirsk, Russia
[5]Institute of Thermal Physics, Novosibirsk, Russia
[6]Budker Institute of Nuclear Physics, Novosibirsk, Russia
[7]Karlsruhe Inst. Technol., Karlsruhe, Germany

Thin film solid oxide fuel cells (SOFC) operating in the intermediate temperature range are now considered as the most promising for distributed, mobile, standby or auxiliary power generation [1]. One of the most demanding problem in their design is caused by the necessity of co-sintering of thin layers (electrolyte, spatially graded cathode layers) to required density without degradation of their functional properties (conductivity, oxygen mobility etc). Traditional sintering approaches requiring too high temperatures often failed in this respect. This work presents results of application of microwave sintering promising for design of anode-supported SOFC [2].

Experimental

Nanocrystalline complex oxides with ionic conductivity (YSZ, GDC etc.) were used as electrolyte and oxides with mixed ionic-electronic conductivity (rare-earth nickelates and cobaltites) were synthesized by polymerized polyester citric acid-ethylene glycol precursors (Pechini) route. Nanocomposites were prepared by ultrasonic dispersion of the mixture of powders in isopropanol with addition of polyvinyl butyral. Functionally graded cathodes comprised of porous perovskites layers (La-Sr-Mn-O, La-Bi-Mn-O, La-Sr-Fe-Ni-O, etc) and dense thin perovskite-electrolyte nanocomposite interlayers were supported by slip casting, screen-printing, air brushing, MO CVD or electrophoretic deposition. Functional layers and uniaxially pressed pellets were sintered by different techniques: conventional heating (CH) in the furnace at temperatures up to 1300 °C (nanocomposites) and 1400 °C (electrolytes) with or without sintering aids (Bi or Ag nitrates, etc) under Ar atmosphere; microwave heating (MH) or radiation-thermal sintering under electron beam action. MH was carried out using a system based on gyrotron with frequency 24 GHz specially designed for heating of ceramics. Samples were heated by the focused radiation (power 0.5–1.5 kW) up to 1000–1200 °C. RTS was carried out on an ILU-6 accelerator that gives electron pulses with a high (2.4 MeV) energy. Temperature was measured by thermocouple and varied in range 900–1200 °C by changing the frequency in the range of 8–20 Hz.

Genesis of the real structure of sintered functional layers and pellets was studied in details by high resolution transmission electron microscopy and scanning electron microscopy with local elemental analysis by EDX, X-ray powder diffraction. Performance of functional layers sintered by using different techniques was tested using respective devices: button-size fuel cells operating with wet H_2 –air feeds.

Effect of sintering on density and real structure of SOFC materials

In this work we study the effect of sintering parameters (temperature, radiation density and duration) on the microstructure (porosity, sizes of domains and spatial uniformity of their distribution) in functional layers and bulk ceramics comprised of a given material (nanocomposite, fluorite-like electrolyte or complex perovskite). Anode substrates were comprised of NiO/YSZ composite either bulk platelets (porosity 20–30 vol.%) or supported as layers with graded porosity on compressed planar Ni-Al foam substrate [3]. Substrates were sintered by conventional or microwave heating and used as a support for solid electrolyte. Sintering parameters were optimized to provide required layers density while avoiding formation of isolating pyrochlores or excessive sintering of anode substrates. Morphology of sintered materials was studied by SEM with local EDX analysis and typical micrographs are presented on Fig. 1 and Fig. 2.

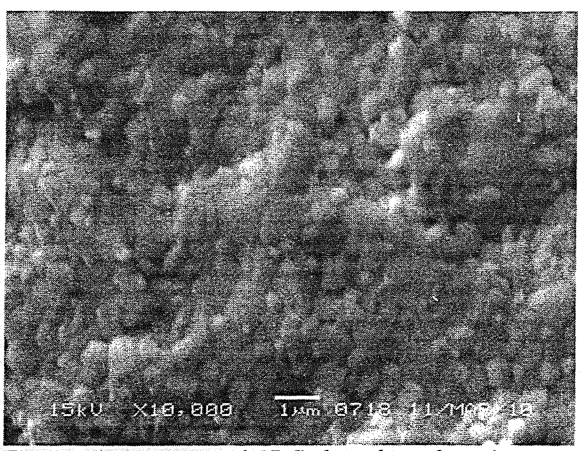

Fig. 1. Microstructure of GDC electrolyte after microwave sintering

Microwave heating allows to achieve complete densification of GDC electrolyte as a bulk disk al-

ready at 1200 °C (Fig. 1). Thin layers of GDC or YSZ supported on the surface of NiO/YSZ anode cermet (either bulk or Ni-Al foam supported) also can be sintered to density close to theoretical without mechanical cracks or flaking.

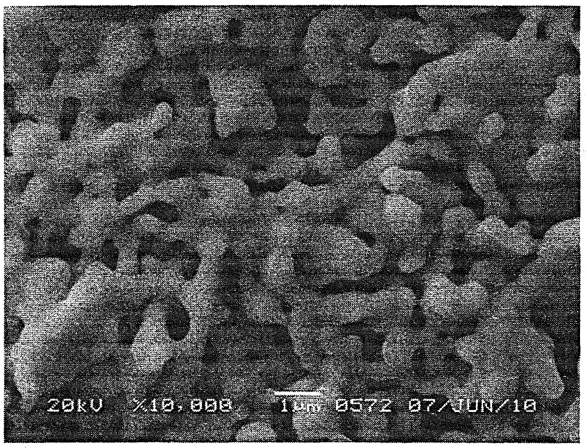

Fig. 2. Typical SEM image of cathodic composite La-Fe-Ni- Ce-Gd-O (LFN-GDC) after radiation thermal sintering at 1200 °C

Microwave heating as well as radiation- thermal sintering allowed to control in the range of 60–95.% the density of layers of cathodic nanocomposites supported on the electrolyte layer as dependent upon the sintering temperature (Fig. 2). These advanced sintering techniques also provide small domains of both phases in dense nanocomposites which result in developed interfaces revealed to be paths for fast oxygen diffusion [4]. Detailed XRD and TEM study confirm that no significant changes in phase composition occurs during sintering using microwave heating or RTS. At the same time, some redistribution of cations in cathodic nanocomposite was observed generating only surface phases with a high mixed ionic-electronic conductivity without nucleation of isolating phases with the pyrochlore structure [4].

Microwave sintering was shown to be much more efficient in achieving required density of functional layers at temperatures less by 200–300 °C as compared with traditional sintering, without layers cracking, their spallation or formation of isolating layers at cathode/electrolyte interface. In comparison with RTS, microwave sintering is more flexible and simple in the technical realization.

Fuel cell performance

For button-size fuel cells with Ni/YSZ anodes, thin (~10 microns) layers of YSZ electrolyte, thin dense perovskite-fluorite nanocomposite interlayers and thick porous perovskite cathode layers sintered to optimum density by MH and RTS, a typical power density was about 600–800 mW/cm^2 at 700 °C without any degradation of performance in middle-term (~ 100 h) tests (Fig. 3).

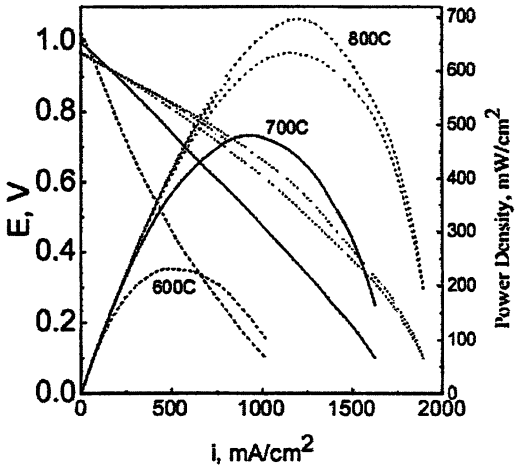

Fig. 3. Electrochemical performance of fuel cell sintered using microwave radiation. Fuel – wet hydrogen, oxidant – air

SEM studies of cross-section of metal – supported cell discharged after testing demonstrated absence of any cracks or isolating pyrochlore-type layers.

Acknowledgements

Support of this research by Integration Project 57 SB RAS-Belarus NAS, Russian Federation Government Grant N 11.G34.31.0033 and Contract 02.740. 11.0852 of the Federal Program "Scientific and Educational Cadres of Russia" is gratefully acknowledged.

References

1. *Noh, H.-S., Lee, H., Lee, J.-H., Lee, H.-W., Son, J.-W.* Thin film electrolyte micro-SOFC: fabrication and performance improvement through thin film electrolyte and nano-structure electrodes // ECS Transactions 2009. V. 25. No. 2. P. 873-879.

2. *Upadhyaya, D.D., Ghosh, A., Dey, G.K., Prasad, R., Suri, A.K.* Microwave sintering of zirconia ceramics // J. Mater. Sci. 2001. V. 36. P. 4707-4710.

3. *Sadykov, V., Mezentseva, N., Usoltsev, V., Smorygo, O., Mikutski, V., Marukovich, A., Bobrenok, O., Uvarov, N.* Metal supported SOFC on the gradient permeable metal foam substrate // Adv. Mater. Res. 2010. V. 123/125. P. 1083-1086.

4. *Sadykov, V., Pavlova, S., Zarubina, V., Bobin, A., Alikina, G., Lukashevich, A., Muzykantov, V., Usoltsev, V., Kharlamova, T., Boronin, A., Koscheev, S., Krieger, T., Ishchenko, A., Mezentseva, N., Salanov, A., Smirnova, A., Bobrenok, O., Uvarov, N.* Design and characterization of functionally graded cathode materials for solid oxide fuel cells // ECS Transaction 2009. V. 25. P. 2403-2412.

Study of the Processes of Ion Boron Doping and High-Temperature Annealing of Epitaxial CVD Diamond Films Grown by Microwave Plasma-Assisted Chemical Vapor Deposition

M.P. Dukhnovsky[1], A.K. Ratnikova[1], Yu.Yu. Fedorov[1] A.L. Vikharev[2], A.M. Gorbachev[2], A.B. Muchnikov[2]

[1] FSUE "Istok", Fryazino, Russia, istok220@mail.ru
[2] Institute of Applied Physics RAS, Nizhny Novgorod, Russia

Diamond is a promising material for creation of electronic devices, e.g., in the class of high-power high-frequency transistors [1].

To create devices based on diamond structures, the latter should be doped with donors or acceptors. The most promising technique of creating doped layers in diamond films is ion doping, which allows obtaining layers with required concentrations of charge carriers in a controllable and well reproducible manner [2].

This paper presents the results of studying the manufacture of diamond films by using the ion doping method, specifically, doping of epitaxial 100-oriented layers on substrates of natural IIa-type diamonds with boron.

Currently, vapour deposition of diamond in plasmochemical reactors with activation of carbon-containing gas by the microwave discharge plasma is the only method of obtaining artificial monocrystal diamond layers, which have high quality reproducible from crystal to crystal [3].

Epitaxial diamond layers were grown in a plasmochemical reactor based on a volume reactor with a microwave discharge maintained by microwave radiation at a frequency of 2.45 GHz [4, 5].

Figure 1 presents optical images of the grown samples obtained in reflected light. The single crystal layers deposited on substrates A049 and A196 are rather uniform, optically transparent, and lacking such defects as growth hillocks or etch pits.

Figure 2 shows the image of the surface of sample A196 (after the deposition) obtained with a JEOL 6390 LA scanning electron microscope. As seen from the Figure, the surface has good uniformity.

The layer of the epitaxial CVD diamond, as well as the natural-diamond IIa-type substrates (the reverse side of the samples) were doped with boron ions.

The multistage doping with boron ions having the energy ranging from 40 to 110 keV was used to upgrade the electrophysical characteristics of the diamond films and reduce graphitization of the surface. The total dose of boron varied in the range from $1.1 \cdot 10^{14}$–$5.7 \cdot 10^{15}$ cm^{-2}.

To restore the crystalline structure of the damaged near-surface diamond layers after doping and activation of the doping agent, we annealed the doped samples in a setup for fast annealing in a nitrogen medium.

The main problem of creating layers of diamond with p-type conductivity by using ion doping is the possibility of graphitization, i.e., transformation of the doped layer under annealing not to diamond, but to graphite [6]. The critical peak concentration of boron ions was determined, above which the considered layer is not transformed to diamond completely in this annealing regime. After annealing, all samples were cleaned to remove graphite traces from their surface by etching them with acid.

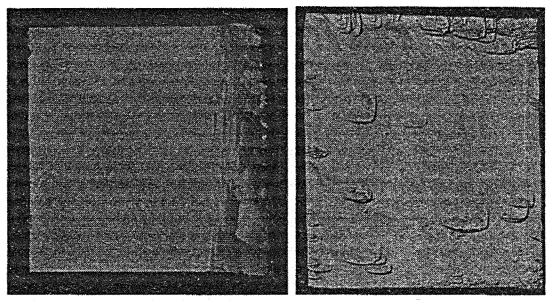

a *b*

Fig. 1. Reflected-light optical images of the grown samples: A049 (*a*) and A196 (*b*)

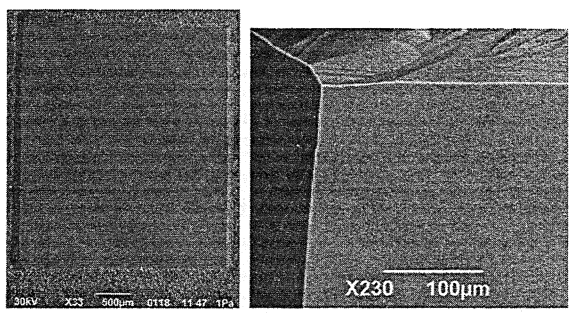

a *b*

Fig. 2. SEM image of sample A196: overall view (*a*) and top left corner (*b*)

To measure characteristics of the layers of semiconducting diamond, metal contacts of Ti and Al, 0.1 and 1.0 μm thick, respectively, were deposited on the surface of the samples. The surface density and mobility of charge carriers were determined by measuring the Hall effect.

The optimal regime to ensure diamond restoration after doping by using the annealing was found. It ensured a carrier mobility of 1150 $cm^2/V \times s$ at 300 K being the highest value of those obtained in ion-doped semiconductor diamond [6]. The manufactured near-surface, highly-doped layer of the p-type allows using as a near-contact layer in electronic devices. The results of doping, annealing and electrical measurements are shown in the table.

№ measurement	Surface of doping	Dose of boron ions, ion/cm^2	Temperature of annealing, °C	Material of contacts and temperature of firing, °C	Surface concentration, cm^{-2}	Mobility of holes, μ, cm^2/Vs	Surface resistivity, Kohm/sq
1	Substrate (natural diamond of IIa type), Sample A049	$5\cdot10^{14}$	1380	Ti, Al, 900	–	–	–
2	CVD layer, Sample A049	$5\cdot10^{14}$	1380	Ti, Al, 900	$4\cdot10^{11}$	1150	13.3
3	CVD layer, Sample A049	$3\cdot10^{15}$	1380	Ti, Al, without firing	$2.7\cdot10^{11}$	780	29.4

References

1. *Sussmann R.* // CVD Diamond for Electronic Devices and Sensors, John Wiley & Sons. 2009.

2. *Vavilov V.S.* // Phys. Usp. 1994. V. 37. P. 407.

3. *Kobashi K.*, Diamond Films, Amsterdam: Elsevier, 2005.

4. *Vikharev A.L., Gorbachev A.M., Koldanov V.A., Radishchev D.B.* // Plasma Physics Reports. 2005. V. 31. P. 338.

5. *Muchnikov A.B., Vikharev A.L., Gorbachev A.M., Radishev D.B., Blank V.D., Terentiev S.A.* Homoepitaxial single crystal diamond growth at different gas pressures and MPACVD reactor configurations // Diamond Relat. Mater. 2010. V. 19. P. 432.

6. *Ueda K., Kasu M., and Makimoto T.* High-pressure and high-temperature annealing as an activation method for ion-implanted dopants in diamond // Appl. Phys. Lett. 2007. V. 90, No. 12. P. 2102.

The Superconducting ECR Ion Source DECRIS-SC2

A. Efremov, V. Bekhterev, S. Bogomolov, V. Drobin, A. Lebedev,
V. Loginov, V. Seleznev, Yu. Shishov, N. Yazvitsky

Joint Institute for Nuclear Research, Dubna, Moscow reg., Russia, efremov@nrmail.jinr.ru

Electron cyclotron resonance (ECR) ion sources have been widely used as the external ion sources for heavy ion accelerators. The production of intense heavy ion beams has become one of the key point for the successful accelerators operation.

It is well known that electron confinement plays a major role in ECR ion sources performances. Therefore the quality of an ECRIS confinement essentially depends upon the value of the axial and radial magnetic fields as experimentally found [1]. Taking into account the experimental laws governing this confinement a "liquid He-free" superconducting ECR ion source DECRIS-SC [2] has been designed and manufactured at the FLNR in collaboration with LHE (JINR). Since April 2004 the source is in operation at the CI-100 cyclotron. Using the experience obtained during construction and operation with the source the new source DECRIS-SC2 was developed.

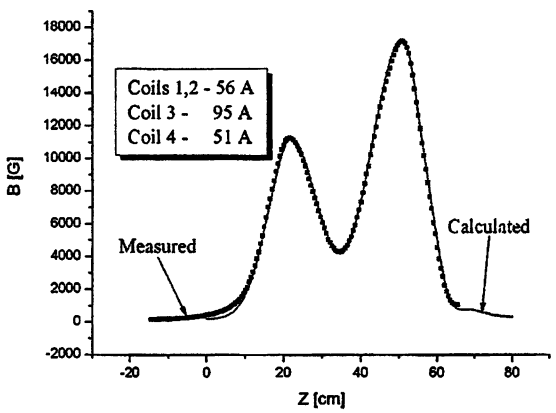

Fig. 1. Calculated (line) and measured (points) axial magnetic field distribution

The technical details of the source have been described elsewhere [3]. The design of the superconducting magnet system of the new source differs essentially from the previous one. To decrease the weight and dimensions of the system it was decided to produce the vacuum vessel from chromium plated soft steel, so it will simultaneously serves also as a magnetic yoke. The magnet contains a set of four solenoid coils. The coils are posed on the framework, fashioned from non-magnetic stainless steel which is free-floating fixed inside a vacuum casing with the help of two supports. The support consists of two stainless steel rings and eight glass textolite rods.

The vacuum vessel is produced from chromium plated soft steel and simultaneously serves also as a magnetic yoke. The magnetic field is formed by magnetic yoke and iron plugs. Combining of the magnetic yoke and vacuum vessel functions allows one to decrease significantly the dimensions and weight of the magnet.

The framework with windings is protected by a reflective aluminium shield and copper screen which is cooled by the first stage of the cryocooler. The copper screen is covered with a multilayer screen-vacuum isolation.

A Nb Ti/Cu monolithic superconducting wire (bare diameter – 0.65 mm, insulated diameter – 0.7 mm) is used in the windings. The working current (up to 100 A) is significantly lower critical current ($\geq$ 270 A at 5 T and 4.5 K). The reserve of the temperature stability has the value about of 2 K and allows this magnet to operate with increased heat loads. The framework and the windings are connected with the second stage of the cryocooler by a high-purity aluminum tape. The copper plates are screwed to the framework. "Cold" diodes are located on the plates. The copper screen is fastened to supports. Six HTSC current leads are posed around the cryocooler head. The pumping of the vacuum casing is performed by forevacuum and turbomolecular pumps.

It should be noted, that the windings are substantially self-protected due to the moderate cross-section dimensions and sufficient thermal conductivity. Besides, the stored energy is not so high (~ 40 kJ). The estimations have shown that coils temperature after a full quench transition is 40–50 K and the maximum temperature of the "hottest" point does not exceed ~120 K.

In the design of the "warm" part of the source most of constructional features of the DECRIS-SC source, such as cylindrical plasma chamber, UHF feed by standard waveguide, bias-electrode etc., are used. The hexapole for radial confinement of plasma has a Halbach structure. It consists of 24 permanent-magnet identical sectors with the corresponding easy axis direction. The inner diameter, the outer diameter and the length of the hexapole are 80 mm, 170 mm and 290 mm, respectively. The desired radial magnetic field strength on the plasma chamber wall is 1 T.

The axial magnetic field distribution is shown in Fig. 1. In Table 1 we summarized the main operating parameters.

Table 1

Operating frequency	14 GHz
Axial magnetic field max. peaks	1.9/1.4 T
Radial magnetic field max.	1.05 T
Hexapole material and structure	NdFeB, 24 pieces
Plasma chamber diameter	64 mm
Plasma chamber length	300 mm
Max. extraction voltage	30 kV

Generally the operation of the DECRIS-SC2 ion source is very stable and reproducible. Till now only oxygen and few noble gases were tested. All of the spectrums were optimized for the production of me-

dium charge states ions. Two of the Ar spectrums when source was optimized for Ar^{8+} and Ar^{11+} production are shown in Fig. 2.

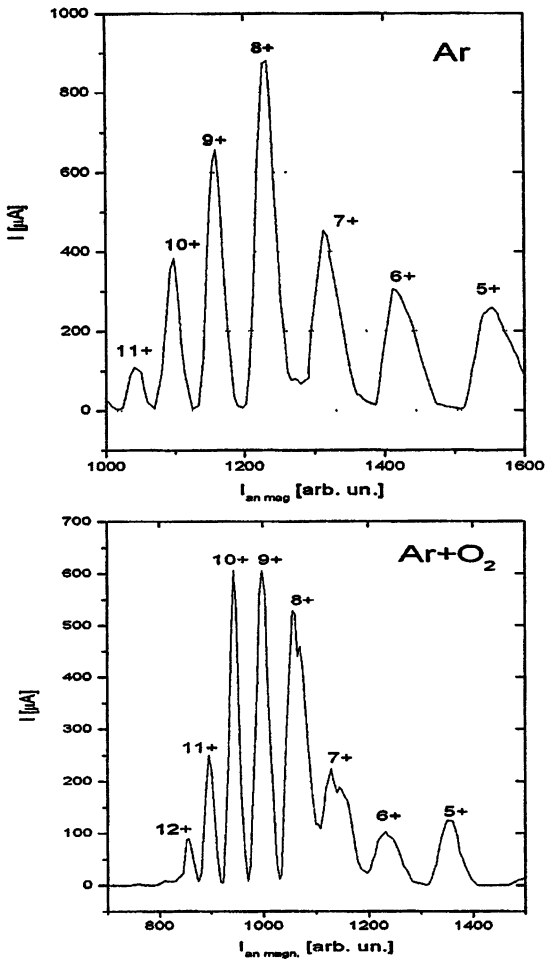

Fig. 2. Ar spectrums when source was optimized for the Ar^{8+} (top) and Ar^{11+} (bottom)

For the preliminary commissioning the TWT generator with the maximum power of about 600 W was used to feed UHF power directly into the plasma chamber through the standard rectangular waveguide. With the primitive one gap extraction and a stainless steel puller installed for the first tests the source can work without discharge at 25 kV. The transmission efficiency right until the faraday cup installed after the analyzing magnet was estimated with an oxygen beam in the range of 40÷60 % for the extraction voltage varied from 15 to 25 kV. The typical analyzed currents obtained during these tests for various beam species are given in Table 2.

It was interesting to compare the performances of the new DECRIS-SC ion source and the DECRIS-4 ion source which was designed with a so called "flat magnetic field" geometry. The last one showed very good performance (see Fig. 3) for low levels of the UHF power (≤ 150 W). The DECRIS-4 ion source can produce about of 490 μA of Ar^{8+} with the UHF power 100 W only meanwhile the new source delivers up to 550 μA with the same power.

Table 2

Ion species	Current (eμA)
O^{6+}	820
Ar^{8+}	880
Ar^{9+}	680
Ar^{11+}	250
Ar^{12+}	120
Kr^{15+}	250

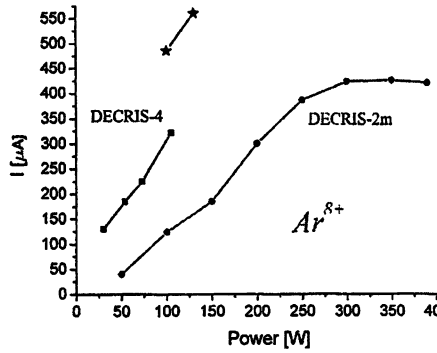

Fig. 3. Comparison of the Ar^{8+} yields from DECRIS-4 (flat field) and DECRIS-2m (classical) ion sources

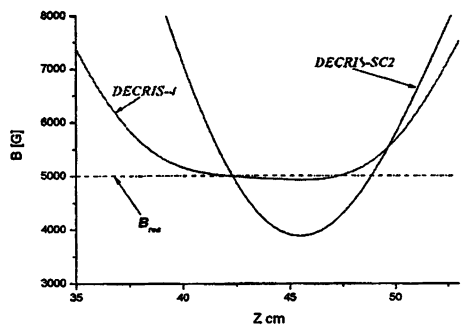

Fig. 4. Magnetic field distribution around the minimum for "classical" and "flat field" ion sources

The main difference between two sources is the magnetic field distribution around the field minimum. Figure 4 shows these distributions for both sources when magnetic fields were optimized for the maximum yields of Ar^{8+}. It is well known that the level and the shape of the "minimum" are responsible for the efficiency of the UHF absorption. The smooth magnetic field gradient helps to heat electrons more efficiently in case of the source with not so good confinement but for higher UHF power levels plasmas became unstable. Meantime the new source with the better confinement can produce up to 880 μA of Ar^{8+} with the UHF power of about 300 W.

References

1. *Hitz, D., Girard, A., Melin, G., Gammino, S.* // Rev. Sci. Instrum. 2002. V. 73. P. 509.

2. *Efremov, A., et al.* // Rev. Sci. Instrum. 2006. V. 77, P. 03A320.

3. *Efremov, A., et al.* Project of the Superconducting ECR Ion Source DECRIS-SC2 // Proc. of the 17th Int. Worckshop on ECR Ion Sources, 2006, Lanzhou, China, edited by H. Zhao and L. Sun, Beijing Kexin Printing House, 2007. ISSN 0254-3052 P. 23-26.

Nd:Y_2O_3 Laser Ceramics Fabricated by Millimeter-Wave Sintering

S.V. Egorov[1], Yu.V. Bykov[1], A.G. Eremeev[1], V.V. Kholoptsev[1], O.N. Eremeykin[1], A.S. Egorov[2], A.P. Savikin[2], V.V. Sharkov[2]

[1] Institute of Applied Physics, Russian Academy of Sciences, Nizhny Novgorod, Russia, egr@appl.sci-nnov.ru
[2] Nizhny Novgorod State University, Nizhny Novgorod, Russia

In the late 1990s, the processing routes for synthesis of a new class of ceramic materials, the so called laser ceramics, have been developed by the Japanese researches [1, 2]. Laser ceramics are fully dense host materials with cubic crystalline structure, such as yttrium-aluminum garnet (YAG) or Y_2O_3, doped with lasing rare-earth elements, usually Nd, Yb, Er, etc. as active laser ions. It was found that a necessary prerequisite for the fabrication of high quality optical ceramics was the use of green bodies with high uniform density, compacted from high-purity nanosize non-agglomerated powders. Pore-free ceramics with optical properties approximating those of single crystals were obtained by sintering at a temperature of 1750–1850 °C for 20 hours in resistive furnaces under a vacuum of $1.3 \cdot 10^{-3}$ Pa. The developed routes have made it possible to obtain polycrystalline ceramics with minimal optical loss, which originate primarily from pores, second phases, grain boundary impurities, compositional gradients, and lattice imperfections.

Microwave sintering of optical ceramics is appealing because it is free of high temperature resistive heaters that may cause pollution of materials. This method eliminates the necessity to perform sintering at high vacuum. In addition, the inverse temperature distribution that exists within the body under volumetric microwave heating is favorable for elimination of porosity. Few studies on microwave sintering of optical YAG- and Y_2O_3-based ceramics [3, 4] have been undertaken to this date. The sintered samples with density over 99% were translucent but not with transparency needed for lasing. This paper reports first results of laser generation on the microwave sintered Nd:Y_2O_3-ceramics.

The details of the fabrication of powders and compacts for sintering are described elsewhere [5]. The ceramic green body samples were fabricated at the Institute of Electrophysics, Ekaterinburg, Russia.

The compacted samples were sintered on a gyrotron-based set-up operating at a frequency of 24 GHz with microwave power up to 6 kW [6, 7]. The samples were placed in the center of a fused quartz crucible filled with granulated Y_2O_3 (99.99 %) powder used for thermal insulation. The vacuum-proof applicator of the set-up with 40 cm inner diameter and 60 cm length was evacuated before the start of microwave heating, and the entire sintering process was performed at a residual air pressure of about 10 Pa. The temperature of samples was measured by the *Luxtron* optical thermometer, model M10. The optical measurements were calibrated up to 1800 °C in separate runs by the readings of a *Pt÷Pt-Rh* thermocouple. The accuracy of the temperature measurements was about 1 % at the holding stage of sintering. The computer-controlled heating of samples was carried out under various temperature-time schedules. The ramp-up rate varied from 3 to 10 °C/min, the temperature of sintering from 1750 to 1900 °C and the holding time from 2 to 20 hours. Upon completion of a preset temperature-time schedule of heating, the microwave power was automatically switched off and a sample cooled down together with thermal insulation at the rate of over 25 °C/min.

The surfaces of sintered samples were mirror-polished with a diamond paste to the sample thickness of about 1.2 mm. The optical transmittance spectrum was measured within the wavelength region from 400 to 1000 nm with the resolution of 0.1 nm using a *CF-56* spectrophotometer. Additionally, the coefficient of extinction at the wavelength of 1.06 μm was measured for some samples. The microstructure of the sintered samples was studied by scanning electron microscopy (*SUPRA 50 VP*). The average grain size in the sintered samples was in the range of 150–250 μm and the porosity was estimated as 20–40 ppm.

The data on the temperature-time schedules of 3%Nd:Y_2O_3 ceramics sintering and the optical properties of some samples are given in the Table.

T (°C)	τ (hours)	Transmittance (%) at 400 / 1000 nm	k (cm^{-1}) at λ = 1.06 μm
1750	3	40 / 70	1.66
1800	6	66 / 75	2.08
1850	20	64 / 75	0.7
1900	4	–	0.045
1900	8	70 / 75	–

Some inconsistency between the schedules of sintering and the corresponding extinction coefficients was probably due to the lack of repeatability in the manufacturing of the green body samples.

The part of the transmittance spectrum of the sample sintered at 1900 °C for 4 hours is shown in Fig. 1. The peaks of strong absorption by Nd^{3+}-ions are observed at the wavelengths of 806.5 and 821.0 nm.

The fiber-coupled diode laser module *LIMO* was used for the study of the luminescence properties and pumping the sintered samples in the laser tests. The spectrum of the diode oscillations was matched the 806.5 nm absorption line of the 3%Nd:Y_2O_3 ceramics by an adjustment of the operational temperature of diodes. The spectrum of diode oscillations at a temperature of 25 °C matches well the absorption peak of the ceramics. About 50 % of the incident power is absorbed in the sample.

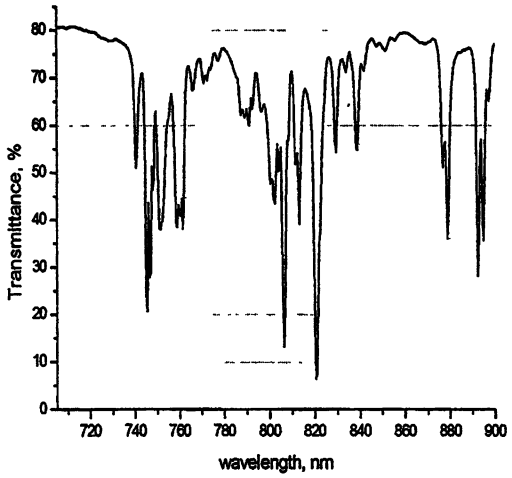

Fig. 1. Transmittance spectrum of 3%Nd:Y_2O_3 sample sintered at 1900 C for 4 hours

The luminescence of the ceramics was studied in order to determine the expected spectrum of the laser oscillation. There were two strong peaks at the wavelength of 1074.6 and 1078.6 nm with the peak width of 1.15 and 1.6 nm, respectively, in the luminescence spectrum of the ceramic sample. The time of luminescence decay was about 50–60 μs which is close to the value observed in [8] for the ceramic material of the same composition. This implies a rather small loss of inversion caused by the nonradiative transitions.

Schematic diagram of the experimental setup for a 3%Nd:Y_2O_3 ceramic laser is given in Fig. 2. The ceramic sample of 9×9×1 mm size was fastened in a non-cooled copper fixture having the 4 mm aperture. The light from the pumping diode LD was focused by a set of lenses L1, L2, L3 via a dichroic mirror HR in the sample. The resonator of 10 mm length was formed by two mirrors HR and OC. The flat mirror HR had the reflection coefficient of 99.7 % in the wavelength range of 1070–1080 nm and a 97 % transmission coefficient. The flat mirror OC with a 0.4 % transmission coefficient at the oscillation wavelength was used as an output mirror. Since the lasing experiments were performed without a system of thermal stabilization the test was carried out in the pulse regime with a 10 ms pulse duration and 10 Hz repetition rate.

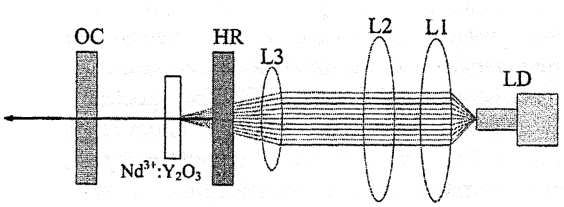

Fig. 2. Schematic diagram of the laser experimental setup: LD – pumping diode, L1, L2, L3 – focusing lenses, HR – blind mirror, OC – output coupling mirror

The threshold of laser oscillation was 0.5 J that corresponded to the 10 W pulse pumping power. At the maximal pumping power of 20 W and the absorbed energy of 1 J, the energy of laser oscillation was 0.08 mJ with a total efficiency of 0.008 % and a differential efficiency of 0.017 %.

Two spectral lines with resolution ~0.02 nm at the wavelengths of 1074.6 and 1078.6 nm with the line half-width of 0.08 nm were observed in the laser spectrum (Fig. 3, curve 1). The intensities of spectral lines were close to each other due to nearly equal intensities of the luminescence at 1074.6 and 1078.6 nm (Fig. 3, curve 2). The distribution of the intensity over the cross-section of the laser beam given in the Fig. 3 (insert) evidences in favor of the excitation of the fundamental mode of the resonator.

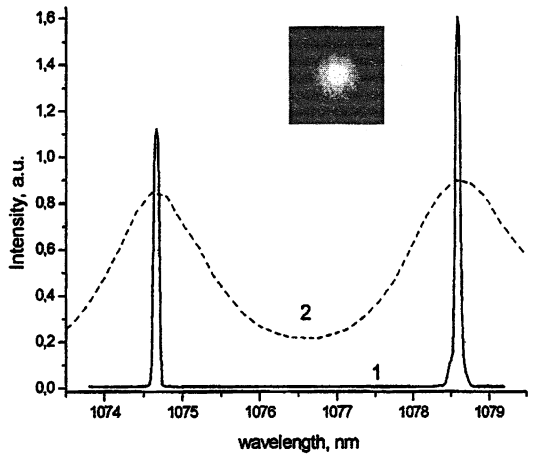

Fig. 3. Laser radiation spectrum near the threshold of oscillation (1); luminescence spectrum (2); Insert: the distribution of intensity over the cross-section of the laser beam

The results of this study have demonstrated the feasibility of fabricating the ceramics of a laser quality using the microwave sintering.

References

1. *Ikesue, A., et al.* Fabrication and optical properties of high-performance polycrystalline Nd:YAG ceramics for solid-state laser // J. Am. Ceram. Soc. 1995. V. 78, No. 4. P. 1033-1040.

2. *Lu, J., et al.* High-power Nd:$Y_3Al_5O_{12}$ ceramic laser // Jpn. J. Appl. Phys. 2000. V. 39, Pt. 2. L 1048-1050.

3. *Panneerselvam, M., et al.* Translucent yttrium aluminum garnet: Microwave-assisted route to synthesis and processing" // J. Mater. Res. 2001. V. 16, No. 10. P. 2273-2776.

4. *Imam, M.A., et al.* Millimeter-wave reactive sintering of neodymium-doped yttrium aluminum garnett // Mater. Sci. Forum. 2010. V. 654-656. P. 2002-2005.

5. *Bagaev, S.N., et al.* Highly transparent Nd^{3+} Y_2O_3 ceramics // Fotonika, 2007. № 5. P. 24-29 (*in Russian*).

6. *Bykov, Yu., et al.* 24-84 GHz gyrotron systems for technological microwave applications // IEEE Trans. on Plasma Science, 2004, V. 32. P. 67-72.

7. *Egorov, S. V., et al.* Transparent Nd:Y_2O_3-ceramics by millimeter-wave sintering // Strong Microwaves: Sources and Applications, Proc. VII Int. Workshop, edited by A. G. Litvak, Nizhny Novgorod. 2008, V. 2. P. 509-513.

8. *Sato, Y., et al.* Spectroscopic properties of neodymium-doped Y2O3 ceramics // Advanced Solid-State Lasers, edited by Ch. Marshall, 2001. V. 50. P. 417-421.

Comparative Study of Neck Formation in Amorphous Silica at Microwave and Conventional Heating

S.V. Egorov, A.G. Eremeev, A.A. Sorokin, Yu.V. Bykov

Institute of Applied Physics, Nizhny Novgorod, Russia, egr@appl.sci-nnov.ru

The results of numerous experimental studies are indicative of differences between the material processing performed under conventional and microwave heating. Most, if not all, of thermally activated processes are characterized by high complexity due to many mass transport mechanisms proceeding simultaneously. Therefore, an important role belongs to the studies of rather simple model processes allowing an observation of features peculiar to the action of microwave field on mass transport. An investigation of neck growth between adjoining particles, firstly performed by Kuczynski [1]. is an example of such a model process. Later, the method was developed for revealing the diffusion mechanisms dominating at different stages of sintering [2].

The results of investigations of neck formation between amorphous SiO_2 spherical particles under microwave and conventional heating are presented here. The samples for the study were prepared by gravitational sedimentation in the distilled water of SiO_2 spheres with 1±0.1 μm diameter (Geltech, Inc.) and subsequent drying of the sediment. An electron microscope image of the sediment is shown in Fig. 1.

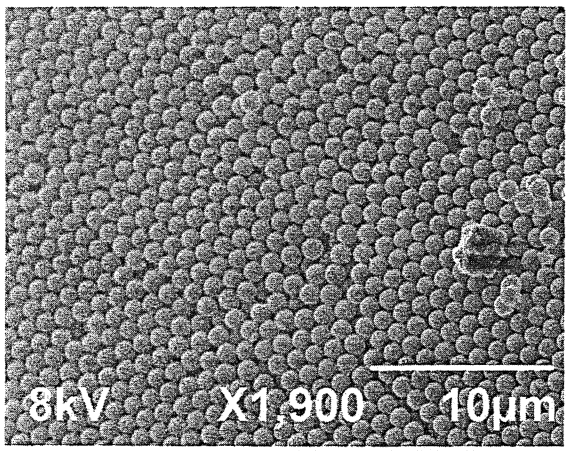

Fig. 1. SEM image of SiO2 particles sediment

The compacts of 6 mm diameter and 0.5 mm thickness were annealed either in the applicator of a 24 GHz 3.5 kW gyrotron set-up [3] or in a conventional resistive oven, in both cases under identical heating regimes: a ramp-up rate of 60 °C/min up to the maximal temperature, then hold at the maximal temperature from 0 to 30 hours. The maximal temperatures varied from 850 °C to 1300 °C. In the case of conventional heating, the samples were put into a preheated oven. At microwave heating the compacts were placed in a two-layer thermal insulation arrangement made of Al_2O_3-based ceramics. The XRD study showed the absence of crystallization in the annealed compacts.

The problem of a paramount importance at the comparative studies is the accordance between the temperature measurements at microwave and conventional heating. A one-colour optical fiber thermometer "*Luxtron*" calibrated by the readings of the *Pt – Pt-Rh* thermocouple was used for measuring the temperature at microwave heating., The correctness of the thermocouple measurements, in turn, was checked by microwave heating of small aluminum and copper pieces making use of their melting temperature as the reference points. The results of these tests showed that the difference between the data of measurements and the reference data did not exceed 5 °C.

The microstructure of samples was studied with the scanning electron microscope JSM-6390LA. The neck size between a pair of adjoining spheres (Fig. 2) was measured using direct manual length measurements on the SEM images of Pt-coated material (the coating layer thickness was approx. 15 nm). The results of measurement were averaged over the ensemble of particles located within a frame of 14 x 11.1 μm (10 000x magnification) which contained 60–100 necks. The resulting neck size error was determined taking into account the measured data dispersion and the inaccuracy of direct length measurements.

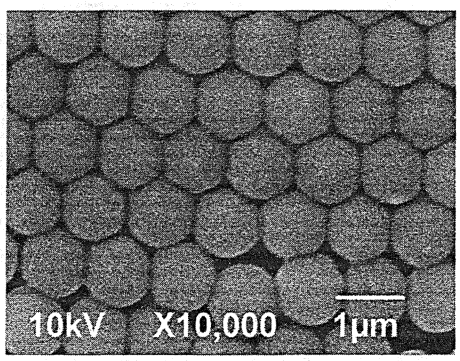

Fig. 2. SEM image of a sample after microwave heating

It is worth noting that the contact zone differed from the ideal point contact even on the images of compacts not subjected to heating, i.e., the apparent necks between adjoining spheres had a non-zero size. The reason for this is an insufficient contrast in the places of touching of the spheres. It is clear that an actual neck size at low annealing temperatures, when it is small, can be veiled by an "apparent neck" effect. Therefore, the neck size observed in unheated samples was taken as a lower limit in the analysis of images. The uncertainty in the initial value of neck size does not affect the results of the analysis because its quantitative characteristics are based on the relative behavior and the relative data on the neck size.

The mechanism of neck formation for amorphous materials is viscous flow. Theoretical models which describe the neck growth are based on Frenkel's approach in which the rate of energy gain from surface-area reduction is equated to the rate of energy dissipation due to viscous flow [4]. The rate of neck growth between two spherical particles of radius, R, is

$$(a/R)^2 = 3\gamma t / 2\eta R \qquad (1)$$

where a is the neck radius, γ – the specific surface energy, t – the annealing time, and $\eta = \eta_0 \exp(Q/kT)$ is the viscosity, Q – activation energy for viscosity, T – the temperature, k – the Boltzmann constant.

As it is obvious from Fig. 3, the neck radius grows much faster with an increase in a temperature at microwave heating.

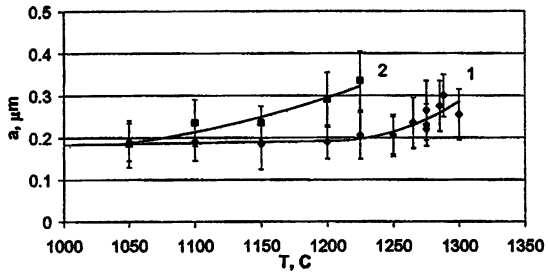

Fig. 3. Neck radius vs. temperature at 15 min hold time: 1 – conventional heating, 2 – microwave heating

The linear dependences of the square of the neck radius a^2 on the time of annealing (Fig. 4) prove the viscous flow mechanism of neck formation under both microwave and conventional heating.

The data given in Fig. 5 illustrate once again a marked distinction between the rates of neck growth under microwave and conventional heating.

The use of the dependence of neck radius on the annealing time and the expression (1) makes it possible to determine the viscosity of the material. The plots of viscosity via temperature for the data obtained in this study and the data of other authors obtained at conventional heating of amorphous silica are shown in Fig. 6. As it is seen, the data on viscosity for conventional heating are close enough to each other.

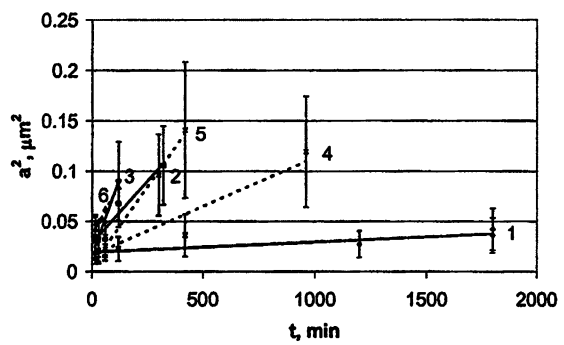

Fig. 4. Square of neck radius vs. time: 1, 2, 3 – conventional heating, 4, 5, 6 – MW heating, 1 – 1050 C, 2 – 1150 C, 3 – 1250 C, 4 – 950 C, 5 – 1000 C, 6 – 1050 C

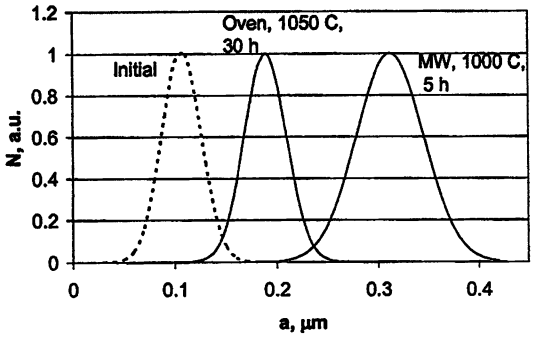

Fig. 5. Neck radii distributions after microwave heating at 1000 C for 5 hours and heating in oven at 1050 C for 30 hours

The viscosity observed in this study at microwave heating is 2–3 orders of magnitude less than the value typical for conventional heating.

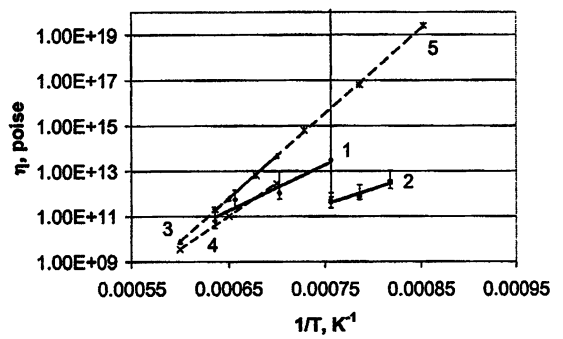

Fig. 6. Viscosity vs. temperature: 1 – conventional heating, 2 – microwave heating, 3 – SiO_2-type 1 from [5], 4 – SiO_2-type 2 from [5], 5 – from [6]

Taking into account the well-known Stokes-Einstein relation between viscosity and diffusion coefficient $\eta(T) = kT / 6\pi DR$ it can be concluded that microwave heating enhances, to the same degree, the diffusion in amorphous silica.

References

1. *Kuczynski, G.C.,* Study of the sintering of glass // J. Appl. Phys. 1949. V. 20, No. 12. P. 1160-1163.

2. *Kingery, W.D., Berg. M.* Study of the initial stages of sintering solids by viscous flow, evaporation – condensation, and self-diffusion // J. Appl. Phys. 1955. V. 26, No. 10. P. 1205-1212.

3. *Bykov, Yu., et al.* 3.5 kW 24 GHz compact gyrotron system for microwave processing of materials // Advances in Microwave and Radio Frequency Processing, edited by M. Willert-Porada. Berlin Heidelberg: Springer-Verlag, 2006. P. 24-30.

4. *Frenkel, J.* Viscous flow of crystalline bodies under the action of surface tension // J. Phys. (USSR). 1945. V. 9, No. 5. P. 385-391.

5. *Brebec, G., et al.* Diffusion du silicium dans la silice amorphe // Acta Metall. 1980. V. 28, No. 2. P. 323-333.

6. *Ojovan, M.I., Lee, W.E.* Viscosity of network liquids within Doremus approach // J. Appl. Phys. 2004. V. 95, No. 7. P. 3803-3810.

Characteristic Features of Epitaxial Growth of CVD Diamond Films by Microwave Plasma-Assisted Chemical Vapor Deposition on Various Substrates

A.L. Vikharev[1], A.M. Gorbachev[1], M.P. Dukhnovsky[2], A.B. Muchnikov[1], A.K. Ratnikova[2], Yu.Yu. Fedorov[2]

[1]Institute of Applied Physics RAS, Nizhny Novgorod, Russia
[2]FSUE "Istok", Fryazino, Russia, istok220@mail.ru

Due to its unique properties, CVD diamond is a promising material for up-to-date electronics. This is due to the fact that diamond has tangible advantages compared with the conventional semiconducting materials, and allows one to develop devices with higher operating temperatures, electric power, and radiation hardness. One of the main factors that hinder its wide application is the small size of the initial substrates of natural or HPHT diamonds, on which further epitaxial growth of CVD diamond films occurs.

In this work, we studied epitaxial growth of diamond films from the gaseous phase on combined substrates 25 mm in diameter, which contained sections of polycrystalline and monocrystalline diamond, for further formation of semiconducting wide-zone diamond structures aiming at creation of high-power microwave semiconductor devices.

Experiments were carried out in microwave plasma assisted CVD reactor at frequency 2.45 GHz [1, 2]. The main part of the setup was a plasma chemical reactor based on a cylindrical cavity. Diamond was grown in a pulsed wave (PW) regime of reactor operation at repetition rate 250 Hz and duty cycle 50 % at a high microwave power density , specifically, 200 W/cm^2.

Combined substrates of monocrystalline and polycrystalline diamond were grown in the following way. On the silicon substrate, 25 mm in diameter, two single crystalline diamond seeds (3×3 mm, thickness about 300 μm) were placed. Then the CVD process of diamond growth was realized at the conditions, under which high-quality monocrystalline layers are deposited. The epitaxial growth of monocrystalline diamond took place on single crystalline diamond seeds and polycrystalline diamond was grown on silicon substrate. During the deposition process, poly- and monocrystalline diamond coalesced forming single structure, Fig. 1.

The conditions for splicing of polycrystalline and monocrystalline diamond films were found and the growth of polycrystalline plates of CVD diamond (200–300 μm thick and 25 mm in diameter) with inclusions of monocrystalline CVD diamonds was studied. Thus by this method combined substrates of monocrystalline and polycrystalline diamond material were obtained.

It was shown that preliminary leveling of the surface of the combined substrate (planarization) leads to an improvement in the quality of epitaxial diamond films. The regimes of substrate planarization using thermal etching on an iron pedestal were studied and optimized.

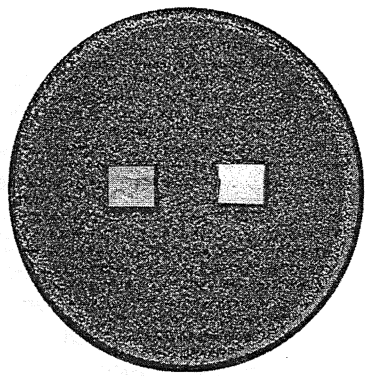

Fig. 1. Combined one inch wafer of mono- and polycrystalline diamond before thermal planarization

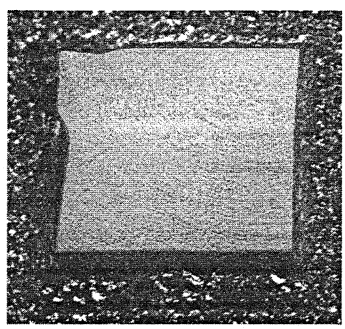

Fig. 2. Monocrystalline diamond crystal after epitaxial growth on combined substrate

Monocrystal layers of CVD diamond were synthesized on monocrystal sections of a combined substrate. Their quality exceeded the quality of the substrate, their orientation was (100), and their thicknesses ranged from 100 to 800 μm. The crystalline structure of the grown monocrystal layers was studied by the method of spectroscopy of combinational (Raman) scattering of laser radiation. The Raman spectrum of high-quality diamond has a fine first-order line with a wave number of 1332 cm^{-1}. FWHM of the diamond peak in Raman spectrum did not exceed 3 cm^{-1} for single crystalline parts and 4–6 cm^{-1} for polycrystalline parts of combined diamond wafers.

At the final stage the combined diamond wafers were subjected to thermal planarization to obtain diamond plates with parallel surfaces, 200–300 μm thick. The plates were optically transparent. It allowed to investigate the boundary between spliced polycrystalline and monocrystalline diamond, Fig. 3.

Thus, the first experimental technique of growing polycrystalline plates of CVD diamond with inclusions of monocrystal diamond was created and then used to

grow epitaxial layers on combined planarized substrates. Experimental prototypes of epitaxial diamond layers on combined substrates have been manufactured.

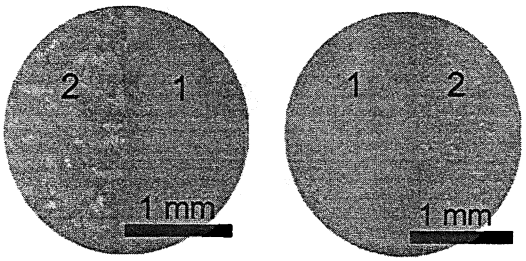

a *b*

Fig. 3. Boundary between monocrystalline (1) and polycrystalline (2) diamond from growth (a) and nucleation (b) sides after thermal planarization of the combined wafer

The obtained structures can be used in development of up-to-date semiconducting devices based on CVD diamonds.

Combined poly- and monocrystalline diamond material can be used for improvement of heat sink from high power single crystal diamond devices, e.g. diamond X-ray monochromators [3].

This work was partially supported by the Russian Foundation for Basic Research (project No. 09–08–00019.

References

1. *A.L. Vikharev, A.M. Gorbachev, V.A. Koldanov, D.B. Radishchev,* Plasma Physics Reports, 31 (2005) 338.

2. *Muchnikov A.B., Vikharev A.L., Gorbachev A.M., Radishev D.B., Blank V.D., Terentiev S.A.* Homoepitaxial single crystal diamond growth at different gas pressures and MPACVD reactor configurations // Diamond Relat. Mater. 2010. V. 19. P. 432.

3. *A.K. Freund, S. Gsell, M. Fischer, M. Schreck, K.H. Andersen, P. Courtois, G. Borchert, M. Skoulatos* // Nucl. Instr. and Meth. A (2010), doi:10.1016/j.nima.2010.05.043.

Requirements and Design Description for the Linear IFMIF Prototype Accelerator

R. Heidinger[1], Ph. Cara[1], A. Facco[2], F. Fantini[1], A. Ibarra[3], V. Massaut[4], A. Mosnier[5], T. Nishitani[6], Ch. Vermare[7], P. Garin[7]

[1]Fusion For Energy, BFD Department, Garching, Germany, roland.heidinger@f4e.europa.eu
[2]INFN, LNL, Legnaro, Italy; [3]CIEMAT, Madrid, Spain; [4]SCK-CEN, Mol, Belgium; [5]CEA, IRFU, Saclay, France; [6]JAEA, Fusion R+D Directorate, Rokkasho, Japan; [7]IFMIF/EVEDA Project Team, Rokkasho, Japan.

The International Fusion Materials Irradiation Facility (IFMIF) is projected to provide an accelerator-based, D-Li neutron source to produce high energy neutrons at sufficient intensity and irradiation volume to allow simulating the first wall neutron spectrum of the future nuclear fusion reactors such as DEMO and Power Plants as closely as possible [1, 2]. By providing the same nuclear responses which affect the material behaviour under irradiation, engineering data will be generated for setting-up DEMO design rules for "End-of-Life" conditions. Further, materials and sub-components will be tested prior to approval for application in Power Plants and by this providing in addition the basis for their licensing.

Currently, Engineering Validation and Engineering Design Activities are being performed by the IFMIF/EVEDA project in the framework of the Broader Approach agreement between EURATOM and Japan [3]. The design of the IFMIF plant is built upon 3 main systems (see. Fig. 1 [2]):

- 40 MeV deuterium Accelerator system with 2 identical Linear Accelerator (Linac) lines;
- Lithium target system providing intense high energy neutron beam;
- Test Facilities with High, Medium and Low Flux Test Modules providing ample space at fusion relevant damage levels.

In order to provide detailed experimental evidence for the soundness of the Engineering Design, prototypes are designed, manufactured, set up, commissioned and operated for these main systems.

This paper focuses on the description of the accelerator prototype (LIPAc) with its general requirements:

- Produce a CW 125 mA D^+ beam with energy of 9 MeV;
- Experimentally confirm the key technologies, as given in the functional scheme (see Fig. 2, and description below))
- Perform a complete follow-up and recording of the beam parameters along the accelerator during each operational phase;
- Study the beam losses along the machine to confirm the "hands-on" maintenance schemes and the beam stability in terms of transversal position and shape.

The beam of LIPAc is generated by an injector (4.4) using an Electron Cyclotron Resonance (ECR) source (4.4.1). After being properly focused and filtered along the Low Energy Beam Transport (LEBT, 4.4.2), the D+ beam is accelerated by two successive systems: a normal conducting Radio Frequency Quadrupole (RFQ, 4.5) and a set of superconducting Half-Wave Resonators located within the Superconducting Radio Frequency Linac (SRF Linac, 4.7). The limitation to the first SRF Linac cryomodule is justified as the low energy parts of the IFMIF accelerators are deemed to be the most critical part. After controls and measurements of the beam parameters, the deuteron current is stopped into a Beam Dump (BD, 4.8.2). Between these systems, specific Medium Energy Beam Transport (MEBT, 4.6) and High Energy Beam

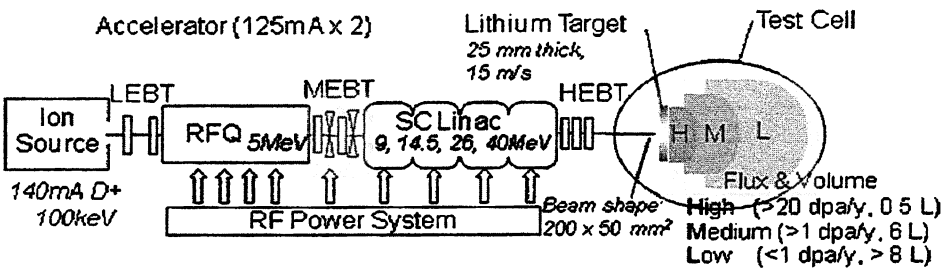

Fig. 1. System concept setting the basis for the Engineering Design of the IFMIF plant [2]

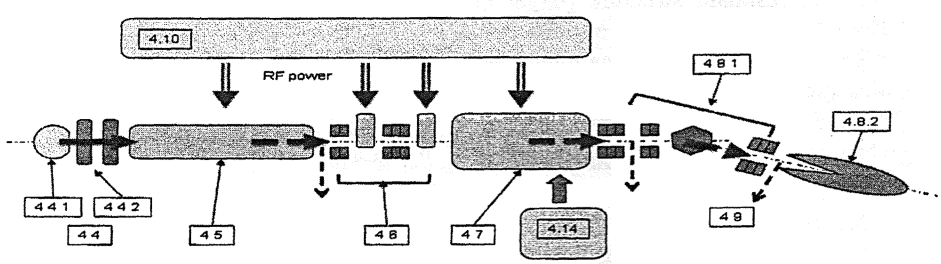

Fig. 2. Functional scheme of the LIPAc sub-systems (part numbers refer to description in the text)

Transport (HEBT, 4.8.1) lines transport and adapt the beam characteristics to the subsequent structures. Amplifiers chains (4.10.2), part of the Radio Frequency Power System (RF Power System, 4.10), supply the RF power required. A Cryoplant (4.14) is needed to cool down and maintain the 4.4 K temperature in the SRF Linac. The Beam Instrumentation (4.9) is distributed along the machine, in addition with the diagnostics included in each subsystem.

The primary parameters of the LIPAc system in comparison to the IFMIF accelerator system are given the following table:

Primary Parameters	LIPAc (EVEDA)	IFMIF	Units
Number of Linacs	1	2	
Duty factor	CW	CW	
Ion type	D^+	D^+	
Beam intensity on target	125	2 x 125	mA
Beam energy on target	9	40	MeV
Beam Power on target	1.125	2 x 5	MW
RF Frequency	175	175	MHz
Target material	Cu (Beam Dump)	Li	
Total length	33.85 (34.00)	84.69	m
Injector length	5.05	5.05	m
RFQ length	9.81	9.81	m
MEBT (MS) length	2.20 (2.35)	2.35	m
SRF Linac length	4.64	22.42	m
Number of cryomodules	1	2 x 4	
HEBT total length	9.65	45.06	m

The two accelerating sub-systems are the RFQ and the SRF Linac. The RFQ bunches and accelerates the beam (from 0.1 to 5 MeV) using the RF fields in a normal conducting Cu resonant structure (target Q factor 11500). The RF power is injected into the cavity by means of RF Power Couplers containing a set of RF Diagnostics (arc detectors, bidirectional couplers and RF detectors to measure the forward and reflected power) which are connected to the local control system of the RF power system. The RF tuning of this long cavity is performed by a complete set of tuners. The field level and field distribution in the cavity is monitored by pick up loops distributed along the cavity. The heat generated by the RF and beam losses is extracted through a highly precise cooling system, which has also a role for the slow tuning of the resonant frequency in the cavity, by acting on the temperature difference between electrodes and external body of the cavity.

The first cryomodule is set up by an arrangement of 8 Superconducting Nb cavity packages and the same number of solenoid packages. By means of the half-wavelength resonators (HWR), each with a targeted Q-factor (unloaded) of $1.4 \cdot 10^9$, the deuteron beam is accelerated from 5 MeV to 9 MeV in CW mode using a mechanical tuning system. The focusing and orbit corrections of the beam are made by the solenoids packages, each one being composed of a solenoid together with a steerer and a beam positioning monitor. 8 RF couplers transfer the RF from the RF power system power into HWRs. A forced air-cooling removes the heat from coupler window area and a water cooling system extracts heat from the coupler antennas and from the Tee-transition. The cryostat has the function of:

- Maintaining the temperature of the superconducting elements at 4.4 K;
- Insulating the internal components from the external 300 K ambient temperature and atmospheric pressure;
- Shielding the HWR components from the earth magnetic field.

The Accelerator Prototype RF Power System contains all the equipment necessary to generate the required conditioned RF power and to feed the IFMIF/EVEDA cavities. These cavities require 18 RF power inputs at 175 MHz distributed as follows: eight 200kW inputs for the RFQ cavity, two 105kW inputs for the Matching Section cavities and another eight 105kW inputs for the SRF Linac (SRF Linac).

The RF Power System (RFPS) evolved from system-level trade-off studies that resulted in the use of common amplifier types in all the RF stations. The result is 18 three stage amplifiers working at 175 MHz (8 of up to 200kW for the RFQ, 8 of up to 105kW for the SRF Linac and 2 more of up to 105kW for the Matching Section) and another 200kW one for a permanent test platform.

References

1. *Ehrlich, K., Bloom, E., Kondo, T.*, International strategy for fusion materials development // J. Nucl. Mater. 2000. V. 283–287. P. 79–88.

2. *Garin, P., Sugimoto, M. et al.*. IFMIF's new design: Status after 2 years of the EVEDA project // J. Nucl. Mater., 2011, doi:10.1016/j.jnucmat.2010.12.272.

3. *Garin, P.*, Start of the engineering validation and design phase of IFMIF // J. Nucl. Mater. 2009. V. 386-388. P. 944-948.

Theoretical and Experimental Study of Microwave Power Absorption by a Multipactor Discharge on a Dielectric

V.A. Ivanov, A.S. Sakharov, M.E. Konyzhev, Yu.A. Tarbeeva

Prokhorov General Physics Institute, Moscow, Russia, ivanov@fpl.gpi.ru

In theoretical studies on multipactor discharges, the secondary electron yield (SEY) is customarily described by Vaughan's formula [1] (Fig. 1, curve *1*):

$$\delta = \delta_{max}(Ve^{1-V})^k, \quad (1)$$

where $V = (\varepsilon - \varepsilon_0)/(\varepsilon_{max} - \varepsilon_0)$. Here, ε is the energy of an incident (primary) electron; ε_0 is the cutoff energy, below which δ is zero; ε_{max} is the energy corresponding to the maximum SEY at a given incident angle θ; $k = 0.62$ for $V < 1$; $k = 0.25$ for $V > 1$; $\delta_{max} = \delta_{max0}(1 + \theta^2/2\pi)$; and $\varepsilon_{max} = \varepsilon_{max0}(1 + \theta^2/\pi)$, with δ_{max0} and ε_{max0} being the peak value of the SEY at $\theta = 0$ and the incident energy corresponding to this peak.

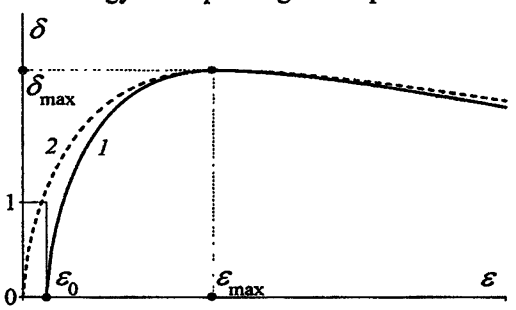

Fig. 1. SEY as a function of the incident energy: (*1*) Vaughan; (*2*) simplified Vaughan (Vaughan_0). The step at $\varepsilon < \varepsilon_0$ shows the reflection coefficient $r = 1$, introduced by Vicente et al. [2]

In numerical simulations, a simplified formula with $\varepsilon_0 = 0$ (Fig. 1, curve *2*), further referred to as Vaughan_0, is also widely used (see, e.g., [3, 4]).

In the saturated (quasi-steady) multipactor, the δ value averaged over the oscillation period of the external field $E_x = E_0 \sin \omega t$ is equal to 1. This means that, at electron oscillation energies $\varepsilon_{osc} = (eE_0/\omega)^2/2m_e$ much exceeding the first crossover energy ε_1, at which $\delta = 1$, the emitted electrons must return to the surface over a time Δt much shorter than ω^{-1}; otherwise, they acquire an energy larger than ε_1 and the number of secondaries continues to grow. In this case, the external field varies only slightly during the flight time of secondary electrons; hence, we can use the so-called "constant-field approximation," in which the multipactor characteristics depend on time parametrically.

In this approximation, the power absorbed per unit area of the dielectric surface can be estimated analytically [5]. Assuming that the external tangential field E_x is constant and the secondaries have a Maxwellian distribution with a temperature T_e, we find that the profiles of the electric potential and electron density along the normal coordinate z are

$$e\varphi = -2T_e \ln(1 + z\omega_{p0}/2^{1/2}v_{Te}), \quad (2)$$

$$n_e = n_0(1 + z\omega_{p0}/2^{1/2}v_{Te})^{-2}, \quad (3)$$

where $\omega_{p0} = (4\pi e^2 n_0/m_e)^{1/2}$ and n_0 is the electron density at $z = 0$. The electron flight time is

$$\Delta t = (2\pi)^{1/2}\Phi((\varepsilon_{z0}/2T_e)^{1/2})\exp(\varepsilon_{z0}/2T_e)/\omega_{p0}, \quad (4)$$

where ε_{z0} is the z component of the initial electron energy and $\Phi(x)$ is the error function.

The density n_0 can be found from the flux balance of incident and emitted electrons. For Vaughan_0 and $\varepsilon_{osc} >> \varepsilon_1 >> T_e$, we have

$$\int(\varepsilon_{inc}(\varepsilon_{z0})/\varepsilon_1)^{0.62}\exp(-\varepsilon_{z0}/T_e)d\varepsilon_{z0} = 1, \quad (5)$$

where $\varepsilon_{inc} \approx (eE_x\Delta t)^2/2m_e$ is the energy with which an electron returns to the surface. Integrating Eq. (5) numerically, we obtain

$$n_0 \approx 17.4(E_x)^2/8\pi\varepsilon_1. \quad (6)$$

The power absorbed per unit area W_{abs} is found by integrating the electron energy flux onto the surface over ε_{z0} from 0 to the energy $\varepsilon_{z0max} \approx T_e \ln(\varepsilon_{osc}/\varepsilon_1)$, at which $\varepsilon_{inc} \sim \varepsilon_{osc}$. Finally, after averaging over time, we obtain

$$\langle W_{abs} \rangle = \kappa c(E_0)^2/8\pi, \quad (7)$$

where

$$\kappa \approx (\pi/2)^{1/2}(v_{Te}/c)\ln(\varepsilon_{osc}/\varepsilon_1). \quad (8)$$

To more thoroughly study the multipactor discharge, we have developed a 1D3V PIC code, that takes into account the electron space charge, secondary electron emission, and elastic and inelastic reflections of electrons from the dielectric surface.

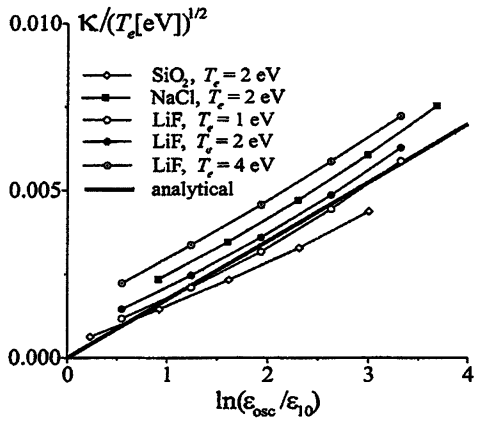

Fig. 2. Calculated dependences of the absorption coefficient κ on ε_{osc} for SiO_2 ($\delta_{max} = 2.4$, $\varepsilon_{max} = 400$ eV, $\varepsilon_{10} = 39.6$ eV), NaCl ($\delta_{max} = 10$, $\varepsilon_{max} = 1200$ eV, $\varepsilon_{10} = 10.5$ eV), and LiF ($\delta_{max} = 7.5$, $\varepsilon_{max} = 1000$ eV, $\varepsilon_{10} = 14.5$ eV). Here, the SEY is described by Vaughan_0, with ε_{10} being the corresponding first crossover energy (electron reflections are ignored)

Figure 2 shows the calculated value of the absorption coefficient κ defined by Eq. (7) as a function of the oscillation energy for different dielectric materials (NaCl, LiF, SiO_2), assuming that the SEY is described by Vaughan_0 (with no reflections). The dependences

$\kappa(\varepsilon_{osc})$ for three values of T_e are shown for LiF. It can be seen that the simulation results agree qualitatively with formula (8): all the curves group around the analytical dependence. As the temperature increases, the curves for LiF progressively deviate away from the analytical dependence.

We also calculated the absorption coefficient by using Vaughan's formula with a finite cutoff energy ε_0 (Eq. (1)). The simulations were performed for SiO_2. The cutoff energy was set at 30 eV (note that this value was chosen rather arbitrarily, because experimental data on the SEY for SiO_2 in the low-energy range are lacking). Curve *1* in Fig. 3 shows the result obtained without electron reflections. It is seen that the absorption coefficient is somewhat lower than in the previous case.

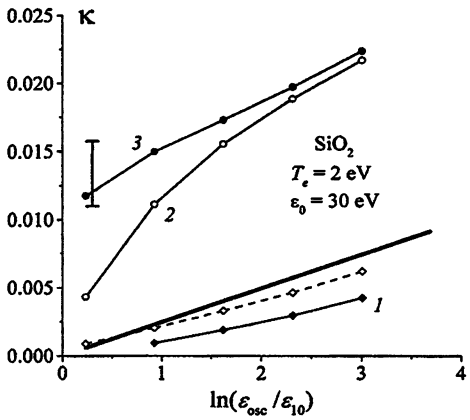

Fig. 3. Absorption coefficient $\kappa(\varepsilon_{osc})$ for SiO_2, calculated using Vaughan's formula with $\varepsilon_0 = 30$ eV: (*1*) no electron reflection, (*2*) coefficient of elastic reflection at $\varepsilon < \varepsilon_0$ is $r = 1$ (see Fig. 1), (*3*) additional elastic and inelastic reflections at $\varepsilon > \varepsilon_0$ with the coefficients $r = \eta = 0.1$. The heavy solid line shows dependence (8), and the dashed line shows the absorption coefficient calculated using Vaughan's formula with no cutoff and reflections

Curve *2* shows the absorption coefficient calculated under the assumption that the coefficient of elastic electron reflections at $\varepsilon < \varepsilon_0$ is $r = 1$, as was proposed by Vicente et al. [2]. It is seen that electron reflections drastically increase the absorption coefficient. Finally, curve 3 shows the absorption coefficient calculated with additionally introduced small elastic and inelastic electron reflections at $\varepsilon > \varepsilon_0$ with the coefficients $r = \eta = 0.1$. It is seen that even small reflections in this energy range additionally increase the absorption coefficient, especially at lower oscillation energies.

We performed experimental measurements of the microwave power absorbed by a multipactor developing on a 0.2×1×6-cm SiO_2 plate placed in the antinode of the 1.95-GHz standing H_{10} mode of a 6×12-cm rectangular waveguide. The experiments were carried out on the BRUS device [6]. Fig. 4 shows signals of the reflected microwave power and the current to the electron collector installed under the dielectric plate.

It is seen that the appearance of the current at the collector, which indicates the onset of a multipactor discharge, is accompanied by a decrease in the reflected microwave power. The height of the step in the reflected signal corresponds to the power absorbed by the multipactor. Taking into account the geometry of the waveguide and dielectric plate, the ratio $\Delta P/P_{inp}$ can be recalculated into the absorption coefficient κ defined by Eq. (7). Unfortunately, we could perform such measurements only at input microwave powers $P_{inp} \leq 85$ kW, only slightly exceeding the threshold power for the onset of a multipactor (≈65 kW), because, at higher powers, the multipactor developed already at the front of the microwave pulse and no step at the top of the reflected signal was observed. The range of κ values obtained experimentally for $P_{inp} = 85$ kW is shown in Fig. 3 by the vertical bar. It is seen that agreement between the simulation and experimental results can be achieved only if electron reflections are taken into account.

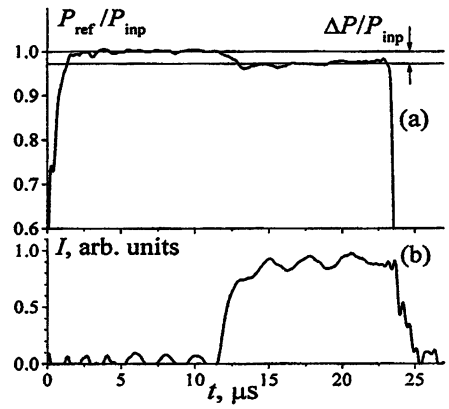

Fig. 4. Signals of (a) the reflected microwave power and (b) the current to the electron collector

Thus, our simulations have shown that secondary electrons reflected from the dielectric surface drastically affect the energy balance in a multipactor, substantially increasing the absorption coefficient.

This work was supported by RFBR-project 09-08-00753-a

References

1. *Vaughan, J.R.M.* A New Formula for Secondary Emission Yield // IEEE Trans. Electron Devices. 1989. V. 36, No. 9. P. 1963–1967.

2. *Vicente, C., Mattes, M., Wolk, D., et al.*, FEST3D – a Simulation Tool for Multipactor Prediction / MULCOPIM 2005, Noordwijk, 2005. P. 11–17.

3. *Sazontov, A., Semenov, V., Buyanova, M., et al.* Multipactor Discharge on a Dielectric Surface: Statistical Theory and Simulations // Phys. Plasmas. V. 12, No. 9. P. 093501.

4. *Kim, H.C., Verboncoeur, J.P.* Time-dependent Physics of a Single-Surface Multipactor Discarge // Phys. Plasmas. V. 12, No. 12. P. 123504.

5. *Ivanov, V. A., Sakharov, A. S., Konyzhev, M.E.* Multipactor Discharge on a Dielectric Surface in the Saturation Regime / XXXVII International Zvenigorod Conference on Plasma Physics and Controlled Fusion, Zvenigorod, 2010. http://www.fpl.gpi.ru/Zvenigorod/XXXVII/Lt/en/MI-Sakharov_e.doc.

6. *Batanov, G.M., Ivanov, V.A., Konyzhev, M.E.* Microwave Breakdown of Ion Crystals Initiated by a Secondary-Electron-Emission Discharge // JETP Lett. V. 59, No. 10. P. 690–694.

Gaz Utilization Efficiency Optimization for Short-Pulsed ECR Ion Source

I.V. Izotov, V.A. Skalyga, V.G. Zorin

Institute of Applied Physics, Russian Academy of Sciences, Nizhny Novgorod, Russian Federation,
izotov@appl.sci-nnov.ru

Introduction

Creation of multicharged ion source of certain short-living isotopes (^{6}He, ^{18}Ne, ^{8}B or ^{8}Li) is needed in order to proceed with "Beta Beam" project intended for neutrino oscillation investigations, hosted in CERN. Present technology of isotopes production is very complicated and limited in performance, which leads to high demands on gas efficiency of ion source. Ion beam pulse duration and repetition rate is limited by further acceleration scheme; pulse duration mustn't exceed 100 μs, which is close to electrons lifetime, and repetition rate should not be more than 10 Hz, which is comparable with isotopes half-life.

Numerical analysis of ^{6}He atoms utilizing efficiency in a ECR ion source (ECRIS) with powerful gyrotron heating is performed in present work using zero-dimensional balanced model of electron-cyclotron resonance (ECR) discharge in a magnetic trap [1]. This model was broadly described in [1, 2] and its references. Good coincidence of plasma parameters simulation with experimental results was shown in [1, 2, 3] and some other works, giving us the ability to use the model for efficiency estimation. Based on obtained numerical results, two ways of effective ECRIS creation are suggested.

Simulation results

Isotopes production rate ($5\cdot10^{13}$ pps) doesn't allow to feed a discharge with isotope atoms up to noticeable densities, thus both ways use a supporting gas.

The first approach implies pulsed injection of working and supporting gas in a discharge chamber of an ECRIS, and strong "ion pumping" (in other words, large extraction hole placed in the plug) to avoid atoms losses between MW pulses. Example of an optimum $^6He^{++}$ current is presented in figure 1 together with $^6He^+$ current while 100% ion pumping (every ion left the discharge is considered as extracted), which could be organized with biased disks, asymmetrical magnetic field etc.

All simulations were done with following parameters, if otherwise isn't mentioned. Microwave frequency f = 60 Ghz; vacuum chamber: 1cm diameter and 10 cm length; magnetic trap mirror ratio k = 4; supporting gas: Nitrogen.

Rapid decrease of a Helium ion current in fig. 1 is determined by a "burning" effect – most of atoms are ionized and extracted.

Hereinafter, we assume that gas efficiency η is a ratio of total amount of utilized ions and total amount of injected atoms:

$$\eta = N_{ext}/N_{inj} \qquad (1)$$

^{6}He utilization efficiency for both Helium ions is plotted in fig. 2 versus microwave power for different supporting gas density.

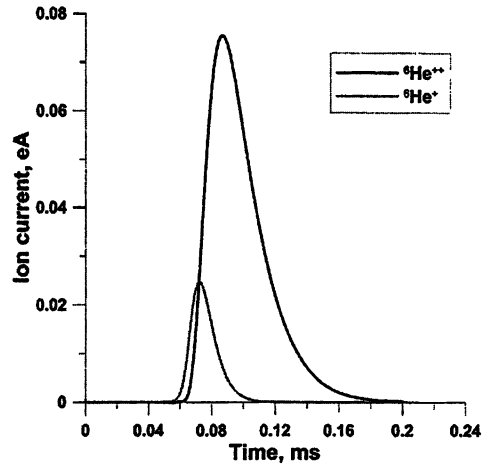

Fig. 1. Calculated $^6He^+$ and $^6He^{++}$ currents while strong ion pumping. Simulation parameters: 60 GHz; 24000 W/cm^2; ^{6}He: $6\cdot10^{11}$ cm^{-3}; N: $1.6\cdot10^{13}$ cm^{-3}. Optimum for $^6He^{++}$.

It should be noted that regime which gives the best efficiency for $^6He^+$ ion is a regime of quasi-stationary ions generation, whereas regime efficient for $^6He^{++}$ utilizes combined Preglow and Afterglow effects (so-called "micropulses" [4]).

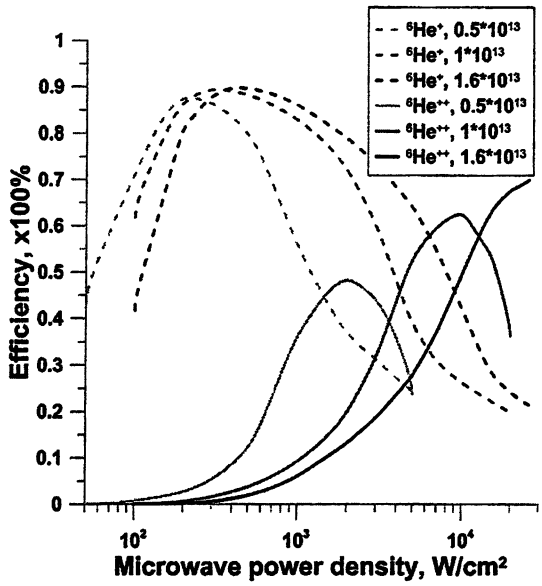

Fig. 2. Calculated $^6He^+$ and $^6He^{++}$ efficiency while strong ion pumping. Simulation parameters: 60 GHz; ^{6}He: $6\cdot10^{11}$ cm^{-3}

One can see that it is possible to reach very good efficiency up to 90 % for $^6He^+$ theoretically. Definitely, a 100 % ion pumping leads to extremely high

total ion currents. For example, the efficiency optimum for the first Helium ion in fig. 2 corresponds to the total ion current (supporting gas ions are dominating) of almost 2 eA.

The second way of efficient ECRIS creation, which turns in lower efficiency, but seems to be much simpler for realization, implies constant supporting and working gas inflows with pulsed microwave heating along with small extraction hole. Described scheme could reach good over-all (averaged over may pulses) efficiency at steady-state regime, when amount of extracted during one MW pulse particles becomes equal to an injected one between MW pulses. Atoms losses through the extraction hole between pulses are low as diameter of the hole is small and partial density of ^{6}He do not exceed $3 \cdot 10^{12}$ cm^{-3} (within calculated optimal parameters range); ions which haven't been extracted during one pulse, have a chance to be extracted in next pulses, thus increasing over-all efficiency.

Stationary efficiency for both Helium ions is plotted in figure 3 versus absorbed microwave power for different extraction hole diameters while constant gases flow.

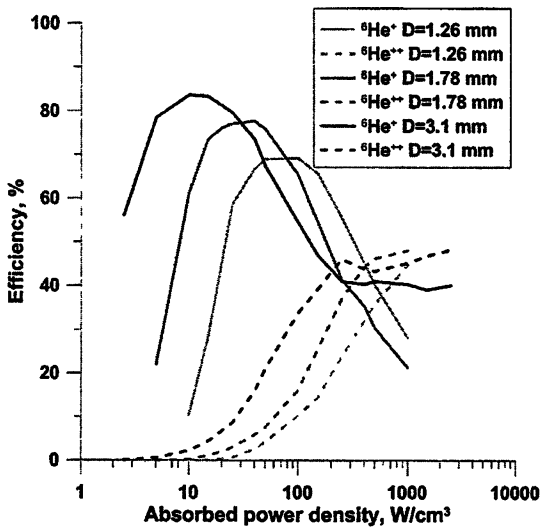

Fig. 3. Stationary efficiency versus microwave power density for different extraction hole diameter D. ^{6}He flow: $5 \cdot 10^{12}$ cm^{-3}/s; N flow: $5 \cdot 10^{13}$ cm^{-3}/s

The same as for 100 % extraction, regime which gives the best efficiency for ^{6}He$^+$ ion is a regime of steady-state ions generation, whereas regime efficient for ^{6}He^{++} utilizes combined Preglow and Afterglow effects.

Small extraction hole naturally leads to a lower total current in comparison with 100 % extraction case. Maximum efficiency for both Helium ions is plotted in figure 4 along with corresponding maximum total ion current versus extraction hole diameter. It is clearly seen that maximum total current is an order of magnitude lower than in case of 100 % extraction.

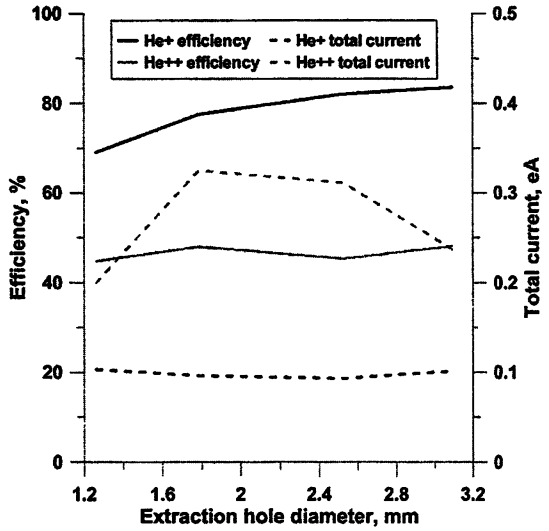

Fig. 4. Maximum stationary efficiency versus extraction hole diameter

Conclusion

Two ways of ECRIS with high gas utilization efficiency are suggested. The first way implies pulsed gas and microwave injection and large extraction hole, resulting in high efficiency (up to 90 % for ^{6}He$^+$, 70 % – ^{6}He^{++}), but very high total ion current must be extracted (several eA). The second way implies more traditional for ECRISes constant gas injection with pulsed MW heating, and small extraction hole, which leads to lower over-all efficiency (80 % – ^{6}He$^+$, 45 % – ^{6}He^{++}) in comparison with the first approach, but lower total current as well as much simpler technical realization.

Acknowledgements

This work was performed in frame of realization of federal targeted program "Scientific and pedagogical labor force for an innovative Russia" for 2009–2013 yy.

We acknowledge the financial support of the European Community under the European Commission Framework Programme 7 Design Study: EUROnu, Project Number 212372. The EC is not liable for any use that may be made of the information contained herein.

References

1. *Skalyga V. et al.*, Gas Breakdown in ECR ion Source. // Review of Scientific Instruments. 2006. V. 77, № 3. P. 03A325-1 – 03A325-3.

2. *Izotov I.V. et al.*, Experimental and Theoretical Investigation of the Preglow in ECRIS // IEEE Transactions on Plasma Science. 2008. V. 36, No. 4. P. 1494-1501.

3. *Thuillier T et al.*, Study of pulsed electron cyclotron resonance ion source plasma near breakdown: The Preglow // Review of Scientific Instruments, 79, 02A314 (2008).

4. *Skalyga V.A. et al.*, Micropulses generation in ECR breakdown stimulated by gyrotron radiation @ 37,5 GHz // present proceedings.

JINR-IAP Experiment on RF Pulse Heating: Results and Data Analysis

A.K. Kaminsky[1], N.S. Ginzburg[2], I.I. Golubev[1], A.P. Kozlov[1], A.F. Kratko[1], S.V. Kuzikov[2], E.A. Perelstein[1], N.Yu. Peskov[2], M.I. Petelin[2], S.N. Sedykh[1], A.A. Vikharev[2], N.I. Zaitsev[2]

[1]Joint Institute for Nuclear Research, Dubna, Russia, alikk@sunse.jinr.ru
[2]Institute of Applied Physics RAS, Nizhny Novgorod, Russia

Problem of surface degradation under RF pulse heating

In recent years, a project of new linear electron–positron collider CLIC with the energy up to 3 TeV has been extensively developed at CERN. For a collider lifetime of ~20 years and an operation cycle frequency of 50 Hz, the total number of cycles will reach on the order of $\sim 2 \cdot 10^{10}$. The projected accelerating gradient in the CLIC collider was selected to be ~100 MV/m at a working frequency of 12 GHz and the microwave field pulse duration of about 200 ns.

For working frequencies of several tens of gigahertz, an important restriction on the working life of accelerating structures is related to their damage and fracture as a result of cyclic heating by short high-power microwave pulses. A physical reason for the material fracture in an accelerating structure is related to large mechanical stresses developed at the metal surface during short pulsed microwave heating, which can exceed the level of plasticity.

The surface damage of copper and other metals has been previously studied in experiments with pulsed UV lasers and equivalent ultrasonic loading [1]. Several research groups at SLAC in cooperation with CERN performed experiments with microwave radiation sources (11.4 GHz klystrons with a power of 50 MW and a pulse duration of about 1500 ns) [2, 3], in which the damage of copper samples was caused by pulsed heating up to $\delta T = 70–120$ K and the number of cycles reached $N = (2–85) \cdot 10^6$.

Experimental facility based on JINR-IAP RAS 30 GHz FEM oscillator

An experimental microwave facility at JINR was designed to obtain experimental data at f = 30 GHz and at much higher levels of pulsed heating ($\delta T \geq 200$ K) as compared to the experiments performed at SLAC. The source of microwave power in the JINR facility was a free-electron maser with the following parameters: output power of 20 MW; frequency of 30 GHz; pulse duration up to 200 ns; spectral width, not exceeding 10 MHz. The FEM was pumped by an electron beam of the linear induction accelerator LIU-3000, which produced electron bunches with an energy of 0.8 MeV, a current amplitude of up to 250 A, and a repetition rate of up to 1 Hz [4].

To simulate the temperature regime of one of the CLIC project high-gradient accelerating structures, we used a high-Q test cavity which provided high intensity RF fields (E ~200 MV/m in the volume and H ~1 MA/m at the surface) when it is fed by the FEM pulses. The Fabry-Perot–type test cavity was designed to operate at TE_{011} mode. It was made from oxygen-free copper and had the form of two diaphragms with a profiled central section ("waistband") in between. The shape of the waistband was optimized to enhance the magnetic field in its center in order to provide the required temperature rise during the RF pulse. Increasing the curvature of the waistband increased the maximum magnetic field and, hence, the peak heating temperature with an inevitable narrowing of the hot area. In different experimental series we could vary the temperature rise from 50 °C to 250 °C. The test cavity operating mode was axially symmetrical and allowed study the pulse heating effect in the absence of a normal to surface electric component, i.e., safely in the viewpoint of the RF breakdown.

Experimental results

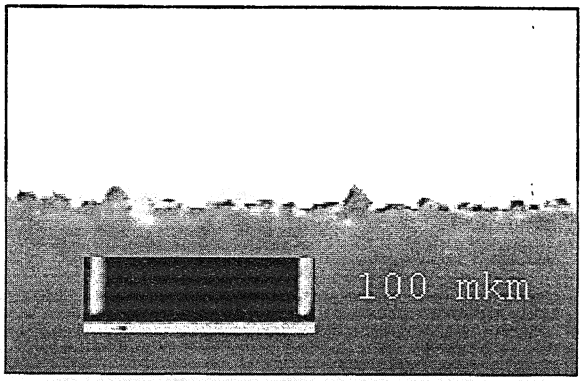

Fig. 1. Microphotograph of the copper ring edge after pulse heating at the temperature rise $\delta T = 250$ °C and the pulse number $N = 1.6 \cdot 10^4$

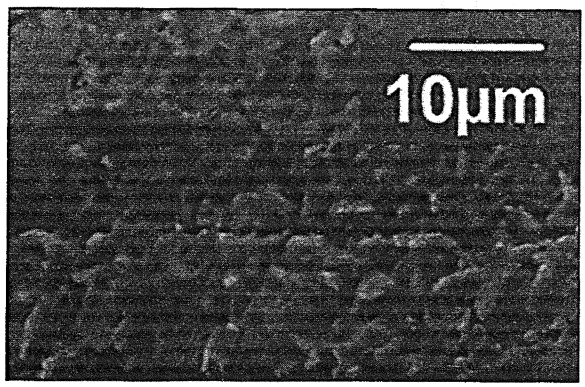

Fig. 2. Electron microscope image of the copper ring surface (near the edge) after pulse heating at the temperature rise $\delta T = 250$ °C and the pulse number $N = 6.0 \cdot 10^4$

To investigate fatigue damage after a number of pulses, the cavity surface was analyzed by means of optical and electronic microscopes. The initial copper surface has mainly small defects oriented along the waistband. These are grooves made by the cutting tool during the creation of the waistband shape, the surface roughness was about ~1 μm. Analysis of the microscope photographs showed different types of the surface damage after RF irradiation. During the first disassembly of the cavity (after $N = 1.6 \cdot 10^4$ pulses), the effects were found only at the middle of the waistband and only in the form of protuberances of ten's microns size (Fig. 1). After the action of $N > 3.2 \cdot 10^4$ pulses, we found that the number of surface damage sites increased and the area subject to damage expanded to either side of the waistband middle.

An electron microscope image of the waistband surface after irradiation by the last series of pulses ($N = 6 \cdot 10^4$ pulses), which was slit and made using an electronic microscope, is shown in Fig. 2. After that number of pulses we have observed regular breakdowns at various azimuth coordinates in the cavity. The local breakdowns are probably caused by discontinuity of the high-frequency Foucault current on cracks in the copper ring, which gives rise to a strong electric field at the edges of cracks with the resulting field and explosive emission of electrons.

Figure 3 contains summary of the results obtained by ultrasonic vibrators, ultraviolet laser heating, RF heating experiments in SLAC and JINR-IAP. We try to analyze and discuss it.

References

1. *Arnau Izquierdo, G., Calatroni, S., Heikkinen, S. et al.* High power RF induced thermal fatique in the high gradient CLIC accelerating structures // CLIC-Note-708. 2007. P. 1-13.

2. *Pritzkau, D.P., Siemann, R.H.* Experimental study of RF pulsed heating on oxygen free electronic copper // Phys. Rev. Special Topics – Accelerator and Beams. 2002. V. 5. 112002. P. 1-22.

3. *Laurent, L., Tantawi, S., Dolgashev, V. et al.* Experimental study of RF pulsed heating // Phys. Rev. Special Topics – Accelerator and Beams. 2011. V. 14. Issue 4. 041001. P. 1-22.

4. *Elzhov, A.V., Ginzburg, N.S., Kaminsky, A.K. et al.* Test facility for investigation of heating of 30 GHz accelerating structure imitator for the CLIC project // Nucl. Instr. And Meth. Phys. Res. A. 2004. V. A528. P. 78-82.

5. *Danilov, Yu.Yu., Ginzburg, N.S., Golubev, I.I. at al.* First full-scale result in CLIC-JINR-IAP RAS experiment on 30 GHz copper cavity heating // Strong Microwaves in Plasmas ed. by A.G. Litvak, Nizhny Novgorod: Institute of Applied Physics. 2009. V. 1. P. 230-235.

6. *Ginzburg, N.S., Golubev, I.I., Kaminsky, A.K. et al.,* Experiment on pulse heating and surface degradation of a copper cavity powered by powerful 30 GHz free electrom maser // Phys. Rev. Special Topics – Accelerator and Beams. 2011. V. 14. Issue 4. 041002. P. 1-7.

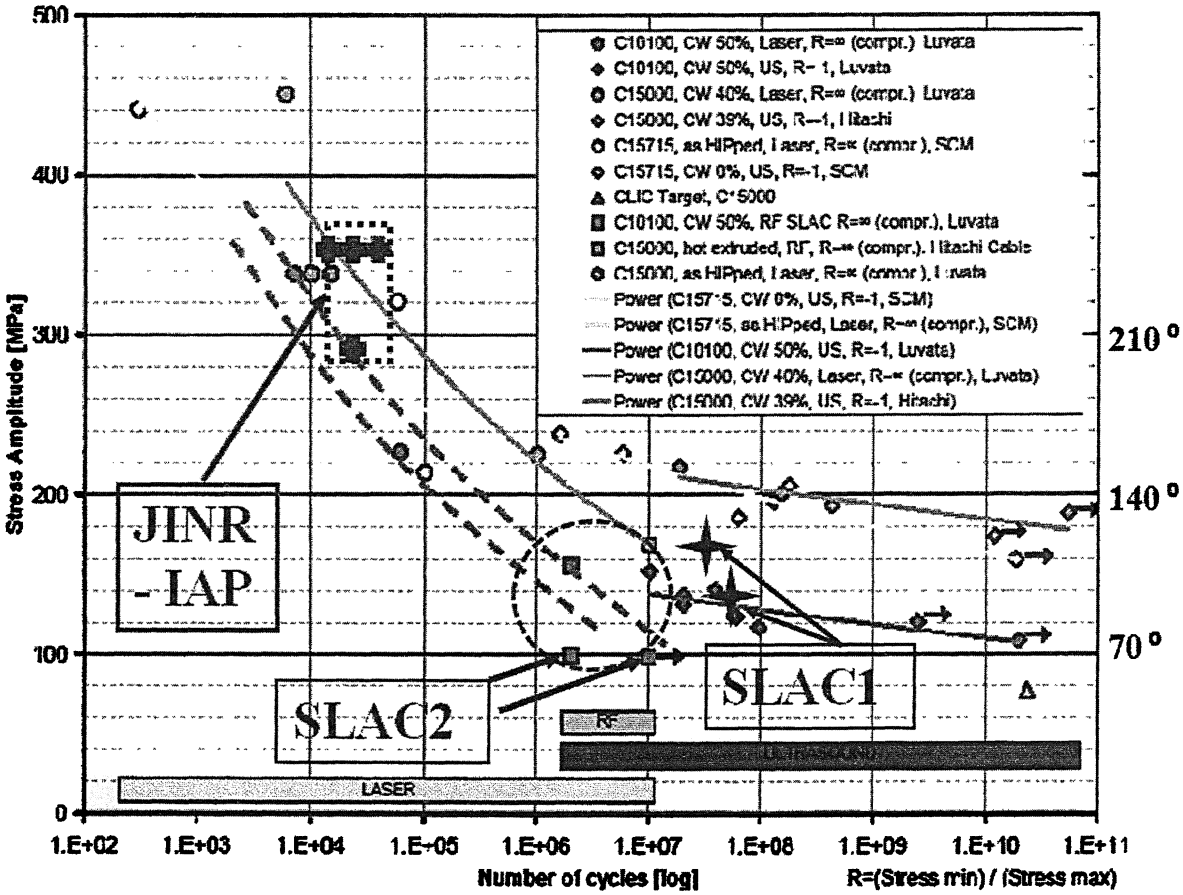

Fig. 3. Summary of the results obtained by ultrasonic vibrators, ultraviolet laser heating, RF heating experiments in SLAC and JINR-IAP

Influence of Small Additions of Noble Gases on Strongly Nonuniform Nonequilibrium Microwave Discharge in Nitrogen

Yu.A. Lebedev, T.B. Mavlyudov, I.L. Epstein, A.V. Tatarinov

Topchiev Institute of Petrochemical Synthesis RAS, Moscow, Russia, lebedev@ips.ac.ru

Gas additions to the basic plasma gas enable to change the plasma parameters and in special cases can be used for plasma diagnostics (e.g., actinometric method). Electrode microwave discharge (EMD) is a representative of non-uniform discharges [1, 2, 3]. EMD was earlier studied in the mixture of hydrogen with Ar and in the mixture of nitrogen with hydrogen [4, 5]. Some results of study of influence of small additions of Ar, Ne, He on the plasma characteristics of nitrogen EMD are presented in this paper.

Experimental setup and the model

Experimental set-up was described in detail elsewhere [1, 2, 3]. Briefly the setup consists of the stainless steel cylindrical discharge chamber with diameter of $R_1 = 7$ cm, the microwave powered (incident power 40–100 W, 2,45 GHz) electrode/antenna with outer diameter of 5 mm, system of gas feeding, and diagnostic devices for study of microwaves and discharge visible emission. The basic plasma gas was N_2 with flow rates 10 and 20 sccm and admixture gases were Ar, Ne, and He with flow rates 0–5 sccm, the total gas pressure in the chamber was 1 Torr. The content of admixtures in nitrogen was 0–5 %. It should be noted that Ar addition is often used for diagnostics of nitrogen close to homogeneous structured discharges as it does not change the plasma properties of such discharges. Discharge light emission through the lateral quartz window is focused by the quartz lens, collected by the optical fiber (spatial resolution was of 150 μm), and recorded with spectrographs AvaSpec-2048 and AvaSpec-2048-4-RM. Discharge visualization is made with video camera, digital photo camera, and electron-optic high time resolution digital camera K-008.

A self-consistent 2D-model for the nitrogen discharge has been used for qualitative analysis of physical-chemical processes of the EMD in mixture of nitrogen with small additives of noble gases [6]. The Poisson equation and balance equations for noble gases atoms excitation and ionization as well as influence of these states on nitrogen kinetics have been added.

The model includes the Maxwell, Poisson and balance equations for charged and neutral species. The rate constants of processes with direct electron impact are assumed to be functions of the local value of the microwave field and are calculated using the EEDF, obtained by solving the time-independent homogeneous Boltzmann equation in the two-term approximation. In the final system of equations the rate constants of reactions are given as functions of the local value of averaged over period microwave field. The influence of vibrationally excited nitrogen molecules of the ground state on plasma processes is taken into account (as it is done in [6]) by applying the well known analytic expression for the VDF of molecules obtained in the diffusion approximation. Detailed modeling was carried out for the mixture of nitrogen with argon.

Results and discussion

Experiments showed that small concentrations of add-on noble gases changed the EMD characteristics and changes have both similar and distinctive features. All add-gases increase the size of the spherical part of EMD (Fig. 1), decrease of intensities of emission 2^+ bands of nitrogen in the near electrode part of EMD, decrease of plasma absorbed power. Vibrational distributions of $N_2(C^3\Pi_u)$-state molecules does not changed by the addition of noble gases. But if addition of argon decreases the intensity of the 1^- system of nitrogen ion (391.4 nm), addition of neon and helium does not decrease this intensity.

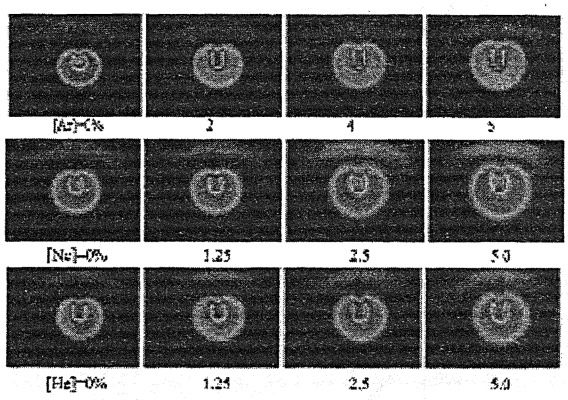

Fig. 1. Influence of add-on noble gases on the EMD size in nitrogen at pressure 1 Torr and incident power 70 W

Electric field strength in the near electrode region was defined in the mixture N_2+Ar from the ratio of intensities of 2^+ and 1^- bands of emission in the approximation of coronal model. It was shown that the microwave field is a decreased function of argon concentration.

Results of 2D modeling of EMD in the mixture of N_2+Ar are in good agreement with the experimental results. Analysis of the spatial distributions of ion components allowed us to determine a mechanism of the influence of small addition of argon on parameters of the nitrogen discharge. The reactions of ion conversion $Ar^+ + N_2\left(X^1\Sigma_g^+\right) \Rightarrow N_2^+ + Ar(^1S_0)$ and $Ar + N_2^+ \Rightarrow N_2 + Ar^+$ were found to be very important. Another important factor was the spatial separa-

tion of peak regions of Ar^+ and N_2^+ densities. This reduces the flux of N_2^+ to the electrode and as a consequence strongly affects the microwave field needed for maintaining of the self-consistent discharge. The latter in its turn leads to changing of all plasma parameters.

The experimental method of determination of electric field described above for argon admixture can not be applied for neon and helium contained plasma since the population of emitting states of molecular ions of nitrogen via electron impact is strongly disturbed by collisions with ionized and metastable atoms of neon and helium. Since the changes of intensities of 2^+ emission bands in the neon and helium contained mixtures are the same as that in the argon contained mixture, it is possible to suppose that decrease of intensities is also related with decreasing electric field.

Analysis of changes of EMD radiation versus the concentration of add-on noble gases gives additional information on physics of EMD. It is known that the higher the energy threshold of emission excitation by the electron impact, the most pronounced changes in the intensity of emission should be observed with decreasing field.

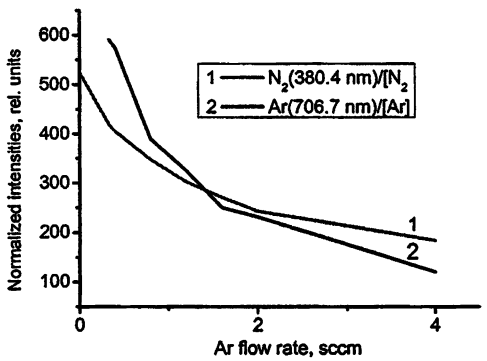

Fig. 2. Changes of the intensity of 2^+ emission band (1) and argon line (2) versus Ar flow rate at pressure 1 Torr and incident power 70 W (N_2 flow rate 20 sccm)

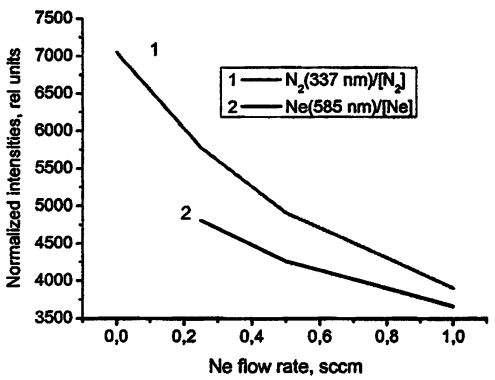

Fig. 3. Changes of the intensity of 2^+ emission band (1) and neon line (2) versus Ne flow rate at pressure 1 Torr and incident power 70 W (N_2 flow rate 20 sccm)

The threshold energies for measured emission intensities are placed in the line of increased thresholds as: $N_2(C^3\Pi_u)$ (11 eV), *Ar* (13.3 eV), *Ne* (18.8 eV), *He* (23.1 eV).

Figure 2 shows that *Ar* emission conforms to the above rule: it failed down rapidly than N_2 emission with lower threshold. In the case of *Ne* admixture the situation is opposite and higher threshold Ne emission failed down slowly than N_2 emission. As the light emission in the near electrode region is initiated by the direct electron impact [1–3], this means that the electron energy distribution function (EEDF) is enriched in high energy region. The emission of *He* lines in the case of *He* addition was observed only if $[He]/[N_2]$ >10 %. Taking into account the high threshold energies of these lines it can be assumed that the EEDF is rapidly depopulated at these energies. Thus the bimodal EEDF can exist in the EMD and the diapason of energies of EEDF enrichment can be determined.

It was assumed earlier that the EMD consists of two luminous parts: self-sustained near electrode region and non-self-sustained external region [1–3]. The results show that the electron beam-like flux can be generated in the near electrode region of EMD. The nature of the second part can be related with the electron beam. This conclusion should be checked by independent methods.

Conclusions

The results show the role of non-uniformity in physics of the electric discharges and point out possible ways for controlling the parameters of the non-uniform discharge. The mechanism described here can take place in plasma with strong spatial non-uniformity of the electric field.

References

1. *Lebedev Yu.A., Shakhatov V.A., Tatarinov A.V., Epstein I. L.* Electrode microwave discharge and plasma self-organization // J. Phys.: Conf. Ser. 2006. V. 44. P. 30-39.

2. *Lebedev Yu.A., Mokeev M.V, Solomakhin P.V.et al.* Physics and microstructure of electrode microwave discharge // J. Phys. D: Appl. Phys. 2008. V. 41. 194001.

3. *Lebedev Yu.A., Shakhatov V.A., TatarinovA.V., Epstein I. L.* Electrode microwave discharge: areas of application and recent results of discharge physics // J. Phys.: Conf. Ser. 2010. V. 207. 012002.

4. *Lebedev Yu.A., Mokeev M.V.* Determination of the electron density and electric field in the plasma of a low-pressure microwave electrode discharge in hydrogen from the measured spectral line intensities // Plasma Phys. Rep. 2003. V. 29. P. 1059-1066.

5. *Lebedev Yu.A., Mavlyudov T.B., Shakhatov V.A., Epstein I.L.* Nonuniform microwave discharge in a nitrogen-hydrogen mixture // High Temp. 2010. V. 48. P. 333-339.

6. *Lebedev Yu.A., Tatarinov A.V. and Epstein I.L.* Modeling of the electrode microwave discharge in nitrogen // Plasma Sources Science and Technology. 2007. V. 16. P. 726-733.

Investigation of Millimeter-Wave Metal Powder Sintering by Application of Dilatometry and In-Situ Resistivity Measurements

G. Link[1], M.M. Mahmoud[1,2], M. Thumm[1,3]

[1] Karlsruhe Institute of Technology, IHM, Germany
[2] Advanced Technology and New Materials Research Institute, MuCSAT, Alexandria, Egypt.
[3] Karlsruhe Institute of Technology, IHE, Germany

Introduction

Microwave sintering technology has been developed in the field of ceramics and composites in the last decades motivated by the potential of a direct and instantaneous volumetric heating. As a result more rapid and homogeneous heating has been demonstrated in comparison to the conventional heating process. Very often enhanced sintering has been reported as well that allows a reduction of process temperature and/or processing time and therefore less energy consumption.

Microwave sintering of metal powders is a new activity with growing interest since Roy, Agrawal and co-workers published their results some years ago [1, 2]. Although metallic materials are known to reflect microwaves rather than absorbing them, it has been demonstrated that sintering of metal powder compacts using microwave heating is possible. Furthermore, in former investigations, a volumetric heating by millimetre waves has been demonstrated by measurement of temperature gradients within the metal powder compact during the heating cycle [3].

The characterization of the sintering progress by density measurement or by using a dilatometer is a standard procedure in case of ceramic materials. For compacts obtained from ductile metal powders with green densities up to 90 %, the classical sintering models can hardly prescribe macroscopic properties in relation to the density. Therefore, different measurement techniques have to be developed.

At the Bayreuth University, Germany, the DC electrical conductivity of steel powder compacts was measured at ambient temperatures after different steps of sintering [4]. In the present study, the progress of sintering process of die-pressed steel powder compacts was investigated using in-situ electrical resistivity measurements during the millimeter-wave sintering cycle in a modified dilatometer set-up [5].

Experimental

The millimeter-wave sintering was performed in a compact 30 GHz gyrotron system [6] that has hexagonal applicator geometry and is equipped with a rotating mode stirrer for homogeneous field distribution. This system was used in combination with a special dilatometer set-up that offers continuous monitoring of the sintering kinetics of a given sample as a function of temperature. It is a commercial dilatometer (type L75 from Linseis Company, Germany) that was adapted to the millimeter-wave applicator in a way that the millimeter-wave leakage could be excluded. This dilatometer set-up was modified so that parallel to the measurement of the changes in sample length, the dc electric resistance could be measured during the sintering process simultaneously. The resistance was measured using a Keithley digital multimeter Model 2002 in combination with the four-wire method. Therefore, two platinum wires were in contact with the top and the bottom surfaces of the cylindrical pressed steel powder compacts sample, respectively. This sample electrode arrangement is assembled into the dilatometer set-up. The benefit of this arrangement with respect to improved electrode contact has to be paid by an additional source of errors in the dilatometer signal, since any length change of the used platinum wire electrodes are superimposed to the intrinsic sample signals. So the dilatometer results will give qualitative information rather than precise quantitative data about the sintering process. The electrical resistivity ρ is thus calculated from the measured resistance R by the relation:

$$\rho = R\frac{(d/2)^2\pi}{l}.$$

Where d is the diameter of the cylindrical sample and l its length.

The heating process was controlled along a preset temperature-time program using the temperature signal of an S-type sheathed thermocouple placed at the sample surface. All experiments were performed in a nitrogen atmosphere at ambient pressure. Samples with 5 mm in diameter and about 20 mm in length were used in two different qualities and with green densities of about 7 g/cm^3. One type of samples was consisted of pure atomized steel powder from KOBE Steel Ltd., Japan with a purity of more than 99.6 %. In the other sample type, the mentioned steel powder was mixed with 0.7 weight% graphite powder from Asubery with purity higher than 95 %. Samples were heated with a rate of 10 °C/min up to 1140 °C and soaked for 10 min. at this temperature. After free cooling, a subsequent identical run was performed, using the same sample.

Results and Discussion

Figures 1 and 2 present the experimental data of both consecutive temperature cycles of the pure iron sample and the sample including some graphite powder, respectively. Both graphs show that the absolute changes in length from the dilatometer and the measured resistivity as a function of temperature. This allows distinguishing extrinsic effects due to sintering from intrinsic temperature dependent effects.

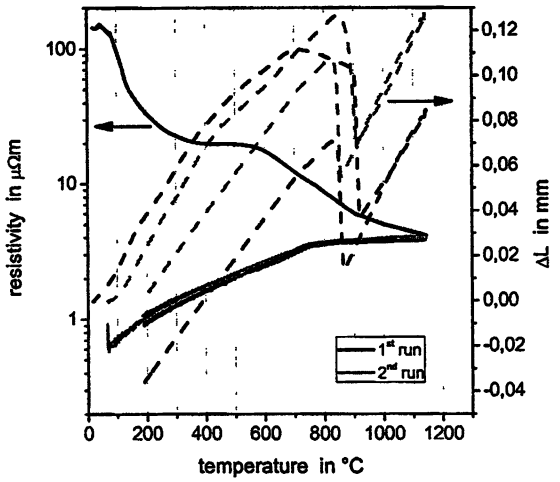

Fig. 1. Dilatometer and resistance measurement of the pure iron sample as a function of temperature

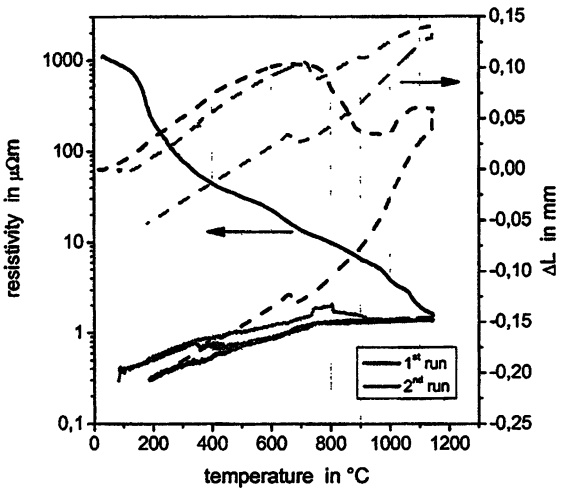

Fig. 2. Dilatometer and resistance measurement of the graphite doped iron sample as a function of temperature

From ambient temperature till about 700 °C a positive slope in the dilatometer curves is observed for both samples due to thermal expansion. Thereafter, the slope gets slightly negative indicating the onset of sintering. In the pure iron sample, at a temperature of about 900 °C, a sudden transformation from the ferrite to the austenite phase is observed as indicated by the dilatometer data. Subsequently thermal expansion is dominating the superimposed sintering effect resulting again a positive slope in the dilatometer curve till the final target temperature 1140 °C was reached for isothermal soaking. In the graphite doped sample, the phase transformation is much smoother and starts already at lower temperatures as compared with the pure iron sample and as expected from the iron carbon phase diagram.

The results of resistivity measurements show a strong decrease in resistivity of about one order of magnitude for the first 300 °C followed by saturation. This was explained by welding of the interparticle contacts by O. Lame and co-authors [7] who performed similar experiments by conventional heating. Above a temperature of about 600 °C to 700 °C, were the start of sintering can be recognized from the dilatometer curve, a second decrease in resistivity comparable in magnitude can be observed. This is followed up by a second saturation phase till the end of the soak time. Thereafter, during the cooling process, the negative slope is measured which can be explained by the intrinsic temperature behaviour of the resistivity. This is confirmed by the curve measured during an identical second heating cycle as can be clearly seen in Figures 1 and 2. The qualitative evolution of the resistivity obtained for the graphite doped sample is similar to the pure iron sample. The main difference is that the initial resistivity was significantly higher in the graphite doped sample. This demonstrates that carbon is acting as an inhibitor for the formation of metallic pressing contacts as prescribed by A. Simchi and co-authors [8].

Conclusions

The sintering progress in millimeter-wave heated metal powder compact has been investigated by application of in-situ resistance measurement. Therefore, an existing dilatometer set-up has been completed with a four-wire test and a high resolution ohm-meter. This test method gives important information about microstructural changes with respect to the interparticle electrical contacts during the sintering process. A direct comparison of the measured data from two identical subsequent thermal process runs allows differentiating extrinsic effect due to sintering from intrinsic temperature dependent effects. This data indicates that tremendous changes already occurring at temperatures below 300 °C where a strengthening of the material cannot be expected.

Acknowledgement

The support of Hitachi Powdered metals Co., Ltd. and of the DFG under the contract GZ TH656/3-1 AOBJ 575894 is kindly acknowledged.

References

1. *Roy R., Agrawal D., Cheng J. and Gedevanishvili S.* // Nature. 1999. V. 399. P. 668-670.

2. *Cheng J., Roy R. and Agrawal D.* // Journal of Materials Science Letters. 2001. V. 20. P. 1561-1563.

3. *Takayama S., Link G., Miksch S., Sato M., Ichikawa J., Thumm M.* // Powder Metallurgy. 2006. V. 49. P. 274-280.

4. *Willert-Porada M., Park H.-S.* // Ceramics Transaction. 2001. V. 111. P. 459-470.

5. Link G., Ichikawa J. and Thumm M. // Proc. Global Congress on Microwave Energy Applications Otsu, Japan, 2008. P. 561-564.

6. *Link G., Feher L., Thumm M., Ritzhaupt-Kleissel H.-J., Böhme R., Weisenburger A.* // IEEE Trans. on Plasma Science. 1999. V. 27 [2]. P. 547-554.

7. *Lame O., Bordère S., Denux D., Bouvard D.* // Materials Science and Engineering. 2003. V. A363. P. 126-133.

8. *Simchi A., Danninger H., Gierl C.* // Powder Metallurgy. 2001. V. 44 [2]. P. 148-156.

Microwave Recycling of PET Waste and Its Technical Realisation

G.A. Morozov, O.G. Morozov, R.R. Samigullin, A.R. Nasibullin

Tupolev Kazan State Technical University, new-1@yandex.ru

Methods of effective recycling of poly(ethylene terephthalate) domestic waste are considered, based on theoretical and experimental studies of efficiency of microwave electromagnetic field application in chemical reactions of polymer decay. The of microwave radiation energy as a heat source ensures improved quality of reaction flow, a decrease of energy costs and time of thermal processing in comparison with classical heating. The interaction with glycols (ethylene glycol, diethylene glycol, propylene glycol) is used to achieve destruction at temperatures of 210–250 °C and atmospheric pressure. The resulting terephthalic acid oligoethers can be used, depending on their purity, to produce new poly(ethylene terephthalate) or other polymer-containing materials.

The major problem for the modern polymeric industry is recycling of the plastics which were in the use. These materials are maintained in natural conditions for a long time because of high stability against environmental effects. The recovery of polymer waste can be viewed not only as the ecological factor, but also as economic as materials and energy arrive in a reuse. It allows one to use natural resources more rationally, to reduce power consumption and to reduce exhausts to the environment. As the most promising directions mechanical and chemical processing are considered, each being characterised by the merits and demerits. Mechanical processing ensures simple secondary use of the same materials at certain losses in their properties. Chemical processing derives a final product in the form of monomer or oligomer which can be used to produce new polymeric raw materials. In this connection there is a problem of selecting optimum methods of recycling.

The greatest contribution to lump polymeric waste is from poly(ethylene terephthalate) (PETP) – approximately 25 %, and annually the volume of the accumulated waste is incremented on 10 million tons. PETP because of a wide spectrum of its properties has found application in various fields of production, but the main use is still in the manufacturing of packagings for foodstuff (bottles and tare designated for food purposes). Plastic is recycled by all basic methods mentioned above. Mechanical processing of PETP consists in preliminary crushing of a waste with the subsequent moulding of the obtained grains under high pressure. The deficiencies of this method are restriction of ranges of application of the substances gained as a result of recycling and high requirements to initial PETP. The chemical method consists in a depolymerization of PETP waste at interaction with various solvents for the purpose of deriving monomers or oligomers, applicable both for manufacturing of various plastic, and for recurrent PETP synthesis. This method incurs significant energy costs and requires use of expensive chemical reagents. However, there is a possibility to use raw materials of lower quality as chemical processes allow additional purification. At chemical processing, it is possible to achieve a drop of energy expenditures, cut the time of thermal handling, and ensure substantial improvement of quality of reaction flow by using the energy of microwave (ultrahigh-frequency) electromagnetic radiation as heat source.

Application of microwave technologies allows one to achieve advantages in comparison with traditional methods of heat treatment to which it is possible to refer: the possibility of volumetric heating, and as consequences fast and more uniform heating of bulk materials, improvement of product quality, power savings, and cutting the cost of production.

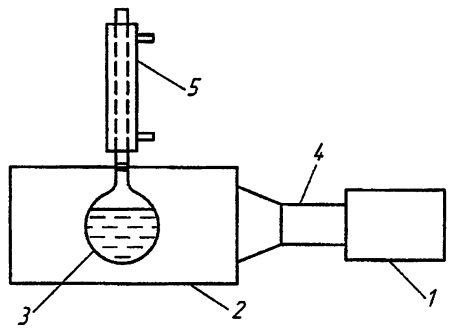

Fig. 1. Schematic diagram of the pilot unit

As the polymer destruction reaction it is suggested to use interaction with ethylene glycol (EG) – glycolysis, deriving bis (2-hydroxyethylene) terephthalate (BHET). This reaction is carried out at atmospheric pressure and a temperature of 210–250 °C. The obtained oligoether, depending on its purity, can be recurrently used at the second stage of polymerisation to obtain new PETP or in various chemical processes. The use of ethylene glycol at dielectric heating is more expedient in comparison with other solvents because of high loss angle, tg δ = 1.35 at room temperature and frequency of 2450 MHz (for water tg δ = 0.123).

To perform physical modeling of the PETP recycling process, a pilot unit (Fig. 1) has been constructed, consisting of a microwave radiation source – a magnetron (1) generating a maximum power of 700 W at a frequency of 2450 MHz with a resonator chamber (2), joined to the magnetron by a segment of a rectangular wave guide (4). The matching of the multimode resonator for frequency of 2450 MHz is implemented by using an E-sectorial horn installed sideways from an axial line of the case on face wall. In the chamber a glass vessel with reactants 500 ml in volume, coupled under reflux (5) through a hole in the upper wall of the resonator chamber, is placed. The resonator construction spots a maximum of intensity of an electromagnetic field in space of determination of the vessel to be heated.

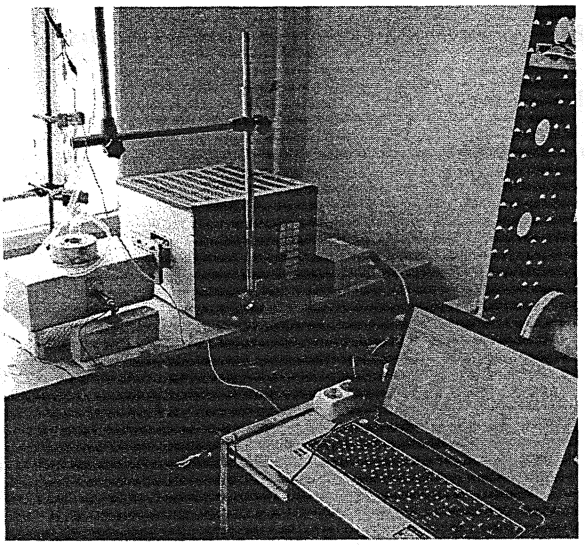

Fig. 2. Appearance of the installation

As reaction catalytic agents usual laboratory chemicals, such as sodium carbonate, sodium bicarbonate, barium hydroxide and zinc acetate were used. The ratio of the initial amount of PETP to ethylene glycols varied from 1:4 to 1:10, whereas the concentration of catalytic agents had a constant value of 1 % of the total intermixture. The PETP bottles were applied to effervescent beverages, beforehand stripped, washed out and grinded to sizes 5×5 mm. The reaction control in the closed resonator chamber was carried out by a video camera with recording of the entire process on the computer, the temperature of the flask surface was registered by means of an infrared temperature sensors. The temperature data was supplied to the PID-thermocontroller in the channel of feedback to maintain the necessary temperature of reaction with optimum power consumption of the inverter power supply of the magnetron.

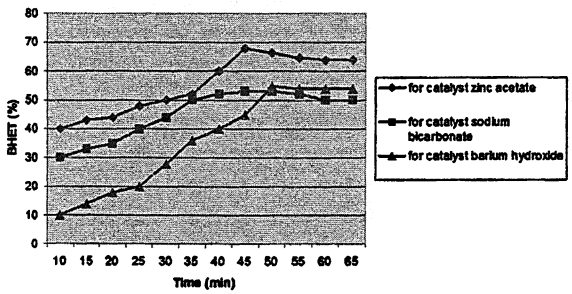

Fig. 3. Results of the experimental study of the microwave effect on the PETP glycolysis reaction

A photograph of the pilot unit is shown in Fig. 2. The glycolysis yield has been gained as the heels after a filtration, containing ethylene glycol, BHET and a small amount of some oligomers.

A comparison of effects was made according to the amount of BHET obtained as a result of treatment vs. time spent on decomposition. In Fig. 3 a dependence of BHET yield on time of depolymerization for the cases of use of three catalytic agents and maximum power of radiation of the generator is shown. Maximum BHET yield (67 %) was observed in the case of zinc acetate use at duration of reaction of 40–50 minutes.

The amount of BHET increases during this time, after which a reduction in the oligomer fraction is observed. This results from the fact that glycolysis is an equilibrium reversible reaction; the reverse reaction is polyfunctional condensation. In the case of heating by a classical method with other factors being equal the depolymerization time is 6–7 hours.

Based on the results of physical and mathematical modelling of a microwave method of PETP recycling, a pre-production model of a complex (Fig. 4) is developed for processing of plastic bottles designated for food purposes, both as an independently functioning unit and as a part of existing complexes. The microwave reactor is part of a complex composition with multi-element excitation; the power supply system of magnetrons is inverter type, for the purpose of flexible control of the temperature of the reaction mixture. The distributed fiber optic temperature sensors control exact location of the temperature profile in the reactor. The response monitoring system checks in visible or infrared light the final product yield.

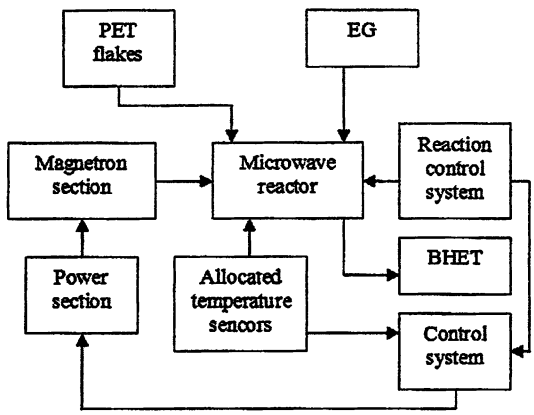

Fig. 4. Schematic diagram of a microwave recycling comlex

The results of the study presented in this paper have confirmed a positive effect of microwave technology application in PETP chemical destruction which leads to a significant (by 15 times) decrease in the time of depolymerization and to reduction of power consumption in comparison with a usual thermal heating while the amount of the produced BHET is approximately equal.

High Power Shot Pulse BWOs on High-Current Relativistic Electron Beams for Applications

M.B. Goykhman[1], A.V. Gromov[1], V.A. Kashin[2], V.V. Kladuhin[3], N.F. Kovalev[1], A.V. Palitsin[1]

[1] IAP RAS, Nizhny Novgorod, Russia
[2] Special Design Bureau «Almaz», Moscow, Russia.
[3] Institute of Electrophysics, Urals Branch, RAS, Ekaterinburg, Russia

Microwave oscillators on high-current relativistic electron beams, emitted from cold explosive cathodes, have unique power characteristics. By now output radiation of these devices exceeds gigawatt level in centimeter band of wavelengths and it could be used in radar system [1], to effect on some biological objects [2], on electronics [3] and etc. Successful application of such devices requires solving of some problems related to improvement of their technical properties. In report we consider the importance and complication of these problems by example of relativistic backward wave oscillator (BWO), since it is most investigated and widely used in various applications.

In report we list main technical problems, the extent of study and possible ways of their solving. The first group is related to study of short pulse generation dynamics, especially the problem of decreasing the starting time of oscillations. Its solution concerns with investigation of initial impact influence. Increasing of stability and duration of microwave pulses of output radiation is also discussed in the report, as well as effect of external signal on microwave generation.

The second group includes problems of increasing pulse repetition rate and average microwave power that supposes development of repetitive explosive-emission electron beam injectors and systems of heat removing, in particular from collector. In the report the possibility is shown to develop BWOs with 500 Hz repletion rate (1 kHz in short series) if the average output microwave power is about 20 kW and peak power – 1 GW.

The third group is concerned with increasing of peak power and breakdown strength of slow wave structure (SWS) and output microwave system, that usually means enlargement of transverse dimensions and solving the mode selection problem. In this aspect the initial impact can be an additional factor of selection as well as a stratification of azimuthal velocities in thin-walled electron beam. Development of high-power oscillators with higher frequencies of radiation also requires SWS with large transverse dimensions and using methods of mode selection.

The fourth group includes the problems of frequency adjusting or, in wider definition, switching short pulse oscillator's regimes from pulse to pulse. This topic is presented briefly.

Concluding part of report covers applied aspects of BWOs, especially for radar systems, where cryogen-free superconducting magnet and ferrite phase array antenna [4] can be used.

References

1. *Clunie D., Mesyats G., Osipov M., Petelin M., Zagulov P., Korovin S., Clutterbuck C., Wardrop B.* The design, construction and testing of an experimental high power, short-pulse radar. // Strong Microwaves in Plasmas. Nizhni Novgorod: IAP RAS, 1996. V. 2. P. 886-902.

2. *Bolshakov M.A., Bugaev S.P., Elchaninov A.A., Evdokimov E.V., Goncharik A.O., Gunin A.V., Korovin S.D., Kutenkov O.P., Pegel I.V., Rostov V.V.* Effect of repetitive nanosecond HPM pulses on some biological objects. // Proc. Of 1 Int. Congress on Radiation Phys., High Current Electr. And Modific. Of Materials, Tomsk, 2000, V. 2. P. 514-518.

3. *Giri D.V., Taylor C.D.* High-power microwave systems and effects // Taylor & Francis, Washington, D.C., 1994. P. 203.

4. *Kolganov N., Kovalev N., Kashin V., Danilov E.* Intense microwave pulse transmission through electrically controlled ferrite phase shifters // Proc. Of the NATO Advanced Workshop on Quasi-Optical Control of Intense Microwave Transmission. Nizhny Novgorod, Russia, 2004. P. 393-398.

The Electromagnetic Microwaves Scattering by Inhomogeneities in CVD-Diamond

O.S. Mocheneva and V.V. Parshin

Institute of Applied Physics RAS, Nizhny Novgorod, Russia, parsh@appl.sci-nnov.ru

The scattering of electromagnetic radiation by structural inhomogeneities of MPACVD-diamond disks at the 100–1000 GHz frequency range are calculated.

. It is shown that the scattering contributes significantly to the attenuation of the radiation from about 100 GHz and becomes a determinant factor closely to 1 THz. The further effect of scattered energy also has been calculated. The loss tangent frequency dependencies of a set of MPACVD-diamond disks are also presented.

Polycrystalline Diamond plates produced by Microwave Plasma Assistant Chemical Vapor Deposition (below CVD-Diamond) technique have a unique set of dielectric, thermal, mechanical properties, which are of primary interest for application both for microelectronics and electronics of high-power. The CVD-Diamonds have solved the key problem of high-power electronics of MM-waves – the creation of output/input windows able to transmit the Megawatt level of power. It is the single material (typical sizes: diameter ~100 mm, thickness ~1.8 mm) for output windows of Megawatts CW gyrotrons for microwave plasma heating in the ITER Project. During the last ten years the lowest loss observed in CVD-Diamonds had been reduced as less 2 orders of magnitude and now it has the lowest loss among all the materials at room temperature. The tanδ value ~ $3 \cdot 10^{-6}$ at 170 GHz and 300 K was found in several CVD-diamonds plates [1].

From the previous studies [2] it follows that at room temperatures the main absorption mechanism at MM waves is absorption due to extrinsic conductivity[1] generated by impurities, defects and non-diamond inclusions (graphite). For this mechanism loss tangent varies inversely with frequency (tanδ ~ 1/f).

So, the absorption value of the plate with fixed thickness does not depend on the frequency! It is a very attractive feature, especially for SubMM application. The important conclusion was made that the theoretical lower loss limit at room temperature is at least one order of magnitude lower than the measured lowest loss [2].

However, on closer examination of the tanδ frequency dependencies of the real Diamond disks (Fig. 1) it is clearly seen that there are not the clear frequency reverse dependencies (like 1/f) and every disc has its own original tanδ frequency dependence.

It was shown that impossible to extract the pure 1/f dependence on the base of any real measured frequency points even at low frequencies.

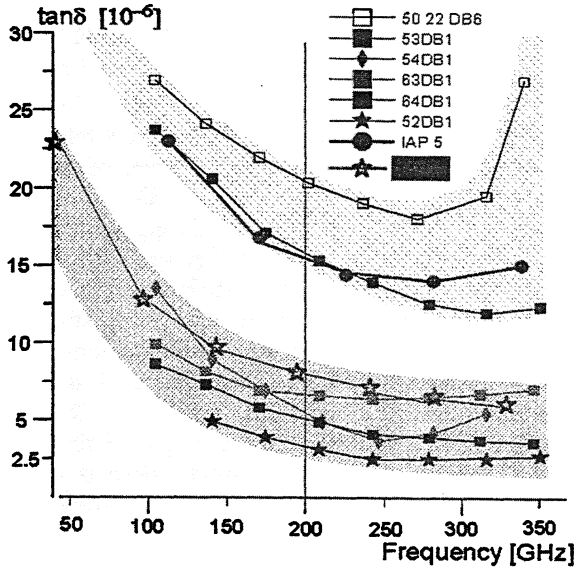

Fig. 1. Loss tangent frequency dependencies of real diamond windows

Also at the higher frequencies the tanδ increasing with frequency was observed in several CVD-Diamond disks. Taking into consideration above mentioned it has been supposed that at frequencies higher than 100 GHz we see the influence of other absorption mechanism [3]. Unfortunately it did take place. The tanδ increasing (like tanδ ~ f) higher than 200 GHz for the discs with loss tangent ~ 10^{-5} (middle quality, the most usable samples) was observed. That means that probably we see the lattice absorption influence (with frequency dependence like tanδ ~ f).

This fact is in contradiction with the understanding that the modern good CVD-Diamond is the oriented polycrystal with perfect crystallites. The great thermoconductivity along the surface, like in the good monocrystals, means that we operate with perfect crystals and the lattice influence should not be observed.

On the total photo of the window Fig. 2 we see the white little stroke in reflected light. In the window centre looking via microscope we see the "dark" spots in the window body (see the microphoto photo in through-passing light on Fig. 3). As it was established in the previous works [3] they are the microcaverns between the crystallites. So we have supposed that the additional losses are caused by wave scattering in disk volume by these microcaverns. (The microscope allows us not only to observe the microcaverns but also estimate its distribution and sizes.)

[1] The Debye temperature is 1900 K, so the intrinsic diamond conductivity at room temperature is negligible

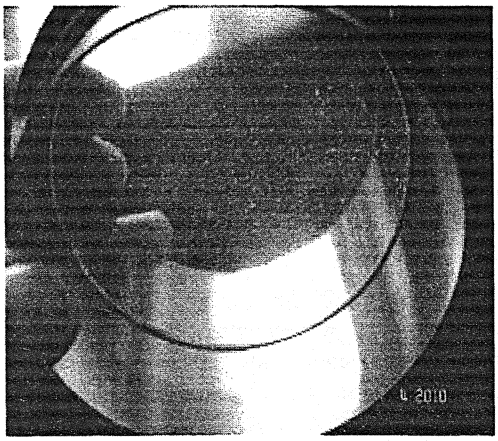

Fig. 2. Photo of the window disc

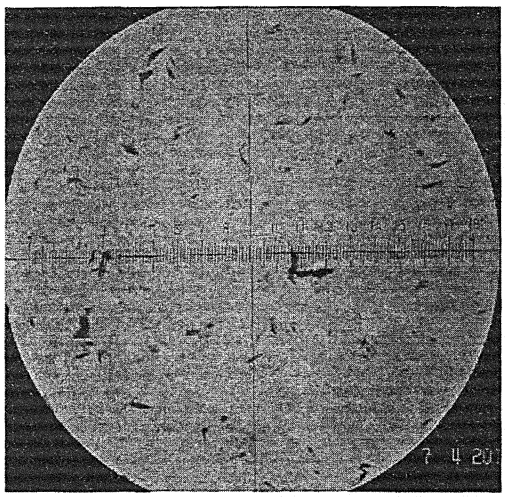

Fig. 3. Microphoto of the window centre

The absorption in CVD-Diamond disks is measured by a resonance technique based on a high Q-factor Fabry-Perot resonator [4], in which the studied dielectric is placed. (The absorption is determined by observing the changes in Q-factor of the empty and loaded resonator.)

It is important to note that only resonator methods permit to measure with good accuracy so negligible absorption like in modern CVD-Diamond films. But in the framework of these methods, it is impossible to separate the losses due to the "pure" absorption and the scattering by structural inhomogeneities in the sample. Also at the wide frequency (40 GHz – 360 GHz) investigations the beam spot diametre changes 3 times as much. So at the different frequencies the different irregular number of caverns participates in the scattering process and so every disk has its own loss tangent frequency dependence which in one's turns depends the beam area in resonator.

Figure 4 shows the scattering influence of one of "big" caverns (Fig. 3).

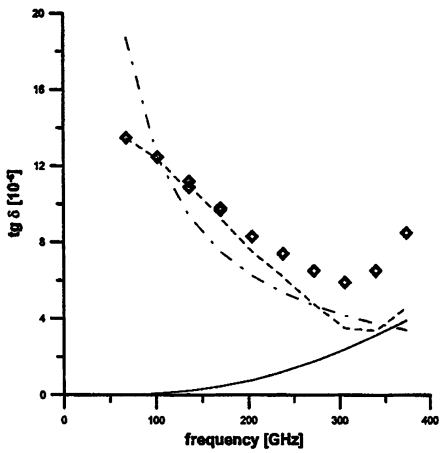

Fig. 4. Illustration to the scattering process:

♦♦♦ is the experimental points,
——— is the scattering calculation by one big cavern,
- - - - - is the difference between experiment and calculation,
—·—·· is the approximation by function 1/f

As it follows from our new careful calculations in the millimeter-wave band, the scattering can be neglected. At frequencies are higher than 170 GHz, the influence of the scattering becomes noticeable and closer to 1 THz, the attenuation caused by the scattering exceeds the absorption in the disk material by many times. Approximately 10 % of scattered energy will be scattered forward and back from the window and ~ 90 % will be "closed" into the disk due to effect of total internal reflection and will dissipates into the window. So it is possible to say that the resonator measurements of absorption are true within 10 % accuracy.

Acknowledgement

Studies described in this work were supported partly by the Grants of RFBR 11-02-91179-ГФЕН_а.

References

1. *Denisov G.G., Litvak A.G., Myasnikov V.E., Tai E.M., Ilin V.I., Zapevalov V.E.* Megawatt-power gyrotrons for fusion // Proceedings of the 6th International Workshop «Strong microwaves in plasmas» Ed. A.G. Litvak. Nizhny Novgorod. 2006. P. 62-75.

2. *Polyakov V.I., Rukovishnikov A.I., Garin B.M., Avdeeva L.A., Heidinger R., Parshin V.V., Ralchenko V.G.* Electrically active defects, conductivity and MM wave dielectric loss in CVD-diamonds // Diamond and Related Materials. 2005. V. 14. P. 604-607.

3. *Mocheneva O.S., Parshin V.V.* Scattering by structural inhomogeneities of CVD diamonds in the 100–1000 GHz range // Radiophysics and Quantum Electronics. 2007. V. 50, № 12. P. 946-954.

4. *Dryagin Yu.A., Parshin V.V.* A method to measure dielectric parameters in 5–0.5 mm wavelength band // Int. J. of Infrared and Millimeter Waves. 1992. V. 13, № 7. P. 1023-1032.

Versions of Grating-Based High-Power-Microwave Combiners, Scanners and Duplexers

M. Petelin

Institute of Applied Physics of the Russian Academy of Sciences,
Nizhny Novgorod, Russia, petelin@appl.sci-nnov.ru

Methods to control 10–1000 GHz high-power wave beams are of interest for the controlled fusion, microwave technologies, diagnostics, radar and communication. Within the band, to reduce Ohmic loss, to avoid RF breakdown and overheating, to provide mode filtration, all wave transmission and control components should be quasi-optical. A considerable number of these functions may be performed with gratings [1–5]. This talk is aimed to discuss some specific versions attractive for using in some near-time collaborative international researches.

Multi-beam combiners. Any plane wave incident to a periodic metallic grating is known to be scattered to a limited number of secondary waves. By adjusting the grating profile, we may redistribute the incident RF power between the scattered waves, in particular, to equalize the diffracted wave powers [6]. The reciprocal process provides combining a set of mutually phased wave beams into a single beam.

Littrow gratings [1, 3, 5] are distinguished with 2 specifications: 1) the grating period is chosen to diffract the incident wave beam only into the 0-th order (mirror) and the –1-st order directions, 2) the –1-st order beam is aimed to the anti-mirror direction. Various Littrow gratings may perform various functions of interest for high power microwave applications:

1) If the corrugation depth is chosen to equalize powers of the two diffracted beams, the resulting configuration represents a ***3 dB hybrid*** [3–5] analogous to the usual magic T and, so, capable to operate as

- a ***phase controlled beam combiner-switcher*** [3–5],
- a beam divider/combiner in a Mach-Zender multiplexer.

2) If the corrugation depth is chosen so that, at the central frequency, the mirror beam power is zero and the total power is reflected into the –1-st order direction, the configuration may be used, within a band around the central frequency, as [2–5]

- a frequency controlled wave beam scanner,
- a component of a multiplexer.

3) The Littrow corrugation profile may be synthesized so that the wave E-polarized relative the groove direction is mirror reflected and the H- polarized wave is reflected in the –1-st order direction. The configuration functions as a ***polarization separator*** [4, 5].

Polarizers. If the grating period is small compared with the wavelength, the total incident wave power is reflected only into the mirror direction. However, in the general case, components of waves E- and H-polarized relative the grating groove direction undergo different phase shifts at the reflection from the grating. So the polarization of the reflected wave differs from that of the incident wave [1, 2].

Duplexers. Various combinations of the above components may be used in transmit-receive configurations with a common antenna. For instance, one of proposed duplexers [5] represents a sequence of a polarization separator and a polarizer; in this case the target is irradiated with the circular polarized wave beam and the receiver sees only the reflected wave of the same circular polarization.

Conclusive note. Most of the above components may be used in systems fed with free-running microwave auto-generators; however the field of applications would be considerably expanded if high microwave powers were produced with phase controlled sources, especially, amplifiers, in particular, high-order-mode gyroklystrons [7].

References

1. *Petit, R. (ed.),* Electromagnetic theory of gratings // Berlin-Hedelberg-New York: Springer-Verlag, 1980.

2. *Belousov, V., Koposova, E., Orlova, I. et al.* Auxiliary elements of high-power quasioptical waveguide ducts // Gyrotrons / Ed. V. Flyagin. IAP, Gorky, USSR. 1989. P. 155-160.

3. *Petelin, M., Caryotakis, G., Tolkachev, A. et al.* Quasi-Optical Components for MMW Fed Radars and Particle Accelerators // High Energy Density Microwaves / Ed. R.M. Phillips. 1998. AIP Conference Proceedings 474, Pajaro Dunes, California, Woodbury, NY. P. 304-315.

4. *Petelin, M.,* High Power Microwave Control by Quasi-Optical Gratings // IVEC 2006. Monterey, USA. P. 553-554.

5. *Petelin, M., Erckmann, V., Hirshfield, J. et al.* New concepts for quasi-optical structures for use with gyrotron systems // IEEE Trans. On Electron Devices. 2009. № 5. P. 561-565.

6. *Koposova, E., Petelin, M.* Scattering of wave by metallic corrugated surface: control of distribution of scattered wave powers with profile optimization // Radiofizika. 1989. V. 32, № 9. P. 1178-1181.

7. *Zaitsev, N., Danilov, Yu., Gvozdev, A. et al.* A pulsed multi-megawatt gyroklystron // this workshop.

Low-Pressure Discharge Induced by Microwave Radiation with Jumping Phase

I.F. Potapenko[1], A.F. Alisov[2], A.M. Artamoshkin[2], V.I. Golota[2], A.M. Egorov[2], I.V. Karas'[2], V.I. Karas'[2], A.N. Starostin[3], A.G. Zagorodny[4], I.A. Zagrebelny[2], V.I. Zasenko[4]

[1]Keldysh Institute of Applied Mathematics RAS, Moscow, RF, irina@keldysh.ru
[2]NSC Kharkov Institute of Physics and Technology, Kharkov, Ukraine
[3]Institute for Innovation and Fusion Research, Troitsk, RF
[4]Bogolyubov Institute for Theoretical Physics, Kiev, Ukraine

The effect of high-power pulsed microwave radiation with a stochastically jumping phase (MWRSJP) on plasmas produced in a rarefied gas filling a coaxial waveguide is studied. The source of a decimetric diapason MWRSJP is the beam-plasma generator (BPG) created at the NSC Kharkov Institute of Physics and Technology [1] and recently upgraded. The conditions of a microwave discharge ignition, its maintenance in air by MWRSJP, and the pressure range at which required power is minimal are found both experimentally and theoretically. To interpret the experimental results, a computer code is developed. Numerical simulation of the process of gas ionization by electrons heated in the MWRSJP field, the behavior of plasma particles in such a field, and the spectral power density along the beam with a known absorption coefficient for different gas mixtures are carried out. The results can be used for the development of a new type of efficient sources of optical radiation with a quasi-solar spectrum.

It was shown in [2–3], both theoretically and experimentally, that the phenomenon of anomalous penetration of microwave radiation into plasma, conditions for gas breakdown and maintenance of a microwave gas discharge, and collisionless electron heating in a microwave field are related to microwave radiation phase jumps. In this case, in spite of the absence of pair collisions or a synchronism between plasma particles and the propagating electromagnetic field, stochastic microwave fields exchange their energy with charged particles. In such fields, random phase jumps of microwave oscillations play the role of collisions and the average energy acquired by a particle over the field period is proportional to the frequency of phase jumps. To ignite an MWRSJP discharge in a low-pressure gas in an evacuated coaxial waveguide with a wave resistance of ~75 Ω, it was connected to the BPG. The BPG operated in the regime of narrow-band signal generation with the short-circuited input. The gas or gas mixture was pumped out through a socket located in the middle of the coaxial waveguide. The gas pressure in the waveguide was monitored using a thermocouple tube mounted in the same socket. With use of a precision valve, the working gases were inputted through 2-mm-diameter channels that located diametrically near the both ends of the waveguide. Diagnostic probes are placed in such a way that the monitoring of the microwave discharge parameters is provided along the waveguide length. Spectroscopic studies are carried out through two 40-mm-diameter 2-mm-thick quartz glass windows that are located on the side wall of the waveguide in a plane perpendicular to the plane in which the diagnostic probes were installed. The standing-wave ratio and the attenuation coefficient of electromagnetic waves in the frequency range 50–1250 MHz are measured with RK2-47 panoramic display. A time-delay circuit is used to vary the instant of triggering the oscilloscopes with respect to the beginning of the high-voltage pulse. This allowed us to observe the shape of the generated signal at different instants after the beginning of the electron beam pulse. A detector head and D2-13 variable resistive-capacitive attenuator connected to the secondary line of the coupler were used to measure the envelope of microwave oscillations. The waveforms and spectral characteristics of MWRSJP at the input and output of the coaxial waveguide were studied using an HP Agilent Infinium four-channel broadband (2.25 GHz) oscilloscope. A PEM-29 photomultiplier powered from a VSV-2 high-voltage stabilized rectifier was used to measure the integral intensity of optical radiation from the plasma. An ISP-51 three-prism glass spectrograph was used for optical spectroscopy of the discharge in the coaxial waveguide. The discharge radiation was focused by a lens onto the input slit of the spectrograph. A PEM-36 photomultiplier was connected to the output slit of the spectrograph.

In certain ranges of the gas pressure, gas composition, and microwave power, a discharge was ignited in the coaxial waveguide. It is found that the discharge radiation intensity decreases along the waveguide.

It should be noted that the discharge color depends on the working gas pressure and the microwave power input in the waveguide. The waveforms of the main BPG parameters (the electron beam current, the electron beam voltage, and the envelopes of the high-frequency signal and integral optical radiation) were measured. It was found that microwave oscillations are excited when the current exceeds a certain critical value and that the discharge continues to glow for a certain time after the end of the electron beam pulse due to recombination processes.

For the pressure P = 2 Pa and the power is sufficient to breakdown the air and maintain the stationary discharge, as can be seen in Fig. 1, the amplitude of realizations MWRSJP and their local spectra at input and output coaxial waveguide are substantially different.

Ignition of the discharge does not affect the penetration into dense plasma MWRSJP evidenced by

nearly constant amplitude at the entrance to the waveguide (curve *1* in Fig. 1), because the same amount of energy radiation on air ionization for the discharge maintenance MWRSJP amplitude at the output of the coaxial waveguide (curve *2* in Fig. 1) exists, but essentially diminished. In addition, it is important that changes significantly as the local spectrum (curve *2'* in Fig. 1) on the output waveguide, it is no peak associated with the main spectral component MWRSJP.

Thus, based on the quantitative indicators such as the electric field intensity, frequency of MWRSJP and phase jumps, etc., it can be expected the following. The prospective creation of an efficient light radiation source of low power (100 W) in a wide range of air pressure, in which the discharge is ignited and maintained stably, becomes a reality. The main task of future research is to optimize the gas mixture for the discharge of quasi-solar optical spectrum.

The results of one- and two-dimensional numerical simulations can be formulated as follows.

(i) The intensity of collisionless electron heating increases with increasing rate of phase jumps in MWRSJP.

(ii) There is an optimal phase jump rate at which the rate of gas ionization and, accordingly, the growth rate of the electron and ion densities growth are maximal. The optimal phase jump rate is equal to the ionization frequency at electron energies close to the ionization energy of the working gas.

(iii) The results of numerical simulations are in qualitative agreement with the experimental data.

The original SPECRAY code has been used to calculate the spectral radiation intensity along a ray for the known profile of the absorption coefficient under the assumption that the medium is in thermodynamic equilibrium and does not scatter radiation.

Due to strong absorption of the MWRSJP power, the discharge ignited in the coaxial waveguide is nonuniform along the waveguide, because the field amplitude decreases by more than one order of magnitude at the waveguide output. It should be noted that the spectral components corresponding to the maximum of the MWRSJP spectrum at the input to the waveguide are practically absent at the waveguide output. In a steady-state discharge maintained by MWRSJP, the main spectral components are damped almost completely due to gas ionization.

The discharge glow decreases substantially with distance from the MWRSJP input and has a filamentary structure.

As the air pressure decreases, the optical radiation spectrum of the discharge shifts toward shorter wavelength range. Thus, at a pressure of 20 Pa, the discharge glow is red, but, as the pressure is decreased by one order of magnitude, the discharge glow becomes blue.

The discharge glow and microwave generation are observed practically over the entire duration of the electron beam pulse in the BPG.

Concluding we can say that results of this work can be used for the development of efficient sources of optical radiation. Also as far as plasma particles responsible for the heat transport are much less collisional than thermal ones, the results might also be of some use in connection with additional plasma heating in nuclear fusion devices due the fact that the radiation source is insensitive to temperature.

The creation of a new type of optical radiation with a quasi-solar spectrum may result in a breakthrough in the field of lighting engineering.

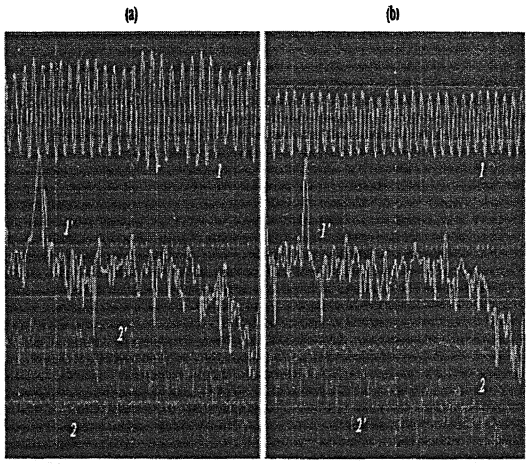

Fig. 1. Waveforms of MWRSJP at the (*1*) input and (*2*) output of the coaxial waveguide, respectively, and local microwave spectra on a logarithmic scale (10 dB/div) at the (*1'*) input and (*2'*) output of the coaxial waveguide, respectively. respectively. The time scale is 5 ns/div, and the voltage scale is 100 (V/cm)/div

References

1. *Berezin, A.K., Fainberg, Ya.B., Artamoshkin, A.M. et al.* The beam-plasma generator of stochastic oscillations of decimeter diapason // Plasma Phys. Rep. 1994. V. 20, No. 9. P. 703-710.

2. *Alisov, A.F., Artamoshkin, A.M., Berdin, S.A. et al.* Low-pressure discharge induced by microwave radiation with a stochastically jumping phase // Plasma Phys. Rep. 2010. V. 36, No. 8. P. 736-749.

3. *Alisov, A.F., Artamoshkin, A.M., Golota, V.I. et al.* Dependence of threshold power for breakedown of the gas pressure in different modes of operation of the generator of microwave radiation with a phase jump // Problems At. Sci. & Tech., Ser. Plasma Electronics & New Accel. Methods. 2008. V. 4, No. 6. P. 199-203.

Study of the Multipactor Avalanche in Two-Wire Transmission Lines

V.E. Semenov[1], E. Rakova[1], J. Rasch[2], D. Anderson[2], J. Johansson[3], J. Puech[4], and M. Lisak[2]

[1]Institute of Applied Physics, Russian Academy of Sciences, Nizhny Novgorod, Russia, sss@appl.sci-nnov.ru
[2]Department of Space and Geophysical Science, Chalmers University of Technology, Gothenburg, Sweden
[3]RUAG Space AB, Gothenburg, Sweden
[4]Centre National d'Etudes Spatiales, Toulouse, France

Currently the multipactor discharge presents an important limiting factor for space born communications. Therefore any design of novel rf components has to include a study of the multipactor threshold. An important example in space applications is the helix antenna, which consists of two helically wound metallic wires (see Fig. 1). Up to recently the multipactor threshold was estimated in these structures using the existing ESA standard [1] which is based mainly on resonance theory and the plane-parallel model. A number of recent papers demonstrated that the ESA standard is not quite applicable to predict the multipactor threshold in many systems with non-uniform rf field (such as hollow [2] and coaxial [3] waveguides, waveguide iris [4], micro-strip lines [5]). However very little attention has so far been given to multipactor breakdown in open antenna structures and the purpose of this paper is to analyze the limits set by multipactor in such antennas by considering a simplified model consisting of two parallel cylindrical wires.

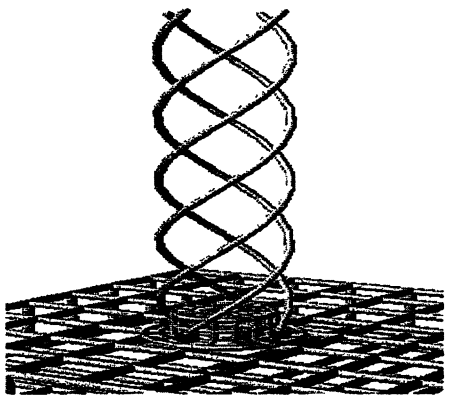

Fig. 1. Configuration of the helix antenna

Under realistic conditions the distance between the wires is considerably larger than the wire radius and the amplitude of the electron oscillations driven by the rf field in the system. This makes it possible (i) to separate drift and oscillatory parts in the electron motion, (ii) to estimate the average impact velocity of the electrons using the polyphase multipactor theory [6]. Specifically, the drift motion is determined mainly by the initial acceleration of the secondary electron in the direction perpendicular to the wire surface. Evidently, a curvature of these surfaces results in a spread of the electron bunch during its passage between the two wires. This spread is accompanied by a decrease of electron density and growth of the multipactor avalanche is possible only when this decrease is balanced by the secondary emission yield. An estimate of the necessary threshold value of the secondary emission yield (SEY), σ_{th}, is very simple for a narrow bunch around the straight line connecting the wire axes in the plane perpendicular to these axes [7]:

$$\sigma_{th} = 1 + d/R \,, \qquad (1)$$

where d and R denote the distance between the wire surfaces and the wire radius respectively. Correspondingly, the multipactor threshold can be expressed as an equality between the averaged (over electron impacts) value of the SEY $\langle\sigma\rangle$ and its threshold value, σ_{th}. In Ref. [7] it was suggested to estimate $\langle\sigma\rangle$ using the average value of the electron impact velocity, $\langle v\rangle$:

$$\langle\sigma\rangle \approx \sigma\left(\langle v\rangle\right) \,, \quad \langle v\rangle = \frac{\int v^2 dt}{\int v dt} \,, \quad v = v_d + v_\omega \cos(\omega t),$$

where v_d denotes the drift velocity, $v_\omega = eE/m\omega$ the amplitude of the electron oscillatory velocity, E the maximum electric field amplitude attained at the wire surface, e, m electron charge and mass respectively and ω the angular field frequency. Taking the maximum possible value of the drift velocity $v_d \doteq v_\omega$, one obtains the following average approximation

$$\langle\sigma\rangle \approx \sigma\left(3v_\omega/2\right) \,, \qquad (2)$$

instead of the equality

$$\langle\sigma\rangle \approx \sigma\left(2v_\omega\right) \,, \qquad (3)$$

used in the resonance theory. To verify the above simple theory, the multipactor avalanche between two parallel wires was simulated numerically using the Monte-Carlo algorithm and Vaughan's approximation for the dependence of the secondary emission yield on electron impact velocity [8]. The simulation results are shown in Figs. 2–4 where the multipactor threshold in terms of the rf voltage amplitude, V, (applied between the wires) is given as a function of the wire radius for different distances between the wires and different parameters of the secondary emission.

When the distance between the wires is small, a spread in initial electron velocity is not important and resonance theory is applicable to estimate the average SEY, as can be seen from Fig. 2. This figure also demonstrates that the above threshold value of the SEY (1) is quite accurate. Nevertheless in Fig. 3 one can see a considerable discrepancy between the simple estimate of the multipactor threshold and the simulation results. This discrepancy is mainly related

to short coming of the approximation $\langle\sigma\rangle \approx \sigma(\langle v\rangle)$ which is caused by the nonlinear dependence of the SEY on electron impact velocity.

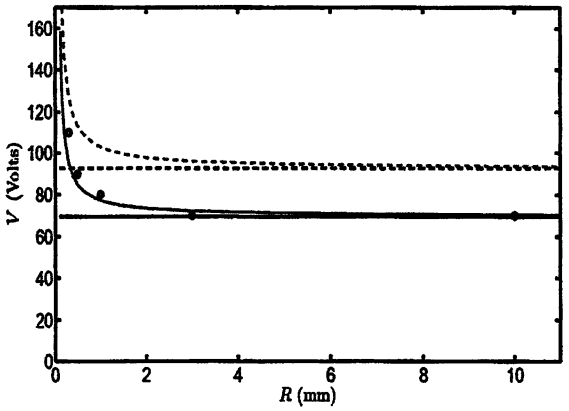

Fig. 2. The threshold voltage, V, vs. wire radius, R, in case of small distance, d = 0.15 mm. Simulation results (circles) are obtained taking ESA standard [1] for the secondary emission yield from silver (maximum SEY = 2.22, the first cross-over point, W_1 = 30 eV) and initial energy of secondary electron, W_0 = 3eV. The solid line shows results of simple estimate ($\langle\sigma\rangle = \sigma_{th}$) taking average approximation (2). The dashed line presents the similar estimate taking resonance approximation (3). The straight solid and dashed lines represent results (resonance and average) of the plane-parallel model

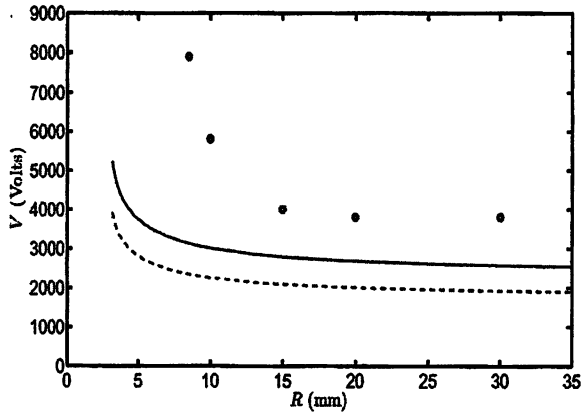

Fig. 3. The threshold voltage, V, vs. wire radius, R, in case of typical distance, d = 3.8 mm. The same SEY parameters and the same notations are used as in Fig. 1

The latter assumption was confirmed in an additional series of simulations where all parameters were taken the same as in Fig. 3 with the exception of the maximum value of SEY which was taken to be 10. In this case the dependence of the SEY on impact velocity is closer to a linear one around the threshold value, $\sigma \approx \sigma_{th}$. The corresponding discrepancy between the simple estimate and the simulation data becomes considerably smaller (see Fig. 4).

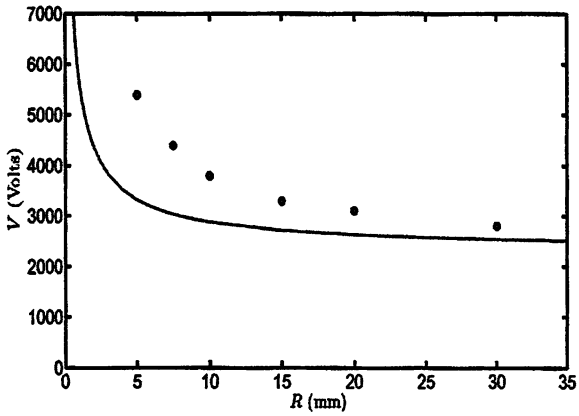

Fig. 4. The threshold voltage, V, vs. wire radius, R, in case of typical distance, d = 3.8 mm. The maximum SEY is taken to be 10 whereas all other parameters and notations are the same as in Fig. 2

References

1. ESA for ECSS, "Space engineering, multipactor design, and test," ESA Publications Division, Noordwijk, The Netherlands, ECSS-E-20-01-01A, 5 May (2003).

2. *Kossyi I.A., Lukyanchikov G.S., Semenov V.E., Rakova E.I., Anderson D., Lisak M., and Puech J.* Polyphase (non-resonant) multipactor in rectangular waveguides // Journal Of Physics D: Applied Physics (J. Phys. D: Appl. Phys.) 41 065203 (p. 1-8) (2008).

3. *Perez A.M., Tienda C., Vicente C., Anza S., Gil J., Gimeno B., Boria V.E., and Raboso D.* Prediction of Multipactor Breakdown Thresholds in Coaxial Transmission Lines for Travelling, Standing, and Mixed Waves // IEEE transactions on Plasma Science, V. 37, No. 10, p. 2031-2040 (2009).

4. *Semenov V.E., Rakova E., Udiljak R., Anderson D., Lisak M., and Puech J.* Conformal mapping analysis of multipactor breakdown in waveguide irises // Phys. Plasmas V. 15, 033501, p. 1-8 (2008).

5. *Semenov V.E., Rakova E.I., Sazontov A.G., Nefedov I.M., Pozdnyakova V.I., Shereshevskii I.A., Anderson D., Lisak M. and Puech J.* Simulations of multipactor thresholds in shielded microstrip lines // J. Phys. D: Appl. Phys. V.42 (2009) 205204 (7 p).

6. *Grishin L.V., Dorofeyuk A.A., Kossyi I.A., Luk'yanchikov G.S., Savchenko M.M.* A study of secondary-emission microwave discharges with large electron transit angles // Lebedev Physics Institute Series (Consultants Bureau, New York, London, 1977), V. 92, p. 63-101.

7. *Rasch J., Anderson D., Johansson J., Lisak M., Puech J., Rakova E., Semenov V.* Microwave multipactor breakdown between two cylinders // IEEE Trans. Plasma Science, V. 38, No. 8, (2010), p. 1997-2005.

8. *Vaughan J. R. M.*, A New Formula for Secondary Emission Yield // IEEE Trans. Electron Devices, V. 36, No. 9, p. 1963-1967, (1989).

On the Thermal Balance of a Small Spherical Microwave Breakdown Region in Atmospheric Air

J. Rasch[1], V.E. Semenov[2], D. Anderson[1], M. Lisak[1] and J. Puech[3]

[1]Chalmers University of Technology, Gothenburg, Sweden, joel.rasch@chalmers.se
[2]Institute of Applied Physics, Nizhny Novgorod, Russia
[3]Centre National d'Études Spatiales, 31401 Toulouse Cedex 9, France

The microwave breakdown of the gas inside transmission systems and other types of RF equipment involves the exponential growth of the number of free electrons in the system due to ionizing collisions of electrons with the neutral molecules of the gas. To this day it remains a serious failure mechanism for any type of high power microwave equipment [1]. Not only because of the noise generated and the changed electromagnetic characteristics of the equipment, but under atmospheric pressure conditions because of the intense heat that is generated in the breakdown region. This heat is caused by the motion of electrons in response to the field coupled with the high frequency of collisions with the neutral molecules. The result is not only the heating of the conducting elements and the direct damage to them, but also the heating of the surrounding gas, the concomitant lowering of the breakdown threshold, and the possible expansion of an initially small breakdown region.

Typically, when there are small protrusions in the conducting parts of the microwave device, these are the most vulnerable sites from the point of view of the risk for microwave breakdown, simply due to the resulting field intensification in the vicinity of the these protrusions. Examples of such irregularities can be tuning screws, welding points, sharp corners etc [2, 3]. In atmospheric pressure Air, microwave breakdown is achieved at 30 kV/cm/Torr, corresponding to the high pressure part of the Paschen curve. The initial breakdown region might be localized completely in an area of field intensification, and initially be quite small. The electron density will rapidly saturate at a level where the internal field in the breakdown region will correspond to the breakdown value. On short time-scales the situation might be stable. However, the motion of the electrons will generate heat and lower the surrounding breakdown threshold, allowing the small breakdown region to expand and consequently generate more heat. The full analytical treatment of this type of non-linear problems is extremely complicated. On short timescales, the electrodynamics of the system will be determined by the intricate interplay between the breakdown region and the external electromagnetic field. And on longer timescales, the heating of the gas will change the dynamics completely. Couple this with suitable boundary conditions and the problem becomes formidable indeed. Computer simulations can indeed model the situation, but for physical understanding simplified scenarios should be analyzed. In Ref. [4] we considered the situation where initially there is a spherical breakdown region in an otherwise homogeneous electric field. The volume of the sphere is assumed to be small in comparison with the wavelength, which allows us to use the quasi-steady approach for the field. At the same time, the sphere is assumed to be much larger than the attachment length $L_a \equiv \sqrt{D/\nu_a}$, where D is the diffusion coefficient, and ν_a is the attachment frequency [5]. This allows us to neglect the process of diffusion inside the sphere, and the electrical field can be approximated as the breakdown threshold field in high pressure Air. This value for the electric field has a temperature dependence, since increasing the gas temperature locally decreases the neutral density and allows the electrons to reach higher energies. The temperature dependence is of the form $E_a(T) \approx E_{a0} T_0 / T$, where E_{a0} is the breakdown field at room temperature, T_0. The electric permittivity, ε, inside the breakdown region is a function of the electron density, and the field is known analytically from $E_a = |3E_0/(\varepsilon+2)|$, where E_0 is the externally applied field. This allows us to express the electron density as a function of the electric field strength and the gas temperature. Consequently, we can derive a heating term valid inside the breakdown region. This heating term will only depend on the temperature, and the equation for the evolution of the gas temperature looks like

$$\frac{\partial}{\partial t}(\rho c_v T) = \nabla(\kappa(t)\nabla T) + q_p(T) \qquad (1)$$

Where $\kappa(T) \approx \kappa_0 (T/T_0)^{3/4}$ is the thermal conductivity of Air [6], ρ is the Air density, c_v the heat capacity of Air at constant volume, and $q_p(T) \approx 3\varepsilon_0 \omega E_0^2 \frac{T_1}{T}\sqrt{1-\left(\frac{T_1}{T}\right)^2}$ is the heating term for the breakdown region. Outside the sphere the heating is zero. The temperature $T_1 = T_0 \frac{E_{a0}}{E_0}$ corresponds to the temperature necessary to achieve breakdown by heating in the external field E_0. ε_0 is the vacuum permeability, and ω is the field frequency in rad/s.

The question is whether the sphere is thermodynamically stable or not. To investigate this we integrate Eq. (1) over the sphere radius, R, and employ the fact that the temperature on the edge of the sphere must be T_1, and the temperature far away must be T_0. We get $\frac{\partial W_{total}}{\partial t} = -Q_{loss} + Q_{Joule}$, where $Q_{loss} \propto R$ is the heat lost over the edge of the sphere, and

$Q_{Joule} \propto R^3$ is the heat generated in the sphere. The two terms are plotted in Fig. 1.

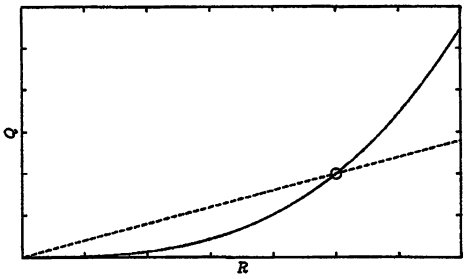

Fig. 1. The dependence on radius for the heat loss term (dashed line), and the heat generation term (solid line)

It is clear from the figure that any deviations from the point of equilibrium (marked by a circle) will lead to instability. If the radius decreases below the equilibrium value, less heat will be generated than what is lost over the edge and the sphere will cool down and contract. If the radius increases from the critical value, more heat is generated inside than what can be transported over the edge, and the sphere will expand.

The critical radius can be expressed as

$$R_{crit} = \sqrt{\frac{8\kappa_0 T_0}{7\varepsilon_0} \frac{((E_{a0}/E_0)^{7/4} - 1)}{\omega E_{a0}^2} (E_{a0}/E_0)^2}$$

and evaluated for any combination of parameters. For example, in room temperature at atmospheric pressure, when $E_{a0}/E_0 \approx 3$, and $\omega = 10^5$ Hz we get $R_{crit} \approx 0.1$ cm. Increasing the frequency decreases the radius, and for GHz values the radius will be below the attachment length. This implies that in the range of sizes between the attachment length and the wavelength in a microwave system, no stable breakdown region can exist inside a homogeneous field. However, it does not tell us if there might be stable situations at smaller sizes, where diffusion is important, or what happens close to very small field enhancements, where experiments seem to imply the existence of stable discharges.

Although the model is approximate, we can use the values given by the critical radius to determine safe sizes for areas of intensified heating or field strength inside otherwise homogeneous microwave systems. This can be a very useful consideration in the design of RF equipment, in order to avoid full scale breakdown.

References

1. *A.D. MacDonald.* Microwave Breakdown in Gases // John Wiley and Sons, New York (1966).

2. *Rasch, J., D. Anderson, M. Lisak, V. E. Semenov and J. Puech.* Gas breakdown in inhomogeneous microwave electric fields // J. Phys. D: Appl. Phys. 2009. V. 42. 205203.

3. *Cohn, S.B.* Rounded corners in Microwave High-Power Filters and Other Components // IRE Transactions on Microwave Theory and Techniques. 1961. V. 9. 389.

4. *Rasch, J., Semenov V.E., Anderson D., Lisak M., and Puech J.* On the microwave breakdown stability of a spherical hot spot in air // J. Phys. D: Appl. Phys. 2010. V. 43, 325204.

5. *Raizer, Yu.* Gas Discharge Physics // Springer. Berlin. (1991).

6. *Zykov, N.A., Semast'yanov, R.M., Voroshilova, K.I.* Transport properties of nitrogen, oxygen, carbon dioxide, and air low pressures and temperatures from 50 to 3000 K // Journal of Engineering Physics and Thermophysics. 1982. V. 43. 762.

Multipactor Breakdown Prediction on a Dielectric: Effects of RF Magnetic Field and Finite Geometry

A.G. Sazontov[1], V.E. Nechaev[1], N.K. Vdovicheva[2]

[1]Institute of Applied Physics, RAS, Nizhny Novgorod, Russia, sazontov@hydro.appl.sci-nnov.ru
[2]Institute of Physics of Microstructures, RAS, Nizhny Novgorod, Russia

Multipactor discharge on a dielectric is an important mechanism of the rf window failure in powerful microwave systems (see, e.g. [1–3]). This phenomenon is commonplace and influences significantly operation of powerful microwave devices. Most of the publications on this problem did not take into account the action of the rf magnetic field component on the electron motion as well as effects of finite geometry. In this context it is worth commenting that the potential importance of the rf magnetic field on the multipactor initiation was discussed first by Neuber *et al.* [2] who revealed that the rf magnetic force pushes high energy secondary electrons to the emission surface and plays a role of restoring force. Later, Valfells *et al.* [3] briefly examined the electromagnetic effects on the structure of the susceptibility diagram under qualitative considerations.

This paper presents the results of a statistical theory for quantitative prediction of how the rf magnetic field and space limitation of transmission window affect the multipacting discharge cutoff conditions.

The geometry of the problem is shown in Fig. 1. A secondary electron emitted at time t_0 from the dielectric surface $(x=0)$ with random velocity v_0 is subjected to the forces imposed by the rf and dc fields. The electromagnetic field is characterized by its components, $E_y(x,t)$ and $H_z(x,t)$ (depending on the propagation coordinate x and time t):

$$E_y(x,t)=E_{rf}\cos(\omega t+kx), \quad H_z(x,t)=-E_y(x,t).$$

Here, E_{rf} is the rf electric field amplitude, ω is the angular frequency, and $k=\omega/c$ is the vacuum wave number (c is the velocity of light). The static electric field E_{dc} (that may result from dielectric charging) acts in the x-direction as shown in Fig. 1. The characteristic window size is designated by a.

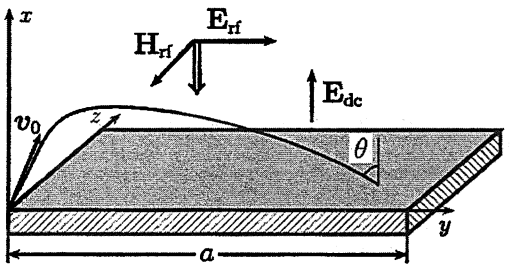

Fig. 1. Geometry of the problem

In what follows, the distribution function for the random initial velocity v_0 of the emitted electrons is assumed to be of the form: $f(\mathrm{v}_0)=\frac{2v_{0x}}{\pi v_{0m}^4}\exp\left(-\frac{v_0^2}{v_{0m}^2}\right)$, where v_{0m} is effective thermal velocity and is related to the most probable emission energy W_{0m} as $W_{0m}=0.5mv_{0m}^2$.

The dependence of the secondary electron yield σ on the impact energy W_i and the impact angle θ is adopted from Vaughan's empirical formula:

$$\sigma=\sigma_{max}\left(1+\frac{k_s\theta^2}{2\pi}\right)[w(1-w)]^{k(w)},\ w=\frac{W_i}{W_{max}}\left(1+\frac{k_s\theta^2}{\pi}\right)^{-1},$$

where σ_{max} is the maximum value of σ, W_{max} being the impact energy which yields σ_{max}, k_s is a surface smoothness factor, $k(w)=0.62$ for $w<1$, and $k(w)=0.25$ for $w>1$.

In this paper, we set $k_s=1$ representing a typical dull surface, $W_{max}=400$ eV, and $W_{0m}=2$ eV.

The governing non-relativistic force equation describing the electron motion in a vacuum half-space $x\ge 0$ possess the following integrals:

$$\begin{aligned} &mv_y-\frac{e}{c}A(x,t)=\text{const}, \quad \mathrm{mv}_z=\text{const},\\ &W+cmv_x+eE_{dc}(x+ct)=\text{const}, \end{aligned} \tag{1}$$

where $A(x,t)=E_{rf}k^{-1}\cos(\omega t+kx)$ is the vector potential of the rf field, W is electron kinetic energy, m and $-e$ stand for electron mass and charge, respectively. These integrals of motion completely describe the electron dynamics. In particular, the normal component of the electron trajectory can be found from Eqs. (1) in parametric form (ξ is parameter):

$$x(\xi)=c\xi-c\int_{\xi_0}^{\xi}\frac{d\zeta}{\sqrt{(1+v_{0x}/c)^2-2U(\zeta)/mc^2}},\ t(\xi)=\xi-\frac{x}{c}, \tag{2}$$

where $U(\xi)=ecE_{dc}(\xi-\xi_0)+\frac{e^2}{2mc^2}[A(\xi)-A(\xi_0)]^2$ is the potential caused by the dc and rf fields. (In writing $U(\xi)$ it is taken into account that for the majority of practical situations $v_{0y}\ll v_{rf}$, where $v_{rf}=eE_{rf}/m\omega$ is the oscillatory velocity.) The time flight t_i is then obtained by letting $x=0$ in Eq. (2). Notice that the corresponding transit time depends on v_{0x}, E_{rf}, E_{dc}, and initial phase $\varphi_0=\omega t_0$ as on parameters.

Knowledge of the arrival time makes it possible to estimate the impact energy and the impact angle, both of which determine the yield.

As an example, Fig. 2 depicts the impact energy *vs* the rf amplitude at $E_{dc}/E_{max}=10^{-3}$ and $\varphi_0=75°$. (The normalization parameter $E_{max}=\omega\sqrt{2mW_{max}/e}$ is

used for electric fields.) This energy is compared to the one obtained by ignoring the rf magnetic field (dashed curve).

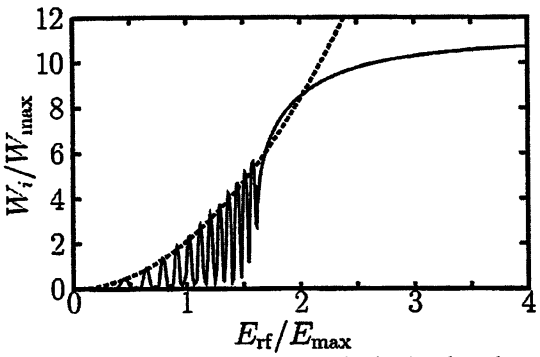

Fig. 2. Impact energy *vs* rf amplitude in the absence (dashed) and in the presence (solid) of rf magnetic field

It can be seen, that under the approximation $H_{rf}=0$ the impact energy increases monotonically and scales as E_{rf}^2, while the action of the rf magnetic field leads to saturation in the energy gain of the multipactoring electrons. The saturation level W_i^{sat} depends only on the initial velocity, i.e., $W_i^{sat}=3mv_{0x}c$. For typical electron emission energy of a few eV the maximum possible value of impact energy is of order 5–10 keV. It is worth commenting that if W_i^{sat} is lower than the second crossover energy, the upper susceptibility boundary is eliminated.

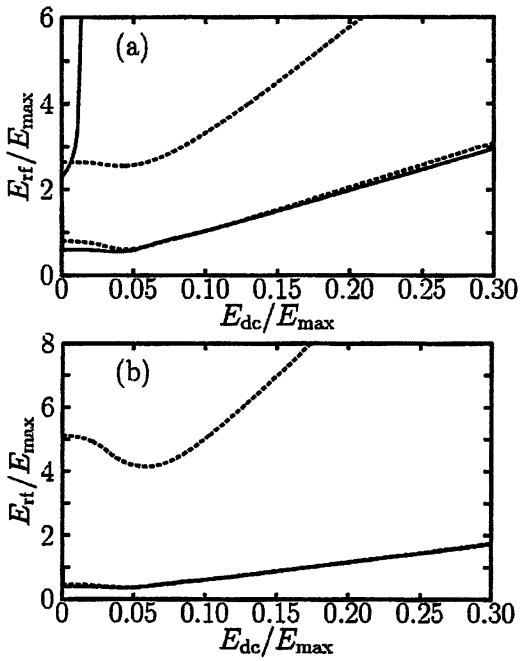

Fig. 3. (a) Susceptibility diagram in the absence (dashed) and in the presence (solid) of rf magnetic field for $\sigma_{max}=1.3$ and (b) for $\sigma_{max}=2$

To predict the multipactor induced breakdown we extend the statistical treatment proposed in Ref. 4 to the subject of interest. The calculation employs the integral equation allowing determining the threshold of multipactor growth.

Figure 3 displays the susceptibility curves in the absence (dashed) and in the presence (solid) of the rf magnetic field effects for two selected values of σ_{max}. It is observed distinctly from this figure that the rf magnetic field qualitatively changes the multipacting discharge cutoff conditions (in comparison with the ones predicted from the theory ignoring the spatial variation of the incident electromagnetic wave) and, depending on the secondary electron yield, leads either to rising of the slope of the upper boundary (Fig. 2a) or to its complete elimination (Fig. 2b). It should be emphasized that the conclusion concerning the elimination of the upper boundary (as well as the saturation of the impact energy) were made first by Valfels *et al.* [3] under qualitative considerations.

The results presented in Fig. 3 have been obtained for unbounded emission surface model. The problem of finding the condition of multipactor initiation on a transmission window with a finite spatial size essentially differs from the traditional approach which ignores the tangential electron motion along the window. For the scenario considered some fraction of the emitted electrons (with the longest time flight) will be lost from the discharge and such a process will significantly alter the threshold multipacting characteristics.

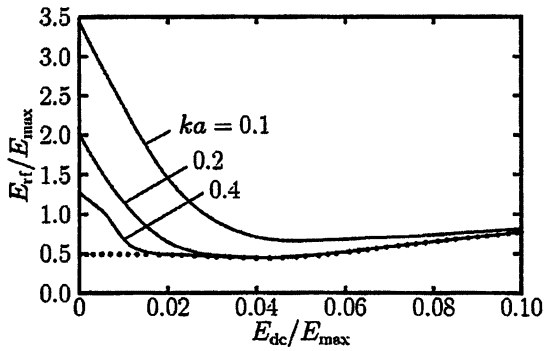

Fig. 4. Susceptibility diagrams for $\sigma_{max}=2$ and several values of ka. Dotted line corresponds to the case $ka\to\infty$

Figure 4 shows the susceptibility diagram for various values of ka. Thus, it is evident from this figure, that the effect of finite geometry is especially strong in the range of weak dc field (at the initiation stage): the decrease of the window wave size gives rise to the growth of its electric strength.

References

1. *Kishek, R.A., Lau, Y.Y.* Multipactor discharge on a dielectric // Phys. Rev. Lett. 1998. V. 80, No. 1. P. 193-196.

2. *Neuber, A., Hemmer, D., Krompholz, H., Hatfield, L., and Kristiansen, M.* Initiation of high power microwave dielectric interface breakdown // J. Appl. Phys. 1999. V. 86, No. 3. P. 1724-1728.

3. *Valfells, A., Ang, L.K., Lau, Y.Y., Gilgenbach, R.M.* Effect of an external magnetic field, and of oblique radio-frequency electric fields on multipactor discharge on a dielectric // Phys. Plasmas. 2000. V. 7, No. 2. P. 750-757.

4. *Vdovicheva, N.K., Sazontov, A.G., Semenov, V.E.* Statistical theory of two-sided multipactor // Radiophysics and Quantum Electronics. 2004. V. 47, No. 3. P. 580-597.

Space-Charge and RF Magnetic Field Effects on Multipactor Development on a Dielectric

V.E. Nechaev and A.G. Sazontov

Institute of Applied Physics, RAS Nizhny Novgorod, Russia, sazontov@hydro.appl.sci-nnov.ru

The present paper gives a statistical analysis of multipactor development on a dielectric. It focuses on how the combined action of the space charge and rf magnetic field affects the temporal evolution of the discharge. To predict the multipactor characteristics we extend the theoretical treatment proposed in [1, 2] to the subject of interest.

We consider a single-surface multipactor discharge on a dielectric exposed to a circularly polarized electromagnetic field which is parallel to that surface and a dc electric field normal to the surface that will be present if the dielectric accumulates any charge. In general, the rf field is a combination of the incident and reflected waves. The vector potential $\mathbf{A}(x,t)$ of this wave field (depending on propagation coordinate x and time t) has the form

$$A_y + iA_z = \frac{E_{rf}}{k}[\exp i(\omega t + kx) - R\exp i(\omega t - kx)]. \quad (1)$$

Here E_{rf} is the electric field amplitude, ω is the angular frequency, $k = \omega/c$ is the wave number (c is the velocity of light), R is reflection coefficient. Notice that the discharge driven by waves of this kind will be polyphase at all the stages (transit time and impact energy do not depend on the rf phase).

Electrons are injected at time t_0 from the dielectric surface $(x=0)$ with a random velocity v_{0x} are subjected to the forces imposed by the rf and dc fields. The distribution function in the initial velocity of the emitted electrons is assumed to be of the form: $f(v_{0x}) = \frac{2v_{0x}}{v_{0m}^2}\exp\left(-\frac{v_{0x}^2}{v_{0m}^2}\right)$, $v_{0m} = \sqrt{2W_{0m}/m}$, where W_{0m} the most probable emission energy and m stands for the electron mass.

As a result of secondary emission the dielectric gains the positive charge which creates the instantaneous dc electric field. The corresponding dc field is spatially dependent and specific form of its profile is determined by the distribution function of emitted secondary electrons [1].

The electron motion in a vacuum half-space $x \geq 0$ is described by the force equation

$$\ddot{x} = -\frac{\partial U_{\text{eff}}(x,t)}{\partial x},$$

$$U_{\text{eff}}(x,t) = e\varphi(x) + \frac{e^2}{2mc^2}[\mathbf{A}(x,t) - \mathbf{A}(0,t_0)]^2,$$

where $\varphi(x)$ is the electrostatic potential caused by the dc field and $\mathbf{A}(x,t)$ is given by Eq. (1). It is evident that the multipactor development occurs when the injected electrons strike back to the emission surface after a finite time of flight t_i defined from the condition $x(t_i) = 0$. The corresponding transit time t_i depends on v_{0x}, E_{rf}, and the surface electric field E_0 as on parameters, i.e.,. $t_i = t_i(v_{0x}, E_{\text{rf}}, E_0)$.

To calculate the secondary electron emission caused by the flux of incident electrons we use Vaughan's empirical formula:

$$\sigma = \sigma_{\max}\left(1 + \frac{k_s\theta^2}{2\pi}\right)[w(1-w)]^{k(w)},\ w = \frac{W_i}{W_{\max}}\left(1 + \frac{k_s\theta^2}{\pi}\right)^{-1},$$

where $\sigma_{\max}$ is the maximum value of σ, $W_{\max}$ being the impact energy which yields $\sigma_{\max}$, k_s is a surface smoothness factor, $k(w) = 0.62$ for $w < 1$, and $k(w) = 0.25$ for $w > 1$.

The temporal behavior of the electron density N per unit area is described by equation

$$\frac{dN}{dt} = (\sigma_{\text{eff}} - 1)\frac{N}{\bar{t}_i}, \quad (2)$$

where $\bar{t}_i = \int_0^\infty t_i(v_{0x}, E_{\text{rf}}, E_0) f(v_{0x}) dv_{0x}$ is the mean transit time and $\sigma_{\text{eff}} = \int_0^\infty \sigma(v_{0x}, E_{\text{rf}}, E_0) f(v_{0x}) dv_{0x}$ is the effective secondary yield. These parameters depend on the electric field strengths. Notice also that the surface electric field E_0 is related to N as: $E_0 = 4\pi eN$, where e is the electron charge.

For the simulations, we use the following parameters: $f = 10$ GHz, $W_{\max} = 400$ eV, $\sigma_{\max} = 2$, $k_s = 1$, and $W_{0m} = 2$ eV. The initial value of the surface electric field is taken to be 10 V/cm.

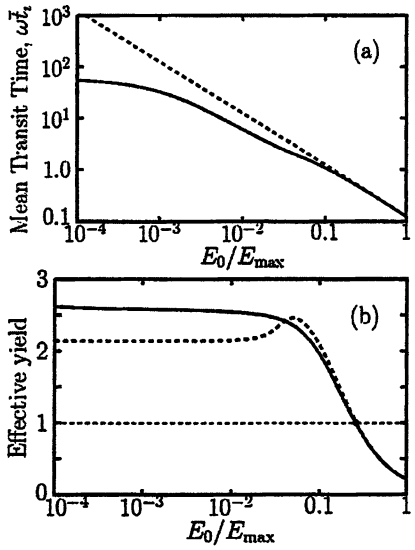

Fig. 1. The mean transit time (a) and effective yield (b) as a function of the surface dc electric field for $E_{\text{rf}}/E_{\max} = 1$

From Eq. (2) it follows that to calculate the temporal electron dynamics for a given rf field amplitude it is necessary to evaluate how $\bar{t}_i$ and σ_{eff} vary with the surface dc field.

Figure 1 demonstrates the dependence of the quantities of interest *vs* E_0 for $E_{rf} = 40$ kV/cm and $R = 0.2$. with and without rf magnetic field effects (the normalization parameter $E_{max} = \omega\sqrt{2mW_{max}/e}$ is used for electric fields). It can be seen, that the effect of the rf magnetic field is especially strong in the range of weak dc field.

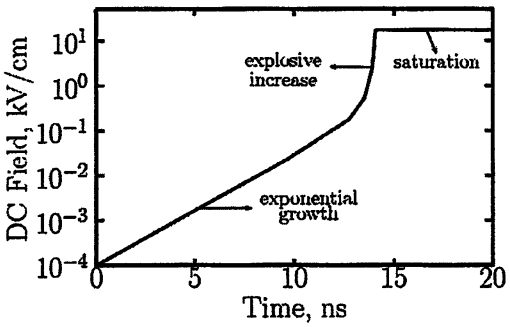

Fig. 2. Temporal evolution of multipactor discharge for $E_{rf} = 40$ kV/cm and $R = 0.2$.

Figure 2 shows the multipactor evolution for $E_{rf} = 40$ kV/cm and $R = 0.2$. At the beginning (when the average transit time and effective yield are almost constant) the electron density grows exponentially. At this stage (which is the longest one) the rf magnetic field force is significant in comparison to the electrostatic force and plays a primary role in the multipactor development. Then, as the number of secondary electrons builds up, dc field grows, and the action of electrostatic force and magnetic force supplement each other leading to explosive instability (due to sharp decreasing of the transit time between impacts). Finally, the charging field becomes very strong, and the multipaction process reaches a saturation condition, when the effective secondary yield has a mean value of unity. The average rf power delivered to the dielectric also grows to a maximum value at saturation. The corresponding saturation level as a function of E_{rf} is shown in Fig. 3.

Figure 4 displays the total time of the discharge development *vs* rf field amplitude for two selected values of R. It is worth commenting that the time required for saturation and the saturation level itself depends significantly on the value of reflection coefficient: with increasing R the characteristic time required to achieve the steady state decreases and the corresponding level becomes smaller.

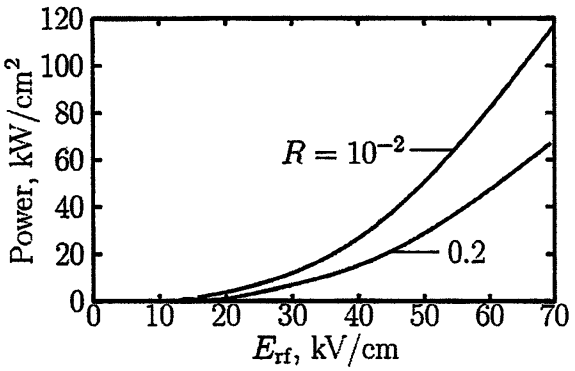

Fig. 3. Average power deposited onto the dielectric *vs* rf field amplitude at sarutation

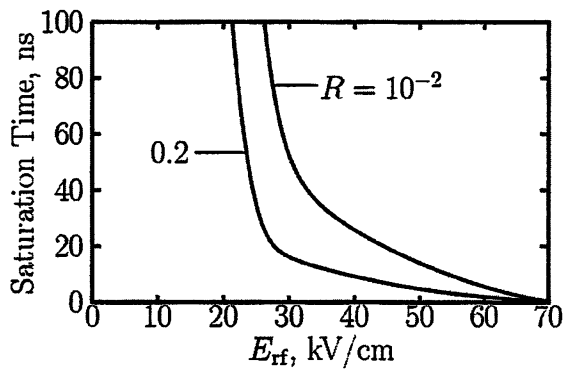

Fig. 4. Total time of the discharge development as a function of rf field amplitude and two selected values of R

Thus, it is found that the rf magnetic field alters the temporal evolution of the discharge leading to the acceleration of the electron avalanche and the shielding effect is responsible for the saturation level.

References

1. *Valfells, A., Verboncoeur, J.P., Lau, Y.Y.* Space-charge effects on multipactor on a dielectric // IEEE Trans. Plasma Sci. 2000. V. 28, No. 3. P. 529-536.

2. *Sazontov, A.G., Nechaev, V.E.* Effects of rf magnetic field and of wave reflections on multipactor discharge on a dielectric // Phys. Plasmas. 2010. V. 17, P. 033509-1 – 033509-9.

CVD Diamond Torus Windows for ITER ECRH – Prototype Design and Experimental Investigations

S. Schreck[1], T.A. Scherer[1], D. Strauss[1], A. Meier[1],
K. Sakomoto[2], K. Takahashi[2], K. Kajiwara[2], Y. Oda[2], G. Saibene[3]

[1]Karlsruhe Institute of Technology KIT, Institute for Applied Materials, IAM (AWP), Eggenstein-Leopoldshafen, Germany, sabine.schreck@kit.edu
[2] Japan Atom Energy Agency (JAEA), Plasma Heating Technology Group, Naka, Japan
[3]Fusion for Energy, Barcelona, Spain

Ultra low mm-wave loss CVD diamond windows are required for the ITER ECRH system, which consists of EC launchers at the upper and the equatorial level [1, 2, 3]. The torus window assemblies are part of the primary vacuum boundary and act as the first tritium barrier. They have to fulfil adequate transmission capability for the high mm-wave power guided into the launcher. The window assembly consists of a diamond disk integrated into a metallic housing. High power RF experiments with a window prototype had shown additional parasitic heating due to small gaps in the housing [4, 5]. An optimized design was developed to minimize these effects; high power experiments at the JAEA gyrotron facility have shown a minimization of the higher order mode excitation in the cavities. The design of both prototypes and the corresponding results of low and high power measurements will be presented.

Design of the CVD diamond window prototypes

The torus window assemblies consist of a low loss diamond disks produced by 'Microwave Plasma Assisted (MPA)' chemical vapour deposition (CVD) brazed to a cooper cuff and integrated into a metallic housing. In Fig. 1 the CAD design of window prototypes I and II is shown.

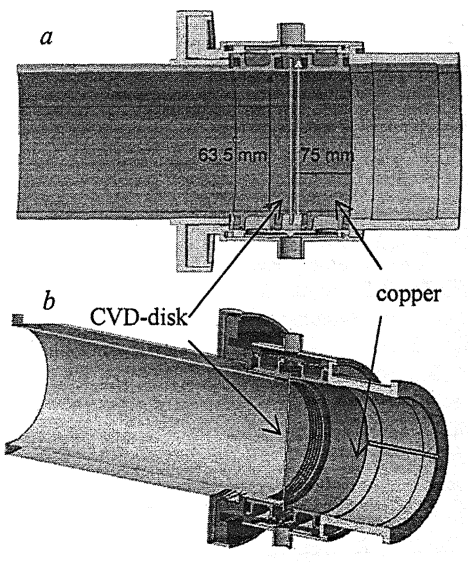

Fig. 1. CAD design of a) prototype I and b) prototype II

For both prototypes an indirect cooling concept was chosen. The cooling circuit formed by two symmetric cooling chambers is separated by a vacuum segment at the edge of the diamond disk. As the high power experiments of prototype I had shown parasitic mode generation and heating of the window a changed design due to improved RF behaviour was developed. By using a waveguide insert, the small gaps (50–100 μm) between the copper cuff and the SS waveguide were covered (illustrated in Fig. 1*b* for the torus side of the window assembly).

The CVD diamond disks have a diameter of $d = 75$ mm and a thickness of $t = 1.1$ mm. The disk for prototype I was grown by ElementSix (Cuijk, Netherlands) and disk II was manufactured by Diamond Materials (Freiburg, Germany).

Experiments and results

At KIT, a dedicated measurement facility (Fabry – Perot – resonator) is available to investigate the dielectric loss and its lateral homogeneity using open resonator setups [6, 7]. The distribution of the dielectric loss of the bare disk is parameterized with a hemi-spherical measurement set-up and the loss tangent at the center of the bare disk is evaluated in a symmetric resonator with two spherical mirrors. In the latter case also complete window assemblies can be measured.

The bare prototype I-disk had shown at 170 GHz a low effective loss at the centre of $\tan\delta = 0.9 \cdot 10^{-5}$ and after brazing a loss tangent of $\tan\delta = 3.4 \cdot 10^{-5}$.

For the Diamond Materials disk the result of the dielectric loss mapping at 145 GHz is shown in Fig. 2.

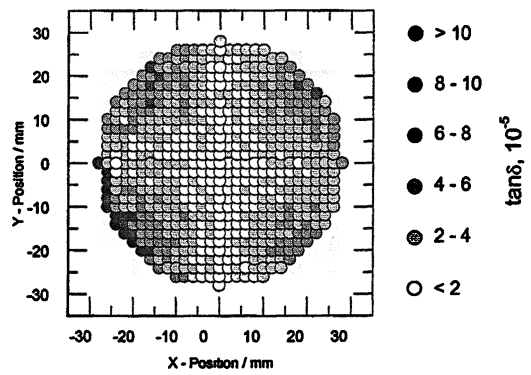

Fig. 2. Dielectric loss mapping of the bare diamond disk II (Diamond Materials) measured at 145 GHz

In the center of this bare disk a very low effective loss of $\tan\delta = 0.4 \cdot 10^{-5}$ was determined for the resonant frequency of 170 GHz. After the brazing the value of diamond disk II was increased slightly to $\tan\delta = 0.55 \cdot 10^{-5}$.

The high power RF experiments of the prototypes have been carried out at the JAEA gyrotron test side within different experimental campaigns. The applied maximum power was 520 kW @ 170 GHz. One side of the window unit was evacuated and mounted to the supply waveguide from the gyrotron source and the opposite side was in air. After a free air transit the RF power was dissipated in a dummy load. IR thermography was used to investigate the temperature distribution over the diamond disk. Additional thermocouples (T/C) were fixed to the housing.

Fig. 3, *a* and *b* show the temperature behaviour of prototype I for a 520 kW/30 s pulse. The temperature distribution at the window surface was not a center peaked distribution and therefore it was assumed that RF wave propagated with some percentage of high order modes. So the beam profile at the end of the waveguide after passing several mitre bends was not purely HE_{11}. Additional parasitic cavity heating can be expected in this case and is an obvious source for the observed additional heating of the housing (point C and thermocouple measurement).

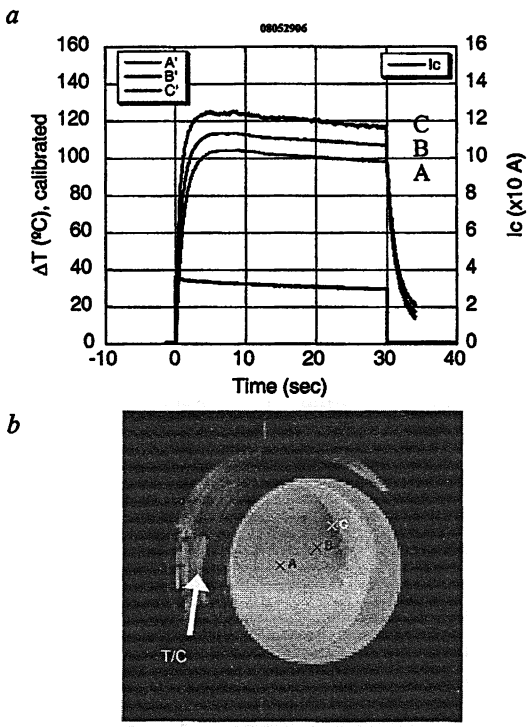

Fig. 3. IR measurements for prototype I during pulse operation (520 kW/30s): a) Temperature/time dependence and b) IR image (at the end of the pulse)

For the optimized prototype II no significant temperature increase on the diamond disk was measured during high power RF experiments (500 kW@ 170 GHz) with pulses up to 20 s neither in the IR measurement nor by thermocouples. To illustrate the behaviour a typical video camera picture and the corresponding IR image is shown in Fig. 4.

The observed visible star lights are usual and well known and caused by the typical hydrocarbon surface bonds. No additional heating of the housing could be detected during the experiments. In the case of the experimental campaign for the prototype II a field pattern measurement was performed using a sheet of paper fixed on the top of the diamond disk (atmospheric side). Based on this field pattern the transmitted modes were estimated as 88.6 % HE_{11}, 0.9 % HE_{12}, 4.6 % (HE_{21}+TM_{02}) and 2.1 % (HE_{21}+TE_{01}).

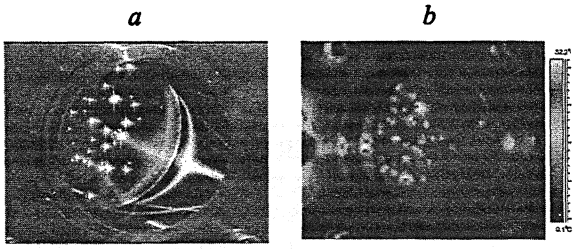

Fig. 4. Prototype II during pulse operation: a) video camera picture and b) IR image with temperature scale

It can be concluded that the sensitivity to parasitic higher order modes, which was observed for prototype I, is minimized for prototype II. Therefore the "mode-problem" can be considered as solved. For prototype II a very low loss tangent was measured at 170 GHz for low and high RF power. Further investigations with longer pulses and increased power are planned, which require an evacuation of both sides of the diamond window assembly.

Acknowledgement

This work was partly supported by Fusion for Energy under the contract No. F4E-2010-OPE-140. The views and opinions expressed herein reflect only the author's views. Fusion for Energy is not liable for any use that may be made of the information contained therein.

References

1. *M.A. Henderson, et al.,* Overview of the ITER EC upper launcher // Nucl. Fusion **48,** (2008) 054013.

2. *P. Späh, et al.,* Design and analysis of struct. comp. in the ITER ECH upper port plug // Fus. Eng. Design **82** (2007) 700.

3. *K. Takahashi, et al.* Progress on Design and Development of ITER Equatorial Launcher // Fusion Science a. Techn. **52** (2007). P. 266-280.

4. *T.A. Scherer et al.* Recent Upgrades of the ITER ECRH CVD Torus Diamond Window Design and investigations of Dielectric Diamond Properties // Proc. EC-16, Sanya, China, 2010.

5. *T.A. Scherer, et al.,* Design aspects and RF characterization of ITER-RF-CVD Diamond windows // Proc. EC-15, Yosemite, (CA) USA, 2008, P. 502-508.

6. *R. Heidinger, et al.,* CVD diamond windows studied with low- and high-power millimeter waves // IEEE Trans. Plasma Sci., v. 30, no. 3, p. 800–807, Jun. 2002.

7. *I. Danilov, R. Heidinger,* New approach for open resonator analysis for dielectric measurement at mm-wavelength // J. Europ. Cer. Soc., 23 (2003). P. 2623-2626.

Action of the High-Power Pulsed RF Radiation on the Micro- and Nano-objects in Dielectric Media

S.N. Sedykh[1], V.G. Baev[2], Yu.A. Fedotova[2], I.I. Golubev[1], S.M. Golubykh[1], A.K. Kaminsky[1], Yu.A. Kovalev[1], A.P. Kozlov[1], I.A. Kryachko[1], A.I. Lesnikovich[2], I.A. Milevich[2], E.A. Perelstein[1], S.I. Tyutyunnikov[1], V.A. Vdovin[3]

[1]Joint Institute for Nuclear Research, Dubna, Russia, snsed@yandex.ru
[2]Belarussian State University, Minsk, Republic of Belarus
[3]Kotel'nikov Institute of Radio-engineering and Electronics of RAS, Moscow, Russia

Brief history of the question

The 30 GHz free-electron maser with the output power of 20 MW, pulse duration of 170 ns and repetition rate up to 1 Hz has been created several years ago in JINR, Dubna, in close collaboration with Institute of Applied Physics, Nizhny Novgorod [1]. It is now used in different research programs [2]. One of them proposes selective destruction of cancer cells in conditions of saturation of the cancer tissue by RF adsorbing media. First promising results have been reported at that conference 3 years ago [3]. This report is devoted to the progress and new ideas in that direction.

Main ideas of the project

We try to convert the features of our facility into the advantages for the developing method. The features are small mean power (1) and high pulse power (2) of the radiation, small pulse duration (3), wavelength in cm region (4).

(1) The stored RF energy is 2–3 J per pulse depending on the FEM regime, so the mean power of the radiation is not more than 3 W. It is small enough to be absolutely safe for living tissue in absence of the local absorbers. Our control experiments have proved it many times.

(2) Our wave beam can be focused into the spot with the diameter about the wavelength, i.e. 1 cm. So the power density can reach the value of 20 MW/cm^2, more than air breakdown threshold. The breakdown into the dielectric media can start at the similar electric fields. It means that we can use not only the Joule heating of the conductors in RF field, but breakdown effects such as field electron emission and explosive electron emission as the possible ways of the RF-wave energy conversion.

(3) The distance of the heat transfer during 170 ns is only several microns even in the copper, and it will be much smaller in organic tissue. It is small with respect to the size of the cancer cell (typically 10 microns). So the action of the temperature rise of the absorber will be local. If the absorber is selectively delivered to the cancer cells by the biochemical method, other tissue will be not damaged.

(4) Frequency of the FEM oscillator is in the common region of the ferromagnetic resonance [4]. This effect can be used for further increasing of the RF energy absorption if the media are ferromagnetic clusters.

Choice of the adsorbing media

One of the key problems of the project is the choice of the efficient wave energy absorbers, which size is small enough to allow delivering to the cancer by biochemical methods. We present experimental results on RF irradiation of conducting and ferromagnetic clusters in media with different dielectric permittivity, including ferromagnetic liquids.

Degradation of metal nano-layers on polymer films during irradiation is also studied, because such films were used in the successful experiments on cancer cell destruction [3].

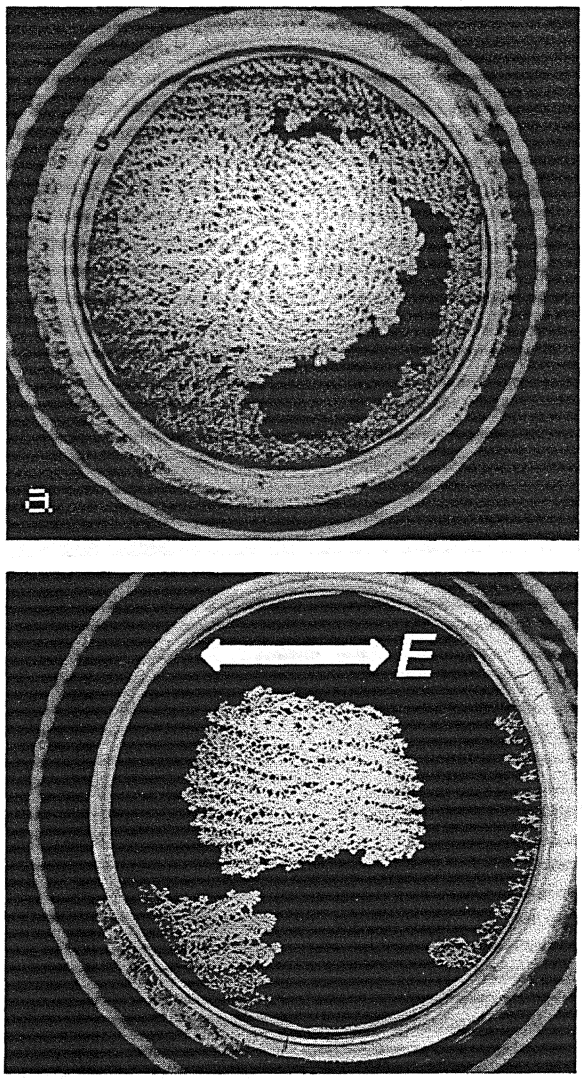

Fig. 1. Metallized polymer film irradiated in alcohol using circularly-polarized (a) and linearly-polarized (b) RF wave

To investigate the role of different channels of RF wave energy absorption we irradiate metallized films immersed in the media with different dielectric permittivity (transformer oil, castor oil, alcohol, distilled water). We compare circularly-polarized and linearly-polarized wave have to see the correlation between metal layer degradation and electric field direction (example on the Fig. 1). Direction of the metal degradation is parallel to the electric field plane, it allows us to reduce the number of possible effects. Special interest is an anomalous absorption (up to 50 %) of the electromagnetic wave in the metal layer with the thickness about 3 nm [5]. It is the result of the effective decreasing of the metal conductivity when the layer thickness is less than the free length of the electrons in solid metal.

Measurement of the absorption efficiency

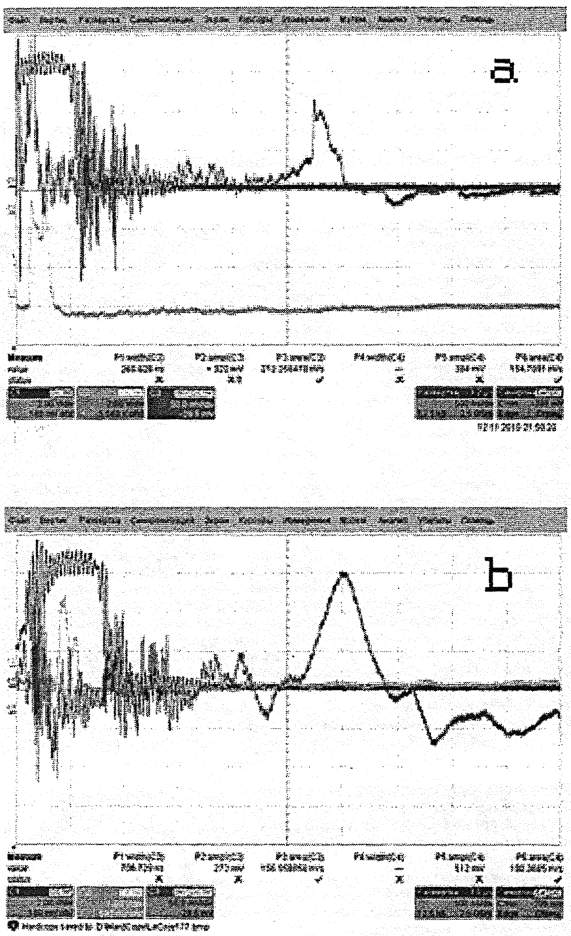

Fig. 2. Signals from thermo-acoustic sensor (pulse in the center): RF radiation is adsorbed by thin metal layer on the input window (*a*) or by distilled water (*b*)

Another key point of the project is the diagnostics of the absorption efficiency. The possible solution is the use of thermo-acoustic RF sensor similar to [5]. The main detail of the sensor is a cylindrical volume filled with liquid (distilled water or alcohol). One face of the cylinder is a quartz window with metal coating about 3 nm thick, absorbing not less than 50% of the wave energy. The opposite face contains an acoustic sensor. The absorbed RF-wave energy causes quick heating of the absorber and hence the sound wave in the liquid. Acoustic signal is delayed with respect to the RF pulse on few microseconds required for sound to reach the acoustic sensor. The delay reduces parasitic signals from high-power facility. If the absorber is the metal layer on the input window, shape of the acoustic signal is similar to the shape of the RF power. If the absorber is the liquid itself, duration of the rise-up of the acoustic signal multiplied by the sound speed in the liquid shows the depth of the layer when the RF energy is fully absorbed (Fig. 2). If the liquid is the colloidal solution of metal clusters or the suspension of ferromagnetic clusters, the signal shape depends on the efficiency of the RF absorption by the clusters. It is very important that the measurements are fulfilled at megawatt power level, so all possible ways of the energy absorption by clusters are taken into account.

Acknowledgements. This project is supported by Russian Foundation for Basic Research, grant # 09-08-00743-a.

References

1. *Ginzburg, N.S., Kaminsky, A.A., Kaminsky, A.K. et al.* High-Efficiency Single Mode FEM-oscillator based on a Bragg Resonator with Step of Phase of Corrugation // Phys. Rev. Lett. 2000. V. 84, Issue 16. P. 3574–3577.

2. *Kaminsky, A.K., Perelshtein, E.A., Sedykh S.N. et al.* Powerful 30-GHz JINR-IAP FEM: Resent results, prospects and applications // Proc. of the 31st Int. FEL Conf., Liverpool, UK, 2009. P. TUPC76.

3. *Besedin, S.P., Kaminsky A.K., Komova O.V. et al.* Experiments on application of high-power microwave radiation to biomedicine using micro- and nanoparticles // Strong Microwaves: sources and applications, edited by A. G. Litvak. Nizhny Novgorod: Institute of Applied Physics. 2009. V. 2. P. 524–528.

4. *Kittel, C.* On the Theory of Ferromagnetic Resonance Absorption // Physical Review, 1948. V. 73. No. 2. P. 524–528.

5. *Andreev, V.G., Vdovin, V.A.* A Thermoacoustic Sensor for Recording High-Power Nanosecond Microwave Pulses // Instrum. and Experim. Techn. 2009. V. 52, No. 2. P. 226–229.

Experimental Study and Numerical Simulations of the Multipactor Discharge in Hollow and Coaxial Waveguides

I.A. Kossyi, G.S. Luk'yanchikov, V.E. Semenov[1], E.I. Rakova[1], N.A. Zharova[1], D. Anderson[2], M. Lisak[2], J. Puech[3]

A.M. Prokhorov General Physics Institute of RAS, Moscow, Russia
[1]Institute of Applied Physics of RAS, Nizhny Novgorod, Russia, sss@appl.sci-nnov.ru
[2]Department of Space and Geophysical Science, Chalmers University of Technology, Gothenburg, Sweden
[3]Centre National d'Etudes Spatiales, Toulouse, France

Multipactor discharges present a serious problem in many modern applications of high power microwaves [1–3]. Therefore it is desirable to develop numerical tools capable of predicting the multipactor threshold in particular rf components. The realization of this purpose requires detailed comparisons of the results of numerical simulations and experiments of the multipactor. Typically an experimental study is restricted to measurements of the multipactor threshold and its dependence on the microwave frequency. However, the multipactor avalanche is also sensitive to the parameters of the secondary emission which could be considerably different from available table data. Therefore only threshold data are insufficient and more detailed experimental investtigations and numerical simulations were completed [4, 5] to verify the reliability of the numerical predicting tool.

The experiments were carried out in vacuum sections of a standard rectangular waveguide and a coaxial cable. The fundamental TE_{10} mode was excited at the frequency 3 GHz in a rectangular waveguide with cross-section 72×34 mm and the multipactor was detected within a wide range of microwave powers from 290 up to 850 kW (see Fig. 1). The waveguide walls were fabricated from stainless steel and the first series of numerical simulations was completed taking the table data for the secondary emission yield (SEY) of steel [6].

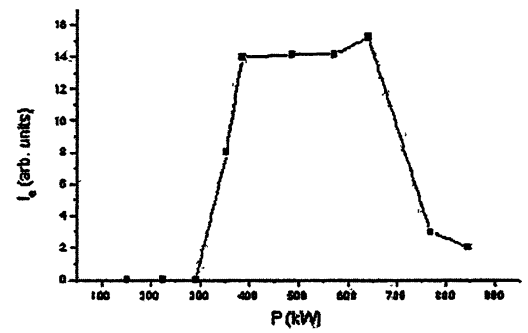

Fig. 1. Electron current at the collector as a function of the microwave power P transmitted through the rectangular waveguide

Specifically, the first cross-over point was taken to be $W_1 = 130$ eV and the maximum SEY value was taken to be $\sigma_{max} = 1.3$. Two different models of the secondary emission were used in these simulations. First, following the paper [7] the electron emission velocity was fixed and directed normally to the emission surface. This assumption resulted in a multipactor threshold about 150 kW which is approximately half of the measured value. Secondly, when a spread of initial electron velocity was taken into account, no multipactor was found in these simulations. One could conclude that a model with fixed emission velocity of electrons is more adequate for the multipactor simulations. However, a more detailed analysis demonstrated considerable discrepancy between the simulation and experimental results (cf. Fig. 1 and Fig. 2). Specifically, as demonstrated in Fig. 2, multipactor growth is possible in a number of separated intervals of power within the investigated range – a feature that was not confirmed in experiments.

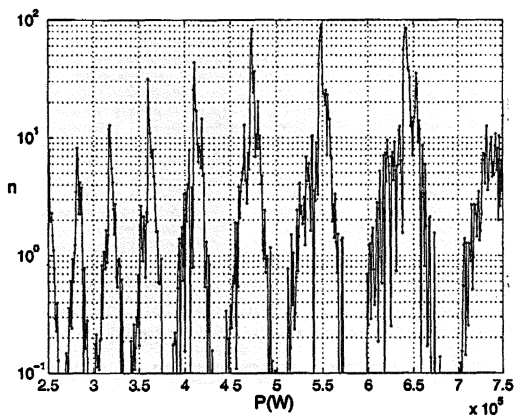

Fig. 2. The increase in the relative number of electrons, n, after 300 microwave periods as a function of power P transmitted through the waveguide in case of fixed value of initial electron velocity. The SEY parameters are: $\sigma_{max} = 1.3$, $W_1 = 130$ eV

Moreover, in experiment, a first cross-over point of $W_1 \approx 20$ eV was measured which is quite different from the table data. This gives the threshold power $P_{th} \approx 25$ kW in the case of fixed initial electron velocity, which is inconsistent with the experiment. After extended numerical simulations it was found that agreement with experimental results can be obtained taking $\sigma_{max} = 3$ and a spread in initial electron velocity corresponding to an average initial energy equal to 3 eV.

The fundamental mode was excited at frequency 2.45 GHz in a coaxial line with an outer electrode (made of brass) of radius 4 mm and an inner electrode (duralumin) of radius 2 mm. In the experiment multipactor was detected at powers exceeding 0.9 kW.

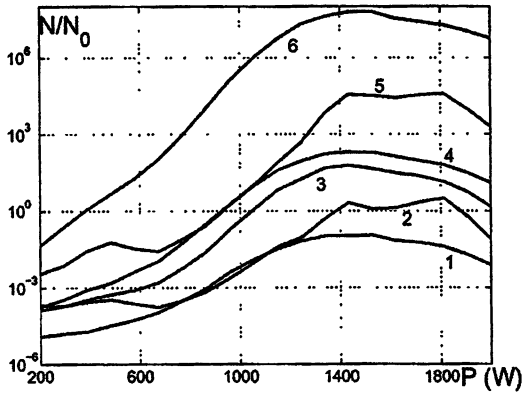

Fig. 3. A dependence of the relative increase of the electron number, N/N_0, after 100 microwave periods on the microwave power, P, and different parameters of the secondary electron emission ($\sigma_{max} = 2$ for all curves, whereas W_0 = 5 eV, W_1 = 30 eV at curve 1; W_0 = 1 eV, W_1 = 20 eV at curve 2; W_0 = 3 eV, W_1 = 20 eV at curve 3; W_0 = 5 eV, W_1 = 20 eV at curve 4; W_0 = 1 eV, W_1 = 10 eV at curve 5; W_0 = 5 eV, W_1 = 10 eV at curve 6)

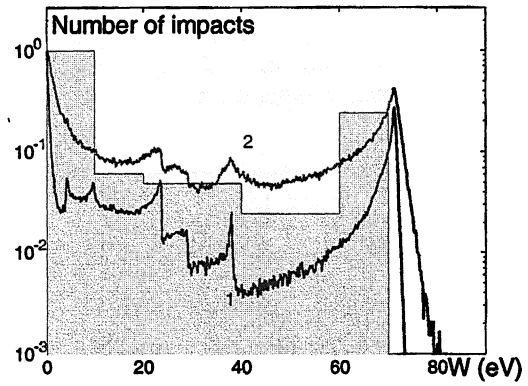

Fig. 4. The distribution of electron impact energy at outer electrode (normalized to maximum value). The curves 1 and 2 presents the simulation results obtained taking P = 1.5 kW, $\sigma_{max} = 2$. The curve 1 corresponds to W_0 = 1 eV, W_1 = = 10 eV. The curve 2 corresponds to W_0 = 5 eV, W_1 = 20 eV. The histogram presents experimental results obtained at power 1.5 kW

Measurements of the SEY in the coaxial line were not possible. However, the distribution of electrons over impact energy was measured at the outer electrode using the dependence of current in the electron collector on the retarding dc bias applied between the collector and the outer electrode. Numerical multipactor simulations in the coaxial line were carried out using a particular PIC software [5] for a wide range of SEY parameters. In these simulations it was found that the multipactor threshold was sensitive to values of the first cross-over point, W_1, and the average initial energy, W_0, of the secondary electrons whereas the threshold dependence on maximum value of SEY was less pronounced. The simulations clearly demonstrated that the measured value of threshold power, $P_{th} \approx$ 900 kW, can be realized using considerably different combinations of parameters (for example, W_0 = 1 eV, W_1 = = 10 eV or W_0 = 5 eV, W_1 = 20 eV as shown in Fig. 3). However only in the case of the second parameter combination, the simulated distribution of electrons over impact energy was in agreement with experimental data (Fig. 4). The observed distribution of electron impact velocities is related to the following effects:

(i) The low energy peak is associated with electrons emitted from the outer electrode at moments when the microwave field pushes them back to the emission surface. These secondary electrons return back in a short time with energies close to their initial energy. In the experiment approximately half of the impacts occurs with low energy which is consistent with the poly-phase nature of the multipactor.

(ii) The intermediate impact energy is caused by electrons emitted during the accelerating phase of the microwave field but returning to the outer electrode due to the action of the Miller force. A measure of their impact velocity is the double oscillatory velocity corresponding to the microwave field amplitude at the outer electrode which corresponds approximately to 25 eV.

(iii) The high energy peak is caused by electrons emitted from the inner electrode. According to a simple estimate their impact energy should have a maximum around 67 eV.

Therefore, based on the simulation results, one can conclude that the multipactor discharge observed in the experiment is excited in the poly-phase regime and that both one-sided and two-sided multipactor avalanches contribute to the discharge.

References

1. *Woode A. & Petit J.* Investigations into Multipactor Breakdown in Satellite Microwave Payloads // ESA Journal, V. 14, No. 1, p. 467-478, (1990).

2. *Kovalev N.F., Nechaev V.E., Petelin M.I., Zaitsev N.I.* Scenario for output pulse shortening in microwave generators driven by relativistic electron beams. IEEE Trans. Plasma Sci. V. PS-36, No. 3, p. 246-251, (1998).

3 *Power J.G., Gai W., Gold S.H., Kinkead A.K., Konecny R., Jing C., Liu W., and Yusof Z.* Observation of Multipactor in an Alumina-Based Dielectric-Loaded Accelerating Structure // Phys. Rev. Letters. V. 92, No. 16, 164801 (p. 1-4) (2004).

4. *Kossyi I.A., Lukyanchikov G.S., Semenov V.E., Rakova E.I., Anderson D., Lisak M., and Puech J.* Polyphase (non-resonant) multipactor in rectangular waveguides // Journal Of Physics D: Applied Physics (J. Phys. D: Appl. Phys.) V. 41, 065203, p. 1-8 (2008).

5. *Kossyi I.A., Luk'yanchikov G.S., Semenov V.E., Zharova N.A., Anderson D., Lisak M., Puech J.* Experimental and Numerical Investigation of Multipactor Discharges in a Coaxial Waveguide // J. Appl. Phys. D: Applied Physics, V. 43, 345206, p. 1-8 (2010).

6. *Bronshtein I.M. and Freiman B.S.* Secondary electron emission, Moscow, Nauka, 1969, 342 p. (in Russian).

7. *Chojnacki E.* Simulations of a multipactor-inhibited waveguide geometry // Phys. Rev. ST Accel. Beams 3, 032001, p. 1-5 (2000).

Surface Microwave Discharge in Air

V.M. Shibkov, L.V. Shibkova

Department of Physics, Moscow State University, Moscow, Russia, shibkov@phys.msu.ru

In the process of searching for optimal methods of generating non-equilibrium plasma in a supersonic flow, a microwave discharge of a new type was suggested in our laboratory, namely, a microwave discharge developed by a surface wave on a dielectric body subjected to supersonic flow of air.

It is known that, in developing a microwave discharge on the dielectric surface the electromagnetic energy delivered to the system transforms to a surface wave. In this case, a self-consistent system arises, where the plasma medium generated by the surface wave proper is required for the existence of surface wave. The wave propagates in space for as long as its energy is sufficient for generating plasma with the electron concentration not lower than the critical density. In the region where the electron density is lower than n_{ec}, the wave does not propagate and the surface discharge is not excited.

In [1–18], a new type of microwave discharge excited by a wave propagating along a dielectric surface was considered. This is a self-consistent system in the form of a plasma waveguide produced by a surface wave propagating along this waveguide; i.e., the plasma so produced is required for the very existence of the surface wave. In this way, a fairly long plasma region of various shapes can be produced in a wide range of the microwave frequency and power. A specific feature of this type of discharge is that it is capable of producing a large-size plasma with a fairly high density because the discharge can exist only at electron densities n_e higher than the critical density n_{ec}.

The experimental setup consisted of a vacuum chamber, a magnetron, a system for inputting microwave power into the chamber, pumping-out and gas-supply systems, and a diagnostics system. The vacuum system allowed us to perform experiments in a wide pressure range, from 10^{-4} to 10^{3} Torr.

As a source of microwave radiation in the centimeter wavelength range, we used a pulsed magnetron which could operate in either a single-pulse or a repetitive mode. The magnetron parameters were as follows: the wavelength λ = 2.4 cm, the pulsed microwave power W up to 100 kW, the pulse duration τ = 1–150 μs, the repetition rate f = 1–100 Hz, the period-to-pulse duration ratio Q = 1000, and the average power up to 100 W. The magnetron was fed from a pulsed modulator with a partial discharge of the storage capacitor. The microwave power was supplied to the discharge chamber through a rectangular waveguide with a cross section of 9.5×19 mm. The input microwave power was measured with the help of a directional coupler, which directed a fraction of the microwave power to the measurement system consisting of an attenuator and a crystalline detector. The waveguide was sealed and was filled with the SF_6 insulating gas at a pressure of 4 atm in order to prevent internal breakdowns. The waveguide end inserted into the discharge chamber was connected through a specially designed junction to the quartz antenna, on the surface of which a microwave discharge in air was initiated. The signal of the microwave pulse envelope was taken by a detector and recorded by a TDS-210 oscilloscope. The shape of the envelope was nearly rectangular.

It was demonstrated (Fig. 1) that, at low pressures of air $p < 1$ torr, with the electron-neutral molecule collision frequency being much lower than the circular frequency of electromagnetic energy, a surface microwave discharge is a large-volume uniform plasma formation, the size of which increases with decreasing pressure. The degree of ionization at $p = 10^{-3}$ torr may be 10 % and higher. The spatial distribution of the electron density is found to depend strongly on the air pressure. This discharge holds promise for developing new sources of plasma for the purposes of micro- and nanoelectronics (plasma treatment of surfaces, etching, deposition of films and coatings, in nanotechnologies).

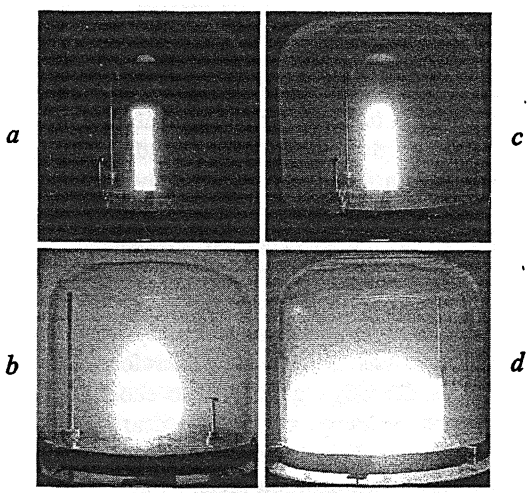

Fig. 1. The surface microwave discharge on the quartz antenna at τ = 100 μs, W = 55 kW and various pressure of air p, torr: a – 5; b – 1; c – 0.5; d – 10^{-3}. Above (a, b) – front view, (c, d) – side view

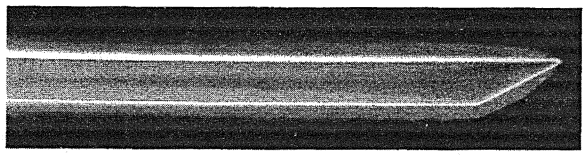

Fig. 2. General (side) view of the surface microwave discharge initiated in air at pressure p = 40 torr. The pulse duration is τ = 100 μs and the pulse power W = 40 kW. The microwave energy propagates from left to right

In the case of moderate pressures of air 10 torr < p < 40 torr a surface microwave discharge in air is a plasma formation with a thickness of the order of or less than 1 mm uniformly covering the surface of an antenna (Fig. 2). At the initial instants of time,

the velocity of propagation of surface microwave discharge reaches a value of 10^7 cm/s. The electric field intensity under conditions of surface microwave discharge is high, and the field is localized in a thin surface layer. Effective dissociation and heating of molecular gas occur under these conditions. These facts are of great importance from the standpoint of reducing the skin friction when a surface microwave discharge is used for energy input into the boundary layer and for initiating the ignition of supersonic flows of gaseous hydrocarbon fuel.

An investigation is performed of a microwave discharge generated on the external surface of a quartz antenna at high pressures of air. Fig. 3 shows a photo of a surface microwave discharge initiated on a quartz antenna at air pressure $p = 760$ Torr.

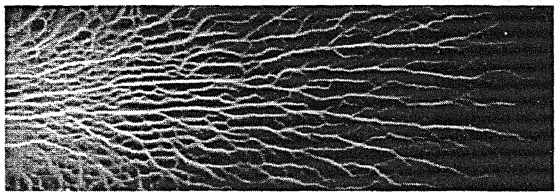

Fig. 3. General (front) view of the surface microwave discharge initiated in atmospheric-pressure air. The pulse duration is $\tau = 10$ μs and the pulse power $W = 75$ kW. The microwave energy propagates from left to right

Under high pressures, the discharge is a complicated system consisting of thin branching plasma channels from 0.1 to 1.0 mm in diameter depending on the time of action, gas pressure, and microwave power input. It is demonstrated that, at the initial stage of forming of discharge, the longitudinal velocity of its propagation reaches a value of 2–30 km/s and, at high pressures of air $p > 30$ torr, the main mechanism providing for the propagation of discharge is the breakdown wave. It has been shown, that the electron concentration in the channels is on the order of 10^{16} cm^{-3}, and the air heats up rapidly within the first ten microseconds to ~1000 K. Therefore, the formation of the discharge gives rise to shock waves, the propagation velocity of which near the antenna reaches 1 km/s. This type of discharge was used to inflame liquid hydrocarbon fuels.

This work was partially supported by the Russian Foundation for Basic Research (grant # 08-02-01251-a and grant # 11-02-01091-a).

References

1. *Shibkov, V.M., Vinogradov, D.A., Voskanyan, A.V., Ershov, A.P., Timofeev, I.B., Shibkova, L.V., and Chernikov, V.A.* Surface microwave discharge in supersonic airflow // Moscow University Physics Bulletin. 2000. V. 55, No. 6. P. 80–82.

2. *Shibkov, V.M., Alexandrov, A.F., Ershov, A.P., Karachev, A.A., Konstantinovskij, R.S., Timofeev, I.B., Chernikov, V.A., and Shibkova, L.V.* Ignition of supersonic stream of hydrocarbon fuel with the help of microwave discharges // Moscow University Physics Bulletin. 2004. V. 59, No. 5. P. 64–66.

3. *Shibkov, V.M., Ershov, A.P., Chernikov, V.A., and Shibkova, L.V.* Microwave discharge on the surface of a dielectric antenna // Technical Physics. 2005. V. 75, No. 4. P. 455–461.

4. *Shibkov, V.M., Dvinin, S.A., Ershov, A.P., and Shibkova, L.V.* Mechanisms of microwave surface discharge propagation // Technical Physics. 2005. V. 75, No. 4. P. 462–467.

5. *Shibkov, V.M., Aleksandrov, A.F., Ershov, A.P., Timofeev, I.B., Chernikov, V.A., and Shibkova, L.V.* Freely localized microwave discharge in a supersonic gas flow // Plasma Physics Reports. 2005. V. 31, No. 9. P.795–801.

6. *Konstantinovskii, R.S., Shibkov, V.M., and Shibkova, L.V.* Effect of a Gas Discharge on the Ignition in the Hydrogen–Oxygen System // Kinetics and Catalysis. 2005. V. 46, No. 6. P. 775–778.

7. *Dvinin, S.A., Shibkov, V.M., and Mikheev, V.V.* On the Theory of Microwave Discharges Excited on the Surface of a Dielectric Antenna // Plasma Phys. Rep. 2006. V. 32, No. 7. P. 601–611.

8. *Shibkov, V.M., Dvinin, S.A., Ershov, A.P., Konstantinovski, R.S., Surkont, O.S., Chernikov, V.A., and Shibkova, L.V.* Surface Microwave Discharges in Air // Plasma Physics Reports. 2007. V. 33, No. 1. P. 72–79.

9. *Shibkova, L.V.* Surface Microwave Discharge at High Pressures in Air // Moscow University Physics Bulletin. 2007. V. 62, No. 5. P. 329–331.

10. *Shibkova, L.V.* Physical Processes in Moving Plasma of Multicomponent Inert and Chemically Active Mixtures // Extended Abstract of Doctoral (Phys.-Math.) Dissertation, Moscow: Joint Inst. for High Temperatures, Russ. Acad. Sci., 2007.

11. *Aleksandrov, A.F., Shibkov, V.M., Shibkova, L.V.* Surface Microwave Discharge in High-Speed Air–Hydrocarbon Flows // Moscow University Physics Bulletin. 2008. V. 63, No. 5. P. 365–366.

12. *Aleksandrov, A.F., Shibkov, V.M., Shibkova, L.V.* Ignition of Hydrocarbon Films under the Conditions of Surface Microwave Discharge // Moscow University Physics Bulletin. 2008. V. 63, No. 6. P. 428–430.

13. *Shibkov, V.M., and Shibkova, L.V.* Inflammation Dynamics of Thin Alcohol Films under the Action of a Surface Microwave Discharge Initiated in Atmospheric-Pressure Air // Technical Physics. 2009. V. 54, No. 10. P. 1467–1475.

14. *Shibkov, V.M., Aleksandrov, A.F., Chernikov, V.A. Ershov, A.P., and Shibkova, L.V.* Microwave and Direct-Current Discharges in High-Speed Flow: Fundamentals and Application to Ignition // Journal of Propulsion and Power. 2009. V. 25, No. 1. P. 123–137.

15. *Shibkov, V.M., Shibkova, L.V., Karachev, A.A.* A Surface Microwave Discharge at High Pressures of Air // High Temperature. 2009. V. 47, No. 5. P. 620–627.

16. *Shibkov, V.M., and Shibkova L.V.* Parameters of the Flame Due to Surface-Microwave Discharge-Initiated Inflammation of Thin Alcohol Films // Technical Physics. 2010. V. 55, No. 1. P. 58–65.

17. *Aleksandrov, A.F., Shibkov, V.M., and Shibkova, L.V.* Gasdynamic Perturbations under Conditions of Surface Microwave Discharge in Air // High Temperature. 2010. V. 48, No. 5. P. 611–619.

18. *Shibkov, V.M., Shibkova, L.V., Gromov, V.G., Karachev, A.A., and Konstantinovskii, R.S.* Influence of Surface Microwave Discharge on Ignition of High-Speed Propane-Air Flows // High Temperature. 2011. V. 49, No. 2. P. 155–167.

Stabilization of Combustion of Liquid Alcohol, Injected into High-Speed Air Stream, Under Condition of Programmable Microwave Discharge

A.A. Karachev, P.V. Kopyl, V.M. Shibkov, N.V. Shibkova, O.S. Surkont

Department of Physics, Moscow State University, Moscow, Russia, shibkov@ph-elec.phys.msu.ru

One of the major practical problems arising by development of the hypersonic direct-flow air-breathing engine is reduction of its longitudinal size. For this purpose it is necessary to apply new unconventional ways of maintenance of fast volumetric ignition and control of process of combustion of hydrocarbon fuel in conditions of a high-speed stream. One of new decisions of the given problem is use of various types of gas discharges.

Under conditions of low-temperature plasma there is an opportunity of generation of active particles in result of molecules dissociation by electronic impact, electron-ionic and ion-molecular reactions, and also reduction in a threshold of chemical reactions with participation of the vibrationally-excited reagents. Therefore essentially not thermal mode of ignition is possible when the creating time of active particles occurs by electronic impact practically on all an extent of reaction. Methods of ignition and combustion control of the air-hydrocarbon streams, based on generation of electric discharges, are represented now by the most perspective. For stationary combustion of hydrocarbon-air mixture at use of non-stationary plasma it is necessary to optimize a mode of initiation of the pulsed discharge. It can be carried out at creation of the discharge in a mode of a programmable pulse [1]. In a programmable pulse mode gas breakdown and creation of plasma is carried out with the help of a short powerful pulse, or a train of short powerful pulses, and maintenance of the formed plasma and energy input occurs during the long low-power pulse following with some time delay after the first pulse.

It is very well-known, that in the motionless gas secondary breakdown becomes easier in comparison with primary breakdown. It is connected to that fact that plasma deionization occurs during some time after switch off of the first pulse of energy, thus the great number of the charged particles can remain to the moment of switch on of the second pulse. Presence in gas of the long-living excited particles also makes easier repeated breakdown as ionization of gas in this case can realize electrons with small energies due to step processes with participation of excited long-living atoms and molecules. Heating of gas during the first pulse at high pressures also results in decrease in secondary breakdown due to reduction of gas density in the zone of the discharge existence. With reference to ignition of motionless air-hydrocarbon mixtures during the first pulse reforming of hydrocarbon fuel (molecules dissociation, creation of the charged and excited particles, active radicals, and also heating of fuel) can occur, that should lead to decrease of induction period during the second pulse and to increase in combustion completeness. As to ignition of high-speed air-hydrocarbon streams the mode of programmable pulses can be used in such combination when the discharge during the first pulse is created before an entrance of combustor where a preparation of fuel takes place whereas during a repeated pulse low-temperature plasma is created in the basic chamber of combustor with the time delay determined in the speed of movement of reformed fuel and distance between area of preliminary excitation of fuel and the combustor chamber.

In the report influence of low temperature plasma of a programmable microwave discharge on efficiency of combustion of liquid hydrocarbon fuel, injected in a drop phase (as a spray) into subsonic ($M \leq 1$) air stream is investigated. The programmable discharge represents a combination of the self-sustained pulse-periodic microwave discharge and the non-self-sustained transversal electrode discharge created on a surface of a dielectric plate. Without use of the microwave discharge the electrode direct current discharge could not exists in a free high-speed air stream.

Experiments were carried out on the installation (look Fig. 1) consisting of a vacuum chamber, a receiver of a high pressure of air, a system for producing a supersonic gas flow, magnetron generator, system for delivering microwave power to the chamber, rectangular aerodynamic channel, a synchronization unit, and a diagnostic system. The basic component of the experimental setup is an evacuated metal cylindrical chamber, which serves simultaneously for high-speed flow creation, and as a tank for the expiration of gases or combustion products. The inner diameter of the vacuum chamber is 1 m, and its length is 3 m. A subsonic flow was produced by filling the vacuum chamber with air through a specially profiled Laval nozzle. The microwave source is a pulsed magnetron generator with parameters: the wavelength is $\lambda = 2.4$ cm, the pulse duration is $\tau = 5$–150 μs, the pulsed microwave power is $W < 100$ kW, and the period-to-pulse duration ratio is $Q = 1000$. Microwave power was delivered to the discharge chamber through a 9.5×19–mm rectangular waveguide. All the components of the microwave transmission line were sealed. To avoid electric breakdowns inside the waveguide, it was filled with an insulating gas (SF_6) at a pressure of 4 atm.

For diagnostics of the investigated phenomenon the automated diagnostic complex consisting from optical refracting gauges, photo electronic multipliers, pulse shadow installation, system for measurement of conductivity of a flame, electric probes, thermocouples, gauges of pressure, a two-wire line, digital monochromaters, spectroscopes, oscillographs, photo and video cameras has been used.

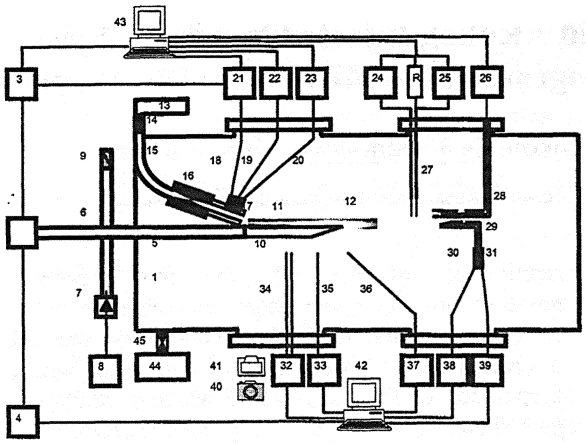

Fig. 1. Experimental installation: 1 – vacuum chamber; 2 – magnetron; 3, 4 – synchronization units; 5 – metal waveguide; 6 – directional coupler; 7 – crystal microwave detector; 8 – pulse voltmeter; 9 – load; 10 – dielectric antenna; 11 – electrodes for DC creation; 12 – programmable discharge; 13 – air high pressure receiver; 14 – electric hydraulic valve; 15 – bringing hose; 16 – Laval nozzle; 17 – aerodynamic channel; 18 – gauge of pressure; 19 – thermocouple; 20 – injector; 21, 22 – amplifiers; 23 – power unitg for injector; 24 – power unitg for double probe; R – measuring resistance; 25 – digital oscilloscope; 26 – amplifier for thermocouple; 27 – double probe; 28 – thermocouple; 29 – nozzles for measurement of static pressure and braking pressure; 30, 31 – gauges of pressure; 32 – digital multichannel spectroscope; 33 – monochromator; 34, 35, 36 – optical waveguides; 37 – photo electronic multiplier; 38, 39 – amplifiers; 40 – video and photo cameras; 41 – pulsed shadow graphics installation; 42, 43 – computers; 44 – vacuum pumps; 45 – valve

It was shown [2], that at ignition of liquid hydrocarbon fuel sharply change common view and characteristics of the discharge (the volt-ampere characteristic of the discharge, time dependences of a discharge current and it is especial voltage on a discharge gap, a spectrum of radiation and integrated intensity of a luminescence of a flame, the thermal stream, registered by thermocouple located on distance of 15 cm downwards on an air stream). The general view of process of combustion is submitted in Fig. 2.



Fig. 2

The separate fragments of dynamics of development of process of ignition and combustion of liquid alcohol are submitted in Fig. 3. An exposition time of one fragment is 4 μs, frequency of shooting is $f = 5000$ Hz. At the left – the discharge in an air stream, in the middle – transient of ignition, on the right – combustion stabilization. Process of stabilization of liquid hydrocarbon fuel combustion can be observed on change of a time dependences of a pulse of a discharge current and especially a pulse of a voltage on a discharge gap (look Fig. 4). Fluctuations of amplitude of a voltage sharply decrease at combustion stabilization.

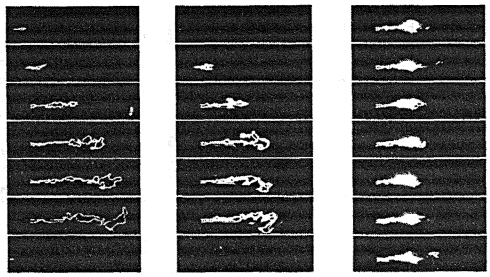

Fig. 3

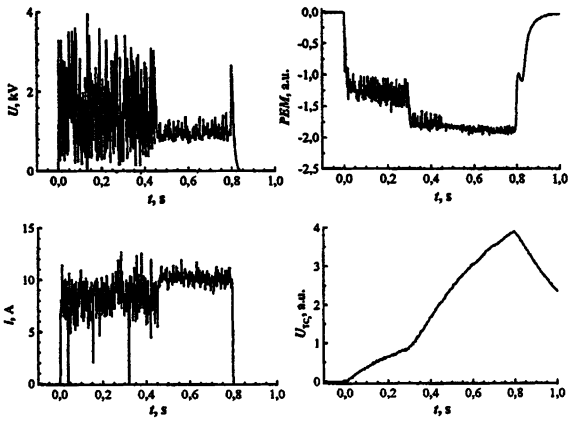

Fig. 4

Completeness of combustion of liquid alcohol reaches of 80 % depending on power. Combustion occurs at a flame temperature ~2000 K (look Fig. 5, curve 2). Integrated intensity of a flame luminescence increases only on 25–30 % at combustion whereas intensity of a hydroxyl luminescence grows in 30 times.

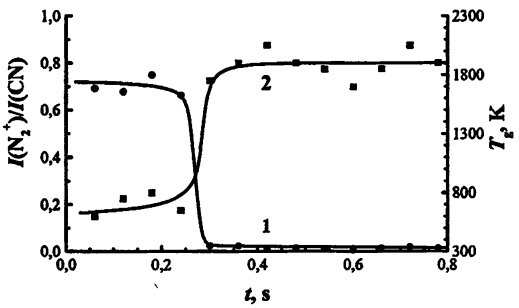

Fig. 5

This work was partially supported by the Russian Foundation for Basic Research (grant # 08-02-01251-a and grant # 11-02-01091-a).

References

1. *Zarin, A.S., Kuzovnikov, A.A., and Shibkov, V.M.* Freely localized microwave discharge in air. M.: Oil and gas. 1996.

2. *Gusev, I.N., Karachev, A.A., Kopyl, P.V., Shibkov, V.M., Shibkova, L.V., Surkont, O.S.* Programmable microwave discharge as the way of combustion stabilization of liquid alcohol, injected into transonic air stream // 10th International Workshop on Magneto-Plasma Aerodynamics. Abstracts. Institute of High Temperature of RAS, Moscow, 21–24 March 2011.

Electromagnetic Band Gap Devices Controlled by Glow Discharges

V.I. Arkhipenko[1], Th. Callegari[2], J. Lo[2], L.V. Simonchik[1], J. Sokoloff[2], M.S. Usachonak[1]

[1]Institute of Physics NAS of Belarus, Minsk, Belarus, simon@imaph.bas-net.by
[2]LAPLACE, University of Toulouse and CNRS, Toulouse, France, thierry.callegari@laplace.univ-tlse.fr

Different electromagnetic band gap (EBG) structures have been receiving growing attention in recent years [1, 2]. Many of them are realized by artificial metallic structures such as using wires to produce effective negative permittivity. However, most EBG materials proposed to date are based on immutable structure of the unit cell and result in a narrow band and not at all tunable. In order to fabricate a broadband and tunable EBG material some of its elements must be replaced by some other structures or materials. Glow discharge plasmas have high potentials as effective control elements in these devices. The flexibility of plasmas in size, density and spatial arrangement can produce novel functional properties in order to control microwave propagation at the frequency range of our interest.

The possibilities to use a DC glow discharge at sub and near atmospheric pressure in an EBG structure has been demonstrated recently in [3, 4]. For this application, significant electronic density in the plasma column is required: $n_e >> n_c$, where the critical density, n_c, is defined by the incident microwave radiation frequency, f_0 (i.e., $2\pi f_0 = \omega_0 = (n_c e^2/\varepsilon_0 m_e)^{1/2}$). In this report we present our results on the propagation characteristics of microwaves through the both the waveguide band filters and EBG structures formed by metallic rods in combination with the plasma columns. We will discuss possibilities of the utilization of non-self-sustained atmospheric pressure glow discharges for EBG structure control.

3-cm waveguide filter. In the first series of our experiments, periodical structures were integrated within a standard WR90 waveguide (22.86×10.16 mm). As seen in Fig. 1, conductive rods (4 mm in diameter) are loaded across the H-plane along the waveguide with a minimal distance between rods of 19 mm. For different configurations, measurements were made with a vector network analyzer (Anritsu 37369C) in the frequency range of 7–12 GHz. Corresponding transmittance-frequency curves are shown for each case: without metallic rods, the transmittance practically does not depend on the frequency (Fig. 1*a*); with 3 rods inserted (Fig. 1*b*), a waveguide filter with direct coupling is formed by two resonators and a resonant frequency is observed at 7.5 GHz; with 5 rods inserted (Fig. 1*c*), a resonant frequency is observed at 10.5 GHz. The bandpass position at around 10.3 GHz does not depend on the resonator length.

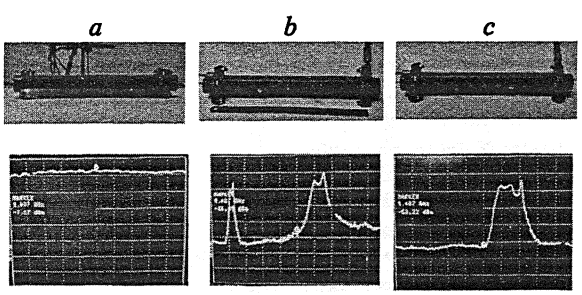

Fig. 1. Photos (upper row) of the waveguide section without rods (*a*), with 3 rods (*b*), with 5 rods (*c*) and their corresponding transmittance-frequency curves (bottom). Axis X – 1 scale division equals 0.5 GHz, axis Y – 10 dB

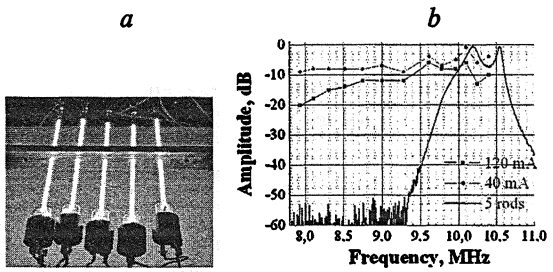

Fig. 2. Photo of waveguide section with 5 lamps (a) and transmittance-frequency curves (b)

Different configurations are tested where several of these rods are replaced by commercial 3 mm internal diameter discharge lamps. The electronic density in these lamps varies in the range of $0.3–2\cdot10^{13}$ cm^{-3} when the current increases from 30 mA up to 130 mA. When five discharge lamps are inserted instead of conductive rods (Fig. 2*a*), the transmittance decreases with the frequency (about 20 dB for frequency 8 GHz at currents of 120 mA) as it can be seen in Fig. 2*b*. The attenuation is much lower than the configuration with 5 conductive rods presented in the same figure with a solid line. This can be explained by low electronic density which is insufficient to create exactly the same periodical conditions as with metallic rods.

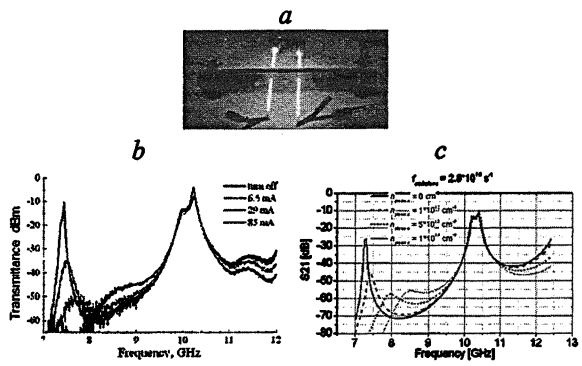

Fig. 3. Measured and calculated transmittances of the waveguide filter with 3 rods and two lamps

In Fig. 3*b*, the transmittance attenuation up to 40/50 dB of waveguide filter at the frequency bands of 7.5 GHz is demonstrated experimentally using both the discharge lamps and conductivity rods (Fig. 3*a*). There is a good qualitative agreement between experimental data and simulated ones (Fig. 3*c*) by Ansoft-HFSS commercial software.

Space triangular EBG structure. Another series of experiments were carried out with a similar space triangular EBG structures in [1, 3, 4] formed by a square network of metallic rods. The EBG structure dimensions are modified for the frequency range of 8 GHz. The rods (with diameter, $d = 3$ mm) are distributed in a square lattice with a step size, $a = 22$ mm (Fig. 4, *a*). One of this EBG's interesting properties is the longitudinal direction is totally forbidden while the diagonal direction is allowed. In order to excite the diagonal mode, we introduce defaults by removing two rods at the EBG interface. We registered a signal of diagonal mode which corresponds to the transmission in the direction of ± 45° to the longitudinal one in this case (Fig. 4*b*). Replacing each of these two rods by a plasma column of gas discharge lamps leads to a decrease of diagonal mode signal on about 10 dB at discharge current of 120 mA, compared to when all the metallic rods are present, the decrease in microwave signal is achieved for more than four order of magnitude.

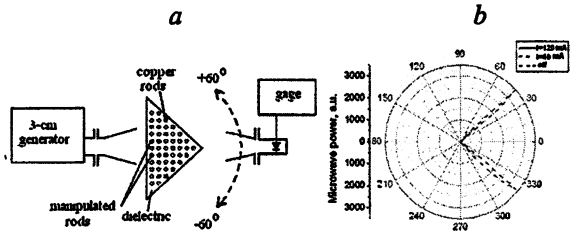

Fig. 4. Schematic of experimental setup (*a*) and directional diagram of the space triangular EBG structure (*b*)

DC non-self-sustained atmospheric pressure glow discharges as a control element of the EBG devices. In order to improve the effective control of electromagnetic wave propagation with plasma discharges, a higher electron concentration is required. It may be obtained by increasing the gas pressure. Therefore, a DC non-self-sustained atmospheric pressure glow discharges (APGD) [5] may be preferable for these purposes. The three electrode configuration shown in Fig. 5*a* may be used in order to create these plasma discharges. In section A, a self-sustained APGD between cathode 1 and anode 2 is occured at a distance of about 2 mm in helium or argon. A gas flow of around 1–2 liter/min is provided through section A for these gases. The gas outlet from this section occurs through a hole (2 mm in diameter) in anode plate 2 (about 1 mm thickness) which divide the discharge chamber into two sections: A and B.

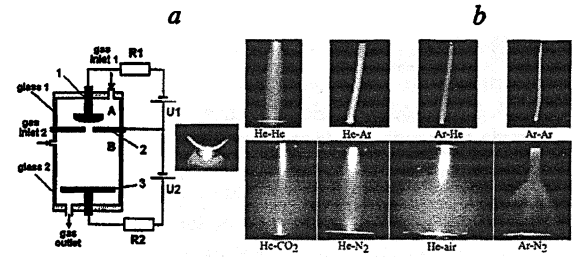

Fig. 5. Schematic of experimental setup for the non-self-sustained atmospheric pressure glow discharge creation (*a*) and images of these discharges in different gases (*b*)

The discharge in section A serves as plasma cathode for the non-self-sustained discharge in section B between anode 3 located in this section at distance about 30 mm from electrode 2. An independent flow of different gases (including molecular ones) is introduced through section B. For various gas combination in sections A and B, long-scale non-self-sustained APGDs are obtained when voltages are applied (Fig. 5*b*). Their size may reach up to 50 mm in height, which is highly interesting to be used in a free space EBG structure as this will offer.

Let's now discuss the main parameter needed for effective control of the EBG devices: the electronic density. In the positive column of the APGDs, the electronic densities are determined for various gases, using two methods, the Stark spectroscopy of the hydrogen H_β line and the estimation from the reduced electric field and current density measurements. Both of the methods are described in [6]. The electronic densities are then plotted against discharge current in Fig. 6.

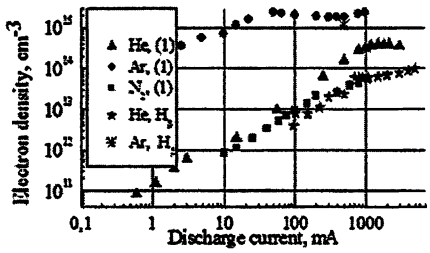

Fig. 6. Electron densities in the APGD positive columns in helium, argon and nitrogen vs discharge current

Thus, the possibilities of the electromagnetic wave propagation control by DC glow discharges at low or medium pressures were demonstrated. To achieve higher performance, a long-scale atmospheric pressure glow discharges maintained by glow discharges in three-electrode system studied in this report seem to be a good candidate.

Financial support of BRFBR-CNRS grants F11F-002 is acknowledged.

References

1. *Giroud, L., Sokoloff, J. and Pigaglio, O.* Reconfigurable EBG at 18 GHz using Perimeter Defects // J. Electromagn. Waves & Appl. 2009. V. 23. P. 1029-1037.

2. *Sakai, O. et al.* Interaction and control of millimetre-waves with microplasma arrays // Plasma Phys. Contr. Fusion. 2005. V. 47. P. B617.

2. *Lo, J., Callegari, Th. et al.* Electromagnetic Band Gap Device Controlled by Microplasma Discharge // PPPT-6, Minsk, Belarus. 2009. V. 1. P. 268.

3. *Lo, J., Sokoloff, J., Callegari, Th. and Boeuf, J.P.* Reconfigurable electromagnetic band gap device using plasma as a localized tunable defect // Applied Physics Letters. 2010. V. 96. 251501.

4. *Arkhipenko, V.I., Kirillov, A.A. et al.* Atmospheric Pressure Air Glow Discharge in Three-electrode Configuration // IEEE Trans.Plasma Phys. 2009. V. 37. P. 1297-1304.

5. *Arkhipenko, V.I., Kirillov, A.A. et al.* Self-sustained dc atmospheric pressure normal glow discharge in helium: from microamps to amps // Plasma Sour. Sci. Techn. 2009. V. 18. 045013.

Enhancing Transformer Ratio of a THz Two-Channel Coaxial Dielectric Structure Using Ramped Bunches

G.V. Sotnikov[1,2], T.C. Marshall[3,2], J.L. Hirshfield[4,2]

[1]NSC Kharkov Institute of Physics and Technology, Kharkov, Ukraine
[2]Omega-P, Inc., New Haven Connecticut, USA
[3]Columbia University, New York City, USA
[4]Yale University, New Haven, Connecticut, USA

Dielectric wakefield accelerator devices have become an attractive alternative to conventional metallic-structure elements used for electron/positron linear colliders. However, other than the possibility to develop high accelerating gradients, an accelerator should have other advantages, such as an attractive transformer ratio (T). Some methods to increase T have been suggested: using a bunch with linearly rising profile of current [1], or using a train of bunches with linearly rising charge, known as the ramped drive bunch train (RBT) technique [2, 3]. Another method to increase T uses a multizone dielectric structure with separate channels for the drive and witness bunches. The cylindrical configuration of a multizone dielectric accelerator structure is a coaxial dielectric wakefield accelerator (CDWA). We have found that T~5–6 can be obtained in a CDWA in the THz frequency range[4]. A natural desire is to combine these two methods in order to increase the transformer ratio of the CDWA even more.

Here we study the applicability of the RBT to a high gradient THz CDWA structure [4]. The question is whether the removal of wakefields due to the group velocity phenomenon will permit the superposition of wakefields from the train of delayed drive bunches, because the THz structure is very lightly loaded with dielectric and so the wave group velocity is very close to the particle velocity.

In this report we show an improved RBT technique [5] that allows a significant increase of T in a THz CDWA. For numerical investigations we take a two-channel CDWA structure using two concentric dielectric tubes of diamond material with dielectric permittivity 5.7. We take for numerical calculations an annular drive bunch with charge (6 nC) and energy (5 GeV) similar to the SLAC bunch. In the Table the dimensions of the dielectric shells calculated for an operating frequency of 0.44 THz (E_{02} mode) are listed.

The results from studies to enhance the transformer ratio are presented in Figs. 1–3. For numerical investigation we used PIC SOLVER of the CST PARTICLE STUDIO.

Fig. 1 shows the axial wakefield trailing a single 6 nC drive bunch, measured on the axis of the unit (along which the witness bunch moves) and along a line parallel to the axis halfway between the outer and inner radii of the drive bunch annulus. From the presented plots it follows that T for this case is 4.73. Here we calculate T as the ratio of maximum accelerating wakefield on the central axis of the structure (~550 MeV/m) to the maximum decelerating wakefield at the drive bunches along the center line (~116 MeV/m). One should observe also that the wakefields are much diminished at 4.2 mm: this shows that the superposition of wakefields is limited to a zone behind the drive bunch depending on the length of the structure and the group velocity of the waves set up by the passage of the drive bunch into the structure [4].

Table: Parameters used for CDWA (Diamond)

Design mode (E_{02} mode)	0.44 THz
External radius of outer coaxial cylinder	790.5 μm
Inner radius of outer coaxial waveguide	707.5 μm
External radius of inner coaxial cylinder	150.0 μm
Accl. channel radius (inner radius of inner coaxial cylinder)	50 μm
Relative dielectric constant ε	5.7
Bunch axial RMS dimension 2σ (Gaussian charge distribution)	277.12 μm
Full bunch length used in PIC simulation	692.8 μm
Outer drive bunch radius (box charge distribution)	578.75 μm
Inner drive bunch radius	278.75 μm
Bunch energy	5 GeV
Total bunch charge	6 nC
Number of bunches	4

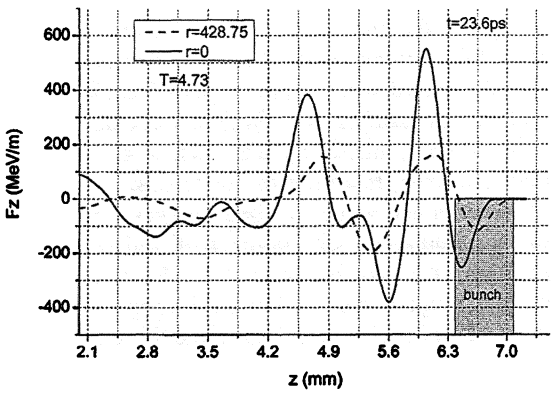

Fig. 1. Axial force from wakefields set up by a single 6 nC, 5 GeV drive bunch in the CDWA structure described in the Table. Solid line is the wakefield at the center of the accelerating channel, the dash line is the wakefield at the center of the drive channel. The head of the drive bunch is located at $z = 7.1$ mm mm (grey rectangle shows the location of the drive bunch current) and the bunch travels from left to right

Figure 2 displays the wakefields set up by a train of four ramped drive bunches [2, 3]. The total bunch charge for the four ramped bunches is the same as for the single bunch (6 nC), and the distribution of charge among the bunches is such that the ratio of bunch

charges increases [3] from the first to the last bunch as 1:3:5:7. Drive bunches are spaced by 1.02 mm (1.5 wakefield wavelengths of the main mode). The T calculated from the last drive bunch is 2.67, which is even less than transformer ratio from the single bunch case. Thus, the conventional algorithm to enhance the transformer ratio with constant bunch spacing does not improve T.

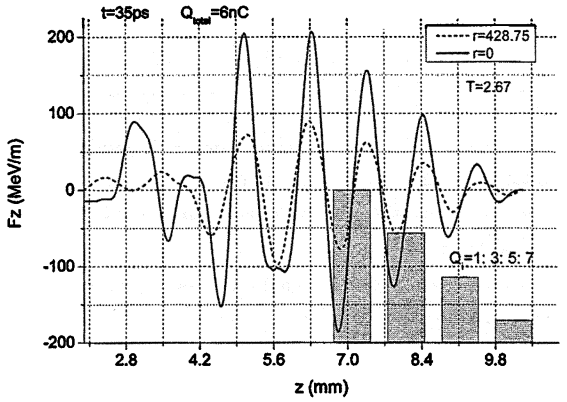

Fig. 2. Axial wakefields excited by a ramped bunch charge train of four drive bunches spaced by 1.5 wakefield wavelengths

This decrease of the transformer ratio can be explained by the multimode excitation of wakefields in the CDWA. To obtain an improved transformer ratio for this case it is necessary to use a modified ramped bunch train [5]. The improved algorithm is based on this theorem [2]: wakefields with maximum transformer ratio are generated by drive bunches whose particles lose the same energy. For a single-mode device, from this statement it follows that for a Gaussian profile of longitudinal bunch charge density, the charge of the *nth*-bunch should change according to the relation [2] $Q_n = Q_1[1+T(n-1)]$, where Q_1 is the charge of the first bunch, and T is the transformer ratio of a single bunch. These bunches should be equally spaced with repetition period equal to an odd half integer number of wakefield wavelengths. In the case of a multimode device, such a simple formula does not exist; therefore to obtain desirable locations of bunches and values of their charges it is necessary to run simulations, the number of which is equal to the number of bunches in the train. First, a calculation with one bunch is carried out, a location of the maximum of an accelerating field in the drive bunch channel is determined, and at this location the second bunch is placed and a new calculation of structure excitation is performed. At the location of the second bunch, the superposition is such that the field there becomes decelerating. Then, each subsequent drive bunch is to be located at the maximum of the accelerating field from the prior bunches, and the charge of the *n*th bunch is set according to the formula [5]: $Q_n = Q_1[1+T_{n-1}]$, where T_{n-1} is the transformer ratio after the $(n-1)st$ bunch. An answer to the goal of improved transformer ratio is provided by the result shown in Fig. 3. The bunch spacing is approximately 1.9 mm, and the charge ratios are 1.0, 2.35, 4.5, and 7.7; again, maintaining the constant total drive bunch charge at 6 nC. The T from the last bunch is 17.3, a factor of 3.7 times as large as the T for the single bunch. Notice the peak wakefield amplitude following the fourth drive bunch is 285.1 MeV/m, down from 550 MeV/m in Figs. 1. This prescription for the drive bunch charge and spacing was obtained by striving for uniform drive bunch deceleration, which means that this arrangement should extract more energy from the entire drive bunch train than that, e.g., shown in Fig. 2. This example establishes that a considerable enhancement of T is possible in the multimode CDWA system using a flexible RBT method. The more complex algorithm (in comparison with [2, 3]) for the bunch charge distribution and bunch locations is related to the multimode excitation of the CDWA.

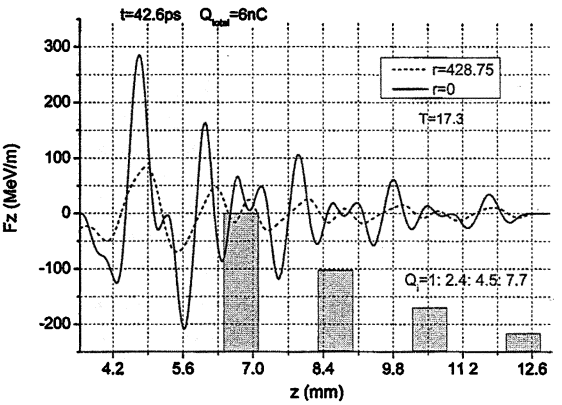

Fig. 3. Axial wakefields set up by an improved ramped train of four drive bunches. The distribution of charge among the bunches is such that the ratios of bunch charges increases from the first to the last bunch as 1:2.4:4.5:7.7. Bunch spacing is approximately 1.9 mm

Acknowledgments. This research was supported by the U.S. Department of Energy, Office of High Energy Physics, Advanced Accelerator R&D.

References

1. *K.L.F. Bane, P. Chen, P.B. Wilson.* On collinear wake field acceleration // IEEE Trans. Nucl.Sci. 1985. V. 32. P. 3524-3526.

2. *S.S. Vaganyan, E.M. Lasiev, and V.M. Tsakanov* // Probl. At. Sci. Technol., Ser. Nucl. Phys. Invest. 1990. V. 7. P. 32-36 (in Russian).

3. *C. Jing, A. Kanareykin, J.G. Power, M. Conde, Z. Yusof, P. Schoessow, and W. Gai.* Observation of Enhanced Transformer Ratio in Collinear Wakefield Acceleration // Phys. Rev. Lett. V. 98, 144801 (2007).

4. *G.V. Sotnikov, T.C. Marshall, and J.L. Hirshfield.* Coaxial two-channel high-gradient dielectric wakefield accelerator // Phys. Rev. ST Accel. Beams, V. 12, 061302 (2009).

5. *G.V. Sotnikov and T.C. Marshall.* Improved ramped bunch train to increase the transformer ratio of a two-channel multimode dielectric wakefield accelerator // Phys. Rev. ST Accel. Beams, V. 14, 031302 (2011).

Electromagnetic PiC Code KARAT in Simulations of EM-propagation in Bio Tissues, Laser-Plasma Interaction, etc.

V.P. Tarakanov

ITES RAS, Moscow, Russia, karat@tarak.msk.su

This paper deals with some last simulations made by code KARAT [1] that is aimed at the solution of 1,2&3D non-stationary electrodynamics problems in a complicated geometry involving plasmas or/and particle beams.

For simulation of electromagnetic processes inside heterogeneous materials with dispersions, for example, water or bio tissues code was supplemented with Lorentz model implicated in FDTD scheme [2]. In frame of this model a dielectric contains electrons bonded to equilibrium position by forces proportional to distance and consequently having a natural frequency. Each oscillator type in Ampere's low corresponds to current density $\vec{j}_n$ from next equation: $(\frac{\partial^2}{\partial t^2}+\Gamma_n\frac{\partial}{\partial t}+\omega_n^2)\vec{j}_n=\frac{\omega_{p,n}^2}{4\pi}\frac{\partial}{\partial t}\vec{E}$, where ω_n – natural frequency, Γ_n – decrement, $\omega_{p,n}$ – frequency of self consistent interaction. The next dielectric permittivity corresponds to $\vec{j}_n: \varepsilon^*=1-\sum_n\frac{\omega_{p,n}^2}{\omega^2-\omega_n^2+i\omega\Gamma_n}$, where the sum via all types of oscillators. Relating it to experimental frequency dependences for ε' and σ one can find coefficients ω_n, Γ_n, $\omega_{p,n}$.

On Fig. 1 there are experimental [3] and corresponding to two component Lorentz-medium dependences via frequency for water.

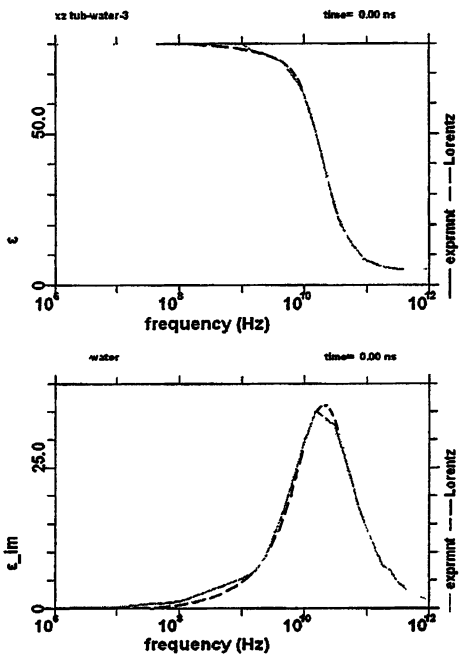

Fig. 1. Dependences of real and image parts of dielectric permittivity vs. frequency for water (solid line – experiment, dashed line – Lorentz-medium)

Parameters of Lorentz-medium for water was used in simulation corresponding to experimental setup. As in region of water layer electromagnetic pulse was close to plane wave we use the XZ-code version where $\partial/\partial y=0$. On Fig. 2 one can see the By component in moment when pulse moves to irradiated object involving water and dielectric ($\varepsilon=3$) layers and also electric field probe spaced at 8 cm.

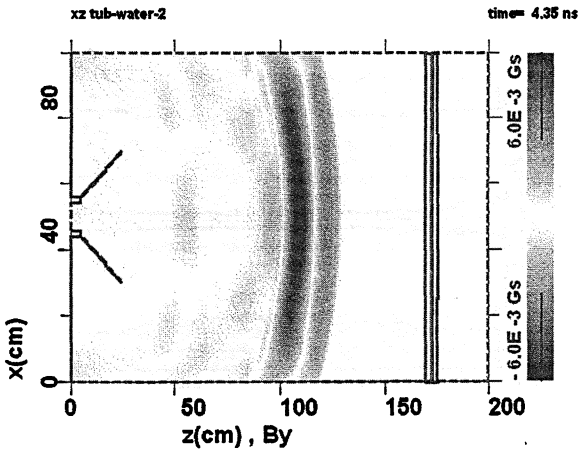

Fig. 2. By component in plane XZ

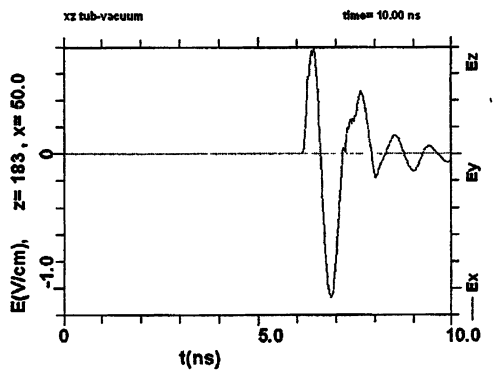

Fig. 3. The history of Ex on probe without water

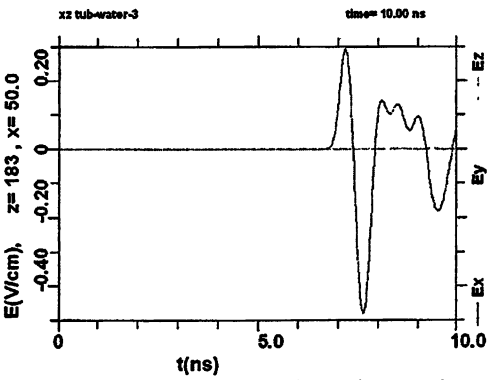

Fig. 4. The history of Ex on probe with water layer 3 cm thick

Last dependencies show the water layer decays the first peak in 3 times that is in good coincidence with experimental result. Simulation demonstrated as processes of reflection and absorbing of the pulse in different heterogeneous materials.

Next simulation concerns of the coaxial electron-string ion source [4] with formation of squeezed state or virtual cathode (VC) of electron flow. The electrons are accumulated in a long trap into which an electron beam is injected. It is shown that a chain of alternating phase holes and squeezed states form in the trap. The dynamical features of such as the double-pulse waveform and strong high-frequency oscillations of the accumulation current and the broadening of the electron distribution function are qualitatively similar to those previously observed in experiments with the Krion-2 ion source operating in the electron-string mode.

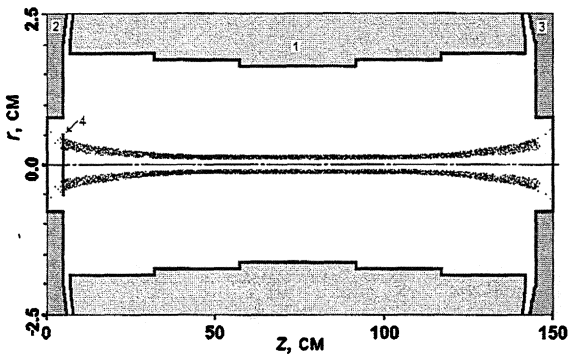

Fig. 5. Geometry of the trap and annular electron beam: (*1*) drift tube, (*2*, *3*) reflectors, and (*4*) cathode grid

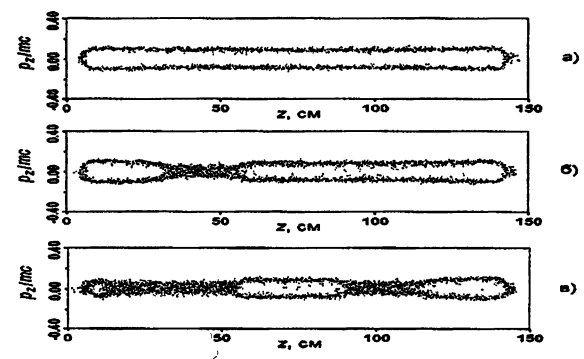

Fig. 6. Instantaneous phase portraits of electrons in the trap for at the instants (a) 3, (b) 4.5, and (c) 6.5 μs

Next simulation concerns of propagation of the surface plasmon polariton (SPP) pulses through a plasmonic crystal with monotonically varying in space parameters is investigated for the case of metal-dielectric structure of a dielectric grating wedge on top of a uniform silver film. We demonstrate that different regimes of the wavepacket motion are possible. In particular, the SPP wavepacket acceleration/deceleration, reflection, and tunneling to the adjacent plasmonic band are possible depending on the SPP pulse central frequency and spectral bandwidth. Aforementioned effects and the fact that they can be easily tuned by variation of the pulses parameters hold a great promise for applications in plasmonic devices.

Next point concerns of a thin film target upon irradiation by intensity $\geq 10^{18}$ W/cm^2 femtosecond laser pulses. The new models include at first γ-quanta generation, then DD-reaction, and at last a field ionization of target. It is shown by the example of a thin gold target that the mean electron energy is twenty five times higher than the mean energy of gamma quanta generated by them. The angular distributions of electrons and gamma quanta are studied. It is shown that only the angular distribution of high-energy gamma quanta repeats the angular distribution of the electrons leaving the target.

The last point concerns the energetic ions and DD neutrons from fusion at the interelectrode space of a low energy nanosecond vacuum discharge with deuterium-loaded Pd anode [5]. To understand better the physics of fusion processes the simulation of the discharge experimental conditions have been developed.

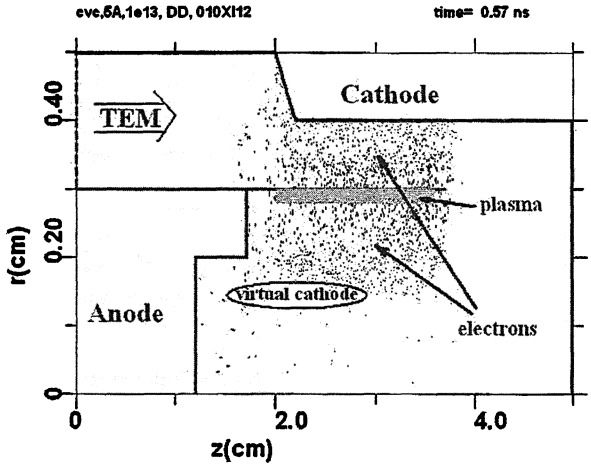

Fig. 7. Configuration simulation region

The dynamics of main charge particle species was reconstructed in time and interelectrode space. The principal role of a VC and the corresponding potential well formed in the interelectrode space are recognised. The calculated depth of the quasistationary potential well of the VC is about 50–60 kV, and the D+ ions being trapped by this well accelerate up to energy values needed to provide collisional DD nuclear synthesis.

References

1. *Tarakanov V.P.* User's Manual for Code KARAT, BRA Inc., Va., USA, (1992).

2. *Лебедев Е.Ф., et al.* Труды III Межд. Конф. Человек и э/м поля, с. 416-425. Саров, 2010. ISBN 978-5-9515.

3. *Barthel, J., et al.* Phys. Chem. 1991. 95(8): p. 853-859.

4. *Donets E.D., Dubinov A.E., et al.* Plasma Physics Reports. 2009. V. 35, No. 1, p. 54-61.

5. *Kurilenkov Yu.K., Skowronek M., Tarakahov V.P. et al.* J. Phys. A: Math & Theor 42, 214041 (2009).

Multi-Mode Accelerating Structures

S.V. Kuzikov[1], J.L. Hirshfield[3,4], Y. Jiang[3,4] M.E. Plotkin[1], A.A. Vikharev[1], V. Vogel[2]

[1]Institute of Applied Physics, Nizhny Novgorod, Russia, kuzikov@appl.sci-nnov.ru
[2]DESY, Hamburg, Germany
[3]Omega-P, Inc., New Haven, CT, USA
[4]Yale University, New Haven, CT, USA

Effects to raising breakdown threshold

RF breakdown is a strong limiting factor towards increase of acceleration gradient, and one needs first of all to prevent the initiation of breakdown. Let us consider a particle beam to be accelerated as a periodic sequence of tight bunches that move along a straight path with a velocity close to the speed of the light. High accelerating fields at the axis of a structure need to exist only during the narrow time intervals when a bunch traverses this structure. During time intervals between bunches fields near the axis should preferably be as small as possible. This principle automatically requires that structure should contain equidistant spectrum of modes with harmonically related frequencies [1, 2]. Such multi-mode accelerating structures operating in several resonant, equidistantly-spaced, axisymmetric, TM-like eigenmodes allows reduction of the exposure time to surface fields. Experimental data obtained for many accelerating structures show that the breakdown probability is dependent on electric field threshold, but also dependent on exposure time. Thus, reducing exposure time one increases breakdown threshold and can obtain higher accelerating gradient.

Additionally, there are two complementary effects (that is reduction of high-field areas and reduction of those fields which are responsible for electron emission) which also help to increase accelerating gradient [2, 3].

A multi-mode, two-beam accelerator

A self-consistent generic theory for a two-beam accelerator ($G > 150$ MeV/m) based on use of a cascade of the detuned multi-mode cavities was developed in [1]. In frames of this theory acceleration cavities were designed as axially symmetrical radial cavities excited by two or three $TM_{0,n,0}$ ($n \geq 1$) modes. This concept does not allow involving a big number of modes (to enhance shunt impedance and accelerating gradient, to reduce overall losses), because a so-called transit time factor decreases with increasing of a radial mode index. In order to increase the mentioned transit time factor, it is attractive to use a cavity where a short RF pulse consequently oscillates between two irises so that in path from left to right it moves in synchronism with a particle, then the pulse returns and begins to interact with next particle (Fig. 1). The waveguide in-between the irises in Fig. 1 is actually a slow wave media (a section filled by some dielectric or a corrugated section). The mentioned RF pulse consists of several (three or more) TM_{01n} modes. These modes with longitudinal indices n–1, n, n+1 are excited by beam current harmonics ω_{s-1}, ω_s, ω_{s+1} correspondingly, because each mode (nearest to n-th mode) satisfies to a condition of the syncronism simultaneously. All these modes are able to have high transit time factors. In Fig. 2 drive and test beams have the separate channels coupled by means of transfer waveguide structure. Principles of mode synchronization with bunches in both cases are shown in Fig. 3.

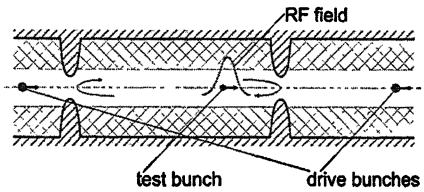

Fig. 1. Conceptual sketch of two-beam accelerator

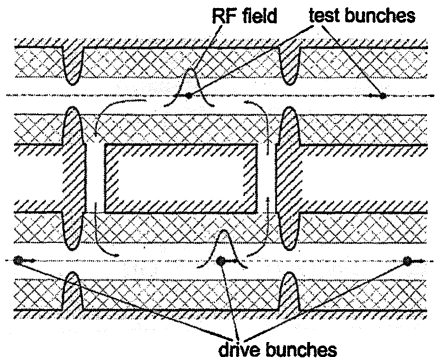

Fig. 2. Conceptual sketch of two-beam accelerator module with transfer waveguides (PETs)

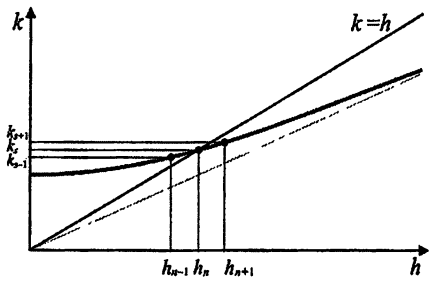

Fig. 3. Equidistant eigen modes of slow wave accelerating cavity

RF photocathode injection gun

A possible application of the described multi-mode principles is so-called high-brightness RF photocathode sources of electrons. An injection gun produces compact bunches of electrons by means of the synchronized high repetition rate laser light and high-power RF field. Modern injection guns also use transverse emittance compensating techniques based on two-solenoid system [4]. Typically RF gun is able

to release electron bunches of 1–10 nc charge and 10–20 ps length with the normalized emittance ε_{rms} = 1–10 μm. Typical view of the 1.5 cell RF gun is shown in Fig. 4.

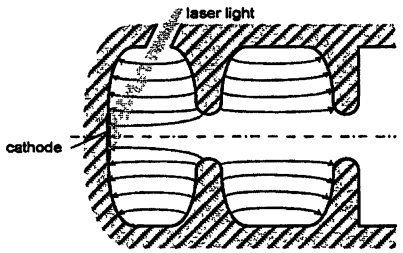

Fig. 4. RF injection gun driven by laser

The reason to drive a RF gun by several ($N \geq 2$) field harmonics is to provide high-quality flatness in time of the accelerating field at the cathode when a bunch is being injected [5] so that each portion of the electrons starts in the same field magnitude. This is important because ideally inevitable difference in energies of the injected electrons should not be accompanied by position difference. In order to satisfy this condition, whole electrons should be injected in the constant field and be accelerated up to a relativistic energy in this field. In the Fig. 6 possible injection time interval lies between $t_1 = -100$ ns and $t_2 = 100$ ns. This idea allows in principle reducing longitudinal bunch emittance. Another potential advantage is associated with the fact that multi-harmonic field, resulted by several coherent RF sources, reaches maxima to be proportional a number N of these sources. This leads to reduction of overall Ohmic losses and the input RF power (for a given peak cathode field). Preliminary calculations show that input power in a symmetric three-mode cavity (f = 0.65 GHz, $2f$ = 1.3 GHz, $6f$ = 3.9 GHz) is nearly half the power needed to feed a single mode with the same cathode field. A further appealing property is the predicted increase of breakdown threshold due to a reduction of the surface exposure time to high fields. The feeding scheme for a multi-mode RF gun is shown in Fig. 5.

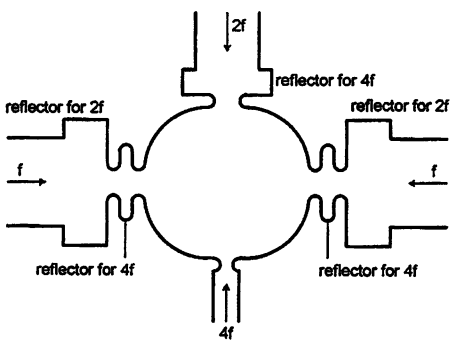

Fig. 5. Feeding of injection gun by external RF sources

The output electron energy in RF gun cavities is limited by breakdown and dark current phenomena. In order to increase bunch energy the "anode-cathode" effect can be used. This effect occurs in longitudinally asymmetric cavity so that emission fields at cathode surface takes place when all modes are in-phase condition. Fields on the right iris at this time are even more than fields on cathode, but these fields do not allow electron emission (this is a virtual "anode"). For a half of a period of the lowest mode these modes becomes out-phased, that is why, an instant "cathode" field at the first iris are less than breakdown threshold. Time-dependent field dynamics on cathode and on the iris surface are shown in Fig. 6, where injection gun frequencies f = 0.65 GHz, $2f$ = 1.3 GHz, $4f$ = 2.6 GHz were used. Calculations show that one can reach bunch energies as high as 3–6 MeV even after the first half cell. In the next cell the mutual phase of RF field and electrons is chosen to compensate energy difference caused by the first cell.

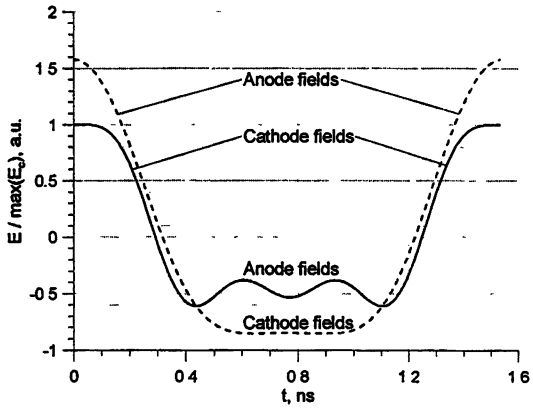

Fig. 6. Time dependence of RF fields at physical cathode (solid curve) and at left side of the first iris (dashed curve)

Conclusion

Multi-mode accelerating structures can provide high acceleration gradient in multi-TeV machines. They can be built as dielectric based or all-metallic structures excited by high-order longitudinal modes.

Application of several harmonically related modes in RF injection gun cavities promises lesser loss and faster acceleration in comparison with traditional single mode gun of the same bunch charge and beam emittance.

References

1. *Kuzikov S.V., S.Yu. Kazakov, Y. Jiang, J.L. Hirshfield.* High-gradient two-beam accelerator structure // Phys. Rev. ST-AB, 2010, v. 13, №7, p. 071303.

2. *Kuzikov S.V., S.Yu. Kazakov, Y. Jiang, J.L. Hirshfield.* Asymmetric bimodal accelerator cavity for raising rf breakdown thresholds // Phys. Rev. Lett., 2010, v. 104, p. 214801.

3. *S.V. Kuzikov, S.Yu. Kazakov, Y. Jiang, M.E. Plotkin, A.A. Vikharev, and J.L. Hirshfield.* Advanced High Gradient RF Structure Development // Proc. of 14th Advanced Accelerator Concepts Workshop, AIP Conf. Proc., Ed. by S.Gold and G.Nusinovich. V. 1299, Issue 1, 2010, p. 307-312.

4. *L. Serafini, J. B. Rosenzweig,* Envelope analysis of intense relativistic quasilaminar beams in rf photoinjectors: A theory of emittance compensation // Phys. Rev. E. V. 55, No. 6, 1997. P. 7568-7589.

5. *D.H. Dowell, M. Ferrario, T. Kimura, J. Lewellen, C. Limborg, P. Raimondi, J.F. Schmerge, L. Serafini, T. Smith and L. Young,* A Two-Frequency RF Photocathode Gun // 25th International Free Electron Laser Conference (FEL 2003) and 10th FEL User Workshop, 8-12 Sep 2003, Tsukuba, Ibaraki, Japan.

INDEX OF AUTHORS

A

Abrosimov N.V. 289
Agapova M.V. 136
Aiello G. 163
Akhmedzhanov R.A. 231
Albajar F. 21
Alberti S. 21, 189
Alisov A.F. 325
Altukhov A.B. 181
Amirov V.Kh. 175
Anderson D. 327, 329, 339
Angeluts A.A. 235
Antonsen T.M., Jr. 285
Ärje J. 43
Arkhipenko V.I. 198, 345
Artamoshkin A.M. 325
Arzhannikov A.V. 57, 86, 131, 209, 237, 295
Askinazi E.E. 287
Asmussen J. 5
Astrelin V.T. 131
Avramides K.A. 99
Azizov E.A. 7

B

Baar M.R, de 21, 147, 167
Baev V.G. 337
Bagryansky P.A. 175
Balakin A.A. 169, 177
Bandurkin I.V. 115, 127
Barik R.K. 223
Baruah U. 21
Batanov G.M. 90
Becket B. 21
Bekhterev V. 299
Bellinger M. 163
Belousov V.I. 91
Ben Rhouma A. 155
Bender S.E. 173
Bera A. 223
Bertelli N. 169
Bertizzolo R. 21
Bespalov V.G. 249
Beveren V., van 167
Bigelow T. 21
Bin W. 15, 71
Bingham R. 191
Bird J. 163
Blackman T. 157
Blank M. 8
Blyakhman A.B. 277
Bobrenok O.F. 295
Bocquet R. 267
Bogdashov A.A. 123
Bogomolov S. 299
Bolshakov A.P. 287
Bondar Yu.V. 90
Bongers W.A. 153, 167
Bonicelli T. 21
Borchard P. 8
Borodin A.B. 39
Borodin A.V. 239, 242
Bouquey F. 157, 163
Braber R., van den 15, 153, 167
Bratman V.L. 9, 32, 75, 88, 115, 125, 252
Braune H. 15, 45, 163
Bruschi A. 15, 21, 71, 153, 163
Burdakov A.V. 209
Butcher P. 163
Buyanova M.N. 169, 177
Bykov Yu.V. 133, 301, 303

C

Cahalan P. 8
Cairns R.A. 191
Callegari Th. 345
Cappa Á. 90, 159
Cara Ph. 307
Cauffman S. 8
Caughman J. 21
Ceccuzzi S. 187
Cengher M. 149
Chang T.-H. 73, 84, 138
Chapman I.T. 157
Chavan R. 21
Chayahara A. 51
Chen Ch.-H. 82
Chen N.C. 73
Cherkasova O.P. 267, 269
Cherkassky V.S. 240
Chernichkin V.I. 213
Chernov V.V. 47
Chernyshev F.V. 173
Chesnokov E.N. 258
Chirkov A.V. 133, 141, 185
Chlechowitz E. 155
Choporova Yu.Yu. 240
Chouli B. 155
Cirant S. 21, 71
Citrin J. 147
Clay R. 163
Conde M. 291
Constable D.A. 115
Constantinescu D. 171
Coquillat D. 217
Corbel E. 157
Coutaz J.-L. 11
Cross A.W. 32, 115, 191
Cuisset A. 267

D

Dammertz G. 45
Danilov Yu.Yu. 140
Daranciang D. 30
Darbos C. 21, 157, 189
Dattoli G. 105
Debray F. 281
Dell'Era F. 71
Denisov G.G. 13, 21, 32, 91, 123, 125, 127, 133, 136, 141, 163, 185
Denisyuk I.Yu. 263
Di Palma E. 105
Djordjevic S. 147
Doelman N. 15, 153, 167
Dolzhenko D.E. 213
Donaldson C.R. 32
Donné A.J.H. 167
Doria A. 17
Drobin V. 299
Drozdov M.N. 289
Dukhnovsky M.P. 297, 305
Dumbrajs O. 171
Dupree R. 61
Dyachenko V.V. 161, 173, 181
Dyakonova N. 217

E

Edlington T. 163
Efremov A. 299
Egorov S.V. 301, 303
Egorov A.M. 325
Egorov A.S. 301
Ejiri A. 151
Elchaninov A.A. 63
Ellis R.A. 149
Eminoglou E. 153, 167
Epstein I.L. 315
Erckmann V. 15, 45, 153, 167
Eremeev A.G. 123, 301, 303
Eremeev N.F. 295
Eremeykin O.N. 301
Eriksson L.-G. 157
Ermolaev D.M. 225
Esalkov M.N. 39
Esaulkov M. N. 242, 239
Esipov L.A. 181
Ezerskaya A.A. 244

F

Facco A. 307
Fadeev D.A. 231
Fanthome J. 163
Fantini F. 307
Farina D. 21, 163
Farthing J. 163
Fedorov Yu.Yu. 297, 305
Fedotov A.E. 9, 75
Fedotova Yu.A. 337
Fedulova E.V. 269
Felch K. 8
Felshtyn M.L. 271
Ferran A. 189
Figini L. 163
Fil'chenkov S.E. 111
Filipovic E. 153
Fisher A. 30
Fix A.Sh. 88
Fritz E. 153
Frolov A.A. 39, 239, 245
Fuchs M.I. 30, 77
Fujii Y. 61
Fujisawa A. 151
Fujiwara T. 61
Fukuyama A. 151

G

Gachev I.G. 123
Gai W. 291
Galant G. 183
Gallerano G.P. 17
Gandini F. 21, 71
Gantenbein G. 15, 45
Garavaglia S. 163
Garcia J. 163
Gardener M. 163
Garet F. 11
Garin P. 307
Gassman T. 21

Gavrilenko V.I. 225
Gelfand A.V. 237
Gerasimov V.V. 247
Gerbaud T. 163
Gillespie K.M. 191
Ginzburg N.S. 57, 69, 86, 97, 113, 129, 131, 313
Giovenale E. 17
Giruzzi G. 157, 163
Glyavin M.Yu. 59, 103, 107
Gnedenkov A.Ph. 136
Godisov O.N. 289
Goede A.P.H. 167
Gold S.H. 95
Goldenberg A.L. 103
Golota V.I. 325
Goltsman G. 211
Golubev I.I. 313, 337
Golubev S.V. 194, 196, 204, 252, 289
Golubok A.O. 271
Golubykh S.M. 337
Goodfellow J. 30
Goodman T.P. 21
Gorbachev A.M. 47, 95, 283, 297, 305
Gorbatushkov V.N. 175, 185
Gorelov Y.A. 149
Gorodetsky A.A. 249
Gospodchikov E.D. 175, 177, 179, 194, 196, 204
Goykhman M B. 79, 321
Grachev Y.V. 249
Granucci G. 163
Graves J.P. 157
Grede A. 80
Gromov A.V. 79, 321
Grünwald G. 49
Gu Y. 5
Gurchenko A.D. 181
Gusakov E.Z. 19, 161, 198
Gusev V.K. 173
Gvozdev A.K. 140

H

Han S.T. 119
Hanada K. 151
Hanatani K. 159
Hasegawa M. 151
Hay J. 163
Hayashi K. 35
He W. 32, 115, 191
Heidinger R. 21, 307
Henderson M. 21, 163, 189, 202
Henke H. 80
Higashijima A. 151
Hintzsche H. 251
Hirshfield J.L. 291, 351, 93, 95, 23, 347
Ho I.-C. 239
Hogeweij G.M.D. 147
Hogge J.-P. 21, 189
Höhnle H. 49
Hollmann F. 153
Holoptsev V.V. 123
Hor'kov D.P. 271
Horii F. 61
Hotchin S. 163
Howell D.F. 157
Huang K.-Y. 82
Huang Y.-Ch. 82
Hung C.-L. 73, 84, 138
Hung C.W. 138
Husainov T.A. 179

I

Ibarra A. 307
Ida K. 41
Idehara T. 61, 65
Idei H. 151
Ido T. 41
Igami H. 41, 151
Igochine V. 171
Ikeda R. 65
Ilin V.I. 13, 136, 185
Ilin V.N. 136
Illy S. 45, 99, 121, 189
Ilyakov I.E. 231
Ilyin V.N. 163
Inyushkin A.V. 287
Irkhin V.I. 277
Irzak M.A. 161, 181
Isaev V.A. 95
Ishiguro M. 151
Isobe M. 151
Ito S. 41
Ivanov D.V. 244
Ivanov O.A. 95
Ivanov V.A. 309
Ivanov V.Yu. 123
Izotov I.V. 43, 200, 204, 281, 311

J

Jastrow Ch. 251
Jennison M. 163
Jensen K.L. 285
Jiang Y. 23, 351
Jin J. 121
Johansson J. 327

K

Kajiwara K. 21, 35, 202, 35
Kalinin P.V. 57, 86, 131, 209, 295
Kalinnikova E. 151
Kalish A.N. 229
Kalvas T. 43
Kalynov Yu.K. 8, 88, 252
Kalynova G.I. 123
Kaminsky A.K. 113, 313, 337
Kanareykin A.D. 279
Kantor M.Yu. 181
Karachev A.A. 343
Karas' I.V. 325
Karas' V.I. 325
Kargovsky A.V. 267, 269
Kashin V.A. 321
Kasparek W. 15, 21, 45, 49, 153, 163, 167
Kasugai A. 21
Kavin A.A. 173
Kawasaki S. 151
Kellett B.J. 191
Kern S. 21, 45, 99, 121, 189
Kharchev N.K. 90
Kharlamova T.S. 295
Khilar P. 163
Khitrov S.A. 161, 173
Khodan A.N. 262
Khokhlov D.R. 213
Kholoptsev V.V. 301
Khomich A.V. 287
Khromov N.A. 173
Khvostenko A.P. 136
Kikuchi M. 151
King M. 191
Kinkead A.K. 95
Kirneva N. 163
Kislov D. 163
Kitaeva G.Kh. 215
Kitsanov S.A. 134
Kladuhin V.V. 321
Kleine-Ostmann T. 251
Klimov A.I. 63
Knap W. 217
Knipe S. 163
Knyazev B.A. 219, 240, 247
Kobayashi N. 21, 202
Kobayashi S. 41, 159
Koivisto H. 43
Koldanov V.A. 252
Kolganov N.G. 111, 125
Kolik L.V. 90
Komppula J. 43
Konev V.Yu. 63
Konoshima S. 159
Konov V.I. 287
Konyzhev M.E. 309
Kopelovich E.A. 133
Kopyl P.V. 343
Kornishin S.Yu. 123
Kossyi I.A. 25, 339
Kostin V.A. 254, 256
Kostyna A.N. 136
Kotelnikov I.A. 242
Kouprienko D.V. 181
Kovalev N.F. 79, 321
Kovalev Yu.A. 337
Kozlov A P. 313, 337
Kozlov A.V. 47
Kozlov S.A. 244, 249
Kratko A.F. 313
Krijger B. 153, 167
Krikunov S.V. 181
Kryachko I.A. 337
Kubarev V.V. 258
Kubo S. 41, 151
Küchler D. 43
Kuftin A.N. 136, 141, 143
Kulipanov G.N. 26, 258
Kulygin M.L. 91
Kumar M. 260
Kuritsin I.I. 39, 242
Kurkin V.S. 123
Kuyanov A. 163
Kuzikov S.V. 23, 93, 127, 140, 313, 351
Kuzmin L. 28
Kuznetsov S.A. 86, 131, 209, 237
Kwon O.J. 223

L

Lackner K. 171
Lamy T. 43, 281

Landis J.D. 21
LaPointe M.A. 291
Laqua H.P. 15, 155
Larionov M.M. 173
Lashkul S.I. 181
Lazorskiy P.A. 237
Lebedev A. 299
Lebedev Yu.A. 315
Lechte C. 15, 45
Lee H.Y. 159
Lennholm M. 157, 163
Leonhardt W. 45
Lesnikovich A.I. 337
Leuterer F. 49
Lheurette E. 11
Li F. 21, 189
Li M. 221
Li W. 221
Liévin C. 45
Lindenberg A.M. 30
Link G. 317
Lippens D. 11
Lisak M. 183, 327, 329, 339
Litaudon X. 163
Litvak A.G. 13, 21, 136, 141, 163, 252
Liu H.Q. 151
Liu M. 77
Lo J. 345
Lo Y C. 138
Lobaev M.A. 95
Lobanov S.E. 173
Loginov V. 299
Lohr J. 34, 149
Loos H. 30
Lu J. 5
Lu X. 53
Lubyako L. 15, 153, 167
Luchinin A.G. 59, 107
Luk'yanchikov G.S. 339
Luna E., de la 163
Lyuteckii A.V. 271

M

Maekawa T. 151, 165
Mahmoud M.M. 317
Makarov M.A. 209
Makhalov P.B. 75
Malakhov D.V. 90
Maleev N.A. 225
Malevich Yu.V. 265
Malkin A.M. 86, 97, 113, 129
Malygin A.V. 99
Malygin V.I. 136, 175, 185
Mansfeld D.A. 196, 204, 289
Manuilov V.N. 103
Manuilov V.N. 65, 88, 101, 143, 123
Mar'ev S.P. 111
Maremyanin K.V. 225
Marie-Jeanne M. 281
Marsen S. 155
Marshall T.C. 93, 291, 347
Martinez J. 90
Marushchenko N.B. 15, 159
Maslov V.V. 123
Massaut V. 307
Masuda K. 159
Matsuoka S. 41
Matveev B.A. 271
Mavlyudov T.B. 315
McConville S.L. 191
Meier A. 335
Mekler K.I. 209
Melnik A.D. 173
Messina G. 17
Mesyats G.A. 63
Meyer-Spasche R. 171
Mezentseva N.V. 295
Michel G. 15, 45, 153
Mihalcea D. 291
Milevich I.A. 337
Min S.H. 223
Minami T. 159
Mirizzi F. 105, 187
Mironov V.A. 231
Mishakin S.V. 123, 125
Mitarai O. 151
Mizuno K. 159
Mizuno Y. 41
Mizuuchi T. 159
Mocheneva O.S. 322
Moiseev M.A. 140, 141, 143
Moisseenko E.V. 265
Mokuno Y. 51
Monaco F. 49
Moriya Y. 159
Moro A. 21, 163
Morozkin M.V. 103, 107
Morozov G.A. 319
Morozov O.G. 319
Mosnier A. 307
Motojima G. 159
Muchnikov A.B. 283, 297, 305
Mukai K. 159
Mukhin V.I. 262
Müller S. 49
Münich M. 49
Murakami S. 159
Mutoh T. 41
Muzzini V. 71
Myasnikov V.E. 13, 21, 136

N

Nagaoka K. 151
Nagasaki K. 159
Nagashima Y. 151
Nakamura K. 151
Nakamura Y. 159
Nakanishi H. 151
Nakashima H. 151
Nasibullin A.R. 319
Nazare C. 21
Nazarov M.M. 11, 235, 262, 263, 265, 267, 269
Nechaev V.E. 331, 333
Nichiporenko V.O. 136
Nicorici A.V. 213
Nikitin A.K. 247
Nishino N. 151
Nishitani T. 307
Nishiura M. 41
Noguchi Y. 165
Noke F. 45, 153
Noland J. 43
Novikov V.N. 136
Novokhatsky A.N. 173
Novoselov E.V. 249
Novozhilova Yu.V. 90, 109
Nowak S. 163
Nuij P.W.J.M. 167
Nusinovich G.S. 285

O

Oda Y. 21, 35, 202, 335
Ogasawara S. 65
Ogawa I. 61, 65
Ohshima S. 159
Okada H. 159
Okada K. 41
Omori T. 21, 202
Orlov V.B. 133
Otte M. 155

P

Paganakis I.Gr. 21, 99, 121, 189
Palitsin A.V. 79, 111, 321
Pan H. 221
Panchenko V.A. 287
Parail V. 163
Park G.S. 223
Parkin A. 163
Parmar D. 21
Parshin V.V. 322
Paulish A.G. 237
Pavelyev A.B. 133, 143
Pavlova S.N. 295
Peregorodova E.N. 117
Perelstein E.A. 113, 313, 337
Peskov N.Yu. 57, 86, 113, 131, 313
Petelin M.I. 15, 90, 140, 153, 167, 313, 324
Peters B. 21
Petrov Yu.V. 173
Petrov A.E. 90
Peura P. 43
Phelps A.D.R. 32, 115, 191, 271
Pihtin N.A. 271
Pikov V. 40
Piosczyk B. 21, 99, 121, 189
Platania P. 21
Plaum B. 15, 21, 153, 163, 167
Plotkin M.E. 140, 351
Plotnikov I.V. 123
Pohl H.-J. 289
Poli E. 21
Polosatkin S.V. 209
Polsky A.V. 287
Ponce D. 149
Popov A.Yu. 19
Popov L.G. 136
Popov V.V. 225
Popovich A.F. 287
Porte L. 21
Postupaev V.V. 209
Potapenko I.F. 325
Power J. 291
Prater R. 34
Preinhaelter J. 155
Pryakhin D.A. 289

Puech J. 327, 329, 339
Purohit D. 21
Purps F. 45, 153

R

Radishev D.B. 47, 283
Rakova E.I. 327, 339
Ralchenko V.G. 287
Ramponi G. 21
Rao S.L. 21
Rasch J. 327, 329
Rasmussen D. 21
Ratnikova A.K. 297, 305
Razin S.V. 200, 252
Reis D. 30
Robertson C.W. 32, 115, 191
Rodin Yu.V. 91, 111
Romanchenko I.V. 63
Ronald K. 32, 115, 191
Ronden D. 21
Ropponen T. 43
Rostov V.V. 63
Rovenskikh A.F. 209
Rozhdestvensky V.V. 181
Rozhnev A.G. 119
Rukavishnikova V.G. 136
Ryabov A.Y. 263
Ryabova L.I. 213
Ryokai T. 151
Ryskin N.M. 109, 117, 119
Rzesnicki T. 121

S

Sadykov V.A. 295
Saibene G. 21, 163, 335
Saito T. 61, 65
Sakaguchi M. 151
Sakamoto K. 21, 35, 151, 159, 202
Sakharov A.S. 309
Sakharov N.V. 173
Sakomoto K. 335
Salanov A.N. 295
Saliba M. 153
Samartsev A. 45, 121
Samigullin R.R. 319
Samoilov L.L. 271
Samsonov S.V. 32, 123, 125
Sanchez F. 21
Sano F. 159
Saparina D.O. 229
Sapozhnikov D.A. 267, 269
Sapozhnikov I.D. 271
Sarsyan K.A. 90
Satake S. 41
Sattorov M.A. 223
Sauter O. 21
Saveliev A.N. 161, 181, 193
Savikin A.P. 301
Savilov A.V. 115, 127
Sazontov A.G. 331, 333
Schamiloglu E. 37, 77
Scherer T.A. 21, 335
Schlaich A. 45, 121
Schmid E. 251
Schmid M. 45
Schrader T. 251
Schreck S. 21, 335
Schubert M. 49
Schulz T. 45
Schütz H. 49
Sedov A.S. 143
Sedykh S.N. 113, 313, 337
Seleznev V. 299
Semenov V.E. 183, 327, 329, 339
Sennikov P.G. 289
Sergeev A.S. 57, 69, 86, 97, 113, 129, 131
Shalashov A.G. 175, 177, 179, 194, 196, 204
Shapiro M. 21, 149
Shapoval S.Yu. 225
SharkovV.V. 301
Sharma S.K. 151
Sharypov A.K. 69
Shashkin V.I. 289
Shatalin S.V. 181
Shchelkunov S.V. 291
Shcherbinin O.N. 161, 173
Shepelev A.V. 265
Shevchenko O.A. 258
Shevchenko V.F. 193
Shevelev A.E. 173
Shibkov V.M. 341, 343
Shibkova L.V. 343
Shibkova N.V. 341
Shikata S. 51
Shimizu A. 41
Shimozuma T. 41
Shishkin B.V. 231
Shishov Yu. 299
Shkurinov A.P. 11, 39, 235, 239, 242, 265, 267, 269
Sidorov A.V. 200, 252, 281
Siegel P.H. 40
Simonchik L.V. 198, 345
Singh N.P. 21
Sinitsky S.L. 57, 86, 131, 209
Sinitsyn O.V. 285
Sizov F. 227
Skalyga V.A. 43, 200, 252, 281, 311
Sklyarov V.F. 209
Skuratov V.A. 265
Skvortsova N.N. 90
Smirnova I.N. 267, 269
Smirnova T.M. 123
Smolyakova O.B. 175
Smolyanskaya O.A. 249
Smorygo O.L. 295
Sokoloff J. 345
Sokolov E.V. 13, 133, 136
Soluyanova E.A. 133, 136, 185
Solyankin P.M. 235
Sorokin A.A. 303
Sortais P. 281
Sotnikov G.V. 93, 291, 347
Sozzi C. 21, 163
Spaeh P. 21
Späh P. 163
Spassovsky I. 17, 105
Speirs D.C. 191
Stange T. 155
Starostin A.N. 325
Steinbuch M. 147
Stepanov A.Yu. 173, 181
Stepanov V.D. 131, 209
Stober J. 49, 153, 167
Stopper H. 251
Strauss D. 21, 163, 335
Strelkov P.S. 67
Suehara T. 61
Sukhorukov A.P. 229
Sulyaev Yu.S. 209
Surkont O.S. 343
Surrenti V. 105
Suvorov E.V. 231
Sypek M. 11

T

Tai E.M. 13, 21, 133, 136, 185
Takahashi K. 21, 35, 202, 335
Takahashi H. 41
Takase Y. 151
Takeuchi M. 159
Takita Y. 41
Taldenkov A.N. 287
Tanaka H. 165
Tarakanov V.P. 349
Tarasov I.S. 271
Tarbeeva Yu.A. 309
Tarvainen O. 43
Tashima S. 151
Tatarinov A.V. 315
Tatematsu Y. 65
Temkin R. 21
Teppe F. 217
Thomas P. 21
Thuillier T. 43, 281
Thumm M. 15, 21, 45, 57, 99, 121, 131, 175, 209, 295, 317
Toi K. 151
Toivanen V. 43
Tokunaga K. 151
Tolkachev A. 90
Totmeninov E.M. 134
Tripathi V.K. 260
Trophime C. 281
Trukhin V.N. 271
Trukhina E. 163
Tsunouchi N. 51
Turco F. 157
Turkin Y. 159
Tyutunnikov S.I. 337

U

Uchida M. 165
Ulihin A.S. 295
Ulmaskulov M.R. 69
Umezawa H. 51
Urban J. 155
Usachev S.V. 136
Usacheva S.A. 109, 117
Usachonak M.S. 198, 345
Usoltsev V.V. 295
Usov V.G. 136
Uvarov N.F. 295

V

Vaccaro A. 163
Vagdama A. 163
Vaks V.L. 233
Vdovicheva N.K. 331

Vdovin V.A. 163, 337
Vdovin V.A. 272
Vermare Ch. 307
Verney E. 281
Vidal N. 281
Vikharev A.A. 91, 93, 127, 313, 351
Vikharev A.L. 297, 305, 283, 47, 95
Viktorov M.E. 196, 204
Vlasov I.I. 287
Vodopyanov A.V. 194, 204, 289
Vogel V. 351
Vorgul I. 191
Vvedenskii N.V. 254, 256
Vyacheslavov L.N. 209
Vykhodtsev P.V. 134

W

Wagner D. 49, 153, 167
Wang J.W. 293
Watanabe F. 165
Watanebe H. 151
Wen H. 30
Westerhof E. 169
Whyte C.G. 32, 115, 191
Witvoet G. 147
Wu J. 221

Y

Yalandin M.I. 63, 69
Yamada H. 51
Yamada I. 41
Yamada N. 65
Yamamoto S. 159
Yashnon Yu.M. 136
Yazvitsky N. 299
Yeh Y.S. 73, 84, 138
Yokoyama M. 41
Yoshida N. 151
Yoshimura Y. 41, 159
Young A.R. 32
Yuan C.P. 73

Z

Zagorodny A.G. 325
Zagrebelny I.A. 325
Zaitsev N.I. 140, 313
Zalesny J. 183
Zamyatina I.N. 277
Zapevalov S.A. 140
Zapevalov V.E. 13, 136, 141, 143
Zasenko V.I. 325
Zaslavsky V.Yu. 86, 113, 129, 131
Zavolsky N.A. 141, 143
Zemlyakov V.E. 225
Zeng H. 221
Zhang L. 32
Zhang X.-C. 53
Zharova N.A. 339
Zhizhin G.N. 247
Zohm H. 21, 49, 171
Zorin V.G. 43, 200, 252, 281, 311
Zotova I.V. 69, 97, 113
Zushi H. 151

CONTENTS

P: Plenary

Microwave Plasma Assisted CVD Synthesis of Single Crystal Diamond at 180–300 Torr 5
Jes Asmussen, Y. Gu, and J. Lu

Hybrid reactors – Prospects of Development and Application 7
E.A. Azizov

Megawatt Class Gyrotron Development at CPI 8
M. Blank, P. Borchard, P. Cahalan, S. Cauffman, K. Felch

Terahertz Electron Sources for EPR and DNP/NMR Spectroscopy 9
V.L. Bratman, A.E. Fedotov, and Yu.K. Kalynov

Interaction of THz Waves with Metals and Related Devices 11
J.-L. Coutaz, F. Garet, M. Nazarov, A. Shkurinov, M. Sypek, E. Lheurette, and D. Lippens

Trends in High-Power Gyrotron Development 13
A.G. Litvak, G.G. Denisov, V.E. Zapevalov, V.E. Myasnikov, E.V. Sokolov, E.M. Tai, V.I. Ilin

ECRH with Advanced CW Systems 15
V. Erckmann, W. Kasparek, M.I. Petelin, A. Bruschi, W. Bin, H. Braune, R. van den Braber, N. Doelman, G. Gantenbein, H.P. Laqua, C. Lechte, L. Lubiako, N.B. Marushchenko, G. Michel, B. Plaum, M. Thumm, and the W7-X ECRH-teams at IPP Greifswald, IPF Stuttgart, and KIT

Development of High Power mm-Wave and THz Sources at ENEA for Novel Biological Applications and Stand-off Detection 17
G.P. Gallerano, A. Doria, E.Giovenale, G. Messina and I. Spassovsky

Anomalous Phenomena at ECRH in Toroidal Devices and Low Threshold Parametric Decay Instabilities 19
E.Z. Gusakov, A.Yu. Popov

Present Status of the 24 MW 170 GHz ITER EC H&CD System 21
M. Henderson, F. Albajar, S. Alberti, U. Baruah, T. Bigelow, B. Becket, R. Bertizzolo, T. Bonicelli, A. Bruschi, J. Caughman, R. Chavan, S. Cirant, C. Darbos, M. de Baar, G. Denisov, D. Farina, F. Gandini, T. Gassman, T.P. Goodman, R. Heidinger, J.P. Hogge, K. Kajiwara, W. Kasparek, A. Kasugai, S. Kern, N. Kobayashi, J.D. Landis, F. Li, A. Litvak, A. Moro, V. Myasnikov, C. Nazare, J. Oda, T. Omori, I. Paganakis, D. Parmar, B. Peters, P. Platania, B. Plaum, E. Poli, L. Porte, B. Piosczyk, D. Purohit, G. Ramponi, S.L. Rao, D. Rasmussen, D. Ronden, G. Saibene, K. Sakamoto, F. Sanchez, T. Scherer, S. Schreck, N.P. Singh, M. Shapiro, C. Sozzi, P. Spaeh, D. Straus, O. Sauter, E. Tai, K. Takahashi, R. Temkin, P. Thomas, M. Thumm, and H. Zohm

High-Gradient Collinear Two-beam Electron Accelerator 23
Y. Jiang, S.V. Kuzikov, J.L. Hirshfield

New Microwave Plasma Sources Based on the Latest Advances of Fundamental Gas-discharge Physics 25
I.A. Kossyi

High Power NovoFEL: Developments and New Results 26
G.N. Kulipanov and NovoFEL team

Ultra-sensitive Cold-Electron Bolometers for High-Performance Cosmology Instruments 28
L. Kuzmin

Ultrafast THz Response of Materials at Extreme Fields: Studies using Laser-based and Accelerator-based Sources 30
D. Daranciang, J. Goodfellow, M. Fuchs, H. Wen, H. Loos, D. Reis, A. Fisher, A.M. Lindenberg

Gyrotron Amplifiers and Gyro-BWOs with Helically Corrugated Waveguides 32
A.D.R. Phelps, V.L. Bratman, A.W. Cross, G.G. Denisov, C.R. Donaldson, W. He, C.W. Robertson, K. Ronald, S.V. Samsonov, C.G. Whyte, A.R. Young, L. Zhang

The Many Applications of ECH on DIII-D 34
R. Prater, J. Lohr, and the DIII-D Physics and Operations Teams

Progress of Gyrotron Development in JAEA 35
Keishi Sakamoto, Ken Kajiwara, Yasuhisa Oda, Koji Takahashi, Kazuo Hayashi

Status of Relativistic Electronics Research in Laboratories in the United States 37
E. Schamiloglu

The Basis of the Plasma Methods of Diagnostics and Detection of THz Radiation 39
A.B. Borodin, M.N. Esalkov, I.I. Kuritsin, A.A. Frolov and A.P. Shkurinov

Impact of Low-Power Millimeter Waves on Cell Membrane Potential 40
P.H. Siegel and V. Pikov

Study of High T_e Plasma Characteristics of LHD Using High Power 77 GHz Gyrotrons 41
H. Takahashi, T. Shimozuma, S. Ito, S. Kubo, Y. Yoshimura, H. Igami, M. Nishiura, S. Kobayashi, Y. Mizuno, K. Okada, Y. Takita, I. Yamada, M. Yokoyama, T. Ido, A. Shimizu, K. Ida, S. Matsuoka, S. Satake, T. Mutoh and the LHD experiment group

Pulsed Operation of ECR Ion Sources – Plasma Physics and Diagnostics 43
O. Tarvainen, T. Ropponen, V. Toivanen, T. Kalvas, J. Komppula, H. Koivisto, J. Ärje, P. Peura, J. Noland, I. Izotov, V. Skalyga, V. Zorin, T. Thuillier, T. Lamy, D. Küchler

Recent Progress on the 1 MW, 140 GHz, CW Series Gyrotrons for W7-X 45
M. Thumm, H. Braune, G. Dammertz, G. Gantenbein, V. Erckmann, S. Illy, S. Kern, W. Kasparek, C. Lechte, W. Leonhardt, C. Liévin, G. Michel, F. Noke, F. Purps, A. Samartsev, A. Schlaich, M. Schmid, T. Schulz

CVD Diamond Films Grown in Millimeter-wave Plasma-assisted Reactor 47
A.L. Vikharev, A.M. Gorbachev, V.V. Chernov, A.V. Kozlov, D.B. Radishev

Advanced Plasma Heating and Control Schemes Using ECRH at ASDEX Upgrade 49
D. Wagner, J. Stober, H. Höhnle, W. Kasparek, G. Grünwald, F. Leuterer, F. Monaco, S. Müller, M. Münich, M. Schubert, H. Schütz, H. Zohm and ASDEX Upgrade Team

Recent Progress in R&D of Synthesis of Large Single-crystal Diamond Wafers by Using MWPCVD 51
H. Yamada, A. Chayahara, Y. Mokuno, N. Tsunouchi, H. Umezawa, S. Shikata

Detection of Intense THz Wave with Air-plasma Photonics 53
Xiaofei Lu and X.-C. Zhang

S: High power microwave sources

Powerful Masers and Lasers with Two-Dimensional Distributed Feedback 57
N.S. Ginzburg, N.Yu. Peskov, A.S. Sergeev, A.V. Arzhannikov, P.V. Kalinin, S.L. Sinitsky and M. Thumm

High Power Pulsed Terahertz Gyrotrons 59
M.Y. Glyavin, A.G. Luchinin

High Power THz Technologies Opened by High Power Radiation Sources – Gyrotron FU CW Series 61
T. Idehara, F. Horii, Y. Fujii, I. Ogawa, T. Saito, T. Fujiwara, T. Suehara and R. Dupree

High Power Nanosecond Microwave Oscillators with Phase Synchronization 63
V.V. Rostov, A.A. Elchaninov, A.I. Klimov, V.Yu. Konev, I.V. Romanchenko, G.A. Mesyats, M.I. Yalandin

Development of High Power Gyrotrons in the Sub Terahertz Region for Application to CTS Measurement 65
T. Saito, Y. Tatematsu, N. Yamada, S. Ogasawara, R. Ikeda, I. Ogawa, T. Idehara, V.N. Manuilov

Recent Progress on Plasma Relativistic Microwave Electronics at General Physics Institute 67
P.S. Strelkov

Amplification, Self-transparancy and Compression of Ultrashort Electromagnetic Pulses Propagating along Quasi-Stationary Electron Beams 69
I.V. Zotova, N.S. Ginzburg, A.S. Sergeev, M.I. Yalandin, M.R. Ulmaskulov, A.K. Sharypov

Beam-spreading Surfaces for Millimeter-wave Matched Loads 71
A. Bruschi, W. Bin, S. Cirant, F. Dell'Era, F. Gandini, V. Muzzini

High-Power, Terahertz Gyrotron with Frequency Tunability 73
T.-H. Chang, N.C. Chen, C.P. Yuan, Y.S. Yeh, and C.L. Hung

Compact Sources of Medium-power Millimeter-wave Radiation 75
V.L. Bratman, A.E. Fedotov, and P.B. Makhalov

Mode Switching and Phase Locking in a Relativistic Magnetron with Diffraction Output 77
M.I. Fuks, M. Liu, E. Schamiloglu

Limiting Currents of Strongly-magnetized Electron Beam in Uniform Transport Channel 79
M.B. Goykhman, A.V. Gromov, N.F. Kovalev, A.V. Palitsin

Corkscrew Modulated Hollow-Beam Klystron 80
A. Grede and H. Henke

Desktop MW Superradiant Free-electron Laser at THz Frequencies 82
Yen-Chieh Huang, Chia-Hsian Chen, Kuan-Yan Huang

A Coaxial-Waveguide Gyrotron Backward-Wave Oscillator with Tapered Waveguide Cross Section 84
C.-L. Hung, Y.S. Yeh, T.H. Chang

Short-wavelength Tunable Bragg Reflectors based on Coupling of Propagating and Cutoff Waves: Modeling and «Cold» Tests 86
P.V. Kalinin, A.V. Arzhannikov, S.A. Kuznetsov, S.L. Sinitsky, N.S. Ginzburg, A.M. Malkin, N.Yu. Peskov, A.S. Sergeev and V.Yu. Zaslavsky

Design of a Powerful CW Terahertz Large-Orbit Gyrotron 88
Yu.K. Kalynov, V.L. Bratman, V.N. Manuilov, A.Sh. Fix

Gyrotron Affected by Modulated Reflection: New Experiments 90
N.K. Kharchev, G.M. Batanov, Yu.V. Bondar, L.V. Kolik, D.V. Malakhov, A.E. Petrov, K.A. Sarsyan, N.N. Skvortsova, M.I. Petelin, Yu.V. Novozhilova, A. Cappa, J. Martinez, A. Tolkachev

Nanosecond Optically Controlled Switches for Sub-Terahertz Radiation 91
M.L. Kulygin, G.G. Denisov, V.I. Belousov, Yu.V. Rodin and A.A. Vikharev

A Short-Period RF Undulator 93
J.L. Hirshfield, S.V. Kuzikov, Th.C. Marshall, G.V. Sotnikov, A.A. Vikharev

High Power Test of Active Microwave Pulse Compressor with Switch Employing Electron Beam Triggering 95
O.A. Ivanov, A.L. Vikharev, M.A. Lobaev, A.M. Gorbachev, V.A. Isaev, J.L. Hirshfield, S.H. Gold and A.K. Kinkead

Generation of Multi-megawatt Terahertz Pulses Based on Superradiance of Picosecond Electron Bunches 97
N.S. Ginzburg, I.V. Zotova, A.M. Malkin, A.S. Sergeev

Three-Dimensional Numerical Studies of Non-uniform Emission in Magnetron Injection Guns 99
A.V. Malygin, I.Gr. Pagonakis, S. Illy, K.A. Avramides, B. Piosczyk, S. Kern, M. Thumm

Dynamic Processes in the Helical Electron Beams with High Pitch-Factor 101
V.N. Manuilov

Low Voltage Non-adiabatic Electron Gun for Technological Gyrotron 103
A.L. Goldenberg, M.Yu. Glyavin, V.N. Manuilov, M.V. Morozkin

Conceptual Design of a High Voltage Electron Gun as a Driver of High Power Millimetre Wave Oscillators 105
F. Mirizzi, E. Di Palma, I. Spassovsky, V. Surrenti, G. Dattoli

Technological Gyrotron with the Wide-Band Fast Frequency Sweeping 107
M.Yu. Glyavin, A.G. Luchinin, M.V. Morozkin

Numerical Simulation of Non-stationary Operation of Oscillator with Reflection from Output Remote Load 109
Yu.V. Novozhilova, N.M. Ryskin, S.A. Usacheva

The Method for Measuring the Spectra of Nanosecond High-Power Microwave (HPM) Sources 111
S.E. Fil'chenkov, N.G. Kolganov, S.P. Mar'ev, A.V. Palitsin, Yu.V. Rodin

Short Wavelength FEM Based on Bragg Coupling of Propagating and Cutoff Waves: Recent Results and Prospects 113
N.Yu. Peskov, N.S. Ginzburg, A.K. Kaminsky, A.M. Malkin, E.A. Perelstein, S.N. Sedykh, A.S. Sergeev, V. Yu. Zaslavsky and I.V. Zotova

Numerical Simulations of a Co-harmonic Gyrotron 115
D.A. Constable, I.V. Bandurkin, A.V. Savilov, W. He, C.G. Whyte, C.W. Robertson, A.D.R. Phelps, A.W. Cross, V.L. Bratman and K. Ronald

Forced Synchronization of a Two-Mode Electronic Maser 117
E.N. Peregorodova, S.A. Usacheva, N.M. Ryskin

Nonstationary Simulation of a Second-Harmonic Sub-Terahertz Frequency-Tunable Gyrotron 119
S.T. Han, A.G. Rozhnev, N.M. Ryskin

2 MW, 170 GHz Coaxial-Cavity Gyrotron for ITER: Results Obtained with a Short Pulse Pre-Prototype at KIT 121
T. Rzesnicki, B. Piosczyk, S. Illy, J. Jin, S. Kern, I.Gr. Pagonakis, A. Samartsev, A. Schlaich and M. Thumm

Development of Helical-Waveguide Gyro-TWT at IAP 123
S.V. Samsonov, A.A. Bogdashov, G.G. Denisov, A.G. Eremeev, I.G. Gachev, V.V. Holoptsev, V.Yu. Ivanov, G.I. Kalynova, S.Yu. Kornishin, V.S. Kurkin, V.N. Manuilov, V.V. Maslov, S.V. Mishakin, I.V. Plotnikov, T.M. Smirnova

Compression of FM Pulses from an X-band Relativistic BWO up to Power of 3 GW 125
S.V. Samsonov, V.L. Bratman, G.G. Denisov, N.G. Kolganov, S.V. Mishakin

Periodic Giant RF Pulse Formation in Electron Masers 127
I.V. Bandurkin, G.G. Denisov, S.V. Kuzikov, A.V. Savilov, A.A. Vikharev

Quasi-Optical Theory of Submillimeter Relativistic Surface-Wave Oscillators 129
N.S. Ginzburg, A.M. Malkin, A.S. Sergeev, V.Yu. Zaslavsky

Planar FEM Driven by Two Microsecond Sheet E-beams 131
S.L. Sinitsky, A.V. Arzhannikov, V.T. Astrelin, N.S. Ginzburg, P.V. Kalinin, S.A. Kuznetsov, N.Yu. Peskov, A.S. Sergeev, V.D. Stepanov, M. Thumm, V.Yu. Zaslavsky

Gyrotron Complexes for Technological Applications 133
E.A. Soluyanova, Yu.V. Bykov, A.V. Chirkov, G.G. Denisov, E.A. Kopelovich, V.B. Orlov, A.B. Pavelyev, E.V. Sokolov, E.M. Tai

Experimental Investigation of the S-band Relativistic Cherenkov Microwave Oscillator Without a Guiding Magnetic Field at the Repetitively Pulsed Modes 134
E.M. Totmeninov, S.A. Kitsanov, P.V. Vykhodtsev

Last Test Results of 170GHz/1MW/50%/CW Gyrotron for ITER 136
S.V. Usachev, L.G. Popov, V.I. Ilin, M.V. Agapova, G.G. Denisov, A.Ph. Gnedenkov, V.N. Ilin, A.P. Khvostenko, A.N. Kostyna, A.N. Kuftin, A.G. Litvak, V.I. Malygin, V.E. Myasnikov, V.O. Nichiporenko, V.N. Novikov, V.G. Rukavishnikova, E.V. Sokolov, E.A. Soluyanova, E.M. Tai, V.G. Usov, Yu.M. Yashnon, V.E. Zapevalov

A Study of Harmonic Multiplying Gyrotron Traveling-wave Amplifiers with Distributed Wall Losses and Attenuating Severs 138
Y.S. Yeh, C.L. Hung, T.H. Chang, Y.C. Lo, C.W. Hung

Pulsed Multimegawatt Gyroklystron 140
N.I. Zaitsev, Yu.Yu. Danilov, A.K. Gvozdev, S.V. Kuzikov, M.A. Moiseev, M.I. Petelin, M.E. Plotkin and S.A. Zapevalov

Preliminary Design of 300 GHz/200kW/cw Gyrotrons for Fusion Research 141
V.E. Zapevalov, A.V. Chirkov, G.G. Denisov, A.N. Kuftin, A.G. Litvak, M.A. Moiseev, N.A. Zavolsky

Development of 395 GHz Gyrotrons for DNP Spectroscopy on the Basis of Experience of Elaboration of a 260 GHz Gyrotron 143
V.E. Zapevalov, A.N. Kuftin, V.N. Manuilov, M.A. Moiseev, A.B. Pavelyev, A.S. Sedov, N.A. Zavolsky

H: Current drive and plasma heating by microwaves in nuclear fusion devices

Control Oriented Application of High Power EC Waves 147
M.R. de Baar, J. Citrin, S. Djordjevic, G.M.D. Hogeweij, G. Witvoet, M. Steinbuch

Status Update on the DIII-D ECH System 149
Y.A. Gorelov, J. Lohr, M. Cengher, D. Ponce, M. Shapiro and R.A. Ellis

Electron Cyclotron / Bernstein Wave Heating and Current Drive Experiments using Phased-array Antenna System in the QUEST 151
H. Idei, H. Zushi, K. Hanada, K. Nakamura, A. Fujisawa, M. Hasegawa, N. Yoshida, M. Sakamoto, H. Watanebe, K. Tokunaga, Y. Nagashima, A. Ejiri, M. Sakaguchi, E. Kalinnikova, M. Ishiguro, S. Tashima, A. Fukuyama H. Igami, S. Kubo, S.K. Sharma, T. Ryokai, H.Q. Liu, M. Isobe, K. Nagaoka, H. Nakanishi, N. Nishino, S. Kawasaki, H. Nakashima A. Higashijima, Y. Takase, T. Maekawa, O. Mitarai, M. Kikuchi and K. Toi

Controlled High-Power Microwave Diplexers 153
W. Kasparek, R. van den Braber, N. Doelman, E. Fritz, V. Erckmann, F. Hollmann, G. Michel, F. Noke, F. Purps, W. Bongers, B. Krijger, E. Eminoglou, M. Petelin, L. Lubyako, A. Bruschi, J. Stober, D. Wagner, B. Plaum, E. Filipovic, M. Saliba, and teams at the contibuting institutes

RF-Experiments at the WEGA-Stellarator 155
H.P. Laqua, A. Ben Rhouma, E. Chlechowitz, B. Chouli, H. Laqua, S. Marsen, T. Stange, M. Otte, J. Preinhaelter, J. Urban

Sawtooth Control in the Presence of Fast Ions 157
M. Lennholm, T. Blackman, F. Bouquey, I. T. Chapman, C. Darbos, L.-G. Eriksson, G. Giruzzi, J.P. Graves, D.F. Howell, E. Corbel, F. Turco and JET EFDA Contributors

Physics Study of ECCD in Heliotron J 159
K. Nagasaki, N.B. Marushchenko, S. Yamamoto, K. Sakamoto, Y. Turkin, T. Mizuuchi, H. Okada, K. Hanatani, T. Minami, K. Masuda, S. Kobayashi, S. Konoshima, M. Takeuchi, Y. Nakamura, S. Ohshima, K. Mukai, H.Y. Lee, K. Mizuno, S. Murakami, Y. Moriya, Y. Yoshimura, G. Motojima, Á. Cappa, F. Sano

LH Current Drive in Spherical Tokamak. Theory and Experiment 161
O.N. Shcherbinin, E.Z. Gusakov, V.V. Dyachenko, M.A. Irzak, S.A. Khitrov, A.N. Saveliev

Conceptual Design of an ECRH System for JET 163
C. Sozzi, G. Giruzzi, M. Lennholm, A. Parkin, G. Aiello, M. Bellinger, J. Bird, F. Bouquey, H. Braune, A. Bruschi, P. Butcher, R. Clay, E. de la Luna, G. Denisov, T. Edlington, J. Fanthome, D. Farina, J. Farthing, L. Figini, S. Garavaglia, J. Garcia, M. Gardener, T. Gerbaud, G. Granucci, J. Hay, M. Henderson, S. Hotchin, V.N. Ilyin, M. Jennison, W. Kasparek, P. Khilar, N. Kirneva, D. Kislov, S. Knipe, A. Kuyanov, X. Litaudon, A.G. Litvak, A. Moro, S. Nowak, V. Parail, B. Plaum, G. Saibene, P. Späh, D. Strauss, E. Trukhina, A. Vaccaro, A. Vagdama, V. Vdovin, and JET EFDA Contributors

Initiation of Closed Flux Surfaces and Subsequent Current Ramp-up by ECH/ECCD in the LATE Device 165
H. Tanaka, T. Maekawa, M. Uchida, F. Watanabe, Y. Noguchi

Progress of CW Compatible Implementations of Line-of-Sight ECE Measurements Within Waveguide Based ECRH Transmission Systems 167
W.A. Bongers, W. Kasparek, M. Petelin, L. Lubyako, E. Eminoglu, M.R. de Baar, V. van Beveren, R. van den Braber, N. Doelman, A.J.H. Donné, V. Erckmann, A.P.H. Goede, B. Krijger, P.W.J.M. Nuij, B. Plaum, J. Stober, and D. Wagner

ECCD Calculations in ITER by Means of the Quasi-Optical Code 169
A.A. Balakin, N. Bertelli, M.N. Buyanova, E. Westerhof

A Low-Dimensional Model System for Quasi-Periodic Plasma Perturbations 171
D. Constantinescu, O. Dumbrajs, V. Igochine, K. Lackner, R. Meyer-Spasche, H. Zohm and ASDEX Upgrade team

Plasma Start-up and Current Generation by RF Waves in Spherical Tokamak Globus-M 173
V.V. Dyachenko, F.V. Chernyshev, V.K. Gusev, S.A. Khitrov, N.A. Khromov, M.M. Larionov, A.D. Melnik, A.N. Novokhatsky, Yu.V. Petrov, N.V. Sakharov, O.N. Shcherbinin, A.E. Shevelev, A.Yu. Stepanov, S.E. Bender, A.A. Kavin, S.E. Lobanov

Design of Auxiliary ECR Heating System for the Gas Dynamic Trap 175
E.D. Gospodchikov, A.G. Shalashov, O.B. Smolyakova, P.A. Bagryansky, V.I. Malygin, V.N. Gorbatushkov, V.Kh. Amirov, M. Thumm

Novel Quasi-Optical Approach to Studying the Linear Mode-Conversion in Magnetic Fusion Devices 177
A.A. Balakin, M.N. Buyanova, E.D. Gospodchikov, A.G. Shalashov

Curvature Effects on Linear Mode-Conversion of Electron Cyclotron Waves in Tokamak Plasmas 179
T.A. Husainov, E.D. Gospodchikov, A.G. Shalashov

Analysis of LHCD Efficiency on FT-2 Tokamak 181
S.I. Lashkul, A.B. Altukhov, A.D. Gurchenko, V.V. Dyachenko, L.A. Esipov, M.Yu. Kantor, D.V. Kouprienko, M.A. Irzak, A.N. Saveliev, V.V. Rozhdestvensky, S.V. Krikunov, S.V. Shatalin, A.Yu. Stepanov

Nonlinear Evolution of Fast Ion Driven Modes at Marginal Stability in Tokamak Plasmas 183
M. Lisak, J. Zalesny, G. Galant, and V.E. Semonov

Transmission Line for Megawatt Power Gyrotron Test Stand 185
V.I. Malygin, G.G. Denisov, A.V. Chirkov, V.N. Gorbatushkov, E.M. Tai, E.A. Solujanova, V.I. Ilin

Analysis of the Main Transmission Line for the Conceptual Design of an ITER-like LHCD System 187
F. Mirizzi, S. Ceccuzzi

The Effect of the ITER Stray Magnetic Field on the Operation of the EU 2 MW Coaxial-Cavity Gyrotron 189
I.Gr. Pagonakis, F. Li, S. Alberti, S. Illy, B. Piosczyk, J.-P. Hogge, S. Kern, A. Ferran, M. Henderson, C. Darbos

Laboratory Reproduction of Auroral Cyclotron Emission Processes 191
D.C. Speirs, S.L. McConville, K.M. Gillespie, A.D.R. Phelps, R. Bingham, A.W. Cross, C.W. Robertson, C.G. Whyte, W. He, M. King, I. Vorgul, R.A. Cairns, B.J. Kellett and K. Ronald

EBW Current Drive and Plasma Heating in MAST-Upgrade 193
A.N. Saveliev, V.F. Shevchenko

Low-Pressure Off-resonant Discharge for the Extreme-Ultraviolet Source 194
A.G. Shalashov, S.V. Golubev, E.D. Gospodchikov, A.V. Vodopyanov

On Interpretation of Multi-Scale Pulsed Regimes of Electron Cyclotron Instabilities in a Mirror Confined Plasma Produced by ECR Discharge 196
A.G. Shalashov, S.V. Golubev, E.D. Gospodchikov, D.A. Mansfeld, M.E. Viktorov

Suppression of Anomalous Power Reflection from Plasma by the Resonant Microwave Frequency Broadening 198
V.I. Arkhipenko, E.Z. Gusakov, L.V. Simonchik, M.S. Usachonak

«Micropulses» Generation in ECR Breakdown Stimulated by Gyrotron Radiation @ 37,5 GHz 200
V. Skalyga, I. Izotov, S. Razin, A. Sidorov, V. Zorin

Present Status of ITER Equatorial EC Launcher Design and R&D 202
K. Takahashi, K. Kajiwara, Y. Oda, N. Kobayashi, K. Sakamoto, T. Omori and M. Henderson

Generation of Wideband Electromagnetic Radiation under Magnetic Compression of a Mirror-Confined Plasma Produced by ECR Discharge 204
M.E. Viktorov, S.V. Golubev, E.D. Gospodchikov, I.V. Izotov, D.A. Mansfeld, A.G. Shalashov, A.V. Vodopyanov

T: Terahertz sources, diagnostics and nonlinear interactions

Subterahertz Generation by Magnetized Plasma at Two-Stream Instability of High Current 1-MeV REB 209
A.V. Arzhannikov, A.V. Burdakov, P.V. Kalinin, S.A. Kuznetsov, M.A. Makarov, K.I. Mekler, S.V. Polosatkin, V.V. Postupaev, A.F. Rovenskikh, S.L. Sinitsky, V.F. Sklyarov, V.D. Stepanov, Yu.S. Sulyaev, M.K.A. Thumm, L.N. Vyacheslavov

Superconducting Hot Electron Bolometer as THz Mixer, Direct Detector and Single-Photon Counter 211
G. Goltsman

Performance of Sensitive Terahertz Photodetectors Based on $Pb_{1-x}Sn_xTe(In)$ 213
D.E. Dolzhenko, V.I. Chernichkin, L.I. Ryabova, A.V. Nicorici, D.R. Khokhlov

The Use of Quantum and Thermal Fluctuations for Calibration of the Terahertz Wave Spectral Brightness 215
G.Kh. Kitaeva

Field Effect Transistors for Terahertz Detection and Emission 217
Wojciech Knap, Nina Dyakonova, Dominique Coquillat, Frederic Teppe

Imaging with a High-Power Monochromatic Terahertz Source: Techniques and Applications 219
B.A. Knyazev

The Control of THz Generation in a Dual-Color Pulse by Molecular Alignment 221
Wenxue Li, Min Li, Haifeng Pan, Jian Wu, Heping Zeng

High Power THz Activities at SNU 223
G.S. Park, S.H. Min, M.A. Sattorov, O.J. Kwon, R.K. Barik, A. Bera

Direct Terahertz Detection by On-chip InGaAs/GaAs Field-Effect-Transistor Array 225
V.V. Popov, D.M. Ermolaev, K.V. Maremyanin, N.A. Maleev, V.E. Zemlyakov, V.I. Gavrilenko, S.Yu. Shapoval

THz/sub-THz Radiation Detectors. Requirements and Restrictions 227
F. Sizov

Nonlinear Terahertz Wave Photonics 229
A.P. Sukhorukov, D.O. Saparina, A.N. Kalish

Plasma Mechanisms of THz Radiation Generation 231
E.V. Suvorov, R.A. Akhmedzhanov, D.A. Fadeev, I.E. Ilyakov, V.A. Mironov, and B.V. Shishkin

Methods of Microwave Spectrometry in the Development of the THz Frequency Range 233
V.L. Vaks

Reflected Signal Analysis in Standoff TDS Terahertz Probing 235
A.A. Angeluts, M.M. Nazarov, A.P. Shkurinov, P.M. Solyankin

Ultra-Thin Submillimeter Wave Absorbers for Bolometric Applications 237
S.A. Kuznetsov, A.V. Arzhannikov, A.G. Paulish, A.V. Gelfand, P.A. Lazorskiy

Low-Frequency Transition Radiation from a Femtosecond Laser-Induced Air-Breakdown Plasma with Sharp Boundaries 239
A.V. Borodin, M.N. Esaulkov, A.A. Frolov, I-Chen Ho, A.P. Shkurinov

In-line and Reference-Beam Holography Experiments at Novosibirsk Free Electron Laser 240
Yu.Yu. Choporova, V.S. Cherkassky, B.A. Knyazev

Role of the Multiphoton Ionization in Generation of Broadband Terahertz Radiation from Optical Breakdown Plasma 242
M.N. Esaulkov, A.V. Borodin, I.I. Kuricyn, I.A. Kotelnikov, A.P. Shkurinov

The Diffraction of One Period Terahertz Electromagnetic Waves 244
A.A. Ezerskaya, D.V. Ivanov, S.A. Kozlov

Emission of Terahertz Waves in the Interaction of a Short Laser Pulse with an Underdense Plasma Slab 245
A.A. Frolov

Experiments on Generation of Surface Plasmons using Terahertz Radiation of a Free-Electron Laser 247
V.V. Gerasimov, B.A. Knyazev, A.K. Nikitin, G.N. Zhizhin

Terahertz Pulse Reflective Tomography System 249
V.G. Bespalov, A.A. Gorodetsky, Y.V. Grachev, E.V. Novoselov, O.A. Smolyanskaya, S.A. Kozlov

THz Radiation Causes Abnormal Mitoses in A_L Cells 251
Henning Hintzsche, Christian Jastrow, Thomas Kleine-Ostmann, Thorsten Schrader, Ernst Schmid and Helga Stopper

Terahertz Discharge in Argon at High and Medium Pressures 252
V.A. Koldanov, V.L. Bratman, S.V. Golubev, Yu.K. Kalynov, A.G. Litvak, S.V. Razin, A.V. Sidorov, V.A. Skalyga, V.G. Zorin

THz Emission from the Near-Surface Ionization of Large-Area DC-Biased Dielectric 254
V.A. Kostin, N.V. Vvedenskii

Broadband THz Emission from a Plasma Formed by the Ionizing Bessel Beam 256
V.A. Kostin, N.V. Vvedenskii

Ultra-Fast Phenomena on Powerful Terahertz NovoFEL 258
V.V. Kubarev, G.N. Kulipanov, E.N. Chesnokov, O.A. Shevchenko

Terahertz Generation in Laser Cluster Interaction 260
Manoj Kumar, V.K. Tripathi

THz Absorption in the Nanodispersed Oxide Materials 262
V.I. Mukhin, A.N. Khodan, M.M. Nazarov

Subwavelength Structures in Metal Film for THz Surface Plasmon Control 263
M.M. Nazarov, A.Y. Ryabov, I.Yu. Denisyuk

Optical Susceptibilities of Carriers in the Terahertz-Frequency Range and Generation in Semiconductors with Controlled Nanostructures 265
Yu.V. Malevich, E.V. Moisseenko, M.M. Nazarov, A.V. Shepelev, A.P. Shkurinov, V.A. Skuratov

Low-Frequency Molecular Motions: Gaseous and Solid State Approaches 267
I.N. Smirnova, A. Cuisset, A.V. Kargovsky, M.M. Nazarov, D.A. Sapozhnikov, O.P. Cherkassova, R. Bocquet and A.P. Shkurinov

Analysis of Spectral Features of Cyclopentaphenanthrene Derivatives in THz Frequency Range 269
O.P. Cherkasova, A.V. Kargovsky, M.M. Nazarov, D.A. Sapozhnikov, I.N. Smirnova, A.P. Shkurinov, E.V. Fedulova

Terahertz Scanning Near-field Microscopy for Diagnostics of Semiconductor Microstructures 271
V.N. Trukhin, A.O. Golubok, A.V. Lyuteckii, B.A. Matveev, N.A. Pihtin, L.L. Samoilov, I. D. Sapozhnikov, I.S. Tarasov, M.L. Felshtyn, D.P. Hor'kov

A Thermoacoustic Sensor for Detecting High-Power Microwave and THz Pulses 272
V.A. Vdovin

A: High power microwave applications (including accelerators, radars, gas discharges, materials processing, biomedical applications etc.)

Quasi-Optimal Filtering of a Non-Coherent Sequence of Echo Signals in a Nanosecond Radar 277
A.B. Blyakhman, I.N. Zamyatina, V.I. Irkhin

Progress on Euclid & ANL/AWA Collaboration on Dielectric Wakefield Accelerator Development 279
A.D. Kanareykin

An ECR Ion Source with a High Power – High Frequency Gyrotron, the 60 GHz «SEISM» Project 281
T. Lamy, F. Debray, I.V. Izotov, M. Marie-Jeanne, A.V. Sidorov, V.A. Skalyga, P. Sortais, T. Thuillier, C. Trophime, E. Verney, N. Vidal, V.G. Zorin

Homoepitaxial Single Crystal Diamond Growth at Different Synthesis Parameters 283
A.B. Muchnikov, A.L. Vikharev, A.M. Gorbachev, D.B. Radishev

Some Problems in the Theory of High-Gradient Accelerating Structures 285
G.S. Nusinovich, T.M. Antonsen, Jr., O.V. Sinitsyn and K.L. Jensen

Growth of Isotope ^{12}C-enriched Polycrystalline and Single Crystal Diamond Films by Microwave Plasma Assisted CVD 287
V.G. Ralchenko, A.P. Bolshakov, A.V. Inyushkin, A.N. Taldenkov, E.E. Askinazi, I.I. Vlasov, A.V. Polsky, A.F. Popovich, A.V. Khomich, V.I. Konov, V.A. Panchenko

Plasma Enhanced Chemical Vapor Deposition of High-Enriched Silicon and Germanium Isotopes 289
P.G. Sennikov, N.V. Abrosimov, S.V. Golubev, A.V. Vodopyanov, D.A. Mansfeld, O.N. Godisov, D.A. Pryakhin, V.I. Shashkin, M.N. Drozdov, H.-J. Pohl

Dielectric Structures for Two-Beam Accelerators, with Parameters Ranging from GHz to THz 291
S.V. Shchelkunov, J.L. Hirshfield, M.A. LaPointe, T.C. Marshall, G. Sotnikov, Wei Gai, M. Conde, J. Power, D. Mihalcea

High Gradient Accelerator Structures R&D at SLAC 293
J.W. Wang for the SLAC Team and Collaborators

Microwave Sintering of Functional Layers in Design of Planar Solid Oxide Fuel Cells 295
V.A. Sadykov, V.V. Usoltsev, N.F. Eremeev, A.N. Salanov, N.V. Mezentseva, T.S. Kharlamova, S.N. Pavlova, O.F. Bobrenok, A.S. Ulihin, N.F. Uvarov, O.L. Smorygo, A.V. Arzhannikov, P.V. Kalinin, M.K.A. Thumm

Study of the Processes of Ion Boron Doping and High-Temperature Annealing of Epitaxial CVD Diamond Films Grown by Microwave Plasma-Assisted Chemical Vapor Deposition 297
M.P. Dukhnovsky, A.K. Ratnikova, Yu.Yu. Fedorov, A.L. Vikharev, A.M. Gorbachev, A.B. Muchnikov

The Superconducting ECR Ion Source DECRIS-SC2 299
A. Efremov, V. Bekhterev, S. Bogomolov, V. Drobin, A. Lebedev, V. Loginov, V. Seleznev, Yu. Shishov, N. Yazvitsky

Nd:Y_2O_3 Laser Ceramics Fabricated by Millimeter-Wave Sintering 301
S.V. Egorov, Yu.V. Bykov, A.G. Eremeev, V.V. Kholoptsev, O.N. Eremeykin, A.S. Egorov, A.P. Savikin, V.V. Sharkov

Comparative Study of Neck Formation in Amporphous Silica at Microwave and Conventional Heating 303
S.V. Egorov, A.G. Eremeev, A.A. Sorokin, Yu.V. Bykov

Characteristic Features of Epitaxial Growth of CVD Diamond Films by Microwave Plasma-Assisted Chemical Vapor Deposition on Various Substrates 305
A.L. Vikharev, A.M. Gorbachev, M.P. Dukhnovsky, A.B. Muchnikov, A.K.Ratnikova, Yu.Yu. Fedorov

Requirements and Design Description for the Linear IFMIF Prototype Accelerator 307
R. Heidinger, Ph. Cara, A. Facco, F. Fantini, A. Ibarra, V. Massaut, A. Mosnier, T. Nishitani, Ch. Vermare, P. Garin

Theoretical and Experimental Study of Microwave Power Absorption by a Multipactor Discharge on a Dielectric 309
V.A. Ivanov, A.S. Sakharov, M.E. Konyzhev, Yu.A. Tarbeeva

Gas Utilization Efficiency Optimization for Short-Pulsed ECR Ion Source 311
I.V. Izotov, V.A. Skalyga, V.G. Zorin

JINR-IAP Experiment on RF Pulse Heating: Results and Data Analysis 313
A.K. Kaminsky, N.S. Ginzburg, I.I. Golubev, A.P. Kozlov, A.F. Kratko, S.V. Kuzikov, E.A. Perelstein, N.Yu. Peskov, M.I. Petelin, S.N. Sedykh, A.A. Vikharev, N.I. Zaitsev

Influence of Small Additions of Noble Gases on Strongly Nonuniform Nonequilibrium Microwave Discharge in Nitrogen 315
Yu.A. Lebedev, T.B. Mavlyudov, I.L. Epstein, A.V. Tatarinov

Investigation of Millimeter-Wave Metal Powder Sintering by Application of Dilatometry and In-Situ Resistivity Measurements 317
G. Link, M.M. Mahmoud, M. Thumm

Microwave Recycling of PET Waste and its Technical Realization 319
G.A. Morozov, O.G. Morozov, R.R. Samigullin, A.R. Nasibullin

High Power Shot Pulse BWOs on High-Current Relativistic Electron Beams for Applications 321
M.B. Goykhman, A.V. Gromov, V.A. Kashin, V.V. Kladuhin, N.F. Kovalev, A.V. Palitsin

The Electromagnetic Microwaves Scattering by Inhomogeneities in CVD-Diamond 322
O.S. Mocheneva and V.V. Parshin

Versions of Grating-Based High-Power-Microwave Combiners, Scanners and Duplexers 324
M. Petelin

Low-Pressure Discharge Induced by Microwave Radiation with Jumping Phase 325
I.F. Potapenko, A.F. Alisov, A.M. Artamoshkin, V.I. Golota, A.M. Egorov, I.V. Karas', V.I. Karas', A.N. Starostin, A.G. Zagorodny, I.A. Zagrebelny, V.I. Zasenko

Study of the Multipactor Avalanche in Two-Wire Transmission Line 327
V.E. Semenov, E. Rakova, J. Rasch, D. Anderson, J. Johansson, J. Puech, and M. Lisak

On the Thermal Balance of a Small Spherical Microwave Breakdown Region in Atmospheric Air 329
J. Rasch, V.E. Semenov, D. Anderson, M. Lisak, and J. Puech

Multipactor Breakdown Prediction on a Dielectric: Effects of RF Magnetic Field and Finite Geometry 331
A.G. Sazontov, V.E. Nechaev, N.K. Vdovicheva

Space-Charge and RF Magnetic Field Effects on Multipactor Development on a Dielectric 333
V.E. Nechaev and A.G. Sazontov

CVD Diamond Torus Windows for ITER ECRH – Prototype Design and Experimental Investigations 335
S. Schreck, T.A. Scherer, D. Strauss, A. Meier, K. Sakomoto, K. Takahashi, K. Kajiwara, Y. Oda, G. Saibene

Action of the High-Power Pulsed RF Radiation on the Micro- and Nano-objects in Dielectric Media 337
S.N. Sedykh, V.G. Baev, Yu.A. Fedotova, I.I. Golubev, S.M. Golubykh, A.K. Kaminsky, Yu.A. Kovalev, A.P. Kozlov, I.A. Kryachko, A.I. Lesnikovich, I.A. Milevich, E.A. Perelstein, S.I. Tyutunnikov, V.A. Vdovin

Experimental Study and Numerical Simulations of the Multipactor Discharge in Hollow and Coaxial Waveguides 339
I.A. Kossyi, G.S. Luk'yanchikov, V.E. Semenov, E.I. Rakova, N.A. Zharova, D. Anderson, M. Lisak, J. Puech

Surface Microwave Discharge in Air 341
V.M. Shibkov, N.V. Shibkova

Stabilization of Combustion of Liquid Alcohol, Injected into High-Speed Air Stream, Under Condition of Programmable Microwave Discharge 343
A.A. Karachev, P.V. Kopyl, V.M. Shibkov, L.V. Shibkova, O.S. Surkont

Electromagnetic Band Gap Devices Controlled by Glow Discharges 345
V.I. Arkhipenko, Th. Callegari, J. Lo, L.V. Simonchik, J. Sokoloff, M.S. Usachonak

Enhancing Transformer Ratio of a THz Two-Channel Coaxial Dielectric Structure Using Ramped Bunches 347
G.V. Sotnikov, T.C. Marshall, J.L. Hirshfield

Electromagnetic PiC Code KARAT in Simulations of EM-propagation in Bio Tissues, Laser-Plasma Interaction, etc. 349
V.P. Tarakanov

Multi-Mode Accelerating Structures 351
S.V. Kuzikov, J.L. Hirshfield, Y. Jiang, M.E. Plotkin, A.A. Vikharev, V. Vogel

Index of authors 353

The Proceedings of the Conference were printed on the Risograph of the Institute of Applied Physics RAS,
46 Ulyanov Street, Nizhny Novgorod, Russia